

# 食品暨化妝品安全研究中心

2020年09月01日~2021年08月31日

## 論文集(下)



長庚科技大學  
CHANG GUNG UNIVERSITY OF SCIENCE AND TECHNOLOGY



CHANG GUNG UNIVERSITY OF SCIENCE AND TECHNOLOGY

長庚科技大學  
食品暨化妝品安全研究中心

2020 年 09 月 01 日~2021 年 08 月 31 日

論文集

目 錄

(下冊)

序號	期刊論文	學校主要 負責教師	頁 碼
72	Chang, L. C., Chung, C. Y., Chiu, C. H., Lin, M. H. C., & Yang, J. T. (2021). The effect of polybutylcyanoacrylate nanoparticles as a protos delivery vehicle on dental bone formation. <i>International Journal of Molecular Sciences</i> , 22(9): 4873. doi: 10.3390/ijms22094873	邱群惠	958
73	Liu, J. C., Chen, Y. T., Hsieh, Y. J., Wu, C. C., Huang, M. C., Hsu, Y. C., Wu, C. T., Chen, C. K., Dash, S., & Yu, J. S. (2021). Association of urinary ketamine and APOA1 levels with bladder dysfunction in ketamine abusers revealed via proteomics and targeted metabolite analyses. <i>Scientific Reports</i> , 11(1): 9583. doi: 10.1038/s41598-021-89089-4	余兆松	974
74	Korinek, M., Hsieh, P. S., Chen, Y. L., Hsieh, P. W., Chang, S. H., Wu, Y. H., & Hwang, T. L. (2021). Randialic acid B and tomentosolic acid block formyl peptide receptor 1 in human neutrophils and attenuate psoriasis-like inflammation <i>in vivo</i> . <i>Biochemical Pharmacology</i> , 190: 114596. doi: 10.1016/j.bcp.2021.114596	黃聰龍	988



- |    |   |            |      |
|----|---|------------|------|
| 75 | Kuo, H. C., Kwong, H. K., Chen, H. Y., Hsu, H. Y., Yu, S. H., Hsieh, C. W., Lin, H. W., Chu, Y. L., & Cheng, K. C. (2021). Enhanced antioxidant activity of <i>Chenopodium formosanum</i> Koidz. by lactic acid bacteria: Optimization of fermentation conditions. <i>PLoS One</i> , 16(5): 1-14. doi: 10.1371/journal.pone.0249250   | 郭星君        | 1008 |
| 76 | Yeh, Y. C., Chen, C. C., Cheng, C. Y., Chang, H. N., & Huang, T. H. (2021). The beneficial effects of moxibustion on overweight adolescent girls. <i>Evidence-based Complementary and Alternative Medicine</i> , 2021: 1943181. doi: 10.1155/2021/1943181   | 鄭靜宜        | 1022 |
| 77 | Chuang, S. Y., Chen, C. Y., Yang, S. C., Alalaiwe, A., Lin, C. H., & Fang, J. Y. (2021). 2, 4-Dimethoxy-6-Methylbenzene-1, 3-diol, a benzenoid from <i>Antrodia cinnamomea</i> , mitigates psoriasiform inflammation by suppressing MAPK/NF- $\kappa$ B phosphorylation and GDAP1L1/Drp1 translocation. <i>Frontiers in Immunology</i> , 12: 664425. doi: 10.3389/fimmu.2021.664425 | 陳琦媛<br>方嘉佑 | 1031 |
| 78 | Wu, S. J., Liou, C. J., Chen, Y. L., Cheng, S. C., & Huang, W. C. (2021). Fucoxanthin ameliorates oxidative stress and airway inflammation in tracheal epithelial cells and asthmatic mice. <i>Cells</i> , 10(6): 1311. doi: 10.3390/cells10061311  | 黃文忠        | 1047 |

- 79 Ayoub, I. M., Korinek, M., El-Shazly, M., Wetterauer, B., El-Beshbishy, H. A., Hwang, T. L., Chen, B. H., Chang, F. R., Wink, M., Singab, A. N. B., & Youssef, F. S. (2021). Anti-allergic, anti-inflammatory and anti-hyperglycemic activity of *Chasmanthe aethiopica* leaf extract and its profiling using LC/MS and GLC/MS. *Plants*, 10(6): 1118. doi: 10.3390/plants10061118 黃聰龍 1065
- 80 Chen, Y. J., Lai, M. H., & Liu, J. F. (2021). Studies of antioxidants and antioxidative activity of fresh juice in Taiwan. *Chang Gung Journal of Science*, 2021(34): 53-60. doi: 10.6192/CGUST.202106\_(34).5 陳頤之 劉珍芳 1085
- 81 Tsai, S. H., Chien, C. C., Lee, S. C., Fan, C. H., Cheng, C. S., Chang, P. C., & Lee, M. Y. (2021). The development of alternative meat industry driven by the trend of net zero carbon emissions, research progress and future challenges. *Chang Gung Journal of Science*, 2021(34): 1-15. doi: 10.6192/CGUST.202106\_(34).1 李明怡 1093
- 82 Uras, I. S., Ebada, S. S., Korinek, M., Albohy, A., Abdulrazik, B. S., Wang, Y. H., Chen, B. H., Horng, J. T., Lin, W., Hwang, T. L., & Konuklugil, B. (2021). Anti-inflammatory, antiallergic, and COVID-19 main protease (Mpro) inhibitory activities of butenolides from a marine-derived fungus *Aspergillus terreus*. *Molecules*, 26(11): 3354. doi: 10.3390/molecules26113354 黃聰龍 1108

- 83 Wu, C. C., Lu, Y. T., Yeh, T. S., Chan, Y. H., Dash, S., & Yu, J. S. (2021). Identification of fucosylated SERPINA1 as a novel plasma marker for pancreatic cancer using lectin affinity capture coupled with iTRAQ-Based quantitative glycoproteomics. *International Journal of Molecular Sciences*, 22(11): 6079. doi: 10.3390/ijms22116079 余兆松 1122
  
- 84 Malla, P., Liao, H. P., Liu, C. H., & Wu, W. C. (2021). Electrochemical immunoassay for serum parathyroid hormone using screen-printed carbon electrode and magnetic beads. *Journal of Electroanalytical Chemistry*, 895: 115463. doi: 10.1016/j.jelechem.2021.115463 劉繼賢 1144
  
- 85 Dash, B. S., Das, S., & Chen, J. P. (2021). Photosensitizer-functionalized nanocomposites for light-activated cancer theranostics. *International Journal of Molecular Sciences*, 22(13): 6658. doi: 10.3390/ijms22136658 陳志平 1154
  
- 86 Peng, K. T., Chen, J. L., Kuo, L. T., Yu, P. A., Hsu, W. H., Lee, C. W., Chang, P. J., & Huang, T. Y. (2021). GMI, an immunomodulatory peptide from *Ganoderma microsporum*, restrains periprosthetic joint infections via modulating the functions of myeloid-derived suppressor cells and effector T cells. *International Journal of Molecular Sciences*, 22(13): 6854. doi: 10.3390/ijms22136854 李江文 1176

- 87 Hsu, S. H., Cheng, A. C., Chang, T. Y., Pao, L. H., Hsiong, C. H., & Wang, H. J. (2021). Precisely adjusting the hepatic clearance of highly extracted drugs using the modified well-stirred model. *Biomedicine and Pharmacotherapy*, 141: 111855. doi: 10.1016/j.biopha.2021.111855 鮑力恒 1190
  
- 88 Chen, Y. C., Sung, H. C., Chuang, T. Y., Lai, T. C., Lee, T. L., Lee, C. W., Lee, I. T., & Chen, Y. L. (2021). Vitamin D3 decreases TNF- $\alpha$ -induced inflammation in lung epithelial cells through a reduction in mitochondrial fission and mitophagy. *Cell Biology and Toxicology*. doi: 10.1007/s10565-021-09629-6 李江文 1198
  
- 89 Dash, B. S., Lu, Y. J., Chen, H. A., Chuang, C. C., & Chen, J. P. (2021). Magnetic and GRPR-targeted reduced graphene oxide/doxorubicin nanocomposite for dual-targeted chemo-photothermal cancer therapy. *Materials Science and Engineering C*, 128: 112311. doi: 10.1016/j.msec.2021.112311 陳志平 1222
  
- 90 Alalaiwe, A., Fang, J. Y., Lee, H. J., Chiu, C. H., & Hsu, C. Y. (2021). The demethoxy derivatives of curcumin exhibit greater differentiation suppression in 3T3-L1 adipocytes than curcumin: A mechanistic study of adipogenesis and molecular docking. *Biomolecules*, 11(7): 1025. doi: 10.3390/biom11071025 方嘉佑 邱群惠 許青雲 1238

- 91 Poorna, M., Jayakumar, R., Chen, J. P., & Mony, U. (2021). Hydrogels: A potential platform for induced pluripotent stem cell culture and differentiation. *Colloids and Surfaces B: Biointerfaces*, 207: 111991. doi: 10.1016/j.colsurfb.2021.111991 陳志平 1256
  
- 92 Lu, Y. J., Anilkumar, T. S., Chuang, C. C., & Chen, J. P. (2021). Liposomal IR-780 as a highly stable nanotheranostic agent for improved photothermal/photodynamic therapy of brain tumors by convection-enhanced delivery. *Cancers*, 13(15): 3690. doi: 10.3390/cancers13153690 陳志平 1269
  
- 93 Liao, P. J., Ting, M. K., Wu, I. W., Chen, S. W., Yang, N. I., & Hsu, K. H. (2021). Higher leptin-to-adiponectin ratio strengthens the association between body measurements and occurrence of type 2 diabetes mellitus. *Frontiers in Public Health*, 9: 678681. doi: 10.3389/fpubh.2021.678681 許光宏 1294
  
- 94 Liu, Y. C., Mok, B. W. Y., Wang, P., Kuo, R. L., Chen, H., & Shih, S. R. (2021). Cellular 5'-3' mRNA exoribonuclease XRN1 inhibits interferon beta activation and facilitates influenza A virus replication. *MBio*, 12(4): 1-18. doi: 10.1128/mBio.00945-21 施信如 1303

- 95 Wu, I. W., Liao, P. J., Ting, M. K., Chen, S. W., Yang, N. I., & Hsu, K. H. (2021). Combination of thigh circumference and indices of central obesity helps predict incident chronic kidney disease: A 14-Year prospective cohort study using a three-dimensional body laser scanner. *Journal of Renal Nutrition*, 2021: 1-9. doi: 10.1053/j.jrn.2021.06.009 許光宏 1321
  
- 96 Chen, M. H., Tsai, S. J., Su, T. P., Li, C. T., Lin, W. C., Chen, T. J., Pan, T. L., & Bai, Y. M. (2021). Increased risk of stroke in patients with obsessive-compulsive disorder: A nationwide longitudinal study. *Stroke*, 52: 2601-2608. doi: 10.1161/STROKEAHA.120.032995 潘台龍 1330
  
- 97 Anwar, D. M., El-Sayed, M., Reda, A., Fang, J. Y., Khattab, S. N., & Elzoghby, A. O. (2021). Recent advances in herbal combination nanomedicine for cancer: Delivery technology and therapeutic outcomes. *Expert Opinion on Drug Delivery*, 18(11): 1-17. doi: 10.1080/17425247.2021.1955853 方嘉佑 1338
  
- 98 Chang, M. L., Hu, J. H., Pao, L. H., Lin, M. S., Kuo, C. J., Chen, S. C., Fan, C. M., Chang, M. Y., & Chien, R. N. (2021). Critical role of triglycerides for adiponectin levels in hepatitis C: A joint study of human and HCV core transgenic mice. *BMC Immunology*, 22(1): 1-12. doi: 10.1186/s12865-021-00445-5 鮑力恒 1355



- 99 Lin, Y. J., Wei, K. C., Chen, P. Y., Lim, M., & Hwang, T. L. (2021). Roles of neutrophils in glioma and brain metastases. *Frontiers in Immunology*, 12: 701383. doi: 10.3389/fimmu.2021.701383 黃聰龍 1367
- 100 Chen, C. H., Cheng, Y. H., Chen, S. H., Chuang, A. D. C., & Chen, J. P. (2021). Functional hyaluronic acid-poly(lactic acid)/silver nanoparticles core-sheath nanofiber membranes for prevention of post-operative tendon adhesion. *International Journal of Molecular Sciences*, 22(16): 8781. doi: 10.3390/ijms22168781 陳志平 1386
- 101 Cheng, K. C., Kuo, H. C., Hsieh, M. C., Huang, C. Y., Teng, C. C., Tung, S. Y., Shen, C. H., Lee, K. F., Yang, Y. L., & Lee, K. C. (2021). Identification of two novel CIL-102 upregulations of ERP29 and FUMH to inhibit the migration and invasiveness of colorectal cancer cells by using the proteomic approach. *Biomolecules*, 11(9): 1280. doi: 10.3390/biom11091280 郭星君 1406
- 102 Tseng, T. H., Lee, H. J., Lee, Y. J., Lee, K. C., Shen, C. H., & Kuo, H. C. (2021). Ailanthoidol, a neolignan, suppresses TGF- $\beta$ 1-induced HepG2 hepatoblastoma cell progression. *Biomedicines*, 9(9): 1110. doi: 10.3390/biomedicines9091110 郭星君 1421



Article

# The Effect of Polybutylcyanoacrylate Nanoparticles as a Protos Delivery Vehicle on Dental Bone Formation

Li-Ching Chang<sup>1,2</sup>, Chiu-Yen Chung<sup>3</sup>, Chun-Hui Chiu<sup>4,5</sup> , Martin Hsiu-Chu Lin<sup>3,\*,†</sup> and Jen-Tsung Yang<sup>3,6,\*,†</sup>

<sup>1</sup> Department of Dentistry, Chang Gung Memorial Hospital, Chiayi 61363, Taiwan; liching@ms39.hinet.net

<sup>2</sup> Department of Nursing, Chang Gung University of Science and Technology, Chiayi 61363, Taiwan

<sup>3</sup> Department of Neurosurgery, Chang Gung Memorial Hospital, Chiayi Branch, 6, Sec. West, Chai-Pu Road, Pu-Tz City, Chia-Yi 61363, Taiwan; yen5103106@gmail.com

<sup>4</sup> Graduate Institute of Health-Industry Technology, Research Center for Food and Cosmetic Safety, College of Human Ecology, Chang Gung University of Science and Technology, Tao-Yuan 33303, Taiwan; chchiu@mail.cgust.edu.tw

<sup>5</sup> Department of Traditional Chinese Medicine, Keelung Chang Gung Memorial Hospital, Keelung 20401, Taiwan

<sup>6</sup> College of Medicine, Chang Gung University, Tao-Yuan 33302, Taiwan

\* Correspondence: martinhclin@hotmail.com (M.H.-C.L.); jents716@ms32.hinet.net (J.-T.Y.);

Tel.: +886-5-3621000 (ext. 2864) (M.H.-C.L.); +886-5-3621000 (ext. 2009) (J.-T.Y.);

Fax: +886-5-3621000 (ext. 3002) (M.H.-C.L. & J.-T.Y.)

† These authors contributed equally to this work.



**Citation:** Chang, L.-C.; Chung, C.-Y.; Chiu, C.-H.; Lin, M.H.-C.; Yang, J.-T. The Effect of Polybutylcyanoacrylate Nanoparticles as a Protos Delivery Vehicle on Dental Bone Formation. *Int. J. Mol. Sci.* **2021**, *22*, 4873. <https://doi.org/10.3390/ijms22094873>

Academic Editor: Pavel Rossner

Received: 15 March 2021

Accepted: 1 May 2021

Published: 5 May 2021

**Publisher's Note:** MDPI stays neutral with regard to jurisdictional claims in published maps and institutional affiliations.



**Copyright:** © 2021 by the authors. Licensee MDPI, Basel, Switzerland. This article is an open access article distributed under the terms and conditions of the Creative Commons Attribution (CC BY) license (<https://creativecommons.org/licenses/by/4.0/>).

**Abstract:** Background: Dental implants are commonly used for missing teeth, for which success depends heavily on the quality of the alveolar bone. The creation of an ideal implant site is a key component in shortening the treatment time, which remains clinically challenging. Strontium ranelate (Protos) is an anti-osteoporotic agent which has previously been used to promote bone formation, however the systemic use of Protos has been linked to serious cardiovascular and venous thromboembolic events, thus local delivery strategies may be better suited for this purpose. In this study, a biodegradable, and biocompatible nanocarrier “polybutylcyanoacrylate” (PBCA) loaded with strontium was constructed and its ability to promote bone formation was assessed. Methodology: PBCA nanoparticles loaded with strontium (PBCA-Sr NPs) were synthesized using the emulsion polymerization method, and their physical properties (zeta potential, size and shape) and entrapment efficiency were characterized. Committed MSCs (osteoblasts) were derived from the differentiation of cultured rat mesenchymal stem cells (MSC), which were tested with the PBCA-Sr NPs for cytotoxicity, inflammatory response, bone formation and mineralization. Scanning electron microscopy was performed following a 7-day treatment of PBCA-Sr NPs on decellularized procaine mandibular bone blocks grafted with osteoblasts. Results: Spherical PBCA-Sr NPs of  $166.7 \pm 2.3$  nm, zeta potential of  $-1.15 \pm 0.28$  mV with a strontium loading efficiency of  $90.04 \pm 3.27\%$  were constructed. The presence of strontium was confirmed by energy-dispersive X-ray spectroscopy. Rat committed MSCs incubated in PBCA-Sr NPs for 24 hrs showed viabilities in excess of 90% for concentrations of up to 250  $\mu\text{g/mL}$ , the cellular expression of osteocalcin and alkaline phosphatase were 1.4 and 1.3 times higher than the untreated control, and significantly higher than those treated with strontium alone. Bone formation was evident following osteoblast engraftment on the decellularized procaine mandibular bone block with PBCA-Sr NPs, which appeared superior to those treated with strontium alone. Conclusion: Treatment of committed MSCs with PBCA-Sr NPs showed higher expression of markers of bone formation when compared with strontium alone and which corresponded to greater degree of bone formation observed on the 3-dimensional decellularized procaine mandibular bone block. Further quantitative analysis on the extent of new bone formation is warranted.

**Keywords:** strontium; bone formation; polybutylcyanoacrylate; nanotechnology

## 1. Introduction

Dental implant therapy is a common reconstructive technique of replacing missing tooth or teeth. The implant fixture must be placed in alveolar bone with sufficient bone quantity and quality [1–3]. Furthermore, shortening the treatment time by hastening the development of an ideal implant site poses a great challenge in modern implant rehabilitation [4–6]. It can be clinically challenging to improve bone density [7], therefore new methods are required to optimize the implant site bone quality.

The bone mineral structure,  $\text{Ca}_{10}(\text{PO}_4)_6(\text{OH})_2$ , is approximated by the formula:  $(\text{Ca},\text{X})_{10}(\text{PO}_4,\text{HPO}_4,\text{CO}_3)_6(\text{OH},\text{Y})_2$ , where X are cations that can be substituted by cations other than calcium ions [8]. Therefore, it is possible to change the bone density by replacing calcium ions with other cations, including strontium. Strontium ranelate (Protos), which is an oral anti-osteoporotic agent, has been shown to decrease bone resorption and increase bone formation in vitro and in vivo (dual action bone agent) [9,10]. In addition, the substitution of calcium ion by strontium is possible, which could alter the calcium ion concentration in bone to affect bone cell adhesion, proliferation and morphology [11,12]. Thus, the interaction between strontium and calcium on biological properties of resident cells would be taken into consideration for bone formation. In previous studies, systemic use of Protos could promote bone formation in healthy rats and ovariectomized rats [13–15]. However, Protos has been taken off the shelf due to its cardiac-vascular risk [16–19].

The local use of strontium for promoting bone growth usually involves the incorporation of strontium into bone grafts [20–22]. Other strontium delivery methods include strontium associated with collagen sponge [23], strontium-containing collagen membrane and strontium dissolved in gel [24–27]. However, these methods are essentially matrices acting as reservoirs of drugs which are released through biolysis. Apart from the promotion of bone growth, strontium has bactericidal effects on *Staphylococcus aureus* and *Streptococcus faecalis* when used locally [28–30]. The bactericidal effect of strontium could improve outcome of dental implant therapy and implant-associated surgery because infection would interfere with bone formation and implant osteointegration. Additionally, the localized injection of strontium in a rat study revealed neither adverse effects on the general health of the animal, nor at the injection site [31]. However, earlier studies showed that a low oral dose of strontium promotes bone growth, but prevents bone formation at a higher dose [32–34]. The optimum concentration of strontium ranelate on bone cell growth is around 0.1 mM [35]. Therefore, the optimal level of strontium in local delivery is also very important for the desired effect.

Because of the properties in biodegradation, biocompatibility, low toxicity, and stability, nanocarriers are often used as drug delivery vehicles. Polybutylcyanoacrylate (PBCA) is a polymeric colloidal carrier system which is widely used in drug delivery in various settings such as central nervous system drug delivery, antiretroviral drug delivery, cancer therapy and osteointegration [36–42]. In addition, the nanotechnology-based delivery system can potentially overcome the pharmacokinetics to provide a slow but long-term release of drugs and easy uptake by cells [41,43,44]. In this study PBCA nanoparticles containing strontium are constructed as a local delivery strategy that differed from previous methods, we hypothesize that the new material will promote bone formation in vitro.

## 2. Results

### 2.1. Characterization of Nanoparticles

The particle sizes and zeta potential of PBCA NPs and PBCA-Sr NPs were analyzed by Zetasizer Nano ZS90 (Malvern, Worcestershire, UK), and the calculated loading efficiencies of strontium of nanoparticles are shown in Table 1. The mean diameter of PBCA NPs was measured at  $126.1 \pm 0.8$  nm. The encapsulation of strontium ranelate into PBCA NPs increased the mean diameter to  $166.7 \pm 2.3$  nm. The zeta potential measurements of PBCA NPs ( $-1.93 \pm 0.24$  mV) and PBCA-Sr ( $-1.15 \pm 0.28$  mV) essentially remained nearly neutral in charge. The acid emulsion polymerization method of nanoparticle synthesis

produced a mono-dispersed sample with an entrapment efficiency for strontium ranelate of more than 90%.

**Table 1.** The average diameter ( $D_{av}$ ), zeta potential, polydispersity (PDI), and entrapment efficiency of strontium of nanoparticles.

Sample	$D_{av}$ (nm)	Zeta Potential (mV)	PDI	$EE_{Sr}$ (%)
PBCA NPs	$126.1 \pm 0.8$	$-1.93 \pm 0.24$	$0.044 \pm 0.009$	-
PBCA-Sr NPs	$166.7 \pm 2.3$	$-1.15 \pm 0.28$	$0.241 \pm 0.019$	$90.04 \pm 3.27$

$n = 3$ .

The morphology, geometry, and the elemental composition of the NPs were acquired by field emission scanning electron microscopy (FE-SEM, SU8220, Tokyo, Japan), transmission electron microscopy (TEM, H-7500, Hitachi, Tokyo, Japan), and energy-dispersive spectrometry (EDS). The results showed that both PBCA NPs and PBCA-Sr NPs had a uniform spheroid shape (Figure 1A). PBCA NPs were dark with smooth boundaries (Figure 1B); whereas PBCA-Sr NPs displayed rough and irregular boundaries. Meanwhile, PBCA NPs were smaller than PBCA-Sr NPs. The result indicated an increase in weight percentage of strontium corresponded to an increase in the size of PBCA NPs. To confirm the encapsulation of strontium into PBCA NPs, PBCA-Sr NPs were analyzed by EDC, which exhibited the presence high intensity of O, S and Sr elemental peaks, and low intensity of C and N elemental peaks when compared with PBCA NPs. This significant increase in O, S and Sr atomic percentage was taken as evidence for the existence of Sr on outer surface layer (10 nm thickness) of PBCA-Sr NPs (Figure 1C).

## 2.2. Morphology and Differentiation Potential of the Rat MSCs

Primary rat bone marrow stromal cells (MSCs) were cultured from the marrows from femurs and tibiae of 5-week-old Sprague-Dawley (SD) rats (BioLasco, Taipei, Taiwan) to generate osteoblasts. The morphology of rat MSCs at passage-1 appeared as discrete colonies similar to ESC aggregates that exhibited a clear boundary, bright large nucleoli and scant cytoplasm in (Figure 2a). The rat MSCs colonies were detached from the cell cluster by subculture over a number of passages. Rat MSCs were morphologically homogeneous, spindle-shape and fibroblast-like at passage-4 (Figure 2b).

To confirm the multi-lineage differentiation of rat MSCs, we assayed for adipogenesis and osteogenesis in vitro. As shown in Figure 2c, after exposure to an adipogenic stimulus for 7 days, morphologic changes in the cells as well as the formation of neutral lipid droplets in the cytoplasm that stained red with Oil Red O were noted. As shown in Figure 2d, after 7 days of culture in an osteogenic medium, morphologic changes in the cells from spindle-shape to a flattened and broadened shape occurred following the induction period. Osteogenic cells were positive for ALP staining. As shown in Figure 2e, after 3 weeks of induced osteogenic differentiation, MSC developed into committed MSCs (osteoblastic cells), as judged by their ability to mineralize the extracellular matrix which was positive for Alizarin Red S staining.

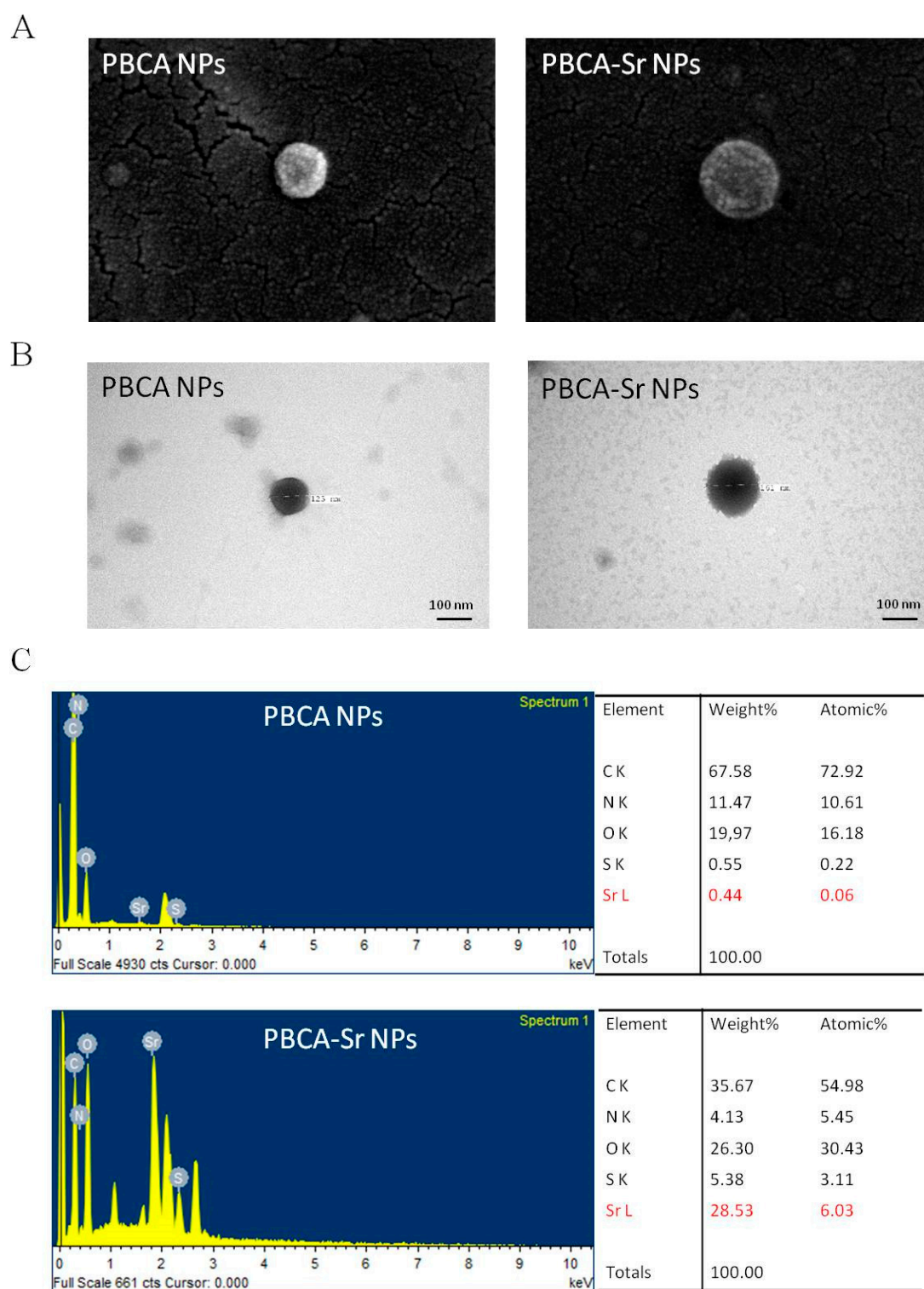


**Figure 1.** Analysis of PBCA-Sr. (A) FE-SEM images of PBCA NPs and PBCA-Sr NPs. Magnification: 200,000 $\times$ . (B) TEM images of PBCA NPs and PBCA-Sr NPs. Magnification: 200,000 $\times$ . (C) EDS analysis for PBCA NPs and PBCA-Sr NPs.



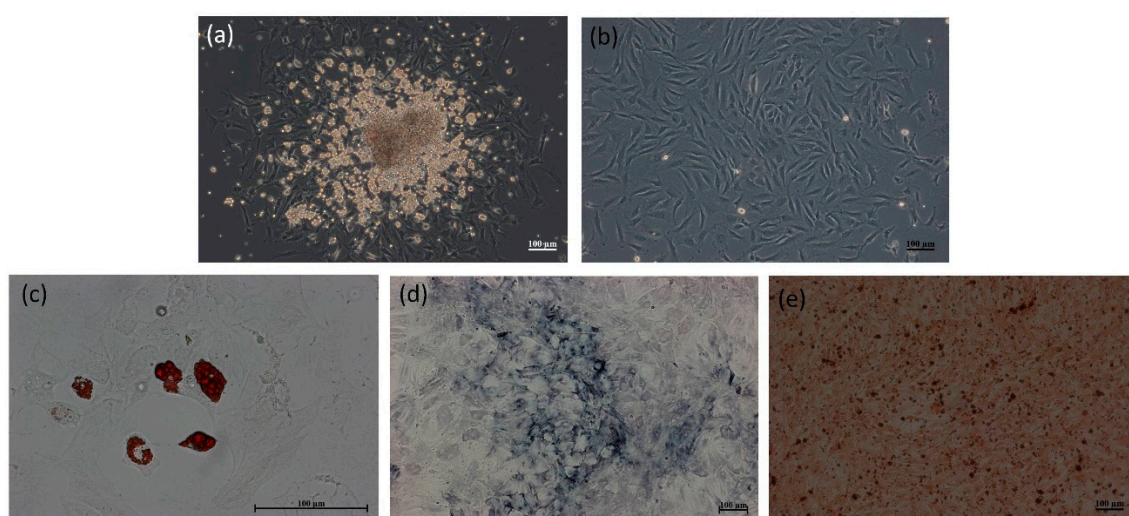


**Figure 2.** The optical images of rat bone marrow stromal cells (MSCs) at passage-1 (a) and passage-4 (b). Differentiation of rat MSCs into adipocytes and osteoblasts. Adipogenic MSC formed phase-bright vacuoles and were stained with oil red O (c). ALP staining (d) and Alizarin Red S staining (e) of osteogenic rat MSCs. Scale bar = 100  $\mu$ m.

### 2.3. Assessment of Cytotoxicity

Cell viability, cell proliferation and cytotoxicity of Sr, PBCA NPs and PBCA-Sr NPs to osteoblasts were estimated by the MTT assay, WST-1 and LDH assays. A concentration-dependent cell viability profile of Sr, PBCA NPs and PBCA-Sr NPs were determined by the MTT assay following 24 h of culture are shown in Figure 3A. The viability of committed MSCs maintained over 90% with Sr concentrations of 0.05 to 10 mM, but Sr concentrations of greater than 10 mM led to significant reductions in viability. PBCA NP concentration in excess of 100  $\mu$ g/mL and PBCA-Sr NPs concentration of more than 250  $\mu$ g/mL were found to be cytotoxic to the osteoblasts. The cell proliferation assay was carried out using the WST-1 assay on committed MSCs cultured with different concentrations of NPs for 24 h. A concentration-dependent cell proliferation profile of Sr, PBCA NPs and PBCA-Sr NPs are shown for Figure 3B. The result showed the viability is more than 90% at Sr concentrations of up to 0.05 mM, PBCA NP concentrations of up to 250  $\mu$ g/mL, and PBCA-Sr NP concentrations of up to 250  $\mu$ g/mL. Toxicity testing was carried out by the LDH assay following 24 h of culture are shown in Figure 3C. The positive control is the amount of LDH released from the lysed committed MSCs which was taken as “100% toxicity”. The negative control is the amount of LDH released from untreated committed MSCs which was denoted as “0% toxicity”. There was no significant difference between any of the concentrations of Sr, PBCA NPs or PBCA-Sr NPs compared with negative control. The result showed no significant toxicity at Sr concentrations of up to 0.05 mM, PBCA NP concentrations of up to 250  $\mu$ g/mL, and PBCA-Sr NP concentrations of up to 250  $\mu$ g/mL. On the other hand, the inflammatory cytokines IL-1 $\alpha$ , IFN- $\gamma$  and TNF were assessed by the CBA kit. Except for TNF, both IL-1 $\alpha$ , IFN- $\gamma$  were not detected when the Sr concentration of 0.2 mM, similar changes were detected on PBCA-Sr NP with a concentration of 100  $\mu$ g/mL.

### 2.4. The effect of Osteogenesis and Mineralization of PBCA-Sr NPs on Committed MSCs

#### 2.4.1. 2D Culture

In order to demonstrate the effect of strontium-loaded nanoparticles on osteogenesis, we examined the expression of osteocalcin and alkaline phosphatase on committed MSCs at day-7 after treatment with PBCA NPs (50  $\mu$ g/mL), Sr (0.1 mM) or PBCA-Sr NPs (50  $\mu$ g/mL containing 0.1 mM Sr) by western blotting analysis. As shown in Figure 4, the protein expression levels of osteocalcin and alkaline phosphatase increased significantly in the cells treated with PBCA-Sr NPs.



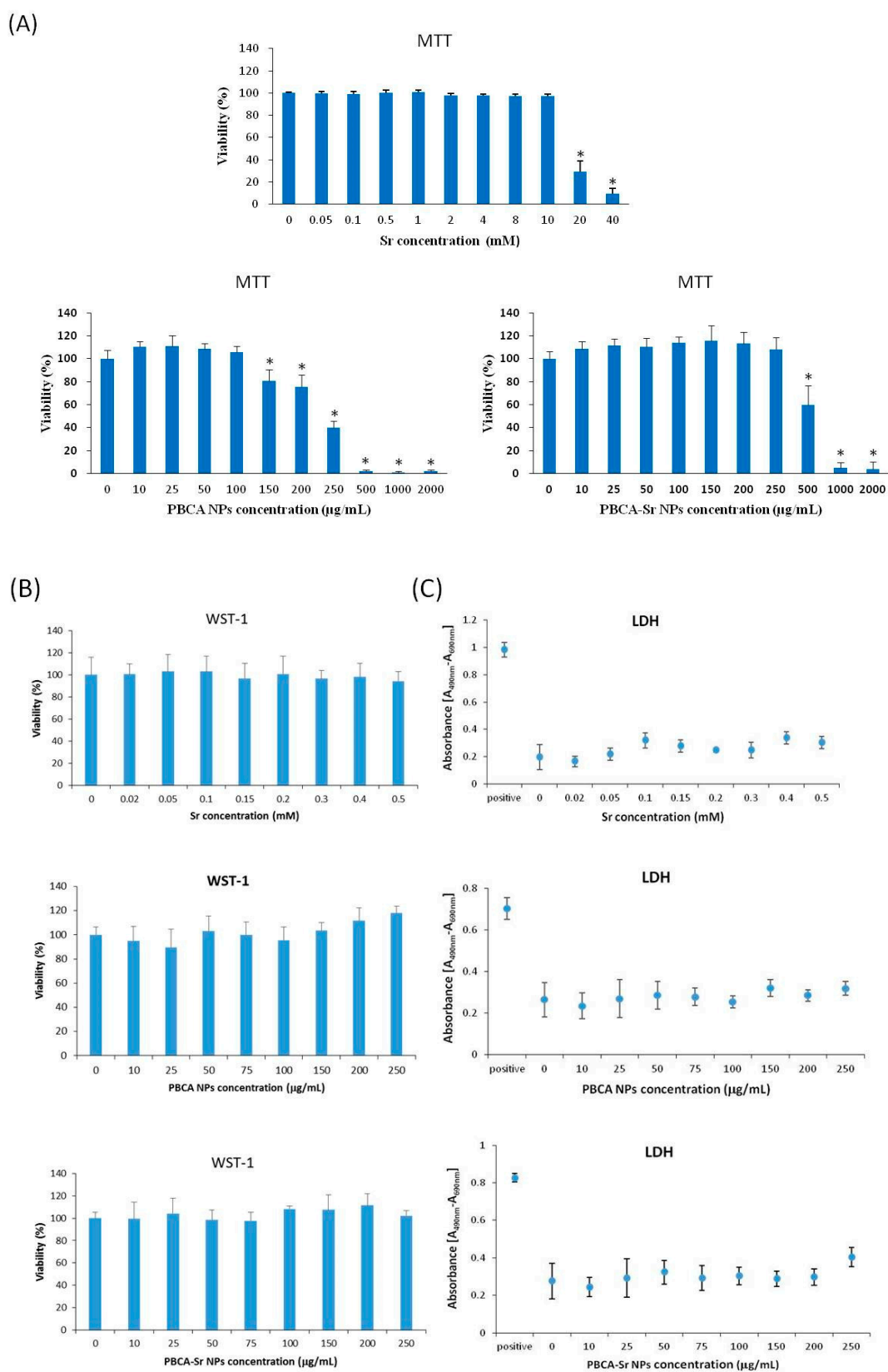
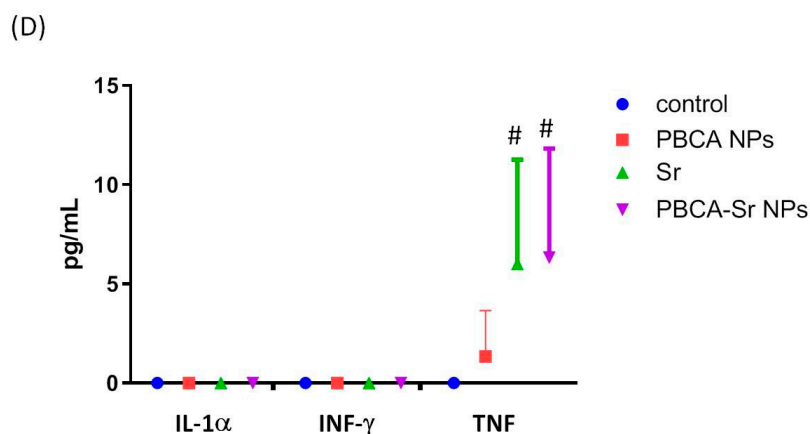
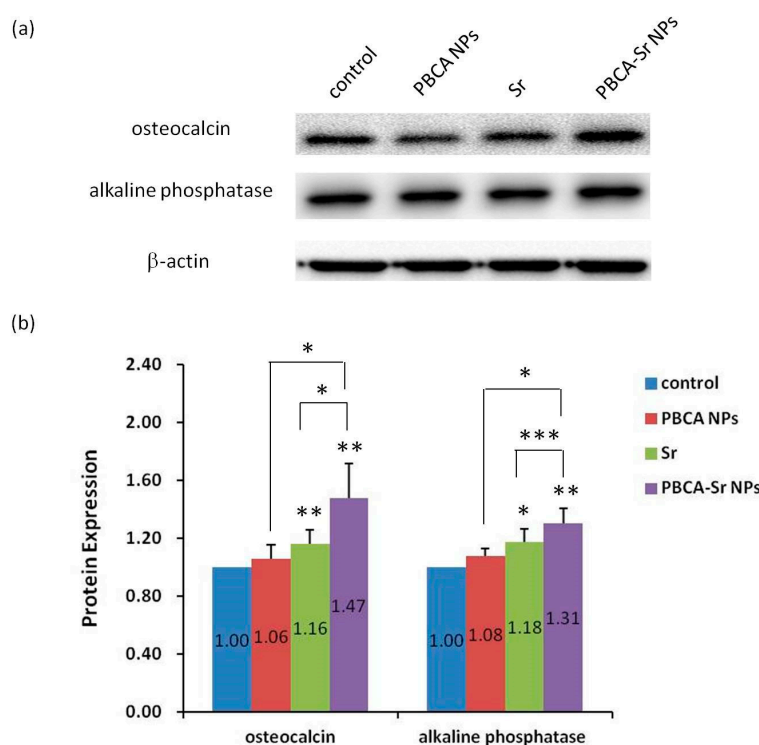


Figure 3. Cont.



**Figure 3.** Cell viability ((A). MTT assay), cell proliferation ((B). WST-1 assay) and cytotoxicity ((C). LDH assay) on committed MSCs treated with strontium ranelate (Sr), and inflammatory cytokines (D), PBCA NPs or PBCA-Sr NPs for 24 h.  $n = 6$ ; \*  $p < 0.001$ , #  $p < 0.05$ .



**Figure 4.** (a) Western blot analysis of osteocalcin and alkaline phosphatase at day-7 after treated with PBCA NPs (50  $\mu\text{g}/\text{mL}$ ), strontium ranelate (0.1 mM) or PBCA-Sr NPs (50  $\mu\text{g}/\text{mL}$  containing 0.1 mM Sr).  $\beta$ -actin was used as a loading control. (b) Quantitative analysis was presented. The expression level of osteocalcin and alkaline phosphatase protein were normalized to control of  $\beta$ -actin. \*  $p < 0.05$ , \*\*  $p < 0.01$  and \*\*\*  $p < 0.001$ .

Moreover, committed MSCs ( $1 \times 10^4$  cells/ $\text{cm}^2$ ) were treated with PBCA NPs (50  $\mu\text{g}/\text{mL}$ ), Sr (0.1 mM) or PBCA-Sr NPs (50  $\mu\text{g}/\text{mL}$  containing 0.1 mM Sr) and incubated for 7 and 21 days. Alkaline phosphatase (ALP) staining and Alizarin Red S (ARS) staining were then performed separately. ALP staining demonstrated that the intensity of ALP activity appeared higher for PBCA-Sr NPs after 7 days (Figure 5a), this was also true for ARS staining (Figure 5b). The quantified staining intensity showed significant increases in ALP and ARS stain intensity for PBCA-Sr-NPs over Sr, PBCA-NPs and control (Figure 5c).

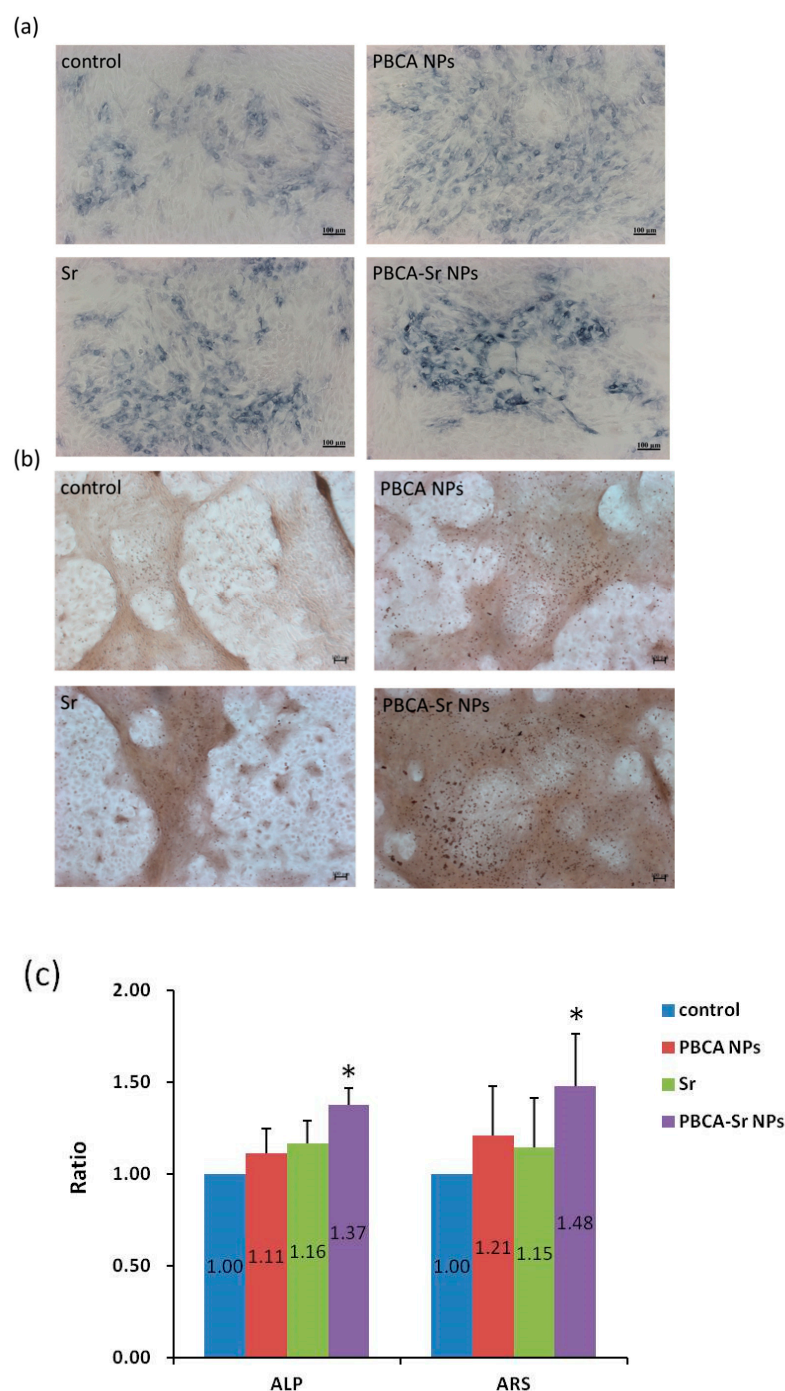


**Figure 5.** Influence of Sr-NPs on committed MSCs. Committed MSCs was treated with strontium ranelate (0.1 mM), PBCA NPs (50  $\mu\text{g}/\text{mL}$ ) or PBCA-Sr NPs (50  $\mu\text{g}/\text{mL}$  containing 0.1 mM Sr). (a) Alkaline phosphatase staining following exposure medium for 7 days. (b) Alizarin Red S staining was performed at 21 days after treatment. Scale bar = 100  $\mu\text{m}$ . (c) Quantification of ALP and ARS as a ratio to control. \*  $p < 0.05$ .

#### 2.4.2. 3D Culture

A 3-D bone model produced by the decellularization of procaine mandible bone block was used to prove that the Sr-NP promote bone formation. Figure 6 shows the SEM images of a decellularized procaine mandible bone block. As indicated in this figure, the pore structure of bone block with different size is clearly evident. The morphology indicated that the typical trabecular structure of cancellous bone is well preserved even after decellularization. The committed MSCs engrafted bone blocks treated with PBCA-Sr

NPs appeared to have better bone matrix deposition as indicated by the roughened surface texture and the coverage of pores less than 30 microns.

In Figure 7, the SEM images shows that the committed MSCs attached on the bone block have similar morphology at day-7 after treated with PBCA NPs (50  $\mu\text{g}/\text{mL}$ ), Sr (0.1 mM) or PBCA-Sr NPs (50  $\mu\text{g}/\text{mL}$  containing 0.1 mM Sr).

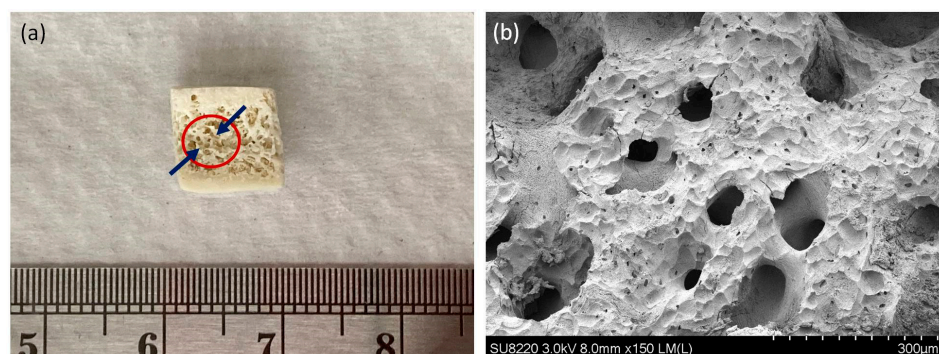


**Figure 6.** The morphology of procaine mandible bone block (a). FE-SEM images of procaine mandible bone block (b). Magnification: 150 $\times$ .

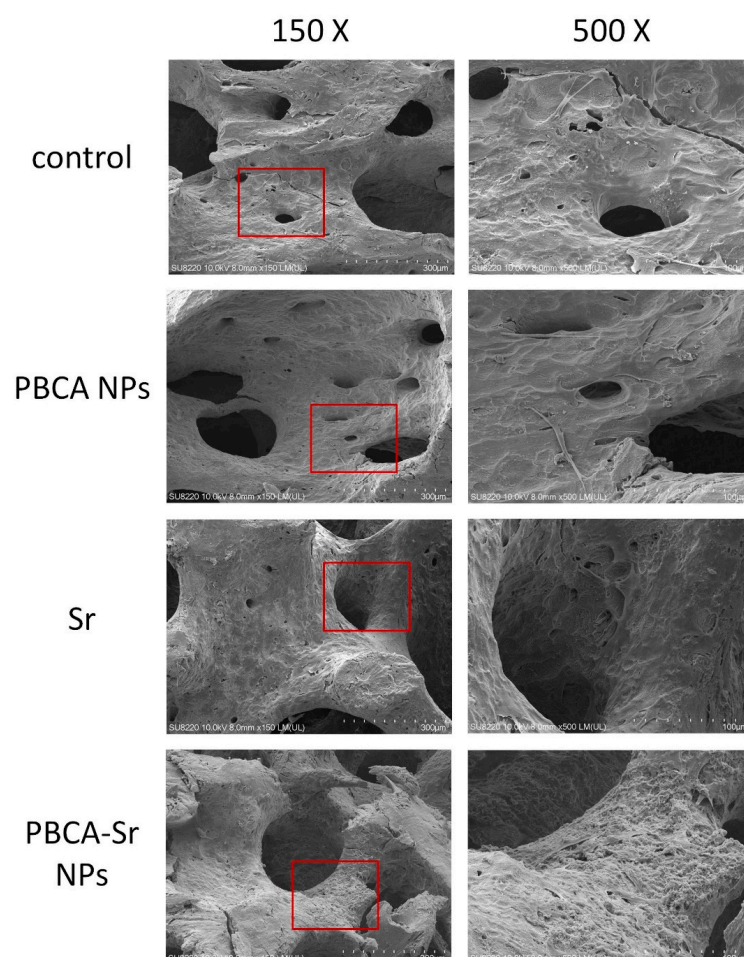


**Figure 7.** FE-SEM images of committed MSCs in procaine mandible bone block. Cells were treated with PBCA NPs (50  $\mu\text{g}/\text{mL}$ ), strontium ranelate (0.1 mM) or PBCA-Sr NPs (50  $\mu\text{g}/\text{mL}$  containing 0.1 mM Sr) for 7 days. Areas highlighted in the red square are displayed under higher magnification on the right side. Magnification: 150 $\times$  and 500 $\times$ .



### 3. Discussion

Strontium (Sr) is a promising trace element that can trigger new bone formation by inducing osteoblasts and preventing osteoclast activity. Strontium ranelate is a kind of strontium-containing anti-osteoporotic drug, which can significantly reduce the probability of fractures in patients with osteoporosis [45]. However, concerns over serious cardiovascular and venous thromboembolic events associated with the systemic administration of Protos has led to the exploration of local delivery strategies [46,47].

In this study, we have successfully synthesized and characterized a novel nanocarrier “polybutylcyanoacrylate nanoparticle” loaded with strontium ranelate as a local drug delivery system by the emulsion polymerization method [48]. The PBCA-Sr NPs were spherical with diameters of  $166.7 \pm 2.3$  nm, zeta potential of  $-1.15 \pm 0.28$  mV, and strontium ranelate loading efficiency of  $90.04 \pm 3.27\%$ . The incorporation of strontium ranelate in the PBCA nanoparticles leads to an increase in particles size, but does not affect the zeta potential.

As a series of in vitro and in vivo studies have shown, strontium ranelate has been demonstrated to modulate bone formation and bone resorption [49], accordingly, it has been shown that different strontium concentrations have different effects on bone formation in vitro; for bone-forming cells, the most effective concentration is between 0.001 and 1 mM, and for the reduction of bone resorbing cells, the most effective concentration is between 0.01 and 1 mM [50]. In our study, the concentration of strontium incorporated into PBCA nanoparticle is within this range. Strontium has been proven to be an anti-inflammatory drug [51]. In this study, when the Sr concentration was 0.2 mM, the PBCA NP concentration was 100 µg/mL, and the PBCA-Sr NP concentration was 100 µg/mL, the inflammatory cytokines IL-1α, IFN-γ were undetected, with only low levels of TNF induced, which is consistent with those reported in literature on the anti-inflammatory effect of Sr [52,53]. Strontium and calcium (Ca) in bones have similar cellular and physiochemical properties. Although the exact mechanism of Sr in bone is not clear, it has been proposed that Sr interacts with cellular targets by activating calcium-sensing receptor (CaSR) similar to  $\text{Ca}^{2+}$ , thereby acting as a signaling transduction pathway related to Ca-driven regulation of bone metabolism [54]. The phosphatase activity (ALP) is one of the most commonly used markers for osteoblast differentiation, and the enzyme activity is considered a necessary prerequisite for bone mineralization. The role of osteocalcin is bone mineralization and calcium ion homeostasis [55]. Strontium induces the higher expression of osteoblastic genes such as alkaline phosphatase (ALP), osteocalcin (OCN) and bone sialoprotein, which is accompanied by an increase in bone nodules and a decrease in the number of mature osteoclasts in vitro [51]. Here, we demonstrated that culturing osteoblasts in vitro with strontium-containing nanomaterials can meaningfully increase the expression of osteogenic proteins such as ALP and OCN, and increase the formation of calcium deposits.

In order to understand the effect of Sr-NP on the growth of osteoblast in the 3-D bone model, procaine mandible bone block decellularization was used to guide bone regeneration. Similar to the expression of osteogenic proteins, the results showed greater degree of bone matrix deposition on the raw surface of the trabecular bone following treatment with PBCA-Sr NP as indicated by the roughened ultrastructural surface texture of the bone blocks and the coverage of pores less than 30 microns on the trabecular bone.

### 4. Materials and Methods

#### 4.1. Synthesis of PBCA-Sr NPs

PBCA NP was synthesized by the emulsion polymerization method with minor modification [48]. 1% (v/v) butylcyanoacrylate (BCA, Sicomet, Sichel Werk, Hanover, Germany) monomers were added drop by drop into 0.1 N HCl acidic polymerization medium containing 1% (w/v) dextran 70,000 (Sigma, St. Louis, MO, USA) and 0.5135 g (100 mM) strontium ranelate (Protos<sup>®</sup>, Servier, France) at pH 2.0 (pH adjusted with 12 N HCl) under 400 rpm and 25 °C for 3 h. 0.1 N NaOH was mixed with NP suspension to terminate polymerization, and then the suspension was centrifuged at  $5250 \times g$  for 10 min. The larger polymer aggregates

were separated from the nanoparticles suspension by filtration through 0.22 µm filtration units. The drug-free NPs were prepared using the same method.

#### 4.2. Characterization

The concentration of PBCA-Sr NPs in DPBS buffer at pH 7.4 was 2 mg/mL in characterization analysis. The particle size and zeta potential of PBCA-Sr NPs were determined by Zetasizer Nano ZS90 (Malvern, Worcestershire, UK) with photo correlation spectroscopy. The geometry, surface morphology and the elemental composition of NPs were obtained by a transmission electron microscope (TEM, H-7500, Hitachi, Tokyo, Japan), field emission scanning electron microscope (FE-SEM, SU8220, Tokyo, Japan) and energy-dispersive spectrometry (EDS).

#### 4.3. Evaluation of Entrapment Efficiency

The free drug in the supernatant was measured using inductively coupled plasma mass spectroscopy (NexION 350X ICP-MS, PerkinElmer, Waltham, MA, USA). The entrapment efficiency of Sr,  $E_e$ , is defined as  $E_e (\%) = (\text{Total weight of Sr} - \text{weight of Sr in supernatant}) / (\text{Total weight of Sr}) \times 100\%$ .

#### 4.4. Isolation of Rat Bone Marrow Stromal Cells

The primary bone marrow stromal cells (MSCs) were from the long bone marrow of 5-week-old Sprague-Dawley (SD) rats (BioLasco, Taipei, Taiwan). The femurs and tibiae were aseptically removed from the animals and dissected clean of attached muscles. Bone marrow were flushed with 10 mL of cold PBS with 1% FBS and cells were washed 2–3 times with 1X PBS. Then, cells were cultured with  $\alpha$ -MEM containing 10% define FBS, antibiotics (100 U/mL penicillin G and 100 mg/mL streptomycin sulfate, Invitrogen, California). Flasks were incubated in a humidified atmosphere with 5% CO<sub>2</sub> at 37 °C. After 8 days, nonadherent cells were removed and remaining adherent cells were detached by trypsinization. When the culture is 80–90% confluence, the cells were passaged at the ratio of 1:4 in 75-cm<sup>2</sup> tissue culture flasks. Cells from the 3th to the 4th (18–24 days) passage were used for this study.

#### 4.5. MSC Differentiation Potential

To induce adipogenesis, fourth-passage cells were seeded in 6-well plates at  $2 \times 10^4$  cells/cm<sup>2</sup> and cultured in growth medium overnight. Cultures were then treated with Complete Adipogenesis Differentiation Medium (StemPro<sup>®</sup> Adipogenesis Differentiation Kit, Gibco, Carlsbad, CA, USA) for 7 days. Refeed cultures twice weekly and adipogenesis was assessed at day 7. Cells were fixed with 4% paraformaldehyde and stained with Oil Red O (Sigma) to evaluate adipogenesis via the accumulation of neutral lipids.

To induce osteogenic differentiation, fourth-passage cells were seeded in 6-well plates at  $2 \times 10^3$  cells/cm<sup>2</sup> and cultured in growth medium overnight. Cultures were then treated with osteogenic medium consists of DMEM containing 10% FBS, antibiotics (100 U/mL penicillin G and 100 mg/mL streptomycin sulfate), 100 nM Dexamethasone (Sigma, Saint Louis), 10 mM  $\beta$ -glycerophosphate (Sigma) and 50 µM L-ascorbate-2-phosphate (Sigma) for 1 week and 3 weeks. Medium was replaced twice weekly. Osteogenic differentiation was revealed after 1 week by ALP accumulation, as detected by microscopy after staining with BCIP/NBT Liquid Substrate System (Sigma-Aldrich). In the other hand, On week 3 of osteogenic differentiation, the cells were stained using 2% alizarin red (Sigma) solution (pH 4.2) to stain the calcium deposits.

#### 4.6. Differentiation of Rat Committed MSCs and Cell Culture

Rat MSCs were seeded with a density of  $1 \times 10^4$  cells/cm<sup>2</sup> and incubated overnight. Then, the medium was replaced with osteogenic medium consists of DMEM containing 10% FBS, antibiotics (100 U/mL penicillin G and 100 mg/mL streptomycin sulfate), 100 nM



Dexamethason (Sigma, Saint Louis), 10 mM  $\beta$ -glycerophosphate (Sigma) and 50  $\mu$ M L-ascorbate-2-phosphate (Sigma) in a humidified CO<sub>2</sub> incubator at 37 °C. When the culture is 80–90% confluence, the cells were passaged at the ratio of 1:4 in 75-cm<sup>2</sup> tissue culture flasks. Cells from the 3th to the 4th passage were used for this study.

#### 4.7. Evaluate the Effect of PBCA-Sr NPs on Osteoblasts in Vitro

##### 4.7.1. Cell Viability Test

###### MTT Assay

The cytotoxicity of PBCA-Sr NPs to committed MSCs was estimated by 3-(4,5-dimethylthiazol-2-yl)-2,5-diphenyltetrazolium bromide (MTT) assay (Sigma). Cells were seeded into a 96-well plate at a density is 10,000 cells/well and incubated overnight. Then the cells were treated with different concentrations of NPs in 100  $\mu$ L growth medium and are incubated for 24 h. Then, the cells were incubation with 100  $\mu$ L of MTT solution (1 mg/mL) for 2 h at 37 °C in a humidified atmosphere of 5% CO<sub>2</sub> incubator. MTT solution was removed and replace with dimethylsulphoxide (DMSO, Sigma-Aldrich) to solubilize the blue formazan crystals. The optical absorbance was measured by an EnSpire Multimode Plate Reader (Perkin Elmer Inc., Waltham, MA, USA) at wavelength of 570 nm. Percentage of cell viability was defined as the relative absorbance of PBCA-Sr NPs -treated cells versus the control cells. The percentage of the absorbance of control cells was taken as 100% viability.

###### WST-1 Assay

WST-1 assay was used to investigate the cell proliferation. Cells were seeded on 96-well plate at a density is 10,000 cells/well and incubated overnight. The cell viability was estimated after cells exposure to different concentration of NPs for 24 h by WST-1 assay (cell proliferation kit, Roche). The absorption is measured by a spectrophotometer (ELISA reader) at a wavelength of 450 nm.

###### LDH Assay

Cells were seeded on 96-well plate at a density is 10,000 cells/well and incubated overnight. Then, cells were added with different concentrations of NPs. After 24 h, the cytotoxicity was estimated by LDH assay (cytotoxicity detection kit, Roche). The absorption is measured by a spectrophotometer (ELISA reader) at a wavelength of 490 nm.

#### Determination of Inflammation

The committed MSCs are seeded into a 96-well plate at a density is  $1 \times 10^4$  cells/cm<sup>2</sup> and incubated overnight. The cell medium was collected after treating with different concentrations of NPs for analyzing IL-1 $\alpha$ , IFN- $\gamma$  and TNF- $\alpha$  by BD cytometric bead array (CBA) kit (BD Biosciences, NJ, USA). The kit was performed according to the manufacturer's instructions and analyzed by flow cytometry.

##### 4.7.2. ALP Staining

The committed MSCs were treated with different concentrations of PBCA-Sr NPs for 7 days. Cells were washed with  $1 \times$  PBS and fixed with 4% formaldehyde for 20 min at room temperature. Then, BCIP/NBT Liquid Substrate System (Sigma-Aldrich) was added for ALP staining.

##### 4.7.3. Analysis of Calcium Deposition

The committed MSCs were treated with different concentrations of PBCA-Sr NPs for 21 days. Cells were washed with  $1 \times$  PBS and fixed with 4% formaldehyde for 20 min at room temperature. Then, 2% alizarin red (pH 4.2) was added for calcium staining.

#### 4.7.4. Western Blot Analysis

The committed MSCs were cultured with different concentrations of PBCA-Sr NPs for 7 days. The cells were lysed using M-PER Mammalian Protein Extraction Reagent (Thermo Fisher Scientific, Waltham, MA, USA) and centrifuged at 12,000 rpm at 4 °C for 15 min. Protein concentration was measured by Bio-Rad protein assay reagent. Protein separation was performed by using SDS polycarylamide gel electrophoresis (SDS-PAGE) and transferred onto PVDF membrane. Blocking of non-specific binding was achieved by placing the PVDF membrane in a 1% BSA blocking solution and stained with antibodies specific for osteocalcin (OCN, 1:1000, Santa Cruz Biotechnology), alkaline phosphatase (1:1000, Abcam, Cambridge, UK) or  $\beta$ -actin (1:10000, Santa Cruz), gently shaken in room temperature for 1 h, then washed 3 times for 15 min with washing buffer (10 mM Tris-base, pH 7.5, 100 mM NaCl 0.1% Tween 20). Secondary antibody diluted in peroxidase-containing blocking buffer is added, incubated for 1 h, then, washed 3 times for 15 min with washing buffer. The PVDF membrane was analyzed by chemiluminescent-base detection system for detection of protein expression.

#### 4.8. Generation of Procaine Mandibular Bone Block by Decellularization

The procaine mandibular bone samples were harvested from maker (Chia-Yi, Taiwan). The procaine mandibular bone has been cut into a cuboid of 10 mm  $\times$  10 mm  $\times$  10 mm and stored at  $-80$  °C until use. The bone blocks were washed with  $1 \times$  PBS+  $1 \times$  PSG (antibiotics, 100 U/mL penicillin G and 100 mg/mL streptomycin sulfate). Then, bone blocks were immersed in distilled water (ddH<sub>2</sub>O) and performed 2 cycle of thermal shock. The solution was changed at every cycle. The step of thermal shock was heated at 121 °C for 20 min, followed by freezing in liquid nitrogen overnight. To remove cellular debris, bone blocks were washed with 1% Triton X-100 and then 0.1% Triton X-100. Bone blocks were washed with ddH<sub>2</sub>O to remove residual Triton X-100. Bone blocks were dehydrated in 50, 75, 95, and 100% ethanol. All these steps were performed under continuous shaking at room temperature with the rotator shaker. Bone blocks were transferred to cell culture dishes and allowed to dry at RT under a sterile laminar flow hood.

#### 4.9. The Morphology of Osteoblasts Attached on Bone Block

After sterilization, pig bone blocks were transferred to 6-well culture plates. The committed MSCs ( $1 \times 10^4$  cells/cm<sup>2</sup>) are seeded into bone block and incubated overnight. The cells were cultured with different concentrations of PBCA-Sr NPs for 7 days. Sample were rinsed in PBS and then fixed with 3% glutaraldehyde and 2% paraformaldehyde in 0.1 M cacodylate buffer (pH 7.4) at 4 °C for 2 h. The fixative was removed by washing with 0.1 M cacodylate buffer and post-fixed in 1% osmium tetroxide in 0.1 M cacodylate buffer at 4 °C or 1 h. Then the cells were dehydrated in a graded ethanol series (30, 50, 70, 95, and 100%). The specimens were coated with platinum and the morphology of osteoblasts attached on pig bone block is characterized by FE-SEM (SU8220).

#### 4.10. Statistics

Results were presented as mean  $\pm$  standard deviation. The data were analyzed with a one-way analysis of variance (ANOVA), and the comparisons between pairs were performed with Tukey HSD test. A *p* value of 0.05 or less indicated a significant statistical difference.

### 5. Conclusions

The nanoparticle-based delivery of Sr using PBCA NPs can aid bone formation by increasing osteocalcin and alkaline phosphatase protein expression and promoting calcium deposition in committed MSCs, which are superior to Sr alone. PBCA-Sr-NPs could potentially be a biocompatible delivery system used locally for optimization of bone quality in dental implantation.

**Author Contributions:** L.-C.C. and C.-Y.C. conceived and designed the experiments; C.-Y.C. and C.-H.C. performed the experiments; J.-T.Y. analyzed the data; C.-Y.C. and M.H.-C.L. contributed reagents/materials/analysis tools; L.-C.C. and J.-T.Y. funding acquisition; L.-C.C., C.-Y.C. and M.H.-C.L. wrote the manuscript; and J.-T.Y. proofread the manuscript. All authors have read and agreed to the published version of the manuscript.

**Funding:** This study was funded by Chang Gung Memorial Hospital, Chiayi (CMRPG6G0131, CMRPG6G0591, CMRPG6J0281, CMRPG6L0051, and BMRP492) and Chang Gung University of Science and Technology (ZRRPF3K0101).

**Institutional Review Board Statement:** The animal experiment project was reviewed, approved and supervised by the Institutional Animal Care and Use Committee (IACUC) of Chang Gung Memorial Hospital in Taiwan. The IACUC approval number is 2017101702, and approval date is 20171201.

**Informed Consent Statement:** Not applicable.

**Acknowledgments:** This work was performed in the Common Laboratory of Chang Gung Memorial Hospital at Chiayi. We thank the Microscope Core Laboratory of Chang Gung Memorial Hospital in Linkou for its assistance in SEM and TEM. Thanks to the Food and Cosmetic Safety Research Center of Chang Gung University of Science and Technology for their assistance in ICP-MS analysis. We would also like to thank the Leica SP5II confocal microscope service provided by the Precious Instrumentation Core Laboratory of Chang Gung Memorial Hospital in Chiayi.

**Conflicts of Interest:** The authors declare no conflict of interest.

## References

1. Al-Nawas, B.; Schiegnitz, E. Augmentation procedures using bone substitute materials or autogenous bone—A systematic review and meta-analysis. *Eur. J. Oral Implantol.* **2014**, *7* (Suppl. 2), S219–S234.
2. Kassim, B.; Ivanovski, S.; Mattheos, N. Current perspectives on the role of ridge (socket) preservation procedures in dental implant treatment in the aesthetic zone. *Aust. Dent. J.* **2014**, *59*, 48–56. [[CrossRef](#)] [[PubMed](#)]
3. Hammerle, C.H.; Araujo, M.G.; Simion, M.; Osteology Consensus, G. Evidence-based knowledge on the biology and treatment of extraction sockets. *Clin. Oral Implant. Res.* **2012**, *23* (Suppl. 5), 80–82. [[CrossRef](#)] [[PubMed](#)]
4. Barndt, P.; Zhang, H.; Liu, F. Immediate loading: From biology to biomechanics. Report of the Committee on Research in fixed Prosthodontics of the American Academy of fixed Prosthodontics. *J. Prosthet. Dent.* **2015**, *113*, 96–107. [[CrossRef](#)] [[PubMed](#)]
5. Stafford, G.L. Different loading times for dental implants—No clinically important differences? *Evid. Based Dent.* **2013**, *14*, 109–110. [[CrossRef](#)]
6. Xu, L.; Wang, X.; Zhang, Q.; Yang, W.; Zhu, W.; Zhao, K. Immediate versus early loading of flapless placed dental implants: A systematic review. *J. Prosthet. Dent.* **2014**, *112*, 760–769. [[CrossRef](#)]
7. Valeria De Risi, M.C. Gianluca Vittorini, Alice Mannocci, Massimo De Sanctis. Alveolar ridge preservation techniques: A systemic review and meta-analysis of histological and histomorphometrical data. *Clin. Oral Implant. Res.* **2013**, 1–19.
8. LeGeros, R.Z. Properties of osteoconductive biomaterials: Calcium phosphates. *Clin. Orthop. Relat. Res.* **2002**, *395*, 81–98. [[CrossRef](#)]
9. Iolascon, L.F.G.; Di Pietro, G.; Capaldo, A.; Luciano, F.; Gimigliano, F. Bone quality and bone strength: Benefits of the bone-forming approach. *Clin. Cases Miner. Bone Metab.* **2014**, *11*, 20–24. [[CrossRef](#)]
10. Subhagit Das, J.C.C. Osteoporosis—A current view of pharmacological prevention and treatment. *Drug Design Dev. Ther.* **2013**, *7*, 435–448.
11. Conserva, E.; Pisciotto, A.; Borghi, F.; Nasi, M.; Pecorini, S.; Bertoni, L.; de Pol, A.; Consolo, U.; Carnevale, G. Titanium Surface Properties Influence the Biological Activity and FasL Expression of Craniofacial Stromal Cells. *Stem Cells Int.* **2019**, *2019*, 4670560. [[CrossRef](#)] [[PubMed](#)]
12. Nayab, S.N.; Jones, F.H.; Olsen, I. Effects of calcium ion implantation on human bone cell interaction with titanium. *Biomaterials* **2005**, *26*, 4717–4727. [[CrossRef](#)]
13. Zacchetti, G.; Dayer, R.; Rizzoli, R.; Ammann, P. Systemic treatment with strontium ranelate accelerates the filling of a bone defect and improves the material level properties of the healing bone. *Biomed Res. Int.* **2014**, *2014*, 549785. [[CrossRef](#)]
14. Karakan, N.C.; Akpinar, A.; Goze, F.; Poyraz, O. Investigating the Effects of Systemically Administered Strontium Ranelate on Alveolar Bone Loss Histomorphometrically and Histopathologically on Experimental Periodontitis in Rats. *J. Periodontol.* **2017**, *88*, e24–e31. [[CrossRef](#)]
15. Tsai, T.T.; Tai, C.L.; Ho, N.Y.; Lai, P.L.; Fu, T.S.; Niu, C.C.; Chen, L.H.; Chen, W.J. Effects of Strontium Ranelate on Spinal Interbody Fusion Surgery in an Osteoporotic Rat Model. *PLoS ONE* **2017**, *12*, e0167296. [[CrossRef](#)] [[PubMed](#)]
16. Reginster, J.Y. Cardiac concerns associated with strontium ranelate. *Expert Opin. Drug Saf.* **2014**, *13*, 1209–1213. [[CrossRef](#)]

17. Reginster, J.Y.; Brandi, M.L.; Cannata-Andia, J.; Cooper, C.; Cortet, B.; Feron, J.M.; Genant, H.; Palacios, S.; Ringe, J.D.; Rizzoli, R. The position of strontium ranelate in today's management of osteoporosis. *Osteoporos. Int.* **2015**, *26*, 1667–1671. [[CrossRef](#)] [[PubMed](#)]
18. Yu, J.; Tang, J.; Li, Z.; Sajjan, S.; O'Regan, C.; Modi, A.; Sazonov, V. History of cardiovascular events and cardiovascular risk factors among patients initiating strontium ranelate for treatment of osteoporosis. *Int. J. Womens Health* **2015**, *7*, 913–918.
19. Zapolski, T.; Wysokinski, A. Current views on the interaction between the treatment of osteoporosis and cardiovascular diseases. *Wiad. Lek.* **2016**, *69*, 665–674.
20. Park, J.W.; Kang, D.G.; Hanawa, T. New bone formation induced by surface strontium-modified ceramic bone graft substitute. *Oral Dis.* **2016**, *22*, 53–61. [[CrossRef](#)]
21. Santocildes-Romero, M.E.; Crawford, A.; Hatton, P.V.; Goodchild, R.L.; Reaney, I.M.; Miller, C.A. The osteogenic response of mesenchymal stromal cells to strontium-substituted bioactive glasses. *J. Tissue Eng. Regen. Med.* **2015**, *9*, 619–631. [[CrossRef](#)]
22. Denry, I.; Goudouri, O.M.; Fredericks, D.C.; Akkouch, A.; Acevedo, M.R.; Holloway, J.A. Strontium-releasing fluorapatite glass-ceramic scaffolds: Structural characterization and in vivo performance. *Acta Biomater.* **2018**. [[CrossRef](#)]
23. Masalskas, B.F.; Martins Junior, W.; Leoni, G.B.; Faloni, A.P.S.; Marcaccini, A.M.; Silva Sousa, Y.T.C.; Castro-Raucci, L.M.S. Local delivery of strontium ranelate promotes regeneration of critical size bone defects filled with collagen sponge. *J. Biomed. Mater. Res. A* **2018**, *106*, 333–341. [[CrossRef](#)] [[PubMed](#)]
24. Suleimenova, D.; Hashimi, S.M.; Li, M.; Ivanovski, S.; Mattheos, N. Gene expression profiles in guided bone regeneration using combinations of different biomaterials: A pilot animal study. *Clin. Oral Implant. Res.* **2017**, *28*, 713–720. [[CrossRef](#)] [[PubMed](#)]
25. Kitayama, S.; Wong, L.O.; Ma, L.; Hao, J.; Kasugai, S.; Lang, N.P.; Mattheos, N. Regeneration of rabbit calvarial defects using biphasic calcium phosphate and a strontium hydroxyapatite-containing collagen membrane. *Clin. Oral Implant. Res.* **2015**, *27*, e206–e214. [[CrossRef](#)]
26. Nahass, H.E.; Din, N.N.E.; Nasry, S.A. The Effect of Strontium Ranelate Gel on Bone Formation in Calvarial Critical Size Defects. *Open Access Maced. J. Med. Sci.* **2017**, *5*, 994–999. [[CrossRef](#)] [[PubMed](#)]
27. Peng, S.; Lai, Z.T.; Hong, D.W.; Chu, I.M.; Lai, P.L. Controlled release of strontium through neutralization reaction within a methoxy(polyethylene glycol)-polyester hydrogel. *J. Appl. Biomater. Funct. Mater.* **2017**, *15*, e162–e169. [[CrossRef](#)]
28. Liu, J.; Rawlinson, S.C.; Hill, R.G.; Fortune, F. Strontium-substituted bioactive glasses in vitro osteogenic and antibacterial effects. *Dent. Mater.* **2016**, *32*, 412–422. [[CrossRef](#)]
29. Brauer, D.S.; Karpukhina, N.; Kedia, G.; Bhat, A.; Law, R.V.; Radecka, I.; Hill, R.G. Bactericidal strontium-releasing injectable bone cements based on bioactive glasses. *J. R. Soc. Interface* **2012**. [[CrossRef](#)]
30. Mao, Z.; Li, Y.; Yang, Y.; Fang, Z.; Chen, X.; Wang, Y.; Kang, J.; Qu, X.; Yuan, W.; Dai, K.; et al. Osteoinductivity and Antibacterial Properties of Strontium Ranelate-Loaded Poly(Lactic-co-Glycolic Acid) Microspheres With Assembled Silver and Hydroxyapatite Nanoparticles. *Front. Pharmacol.* **2018**, *9*, 368. [[CrossRef](#)] [[PubMed](#)]
31. Munad, J. Al-Duliamy, N.H.G. Omar, A.; Kader, Bashar, H.; Abdullah, Enhancement of orthodontic anchorage and retention by the local injection of strontium: An experimental study in rats. *Saudi Dent. J.* **2015**, *27*, 22–29.
32. Marie, P.J.; Garba, M.T.; Hott, M.; Miravet, L. Effect of low doses of stable strontium on bone metabolism in rats. *Min. Electrolyte Metab* **1985**, *11*, 5–13.
33. Morohashi, T.; Sano, T.; Yamada, S. Effects of strontium on calcium metabolism in rats. I. A distinction between the pharmacological and toxic doses. *Jpn. J. Pharmacol.* **1994**, *64*, 155–162. [[CrossRef](#)]
34. Pasqualetti, S.; Banfi, G.; Mariotti, M. The effects of strontium on skeletal development in zebrafish embryo. *J. Trace Elem Med. Biol.* **2013**, *27*, 375–379. [[CrossRef](#)] [[PubMed](#)]
35. Silva, G.A.B.; Bertassoli, B.M.; Sousa, C.A.; Albergaria, J.D.; de Paula, R.S.; Jorge, E.C. Effects of strontium ranelate treatment on osteoblasts cultivated onto scaffolds of trabeculae bovine bone. *J. Bone Miner. Metab.* **2018**, *36*, 73–86. [[CrossRef](#)]
36. Fatemeh, D.R.; Ebrahimi Shahmabadi, H.; Abedi, A.; Alavi, S.E.; Movahedi, F.; Koochi Moftakhari Esfahani, M.; Zadeh Mehrizi, T.; Akbarzadeh, A. Polybutylcyanoacrylate nanoparticles and drugs of the platinum family: Last status. *Indian J. Clin. Biochem.* **2014**, *29*, 333–338. [[CrossRef](#)] [[PubMed](#)]
37. Mitra, A.; Lin, S. Effect of surfactant on fabrication and characterization of paclitaxel-loaded polybutylcyanoacrylate nanoparticle delivery systems. *J. Pharm. Pharmacol.* **2003**, *55*, 895–902. [[CrossRef](#)]
38. Lu, B.; Feng, J.F.; Yang, X.C. Human recombinant interferon-alpha 2a polybutylcyanoacrylate sustained release lyophilized nanospheres for liver-targeting. *Sichuan Da Xue Xue Bao Yi Xue Ban* **2004**, *35*, 1–4. [[PubMed](#)]
39. Yang, Y.X.; Zhu, L.; He, X.; Bao, D.Y.; Bao, X. Antitumor activity of mitoxantrone-nanosphere against murine liver tumor H22. *Sichuan Da Xue Xue Bao Yi Xue Ban* **2004**, *35*, 68–70.
40. Gao, H.; Wang, J.Y.; Shen, X.Z.; Deng, Y.H.; Zhang, W. Preparation of magnetic polybutylcyanoacrylate nanospheres encapsulated with aclacinomycin A and its effect on gastric tumor. *World J. Gastroenterol.* **2004**, *10*, 2010–2013. [[CrossRef](#)] [[PubMed](#)]
41. Kolter, M.; Ott, M.; Hauer, C.; Reimold, I.; Fricker, G. Nanotoxicity of poly(n-butylcyano-acrylate) nanoparticles at the blood-brain barrier, in human whole blood and in vivo. *J. Control. Release* **2015**, *197*, 165–179. [[CrossRef](#)]
42. Lissarrague, M.H.; Fascio, M.L.; Goyanes, S.; D'Accorso, N.B. Acrylic bone cements: The role of nanotechnology in improving osteointegration and tunable mechanical properties. *J. Biomed. Nanotechnol.* **2014**, *10*, 3536–3557. [[CrossRef](#)]
43. Bagad, M.; Khan, Z.A. Poly(n-butylcyanoacrylate) nanoparticles for oral delivery of quercetin: Preparation, characterization, and pharmacokinetics and biodistribution studies in Wistar rats. *Int. J. Nanomed.* **2015**, *10*, 3921–3935.

44. Lin, M.H.; Chung, C.Y.; Chen, K.T.; Yeh, J.C.; Lee, T.H.; Lee, M.H.; Lee, I.N.; Huang, W.C.; Yang, J.T. Comparison between Polybutylcyanoacrylate Nanoparticles with Either Surface-Adsorbed or Encapsulated Brain-Derived Neurotrophic Factor on the Neural Differentiation of iPSCs. *Int. J. Mol. Sci.* **2019**, *20*, 182. [[CrossRef](#)]
45. Zhang, S.; Dong, Y.; Chen, M.; Xu, Y.; Ping, J.; Chen, W.; Liang, W. Recent developments in strontium-based biocomposites for bone regeneration. *J. Artif. Organs* **2020**, *23*, 191–202. [[CrossRef](#)] [[PubMed](#)]
46. Atteritano, M.; Catalano, A.; Santoro, D.; Lasco, A.; Benvenga, S. Effects of strontium ranelate on markers of cardiovascular risk in postmenopausal osteoporotic women. *Endocrine* **2016**, *53*, 305–312. [[CrossRef](#)]
47. Ali, M.S.; Berencsi, K.; Marinier, K.; Deltour, N.; Perez-Guthann, S.; Pedersen, L.; Rijnbeek, P.; Lapi, F.; Simonetti, M.; Reyes, C.; et al. Comparative cardiovascular safety of strontium ranelate and bisphosphonates: A multi-database study in 5 EU countries by the EU-ADR Alliance. *Osteoporos. Int.* **2020**, *31*, 2425–2438. [[CrossRef](#)]
48. Chung, C.Y.; Yang, J.T.; Kuo, Y.C. Polybutylcyanoacrylate nanoparticles for delivering hormone response element-conjugated neurotrophin-3 to the brain of intracerebral hemorrhagic rats. *Biomaterials* **2013**, *34*, 9717–9727. [[CrossRef](#)] [[PubMed](#)]
49. Marx, D.; Rahimnejad Yazdi, A.; Papini, M.; Towler, M. A review of the latest insights into the mechanism of action of strontium in bone. *Bone Rep.* **2020**, *12*, 100273. [[CrossRef](#)]
50. Quade, M.; Vater, C.; Schlötz, S.; Bolte, J.; Langanke, R.; Bretschneider, H.; Gelinsky, M.; Goodman, S.B.; Zwingenberger, S. Strontium enhances BMP-2 mediated bone regeneration in a femoral murine bone defect model. *J. Biomed. Mater. Res. B Appl. Biomater.* **2020**, *108*, 174–182. [[CrossRef](#)]
51. Pilmane, M.; Salma-Ancane, K.; Loca, D.; Locs, J.; Berzina-Cimdina, L. Strontium and strontium ranelate: Historical review of some of their functions. *Mater. Sci. Eng. C* **2017**, *78*, 1222–1230. [[CrossRef](#)] [[PubMed](#)]
52. Wei, L.; Jiang, Y.; Zhou, W.; Liu, S.; Liu, Y.; Rausch-Fan, X.; Liu, Z. Strontium ion attenuates lipopolysaccharide-stimulated proinflammatory cytokine expression and lipopolysaccharide-inhibited early osteogenic differentiation of human periodontal ligament cells. *J. Periodontol. Res.* **2018**, *53*, 999–1008. [[CrossRef](#)] [[PubMed](#)]
53. Berksoy Hayta, S.; Durmus, K.; Altuntas, E.E.; Yildiz, E.; Hisarciklio, M.; Akyol, M. The reduction in inflammation and impairment in wound healing by using strontium chloride hexahydrate. *Cutan. Ocul. Toxicol.* **2018**, *37*, 24–28. [[CrossRef](#)]
54. Wan, B.; Wang, R.; Sun, Y.; Cao, J.; Wang, H.; Guo, J.; Chen, D. Building Osteogenic Microenvironments With Strontium-Substituted Calcium Phosphate Ceramics. *Front. Bioeng. Biotechnol.* **2020**, *8*, 591467. [[CrossRef](#)] [[PubMed](#)]
55. Raucci, M.G.; Alvarez-Perez, M.; Giugliano, D.; Zeppetelli, S.; Ambrosio, L. Properties of carbon nanotube-dispersed Sr-hydroxyapatite injectable material for bone defects. *Regen. Biomater.* **2016**, *3*, 13–23. [[CrossRef](#)] [[PubMed](#)]



OPEN

# Association of urinary ketamine and APOA1 levels with bladder dysfunction in ketamine abusers revealed via proteomics and targeted metabolite analyses

Jo-Chuan Liu<sup>1</sup>, Yi-Ting Chen<sup>1,2,3</sup>, Ya-Ju Hsieh<sup>2</sup>, Chia-Chun Wu<sup>2</sup>, Ming-Chyi Huang<sup>4,5</sup>, Yu-Chao Hsu<sup>6,7</sup>, Chun-Te Wu<sup>7,8</sup>, Chih-Ken Chen<sup>7,9</sup>, Srinivas Dash<sup>1</sup> & Jau-Song Yu<sup>1,2,10,11</sup>✉

Chronic ketamine abuse is associated with bladder dysfunction and cystitis. However, the effects of ketamine abuse on the urinary proteome profile and the correlations among urinary proteins, urinary ketamine (and metabolites) and clinicopathological features of ketamine-induced bladder dysfunction remain to be established. Here, we recruited 56 ketamine abusers (KA) and 40 age-matched healthy controls (HC) and applied the iTRAQ-based proteomics approach to unravel quantitative changes in the urine proteome profile between the two groups. Many of the differentially regulated proteins are involved in the complement and coagulation cascades and/or fibrotic disease. Among them, a significant increase in APOA1 levels in KA relative to control samples ( $392.1 \pm 59.9$  ng/ml vs.  $13.7 \pm 32.6$  ng/ml,  $p < 0.0001$ ) was detected via ELISA. Moreover, urinary ketamine, norketamine and dehydronorketamine contents (measured via LC-SRM-MS) were found to be positively correlated with overactive bladder syndrome score (OABSS) and APOA1 levels with urinary RBC, WBC, OABSS and numeric pain rating scale in KA. Collectively, our results may aid in developing new molecular tool(s) for management of ketamine-induced bladder dysfunction. Moreover, information regarding the differentially regulated proteins in urine of KA provides valuable clues to establish the molecular mechanisms underlying ketamine-induced cystitis.

## Abbreviations

APOA1	Apolipoprotein A1
AUC	Area under the ROC curve
GO	Gene ontology
HPF	High power field
iTRAQ	Isobaric tag for relative and absolute quantitation
HC	Healthy control
KA	Ketamine abuser
LC-MS/MS	Liquid chromatography tandem mass spectrometry
RBC	Red blood cell
ROC	Receiver operating characteristic curve
SAA4	Serum amyloid A-4 protein

<sup>1</sup>Graduate Institute of Biomedical Sciences, College of Medicine, Chang Gung University, Taoyuan, Taiwan. <sup>2</sup>Molecular Medicine Research Center, Chang Gung University, Taoyuan, Taiwan. <sup>3</sup>Department of Biomedical Sciences, College of Medicine, Chang Gung University, Taoyuan, Taiwan. <sup>4</sup>Department of Addiction Sciences, Taipei City Psychiatric Center, Taipei City Hospital, Taipei, Taiwan. <sup>5</sup>Department of Psychiatry, School of Medicine, College of Medicine, Taipei Medical University, Taipei, Taiwan. <sup>6</sup>Department of Urology, Linkou Chang Gung Memorial Hospital, Taoyuan, Taiwan. <sup>7</sup>College of Medicine, Chang Gung University, Taoyuan, Taiwan. <sup>8</sup>Department of Urology, Chang Gung Memorial Hospital, Keelung, Taiwan. <sup>9</sup>Department of Psychiatry, Chang Gung Memorial Hospital, Keelung, Taiwan. <sup>10</sup>Liver Research Center, Linkou Chang Gung Memorial Hospital, Taoyuan, Taiwan. <sup>11</sup>Research Center for Food and Cosmetic Safety, College of Human Ecology, Chang Gung University of Science and Technology, Taoyuan 33303, Taiwan. ✉email: yusong@mail.cgu.edu.tw



SRM	Selected reaction monitoring
WBC	White blood cell
K	Ketamine
NK	Norketamine
DHNM	Dehydronorketamine

Ketamine hydrochloride, initially synthesized in 1962 by Calvin Stevens, a scientist at Parke-Davis Laboratories, is a noncompetitive antagonist of N-methyl-D-aspartic acid receptor used as a general anesthetic with short-term effect in both human and veterinary settings<sup>1</sup>. Ketamine undergoes N-demethylation by liver microsomal cytochrome P450 enzymes to generate the primary metabolite norketamine<sup>2</sup>. Dehydrogenation of norketamine generates dehydronorketamine, which is conjugated to glucuronic acid before excretion in urine. Levels of ketamine and its metabolites are detectable in urine up to 2 weeks after consumption using enzyme-linked immunosorbent assay (ELISA)<sup>3</sup> or liquid chromatography-tandem mass spectrometry (LC-MS/MS)<sup>4</sup>.

In addition to its medical applications, ketamine is widely used as a recreational drug, especially in nightclubs and parties. Besides several negative effects (increased heart and respiratory rates, convulsions, temporary paralysis, nausea, vomiting, and hallucinations), use of ketamine can cause addictive effects, such as altered sensations, out-of-body experiences and a euphoric rush<sup>5</sup>. Since the first report of “ketamine-associated ulcerative cystitis” as a new clinical entity in 2007<sup>6</sup>, accumulating evidence has supported an association of chronic ketamine abuse with harmful physical effects, such as acute cardiac risk, ulcerative cystitis, lower urinary tract symptoms (LUTS), kidney dysfunction, intense abdominal pain and unexplained deaths<sup>7</sup>. Secondary and irreversible renal damage may occur in critical cases, leading to complete dependence on dialysis. Street ketamine abuse is not only a drug problem but also correlated with severe urological conditions that cause a significant burden to the healthcare system<sup>8,9</sup>. This highlights the critical need to clarify the mechanisms underlying development of ketamine-induced lower urinary tract dysfunction, which could provide useful clues for its clinical management.

Bladder dysfunction is one of the main characteristics of ketamine-induced LUTS, including irregular voiding frequency, decreased intercontraction intervals and bladder capacity, tissue fibrosis, injury to the urinary barrier and reduced urothelium areas of the bladder wall<sup>10–12</sup>. Serious bladder inflammation induces overactive bladder syndrome, irritative bladder symptoms and bladder pain. For evaluation of overactive bladder syndrome, scientists have developed a symptom assessment tool designated ‘overactive bladder symptom score’ (OABSS) that includes symptoms such as urgency, frequency (daytime and nighttime) and urinary incontinence<sup>13</sup>. It has been reported that overactive bladder syndrome caused by serious bladder inflammation is frequently observed in KA<sup>14</sup>. These observations support the correlation between OABSS and urinary ketamine and its metabolites.

Ketamine and its metabolites are excreted via urine. Direct toxic effects of these compounds on uroepithelial cells have been documented as one of the possible mechanisms underlying ketamine-induced bladder dysfunction<sup>15,16</sup>. Urine is in direct contact with uroepithelial cells and proteins released from damaged uroepithelial cells and/or bladder wall during long-term exposure to ketamine and its metabolites may be enriched in urine of KA. Therefore, non-invasive urine specimens of KA represent an ideal sample to identify useful indicators and/or the pathological mechanisms underlying ketamine-induced bladder dysfunction. Although a number of investigations have focused on the global changes in gene or protein expression levels in tissue specimens from bladders of mice subjected to long-term consumption of ketamine<sup>17–19</sup> and KA<sup>20</sup>, to our knowledge, no studies have analyzed the proteome profile of urine samples from KA and relevant associations with ketamine-induced LUTS or urinary ketamine and its metabolites.

Chronic ketamine abuse can induce bladder dysfunction but the molecular mechanism still remains unclear. We supposed that direct toxic effects of ketamine and its metabolites may strongly affect uroepithelial cells or bladder wall, cause release of proteins into urine, and induce bladder dysfunction, including overactive bladder syndrome. The effects of ketamine abuse on the urinary proteome profile and the correlations among urinary proteins, urinary ketamine (and metabolites) and clinicopathological features of ketamine-induced bladder dysfunction need to be established. In the present investigation, we collected urine samples from KA and age-matched healthy controls along with clinical information, including laboratory data on urine/serum samples, OABSS and pain rating scales. LC-MS/MS was applied to measure the ketamine and metabolite contents in urine samples of KA and the urine proteome profile alterations in KA versus healthy controls investigated using the iTRAQ-based quantitative proteomics approach. Proteins displaying significantly altered levels were subjected to bioinformatics analysis for disrupted biological pathways in KA, and the urinary levels of two target proteins, APOA1 and SAA4, determined via ELISA in all enrolled subjects. Finally, the potential associations among urinary target protein levels, ketamine and metabolite contents and clinicopathological features of KA were evaluated.

## Results

**Study population and experimental design.** We recruited 56 KA (41 males and 15 females) and 40 age-matched healthy controls (25 males and 15 females) for study. Examination times after ketamine uptake for male and female KA were  $6.0 \pm 6.0$  and  $6.0 \pm 4.8$  days and average doses of ketamine uptake in the 90 days before admission were  $4.0 \pm 2.2$  and  $3.4 \pm 2.6$  g per day, respectively (Table 1). Urine samples were collected from all subjects for measurement of ketamine (and metabolite) contents as well as proteome profile analysis. A schematic presentation of the strategy used is shown in Fig. 1. We initially assessed the ketamine, norketamine and dehydronorketamine contents in individual KA urine samples via targeted metabolite analysis using LC-SRM-MS. Subsequently, pooled urine protein samples from 4 subgroups (male HC, male KA, female HC and female KA; 10 cases per group) were prepared for iTRAQ-based quantitative proteomics analysis to compare the urinary proteome profiles between HC and KA for both genders. Proteins showing differential expression

	Male		Female	
Total enrolled subjects in this study				
Group	HC	KA	HC	KA
Case no	25	41	15	15
Age (year)	31.4 ± 6.7	31.4 ± 6.7	31.6 ± 3.6	30.9 ± 5.1
Inspection time after ketamine uptake (day)	NA	6.0 ± 6.0	NA	6.0 ± 4.8
Average dose before admission for 90 days (g/day)	NA	4.0 ± 2.2	NA	3.4 ± 2.6
Enrolled subjects used for ITRAQ-based quantitative proteomics study				
Group	HC	KA	HC	KA
Case no	10	10	10	10
Age (year)	31.9 ± 5.2	31.8 ± 13.7	31.6 ± 1 3.6	28.9 ± 4.5
Inspection time after ketamine uptake (day)	NA	6.0 ± 15.6	NA	6.8 ± 5.3
Average dose before admission for 90 days (g/day)	NA	4.9 ± 2.8	NA	3.8 ± 3.0

**Table 1.** Demographic characteristics of enrolled subjects. *HC* healthy controls, *KA* ketamine abusers, *NA* not applicable.

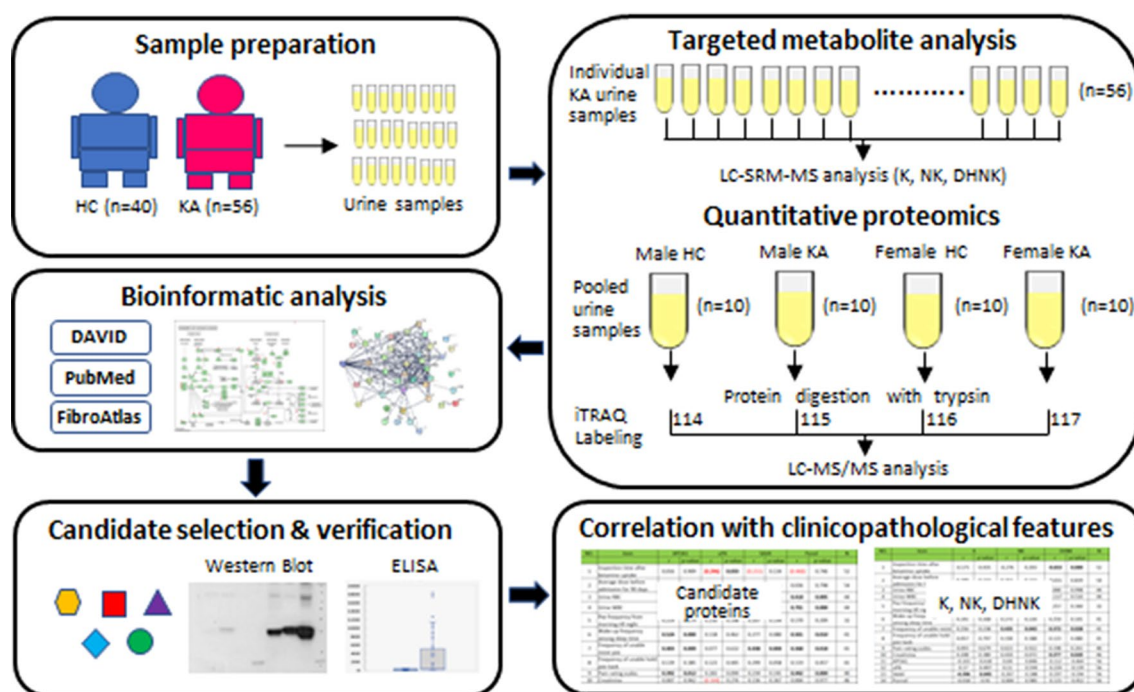


**Figure 1.** Workflow for exploring urine proteome alteration in KA and the association between urine protein levels, contents of ketamine and its metabolites and clinicopathological features of KA. Please refer to the text for details.

patterns between HC and KA groups were selected for subsequent bioinformatics analysis to determine the biological network(s) potentially related to ketamine-induced bladder dysfunction. Several candidate proteins were further selected for verification using western blot and ELISA in pooled and individual urine samples. The correlations among urinary protein levels, contents of ketamine and its metabolites and clinicopathological features of KA were additionally evaluated.

**Clinicopathological features of KA.** Clinical data on the 56 KA detailed in Table S1 are summarized in Table 2. Different clinical data were available from 40 to 54 cases. Forty cases (77%, 40/52) visited the addiction center for ketamine detoxification 1 day or more after ketamine uptake and 46 cases (85%, 46/54) had consumed more than 2 g ketamine per day over the 3 months before admission. Laboratory data showed that 10 (23%, 10/44) and 17 (39%, 17/44) subjects contained urine RBC and WBC > 5/HPF, respectively, implicating inflammation in the lower urinary tract for more than a third of KA cases. Questionnaire-based survey data revealed that 21 (51%, 21/41) and 14 (35%, 14/40) cases had overactive bladder syndrome score (OABSS) > 6 and pain rating scale > 50 mm, respectively, suggesting that a significant proportion of the KA group developed ketamine-induced LUTS.

Features	Case no. <sup>a</sup>	Mean $\pm$ SD
<b>Inspection time after ketamine uptake (day)</b>	(n = 52)	
< 1	12	0.75 $\pm$ 0.45
2–7	24	3.88 $\pm$ 1.62
> 7	16	13.13 $\pm$ 4.65
<b>Average dose before admission for 90 days (g/day)</b>	(n = 54)	
< 1	8	0.89 $\pm$ 0.21
2–5	37	3.56 $\pm$ 1.46
> 5	9	7.44 $\pm$ 1.59
<b>Urine RBC (RBC/HPF)</b>	(n = 44)	
< 5	34	1.16 $\pm$ 0.67
> 5	10	142.54 $\pm$ 164.68
<b>Urine WBC (WBC/HPF)</b>	(n = 44)	
< 5	27	1.78 $\pm$ 1.30
> 5	17	94.15 $\pm$ 137.26
<b>Serum creatinine (mg/dL)</b>	(n = 46)	
< 1	41	0.75 $\pm$ 0.14
> 1	5	4.24 $\pm$ 6.22
<b>OABSS (overactive bladder syndrome score)</b>	(n = 41)	
0–5	20	2.45 $\pm$ 1.61
6–9	13	7.15 $\pm$ 1.14
10–15	8	11.63 $\pm$ 1.77
<b>Pain rating scale (mm)<sup>b</sup></b>	(n = 40)	
0–50	26	11.19 $\pm$ 13.87
51–100	14	77.32 $\pm$ 13.85

**Table 2.** Clinicopathological features of ketamine abusers enrolled in this study. <sup>a</sup>Data from 2 to 16 cases of KA are not available for each feature. <sup>b</sup>A person rates his/her pain on a scale of 0 to 100 mm. Zero means “no pain”, and 100 means “the worst possible pain”.

**Urinary ketamine, norketamine and dehydronorketamine contents in KA.** Ketamine and its metabolites can be detected in biofluids, such as urine and plasma. Using tetra-deuterated ketamine, norketamine and dehydronorketamine as internal standards, we developed a LC-SRM-MS method to estimate the contents of ketamine and its metabolites in KA urine samples (“[Material and methods](#)” section). Figure S1 depicts the response curves of ketamine, norketamine and dehydronorketamine in a urine matrix background. The limit of detection (LOD) of ketamine, norketamine and dehydronorketamine with LC-SRM-MS was determined as 7.6, 36 and 176.8 ng/ml, respectively. Levels of ketamine and its metabolites in urine specimens of each KA were determined in triplicate (Table S2). Ketamine, norketamine and dehydronorketamine were detected and quantified in 26, 17 and 29 KA subjects, respectively, with concentration ranges of 47–7121 (ketamine), 64–5461 (norketamine) and 202–12,953 (dehydronorketamine) ng/ml. Notably, levels of ketamine and its metabolites were highly correlated (ketamine vs. norketamine ( $r = 0.96$ ,  $p < 0.001$ ), ketamine vs. dehydronorketamine ( $r = 0.924$ ,  $p < 0.001$ ), norketamine vs. dehydronorketamine ( $r = 0.943$ ,  $p < 0.001$ ); Fig. S2). In general, higher levels of ketamine and metabolites were detected in urine samples from KA with higher ketamine uptake before hospital admission and shorter examination time after ketamine uptake.

**Quantitative proteome profiling of urine samples from KA and healthy controls.** We applied the iTRAQ-based proteomics approach for quantitative comparison of the urinary proteome profiles for both genders of HC and KA groups using pooled urine protein samples from 4 subgroups (male HC, male KA, female HC and female KA; 10 cases for each group) as shown in Table 1. Prior to iTRAQ labeling, each urine sample was assessed via SDS-PAGE and silver staining to ensure protein quality. Starting from 36  $\mu$ g, a total of 1113 urinary proteins were quantified. Among the quantified proteins, levels of 143 and 137 proteins were elevated ( $> \text{mean} + 1\text{SD}$ ) and those of 104 and 118 proteins were reduced ( $< \text{mean} - 1\text{SD}$ ) in urine samples of male and female KA, respectively, with 93 elevated and 33 diminished proteins common to both genders (Table S3, Fig. 2A). A complete list of quantified proteins in urine samples of KA and healthy controls is presented in Table S4, and up- and downregulated proteins listed in Tables S5 and S6, respectively. The results showed that 1/10–1/5 urinary proteins are significantly altered in KA compared to healthy subjects, clearly indicating a profound effect of ketamine abuse on the urine protein profile. Assessment of the quantification data further revealed a good correlation between fold changes of up- and down-regulated proteins in both men and women (Fig. 2B), suggesting a similar effect of ketamine abuse on the urine protein profile in both genders. Determination of urinary proteins that are significantly altered in KA may be helpful in clarifying the mechanisms underlying ketamine induced cystitis frequently observed in cases of long-term ketamine abuse.

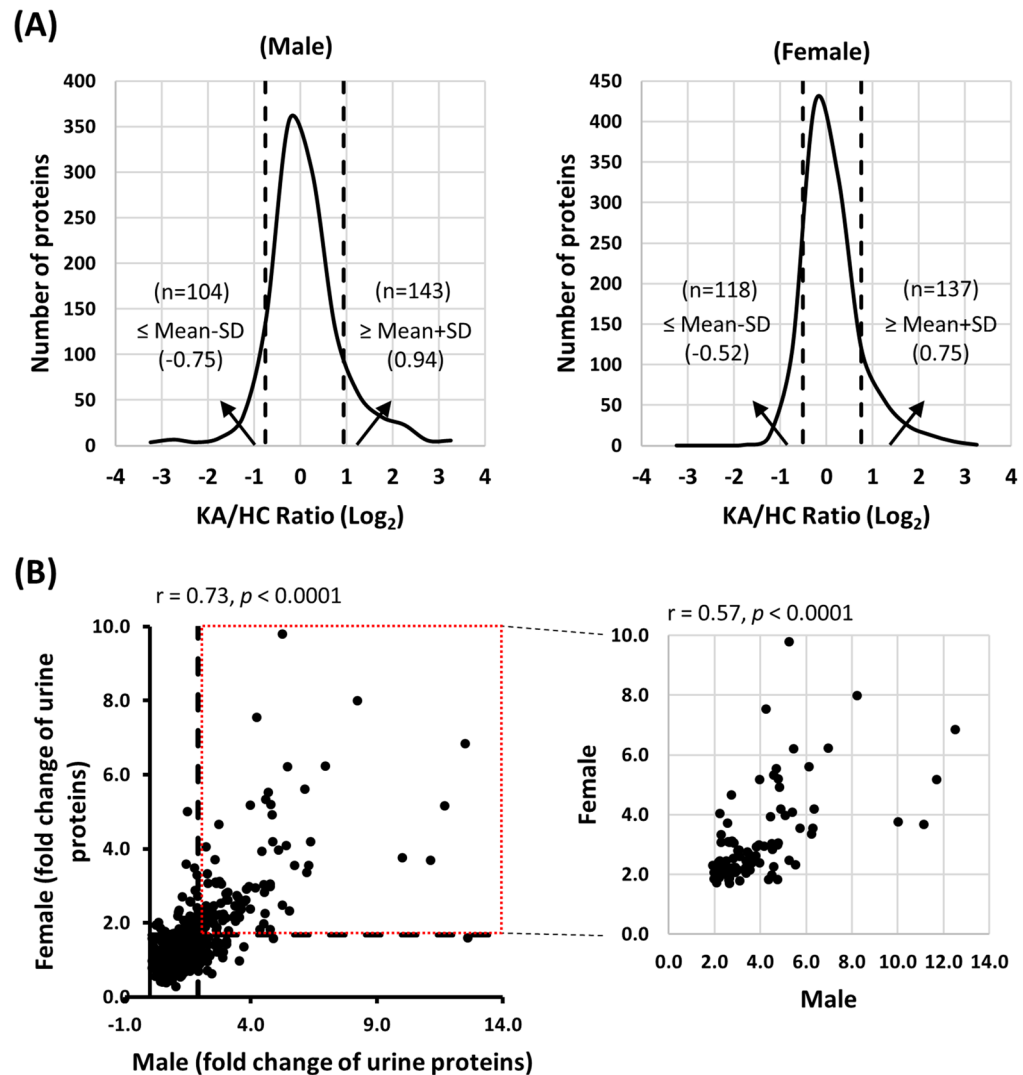
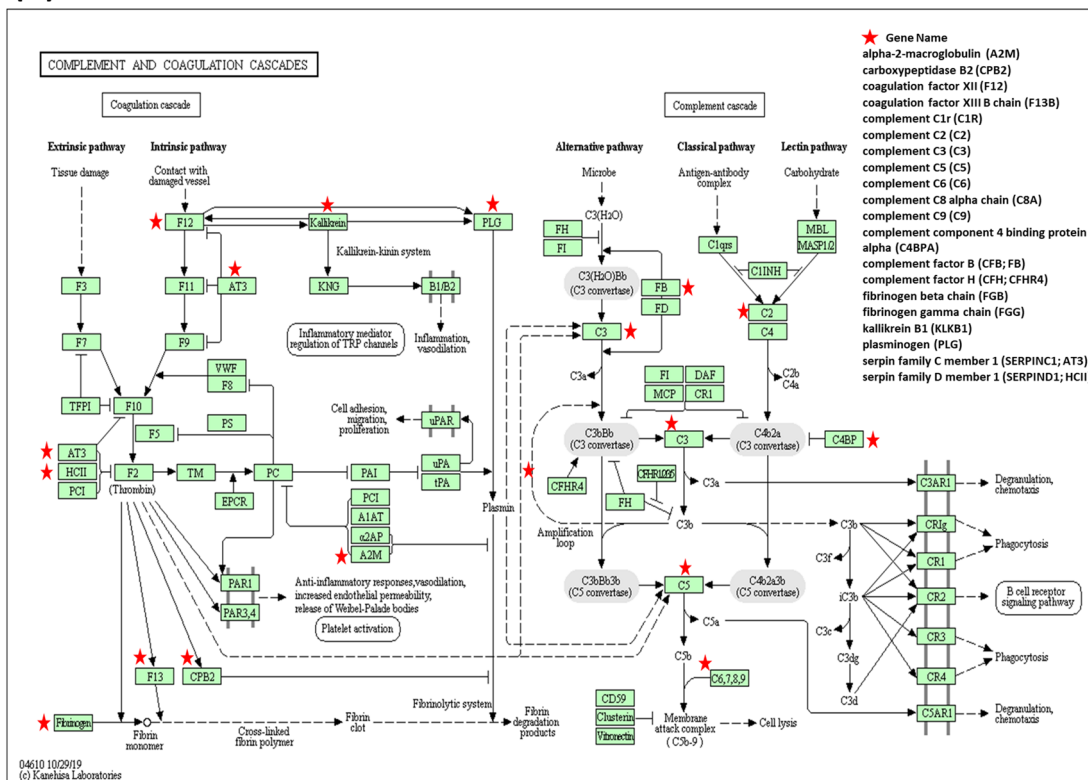


**Figure 2.** Quantitative comparison of urine proteome profiles between KA and HC for both genders. (A) Log<sub>2</sub> ratio distribution of the 1113 quantified urine proteins between KA and HC of male (left panel) and female (right panel) groups. The dashed lines indicate the boundaries at mean  $\pm$  SD. (B) Assessment of the correlation between fold changes of up- and downregulated proteins in both genders. Good correlation ( $r = 0.73$ ,  $p < 0.0001$ ) was observed for all the quantified proteins (left panel). Correlations of proteins showing  $>$  twofold changes in both genders were further analyzed ( $r = 0.57$ ,  $p < 0.0001$ ; right panel).

**Biological process network analysis of differentially regulated urinary proteins in KA.** To explore the biological processes potentially involved in the pathogenesis of ketamine cystitis, we applied DAVID, an integrated software suite for functional analysis of experimental data, to analyze the 126 differentially regulated urine proteins (93 elevated and 33 diminished) in both genders of the KA group. Gene ontology (GO) network analysis showed involvement of these differentially regulated proteins in networks of complement activation, proteolysis, fibrinolysis, innate immune response, platelet degranulation, and blood coagulation, among other functions (Table S7). Further KEGG pathway analysis confirmed ‘complement and coagulation cascades’ as the top pathway enriched from a proportion of differentially expressed proteins (protein count = 20,  $p$  value =  $1.001\text{E}-25$ , FDR =  $1.04\text{E}-22$ ; Table S8), which involves interactions among coagulation, complement system and fibrinolysis (Fig. 3A).

Bladder fibrosis resulting from irreversible injury to the bladder is one of the major symptoms of ketamine cystitis in heavy ketamine users. We searched FibroAtlas, a database of fibrotic diseases and associated genes<sup>21</sup>, to examine for fibrosis-related proteins in differentially expressed urinary proteins of KA. More than one-third (46 of 126) of the proteins were annotated as fibrosis-related proteins in the FibroAtlas database (Table S9). Among the 46 proteins, 32 were found to be related to hepatic fibrosis, cystic fibrosis, pulmonary fibrosis, idiopathic pulmonary fibrosis, cardiac fibrosis, renal fibrosis and/or acute interstitial pneumonia. Notably, ten have been identified as fibrosis biomarkers, specifically, apolipoprotein A-I, alpha-2-macroglobulin, serotransferrin, vitamin D-binding protein, chitinase-3-like protein 1, protein S100-A9, matrilysin, hemopexin, retinol-binding

(A)



(B)

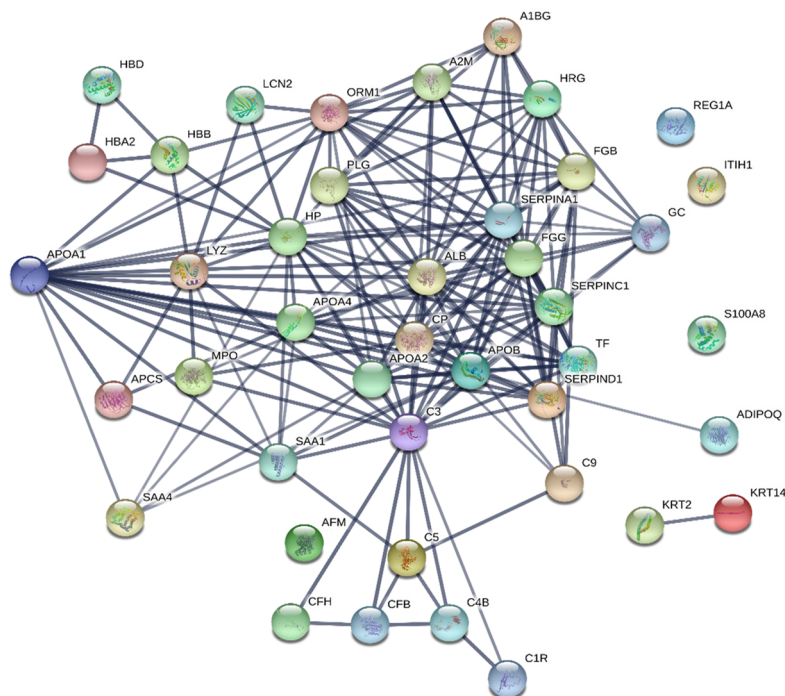


**Figure 3.** Biological process network analysis of differentially regulated urine proteins in KA. **(A)** KEGG pathway map for the complement and coagulation cascades identified as the top pathway enriched from a proportion of differentially expressed proteins (protein count = 20, denoted by asterisks). **(B)** Protein–protein interaction networks for 46 fibrosis-related proteins analyzed using STRING (PPI enrichment p-value < 10e-16, average local clustering coefficient of 0.583). Line thickness indicates the strength of data support.



protein 4 and osteopontin. Further analysis using the functional protein association network database (STRING) with a high confidence setting (0.7) showed tight/complex associations between fibrosis-related proteins (PPI enrichment  $p$ -value  $< 10^{-16}$ , average local clustering coefficient of 0.583; Fig. 3B).

Interestingly, several complement proteins, including complement C2, C3 and C5, have strong links to other fibrosis-related proteins ( $n = 16$ ,  $0.749 < \text{score} < 0.998$ ), some of which (APOA1, GC, SPP1, TF) are known biomarkers in idiopathic pulmonary, hepatic and cardiac fibrosis. The complement system stimulates immune functions, including inflammation, phagocytosis and membrane attack, and a series of immune responses<sup>22</sup>. Additionally, APOA1 acts as a hub linking other fibrosis-related proteins in this network analysis ( $n = 16$ ,  $0.740 < \text{score} < 0.999$ ; Fig. 3B), such as alpha-2-macroglobulin (A2M), apolipoprotein C-I (APOC1), fibrinogen gamma chain (FGG), haptoglobin (HP), hemopexin (HPX), and osteopontin (SPP1), most of which are activated in hepatic fibrosis. These results support an important role of APOA1 in ketamine-induced disorders.

**Verification of differentially regulated proteins in urine samples of healthy controls and KA.** According to iTRAQ results and relevance to ketamine cystitis, four upregulated (apolipoprotein A-I (APOA1), serum amyloid A-4 protein (SAA4), heparin cofactor 2 (SERPIND1) and plasminogen (PLG)) and one down-regulated (osteopontin (SPP1)) candidate proteins were selected for further verification in urine samples. Figure 4 depicts the results of MS analyses for quantification and identification of the five selected candidates (Fig. 4A) as well as western blot of urine samples originally used for iTRAQ experiments using specific antibodies against the five proteins (Fig. 4B). Our findings clearly showed consistency between MS-based and antibody-based quantification results, although the fold difference for target proteins was generally higher using western blot.

Next, we assessed levels of the five proteins in the 96 urine samples collected from 40 healthy controls and 56 KA via ELISA. However, upon testing of several commercially available ELISA kits, only two (for APOA1 and SAA4) could be confidently used for measuring levels in urine. Notably, levels of APOA1, but not SAA4, were significantly increased in KA relative to control samples ( $392.1 \pm 59.9$  ng/ml vs.  $13.7 \pm 32.6$  ng/ml for APOA1,  $p < 0.0001$ ;  $1.0 \pm 1.3$  ng/ml vs.  $0.99 \pm 2.1$  ng/ml for SAA4,  $p = 0.9$ ) (Fig. 4C). Three representative cases of increased APOA1 levels in individual urine samples detected via western blot are shown in Fig. 4D. The AUC value of ROC curve analysis for APOA1 in discrimination of KA ( $n = 56$ ) from controls ( $n = 40$ ) was 0.785 (Fig. 4E), supporting the utility of APOA1 as a potential urinary indicator of chronic ketamine abuse.

**Associations between urinary levels of ketamine and its metabolites and clinicopathological features.** Data on associations between urinary ketamine and metabolite levels and clinicopathological features (5 items) are shown in Table 3. OABSS of the KA group were significantly associated with levels of ketamine ( $r = 0.338$ ,  $p = 0.038$ ), norketamine ( $r = 0.348$ ,  $p = 0.030$ ) and dehydronorketamine ( $r = 0.463$ ,  $p = 0.003$ ). Ketamine ( $r = 0.358$ ,  $p = 0.030$ ), but not norketamine and dehydronorketamine, showed significant association with the pain rating scale of KA. Urinary RBC and WBC counts and serum creatinine levels were not significantly associated with levels of ketamine and its metabolites.

**Associations between urinary APOA1/SAA4 levels and clinicopathological features of KA.** Urinary APOA1 was significantly associated with RBC ( $r = 0.463$ ,  $p = 0.002$ ), WBC ( $r = 0.721$ ,  $p < 0.001$ ), OABSS ( $r = 0.426$ ,  $p = 0.006$ ) and pain rating scale ( $r = 0.392$ ,  $p = 0.012$ ), but not serum creatinine, or urinary levels of ketamine and its metabolites (Table 4). Urinary SAA4 was significantly correlated with OABSS ( $r = 0.415$ ,  $p = 0.007$ ) but no other clinicopathological features or urinary levels of ketamine and its metabolites.

## Discussion

Urine is an information-rich fluid containing numerous proteins produced or shed in the kidney and urogenital tract. Alterations of the human urinary proteome profile have been reported in response to disease or drug toxicity, particularly those affecting the kidney and urogenital tract<sup>23</sup>. Although the detrimental effect of ketamine abuse on the lower urinary tract has been well established for more than a decade, very little is known about the urinary proteome profile and its association with ketamine-induced LUTS in KA. To our knowledge, the present study is the first to explore this issue by simultaneously evaluating the levels of urine ketamine and its metabolites in KA, comparing the urinary proteome profiles between KA and control subjects, and assessing their relationships with the clinicopathological features of KA.

Using LC-SRM-MS, the concentration ranges of ketamine and its metabolites in urine specimens of KA collected in this study were determined as 47–7121 ng/ml (for ketamine, median 584 ng/ml), 64–5461 ng/ml (for norketamine, median 730 ng/ml) and 202–12,953 ng/ml (for dehydronorketamine, median 2212 ng/ml). Our data are consistent with the findings of Cheng et al.<sup>24</sup> on levels of ketamine and its metabolites in 22 urine specimens collected from suspected drug users in Taiwan in 2004 determined via gas chromatography–mass spectrometry (GC–MS). The group found that the concentration range of ketamine was the narrowest (20–7196 ng/ml) with the lowest median (332 ng/ml) while that of dehydronorketamine was the widest (36–17,629 ng/ml) with the highest median (891 ng/ml). The concentration range of NK was between 25 and 7685 ng/ml<sup>24</sup>. It is noted that only in half of the KA subjects that ketamine, norketamine and/or dehydronorketamine were detected (Table S2). The reasons for this observation can be manifold. First, inspection time after ketamine uptake varied significantly between KA subjects (0–24 days). Longer inspection time after ketamine uptake would allow metabolization of more ketamine and removal of more metabolized ketamine from the body via urinary excretion. Second, average dose of ketamine consumption for 90 days prior to admission differed significantly between KA subjects (0.5–10 g/day). Clearing of ketamine from the body would be faster in KA subjects with less dose of ketamine consumption. Third, personal variation of KA subjects in the ability to metabolize ketamine

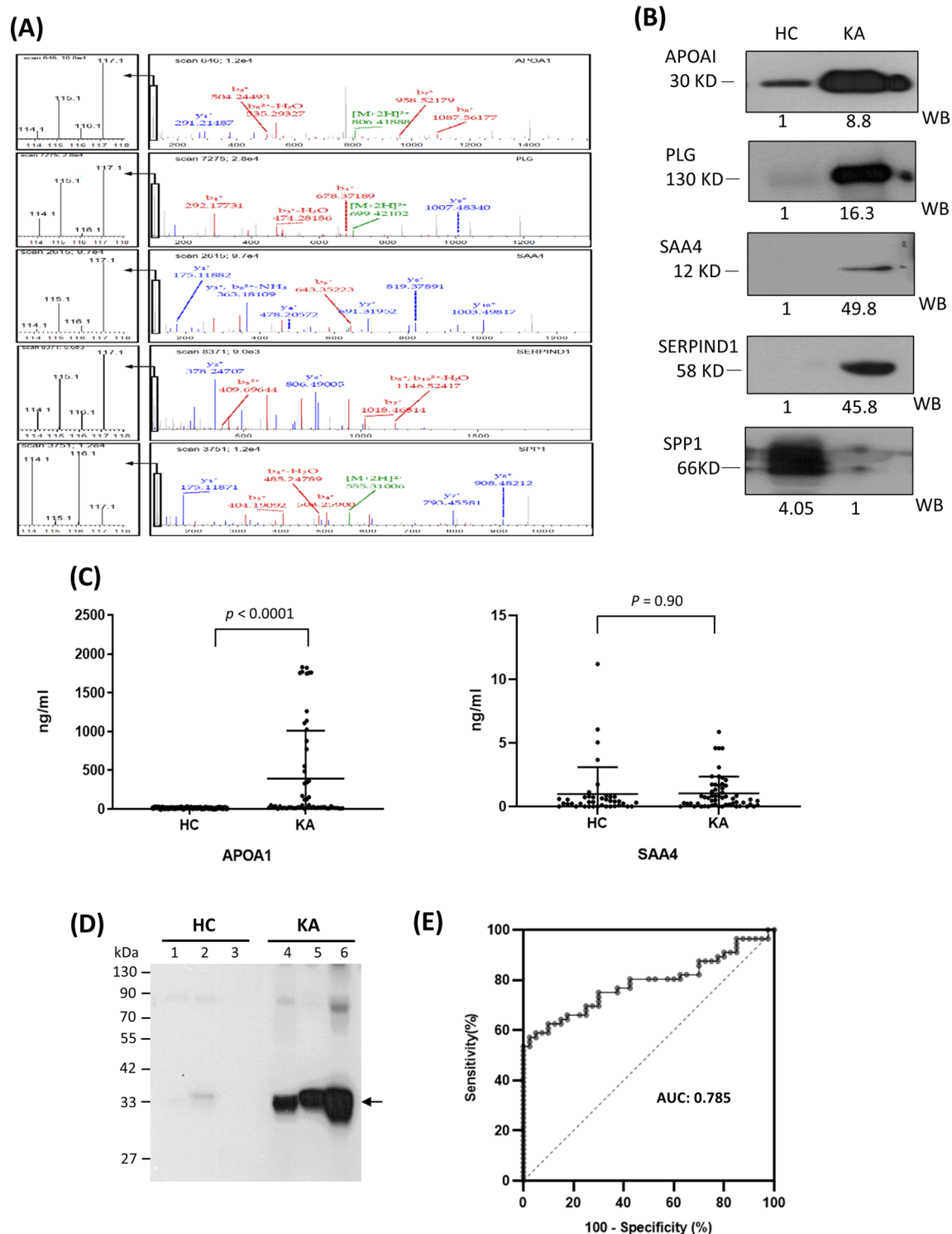


**Figure 4.** Validation of differentially regulated proteins in urine samples of HC and KA groups. **(A)** LC-MS/MS quantification of five selected proteins (APOA1, PLG, SAA4, SERPIND1 and SPP1) with significantly altered urinary levels between HC and KA. The low mass reporter ion region (used for quantification) in the right panel is enlarged in the left panel. **(B)** Western blot analysis of the five selected proteins (50  $\mu$ g) in urine samples pooled respectively from HC and KA (three males and three females per group). Relative levels of each protein quantified from the Western blot are denoted below the respective image. Full images of the cropped blots are detailed in Fig. S3. **(C)** ELISA analysis of APOA1 and SAA4 levels in individual urine samples from 40 HC and 56 KA. **(D)** Western blot analysis of APOA1 in urine samples (50  $\mu$ g protein) from three HC and three KA. The position of APOA1 is denoted with an arrow. **(E)** ROC curve analysis of APOA1 with utility in differentiating KA from HC.

Item	Feature (case no.)	K		NK		DHNK	
		r	p-value	r	p-value	r	p-value
1	Urine RBC (n = 44)	0.209	0.207	0.083	0.610	0.177	0.257
2	Urine WBC (n = 44)	0.127	0.447	−0.045	0.781	0.061	0.699
3	Serum creatinine (n = 46)	0.210	0.193	0.226	0.149	0.210	0.166
4	OABSS (n = 41)	0.338	0.038	0.348	0.030	0.463	0.003
5	Pain rating scale (n = 40)	0.358	0.030	0.255	0.122	0.231	0.158

**Table 3.** Associations between urinary contents of ketamine and metabolites and clinicopathological features of KA. *K* ketamine, *NK* norketamine, *DHNK* dehydronorketamine, *OABSS* overactive bladder syndrome score.

Item	Feature (case no.)	APOA1		SAA4	
		r	p-value	r	p-value
1	Urine RBC (n = 44)	0.463	0.002	0.108	0.485
2	Urine WBC (n = 44)	0.721	0.000	0.090	0.562
3	Serum creatinine (n = 46)	0.007	0.962	0.136	0.367
4	OABSS (n = 41)	0.426	0.006	0.415	0.007
5	Pain rating scale (n = 40)	0.392	0.012	0.279	0.082
6	[K] (n = 56)	0.202	0.16	0.101	0.486
7	[NK] (n = 56)	0.066	0.641	0.017	0.906
8	[DHNK] (n = 56)	0.196	0.151	0.159	0.247

**Table 4.** Correlations among clinicopathological features, APOA1 and SAA4 urine levels in 56 KA.

and remove metabolized ketamine from the body. All these factors can affect the detection/quantification of ketamine, norketamine and dehydronorketamine in the urine specimens of KA subjects enrolled in the present cross-sectional study.

Overactive bladder syndrome caused by serious bladder inflammation is frequently observed in KA. A recent survey on 106 KA cases in Taiwan reported that 84% ketamine users developed LUTS after two years, with an estimated OABSS of  $5.25 \pm 4.43^{14}$ . Among the 41 KA with available OABSS data enrolled in this study, 21 (51%, 21/41) had OABSS > 6 (Table 2), indicating moderate to severe overactive bladder syndrome in more than half the KA participants. Based on both sets of available data (urinary levels of ketamine and metabolites and clinicopathological features of KA), we observed a positive association between overactive bladder syndrome (assessed via OABSS) and urinary levels of ketamine and its metabolites in KA (Table 3). While the reason for this correlation is currently unknown, recent findings on the ability of ketamine to induce inflammation and promote apoptosis in bladder tissues of a rat model and human SV-HUC-1 uroepithelial cells through regulating the NLRP3/TXNIP axis may provide an important clue<sup>18</sup>. It is possible that urinary ketamine directly activates the TXNIP/NLRP3 signaling pathway in uroepithelial cells to generate an inflammatory microenvironment in the affected bladder, which serves as one of the main factors causing overactive bladder syndrome<sup>25</sup>. However, some confounding factors need to be considered in the study of association between OABSS and urinary levels of ketamine and its metabolites in KA, including high variation of examination times after ketamine uptake, detoxification treatment, duration of ketamine use, and any other diseases which might influence the results potentially, such as urinary infection and sexually transmitted diseases.

Using pooled urine protein samples and the iTRAQ-based proteomics approach, we generated the first quantitative urine proteome map comparing KA and healthy control subjects of both genders. Consequently, a total of 126 differentially regulated proteins were identified (Table S3). Further bioinformatics analysis revealed 'complement and coagulation cascades' as the top pathway enriched from these differentially regulated proteins (Table S7, Fig. 3A). Moreover, one-third (46 out of 126) of the differentially regulated proteins were annotated as fibrosis-related proteins in the FibroAtlas database, including several (A2M, FGG, CPB2, C3, F13B, CFB, C2 and C5) in the complement and coagulation cascades (Table S8). An association between the complement and coagulation cascades and specific fibrotic diseases has been previously reported<sup>26,27</sup>. For example, the extrinsic coagulation pathway together with C5a can promote fibrosis in bronchopulmonary dysplasia (a serious pulmonary fibrotic disorder) via the endothelin-1 signaling pathway<sup>26</sup>. Moreover, significant upregulation of proteins in the complement and coagulation cascades has been observed in colon and rectal tissues in a rat model of radiation-induced colorectal fibrosis<sup>27</sup>. These observations, together with our findings, raise the intriguing possibility that the complement and coagulation cascades are involved in the process of bladder fibrosis frequently observed in heavy ketamine users. Further experiments are essential to validate this hypothesis and the associated mechanisms.

Among the upregulated candidate proteins in urine samples, we successfully detected increased levels of APOA1 via ELISA in KA (n = 56) relative to healthy controls (n = 40) (Fig. 4C–E). This increase was significant,



since all 40 healthy controls contained low urinary APOA1 levels (0–26.2 ng/ml) whereas more than half (30 out of 56) KA displayed markedly higher urinary APOA1 levels (27.2–1830.8 ng/ml), indicating good power of urinary APOA1 to discriminate KA from control subjects ( $AUC = 0.785$ ). Notably, we observed significant association of urinary APOA1 levels with OABSS and pain rating scale in addition to urinary RBC/WBC levels (Table 4). To our knowledge, APOA1 represents the first urine protein component associated with ketamine-induced bladder dysfunction. Moreover, among the clinical parameters, urinary APOA1 showed the highest correlation with WBC level ( $r = 0.721$ ,  $p < 0.001$ ) (Table 4), an important quantitative indicator of inflammation in the kidney or lower urinary tract. This finding suggests that ketamine-induced inflammation in the kidney or lower urinary tract serves as the major factor underlying elevation of urinary APOA1.

The issue of whether the drastic increase in urinary APOA1 plays a pathophysiological role in the disease process of ketamine-induced bladder dysfunction remains unclear. APOA1, a major component of high-density lipoprotein (HDL) in plasma, mediates the reverse transport of cholesterol from peripheral cells to the liver for excretion<sup>28,29</sup>. In addition to its potential protective effects on the cardiovascular system and lowering of cardiovascular disease risk, accumulating evidence over the past decade supports the multifunctional nature of APOA1 with immunity, anti-inflammation, apoptosis, anti-clotting and anti-aggregatory effects<sup>30</sup>. Regarding anti-inflammation activity, APOA1 acts as a “negative” acute-phase protein that inhibits the production of interleukin-1 $\beta$  and tumor necrosis factor- $\alpha$  by blocking contact-mediated activation of monocytes by T lymphocytes<sup>31</sup>. Interestingly, an idiopathic pulmonary fibrosis (IPF) animal model study showed that intranasal treatment with APOA1 protein reduced the bleomycin-induced increase in the number of inflammatory cells and collagen deposition in sham-treated mice in a dose-dependent manner, demonstrating anti-inflammatory and anti-fibrotic effects of APOA1 protein on experimental lung injury and fibrosis<sup>32</sup>. These previous findings raise another intriguing possibility that elevated urinary APOA1 modulates acute or chronic inflammation during ketamine-induced stress on bladder cells, which warrants further in-depth investigation.

One of the main limitations of this study is the small sample size used to verify the differentially regulated proteins identified via iTRAQ proteomics. The validity of our findings should be tested with larger collections of samples from different hospitals. Another limitation is the cross-sectional design of our study in which only one urine specimen was obtained for each KA. Multiple urine samples longitudinally collected from a set of KA subjects during the entire detoxification period should allow in-depth analysis of the correlations among urine ketamine and its metabolites, urinary proteins and clinical features for individual subjects and minimize the effects of personal variability.

Using the iTRAQ-based proteomics approach, we have demonstrated quantitative changes in the urine proteome profile in KA relative to healthy controls. Many of the differentially regulated proteins are involved in the complement and coagulation cascades and/or fibrotic disease. Among numerous up- and downregulated candidate proteins, a significant increase in APOA1 expression in urine samples of KA was detected via ELISA. This information, together with the urinary levels of ketamine, norketamine and dehydronorketamine (measured via LC-SRM-MS) and clinical data (assessed via laboratory tests and a questionnaire-based survey), supports positive associations of urinary ketamine and APOA1 with OABSS and pain rating scale, two of the main bladder dysfunction symptoms of KA. Identification of APOA1 as the first urinary protein component associated with ketamine-induced bladder dysfunction may aid in developing new molecular tool(s) for management of ketamine-associated LUTS. Moreover, information regarding the differentially regulated proteins in urine of KA provides valuable clues to establish the molecular mechanisms underlying ketamine-induced cystitis.

## Material and methods

**Study subjects and sample collection.** All ketamine abusers (KA) and age-matched healthy controls (HC) included for study were over 20 years of age. All HC urine samples ( $n = 40$ ) were collected at Chang Gung University, Taoyuan, Taiwan, and urine samples of KA ( $n = 56$ ) admitted to an addiction center for ketamine detoxification obtained at Taipei City Psychiatric Center between 2014 and 2017. All urine samples were stored at  $-80^{\circ}\text{C}$ . The study protocol was approved by the Medical Ethics and Human Clinical Trial Committee at Chang Gung Memorial Hospital, Taiwan, and Taipei City Hospital (Taipei, Taiwan). Experiments were conducted according to the principles of the Declaration of Helsinki and reviewed and approved by the Institutional Review Board (IRB) of Chang Gung Medical Foundation (Taoyuan, Taiwan; IRB no:106-0191C), and Taipei City Hospital (Taipei, Taiwan; IRB no: TCHIRB-1030408). Prior to sample collection, an IRB-approved informed consent form was signed by each participant. The inclusion criteria were as follows: (1) age between 18 and 60 years; (2) fulfilling DSM-IV-TR criteria for ketamine dependence as verified by two board-certified psychiatrists; (3) last ketamine use within 30 days (by self-report) prior to admission; (4) an ability to read Chinese and provide informed consent. The exclusion criteria were: (1) other substance use disorder (including abuse and dependence) in the past year except nicotine; (2) history of schizophrenia, bipolar disorder, or major depressive disorder, or having been treated with antipsychotics, mood stabilizers (including lithium, valproic acid, carbamazepine, and quetiapine), or antidepressants; (3) history of systemic medical illnesses such as hypertension, metabolic disorders (e.g., diabetes mellitus), or renal or liver diseases; (4) history of head injury, loss of consciousness, or neurological disorders; (5) inability or refusal to provide urine sample. Healthy controls were enrolled from the volunteers in Chang Gung University with inclusion criteria as follows: (1) age between 18 and 60 years; (2) no other substance use disorder (including abuse and dependence) in the past year, except nicotine; (3) no known systemic or neurological diseases such as hypertension, metabolic disorders (e.g., diabetes mellitus), or renal or liver diseases; (4) an ability to read Chinese and provide informed consent. All the participants were given a comprehensive description of the study and then recruited after giving written informed consent. The demographic characteristics of the 96 enrolled subjects are shown in Table 1 and clinical information on 56 KA (including laboratory data on urine/serum samples, OABSS and pain rating scales) in Table S1. For evalu-

ation of overactive bladder syndrome, a total OABS score of  $\leq 5$  is defined as mild, 6–11 as moderate, and  $\geq 12$  as severe<sup>13</sup>. The first morning urine samples were collected in the presence of a protease inhibitor cocktail tablet (one tablet per 50 ml urine; Roche, Mannheim, Germany) and 1 mM sodium azide. Samples were centrifuged at 5000×g for 30 min at 4 °C within 5 h to remove cells and debris, and supernatant fractions stored at –20 °C until further use.

**LC-SRM-MS analysis of ketamine and metabolites in urine samples.** Ketamine and its metabolites (norketamine and dehydronorketamine) were quantified using the LC-MS/MS-based assay according to the method of Parkin et al.<sup>33</sup>, with slight modifications. Briefly, urine samples were spiked with an equal volume of a mixture of tetra-deuterated ketamine (ketamine-D4) (Cerilliant, Round Rock, TX, USA) and its derivatives (norketamine-D4 and dehydronorketamine-D4) (Toronto Research Chemicals, Ontario, Canada) at 1 pmol/μl in 0.1% formic acid in methanol. Urine samples were centrifuged at 10,000×g for 10 min at 4 °C, and the collected supernatant fractions subjected to LC-MS/MS analysis in the selected reaction monitoring (SRM) mode using Waters ACQUITY UPLC (ultra-performance liquid chromatography; Hertfordshire, UK) coupled with a HCT ultra mass spectrometer (Bruker Daltonik GmbH, Bremen, Germany). The mobile system was as follows: A, 0.1% formic acid in water and B, acetonitrile with 0.1% formic acid. The flow rate was 60 μl/min and a linear gradient was set as follows: 0 min, 8% B; 2 min, 8% B; 12 min, 18% B; 14 min, 20% B; 15 min, 95% B; 18 min, 95% B. MS data were acquired in the SRM mode: isolation with a 10 amu peak width the first time and 1 amu the second time, followed by smart fragmentation ramping from 0.3 to 2 V. The peak areas of fragments were detected and integrated using the software package DataAnalysis 4.2. (Bruker Corporation, MA, USA).

Quantification was performed by calculating the peak area ratio of the product ion for ketamine (m/z 220.1) to its tetra-deuterated analog (m/z 224.1) ketamine-d4, norketamine (m/z 207.1) to norketamine-d4 (m/z 211.1), and likewise, dehydronorketamine (m/z 205.0) to dehydronorketamine-d4 (m/z 209.0). Each urine sample was analyzed in triplicate, and levels of ketamine, norketamine and dehydronorketamine calculated as mean ± SD (ng/ml). Assay linearity for ketamine, norketamine and dehydronorketamine was determined by constructing response curves from urine to which no or nine different concentrations (fivefold serial dilutions ranging from 50 to 0.128 fmol/μl) of ketamine, norketamine and dehydronorketamine were added as calibrants (0.5 pmol/μl tetra-deuterated analog). A linear regression model with a weighting function of log-transformed light to heavy ratio (X axis) and peak area (Y axis) was applied and linearity achieved with  $R^2 \geq 0.995$ . The limit of detection (LOD) was defined as the lowest concentration with a mean signal-to-noise ratio of  $\geq 3$  based on the peak height of all three ion transitions and limit of quantification (LOQ) as signal-to-noise ratio  $\geq 10$  of the quantifying ion and at least 3 for the two qualifying transitions.

**Concentration and desalting of urine samples.** Urine proteins were concentrated using a 10 kDa centrifugal filter (Millipore, Carrigtwohill, Ireland) as described previously<sup>34</sup>. Briefly, urine samples (12.5 ml) were centrifuged at 5000×g for 30 min at 4 °C in a filter tube, followed by the addition of 12.5 ml of 20% acetonitrile/H<sub>2</sub>O and re-centrifugation. This process was repeated once using pure water for desalting. Samples were subjected to an additional desalting step using 4 ml H<sub>2</sub>O to avoid possible interference from metabolites in the labeling reaction for iTRAQ labeling. After estimation of protein quantity with a Pierce BCA protein assay kit (Thermo Scientific, MA, USA), each concentrated/desalted urine sample was lyophilized and stored at –80 °C for subsequent processing.

**Tryptic digestion of urinary proteins and iTRAQ reagent labeling.** We applied pooled urine samples from different groups (male HC, male KA, female HC and female KA; 10 cases per group) for iTRAQ-based quantitative proteomics analysis to minimize individual variations and enhance signals. The 10 cases were randomly selected from each subgroup with age between 26 and 36 to generate gender- and age-matched subgroups. Equal amounts of protein (10 μg) from individual samples were pooled into a subgroup. Pooled urinary protein (100 μg) from each subgroup was reduced, cysteine-blocked and digested with trypsin at 37 °C for 16 h as described previously<sup>34</sup>. Digested peptides were labeled with iTRAQ reagent (Applied Biosystems, Foster City, CA, USA) according to the manufacturer's protocol. Peptide mixtures of male HC, male KA, female HC and female KA were labeled with iTRAQ tags 114, 115, 116 and 117, respectively. After incubation at room temperature for 1 h, peptide mixtures were pooled and desalted via SPE (solid phase extraction) of Oasis HLB (30 μm) cartridges (Waters, Massachusetts, USA) and vacuum dried.

**Two-dimensional LC-MS/MS analysis.** Dried iTRAQ labeling peptides (30 μg) were reconstituted in 50 μl HPLC mobile phase A (30% acetonitrile/0.1% formic acid) and loaded onto a homemade strong cation exchange chromatography (SCX) column (Luna SCX 5 μm, 0.5 × 255 mm, Phenomenex, Torrance, CA, USA) at flow rate of 5 μl/min for 30 min. Peptides were eluted with 0–100% HPLC mobile phase B (0.5 M ammonium chloride/30% acetonitrile/0.1% formic acid) and separated into 66 fractions using online 2D-HPLC (Dionex Ultimate 3000; Thermo Fisher, San Jose, CA, USA). Each SCX fraction was further diluted in-line prior to trap of reverse-phase column (Zorbax 300SB-C18 5 μm, 0.3 × 5 mm; Agilent Technologies, Wilmington, DE, USA) and diluted peptides were resolved on an analytical C18 column (Synergi Hydro-RP 2.5 μm, 0.075 × 200 mm with a 15 μm tip; Phenomenex, Torrance, CA, USA). A linear gradient of fractionation was applied as follows: 3–28% HPLC mobile phase C (99.9% acetonitrile/0.1% formic acid) for 37 min, 28–50% mobile phase C for 12 min, 50–95% mobile phase C for 2 min, 95% mobile phase C for 5 min, and 3% mobile phase C for 9 min), with a flow rate of 0.3 μl/min. LC apparatus was coupled with a two-dimensional linear ion trap mass spectrometer (LTQ-Orbitrap ELITE; Thermo Fisher, San Jose, CA, USA) controlled by Xcalibur 2.2 software (Thermo Fisher, San Jose, CA, USA). Full-scan MS was performed in the Orbitrap over a range of 400 to 2000 Da and a resolu-

tion of 60,000 at  $m/z$  400. Internal calibration was performed using the ion signal of  $[\text{Si}(\text{CH}_3)_2\text{O}]_6\text{H}^+$  at  $m/z$  445.120025, 462.146574, and 536.165365 as lock masses. The twelve data-dependent MS/MS scan events of six collision-induced dissociation (CID) mode and six high-energy collision induced dissociation (HCD) mode were followed with one MS scan for the six most abundant precursor ions in a preview MS scan.

**Sequence database search and quantitative data analysis.** Data analysis was performed using Proteome Discoverer software (version 1.4, Thermo Fisher Scientific) involving the reporter ion quantifier node for iTRAQ quantification. MS/MS spectra were searched against the Swiss-Prot human sequence database (released on 20,150,429, selected for *Homo sapiens*, 20,199 entries) using the Mascot search engine (Matrix Science, London, UK; version 2.2.6). For protein identification, the precursor mass tolerance was set to 10 ppm and fragment ion mass tolerance to 0.5 Da for CID mode by ion analysis and 0.05 Da for HCD mode by orbitrap analysis, with allowance for one missed cleavage from tryptic digestion. Fixed modification was set to methylthiolation at cysteine (+45.99 Da) and variable modification to acetylation at protein N-terminus (+42.01 Da), oxidation at methionine (+15.99 Da), pyroglutamate conversion at N-terminal glutamine (−17.03 Da) and iTRAQ4-plex labeling at lysine and peptide N-terminus (+144.10 Da). Data were filtered based on medium confidence of peptide identification to ensure an overall false discovery rate below 0.01. Proteins with a single peptide hit were removed, and quantitative data exported as Excel files from Proteome Discoverer and manually normalized, such that  $\log_2$  of iTRAQ ratio displayed a median value of zero for all peptides in a single given protein. Proteins with  $\log_2$  ratios above the mean of all  $\log_2$  ratios plus one standard deviation (SD) of all  $\log_2$  ratios were considered upregulated, and those with  $\log_2$  ratios below the mean minus one SD were classified as downregulated.

**Bioinformatics and network analysis.** The Database for Annotation, Visualization, and Integrated Discovery (DAVID, v6.7, <http://david.abcc.ncifcrf.gov/>) and Kyoto Encyclopedia of Genes and Genomes (KEGG) database resource were used to test for the enrichment of biological processes<sup>35,36</sup>. Proprietary gene ontology (GO) biological process with a false-discovery rate (FDR) < 0.05 was considered significant in enrichment analysis. Fibrosis-related proteins were retrieved from FibroAtlas, a database for the exploration of fibrotic diseases and their genes<sup>21</sup>. Protein–protein interaction networks were analyzed using STRING: functional protein association networks (version 11.0)<sup>37</sup>.

**Western blot analysis.** Western blot was analysis performed as described previously<sup>34</sup>. Briefly, urine samples (containing 50  $\mu\text{g}$  protein) were resolved on 10% SDS gels and transferred to PVDF membrane that were probed using primary antibodies against the candidate proteins of interest, including anti-APOA1 (Proteintech, Rosemont, USA), anti-SERPIND1 (Proteintech), anti-osteopontin (Proteintech), anti-plasminogen (Thermo Fisher, Rockford, USA) and anti-SAA4 (Abnova, Taipei, Taiwan). The relative signal intensity of each target protein detected in the blots was quantified using a computing densitometer (Molecular Dynamics, Sunnyvale, CA).

**Quantification of APOA1 and SAA4 by ELISA.** APOA1 and SAA4 levels in urine samples were measured using sandwich ELISA kits (R&D Systems, MN, USA) and Elabscience (Hubei, China), respectively, according the manufacturers' protocols. Briefly, 100  $\mu\text{l}$  of each urine sample (2- and fourfold diluted for HC and KU subjects, respectively) was added to the wells of antibody-coated microplates and incubated at room temperature for 2 h, followed by five washes with wash buffer. Biotinylated antibody was added to the wells and incubated for 1 h. After a further five washes with wash buffer, 200  $\mu\text{l}$  substrate solution was added to each well and incubated for 30 min at room temperature. Finally, 50  $\mu\text{l}$  stop solution was added to each well and the color intensity measured at different times at a wavelength of 450 nm using a Spectra Max M5 microplate reader (Molecular Devices, Sunnyvale, CA).

**Statistical analysis.** The correlations between ELISA data and clinicopathological features of patients were analyzed with the non-parametric Mann–Whitney U test using the statistical package SPSS 15.0 (SPSS Inc., Chicago, IL, USA). Receiver operator characteristic (ROC) curve and area under the curve (AUC) analyses were utilized to detect the optimal cutoff point that produced the greatest total accuracy for clinical classification. Spearman correlation analysis was applied to assess the correlations between urine contents of ketamine (and metabolites), ELISA data and clinicopathological features of ketamine users. Results are presented as coefficient of correlation ( $r$ ) and the corresponding  $p$ -value. Statistical assessments were two-tailed and significance set at  $p < 0.05$ .

**Ethics approval and consent to participate.** The study protocol was approved by the Medical Ethics and Human Clinical Trial Committee at Chang Gung Memorial Hospital, Taiwan and Taipei City Hospital, Taipei, Taiwan. This study was conducted according to the principles expressed in the Declaration of Helsinki and was reviewed and approved by the Institutional Review Board (IRB) of Chang Gung Medical Foundation, Taoyuan, Taiwan (IRB no:106-0191C) and Taipei City Hospital, Taipei, Taiwan (IRB no: TCHIRB-1030408). All subjects gave their written informed consent.

### Data availability

The datasets generated and/or analyzed in the current study are not publicly available due to patient privacy, however they are available from the corresponding author on reasonable request.

Received: 22 December 2020; Accepted: 21 April 2021

Published online: 05 May 2021

# References

- Domino, E. F. Taming the ketamine tiger. 1965. *Anesthesiology* **113**, 678–684. <https://doi.org/10.1097/ALN.0b013e3181ed09a2> (2010).
- Hijazi, Y. & Boulieu, R. Contribution of CYP3A4, CYP2B6, and CYP2C9 isoforms to N-demethylation of ketamine in human liver microsomes. *Drug Metab. Dispos.* **30**, 853–858. <https://doi.org/10.1124/dmd.30.7.853> (2002).
- Huang, M. H. *et al.* Performance characteristics of ELISAs for monitoring ketamine exposure. *Clin. Chim. Acta* **379**, 59–65. <https://doi.org/10.1016/j.cca.2006.12.013> (2007).
- Harun, N., Anderson, R. A. & Miller, E. I. Validation of an enzyme-linked immunosorbent assay screening method and a liquid chromatography-tandem mass spectrometry confirmation method for the identification and quantification of ketamine and nor-ketamine in urine samples from Malaysia. *J. Anal. Toxicol.* **33**, 310–321. <https://doi.org/10.1093/jat/33.6.310> (2009).
- Dillon, P., Copeland, J. & Jansen, K. Patterns of use and harms associated with non-medical ketamine use. *Drug Alcohol Depend.* **69**, 23–28. [https://doi.org/10.1016/s0376-8716\(02\)00243-0](https://doi.org/10.1016/s0376-8716(02)00243-0) (2003).
- Shahani, R., Streutker, C., Dickson, B. & Stewart, R. J. Ketamine-associated ulcerative cystitis: A new clinical entity. *Urology* **69**, 810–812. <https://doi.org/10.1016/j.urology.2007.01.038> (2007).
- Morgan, C. J., Curran, H. V. & Independent Scientific Committee on Drugs. Ketamine use: A review. *Addiction* **107**, 27–38. <https://doi.org/10.1111/j.1360-0443.2011.03576.x> (2012).
- Chu, P. S. *et al.* The destruction of the lower urinary tract by ketamine abuse: A new syndrome?. *BJU Int.* **102**, 1616–1622. <https://doi.org/10.1111/j.1464-410X.2008.07920.x> (2008).
- En-Meng, S.-T.W., Cha, T.-L., Sun, G.-H., Yu, D.-S. & Chang, S.-Y. A murderer of young bladders: Ketamine-associated cystitis. *Urol. Sci.* **24**, 113–116 (2013).
- Gu, D. *et al.* Long-term ketamine abuse induces cystitis in rats by impairing the bladder epithelial barrier. *Mol. Biol. Rep.* **41**, 7313–7322. <https://doi.org/10.1007/s11033-014-3616-5> (2014).
- Lin, C. C., Lin, A. T., Yang, A. H. & Chen, K. K. Microvascular injury in ketamine-induced bladder dysfunction. *PLoS ONE* **11**, e0160578. <https://doi.org/10.1371/journal.pone.0160578> (2016).
- Duan, Q. *et al.* Changes to the bladder epithelial barrier are associated with ketamine-induced cystitis. *Exp. Ther. Med.* **14**, 2757–2762. <https://doi.org/10.3892/etm.2017.4913> (2017).
- Yamaguchi, O. *et al.* Clinical guidelines for overactive bladder. *Int. J. Urol.* **16**, 126–142. <https://doi.org/10.1111/j.1442-2042.2008.02177.x> (2009).
- Li, C. C. *et al.* A survey for ketamine abuse and its relation to the lower urinary tract symptoms in Taiwan. *Sci. Rep.* **9**, 7240. <https://doi.org/10.1038/s41598-019-43746-x> (2019).
- Baker, S. C., Shabir, S., Georgopoulos, N. T. & Southgate, J. Ketamine-induced apoptosis in normal human urothelial cells: A direct, N-methyl-D-aspartate receptor-independent pathway characterized by mitochondrial stress. *Am. J. Pathol.* **186**, 1267–1277. <https://doi.org/10.1016/j.ajpath.2015.12.014> (2016).
- Gu, D. *et al.* Ketamine induces endoplasmic reticulum stress in rats and SV-HUC-1 human uroepithelial cells by activating NLRP3/TXNIP axis. *Biosci. Rep.* <https://doi.org/10.1042/BSR20190595> (2019).
- Gu, D. *et al.* Effects of long-term ketamine administration on rat bladder protein levels: A proteomic investigation using two-dimensional difference gel electrophoresis system. *Int. J. Urol.* **20**, 1024–1031. <https://doi.org/10.1111/iju.12100> (2013).
- Shen, C. H. *et al.* Biological effect of ketamine in urothelial cell lines and global gene expression analysis in the bladders of ketamine-injected mice. *Mol. Med. Rep.* **11**, 887–895. <https://doi.org/10.3892/mmr.2014.2823> (2015).
- Shen, C. H. *et al.* Evaluation of urinary bladder fibrogenesis in a mouse model of long-term ketamine injection. *Mol. Med. Rep.* **14**, 1880–1890. <https://doi.org/10.3892/mmr.2016.5482> (2016).
- Yang, H. H., Zhai, W. J. & Kuo, H. C. The putative involvement of actin-binding proteins and cytoskeleton proteins in pathological mechanisms of ketamine cystitis—Revealed by a prospective pilot study using proteomic approaches. *Proteomics Clin. Appl.* <https://doi.org/10.1002/prca.201600085> (2017).
- Liu, J. *et al.* FibroAtlas: A database for the exploration of fibrotic diseases and their genes. *Cardiol. Res. Pract.* **2019**, 4237285. <https://doi.org/10.1155/2019/4237285> (2019).
- Merle, N. S., Noe, R., Halbwachs-Mecarelli, L., Fremaux-Bacchi, V. & Roumenina, L. T. Complement system part II: Role in immunity. *Front. Immunol.* **6**, 257. <https://doi.org/10.3389/fimmu.2015.00257> (2015).
- Decramer, S. *et al.* Urine in clinical proteomics. *Mol. Cell Proteomics* **7**, 1850–1862. <https://doi.org/10.1074/mcp.R800001-MCP200> (2008).
- Cheng, P. S., Fu, C. Y., Lee, C. H., Liu, C. & Chien, C. S. GC-MS quantification of ketamine, norketamine, and dehydronorketamine in urine specimens and comparative study using ELISA as the preliminary test methodology. *J. Chromatogr. B Anal. Technol. Biomed. Life Sci.* **852**, 443–449. <https://doi.org/10.1016/j.jchromb.2007.02.005> (2007).
- Meng, E., Lin, W. Y., Lee, W. C. & Chuang, Y. C. Pathophysiology of overactive bladder. *Low Urin Tract Symptoms* **4**(Suppl 1), 48–55. <https://doi.org/10.1111/j.1757-5672.2011.00122.x> (2012).
- Kambas, K. *et al.* Endothelin-1 signaling promotes fibrosis in vitro in a bronchopulmonary dysplasia model by activating the extrinsic coagulation cascade. *J. Immunol.* **186**, 6568–6575. <https://doi.org/10.4049/jimmunol.1003756> (2011).
- Huang, S. *et al.* TMT-labelled quantitative proteomic analysis to identify the proteins underlying radiation-induced colorectal fibrosis in rats. *J. Proteomics* **223**, 103801. <https://doi.org/10.1016/j.jpro.2020.103801> (2020).
- Phillips, J. C., Wriggers, W., Li, Z., Jonas, A. & Schulten, K. Predicting the structure of apolipoprotein A-I in reconstituted high-density lipoprotein disks. *Biophys. J.* **73**, 2337–2346. [https://doi.org/10.1016/S0006-3495\(97\)78264-X](https://doi.org/10.1016/S0006-3495(97)78264-X) (1997).
- Wasan, K. M., Brocks, D. R., Lee, S. D., Sachs-Barrable, K. & Thornton, S. J. Impact of lipoproteins on the biological activity and disposition of hydrophobic drugs: Implications for drug discovery. *Nat. Rev. Drug Discov.* **7**, 84–99. <https://doi.org/10.1038/nrd2353> (2008).
- Mangaraj, M., Nanda, R. & Panda, S. Apolipoprotein A-I: A molecule of diverse function. *Indian J. Clin. Biochem.* **31**, 253–259. <https://doi.org/10.1007/s12291-015-0513-1> (2016).
- Hyka, N. *et al.* Apolipoprotein A-I inhibits the production of interleukin-1 $\beta$  and tumor necrosis factor- $\alpha$  by blocking contact-mediated activation of monocytes by T lymphocytes. *Blood* **97**, 2381–2389. <https://doi.org/10.1182/blood.v97.8.2381> (2001).
- Kim, T. H. *et al.* Role of lung apolipoprotein A-I in idiopathic pulmonary fibrosis: Antiinflammatory and antifibrotic effect on experimental lung injury and fibrosis. *Am. J. Respir. Crit. Care Med.* **182**, 633–642. <https://doi.org/10.1164/rccm.200905-0659OC> (2010).
- Parkin, M. C. *et al.* Detection of ketamine and its metabolites in urine by ultra high pressure liquid chromatography-tandem mass spectrometry. *J. Chromatogr. B Anal. Technol. Biomed. Life Sci.* **876**, 137–142. <https://doi.org/10.1016/j.jchromb.2008.09.036> (2008).
- Chen, Y. T. *et al.* Discovery of novel bladder cancer biomarkers by comparative urine proteomics using iTRAQ technology. *J. Proteome Res.* **9**, 5803–5815. <https://doi.org/10.1021/pr100576x> (2010).



35. da Huang, W., Sherman, B. T. & Lempicki, R. A. Systematic and integrative analysis of large gene lists using DAVID bioinformatics resources. *Nat. Protoc.* **4**, 44–57. <https://doi.org/10.1038/nprot.2008.211> (2009).
36. Kanehisa, M. & Goto, S. KEGG: Kyoto encyclopedia of genes and genomes. *Nucleic Acids Res.* **28**, 27–30. <https://doi.org/10.1093/nar/28.1.27> (2000).
37. Szklarczyk, D. *et al.* STRING v11: Protein-protein association networks with increased coverage, supporting functional discovery in genome-wide experimental datasets. *Nucleic Acids Res.* **47**, D607–D613. <https://doi.org/10.1093/nar/gky1131> (2019).

## Acknowledgements

We are grateful to the technical services provided by the Proteomics Core Facility, Molecular Medicine Research Center, Chang-Gung University. We also thank all lab technicians, nurses and physicians for their excellent cooperation and help. This study was supported by the “Molecular Medicine Research Center, Chang Gung University” from The Featured Areas Research Center Program within the framework of the Higher Education Sprout Project by the Ministry of Education (MOE) in Taiwan. This work was also supported by grants from the Ministry of Science and Technology, Taiwan (MOST 106-2320-B-182-029-MY3 and MOST 109-2320-B-182-009-MY3 to JSY; MOST 109-2113-M-182-003 to YTC); and the Chang Gung Memorial Hospital, Linkou, Taiwan (CLRPD1J0012, CMRPD1D0301-303, and CMRPD1H0251-253 to JSY; CMRPD1G0133 to YTC).

## Author contributions

J.C.L., Y.T.C. and J.S.Y. conceived and designed the experiments; J.C.L., C.C.W. and Y.J.H. performed the experiments; J.C.L., Y.J.H. and C.C.W. analyzed the data; M.C.H., Y.C.H., C.T.W., C.K.C., Y.T.C. and J.S.Y. contributed reagents/materials; J.C.L., S.D. and J.S.Y. wrote the paper. All authors read and approved the final manuscript.

## Competing interests

The authors declare no competing interests.

## Additional information

**Supplementary Information** The online version contains supplementary material available at <https://doi.org/10.1038/s41598-021-89089-4>.

**Correspondence** and requests for materials should be addressed to J.-S.Y.

**Reprints and permissions information** is available at [www.nature.com/reprints](http://www.nature.com/reprints).

**Publisher’s note** Springer Nature remains neutral with regard to jurisdictional claims in published maps and institutional affiliations.



**Open Access** This article is licensed under a Creative Commons Attribution 4.0 International License, which permits use, sharing, adaptation, distribution and reproduction in any medium or format, as long as you give appropriate credit to the original author(s) and the source, provide a link to the Creative Commons licence, and indicate if changes were made. The images or other third party material in this article are included in the article’s Creative Commons licence, unless indicated otherwise in a credit line to the material. If material is not included in the article’s Creative Commons licence and your intended use is not permitted by statutory regulation or exceeds the permitted use, you will need to obtain permission directly from the copyright holder. To view a copy of this licence, visit <http://creativecommons.org/licenses/by/4.0/>.

© The Author(s) 2021



# Randialic acid B and tomentosolic acid block formyl peptide receptor 1 in human neutrophils and attenuate psoriasis-like inflammation *in vivo*

Michal Korinek<sup>a,b,c</sup>, Pei-Shan Hsieh<sup>a</sup>, Yu-Li Chen<sup>a,b</sup>, Pei-Wen Hsieh<sup>a,d</sup>, Shih-Hsin Chang<sup>a,b</sup>, Yi-Hsiu Wu<sup>a</sup>, Tsong-Long Hwang<sup>a,b,d,e,\*</sup>

<sup>a</sup> Graduate Institute of Natural Products, College of Medicine, Chang Gung University, Taoyuan 33302, Taiwan

<sup>b</sup> Research Center for Chinese Herbal Medicine, Research Center for Food and Cosmetic Safety, and Graduate Institute of Health Industry Technology, College of Human Ecology, Chang Gung University of Science and Technology, Taoyuan 33302, Taiwan

<sup>c</sup> Graduate Institute of Natural Products, College of Pharmacy, Kaohsiung Medical University, Kaohsiung 80708, Taiwan

<sup>d</sup> Department of Anesthesiology, Chang Gung Memorial Hospital, Taoyuan 33305, Taiwan

<sup>e</sup> Department of Chemical Engineering, Ming Chi University of Technology, New Taipei City 24301, Taiwan

## ARTICLE INFO

### Keywords:

Neutrophilic inflammation  
FPR1 antagonist  
Triterpene  
*Ilex kaushue*  
Psoriasis

## ABSTRACT

Psoriasis is a long-lasting inflammatory skin disease lacking proper cure. Dysregulated activation of neutrophils is a major pathogenic factor in psoriasis. Formyl peptide receptor 1 (FPR1) triggers neutrophil activation in response to bacteria- or mitochondria-derived *N*-formyl peptides, but its significance in neutrophilic psoriasis remains unknown. In this study, we discovered two derivatives of ursolic acid, 3 $\beta$ -hydroxyurs-12,18-dien-28-oic acid (randialic acid B, RAB) and 3 $\beta$ -hydroxyurs-12,19-dien-28-oic acid (tomentosolic acid, TA), as FPR1 inhibitors in human neutrophils with ability to suppress psoriatic symptoms in mice. Both RAB and TA, triterpenoids of traditional medicinal plant *Ilex kaushue*, selectively inhibited reactive oxygen species production, elastase release, and CD11b expression in human neutrophils activated by FPR1, but not non-FPR1 agonists. Importantly, RAB and TA inhibited the binding of *N*-formyl peptide to FPR1 in human neutrophils, neutrophil-like THP-1 cells, and hFPR1-transfected HEK293 cells, indicating FPR1 antagonism. Moreover, in assays induced by various concentrations of FPR1 agonist, both RAB and TA acted competitively for its binding to the FPR1 receptor. The FPR1-downstream signaling such as Ca<sup>2+</sup> mobilisation and activation of Akt and MAPKs was also competitively inhibited. In addition, imiquimod-induced psoriasis-like symptoms, including epidermal hyperplasia, desquamation with scaling, neutrophil skin infiltration, and transepidermal water loss were significantly reduced by both RAB and TA. The results illustrate a possible role of human neutrophils FPR1 receptor in psoriasis-like inflammation. Accordingly, triterpenoids RAB and TA represent novel FPR1 antagonists and exhibit therapeutic potential for treating neutrophilic inflammatory skin diseases.

## 1. Introduction

The immune system is the first line of defense against human pathogens, where neutrophils participate in both innate and adaptive immune responses [1,2]. When a pathogen invades the host, bacterial *N*-formyl peptide is associated with the formyl peptide receptor 1 (FPR1), a G<sub>i</sub>-protein coupled receptor (GPCR) expressed on the surface of host

neutrophil cell membrane. Then, the neutrophils activated via FPR1 migrate to the site of infection, produce reactive oxygen species (ROS), release proteases and neutrophil extracellular traps (NETs) in order to kill pathogens [3]. But when neutrophils are overactivated in response to pathogen or aberrant immune signal, these toxic substances will also cause injury to host tissues, leading to various acute, chronic or autoimmune inflammatory diseases such as life-threatening sepsis [4],

**Abbreviations:** ABTS, 2,2'-azino-bis (3-ethylbenzothiazoline-6-sulfonic acid) diammonium salt; CB, cytochalasin B; DPPH, 1,1-diphenyl-2-picryl-hydrazyl; Fluo-3/AM, Fluo-3 acetoxymethyl ester; fMLF, *N*-formyl-methionyl-leucyl-phenylalanine; fMMYALF, *N*-formyl-Met-Met-Tyr-Ala-Leu-Phe; fNLFNYK, *N*-formyl-Nle-Leu-Phe-Nle-Tyr-Lys-fluorescein; GPCR, G<sub>i</sub>-protein coupled receptor; HE, hydroethidine; IMQ, imiquimod; Ly6G, lymphocyte antigen 6 complex locus G6D; m3M3FBS, *N*-(3-trifluoromethylphenyl)-2,4,6-trimethylbenzenesulfonamide; MPO, myeloperoxidase; PMA, phorbol 12-myristate 13-acetate; PLC, phospholipase C; PKC, protein kinase C; RAB, randialic acid; TA, tomentosolic acid; WST-1, water-soluble tetrazolium-1.

\* Corresponding author at: Graduate Institute of Natural Products, Chang Gung University, 259 Wen-Hwa 1st Road, Kweishan, Taoyuan 333, Taiwan.

E-mail address: [htl@mail.cgu.edu.tw](mailto:htl@mail.cgu.edu.tw) (T.-L. Hwang).

<https://doi.org/10.1016/j.bcp.2021.114596>

Received 14 March 2021; Received in revised form 2 May 2021; Accepted 3 May 2021

Available online 6 May 2021

0006-2952/© 2021 Elsevier Inc. All rights reserved.



rheumatoid arthritis [5], chronic obstructive pulmonary disease (COPD) and asthma [6], psoriasis [7], or atherosclerosis [8], but also coronavirus-associated acute respiratory distress syndrome (ARDS) [9]. Therefore, the inhibition of the FPR1 is considered as an effective strategy for the treatment of inflammation-related diseases [10].

Psoriasis is a chronic and recurrent immune skin disease, affecting approx. 2 to 3% of the world's total population. Histopathological features caused by psoriasis include epidermis thickening and infiltration of immune cells, resulting in abnormal skin production [7]. The cause of psoriasis is still not fully understood, but unlike other inflammatory skin diseases, there are multiple types of immune cells participating in the pathogenesis of psoriasis, including macrophages, lymphocytes and neutrophils with growing evidence for a crucial role of neutrophils [11]. However, the available treatments do not fully utilize important role of neutrophils in psoriasis.

Triterpenoids represent phytochemicals abundant in nature that possess anti-inflammatory [12] and anticancer activities [13]. Previously, 3 $\beta$ -hydroxyurs-12,18-dien-28-oic acid (randialic acid B, RAB) and 3 $\beta$ -hydroxyurs-12,19-dien-28-oic acid (tomentosolic acid, TA), the unsaturated derivatives of ursolic acid, were isolated from *Ilex kaushue* (syn. *I. kudingcha*) [14], a traditional Chinese medicine used for millennia to treat inflammation-related health disorders [15]. There is a lack of knowledge on the anti-inflammatory effects of these triterpenoids but also the correlation between FPR1 expression and psoriasis is rather unknown.

Thus, in the current study, we delve into the anti-inflammatory effects of triterpenoids RAB and TA in human neutrophils, molecular mechanism targeting FPR1 and effects on psoriasis-like inflammation in mice.

## 2. Materials and methods

### 2.1. Reagents and antibodies

Randialic acid B and tomentosolic acid were obtained from *Ilex kaushue* and identified using comprehensive spectroscopic data analysis including 1D and 2D NMR as previously described [14]. Compounds were dissolved in DMSO for experiments. Dextran, ferricytochrome c, cytochalasin B (CB), Triton X-100,  $\alpha$ -tocopherol (vitamin E), 1,1-disphenyl-2-picryl-hydrazyl (DPPH), *N*-formyl-methionyl-leucyl-phenylalanine (fMLF), 2,2'-azino-bis (3-ethylbenzothiazoline-6-sulfonic acid) diammonium salt (ABTS), xanthine oxidase, DMSO, phorbol 12-myristate 13-acetate, PMA and *N*-(3-trifluoromethylphenyl)-2,4,6-trimethylbenzenesulfonamide (m3M3FBS), butyryl cAMP, luminol were purchased from Sigma-Aldrich (St. Louis, MO, USA). Ficoll-Paque TM PLUS was purchased from GE Healthcare (Buckinghamshire, UK). Fetal bovine serum (FBS), HBSS and DMEM, were purchased from Gibco (Grand Island, NY, USA). Trypan blue was purchased from Biological Industries (Beit Haemek, Israel). Methoxysuccinyl-Ala-Ala-Pro-Val-p-nitroanilide was purchased from Calbiochem (La Jolla, CA, USA). Hydroethidine (dihydroethidine, HE) and Hoechst 33342 (Trihydrochloride, Trihydrate - 10 mg/mL solution in water, Cat# H3570) were purchased from Invitrogen (Carlsbad, CA, USA). *N*-Formyl-Met-Met-Tyr-Ala-Leu-Phe (fMMYALF) was purchased from GeneDireX (Las Vegas, NV, USA). MMK1 and LTB4 were purchased from Tocris Bioscience (Bristol, United Kingdom). IL8 was purchased from ProSpec (Ness-Ziona, Israel). Anti-human CD11b (activation epitope) FITC (CBRM1/5) antibody (Thermo Fisher Scientific, Cat# 11-0113-42, RRID: AB\_2572437, Waltham, MA, USA) was purchased from eBioscience (San Diego, CA, USA). Anti-mouse lymphocyte antigen 6 complex locus 6D (Ly6G) antibody (BioLegend Cat# 127602, RRID:AB\_1089180; San Diego, CA, USA), anti-mouse Ki67 [SP6] antibody (GeneTex Cat# GTX16667, RRID:AB\_422351; Hsinchu, Taiwan), and anti-human myeloperoxidase (MPO) antibody (Abcam Cat# ab9535, RRID:AB\_307322; Cambridge, MA, USA), anti-rabbit Poly-HRP-IgG (<25 $\mu$ g/mL) containing 10% (v/v) animal serum in tris-buffered saline/0.1% ProClin™ 950

and anti-rat IgG (H&L) Affinity Pure, HRP conjugate (ImmunoReagents Inc., RbxRt-003-DHRPX; Raleigh, NC, USA) were used for immunohistochemical experiments. Fluo-3 acetoxymethyl ester (Fluo-3/AM) and *N*-formyl-Nle-Leu-Phe-Nle-Tyr-Lys-fluorescein (fNLFNYK) were purchased from Molecular Probes (Eugene, OR, USA). Xanthine was purchased from Santa Cruz Biotechnology (Dallas, TX, USA). 2-(4-Iodophenyl)-3-(4-nitrophenyl)-5-(2,4-disulphophenyl)-2H-tetrazolium monosodium salt (water-soluble tetrazolium-1, WST-1) was purchased from Dojindo Laboratories (Kunamoto, Japan). Antibody for p38 MAPK (Cell Signaling Technology Cat# 9212, RRID:AB\_330713), phospho-p38 MAPK (Thr180/Tyr182) (Cell Signaling Technology Cat# 9211, RRID: AB\_331641), SAPK/JNK (56G8) (Cell Signaling Technology Cat# 9258, RRID:AB\_2141027), phospho-SAPK/JNK (Thr183/Tyr185) (Cell Signaling Technology Cat# 9251, RRID:AB\_331659), Akt (pan) (C67E7) (Cell Signaling Technology Cat# 4691, RRID:AB\_915783), phospho-Akt (Ser-473) (193H12) (Cell Signaling Technology Cat# 4058, RRID: AB\_331168), ERK p44/42 MAPK (Erk1/2) (137F5) (Cell Signaling Technology Cat# 4695, RRID:AB\_390779) and phospho-ERK p44/42 MAPK (Erk1/2) (Thr202/Tyr204) (Cell Signaling Technology Cat# 4370, RRID:AB\_2315112) antibodies were purchased from Cell Signaling (Beverly, MA, USA). Secondary goat anti-rabbit IgG (H+L) antibody, HRP-linked (Thermo Fisher Scientific Cat# 31460, RRID: AB\_228341) was used for Western blotting experiments.

### 2.2. Preparation of human neutrophils

The experiment was approved by the Institutional Review Board of Chang Gung University Hospital (Registration number: IRB 100 1278C) and written consent was obtained from every blood donor. Elbow vein blood was collected from healthy volunteers 20 to 30 years of age without medication using a vacuum sterile blood collection tube containing heparin as anticoagulant [16]. The blood was centrifuged at 650 g and 25 °C for 10 min. After removing the plasma supernatant, 3% dextran was added, mixed, and left at room temperature for 25 min to allow the red blood cells to settle. The upper suspension containing neutrophil was centrifuged with Ficoll-Paque, using gradient centrifugation at 200  $\times$  g at 20 °C for 35 min to separate different types of white blood cells. Residual red blood cells were washed with a hypotonic solution and removed after centrifugation at 200  $\times$  g for 8 min at 4 °C. More than 98% of viable neutrophils were calculated using trypan blue exclusion technique. Finally, the isolated neutrophils were suspended in Ca<sup>2+</sup>-free HBSS at pH 7.4 and kept at 4 °C before subsequent experiments.

### 2.3. Cell culture and differentiation of THP-1 cells

THP-1 cell line (purchased from the Center for Bioresources Conservation and Research, Institute of Food Science; ATCC Cat# TIB-202, RRID:CVCL\_0006) was human monocytic leukemia cell line and was cultured in Roswell Park Memorial Institute (RPMI) 1640 culture medium (containing 10% FBS, 1% glutamine and 1% antibiotic-antimycotic solution, i.e. 100 U·mL<sup>-1</sup> penicillin, 100  $\mu$ g·mL<sup>-1</sup> streptomycin, and 2.5  $\mu$ g·mL<sup>-1</sup> amphotericin B) in a constant temperature incubator at 37 °C and 5% CO<sub>2</sub> incubator. When the THP-1 cell line was incubated with 300  $\mu$ M dibutyl cAMP for 48 h, the cells differentiated into a large number of neutrophil-like cells expressing FPR1 used for subsequent experiments [17].

### 2.4. HEK293 cells transfection with human FPR1 (hFPR1)

HEK293 cell line (purchased from the Center for Bioresources Conservation and Research, Institute of Food Science; ATCC Cat# CRL-1573, RRID:CVCL\_0045), a human embryonic kidney cell line, was cultured using DMEM medium (containing 10% FBS, 1% non-essential amino acid, 1% glutamine and 1% antibiotic-antimycotic solution) in 37 °C with 5% CO<sub>2</sub> incubator. The cell line was transfected with a pCMV6-AC

vector containing the human FPR1 gene (hFPR1) (NM-002029, OriGene, Rockville, MD, USA) for 72 hr using X-tremeGENE, Hp DNA Transfection reagent (Roche, Mannheim, Germany) according to the instructions of the manufacturer. The transfected HEK293 cells were cultured with G418 (geneticin, 3 mg·mL<sup>-1</sup>) and only G418-resistant clones were used for subsequent experiments [17]. Because hFPR1-transfected HEK293 cells may express different FPR1 receptor expression levels, a further selection of high FPR1 expressing cells was performed. The hFPR1-transfected HEK293 cells were subcultured, diluted, regrown, and incubated with G418 medium. The cells ( $5 \times 10^5$  cells·mL<sup>-1</sup>) were activated by fNLFNYK (3 nM) in HBSS at 4 °C for 30 min, and FPR1 expression was detected by flow cytometer. The FPR1 expressing cells were recultured again until a single type of cells with high FPR1 expression was obtained.

## 2.5. Reactive oxygen species (ROS) and reactive nitrogen species (RNS)

When the neutrophils are activated, the protein complex NADPH oxidase located on the cell membrane and in the cytoplasm will consume oxygen in the process of respiratory burst to produce a large number of reactive oxygen molecules such as superoxide radicals.

### 2.5.1. Determination of extracellular superoxide anion generation

Extracellular superoxide was measured using assay utilizing ferricytochrome *c* which cannot penetrate into the cell, and thus can only interact with superoxide from outside the cell [18]. Upon the reaction with radicals, ferricytochrome *c* is reduced, and it has a light-absorbing reaction at a wavelength of 550 nm. The neutrophil suspension ( $6 \times 10^5$  cells·mL<sup>-1</sup>) and 0.5 mg·mL<sup>-1</sup> ferricytochrome *c* solution containing 1 mM CaCl<sub>2</sub> were preheated at 37 °C for 5 min. The test compounds or DMSO were added, and after 2 min, the priming agent cytochalasin B (CB, 1 µg·mL<sup>-1</sup>; except PMA) was added to amplify the reaction. After another 3 min, the cells were stimulated with 0.1 µM fMLF, 0.1 µM fMMYALF, 0.3 µM MMK-1, 15 µM m3M3FBS, or 10 nM PMA ( $3 \times 10^5$  cells·mL<sup>-1</sup>) for 10 min, and the change in absorbance at a wavelength of 550 nm (Hitachi, U-3010, Tokyo) was continuously measured to evaluate the effect of the test compounds. The superoxide generation was calculated based on the absorbance differences between measurements with and without SOD (100 U·mL<sup>-1</sup>) divided by the extinction coefficient for the reduction of ferricytochrome *c* ( $\epsilon = 21.1 \cdot \text{mM}^{-1} \cdot 10 \text{ mm}^{-1}$ ).

### 2.5.2. Determination of total ROS release

The total, i.e. intracellular and extracellular reactive oxygen species (ROS) were determined using 5-amino-2,3-dihydrophthalazine-1,4-dione (luminol) to react with reactive oxygen molecules which generates chemiluminescence and was further enhanced by horseradish peroxidase (HRP) to detect the total amount of ROS inside and outside the cells [19]. The experiment was performed on a 96 well microplate, and 37.5 µM luminol was added to the test compounds at 37 °C for 5 min. Finally, the cells were primed with CB (1 µg·mL<sup>-1</sup>) and activated with 0.1 µM fMLF and 0.1 µM fMMYALF. The generation of ROS radicals was measured using a 96-well chemiluminometer (Tecan, Infinite F200 Pro; Tecan Group, Männedorf, Switzerland).

### 2.5.3. Determination of intracellular superoxide anion generation

The intracellular superoxide radicals were determined using hydroethidine (HE), a molecule that penetrates into the cell and reacts with intracellular superoxide radicals to produce a red fluorescence (ethidium E<sup>+</sup>) [20]. The experiment was performed at 37 °C in the presence of 1 mM CaCl<sub>2</sub>. Neutrophils ( $1 \times 10^6$  cells·mL<sup>-1</sup>) were incubated with 1 µM HE for 12 min, and then the test compounds or DMSO were added. After 2 min, a priming agent CB (1 µg·mL<sup>-1</sup>) was added. Finally, 3 min after the priming agent, fMLF (0.1 µM) and MMK1 (0.3 µM) were added for another 5 min, and the fluorescence intensity was measured by a flow cytometer.

### 2.5.4. Determination of ROS/RNS scavenging activity

In order to clarify whether RAB and TA have the ability to directly scavenge free radicals, a cell-free system assays of superoxide (xanthine/xanthine oxidase) and nitrogen radicals 1,1-disphenyl-2-picryl-hydrazyl (DPPH) and 2,2'-azinobis-3-ethylbenzothiazoline-6-sulfonic acid (ABTS) in cell-free systems were utilized [21].

Superoxide anion scavenging assay uses xanthine/xanthine oxidase to produce superoxide which further reduces WST-1. Compounds scavenging effect was evaluated by measuring the amount of reduced WST-1. In a 50 mM Tris buffer (pH 7.4), 0.3 mM WST-1 and 0.02 U·mL<sup>-1</sup> xanthine oxidase were mixed and the test compounds or SOD were added, followed by incubation at 30 °C for 3 min, and addition of 0.1 mM xanthine for 10 min. Changes in absorbance were measured at 450 nm, and SOD was used as a positive control.

Nitrogen radicals (RNS) were detected using 1,1-disphenyl-2-picryl-hydrazyl (DPPH), a stable nitrogen-centered free radical. DPPH was dissolved in 99% ethanol to prepare a 100 µM solution. In the experiment, the tested compounds were reacted with DPPH for 15 min at 25 °C, and the absorbance at 517 nm was measured.  $\alpha$ -Tocopherol (vitamin E), which is known to have strong scavenging activity, was used as a positive control.

Also, 2,2'-azinobis-3-ethylbenzothiazoline-6-sulfonic acid (ABTS) is a nitrogen-centered radical. In a cell-free system, 7 mM ABTS and 2.45 mM potassium persulfate were dissolved in ddH<sub>2</sub>O, to form stable nitrogen radical ABTS<sup>•</sup>, reacted with the test compounds for 15 min at room temperature, and measured the absorbance at 734 nm.  $\alpha$ -Tocopherol was used as a positive control.

## 2.6. Cytotoxicity test

When a cell is damaged or dying, the cell membrane loses its integrity, and LDH stored in the cytoplasm is released outside the cell. By detecting the amount of LDH, we could evaluate whether the test compound is toxic to the cells [22]. The human neutrophil suspension ( $6 \times 10^5$  cells·mL<sup>-1</sup>) were preheated at 37 °C for 5 min in the presence of CaCl<sub>2</sub> (1 mM). Then the test compounds were added to interact with the cells for 15 min, 1 h or 3 h. In a total LDH release control, 0.1% of Triton X-100 were incubated with cells for 30 min to completely lyse the cells. The cells were centrifuged at 4 °C for 200 × g for 8 min, and LDH reagent was added to supernatant reacted at room temperature for 30 min in the dark. The absorbance was measured at 492 nm, and the LDH release was calculated and compared to the total LDH release set as 100%.

## 2.7. Determination of elastase release

Activated neutrophils release large amount of elastase through the degranulation of azurophilic granules [22]. In this experiment, elastase specific substrate (methoxysuccinyl-Ala-Ala-Pro-Val-p-nitroanilide) was used to evaluate the effect of test compounds on elastase release. Neutrophils ( $6 \times 10^5$  cells·mL<sup>-1</sup>) were mixed with the substrate (0.1 mM) containing CaCl<sub>2</sub> (1 mM) at 37 °C for 5 min and then the test compounds were added. After 2 min, CB (0.5 µg·mL<sup>-1</sup>; except for LTB4 and IL8 2 µg·mL<sup>-1</sup>) was added for 3 min to amplify the reaction, and finally cells were stimulated with 0.1 µM fMLF, 0.1 µM fMMYALF, 0.3 µM MMK1, 15 µM m3M3FBS, 0.1 µM LTB4, or 100 ng·mL<sup>-1</sup> IL8 for 10 min. The change in absorbance was measured at 405 nm to evaluate the percentage of elastase release of the test compounds in comparison with the fMLF/CB-activated, drug-free control.

## 2.8. Determination of elastase enzymatic activity

The compounds were further tested for direct inhibition of elastase enzymatic activity [19]. The neutrophil suspension ( $6 \times 10^5$  cells·mL<sup>-1</sup>) was preheated for 5 min in the presence of CaCl<sub>2</sub> (1 mM) at 37 °C. Priming agent CB (1.5 µg·mL<sup>-1</sup>) was added for 2 min, followed by fMLF (0.1 µM) for 20 min to release the elastase. The supernatant was

centrifuged at 1000 g for 5 min at 4 °C. Then, the supernatant containing elastase was preheated at 37 °C for 5 min, and the test compounds were added. Finally, 0.1 mM of substrate methoxysuccinyl-Ala-Ala-Pro-Val-p-nitroanilide was added for 10 min. The effect of the test compounds was evaluated by measuring the absorbance at 405 nm.

## 2.9. Cell surface CD11b expression measurement

The following experiment was performed to evaluate the effect on CD11b integrin expression on the cell surface in stimulated neutrophils, important for the regulation of cell adhesion and migration [20]. Human neutrophils ( $2.5 \times 10^5$  cells·mL<sup>-1</sup>) containing CaCl<sub>2</sub> (1 mM) were mixed with the test compounds for 5 min at 37 °C. After 2 min, CB (0.5 µg·mL<sup>-1</sup>) was added and then cells were stimulated with 0.1 µM fMLF or 0.3 µM MMK1 for 5 min. The reaction was stopped on ice. The cells were centrifuged at  $200 \times g$  at 4 °C for 8 min, the supernatant was removed and cells were resuspended in HBSS containing 0.5% (w/v) BSA. FITC-labeled anti-CD11b (1 µg) was added at 4 °C for 90 min in the dark, and the immunofluorescence was immediately measured by flow cytometry.

## 2.10. Cell adhesion assay

The mouse brain microvascular endothelial cell line bEnd.3 was used to simulate the environment of neutrophils in the microvasculature and observe the effect of test compounds on the neutrophils' adhesion [23]. bEnd.3 cell line (purchased from the Center for Bioresources Conservation and Research, Institute of Food Science, ATCC Cat# CRL-2299, RRID:CVCL\_0170) is a mouse brain microvascular endothelial cell line and was cultured using DMEM (containing 10% FBS and 1% antibiotic-antimycotic solution) at 37 °C with 5% CO<sub>2</sub>. Neutrophils were pretreated with 1 ng·mL<sup>-1</sup> Hoechst 33342 dye at 37 °C. After washing away the dye by centrifugation at  $200 \times g$  for 8 min, the neutrophils suspension containing CaCl<sub>2</sub> (1 mM) was incubated at 37 °C for 5 min, and the test compounds were added for 2 min, followed by CB (0.5 µg·mL<sup>-1</sup>) for another 3 min. Afterwards, a solution of 0.1 µM fMLF was added to bEnd.3 cells, and then mixed and co-cultured with the neutrophil suspension at 37 °C for 15 min. The unattached neutrophils to bEnd.3 were removed by rinsing with HBSS. Then, 4% paraformaldehyde (PFA) was added to fix the cells, and adherent neutrophils were counted using a fluorescence microscope (IX81; Olympus, Center Valley, PA, USA).

## 2.11. Receptor binding test

The potency of compounds to directly inhibit binding to the cell surface receptor FPR1 was investigated (24). Fluorescent labelled peptide N-formyl-Nle-Leu-Phe-Nle-Tyr-Lys-fluorescein (fNLFNYK) is a structural analog of fMLF that specifically binds to FPR1. Human neutrophils ( $2 \times 10^6$  cells·mL<sup>-1</sup>), THP-1 cells differentiated into neutrophil-like cells ( $5 \times 10^5$  cells·mL<sup>-1</sup>), or HEK293 cells transfected with hFPR1 ( $2.5 \times 10^5$  cells·mL<sup>-1</sup>) were incubated with tested compounds at 4 °C for 5 min. Then fNLFNYK (3 nM) was added and reacted for 30 min. Collected cells were analysed by flow cytometry and a decrease in fluorescence level indicated the amount of receptor bound by the test compounds, where fMLF was used as a control.

## 2.12. Determination of intracellular calcium concentration ( $[Ca^{2+}]_i$ )

For measurement of intracellular calcium, neutrophils ( $6 \times 10^6$  cells·mL<sup>-1</sup>) were incubated with Fluo-3/AM (2 µM) at 37 °C for 30 min, and then the supernatant was removed after centrifugation at  $200 \times g$  at 4 °C for 8 min [22]. The resuspended cells in HBSS stained with Fluo-3/AM were treated with test compounds for 5 min in the presence of 1 mM CaCl<sub>2</sub> at 37 °C and then stimulated by 0.1 µM fMLF (or 0.1 µM – 1 µM), 0.3 µM MMK-1, 15 µM m3M3FBS, 0.1 µM LTB<sub>4</sub>, or 100 µg·mL<sup>-1</sup> IL8. The

fluorescence changes were monitored using a Hitachi F-4500 spectrofluorometer (Tokyo, Japan) with continuous stirring at 37 °C in a quartz cuvette. The excitation and emission wavelengths were set to 488 nm and 520 nm, respectively. Finally, 0.05% Triton X-100 was added to obtain the maximum fluorescence value ( $F_{max}$ ), and 20 mM EGTA was added to obtain the minimum fluorescence value ( $F_{min}$ ). The amount of change in intracellular  $Ca^{2+}$  concentration was calculated according to the following formula:  $[Ca^{2+}]_i = K_d \times [(F - F_{min}) / (F_{max} - F)]$ , where  $F$ ,  $F_{max}$  and  $F_{min}$  are measured fluorescence intensities and  $K_d$  is the dissociation constant of Fluo-3/AM, set as 400 nM.

## 2.13. Immunoblotting analysis

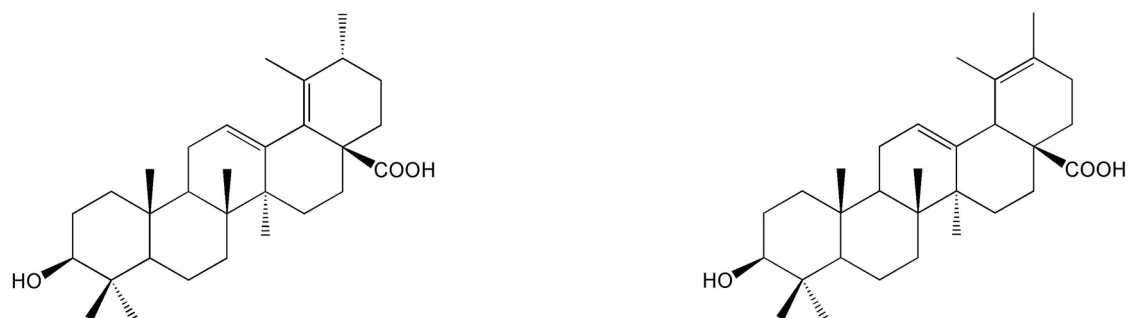
Intracellular protein expression and phosphorylation regulate different cellular physiological functions. Immunoblotting of target proteins by specific antibodies is used to bind and quantify the changes in intracellular proteins [25]. Human neutrophils ( $2.5 \times 10^7$  cells·mL<sup>-1</sup>) containing CaCl<sub>2</sub> (1 mM) were incubated at 37 °C and the test compounds were added for 5 min, followed by the addition of fMLF for 25 sec. The reaction was stopped by the addition of sample buffer (62.5 mM Tris-HCl, pH = 6.8, 2% SDS, 10% glycerol, 0.01% bromophenol blue and 5% 2-mercaptoethanol). The cells were mixed and heated at 100 °C for 15 min to fully lyse the cells and release the protein. The lysed cells were centrifuged at 14,000 rpm at 4 °C for 20 min and the supernatant was collected. Proteins were quantified and separated by SDS-PAGE gel electrophoresis using 12% acrylamide gel. The proteins were then transferred to a nitrocellulose membrane, which was soaked by 5% skim milk powder (in TBST containing 0.1% tween 20) at room temperature for one hour to block non-specific binding. Then, the membrane was immersed with corresponding primary antibodies in 5% BSA at 4 °C overnight. Finally, the membrane was incubated with HRP secondary antibodies in 5% BSA at room temperature for one hour, and then enhanced chemiluminescence reagent (Amersham Bioscience, Piscataway, NJ, USA) was added. The fluorescent bands of phosphorylated and total proteins were visualised using a densitometer (UVP Biospectrum Imaging System, LLC, Upland, CA, USA). Corresponding rabbit primary antibodies for p38, phospho-p38, JNK, phospho-JNK, Akt, phospho-Akt (Ser-473), ERK, phospho-ERK (1:2000) and HRP-linked anti-rabbit IgG, antibodies (1:10000) were used for quantification of total and phosphorylated MAPK and Akt proteins [26]. The quantitative ratios for all samples were normalized to the corresponding total protein.

## 2.14. Psoriasis skin model

### 2.14.1. Psoriasis-like skin inflammation induced by imiquimod (IMQ)

Imiquimod (IMQ)-induced model of psoriatic-like skin symptoms is widely accepted psoriasis animal model when employed appropriately [27–29]. The effect of compounds on psoriasis-like inflammation was evaluated in mice [30]. This study was performed with approval by the Institutional Animal Care and Use Committee of Chang Gung University, Taiwan (IACUC approval No. CGU14-150). Experimental procedures were carried out in accordance with the ARRIVE [31,32] with all efforts made to minimize the number of animals used and their sufferings. In the experiment, 7-week-old BALB/c white female mice (20 g weight) were housed in an air-conditioned room with 12 h light–dark cycle. On the first day, the hair on the back of mice was shaved with a razor, and then hair removal cream was applied. After 10 to 15 min, hair removal cream was washed to completely remove the hair on the back of the mouse. The mice were randomly divided into four groups for each treatment: sham treated with vehicle only (i.v.); compound only (i.v.); IMQ + vehicle (i.v.), and IMQ + compound (i.v.). Compounds RAB (10 mg·kg<sup>-1</sup>) or TA (10 mg·kg<sup>-1</sup>) were dissolved in DMSO, tween 80, and saline (1:2:7) and the solution of RAB, TA or vehicle alone was administered intravenously (50 µL, i.v.) every other day. A dose of 62.5 mg of a 5% w/w IMQ cream (Aldara, 3 M Health Care Limited, Loughborough,

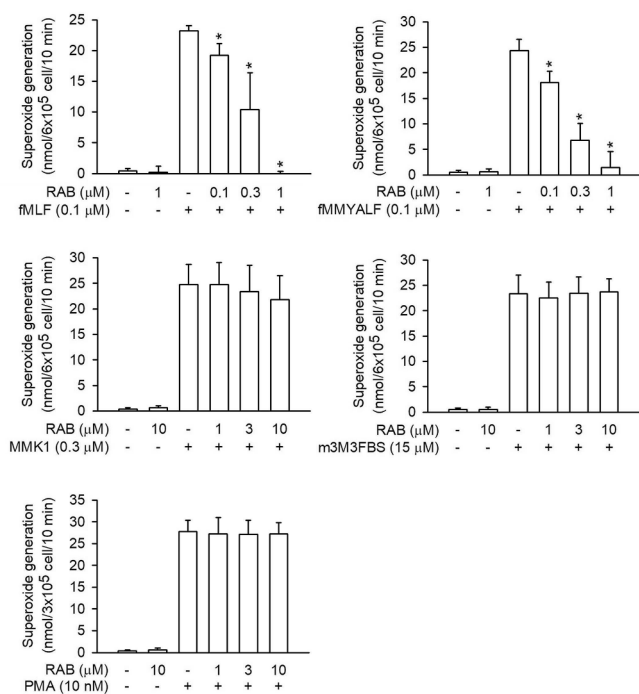
(A)



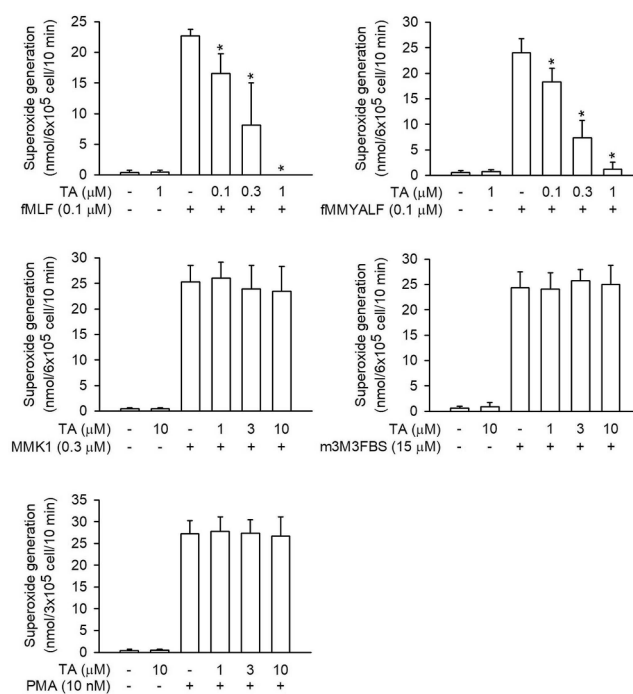
(B)

Compound	Superoxide anion, IC <sub>50</sub> (μM)				
	fMLF	fMMYALF	MMK1	m3M3FBS	PMA
RAB	0.43 ± 0.37	0.18 ± 0.04	>10	>10	>10
TA	0.23 ± 0.14	0.21 ± 0.07	>10	>10	>10

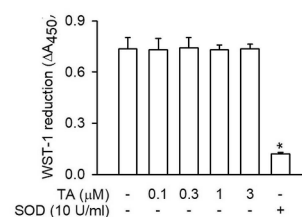
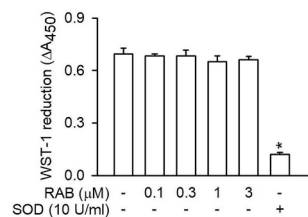
(C) RAB



TA



(D)



(caption on next page)



**Fig. 1.** Randialic acid B (left panel) and tomentosolic acid (right panel) significantly inhibit superoxide anion generation in human neutrophils induced by activators of FPR1, but not by non-FPR1 activators. None of them have antioxidant effects. (A) The chemical structures of randialic acid B (RAB, left) and tomentosolic acid (TA, right). (B) RAB and TA significantly inhibit activators of FPR1, but not non-FPR1, induced superoxide anion generation in human neutrophils. Human neutrophils were incubated with DMSO (as control), randialic acid B (RAB, 0.1–10  $\mu\text{M}$ , left panel) or tomentosolic acid (TA, 0.1–10  $\mu\text{M}$ , right panel) for 5 min and then activated by fMLF (0.1  $\mu\text{M}$ )/CB (1  $\mu\text{g}\cdot\text{mL}^{-1}$ ), fMMYALF (0.1  $\mu\text{M}$ )/CB (1  $\mu\text{g}\cdot\text{mL}^{-1}$ ), MMK1 (0.3  $\mu\text{M}$ )/CB (1  $\mu\text{g}\cdot\text{mL}^{-1}$ ), m3M3FBS (15  $\mu\text{M}$ )/CB (1  $\mu\text{g}\cdot\text{mL}^{-1}$ ), or PMA (10 nM) for another 10 min. Extracellular superoxide anion generation was measured based on ferricytochrome c reduction. Results are expressed as  $\text{IC}_{50}$  values, i.e., concentration necessary for 50% inhibition. (C) Concentration-dependent effects of RAB and TA on superoxide generation using FPR1 activators (fMLF and fMMYALF) and non-FPR1 activators (MMK1, m3M3FBS or PMA). All data are presented as means  $\pm$  SD ( $n = 6$ ). \*  $p < 0.05$  compared with activator alone (*t*-test). (D) Superoxide anion scavenging effects of RAB or TA (0.1–3  $\mu\text{M}$ ) were assayed in a cell-free xanthine/xanthine oxidase system. Reduction of WST-1 was measured spectrophotometrically at 450 nm. SOD (10 U/ml) was used as the positive control. Data are presented as means  $\pm$  SD ( $n = 3$ ).

United Kingdom) was applied on the back of the mice to induce the psoriasis-like symptoms in the mouse skin, daily for five consecutive days. When both drug and IMQ were applied on the same day, it was performed with a 30 min interval. Mice were sacrificed on the sixth day after the first IMQ application using overdose of 30 mg/kg Zoletil 50 and 6 mg/kg xylazine. The skin appearance was observed (photographed by a digital camera and by hand-held digital microscope), histology, immunological staining and degree of water dispersion (described below in next Section 2.14.2) tests were performed to evaluate the level of psoriasis-like symptoms in mice [33]. For the analysis, the skin samples were isolated, fixed in 10% paraformaldehyde, and buffered in phosphate saline. Afterwards, the skin histology was observed by staining with hematoxylin-eosin (H&E), and the stained slides were visualized by a light microscope. For immunohistochemical analysis, the unstained slides of formalin-fixed paraffin-embedded skin sections were dewaxed and rehydrated, followed by the heat-induced epitope retrieval treatment with Bond Epitope Retrieval Solution 2, pH 9 (Leica Biosystems DS9800) according to manufacturer's protocol. The reaction was blocked using normal serum solution. Skin samples sections were then incubated with primary antibodies, i.e., rabbit polyclonal anti-mouse Ki67, goat polyclonal anti-mouse Ly6G or goat polyclonal anti-human MPO antibodies for 1 h at 25–27 °C. After washing with phosphate saline solution containing 0.5% Tween 20, the sections were incubated with the biotinylated donkey anti-goat IgG secondary antibodies (Jackson ImmunoResearch Labs Cat# 705–001-003, RRID:AB\_2340383) for 20 min at 25–27 °C. Vectastatin Elite avidin-biotin complex kit (Vector Laboratories, Burlingame, CA, United States) was utilized for color reaction and the photomicrographs were captured using a microscope equipped with Olympus DP72 digital color camera.

#### 2.14.2. Transepidermal water loss (TEWL)

The skin is the largest organ of the human body and covers the entire body surface. Skin serves as the first line of defense against pathogens but is also regulating body temperature and preventing water loss. Many of the symptoms of psoriasis such as redness, scaling, and dry skin desquamation are the result of immune response causing damage to the stratum corneum and thus affecting the skin's water retention function. Tewameter® (Courage & Khazawa, Cologne, Germany) was used to measure the humidity in a moisture-proof box to maintain the humidity of the environment and prevent errors caused by atmospheric disturbances. The instrument's probe was placed on the back of the mouse and pressed against the skin, while the degree of skin damage was estimated by detecting the moisture lost by the stratum corneum. Each measurement was detected for 30 sec, monitoring the change in relative humidity and temperature to reach a stable curve. The average value was then expressed as a value of water dispersion with the unit of  $\text{g}\cdot\text{m}^{-2}\cdot\text{h}$ .

#### 2.15. Data and statistical analysis

Experimental data were expressed as means  $\pm$  SD of at least three independent measurements. Comparisons were carried out using Student's *t*-test for two groups, or two-way ANOVA with Bonferroni's post-hoc test (when *F* achieved  $p < 0.05$  and no significant variance inhomogeneity) for multiple groups (SigmaPlot, Systat Software, San Jose, CA, USA). A value of  $p < 0.05$  was considered statistically significant.

The 50% inhibitory concentration ( $\text{IC}_{50}$ ) was calculated from the dose–response curve obtained by plotting the percentage of inhibition versus concentrations (linear function, Microsoft Office). Graphs were plotted using SigmaPlot software. Equalization, randomization, and blinding were used for each group in both *in vitro* and *in vivo* experiments.

In ligand-receptor inhibitory assay (Fig. 7), superoxide generation or elastase release versus log [fMLF] were plotted to generate familiar sigmoid concentration-effect curve. Data normalization was employed as follows: For experiments where fluorescence intensity was measured employing flow cytometry (Fig. 3; 5A and 5B; 6) and adhesion assay (Fig. 5C), each value was divided by the mean of basal values and expressed in the form of fold of basal (labelled as 'Fold of basal' in Y axis of the figures). When analyzing the expression of phosphorylated protein levels in cells by Western blot (Fig. 9), detected protein expression intensities were first divided by the total protein and then expressed as % of the maximal detected value (labelled as '% of maximal' in Y axis of the figure). This was done to control for unwanted sources of variation.

### 3. Results

#### 3.1. Randialic acid B and tomentosolic acid selectively inhibit FPR1 stimulant-activated extracellular and intracellular superoxide anion generation by human neutrophils

First, we aimed to explore whether randialic acid B (RAB) and tomentosolic acid (TA) (Fig. 1A) have anti-inflammatory effects in human neutrophils. Neutrophils feature several offensive strategies to fight pathogens, one of which is the formation and release of ROS, mostly superoxide radicals, during a process called the respiratory burst. We used various neutrophil activators, including FPR stimulators such as fMLF (exogenous FPR1 stimulator), fMMYALF (endogenous FPR1 stimulator), or MMK1 (FPR2 stimulator), and stimulators of specific molecular signaling pathways, such as m3M3FBS (phospholipase C, PLC inducer) and PMA (protein kinase C, PKC inducer). According to the results (Fig. 1B and C), both RAB and TA demonstrated a concentration-dependent effect on the inhibition of extracellular superoxide production upon activation by both FPR1 stimulators, the exogenous fMLF or endogenous fMMYALF, with submicromolar  $\text{IC}_{50}$  values. In addition, both RAB and TA were unable to inhibit extracellular superoxide radicals produced by using the FPR2 stimulator MMK1 as well as the inducers of PLC signaling (m3M3FBS) and PKC signaling (PMA) pathways, indicating that FPR2 and the PLC or PKC pathways are not main molecular targets of RAB and TA (Fig. 1B and C). Also, RAB and TA did not trigger superoxide generation in resting neutrophils. These results suggested that RAB and TA selectively inhibit interaction with FPR1.

Furthermore, the production of total (intracellular and extracellular) ROS radicals was evaluated using luminol peroxidase system. The results showed that RAB and TA had a significant and concentration-dependent inhibitory effect on the ROS production in neutrophils activated by FPR1 stimulators fMLF and fMMYALF (Fig. 2).

Further, to verify the effect of RAB and TA on the intracellular superoxide radicals in the neutrophils activated by FPR1 (fMLF) or FPR2 stimulator (MMK1), hydroethidine (HE) was utilized. The results revealed that RAB and TA inhibited fMLF-stimulated intracellular

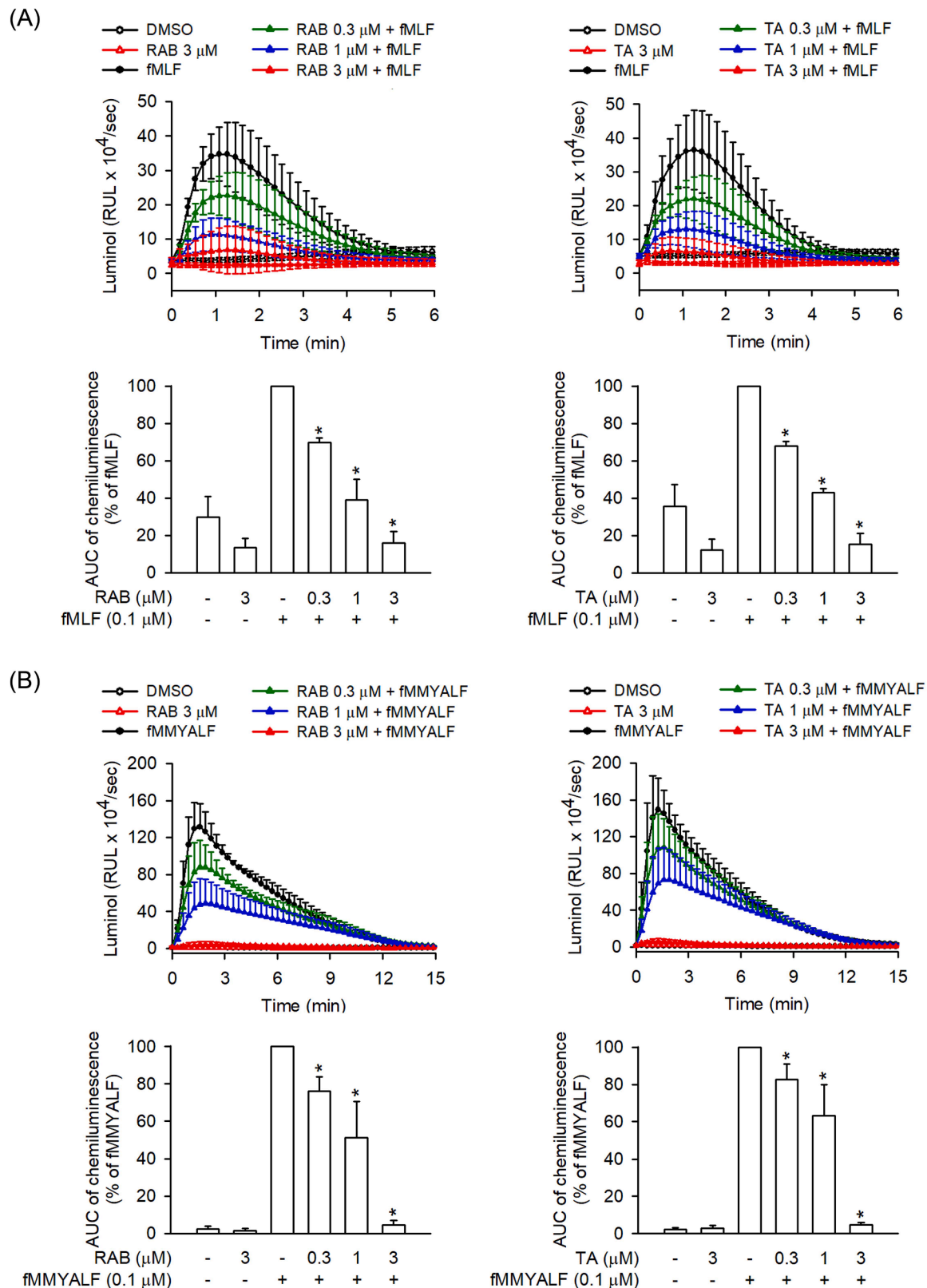
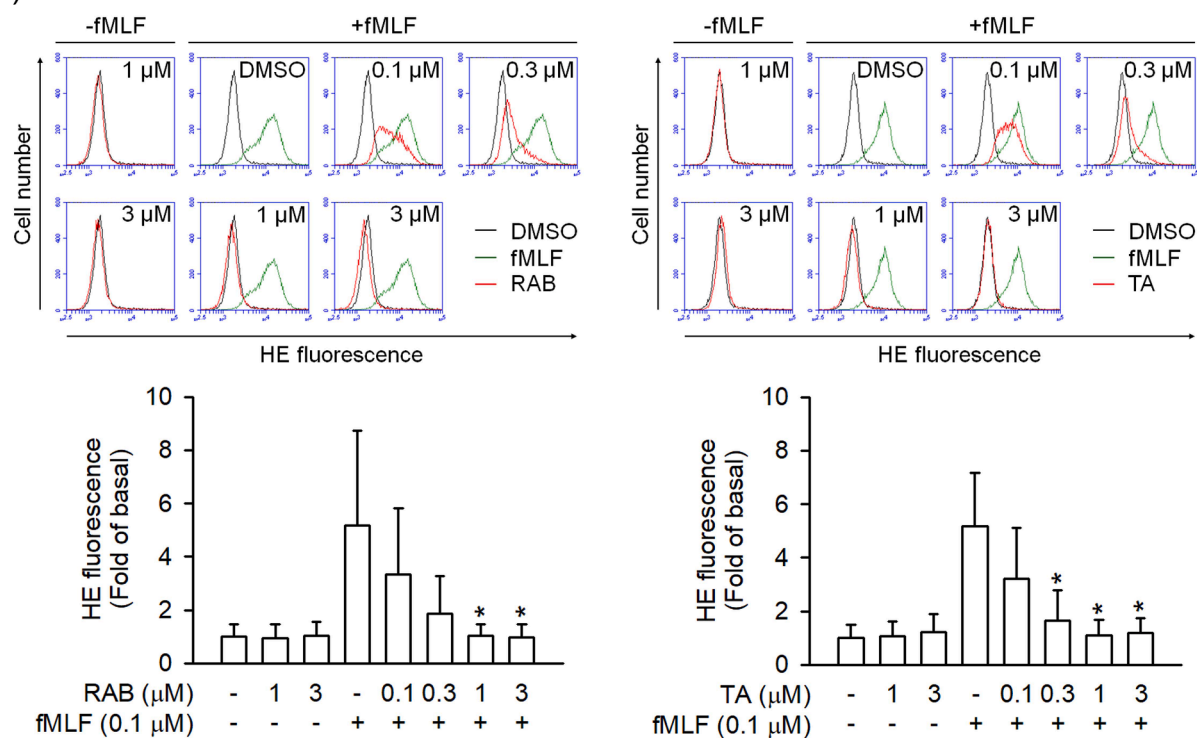


**Fig. 2.** Randialic acid B (left panel) and tomentosolic acid (right panel) inhibit ROS generation in FPR1 stimulators-activated human neutrophils in the luminol-enhanced chemiluminescence. Human neutrophils were incubated with DMSO (as control) or randialic acid B (RAB, 0.1–3 μM, left) or tomentosolic acid (TA, 0.1–3 μM, right) for 5 min and activated by (A) fMLF (0.1 μM), and (B) fMMYALF (0.1 μM)/CB (1 μg/ml) for another 6 or 15 min. The ROS formation was measured using the luminol peroxidase system. Peak chemiluminescence expressed as area under curve (AUC) of chemiluminescence levels was calculated and is presented as the means ± SD (n = 3).



(A)



(B)

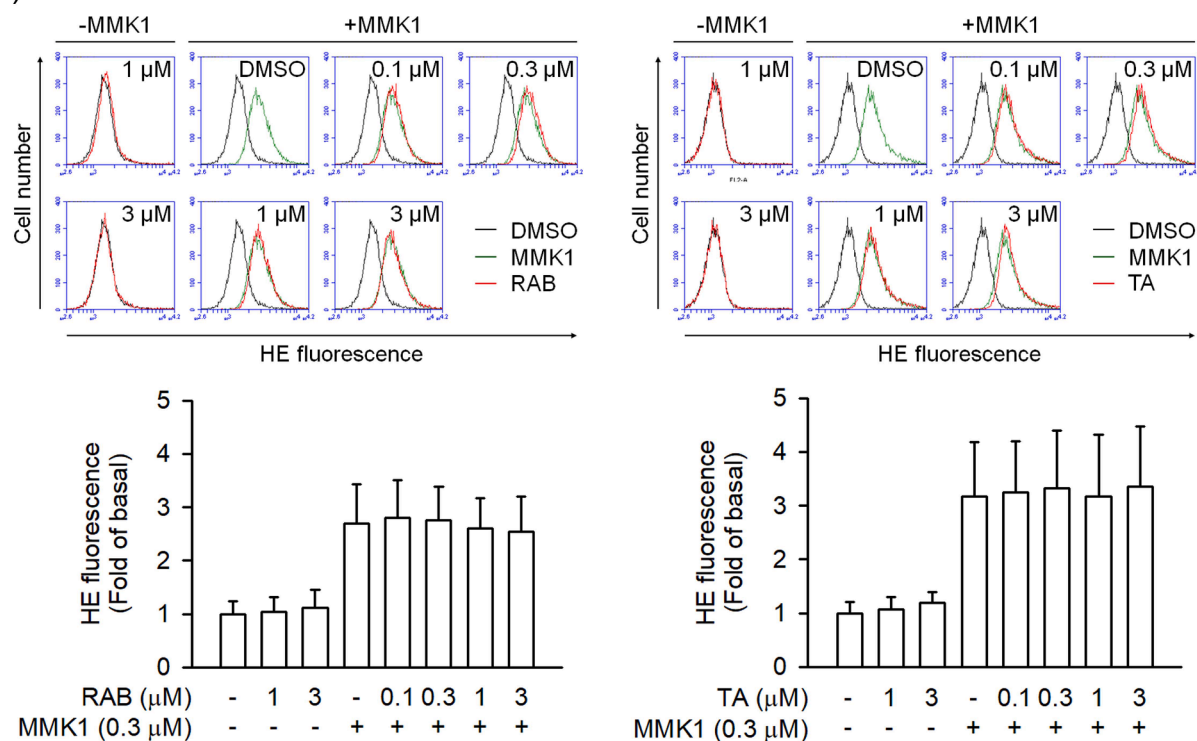
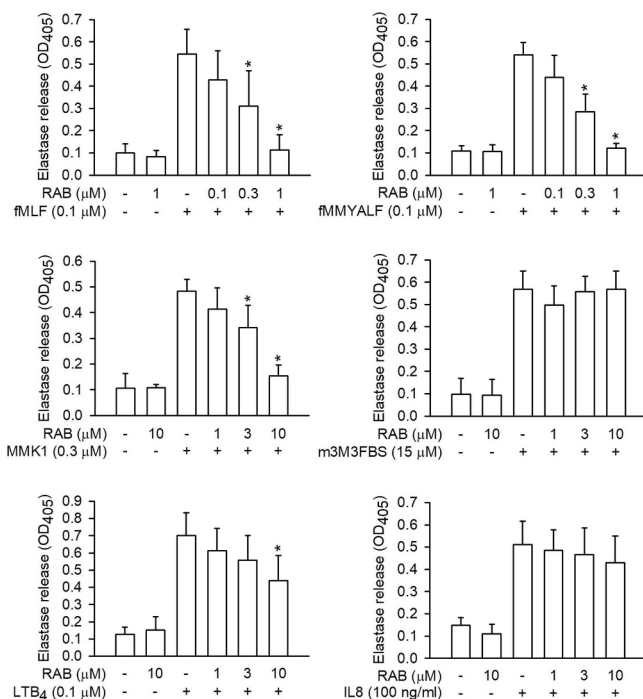


**Fig. 3.** Randialic acid B (left panel) and tomentosolic acid (right panel) selectively inhibits reactive oxygen species (ROS) generation in human neutrophils activated by FPR1 stimulator, but not by FPR2 stimulator. Hydroethidine (HE)-labeled human neutrophils were incubated with DMSO (as control), randialic acid B (RAB, 0.1–3  $\mu$ M, left panel) or tomentosolic acid (TA, 0.1–3  $\mu$ M, right panel) for 5 min and then activated by (A) fMLF (0.1  $\mu$ M)/CB (1  $\mu$ g·mL<sup>-1</sup>) or (B) MMK1 (0.3  $\mu$ M)/CB (1  $\mu$ g·mL<sup>-1</sup>) for another 5 min. The ROS formation was determined based on HE fluorescence intensity by flow cytometry. Representative histograms of flow cytometry are shown. Fluorescent intensities were calculated and are presented as means  $\pm$  SD ( $n = 6$ ). \*  $p < 0.05$  compared with the activator alone ( $t$ -test). HE, hydroethidine; FPR, formyl peptide receptor.

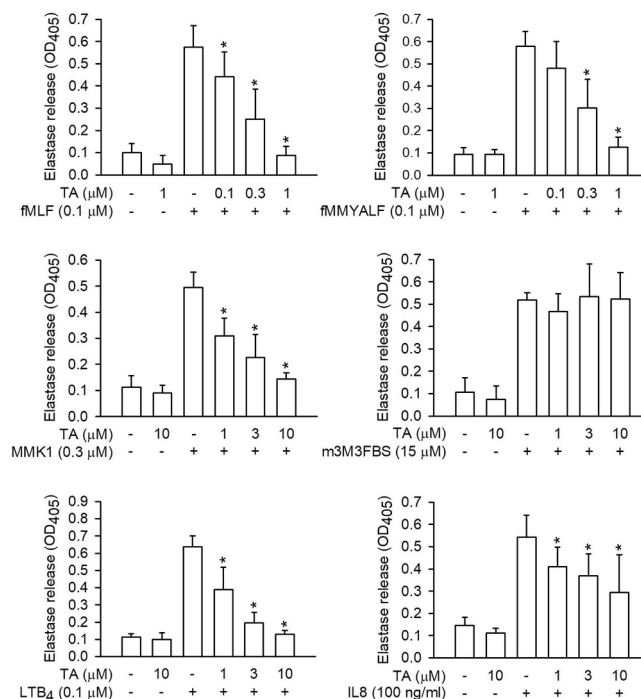
(A)

Compound	Elastase release, IC <sub>50</sub> (μM)					
	fMLF	fMMYALF	MMK1	m3M3FBS	LTB <sub>4</sub>	IL8
RAB	0.25 ± 0.14	0.24 ± 0.07	4.20 ± 1.55	>10	>10	>10
TA	0.27 ± 0.15	0.25 ± 0.12	2.87 ± 2.19	>10	1.42 ± 0.51	>10

(B) RAB



TA



(C)

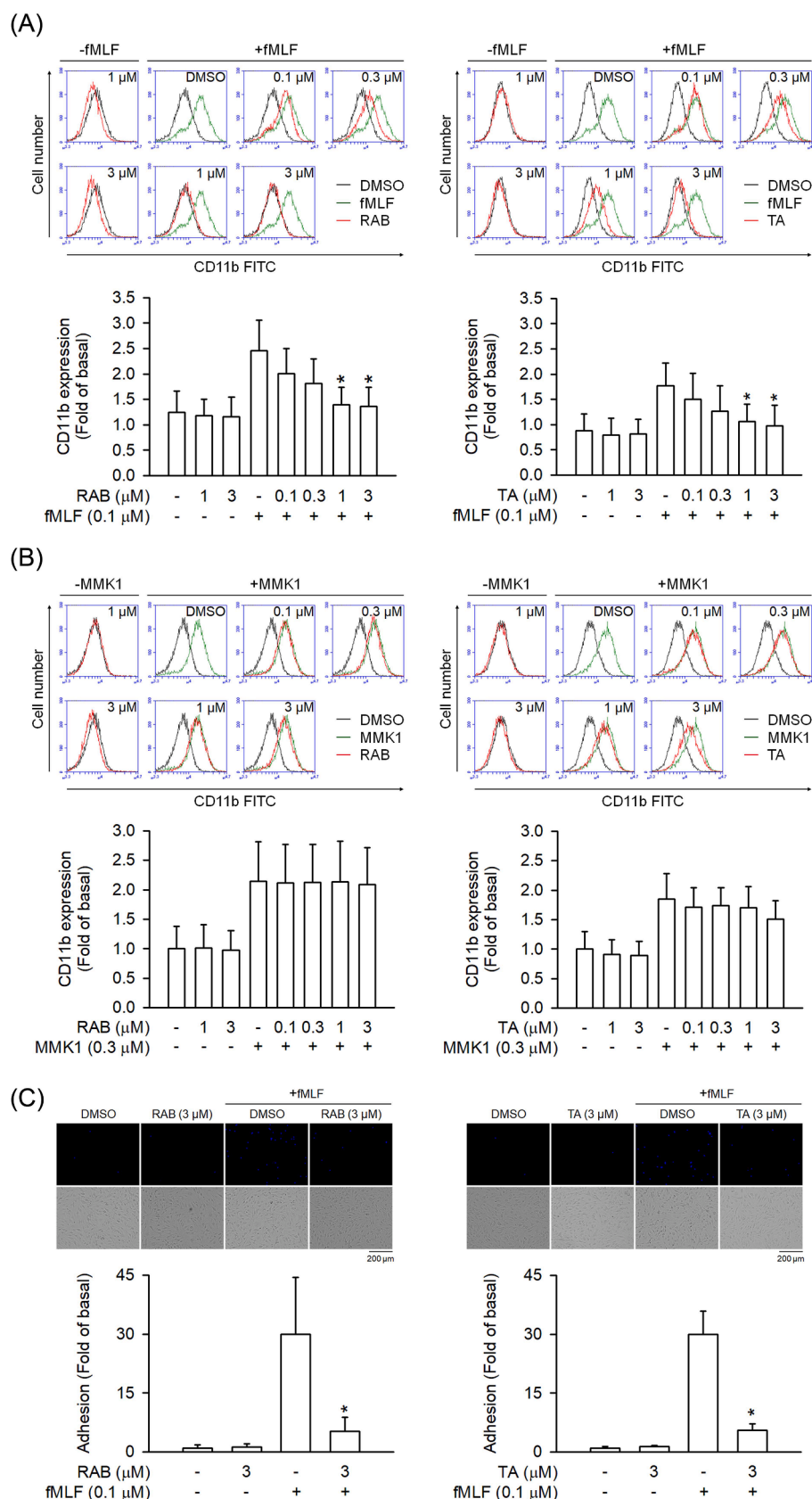


**Fig. 4.** Randialic acid B (left panel) and tomentosolic acid (right panel) significantly inhibit elastase release induced by activators of FPR1, but not by non-FPR1 activators. None of them inhibit elastase enzymatic activity at an effective concentration range. (A) RAB and TA significantly inhibit activators of FPR1, but not non-FPR1, induced elastase release in human neutrophils. Human neutrophils were incubated with DMSO (as control), randialic acid B (RAB, 0.1–10 μM, left panel) or tomentosolic acid (TA, 0.1–10 μM, right panel) for 5 min and then activated by fMLF (0.1 μM)/CB (0.5 μg·mL<sup>-1</sup>), fMMYALF (0.1 μM)/CB (0.5 μg·mL<sup>-1</sup>), MMK1 (0.3 μM)/CB (0.5 μg·mL<sup>-1</sup>), m3M3FBS (15 μM)/CB (0.5 μg·mL<sup>-1</sup>), LTB<sub>4</sub> (0.1 μM)/CB (2 μg·mL<sup>-1</sup>), and IL8 (100 ng·mL<sup>-1</sup>)/CB (2 μg·mL<sup>-1</sup>) for another 10 min. Results are expressed as IC<sub>50</sub> values, i.e., concentration necessary for 50% inhibition. (B) Concentration-dependent effects of RAB and TA on elastase release using FPR1 activators (fMLF and fMMYALF) and non-FPR1 activators (MMK1, m3M3FBS, LTB<sub>4</sub> or IL8). Elastase release was measured spectrophotometrically at 405 nm. All data are presented as means ± SD (n = 6). \* p < 0.05 compared with activator alone (t-test). (C) Human neutrophils were incubated with fMLF/CB for 15 min. The elastase supernatant was obtained and incubated with DMSO (as control), randialic acid B (RAB, 0.1–10 μM) or tomentosolic acid (TA, 0.1–10 μM) for 2 min before the addition of substrate (100 μM). Elastase activity was measured at 405 nm. Data are presented as means ± SD (n = 6). \* p < 0.05 compared with the control group (t-test).

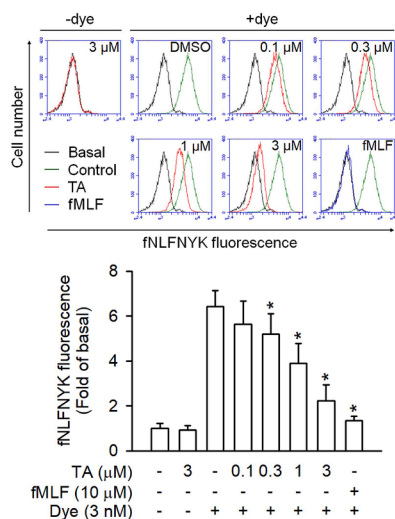
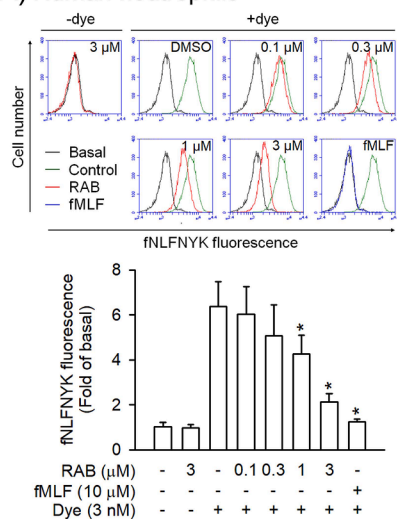
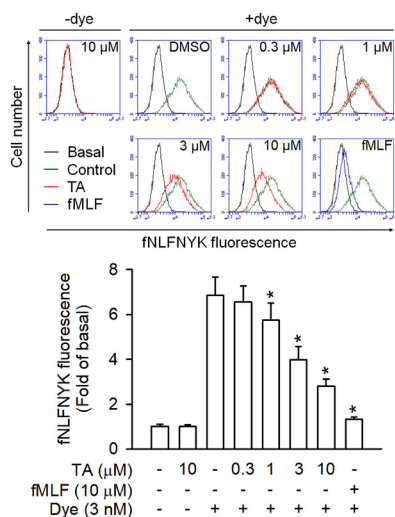
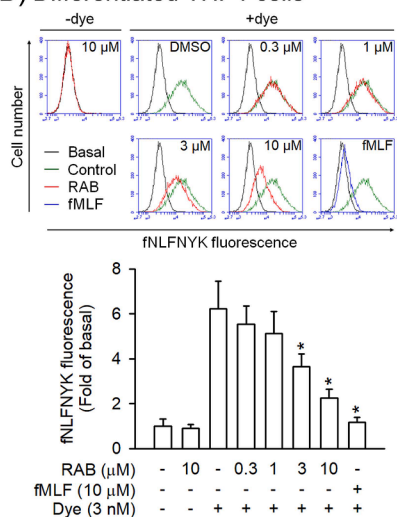
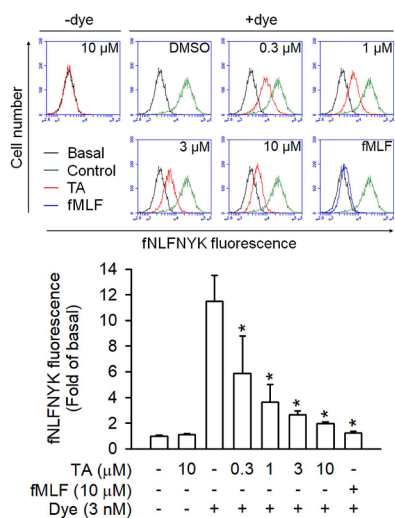
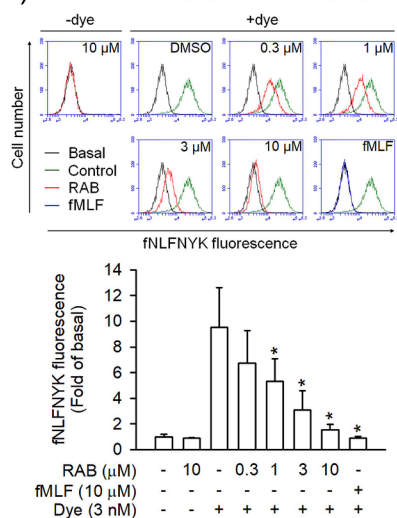
superoxide production in a concentration-dependent manner with IC<sub>50</sub> of 0.10 ± 0.02 μM and 0.11 ± 0.02 μM, respectively (Fig. 3A). None of the compounds inhibited the production of intracellular superoxide radicals induced by MMK1 (Fig. 3B) which further suggested a selective effect on the FPR1 pathway.

### 3.2. Randialic acid B and tomentosolic acid do not directly scavenge superoxide radicals and nitrogen radicals or cause cytotoxicity

The inhibitory effects of RAB and TA on superoxide anion generation didn't exclude a possibility of their direct interaction with radicals themselves. Therefore, the cell-free system was utilized to determine



**Fig. 5.** Randialic acid B (left panel) and tomentosolic acid (right panel) inhibit CD11b expression and adhesion in human neutrophils activated by FPR1 stimulator, but not by FPR2 stimulator. Human neutrophils were incubated with DMSO (as control), randialic acid B (RAB,  $0.1\text{--}3 \mu\text{M}$ , left panel), or tomentosolic acid (TA,  $0.1\text{--}3 \mu\text{M}$ , right panel) for 5 min and then activated by (A) fMLF ( $0.1 \mu\text{M}$ )/CB ( $0.5 \mu\text{g}\cdot\text{mL}^{-1}$ ) or (B) MMK1 ( $0.3 \mu\text{M}$ )/CB ( $0.5 \mu\text{g}\cdot\text{mL}^{-1}$ ) for another 5 min. The fluorescence intensity of the FITC-CD11b antibody was determined by flow cytometry. Fluorescence intensities are shown as means  $\pm$  SD (Fig. 5A,  $n = 4$ ; Fig. 5B,  $n = 5$ ; Fig. 5C,  $n = 6$ ). \*  $p < 0.05$  compared with activator alone ( $t$ -test). FPR, formyl peptide receptor. (C) Hoechst-labelled neutrophils were incubated with DMSO (as control), RAB ( $3 \mu\text{M}$ , left), or TA ( $3 \mu\text{M}$ , right) for 5 min, and then co-cultured with epithelial cells in fMLF ( $0.1 \mu\text{M}$ )/CB ( $0.5 \mu\text{g}\cdot\text{mL}^{-1}$ ) for another 15 min. Adherent neutrophils on bEND.3 cells were detected by fluorescent microscopy. Bar  $200 \mu\text{m}$ . Representative histograms for fluorescent microscopy are shown. Adherent neutrophils were counted and quantified. All data are expressed as means  $\pm$  SD ( $n = 6$ ). \*  $p < 0.05$  compared with fMLF alone ( $t$ -test). FPR, formyl peptide receptor.

**(A) Human neutrophils****(B) Differentiated THP1 cells****(C) hFPR1-transfected HEK293 cells**

**Fig. 6.** Randialic acid B (left panel) and tomentosolic acid (right panel) decrease fNLFNYK binding to FPR1 in human neutrophils, in differentiated THP1 cells, or hFPR1-transfected HEK293 cells. (A) Human neutrophils, (B) differentiated THP1 cells, or (C) hFPR1-transfected HEK293 cells were pre-incubated with DMSO (as control), randialic acid B (RAB, 0.1–10 μM, left panel), tomentosolic acid (TA, 0.1–10 μM, right panel), or fMLF (10 μM) for 5 min and labeled with FPR1-specific fluorescent ligand fNLFNYK (3 nM) for 30 min. Representative histograms demonstrating typical fluorescence in the absence or presence of fNLFNYK dye (control), fNLFNYK with RAB (left) or fNLFNYK with TA (right) are displayed. Mean fluorescence intensity was calculated and is presented as means  $\pm$  SD ( $n = 6$ ). \*  $p < 0.05$  compared with fNLFNYK alone ( $t$ -test).

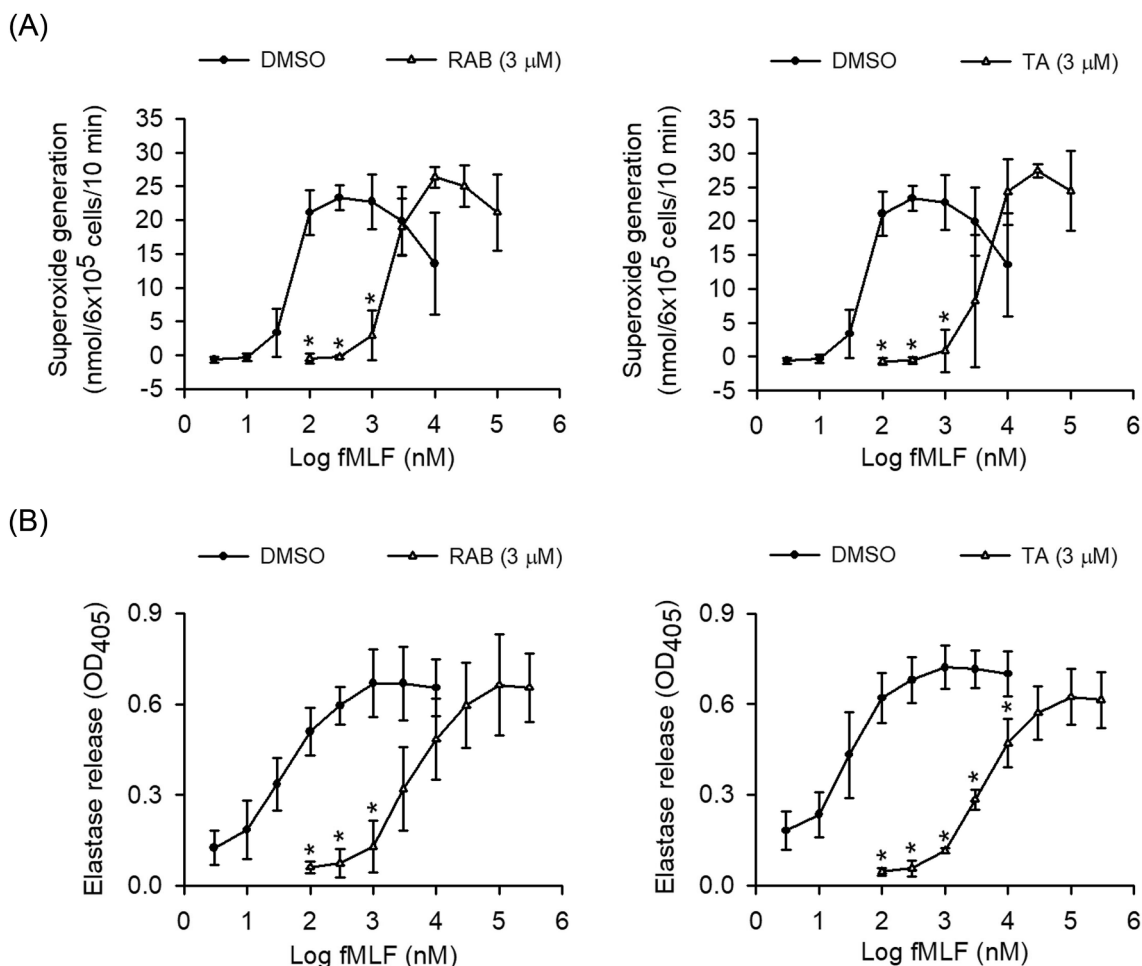


**Fig. 7.** Randialic acid B (left panel) and tomentosolic acid (right panel) competitively inhibit (A) superoxide anion generation and (B) elastase release in fMLF-activated human neutrophils. Human neutrophils were incubated with DMSO (as control), randialic acid B (RAB, 3 μM, left panel), or tomentosolic acid (TA, 3 μM, right panel) for 5 min and then activated by fMLF (0.003–100 μM for superoxide, 0.003–300 μM for elastase)/CB (1 μg·mL<sup>-1</sup> for superoxide, 0.5 μg·mL<sup>-1</sup> for elastase) for another 10 min. (A) Superoxide anion generation was measured based on ferricytochrome c reduction. (B) Elastase release was measured spectrophotometrically at 405 nm. All data are presented as means ± SD (n = 6). \* *p* < 0.05 compared to the fMLF alone (two-way ANOVA).

whether the test compounds can directly scavenge free radicals. The experiment revealed no scavenging effect of RAB and TA on scavenging superoxide radicals produced by xanthine/xanthine oxidase (Fig. 1D) or nitrogen radicals DPPH and ABTS (data not shown). Another concern, a toxic effect of RAB and TA towards human neutrophils, was eliminated by detecting the amount of LDH enzyme. The result showed that neither RAB nor TA were toxic at concentrations 0.1–10 μM during 15 min to 3 h treatment (data not shown).

### 3.3. Randialic acid B and tomentosolic acid selectively inhibit FPR1 stimulant-activated elastase release in human neutrophils

Degranulation is another important offensive feature of neutrophils where enzymes and proteases are released from granules. Neutrophils were activated by various specific inducers, including fMLF, fMMYALF (both FPR1), MMK1 (FPR2), LTB<sub>4</sub> (BLT1 receptor), IL8 (CXC chemokine receptors), and m3M3FBS (PLC pathway). The results (Fig. 4A and B) demonstrated that RAB and TA selectively and dose-dependently inhibited elastase release activated by both exogenous and endogenous FPR1 stimulators, fMLF and fMMYALF, with submicromolar IC<sub>50</sub> values. The effects of RAB and TA on the FPR2 stimulant, MMK1-induced degranulation were noticeably weaker (over 10-folds). Similarly, weak to no effects on elastase release were observed by using stimulators specific for different signal transduction, such as m3M3FBS,

LTB<sub>4</sub>, and IL8 (Fig. 4A and B). Overall, the results demonstrated the specificity of RAB and TA towards the FPR1 pathway. The profound effects of RAB and TA on elastase release didn't exclude direct binding and inhibition of elastase enzymatic activity. Therefore, collected elastase was incubated with RAB and TA in the cell-free system. Neither RAB nor TA could inhibit elastase enzymatic activity at an effective concentration range 0.1 to 3 μM (Fig. 4C).

### 3.4. Randialic acid B and tomentosolic acid inhibit the expression of CD11b, a surface neutrophil adhesion molecule, and adhesion induced by FPR1 stimulator

When neutrophils are activated, the expression of integrin CD11b/CD18 on the cell membrane is enhanced, thereby increasing the affinity with vascular endothelial cells, which facilitates the adherence of neutrophils to the vessel wall and finally allows the penetration via endothelial cells to reach the infected tissues [34]. In the first experiment, we detected the expression of CD11b fluorometrically using FITC-calibrated CD11b antibody in neutrophils activated either by fMLF, an FPR1 agonist, or by MMK1, an FPR2 agonist. The results showed that RAB and TA inhibited CD11b expression in fMLF-activated neutrophils in a concentration-dependent manner (Fig. 5A) but had no effect on MMK1-activated CD11b expression (Fig. 5B) indicating specificity for FPR1 pathway. In the following experiment, the mouse brain microvascular



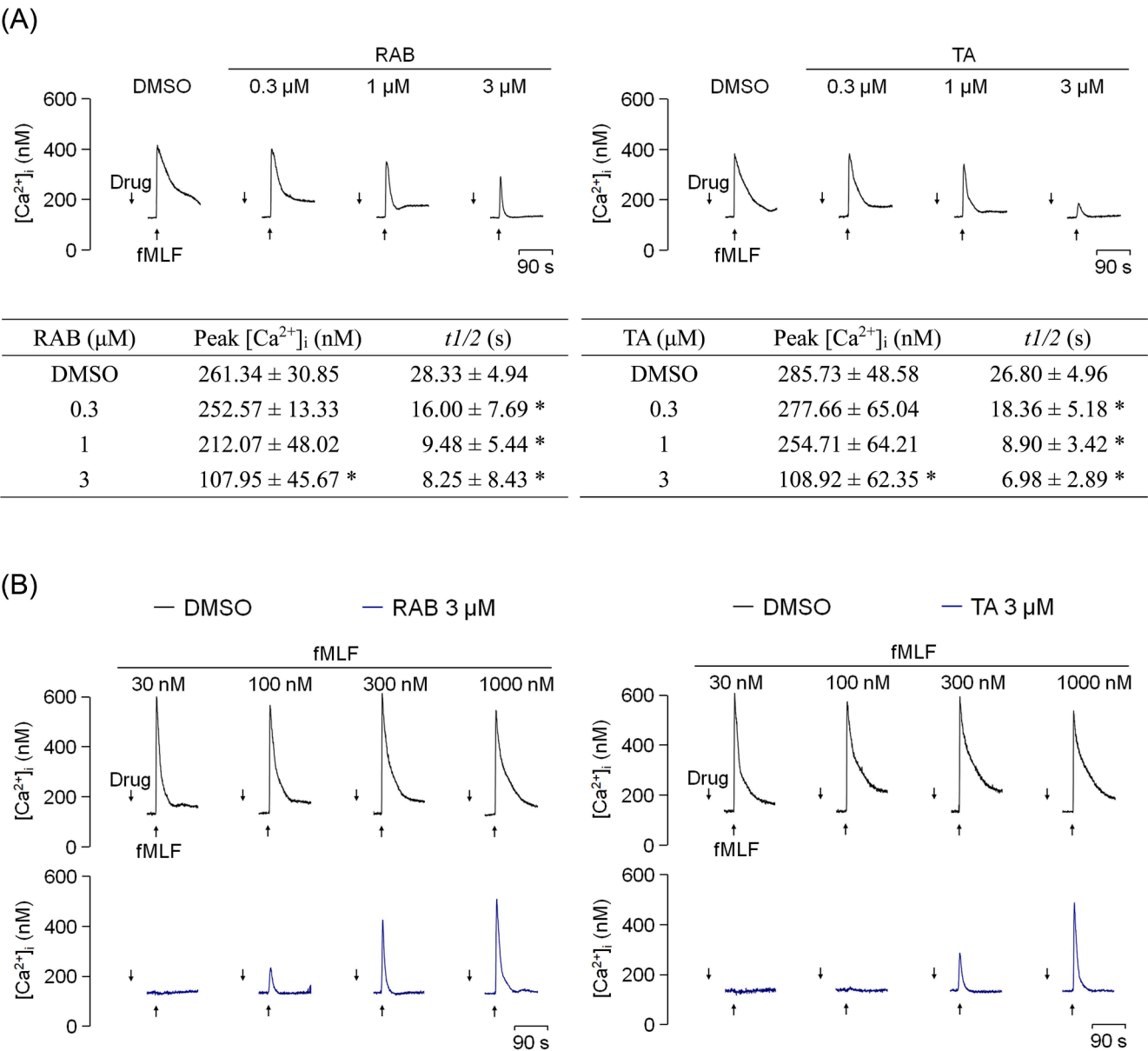


**Fig. 8.** Randialic acid B (left panel) and tomentosolic acid (right panel) competitively inhibit calcium mobilisation in fMLF-activated human neutrophils. (A) Fluo-3/AM-labeled neutrophils were incubated with DMSO (as control), randialic acid B (RAB, 0.3–3 μM, left), or tomentosolic acid (TA, 0.3–3 μM, right) and then activated with fMLF (0.1 μM) in the presence of Ca<sup>2+</sup> (1 mM). Fluorescence was monitored at 37°C with stirring. All data are presented as means ± SD (n = 5). \* *p* < 0.05 compared with the control (*t*-test). (B) Fluo-3/AM-labeled neutrophils were incubated with DMSO (as control), randialic acid B (RAB, 3 μM, left), or tomentosolic acid (TA, 3 μM, right) and then activated with fMLF (0.03–1 μM). All data are presented as the means ± SD (n = 3).

endothelial cell line bEnd.3 was used to mimic the adhesion of neutrophils in the vascular endothelium. The results revealed that RAB and TA effectively inhibited the adhesion of fMLF-activated neutrophils to bEnd.3 endothelial cells (Fig. 5C).

3.5. Randialic acid B and tomentosolic acid bind to FPR1 on the surface of the neutrophil cell membrane, as well as neutrophil-like cells and hFPR1-transfected cells

A stimulus, such as *N*-formyl peptide fMLF, combines with the FPR1 receptor present on the neutrophil cell membrane which triggers a cascade leading to respiratory burst, degranulation and production of inflammatory mediators by human neutrophils [9]. To understand whether RAB and TA inhibit neutrophil activation by binding to FPR1, the receptor-binding assay was performed utilizing the fluorescent labelled FPR1 specific ligand, an fMLF analog, fNLFNYK fluorescein dye

[24]. According to the results, both RAB and TA decreased fNLFNYK binding to FPR1 on the surface of human neutrophils in a dose-dependent manner as illustrated by a marked shift of the fluorescent peak to the left (Fig. 6A). The IC<sub>50</sub> for RAB and TA to FPR1 in human neutrophils was calculated as 1.28 ± 0.26 μM and 1.23 ± 0.22 μM, respectively. An FRP1 agonist, fMLF, served as positive control which completely inhibited the binding of fNLFNYK dye to the receptor. This result demonstrates that both RAB and TA interact with the FPR1 receptor and thus prevent the exposure of the FPR1 receptor to its fNLFNYK ligand. Furthermore, to understand whether RAB and TA also bind to FPR1 in different cell types, we used THP-1 cells (human monocytic cell line) differentiated into neutrophil-like cells and HEK293 cells (human embryonic kidney cells) with human FPR1 receptor (hFPR1) transfected onto the cell membrane. Both RAB and TA decreased fNLFNYK binding to FPR1 on the surface of differentiated THP-1 cells in a concentration-dependent manner with the IC<sub>50</sub> of 4.08



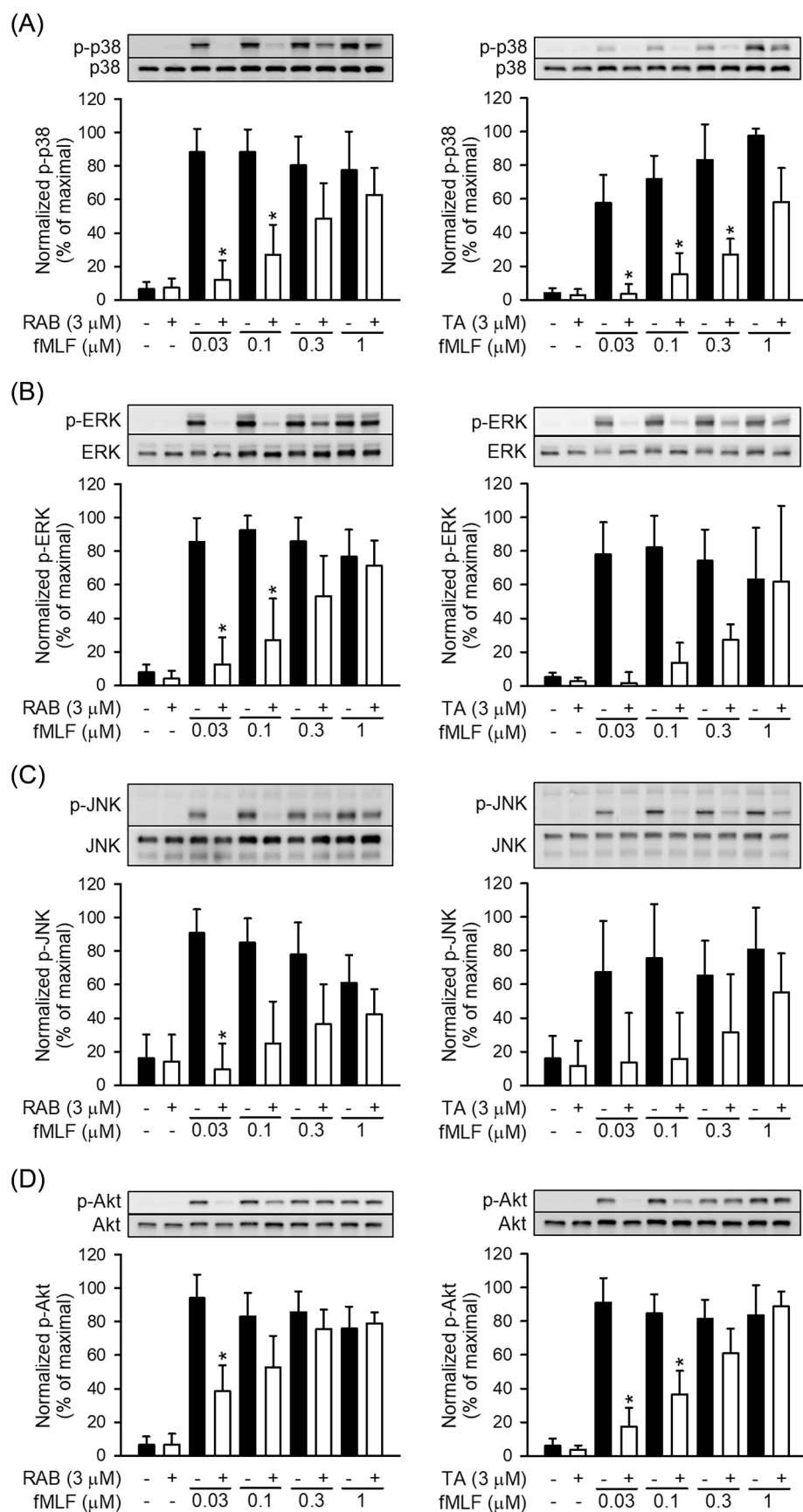


**Fig. 9.** Randialic acid B (left panel) and tomentosolic acid (right panel) competitively inhibit fMLF-induced phosphorylation of p38, ERK, JNK or Akt in human neutrophils. Human neutrophils were incubated with DMSO (as control), randialic acid B (RAB, 3  $\mu$ M, left) or tomentosolic acid (TA, 0.1–10  $\mu$ M, right) for 5 min before stimulation with or without fMLF for another 25 s. Phosphorylation of (A) p38, (B) ERK, (C) JNK and (D) Akt analyzed by immunoblotting with antibodies raised against the phosphorylated and total form of each protein. Data are normalized to the corresponding total protein level and expressed as means  $\pm$  SD relative to the mean maximal ratio ( $n = 6$ ). \*  $p < 0.05$  compared with the corresponding control group (two-way ANOVA).

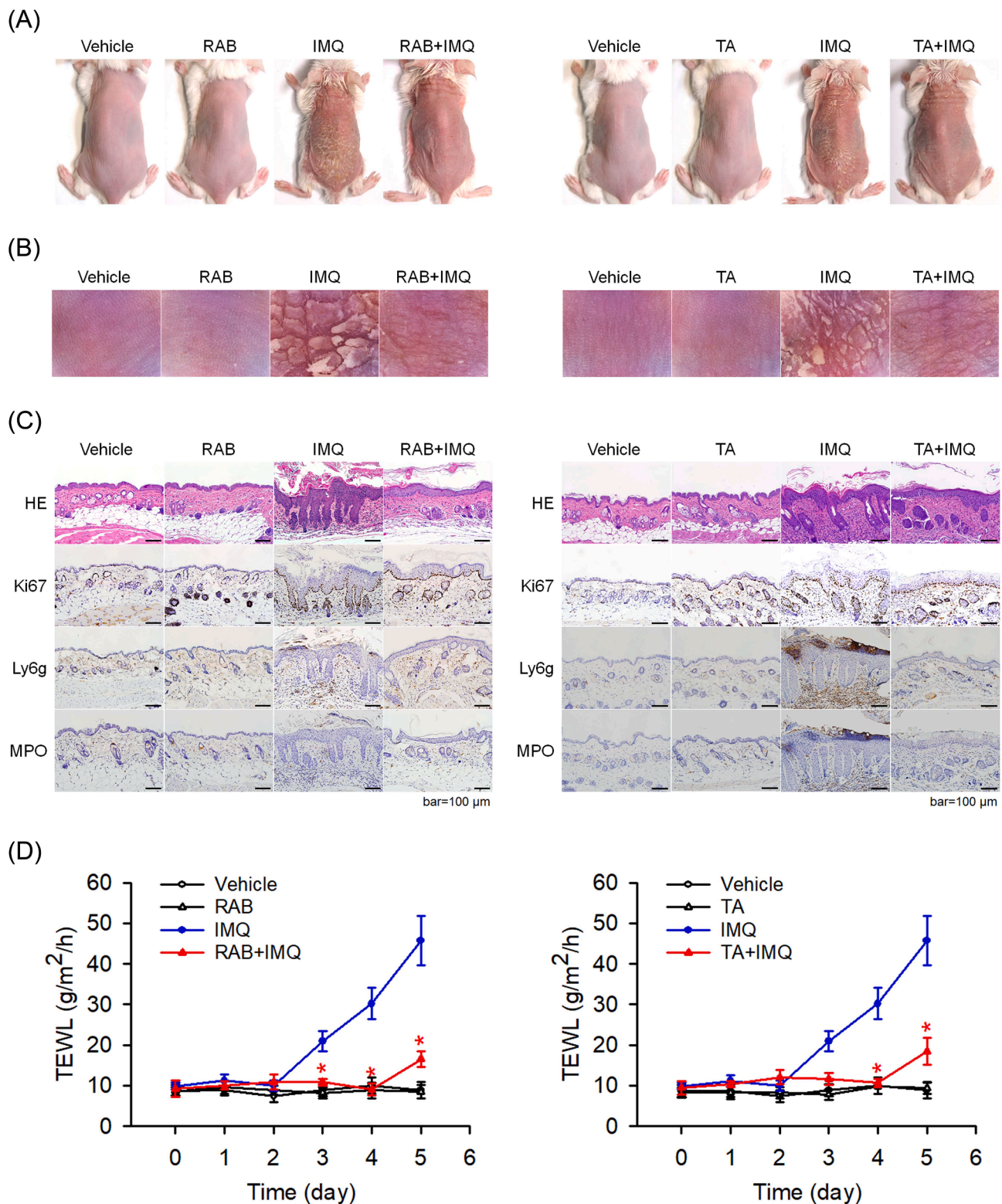


**Fig. 10.** Randialic acid B (left panel) and tomentosolic acid (right panel) reduce imiquimod (IMQ)-induced psoriasis-like skin lesions in mice. BALB/c mice were treated daily with vehicle (10% DMSO), randialic acid B (RAB, 10 mg·kg<sup>-1</sup>, left) or tomentosolic acid (TA, 10 mg·kg<sup>-1</sup>, right) by intravenous injection before induction of psoriasis-like inflammation by applying 5% imiquimod (IMQ) cream on the shaved back skin for 5 consecutive days. (A) Phenotypic presentation of the back skin at day 5. (B) Microscopic presentation of the back skin. (C) Histological analyses of mouse back skin by H&E staining and immunohistochemistry staining for Ki67, Ly6g, and MPO (n = 6 mice). Scale bars, 100 μm. (D) RAB (left) and TA (right) attenuate the degree of transepidermal water loss (TEWL) in IMQ-treated mice. The transepidermal water loss was measured by tewameter and expressed as means ± SD (n = 6). \* *p* < 0.05 compared with the corresponding control group (two-way ANOVA).

$\pm 0.48 \mu\text{M}$  and  $3.39 \pm 0.32 \mu\text{M}$ , respectively (Fig. 6B). Similarly, both RAB and TA reduced binding of the activating ligand fNLFFNYK to its cell surface receptor in HEK293 cells transfected with hFPR1 with  $\text{IC}_{50}$  of  $0.98 \pm 0.06 \mu\text{M}$  and  $0.27 \pm 0.10 \mu\text{M}$ , respectively (Fig. 6C).

### 3.6. Randialic acid B and tomentosolic acid attenuate the activation of neutrophils by competitively inhibiting fMLF

The above experiments proved that both RAB and TA can inhibit the binding of fMLF to FPR1, thus the next aim was to explore the type of ligand-receptor inhibition. In this test, we used different concentrations of fMLF (0.003–100  $\mu\text{M}$ ) to stimulate human neutrophils. Both RAB (3  $\mu\text{M}$ ) and TA (3  $\mu\text{M}$ ) markedly inhibited superoxide radical production (Fig. 7A) or elastase release (Fig. 7B) upon stimulation with low concentrations of fMLF, but the effect diminished with high concentrations of fMLF, producing parallel rightward shift in the concentration–response curve of fMLF. This demonstrated that both RAB and TA act as competitive inhibitors of fMLF binding to the FPR1 receptor.

### 3.7. Randialic acid B and tomentosolic acid inhibit fMLF-stimulated $\text{Ca}^{2+}$ modulation in human neutrophils

When a GPCR receptor FPR1 is stimulated, a downstream molecular cascade is turned on leading to calcium mobilisation via inositol-1,4,5-triphosphate (IP3) and PLC pathway, followed by activation of signaling proteins and the release of effector molecules by neutrophils [35]. We evaluated the effect of RAB and TA on intracellular calcium concentration ( $[\text{Ca}^{2+}]_i$ ) in neutrophils stimulated by fMLF, an FPR1 agonist. Such activation in the presence of extracellular calcium would cause a transient increase in  $[\text{Ca}^{2+}]_i$  until reaching a maximum ( $[\text{Ca}^{2+}]_i$  peak) and subsequently  $[\text{Ca}^{2+}]_i$  would come back to equilibrium, usually within a minute. Experimental results illustrated that RAB and TA cause a concentration-dependent inhibition of the transient increase of  $[\text{Ca}^{2+}]_i$  stimulated by fMLF in neutrophils (Fig. 8A). Both RAB and TA reduced the maximum peak of calcium influx triggered by FPR1 agonist as well as shortened the calcium recovery time  $t_{1/2}$  indicating downstream effects of RAB and TA on neutrophil activation. In additional experiments, we evaluated the effects of RAB and TA on calcium mobilisation in neutrophils stimulated by non-FPR1 stimulators, including MMK1 (FPR2 agonist), m3M3FBS (PLC agonist), LTB4 (BLT1 receptor), and IL8 (CXCR receptor). The results revealed that RAB and TA did not affect  $[\text{Ca}^{2+}]_i$  in the neutrophils activated by non-FPR1 stimuli (data not shown). We also used increasing concentrations of fMLF (0.03–1  $\mu\text{M}$ ) to activate neutrophils and the results indicated that both RAB and TA competitively inhibited calcium mobilisation (Fig. 8B). These findings indicated that RAB and TA competitively and selectively inhibit FPR1 agonist-activated calcium mobilisation.

### 3.8. Randialic acid B and tomentosolic acid competitively inhibit the phosphorylation of MAPKs and Akt downstream signals in FPR1 agonist-induced neutrophils.

The activation and phosphorylation of signaling proteins, such as MAPK or Akt, regulate physiological functions of neutrophils, including respiratory burst, degranulation or adhesion. Immunoblotting experiments revealed that RAB and TA (3  $\mu\text{M}$ ) markedly inhibited the phosphorylation of MAPK (p38, Fig. 9A; ERK, Fig. 9B; JNK, Fig. 9C) and Akt (Fig. 9D) proteins in fMLF-activated human neutrophils. It was also demonstrated that MAPKs and Akt phosphorylation is gradually impaired upon activation of neutrophils with increasing concentration of FPR1 inducer (fMLF, 0.03–1  $\mu\text{M}$ ). This result confirmed that RAB and TA act as antagonists of FPR1 and have a competitive relationship with fMLF.

### 3.9. Randialic acid B and tomentosolic acid are effective in attenuating the symptoms of psoriasis induced by IMQ in mice

In our experiments, both RAB and TA have been proven to act as FPR1 competitive antagonists, however, there is a lack of understanding whether inhibitor of FPR1 would be effective in the treatment of psoriasis. Therefore, we utilized a psoriasis-like inflammation mouse model induced by imiquimod (IMQ), an agonist of toll-like receptors [36]. The typical psoriatic skin symptoms include erythema, plaques, silvery-white scales, hyperkeratosis, epidermis thickening, and importantly, neutrophil infiltration concentrated within so-called Munro's microabscesses. To understand whether RAB and TA, antagonists of FPR1, are applicable for the treatment of psoriasis, we administered a dose of 10  $\text{mg}\cdot\text{kg}^{-1}$  of RAB or TA intravenously every second day and applied IMQ to the shaved back of the mouse daily for five consecutive days. Daily observation of the skin structure indicated that the IMQ-treated skin began to appear slightly dry on the third day, and consequently, erythema and skin scaling were observed on the fifth day (Fig. 10A). The microscopic observation of the IMQ-experimental group of mice clearly revealed the formation of erythema and silvery-white scales compared with the healthy, rosy and smooth skin of the IMQ-free group (Fig. 10B). On the contrary, the skin condition of RAB or TA-treated groups was markedly improved showing almost no scaling, reduced erythema and dryness (Fig. 10B). The skin samples from the back of the mice were further analysed, using hematoxylin-eosin (H&E) staining for histology, immunohistochemical staining by Ki67 for the epidermal proliferation, and using Ly6G and MPO as markers for neutrophil infiltration (Fig. 10C). IMQ-treated skin featured hyperkeratosis, epidermis thickening and neutrophil infiltration with the formation of Munro's microabscesses while these hallmarks of psoriasis were significantly reduced in the mice treated with RAB and TA.

In psoriatic skin, the stratum corneum is damaged which affects the skin's water retention function. The transepidermal water loss (TEWL) reflects the integrity of the stratum corneum and is commonly used as a reference index in the evaluation of psoriasis severity or treatment progress. According to our data, TEWL of the IMQ group was increased continuously, indicating compromised integrity of the stratum corneum, resulting in a significant increase in the water loss through the skin. Importantly, in both RAB and TA treatment groups, the TEWL values were significantly reduced with only a slight difference from normal skin group (Fig. 10D). The aforementioned results indicated that both RAB and TA, which were demonstrated to act as FPR1 antagonists, can effectively ameliorate the symptoms of psoriasis induced by IMQ.

## 4. Discussion and conclusions

Psoriasis is a long-lasting inflammatory skin disease caused by poor regulation of the immune response. Up to date, there is still no radical cure available. In the pathogenesis of psoriasis, the keratinocytes are activated, a large number of immune cells is attracted and infiltrated to the skin causing damage to the skin cells and leading to abnormal proliferation of the skin epidermis and dermis, thereby forming a dry lesion. The process includes binding DNA fragments of keratinocytes with antimicrobial peptide LL-37 and the release of various interleukins (particularly IL-17) from dendritic cells, Th1, and Th17 cells [36]. Recently, an increasing number of studies point to the importance of neutrophils involvement in psoriasis [37]. One of the key features is the formation of Munro's microabscesses that is correlated with the accumulation of neutrophils in the epidermis [38]. It has been demonstrated that experimental depletion of neutrophils improved the course of psoriasis in patients [10,39].

Neutrophils usually respond to pathogen- or damage-associated chemotactic molecular patterns (PAMPs and DAMPs) from the environment, which are recognized by transmembrane GPCRs (such as FPR1) on the cell surface [40]. Respiratory burst and degranulation are key inflammatory features of neutrophils to fight pathogens or sterile

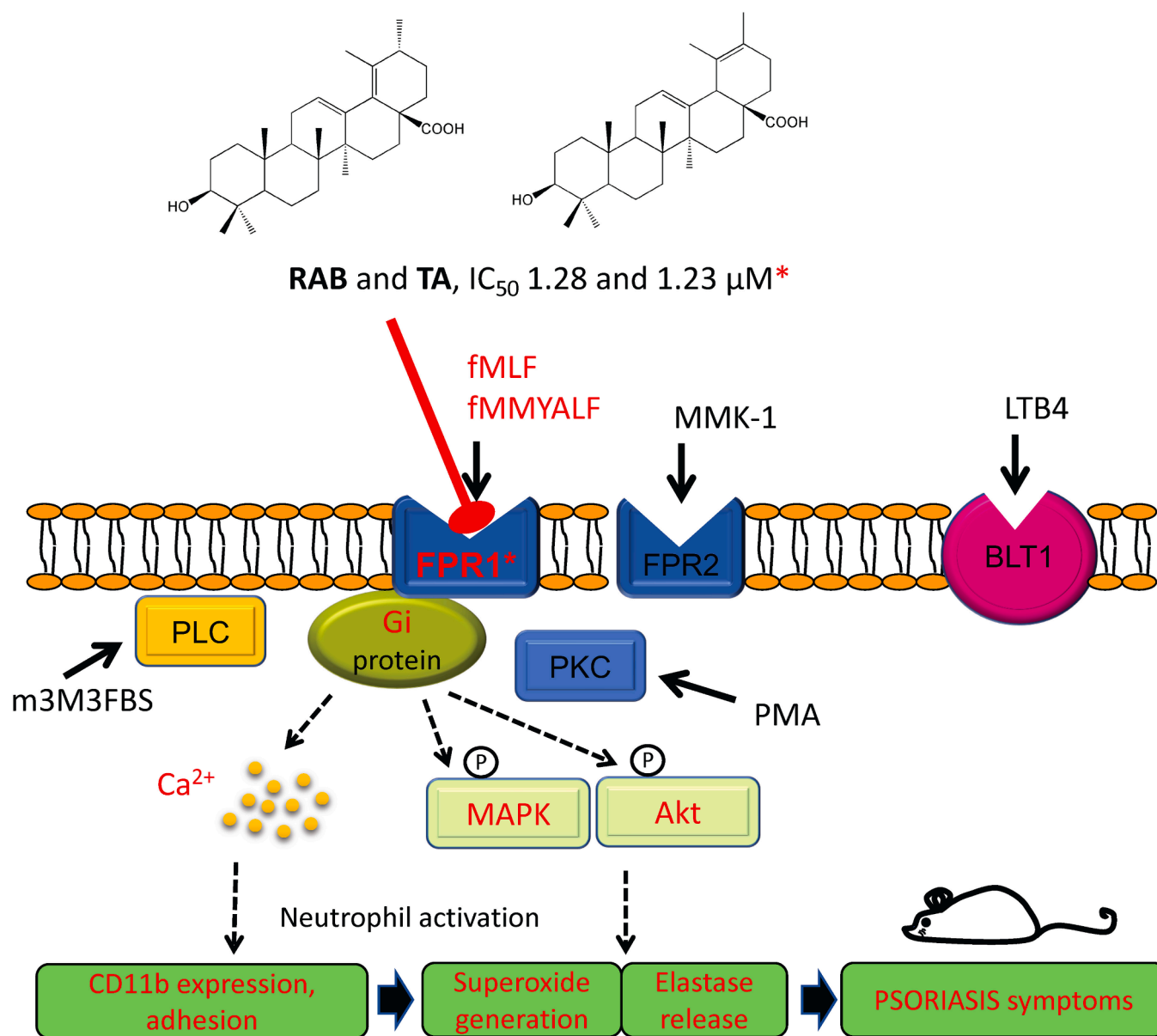


**Fig. 11.** Schematic mechanism of suppressive effects of randialic acid B (RAB) and tomentosolic acid (TA) on neutrophilic activation and psoriasis-like inflammation. Molecular targets inhibited by RAB and TA are indicated in red. RAB and TA selectively and competitively inhibited FPR1 and subsequently neutrophils activation, including calcium mobilisation, Akt and MAPKs signaling, respiratory burst, degranulation and adhesion. The results were further illustrated *in vivo* using the IMQ-induced psoriasis-like inflammation mouse model. FPR1, formyl peptide receptor 1. (For interpretation of the references to color in this figure legend, the reader is referred to the web version of this article.)

inflammation. These offensive features are usually initiated by activation of FPR1 pathway. The modulation of FPR1 function by natural products such as triterpenoids RAB and TA demonstrated in the present study can facilitate the development of new anti-inflammatory agents.

Triterpenes are pentacyclic compounds abundant in nature with more than 20,000 combinations that exert various bioactivity profiles with particular importance of ursane, oleanane and lupane type [41]. The presence of a C-28 carboxylic group (RAB and TA, Fig. 1A) has been reported as a structural prerequisite for anti-inflammatory activity *in vivo* [42]. Ursolic acid has been previously isolated from various plants of different families, such as *Ilex* (Aquifoliaceae) [14], *Eucalyptus* (Myrtaceae) [43] or *Pyrola* (Pyrolaceae) [44]. On the other hand, very few studies reported on the isolation of unsaturated derivatives of ursolic acid, i.e., tomentosolic acid (TA, also known as sanguisorbinin) or randialic acid B (RAB, also known as vangerolic acid). TA was isolated only from *Sanguisorba officinalis* (Rosaceae) [45] and *Vangueria*

*tomentosa* (Rubiaceae) [46] while RAB from *Randia dumetorum* (Rubiaceae) [47], *Vangueria tomentosa* [46] and *Ilex cornuta* [48]. However, these triterpenes could be also obtained from triterpenoid saponins of various plants such as *Sanguisorba* [49] or *Ilex* [14], simply by hydrolysis of the glycosidic bond. For instance, RAB and TA were previously obtained from a saponin glycoside latifolioside G, one of the major components of *Ilex kaushue* [14]. Both *Ilex kaushue* and *Sanguisorba officinalis* are traditional medicines used for the treatment of inflammatory diseases [50]. Interestingly, the plants are either roasted or boiled before consumption which may facilitate hydrolysis of these saponins and production of active aglycons RAB or TA [51]. Thus, the potent activity of RAB and TA to treat neutrophilic inflammation may be correlated to the therapeutic effect and traditional use of *I. kaushue*.

Ursolic acid has been reported to exert anti-inflammatory activities through suppression of NO synthase, COX-2, and the NF-κB pathway [52]. A previous study revealed the inhibitory effects of ursolic acid on



respiratory burst and degranulation in human neutrophils induced by fMLF [18]. Interestingly, in agreement with previous preliminary results [14], we found that both RAB and TA are up to five-folds more active in the inhibition of superoxide generation and elastase release compared to ursolic acid. That motivated us to study the regulation of neutrophil activation by RAB and TA. Previously, ursolic acid inhibited superoxide generation in vitro while did not possess the radicals scavenging abilities [18,53]. Similarly, RAB and TA did not scavenge the superoxide or other radicals. Furthermore, the experimental results of respiratory burst, degranulation, adhesion, binding and calcium influx assays, suggested that RAB and TA selectively inhibit interaction with FPR1 in the competitive manner with fMLF, a physiological FPR1 agonist. The selectivity towards the FPR1 receptor was proved by multiple experiments. Most importantly, the FPR1 on the surface of the cell membrane of different cells (neutrophils, THP1 neutrophil-like cells, hFPR1-transfected HEK293) was blocked by both RAB and TA in FPR1 receptor-binding assay. Both compounds inhibited FPR1 binding with fNLFNYK, a specific and well-established FPR1 analog for FPR1 binding evaluation [17,23] which confirmed interaction with FPR1 regardless the cells origin. Furthermore, the ligand-receptor interaction experiment demonstrated a competitive inhibitory relationship with FPR1. Thus, RAB and TA proved to block FPR1, preventing transmission of transduction signals to downstream which leads to the suppression of inflammatory response [54]. The downstream signals, such as intracellular  $\text{Ca}^{2+}$ , an important second messenger, together with MAPK and Akt signaling transduction were all inhibited by RAB and TA pretreatment. These processes would ultimately affect multiple cellular physiological functions, including respiratory burst and degranulation in human neutrophils [54].

Previously, it was demonstrated that modulation of FPR1 signalling might be a good approach to treat COPD [55], hepatic injury [56], lung injury [17], colitis or sterile inflammation (9). It has been revealed that both genetic ablation of the FPR1 and application of FPR1 antagonist (cyclosporine H) could attenuate smoking-induced lung emphysema in mice [55]. It is important to note that there are currently no FPR1 inhibitors available in clinical use. Among experimental FPR1 antagonists, several compounds were identified, including the clinical drug propofol [57], neolignan honokiol [23], dipeptide HCH6-1 [17] or hederagenin saponin SMG-1 [58]. Both RAB and TA can be obtained by simple hydrolysis of saponins abundant in nature. Also, the triterpenoid structure of RAB and TA may serve as a lead compound for development of FPR1 antagonists.

Interestingly, a calcium-sensing molecule STIM1 knock-out mice were evaluated using IMQ-induced psoriasis-like skin model, and the mice displayed improved symptoms of psoriasis and reduced neutrophil infiltration in the epidermis. The gene ablation of STIM1, which is related to the chemoattractant FPR1 pathway, impaired neutrophils contribution to psoriatic inflammation [59]. Moreover, FPR1 gene is among the genes consistently elevated by IMQ and associated with upregulated inflammation, and immune response [60]. It is known, that effective regulation of immune cells over-activation in psoriasis disease can help improve the psoriatic symptoms [61]. However, there are currently no studies using FPR1 antagonists to treat psoriasis. Therefore, we used the psoriatic mouse model induced by IMQ, where mice developed dry skin, silver scales and erythema. Meanwhile, the skin of mice treated with RAB or TA was improved, i.e., the symptoms of dry skin and silver scales were suppressed, and neutrophils dissemination which is correlated with the presence of Munro's microabscesses was reduced. The number of  $\text{Ly6G}^{+}$  cells in the dermis and subcutaneous tissue, which was also previously correlated with the scaling [62] was diminished. The profound effect of FPR1 antagonists on psoriatic skin suggests a potential utilization of FPR1 inhibitors in the treatment of autoimmune neutrophilic skin diseases.

In conclusion, RAB and TA are selective inhibitors of FPR1, acting primarily by reducing the stimulation of *N*-formyl peptide by binding to FPR1 on the neutrophil cell membrane (Fig. 11). The inhibition of FPR1

by RAB or TA is competitive and leads to the inhibition of superoxide radical production, elastase release, adhesion and downstream signaling by neutrophils. The FPR1 competitive antagonists RAB and TA proved effective in improving the appearance of the IMQ-induced psoriatic skin, reducing neutrophil infiltration, and also reversing the aberrant degree of skin water dispersion. Therefore, RAB and TA have the potential for further development as effective FPR1 antagonists in the treatment of neutrophilic inflammatory disorders including psoriasis.

## CRediT authorship contribution statement

**Michal Korinek:** Validation, Visualization, Writing - original draft. **Pei-Shan Hsieh:** Investigation, Methodology, Data curation, Writing - original draft. **Yu-Li Chen:** Writing - review & editing. **Pei-Wen Hsieh:** Conceptualization. **Shih-Hsin Chang:** Validation, Visualization. **Yi-Hsiu Wu:** Investigation, Methodology, Data curation, Validation, Visualization. **Tsong-Long Hwang:** Conceptualization, Writing - review & editing, Supervision, Methodology, Funding acquisition.

## Declaration of Competing Interest

The authors declare that they have no known competing financial interests or personal relationships that could have appeared to influence the work reported in this paper.

## Acknowledgements

This research was supported by the grants from the Ministry of Science and Technology (MOST 106-2320-B-255-003-MY3 and MOST 108-2320-B-255-003-MY3, MOST 109-2327-B-255-001, MOST 109-2327-B-182-002 and MOST 109-2811-I-006-500), Chang Gung Memorial Hospital (CMRPF1G0241 ~ 3, CMRPF1J0051 ~ 3, and BMRP450), Chang Gung University (104-6576A3), Taiwan. The funders had no role in the study design, data collection and analysis, decision to publish, or preparation of the manuscript. All authors had full access to the full data in the study and accept responsibility to submit for publication.

## References

- [1] E. Kolaczowska, P. Kubes, Neutrophil recruitment and function in health and inflammation, *Nat Rev Immunol.* 13 (3) (2013) 159–175.
- [2] S. Jaillon, M.R. Galdiero, D. Del Prete, M.A. Cassatella, C. Garlanda, A. Mantovani, Neutrophils in innate and adaptive immunity, *Semin Immunopathol.* 35 (4) (2013) 377–394.
- [3] P.H. Leliefeld, C.M. Wessels, L.P. Leenen, L. Koenderman, J. Pillay, The role of neutrophils in immune dysfunction during severe inflammation, *Crit Care.* 20 (2016) 73.
- [4] B. McDonald R.P. Davis S.-J. Kim M. Tse C.T. Esmon E. Kolaczowska C.N. Jenne Platelets and neutrophil extracellular traps collaborate to promote intravascular coagulation during sepsis in mice 129 10 2017 1357 1367.
- [5] J. Talbot, F.J. Bianchini, D.C. Nascimento, R.D.R. Oliveira, F.O. Souto, L.G. Pinto, R.S. Peres, J.R. Silva, S.C.L. Almeida, P. Louzada-Junior, T.M. Cunha, F.Q. Cunha, J.C. Alves-Filho, CCR2 Expression in neutrophils plays a critical role in their migration into the joints in rheumatoid arthritis, *Arthritis Rheumatol.* 67 (7) (2015) 1751–1759.
- [6] T.K. Wright, P.G. Gibson, J.L. Simpson, V.M. McDonald, L.G. Wood, K.J. Baines, Neutrophil extracellular traps are associated with inflammation in chronic airway disease, *Respirology.* 21 (3) (2016) 467–475.
- [7] C.-C. Chiang, W.-J. Cheng, M. Korinek, C.-Y. Lin, T.-L. Hwang, Neutrophils in Psoriasis, *Front Immunol.* 10 (2019) 2376.
- [8] A. Warnatsch, M. Ioannou, Q. Wang, V. Papayannopoulos, Inflammation. Neutrophil extracellular traps license macrophages for cytokine production in atherosclerosis, *Science.* 349 (6245) (2015) 316–320.
- [9] C.C. Chiang, M. Korinek, W.J. Cheng, T.L. Hwang, targeting neutrophils to treat acute respiratory distress syndrome in coronavirus disease, *Front Pharmacol.* 11 (2020), 572009.
- [10] S.C. Yang, T.L. Hwang, The potential impacts of formyl peptide receptor 1 in inflammatory diseases, *Front Biosci (Elite Ed).* 8 (2016) 436–449.
- [11] S. Ikeda, H. Takahashi, Y. Suga, H. Eto, T. Etoh, K. Okuma, K. Takahashi, T. Kanbara, M. Seishima, A. Morita, Y. Imai, T. Kanekura, Therapeutic depletion of myeloid lineage leukocytes in patients with generalized pustular psoriasis indicates a major role for neutrophils in the immunopathogenesis of psoriasis, *J Am Acad Dermatol.* 68 (4) (2013) 609–617.

- [12] S. Fukumitsu, M.O. Villareal, T. Fujitsuka, K. Aida, H. Isoda, Anti-inflammatory and anti-arthritis effects of pentacyclic triterpenoids maslinic acid through NF-kappaB inactivation, *Mol Nutr Food Res*. 60 (2) (2016) 399–409.
- [13] M.J. Hsu, J.S. Cheng, H.C. Huang, Effect of saikosaponin, a triterpene saponin, on apoptosis in lymphocytes: association with c-myc, p53, and bcl-2 mRNA, *Br J Pharmacol*. 131 (7) (2000) 1285–1293.
- [14] Y.-L. Chen, T.-L. Hwang, H.-P. Yu, J.-Y. Fang, K.Y. Chong, Y.-W. Chang, C.-Y. Chen, H.-W. Yang, W.-Y. Chang, P.-W. Hsieh, *Ilex kaushue* and its bioactive component 3,5-dicaffeoylquinic acid protected mice from lipopolysaccharide-induced acute lung injury, *Sci Rep*. 6 (1) (2016), <https://doi.org/10.1038/srep34243>.
- [15] L.-i. Li, L.-J. Xu, G.-Z. Ma, Y.-M. Dong, Y. Peng, P.-G. Xiao, The large-leaved Kudungcha (*Ilex latifolia* Thunb and *Ilex kudingcha* C.J. Tseng): a traditional Chinese tea with plentiful secondary metabolites and potential biological activities, *J Nat Med*. 67 (3) (2013) 425–437.
- [16] C.-Y. Chen, C.-C. Liaw, Y.-H. Chen, W.-Y. Chang, P.-J. Chung, T.-L. Hwang, A novel immunomodulatory effect of ugonin U in human neutrophils via stimulation of phospholipase C, *Free Radic Biol Med*. 72 (2014) 222–231.
- [17] S.-C. Yang, S.-H. Chang, P.-W. Hsieh, Y.-T. Huang, C.-M. Ho, Y.-F. Tsai, T.-L. Hwang, Dipeptide HCH6-1 inhibits neutrophil activation and protects against acute lung injury by blocking FPR1, *Free Radic Biol Med*. 106 (2017) 254–269.
- [18] T.-L. Hwang, H.-I. Shen, F.-C. Liu, H.-I. Tsai, Y.-C. Wu, F.-R. Chang, H.-P. Yu, D. Ma, Ursolic acid inhibits superoxide production in activated neutrophils and attenuates trauma-hemorrhage shock-induced organ injury in rats. *PLoS One* 9 (10) (2014) e111365-e.
- [19] Y.F. Tsai, H.P. Yu, W.Y. Chang, F.C. Liu, Z.C. Huang, T.L. Hwang, Sirtinol inhibits neutrophil elastase activity and attenuates lipopolysaccharide-mediated acute lung injury in mice, *Sci Rep*. 5 (2015) 8347.
- [20] S.-C. Yang, P.-J. Chen, S.-H. Chang, Y.-T. Weng, F.-R. Chang, K.-Y. Chang, C.-Y. Chen, T.-I. Kao, T.-L. Hwang, Luteolin attenuates neutrophilic oxidative stress and inflammatory arthritis by inhibiting Raf1 activity, *Biochem Pharmacol*. 154 (2018) 384–396.
- [21] Y.-K. Lin, Y.-L. Leu, T.-H. Huang, Y.-H. Wu, P.-J. Chung, J.-H. Su Pang, T.-L. Hwang, Anti-inflammatory effects of the extract of indigo naturalis in human neutrophils, *J Ethnopharmacol*. 125 (1) (2009) 51–58.
- [22] T.-L. Hwang, Y.-C. Su, H.-L. Chang, Y.-L. Leu, P.-J. Chung, L.-M. Kuo, Y.-J. Chang, Suppression of superoxide anion and elastase release by C18 unsaturated fatty acids in human neutrophils, *J Lipid Res*. 50 (7) (2009) 1395–1408.
- [23] F.-C. Liu, H.-P. Yu, Y.-T. Syu, J.-Y. Fang, C.-F. Lin, S.-H. Chang, Y.-T. Lee, T.-L. Hwang, Honokiol suppresses formyl peptide-induced human neutrophil activation by blocking formyl peptide receptor 1, *Sci Rep*. 7 (1) (2017), <https://doi.org/10.1038/s41598-017-07131-w>.
- [24] A.-L. Stenfeldt, J. Karlsson, C. Wennerås, J. Bylund, H. Fu, C. Dahlgren, The non-steroidal anti-inflammatory drug piroxicam blocks ligand binding to the formyl peptide receptor but not the formyl peptide receptor like 1, *Biochem Pharmacol*. 74 (7) (2007) 1050–1056.
- [25] F.-C. Liu, H.-P. Yu, P.-J. Chen, H.-W. Yang, S.-H. Chang, C.-C. Tzeng, W.-J. Cheng, Y.-R. Chen, Y.-L. Chen, T.-L. Hwang, A novel NOX2 inhibitor attenuates human neutrophil oxidative stress and ameliorates inflammatory arthritis in mice, *Redox Biol*. 26 (2019) 101273, <https://doi.org/10.1016/j.redox.2019.101273>.
- [26] P.-J. Chen, I.-L. Ko, C.-L. Lee, H.-C. Hu, F.-R. Chang, Y.-C. Wu, Y.-L. Leu, C.-C. Wu, C.-Y. Lin, C.-Y. Pan, Y.-F. Tsai, T.-L. Hwang, Targeting allosteric site of AKT by 5,7-dimethoxy-1,4-phenanthrenequinone suppresses neutrophilic inflammation, *EBioMedicine*. 40 (2019) 528–540.
- [27] W.R. Swindell, A. Johnston, S. Carbajal, G. Han, C. Wohn, J. Lu, X. Xing, R.P. Nair, J.J. Voorhees, J.T. Elder, X.-J. Wang, S. Sano, E.P. Prens, J. DiGiovanni, M. R. Pittelkow, N.L. Ward, J.E. Gudjonsson, S. Bereswill, Genome-wide expression profiling of five mouse models identifies similarities and differences with human psoriasis, *PLoS One*. 6 (4) (2011) e18266.
- [28] J. Bai, Y. Gao, L. Chen, Q. Yin, F. Lou, Z. Wang, Z. Xu, H. Zhou, Q. Li, W. Cai, Y. Sun, L. Niu, H. Wang, Z. Wei, S. Lu, A. Zhou, J. Zhang, H. Wang, Identification of a natural inhibitor of methionine adenosyltransferase 2A regulating one-carbon metabolism in keratinocytes, *EBioMedicine*. 39 (2019) 575–590.
- [29] A. Achek, H.K. Kwon, M.C. Patra, M. Shah, R. Hong, W.H. Lee, et al., A peptide derived from the core beta-sheet region of TIRAP decoys TLR4 and reduces inflammatory and autoimmune symptoms in murine models, *EBioMedicine*. 52 (2020), 102645.
- [30] C.-C. Chiang, W.-J. Cheng, C.-Y. Lin, K.-H. Lai, S.-C. Ju, C. Lee, S.-H. Yang, T.-L. Hwang, Kan-Lu-Hsiao-Tu-Tan, a traditional Chinese medicine formula, inhibits human neutrophil activation and ameliorates imiquimod-induced psoriasis-like skin inflammation, *J Ethnopharmacol*. 246 (2020) 112246, <https://doi.org/10.1016/j.jep.2019.112246>.
- [31] C. Kilkenny W. Browne I.C. Cuthill M. Emerson D.G. Altman Animal research: reporting in vivo experiments: the ARRIVE guidelines 160 7 2010 1577 1579..
- [32] N. Percie du Sert, V. Hurst, A. Ahluwalia, S. Alam, M.T. Avey, M. Baker, W.J. Browne, A. Clark, I.C. Cuthill, U. Dirnagl, M. Emerson, P. Garner, S.T. Holgate, D. W. Howells, N.A. Karp, S.E. Lazic, K. Lidster, C.J. MacCallum, M. Macleod, E.J. Pearl, O.H. Petersen, F. Rawle, P. Reynolds, K. Rooney, E.S. Sena, S.D. Silberberg, T. Steckler, H. Würbel, I. Bouteron, The ARRIVE guidelines 2.0: Updated guidelines for reporting animal research. *PLoS Biol*. 18 (7) (2020) e3000410.
- [33] L. van der Fits, S. Mourits, J.S.A. Voerman, M. Kant, L. Boon, J.D. Laman, F. Cornelissen, A.-M. Mus, E. Florencia, E.P. Prens, E. Lubberts, Imiquimod-induced psoriasis-like skin inflammation in mice is mediated via the IL-23/IL-17 axis, *J Immunol*. 182 (9) (2009) 5836–5845.
- [34] A. Mantovani, M.A. Cassatella, C. Costantini, S. Jaillon, Neutrophils in the activation and regulation of innate and adaptive immunity, *Nature Reviews Immunology*. 11 (8) (2011) 519–531.
- [35] G. Tintinger, H.C. Steel, R. Anderson, Taming the neutrophil: calcium clearance and influx mechanisms as novel targets for pharmacological control, *Clin Exp Immunol*. 141 (2) (2005) 191–200.
- [36] K. El Malki, S.H. Karbach, J. Huppert, M. Zayoud, S. Reißig, R. Schüler, A. Nikolaev, K. Karraam, T. Münzel, C.R.W. Kuhlmann, H.J. Luhmann, E. von Stebut, S. Wörtge, F.C. Kurschus, A. Waisman, An alternative pathway of imiquimod-induced psoriasis-like skin inflammation in the absence of interleukin-17 receptor a signaling, *J Invest Dermatol*. 133 (2) (2013) 441–451.
- [37] S. Shao, T. Cao, L. Jin, B. Li, H. Fang, J. Zhang, Y. Zhang, J. Hu, G. Wang, Increased lipocalin-2 contributes to the pathogenesis of psoriasis by modulating neutrophil chemotaxis and cytokine secretion, *J Invest Dermatol*. 136 (7) (2016) 1418–1428.
- [38] M. Uribe-Herranz, L.-H. Lian, K.M. Hooper, K.A. Milora, L.E. Jensen, IL-1R1 signaling facilitates Munro's microabscess formation in psoriasisform imiquimod-induced skin inflammation, *J Invest Dermatol*. 133 (6) (2013) 1541–1549.
- [39] H. Sumida, K. Yanagida, Y. Kita, J. Abe, K. Matsushima, M. Nakamura, S. Ishii, S. Sato, T. Shimizu, Interplay between CXCR2 and BLT1 facilitates neutrophil infiltration and resultant keratinocyte activation in a murine model of imiquimod-induced psoriasis, *J Immunol*. 192 (9) (2014) 4361–4369.
- [40] K. Chen, Z. Bao, W. Gong, P. Tang, T. Yoshimura, J.M. Wang, Regulation of inflammation by members of the formyl-peptide receptor family, *J Autoimmun*. 85 (2017) 64–77.
- [41] R.A. Hill, J.D. Connolly, Triterpenoids, *Nat Prod Rep*. 37 (7) (2020) 962–998.
- [42] M. del Carmen Recio, R. Giner, S. Mániz, J. Ríos, Structural requirements for the anti-inflammatory activity of natural triterpenoids, *Planta Med*. 61 (02) (1995) 182–185.
- [43] S. Ceballos, A. Guillén, D.L. Muñoz, A. Castaño, L.F. Echeverri, S. Acín, N. Balcázar, Immunometabolic regulation by triterpenes of *Eucalyptus tereticornis* in adipose tissue cell line models, *Phytomedicine*. 50 (2018) 109–117.
- [44] X. Yang, J. She, J. Liu, T. Yang, G. An, Q. Chen, C. Fan, S. Li, Q. Liu, C. Qian, Y. Liu, Y. Zhou, J. Zhao, A comprehensive review of the genus *Pyrola* herbs in traditional uses, phytochemistry and pharmacological activities, *Curr Top Med Chem*. 20 (1) (2020) 57–77.
- [45] H. Wada, H. Nakata, Hirata Y (Structure of Sanguisorbigenin, a Triterpene Obtained from *Sanguisorba officinalis* L.), *Yakugaku Zasshi* 84 (1964) 477–479.
- [46] D.H.R. Barton, H.T. Cheung, P.J.L. Daniels, K.G. Lewis, J.F. McGhie, 994. Triterpenoids. Part XXVI. The triterpenoids of *Vangueria tomentosa*, *Journal of the Chemical Society (Resumed)* (1962) 5163, <https://doi.org/10.1039/jr9620005163>.
- [47] J.S. Tandon, K.P. Agrawal, M.M. Dhar, Chemistry of triterpenoids from *Randia dumetorum*, *Indian J Chem*. 4 (1966) 483.
- [48] S.S. Li, Y.L. Liu, Q.M. Xu, C.M. Mao, S.L. Yang, Three new triterpenoids isolated from the aerial parts of *Ilex cornuta* and protective effects against H<sub>2</sub>O<sub>2</sub>-induced myocardial cell injury, *Chin J Nat Med*. 15 (2) (2017) 115–120.
- [49] X. Liu, Y. Cui, Q. Yu, B. Yu, Triterpenoids from *Sanguisorba officinalis*, *Phytochemistry*. 66 (14) (2005) 1671–1679.
- [50] T.-L. Kang, M.-K. Park, Study on the process of *Sanguisorbae Radix* - tomentosolic acid isolated from roasted *Sanguisorbae Radix*, *Yakhak Hoeji*. 38 (6) (1994) 712–714.
- [51] H.H. Yoo, S.W. Kwon, J.H. Park, The cytotoxic saponin from heat-processed *Achyranthes fauriei* roots, *Biol Pharm Bull*. 29 (5) (2006) 1053–1055.
- [52] S. Mlala, A.O. Oyedemi, M. Gondwe, O.O. Oyedemi, Ursolic acid and its derivatives as bioactive agents, *Molecules*. 24 (15) (2019) 2751.
- [53] M.S. Ali, S.A. Ibrahim, S. Jalil, M.I. Choudhary, Ursolic acid: a potent inhibitor of superoxides produced in the cellular system, *Phytother Res*. 21 (6) (2007) 558–561.
- [54] W.M. Nauseef, N. Borregaard, Neutrophils at work, *Nat Immunol*. 15 (7) (2014) 602–611.
- [55] S. Cardini, J. Dalli, S. Fineschi, M. Perretti, G. Lungarella, M. Lucatelli, Genetic ablation of the fpr1 gene confers protection from smoking-induced lung emphysema in mice, *Am J Respir Cell Mol Biol*. 47 (3) (2012) 332–339.
- [56] M. Honda, T. Takeichi, S. Hashimoto, D. Yoshii, K. Isono, S. Hayashida, Y. Ohya, H. Yamamoto, Y. Sugawara, Y. Inomata, Intravital imaging of neutrophil recruitment reveals the efficacy of FPR1 blockade in hepatic ischemia-reperfusion injury, *J Immunol*. 198 (4) (2017) 1718–1728.
- [57] S.-C. Yang, P.-J. Chung, C.-M. Ho, C.-Y. Kuo, M.-F. Hung, Y.-T. Huang, W.-Y. Chang, Y.-W. Chang, K.-H. Chan, T.-L. Hwang, Propofol inhibits superoxide production, elastase release, and chemotaxis in formyl peptide-activated human neutrophils by blocking formyl peptide receptor 1, *J Immunol*. 190 (12) (2013) 6511–6519.
- [58] T.-L. Hwang, C.-C. Wang, Y.-H. Kuo, H.-C. Huang, Y.-C. Wu, L.-M. Kuo, Y.-H. Wu, The hederagenin saponin SMG-1 is a natural FMLP receptor inhibitor that



- suppresses human neutrophil activation, *Biochem Pharmacol.* 80 (8) (2010) 1190–1200.
- [59] N. Steinckwich, P. Myers, K.S. Janardhan, N.D. Flagler, D. King, J.G. Petranka, J. W. Putney, Role of the store-operated calcium entry protein, STIM1, in neutrophil chemotaxis and infiltration into a murine model of psoriasis-inflamed skin, *FASEB J.* 29 (7) (2015) 3003–3013.
- [60] W.R. Swindell, K.A. Michaels, A.J. Sutter, D. Diaconu, Y.i. Fritz, X. Xing, M. K. Sarkar, Y. Liang, A. Tsoi, J.E. Gudjonsson, N.L. Ward, Imiquimod has strain-dependent effects in mice and does not uniquely model human psoriasis, *Genome Med.* 9 (1) (2017), <https://doi.org/10.1186/s13073-017-0415-3>.
- [61] J.E. Greb, A.M. Goldminz, J.T. Elder, M.G. Lebwohl, D.D. Gladman, J.J. Wu, N. N. Mehta, A.Y. Finlay, A.B. Gottlieb, Psoriasis. *Nat Rev Dis Primers.* 2 (1) (2016), <https://doi.org/10.1038/nrdp.2016.82>.
- [62] N. Shimoura, H. Nagai, S. Fujiwara, H. Jimbo, C. Nishigori, Exacerbation and prolongation of psoriasiform inflammation in diabetic obese mice: a synergistic role of CXCL5 and endoplasmic reticulum stress, *J Invest Dermatol.* 138 (4) (2018) 854–863.

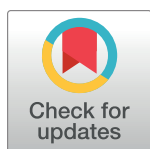
RESEARCH ARTICLE

# Enhanced antioxidant activity of *Chenopodium formosanum* Koidz. by lactic acid bacteria: Optimization of fermentation conditions

Hsing-Chun Kuo<sup>1,2,3,4</sup>, Ho Ki Kwong<sup>5</sup>, Hung-Yueh Chen<sup>6</sup>, Hsien-Yi Hsu<sup>7,8</sup>, Shu-Han Yu<sup>5</sup>, Chang-Wei Hsieh<sup>9</sup>, Hui-Wen Lin<sup>10</sup>, Yung-Lin Chu<sup>11\*</sup>, Kuan-Chen Cheng<sup>12\*</sup>

**1** Division of Basic Medical Sciences, Department of Nursing, Chang Gung University of Science and Technology, Chiayi, Taiwan, **2** Chang Gung Memorial Hospital, Chiayi, Taiwan, **3** Research Center for Industry of Human Ecology, Chang Gung University of Science and Technology, Taoyuan, Taiwan, **4** Chronic Diseases and Health Promotion Research Center, CGUST, Chiayi, Taiwan, **5** Institute of Biotechnology, College of Bioresources and Agriculture, National Taiwan University, Taipei, Taiwan, **6** Institute of Food Science and Technology, College of Bioresources and Agriculture, National Taiwan University, Taipei, Taiwan, **7** Department of Materials Science and Engineering, School of Energy and Environment, City University of Hong Kong, Kowloon Tong, Hong Kong, China, **8** Shenzhen Research Institute of City University of Hong Kong, Shenzhen, China, **9** Department of Food Science and Biotechnology, National Chung Hsing University, Taichung, Taiwan, **10** Department of Optometry, Asia University, Wufeng, Taichung, Taiwan, **11** Department of Food Science, College of Agriculture, National Pingtung University of Science and Technology, Pingtung, Taiwan, **12** Department of Medical Research, China Medical University Hospital, China Medical University, Taichung, Taiwan

\* [kccheng@ntu.edu.tw](mailto:kccheng@ntu.edu.tw) (KCC); [ylichu@mail.npust.edu.tw](mailto:ylichu@mail.npust.edu.tw) (YLC)



## OPEN ACCESS

**Citation:** Kuo H-C, Kwong HK, Chen H-Y, Hsu H-Y, Yu S-H, Hsieh C-W, et al. (2021) Enhanced antioxidant activity of *Chenopodium formosanum* Koidz. by lactic acid bacteria: Optimization of fermentation conditions. PLoS ONE 16(5): e0249250. <https://doi.org/10.1371/journal.pone.0249250>

**Editor:** Branislav T. Šiler, Institute for Biological Research, SERBIA

**Received:** November 2, 2020

**Accepted:** March 10, 2021

**Published:** May 11, 2021

**Peer Review History:** PLOS recognizes the benefits of transparency in the peer review process; therefore, we enable the publication of all of the content of peer review and author responses alongside final, published articles. The editorial history of this article is available here: <https://doi.org/10.1371/journal.pone.0249250>

**Copyright:** © 2021 Kuo et al. This is an open access article distributed under the terms of the [Creative Commons Attribution License](https://creativecommons.org/licenses/by/4.0/), which permits unrestricted use, distribution, and reproduction in any medium, provided the original author and source are credited.

**Data Availability Statement:** All relevant data are within the paper and its [Supporting information](#) files.

## Abstract

In this study, different probiotics commonly used to produce fermented dairy products were inoculated independently for *Chenopodium formosanum* Koidz. fermentation. The strain with the highest level of antioxidant activity was selected and the fermentation process was further optimized via response surface methodology (RSM). *Lactobacillus plantarum* BCRC 11697 was chosen because, compared to other lactic acid bacteria, it exhibits increased free radical scavenging ability and can produce more phenolic compounds, DPPH (from 72.6% to 93.2%), and ABTS (from 64.2% to 76.9%). Using RSM, we further optimize the fermentation protocol of BCRC 11697 by adjusting the initial fermentation pH, agitation speed, and temperature to reach the highest level of antioxidant activity (73.5% of DPPH and 93.8% of ABTS). The optimal protocol (pH 5.55, 104 rpm, and 24.4°C) resulted in a significant increase in the amount of phenolic compounds as well as the DPPH and ABTS free radical scavenging ability of BCRC 11697 products. The IC<sub>50</sub> of the DPPH and ABTS free radical scavenging ability were 0.33 and 2.35 mg/mL, respectively, and both protease and tannase activity increased after RSM. An increase in lower molecular weight (<24 kDa) protein hydrolysates was also observed. Results indicated that *djulis* fermented by *L. plantarum* can be a powerful source of natural antioxidants for preventing free radical-initiated diseases.

**Funding:** This project was funded by the Ministry of Science and Technology, Taiwan (MOST 109-2628-E-002-007-MY3 and MOST 107-2320-B-255-001-MY3). HC Kuo received grant of MOST 107-2320-B-255-001-MY3. KC Cheng received grant of MOST 109-2628-E-002-007-MY3. URL: <https://www.most.gov.tw/?l=en>. HC Kuo also received funding grant of BMRPD42 for this study was also provided in part by research grants from the Chang Gung Memorial Hospital, Chiayi, Taiwan. The funders had no role in study design, data collection and analysis, decision to publish, or preparation of the manuscript.

**Competing interests:** The authors have declared that no competing interests exist.

## Introduction

Djulis (*Chenopodium formosanum* Koidz.) is a traditional crop from the same genus as quinoa (*Chenopodium quinoa*), and it is cultivated and consumed as food or used as a wine starter in Taiwan [1]. Reports have shown that djulis exhibits beneficial effects on anti-inflammation, anti-diabetes, anti-oxidation, and immune regulation [1, 2]. Bioactive components and pigments such as peptides, betacyanin (red), betaxanthins (yellow), and polyphenols contribute to the aforementioned effects. Other ingredients, such as rutin and chlorogenic acid, can also restore the injury from UVB on HaCaT cells by reducing the level of interleukin-6 and reactive oxygen species (ROS) [3].

Lactic acid bacteria (LAB) are widely known strains of probiotics. Several studies have indicated that LAB exhibit multiple functions, such as modulating gut health, improving liver function, and decreasing cholesterol levels and blood pressure [4–6]. LAB can also enhance the flavor of fermented products and increase the amount of antioxidative compounds in dairy products through bioconversion [7]. For example, Hsieh et al. [8] reported that heat killed cells and cytoplasmic fraction forms of *Lactobacillus acidophilus* BCRC 14079 grown in taro waste medium showed enhanced anti-tumor and immune-modulatory properties. Bianchi et al. [9] reported that synbiotic fermented beverages combining quinoa and soy had favorable nutritional, rheological, and sensory characteristics.

Traditionally, optimal fermentation condition are determined using a one-factor-at-a-time approach [10]. However, this method is both time-consuming and costly in terms of materials and human resources. In worst-case scenarios, the interactions among parameters are often overlooked, resulting in misleading conclusions. As an alternative, response surface methodology (RSM) is a statistical method for simultaneously validating the effects of and interactions among different parameters [8, 11]. RSM has been used in various fermentation applications such as wine making [12], bioethanol production [13], exopolysaccharides [14], and biomass production [8, 15].

The aim of the present study was to select suitable LAB strains for djulis fermentation to enhance antioxidant activity for the development of health-promoting beverages. Antioxidant activity of LAB-fermented djulis was evaluated according to 2,2'-azino-bis-(3-ethylbenzthiazoline-6-sulphonate) (ABTS) and 2,2-diphenyl-1-picrylhydrazyl (DPPH) free radical scavenging ability. We employed RSM to determine the optimal fermentation parameters (initial pH, agitation speed and cultivation temperature) for achieving the highest level of antioxidant activity. Possible causes for the increased bioactivity after djulis fermentation and composition analysis of djulis samples before and after fermentation were also investigated.

## Materials and methods

### Materials

Domestic djulis was purchased from Pingtung, Taiwan. Lactobacilli MRS Broth was provided by Hardy diagnostics (Santa Maria, CA, USA). We purchased 95% Ethanol and methanol from Echo Chemical, Co., Ltd. (Taipei, Taiwan), and 2,2'-Azino-bis(3-ethylbenzothiazoline-6-sulfonic acid) diammonium salt (ABTS), gallic acid, Folin-Ciocalteu phenol reagent, and  $\alpha$ ,  $\alpha$ -diphenyl- $\beta$ -picrylhydrazyl (DPPH) from Sigma-Aldrich Co. (St. Louis, MO, USA). Agar and peptone were provided by Bioshop Inc. (Burlington, ON, Canada).

### Microorganisms and medium

*Bifidobacterium infantis* BCRC14602, *Bifidobacterium adolescentis* BCRC14606, *Bifidobacterium bifidum* BCRC14615, *Bifidobacterium longum* BCRC14634, *Bifidobacterium breve*

BCRC11846, *Lactobacillus rhamnosus* GG BCRC16000, *Lactobacillus delbrueckii* subsp. *bulgaricus* BCRC10696, *Lactobacillus plantarum* BCRC11697, *Lactobacillus acidophilus* BCRC14079, *Streptococcus salivarius* subsp. *thermophiles* BCRC14085 were purchased from Bioresource Collection and Research Center (BCRC, Hsinchu city, Taiwan). All LAB strains were grown in MRS medium (Sigma-Aldrich, MI, USA). For storage, stock cultures were kept in 20% glycerol at -80°C. Viable cells were grown in MRS medium at 37°C for 20 hours as inoculum and sub-cultured twice a month [16]. The standard growth curve was measured at 600 nm using a Multiskan GO microplate spectrophotometer (Thermo Scientific, Waltham, MA, USA).

## Djulis fermentation

Djulis was crushed into powder, filtered using a 0.6 mm mesh and then stored at -20°C until use. Djulis powder was combined with 10 times the amount of ddH<sub>2</sub>O (w/v) and sterilized at 90°C for 10 minutes. After cooling to room temperature, samples were inoculated with 1% LAB (~7 log CFU mL<sup>-1</sup>) as a seed culture and then fermented at 37°C for 48 hours. To determine the optimal fermentation time, LAB samples were taken every 12 hours and monitored for their pH, bacteria number, total phenolic content (TPC), ABTS, and DPPH. The optimal LAB was chosen based on the ABTS and DPPH assay results.

## Anti-oxidant activity

**DPPH assay.** Fermented djulis samples were freeze-dried and diluted to 5 mg/mL (deionized water). They were then mixed with DPPH ethanol solution (100 µM) at 1:1 ratio in a 96-well tissue culture plate to carry out the reaction in the dark for 30 minutes. Finally, the samples were analyzed at the 517 nm wavelength using the microplate spectrophotometer [17]. DPPH scavenging activity of the djulis extracts was calculated as follows:

$$\text{DPPH scavenging activity(\%)} = [1 - (A1 - A2)/A0] \times 100. \quad (1)$$

where A0 = DPPH (without samples), A1 = Sample + DPPH, and A2 = Sample (without DPPH). We used this method to screen the optimal LAB for djulis fermentation. Once the optimal fermentation protocol was evaluated, the IC<sub>50</sub> was calculated to provide an absolute number. IC<sub>50</sub> of the djulis samples was obtained from the regression curve between concentration and DPPH scavenging activity.

**ABST assay.** Fermented djulis samples were freeze-dried and diluted to 5 mg/mL (80% methanol). A 2.5 mM K<sub>2</sub>O<sub>8</sub>S<sub>2</sub> solution was prepared with K<sub>2</sub>O<sub>8</sub>S<sub>2</sub> and 7 mM 2,2'-azinobis (3-ethylbenzothiazoline-6-sulfonic acid) solution. The solution was placed in the dark for 12–16 hours until it became blue-green due to the formation of ABTS<sup>+</sup>. The ABTS<sup>+</sup> solution was diluted with 0.2 M phosphate buffer solution (pH 7.4) until its OD<sub>734</sub> reached to 0.7±0.02. Each sample (3 µL) was added to ABTS<sup>+</sup> solution (300 µL) in the dark for 6 minutes [17]. After the reaction was completed, the samples were analyzed at 734 nm using the microplate spectrophotometer. The ABTS scavenging activity of the djulis was calculated as follows:

$$\text{ABTS(\%)} = [AC - AS]/AC \times 100. \quad (2)$$

where AC = ABTS (without samples); AS = Sample + ABTS.

**Determination of the TPC.** The TPCs was determined using Folin–Ciocâlteu's reagent following the methods described by Wu et al. [13] but with slight modifications. Briefly, each extract (100 mg) was dissolved in a solution of 5 mL of 3% HCl in methanol/deionized water (1:1), and the resulting mixture (100 µL) was added to 100 µL of 10% aqueous sodium carbonate solution. After 2 minutes, 100 µL of 50% Folin–Ciocâlteu's reagent was added to the

mixture. After the solution had stood for 30 minutes, absorbance was measured at 750 nm against a blank. TPC was calculated based on the calibration curve of gallic acid, and this is reported as mg gallic acid equivalent per 1 g of dry djulis powder (mg GAE/1 gdw).

**Enzyme activity.** Protease activity was determined by taking aliquots of 100  $\mu$ L of the fermented liquid and adding 100  $\mu$ L of 0.1 M sodium phosphate buffer (pH 5.7). To this mixture, 100  $\mu$ L of substrate was added and incubated for 30 minutes at 50°C for the two cultivars. The reaction was stopped by adding 500  $\mu$ L of trichloroacetic acid at 10% (v/v) and centrifuged at 10,000  $\times$  g for 5 minutes. We then added 200  $\mu$ L of 1.8 M NaOH to the supernatant. Readings were taken using a spectrophotometer at 280nm. For quantification, an enzymatic unit was considered the amount of enzyme required to increase the absorbance by 0.01 [18]. To measure the tannase activity, the sample solution (100  $\mu$ L) was incubated with 300  $\mu$ L of 1.0% (w/v) tannic acid within a 0.2 M acetate buffer (pH 5.0) at 40°C for 30 minutes. The reaction was then terminated at 0°C by adding 2 mL bovine serum albumin (1 mg/mL), causing the remaining tannic acid to precipitate out of the solution. The samples were then centrifuged (5,000  $\times$  g, 10 min), and the precipitate was dissolved in 2 mL of sodium dodecyl sulfate (SDS)–triethanolamine (1% w/v, triethanolamine) solution. Absorbency was measured at 550 nm after addition of 1 mL of FeCl<sub>3</sub> (0.13 M). One unit of tannase was defined as the amount of enzyme required to hydrolyze 1  $\mu$  mole of ester linkage of tannic acid in 1 minute under specific conditions [19].

**Optimization for djulis fermentation.** RSM using the Box-Behnken design was performed to select the optimal conditions for djulis fermentation. Three variables, namely the initial pH (5, 6, 7), agitation speed (50, 100, 150 rpm), and cultivation temperature (20, 25, 30°C), were optimized based on the results of a set of experiments. A total of 15 runs were performed to establish a model and predict the optimal conditions. Three levels of design were introduced: low, medium, and high (respectively labeled as -1, 0, and 1 in Table 1. Minitab software was used to predict the optimal values of the three variables according to the following second-order polynomial equation:

$$Y = B_0 + \sum B_i X_i + \sum B_{ii} X_i^2 + \sum \sum B_{ij} X_i X_j$$

where  $Y$  is the dependent variable and represents the predicted response on ABTS ability;  $B_0$  represents the fitted response at the design's center point;  $B_i$ ,  $B_{ii}$ , and  $B_{ij}$  are the coefficient for linear, quadratic, and cross-product regression, respectively; and  $X_i$  and  $X_j$  (with  $j = i + 1$ ) are the coded independent variables ( $X_1$  = initial pH,  $X_2$  = agitation speed, and  $X_3$  = fermentation temperature).

**SDS gel electrophoresis.** Djulis samples weighing approximately 0.1 g were mixed with 15 mL of deionized water and stirred for 30 minutes at room temperature. Next, 0.1 M NaOH was added to adjust the pH to 9.0, and the samples were stirred for another 30 minutes, centrifuged at 4,500  $\times$  g for 20 minutes, and then 0.1 N HCL was added to adjust the pH to 5.0. After removal of the supernatant, the samples were mixed with 500  $\mu$ L of 63 mM Tris-HCl solution (pH 8.0). The obtained djulis protein samples were quantitated with a protein assay kit (Bio-

**Table 1. Range and corresponding levels of the independent variables.**

Variable	Range values of coded levels		
	-1	0	1
pH ( $X_1$ )	5	6	7
Rpm ( $X_2$ )	50	100	150
Temperature ( $X_3$ , °C)	20	25	30

<https://doi.org/10.1371/journal.pone.0249250.t001>



Rad Laboratories, Hercules, CA, USA) [20]. The total proteins were used for SDS gel electrophoresis analysis, and all samples were subjected to 15% SDS-polyacrylamide gel electrophoresis (SDS-PAGE) for 180 minutes at 60 V (stacking gel) and 120 V (separating gel). The separating gel was shaken and washed with deionized water three times at 70 rpm. After the deionized water was removed, RAPIDStain was added to completely submerge the gel, and it was shaken at 70 rpm for 1 hour. Finally, the gel was washed with two to three times deionized water at 70 rpm (10–15 minutes/time).

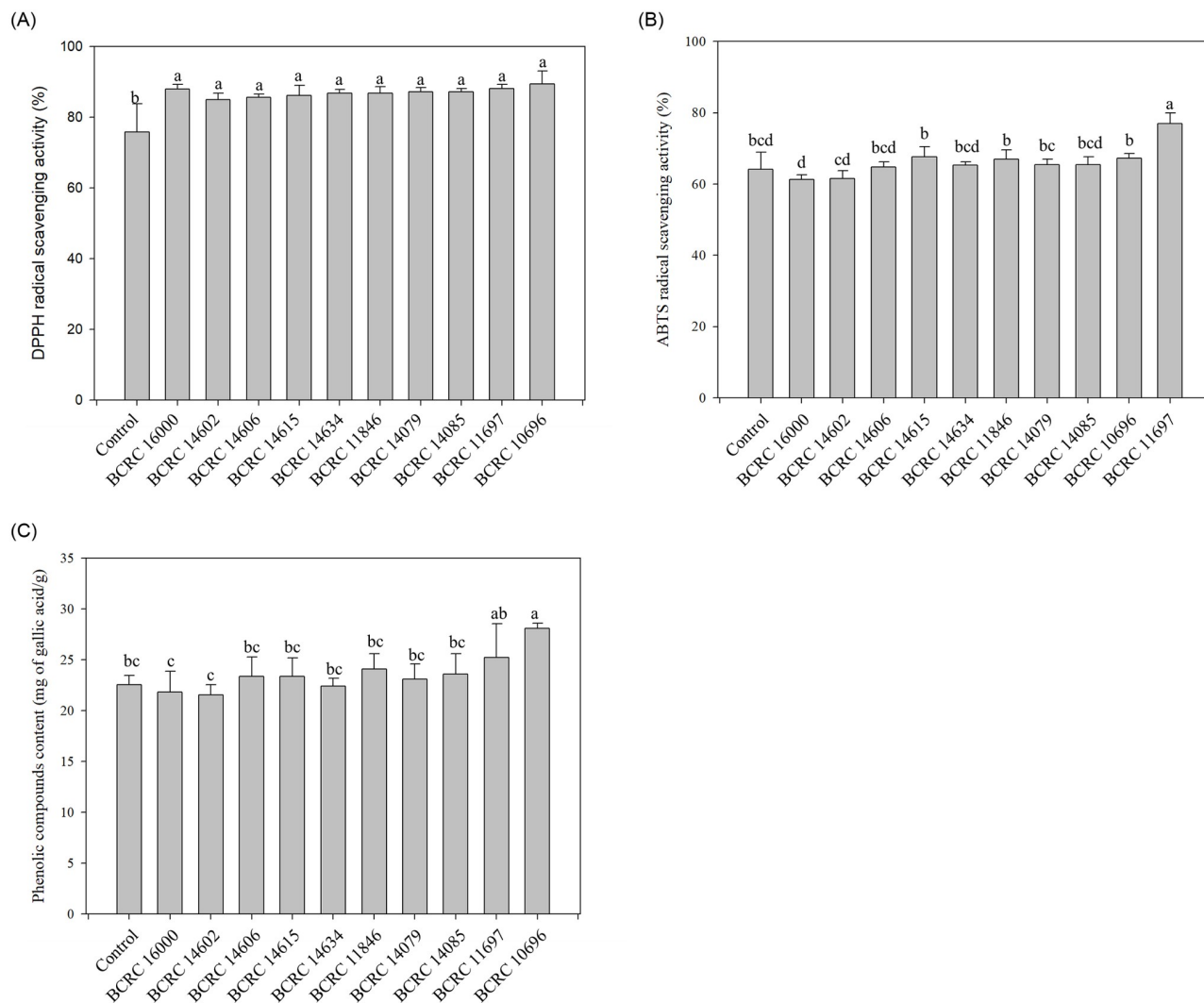
**Composition analysis of fermented djulis samples.** Fermented djulis samples were analyzed for their moisture, carbohydrate, protein, fat, and ash content following methods described in the literature [13] but with slight modifications. Crude protein content (g/100 g dry matter) was evaluated using the Kjeldahl method on the basis of nitrogen level and multiplied by 5.7. Crude fat content (g/100 g dry matter) was measured using Soxhlet extraction with petroleum ether. Moisture was determined by oven-drying at 105°C. Ash content was determined by placing samples overnight in a furnace at 600°C. Total carbohydrate content (g/100 g dry matter) was obtained by taking the difference between 100 and the sum of the ash content, moisture, crude fat, and crude protein.

**Statistical analysis.** All experiments were conducted with three independent evaluations and with three replications for each sample. Values are expressed as the mean  $\pm$  SD. Minitab software (Minitab Inc., University City, Pennsylvania, USA) was used to perform one-way ANOVA and Duncan's new multiple range tests as well as RSM evaluation and analysis. Differences were considered statistically significant differences where  $p < 0.05$ .

## Results and discussions

### Strain selection for djulis fermentation

To improve the functional properties, nutritional value, and taste of djulis, we fermented djulis grains using different strains of LAB. Djulis samples were inoculated with 10 strains of LAB, and were measured for their DPPH and ABTS radical scavenging activity after 24 hours of fermentation. The results showed that all 10 strains of LAB promoted the antioxidant activity of djulis. However, amongst all samples, *L. plantarum* BCRC 16000 and 11697 exhibited relatively higher performance for DPPH activity (93.2%) (Fig 1A). Additionally, the ABTS radical scavenging activity assay demonstrated that *L. plantarum* BCRC 11697 showed significantly higher ABTS radical scavenging activity (76.9%) compared to the control (64.2%) ( $p < 0.05$ ). Fig 1C shows the TPC was in line with the results regarding *L. plantarum* BCRC 11697 fermentation and antioxidant activity. *L. plantarum* BCRC 11697 produced more phenolic compounds than did the other strains. Past studies have reported that a correlation coefficient of  $R = 0.966$  between ABTS and TPC, and  $R = 0.939$  between DPPH and TPC [21]. Turkan [22] also reported that polyphenols are antioxidants that reduce ROS and reactive nitrogen species. This could explain why *L. plantarum* BCRC 11697 performed the best in the DPPH and ABTS tests. *L. plantarum* is a common LAB strain used in fermented plant-based foods, and it is often applied to the metabolic bacteria model of phenolic compounds [23]. Moreover, it can degrade phenolic compounds in food, and produce some compounds that affect food flavor and enhance antioxidant activity [23]. For example, all strains of *L. plantarum* secretes TanBLp (tannase), and tannase can hydrolyze the ester bond of gallic acids and protocatechuic acids [23]. Furthermore, feruloyl esterases are involved in releasing enzymes from plant cell walls and promoting antioxidant activity [24]. ABTS and DPPH assays are widely used methods for assessing antioxidant activity in natural herbal products. Both assays are spectrophotometric techniques based on the quenching of stable colored radicals (ABTS or DPPH) and show the radical scavenging ability of antioxidants even when present in complex plant extracts [25].

**Fig 1.**

<https://doi.org/10.1371/journal.pone.0249250.g001>

Both methods are rapid, simple, inexpensive and widely used to measure the ability of compounds to act as free radical scavengers or hydrogen donors, and to evaluate the antioxidant activity of complex extracts. Several studies have also adopted ABTS and DPPH assays to evaluate the quinoa antioxidant activity [17, 26, 27].

To determine the optimal djlus fermentation time for *L. plantarum* BCRC 11697, we carried out 54-hour cultivation with samples collected every 6 hours. As shown in Fig 1(A), all LAB strains exhibited similar DPPH scavenging effect, while BCRC11697 showed significantly higher ABTS amongst all the strains (Fig 1(B)); as such, we chose BCRC 11697 for the remainder of the study and used ABTS as the indicator.

Fig 2 shows the results of the ABTS radical scavenging activity, CFU, and pH values during fermentation. ABTS activity in the fermented djlus samples peaked after 24 hours of fermentation (77%) and then decreased gradually after 48 hours. Therefore, 24 hours was selected as the fermentation time for the remainder of the study. Moreover, lactic acidification improved the extraction of total phenols when the selected strain was used, and this has also been

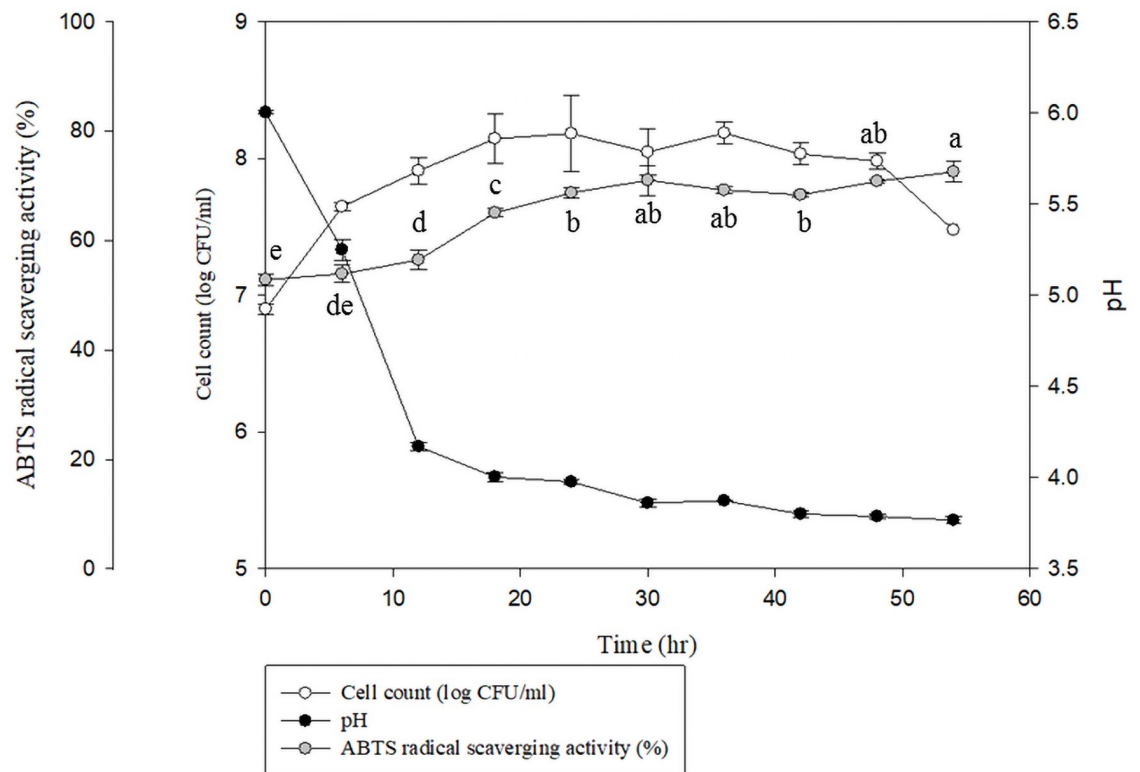


Fig 2.

<https://doi.org/10.1371/journal.pone.0249250.g002>

reported in previous research [26]. Esterase activity released the complex glycosylated-phenolic compounds into the corresponding phenolic acids during fermentation.

### RSM optimization

A set of individual experiments was conducted for each variable ( $X_1$ : initial pH,  $X_2$ : agitation speed, and  $X_3$ : temperature) in order to elucidate the specific effect of each parameter on ABTS antioxidation ability. We investigated initial pH values ranging from 2 to 10 for solutions of djulis powder mixed with deionized water for cultivation. An initial pH of 6 yielded the highest ABTS antioxidant activity ( $IC_{50}$ : 2.59 mg/mL) among the fermented samples (S1A Fig). Initial pH values of 5, 6, and 7 were chosen as experimental values. Different agitation speeds were also evaluated for ABTS antioxidant ability. Results showed that samples obtained at 100 rpm of agitation had the best ABTS ( $IC_{50}$ : 2.39 mg/mL). Therefore, agitation speeds of 50, 100 and 150 rpm were chosen as experimental values (S1B Fig). For the temperature parameter, we evaluated temperatures ranging from 15°C to 40°C. Results showed the best fermentation temperature to be 25°C, which gave the lowest ABTS  $IC_{50}$ : 2.44 mg/mL). Therefore, fermentation temperatures of 20°C, 25°C, and 30°C were chosen as experimental values (S1C Fig). Based on the results from the one-factor-at-a-time approach, RSM was applied to determine and to optimize the three fermentation parameters in order to achieve the highest ABTS anti-oxidation ability in the fermented djulis product (Table 1). The results are summarized in Table 2. Multiple regression was applied to the experimentally determined data in Eq (1) to estimate the regression coefficients, and the following second-order polynomial equation was

Table 2. Experimental range and values in the central composite design for optimizing the fermentation conditions.

StdOrder	RunOrder	PtType	Blocks	Initial pH	RPM	Tm. (°C)	ABTS-IC <sub>50</sub> (mg/mL)
12	1	2	1	6	150	30	3.50
8	2	2	1	7	100	30	3.65
5	3	2	1	5	100	20	3.26
9	4	2	1	6	50	20	3.50
7	5	2	1	5	100	30	3.57
4	6	2	1	7	150	25	3.20
2	7	2	1	7	50	25	3.41
11	8	2	1	6	50	30	4.04
14	9	0	1	6	100	25	2.97
3	10	2	1	5	150	25	3.24
1	11	2	1	5	50	25	3.28
10	12	2	1	6	150	20	3.66
6	13	2	1	7	100	20	3.65
15	14	0	1	6	100	25	3.14
13	15	0	1	6	100	25	2.83

<https://doi.org/10.1371/journal.pone.0249250.t002>

obtained using Minitab software:

$$Y = 13.2626 - 0.4305X_1 + 0.0031X_2 - 0.7593X_3 + 0.0804X_1^2 + 0.00009X_2^2 + 0.0188X_3^2 - 0.00085X_1X_2 - 0.0152X_1X_3 - 0.0007X_2X_3.$$

where Y = ABTS free radical scavenging ability-IC<sub>50</sub>; theory value; X<sub>1</sub> = initial pH; X<sub>2</sub> = agitation speed (rpm); X<sub>3</sub> = fermentative temperature (°C).

The predicted optimal parameters of X<sub>1</sub>, X<sub>2</sub>, and X<sub>3</sub> were obtained by applying the regression analysis of Eq (2); these were pH 5.55, 104 rpm, and 24.4°C. The predicted value of ABTS-IC<sub>50</sub> was 2.42 mg/mL which approximates our experimental result (2.35 mg/mL).

The coefficient of determination of the regression for the response related to the significant effects in the model was R<sup>2</sup> = 0.946 (Table 3). Hence, the sample variation of 94.6% for ABTS-IC<sub>50</sub> was associated with the three independent variables. The interaction between temperature and agitation speed can be observed from the results (p < 0.05). We hypothesize that is because the heating process can be accelerated by the increased agitation speed, resulting in a favored environment for LAB growth and TPC production. Similar results were reported by Dinarvand et al. [28]. They reported that the interaction between temperature and agitation speed affected the production of invertase from *Aspergillus niger*. The surface plots for ABTS-IC<sub>50</sub> are shown in Fig 3. The initial ABTS-IC<sub>50</sub> increased with the initial pH, reaching an optimal ABTS-IC<sub>50</sub> value approximately 5.55, which declined gradually above the optimal pH due to inactivation of the tannase, which accords with previous reports [23, 25]. The adequacy of the full quadratic model of liquefaction was also evaluated via ANOVA. The model summary statistics in Table 3 indicate the adequacy of the models including linear, 2-factor interactions and quadratic terms (P < 0.05). The lack-of-fit error was nonsignificant (p = 0.842), verifying the accuracy fit of the second-order model (Eq 2) to the true response of ABTS-IC<sub>50</sub>.

For the following assay, we chose pH 5.55, 104 rpm and 24.4°C as our fermentation conditions. Between the unfermented and fermented djulis samples, the fermented sample exhibited markedly higher antioxidant ability. For example, the IC<sub>50</sub> of ABTS was 3.4 mg/mL before fermentation, and this decreased to 2.35 mg/ml after optimization. In addition, the IC<sub>50</sub> of DPPH

Table 3. Estimated regression coefficients for ABTS free radical scavenging ability-IC<sub>50</sub>.

Sources	DF	Sum of squares	Mean squares	F-value	P-value	
Model	9	1.24941	0.138824	9.74	0.011	Significant
pH	1	0.0386	0.038597	2.71	0.161	
RPM	1	0.04905	0.049049	3.44	0.123	
Tm.	1	0.06107	0.061074	4.29	0.093	
pH <sup>2</sup>	1	0.00356	0.023883	1.68	0.252	
RPM <sup>2</sup>	1	0.13241	0.186733	13.1	0.015	Significant
Tm. <sup>2</sup>	1	0.812	0.812001	56.98	0.001	Significant
pH*RPM	1	0.00728	0.007285	0.51	0.507	
pH*Tm.	1	0.02307	0.023075	1.62	0.259	
RPM*Tm.	1	0.12236	0.12236	8.59	0.033	Significant
Residual error	5	0.07126	0.014251			
Lack of fit	3	0.02082	0.006939	0.28	0.842	
Pure error	2	0.05044	0.025219			
					R <sup>2</sup>	94.60%
					Adjusted R <sup>2</sup>	84.89%

DF refers to degrees of freedom, which differs significantly ( $p < 0.05$ ). The optimal starting reaction conditions for anti-oxidation were pH 5.55, 104 rpm and 24.4°C.

<https://doi.org/10.1371/journal.pone.0249250.t003>

was 1.11 mg/mL before fermentation, decreasing to 0.33 mg/mL ( $p < 0.05$ ) after RSM (Table 4). Compared to the TPC in the unfermented djulis samples, that in the fermented samples exhibited a significant increased from 9.33 to 28.97 (mg of gallic acid/gdw) ( $p < 0.05$ ). (Table 4).

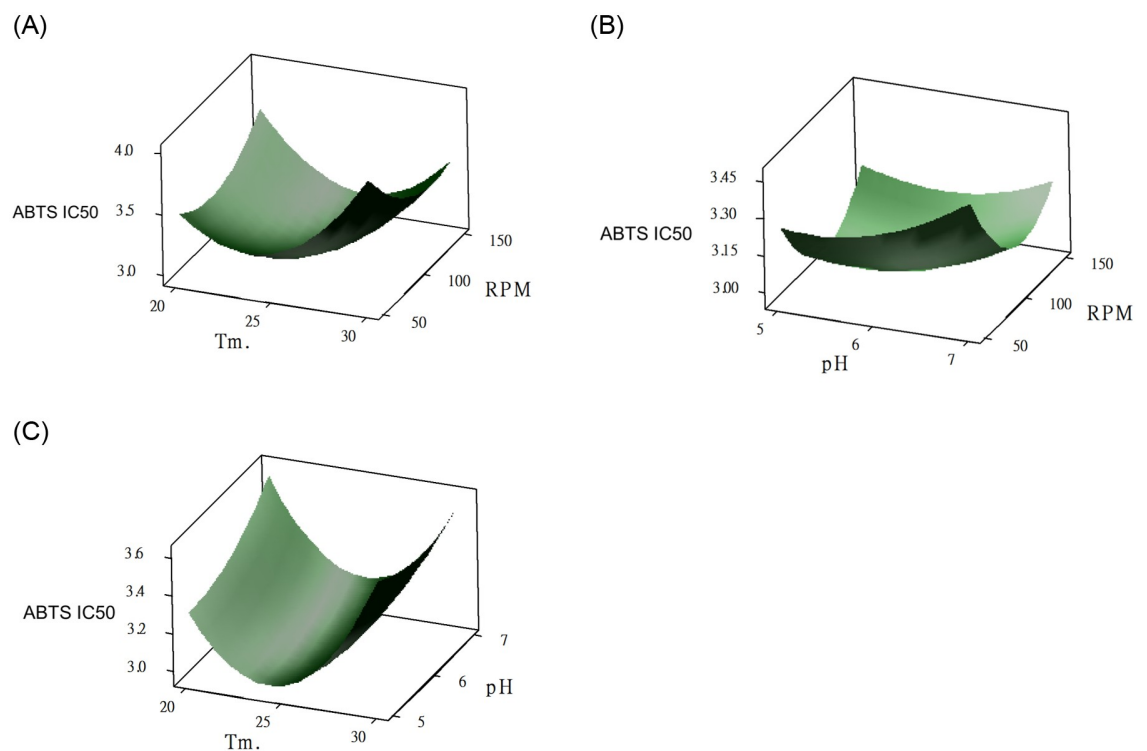


Fig 3.

<https://doi.org/10.1371/journal.pone.0249250.g003>



Table 4. Changes in TPC, cell number, pH, and DPPH and ABTS radical scavenging activity in djulis fermented with *L. plantarum* BCRC 11697.

Group	TCP (mg of gallic acid/gdw)	ABTS-IC <sub>50</sub> (mg/ml)	DPPH-IC <sub>50</sub> (mg/ml)	log CFU/ml	pH	Protease activity (U/mg-protein)	Tannase activity (U/mg-protein)
Unfermented	9.33 ± 0.25 <sup>a</sup>	3.40 ± 0.32 <sup>a</sup>	1.11 ± 0.20 <sup>a</sup>	7.31 ± 0.04 <sup>a</sup>	5.55 ± 0.02 <sup>a</sup>	ND	ND
Fermented	27.68 ± 0.21 <sup>b</sup>	2.44 ± 0.26 <sup>b</sup>	1.01 ± 0.17 <sup>a</sup>	7.42 ± 0.08 <sup>a</sup>	4.21 ± 0.03 <sup>b</sup>	1.69 ± 0.17 <sup>a</sup>	0.88 ± 0.11 <sup>a</sup>
Fermented-RSM	28.97 ± 0.19 <sup>b</sup>	2.35 ± 0.46 <sup>b</sup>	0.33 ± 0.02 <sup>b</sup>	8.61 ± 0.32 <sup>b</sup>	4.09 ± 0.01 <sup>b</sup>	2.53 ± 0.21 <sup>b</sup>	1.12 ± 0.09 <sup>b</sup>

Statistical differences were calculated using Duncan's new multiple range test. Values are presented as the mean ± SD of three independent experiments with the different superscripts (a, b) indicating significantly differences ( $p < 0.05$ ). ND: not detected.

<https://doi.org/10.1371/journal.pone.0249250.t004>

The increase of TPC is due to the presence of protease (2.53 U/mg-protein), tannase (1.12 U/mg-protein), and other enzymes used in enzymatic hydrolysis. Solid-state fermentation has also been adopted for cereal grains fermentation using fungi in previous research [29] that reported significantly greater antioxidant properties in the fermented products than unfermented grains. In the case of quinoa fermentation, that study reported an increase of 2.46 mg/g in TPC content after 35 days of fermentation. For our case, the TPC content of fermented djulis increased by 19.64 mg/g after 24 hours, which provided a fast and economically feasible method for the up-scaled production of antioxidant-rich ingredients.

### Changes of djulis components through fermentation

Principal components analysis showed that the freeze-dried powder of the fermented djulis contained 68.80% carbohydrates, 17.01% crude protein, 4.12% crude fat, 5.71% ash, and 4.37% moisture (Table 5). A slight decrease in carbohydrates, protein, and fat was observed due to the presence of enzymes partaking in hydrolysis and oxidation, which was discussed in a previous study [29]. LAB utilized the carbohydrates, protein and fat of the djulis since it was the only nutrient within the medium. Some nutrients could be hydrolyzed into small molecules such as peptides, oligosaccharides, and short-chain fatty acids due to the presence of related enzymes.

### Protein hydrolyzation

Fermented grain products are consumed in many countries and are one of the most crucial sources of bioactive peptides [29]. Grains fermented using bacteria (LAB and *Bacillus* spp.) yield many different types of fermented products that possess a multitudinous array therapeutic properties, such as antioxidant, antihypertensive, antimicrobial, antidiabetic, and anticancer activity [29].

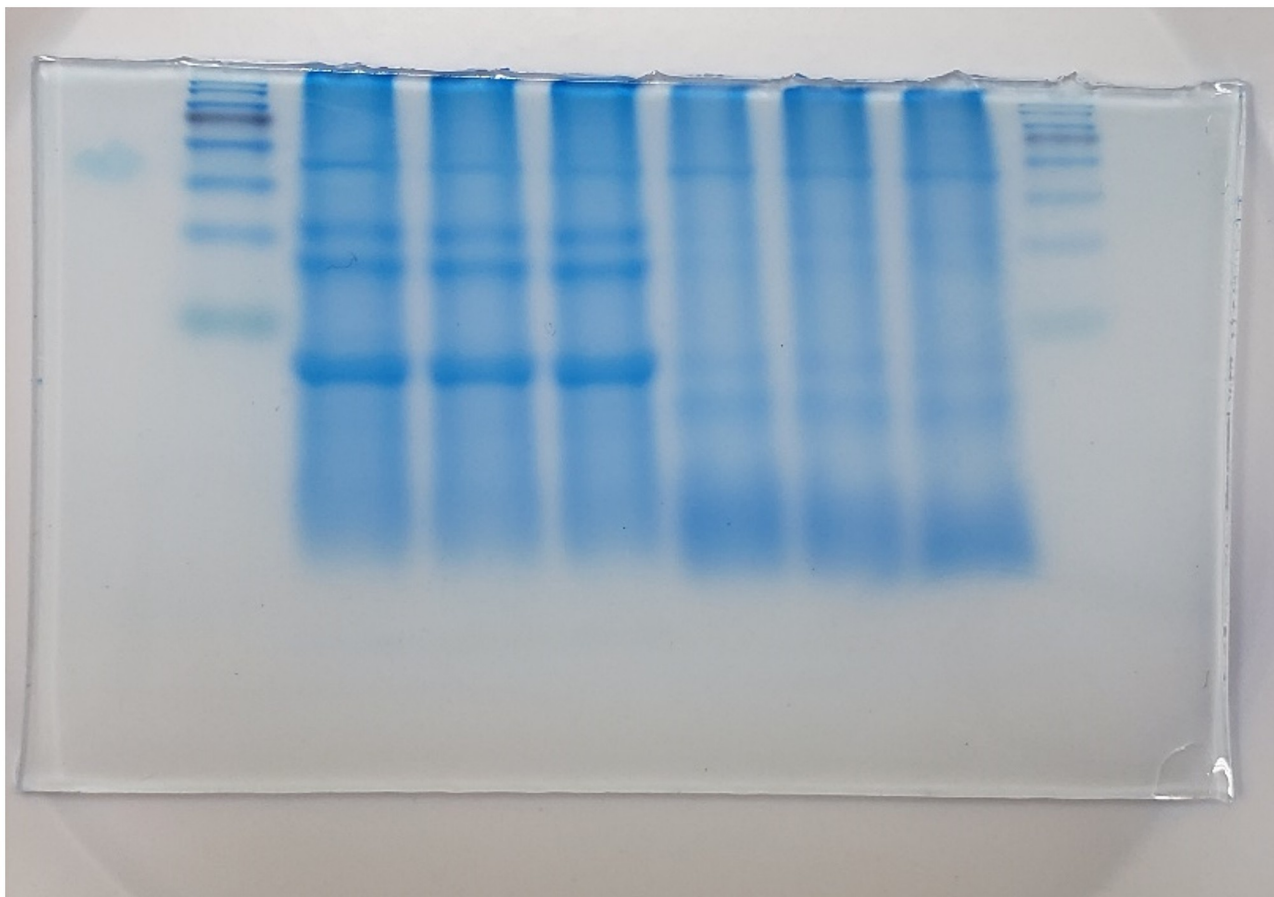
A previous study identified five peptides with antioxidant activity (ABTS and DPPH) after LAB fermentation through the hydrolysis of quinoa protein [26]. The size of each peptide was approximately 5–9 amino acid residues. Another study demonstrated that the bands between

Table 5. Carbohydrates, protein, fat, ash and moisture of *Chenopodium formosanum* Koidz. fermented product.

	Carbohydrates (g/100 g)	Protein (g/100 g)	Fat (g/100 g)	Ash (g/100 g)	Moisture (g/100 g)
Quinoa	74	16.3	7	2.7	0
Djulis	70.62 ± 0.15	19.15 ± 0.32	4.34 ± 0.17	2.62 ± 0.08	3.27 ± 0.21
Dry powder of fermented djulis	68.80 ± 0.16	17.01 ± 0.29	4.12 ± 0.54	5.71 ± 0.08	4.37 ± 0.21

Values are presented as mean ± SD of three independent experiments.

<https://doi.org/10.1371/journal.pone.0249250.t005>



**Fig 4.**

<https://doi.org/10.1371/journal.pone.0249250.g004>

53 and 41 kDa, two bands around 32 to 24 kDa, and bands under 24 kDa potentially have antioxidant activity as well [30]. The present study employed SDS-PAGE to determine the protein distribution of unfermented and fermented djulis. Our results showed that proteins of djulis had been hydrolyzed after fermentation. For example, two bands were between 24 and 32 kDa, one major band under 24 kDa disappeared after fermentation, and more bands with lower molecular weight were observed after fermentation (Fig 4). These results aligned with the behavior of wheat after *L. plantarum* M616 fermentation [30]. Virtanen et al. [30] also reported that milk whey protein hydrolysate weighing 4–20 kDa showed remarkably high antioxidant activity compared to that of the original milk whey protein.

## Conclusions

We applied RSM to determine the optimal fermentation conditions and to evaluate the interaction among the initial pH, agitation speed, and temperature. Our results show that *L. plantarum* BCRC 11697 is the optimal LAB strain for djulis submerged fermentation among the 10 candidates of LAB strains were investigated. After RSM-assisted optimization, we observed significant improvement in the free radical scavenging activity of DPPH and ABTS and in TPC. The presence of protease and tannase activity also supports that *L. plantarum* BCRC 11697 enhances free radical scavenging bioactivity through protein hydrolysis and the release of bound-phenolic compounds. In conclusion, fermented djulis using LAB shows potential for

commercialization as a beverage. Future studies will need to investigate the up-scaled production of djulis content, determination of the specific mechanisms of antioxidation and identification of bioactive peptides for the findings of this study to be employed in commercial applications.

## Supporting information

**S1 Fig.** (A) Initial pH-The ABTS radical scavenging activity of *Chenopodium formosanum* Koidz. fermented with *Lactobacillus plantarum* BCRC 11697. (B) RPM-The ABTS radical scavenging activity of *Chenopodium formosanum* Koidz. fermented with *Lactobacillus plantarum* BCRC 11697. (C) Fermentation temperature-The ABTS radical scavenging activity of *Chenopodium formosanum* Koidz. fermented with *Lactobacillus plantarum* BCRC 11697. Statistical differences were calculated by Duncan's new multiple range test. Values are presented as mean  $\pm$  SD of three independent experiments with different superscripts (a, b, c, d) are significantly different ( $p < 0.05$ ).

(TIF)

**S1 Raw image.**

(PDF)

**S1 Graphical abstract.**

(JPG)

## Acknowledgments

The authors greatly acknowledge the article proofreading by Iris YS Wu who is a native speaker from Molecular Environmental Biology, University of California, Berkeley (Berkeley, CA, USA).

## Author Contributions

**Conceptualization:** Hsing-Chun Kuo, Hsien-Yi Hsu, Chang-Wei Hsieh, Yung-Lin Chu, Kuan-Chen Cheng.

**Data curation:** Ho Ki Kwong, Hung-Yueh Chen.

**Formal analysis:** Ho Ki Kwong.

**Investigation:** Hsien-Yi Hsu.

**Methodology:** Hung-Yueh Chen, Shu-Han Yu, Hui-Wen Lin, Yung-Lin Chu.

**Resources:** Hsing-Chun Kuo.

**Supervision:** Hsing-Chun Kuo, Hung-Yueh Chen, Hsien-Yi Hsu, Shu-Han Yu, Chang-Wei Hsieh, Kuan-Chen Cheng.

**Validation:** Chang-Wei Hsieh.

**Writing – original draft:** Yung-Lin Chu.

**Writing – review & editing:** Shu-Han Yu, Hui-Wen Lin, Kuan-Chen Cheng.

## References

1. Tsai PJ, Sheu CH, Wu PH, Sun YF. Thermal and pH stability of betacyanin pigment of Djulis (*Chenopodium formosanum*) in Taiwan and their relation to antioxidant activity. *J Agric Food Chem.* 2010; 58 (2):1020–5. Epub 2009/12/25. <https://doi.org/10.1021/jf9032766> PMID: 20030318.

2. Chyau CC, Chu CC, Chen SY, Duh PD. The Inhibitory Effects of Djulis (*Chenopodium formosanum*) and Its Bioactive Compounds on Adipogenesis in 3T3-L1 Adipocytes. *Molecules*. 2018; 23(7). Epub 2018/07/22. <https://doi.org/10.3390/molecules23071780> PMID: 30029534
3. Lee KS, Cha HJ, Lee GT, Lee KK, Hong JT, Ahn KJ, et al. Troxerutin induces protective effects against ultraviolet B radiation through the alteration of microRNA expression in human HaCaT keratinocyte cells. *Int J Mol Med*. 2014; 33(4):934–42. Epub 2014/02/08. <https://doi.org/10.3892/ijmm.2014.1641> PMID: 24503859.
4. Higashikawa F, Noda M, Awaya T, Nomura K, Oku H, Sugiyama M. Improvement of constipation and liver function by plant-derived lactic acid bacteria: a double-blind, randomized trial. *Nutrition*. 2010; 26(4):367–74. Epub 2009/07/25. <https://doi.org/10.1016/j.nut.2009.05.008> PMID: 19628371.
5. Zhang Q, Song X, Sun W, Wang C, Li C, He L, et al. Evaluation and application of different cholesterol-lowering lactic acid bacteria as potential meat starters. *J Food Prot*. 2020. Epub 2020/08/21. <https://doi.org/10.4315/JFP-20-225> PMID: 32818231.
6. Albano C, Morandi S, Silveti T, Casiraghi MC, Manini F, Brasca M. Lactic acid bacteria with cholesterol-lowering properties for dairy applications: In vitro and in situ activity. *J Dairy Sci*. 2018; 101(12):10807–18. Epub 2018/09/24. <https://doi.org/10.3168/jds.2018-15096> PMID: 30243635.
7. Zhao D, Shah NP. Concomitant ingestion of lactic acid bacteria and black tea synergistically enhances flavonoid bioavailability and attenuates d-galactose-induced oxidative stress in mice via modulating glutathione antioxidant system. *J Nutr Biochem*. 2016; 38:116–24. Epub 2016/10/14. <https://doi.org/10.1016/j.jnutbio.2016.09.005> PMID: 27736731.
8. Hsieh SC, Liu JM, Pua XH, Ting Y, Hsu RJ, Cheng KC. Optimization of *Lactobacillus acidophilus* cultivation using taro waste and evaluation of its biological activity. *Appl Microbiol Biotechnol*. 2016; 100(6):2629–39. Epub 2015/11/18. <https://doi.org/10.1007/s00253-015-7149-1> PMID: 26572522.
9. Bianchi F, Rossi EA, Gomes RG, Sivieri K. Potentially synbiotic fermented beverage with aqueous extracts of quinoa (*Chenopodium quinoa* Willd) and soy. *Food Sci Technol Int*. 2015; 21(6):403–15. Epub 2014/06/25. <https://doi.org/10.1177/1082013214540672> PMID: 24958776.
10. Lin SP, Kuo TC, Wang HT, Ting Y, Hsieh CW, Chen YK, et al. Enhanced bioethanol production using atmospheric cold plasma-assisted detoxification of sugarcane bagasse hydrolysate. *Bioresour Technol*. 2020; 313:123704. Epub 2020/06/27. <https://doi.org/10.1016/j.biortech.2020.123704> PMID: 32590306.
11. Bezerra MA, Santelli RE, Oliveira EP, Villar LS, Escalera LA. Response surface methodology (RSM) as a tool for optimization in analytical chemistry. *Talanta*. 2008; 76(5):965–77. <https://doi.org/10.1016/j.talanta.2008.05.019> PMID: 18761143.
12. Lai YT, Cheng KC, Lai CN, Lai YJ. Isolation and identification of aroma producing strain with esterification capacity from yellow water. *PLoS One*. 2019; 14(2):e0211356. Epub 2019/02/15. <https://doi.org/10.1371/journal.pone.0211356> PMID: 30763353
13. Wu WH, Hung WC, Lo KY, Chen YH, Wan HP, Cheng KC. Bioethanol production from taro waste using thermo-tolerant yeast *Kluyveromyces marxianus* K21. *Bioresour Technol*. 2016; 201:27–32. Epub 2015/11/30. <https://doi.org/10.1016/j.biortech.2015.11.015> PMID: 26615498.
14. Hsu KD, Wu SP, Lin SP, Lum CC, Cheng KC. Enhanced active extracellular polysaccharide production from *Ganoderma formosanum* using computational modeling. *J Food Drug Anal*. 2017; 25(4):804–11. Epub 2017/10/11. <https://doi.org/10.1016/j.jfda.2016.12.006> PMID: 28987356.
15. Shella Permatasari Santoso C-CC, Shin-Ping Lin, Felicia Edi Soetaredjo, Suryadi Ismadji, Chang-Wei Hsieh, Kuan Chen Cheng. Enhanced production of bacterial cellulose by *Komactobacter intermedius* using statistical modeling. *Cellulose* 2020; 27:2497–509. <https://link.springer.com/article/10.1007/s10570-019-02961-5?shared-article-renderer>.
16. Yang WC, Hsu TC, Cheng KC, Liu JR. Erratum to: Expression of the *Clonostachys rosea* lactonohydrolase gene by *Lactobacillus reuteri* to increase its zearalenone-removing ability. *Microb Cell Fact*. 2017; 16(1):102. Epub 2017/06/14. <https://doi.org/10.1186/s12934-017-0714-9> PMID: 28606142
17. Hu Y, Zhang J, Zou L, Fu C, Li P, Zhao G. Chemical characterization, antioxidant, immune-regulating and anticancer activities of a novel bioactive polysaccharide from *Chenopodium quinoa* seeds. *Int J Biol Macromol*. 2017; 99:622–9. Epub 2017/03/10. <https://doi.org/10.1016/j.ijbiomac.2017.03.019> PMID: 28274868.
18. Luciane Santos SOUSA FdSR, Paulo Túlio de Souza SILVEIRA, Eliete da Silva BISPO, Sérgio Eduardo SOARES. Enzymatic activity of proteases and its isoenzymes in fermentation process in cultivars of cocoa (*Theobroma cacao* L.) produced in southern Bahia, Brazil. *Food Science and Technology*. 2016; 36. Epub Nov 21, 2016 [https://www.scielo.br/scielo.php?script=sci\\_arttext&pid=S0101-20612016000400656&lng=en&tlng=en](https://www.scielo.br/scielo.php?script=sci_arttext&pid=S0101-20612016000400656&lng=en&tlng=en).
19. Jana A, Maity C, Halder SK, Pati BR, Mondal KC, Mohapatra PK. Rapid screening of tannase producing microbes by using natural tannin. *Braz J Microbiol*. 2012; 43(3):1080–3. Epub 2012/07/01. <https://doi.org/10.1590/S1517-838220120003000034> PMID: 24031931

20. Aloisi I, Parrotta L, Ruiz KB, Landi C, Bini L, Cai G, et al. New Insight into Quinoa Seed Quality under Salinity: Changes in Proteomic and Amino Acid Profiles, Phenolic Content, and Antioxidant Activity of Protein Extracts. *Front Plant Sci.* 2016; 7. ARTN 656 <https://doi.org/10.3389/fpls.2016.00656> PMID: 27242857
21. Dudonne S, Vitrac X, Coutiere P, Woillez M, Merillon JM. Comparative study of antioxidant properties and total phenolic content of 30 plant extracts of industrial interest using DPPH, ABTS, FRAP, SOD, and ORAC assays. *J Agric Food Chem.* 2009; 57(5):1768–74. <https://doi.org/10.1021/jf803011r> PMID: 19199445.
22. Turkan I. ROS and RNS: key signalling molecules in plants. *J Exp Bot.* 2018; 69(14):3313–5. Epub 2018/06/23. <https://doi.org/10.1093/jxb/ery198> PMID: 29931350
23. Esteban-Torres M, Landete JM, Reveron I, Santamaria L, de las Rivas B, Munoz R. A *Lactobacillus plantarum* esterase active on a broad range of phenolic esters. *Appl Environ Microbiol.* 2015; 81(9):3235–42. <https://doi.org/10.1128/AEM.00323-15> PMID: 25746986
24. Gasparova Z, Stara V, Stolic S. Effect of antioxidants on functional recovery after in vitro-induced ischemia and long-term potentiation recorded in the pyramidal layer of the CA1 area of rat hippocampus. *Gen Physiol Biophys.* 2014; 33(1):43–52. [https://doi.org/10.4149/gpb\\_2013062](https://doi.org/10.4149/gpb_2013062) PMID: 23940087.
25. Koleva II, van Beek TA, Linssen JP, de Groot A, Evstatieva LN. Screening of plant extracts for antioxidant activity: a comparative study on three testing methods. *Phytochem Anal.* 2002; 13(1):8–17. Epub 2002/03/20. <https://doi.org/10.1002/pca.611> PMID: 11899609.
26. Yao Y, Shi Z, Ren G. Antioxidant and immunoregulatory activity of polysaccharides from quinoa (*Chenopodium quinoa* Willd.). *Int J Mol Sci.* 2014; 15(10):19307–18. Epub 2014/10/25. <https://doi.org/10.3390/ijms151019307> PMID: 25342323
27. Khan Nadiya Jan PSP, Sukhcham Singh. Optimization of antioxidant activity, textural and sensory characteristics of gluten-free cookies made from whole indian quinoa flour. *LWT—Food Science and Technology.* 2018; 93:573–82. <https://doi.org/10.1016/j.lwt.2018.04.013>.
28. Dinarvand M, Rezaee M, Foroughi M. Optimizing culture conditions for production of intra and extracellular inulinase and invertase from *Aspergillus niger* ATCC 20611 by response surface methodology (RSM). *Braz J Microbiol.* 2017; 48(3):427–41. Epub 2017/04/01. <https://doi.org/10.1016/j.bjm.2016.10.026> PMID: 28359854
29. Bhanja Dey T, Kuhad RC. Upgrading the antioxidant potential of cereals by their fungal fermentation under solid-state cultivation conditions. *Lett Appl Microbiol.* 2014; 59(5):493–9. Epub 2014/06/27. <https://doi.org/10.1111/lam.12300> PMID: 24964826.
30. Virtanen T, Pihlanto A, Akkanen S, Korhonen H. Development of antioxidant activity in milk whey during fermentation with lactic acid bacteria. *J Appl Microbiol.* 2007; 102(1):106–15. Epub 2006/12/23. <https://doi.org/10.1111/j.1365-2672.2006.03072.x> PMID: 17184325.



## Research Article

# The Beneficial Effects of Moxibustion on Overweight Adolescent Girls

Yuan-Chieh Yeh <sup>1,2</sup>, Chin-Chang Chen,<sup>1,3</sup> Ching-Yi Cheng,<sup>4,5</sup> Hsin-Ning Chang,<sup>1,6</sup>  
and Tse-Hung Huang <sup>1,4,7</sup>

<sup>1</sup>Department of Traditional Chinese Medicine, Chang Gung Memorial Hospital, Keelung, Taiwan

<sup>2</sup>Program in Molecular Medicine, School of Life Sciences, National Yang Ming University, Taipei, Taiwan

<sup>3</sup>Department of Anatomy, School of Medicine, China Medical University, Taichung, Taiwan

<sup>4</sup>Graduate Institute of Health Industry Technology,  
Research Center for Chinese Herbal Medicine and Research Center for Food and Cosmetic Safety, College of Human Ecology,  
Chang Gung University of Science and Technology, Taoyuan, Taiwan

<sup>5</sup>Department of Pulmonary Infection and Immunology, Chang Gung Memorial Hospital at Linkou, Taoyuan, Taiwan

<sup>6</sup>Graduate Institute of Clinical Medicine Sciences, College of Medicine, Chang Gung University, Taiwan

<sup>7</sup>School of Nursing, National Taipei University of Nursing and Health Sciences, Taipei, Taiwan

Correspondence should be addressed to Tse-Hung Huang; [tcmhuang168@gmail.com](mailto:tcmhuang168@gmail.com)

Received 3 May 2020; Revised 15 November 2020; Accepted 24 April 2021; Published 11 May 2021

Academic Editor: Jose C Adsuar

Copyright © 2021 Yuan-Chieh Yeh et al. This is an open access article distributed under the Creative Commons Attribution License, which permits unrestricted use, distribution, and reproduction in any medium, provided the original work is properly cited.

Among adolescent girls, overweight or obesity has both physical and psychological involvement. We conducted a randomized controlled trial of moxibustion using a moxa burner. Fifty-four eligible girls aged 15–18 years with a body mass index (BMI) greater than 25.3 were enrolled in the study. The girls were randomly allocated to the treatment ( $n = 27$ ) and control ( $n = 27$ ) groups. The girls underwent treatment three times per week for 8 weeks (24 treatments). Moxibustion was applied to the RN12, RN6, ST25, ST36, and SP6 acupoints. Physical assessments were BMI, waist-to-hip ratio (WHR), and body fat ratio (BFR). Psychological outcomes were measured using the Rosenberg Self-Esteem Scale (RSE). Data were collected at the beginning of the study (baseline), week 4, and week 8. Of the 54 participants, 46 completed the trial. The difference in mean BMI from baseline between the two groups was 0.097 ( $p = 0.655$ ) at week 4 and  $-0.794$  ( $p = 0.001$ ) at week 8. The mean WHR of the treatment group was significantly reduced compared with baseline, with a  $-0.011$  ( $p = 0.017$ ) and  $-0.035$  ( $p < 0.001$ ) mean change at weeks 4 and 8, respectively. The mean BFR was slightly reduced ( $-0.253$ ;  $p = 0.474$ ) at week 4 compared with baseline in the treatment group. At week 8, it was significantly reduced ( $-2.068$ ;  $p < 0.001$ ) from baseline in the treatment group. The mean RSE in the treatment group showed no significant increase from baseline at week 4 (0.155 points,  $p = 0.803$ ), but it improved significantly from baseline at week 8 (1.606 points,  $p = 0.021$ ) compared to that in the control group. No obvious adverse effect was reported during this study. Moxibustion using a moxa burner may be an effective and safe intervention for overweight adolescent girls, having both physical and psychological benefits.

## 1. Introduction

Overweight in adolescents is a major health concern worldwide because it is a strong predictor of high risks of cardiovascular disease, type 2 diabetes, and other health problems [1, 2]. Moreover, adolescents with overweight or obesity have a greater risk of adulthood overweight or

obesity regardless of race or ethnicity [3]. Because the prevalence of overweight in adolescents has increased in several developed and developing countries [4–6], it has garnered more public attention to promote health improvements. In Taiwan, the prevalence of adolescent overweight was 12%–34% in a large-scale nationwide survey [7]. Being overweight or obese is more likely to contribute to

major psychological problems among girls than among boys [8, 9]. Adolescent girls who developed a negative body image were found to be at a greater risk of subsequent psychological difficulties, such as frustration or a sense of failure [10]. Social aspects of overweight or obesity, such as prejudice and discrimination, also play a role in adolescent mental development as adolescents mature into adulthood.

Traditional Chinese medicine (TCM) techniques, including acupuncture, body or auricular acupoint stimulation, and acupoint catgut embedding, have become increasingly widely applied for controlling overweight and obesity. Moxibustion is a thermal stimulation method that employs ignited material applied onto or above the surface of the skin of a patient [11]. It can also be applied above acupoints on the surface of the patient's skin by using moxa sticks [12]. From the viewpoint of traditional Chinese medicine, moxibustion dredges meridians, relieves stagnation, and regulates qi-blood balance. This simple and safe therapeutic technique has been employed to treat myriad diseases [13] and is relatively noninvasive compared with acupuncture or acupoint catgut embedding. However, clinical trials on moxibustion and adolescents with overweight remain scant.

This clinical trial evaluated the effectiveness of moxibustion on adolescent girls with overweight. We hypothesized that, at the end of the 8-week intervention period, patients in the moxibustion group would exhibit more substantial improvement in both physical and psychological function than would those in the control group.

## 2. Materials and Methods

**2.1. Subject Selection.** A randomized controlled trial was executed to ascertain the effectiveness of moxibustion among adolescent girls with overweight who were from a nursing school in Northern Taiwan. In total, 54 eligible participants aged from 15 to 18 years were enrolled. The participants all had a body mass index (BMI) greater than 25.3, which is the World Health Organization's (WHO's) definition of overweight. Participants were randomly allocated to the treatment group ( $N=27$ ) or control group ( $N=27$ ) using computer-generated numbers. Participants who, during the trial, had catastrophic diseases, wounds on the abdomen, or any signs of acute inflammation, as well as those who were pregnant, were excluded. Moreover, participants who missed more than three consecutive sessions during the 8-week intervention were excluded from the trial. The process of this randomized controlled trial was approved by the Institutional Review Board of the Chang Gung Memorial Foundation (95-1478B).

**2.2. Moxibustion Intervention.** Moxibustion interventions were performed thrice weekly for 8 weeks (24 treatments in total). Moxibustion was applied to the RN12 (*zhong wan*), RN6 (*qi hai*), ST25 (*tian shu*), ST36 (*zu san li*), and SP6 (*san yin jiao*) acupoints. The intervention was performed using a moxa burner (Figure 1(a)), with placing one end of a moxa stick; therefore, the distance between the lit end of the moxa

stick and the corresponding acupoint was stable. A metal mesh was attached to the bottom of the moxa burner to prevent burns resulting from falling ash. Each standardized moxa stick weighed 30–32 g. For moxibustion intervention of 10 min/acupoint,  $4 \pm 1$  g of moxa material was ignited. After a brief introductory session of the usage of a moxa burner and the locations of all acupoints to ensure standardization of the treatment process, the participants were asked to work in pairs. One participant lay down and held two moxa burners applied to bilateral ST25, while another fellow participant held two burners applied to bilateral SP6 (Figure 1(b)) for the first 10 minutes. Then, the participants took out all moxa sticks to clean the ashes in the moxa burners, kept moxa sticks ignited, and inserted them into burners. Afterwards, the participant shifted two moxa burners to RN12 and RN6, while the fellow participant applied the moxa burners to bilateral ST36 for another 10 minutes. After a complete 20-minute moxibustion treatment, the participant and her partner exchanged their positions for another 20-minute intervention. During the entire 40-minute intervention, the participants could adjust the moxa sticks if they felt the skin too hot or not hot enough; otherwise, they were told to keep the moxa sticks in place to avoid experimental bias. Participants were told to maintain their daily routines following each intervention. Participants who missed one treatment were asked to perform moxibustion at home using moxa burners and material provided by the research staff.

**2.3. Control Intervention.** Participants in the control group were encouraged to maintain their daily routines during the 8-week study period. They were asked not to participate in moxibustion or acupuncture treatment or new exercise programs or diets. They received a 1-week (i.e., three treatments) supply of moxa burners and material following the study period and were taught how to use them, in return for their participation.

**2.4. Assessment.** The physical and psychological variables were measured at the beginning of the study (baseline), week 4, and week 8. The physical outcomes were changes in the BMI, waist-to-hip ratio (WHR), and body fat ratio (BFR). Data were acquired using a digital medical scale (HW-999, Super View, Taiwan) for BMI measurement and In Body 3.0 for WHR and BFR measurement in the laboratory to avoid measurement bias.

The Rosenberg Self-Esteem Scale (RSE) was used to assess the psychological changes in the participants during the intervention [14]. The RSE is a validated social survey questionnaire and has been widely used in studies on adolescents with obesity [15–17]. In total, 10 items are rated on a 4-point scale on the RSE; total scores range from 10 to 40. Heavier weights of adolescent girls are correlated with lower RSE scores [18].

**2.5. Data Analysis.** SPSS v.15 for Windows was used for data processing and analysis. A statistically significant change was defined as  $p < 0.05$ . Differences in general demographic

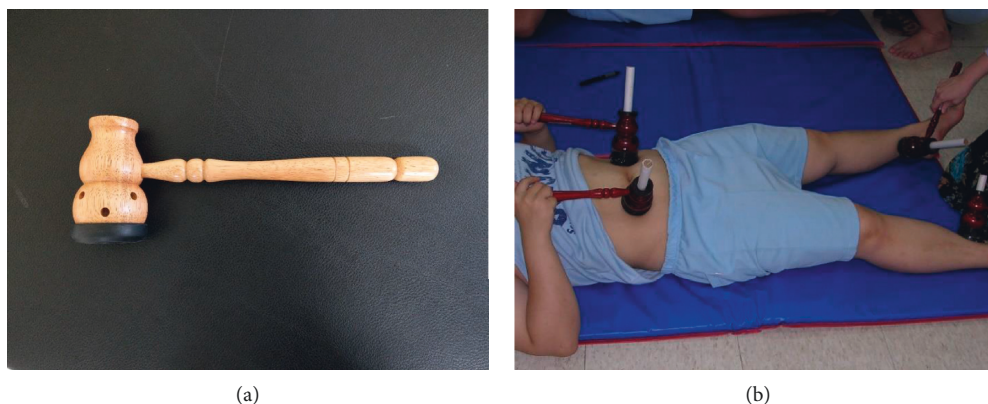


FIGURE 1: Moxa burner (a) and an example of moxibustion intervention (b). The participant (lay down) held two moxa burners applied to bilateral ST25, while the fellow participant held two burners applied to bilateral SP6 for the first 10 minutes. After the moxa burners were cleaned, the participant shifted two moxa burners to RN12 and RN6, while the fellow participant applied the moxa burners to bilateral ST36 for another 10 minutes. After a complete 20-minute intervention, the two participants swapped their positions for another 20-minute moxibustion treatment.

information between the two groups were measured using the chi-squared test. An independent-sample *t*-test was performed to compare the BMI, WHR, BFR, and RSE score between the two groups at the beginning of the study. Moreover, generalized estimating equations (GEEs) were used to assess the improvements in the BMI, WHR, BFR, and RSE score at the end of week 4 and week 8.

### 3. Results

In total, 54 participants were enrolled in this study. Figure 2 shows the screening, randomization, and evaluation algorithm used in this study. Three participants in the treatment group and four participants in the control group dropped out of the study because of scheduling conflicts; one participant in the control group dropped out of the study because of dysmenorrhea at week 2. The dropout rate of this study was 14.9%.

**3.1. Baseline Data of the Participants.** Table 1 presents the baseline data of the participants after randomization, and no difference between the mean age, BMI, WHR, BFR, and RSE score was observed. The average participant was obese (mean BMI > 30), had high cardiovascular risk (mean WHR > 0.85), and had a high amount of body fat (mean BFR > 40). The mean RSE score was between 26 and 27.

Questionnaires on diet preference and medicine usage also revealed no differences (Table 2). Participants in the treatment group were more likely to have attempted to lose weight ( $N = 21$ , 87.5%) than were those in the control group ( $N = 14$ , 63.5%); however, this result was not statistically significant ( $p = 0.058$ ). Most participants did not take regular food supplements or medicine to lose weight. Heterogeneity was examined, and the result showed no statistical significance ( $p > 0.05$ ).

**3.2. Moxibustion Improved Both Physical and Psychological Outcomes of the Participants.** The physical and psychological evaluation data were analyzed using GEEs and are

summarized in Table 3. Line charts of our data are provided in Figures 3(a)–3(d).

At week 4, the BMI of the treatment group was slightly increased compared with that of the control group (Table 3, Figure 3(a)). The difference in BMI change from baseline between the treatment group and control group was 0.097 ( $p = 0.655$ ) at week 4 and  $-0.794$  ( $p = 0.001$ ) at week 8. In summary, after 8 weeks of moxibustion intervention, the treatment group participants' mean BMI score was 0.794 lower than that of the control group participants.

The treatment group exhibited a significant decrease ( $-0.011$ ;  $p = 0.017$  and  $-0.035$ ;  $p < 0.001$ ) in WHR after 4 and 8 weeks' intervention, respectively, from baseline (Table 3, Figure 3(b)).

The treatment group showed a slight, nonsignificant decrease ( $-0.253$ ;  $p = 0.474$ ) in BFR from baseline at week 4. However, at week 8, a significant decrease ( $-2.068$ ;  $p < 0.001$ ) in BFR from baseline was observed (Table 3, Figure 3(c)).

The RSE score of the treatment group was slightly higher (0.155;  $p = 0.803$ ) at week 4. At week 8, the treatment group showed a significant improvement from baseline (1.606 points;  $p = 0.021$ ) than the control group (Table 3, Figure 3(d)).

**3.3. Moxibustion Caused No Adverse Effects during the Trial.** No obvious adverse effects, such as burn injuries or irritation, were observed during the 8-week intervention. One participant dropped out of the control group because of dysmenorrhea at week 2; this was unrelated to the moxibustion intervention.

### 4. Discussion

To the best of our knowledge, this is the first integrated clinical trial to evaluate the effects of moxibustion on adolescent girls with overweight. Moxibustion is usually applied in combination with other acupuncture treatments,

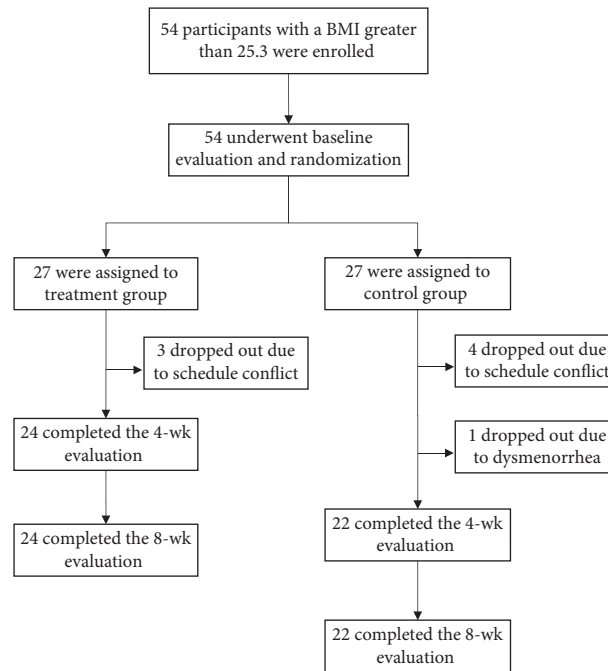


FIGURE 2: Screening, randomization, and evaluation algorithm.

TABLE 1: Baseline characteristics of the participants.

Variable	Treatment group (N = 24)	Control group (N = 22)	<i>P</i>
	Mean $\pm$ SD	Mean $\pm$ SD	
Age, yr	17.17 $\pm$ 0.92	17.50 $\pm$ 1.01	0.247
Body mass index	31.26 $\pm$ 3.80	31.63 $\pm$ 4.39	0.761
Waist-to-hip ratio	0.94 $\pm$ 0.06	0.94 $\pm$ 0.62	0.978
Body fat ratio	40.93 $\pm$ 4.18	40.51 $\pm$ 3.86	0.728
RSE*	26.58 $\pm$ 4.13	26.36 $\pm$ 3.82	0.853

\*RSE: Rosenberg Self-Esteem Scale.

such as needle acupuncture, electroacupuncture, laser acupuncture, or even more invasive acupoint catgut embedding therapy [19, 20]. On the aspect of weight reduction, moxibustion with warming needle acupuncture may be one of the optimal methods in losing weight [20]. However, there was no clinical trial investigating purely moxibustion in losing weight. Among 34 eligible trials analyzed in one literature review, only one study used moxibustion with other acupuncture therapies to lose weight [20]. Herein, we conducted a randomized controlled trial to apply simply moxibustion in treating obesity or overweight. Our results support moxibustion's efficacy in reducing the BMI, WHR, and BFR, as well as increasing self-esteem in adolescent girls with overweight. All participants tolerated moxibustion using the noninvasive and easy-to-use moxa burner favorably without severe adverse events. The findings of this study may have important implications for managing the global health issue—adolescent obesity or overweight.

We enrolled all participants according to the WHO definition of overweight (i.e., a BMI greater than 25.3). However, the average BMI in our study participants was more than 30 in both groups (Table 1), which is defined as obese.

The results of our questionnaires revealed that 35 (76.08%) of the participants had previously attempted to lose weight (Table 2). Most adolescents with overweight or obesity reported that they had attempted to lost weight, according to an international survey [21]. Furthermore, most respondents to the survey in our study stated that they did not spend money on losing weight, which may have been because of economic status. Additionally, more than 90% of participants in one study reported a habit of late-night snacking, which is a risk factor for adolescent obesity [22]. Another study indicated that circadian rhythm and food intake interact to play a pivotal role in the development of adolescent obesity, perhaps because of the strong adverse association between glucose and insulin at nighttime [23].

According to the viewpoint of traditional Chinese medicine, the disease pattern observed in obese adolescents was yang deficiency and qi stagnation. Moxibustion has been used for warming yang and dredging meridians, which is favorably indicated for treating obesity. In addition to moxibustion, acupuncture and acupoint catgut embedding are used to treat adolescents with obesity in Taiwan. However, several adverse effects of these treatments—such as pain, hematoma, and granuloma—have been reported



TABLE 2: Results of the questionnaire on diet habits and medicine use of the participants.

Variable	Treatment group (N=24) Number (%)	Control group (N=22) Number (%)	P
Ever attempted to lose weight			0.058
No	3 (12.5)	8 (36.4)	
Yes	21 (87.5)	14 (63.6)	
Exercised to lose weight			0.253
No	7 (29.2)	10 (45.5)	
Yes	17 (70.8)	12 (54.5)	
On diet to lose weight			0.253
No	7 (29.2)	10 (45.5)	
Yes	17 (70.8)	12 (54.5)	
Use of food supplement to lose weight			0.187
No	20 (83.3)	21 (95.5)	
Yes	4 (16.7)	1 (4.5)	
Use of herbal medicine to lose weight			0.268
No	19 (79.2)	20 (90.9)	
Yes	5 (20.8)	2 (9.1)	
Use of other medicine to lose weight			0.333
No	23 (95.8)	22 (100)	
Yes	1 (4.2)	0 (0)	
Cost per month to lose weight			0.229
0 TWD	16 (66.7)	19 (86.4)	
1–1000 TWD	4 (16.7)	3 (13.6)	
1001–2000 TWD	1 (4.2)	0 (0)	
>2001 TWD	3 (12.5)	0 (0)	
A habit of a midnight snack			0.642
No	2 (8.3)	2 (9.1)	
Yes	22 (91.7)	20 (90.9)	
Prefer Chinese eating style			0.243
No	5 (20.8)	8 (36.4)	
Yes	19 (79.2)	14 (63.6)	
Prefer Western eating style			0.136
No	10 (41.7)	14 (63.6)	
Yes	14 (58.3)	8 (36.4)	

[24]. The safe and easy-to-use moxa burner and material used in our study may have contributed to the low withdrawal rate (14.8%) compared with that in studies using needle acupuncture (25%–27%) [25].

Our results revealed that moxibustion reduced the WHR earlier than the other measures, with a significant reduction ( $p = 0.017$ ) in WHR observed at week 4 (Table 3, Figure 3(b)). This anthropometrical change may reduce the risk of cardiovascular disease because WHR is strongly associated with coronary artery calcification in young adults, and this parameter is frequently used for cardiovascular risk evaluation [26]. This is consistent with the correlation between visceral fat and coronary atherosclerosis. The body shape of the participants was more “apple-shaped” (WHR > 0.85) at baseline and seemed to be more “pear-shaped” following the moxibustion intervention. The results revealed that moxibustion reduces the cardiovascular risk of girls with overweight or obesity.

Our findings were broadly consistent with those of other studies on acupuncture or moxibustion [19, 27]. The results may be because of the abdominal acupoints used in our study: RN12, RN6, and bilateral ST25 are traditionally used for adjusting bowel movements and treating constipation, whereas ST36 and SP6 are used for dredging

meridians and relieving stagnation, especially in the stomach and spleen channels, with stagnation also correlated with obesity. One clinical trial indicated that warming needle acupuncture applied to abdominal acupoints (RN12, RN9, RN6, RN3, ST25, and ST28) may have long-term therapeutic effect on simple obesity with spleen deficiency pattern [28]. Previous study indicated that moxibustion-like thermal stimulation to the mouse abdomen decreased the size of white adipose tissue and induced formation of beige adipocytes [29]. Electroacupuncture stimulation to acupoints RN12, SP6, and ST36 may regulate gastrointestinal motility *in vivo* through the vagus-gastric neural pathway [30, 31]. Similarly, diet-induced obese rats treated by electroacupuncture applied to ST25, RN12, SP6, and ST36 showed the mechanisms to reduce weight and appetite may be related to hypothalamic Tsc1 promoter demethylation and mTORC1 signaling pathway inhibition [32]. However, the detailed molecular mechanism responsible for weight reduction by simply moxibustion is yet to be clearly identified.

Other physical variables, such as BMI and BFR, showed no significant decrease until week 8. These results were similar to those of other studies that used acupuncture to treat children with obesity [33], suggesting that acupuncture



TABLE 3: Generalized estimating equation analysis of outcome measurements.

(A) body mass index	$\beta$	Standard error	<i>p</i>
Group			
Treatment vs. control	31.627		
Time course			
4 <sup>th</sup> week vs. baseline	-0.268		
8 <sup>th</sup> week vs. baseline	-0.077		
Group * time course (treatment vs. control)			
4 <sup>th</sup> week vs. baseline	0.097	0.218	0.655
8 <sup>th</sup> week vs. baseline	-0.794	0.248	0.001**
(B) waist-to-hip ratio			
Group			
Treatment vs. control	0.944		
Time course			
4 <sup>th</sup> week vs. baseline	-0.002		
8 <sup>th</sup> week vs. baseline	-4.63		
Group * time course (treatment vs. control)			
4 <sup>th</sup> week vs. baseline	-0.011	0.004	0.017*
8 <sup>th</sup> week vs. baseline	-0.035	0.007	<0.001***
(C) body fat ratio			
Group			
Treatment vs. control	40.509		
Time course			
4 <sup>th</sup> week vs. baseline	-0.268		
8 <sup>th</sup> week vs. baseline	0.068		
Group * time course (treatment vs. control)			
4 <sup>th</sup> week vs. baseline	-0.253	0.353	0.474
8 <sup>th</sup> week vs. baseline	-2.068	0.548	<0.001***
(D) Rosenberg self-Esteem Scale			
Group			
Treatment vs. control	26.364		
Time course			
4 <sup>th</sup> week vs. baseline	0.136		
8 <sup>th</sup> week vs. baseline	0.227		
Group * time course (treatment vs. control)			
4 <sup>th</sup> week vs. baseline	0.155	0.622	0.803
8 <sup>th</sup> week vs. baseline	1.606	0.698	0.021*

The outcome measurements are body mass index (A), waist-to-hip ratio (B), body fat ratio (C), and Rosenberg Self-Esteem Scale (D) ( $N = 46$ ). \*  $p < 0.05$ , \*\*  $p < 0.01$ , \*\*\*  $p < 0.001$ .

significantly reduces visceral fat and WHR without significantly changing body weight.

The association between overweight or obesity and self-esteem was reported to be tenuous in other studies on Han and other ethnic groups [9, 34, 35]. However, overweight or obesity may increase the risk of developing body image dissatisfaction, which may in turn impair self-esteem [36]. In particular, girls with overweight in our study reported an increase in self-esteem after moxibustion (Table 3, Figure 3(d)). The mean baseline RSE scores of the two groups were 26.58 (treatment) and 26.36 (control), which did not statistically differ. As expected, moxibustion successfully increased the mean RSE score by 1.606 in the treatment group, indicating that the self-esteem of the participants was increased by the intervention.

The moxa burner is a relatively safe device, according to our study. The burner, which has a fine metal mesh at the bottom, allows heat to pass without ashes falling onto the skin. During the 8-week intervention, no adverse effects or burns were reported, probably because this safe moxibustion

device was used and its method of use was effectively explained. Although other studies have reported potentially adverse effects from moxibustion, such as allergies, burns, and infections [37], no participant in our treatment group withdrew because of these adverse effects.

**4.1. Limitations.** Our study had several limitations. First, the trial was not double blinded because performing sham moxibustion is difficult. To date, no validated double-blinded studies on moxibustion have been reported in the literature. Other studies have performed sham moxibustion by using devices to prevent heat radiating from the moxa burner to the patient's skin [38]. However, the sensation of heat may play a role in the process of moxibustion. Second, this study was conducted in only one nursing school in Northern Taiwan. Thus, the generalization of the results to other populations with different backgrounds may be limited. Third, the measurements were taken thrice only, without long-term follow-up, because of our limited

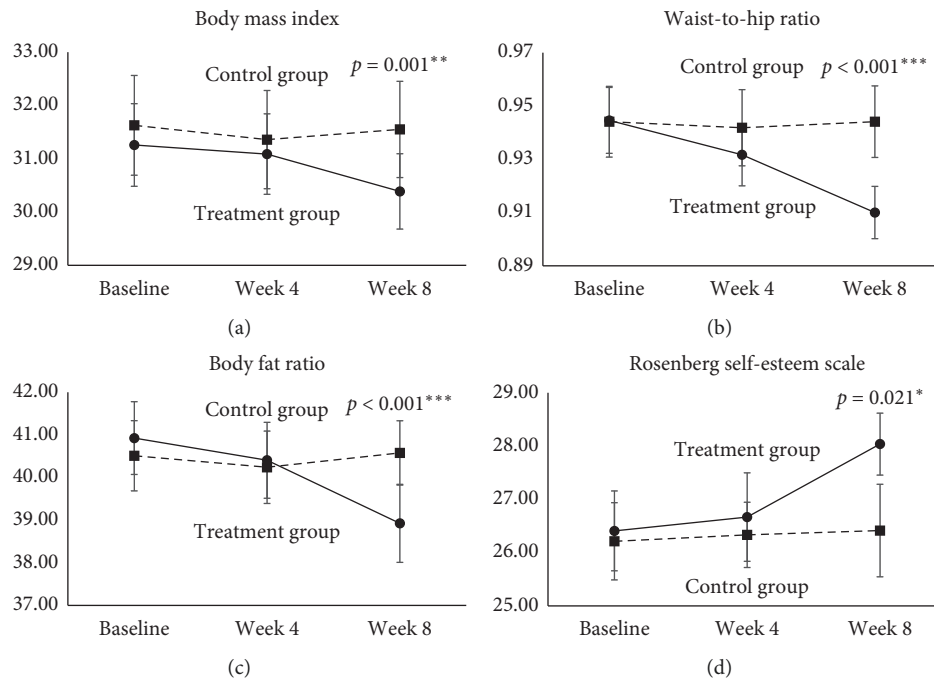


FIGURE 3: Mean changes in four variables at weeks 4 and 8 by the treatment group. The mean changes in body mass index (a), waist-to-hip ratio (b), body fat ratio (c), and rosenberg self-esteem scale (d) were measured at baseline, week 4, and week 8 between the treatment group and control group. \* $p < 0.05$ , \*\* $p < 0.01$ , and \*\*\* $p < 0.001$ .

research funding and resources. Fourth, we may enroll more eligible samples in our further study to strengthen our results because the error bars in Figure 3 seem to be excessive. We believe the results of our study may provide a comprehensive knowing in designing a larger-scale randomized controlled trial in the future to improve statistical power.

## 5. Conclusions

Moxibustion intervention may help improve some physical and psychological variables of adolescent girls with overweight, including the WHR and BFR, as well as the BMI and RSE score. This simple and safe therapeutic method is worthy of promotion by public health authorities.

## Abbreviations

TCM: Traditional Chinese medicine  
 BMI: Body mass index  
 WHR: Waist-to-hip ratio  
 BFR: Body fat ratio  
 RSE: Rosenberg Self-Esteem Scale.

## Data Availability

The data supporting the findings of this study are available from the corresponding author upon request.

## Disclosure

Two oral presentations of the data in the manuscript were presented in the International Conference on Medical and

Health Informatics (ICMHI) 2018 Japan and International Brazilian Acupuncture Congress (CMAESP & CMBA) 2018 Brazil.

## Conflicts of Interest

The authors declare no conflicts of interest.

## Acknowledgments

The authors thank all patients for participation in this study and Tay-Wey Lee at the Department of Medical Research and Development, Keelung Chang Gung Memorial Hospital, for data analysis and statistical consultation. The authors are grateful for the financial support by Chang Gung Memorial Hospital (CMRPG2G0333, CMRPG2H0121, CMRPG2H0361, CMRPG2H0362, CMRPG2J0041, and CMRPG2J0042) and the Ministry of Science and Technology (MOST 107-2320-B-182A-019-MY3).

## References

- [1] D. S. Freedman, Z. Mei, S. R. Srinivasan, G. S. Berenson, and W. H. Dietz, "Cardiovascular risk factors and excess adiposity among overweight children and adolescents: the Bogalusa Heart Study," *The Journal of Pediatrics*, vol. 150, no. 1, pp. 12–17 e12, 2007.
- [2] I. M. Libman, E. Barinas-Mitchell, A. Bartucci, D. Chaves-Gnecco, R. Robertson, and S. Arslanian, "Fasting and 2-hour plasma glucose and insulin: relationship with risk factors for cardiovascular disease in overweight nondiabetic children," *Diabetes Care*, vol. 33, no. 12, pp. 2674–2676, 2010.

- [3] K. M. Harris, P. Gordon-Larsen, K. Chantala, and J. R. Udry, "Longitudinal trends in race/ethnic disparities in leading health indicators from adolescence to young adulthood," *Archives of Pediatrics & Adolescent Medicine*, vol. 160, no. 1, pp. 74–81, 2006.
- [4] E. Stamatakis, P. Zaninotto, E. Falaschetti, J. Mindell, and J. Head, "Time trends in childhood and adolescent obesity in England from 1995 to 2007 and projections of prevalence to 2015," *Journal of Epidemiology & Community Health*, vol. 64, no. 2, pp. 167–174, 2010.
- [5] D. I. Musa, A. L. Toriola, M. A. Monyeke, and B. Lawal, "Prevalence of childhood and adolescent overweight and obesity in Benue State, Nigeria," *Tropical Medicine & International Health*, vol. 17, no. 11, pp. 1369–1375, 2012.
- [6] S. Gee, D. Chin, L. Ackerson, D. Woo, and A. Howell, "Prevalence of childhood and adolescent overweight and obesity from 2003 to 2010 in an integrated health care delivery system," *Journal of Obesity*, vol. 2013, Article ID 417907, 8 pages, 2013.
- [7] N. F. Chu, "Prevalence of obesity in taiwan," *Obesity Reviews*, vol. 6, no. 4, pp. 271–274, 2005.
- [8] C. Saloumi and H. Plourde, "Differences in psychological correlates of excess weight between adolescents and young adults in Canada," *Psychology, Health & Medicine*, vol. 15, no. 3, pp. 314–325, 2010.
- [9] D. Young-Hyman, D. G. Schlundt, L. Herman-Wenderoth, and K. Bozylinski, "Obesity, appearance, and psychosocial adaptation in young African American children," *Journal of Pediatric Psychology*, vol. 28, no. 7, pp. 463–472, 2003.
- [10] W. H. Dietz, "Health consequences of obesity in youth: childhood predictors of adult disease," *Pediatrics*, vol. 101, no. 3, pp. 518–525, 1998.
- [11] WHO and W. P. Region, *WHO International Standard Terminologies on Traditional Medicine in the Western Pacific Region*, World Health Organization Western Pacific Region, Geneva, Switzerland, 2007.
- [12] J. H. Chiu, "How does moxibustion possibly work?," *Evidence-Based Complementary and Alternative Medicine*, vol. 2013, Article ID 198584, 8.
- [13] H. Deng and X. Shen, "The mechanism of moxibustion: ancient theory and modern research," *Evidence-Based Complementary and Alternative Medicine*, vol. 2013, Article ID 379291, 7.
- [14] M. Rosenberg, *Society and the Adolescent Self-Image*, Wesleyan University Press, Middletown, CT, USA, 1989.
- [15] K. Setiloane, "Being overweight: negative outcomes for African American adolescents," *Nutrition and Health*, vol. 18, no. 1, pp. 61–66, 2004.
- [16] J. S. Huang, G. J. Norman, M. F. Zabinski, K. Calfas, and K. Patrick, "Body image and self-esteem among adolescents undergoing an intervention targeting dietary and physical activity behaviors," *Journal of Adolescent Health*, vol. 40, no. 3, pp. 245–251, 2007.
- [17] E. S. Pearson, J. D. Irwin, D. Morrow, and C. R. Hall, "The CHANGE program: comparing an interactive versus prescriptive obesity intervention on university students' self-esteem and quality of life," *Applied Psychology: Health and Well-Being*, vol. 4, no. 3, pp. 369–389, 2012.
- [18] S. Martin, K. Housley, H. McCoy et al., "Self-esteem of adolescent girls as related to weight," *Perceptual and Motor Skills*, vol. 67, no. 3, pp. 879–884, 1998.
- [19] J. M. Garcia-Vivas, C. Galaviz-Hernandez, F. Becerril-Chavez et al., "Acupoint catgut embedding therapy with moxibustion reduces the risk of diabetes in obese women," *Journal of Research in Medical Sciences*, vol. 19, no. 7, pp. 610–616, 2014.
- [20] Y. Zhang, J. Li, G. Mo et al., "Acupuncture and related therapies for obesity: a network meta-analysis," *Evidence-Based Complementary and Alternative Medicine*, vol. 2018, Article ID 9569685, 2018.
- [21] K. Ojala, C. Vereecken, R. Valimaa et al., "Attempts to lose weight among overweight and non-overweight adolescents: a cross-national survey," *International Journal of Behavioral Nutrition and Physical Activity*, vol. 4, p. 50, 2007.
- [22] S. Eng, D. A. Wagstaff, and S. Kranz, "Eating late in the evening is associated with childhood obesity in some age groups but not in all children: the relationship between time of consumption and body weight status in U.S. children," *International Journal of Behavioral Nutrition and Physical Activity*, vol. 6, p. 27, 2009.
- [23] L. Q. Qin, J. Li, Y. Wang, J. Wang, J. Y. Xu, and T. Kaneko, "The effects of nocturnal life on endocrine circadian patterns in healthy adults," *Life Sciences*, vol. 73, no. 19, pp. 2467–2475, 2003.
- [24] Y. T. Chuang, T. S. Li, T. Y. Lin, and C. J. Hsu, "An unusual complication related to acupuncture point catgut embedding treatment of obesity," *Acupuncture in Medicine*, vol. 29, no. 4, pp. 307–308, 2011.
- [25] R. Q. Zhang, J. Tan, F. Y. Li, Y. H. Ma, L. X. Han, and X. L. Yang, "Acupuncture for the treatment of obesity in adults: a systematic review and meta-analysis," *Postgraduate Medical Journal*, vol. 93, no. 1106, pp. 743–751, 2017.
- [26] C. D. Lee, D. R. Jacobs Jr., P. J. Schreiner, C. Iribarren, and A. Hankinson, "Abdominal obesity and coronary artery calcification in young adults: the coronary artery risk development in young adults (CARDIA) study," *The American Journal of Clinical Nutrition*, vol. 86, no. 1, pp. 48–54, 2007.
- [27] Z. Liu, F. Sun, J. Li, Y. Han, Q. Wei, and C. Liu, "Application of acupuncture and moxibustion for keeping shape," *Journal of Traditional Chinese Medicine*, vol. 18, no. 4, pp. 265–271, 1998.
- [28] Y. Shi, L. S. Zhang, C. Zhao, and X. Y. Zuo, "[Controlled study of needle warming therapy and electroacupuncture on simple obesity of spleen deficiency type]," *Zhongguo Zhen Jiu*, vol. 25, no. 7, pp. 465–467, 2005.
- [29] Y. J. Koh, J. H. Lee, and S. Y. Park, "Moxibustion-simulating bipolar radiofrequency suppresses weight gain and induces adipose tissue browning via activation of UCP1 and FGF21 in a mouse model of diet-induced obesity," *Evidence-Based Complementary and Alternative Medicine*, vol. 2018, Article ID 4737515, 12 pages, 2018.
- [30] A. Tabosa, Y. Yamamura, E. R. Forno, and L. E. Mello, "Effect of the acupoints ST-36 (Zusanli) and SP-6 (Sanyinjiao) on intestinal myoelectric activity of Wistar rats," *Brazilian Journal of Medical and Biological Research*, vol. 35, no. 6, pp. 731–739, 2002.
- [31] H. Wang, W. J. Liu, G. M. Shen, M. T. Zhang, S. Huang, and Y. He, "Neural mechanism of gastric motility regulation by electroacupuncture at RN12 and BL21: a paraventricular hypothalamic nucleus-dorsal vagal complex-vagus nerve-gastric channel pathway," *World Journal of Gastroenterology*, vol. 21, no. 48, pp. 13480–13489, 2015.
- [32] J. Leng, F. Xiong, J. Yao et al., "Electroacupuncture reduces weight in diet-induced obese rats via hypothalamic Tsc1 promoter demethylation and inhibition of the activity of mTORC1 signaling pathway," *Evidence-Based Complementary and Alternative Medicine*, vol. 2018, Article ID 3039783, 10.

- [33] H. Zhang, Y. Peng, Z. Liu et al., "Effects of acupuncture therapy on abdominal fat and hepatic fat content in obese children: a magnetic resonance imaging and proton magnetic resonance spectroscopy study," *The Journal of Alternative and Complementary Medicine*, vol. 17, no. 5, pp. 413–420, 2011.
- [34] N. Y. Shin and M. S. Shin, "Body dissatisfaction, self-esteem, and depression in obese Korean children," *The Journal of Pediatrics*, vol. 152, no. 4, pp. 502–506, 2008.
- [35] R. Y. Sung, C. W. Yu, R. C. So, P. K. Lam, and K. T. Hau, "Self-perception of physical competences in preadolescent overweight Chinese children," *European Journal of Clinical Nutrition*, vol. 59, no. 1, pp. 101–106, 2005.
- [36] K. H. Chung, H. Y. Chiou, and Y. H. Chen, "Psychological and physiological correlates of childhood obesity in Taiwan," *Scientific Reports*, vol. 5, Article ID 17439, 2015.
- [37] J. E. Park, S. S. Lee, M. S. Lee, S. M. Choi, and E. Ernst, "Adverse events of moxibustion: a systematic review," *Complementary Therapies in Medicine*, vol. 18, no. 5, pp. 215–223, 2010.
- [38] J. E. Park, J. U. Sul, K. Kang, B. C. Shin, K. E. Hong, and S. M. Choi, "The effectiveness of moxibustion for the treatment of functional constipation: a randomized, sham-controlled, patient blinded, pilot clinical trial," *BMC Complementary and Alternative Medicine*, vol. 11, p. 124, 2011.



OPEN ACCESS

**Edited by:**

Frank Martin,  
Juvenile Diabetes Research  
Foundation, United States

**Reviewed by:**

Julie Worrell,  
University of Glasgow,  
United Kingdom  
Florence Apparailly,  
INSERM U1183 Cellules Souches,  
Plasticité Cellulaire,  
Médecine Régénératrice Et  
Immunothérapies, France

**\*Correspondence:**

Chih-Hung Lin  
chlin@mail.cgu.edu.tw  
Jia-You Fang  
fajy@mail.cgu.edu.tw

**Specialty section:**

This article was submitted to  
Autoimmune and  
Autoinflammatory Disorders,  
a section of the journal  
Frontiers in Immunology

**Received:** 05 February 2021

**Accepted:** 30 April 2021

**Published:** 14 May 2021

**Citation:**

Chuang S-Y, Chen C-Y, Yang S-C,  
Alalaiwe A, Lin C-H and Fang J-Y  
(2021) 2,4-Dimethoxy-6-  
Methylbenzene-1,3-diol, a Benzenoid  
From *Antrodia cinnamomea*, Mitigates  
Psoriasisform Inflammation  
by Suppressing MAPK/  
NF- $\kappa$ B Phosphorylation and  
GDAP1L1/Drp1 Translocation.  
Front. Immunol. 12:664425.  
doi: 10.3389/fimmu.2021.664425

# 2,4-Dimethoxy-6-Methylbenzene-1,3-diol, a Benzenoid From *Antrodia cinnamomea*, Mitigates Psoriasisform Inflammation by Suppressing MAPK/NF- $\kappa$ B Phosphorylation and GDAP1L1/Drp1 Translocation

Shih-Yi Chuang<sup>1</sup>, Chi-Yuan Chen<sup>2,3,4</sup>, Shih-Chun Yang<sup>5</sup>, Ahmed Alalaiwe<sup>6</sup>,  
Chih-Hung Lin<sup>7\*</sup> and Jia-You Fang<sup>1,3,8\*</sup>

<sup>1</sup> Pharmaceuticals Laboratory, Graduate Institute of Natural Products, Chang Gung University, Taoyuan, Taiwan, <sup>2</sup> Graduate Institute of Health Industry Technology, Chang Gung University of Science and Technology, Taoyuan, Taiwan, <sup>3</sup> Research Center for Food and Cosmetic Safety and Research Center for Chinese Herbal Medicine, Chang Gung University of Science and Technology, Taoyuan, Taiwan, <sup>4</sup> Tissue Bank, Chang Gung Memorial Hospital, Taoyuan, Taiwan, <sup>5</sup> Department of Cosmetic Science, Providence University, Taichung, Taiwan, <sup>6</sup> Department of Pharmaceutics, College of Pharmacy, Prince Sattam Bin Abdulaziz University, Al Kharj, Saudi Arabia, <sup>7</sup> Center for General Education, Chang Gung University of Science and Technology, Taoyuan, Taiwan, <sup>8</sup> Department of Anesthesiology, Chang Gung Memorial Hospital, Taoyuan, Taiwan

*Antrodia cinnamomea* exhibits anti-inflammatory, antioxidant, and immunomodulatory activities. We aimed to explore the antipsoriatic potential of 2,4-dimethoxy-6-methylbenzene-1,3-diol (DMD) derived from *A. cinnamomea*. The macrophages activated by imiquimod (IMQ) were used as the cell model for examining the anti-inflammatory effect of DMD *in vitro*. A significantly high inhibition of IL-23 and IL-6 by DMD was observed in THP-1 macrophages and bone marrow-derived mouse macrophages. The conditioned medium of DMD-treated macrophages could reduce neutrophil migration and keratinocyte overproliferation. DMD could downregulate cytokine/chemokine by suppressing the phosphorylation of mitogen-activated protein kinases (MAPKs) and NF- $\kappa$ B. We also observed inhibition of GDAP1L1/Drp1 translocation from the cytoplasm to mitochondria by DMD intervention. Thus, mitochondrial fission could be a novel target for treating psoriatic inflammation. A psoriasisform mouse model treated by IMQ showed reduced scaling, erythema, and skin thickening after topical application of DMD. Compared to the IMQ stimulation only, the active compound decreased epidermal thickness by about 2-fold. DMD diminished the number of infiltrating macrophages and neutrophils and their related cytokine/chemokine



production in the lesional skin. Immunostaining of the IMQ-treated skin demonstrated the inhibition of GDAP1LI and phosphorylated Drp1 by DMD. The present study provides insight regarding the potential use of DMD as an effective treatment modality for psoriatic inflammation.

**Keywords:** *Antrodia cinnamomea*, 2,4-dimethoxy-6-methylbenzene-1,3-diol, psoriasis, macrophage, GDAP1L1, Drp1

## INTRODUCTION

Psoriasis is one of the most common autoimmune skin disorders. Patients with psoriasis are characterized by red and thick plaques covered with silver multilayered scales. IL-23/helper T cell type 17 (Th17) axis is recognized to have a key role in psoriasis (1). Typical histopathology of psoriatic lesions includes epidermal hyperplasia, elongated rete ridge, and immune cell infiltration. The estimated global prevalence of psoriasis is 2%–3% (2). Approximately 80% of the patients with psoriasis are classified as mild-to-moderate (3), for which topical drug treatment is feasible. However, the topical treatment is far from satisfactory due to the time-consuming therapeutic course, frustration with efficacy, and side effects (4). There is an urgent need to develop new antipsoriatic agents with improved therapeutic efficiency and safety. The development of antipsoriatic candidates from natural resources can potentially achieve the purposes of superior therapeutic effectiveness and fewer adverse effects (5). Nearly 39%–62% patient population in Asia and the Middle East use complementary and alternative medicine for treating psoriasis (6). And nearly 47% of the patients in South Europe use plant extracts as a remedy against psoriasis (7).

Many natural compounds derived from mushrooms are known to exhibit anti-inflammatory and immunomodulatory activities (8). The mushroom *Antrodia cinnamomea* is used as a medicinal herb because of its biological properties. *A. cinnamomea* is traditionally used to treat diarrhea, abdominal pain, hypertension, cancers, and itchy skin (9). The extracts and bioactive compounds from *A. cinnamomea* are reported to show biological effects such as anti-inflammatory, antioxidant, antitumor, antihyperlipidemic, and hepatoprotective activities (10). The ethanolic extract derived from *A. cinnamomea* inhibits Th17 cell infiltration in the dermis of the psoriasiform lesion and can thus be a therapeutic option for psoriasis (11). Previous investigations (12, 13) suggest the anti-inflammatory activity of some benzenoids isolated from *A. cinnamomea* on the activated T cells and macrophages. Likewise, we demonstrated in a previous study (14) that the benzenoid 2,4-dimethoxy-6-methylbenzene-1,3-diol (DMD) from *A. cinnamomea* exerts anti-inflammatory activity in atopic dermatitis-like skin in mice. In that study, we mainly explored the therapeutic potential of DMD on psoriasis treatment based upon the cell-based and *in vivo* animal studies.

Psoriasis is generally regarded as a T cell-mediated disease. Nevertheless, there is increasing evidence indicating that macrophages also play an essential role in psoriasis pathogenesis (15). Macrophages differentiate from monocytes in the blood, enter

the host tissue, and are influenced by the local environment. Macrophages are largely infiltrated in the dermal layer of psoriasis to release cytokines IL-23, IL-6, and TNF- $\alpha$  during the development of the lesion (16). We aimed to explore an effective strategy to treat psoriasis by regulating macrophage activation and to elucidate the possible mechanisms of DMD-mediated inhibition of inflammation using the macrophages (the differentiated THP-1 cells) as the cell model. Imiquimod (IMQ) is a Toll-like receptor (TLR)7 ligand which acts as an immune stimulator for macrophages (17). We used IMQ to activate macrophages and induce psoriasis-like plaque in mice for evaluating the anti-inflammatory effect of DMD in psoriasis treatment.

## MATERIALS AND METHODS

### Reagents and Antibodies

Menadione, tert-butylhydroquinone (TBHQ) and phorbol 12-myristate 13-acetate (PMA) were purchased from Sigma-Aldrich (St. Louis, MO, USA). IMQ cream (Aldara<sup>®</sup>, 5%) was acquired from 3M Pharmaceuticals (Leicestershire, UK). Phospho (p)-JNK, p-ERK, p-p38, p-p65, JNK, ERK, p38, CCR7, Drp1 and GAPDH antibodies were purchased from Santa Cruz Biotechnology (Santa Cruz, CA, USA). F4/80 and Ly6G antibodies were purchased from Abcam (Cambridge, MA, USA). The anti-Ly6G antibody was purchased from eBiosciences (San Diego, CA, USA). GDAP1L1 and mtHSP70 antibodies were purchased from Invitrogen (Carlsbad, CA, USA). The antibody targeting phospho-Drp1-S616 was obtained from Biorbyt (St. Louis, MO, USA).

### DMD From *A. cinnamomea*

DMD was obtained by partitioning and silica gel column chromatography. The detailed information of the extraction and isolation was described earlier (14). The chemical structure of DMD is illustrated in **Supplementary Figure 1**.

### Cell Lines, Primary Cells, and Cell Culture

Human monocytic leukemia THP-1 cell line was maintained in RPMI 1640 supplemented with 10% heat-inactivated FBS and 100 U/mL penicillin and streptomycin. Before the experiments, THP-1 cells were differentiated into macrophages by treating with phorbol 12-myristate 13-acetate (100 ng/mL) for 36 h, followed by overnight incubation in a fresh medium. Bone marrow was collected from the femur and tibia of BALB/c mice to generate bone marrow-derived macrophages (BMDMs) following an earlier published protocol (18). For

testing the effect of DMD on activated THP-1 and BMDMs, the cells were pretreated with DMD for 1 h and then incubated with IMQ (10  $\mu\text{g}/\text{mL}$ ) for 24 h. HaCaT cells, the immortalized cell line of human keratinocytes, were cultured in DMEMs supplemented with 10% FBS and 100 U/mL penicillin-streptomycin at 37°C. Human primary neutrophils were obtained from healthy, 20-30 years old volunteers using a protocol approved by the Institutional Review Board at Chang Gung Memorial Hospital (201701925B0). All volunteers provided written informed consent for participation. The neutrophils were purified by sedimentation prior to centrifugation and erythrocyte lysis following the protocol in a previous report (19).

### Cytotoxicity Assay

The cytotoxicity of DMD was studied by 3-(4,5-dimethylthiazol-2-yl)-2,5-diphenyltetrazolium bromide (MTT) analysis. The macrophages were cultured in DMEM at a density of  $2 \times 10^6$  cells/well and incubated at 37°C for 24 h. Then DMD (1–40  $\mu\text{g}/\text{mL}$ ) was added into the cell suspension and incubated for 24 h. The cells in a blank medium were used as the control. MTT (0.5 mg/mL) present in culture medium (200  $\mu\text{L}$ ) was incorporated in the cell suspension, which was further incubated at 37°C for 4 h. The THP-1 viability was detected by a spectrophotometer at 570 nm. The trypan blue assay was also used to evaluate the cell viability. After treating DMD for 24 h, the cells were removed and stained with 0.4% trypan blue. The number of unstained viable cells was counted in a hemocytometer under light microscope (Leica DMi8).

### Total RNA Extraction and Real-Time Quantitative Polymerase Chain Reaction (RT-qPCR)

Total cellular RNA was extracted using the Direct-zol kit with RNase-free DNase 1 digestion to remove genomic DNA contamination according to the manufacturer's instructions. Reverse transcription to cDNA was performed by iScript cDNA Synthesis kit. RT-qPCR was carried out by a CFX Connect RT PCR Detection System using iQ SYBR Green Supermix. The level of GAPDH was used to normalize the mRNA level. The primer sequences used for amplification from mouse and human species are listed in **Supplementary Table 1** and **Supplementary Table 2**, respectively.

### Enzyme-Linked Immunosorbent Assay (ELISA)

The level of cytokines and chemokines in the supernatant of the cell medium was quantified using ELISA kits (BioLegend) according to the manufacturer's instructions. The absorbance was measured at 450 nm on a microplate spectrophotometer. The concentration of cytokines and chemokines was estimated based on the corresponding standard curves.

### Immunoblotting

The level of mitogen-activated protein kinases (MAPKs), NF- $\kappa\text{B}$ , ganglioside-induced differentiation-associated protein 1 like 1 (GDAP1L1), dynamin-related protein 1 (Drp1), and Drp1 S616

were estimated by western blotting. The cells were collected and added to the lysis buffer. The nuclear pellets were obtained after centrifugation at  $400 \times g$  and 4°C for 5 min. After probe sonication, the protein fraction was obtained by centrifugation at  $8,000 \times g$  and 4°C for 10 min. For quantification, protein assay dye was mixed with the protein fraction, and separated by 10% acrylamide SDS-PAGE, and transferred to a polyvinylidene difluoride membrane. The membrane was incubated with the primary antibody (1:1000 dilution) at 4°C overnight. Subsequently, the membrane was washed using tris-buffered saline and incubated with horseradish peroxidase-conjugated secondary antibody (1:5000 dilution) for 1 h. The immunoreactive bands were detected by Western Lightning Plus-ECL. Anti-GAPDH or anti-actin antibody was used as the loading control.

### Wound Healing Assay

Fresh neutrophils ( $4 \times 10^5$  cells/well) were seeded in a six-well plate and cultured in the complete DMEM medium. The cells were scraped using a 200  $\mu\text{L}$  pipette tip to achieve a noncellular region, and the culture medium was then replaced by the conditioned medium of THP-1 cells after IMQ stimulation with or without DMD intervention (10  $\mu\text{g}/\text{mL}$ ). After 4 h, the migration number of the neutrophils was measured by using ImageJ software.

### Chemotaxis Assay

The neutrophil migration initiated by the conditioned medium of THP-1 cells was evaluated by the Boyden chamber migration analysis. Briefly, the isolated human neutrophils were added to DMEM supplemented with 0.25% BSA. The neutrophils ( $4 \times 10^5$  cells/well) were added to the upper well of the Boyden chamber. The conditioned medium harvested from macrophages was added into the lower well. The plate was stored at 37°C for 4 h before placing it on ice, and 100  $\mu\text{L}$  of 0.5 M EDTA was incorporated into the well at 4°C for 10 min. The well insert was removed and the cell suspension was collected. Then neutrophil count was estimated using a Moxi Z Mini-Automated Cell Counter kit.

### Isolation of Cytosolic and Mitochondrial Fractions

GDAP1L1 and Drp1 levels in cytosol and mitochondria of macrophages were determined by western blotting. The separation of mitochondria from cytoplasm was performed as described previously (18). In brief, the macrophages were collected, then the Mitochondria Isolation kit was used to separate the cellular components according to the manufacturer's instructions. Cytoplasmic and mitochondrial proteins were quantified by western blotting using the same method described in the section of immunoblotting. The p38 and mitochondrial HSP70 (mtHSP70) were employed as the loading control for cytosolic and mitochondrial fractions, respectively.

### Immunofluorescence Staining

To appraise the expression of GDAP1L1 and Drp1 S616 in THP-1 cells, immunofluorescence staining was carried out. The

cells were cultured on coverslips and then labeled with MitoTracker Red for staining mitochondria. The macrophages were fixed with 4% paraformaldehyde for 15 min at room temperature. The fixed macrophages were permeabilized with Triton X-100 for 5 min and then blocked with 1% BSA for 30 min. For immunofluorescence staining, primary antibodies against GDAP1L1 or Drp1 S616 were used followed by the incubation of secondary antibody conjugated with Alexa Fluor 488 or 594. The cells were monitored under a confocal microscope (Zeiss LSM780). Quantification and measurement of mitochondrial length was performed with MetaMorph (Molecular Devices) by an investigator blinded to experimental groups. Mitochondrial length was classified into three categories;  $<0.5\ \mu\text{m}$ ,  $0.5\text{--}2\ \mu\text{m}$ , and  $>2\ \mu\text{m}$ . The resulting data were visualized using GraphPad Prism software.

### Immunoprecipitation

Total mitochondrial fraction extract (100  $\mu\text{g}$ ) was incubated with GDAP1L1 antibody overnight at  $4^{\circ}\text{C}$ . Protein A beads were added to the mixtures and incubated for 1 h at  $4^{\circ}\text{C}$ . After five washings with lysis buffer, the immunoprecipitants were subjected to SDS/PAGE and analyzed by immunoblotting as indicated antibodies.

### Animals

Female BALB/c mice (8-weeks old) were purchased from the National Laboratory Animal Center (Taipei, Taiwan). All animal experiments were approved by the Institutional Animal Care and Use Committee of Chang Gung University and complied with Directive 86/109/EEC from the European Commission (CGU108-101).

### IMQ-Induced Psoriasiform Skin in Mice

A psoriasis-like lesion was evoked on the back of the BALB/c mouse following a protocol from van der Fits et al., with modifications (20). The mouse received a daily topical dose of 62.5 mg 5% IMQ cream (Aldara, 3M) on the shaved area of the dorsal skin for five consecutive days. Before 30 min of IMQ cream treatment, 100  $\mu\text{L}$  DMD (1 mg/mL) in PEG400/PBS (3:7) was topically administered on the back. The vehicle was dried during this 30-min period. The skin surface appearance was visualized using a portable digital magnifier (Mini Scope-V, M&T Optics). The subjective evaluation of the severity was estimated by the cumulative score (scaling plus erythema) with a scale from 0 to 8 based on the Psoriasis Area and Severity Index (PASI). Transepidermal water loss (TEWL) was detected by a Tewameter TM300 (Courage and Khazaka). The animals were sacrificed on day 6 for further histological examination and detection of cytokine/chemokine expression. The skin was extracted following a previously described method (21). The skin extract was used to determine proinflammatory mediators by RT-qPCR. The protocol for RT-qPCR was the same as that mentioned in the section for the *in vitro* THP-1 study.

### Histology

The skin sample was fixed in 10% formaldehyde and embedded in paraffin and then stained with hematoxylin and eosin (H&E).

The unstained slice of skin sample was prepared for immunohistochemistry (IHC). After dewaxing and rehydration, the skin section was subjected to heat-induced epitope retrieval using the Bond Epitope Retrieval Solution 2 according to the manufacturer's instructions, followed by the blocking with diluted normal serum. The section was incubated with rabbit polyclonal anti-mouse Ki67, Ly6G, F4/80, GDAP1L1, or Drp1 S616 antibody (1:100 dilution) for 1 h at room temperature, washed with 0.5% Tween 20 in saline, and subsequently incubated with biotinylated donkey anti-rabbit IgG at ambient temperature for 20 min. The photomicrographs were observed under an optical microscope (Leica DMI8). Quantification of the IHC-stained sections was performed by AlphaView software. Each section was examined independently by two investigators in a blinded manner. Numbers of positive cells were evaluated by counting the numbers of cells (original manifestation  $\times 200$ ) for three sections of three mice per group.

### Statistical Analysis

The statistical differences in the data of different treatment groups were measured using the one-way analysis of variance followed by Tukey's multiple comparison test. The data distribution was checked by Kolmogorov-Smirnov test. The levels of probability including 0.05, 0.01, and 0.001 were considered statistically significant.

## RESULTS

### DMD Inhibits Cytokine/Chemokine Expression in Activated Macrophages

IMQ was used as the activator to evoke the macrophage stimulation in this study. We tested the effect of IMQ on THP-1 viability to determine its cytotoxicity to the macrophages. Although slight cytotoxicity determined by MTT assay was found after IMQ treatment, the viability could still surpass 80% for the activator concentrations between 1 and 20  $\mu\text{g/mL}$  (the left panel of **Figure 1A**). In addition to the evaluation of cell viability, MTT assay is a method to assess cell metabolic activity. The MTT assay is dependent on the mitochondrial respiration. The slight reduction of MTT by IMQ may suggest the involvement of IMQ in the metabolic activity of THP-1 cells. No cell viability reduction by IMQ was detected using trypan blue analysis (the right panel of **Figure 1A**), demonstrating a minimal cytotoxicity of IMQ. Then, an IMQ dose of 10  $\mu\text{g/mL}$  was used in the subsequent experiments. Up to a concentration of 20  $\mu\text{g/mL}$ , DMD had no effect on the viability for both MTT and trypan blue analyses (**Figure 1B**), while following the treatment with 40  $\mu\text{g/mL}$  DMD the viability percentage was 94% in the MTT assay. The non-cytotoxic dose of 10  $\mu\text{g/mL}$  DMD was selected to investigate the anti-inflammatory effect on macrophages.

To further elucidate the role of DMD on the cytokine expression, RT-qPCR analysis was carried out for the five genes

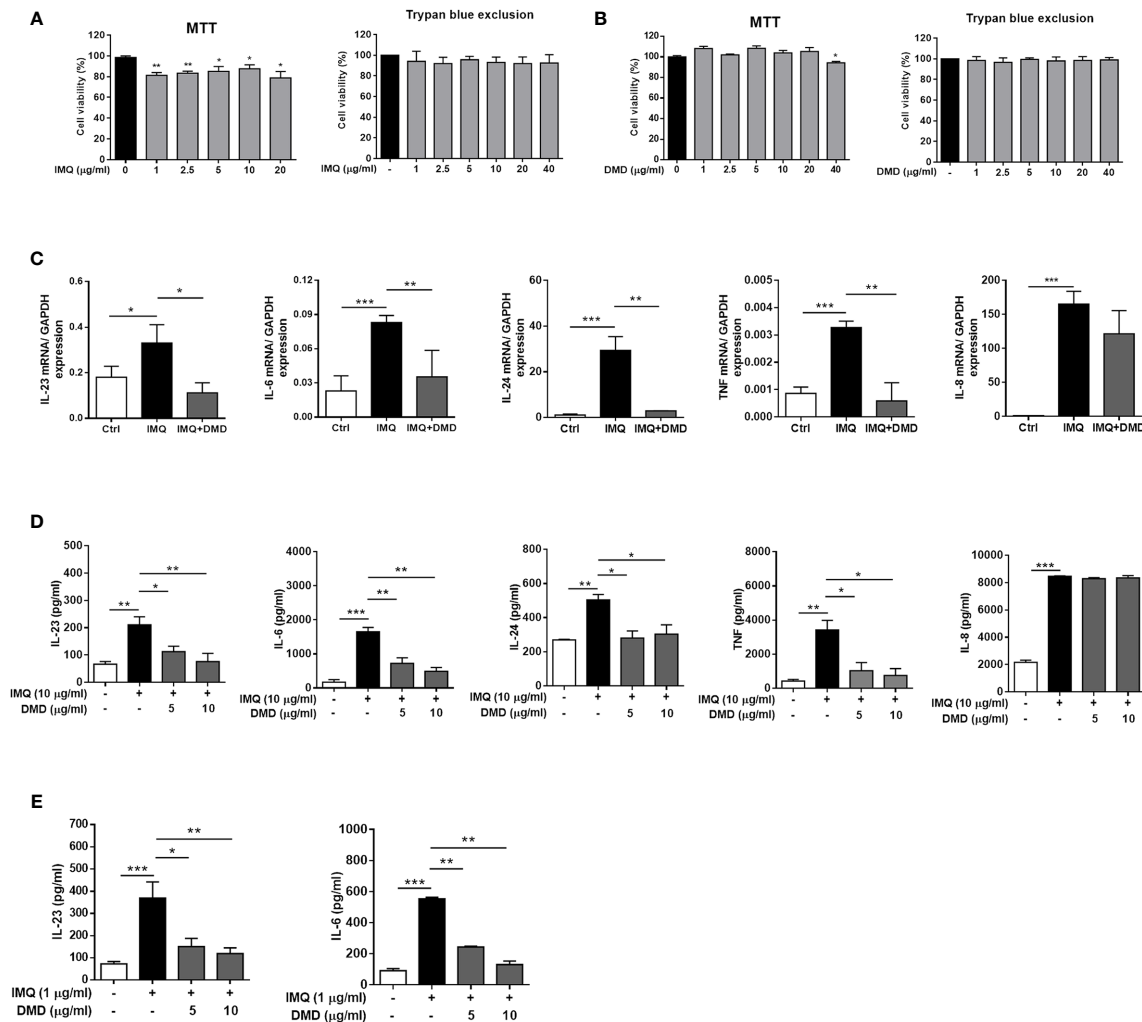


**FIGURE 1 |** DMD inhibit IMQ-induced inflammatory cytokines in THP-1 and BMDMs. **(A, B)** Cell viability in THP-1 cells determined by MTT and trypan blue assays after incubation with IMQ and DMD in the indicated concentration, respectively, for 24 h ( $n=3$ ). **(C)** RT-qPCR analysis of the cytokines in IMQ-stimulated THP-1 cells following DMD treatment ( $n=3$ ). **(D)** ELISA analysis of the cytokines in IMQ-stimulated THP-1 cells following DMD treatment ( $n=3$ ). **(E)** ELISA analysis of the cytokines in IMQ-stimulated BMDMs following DMD treatment ( $n=3$ ). The data shown are representative of three independent experiments. GAPDH is served as an internal control. \* $P < 0.05$ , \*\* $P < 0.01$ , and \*\*\* $P < 0.001$  when compared to IMQ group. Data are represented as mean  $\pm$  SEM.

of IL-23, IL-6, IL-24, TNF, and IL-8. IMQ was able to increase the expression of these inflammatory factors with a statistical significance (**Figure 1C**). The mRNA detection verified a decrease in cytokine level after DMD versus IMQ stimulation. At 10  $\mu\text{g/mL}$ , DMD totally inhibited IL-23, IL-6, IL-24, and TNF to the baseline control. The expression of the cytokines in macrophages was further confirmed by ELISA. The protein and mRNA expression showed a consistent trend (**Figure 1D**). BMDMs, the primary macrophages derived from the mouse, were used as another macrophage model for treating the effect of DMD on inflammation attenuation. Similar to THP-1 cells, IMQ induced some cytotoxicity against BMDMs (**Supplementary Figure 2**). DMD produced a limited cytotoxicity on BMDMs. The viability of BMDMs could be maintained to 75% after DMD

treatment at the highest concentration (40  $\mu\text{g/mL}$ ). *In vitro*, BMDMs also expressed IL-23 and IL-6 at high levels after IMQ stimulation (**Figure 1E**), and this upregulation could be reduced in the DMD-treated groups. To understand the capacity of chemokines, we analyzed mRNA expression of nine chemokines in IMQ-activated macrophages and observed a high level of CCR7, CCL1, CCL2, CCL4L2, CCL20, CCL22, CXCL3, CXCL6, and CXCR5 in stimulated THP-1 (**Figure 2A**), and this could be abolished by DMD treatment. This result suggests the involvement of DMD in the regulation of macrophage chemotaxis. We also observed upregulated GDAP1L1 mRNA by IMQ and a 70-fold decrease to that of the baseline after DMD treatment (**Figure 2B**). GDAP1L1 is a paralog of GDAP1 and predominantly governs mitochondrial dynamics.



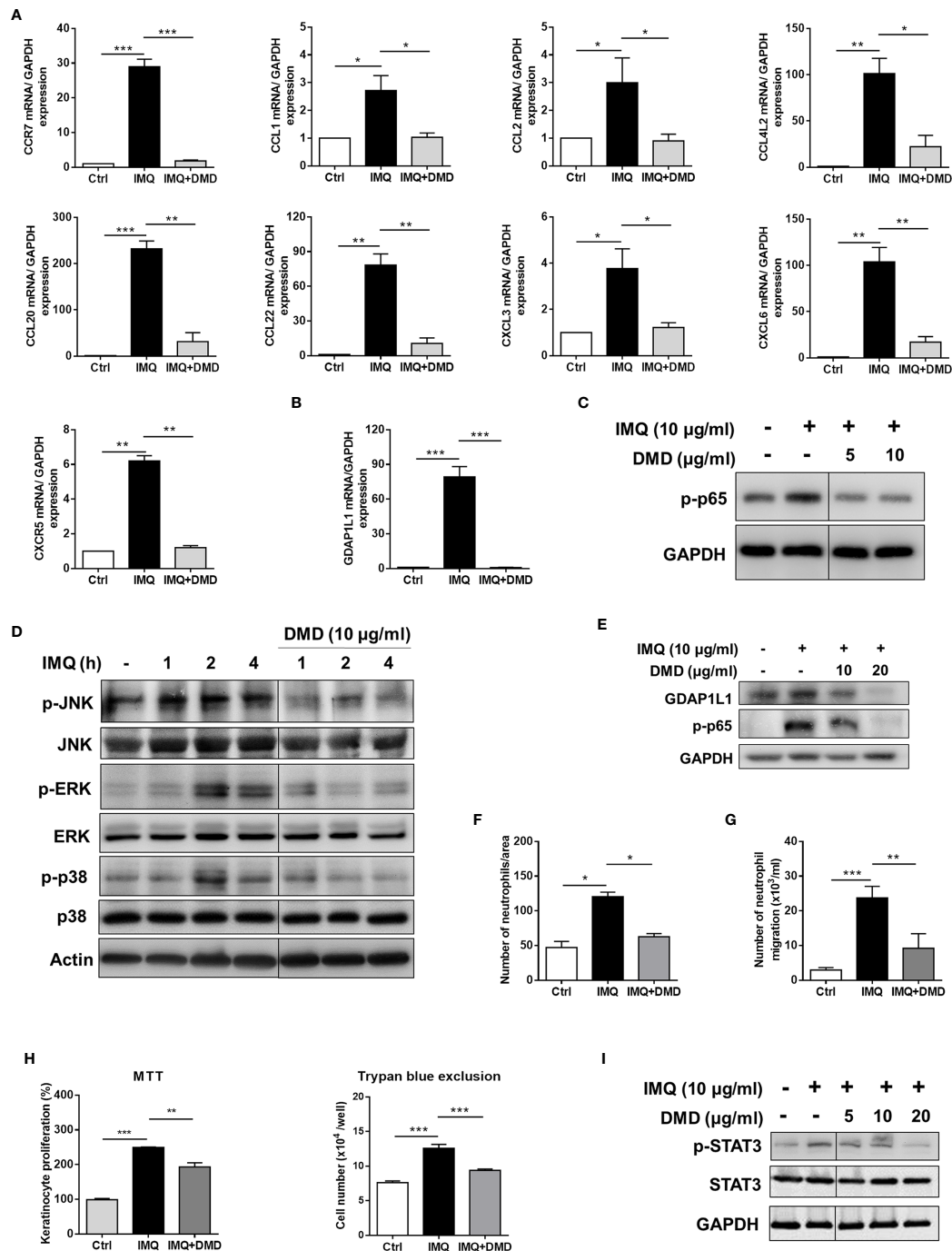


**FIGURE 2 |** DMD inhibit IMQ-induced activation in THP-1 cells through MAPK and NF- $\kappa$ B pathways, and block neutrophil invasion and keratinocyte proliferation. **(A)** RT-qPCR analysis of the chemokines in IMQ-stimulated THP-1 cells following DMD treatment ( $n=4$ ). **(B)** RT-qPCR analysis of GAPDH in IMQ-stimulated THP-1 cells following DMD treatment ( $n=4$ ). **(C-E)** THP-1 cells were treated with IMQ in the presence or absence of DMD. Immunoblotting analysis of phosphorylation of NF- $\kappa$ B, MAPKs, and GAPDH was determined, respectively. **(F)** Neutrophil migration was measured by wound healing assay. Neutrophils were treated with the conditioned medium of THP-1 cells for 24 h to determine the rate of migration into the scratched area. Wound healing was quantified by measuring the distance between scratch edges at 0 and 24 h. **(G)** Neutrophil invasion was measured by the Boyden chamber invasion assay. Neutrophils were loaded on the top chambers. The cells were allowed to invade for 4 h, and the rate of invasion was quantified ( $n=4$ ). **(H)** Keratinocyte proliferation induced by the conditioned medium of THP-1 cells was measured using the MTT and trypan blue assays ( $n=3$ ). **(I)** Immunoblotting of the phosphorylation of STAT3 in keratinocytes stimulated with the conditioned medium of THP-1 cells for 24 h. One out of three independent experiments is shown. \* $P < 0.05$ , \*\* $P < 0.01$ , and \*\*\* $P < 0.001$  when compared to IMQ group. Data are represented as mean  $\pm$  SEM.



## DMD Inhibits Cytokine/Chemokine Expression by Blocking the MAPK/NF- $\kappa$ B Signaling

To elucidate the signaling pathways through which DMD attenuated the inflammation, we checked the possible role of NF- $\kappa$ B. Western blot analysis displayed that IMQ upregulated the expression of p-p65 that was a subunit of p-NF- $\kappa$ B (Figure 2C), while a significantly opposite effect was observed after DMD treatment in macrophages. DMD inhibited the phosphorylation of p65 by 2-fold as measured by densitometry (Supplementary Figure 3A). To examine the possible role of MAPKs in the inflammation suppression by DMD, we studied the IMQ-induced phosphorylation of JNK, ERK, and p38 in macrophages. The maximum expression of the phosphorylated MAPKs was detected at 2 h after IMQ stimulation (Figure 2D and Supplementary Figure 3B), while DMD could reverse the phosphorylation, clearly indicating the anti-inflammatory activity of DMD through the downregulation of MAPKs and NF- $\kappa$ B. GDAP1L1 is an important marker that showed a significant decrease after DMD treatment of activated THP-1 macrophages. Immunoblotting revealed that GDAP1L1 protein level increased after IMQ and arrested by DMD treatments in a dose-dependent manner (Figure 2E and Supplementary Figure 3C).

## The Conditioned Medium of DMD-Treated Macrophages Prevents Neutrophil Migration and Keratinocyte Proliferation

In psoriasis, macrophage chemotaxis may mediate the interplay between the macrophages and the other cells. To gain an in-depth understanding of the chemotaxis, we validated the effect of IMQ-activated macrophage conditioned medium on neutrophil invasion and keratinocyte proliferation. The wound-healing assay showed that DMD-treated macrophage medium suppressed wound closure in neutrophils (Figure 2F). Moreover, the DMD-treated group had lowered the average number of migrating neutrophils permeating the transwell membrane (Figure 2G). The conditioned medium from IMQ-stimulated macrophages promoted keratinocyte proliferation by about 2-fold as measured by both MTT and trypan blue assays (Figure 2H). This effect was inhibited by DMD at 10  $\mu$ g/mL. The keratinocyte proliferation in psoriasis is in close association with the signal transducer and activator of transcription 3 (STAT3) pathway. The IMQ-treated conditioned medium enhanced STAT3 activation in keratinocytes, which was observed in the form of increased p-STAT3 (Figure 2I and Supplementary Figure 3D), which was considerably reduced upon the intervention of DMD. Our data demonstrated that DMD was effective in suppressing neutrophil and keratinocyte activation *via* the inhibition of macrophage chemotaxis.

## GDAP1L1/Drp1 Axis Participates in DMD-Induced Inhibition on Macrophage Activation

According to the cell-based study, we found a possible role of GDAP1L1 in the inhibition of activated macrophage by DMD.

GDAP1L1 is a mitochondrial fission factor. Mitochondrial fission and fusion are required for maintaining mitochondrial functions related to biogenesis, apoptosis, neurodegeneration, and inflammation. Following IMQ stimulation, the GDAP1L1 level was significantly increased at the indicated times as verified by densitometry (Figure 3A and Supplementary Figure 4). DMD treatment at 10  $\mu$ g/mL blocked IMQ-stimulated GDAP1L1 expression. The activity of GDAP1L1 to induce mitochondrial fission depends upon another fission factor Drp1. The fission needs the phosphorylated Drp1 at the S616 site and translocation of Drp1 from the cytoplasm to mitochondria. We found an increase in IMQ-mediated Drp1 phosphorylation in THP-1 (Figure 3A), and this elevation could be reduced by DMD. GDAP1L1 is a cytosolic protein that is also delivered to the mitochondria in response to external stimuli. We found the association between GDAP1L1 and mitochondria after IMQ treatment (Supplementary Figure 5), which increased following the increase in treatment duration. To appraise whether DMD affected GDAP1L1 and Drp1 location, cytosol and mitochondria were isolated from IMQ-treated macrophages and more GDAP1L1 was expressed in the mitochondria after IMQ stimulation (Figure 3B). We found a minimal expression of the cytosolic specific marker p38 in the mitochondrial fraction. Menadione is a quinone-related derivative used as a positive control in oxidative stress-induction studies. Mitochondrial translocation of GDAP1L1 was found after menadione treatment. DMD not only reduced GDAP1L1 production but also decreased IMQ- and menadione-induced GDAP1L1 translocation. Menadione is conjugated to form menadione-S-glutathione by glutathione S-transferase to induce stress. Glutathione conjugation detoxifies tertiary butylhydroquinone (TBHQ). TBHQ could reduce the GDAP1L1 transfer to mitochondria sensitized by menadione. IMQ and menadione also strongly increased the expression of Drp1 in mitochondria without a significant change of total Drp1. DMD treatment abolished the elevated GDAP1L1 in mitochondria. However, this phenomenon was not detected in the case of menadione-treated cells intervened by TBHQ.

We then examined the phosphorylated Drp1 at S616 in mitochondria. The level of mitochondrial Drp1 and Drp1 S616 increased in THP-1 stimulated with IMQ and menadione (Figure 3C) and this increase in the active form of Drp1 in mitochondria was blocked by DMD, as was confirmed by immunofluorescence analysis (the left panel of Figure 3D). Colocalization of Drp1 S616 with mitochondria was observed using double immunofluorescence staining. The estimation of mitochondrial length showed a decreased average length after IMQ intervention (the upper right panel of Figure 3D), suggesting a fission of mitochondria after an inflammation stimulation. DMD treatment could reverse this reduction to the control baseline level. We also found an increased proportion of mitochondria with short length (<0.5  $\mu$ m) by IMQ stimulation (the lower right panel of Figure 3D). Again, this increase could be reversed to baseline control by DMD. Based on the above-mentioned results, we speculated that Drp1 might complex with GDAP1L1. We employed

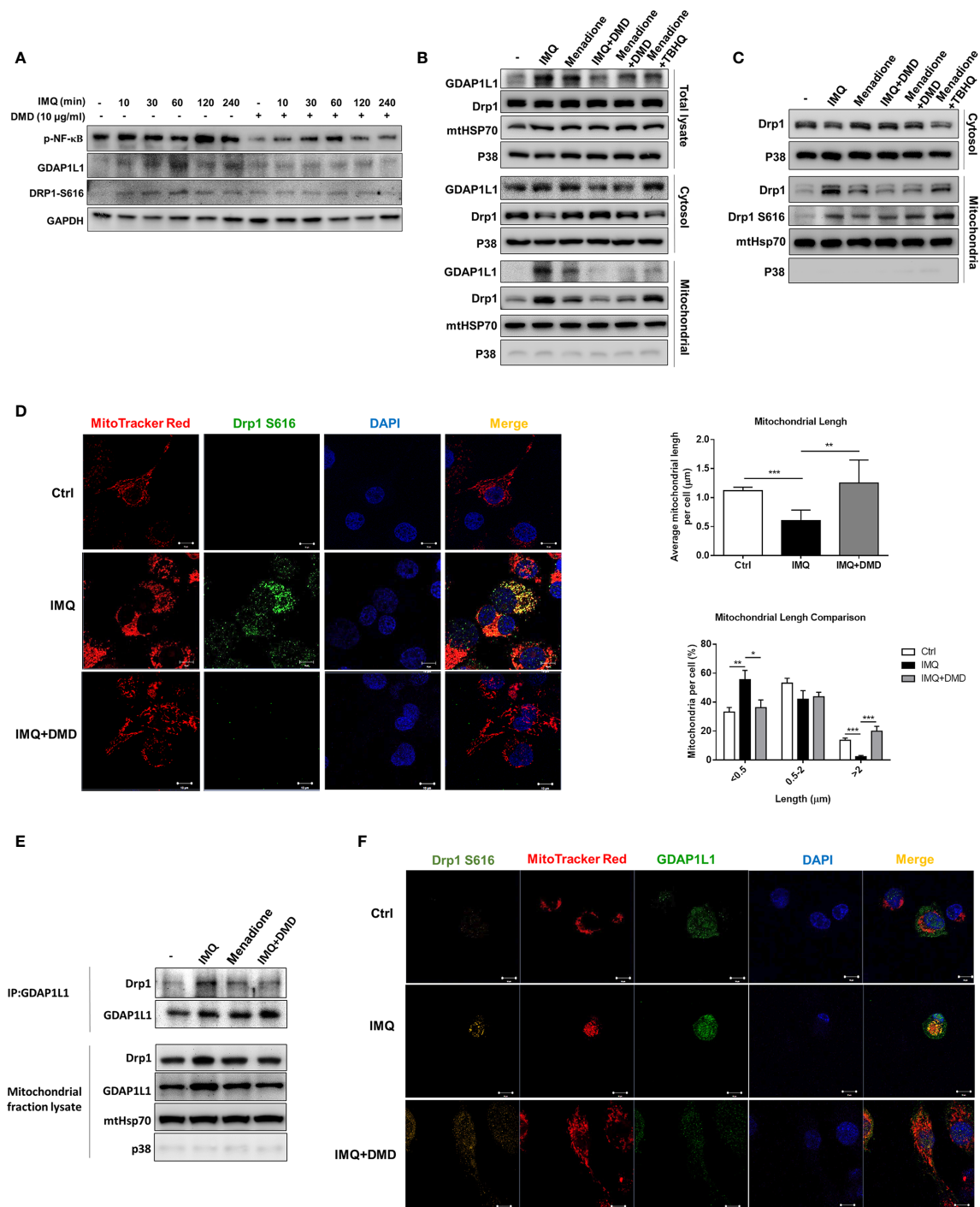


**FIGURE 3 |** DMD inhibit IMQ-induced activation in THP-1 cells through decreasing Drp1 phosphorylation and GDAP1L1/Drp1 translocation. **(A)** Immunoblotting of GDAP1L1 and Drp1 S616 in IMQ-stimulated THP-1 cells following DMD treatment. **(B)** THP-1 cells were pretreated by DMD or TBHQ and then stimulated with IMQ or menadione for 2 h. Cells were fractionated into cytosolic and mitochondrial fractions and subjected to immunoblotting assay to determine GDAP1L1 and Drp1. **(C)** THP-1 cells were pretreated by DMD or TBHQ and then stimulated with IMQ or menadione for 2 h. Cells were fractionated into cytosolic and mitochondrial fractions and subjected to immunoblotting assay to determine Drp1 and its phosphorylated form (Drp1 S616). **(D)** THP-1 cells were stimulated with IMQ for 2 h, and then stained with MitoTracker Red. Cells were fixed and immunostained with the antibody against Drp1 S616 followed by confocal microscopy. Average mitochondrial length (μm) and comparison of mitochondrial length distribution in the indicated groups is shown in the right panel. **(E)** Immunoprecipitation of GDAP1L1 and Drp1 in mitochondria of THP-1 cells as shown in the immunoblotting. **(F)** THP-1 cells were stimulated with IMQ for 2 h, and then stained with MitoTracker Red. Cells were fixed and immunostained with the antibody against GDAP1L1 or Drp1 S616 followed by confocal microscopy. Scale bars, 10 μm. All experiments were repeated two or three times with similar results.

immunoprecipitation to check if GDAP1L1 and Drp1 were associated to interact with each other. The GDAP1L1 antibody could successfully pull down both GDAP1L1 and Drp1 (**Figure 3E**). GDAP1L1 indeed coprecipitated with Drp1 when transiently expressed in THP-1 cells. Both Drp1 S616 and GDAP1L1 expression was upregulated in mitochondria after IMQ stimulation, as shown by the immunofluorescence image (**Figure 3F**). An appreciable overlap was observed between both fission factors and mitochondria. GDAP1L1 possibly colocalized with phosphorylated Drp1 in mitochondria. We verified that the DMD-induced inflammation suppression was mediated by regulating GDAP1L1/Drp1 translocation to mitochondria.

## DMD Alleviates Psoriasiform Lesion in IMQ-Induced Mouse Model

IMQ was topically applied on mouse skin to generate psoriasis-like plaque for evaluating the anti-inflammatory activity of DMD. The pure compound from *A. cinnamomea* was topically administered on the skin of the back treated with IMQ cream for five consecutive days (**Figure 4A**). Compared to the healthy skin, scaling, erythema, and thickening in the IMQ-treated skin were observed in the macroscopic and microscopic visualization of the skin surface (**Figure 4B**). These symptoms suggest a typical psoriasis feature. DMD-treated groups displayed the clearance of these signs compared to the only IMQ-treated group. The cumulative score estimated by scaling and redness was

significantly reduced by DMD as compared to the only IMQ treatment group (**Figure 4C**). TEWL, as an indicator of cutaneous barrier property, exhibited a 4-fold increase after IMQ stimulation (**Figure 4D**). No improvement of skin barrier dysfunction was detected after DMD intervention. The epidermal thickness increased by about 3-fold by IMQ activation as compared to normal skin (**Figure 4E**). This histological sign was relieved by DMD. The epidermal thickness of IMQ-treated skin was reduced from 77 to 50  $\mu\text{m}$  after DMD treatment. The Munro's microabscess in IMQ-stimulated lesion was reduced by 6.8-fold after treatment of DMD (**Figure 4F**).

*In vivo* efficacy of DMD on psoriasiform lesions was qualitatively monitored using histology. Representative H&E staining from healthy skin revealed normal morphology with no damage to the epidermis and dermis (**Figure 5A**). H&E-stained IMQ-treated skin showed typical histological hallmarks of psoriasis, including acanthosis, hyperkeratosis, elongated rete ridge, and immune cell infiltration. IHC staining for Ki67, a proliferation biomarker revealed a remarkable increase of Ki67 in the basal layer after IMQ treatment (red arrows in **Figure 5B**). The higher power magnification of the histology is revealed in the upper left corner of each image. DMD effectively suppressed epidermal hyperproliferation in mice. The neutrophil infiltration in the stratum corneum and dermis could be visualized by Ly6G staining (red arrows in **Figure 5C**). The IHC showed clouds of

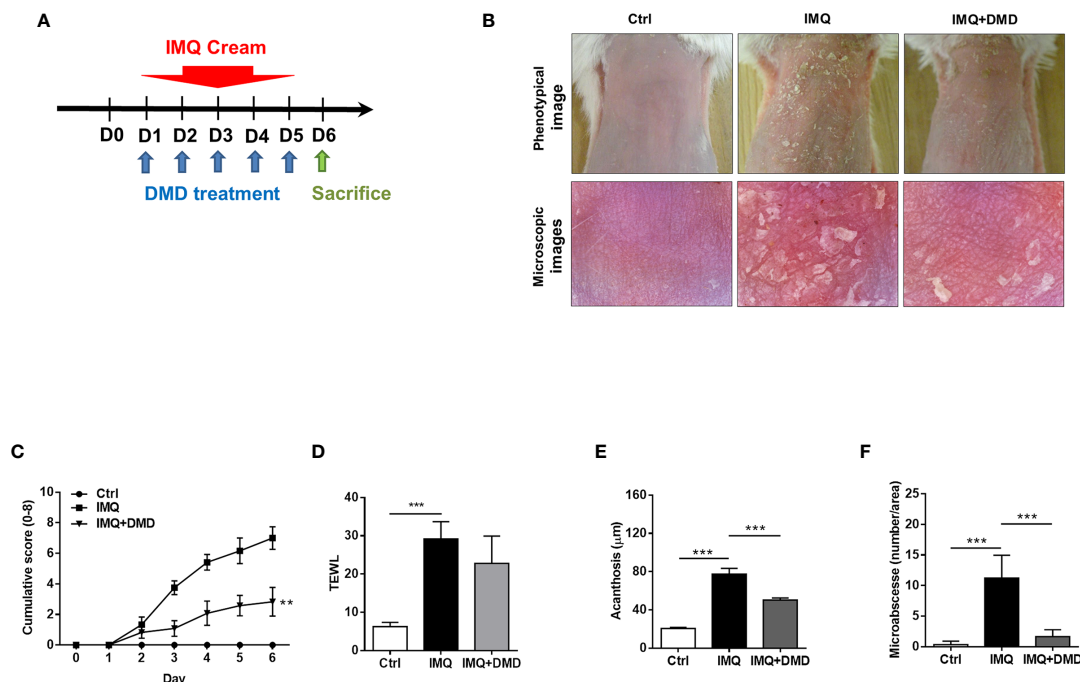


**FIGURE 4 |** DMD attenuate IMQ-induced psoriasis-like inflammation in a mouse model. **(A)** Scheme of the experimental protocol for AC or DMD treatment in IMQ-induced psoriasis-like inflammation model in mice. **(B)** Phenotypic and microscopic images of IMQ-induced psoriasis-like inflammation on mouse skin with and without the treatment by AC or DMD after 5 days. **(C)** The cumulative score (scaling plus erythema from 0 to 4 each) is depicted. **(D)** TEWL was measured on Day 6. **(E)** Epidermal thicknesses measured according to H&E-stained histology. **(F)** Munro's microabscesses measured using an image analysis system. All experiments were performed at least three times. \*\* $P < 0.01$  and \*\*\* $P < 0.001$  when compared to IMQ group. Scale bar, 100  $\mu\text{m}$ . Data are represented as mean  $\pm$  SEM. ( $n=6$ ).



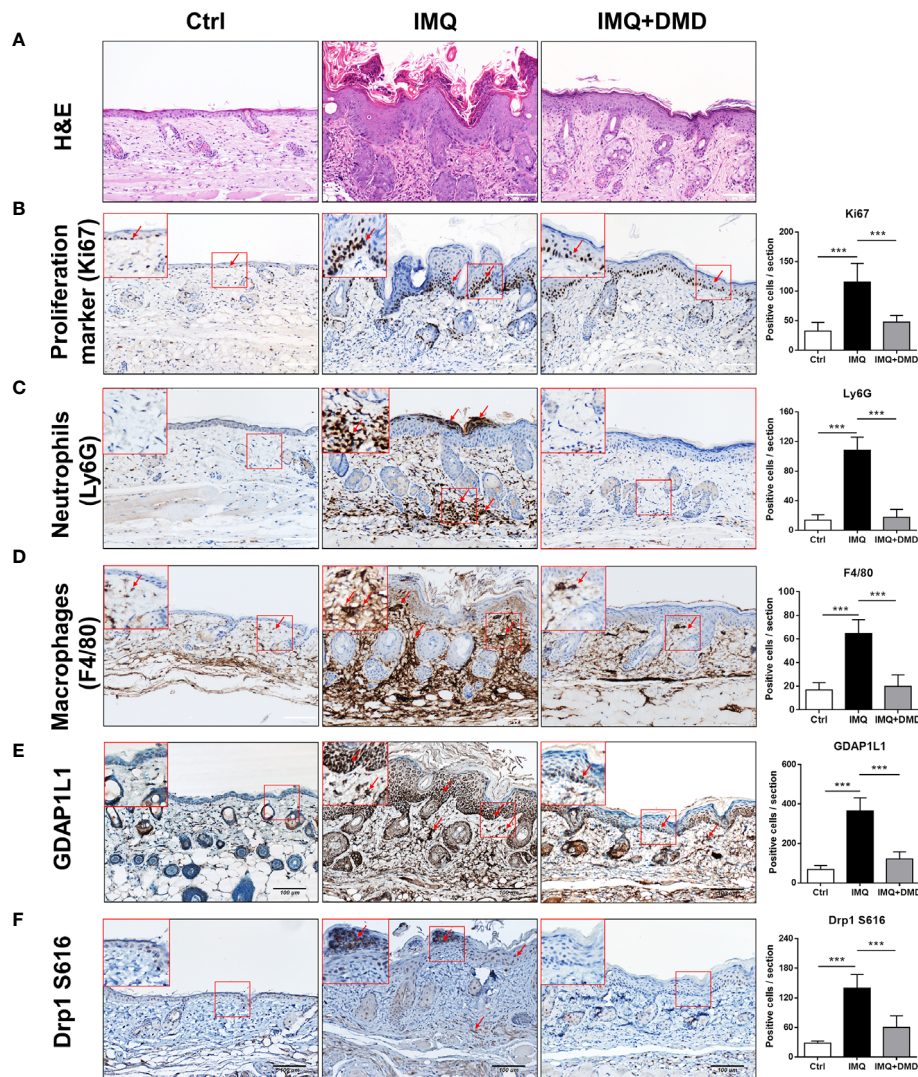


**FIGURE 5** | DMD attenuate IMQ-induced psoriasis-like inflammation in a mouse model as observed by skin histology. **(A)** Histological assessment of the skin by H&E staining. **(B)** Histological assessment of the skin by Ki67 staining. **(C)** Histological assessment of the skin by Ly6G staining. **(D)** Histological assessment of the skin by F4/80 staining. **(E)** Histological assessment of the skin by GDAP1L1 staining. **(F)** Histological assessment of the skin by Drp1 S616 staining. The upper left corner of each image indicates the higher power magnification of the red frame. The red arrow indicates the location of the antibody-stained cells. The quantification of the antibody-positive cells is shown in the right panel of each figure. \*\*\* $P < 0.001$  when compared to IMQ group. Data are represented as mean  $\pm$  SEM. ( $n=9$ ).

Ly6G expression in the dermis after the IMQ challenge. In addition, DMD inhibited infiltrating neutrophils to a certain level. To detect macrophages, the skin was immunostained with F4/80 and its expression was observed in epidermal and dermal layers in IMQ-treated mouse (red arrows in **Figure 5D**), suggesting that macrophages were recruited to the lesional plaque. DMD could mitigate the macrophage infiltration. Strong immunoreactivity for GDAP1L1 and Drp1 S616 was observed in the psoriasiform lesion (red arrows in **Figures 5E, F**). Like the macrophage distribution, GDAP1L1 mainly expressed throughout the viable epidermis and dermis. Expression of both fission factors decreased after and DMD-treatment of the skin compared to IMQ stimulation alone. All quantification of the antibody-positive cell count was

estimated by AlphaView software and depicted in the right panel of **Figure 5**. A statistically significant reduction of antibody-positive cell count was observed after topical administration of DMD on IMQ-treated mouse skin.

The mRNA level of the inflammation-related cytokines and chemokines including IL-23, IL-6, IL-17A, IL-24, TNF, and CXCL2 in mouse skin was determined through RT-qPCR and a dramatic increase in proinflammatory mediator expression was observed after the IMQ challenge (**Figures 6A–F**). The cytokines/chemokines in psoriasiform skin could be restrained to baseline control by DMD. These data clearly demonstrate the ability of DMD to reduce inflammation caused by IMQ. F4/80 mRNA level was significantly increased in IMQ-activated mouse skin and decreased after DMD application (**Figure 6G**).

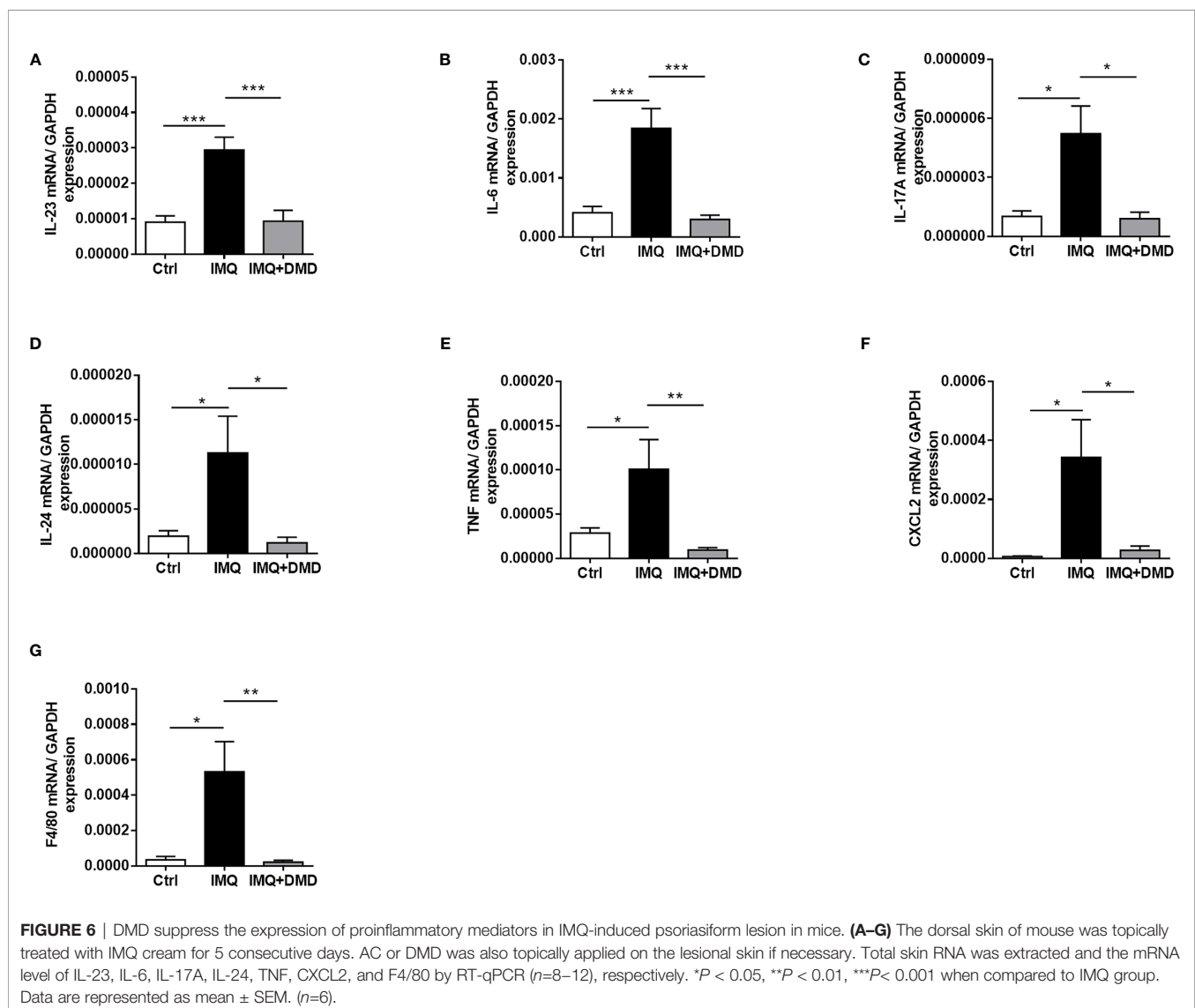
Collectively, the *in vivo* data prove the anti-inflammatory potential of DMD on the psoriasis-like lesions, especially on macrophages and IL-23/Th17 signaling.

## DISCUSSION

Macrophages are thought to have a vital role in the induction of inflammation and autoimmune skin diseases such as psoriasis (1, 16). Therefore, we employed macrophages as the main cell model for evaluating the effect of DMD on the attenuation of psoriasis. The cutaneous macrophages in psoriatic plaque can release cytokines IL-6, TNF, and IL-1 $\beta$  for developing inflammation (22). Cytokines influence cell proliferation in psoriasis (23). Multiple cytokine-signaling including IL-23, IL-6, IL-24, and TNF is known to be important in psoriatic pathogenesis (24). The TLR stimulated by IMQ can initiate macrophage activation to express proinflammatory cytokines (25). Among these

cytokines, IL-23 plays a preliminary role in macrophages to initiate psoriasis development (26). IL-23 is important for inducing IL-6-dependent epidermal hyperplasia and cytokine production in psoriasis. DMD could restrain the upregulation of IL-23 in the activated macrophages in the early stage, followed by the inhibition of IL-6 expression. In the psoriatic skin, one of the major sources of TNF is macrophage (4, 16). Upregulation of TNF was also largely inhibited by DMD. Psoriasis development can be triggered by TNF receptor 1-dependent upregulation of IL-24 (27). IL-24 is a member of the IL-20 family induced by IL-6, TNF, and IL-1 $\beta$  in psoriasis. Macrophages and T lymphocytes are the primary cells expressing IL-24 (28). Here, we confirmed the repression of IL-24 by DMD.

The cytokines including IL-24 and TNF- $\alpha$  mediate the crosstalk between immune cells and keratinocytes. The release of these cytokines stimulates keratinocyte proliferation and amplifies the inflammation in the psoriatic lesions (29). Macrophages accumulate in the psoriatic lesions and release





cytokines to prompt the excessive proliferation of keratinocytes (30). We found that the conditioned medium of DMD-treated THP-1 could successfully inhibit keratinocyte proliferation and p-STAT3 expression. Hyperproliferation of keratinocytes in psoriasis correlates with the STAT3 pathway (31). STAT3 activation in keratinocytes is regarded as the main effector producing cytokines, which in turn leads to the positive feedback loop of psoriasis. DMD not only suppressed macrophage activation but also restrained the following interplay between macrophages and keratinocytes to restrict inflammation.

Another key factor generating the crosstalk between immune cells and keratinocytes is chemotaxis. Immune cell recruitment in psoriatic lesions depends on the chemotactic proteins, including chemokines and their receptors (32). The function of chemokines and cytokines shows some overlaps, but chemokines are primarily recognized for their capacity to modulate cell migration. Among the chemokines, CCL20 is a major contributor to immune cell infiltration in psoriasis (33). CCL20 expression is largely increased by TNF- $\alpha$ , IL-24, and IFN- $\gamma$  (27, 29). CCL20 attracts dendritic cells and Th17 cells to sustain the inflammatory response through a feedback loop (26). DMD was found to significantly suppress CCL20, resulting in the blockage of the vicious inflammatory cycle. Besides CCL20, DMD was capable of inhibiting a series of chemokines and the receptors including CC, and CXC chemokines. CC chemokines majorly recruit T cells and monocytes, whereas CXC chemokines predominantly recruit neutrophils in psoriasis (34). For instance, enhanced CCL2 release by macrophages induces monocyte migration to the psoriasiform lesions in mice (35). CCL4L2 and CCL22 are pivotal chemokines in patients with psoriasis to stimulate the chemotactic infiltration of dendritic cells and macrophages (36, 37). A principal histopathological feature of psoriasis is the inflammatory infiltration of neutrophils in the stratum corneum (Munro's microabscess) and dermis. Chemokine production by the stimulated macrophages acts as a chemoattractant for neutrophil accumulation (38). Our *in vitro* wound healing and transwell assays demonstrated the blockage of neutrophil migration after the suppression of chemokine subset in macrophages treated by DMD.

The binding of chemokines and some stimulators to the corresponding receptors can activate the downstream signaling pathways including those of MAPKs and NF- $\kappa$ B. IMQ is reported to bind with TLR, resulting in MAPKs phosphorylation and NF- $\kappa$ B to generate cytokines and chemokines (39). Overexpression of p-JNK, p-ERK, and p-p38 was inhibited by DMD, suggesting the possible role of this compound in MAPK regulation. Among MAPKs, ERK regulates IL-24 expression in psoriatic lesions (40). Our result verified IL-24 downregulation by DMD through the ERK-dependent signaling. MAPKs regulate the downstream signaling of the transcription factor NF- $\kappa$ B in macrophages to produce cytokines and chemokines for psoriasis development (41). We speculated that both MAPKs and NF- $\kappa$ B pathways participate in DMD-induced cytokine/chemokine arrest.

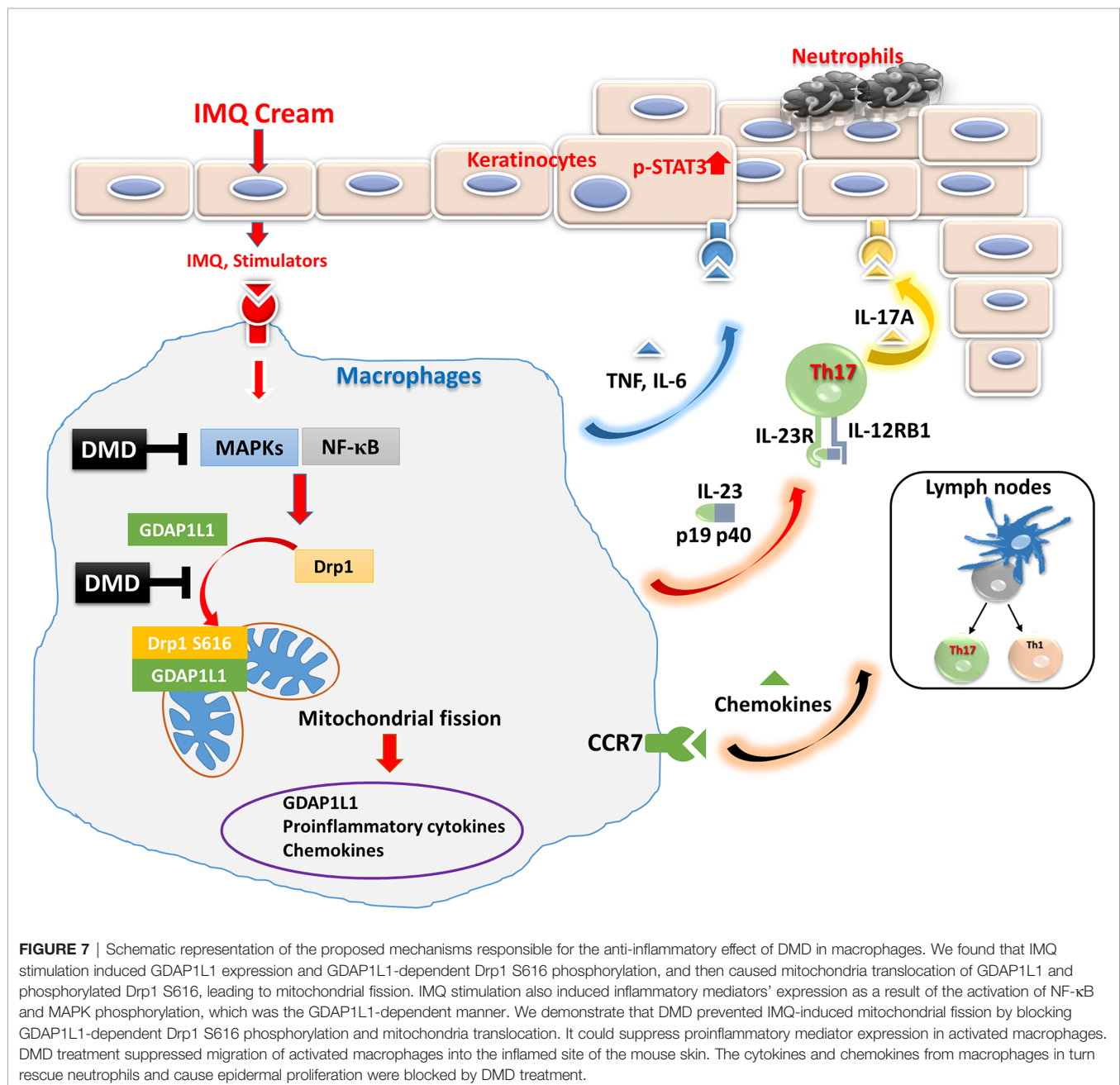
The RNA sequencing study showed a potential role of GDAP1L1 in the anti-inflammatory activity of DMD against macrophages. GDAP1L1 is a mitochondrial fission factor governing the mitochondrial dynamics. Under oxidative stress, GDAP1L1 translocates to the mitochondria. Mitochondrial fission and fusion need to be controlled to keep the balance required for the persistence of mitochondrial morphology. Mitochondrial dynamics mediate energy output, quality control, and the generation of reactive oxygen species (ROS) (42). The defect in mitochondrial membrane dynamics predominantly affects neuron functions to cause neurodegenerative diseases (43). Mitochondrial fission raised as a result of a high level of stress may be one of the main causes of inflammation and immune dysregulation (44). Due to its central role in mitochondrial fission, Drp1 is a prime target for regulatory pathways. Drp1 mainly exists in the cytosol but partially moves to the outer membrane of mitochondria for mediating the process of fission (45). Drp1-mediated fragmentation leads to ROS generation, which is implicated in the pathogenesis of Alzheimer's and Parkinson's diseases (46). Translocation of Drp1 to mitochondria depends on the phosphorylation at S616. Phosphorylation regulates the cycling of Drp1 between the cytoplasm and mitochondrial membrane to prompt fission (47). In this study, IMQ treatment-induced GDAP1L1 expression and translocation, which is involved in the proinflammatory factor expression. GDAP1L1 could induce inflammation in the presence of Drp1 and inhibition of GDAP1L1 and Drp1 S616 translocation to mitochondria mediated by DMD prevented macrophage activation. Some fission factors are associated with apoptotic induction, whereas GDAP1L1 elicits mitochondrial fragmentation without inducing apoptosis (48). Thus, we ruled out the apoptosis pathway mediating the effect of DMD on macrophage activation.

Mitochondrial fission may be fundamental for dominating the production of proinflammatory mediators. A previous study (49) demonstrated that downregulation of Drp1 attenuates proinflammatory factors *via* the reduced MAPK and NF- $\kappa$ B signaling in microglial cells. ERK can trigger mitochondrial fission through phosphorylation of Drp1 at S616 and its translocation to mitochondria (50). Our experimental data inferred that DMD arrested MAPK signaling, blocking the translocation of Drp1 S616 and the subsequent fission. The mechanisms by which GDAP1L1/Drp1 axis regulates macrophage activation are unclear. There is little evidence to link GDAP1L1/Drp1 with inflammation. Zhang et al. (51) reported that Drp1 gene expression increases in atopic dermatitis, and other autoimmune skin diseases. However, Therianou et al. (52) demonstrated a contrary result in lesional psoriatic skin. Further study is needed to yield detailed insight into the molecular pathways that mediate GDAP1L1/Drp1 translocation in psoriasis.

The topical treatment of IMQ cream on murine skin creates inflammation resembling the symptoms of human psoriasis (20). IMQ caused phenotypic changes in psoriasis, including epidermal hyperplasia, inflammatory cell infiltration, and IL-23/Th17 axis activation. Relieving these pathological events is

critical for psoriasis management. DMD effectively ameliorated IMQ-triggered inflammation and hyperproliferation. The epidermal thickness of IMQ-treated mouse skin could be reduced by 47% after DMD application. Based on the same protocol of psoriasis-like lesion induction by IMQ, our previous data (53) demonstrated that betamethasone as a positive control could decrease epidermal thickness by 43%. This indicates a comparable therapeutic efficacy between DMD and the drug used in clinics. IHC and RT-qPCR results manifested a large accumulation of macrophages and neutrophils in viable skin of the psoriasiform lesion. This observation confirmed the macrophage recruitment in the epidermis and dermis of IMQ-

treated mouse skin as was proved in the previous study (54). Our experimental data convincingly demonstrated that a decrease in macrophage recruitment by topical DMD contributed to the resolution of psoriasiform inflammation. We found that DMD application inhibited IMQ-induced overexpression of GDAP1L1 and Drp1 in mouse skin. IL-23 and IL-17 are highly involved in the IMQ-induced animal model of psoriasis (55). In psoriatic lesions, IL-23 is greatly expressed in dendritic cells and macrophages (56). IL-17A is important in relieving psoriasis by upregulating cytokines IL-6, IL-1 $\beta$ , and TNF- $\alpha$  (57). Overexpressed IL-17A in psoriatic skin leads to the proliferation and abnormal differentiation of keratinocytes



(58). Macrophages express low levels of IL-17A (16). Psoriasis is a complex disease with a dynamic interaction between immune cells and keratinocytes, as well as their cytokines and chemokines (59). Activation of a confederacy of cell types in psoriasis includes T cells, mast cells, dendritic cells, neutrophils, macrophages, and keratinocytes. As psoriasis develops, T cells and neutrophils are reported to release IL-17A (16, 60). Our data manifested downregulation of IL-17A in IMQ-treated skin by DMD, which might directly or indirectly act on different immune cells with or without macrophage intervention. IL-17A further recruits dendritic cells and Th17 cells to the psoriatic lesion. The production of IL-1 $\beta$  and TNF- $\alpha$  from macrophages can be stimulated by IL-17A (61), which also acts on keratinocytes to increase their proliferation and chemokine expression. Blocking IL-17A by DMD led to the inhibition of epidermal thickening as detected in our study. IL-24 is another cytokine largely produced by macrophages to direct keratinocyte proliferation (33). In addition to macrophages, IL-24 is produced by T cells, mast cells, and keratinocytes in psoriatic plaque (40). The inhibition of IL-24 by topically applied DMD could be beneficial in diminishing keratinocyte proliferation according to IHC. Neutralization of cytokines by DMD not only decreased the number of macrophages in viable skin, but also the number of neutrophils in the stratum corneum and dermis. Inhibition of neutrophil recruitment impeded the aberrant interplay between neutrophils and keratinocytes, thus blocking the keratinocyte hyperproliferation induced by neutrophil cytokines/chemokines. The significant reduction of GDAP1L1 and Drp1 S616 in IMQ-stimulated skin by DMD corroborated with the *in vitro* result of translocation inhibition.

The findings in the mechanistic and animal studies suggest the multiple antipsoriatic mechanisms of DMD. This compound suppressed IMQ-induced expression of proinflammatory cytokines/chemokines by obstructing of MAPK and NF- $\kappa$ B phosphorylation in macrophages. We also verified that DMD downregulated proinflammatory factors *via* the inhibition of GDAP1L1 and Drp1 translocation and Drp1 phosphorylation. This inhibition might be mediated by decreasing the overexpression of p-NF- $\kappa$ B. Further neutrophil recruitment and keratinocyte hyperproliferation could be prevented by inhibiting macrophage activation after DMD management. The possible mechanisms of action of DMD are depicted in **Figure 7**. The safety of topically applied DMD was examined earlier and shows a negligible irritation in healthy mouse skin (14). A satisfactory therapeutic efficacy and safety could be achieved for topical DMD application.

## CONCLUSIONS

The present work investigated the anti-inflammatory potential of a pure compound (DMD) derived from *A. cinnamomea* for mitigating psoriasiform plaque. The *in vitro* assay on THP-1 cells presented DMD-mediated inhibition of overexpressed cytokine/chemokine. The conditioned medium of the activated

macrophages treated with DMD could suppress neutrophil migration and keratinocyte proliferation. The *in vivo* animal study showed relief in psoriasiform symptoms after DMD treatment. In addition, cytokine/chemokine upregulation and macrophage recruitment in the psoriasis-like lesion were alleviated *in vivo*. DMD downregulated proinflammatory mediators through the MAPKs and NF- $\kappa$ B pathways. The finding in this study also revealed that the GDAP1L1/Drp1 signaling axis plays a critical role in macrophages as an activator of IMQ-induced proinflammatory factors. This axis could be a target of anti-inflammatory DMD to reduce the lesions. This natural compound, DMD, sheds new light on the therapeutic approach against psoriasis.

## DATA AVAILABILITY STATEMENT

The datasets of transcriptomic analysis for this study can be found on the website Gene Expression Omnibus (<https://www.ncbi.nlm.nih.gov/geo/>). The accession number is GSE171667.

## ETHICS STATEMENT

The studies involving human participants were reviewed and approved by Institutional Review Board at Chang Gung Memorial Hospital. The patients/participants provided their written informed consent to participate in this study.

## AUTHOR CONTRIBUTIONS

S-YC initiated the study and drafted the manuscript. C-YC involved in the design of all experiments. S-YC and S-CY carried out the experiments. S-YC and AA analyzed data and wrote the manuscript. C-HL and J-YF supervised the entire project. J-YF reviewed critically and approved the final manuscript. All authors contributed to the article and approved the submitted version.

## ACKNOWLEDGEMENTS

The authors are grateful for the financial support from Ministry of Science and Technology of Taiwan (MOST-107-2320-B-182-016-MY3) and Chang Gung Memorial Hospital (CMRPD1J0061-3).

## SUPPLEMENTARY MATERIAL

The Supplementary Material for this article can be found online at: <https://www.frontiersin.org/articles/10.3389/fimmu.2021.664425/full#supplementary-material>

## REFERENCES

- Kamiya K, Kishimoto M, Sugai J, Komine M, Ohtsuki M. Risk Factors for the Development of Psoriasis. *Int J Mol Sci* (2019) 20:4347. doi: 10.3390/ijms20184347
- Greb JE, Goldminz AM, Elder JT, Lebwohl MG, Gladman DD, Wu JJ, et al. Psoriasis. *Nat Rev Dis Primers* (2016) 2:1–7. doi: 10.1038/nrdp.2016.82
- Boehncke WH, Schön MP. Psoriasis. *Lancet* (2015) 386:983–94. doi: 10.1016/S0140-6736(14)61909-7
- Weng JR, Huang TH, Lin ZC, Alalaiwe A, Fang JY. Cutaneous Delivery of [1-(4-chloro-3-nitrobenzenesulfonyl)-1H-indol-3-yl]-methanol, an indole-3-carbinol Derivative, Mitigates Psoriasisform Lesion by Blocking MAPK/NF- $\kappa$ B/AP-1 Activation. *BioMed Pharmacother* (2019) 119:109398. doi: 10.1016/j.biopha.2019.109398
- Huang TH, Lin CF, Alalaiwe A, Yang SC, Fang JY. Apoptotic or Antiproliferative Activity of Natural Products Against Keratinocytes for the Treatment of Psoriasis. *Int J Mol Sci* (2019) 20:2558. doi: 10.3390/ijms20102558
- Damevska K, Neloska L, Nikolovska S, Gocev G, Duma S. Complementary and Alternative Medicine Use Among Patients With Psoriasis. *Dermatol Ther* (2014) 27:281–3. doi: 10.1111/dth.12139
- Deng S, May BH, Zhang AL, Lu C, Xue CC. Plant Extracts for the Topical Management of Psoriasis: A Systematic Review and Meta-Analysis. *Br J Dermatol* (2013) 169:769–82. doi: 10.1111/bjd.12557
- Muszyńska B, Grzywacz-Kisielewska A, Kała K, Gdula-Argasińska J. Anti-Inflammatory Properties of Edible Mushrooms: A Review. *Food Chem* (2018) 243:373–81. doi: 10.1016/j.foodchem.2017.09.149
- Wang C, Zhang W, Wong JH, Ng T, Ye X. Diversity of Potentially Exploitable Pharmacological Activities of the Highly Prized Edible Medicinal Fungus. *Antrodia camphorata Appl Microbiol Biotechnol* (2019) 103:7843–67. doi: 10.1007/s00253-019-10016-9
- Ganesan N, Baskaran R, Velmurugan BK, Thanh NC. *Antrodia Cinnamomea*—an Updated Minireview of its Bioactive Components and Biological Activity. *J Food Biochem* (2019) 43:e12936. doi: 10.1111/jfbc.12936
- Li MH, Wu HC, Yao HJ, Lin CC, Wen SF, Pan IH. *Antrodia Cinnamomea* Extract Inhibits Th17 Cell Differentiation and Ameliorates Imiquimod-Induced Psoriasisform Skin Inflammation. *Am J Chin Med* (2015) 43:1401–17. doi: 10.1142/S0192415X15500792
- Buccini M, Punch KA, Kaskow B, Flematti GR, Skelton BW, Abraham LJ, et al. Ethynylbenzoid Metabolites of *Antrodia Camphorata*: Synthesis and Inhibition of TNF Expression. *Org Biomol Chem* (2014) 12:1100–13. doi: 10.1039/C3OB42333F
- Shie PH, Wang SY, Lay HL, Huang GJ. 4,7-Dimethoxy-5-methyl-1,3-benzodioxole From *Antrodia Camphorata* Inhibits LPS-induced Inflammation Via Suppression of NF- $\kappa$ B and Induction HO-1 in RAW264.7 Cells. *Int Immunopharmacol* (2016) 31:186–94. doi: 10.1016/j.intimp.2015.12.030
- Yang SC, Huang TH, Chiu CH, Chou WL, Alalaiwe A, Yeh YC, et al. The Atopic Dermatitis-Like Lesion and the Associated MRSA Infection and Barrier Dysfunction can be Alleviated by 2,4-dimethoxy-6-methylbenzene-1,3-diol From *Antrodia Camphorata*. *J Dermatol Sci* (2018) 92:188–96. doi: 10.1016/j.jdermsci.2018.09.002
- Fuentes-Duculan J, Suárez-Fariñas M, Zaba LC, Nogales KE, Pierson KC, Mitsui H, et al. A Subpopulation of CD163-positive Macrophages is Classically Activated in Psoriasis. *J Invest Dermatol* (2010) 130:2412–22. doi: 10.1038/jid.2010.165
- Wang Y, Edelmayer R, Wetter J, Salte K, Gauvin D, Leys L, et al. Monocytes/Macrophages Play a Pathogenic Role in IL-23 Mediated Psoriasis-Like Skin Inflammation. *Sci Rep* (2019) 9:5310. doi: 10.1038/s41598-019-41655-7
- Chuang SY, Lin CH, Sung CT, Fang JY. Murine Models of Psoriasis and Their Usefulness for Drug Discovery. *Expert Opin Drug Discov* (2018) 13:551–62. doi: 10.1080/17460441.2018.1463214
- Chuang SY, Yang CH, Chou CC, Chiang YP, Chuang TH, Hsu LC. TLR-Induced PAI-2 Expression Suppresses IL-1 $\beta$  Processing Via Increasing Autophagy and NLRP3 Degradation. *Proc Natl Acad Sci U S A* (2013) 110:16079–84. doi: 10.1073/pnas.1306556110
- Chen CY, Lee YH, Chang SH, Tsai YF, Fang JY, Hwang TL. Oleic Acid-Loaded Nanosstructured Lipid Carrier Inhibit Neutrophil Activities in the Presence of Albumin and Alleviates Skin Inflammation. *Int J Nanomed* (2019) 14:6539–53. doi: 10.2147/IJN.S208489
- van der Fits L, Mourits S, Voerman JS, Kant M, Boon L, Laman JD, et al. Imiquimod-Induced Psoriasis-Like Skin Inflammation in Mice is Mediated Via the IL-23/IL-17 Axis. *J Immunol* (2009) 182:5836–45. doi: 10.4049/jimmunol.0802999
- Lin ZC, Hsieh PW, Hwang TL, Chen CY, Sung CT, Fang JY. Topical Application of Anthranilate Derivatives Ameliorates Psoriatic Inflammation in a Mouse Model by Inhibiting Keratinocyte-Derived Chemokine Expression and Neutrophil Infiltration. *FASEB J* (2018) 32:6783–95. doi: 10.1096/fj.201800354
- Clark RA, Kupper TS. Misbehaving Macrophages in the Pathogenesis of Psoriasis. *J Clin Invest* (2006) 116:2084–7. doi: 10.1172/JCI29441
- Nickoloff BJ, Xin H, Nestle FO, Qin JZ. The Cytokine and Chemokine Network in Psoriasis. *Clin Dermatol* (2007) 25:568–73. doi: 10.1016/j.clindermatol.2007.08.011
- Jiang S, Hinchliffe TE, Wu T. Biomarkers of an Autoimmune Skin Disease—Psoriasis. *Genom Proteomics Bioinf* (2015) 12:224–33. doi: 10.1016/j.gpb.2015.04.002
- Uttarkar S, Brembilla NC, Boehncke WH. Regulatory Cells in the Skin: Pathophysiologic Role and Potential Targets for Anti-Inflammatory Therapies. *J Allergy Clin Immunol* (2019) 143:1302–10. doi: 10.1016/j.jaci.2018.12.1011
- Tokuyama M, Mabuchi T. New Treatment Addressing the Pathogenesis of Psoriasis. *Int J Mol Sci* (2020) 21:7488. doi: 10.3390/ijms21207488
- Kumari S, Bonnet MC, Ulvmar MH, Wolk K, Karagianni N, Witte E, et al. Tumor Necrosis Factor Receptor Signaling in Keratinocytes Triggers interleukin-24-dependent Psoriasis-Like Skin Inflammation in Mice. *Immunity* (2013) 39:899–911. doi: 10.1016/j.immuni.2013.10.009
- Poindexter NJ, Walch ET, Chada S, Grimm EA. Cytokine Induction of interleukin-24 in Human Peripheral Blood Mononuclear Cells. *J Leukoc Biol* (2005) 78:745–52. doi: 10.1189/jlb.0205116
- Lee CH, Hwang STY. Pathophysiology of Chemokines and Chemokine Receptors in Dermatological Science: A Focus on Psoriasis and Cutaneous T-cell Lymphoma. *Dermatol Sin* (2012) 30:128–35. doi: 10.1016/j.dsi.2012.08.004
- Sun Y, Zhang J, Huo R, Zhai T, Li H, Wu P, et al. Paeoniflorin Inhibits Skin Lesions in Imiquimod-Induced Psoriasis-Like Mice by Downregulating Inflammation. *Int Immunopharmacol* (2015) 24:392–9. doi: 10.1016/j.intimp.2014.12.032
- Miao X, Xiang Y, Mao W, Chen Y, Li Q, Fan B. TRIM27 Promotes IL-6-induced Proliferation and Inflammation Factor Production by Activating STAT3 Signaling in HaCaT Cells. *Am J Physiol Cell Physiol* (2020) 318:272–81. doi: 10.1152/ajpcell.00314.2019
- Luo Y, Luo Y, Chang J, Xiao Z, Zhou B. Identification of Candidate Biomarkers and Pathways Associated With Psoriasis Using Bioinformatics Analysis. *Hereditas* (2020) 157:30. doi: 10.1186/s41065-020-00141-1
- Singh TP, Lee CH, Farber JM. Chemokine Receptors in Psoriasis. *Expert Opin Ther Targets* (2013) 17:1405–22. doi: 10.1517/14728222.2013.838220
- Kim HO, Cho SI, Chung BY, Ahn HK, Park CW, Lee CH. Expression of CCL1 and CCL18 in Atopic Dermatitis and Psoriasis. *Exp Dermatol* (2012) 37:521–6. doi: 10.1111/j.1365-2230.2011.04295.x
- Schuster C, Huard A, Sirait-Fischer E, Dillmann C, Brüne B, Weigert A. S1PR4-Dependent CCL2 Production Promotes Macrophage Recruitment in a Murine Psoriasis Model. *Eur J Immunol* (2020) 50:839–45. doi: 10.1002/eji.201948349
- Pedrosa E, Carretero-Iglesia L, Boada A, Colobran R, Faner R, Pujol-Autonell I, et al. CCL4L Polymorphisms and CCL4/CCL4L Serum Levels are Associated With Psoriasis Severity. *J Invest Dermatol* (2011) 131:1830–7. doi: 10.1038/jid.2011.127
- Kusumoto S, Kajihara I, Nanamoto E, Makino K, Ichihara A, Aoi J, et al. Increased CCL22 Expression in Psoriatic Skin Predicts a Good Response to Infliximab Therapy. *Br J Dermatol* (2014) 171:1259–61. doi: 10.1111/bjd.13091
- De Filippo K, Dudeck A, Hasenberg M, Nye E, van Rooijen N, Hartmann K, et al. Mast Cell and Macrophage Chemokines CXCL1/CXCL2 Control the Early Stage of Neutrophil Recruitment During Tissue Inflammation. *Blood* (2013) 121:4930–7. doi: 10.1182/blood-2013-02-486217



39. Zhao W, Xiao S, Li H, Zheng T, Huang J, Hu R, et al. MAPK Phosphatase-1 Deficiency Exacerbates the Severity of Imiquimod-Induced Psoriasiform Skin Disease. *Front Immunol* (2018) 9:569. doi: 10.3389/fimmu.2018.00569
40. Mitamura Y, Nunomura S, Furue M, Izuhara K. IL-24: A New Player in the Pathogenesis of Pro-Inflammatory and Allergic Skin Diseases. *Allergol Int* (2020) 69:405–11. doi: 10.1016/j.alit.2019.12.003
41. Li L, Zhang HY, Zhong XQ, Lu Y, Wei J, Li L, et al. Psori-CM02 Formula Alleviates Imiquimod-Induced Psoriasis Via Affecting Macrophage Infiltration and Polarization. *Life Sci* (2020) 243:117231. doi: 10.1016/j.lfs.2019.117231
42. Sabouny R, Shutt TE. Reciprocal Regulation of Mitochondrial Fission and Fusion. *Trends Biochem Sci* (2020) 45:564–77. doi: 10.1016/j.tibs.2020.03.009
43. Westermann B. Mitochondrial Fusion and Fission in Cell Life and Death. *Nat Rev Mol Cell Biol* (2010) 11:872–84. doi: 10.1038/nrm3013
44. Giacomello M, Pyakurel A, Glytsou C, Scorrano L. The Cell Biology of Mitochondrial Membrane Dynamics. *Nat Rev Mol Cell Biol* (2020) 21:204–24. doi: 10.1038/s41580-020-0210-7
45. Lee YJ, Jeong SY, Karbowski M, Smith CL, Youle RJ. Roles of the Mammalian Mitochondrial Fission and Fusion Mediators Fis1, Drp1, and Opa1 in Apoptosis. *Mol Biol Cell* (2004) 15:5001–11. doi: 10.1091/mbc.e04-04-0294
46. Liu YJ, McIntyre RL, Janssens GE, Houtkooper RH. Mitochondrial Fission and Fusion: A Dynamic Role in Aging and Potential Target for Age-Related Disease. *Mech Ageing Dev* (2020) 186:111212. doi: 10.1016/j.mad.2020.111212
47. van der Blik AM, Shen Q, Kawajiri S. Mechanisms of Mitochondrial Fission and Fusion. *Cold Spring Harb Perspect Biol* (2013) 5:a011072. doi: 10.1101/cshperspect.a011072
48. Niemann A, Ruegg M, La Padula V, Schenone A, Suter U. Ganglioside-Induced Differentiation Associated Protein 1 is a Regulator of the Mitochondrial Network: New Implications for Charcot-Marie-Tooth Disease. *J Cell Biol* (2005) 170:1067–78. doi: 10.1083/jcb.200507087
49. Park J, Choi H, Min JS, Park SJ, Kim JH, Park HJ, et al. Mitochondrial Dynamics Modulate the Expression of Pro-Inflammatory Mediators in Microglial Cells. *J Neurochem* (2013) 127:221–32. doi: 10.1111/jnc.12361
50. Huang CY, Lai CH, Kuo CH, Chiang SF, Pai PY, Lin JY, et al. Inhibition of ERK-Drp1 Signaling and Mitochondria Fragmentation Alleviates IGF-IIR-induced Mitochondria Dysfunction During Heart Failure. *J Mol Cell Cardiol* (2018) 122:58–68. doi: 10.1016/j.yjmcc.2018.08.006
51. Zhang B, Alysandratos KD, Angelidou A, Asadi S, Sismanopoulos N, Delivanis DA, et al. Human Mast Cell Degranulation and Preformed TNF Secretion Require Mitochondrial Translocation to Exocytosis Sites: Relevance to Atopic Dermatitis. *J Allergy Clin Immunol* (2011) 127:1522–31. doi: 10.1016/j.jaci.2011.02.005
52. Therianou A, Vasiadi M, Delivanis DA, Petrakopoulou T, Katsarou-Katsari A, Antoniou C, et al. Mitochondrial Dysfunction in Affected Skin and Increased Mitochondrial DNA in Serum From Patients With Psoriasis. *Exp Dermatol* (2019) 28:72–5. doi: 10.1111/exd.13831
53. Cheng CY, Lin YK, Yang SC, Alalaiwe A, Lin CJ, Fang JY, et al. Percutaneous Absorption of Resveratrol and its Oligomers to Relieve Psoriasiform Lesions: *in Silico*, *In Vitro* and *In Vivo* Evaluations. *Int J Pharm* (2020) 585:119507. doi: 10.1016/j.ijpharm.2020.119507
54. Terhorst D, Chelbi R, Wohn C, Malosse C, Tamoutounour S, Jorquera A, et al. Dynamics and Transcriptomics of Skin Dendritic Cells and Macrophages in an Imiquimod-Induced, Biphasic Mouse Model of Psoriasis. *J Immunol* (2015) 195:4953–69. doi: 10.4049/jimmunol.1500551
55. Hou Y, Zhu L, Tian H, Sun HX, Wang R, Zhang L, et al. IL-23-induced Macrophage Polarization and its Pathological Roles in Mice With Imiquimod-Induced Psoriasis. *Protein Cell* (2018) 9:1027–38. doi: 10.1007/s13238-018-0505-z
56. Yawalkar N, Tschanner GG, Hunger RE, Hassan AS. Increased Expression of IL-12p70 and IL-23 by Multiple Dendritic Cell and Macrophage Subsets in Plaque Psoriasis. *J Dermatol Sci* (2009) 54:99–105. doi: 10.1016/j.jdermsci.2009.01.003
57. Li HJ, Wu NL, Lee GA, Hung CF. The Therapeutic Potential and Molecular Mechanism of Isoflavone Extract Against Psoriasis. *Sci Rep* (2018) 8:6335. doi: 10.1038/s41598-018-24726-z
58. Sato Y, Ogawa E, Okuyama R. Role of Innate Immune Cells in Psoriasis. *Int J Mol Sci* (2020) 21:6604. doi: 10.3390/ijms21186604
59. Benhadou F, Mintoff D, del Marmol V. Psoriasis: Keratinocytes or Immune Cells—Which is the Trigger? *Dermatology* (2019) 235:91–100. doi: 10.1159/000495291
60. Katayama H. Development of Psoriasis by Continuous Neutrophil Infiltration Into the Epidermis. *Exp Dermatol* (2018) 27:1084–91. doi: 10.1111/exd.13746
61. Girolomoni G, Mrowietz U, Paul C. Psoriasis: Rationale for Targeting Interleukin-17. *Br J Dermatol* (2012) 167:717–24. doi: 10.1111/j.1365-2133.2012.11099.x




**Conflict of Interest:** The authors declare that the research was conducted in the absence of any commercial or financial relationships that could be construed as a potential conflict of interest.

Copyright © 2021 Chuang, Chen, Yang, Alalaiwe, Lin and Fang. This is an open-access article distributed under the terms of the Creative Commons Attribution License (CC BY). The use, distribution or reproduction in other forums is permitted, provided the original author(s) and the copyright owner(s) are credited and that the original publication in this journal is cited, in accordance with accepted academic practice. No use, distribution or reproduction is permitted which does not comply with these terms.



Article

# Fucoxanthin Ameliorates Oxidative Stress and Airway Inflammation in Tracheal Epithelial Cells and Asthmatic Mice

Shu-Ju Wu <sup>1,2,†</sup>, Chian-Jiun Liou <sup>3,4,†</sup> , Ya-Ling Chen <sup>5</sup>, Shu-Chen Cheng <sup>6,\*</sup>  and Wen-Chung Huang <sup>4,7,\*</sup> 

- <sup>1</sup> Department of Nutrition and Health Sciences, Research Center for Chinese Herbal Medicine, Chang Gung University of Science and Technology, Taoyuan City 33303, Taiwan; sjwu@mail.cgust.edu.tw
  - <sup>2</sup> Aesthetic Medical Center, Department of Dermatology, Chang Gung Memorial Hospital, Linkou, Taoyuan City 33303, Taiwan
  - <sup>3</sup> Department of Nursing, Division of Basic Medical Sciences, Research Center for Chinese Herbal Medicine, Chang Gung University of Science and Technology, Taoyuan City 33303, Taiwan; ccliu@mail.cgust.edu.tw
  - <sup>4</sup> Division of Allergy, Asthma, and Rheumatology, Department of Pediatrics, Chang Gung Memorial Hospital, Linkou, Guishan Dist., Taoyuan City 33303, Taiwan
  - <sup>5</sup> School of Nutrition and Health Sciences, Taipei Medical University, Taipei City 11031, Taiwan; ylchen01@tmu.edu.tw
  - <sup>6</sup> Department of Traditional Chinese Medicine, Chang Gung Memorial Hospital, Taoyuan City 33378, Taiwan
  - <sup>7</sup> Graduate Institute of Health Industry Technology, Research Center for Food and Cosmetic Safety, Research Center for Chinese Herbal Medicine, College of Human Ecology, Chang Gung University of Science and Technology, Taoyuan City 33303, Taiwan
- \* Correspondence: kkaren0330@gmail.com (S.-C.C.); wchuang@mail.cgust.edu.tw (W.-C.H.); Tel.: +886-3-3196200 (S.-C.C.); +886-3-2118999 (ext. 5112) (W.-C.H.)
- † Shu-Ju Wu and Chian-Jiun Liou contributed equally to this paper.



**Citation:** Wu, S.-J.; Liou, C.-J.; Chen, Y.-L.; Cheng, S.-C.; Huang, W.-C. Fucoxanthin Ameliorates Oxidative Stress and Airway Inflammation in Tracheal Epithelial Cells and Asthmatic Mice. *Cells* **2021**, *10*, 1311. <https://doi.org/10.3390/cells10061311>

Academic Editor: Alessandro Poggi

Received: 17 April 2021

Accepted: 23 May 2021

Published: 25 May 2021

**Publisher's Note:** MDPI stays neutral with regard to jurisdictional claims in published maps and institutional affiliations.



**Copyright:** © 2021 by the authors. Licensee MDPI, Basel, Switzerland. This article is an open access article distributed under the terms and conditions of the Creative Commons Attribution (CC BY) license (<https://creativecommons.org/licenses/by/4.0/>).

**Abstract:** Fucoxanthin is isolated from brown algae and was previously reported to have multiple pharmacological effects, including anti-tumor and anti-obesity effects in mice. Fucoxanthin also decreases the levels of inflammatory cytokines in the bronchoalveolar lavage fluid (BALF) of asthmatic mice. The purpose of the present study was to investigate the effects of fucoxanthin on the oxidative and inflammatory responses in inflammatory human tracheal epithelial BEAS-2B cells and attenuated airway hyperresponsiveness (AHR), airway inflammation, and oxidative stress in asthmatic mice. Fucoxanthin significantly decreased monocyte cell adherence to BEAS-2B cells. In addition, fucoxanthin inhibited the production of pro-inflammatory cytokines, eotaxin, and reactive oxygen species in BEAS-2B cells. Ovalbumin (OVA)-sensitized mice were treated by intraperitoneal injections of fucoxanthin (10 mg/kg or 30 mg/kg), which significantly alleviated AHR, goblet cell hyperplasia and eosinophil infiltration in the lungs, and decreased Th2 cytokine production in the BALF. Furthermore, fucoxanthin significantly increased glutathione and superoxide dismutase levels and reduced malondialdehyde (MDA) levels in the lungs of asthmatic mice. These data demonstrate that fucoxanthin attenuates inflammation and oxidative stress in inflammatory tracheal epithelial cells and improves the pathological changes related to asthma in mice. Thus, fucoxanthin has therapeutic potential for improving asthma.

**Keywords:** airway hyperresponsiveness; asthma; fucoxanthin; oxidative stress; tracheal epithelial cells

## 1. Introduction

Bronchial asthma is one of the most common respiratory allergies and inflammatory diseases globally. Severe air pollution produces more suspended particles and chemical irritants and increases the prevalence of asthma and respiratory disease in developing and developed countries [1]. The characteristics of sudden asthma include chest tightness, difficulty breathing, shortness of breath, dry cough, and paroxysmal wheezing [2]. Many studies have pointed out that the airways of patients with chronic asthma are excessively

sensitive to allergens, chemical irritants, and particle pollution. Other studies have confirmed that mites, cigarette smoke, pollen, cold air, and ozone may stimulate sudden allergic reactions in the airways and asthma attacks [3]. Continuous inflammation of the respiratory tract is an important factor that worsens the pathological symptoms of asthma. In patients with asthma, allergic stimulants also induce hyperplasia and sensitivity of the tracheal epithelial cells. These tracheal epithelial cells increase mucus secretion, leading to airway obstruction, breathing difficulties, and even suffocation [4].

Recent studies have shown that activated T cells and inflamed macrophages in the lungs of asthmatic patients release high amounts of IL-4 and TNF- $\alpha$  [5]. These cytokines lead to the inflammation and oxidation of the tracheal epithelial cells and the secretion of more inflammatory cytokines, chemokines, and eotaxins. Eotaxins not only attract more eosinophils to infiltrate the lungs, but inflammatory cytokines and chemokines also cause more severe airway inflammation, oxidative cell damage, and airway remodeling, leading to worsening lung function and aggravated breathing difficulties in patients with asthma [6]. Therefore, inflamed tracheal epithelial cells play an important role in the pathological features of patients with acute asthma and severe persistent asthma.

Many studies have confirmed that the deterioration of allergic asthma is closely related to immune system disorders or imbalanced immune cell activation. Massive proliferation and activation of Th2 cells and ILC2 are important factors in the induction of immune system disorders in asthma patients [7]. Excessive activation of Th2 cells results in the release of a large amount of cytokines IL-4, IL-5, and IL-13, causing eosinophil infiltration into the lungs, airway hyperresponsiveness (AHR), and the induction of mast cell and eosinophil release of inflammatory, oxidative, and allergic molecules to damage the epithelial cells in airways [5]. Th2 cell-associated cytokines can also induce goblet cell proliferation in the trachea, stimulating the secretion of large amounts of mucus to block the airways [8]. In sudden asthma attacks, the airway epithelial cells secrete more inflammatory chemokines to attract more immune cells to infiltrate the lungs, including neutrophils, macrophages, and eosinophils. These activated immune cells and airway epithelial cells may release excess reactive oxygen species (ROS), exacerbating the inflammation and oxidative damage to the lungs of asthmatic patients and causing damage to the lung cells and tissues [9]. In the lungs of asthma patients, the synergistic effect of excessive ROS and IL-13 leads to more serious AHR and airway remodeling, increase the thickness of airway smooth muscle, and reduce the gas exchange rate of the respiratory system [7]. Therefore, reducing the activity of Th2 cells in the lungs and the expression of ROS and inflammation-related signaling molecules in the lung and airway epithelial cells is a strategy to improve the development of asthma.

Clinically, drugs commonly used to treat or prevent asthma include bronchodilators as well as anti-inflammatory and anti-allergy drugs. Inhaled steroids and oral steroids are commonly used to treat or prevent asthma, but some patients have side effects on steroids [10]. The use of steroid drugs is limited and invalid for treating neutrophilic asthma or severe asthma patients [11]. Therefore, the development of new effective drugs for treating asthma is expected by many researchers and clinicians.

Some traditional Chinese herbs and pure plant compounds have been found to improve asthma [12–14]. However, the relationship between the pure compounds or extracts isolated from algae and the improvement of asthma symptoms has been studied infrequently. Fucoxanthin is a carotenoid pigment and is abundant in brown seaweeds (Phaeophyceae) and marine diatoms (Bacillariophyta) [15]. Fucoxanthin has multiple biological functions and potential health benefits in animal models and cell experiments [16–18]. Fucoxanthin has been demonstrated to inhibit inflammatory mediators and pro-inflammatory cytokines in LPS-stimulated macrophages, and it could decrease lung fibrosis in bleomycin-induced mice [19,20]. Furthermore, fucoxanthin could decrease ROS expression by promoting neuroprotective effects by regulating the Nrf2-autophagy pathways in a mouse model of traumatic brain injury [21]. Recently, fucoxanthin was found to decrease inflammatory cytokine expression in the bronchoalveolar lavage fluid (BALF) of asthmatic mice

and reduce the levels of total IgE, histamine, and malondialdehyde (MDA) in the serum of mice with allergic rhinitis [22,23]. However, whether fucoxanthin reduces oxidative stress in the lungs, goblet cell hyperplasia, and mucus hypersecretion in the trachea is still unclear. In the current study, we examined whether fucoxanthin attenuates the oxidative responses and inflammatory cytokine expression in human tracheal epithelial cells. We also investigated whether fucoxanthin ameliorated the molecular mechanisms underlying oxidative stress in the lungs, airway inflammation, and pathological lesions in the lungs of asthmatic mice.

## 2. Materials and Methods

### 2.1. Materials

Fucoxanthin (the purity was  $\geq 95\%$  by HPLC) was purchased from Sigma Aldrich (St. Louis, MO, USA). For cell experiments, the concentration of the stock solution was 100 mM, with DMSO as the solvent. DMSO was  $\leq 0.1\%$  of the culture medium as described previously [24]. For asthmatic animal experiments, fucoxanthin was dissolved in DMSO, and the working solution was formulated as 10 mg/50  $\mu$ L and 30 mg/50  $\mu$ L.

### 2.2. Cell Viability Assay

Cell viability was assayed using cell counting kit-8 (CCK-8, Sigma) as described previously [25]. Cells ( $10^4$ /well) were seeded in 96-well culture plates and treated with various concentrations of fucoxanthin for 24 h. Cells treated with the CCK-8 solution were used to determine cell viability using a microplate reader (Multiskan FC, Thermo, Waltham, MA, USA).

### 2.3. BEAS-2B Cell Culture and Fucoxanthin Treatment

Human bronchial epithelial cells (BEAS-2B; American Type Culture Collection, Manassas, VA, USA) were seeded into 24-well culture plates in DMEM/F12 medium supplemented with 10% FBS and 100 U/mL penicillin and streptomycin. BEAS-2B cells were treated with various concentrations of fucoxanthin (0–30  $\mu$ M) for 1 h. Subsequently, the cells were induced with 10 ng/mL TNF- $\alpha$  and 10 ng/mL IL-4 for 24 h. The supernatants were collected, and the chemokine or cytokine levels were detected using specific ELISA kits.

### 2.4. Cell-Cell Adhesion Assay

BEAS-2B cells were treated with fucoxanthin and incubated with 10 ng/mL TNF- $\alpha$ /IL-4 for 24 h. Human monocytic THP-1 cells were purchased from the Bioresource Collection and Research Center (BCRC, Taiwan) and cultured in RPMI 1640 medium. The THP-1 cells were treated with calcein-AM solution (Sigma) for 30 min as described previously [26]. We co-cultured the THP-1 and BEAS-2B cells and detected the adherent THP-1 cells using fluorescence microscopy (Olympus, Tokyo, Japan).

### 2.5. ROS Production in BEAS-2B Cells

BEAS-2B cells were treated with fucoxanthin for 1 h and incubated with TNF- $\alpha$ /IL-4 for 24 h. Next, the BEAS-2B cells were stimulated with 2',7'-dichlorofluorescein diacetate (DCFH-DA) for 30 min, and the intracellular ROS was observed using fluorescence microscopy (Olympus) as described previously [26]. Moreover, the cells were lysed, and the ROS production was detected, both using a multi-mode microplate reader (BioTek synergy HT, Winooski, VT, USA).

### 2.6. Animal Experiments

Six-week-old female BALB/c mice were purchased from the National Laboratory Animal Center (Taipei, Taiwan). All mice were housed in temperature-controlled animal housing under a 12-h light-dark cycle and were raised with food and water available ad libitum. The animal experiments were approved and carried out in accordance with the guidelines from the Laboratory Animal Care Committee of Chang Gung University

of Science and Technology (IACUC approval number: 2019-003). Mice were randomly divided into the five following experimental groups ( $n = 10$  each): normal control group (N) mice were sensitized with normal saline and treated with DMSO by intraperitoneal injection; OVA control group (OVA) mice were sensitized with OVA and treated with DMSO by intraperitoneal injection; prednisolone positive control group (P) mice were sensitized with OVA and treated with 5 mg/kg prednisolone by intraperitoneal injection; or fucoxanthin experiment groups, in which OVA-sensitized mice were treated with 10 mg/kg or 30 mg/kg fucoxanthin (Fu10 and Fu30 groups, respectively) by intraperitoneal injection.

#### 2.7. Mouse Sensitization and Administration of Fucoxanthin

Mice were treated with or without the sensitized solution containing 0.8 mg aluminum hydroxide (Thermo, Rockford, IL, USA) and 50  $\mu$ g ovalbumin (OVA; Sigma) in 200  $\mu$ L normal saline by intraperitoneal injections on days 1–3 and 14. Subsequently, mice were challenged with 2% OVA via an inhaled atomized vapor for 30 min on days 14, 17, 20, 23, and 27 using an ultrasonic nebulizer. The mice were treated with fucoxanthin, prednisolone, or DMSO solution by intraperitoneal injection 1 h before the challenge of OVA or methacholine (Sigma) inhalation (on day 28). AHR was detected on day 28, and the mice were sacrificed to evaluate oxidative stress, inflammatory response, asthma pathology, and immune regulation on day 29.

#### 2.8. Airway Hyperresponsiveness

AHR was assessed to demonstrate airway function as described previously [27]. Mice were put in a single chamber and allowed to inhale 0 to 40 mg/mL aerosolized methacholine to detect the enhanced pause (Penh) using whole-body plethysmography (Buxco Electronics, Troy, NY, USA).

#### 2.9. Histological Analysis of Lung Tissue

Lung tissues were removed and fixed with 10% formalin before being embedded in paraffin and cut into 6- $\mu$ m sections. A section of lung biopsy was treated with Masson's trichrome stain to detect collagen expression. The lung section was also stained using hematoxylin and eosin (HE) solution to examine the eosinophil infiltration of the lungs using a 5-point scoring system and stained with periodic acid-Schiff (PAS) solution (Sigma) to observe the goblet cell hyperplasia of the trachea as described previously [27].

#### 2.10. Serum Collection and Splenocyte Culture

Mice were anesthetized with isoflurane and blood was collected from the orbital vascular plexus. The blood was centrifuged at 6000 rpm for 5 min; the serum was then collected and stored at  $-80^{\circ}\text{C}$ . The serum would detect OVA-specific antibody expression by ELISA as described previously [28]. In addition,  $5 \times 10^6$  splenocytes/mL were incubated with 100  $\mu$ g/mL OVA for 5 continuous days, and cytokine levels were detected using a specific ELISA kit as described previously [29].

#### 2.11. Bronchoalveolar Lavage Fluid and Cell Counting

The BALF was collected as described previously [30]. Mice were anesthetized and sacrificed using an indwelling needle to intubate the trachea to wash the lungs and airways. The lavage fluid was centrifuged, and the supernatant was collected to detect cytokine and chemokine levels. We used Giemsa stain solution (Sigma) to identify the morphology of the different immune cells.

#### 2.12. RNA Isolation and Quantitative Real-Time PCR

Lung tissues were homogenized, and RNA were extracted, both using TRI reagent (Sigma). Using the cDNA synthesis kit (Bio-Rad, San Francisco, CA, USA), we synthesized the cDNA and investigated the specific gene expression using SYBR Green in the quantitative real-time PCR procedure using a spectrofluorometric thermal cycler (iCycler; Bio-Rad).

### 2.13. ELISA

Supernatant from BEAS-2B cell culture medium and BALF was used to detect CCL5, CCL11, CCL24, MCP-1, TNF- $\alpha$ , IL-4, IL-5, IL-6, IL-8, and IL-13 levels using specific ELISA kits (R&D Systems, Minneapolis, MN, USA) as described previously [28]. Serum OVA-specific IgG1, IgG2a, and IgE were assayed by specific ELISA kits (BD Biosciences, San Diego, CA, USA). OVA-IgG1 and OVA-IgG2a standard curves were obtained using serum from OVA-sensitized mice; the serum was diluted 5-fold to observe OVA-IgE by measuring absorbance at 450 nm.

### 2.14. Immunohistochemical Staining

Paraffin-embedded sections of lung tissues were incubated with a specific COX-2 antibody (1:100; ab15191, Abcam, Cambridge, UK) overnight, followed by a secondary antibody. The slides were treated with DAB substrate solution to detect COX-2 expression as described previously [31].

### 2.15. MDA Activity

MDA activity in the lungs was detected using a lipid peroxidation assay kit (Sigma) according to the manufacturer's instructions. The lung tissues were homogenized using a homogenizer (FastPrep-24, MP Biomedicals, Santa Ana, CA, USA) and treated with perchloric acid (150  $\mu$ L, 2N) for protein precipitation. The samples were centrifuged to collect the supernatant, and MDA activity was detected using a multi-mode microplate reader (BioTek Synergy HT).

### 2.16. Glutathione (GSH), Superoxide Dismutase (SOD), and Catalase (CAT) Assay

We used a glutathione assay kit, a superoxide dismutase assay kit, and a catalase assay kit (Sigma) to detect the levels of GSH, SOD, and CAT in the lung tissues according to the manufacturer's instructions.

### 2.17. Statistical Analysis

Statistical analysis was performed using one-way analysis of variance (ANOVA) followed by a Kruskal–Wallis test. All data are expressed as the mean  $\pm$  standard error of the mean (SEM), and at least three independent experiments were analyzed. A  $p$  value  $< 0.05$  was considered significant.

## 3. Results

### 3.1. Fucoxanthin Reduced Inflammatory Mediators and Cell Adhesion in BEAS-2B Cells

The cytotoxicity of fucoxanthin in the BEAS-2B cells was determined using the CCK8 assay. Fucoxanthin did not demonstrate significant cytotoxic effects at a concentration  $\leq 50$   $\mu$ M, and subsequent experiments used fucoxanthin at 0–30  $\mu$ M (Figure 1A). In the BEAS-2B cells, fucoxanthin significantly decreased the levels of CCL5, CCL11, CCL24, IL-6, IL-8, and MCP-1 compared to the TNF- $\alpha$ /IL-4-stimulated BEAS-2B cells (Figure 1B–G). Fucoxanthin also reduced THP-1 cell adherence to the TNF- $\alpha$ /IL-4-activated BEAS-2B cells (Figure 2A,B).



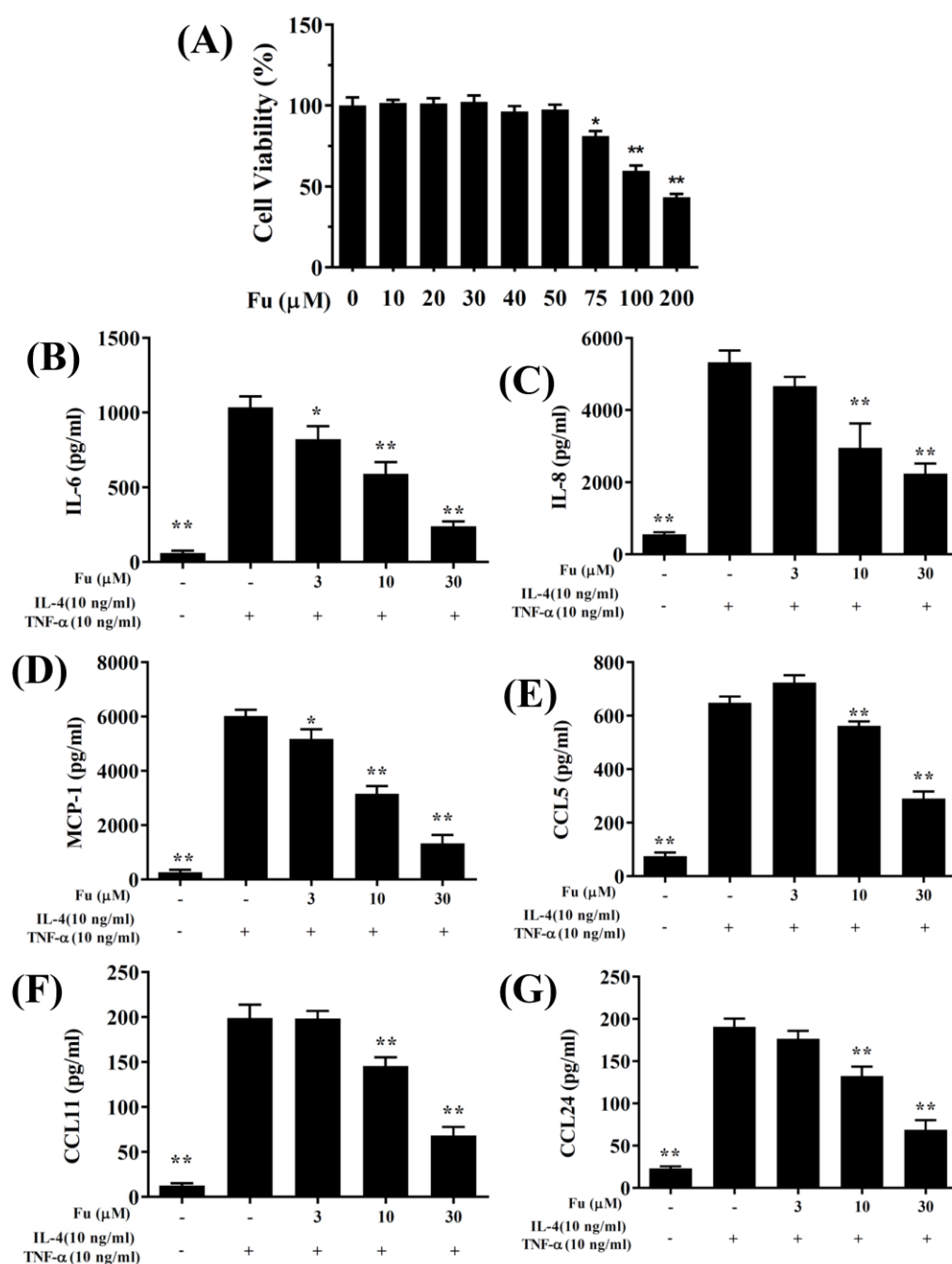


**Figure 1.** The effects of fucoxanthin (Fu) on cytokine and chemokine production in BEAS-2B cells. (A) Cell viability with increasing concentrations of Fu. (B) ELISA results for IL-6, (C) IL-8, (D) MCP-1, (E) CCL5, (F) CCL11, and (G) CCL24 levels in BEAS-2B cells treated with TNF- $\alpha$ /IL-4 and/or Fu. Three independent experiments were analyzed. Data are presented as the mean  $\pm$  SEM. \*  $p < 0.05$ , \*\*  $p < 0.01$  compared to BEAS-2B cells stimulated with TNF- $\alpha$  and IL-4.

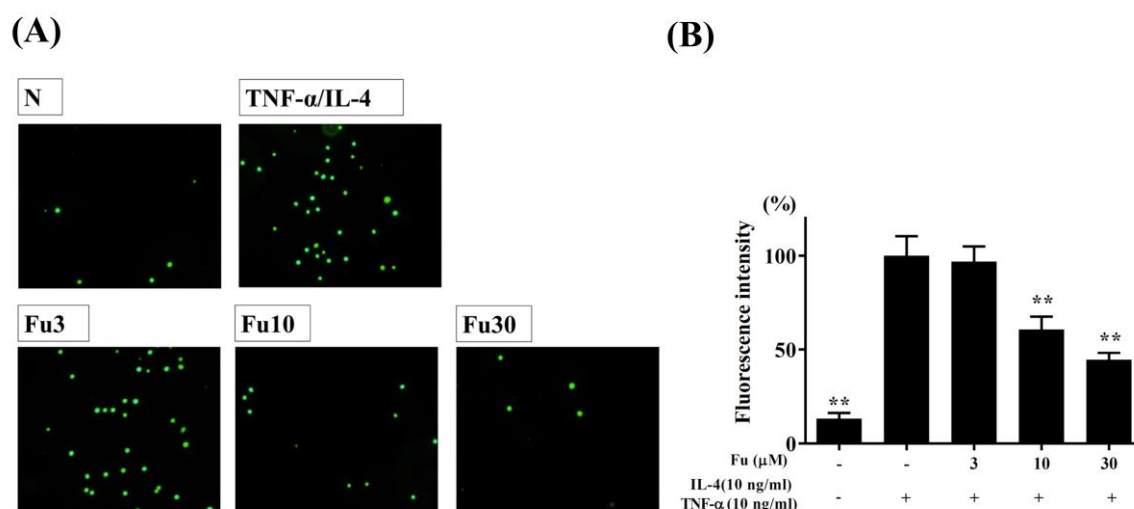


**Figure 2.** Fucoxanthin (Fu) inhibited THP-1 cell adherence to activated BEAS-2B cells. (A) Fluorescence microscopy images of THP-1 cells labeled with calcein-AM and mixed with normal (N) and TNF- $\alpha$ /IL-4-activated BEAS-2B cells in the absence or presence of Fu. (B) Fluorescence intensity of monocytic cell adhesion to BEAS-2B cells. Three independent experiments were analyzed. Data are presented as the mean  $\pm$  SEM. \*\*  $p < 0.01$  compared to BEAS-2B cells stimulated with TNF- $\alpha$  and IL-4.

### 3.2. Effect of Fucoxanthin on ROS Production

Fluorescence microscopy showed that fucoxanthin reduced intracellular ROS production compared to TNF- $\alpha$ /IL-4-stimulated BEAS-2B cells (Figure 3A,B). Furthermore, in the BEAS-2B cells treated with DCFH-DA, fucoxanthin significantly attenuated ROS levels in the TNF- $\alpha$ /IL-4-stimulated BEAS-2B cells (Figure 3C).

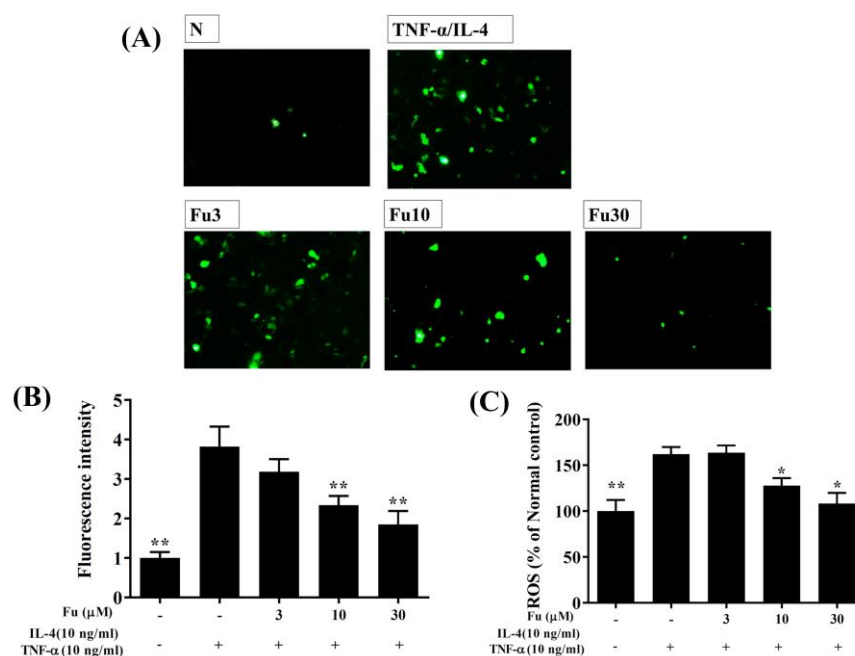


**Figure 3.** The effects of fucoxanthin (Fu) on ROS production in activated BEAS-2B cells. (A) Fluorescence microscopy images of intracellular ROS. (B) Fluorescence intensity of intracellular ROS. (C) Percentages of ROS detected in TNF- $\alpha$ /IL-4-activated BEAS-2B cells in the absence or presence of Fu compared to untreated cells (N). Three independent experiments were analyzed. Data are presented as mean  $\pm$  SEM. \*  $p < 0.05$ , \*\*  $p < 0.01$  compared to BEAS-2B cells stimulated with TNF- $\alpha$  and IL-4.

### 3.3. Fucoxanthin Attenuated AHR in Asthmatic Mice

The process of sensitization and asthma induction is shown in Figure 4A. Penh values can be used as indicators of AHR. Mice inhaled gradually increasing doses of methacholine (0–40 mg/mL) to assess whether fucoxanthin could recover airway function in an OVA-induced allergic asthma murine model. The Penh values significantly increased when OVA-sensitized mice inhaled gradually increasing doses of methacholine compared to normal mice (Figure 4B). Inhalation of high-dose methacholine (40 mg/mL), fucoxanthin treatment, or prednisolone treatment significantly reduced the Penh values compared to the OVA group ( $7.99 \pm 0.47$  vs.  $P: 4.10 \pm 0.18$ ,  $p < 0.01$ ; Fu10:  $6.08 \pm 0.46$ ,  $p < 0.05$ ; and Fu30:  $5.09 \pm 0.35$ ,  $p < 0.01$ ). Therefore, the experimental results confirmed that fucoxanthin can significantly decrease AHR in asthmatic mice.

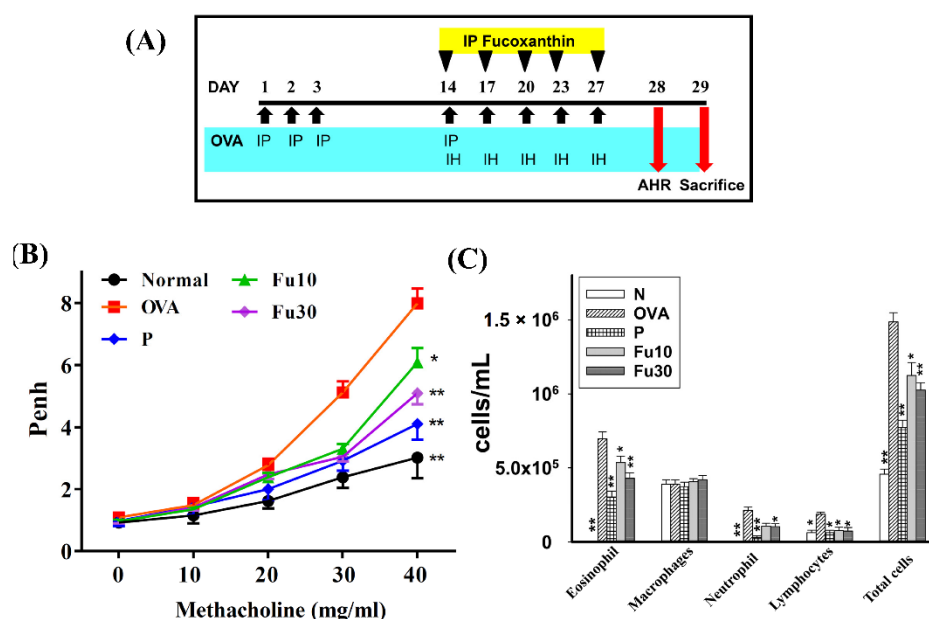


**Figure 4.** The effect of fucoxanthin (Fu) on AHR and cell counts in the BALF of asthmatic mice. (A) On days 1–3 and 14, the mice were sensitized with OVA via intraperitoneal injection (IP) and then challenged with 2% OVA inhalation (IH) on days 14, 17, 20, 23, and 27. One hour before the OVA challenge or methacholine inhalation, the mice were treated with fucoxanthin or DMSO ( $n = 10$  mice/group) via intraperitoneal injection. (B) The mice inhaled increasing doses of methacholine and AHR, assessed as Penh values. (C) The inflammatory cells in the BALF were measured. Three independent experiments were analyzed. Data are presented as mean  $\pm$  SEM. \*  $p < 0.05$ , \*\*  $p < 0.01$  compared to the OVA control group. 10 mg/kg and 30 mg/kg fucoxanthin were named as Fu10 and Fu30, respectively. 5 mg/kg prednisolone was named as P.

### 3.4. Fucoxanthin Inhibited Eosinophils in the BALF

Inflammatory cells in the BALF stained with Giemsa solution in the OVA group of asthmatic mice had higher numbers of eosinophils than normal mice. The OVA-sensitized asthmatic mice treated with fucoxanthin had significantly reduced numbers of eosinophils compared to the OVA control group. We also found that the total number of cells in asthmatic mice was significantly reduced after treatment with fucoxanthin (Fu10:  $1.13 \times 10^6 \pm 8.75 \times 10^4$ ,  $p < 0.01$ ; Fu30:  $1.02 \times 10^6 \pm 4.97 \times 10^4$ ,  $p < 0.01$ ) or prednisolone ( $7.72 \times 10^5 \pm 4.98 \times 10^4$ ,  $p < 0.01$ ) compared to the OVA control group ( $1.49 \times 10^6 \pm 6.21 \times 10^4$ ; Figure 4C).

### 3.5. Fucoxanthin Modulated Chemokine and Cytokine Expression in the BALF and Lung Tissue

In the BALF, fucoxanthin significantly inhibited the levels of TNF- $\alpha$ , IL-4, IL-5, IL-6, IL-13, CCL11, and CCL24 compared to the OVA-sensitized mice (Figure 5). Fucoxanthin

also resulted in significantly higher IFN- $\gamma$  expression in the BALF than in the OVA group (Figure 5D). In the lung tissues, fucoxanthin significantly suppressed MUC5AC, TNF- $\alpha$ , IL-6, IL-4, IL-5, IL-13, CCL11, and CCL-24 expression and significantly increased IFN- $\gamma$  expression compared to the OVA-sensitized asthmatic mice (Figure 6).

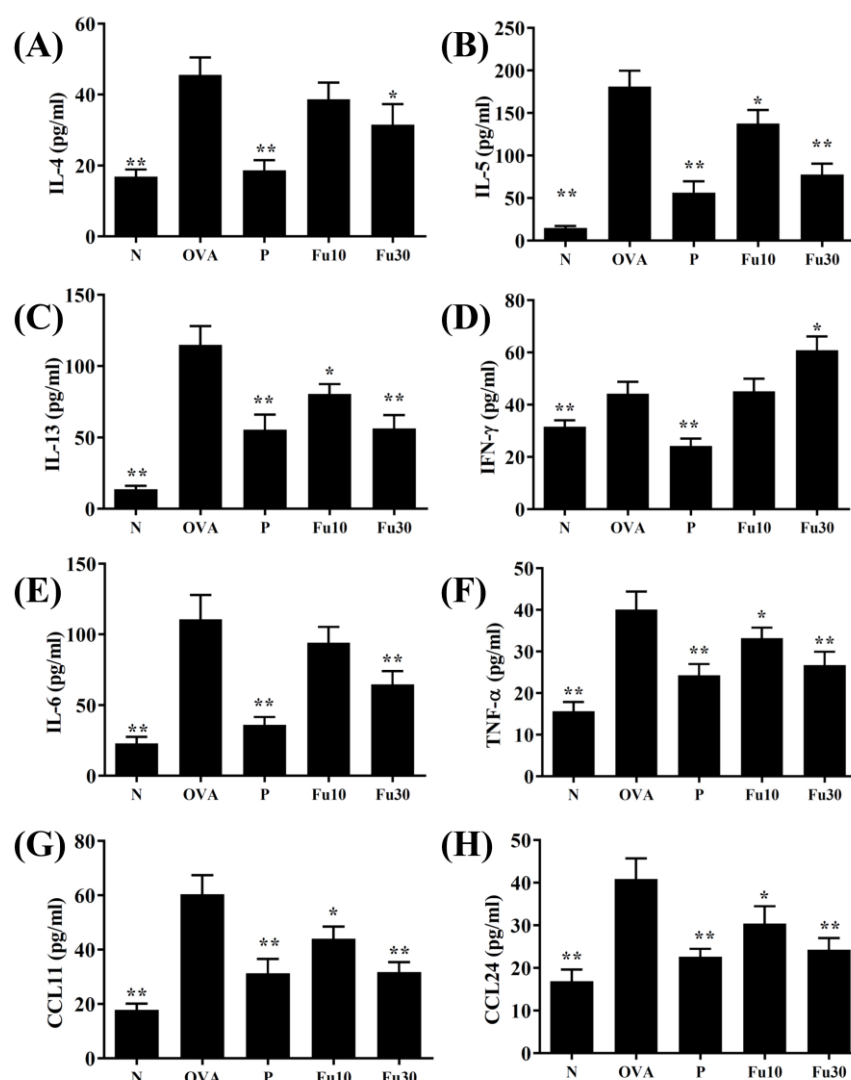


**Figure 5.** The effects of fucoxanthin (Fu) on the cytokine and chemokine levels in the BALF. (A) The concentrations of IL-4, (B) IL-5, (C) IL-13, (D) IFN- $\gamma$ , (E) IL-6, (F) TNF- $\alpha$ , (G) CCL11, and (H) CCL24 were measured by ELISA using BALF from normal (N) and OVA-stimulated (OVA) mice with or without Fu (10 or 30  $\mu$ M) treatment. Three independent experiments were analyzed. Data are presented as mean  $\pm$  SEM. \*  $p < 0.05$ , \*\*  $p < 0.01$  compared to the OVA control group. 10 mg/kg and 30 mg/kg fucoxanthin were named as Fu10 and Fu30, respectively. 5 mg/kg prednisolone was named as P.

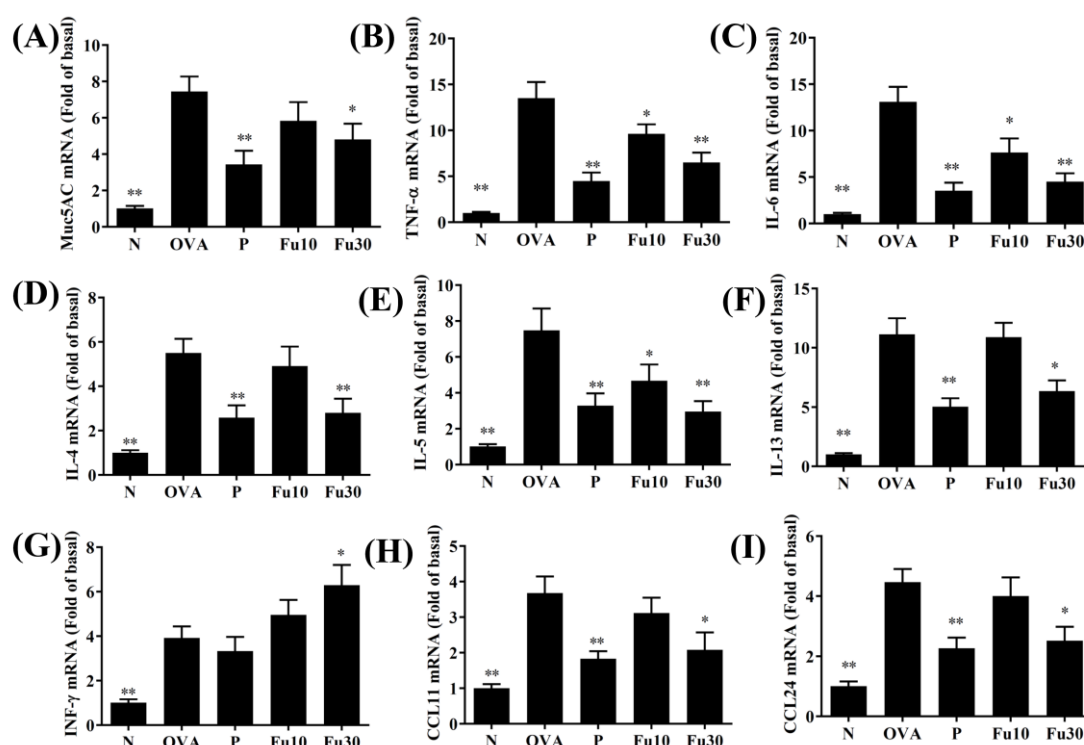


**Figure 6.** The effects of fucoxanthin (Fu) on cytokine, chemokine, and inflammatory mediator mRNA expression in the lungs. Gene expression levels were determined by the real-time RT-PCR of RNA extracted from the lung tissues of normal (N) and OVA-stimulated (OVA) mice with or without Fu (10 or 30  $\mu$ M) treatment. (A) Muc5AC, (B) TNF- $\alpha$ , (C) IL-6, (D) IL-4, (E) IL-5, (F) IL-13, (G) IFN- $\gamma$ , (H) CCL11, and (I) CCL24. Fold changes in expression were measured relative to  $\beta$ -actin (internal control). Three independent experiments were analyzed. Data are presented as mean  $\pm$  SEM. \*  $p < 0.05$ , \*\*  $p < 0.01$  compared to the OVA control group. 10 mg/kg and 30 mg/kg fucoxanthin were named as Fu10 and Fu30, respectively. 5 mg/kg prednisolone was named as P.

### 3.6. Fucoxanthin Reduced Goblet Cell Hyperplasia and Eosinophil Infiltration in Lung Tissue

HE staining demonstrated that OVA-sensitized mice treated with fucoxanthin or prednisolone had reduced eosinophil infiltration of the lungs compared to the OVA control group (Figure 7A). Thus, fucoxanthin and prednisolone significantly decreased the inflammatory pathology score in the OVA-sensitized asthmatic mice (Figure 7B). Goblet cells were detected in the trachea by PAS staining, and fucoxanthin or prednisolone treatment of the OVA-sensitized mice significantly reduced goblet cell hyperplasia compared to the OVA control group (Figure 7C,D).

### 3.7. Fucoxanthin Reduced Collagen and COX-2 Expression in the Lungs

Lung collagen accumulation was indicated by Masson's trichrome stain. Fucoxanthin decreased collagen expression in the lung tissues from asthmatic mice (Figure 7E,F). Moreover, fucoxanthin significantly decreased the gene expression of COX-2 in the lungs of OVA-sensitized mice (Figure 8A). Subsequently, immunohistochemical staining demonstrated that fucoxanthin could decrease COX-2 expression in the lung tissue compared to the OVA control group (Figure 8B).



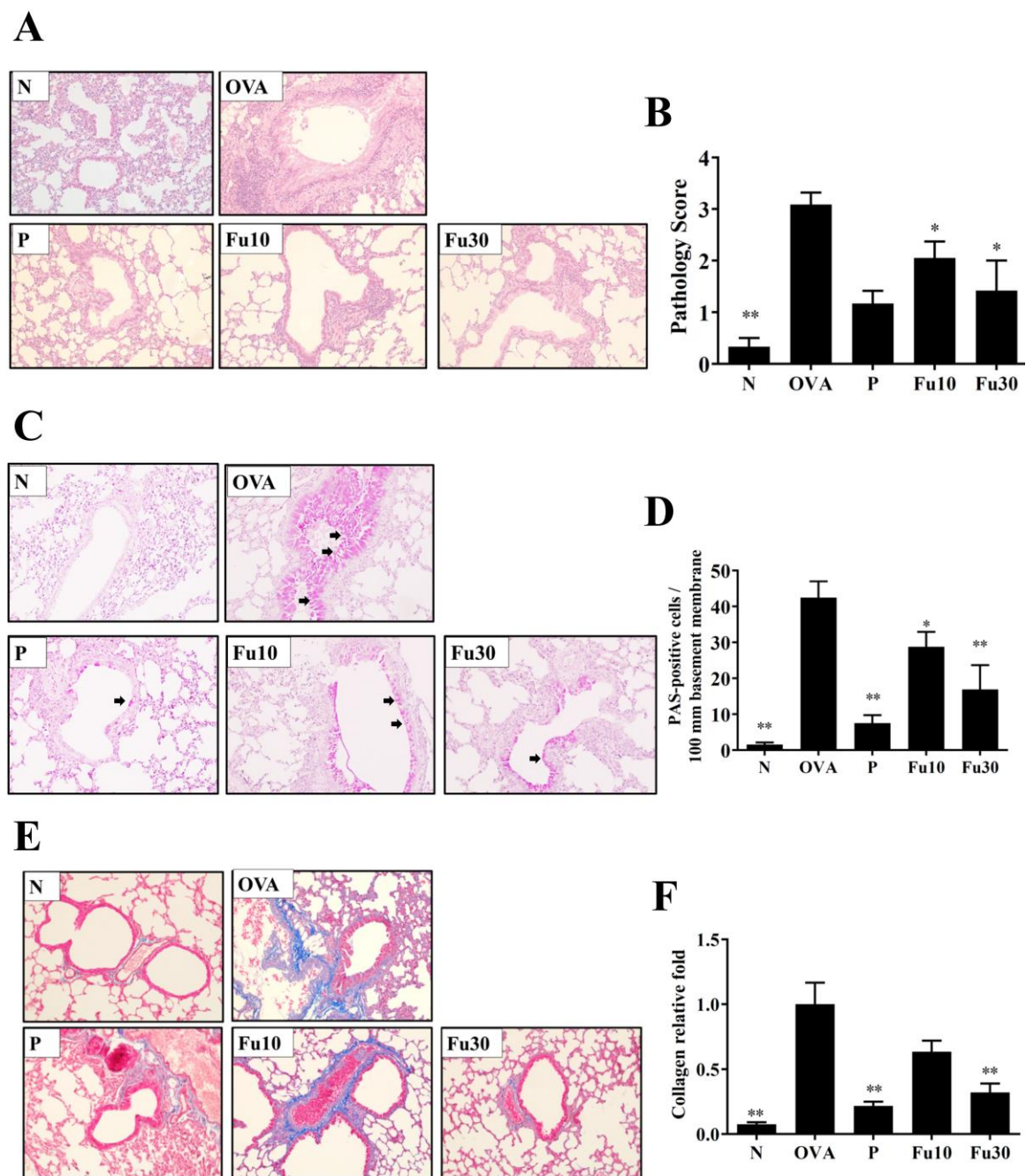


**Figure 7.** The effects of fucoxanthin (Fu) on asthmatic lung tissue. Histological sections of lung tissues from normal (N) and OVA-stimulated (OVA) mice with or without Fu (10 or 30  $\mu$ M) treatment. (A) Fu reduced eosinophil infiltration. HE stain, 200 $\times$  magnification. (B) Inflammation was scored by a pathological evaluation of inflammatory cell infiltration in lung sections. (C) PAS-stained lung sections show goblet cell hyperplasia. Goblet cells are indicated by arrows. 200 $\times$  magnification. (D) Results were expressed as the number of PAS-positive cells per 100  $\mu$ m of the basement membrane. (E) Lung sections were stained with Masson's trichrome stain to detect collagen expression. 200 $\times$  magnification. (F) Quantitative analysis of collagen in lung sections. Three independent experiments were analyzed. Data are presented as mean  $\pm$  SEM. \*  $p < 0.05$ , \*\*  $p < 0.01$  compared to the OVA control group. 10 mg/kg and 30 mg/kg fucoxanthin were named as Fu10 and Fu30, respectively. 5 mg/kg prednisolone was named as P.

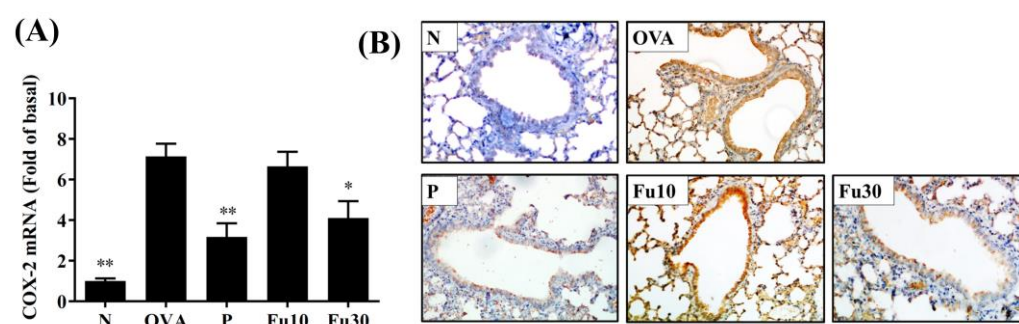


**Figure 8.** The effects of fucoxanthin (Fu) on COX-2 expression in the lung tissues from OVA-sensitized mice. **(A)** COX-2 gene expression was detected by real-time RT-PCR and fold-changes in expression measured relative to  $\beta$ -actin (internal control). **(B)** COX-2 expression was analyzed by immunohistochemistry staining and labeled as a brown colored drop. Three independent experiments were analyzed. Data are presented as mean  $\pm$  SEM. \*  $p < 0.05$ , \*\*  $p < 0.01$  compared to the OVA control group. 10 mg/kg and 30 mg/kg fucoxanthin were named as Fu10 and Fu30, respectively. 5 mg/kg prednisolone was named as P.

### 3.8. Fucoxanthin Modulated Antioxidant Enzyme Levels in the Lungs

Fucoxanthin significantly increased GSH, SOD, and CAT expression and decreased MDA activity in the lung tissues compared to the OVA-sensitized mice (Figure 9A–D).

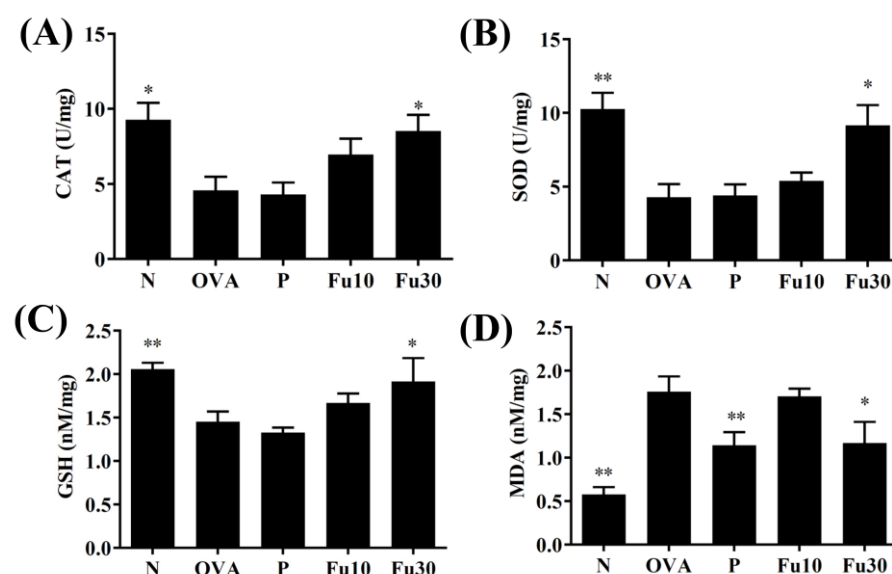


**Figure 9.** The effect of fucoxanthin (Fu) on oxidative stress factors. **(A)** CAT, **(B)** SOD, **(C)** GSH, and **(D)** MDA activity in the lung tissues from the mice. Three independent experiments were analyzed. Data are presented as mean  $\pm$  SEM. \*  $p < 0.05$ , \*\*  $p < 0.01$  compared to the OVA control group. 10 mg/kg and 30 mg/kg fucoxanthin were named as Fu10 and Fu30, respectively. 5 mg/kg prednisolone was named as P.

### 3.9. Fucoxanthin Modulated Serum Antibody and Splenocyte Cytokine Levels

In the serum from OVA-sensitized mice, fucoxanthin significantly decreased OVA-IgG1 and OVA-IgE and increased OVA-IgG2a levels (Figure 10A–C). In the supernatant from splenocyte cultures, fucoxanthin also clearly reduced IL-4, IL-5, and IL-13 expression and promoted IFN- $\gamma$  expression compared to OVA-sensitized mice (Figure 10D–G).

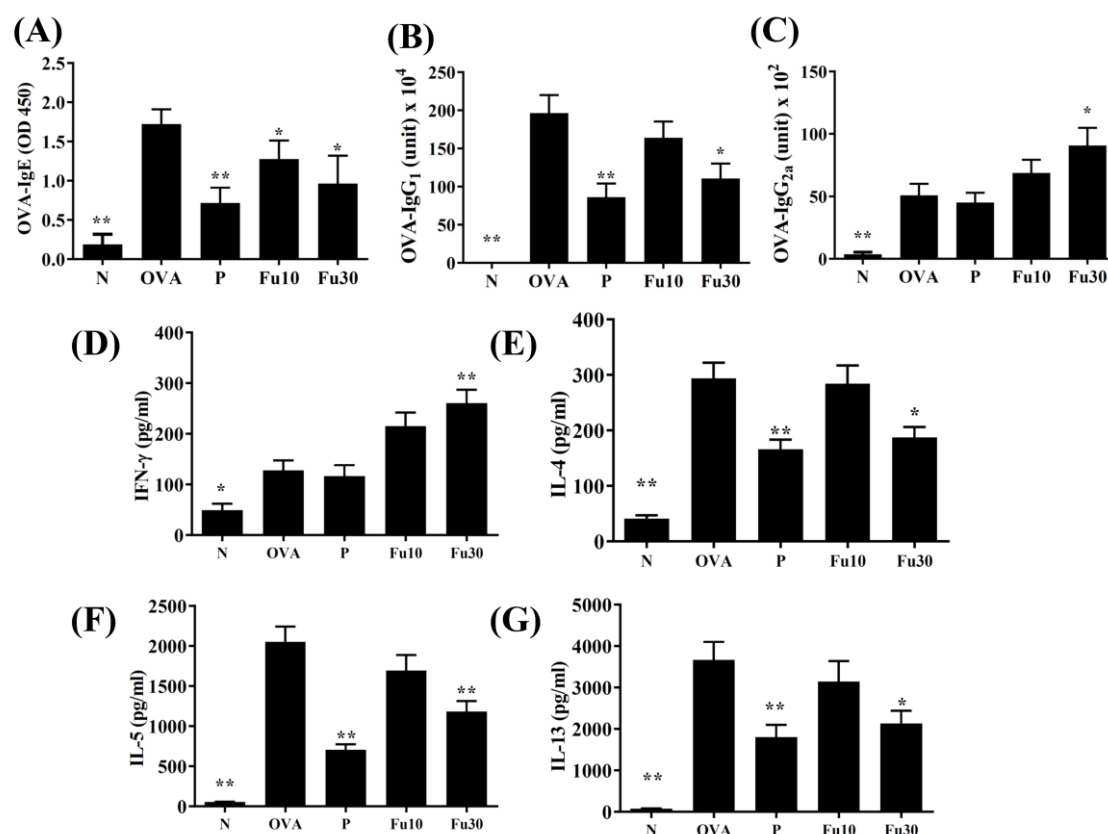


**Figure 10.** The Fucoxanthin (Fu) effects on OVA-specific antibodies in serum. The serum levels of (A) OVA-IgE, (B) OVA-IgG<sub>1</sub>, and (C) OVA-IgG<sub>2a</sub> are shown for normal (N) and OVA-stimulated (OVA) mice treated without or with prednisolone (P) or fucoxanthin (Fu10 and Fu30). Fu modulated the levels of (D) IFN-γ, (E) IL-4, (F) IL-5, and (G) IL-13 produced by OVA-activated splenocytes. All data are the means ± SEM. \*  $p < 0.05$ , \*\*  $p < 0.01$  compared to the OVA control group. 10 mg/kg and 30 mg/kg fucoxanthin were named as Fu10 and Fu30, respectively. 5 mg/kg prednisolone was named as P.

#### 4. Discussion

Brown seaweeds contain a variety of biologically active compounds, including polyphenols, omega-3 polyunsaturated fatty acids, fucosterol, fucoidan, and fucoxanthin [32]. Fucoxanthin is a carotenoid, an orange-red pigment found in the chloroplasts [16]. Recent studies have shown that fucoxanthin has anti-inflammatory, anti-oxidant, and anti-tumor effects in cell and animal experiments [15,18,20,33]. Fucoxanthin also inhibits the expression of inflammatory cytokines and inflammatory signaling molecules in LPS-induced macrophages, and can decrease oxygen-glucose deprivation and re-oxygenation-induced ROS expression in neurons [33]. Fucoxanthin could protect cerebral ischemic/reperfusion injury rats from nerve inflammation and oxidative stress by promoting the Nrf2/HO-1 signaling pathway [21]. Previous studies have shown that 50 mg/kg fucoxanthin can reduce the inflammatory cytokine levels in the BALF of mice [22]. Furthermore, in the mouse allergic rhinitis model induced by OVA, fucoxanthin treatment reduces the MDA levels in the nasal mucosa and serum, and reduces eosinophil infiltration in the nasal cavity [23]. However, whether fucoxanthin can improve lung inflammation and antioxidant effects in the tracheal epithelial cells and asthmatic mice is unclear. In addition, in the current study, the mice were treated with different doses of fucoxanthin for 7 consecutive days for animal toxicity testing, which demonstrated that daily administration of 100 mg/kg, 50 mg/kg, and 30 mg/kg fucoxanthin caused 37.5%, 12.5%, and 0% mortality, respectively (data not shown). We also found that the mice treated with 100 mg/kg and 50 mg/kg fucoxanthin by intraperitoneal injection had significantly lower activity and appetite than the normal mice and the mice treated with 30 mg/kg fucoxanthin (data not shown). Therefore, the animal experiments used 10 mg/kg or 30 mg/kg fucoxanthin to investigate whether fucoxanthin

can improve the asthma pathology in OVA-sensitized asthmatic mice. We also evaluated the molecular mechanism by which fucoxanthin reduces airway inflammation and oxidative stress in asthmatic mice and analyzed the effect of fucoxanthin on inflammation and oxidative stress in inflamed tracheal epithelial cells.

Our experiments used TNF- $\alpha$ /IL-4 to stimulate human tracheal epithelial cells, simulating lung inflammation immune cells that release TNF- $\alpha$  and IL-4 to induce tracheal epithelial cell activation. Under the protection of fucoxanthin treatment, we found that TNF- $\alpha$ /IL-4-stimulated BEAS-2B cells had reduced IL-6 secretion to inhibit the inflammatory response in the airways. Previous experiments in asthmatic animals have found that ROS can stimulate the activation of the airway and tracheal epithelial cells, and the release of more chemokines to attract inflammatory immune cell infiltration into the lungs for the release of more inflammatory mediators, causing lung cell damage and apoptosis [34,35]. In the current study, under the protection of fucoxanthin treatment, we found that TNF- $\alpha$ /IL-4-stimulation in BEAS-2B cells reduced the release of IL-8, MCP-1, and CCL5, which would contribute to a reduction in macrophage and neutrophil infiltration of the lungs as well as inflammation and oxidative damage in the lung tissue. Therefore, we think that fucoxanthin could inhibit the inflammation of tracheal epithelial cells to release more ROS and chemokines, reducing lung cell damage.

Asthma attacks are mainly induced by allergens or airway irritants to cause acute allergies and inflammatory reactions in the airways. However, chronic asthma is often caused by long-term allergic stimulation of the airways, causing inflammation and oxidative damage, and gradually weakening the physiological function of the respiratory system [36]. We found that fucoxanthin can reduce ROS levels in inflamed BEAS-2B cells, indicating that fucoxanthin can reduce oxidative damage to tracheal epithelial cells. In addition, fucoxanthin inhibited the expression of MCP-1, CCL5, and IL-8, which would suppress the migration of neutrophils or macrophages into the lungs. Therefore, we think that fucoxanthin can inhibit the activation of inflammatory tracheal epithelial cells and reduce ROS release and chemokine secretion in tracheal epithelial cells.

SOD, CAT, and GSH are common antioxidant enzymes that can reduce lung cell damage and fibrosis in the lungs of patients with COPD or asthma [37]. Lipid peroxidation is a danger signal of cell damage and would produce abundant MDA as a marker of oxidative stress in cells and tissues [38,39]. In the current study, fucoxanthin promoted SOD, CAT, and GSH expression and decreased MDA expression in the lungs of asthmatic mice (Figure 9). Thus, fucoxanthin could regulate and improve lung peroxidation in asthmatic mice. Previous studies found that fucoxanthin can enhance the Nrf2/HO-1 pathway to improve GSH and SOD expression and reduce brain damage in rat models of traumatic brain injury [21]. Therefore, fucoxanthin has a protective ability against oxidative stress for maintaining lung function in asthmatic mice.

AHR can detect the airflow and frequency of breathing, and has clinical value as an important indicator to evaluate lung function [40]. Previous studies have found that inflammation and oxidative stress stimulate excessive AHR and exacerbate the deterioration of lung function [41]. Allergens or respiratory irritants can induce excessive tracheal contraction and mucus hypersecretion in asthmatic patients, leading to airway obstruction and dyspnea during asthma attacks. Therefore, patients need to breathe more quickly to increase the rate of ventilation, resulting in an increased AHR value in patients with asthma [42]. We used whole body plethysmography to detect AHR in mice and demonstrated that fucoxanthin reduced the AHR and the breathing difficulties caused by rapid breathing in asthmatic mice. Many previous studies have pointed out that the lungs of asthmatic patients have increased IL-13 expression, and activated Th2 cells increase IL-13 secretion to promote AHR [43]. Our experiments showed that the lung tissues, BALF, and spleen cell culture medium for asthmatic mice had significantly reduced IL-13 levels and reduced AHR values after treatment with fucoxanthin (Figures 4–6 and 10). Therefore, our results confirmed that fucoxanthin mainly inhibited IL-13 production to reduce AHR in asthmatic mice.



Asthma patients have a lot of eosinophilic infiltration in the lungs and respiratory tract. Activated Th2 cells in the lungs of asthmatic patients release excess IL-5, which induces the differentiation of bone marrow cells to produce mature eosinophils [44]. In addition, tracheal epithelial cells from asthmatic patients release eotaxins (CCL11 and CCL24) to attract mature eosinophil migration into the lungs [45]. The activated eosinophils release a large amount of basic proteins, stimulate mast cell activation and degranulation, and release allergic mediators to cause allergic reactions in the lungs of asthmatic patients [5]. In addition, IL-4 could activate B-cell differentiation and secrete IgE to bind the FcεR1 of mast cells. After exposure to allergens, the mast cells are activated to release leukotrienes and histamine, causing respiratory sensitization and inflammation [46]. Therefore, fucoxanthin reduces the production of IL-4 and IgE by inhibiting Th2 cell activity, decreasing mast cell activation, and improving the pathological changes in bronchial asthma. Previous researchers have found that fucoxanthin can suppress the levels of histamine and total IgE in serum from allergic rhinitis mice [23]. In our asthmatic mouse model, the BALF and lungs expressed higher IL-5 and eotaxin levels than normal mice (Figures 5 and 6). Fucoxanthin has the ability to reduce IL-5 production to suppress eosinophil infiltration in the lungs of asthmatic mice. In addition, fucoxanthin inhibits CCL11 and CCL24 levels in tracheal epithelial cells and lung tissue, which reduces eosinophil migration into the lungs. Therefore, fucoxanthin could reduce the infiltration of eosinophils into the lungs and BALF of asthmatic mice.

THP-1 cells simulated the adherence of immune cells in the inflamed tracheal epithelial cell model. Fucoxanthin reduced the adherence of THP-1 cells to tracheal epithelial cells (Figure 2). We think that fucoxanthin could inhibit IL-5 secretion in the lung and BALF to reduce the inflammatory response of tracheal epithelial cells to release eotaxins.

The airway epithelial cells secreted appropriate glycoprotein mucus that could adhere to air pollution particles and microorganisms, reducing damage in the lungs and respiratory tract [9]. However, the airway remodeling in asthmatic patients leads to the thickening of the tracheal smooth muscle and the narrowing of the airways [4]. Induced by allergens or chemical stimuli, tracheal epithelial cells increase and differentiate into sensitive goblet cells. These goblet cells secrete excessive mucus and block the airways [47]. Our experiments used PAS staining to observe the goblet cell hyperplasia in asthmatic mice and demonstrated that fucoxanthin significantly reduces tracheal goblet cell hyperplasia and decreases Muc5Ac gene expression in the lungs of asthmatic mice (Figures 6 and 7). Therefore, fucoxanthin can reduce the symptoms of dyspnea caused by excessive secretion of respiratory mucus in asthmatic mice.

Previous studies found that IL-4 and IL-13 released by activated Th2 cells increase goblet cell proliferation in the tracheas of asthmatic mice [48]. However, fucoxanthin has the ability to reduce the expression of IL-4 and IL-13 in spleen cell culture medium, BALF, and lung tissue from asthmatic mice. Therefore, we think that fucoxanthin could reduce the secretion of IL-4 and IL-13 by Th2 cells to reduce the proliferation of goblet cells in the trachea and reduce the breathing difficulties caused by excessive mucus secretion.

Continued inflammation and oxidative damage will increase collagen deposition in the lungs and cause severe pulmonary fibrosis, worsening the respiratory physiology of the lungs [49]. The BALF and lungs of asthmatic patients have increased expression of TGF-β and lung tissue fibrosis [50]. Some studies have pointed out that IL-13 would also drive the expression of TGF-β, exacerbating lung fibrosis [5,51]. Anti-IL-13 (tralokinumab) can improve lung fibrosis in asthmatic patients [52]. In the current study, fucoxanthin significantly inhibited collagen deposition in the lungs of asthmatic mice (Figure 7). Therefore, we speculate that fucoxanthin improves pulmonary fibrosis and AHR in asthmatic mice by reducing the activity of IL-13.

## 5. Conclusions

Collectively, we confirmed that fucoxanthin significantly suppresses AHR, eosinophil infiltration, and mucus secretion by suppressing airway inflammation, oxidative stress,



and Th2 cytokine expression in asthmatic mice. Fucoxanthin also decreased ROS, pro-inflammatory cytokine, and eotaxin levels in BEAS-2B cells, and suppressed monocyte cell adherence to inflammatory BEAS-2B cells. Therefore, this study demonstrates that fucoxanthin has excellent potential for ameliorating or regulating inflammation and oxidative stress in asthma.

**Author Contributions:** Designed and performed the experiments: S.-J.W., C.-J.L., Y.-L.C., and W.-C.H.; Analysis and interpretation of data: C.-J.L. and S.-C.C.; Drafting the manuscript: S.-J.W., S.-C.C., and W.-C.H. All authors have read and agreed to the published version of the manuscript.

**Funding:** This study was supported in part by grants from Chang Gung Memorial Hospital (CMRPF1J0061, CMRPF1J0062, CMRPF1K0031, CMRPF1K0041, CMRPF1G0231, and CMRPF1G0232) and the Ministry of Science and Technology in Taiwan (109-2320-B-255-002-MY3 and 109-2320-B-255-008-MY3).

**Institutional Review Board Statement:** Animal experiments were approved and carried out in accordance with the guidelines from the Laboratory Animal Care Committee of Chang Gung University of Science and Technology (IACUC approval number: 2019-003).

**Informed Consent Statement:** Not applicable.

**Data Availability Statement:** The data presented in this study are available on request from the corresponding author.

**Conflicts of Interest:** The authors have no conflict of interest to declare.

## References








1. Nanda, A.; Wasan, A.N. Asthma in adults. *Med. Clin. N. Am.* **2020**, *104*, 95–108. [[CrossRef](#)] [[PubMed](#)]
2. Carpaij, O.A.; Burgess, J.K.; Kerstjens, H.A.M.; Nawijn, M.C.; van den Berge, M. A review on the pathophysiology of asthma remission. *Pharmacol. Ther.* **2019**, *201*, 8–24. [[CrossRef](#)] [[PubMed](#)]
3. Song, W.J.; Lee, J.H.; Kang, Y.; Joung, W.J.; Chung, K.F. Future risks in patients with severe asthma. *Allergy Asthma Immunol. Res.* **2019**, *11*, 763–778. [[CrossRef](#)] [[PubMed](#)]
4. Goleva, E.; Berdyshev, E.; Leung, D.Y. Epithelial barrier repair and prevention of allergy. *J. Clin. Investig.* **2019**, *129*, 1463–1474. [[CrossRef](#)]
5. Lambrecht, B.N.; Hammad, H.; Fahy, J.V. The cytokines of asthma. *Immunity* **2019**, *50*, 975–991. [[CrossRef](#)]
6. Coleman, J.M.; Naik, C.; Holguin, F.; Ray, A.; Ray, P.; Trudeau, J.B.; Wenzel, S.E. Epithelial eotaxin-2 and eotaxin-3 expression: Relation to asthma severity, luminal eosinophilia and age at onset. *Thorax* **2012**, *67*, 1061–1066. [[CrossRef](#)]
7. Symowski, C.; Voehringer, D. Th2 cell-derived IL-4/IL-13 promote ILC2 accumulation in the lung by ILC2-intrinsic STAT6 signaling in mice. *Eur. J. Immunol.* **2019**, *49*, 1421–1432. [[CrossRef](#)]
8. Bonser, L.R.; Erle, D.J. Airway mucus and asthma: The role of MUC5AC and MUC5B. *J. Clin. Med.* **2017**, *6*, 112. [[CrossRef](#)]
9. Roan, F.; Obata-Ninomiya, K.; Ziegler, S.F. Epithelial cell-derived cytokines: More than just signaling the alarm. *J. Clin. Investig.* **2019**, *129*, 1441–1451. [[CrossRef](#)]
10. Wadhwa, R.; Dua, K.; Adcock, I.M.; Horvat, J.C.; Kim, R.Y.; Hansbro, P.M. Cellular mechanisms underlying steroid-resistant asthma. *Eur. Respir. Rev.* **2019**, *28*, 190096. [[CrossRef](#)]
11. Rodriguez, J.M.; Monsalves-Alvarez, M.; Henriquez, S.; Llanos, M.N.; Troncoso, R. Glucocorticoid resistance in chronic diseases. *Steroids* **2016**, *115*, 182–192. [[CrossRef](#)] [[PubMed](#)]
12. Bielory, L. Complementary and alternative interventions in asthma, allergy, and immunology. *Ann. Allergy Asthma Immunol.* **2004**, *93*, S45–S54. [[CrossRef](#)]
13. Fouladi, S.; Masjedi, M.; Ganjalikhani Hakemi, M.; Eskandari, N. The review of in vitro and in vivo studies over the glycyrrhizic acid as natural remedy option for treatment of allergic asthma. *Iran. J. Allergy Asthma Immunol.* **2019**, *18*, 1–11. [[CrossRef](#)]
14. Li, J.; Zhang, F. The immunoregulatory effects of traditional chinese medicine on treatment of asthma or asthmatic inflammation. *Am. J. Chin. Med.* **2015**, *43*, 1059–1081. [[CrossRef](#)] [[PubMed](#)]
15. Bae, M.; Kim, M.B.; Park, Y.K.; Lee, J.Y. Health benefits of fucoxanthin in the prevention of chronic diseases. *Biochim. Biophys. Acta. Mol. Cell Biol. Lipids* **2020**, *10*, 158618. [[CrossRef](#)]
16. Muradian, K.; Vaiserman, A.; Min, K.J.; Fraifeld, V.E. Fucoxanthin and lipid metabolism: A minireview. *Nutr. Metab. Cardiovasc. Dis.* **2015**, *25*, 891–897. [[CrossRef](#)] [[PubMed](#)]
17. Gammone, M.A.; D’Orazio, N. Anti-obesity activity of the marine carotenoid fucoxanthin. *Mar. Drugs* **2015**, *13*, 2196–2214. [[CrossRef](#)]
18. Satomi, Y. Antitumor and cancer-preventative function of fucoxanthin: A marine carotenoid. *Anticancer Res.* **2017**, *37*, 1557–1562. [[CrossRef](#)]

19. Ma, S.Y.; Park, W.S.; Lee, D.S.; Choi, G.; Yim, M.J.; Lee, J.M.; Jung, W.K.; Park, S.G.; Seo, S.K.; Park, S.J.; et al. Fucoxanthin inhibits profibrotic protein expression in vitro and attenuates bleomycin-induced lung fibrosis in vivo. *Eur. J. Pharmacol.* **2017**, *811*, 199–207. [\[CrossRef\]](#)
20. Robertson, R.C.; Guihéneuf, F.; Bahar, B.; Schmid, M.; Stengel, D.B.; Fitzgerald, G.F.; Ross, R.P.; Stanton, C. The anti-inflammatory effect of algae-derived lipid extracts on lipopolysaccharide (LPS)-stimulated human THP-1 macrophages. *Mar. Drugs* **2015**, *13*, 5402–5424. [\[CrossRef\]](#)
21. Zhang, L.; Wang, H.; Fan, Y.; Gao, Y.; Li, X.; Hu, Z.; Ding, K.; Wang, Y.; Wang, X. Fucoxanthin provides neuroprotection in models of traumatic brain injury via the Nrf2-ARE and Nrf2-autophagy pathways. *Sci. Rep.* **2017**, *7*, 46763. [\[CrossRef\]](#)
22. Yang, X.; Guo, G.; Dang, M.; Yan, L.; Kang, X.; Jia, K.; Ren, H. Assessment of the therapeutic effects of fucoxanthin by attenuating inflammation in ovalbumin-induced asthma in an experimental animal model. *J. Environ. Pathol. Toxicol. Oncol.* **2019**, *38*, 229–238. [\[CrossRef\]](#) [\[PubMed\]](#)
23. Li, S.; Zhang, Y.; Veeraghavan, V.P.; Mohan, S.K.; Ma, Y. Restorative effect of fucoxanthin in an ovalbumin-induced allergic rhinitis animal model through NF- $\kappa$ B p65 and STAT3 signaling. *J. Environ. Pathol. Toxicol. Oncol.* **2019**, *38*, 365–375. [\[CrossRef\]](#) [\[PubMed\]](#)
24. Chang, Y.H.; Chen, Y.L.; Huang, W.C.; Liou, C.J. Fucoxanthin attenuates fatty acid-induced lipid accumulation in FL83B hepatocytes through regulated Sirt1/AMPK signaling pathway. *Biochem. Biophys. Res. Commun.* **2018**, *495*, 197–203. [\[CrossRef\]](#)
25. Huang, W.C.; Su, H.H.; Fang, L.W.; Wu, S.J.; Liou, C.J. Licochalcone A inhibits cellular motility by suppressing E-cadherin and MAPK signaling in breast cancer. *Cells* **2019**, *8*, 218. [\[CrossRef\]](#) [\[PubMed\]](#)
26. Liou, C.J.; Chen, Y.L.; Yu, M.C.; Yeh, K.W.; Shen, S.C.; Huang, W.C. Sesamol alleviates airway hyperresponsiveness and oxidative stress in asthmatic mice. *Antioxidants* **2020**, *9*, 295. [\[CrossRef\]](#)
27. Huang, W.C.; Liu, C.Y.; Shen, S.C.; Chen, L.C.; Yeh, K.W.; Liu, S.H.; Liou, C.J. Protective effects of licochalcone A improve airway hyper-responsiveness and oxidative stress in a mouse model of asthma. *Cells* **2019**, *8*, 617. [\[CrossRef\]](#)
28. Huang, W.C.; Fang, L.W.; Liou, C.J. Phloretin attenuates allergic airway inflammation and oxidative stress in asthmatic mice. *Front. Immunol.* **2017**, *8*, 134. [\[CrossRef\]](#)
29. Huang, W.C.; Chan, C.C.; Wu, S.J.; Chen, L.C.; Shen, J.J.; Kuo, M.L.; Chen, M.C.; Liou, C.J. Matrine attenuates allergic airway inflammation and eosinophil infiltration by suppressing eotaxin and Th2 cytokine production in asthmatic mice. *J. Ethnopharmacol.* **2014**, *151*, 470–477. [\[CrossRef\]](#)
30. Liou, C.J.; Cheng, C.Y.; Yeh, K.W.; Wu, Y.H.; Huang, W.C. Protective effects of casticin from *Vitex trifolia* alleviate eosinophilic airway inflammation and oxidative stress in a murine asthma model. *Front. Pharmacol.* **2018**, *9*, 635. [\[CrossRef\]](#)
31. Liou, C.J.; Huang, W.C. Dehydroepiandrosterone suppresses eosinophil infiltration and airway hyperresponsiveness via modulation of chemokines and Th2 cytokines in ovalbumin-sensitized mice. *J. Clin. Immunol.* **2011**, *31*, 656–665. [\[CrossRef\]](#)
32. Sanjeewa, K.K.A.; Kim, E.A.; Son, K.T.; Jeon, Y.J. Bioactive properties and potentials cosmeceutical applications of phlorotannins isolated from brown seaweeds: A review. *J. Photochem. Photobiol. B* **2016**, *162*, 100–105. [\[CrossRef\]](#)
33. Hu, L.; Chen, W.; Tian, F.; Yuan, C.; Wang, H.; Yue, H. Neuroprotective role of fucoxanthin against cerebral ischemic/reperfusion injury through activation of Nrf2/HO-1 signaling. *Biomed. Pharmacol.* **2018**, *106*, 1484–1489. [\[CrossRef\]](#) [\[PubMed\]](#)
34. Ma, Y.; Ge, A.; Zhu, W.; Liu, Y.N.; Ji, N.F.; Zha, W.J.; Zhang, J.X.; Zeng, X.N.; Huang, M. Morin attenuates ovalbumin-induced airway inflammation by modulating oxidative stress-responsive MAPK signaling. *Oxid. Med. Cell Longev.* **2016**, *2016*, 5843672. [\[CrossRef\]](#)
35. Kim, S.R.; Kim, D.I.; Kim, S.H.; Lee, H.; Lee, K.S.; Cho, S.H.; Lee, Y.C. NLRP3 inflammasome activation by mitochondrial ROS in bronchial epithelial cells is required for allergic inflammation. *Cell Death Dis.* **2014**, *5*, 460. [\[CrossRef\]](#) [\[PubMed\]](#)
36. Chen, X.; Corry, D.B.; Li, E. Mechanisms of allergy and adult asthma. *Curr. Opin. Allergy Clin. Immunol.* **2020**, *20*, 36–42. [\[CrossRef\]](#) [\[PubMed\]](#)
37. Rogers, L.K.; Cismowski, M.J. Oxidative stress in the lung—The essential paradox. *Curr. Opin. Toxicol.* **2018**, *7*, 37–43. [\[CrossRef\]](#) [\[PubMed\]](#)
38. Menzel, M.; Ramu, S.; Calven, J.; Olejnicka, B.; Sverrild, A.; Porsbjerg, C.; Tufvesson, E.; Bjermer, L.; Akbarshahi, H.; Uller, L. Oxidative stress attenuates TLR3 responsiveness and impairs anti-viral mechanisms in bronchial epithelial cells from COPD and asthma patients. *Front. Immunol.* **2019**, *10*, 2765. [\[CrossRef\]](#) [\[PubMed\]](#)
39. Araujo, J.A.; Zhang, M.; Yin, F. Heme oxygenase-1, oxidation, inflammation, and atherosclerosis. *Front. Pharmacol.* **2012**, *3*, 119. [\[CrossRef\]](#)
40. Charron, C.B.; Pakhalé, S. The role of airway hyperresponsiveness measured by methacholine challenge test in defining asthma severity in asthma-obesity syndrome. *Curr. Opin. Allergy Clin. Immunol.* **2016**, *16*, 218–223. [\[CrossRef\]](#)
41. McGovern, T.K.; Chen, M.; Allard, B.; Larsson, K.; Martin, J.G.; Adner, M. Neutrophilic oxidative stress mediates organic dust-induced pulmonary inflammation and airway hyperresponsiveness. *Am. J. Physiol. Lung Cell Mol. Physiol.* **2016**, *310*, 6. [\[CrossRef\]](#) [\[PubMed\]](#)
42. Nair, P.; Martin, J.G.; Cockcroft, D.C.; Dolovich, M.; Lemiere, C.; Boulet, L.P.; O’Byrne, P.M. Airway hyperresponsiveness in asthma: Measurement and clinical relevance. *J. Allergy Clin. Immunol. Pr.* **2017**, *5*, 649–659 e642. [\[CrossRef\]](#) [\[PubMed\]](#)
43. Chen, W.; Sivaprasad, U.; Gibson, A.M.; Ericksen, M.B.; Cunningham, C.M.; Bass, S.A.; Kinker, K.G.; Finkelman, F.D.; Wills-Karp, M.; Khurana Hershey, G.K. IL-13 receptor  $\alpha$ 2 contributes to development of experimental allergic asthma. *J. Allergy Clin. Immunol.* **2013**, *132*, 951–958 e951–956. [\[CrossRef\]](#)

44. Chow, K.; Cosetti, M.K. Use of IL-5 inhibitor benralizumab as a novel therapy for eosinophilic otitis media: Clinical capsule and review of literature. *Otol. Neurotol.* **2020**, *41*, e238–e240. [[CrossRef](#)] [[PubMed](#)]
45. Teixeira, A.L.; Gama, C.S.; Rocha, N.P.; Teixeira, M.M. Revisiting the role of eotaxin-1/CCL11 in psychiatric disorders. *Front. Psychiatry* **2018**, *9*, 241. [[CrossRef](#)] [[PubMed](#)]
46. Caminati, M.; Pham, D.L.; Bagnasco, D.; Canonica, G.W. Type 2 immunity in asthma. *World Allergy Organ. J.* **2018**, *11*, 13. [[CrossRef](#)]
47. Persson, C. Airways exudation of plasma macromolecules: Innate defense, epithelial regeneration, and asthma. *J. Allergy Clin. Immunol.* **2019**, *143*, 1271–1286. [[CrossRef](#)] [[PubMed](#)]
48. Moran, A.; Pavord, I.D. Anti-IL-4/IL-13 for the treatment of asthma: The story so far. *Expert. Opin. Biol.* **2020**, *20*, 283–294. [[CrossRef](#)]
49. Kudo, M.; Ishigatsubo, Y.; Aoki, I. Pathology of asthma. *Front. Microbiol.* **2013**, *4*, 263. [[CrossRef](#)]
50. Stewart, A.G.; Thomas, B.; Koff, J. TGF-beta: Master regulator of inflammation and fibrosis. *Respirology (Carltonvic)* **2018**, *23*, 1096–1097. [[CrossRef](#)]
51. Royce, S.G.; Cheng, V.; Samuel, C.S.; Tang, M.L. The regulation of fibrosis in airway remodeling in asthma. *Mol. Cell Endocrinol.* **2012**, *351*, 167–175. [[CrossRef](#)] [[PubMed](#)]
52. Russell, R.J.; Chachi, L.; FitzGerald, J.M.; Backer, V.; Olivenstein, R.; Titlestad, I.L.; Ulrik, C.S.; Harrison, T.; Singh, D.; Chaudhuri, R.; et al. Effect of tralokinumab, an interleukin-13 neutralising monoclonal antibody, on eosinophilic airway inflammation in uncontrolled moderate-to-severe asthma (MESOS): A multicentre, double-blind, randomised, placebo-controlled phase 2 trial. *Lancet Respir. Med.* **2018**, *6*, 499–510. [[CrossRef](#)]

## Article

# Anti-Allergic, Anti-Inflammatory, and Anti-Hyperglycemic Activity of *Chasmanthe aethiopica* Leaf Extract and Its Profiling Using LC/MS and GLC/MS

Iriny M. Ayoub <sup>1</sup> , Michal Korinek <sup>2,3,4,5</sup> , Mohamed El-Shazly <sup>1,6</sup>, Bernhard Wetterauer <sup>7</sup>, Hesham A. El-Beshbishy <sup>8,9</sup> , Tsong-Long Hwang <sup>4,5,10</sup> , Bing-Hung Chen <sup>3</sup>, Fang-Rong Chang <sup>2,11,12,13,\*</sup> , Michael Wink <sup>7,\*</sup> , Abdel Nasser B. Singab <sup>1,14,\*</sup> and Fadia S. Youssef <sup>1</sup> 

- <sup>1</sup> Department of Pharmacognosy, Faculty of Pharmacy, Ain Shams University, Abbassia, Cairo 11566, Egypt; irinyayoub@pharma.asu.edu.eg (I.M.A.); mohamed.elshazly@pharma.asu.edu.eg (M.E.-S.); fadiayoussef@pharma.asu.edu.eg (F.S.Y.)
- <sup>2</sup> Graduate Institute of Natural Products, College of Pharmacy, Kaohsiung Medical University, Kaohsiung 80708, Taiwan; mickorinek@hotmail.com
- <sup>3</sup> Department of Biotechnology, College of Life Science, Kaohsiung Medical University, Kaohsiung 80708, Taiwan; bhchen@kmu.edu.tw
- <sup>4</sup> Graduate Institute of Natural Products, College of Medicine, Chang Gung University, Taoyuan 33302, Taiwan; htl@mail.cgu.edu.tw
- <sup>5</sup> Research Center for Chinese Herbal Medicine, Research Center for Food and Cosmetic Safety, and Graduate Institute of Health Industry Technology, College of Human Ecology, Chang Gung University of Science and Technology, Taoyuan 33302, Taiwan
- <sup>6</sup> Department of Pharmaceutical Biology, Faculty of Pharmacy and Biotechnology, German University in Cairo, Cairo 11835, Egypt
- <sup>7</sup> Institute of Pharmacy and Molecular Biotechnology, Heidelberg University, INF 364, D-69120 Heidelberg, Germany; bernhard.wetterauer@uni-heidelberg.de
- <sup>8</sup> Medical Laboratory Sciences Department, Fakeeh College for Medical Sciences, Jeddah 21461, Saudi Arabia; hesham\_elbeshbishy@hotmail.com
- <sup>9</sup> Biochemistry and Molecular Biology Department, Faculty of Pharmacy, Al-Azhar University, Nasr City, Cairo 11231, Egypt
- <sup>10</sup> Department of Anesthesiology, Chang Gung Memorial Hospital, Taoyuan 33302, Taiwan
- <sup>11</sup> Drug Development and Value Creation Research Center, Kaohsiung Medical University, Kaohsiung 80708, Taiwan
- <sup>12</sup> Department of Medical Research, Kaohsiung Medical University Hospital, Kaohsiung Medical University, Kaohsiung 80708, Taiwan
- <sup>13</sup> Department of Marine Biotechnology and Resources, National Sun Yat-sen University, Kaohsiung 80424, Taiwan
- <sup>14</sup> Center for Drug Discovery Research and Development, Faculty of Pharmacy, Ain Shams University, Abbassia, Cairo 11566, Egypt
- \* Correspondence: aaronfrc@kmu.edu.tw (F.-R.C.); wink@uni-heidelberg.de (M.W.); dean@pharma.asu.edu.eg (A.N.B.S.)



**Citation:** Ayoub, I.M.; Korinek, M.; El-Shazly, M.; Wetterauer, B.; El-Beshbishy, H.A.; Hwang, T.-L.; Chen, B.-H.; Chang, F.-R.; Wink, M.; Singab, A.N.B.; et al. Anti-Allergic, Anti-Inflammatory, and Anti-Hyperglycemic Activity of *Chasmanthe aethiopica* Leaf Extract and Its Profiling Using LC/MS and GLC/MS. *Plants* **2021**, *10*, 1118. <https://doi.org/10.3390/plants10061118>

Academic Editors: Rodica-Mihaela Dinică and Bianca Furdui

Received: 6 May 2021

Accepted: 28 May 2021

Published: 31 May 2021

**Publisher's Note:** MDPI stays neutral with regard to jurisdictional claims in published maps and institutional affiliations.



**Copyright:** © 2021 by the authors. Licensee MDPI, Basel, Switzerland. This article is an open access article distributed under the terms and conditions of the Creative Commons Attribution (CC BY) license (<https://creativecommons.org/licenses/by/4.0/>).

**Abstract:** This study aims to comprehensively explore the phytoconstituents as well as investigate the different biological activities of *Chasmanthe aethiopica* (Iridaceae) for the first time. Metabolic profiling of the leaf methanol extract of *C. aethiopica* (CAL) was carried out using HPLC-PDA-ESI-MS/MS. Twenty-nine compounds were annotated belonging to various phytochemical classes including organic acids, cinnamic acid derivatives, flavonoids, isoflavonoids, and fatty acids. Myricetin-3-O-rhamnoside was the major compound identified. GLC/MS analysis of the *n*-hexane fraction (CAL-A) resulted in the identification of 45 compounds with palmitic acid (16.08%) and methyl hexadecanoic acid ester (11.91%) representing the major constituents. CAL-A exhibited a potent anti-allergic activity as evidenced by its potent inhibition of  $\beta$ -hexosaminidase release triggered by A23187 and IgE by 72.7% and 48.7%, respectively. Results were comparable to that of dexamethasone (10 nM) in the A23187 degranulation assay showing 80.7% inhibition for  $\beta$ -hexosaminidase release. Both the *n*-hexane (CAL-A) and dichloromethane (CAL-B) fractions exhibited potent anti-inflammatory activity manifested by the significant inhibition of superoxide anion generation and prohibition of elastase release. CAL showed anti-hyperglycemic activity in vivo using streptozotocin-induced

diabetic rat model by reducing fasting blood glucose levels (FBG) by 53.44% as compared with STZ-treated rats along with a substantial increase in serum insulin by 22.22%. Molecular modeling studies indicated that dicaffeoylquinic acid showed the highest fitting with free binding energies ( $\Delta G$ ) of  $-47.24$  and  $-60.50$  Kcal/mol for human  $\alpha$ -amylase and  $\alpha$ -glucosidase, respectively confirming its anti-hyperglycemic activity. Thus, *C. aethiopica* leaf extract could serve as an effective antioxidant natural remedy combating inflammation, allergy, and hyperglycemia.

**Keywords:** anti-allergic; antihyperglycemic; *Chasmanthe aethiopica*; anti-inflammatory; GC/MS; LC/MS

## 1. Introduction

Oxidative stress can be defined as the disturbance in the balance between antioxidants and free radicals within the body that leads to cell and tissue destruction. During the normal process of metabolism, the body releases free radicals with the concomitant production of natural antioxidants to antagonize and neutralize these free radicals. However, a multitude of factors results in the massive production of free radicals that exaggerates oxidative stress including the unhealthy diet and lifestyle, environmental factors such as exposure to radiation and pollution as well as the natural body immune response that temporarily contributes to oxidative stress [1]. Oxidative stress can provoke an inflammation that consequently releases excess free radicals that in turn promote more oxidative stress resulting in a vicious cycle. Chronic exposure to inflammation because of oxidative stress can elicit various human ailments such as diabetes mellitus, allergy, and cardiovascular disease in addition to cancer, and neurodegenerative disorders [2]. ROS can oxidize guanosine in DNA to 8-oxoguanosine which can lead to mutations and in consequence the genetic diseases such as cancer.

Diabetes mellitus has been recently considered the third leading cause of death following cancer and cardiovascular disorders with high prevalence all over the globe [3]. It adversely affects human health causing serious harmful changes in all parts of the body particularly the nerves and blood vessels [4]. Allergy is another global health threat that is also triggered by oxidative stress. It can threaten life in cases of severe asthma and anaphylaxis and can also interfere with the quality of life in cases of chronic allergic conditions exemplified by allergic rhinitis and eczema [5]. Despite the presence of numerous synthetic agents that could alleviate inflammation, relieve allergy, or manipulate hyperglycemia, drugs of natural origin always constitute the main key player in curing various human ailments due to their acceptable prices and safety in comparison with synthetic agents [6].

*Chasmanthe aethiopica* (Iridaceae) (syn. *Antholyza aethiopica* L.) is native to South Africa and is characterized by being a deciduous, bulbous plant that grows up to a height of 0.6 m with pale green lanceolate leaves [7]. Although members of family Iridaceae are popular by the presence of a wide array of compounds represented by flavonoids, isoflavonoids, xanthenes, and quinones to which numerous biological activities including antioxidant, anti-inflammatory, antidiabetic, and phytoestrogenic effects are attributed [8,9], nothing was found in the literature regarding the phytochemical profile or the biological potential of *C. aethiopica*.

This study aims to comprehensively study the phytoconstituents as well as biologically investigate the different activities of the plant for the first time. Herein, we evaluated the anti-allergic and anti-inflammatory activity of the 80% methanol leaf extract of *C. aethiopica* (CAL) as well as its successive fractions in vitro. Additionally, the antihyperglycemic potential of CAL was assessed using streptozotocin-induced diabetes in a rat model. Moreover, metabolic profiling of CAL and its bioactive fractions was performed using LC/MS (Liquid Chromatography coupled with Mass Spectrometry) and GLC/MS (Gas-Liquid Chromatography coupled with Mass Spectrometry). To understand the reasons behind the antihyperglycemic activity, molecular modeling experiments were performed



on the identified compounds from the bioactive fractions using human  $\alpha$ -glucosidase and  $\alpha$ -amylase, as crucial enzymes entangled in the occurrence and dissemination of diabetes.

## 2. Results and Discussion

### 2.1. Gas–Liquid Chromatography Coupled with Mass Spectroscopy (GLC-MS) Analysis

Characterization of the *n*-hexane fraction (CAL-A) of the leaf methanol extract (CAL) of *C. aethiopica* using GLC analysis (Figure 1) resulted in the tentative identification of 45 compounds belonging to sterols and fatty acids accounting for 91.62% of the total *n*-hexane fraction constituents as illustrated in Table 1. Palmitic acid (16.08 %) and methyl hexadecanoic acid ester (11.91%) represent the major constituents in the CAL-A fraction.

**Table 1.** Chemical profile of *C. aethiopica* L. *n*-hexane fraction (CAL-A) by GLC-MS.

No.	Rt	Compound Name	RI <sub>Exp.</sub> <sup>a</sup>	RI <sub>Lit.</sub> <sup>b</sup>	Content%	Molecular Formula	Identification <sup>c</sup>
1.	31.44	Methyl pentadecanoic acid ester	1806	1812	0.15	C <sub>16</sub> H <sub>32</sub> O <sub>2</sub>	MS, RI
2.	31.68	Neophytadiene	1818	1817	0.50	C <sub>20</sub> H <sub>38</sub>	MS, RI
3.	31.85	Hexahydrofarnesyl acetone	1826	1825	5.30	C <sub>18</sub> H <sub>36</sub> O	MS, RI
4.	33.47	7-Hexadecenoic acid methyl ester (Z)	1903	1900	0.68	C <sub>17</sub> H <sub>34</sub> O <sub>2</sub>	MS, RI
5.	33.54	Hexadecanoic acid methyl ester	1907	1907	11.91	C <sub>17</sub> H <sub>34</sub> O <sub>2</sub>	MS, RI
6.	34.45	Palmitic acid	1950	1950	16.08	C <sub>16</sub> H <sub>32</sub> O <sub>2</sub>	MS, RI
7.	34.99	Heptadecanoic acid methyl ester	1976	1978	0.14	C <sub>18</sub> H <sub>36</sub> O <sub>2</sub>	MS, RI
8.	35.55	15-Methyl hexadecanoic acid methyl ester	2003	1996	0.52	C <sub>18</sub> H <sub>36</sub> O <sub>2</sub>	MS, RI
9.	36.77	16-Methyl heptadecanoic acid methyl ester	2070	2077	0.25	C <sub>19</sub> H <sub>38</sub> O <sub>2</sub>	MS, RI
10.	36.90	Linoleic acid methyl ester	2077	2075	2.42	C <sub>19</sub> H <sub>34</sub> O <sub>2</sub>	MS, RI
11.	37.03	Oleic acid methyl ester	2085	2085	4.10	C <sub>19</sub> H <sub>36</sub> O <sub>2</sub>	MS, RI
12.	37.25	Phytol	2096	2096	1.50	C <sub>20</sub> H <sub>40</sub> O	MS, RI
13.	37.48	Methyl stearate	2109	2109	2.08	C <sub>19</sub> H <sub>38</sub> O <sub>2</sub>	MS, RI
14.	37.89	Linolenic acid	2131	2134	3.74	C <sub>18</sub> H <sub>30</sub> O <sub>2</sub>	MS, RI
15.	38.24	Stearic acid	2150	2155	0.83	C <sub>18</sub> H <sub>36</sub> O <sub>2</sub>	MS, RI
16.	41.08	Eicosanoic acid methyl ester	2306	2307	0.57	C <sub>21</sub> H <sub>42</sub> O <sub>2</sub>	MS, RI
17.	41.62	4,8,12,16-Tetramethylheptadecan-4-olide	2336	2364	1.99	C <sub>21</sub> H <sub>40</sub> O <sub>2</sub>	MS
18.	42.84	2,2'-Methylene-bis-(6-tert butyl-4-methylphenol)	2403	2398	0.13	C <sub>23</sub> H <sub>32</sub> O <sub>2</sub>	MS, RI
19.	43.86	<i>n</i> -Pentacosane	2469	2500	1.46	C <sub>25</sub> H <sub>52</sub>	MS
20.	44.22	Palmitic acid $\beta$ -monoglyceride	2492	2498	0.16	C <sub>19</sub> H <sub>38</sub> O <sub>4</sub>	MS, RI
21.	44.41	Docosanoic acid methyl ester	2504	2492	0.40	C <sub>23</sub> H <sub>46</sub> O <sub>2</sub>	MS, RI
22.	45.44	Behenic acid methyl ester	2570	2565	1.99	C <sub>26</sub> H <sub>54</sub>	MS, RI
23.	45.97	Tricosanoic acid methyl ester	2605	2615	0.05	C <sub>24</sub> H <sub>48</sub> O <sub>2</sub>	MS, RI
24.	46.95	2-Methylhexacosane	2668	2663	2.41	C <sub>27</sub> H <sub>56</sub>	MS, RI
25.	47.49	Tetracosanoic acid methyl ester	2702	2714	0.14	C <sub>25</sub> H <sub>50</sub> O <sub>2</sub>	MS, RI
26.	48.42	2-Methylheptacosane	2762	2762	2.47	C <sub>28</sub> H <sub>58</sub>	MS
27.	49.43	$\alpha$ -Tocospiro A	2827	2860	4.13	C <sub>29</sub> H <sub>50</sub> O <sub>4</sub>	MS
28.	49.74	$\alpha$ -Tocospiro B	2847	2881	4.62	C <sub>29</sub> H <sub>50</sub> O <sub>4</sub>	MS
29.	49.83	2-Methyl octacosane,	2852	2857	3.57	C <sub>29</sub> H <sub>60</sub>	MS, RI
30.	50.20	Cholesta-2,4-diene	2876	2872	0.09	C <sub>27</sub> H <sub>44</sub>	MS, RI
31.	51.19	15-Methylnonacosane	2940	2935	2.05	C <sub>30</sub> H <sub>62</sub>	MS, RI
32.	52.51	<i>n</i> -Triacotane	3025	3003	2.02	C <sub>30</sub> H <sub>62</sub>	MS, RI
33.	52.94	$\beta$ -Sitosterol propionate	3053	-	1.77	C <sub>32</sub> H <sub>54</sub> O <sub>2</sub>	MS
34.	53.31	$\alpha$ -Tocopherol	3076	3112	1.76	C <sub>29</sub> H <sub>50</sub> O <sub>2</sub>	MS
35.	53.84	Hentriacontane	3110	3103	1.33	C <sub>31</sub> H <sub>64</sub>	MS, RI
36.	55.31	Dotriacontane	3205	3202	0.64	C <sub>32</sub> H <sub>66</sub>	MS, RI
37.	56.36	Chondrillasterol	3272	3295	1.54	C <sub>29</sub> H <sub>48</sub> O	MS, RI
38.	57.16	$\beta$ -Amyrin	3323	3337	0.42	C <sub>30</sub> H <sub>50</sub> O	MS, RI
39.	57.43	$\gamma$ -Sitosterol	3341	3351	0.17	C <sub>29</sub> H <sub>50</sub> O	MS, RI
40.	58.06	$\alpha$ -Amyrin	3381	3376	1.53	C <sub>30</sub> H <sub>50</sub> O	MS, RI
41.	58.23	Stigmasta-3,5-dien-7-one	3392	-	0.29	C <sub>29</sub> H <sub>46</sub> O	MS
42.	59.07	$\beta$ -Amyrin acetate	3446	3438	0.76	C <sub>32</sub> H <sub>52</sub> O <sub>2</sub>	MS, RI
43.	60.05	Lupeol acetate	3509	3525	0.64	C <sub>32</sub> H <sub>52</sub> O <sub>2</sub>	MS, RI
44.	60.42	Hexadecanoic acid, 3,7,11,15-tetramethyl-2-hexadecenyl ester	3533	3568	2.32	C <sub>36</sub> H <sub>70</sub> O <sub>2</sub>	MS, RI
Total identified (%)					91.62		

<sup>a</sup> Retention index determined experimentally on RTX-5MS column relative to *n*-alkane series (C8–C28), <sup>b</sup> Published retention indices,

<sup>c</sup> Identification was based on comparison of mass spectral data (MS) and retention indices (RI) with those of NIST Mass Spectral Library (2017), Wiley Registry of Mass Spectral Data 8th edition and literature.

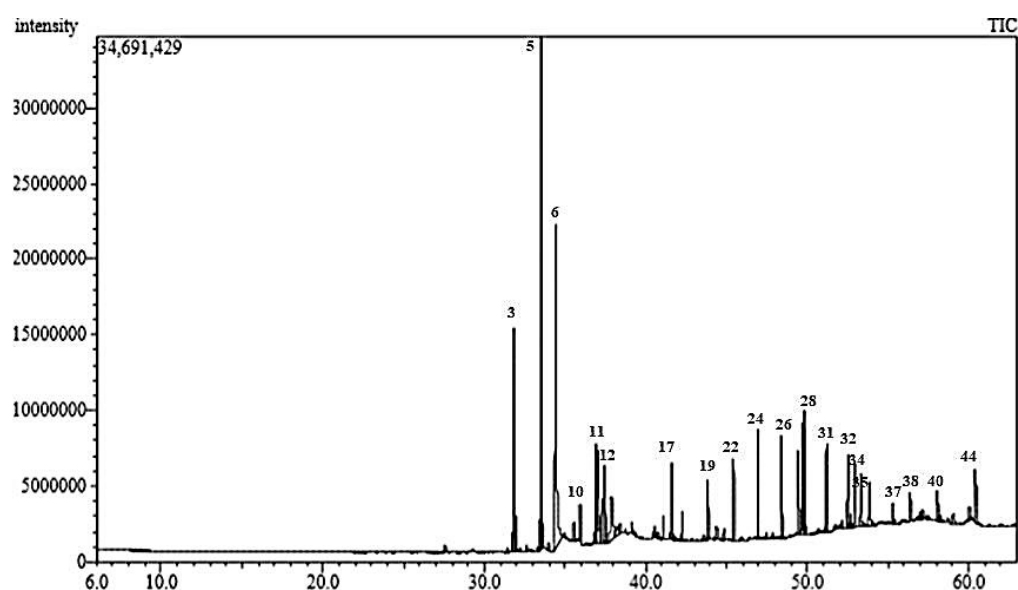


Figure 1. GLC-chromatogram of *C. aethiopica* L. *n*-hexane fraction (CAL-A) on Rtx-5MS column.

## 2.2. HPLC-PDA-ESI-MS/MS Analysis for Characterization of *C. aethiopica* Methanol Extract

Metabolite profiling of *C. aethiopica* total leaf extract (CAL) was carried out using HPLC-PDA-ESI-MS/MS analysis. A total of 29 chromatographic peaks were annotated using simultaneously acquired HPLC-PDA, and HPLC-MS base peak chromatograms (Figure 2). Tentative metabolite assignments were achieved by comparison of mass and UV spectral data of the detected compounds in both negative and positive ionization modes with reported data alongside online public databases. The identified secondary metabolites are listed in Table 2 along with their spectroscopic data. Compounds were illustrated in Figure 3. Several classes of compounds were identified in *C. aethiopica* total leaf extract including organic acids, cinnamic acid derivatives, flavonoids, isoflavonoids, and fatty acids. Flavonoids represented the most abundant class of metabolites detected in CAL. This is the first comprehensive metabolites profiling of genus *Chasmanthe* using HPLC-ESI-MS.

### 2.2.1. Flavonoids

Flavonols, mainly myricetin, in addition to several distinct flavones, markedly tricetin and 6-hydroxyluteolin derivatives, were reported in Ixieae as important chemotaxonomic markers [10,11]. In the current study, tricetin-*O*-rhamnoside (12), myricetin-3-*O*-rhamnoside (15), myricetin (16), 6-hydroxyluteolin-*O*-rhamnoside (18), and 6-hydroxyluteolin (19) were identified in *C. aethiopica* methanol extract. A mass loss of 308 amu suggested a loss of 6-rhamnosylhexose (rutinose) or a *p*-coumaroylhexose. However, acylation with *p*-coumaric acid results in a typical bathochromic shift in band I to  $\lambda_{\max}$  of 310–316 nm in the ultraviolet/visible (UV-VIS) spectra of flavonols and a pseudo molecular ion that is 146 amu greater than the parent glycoside. Moreover, acylation of the sugar residue causes a subsequent increase in the retention time in a chromatographic analysis [12,13]. Myricetin-*O*-coumaroyl-hexoside (9, 11) and myricetin-*p*-coumaroyl-rhamnosyl-hexoside (20) were identified herein, exhibiting  $\lambda_{\max}$  of 310–316 nm and pseudomolecular ions  $[M - H]^-$  at  $m/z$  625 and 771, respectively.

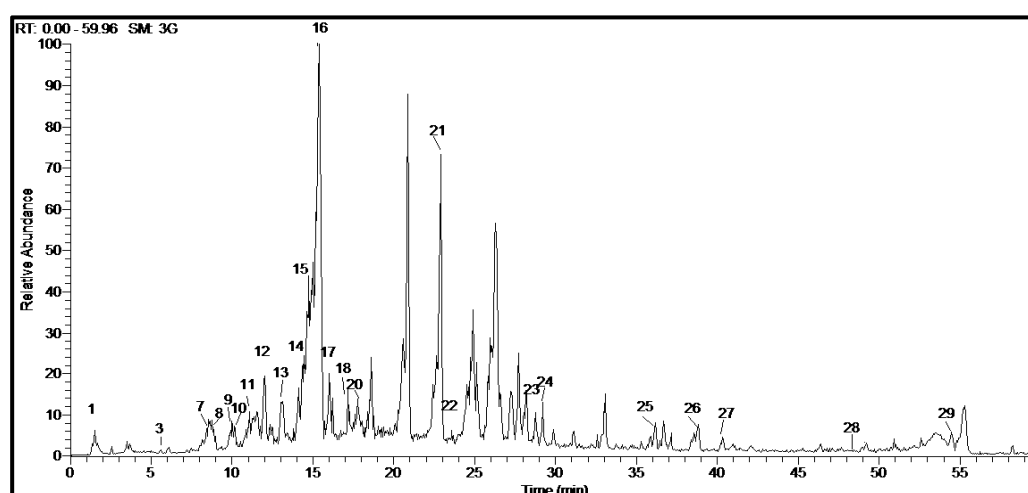
Several isoflavonoids were identified in *C. aethiopica* methanol extract including irisorictorin A/B (10), irigenol-C-hexoside (14), hydroxy-iristectrigenin-*O*-hexoside (17), iriflogenin (21), dihydroxy-methoxy-6,7-methylenedioxy isoflavone (22). Mass spectrometry cannot generally distinguish isoflavones from flavones, where both classes follow a similar fragmentation pathway via retro Diels–Alder (RDA) fragmentation resulting in identical product ions for both classes of compounds [14]. However, conjugation between A- and B-rings is lacking in isoflavone structures. Thus, UV spectra of isoflavones could be distinguished from those of flavones by displaying a low-intensity band I absorption.

Moreover, the increased A-ring oxygenation results in a bathochromic shift in band II from 249 nm in 7,4'-dihydroxyisoflavone to 261 nm in 5,7,4'-trihydroxyisoflavone and 270 nm in 5,6,7,4'-tetrahydroxyisoflavone. The spectra of isoflavones are not affected by changes in B-ring oxygenation patterns [14].

### 2.2.2. Fatty Acids

Several fatty acids could be annotated in the second half of the base peak chromatogram in ESI negative mode of *C. aethiopica* methanol extract exhibiting intense  $[M - H]^-$  pseudo-molecular ions characteristic of fatty acids. Monohydroxy unsaturated fatty acids including hydroxy-octadecatrienoic acid (25), hydroxy-octadecadienoic acid (26), and hydroxy-octadecenoic acid (27) could be detected exhibiting quasi molecular ions  $[M - H]^-$  at  $m/z$  293, 295, 297, respectively. A mass difference of 2 amu between the identified fatty acids indicates an additional double bond [15]. A dihydroxy polyunsaturated fatty acid was identified as dihydroxy-octadecadienoic acid (24) exhibiting  $[M - H]^-$  at  $m/z$  311. Monohydroxy saturated fatty acids including hydroxy-hexadecanoic acid (28) and hydroxy-octadecanoic acid (29) were also assigned. Moreover, dihydroxy-23-oxo-12-oleanen-28-oic acid-*O*-pentosyl dihexoside (23) was identified in *C. aethiopica* methanol extract.

Miscellaneous compounds including quinic acid (1), phenylalanine (2), protocatechuic acid (3), dicaffeoyl quinic acid and its isomer (4–5), hydroxy-methoxy acetophenone-*O*-hexoside (6), caffeoyl quinic acid and its isomer (7–8) were also identified in *C. aethiopica* methanol extract.



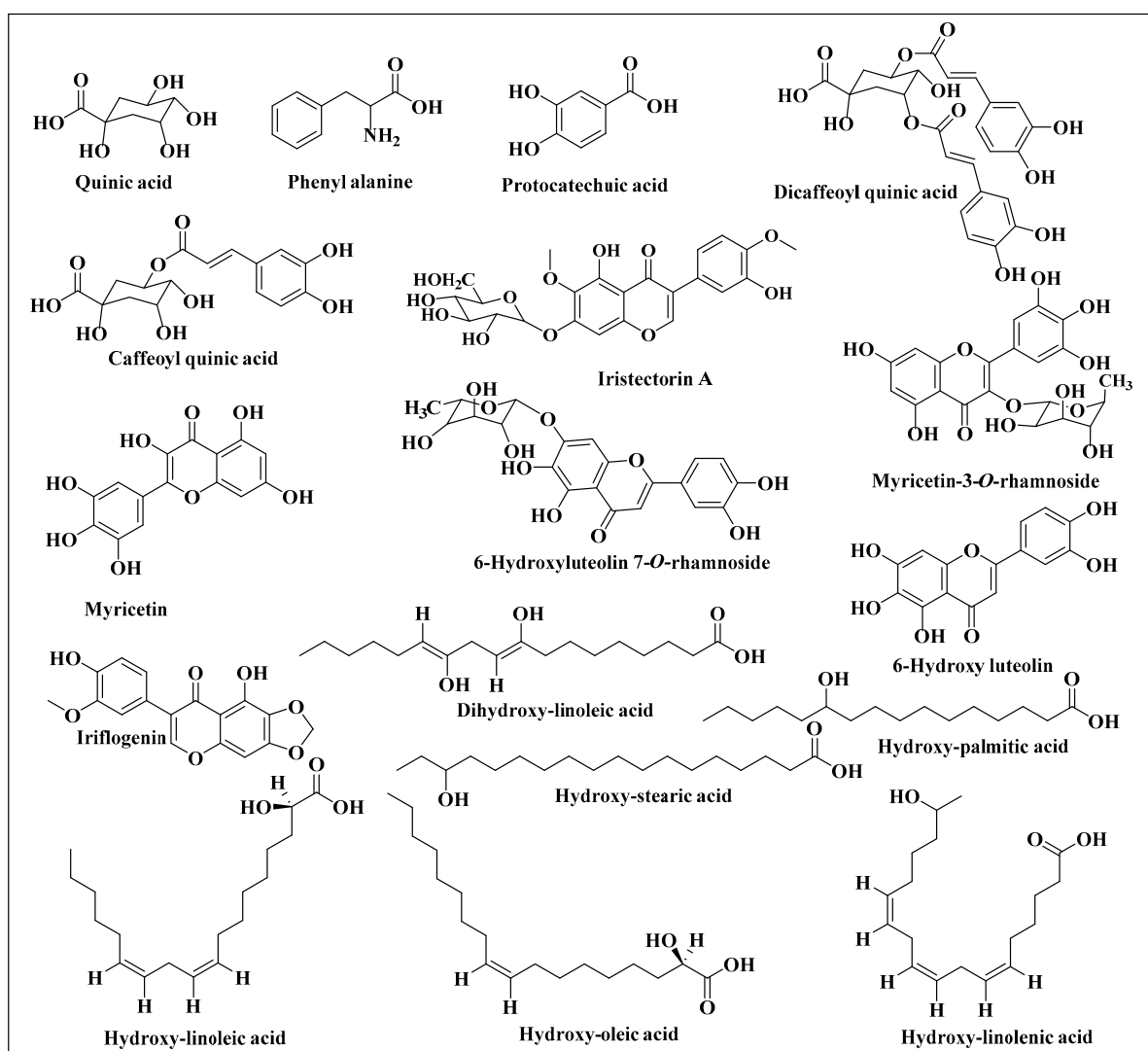
**Figure 2.** HPLC-ESI-MS base peak chromatogram of *C. aethiopica* leaf total methanol extract in the negative ion mode.

Table 2. Metabolite profiling of *C. aethiopica* leaf total methanol extract via HPLC-PDA-ESI-MS/MS in the positive and negative ion mode.

Peak No.	$t_R$ (min)	Name	UV $\lambda_{max}$ (nm)	$[M - H]^+$ (m/z)	$[M - H]^-$ (m/z)	$MS^2$ (m/z)	Molecular Formula	References
1.	2.59	Quinic acid	274		191	173, 127, 85	$C_7H_{12}O_6$	[16]
2.	5.09	Phenyl alanine	252, 275	166	164	147, 119	$C_9H_{11}NO_2$	[17]
3.	5.75	Protocatechuic acid	254, 286		153	109	$C_7H_6O_4$	[18]
4.	7.21	Dicaffeoyl quinic acid	269, 310		515	353, 341, 323, 191, 179	$C_{25}H_{34}O_{12}$	[19]
5.	7.54	Dicaffeoyl quinic acid isomer	282, 310		515	353, 341, 323, 191, 179	$C_{25}H_{34}O_{12}$	[19]
6.	7.65	Hydroxy-methoxy acetophenone-O-hexoside	283		327	295, 283, 179, 165, 147, 119	$C_{15}H_{20}O_8$	[20]
7.	8.07	Caffeoylquinic acid	289, 322		353	191, 179, 135	$C_{16}H_{18}O_9$	[21]
8.	9.24	Caffeoylquinic acid isomer	288, 315		353	191, 179, 135	$C_{16}H_{18}O_9$	[22]
9.	9.88	Myricetin-O-coumaroyl- hexoside	270, 316		625	479, 478, 463, 317, 271, 179	$C_{30}H_{26}O_{15}$	[23]
10.	10.34	Iristectorin A/B	265		491	473, 447, 401, 371, 343, 329, 311, 283, 241, 191, 146, hexoside)	$C_{23}H_{24}O_{12}$	[24]
11.	11.12	Myricetin-O-coumaroyl-hexoside	263, 311		625	479, 478, 463, 317, 287, 271	$C_{30}H_{26}O_{15}$	[25]
12.	11.75	Tricin-O-rhamnoside	264, 310	477	475	329, 328, 315, 299	$C_{23}H_{24}O_{11}$	[23]
13.	13.33	(Trihydroxy-dimethoxy-flavone-O-rhamnoside)	265, 310	477	475	457, 447, 431, 329, 328, 301, 175, 145	$C_{23}H_{24}O_{11}$	[26]
14.	14.21	Trihydroxy-dimethoxy-flavone-O-rhamnoside	264, 322		479	461, 433, 389, 359, 317, 316, 271, 151	$C_{21}H_{20}O_{13}$	[27]
15.	14.92	Hexahydroxy-isoflavone-C-hexoside (Irigenol-C-hexoside)	255, 346	465	463	317, 316, 287, 271, 262, 179, 151	$C_{21}H_{20}O_{12}$	[23]
16.	15.36	Myricetin-3-O-rhamnoside	255, 350	319		319, 301, 273, 263, 165, 179, 153, 109	$C_{15}H_{10}O_8$	[28]
17.	15.87	Myricetin			507	489, 476, 475, 463, 345, 329, 301, 273, 191, 175	$C_{23}H_{24}O_{13}$	[29]
18.	17.19	Tetrahydroxy dimethoxy isoflavone-O-hexoside (Hydroxy-iristectorigenin-O-hexoside)	234, 270, 311	509			$C_{21}H_{20}O_{11}$	[30]
19.	17.46	6-Hydroxyluteolin	316		447	301	$C_{15}H_{10}O_7$	[30]
20.	17.75	Myricetin-p-coumaroyl-rhamnosyl-hexoside	234, 315	303		303, 285, 257, 165, 153, 137	$C_{36}H_{36}O_{19}$	[31]
21.	23.20	5,4'-Dihydroxy-3'-methoxy-6,7-methylenedioxy isoflavone (Iriflogenin)	316	773	771	625, 463, 317		[32]
22.	23.73	Dihydroxy-methoxy-6,7-methylenedioxy isoflavone	276		327	309, 291, 283, 180, 165, 137	$C_{17}H_{12}O_7$	[32]
23.	29.14	Dihydroxy-23-oxo-12-oleanen-28-oic acid-O-pentosyl dihexoside	276		327	309, 291, 283, 229, 179, 165	$C_{17}H_{12}O_7$	[32]
24.	29.41	Dihydroxy-octadecadienoic acid (Dihydroxy-linoleic acid)	275		941	779, 617, 485	$C_{48}H_{77}O_{18}$	[33]
25.	35.93	Hydroxy octadecatrienoic acid (Hydroxy-linolenic acid)	274		311	293, 267, 171, 153	$C_{18}H_{32}O_4$	[15]
26.	38.45	Hydroxy octadecadienoic acid (Hydroxy-linoleic acid)	276		293	275, 249, 211, 183, 171, 121	$C_{18}H_{30}O_3$	[15]
27.	41.33	Hydroxy octadecenoic acid (Hydroxy-oleic acid)	277		295	277, 251, 211, 195, 183, 171	$C_{18}H_{32}O_3$	[15]
28.	48.29	Hydroxyhexadecanoic acid (Hydroxy-palmitic acid)	276		297	279, 253, 171	$C_{18}H_{34}O_3$	[15]
29.	54.51	Hydroxyoctadecanoic acid (Hydroxy-stearic acid)	Nd		271	253, 225, 210	$C_{16}H_{32}O_3$	[18]
			Nd		299	253	$C_{18}H_{36}O_3$	[18]

### 2.3. In Vitro Evaluation of the Anti-Allergic Activity

*C. aethiopica* leaf total methanol extract (CAL), as well as its various fractions, were assessed for their anti-allergic potential using A23187- and antigen (IgE+DNP-BSA)-induced degranulation assays, and the results were illustrated in Table 3. The cytotoxic effect against rat basophilic leukemia (RBL-2H3) for all the samples was evaluated using MTT assay. All samples exhibited toxic effects to RBL-2H3 cells (viability below 80%) at concentration  $\geq 10 \mu\text{g/mL}$  except for CAL-A which showed no cytotoxicity at the tested doses. Samples that were nontoxic were further examined for their anti-allergic effect. All the tested samples revealed weak inhibition percentage in both degranulation assays as illustrated in Table 3 except for CAL-A. It exhibited potent anti-allergic activity as evidenced by its pronounced inhibition percentage on  $\beta$ -hexosaminidase release triggered by A23187 and IgE by 72.7 and 48.7%, respectively, approaching that of dexamethasone especially in A23187 degranulation assay that revealed 80.7% inhibition for  $\beta$ -hexosaminidase release at 10 nM. This considerable anti-allergic activity comes following the anti-asthmatic and anti-allergic potential of previously studied Iridaceae plants such as *Crocus sativus* [34] and *Dietes bicolor* [35]. The hydroxy fatty acids and their esters, the predominant compounds in CAL-A, were previously reported to possess a significant anti-allergic activity as demonstrated in vitro and by ChemGPS-NP (chemical global positioning system for natural products) [36].



**Figure 3.** Major compounds identified in *C. aethiopica* leaf total methanol extract using HPLC-ESI-MS in the negative ion mode.



**Table 3.** Anti-allergic effects of *C. aethiopica* leaf total methanol extract and its fractions at different concentrations using degranulation assay in RBL-2H3 cell line.

Sample	Inhibition % of A23187-Induced $\beta$ -Hexosaminidase Release <sup>a</sup>				Inhibition % of Antigen-Induced $\beta$ -Hexosaminidase Release <sup>a</sup>			
	1 $\mu$ g/mL	10 $\mu$ g/mL	100 $\mu$ g/mL	200 $\mu$ g/mL	1 $\mu$ g/mL	10 $\mu$ g/mL	100 $\mu$ g/mL	200 $\mu$ g/mL
CAL	NS <sup>c</sup>	TOX <sup>d</sup>	TOX <sup>d</sup>	TOX <sup>d</sup>	NS <sup>c</sup>	TOX <sup>d</sup>	TOX <sup>d</sup>	TOX <sup>d</sup>
CAL-A	NS <sup>b</sup>	8.0 $\pm$ 4.9	41.3 $\pm$ 5.4 ***	72.7 $\pm$ 2.2 **** <sup>e</sup>	NS <sup>b</sup>	4.0 $\pm$ 1.7	12.0 $\pm$ 5.2	48.7 $\pm$ 8.6 ***
CAL-B	NS <sup>c</sup>	TOX <sup>d</sup>	TOX <sup>d</sup>	TOX <sup>d</sup>	NS <sup>c</sup>	TOX <sup>d</sup>	TOX <sup>d</sup>	TOX <sup>d</sup>
CAL-C	NS <sup>c</sup>	TOX <sup>d</sup>	TOX <sup>d</sup>	TOX <sup>d</sup>	NS <sup>c</sup>	TOX <sup>d</sup>	TOX <sup>d</sup>	TOX <sup>d</sup>
CAL-D	NS <sup>c</sup>	TOX <sup>d</sup>	TOX <sup>d</sup>	TOX <sup>d</sup>	NS <sup>c</sup>	TOX <sup>d</sup>	TOX <sup>d</sup>	TOX <sup>d</sup>
CAL-E	NS <sup>c</sup>	TOX <sup>d</sup>	TOX <sup>d</sup>	TOX <sup>d</sup>	NS <sup>c</sup>	TOX <sup>d</sup>	TOX <sup>d</sup>	TOX <sup>d</sup>

CAL: *C. aethiopica* leaf total methanol extract; CAL-A: *C. aethiopica* *n*-hexane fraction; CAL-B: *C. aethiopica* dichloromethane fraction; CAL-C: *C. aethiopica* ethyl acetate fraction; CAL-D: *C. aethiopica* *n*-butanol fraction; CAL-E: *C. aethiopica* remaining aqueous fraction. <sup>a</sup> Results are presented as mean  $\pm$  S.E.M. value (n = 3). \*\*\*  $p < 0.001$  compared with the control value (A23187 or antigen only). Dexamethasone, a positive control, inhibited 80.7  $\pm$  3.8% (A23187-induced) and 79.7  $\pm$  2.5% (antigen-induced) degranulation at a concentration of 10 nM. <sup>b</sup> NS: Not significant inhibition (degranulation more than 85 % of control) (n = 1). <sup>c</sup> NS: Not significant inhibition (degranulation more than 85 % of control) (n = 2). <sup>d</sup> TOX: toxic (viability less than 80% of control). <sup>e</sup> CAL-A inhibited A23187-induced  $\beta$ -hexosaminidase release with IC<sub>50</sub> 127.7  $\mu$ g/mL.

#### 2.4. In Vitro Evaluation of Anti-Inflammatory Activity

The anti-inflammatory activity of *C. aethiopica* leaf total methanol extract and its fractions on superoxide anion generation and elastase release in FMLF/CB-induced human neutrophils was evaluated. Results displayed in Table 4 showed that both *n*-hexane (CAL-A) and dichloromethane (CAL-B) fractions revealed potent anti-inflammatory activity manifested by significant inhibition in the generation of superoxide anion and prohibition of elastase release. CAL-A inhibited the generation of superoxide anion and elastase release by 68.68 and 65.18%, respectively at 10  $\mu$ g/mL showing IC<sub>50</sub> equal to 5.32 and 5.8  $\mu$ g/mL, respectively. CAL-B exhibited 58.31 and 68.08% inhibition of superoxide anion generation and elastase release, respectively, at 10  $\mu$ g/mL exhibiting IC<sub>50</sub> values of 7.04 and 5.73  $\mu$ g/mL, respectively. Many Iridaceae plants showed potent anti-inflammatory and immunomodulating effects in previous studies [35]. Noteworthy to highlight that the cellular model of isolated human neutrophils was established to elucidate the anti-inflammatory effect in this study as neutrophils are considered the first line of defense versus microbial infections in addition to being the most abundant circulating leukocytes. Moreover, they greatly contribute to the damage of tissues during several autoimmune and inflammatory diseases [37]. Elastase is a serine protease released by activated human neutrophils and can break several biomarkers comprising elastin in addition to being considered as inflammatory disorders marker. Initiation of elastase release is triggered by formyl peptides such as fMLF in neutrophils; thus, efficient elastase inhibitors can act as a logic strategy to protect tissue from excessive damage caused by inflammatory mediators [38]. The superoxide radical plays a pivotal role in the neutrophil-mediated acute inflammatory response. Superoxide radicals are produced by neutrophils to help in killing invasive microbes where superoxide evolved from actively phagocytizing neutrophils that attracts additional neutrophils via reaction and activation of latent chemotactic factors present in plasma. Hence, natural products that effectively prohibit superoxide-dependent chemotactic factor, serve as promising anti-inflammatory agents [39]. Thus, the anti-inflammatory effect is measured through the inhibition of superoxide anion generation and elastase liberation in our ongoing study.

**Table 4.** Inhibitory effects of *C. aethiopica* leaf total methanol extract and its fractions on superoxide anion generation and elastase release in FMLF/CB-induced human neutrophils.

Sample	Superoxide Anion		Elastase Release	
	IC <sub>50</sub> (µg/mL) <sup>a</sup>	Inhibition%	IC <sub>50</sub> (µg/mL) <sup>a</sup>	Inhibition%
CAL	>10	36.45 ± 2.58 ***	>10	15.27 ± 2.13 **
CAL-A	5.32 ± 0.46	68.68 ± 3.87 ***	5.80 ± 0.34	65.18 ± 6.81 ***
CAL-B	7.04 ± 1.28	58.31 ± 3.76 ***	5.73 ± 0.64	68.08 ± 7.25 ***
CAL-C	>10	43.84 ± 1.94 ***	>10	24.51 ± 4.05 **
CAL-D	>10	22.47 ± 5.53 *	b	b
CAL-E	>10	26.49 ± 2.73 ***	>10	5.30 ± 2.67

CAL: *C. aethiopica* leaf total methanol extract; CAL-A: *C. aethiopica* *n*-hexane fraction; CAL-B: *C. aethiopica* dichloromethane fraction; CAL-C: *C. aethiopica* ethyl acetate fraction; CAL-D: *C. aethiopica* *n*-butanol fraction; CAL-E: *C. aethiopica* remaining aqueous fraction. <sup>a</sup> Percentage of inhibition at 10 µg/mL concentration. Results are presented as mean ± S.E.M. (n = 3). \* *p* < 0.05, \*\* *p* < 0.01, \*\*\* *p* < 0.001 compared with the control value (fMLF/CB). <sup>b</sup> Sample CAL-D had promoting effects (23.86 ± 3.78% in the presence of CB) on elastase release in human neutrophils.

## 2.5. In Vitro Antioxidant Activity Using DPPH Assay

The main mechanistic basis for most in vitro antioxidant assays takes place by either HAT (hydrogen atom transfer) or ET (electron transfer) reactions. DPPH is monitored by determining the color change of the DPPH radical. The DPPH assay relied upon electron transfer reaction, wherein DPPH itself reacts as a radical and a probe. The presence of antioxidants in any sample lightens the color of DPPH by donating an electron/hydrogen atom to the unpaired electron of DPPH that turns the purple color of DPPH colorless, which is measured using UV–VIS spectrophotometer at a wavelength of 517 nm [40]. The DPPH assay showed that *C. aethiopica* leaf total methanol extract showed substantial antioxidant potential with an IC<sub>50</sub> equals of 0.56 mg/mL that may be attributed to the richness of the extract with phytoconstituents belonging to different classes represented mainly by flavonoids and phenolic acid as revealed from the LC/MS analysis.

## 2.6. In Vitro Anti-Hyperglycemic Activity

The anti-hyperglycemic activity of the *C. aethiopica* leaf total methanol extract (CAL) was evaluated in vitro using 3T3-L1 adipocytes using two concentrations which are 30 and 50 µg/mL that were further compared with insulin and pioglitazone, positive controls, using the same concentrations. Results displayed in Table 5 clarified that the concentration of glucose was decreased from 23.9 and 24.1 mmol/L to 22.8 and 22.6 mmol/L after treatment with 30 and 50 µg/mL of CAL, respectively. This showed a moderate reduction in the culture medium glucose concentration estimated by 4.6 and 6.2% as compared to untreated control group. CAL approaches in this regard insulin and pioglitazone that showed 6.3 and 4.37% reduction at 30 µg/mL and 10.5% reduction at 50 µg/mL as compared to untreated control group.

**Table 5.** Effect of *C. aethiopica* leaf total methanol extract (CAL) at concentrations of 30 and 50 µg/mL on glucose consumption in media of 3T3-L1 adipocyte cultures.

	Glucose Concentration in mmol/L	
	30 µg/mL	50 µg/mL
Pioglitazone	22.9 ± 0.7	21.10 ± 0.6 *
Insulin	22.4 ± 0.4 *	21.56 ± 0.7 *
CAL	22.8 ± 0.9	22.6 ± 0.1 *
Control	23.9 ± 0.7	24.1 ± 0.6
Medium	25.3 ± 0.6	25.0 ± 0.6

Data are measured in triplicates (n = 3) and presented as means ± SEM. \* Significantly different from the untreated control group at *p* < 0.05.

### 2.7. In Vivo Assessment of the Antihyperglycemic Activity

The antihyperglycemic effect of *C. aethiopica* leaf total methanol extract (CAL) was evaluated in STZ-induced diabetic rats. The injection of STZ into animals triggered a considerable increase in FBG level by 278% when compared to the normal control group (Figure 4). This change was concomitant with a significant reduction in the serum insulin level by 52.63%, with regard to the normal group. Meanwhile when GLB was administered to STZ-diabetic rats it caused a notable decrease in FBG level by 28.57% accompanied by a marked increase in serum insulin level by 22.22% in comparison with STZ-treated rats. However, the administration of the CAL to STZ-treated rats elicited a significant reduction in FBG level by 53.44%, as compared with the STZ-treated rats with concomitant elevation in serum insulin estimated by 22.22%. The results of CAL suggested a potent antihyperglycemic effect approaching that of GLB. The effectiveness of CAL as a promising antihyperglycemic is attributed to its richness by flavonoids and phenolic acids. These secondary metabolites were previously showed to possess antihyperglycemic activity via acting as potent  $\alpha$ -glucosidase inhibitors [41,42]. It is noteworthy to mention that myricetin derivatives exhibited considerable  $\alpha$ -amylase as well as  $\alpha$ -glucosidase inhibitory activity. They also displayed an insulin-like action via stimulating glucose and lipid uptake as well as enhancing adiponectin production by stimulating the insulin signaling pathway in a manner similar to insulin. Myricetin derivatives trigger Akt1, protein kinase B, peroxisome proliferator-activated receptor gamma, and Slc2a4, glucose transporter, genes up-regulation resulting in antihyperglycemic activity [43]. Moreover, quinic acid and its derivatives effectively stimulate  $\text{Ca}^{2+}$ -dependent mitochondrial function and increase insulin production from  $\beta$ -cells of the pancreas [44]. The plant product quinic acid activates  $\text{Ca}^{2+}$ -dependent mitochondrial function and promotes insulin secretion from pancreatic beta cells. The plant product quinic acid activates  $\text{Ca}^{2+}$ -dependent mitochondrial function and promotes insulin secretion from pancreatic beta cells. The plant product quinic acid activates  $\text{Ca}^{2+}$ -dependent mitochondrial function and promotes insulin secretion from pancreatic beta cell [44].

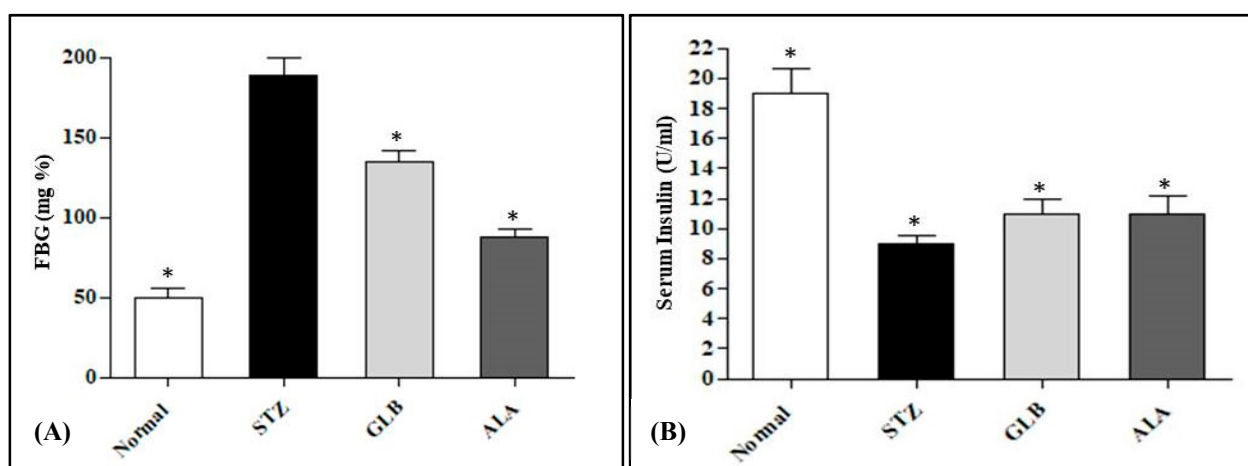


**Figure 4.** Effect of intraperitoneal injection of 20 mg/kg/day of *C. aethiopica* leaf total methanol extract (CAL) and 600 µg/kg/day glibenclamide (GLB) on FBG (A) and serum insulin (B) levels in STZ-induced diabetic rats. Data are measured in triplicates ( $n = 3$ ) and presented as means  $\pm$  S.E.M. \* Significantly different from the STZ-treated group at  $p < 0.05$ ; FBG was assessed using a glucose oxidase kit; serum insulin was determined by an immunoassay kit.

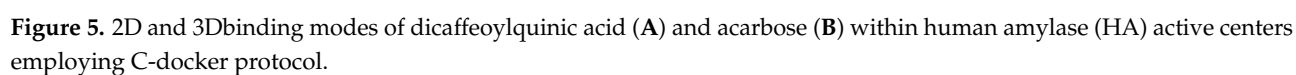
### 2.8. Molecular Modeling

Docking of most of the major compounds identified from *C. aethiopica* leaf total methanol extract inside the active centers of human  $\alpha$ -amylase (HA) and human  $\alpha$ -glucosidase (HG) was performed to further ascertain the results of the in vitro and in vivo study and provides an outline for the probable mechanism of action. Most of the docked

compounds showed certain fitting within the active sites of both examined enzymes. Dicafeoylquinic acid revealed the highest fitting with free binding energies ( $\Delta G$ ) equals to  $-47.24$  and  $-60.50$  Kcal/mol for human  $\alpha$ -amylase (HG) and human  $\alpha$ -glucosidase (HG), respectively (Table 6). The highest fitting of dicafeoylquinic acid at human  $\alpha$ -amylase (HA) is attributed to the formation of two conventional H-bonds with His 305 and Arg 195, two  $\pi$ -alkyl interactions with Ile 235 and Leu 162, two C-H bonds with Asp 300 and Thr 163 in addition to the formation of many Van der Waals interactions. Regarding acarbose, it forms six conventional H-bonds with Gly 306, Asp197, Gln 63, His 291, Arg 195 and Asp 300, two alkyl interactions with Leu 162 and Leu 165, two C-H bonds with Glu 233 and His 305 in addition to Van der Waals interactions with many amino acid residues at the active site (Figure 5). The firm binding of dicafeoylquinic acid at the active site of human  $\alpha$ -glucosidase (HG) can be interpreted by the formation of multiple tight bonds at the active sites, namely, seven conventional H-bonds with Gln 1561, His 1584, Asp 1279, Lys 1460, and Asp 1157; two  $\pi$ - $\pi$  interactions with Phe 1560 and Tyr 1251; and hydrophobic C-H bonds with Pro 1159 and Tyr 125 in addition to the formation of many Van der Waals interactions with most of the amino acid moieties present at the active site of the enzyme together with an attractive charged ionic bond formation between the carboxylic acid moiety of the quinic acid and Lys 1460 residue in the active site (Figure 6). These results for dicafeoylquinic acid approached that of acarbose, the standard antihyperglycemic agent that displayed  $\Delta G$  of  $-76.29$  and  $-89.19$  Kcal/mol for human  $\alpha$ -amylase (HG) and human  $\alpha$ -glucosidase (HG), respectively. Acarbose formed eleven H-bonds with Gln 1158, Lys 1460, Lys 1164, Asp 1157, Arg 1510, and Asp 1420, in addition to two C-H bonds with Trp 1369 and Asp 1526 at the human  $\alpha$ -glucosidase (HG) active center.

**Table 6.** Free binding energies ( $\Delta G$ ) of the major identified compounds with human  $\alpha$ -amylase (HA) and human  $\alpha$ -glucosidase (HG) enzymes active centers using molecular docking with pH- and rule-based methods and expressed in kcal/mol.

Compound	Human $\alpha$ -Amylase (HA)		Human $\alpha$ -Glucosidase (HG)	
	pH-Based	Rule-Based	pH-Based	Rule-Based
Quinic acid	$-15.49$	$-15.49$	$-15.23$	$-15.23$
Phenyl alanine	$-32.81$	$-32.81$	$-28.53$	$-28.53$
Protocatecheuic acid	$-31.44$	$-31.40$	$-31.84$	$-31.80$
Dicafeoylquinic acid	$-47.24$	$-47.24$	$-60.50$	$-60.50$
Caffeoyl quinic acid	$-38.43$	$-38.43$	$-37.68$	$-37.68$
Iristectorin	$-4.17$	$-4.17$	$-14.84$	$-14.84$
Myricetin-3-O-rhamnoside	$-26.44$	$-21.14$	$-27.30$	$-22.92$
Myricetin	$-44.05$	$-41.05$	$-45.83$	$-41.82$
6-Hydroxyluteolin 7-O-rhamnoside	$-39.66$	$-20.66$	$-45.68$	$-23.64$
6-Hydroxyluteolin	$-33.45$	$-21.66$	$-36.10$	$-23.82$
Iriflogenin	$-11.57$	$-11.57$	$-13.41$	$-13.41$
Dihydroxy-linoleic acid	$-23.28$	$-23.28$	$-29.60$	$-29.60$
Hydroxy-linolenic acid	$-3.89$	$-3.69$	$0.17$	$0.12$
Hydroxy-oleic acid	$-32.61$	$-32.61$	$-35.86$	$-35.86$
Hydroxy-stearic acid	$-44.62$	$-44.62$	$-52.17$	$-52.17$
Hydroxy-palmitic acid	$-44.62$	$-44.62$	$-48.43$	$-48.43$
Acarbose	$-76.29$	$-76.29$	$-89.19$	$-89.19$







(fetal bovine serum) were obtained from Merck (Kenilworth, NJ, USA) and Hyclone (Logan, UT, USA), respectively. Other kits used for assessment of LPO (lipid peroxidation) and MDA (malondialdehyde) were obtained from Fluka (Buchs, Switzerland). Dr. Daniel H. Conrad (Virginia Commonwealth University, Richmond, VA, USA) generously supplied Mouse anti-DNP IgE antibody. All other solvents for LC/MS as well as GLC/MS analyses were of analytical grade.

### 3.2. Plant Material

*C. aethiopica* (Iridaceae) leaves were collected from El-Rai botanical garden, El Kanater El Khayreya, Qalyubiya, Egypt. The plants were kindly identified and authenticated by Mrs. Therese Labib, Consultant of Plant Taxonomy at the Ministry of Agriculture and former Director of Orman Botanical Garden, Giza, Egypt, and Dr. Mohammed El-Gebaly, Department of Botany, National Research Centre (NRC), Giza, Egypt. Voucher specimens were deposited in the herbarium of Pharmacognosy Department, Faculty of Pharmacy, Ain Shams University (voucher specimen number: PHG-P-CA-261).

### 3.3. Preparation of the Plant Extract and Its Fractions

Air-dried leaves of *C. aethiopica* L. (100 g) were powdered and percolated in 80% methanol (1 L  $\times$  3) followed by its filtration. The obtained filtrate was concomitantly evaporated under reduced pressure and temperature (45 °C) until dryness and lyophilized to give 25.50 g of the total methanol extract (CAL). The solid residue (20 g) was dissolved in water: methanol (1: 4) and then partitioned successively with *n*-hexane, dichloromethane, ethyl acetate, and *n*-butanol to give CAL-A (2.67 g), CAL-B (3.74 g), CAL-C (2.34 g), and CAL-D (1.16 g), respectively. The remaining aqueous fraction CAL-E was 9.58 g.

### 3.4. Gas–Liquid Chromatography Coupled with Mass Spectroscopy (GLC-MS) Analysis

GLC-MS analysis was achieved on Shimadzu GCMS-QP 2010 (Shimadzu Corporation, Koyoto, Japan) equipped with Rtx-5MS (30 m  $\times$  0.25 mm i.d.  $\times$  0.25  $\mu$ m film thickness) capillary column (Restek, PA, USA) and coupled to a Shimadzu mass spectrometer. Initial column temperature was set at 50 °C for 3 min; 50–300 °C at a rate of 5 °C/min and then 10 min isothermal at 300 °C. The injector temperature was 280 °C. The carrier gas (helium) flow rate was set at 1.37 mL/min. The interface and ion source temperatures were adjusted to 280 and 220 °C, respectively. Diluted samples (1% *v/v*) were injected in split mode with split ratio 15:1. The injection volume was 1  $\mu$ L. Mass spectra were recorded in EI mode of 70 eV, scanning from *m/z* 35 to 500.

### Compound Identification

The tentative identification of the compounds found by GLC-MS was performed based on their retention indices relative to a homologous series of *n*-alkanes (C<sub>8</sub>–C<sub>28</sub>) injected under the same conditions and comparing their mass spectra with those in the National Institute of Standards and Technology (NIST) and Wiley library database in addition to literature [45–52].

### 3.5. HPLC-PDA-ESI-MS/MS Analysis

HPLC-PDA-ESI-MS/MS analysis was carried out on a Finnigan LCQ-Duo ion trap mass spectrometer (Thermo Quest, San Jose, CA, USA) with an ESI source coupled to a Finnigan Surveyor HPLC system (Accela autosampler, MS pump plus, and PDA detector plus) (Thermo, San Jose, CA, USA) with an EC 150/3 Nucleodur 100-3 C18ec column (Macherey-Nagel, Düren, Germany). A gradient of water and acetonitrile (ACN) (with 0.1% formic acid for ESI<sup>+</sup> mode and without formic acid for ESI<sup>−</sup> mode) was applied from 2% to 100% ACN in 60 min at 30 °C at a flow rate of 0.5 mL/min. The injection volume was 20  $\mu$ L. All samples were measured in the positive and negative ion mode. The MS was operated at +10 V capillary voltage for ESI<sup>+</sup> and −10 V for ESI<sup>−</sup>, 240 °C source temperature, and high purity nitrogen as a sheath and auxiliary gas at a flow rate of 80 and 40 (arbitrary

units), respectively. The ions were detected in a mass range of 50–2000  $m/z$ . A collision energy of 35 eV was used in MS/MS fragmentation. Data acquisitions and analyses were executed by Xcalibur™ 2.0.7 software (Thermo Scientific, Karlsruhe, Germany). Tentative metabolite assignments were achieved by comparison of mass and UV spectral data of the detected compounds in both negative and positive ionization modes with reported data alongside online public databases where references are added Table 2.

### 3.6. In Vitro Biological Evaluation

#### 3.6.1. In Vitro Assessment of the Anti-Allergic Activity

##### Cell Culture and Cell Viability Assay

The mucosal mast cell-derived rat basophilic leukemia (RBL-2H3) cell line was obtained from the American Type Culture Collection. The growth of RBL-2H3 was carried out in a DMEM medium containing 10% FBS in addition to 100 U/mL penicillin and 100 µg/mL streptomycin. The culturing of cells was done in 10 cm cell culture dishes (Cellstar) using a humidified chamber containing 5% CO<sub>2</sub> in the air and were kept at 37 °C. A methyl thiazole tetrazolium (MTT) assay was performed to assess the probable toxic effects of the tested samples concerning RBL-2H3 cells [53] as previously described [54–57].

##### Degranulation Assays in Mast Cells

The extent of A23187-induced degranulation in RBL-2H3 cells was evaluated using a  $\beta$ -hexosaminidase activity assay as formerly described [54,58]. The release of  $\beta$ -hexosaminidase from activated RBL-2H3 cells induced by IgE was assessed following the method described earlier [59]. Dexamethasone (10 nM) was used as a positive control. Absorbance was determined using a microplate reader at  $\lambda = 405$  nm. The percentage of inhibition of  $\beta$ -hexosaminidase release from RBL-2H3 cells was computed using the following equation, calculated as a percentage of the control value (untreated stimulated cells):

$$\text{Inhibition (\%)} = \left[ 1 - \frac{(\text{OD}_{\text{sample}} - \text{OD}_{\text{spontaneous}})}{(\text{OD}_{\text{control}} - \text{OD}_{\text{spontaneous}})} \right] \times 100$$

#### 3.6.2. In Vitro Assessment of Anti-Inflammatory Activity

The assessment of anti-inflammatory activity was performed using human neutrophils in which blood was withdrawn from healthy volunteers (20–35 years old) following a protocol approved by the institutional review board at Chang Gung Memorial Hospital adopting a standard method as formerly described [60]. However, the inhibition of superoxide generation was assessed using the assay based on the reduction of ferricytochrome c as previously reported [60]. Meanwhile, the release of elastase from activated neutrophils was measured using the elastase substrate, *N*-methoxysuccinyl-Ala-Pro-Val-*p*-nitroanilide, following the previously described procedure [60].

#### 3.6.3. In Vitro Antioxidant Activity Evaluation Using DPPH Assay

The ability of CAL to donate hydrogen atom or an electron was determined via bleaching the purple color of DPPH• methanol solution 0.2, 0.4, 0.6, and 1.0 mg/mL that was performed in triplicate. Briefly, 50 µL of each concentration of the tested sample was added to 5 mL of 0.004% methanol solution of DPPH. After 30 min incubation at room temperature, the absorbance was measured versus a blank at  $\lambda = 517$  nm using a Shimadzu UV-1601 spectrophotometer (Kyoto, Japan). The percentage of inhibition of DPPH• was calculated using the following equation: Free radical scavenging activity =  $[\text{Ac} - \text{As} / \text{Ac}] \times 100$ , where Ac: absorbance of control and As: absorbance of sample. The IC<sub>50</sub> of ascorbic acid, positive control, was 1.6 µg/mL [61].

#### 3.6.4. In Vitro Anti-Hyperglycemic Evaluation Using 3T3-L1 Adipocyte Culture

Stock solutions of the tested sample at 30 and 50 µg/mL in DMSO were used in which DMSO concentration does not exceed 0.1% in the medium of working solutions. However,

the stock solution of insulin was prepared by dissolving  $10^2$  M of insulin in 0.01 M of acetic acid; pH 3.0 [62].  $5 \times 10^5$  cells/mL of mouse pre-adipocytes 3T3-L1 cells obtained from the American Type Culture Collection (ATCC) were used and cultured in DMEM medium supplemented with 5.56 mmol/L D-glucose, 10% FBS, and 1% PS (penicillin–streptomycin) solutions. The cells were kept at 37 °C in a humidified condition composing of 95% air and 5% CO<sub>2</sub>. After achieving 100% confluence, the cells were treated with 25 mmol/L D-glucose, 0.32 µM insulin, 0.5 mM 3-isobutyl-1-methylxanthine, and 1 µM dexamethasone for 48 h to improve their differentiation. Cells treated with CAL as well as control untreated cells were kept in DMEM media with 25 mmol/L D-glucose for 24 h. Pioglitazone and insulin were employed as a positive control meanwhile the concentrations of glucose in the medium were employed as a tool to assess anti-hyperglycemic effectiveness of the tested sample [62].

### 3.7. In Vivo Biological Evaluation

#### 3.7.1. Animals and Animal Treatment

Rats (Wister male) of 150–250 g, were provided by King Fahd Medical Research Center, King Abdulaziz University, Jeddah, Saudi Arabia, animal facility. The study protocol received approval from the local ethics committee for animal care, Taibah University, Saudi Arabia (Approval number TUCDREC/20160131). The animals were kept under standard conditions of temperature, relative humidity, as well as day and light cycle. Animals were allowed free access to standard laboratory food as previously reported [62] and as indicated by the WHO (World Health Organization) [62].

#### 3.7.2. Diabetes Induction in Rats

The induction of diabetes in rats was achieved by the intraperitoneal administration of streptozotocin (mg/kg) as a single dose as previously described [63]. Enzymatic strips were used to examine the existence of glucose in the urine on the third day. Glibenclamide was utilized as a positive control.

#### 3.7.3. Experimental Protocol

The animals were randomly distributed into four groups, 8 animals per group. The experimental protocol was done following what was previously reported in which groups 1, 2, and 3 represented the normal, streptozotocin (STZ), and glibenclamide (GLB) administered groups, respectively [62]. The fourth group orally received 20 mg/kg body weight of the leaf methanol extract of *C. aethiopica* L. (CAL) for ten successive days. Scarification was done on the 11th day of treatment by cervical dislocation after light ether anesthesia. The separated serum was subjected to centrifugation and used for the determination of glucose and insulin levels.

#### 3.7.4. Assessment of the Biochemical Parameters

Serum glucose and insulin were assessed using the glucose oxidase assay and Amer-sham insulin immune reactive kit, respectively [62,64], as listed by the manufacturer [65].

### 3.8. Statistical Analysis

Statistical analysis was done using one-way ANOVA followed by Dunnet's test which was done using Sigma Plot (Systat software, San Jose, CA, USA) in case of anti-allergic evaluation; student's *t*-test (SigmaPlot) for anti-inflammatory assay; however, for the antihyperglycemic determination, ANOVA was followed by Tukey–Kramer multiple comparison test ( $p < 0.05$ ). Results were given as means  $\pm$  S.E.M. Graphs were plotted using GraphPad Prism 6 software (GraphPad Inc., La Jolla, CA, USA).

### 3.9. Molecular Modeling

Molecular docking of the identified compounds from the total methanol leaf extract (CAL) was performed using Discovery Studio 2.5 (Accelrys Inc., San Diego, CA, USA)

implementing C-docker protocol on human  $\alpha$ -amylase (HA) (PDB ID 1B2Y) and human  $\alpha$ -glucosidase (HG) (PDB ID 3TOP), retrieved from the protein data bank ([www.pdb.org](http://www.pdb.org), accessed on 28 May 2021) using both pH based and rule-based methods. This was done following the previously reported method [3,35,66].

#### 4. Conclusions

This study comprehensively studies the phytoconstituents as well as the different biological activities of the *C. aethiopica* for the first time. GC analyses revealed that palmitic acid and methyl hexadecanoic acid ester are the predominant compounds in *C. aethiopica* *n*-hexane fraction of the leaf extract. Meanwhile, myricetin-3-O-rhamnoside was the major compound in *C. aethiopica* total methanol extract as displayed in HPLC-PDA-ESI-MS/MS analysis. *C. aethiopica* *n*-hexane exhibited the highest anti-allergic and anti-inflammatory potential whereas *C. aethiopica* total methanol extract showed a potent antihyperglycemic activity in streptozotocin-induced diabetes in an animal model that was further confirmed using in silico studies. *C. aethiopica* could serve as an effective antioxidant natural remedy combating inflammation, allergy, and hyperglycemia that will be welcomed by a large category of patients worldwide. Further studies are recommended for the isolation and structural elucidation of the compounds existing in the extract with subsequent assessment of their biological activities.

**Author Contributions:** Conceptualization, methodology, software, writing—original draft preparation, I.M.A. and F.S.Y.; methodology, resources, writing—review and editing; M.K., H.A.E.-B., B.W., T.-L.H., and B.-H.C.; supervision, funding acquisition, writing—review and editing, F.-R.C.; supervision and writing—review and editing, M.E.-S., M.W., and A.N.B.S. All authors have read and agreed to the published version of the manuscript.

**Funding:** This work was supported by grants from the Ministry of Science and Technology of Taiwan (Grant number: MOST 106-2320-B-037-008-MY2, MOST 108-2320-B-037-022-MY3, 108-2811-B-037-511, and 109-2927-I-037-502, awarded to F.-R. Chang, and MOST 108-2320-B-037-004, awarded to B.-H. Chen). In addition, this research was funded by the Drug Development and Value Creation Research Center, Kaohsiung Medical University & Department of Medical Research, Kaohsiung Medical University Hospital (Grant number: KMU-TC108A03-11, KMU-TC109A03-2) and Chang Gung Memorial Hospital (CMRPF1G0241-3; BMRP450).

**Institutional Review Board Statement:** The study protocol received approval from the local ethics committee for animal care, Taibah University, Saudi Arabia (Approval number TUCDREC/20160131).

**Informed Consent Statement:** Not applicable.

**Data Availability Statement:** Data are available upon request from the first author.

**Acknowledgments:** I. M. A. acknowledges Science and Technology Development Fund in Egypt (STDF, project ID 25448) for funding the postdoctoral fellowship in Heidelberg, Germany.

**Conflicts of Interest:** The authors declare no conflict of interest.

#### References

1. Youssef, F.S.; Labib, R.M.; Eldahshan, O.A. Synergistic hepatoprotective and antioxidant effect of artichoke, fig, mulberry herbal mixture on HepG2 cells and their metabolic profiling using NMR coupled with chemometrics. *Chem. Biodivers.* **2017**, *14*, e1700206. [CrossRef]
2. Ashour, M.L.; Youssef, F.S.; Gad, H.A.; El-Readi, M.Z.; Bouzabata, A.; Abuzeid, R.M.; Sobeh, M.; Wink, M. Evidence for the anti-inflammatory activity of *Bupleurum marginatum* (Apiaceae) extracts using in vitro and in vivo experiments supported by virtual screening. *J. Pharm. Pharmacol.* **2018**, *70*, 952–963. [CrossRef]
3. Janibekov, A.A.; Youssef, F.S.; Ashour, M.L.; Mamadalieva, N.Z. New flavonoid glycosides from two *Astragalus* species (Fabaceae) and validation of their antihyperglycaemic activity using molecular modelling and in vitro studies. *Ind. Crops Prod.* **2018**, *118*, 142–148. [CrossRef]
4. Salib, J.Y.; Michael, H.N.; Eskande, E.F. Anti-diabetic properties of flavonoid compounds isolated from *Hyphaene thebaica* epicarp on alloxan induced diabetic rats. *Pharmacogn. Res* **2013**, *5*, 22–29. [CrossRef]
5. Broide, D.H. Immunomodulation of allergic disease. *Annu. Rev. Med.* **2009**, *60*, 279–291. [CrossRef] [PubMed]



6. Youssef, F.S.; Hamoud, R.; Ashour, M.L.; Singab, A.N.; Wink, M. Volatile oils from the aerial parts of *Eremophila maculata* and their antimicrobial activity. *Chem. Biodivers.* **2014**, *11*, 831–841. [[CrossRef](#)] [[PubMed](#)]
7. Goldblatt, P.; Manning, J.; Dunlop, G. *Crocasmia and Chasmanthe*; Timber Press: Portland, OR, USA, 2004.
8. Singab, A.N.B.; Ayoub, I.M.; El-Shazly, M.; Korinek, M.; Wu, T.-Y.; Cheng, Y.-B.; Chang, F.-R.; Wu, Y.-C. Shedding the light on Iridaceae: Ethnobotany, phytochemistry and biological activity. *Ind. Crops Prod.* **2016**, *92*, 308–335. [[CrossRef](#)]
9. Divya, G.; Albert, A.; Singab, A.N.B.; Ayoub, I.M.; Al-Sayed, E.; Paul, E.; Manoharan, K.; Saso, L.; Selvam, G.S. Renoprotective effect of tectorigenin glycosides isolated from *Iris spuria* L. (Zeal) against hyperoxaluria and hyperglycemia in NRK-49Fcells. *Nat. Prod. Res.* **2019**, 1–6. [[CrossRef](#)] [[PubMed](#)]
10. Harborne, J.; Williams, C. The phytochemical richness of the Iridaceae and its systematic significance. *Ann. Bot.* **2000**, *58*. [[CrossRef](#)]
11. Williams, C.A.; Harborne, J.B.; Goldblatt, P. Correlations between phenolic patterns and tribal classification in the family Iridaceae. *Phytochemistry* **1986**, *25*, 2135–2154. [[CrossRef](#)]
12. Rezende, F.M.; Ferreira, M.J.P.; Clausen, M.H.; Rossi, M.; Furlan, C.M. Acylated flavonoid glycosides are the main pigments that determine the flower colour of the Brazilian native tree *Tibouchina pulchra* (Cham.) Cogn. *Molecules* **2019**, *24*, 718. [[CrossRef](#)]
13. Lin, L.-Z.; Chen, P.; Harnly, J.M. New phenolic components and chromatographic profiles of green and fermented teas. *J. Agr. Food Chem.* **2008**, *56*, 8130–8140. [[CrossRef](#)]
14. Markham, K.; Geiger, H.; Harborne, J. The flavonoids: Advances in research since 1986. *Chap* **1994**, *10*, 441–493.
15. Farag, M.A.; Gad, H.A.; Heiss, A.G.; Wessjohann, L.A. Metabolomics driven analysis of six *Nigella* species seeds via UPLC-qTOF-MS and GC-MS coupled to chemometrics. *Food Chem.* **2014**, *151*, 333–342. [[CrossRef](#)] [[PubMed](#)]
16. Farrag, A.R.H.; Abdallah, H.M.I.; Khattab, A.R.; Elshamy, A.I.; Gendy, A.; Mohamed, T.A.; Farag, M.A.; Efferth, T.; Hegazy, M.F. Antiulcer activity of *Cyperus alternifolius* in relation to its UPLC-MS metabolite fingerprint: A mechanistic study. *Phytomedicine* **2019**, *62*, 152970. [[CrossRef](#)] [[PubMed](#)]
17. Liu, M.H.; Zhang, Q.; Zhang, Y.H.; Lu, X.Y.; Fu, W.M.; He, J.Y. Chemical analysis of dietary constituents in *Rosa roxburghii* and *Rosa sterilis* Fruits. *Molecules* **2016**, *21*, 1204. [[CrossRef](#)] [[PubMed](#)]
18. Otfy, A.M.; El-Sayed, A.M.; Michel, C.G.; Farag, M.A. Metabolites profiling of date palm (*Phoenix dactylifera* L.) commercial by-products (pits and pollen) in relation to its antioxidant effect: A multiplex approach of MS and NMR metabolomics. *Metabolomics* **2019**, *15*, 119. [[CrossRef](#)] [[PubMed](#)]
19. Olennikov, D.N.; Kashchenko, N.I.; Chirikova, N.K.; Vasil'eva, A.G.; Gadimli, A.I.; Isaev, J.I.; Vennos, C. Caffeoylquinic acids and flavonoids of fringed sagewort (*Artemisia frigida* Willd.): HPLC-DAD-ESI-QQQ-MS profile, HPLC-DAD quantification, in vitro digestion stability, and antioxidant capacity. *Antioxidants* **2019**, *8*, 307. [[CrossRef](#)]
20. Alperth, F.; Mitić, B.; Mayer, S.; Maleš, Ž.; Kunert, O.; Hrušev, D.; Bucar, F. Metabolic profiling of rhizomes of native populations of the strictly endemic Croatian species *Iris adriatica*. *Plant Biosyst.* **2019**, *153*, 317–324. [[CrossRef](#)]
21. Ibrahim, S.R.; Mohamed, G.A.; Al-Musayeib, N.M. New constituents from the rhizomes of Egyptian *Iris germanica* L. *Molecules* **2012**, *17*, 2587–2598. [[CrossRef](#)]
22. Elshamy, A.I.; Farrag, A.R.H.; Ayoub, I.M.; Mahdy, K.A.; Taher, R.F.; Gendy, A.E.-N.G.E.; Mohamed, T.A.; Al-Rejaie, S.S.; El-Amier, Y.A.; Abd-ElGawad, A.M.; et al. UPLC-qTOF-MS phytochemical profile and antiulcer potential of *Cyperus conglomeratus* Rottb. alcoholic extract. *Molecules* **2020**, *25*, 4234. [[CrossRef](#)] [[PubMed](#)]
23. Rached, W.; Bennaceur, M.; Barros, L.; Calhelha, R.C.; Heleno, S.; Alves, M.J.; Carvalho, A.M.; Marouf, A.; Ferreira, I.C. Detailed phytochemical characterization and bioactive properties of *Myrtus nivelii* Batt & Trab. *Food Funct.* **2017**, *8*, 3111–3119.
24. Zhang, Y.-Y.; Wang, Q.; Qi, L.-W.; Qin, X.-Y.; Qin, M.-J. Characterization and determination of the major constituents in *Belamcandae Rhizoma* by HPLC-DAD-ESI-MS<sup>n</sup>. *J. Pharm. Biomed. Anal.* **2011**, *56*, 304–314. [[CrossRef](#)]
25. Li, J.; Li, W.Z.; Huang, W.; Cheung, A.W.; Bi, C.W.; Duan, R.; Guo, A.J.; Dong, T.T.; Tsim, K.W. Quality evaluation of *Rhizoma Belamcandae* (*Belamcanda chinensis* (L.) DC.) by using high-performance liquid chromatography coupled with diode array detector and mass spectrometry. *J. Chromatogr. A* **2009**, *1216*, 2071–2078. [[CrossRef](#)]
26. Ma, C.; Hu, L.; Kou, X.; Lv, W.; Lou, Z.; Wang, H. Rapid screening of potential  $\alpha$ -amylase inhibitors from *Rhodiola rosea* by UPLC-DAD-TOF-MS/MS-based metabolomic method. *J. Funct. Foods* **2017**, *36*, 144–149. [[CrossRef](#)]
27. Buckingham, J.; Munasinghe, V.R.N. *Dictionary of Flavonoids with CD-ROM*; CRC Press: Boca Raton, FL, USA, 2015.
28. Faheem, S.A.; Saeed, N.M.; El-Naga, R.N.; Ayoub, I.M.; Azab, S.S. Hepatoprotective effect of cranberry nutraceutical extract in non-alcoholic fatty liver model in rats: Impact on insulin resistance and Nrf-2 expression. *Front. Pharmacol.* **2020**, *11*, 218. [[CrossRef](#)]
29. Moriyasu, M.; Igi, Y.; Ichimaru, M.; Iwasa, K.; Kobayakawa, J.; Sato-Nishimori, F.; Matsukawa, Y.; Nagase, C. New isoflavones from *Belamcandae Rhizoma*. *J. Nat. Med.* **2007**, *61*, 329–333. [[CrossRef](#)]
30. Es-Safi, N.E.; Kerhoas, L.; Ducrot, P.H. Application of positive and negative electrospray ionization, collision-induced dissociation and tandem mass spectrometry to a study of the fragmentation of 6-hydroxyluteolin 7-O-glucoside and 7-O-glucosyl-(1→3)-glucoside. *Rapid Commun. Mass Spectr.* **2005**, *19*, 2734–2742. [[CrossRef](#)] [[PubMed](#)]
31. Zhang, Y.; De Stefano, R.; Robine, M.; Butelli, E.; Bulling, K.; Hill, L.; Rejzek, M.; Martin, C.; Schoonbeek, H.-j. Different reactive oxygen species scavenging properties of flavonoids determine their abilities to extend the shelf life of tomato. *Plant. Physiol.* **2015**, *169*, 1568–1583. [[CrossRef](#)]

32. Wollenweber, E.; Stevens, J.F.; Klimo, K.; Knauff, J.; Frank, N.; Gerhauser, C. Cancer chemopreventive in vitro activities of isoflavones isolated from *Iris germanica*. *Planta Med.* **2003**, *69*, 15–20. [\[CrossRef\]](#)
33. Maamoun, A.A.; El-akkad, R.H.; Farag, M.A. Mapping metabolome changes in *Luffa aegyptiaca* Mill fruits at different maturation stages via MS-based metabolomics and chemometrics. *J. Adv. Res.* **2019**. [\[CrossRef\]](#)
34. Boskabady, M.; Tabatabaee, A.; Byrami, G. The effect of the extract of *Crocus sativus* and its constituent safranal, on lung pathology and lung inflammation of ovalbumin sensitized guinea-pigs. *Phytomedicine* **2012**, *19*, 904–911. [\[CrossRef\]](#)
35. Ayoub, I.M.; Korinek, M.; Hwang, T.-L.; Chen, B.-H.; Chang, F.-R.; El-Shazly, M.; Singab, A.N.B. Probing the antiallergic and anti-inflammatory activity of biflavonoids and dihydroflavonols from *Dietes bicolor*. *J. Nat. Prod.* **2018**, *81*, 243–253. [\[CrossRef\]](#) [\[PubMed\]](#)
36. Korinek, M.; Tsai, Y.-H.; El-Shazly, M.; Lai, K.-H.; Backlund, A.; Wu, S.-F.; Lai, W.-C.; Wu, T.-Y.; Chen, S.-L.; Wu, Y.-C. Anti-allergic hydroxy fatty acids from *Typhonium blumei* explored through ChemGPS-NP. *Front. Pharmacol.* **2017**, *8*, 356. [\[CrossRef\]](#) [\[PubMed\]](#)
37. Hwang, T.-L.; Wang, C.-C.; Kuo, Y.-H.; Huang, H.-C.; Wu, Y.-C.; Kuo, L.-M.; Wu, Y.-H. The hederagenin saponin SMG-1 is a natural FMLP receptor inhibitor that suppresses human neutrophil activation. *Biochem. Pharmacol.* **2010**, *80*, 1190–1200. [\[CrossRef\]](#) [\[PubMed\]](#)
38. Braga, P.C.; Dal Sasso, M.; Culici, M.; Bianchi, T.; Bordoni, L.; Marabini, L. Anti-inflammatory activity of thymol: Inhibitory effect on the release of human neutrophil elastase. *Pharmacology* **2006**, *77*, 130–136. [\[CrossRef\]](#)
39. McCord, J.M.; Roy, R.S. The pathophysiology of superoxide: Roles in inflammation and ischemia. *Can. J. Physiol. Pharmacol.* **1982**, *60*, 1346–1352. [\[CrossRef\]](#)
40. Roy, M.K.; Koide, M.; Rao, T.P.; Okubo, T.; Ogasawara, Y.; Juneja, L.R. ORAC and DPPH assay comparison to assess antioxidant capacity of tea infusions: Relationship between total polyphenol and individual catechin content. *Int. J. Food Sci. Nutr.* **2010**, *61*, 109–124. [\[CrossRef\]](#)
41. Chen, J.; Wu, Y.; Zou, J.; Gao, K.  $\alpha$ -Glucosidase inhibition and antihyperglycemic activity of flavonoids from *Ampelopsis grossedentata* and the flavonoid derivatives. *Bioorg. Med. Chem.* **2016**, *24*, 1488–1494. [\[CrossRef\]](#)
42. Rauter, A.P.; Martins, A.; Borges, C.; Mota-Filipe, H.; Pinto, R.; Sepodes, B.; Justino, J. Antihyperglycaemic and protective effects of flavonoids on streptozotocin-induced diabetic rats. *Phytother. Res.* **2010**, *24*, S133–S138. [\[CrossRef\]](#)
43. Arumugam, B.; Palanisamy, U.D.; Chua, K.H.; Kuppasamy, U.R. Potential antihyperglycaemic effect of myricetin derivatives from *Syzygium malaccense*. *J. Funct. Foods* **2016**, *22*, 325–336. [\[CrossRef\]](#)
44. Heikkilä, E.; Hermant, A.; Thevenet, J.; Bermont, F.; Kulkarni, S.S.; Ratajczak, J.; Santo-Domingo, J.; Dioum, E.H.; Canto, C.; Barron, D. The plant product quinic acid activates  $\text{Ca}^{2+}$ -dependent mitochondrial function and promotes insulin secretion from pancreatic beta cells. *Br. J. Pharmacol.* **2019**, *176*, 3250–3263. [\[PubMed\]](#)
45. Adams, R.P. *Identification of Essential Oil Components by Gas Chromatography/Quadrupole Mass Spectroscopy*, 3rd ed.; Allured Pub Corp: Carol Stream, IL, USA, 2004.
46. Ayoub, I.M.; Youssef, F.S.; El-Shazly, M.; Ashour, M.L.; Singab, A.N.; Wink, M. Volatile constituents of *Dietes bicolor* (Iridaceae) and their antimicrobial activity. *Z. Nat. C* **2015**, *70*, 217–225. [\[CrossRef\]](#)
47. Elkady, W.M.; Ayoub, I.M. Chemical profiling and antiproliferative effect of essential oils of two *Araucaria* species cultivated in Egypt. *Ind. Crops Prod.* **2018**, *118*, 188–195. [\[CrossRef\]](#)
48. Gad, H.A.; Ayoub, I.M.; Wink, M. Phytochemical profiling and seasonal variation of essential oils of three *Callistemon* species cultivated in Egypt. *PLoS ONE* **2019**, *14*, e0219571. [\[CrossRef\]](#) [\[PubMed\]](#)
49. Labib, R.M.; Ayoub, I.M.; Michel, H.E.; Mehanny, M.; Kamil, V.; Hany, M.; Magdy, M.; Moataz, A.; Maged, B.; Mohamed, A. Appraisal on the wound healing potential of *Melaleuca alternifolia* and *Rosmarinus officinalis* L. essential oil-loaded chitosan topical preparations. *PLoS ONE* **2019**, *14*, e0219561. [\[CrossRef\]](#)
50. Saeed Kotb, S.; Ayoub, I.M.; El-Moghazy, S.A.; Singab, A.N.B. Profiling the lipophilic fractions of *Pithecellobium dulce* bark and leaves using GC/MS and evaluation of their antioxidant, antimicrobial and cytotoxic activities. *Chem. Biodivers.* **2020**, *17*, e2000048. [\[CrossRef\]](#)
51. Ashmawy, A.M.; Ayoub, I.M.; Eldahshan, O.A. Chemical composition, cytotoxicity and molecular profiling of *Cordia africana* Lam. on human breast cancer cell line. *Nat. Prod. Res.* **2020**, 1–6. [\[CrossRef\]](#)
52. Gad, H.; Al-Sayed, E.; Ayoub, I. Phytochemical discrimination of *Pinus* species based on GC–MS and ATR-IR analyses and their impact on *Helicobacter pylori*. *Phytochem. Anal.* **2021**. [\[CrossRef\]](#)
53. Chen, B.-H.; Wu, P.-Y.; Chen, K.-M.; Fu, T.-F.; Wang, H.-M.; Chen, C.-Y. Antiallergic potential on RBL-2H3 cells of some phenolic constituents of *Zingiber officinale* (Ginger). *J. Nat. Prod.* **2009**, *72*, 950–953. [\[CrossRef\]](#)
54. Thabet, A.A.; Youssef, F.S.; Korinek, M.; Chang, F.-R.; Wu, Y.-C.; Chen, B.-H.; El-Shazly, M.; Singab, A.N.B.; Hwang, T.-L. Study of the anti-allergic and anti-inflammatory activity of *Brachychiton rupestris* and *Brachychiton discolor* leaves (Malvaceae) using in vitro models. *BMC Complement. Altern. Med.* **2018**, *18*, 299. [\[CrossRef\]](#) [\[PubMed\]](#)
55. Samir, N.; George, R.F.; Elrazaz, E.Z.; Ayoub, I.M.; Shalaby, E.M.; Plaisier, J.R.; Demitri, N.; Wink, M. Synthesis of some tropane-based compounds targeting colon cancer. *Future Med. Chem.* **2020**, *12*, 2123–2140. [\[CrossRef\]](#) [\[PubMed\]](#)
56. George, R.F.; Samir, N.; Ayoub, I.M.; Shalaby, E.M.; Demitri, N.; Wink, M. Synthesis, antiproliferative activity and 2D-QSAR study of some 8-alkyl-2,4-bisbenzylidene-3-nortropinones. *Future Med. Chem.* **2018**, *10*, 2815–2833. [\[CrossRef\]](#) [\[PubMed\]](#)
57. Ayoub, I.; El-Shazly, M.; Lu, M.-C.; Singab, A. Antimicrobial and cytotoxic activities of the crude extracts of *Dietes bicolor* leaves, flowers and rhizomes. *S. Afr. J. Bot.* **2014**, *95*, 97–101. [\[CrossRef\]](#)

58. Matsuda, H.; Tewtrakul, S.; Morikawa, T.; Nakamura, A.; Yoshikawa, M. Anti-allergic principles from Thai zedoary: Structural requirements of curcuminoids for inhibition of degranulation and effect on the release of TNF- $\alpha$  and IL-4 in RBL-2H3 cells. *Bioorg. Med. Chem.* **2004**, *12*, 5891–5898. [[CrossRef](#)] [[PubMed](#)]
59. Chen, B.-H.; Hung, M.-H.; Chen, J.Y.-F.; Chang, H.-W.; Yu, M.-L.; Wan, L.; Tsai, F.J.; Wang, T.-P.; Fu, T.-F.; Chiu, C.-C. Anti-allergic activity of grapeseed extract (GSE) on RBL-2H3 mast cells. *Food Chem.* **2012**, *132*, 968–974. [[CrossRef](#)]
60. Chung, Y.-M.; Chang, F.-R.; Tseng, T.-F.; Hwang, T.-L.; Chen, L.-C.; Wu, S.-F.; Lee, C.-L.; Lin, Z.-Y.; Chuang, L.-Y.; Su, J.-H. A novel alkaloid, aristopyridinone A and anti-inflammatory phenanthrenes isolated from *Aristolochia manshuriensis*. *Bioorg. Med. Chem. Lett.* **2011**, *21*, 1792–1794. [[CrossRef](#)]
61. Youssef, F.; Ashour, M.; Sobeh, M.; El-Beshbishy, H.; Singab, A.; Wink, M. *Eremophila maculata* Isolation of a rare naturally-occurring lignan glycoside and the hepatoprotective activity of the leaf extract. *Phytomedicine* **2016**, *23*, 1484–1493. [[CrossRef](#)]
62. Youssef, F.S.; Ashour, M.L.; Ebada, S.S.; Sobeh, M.; El-Beshbishy, H.A.; Singab, A.N.; Wink, M. Antihyperglycaemic activity of the methanol extract from leaves of *Eremophila maculata* (Scrophulariaceae) in streptozotocin-induced diabetic rats. *J. Pharm. Pharmacol.* **2017**, *69*, 733–742. [[CrossRef](#)]
63. Thabet, A.A.; Youssef, F.S.; El-Shazly, M.; El-Beshbishy, H.A.; Singab, A.N.B. Validation of the antihyperglycaemic and hepatoprotective activity of the flavonoid rich fraction of *Brachychiton rupestris* using in vivo experimental models and molecular modelling. *Food Chem. Toxicol.* **2018**, *114*, 302–310. [[CrossRef](#)]
64. Trinder, P. Determination of glucose in blood using glucose oxidase with an alternative oxygen acceptor. *Ann. Clin. Biochem.* **1969**, *6*, 24–27. [[CrossRef](#)]
65. Gordon, C.; Yates, A.; Davies, D. Evidence for a direct action of exogenous insulin on the pancreatic islets of diabetic mice: Islet response to insulin pre-incubation. *Diabetologia* **1985**, *28*, 291–294. [[CrossRef](#)]
66. Elkady, M.W.; Ayoub, M.I.; Abdel-Mottaleb, Y.; ElShafie, M.F.; Wink, M. *Euryops pectinatus* L. flower extract inhibits P-glycoprotein and reverses multi-drug resistance in cancer cells: A mechanistic study. *Molecules* **2020**, *25*, 647. [[CrossRef](#)] [[PubMed](#)]

## 國產水果之鮮榨果汁抗氧化劑及抗氧化能力分析

陳頤之<sup>1</sup> 賴明宏<sup>2</sup> 劉珍芳<sup>3\*</sup>Studies of Antioxidants and Antioxidative Activity  
of Fresh Juice in TaiwanYi-Jr Chen<sup>1</sup>, Ming-Hoang Lai<sup>2</sup>, Jen-Fang Liu<sup>3\*</sup>

## 摘 要

水果中含有豐富的抗氧化劑，包括營養素及物質，具有防止人體氧化性傷害的能力。本研究擬評估木瓜、白肉火龍果、珍珠芭樂及雪梨等四種產自台灣的市售水果，經慢磨機榨汁，測量各種果汁抗氧化劑及抗氧化能力，包括維生素 C 及總多酚；總抗氧化力、自由基清除力及亞硝酸鹽清除力等。結果顯示，維生素 C 及總多酚含量，皆以珍珠芭樂汁的含量最高。在抗氧化能力方面，總抗氧化力以珍珠芭樂汁最強，自由基清除力以木瓜汁及珍珠芭樂汁為最強，亞硝酸鹽清除力以木瓜汁為最強。進一步性分析顯示，本實驗所有果汁樣本的維生素 C 含量及總多酚含量，均與總抗氧化力呈高度正相關性。

關鍵詞：果汁、抗氧化劑、維生素 C、總多酚、總抗氧化力、自由基清除力、亞硝酸鹽清除力

## ABSTRACT

Fruits are rich in antioxidants, including nutrients and substances, which have the ability to prevent oxidative damage. The purpose of this study was to evaluate the antioxidants and antioxidative activity of guava, papaya, pitaya (white meat), and pyrus nivalis in Taiwan. The juice was extracted by masticating juicer. The antioxidant nutrient and substance, including vitamin C and total polyphenols, and the antioxidant activity, including trolox equivalent antioxidant activity, radical scavenging activity and nitrite scavenging activity were analyzed. The results showed that the contents of vitamin C and total polyphenols were the highest in guava juice. In terms of antioxidant activity, guava juice had the strongest total antioxidant activity, papaya juice and guava juice had the strongest free radical scavenging activity, and papaya juice had the strongest nitrite scavenging capacity. The Pearson Correlation test showed that the vitamin C content and total polyphenol content of all juice samples were highly positively correlated

<sup>1</sup> 長庚科技大學保健營養系、食品暨化妝品安全研究中心、中草藥研究中心副教授

<sup>2</sup> 耕莘健康管理專科學校嬰幼兒保育科及護理科助理教授

<sup>3</sup> 長庚科技大學保健營養系、食品暨化妝品安全研究中心、中草藥研究中心教授



with the trolox equivalent antioxidant activity.

**Keywords:** juice, vitamin C, total polyphenols, Trolox equivalent antioxidant activity, radical scavenging activity, nitrite scavenging activity

## 壹、緒論

人體在正常代謝過程中會產生許多活性氧物質 (Reactive oxygen species, ROS), 例如過氧化氫 (hydrogen peroxide,  $H_2O_2$ )、單重態氧 (singlet oxygen,  $^1O_2$ )、超氧陰離子 (superoxide anion radical,  $\cdot O_2^-$ ) 及羥基自由基 (hydroxyl radical,  $\cdot OH$ ) 等 (Zorov, Juhaszova, & Sollott, 2014), 可導致人體氧化性傷害, 包括損傷細胞膜、影響酵素活性及攻擊細胞內遺傳物質 - 去氧核糖核酸 (deoxyribonucleic acid, DNA) 等。許多研究指出, 自由基與癌症、心血管疾病、糖尿病、白內障、巴金森氏症等疾病之形成及老化有關 (Fehrenbach & Northoff, 2001; Ross & Jenkin, 1998)。

許多水果中含有豐富的抗氧化劑 (Antioxidants), 包括營養素及物質, 具有防止人體氧化性傷害的能力。水果的抗氧化劑受到許多因素影響, 包括品種、栽種過程、成熟度、採收時間、貯存時間、貯存溫度、後熟處理方式等等 (吳喜正, 2007)。例如芭樂隨著後熟程度的增加, 維生素 C (vitamin C) 及總多酚 (total polyphenols) 含量有減少的現象, 相對的  $\beta$ -胡蘿蔔素 ( $\beta$ -carotene) 則會增加 50-139%; 西瓜置於 21°C 儲存 14 天後, 茄紅素 (lycopene) 增加 11~14% (Bashir & Abu-Goukh, 2003; Perkins-Veazie & Collins, 2006)。而水果的抗氧化能力, 以亞硝酸鹽清除力而言, 曾有研究指出: 進口水果清除亞硝酸鹽的功能不如國產水果, 可能是進口水果輸運來台販售需要花費時間, 使抗氧化劑流失所致 (楊淑惠 & 謝源業, 2015)。

水果的食用, 除了直接吃之外, 也有人會將

之榨汁。榨汁可以手動或者以機器輔助, 例如離心榨汁機 (Centrifugal Juicer)、慢磨機 (Masticating Juicer)、磨碎榨汁機 (Triturating Juicer) 及壓榨汁機 (Press Juicer) 等 (Nnamdi, Onyejiuwa, & Ogbuke, 2020)。對於果汁之抗氧化相關研究方面, 曾有研究以台灣市售果汁為樣本, 進行抗氧化分析, 發現 100% 柳橙汁之維生素 C 含量與總抗氧化力及自由基清除力有高度正向相關 ( $r > 0.9$ ), 且精胺酸含量與總抗氧化力及自由基清除力之亦有高度相關性 ( $r > 0.8$ ), 但總多酚含量與總抗氧化力及自由基清除力相關性則不高 ( $r < 0.13$ ) (劉昀達 & 姚賢宗, 2013)。而對於台灣市售水果, 則少見以慢磨機鮮榨果汁進行抗氧化分析, 因此本研究依據臺灣民眾的飲食中將水果製備為果汁食用之習慣, 並參考衛生福利部食品藥物管理署之食品營養成分資料庫臺灣產維生素 C 含量較高、居中及較低的四種水果包括珍珠芭樂、木瓜、白肉火龍果 (以下簡稱白火龍果) 及雪梨, 作為受測之水果 (衛生福利部食品藥物管理署, 2017)。將選取之水果以慢磨機榨汁, 分析果汁之抗氧化劑含量及抗氧化力, 並評估抗氧化劑及抗氧化能力之間的相關性。

## 貳、材料與方法

### 一、實驗流程

本實驗之水果, 購入後首先進行果實性質分析, 包括硬度、pH 值、糖度及糖/酸比。將珍珠芭樂、木瓜、白火龍果及雪梨分別為各三批。每個實驗每批樣本取 2 顆, 去除外皮、籽等不食用區塊, 取可食部位, 處理成一般常見的食用狀態



進行分析。之後將樣本以慢磨機榨汁，置入微量離心管，以微量離心機於 4°C 下以 10,000 rpm 離心 3 分鐘，取上清液進行抗氧化劑及抗氧化力分析 (楊淑惠 & 謝源業, 2015)。抗氧化劑分析包括維生素 C 及總酚含量；抗氧化能力分析包括總抗氧化力 (Trolox equivalent antioxidant capacity, TEAC)，自由基清除力 (Radical scavenging activity) 及亞硝酸鹽清除力 (Nitrite scavenging activity) 等。每份樣本之果實性質分析之糖度、抗氧化劑及抗氧化力分析各進行三重覆實驗；果實性質分析之硬度進行二重覆實驗；果實性質分析之可滴定酸度及 pH 值進行一次實驗。實驗流程如圖一。



## 二、樣本

珍珠芭樂 (彰化溪洲, 臺灣) 購自四季田水果行 (新北市, 臺灣), 於 2016 年 9 月至 2017 年 2 月間購得；木瓜 (屏東, 臺灣)、白火龍果 (南投信義鄉, 臺灣) 及雪梨 (梨山新興里, 臺灣) 購自南臺灣頂級水果專賣店 (新北市, 臺灣)。木瓜及雪梨於 2016 年 12 月至 2017 年 2 月間購得，火龍果於 2016 年 11 月至 2017 年 2 月間購得。本研究樣本之取樣方式比照一般消費者購買水果的方

式，選擇水果熟度為立即可食用之狀態。

## 三、果實性質分析

### 1. 硬度

利用硬度計測定果肉食用部位。削去約 1 平方公分大小的果皮，測量果肉。分別選取果實中段區域及旋轉 90 度區域各測 1 次，求其平均值，單位為  $\text{kg}/\text{cm}^2$ 。

### 2. 榨汁率、糖度、酸度及糖 / 酸比

榨汁率是取水果可食部位，以慢磨機 (HB666R, HUROM) 榨汁後，汁液 (mL)  $\div$  可食重 (g) 計算而得。汁液是取汁液利用糖度計 (MASTER-M, ATAGO) 測量，單位為  $^{\circ}\text{Brix}$ 。可滴定酸度的測量是取 14 mL 汁液，以 0.1N NaOH 滴定，pH 值 8.1 為滴定終點，以酸鹼值測定器 (pH meter) 測定 pH 值。酸度以 % 表示，酸度計算方式為： $A \times F \times B \times (100/S) \times (1/25) \times 100$ ；A 代表 0.1N NaOH 消耗的體積 (mL)，F 代表 0.1N NaOH 溶液的力價，其值為 1，B 代表與 0.1N NaOH 溶液 1 mL 相當的有機酸量 (g)，檸檬酸為 0.0064，S 代表試料秤取量，即 10 g (段盛秀 & 楊海明, 2005)。pH 值以酸鹼值測定器測定。糖 / 酸比以糖度 ( $^{\circ}\text{Brix}$ )  $\div$  可滴定酸度 (%) 計算而得。

## 四、抗氧化劑分析

### 1. 維生素 C 含量

取 200  $\mu\text{L}$  的樣本，加入 300  $\mu\text{L}$  的 5% Trichloroacetic acid (TCA) 於 4°C 下以 12,000 rpm 離心 5 分鐘。取出上清液加入 100  $\mu\text{L}$  的 DNPH working reagent，於 60°C 下處理 60 分鐘，冰浴 5 分鐘，再加入 400  $\mu\text{L}$  的 85%  $\text{H}_2\text{SO}_4$  solution 避光反應 20 分鐘後，以分光光度計於波長 520 nm 下測定吸光值 (Roe & Kuether, 1943)，並利用維生素 C 標準品配製不同濃度包括 0  $\mu\text{g}/\text{mL}$ 、20  $\mu\text{g}/\text{mL}$ 、40  $\mu\text{g}/\text{mL}$ 、60  $\mu\text{g}/\text{mL}$ 、80  $\mu\text{g}/\text{mL}$ 、100  $\mu\text{g}/\text{mL}$ ，進

行簡單線性回歸分析 (simple linear regression)，利用此回歸直線計算樣本之相對濃度。DNPH working reagent 配製方法：以 9N  $\text{H}_2\text{SO}_4$  配製 2.2% 2,4-Dinitrophenylhydrazine 溶液，與 5% Thiourea 溶液及 0.6%  $\text{CuSO}_4 \cdot 5\text{H}_2\text{O}$  溶液以 20 : 1 : 1 比例混合 (吳雨杰，2011)。

## 2. 總多酚含量

取 0.5 mL 樣本加入 4°C 之 10% TCA 0.5 mL 作用 24 小時後，以 10,000 rpm 離心 3 分鐘，取上清液進行分析。將每 0.2 mL 上清液加入 1 mL  $\text{ddH}_2\text{O}$ ，再加入 0.1 mL Folin-Ciocalteus reagent 混合均勻後，靜置 5 分鐘，再加入 0.1 mL 20%  $\text{Na}_2\text{CO}_3$  混合均勻，使作用 2 小時，以分光光度計於波長 750 nm 下測定吸光值。並利用 Gallic acid 配製不同濃度包括 0  $\mu\text{g/mL}$ 、20  $\mu\text{g/mL}$ 、40  $\mu\text{g/mL}$ 、60  $\mu\text{g/mL}$ 、80  $\mu\text{g/mL}$ 、100  $\mu\text{g/mL}$ ，進行簡單線性回歸分析 (simple linear regression)，利用此回歸直線計算樣本之相對濃度 (楊淑惠 & 謝源業，2015)。

## 五、抗氧化能力分析

### 1. 總抗氧化力

取 10  $\mu\text{L}$  樣本加入 990  $\mu\text{L}$  ABTS (2, 2'-Azino-bis-[3-ethylbenthiazoline sulfonic acid]) 自由基溶液混合均勻，反應 10 分鐘，以分光光度計於波長 734 nm 下測定吸光值。並利用 Trolox 配製不同濃度 (0-4 mM)，進行簡單線性回歸分析 (simple linear regression)，利用此回歸直線計算樣本之相對濃度。ABTS 自由基溶液配製方法：將 7 mM ABTS 以二次水稀釋到在 734 nm 下，吸光值為  $0.700 \pm 0.020$ 。ABTS 自由基貯存溶液配製方法：以 2.45 mM  $\text{K}_2\text{S}_2\text{O}_8$  配製 7 mM ABTS，室溫避光靜置 12 至 16 小時，會呈藍綠色 (陳佳惠等，2012)。

### 2. 自由基清除力

取 300  $\mu\text{L}$  樣本加入 75  $\mu\text{L}$  1 mM 2,2-Diphenyl-1-picrylhydrazyl (DPPH) (需新鮮配製，以甲醇為溶劑)，震盪混合均勻，在室溫下反應 30 分鐘，取 200  $\mu\text{L}$  反應液以分光光度計於波長 517 nm 下測定吸光值 ( $\text{OD}_{517}$ )；另以  $\text{ddH}_2\text{O}$  進行上述相同實驗作為空白組。清除力以清除率 (scavenging effect %) 表示，清除率計算方式為  $[1 - (\text{樣本 } \text{OD}_{517} / \text{空白組 } \text{OD}_{517})] \times 100$  (湯淑貞，2000)。

### 3. 亞硝酸鹽清除力

取 0.4 mL 樣本加入  $\text{NaNO}_2$  (濃度 5  $\mu\text{g/mL}$ ) 0.3 mL 於 37°C 反應 10 分鐘，再加入 0.4 % Sulfanilic acid 0.2 mL，於室溫反應 5 分鐘；最後加入 0.2 % N-(1-Naphthyl)ethylenediamine dihydrochloride (NEDA) 0.1 mL，於室溫反應 5 分鐘。以分光光度計於波長 538 nm 下測定吸光值。並利用  $\text{NaNO}_2$  配製不同濃度包括 0  $\mu\text{g/mL}$ 、1  $\mu\text{g/mL}$ 、2  $\mu\text{g/mL}$ 、3  $\mu\text{g/mL}$ 、4  $\mu\text{g/mL}$ 、5  $\mu\text{g/mL}$ ，進行簡單線性回歸分析 (simple linear regression)，利用此回歸直線計算樣本之相對濃度 (楊淑惠 & 謝源業，2015)。清除力以清除率 (scavenging effect %) 表示，清除率計算方式為  $[1 - (\text{樣本 } \text{OD}_{538} / \text{空白組 } \text{OD}_{538})] \times 100$ 。

## 六、統計方法

以  $t$  test 分析進行各種水果間之各項數據之比較，當  $p < 0.05$  表示達到統計差異。以 Pearson Correlation test 進行實驗樣本數據相關性之分析，當相關係數 (correlation coefficient,  $r$ ) 為 -1 或 1，表示完全相關。介於 -0.3 及 0.3 之間，表示正向及負向低度相關；介於 -0.3 至 -0.6 及 0.3 至 0.6 之間，表示正向及負向中度相關；介於 -0.6 至 -0.9 及 0.6 至 0.9 之間，表示正向及負向高度相關。

## 參、結果與討論

### 一、果實性質

果實的硬度、糖度、酸度等果實性質，為果實品質及熟度之指標，也影響水果的口感及風味。本實驗四種水果之熟度皆為立即可食用的狀態，其果實性質列於表一，四種水果中，果實硬度以珍珠芭樂之最高，白火龍果為最低。果汁之糖度及糖酸比皆以雪梨為最高，糖度以珍珠芭樂為最低，而糖酸比則以白火龍果為最低。此四種水

果中以慢磨機研磨之榨汁率介於  $68 \pm 10.41\%$  至  $77 \pm 1.80\%$  之間，其中以珍珠芭樂為最低，雪梨則最高。

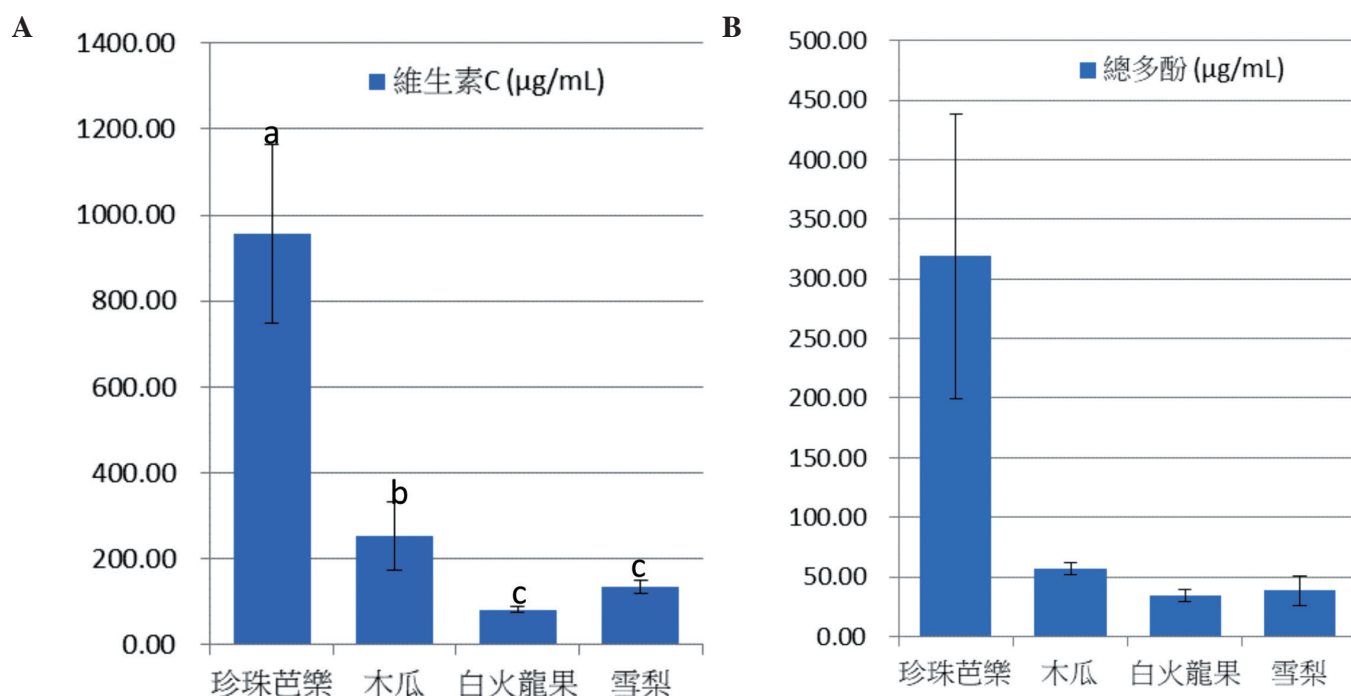
### 二、抗氧化劑及抗氧化能力

#### 1. 抗氧化劑

四種水果其果汁之抗氧化劑結果見圖二，維生素 C 含量由高至低依序為珍珠芭樂、木瓜、白火龍果及雪梨，珍珠芭樂顯著高於其他三種水果，木瓜亦顯著高過白火龍果及雪梨，白火龍果及雪

表一：四種水果之果實性質

	鮮果重 (g)	可食重 (g)	榨汁率 (%)	硬度 (kg/cm <sup>3</sup> )	pH 值	糖度 (°Brix)	酸度 (%)	糖 / 酸比
珍珠芭樂	280.43±31.91	213.00±28.02	68±10.41	5.90±1.28	3.93±0.07	8.90±0.33	0.22±0.04	42.1±8.8
木瓜	654.92±30.62	565.62±39.39	76±3.26	1.00±0.25	5.22±0.10	11.23±0.18	0.09±0.02	133.3±22.3
白火龍果	827.10±139.05	582.63±57.95	73±5.19	0.53±0.06	5.43±0.17	10.97±1.36	0.05±0.01	24.2±4.3
雪梨	446.13±73.42	370.10±59.76	77±1.80	3.47±0.57	4.64±0.25	12.73±0.44	0.10±0.05	154.8±78.5



A 維生素 C 含量；B 總多酚含量。a,b,c 相同英文小寫字母表示不具顯著差異。

圖二：四種水果之抗氧化劑



梨二者則無顯著差異。總多酚含量由高至低依序為珍珠芭樂及木瓜，白火龍果及雪梨，珍珠芭樂顯著高於其他三種水果，木瓜，白火龍果及雪梨三者間無顯著差異。此趨勢在維生素 C 含量及總多酚含量方面之高低，與先前有關國產水果之抗氧化劑的研究一致 (楊淑惠 & 謝源業, 2015)。

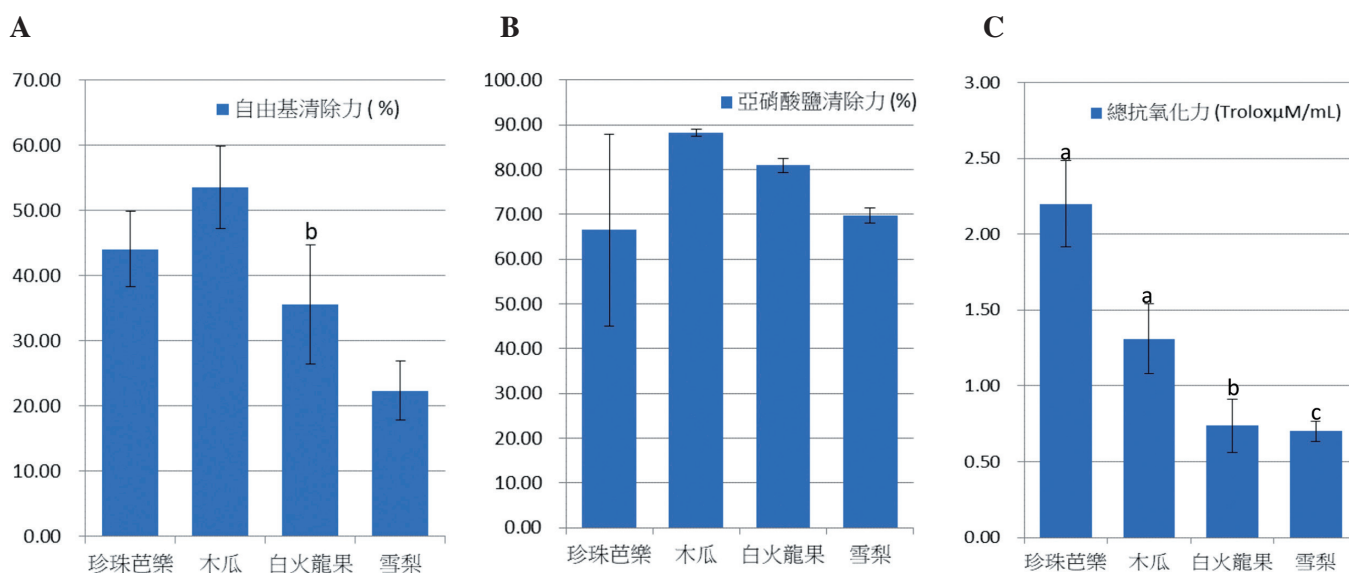
## 2. 抗氧化能力

四種水果其果汁之抗氧化力結果如圖三，總抗氧化力由高至低依序為珍珠芭樂、木瓜、白火龍果及雪梨，珍珠芭樂及木瓜此二者間無顯著差異，但顯著高過其他兩種水果。自由基清除力由高至低依序為木瓜、珍珠芭樂、白火龍果、雪梨。前兩者無顯著差異，但顯著高過其他兩種水果。亞硝酸鹽清除力由高至低依序為木瓜、白火龍果、雪梨及珍珠芭樂，木瓜與白火龍果顯著高過雪梨及珍珠芭樂。先前一項 2015 年所發表對國產水果之亞硝酸鹽清除力的研究，顯示珍珠芭樂的清除力優於木瓜及雪梨 (楊淑惠 & 謝源業, 2015)，推測其間的差異可能源於水果的來源、產地，或樣本製備方式不同所致。

## 3. 抗氧化劑及抗氧化能力之相關性

將本實驗其鮮榨果汁之抗氧化劑：維生素 C 及總多酚之含量，分別與抗氧化能力：總抗氧化力、自由基清除力及亞硝酸鹽清除力等進行相關性分析，見表二及圖四，結果顯示，全部四種果汁的維生素 C 含量與總抗氧化力之相關係數為 0.93，總多酚含量與總抗氧化力之相關係數為 0.75，意即維生素 C 含量及總多酚含量與總抗氧化力皆呈高度正向相關；而維生素 C 含量與亞硝酸鹽清除力則僅在芭樂汁可見到高度正向相關性。

本實驗結果在維生素 C 含量與總抗氧化力間相關性之趨勢，與先前一項國內於 2013 年所發表與評估 100% 柳橙汁之研究結果一致 (劉昀達 & 姚賢宗, 2013)。顯示在不同種類的數種鮮榨果汁或者市售果汁，維生素 C 含量與總抗氧化力間可見到呈現高度正向相關之趨勢。而在維生素 C 含量與自由基清除力及總多酚含量與總抗氧化力間之相關性則不一致，此可能與各類果汁中其他營養素之組成差異有關。此有待進一步進行探討。

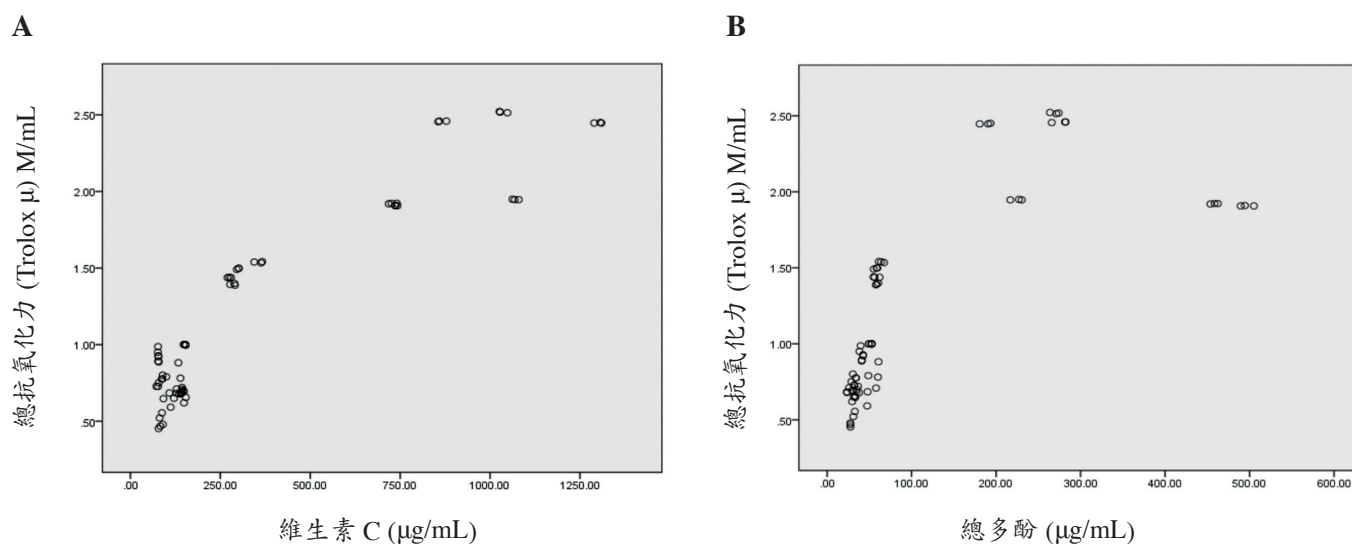


A 總抗氧化力；B 自由基清除力；C 亞硝酸鹽清除力。a,b,c 相同英文小寫字母表示不具顯著差異。

圖三：四種水果之抗氧化力

表二：四種水果之抗氧化劑與抗氧化能力間的相關性分析

水果種類		全部四種 樣本數 = 24		芭樂 樣本數 = 6		木瓜 樣本數 = 6		白火龍果 樣本數 = 6		雪梨 樣本數 = 6	
抗氧化劑	抗氧化能力	<i>r</i>	<i>p</i>	<i>r</i>	<i>p</i>	<i>r</i>	<i>p</i>	<i>r</i>	<i>p</i>	<i>r</i>	<i>p</i>
VitC ( $\mu\text{g/mL}$ )	總抗氧化力 (Trolox $\mu\text{M/mL}$ )	0.93	0.0000	0.55	0.0175	0.98	0.0000	-0.42	0.084	-0.09	0.7231
	自由基清除力 (%)	0.08	0.5173	0.34	0.1627	-0.79	0.0001	-0.2	0.4223	-0.79	0.0001
	亞硝酸鹽清除力 (%)	-0.02	0.8996	0.78	0.0001	-0.62	0.0058	-0.17	0.5066	0.04	0.8615
總多酚 ( $\mu\text{g/mL}$ )	總抗氧化力 (Trolox $\mu\text{M/mL}$ )	0.75	0.0000	-0.65	0.0033	0.83	0.0000	0.84	0.0000	0.56	0.0148
	自由基清除力 (%)	-0.01	0.8916	-0.09	0.7106	-0.8	0.0001	0.28	0.2675	0.19	0.4458
	亞硝酸鹽清除力 (%)	-0.38	0.0010	-0.94	0.0000	-0.54	0.0198	-0.17	0.5023	-0.9	0.000



A：總抗氧化力與與維生素 C；B：總抗氧化力與總多酚。

圖四：全部四種水果其總抗氧化力與抗氧化營養素相關性之散佈圖

## 肆、結論

本實驗所分析之四種市售水果其果汁中，在抗氧化劑方面，包括維生素 C 及總多酚均以珍珠芭樂汁的含量最高。在抗氧化力方面，總抗氧化力則以珍珠芭樂汁為最高，而自由基清除力及亞硝酸鹽清除力則以木瓜汁為最高。此外，維生素 C 含量及總多酚含量與總抗氧化力皆呈高度正向相關。

## 伍、致謝

感謝長庚科技大學助理詹凱筑小姐協助本文之實驗執行及高宇田小姐協助本文之統計分析。

## 參考文獻

吳雨杰 (2011)．不同顏色蔬果的介入對健康成年女性體內抗氧化狀態之影響．臺北醫學大



- 學保健營養學系碩士論文。
- 吳喜正 (2007) · 貯藏溫度及成熟度對數種熱帶水果之抗氧化能力之影響 · 國立屏東科技大學熱帶農業暨國際合作系所碩士論文。
- 段盛秀 & 楊海明 (2005) · 食品化學分析與檢驗。藝軒圖書出版社。
- 陳佳惠、黃秋菁、陳雅筑、王曉芬及易光輝 (2012) · 化妝品常用二十八種精油之總酚含量測定、清除 DPPH 自由基能力、總抗氧化能力及主要精油化學成分分析之研究 · 弘光學報, 69:1-11。
- 湯淑貞 (2000) · 臺灣紅色鄉土蔬菜萃取物之抗氧化效力研究 · 中國文化大學生活應用科學研究所碩士論文。
- 楊淑惠 & 謝源業 (2015) · 國產水果之抗氧化力 - 以亞硝酸鹽清除力為例 · 農業試驗所技術服務季刊, 103:1-3。
- 劉昀達 & 姚賢宗 (2013) · 臺灣市售果汁之主要成分與其自由基清除能力分析 · 臺灣農業化學與食品科學, 51(1):25-33。
- Bashir, H. A. & Abu-Goukh, A.-B. A. (2003). Compositional changes during guava fruit ripening. *Food Chemistry*, 80(4):557-563.
- Fehrenbach, E. & Northoff, H. (2001). Free radicals, exercise, apoptosis, and heat shock proteins. *Exercise immunology Review*, 7:66-89.
- Nnamdi, U. B., Onyejiuwa, C. T. & Ogbuke, C. R. (2020). Review of Orange Juice Extractor Machines. *Advances in Science, Technology and Engineering Systems Journal*, 5:485-492.
- Perkins-Veazie, P. & Collins, J. K. (2006). Carotenoid changes of intact watermelons after storage. *Journal of Agricultural and Food Chemistry*, 54(16):5868-5874.
- Roe, J. H. & Kuether, C. A. (1943). The determination of ascorbic acid in whole blood and urine through the 2, 4-dinitro-phenylhydrazine. *J Biol Chem*, 339-407.
- Ross, K. & Jenkin, R. (1998). Free radical chemistry relationship to exercise. *Sports Med*, 10:236-254.
- Zorov, D. B., Juhaszova, M. & Sollott, S. J. (2014). Mitochondrial reactive oxygen species (ROS) and ROS-induced ROS release. *Physiological Reviews*, 94(3):909-950.
- 衛生福利部食品藥物管理署 (2017) · 食品營養成分資料庫 · 取自 <https://consumer.fda.gov.tw/Food/TFND.aspx?nodeID=178>

## 淨零碳排趨勢帶動之替代性肉品的產業發展、研究進展及未來挑戰

蔡書憲<sup>1</sup> 簡全基<sup>2</sup> 李士哇<sup>3</sup> 范植軒<sup>4</sup> 鄭俊昇<sup>4</sup> 張佩琪<sup>4</sup> 李明怡<sup>5\*</sup>

## The Development of Alternative Meat Industry Driven by the Trend of Net Zero Carbon Emissions, Research Progress and Future Challenges

Shu-Hsien Tsai<sup>1</sup>, Chuan-Chi Chien<sup>2</sup>, Shih-Chi Lee<sup>3</sup>, Chin-Hsuan Fan<sup>4</sup>,  
Chun-Shen Cheng<sup>4</sup>, Pei-Chi Chang<sup>4</sup>, Ming-Yi Lee<sup>5\*</sup>

## 摘 要

全球消費者飲食習慣改變的趨勢中，由於消費者在飲食上對未來環境與健康意識的提升，如動物疾病、自然資源的枯竭及溫室氣體排放的顧慮，使肉類替代品的重要性日益增加。本篇詳細介紹了人造肉的發展及市場現況，並針對不同人造肉種類、成分進行分類，並以營養、健康和安全性等角度進行分析。同時闡述目前人造肉相關加工技術、生產效率、產品特性，最後討論人造肉目前所遇到之困境及未來挑戰。目前市售的人造肉產品以植物肉為主，利用植物性蛋白質進行加工，使其質地和口味與肉品相似，不同植物來源的蛋白質對植物肉的貢獻也有所不同，擠壓、剪切、折疊等技術的應用賦予植物肉不同的物性特質。現今植物肉主要在西方國家銷售，由於消費者對此產品的興趣與日俱增，亞洲國家也將在不久的將來成為潛在的市場，在環境方面，植物肉也有利於減少碳排放、能源消耗與土地利用，對未來經濟糧食的永續經營皆具有高度潛力，有望在未來推動食品市場。

關鍵詞：人造肉、植物肉、肉類替代品

## ABSTRACT

In the changing trend of global consumers' dietary habits, the importance of meat alternatives is increasing due to consumers' increasing awareness of the future environment and health in their diets, such as animal diseases, depletion of natural resources and greenhouse gas emissions. We introduced in detail the types, ingredients, processing technology, production efficiency, product characteristics and market conditions of artificial meat information, advantages, and challenges. We also analyzed the

<sup>1</sup> 工業技術研究院中分院科技經理<sup>2</sup> 工業技術研究院中分院副組長<sup>3</sup> 工業技術研究院中分院副執行長<sup>4</sup> 工業技術研究院中分院科技副研究員<sup>5</sup> 長庚科技大學保健營養系、食品暨化妝品安全研究中心、中草藥研究中心助理教授

trends, nutrition, health and safety of artificial meat research. At present, the artificial meat products on the market are plant-based meat, using plant protein for processing to make the texture and taste similar to meat products. Proteins from different plant sources also make different contributions to plant-based meat. The application of techniques such as extruding gives plant-based meat different physical properties. Nowadays, plant-based meat is mainly sold in Western countries. As consumers' interest in this product is increasing day by day, Asian countries will also become potential markets in the future. In terms of the environment, plant-based meat is also conducive to reducing carbon emissions, energy consumption and land use. This sustainable development of future has high potential. plant-based meat is expected to promote the food market in the future.

**Keywords:** artificial meat, plant-based meat, meat alternatives

## 壹、前言 (Introduction)

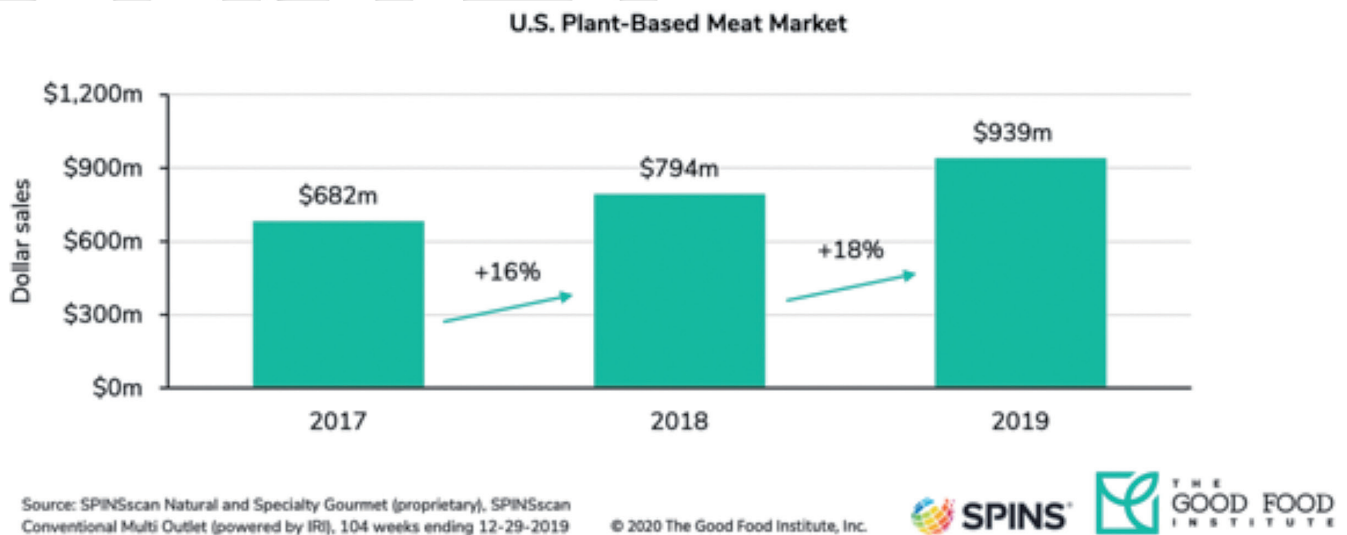
食物一直都是人類需求的必需品，依據聯合國農糧組織 (Food and Agriculture Organization, FAO) 數據，隨著人口的增長，約在 2050 年肉類消費量將從 2007 年的 2.84 億噸上漲到 2050 年的 6 億噸，大量成長的畜牧業排放之排泄物會污染土地和水源，養殖生物中如牛及羊 (反芻類動物) 都排放大量的甲烷氣體，而甲烷的溫室效應要比二氧化碳高 25 倍，另外宰殺動物後的蹄、角、骨、皮和內臟往往會造成了大量的污染。根據美國農業部 (United States Department of Agriculture, USDA) 統計，美國的牲畜屠宰業每年會拋下 14 億噸的垃圾。根據 FAO 統計，當前全球陸地面積有 30% 都被用於養殖業 (包括牧場和飼料田)，人類活動導致的溫室氣體排放中，有 18% 來自養殖業。

人造肉的概念並非近幾年才開始，早在幾個世紀前，就以植物性蛋白來源作為肉的概念及技術開發，但是此階段植物性肉類產品發展都以素食者的需求進行設計，因此早期植物性肉類產品並沒有嘗試完全複製或仿製傳統肉，在口感及營養性上還有十分大的進步空間。為了因應肉品市場轉型趨勢，全球最大的肉類公司 JBS 於 2020

年 6 月推出了無肉蛋白，而其他傳統肉類供應商龍頭，如：Tyson、Smithfield、Perdue Farms 和 Hormel Foods 等也宣布投入人造肉市場，開發自己的植物性人造肉產品及品牌。人造肉包括在質地、風味和外觀上緊密模擬動物全肌肉的類似物及模仿加工肉類的重組產品，例如漢堡、小餡餅、香腸和塊狀食品。因其原物料來源可分為植物類 (大豆、豌豆、鷹嘴豆等)，細胞類 (體外或培養的肉類) 和發酵類 (微生物、真菌蛋白等)。近幾年的研究還包括其他蛋白質來源，例如從螺旋藻中提取的藻類蛋白 (Percival, 2019 年) 和從昆蟲中分離的蛋白 (Megido 等人, 2016 年)。

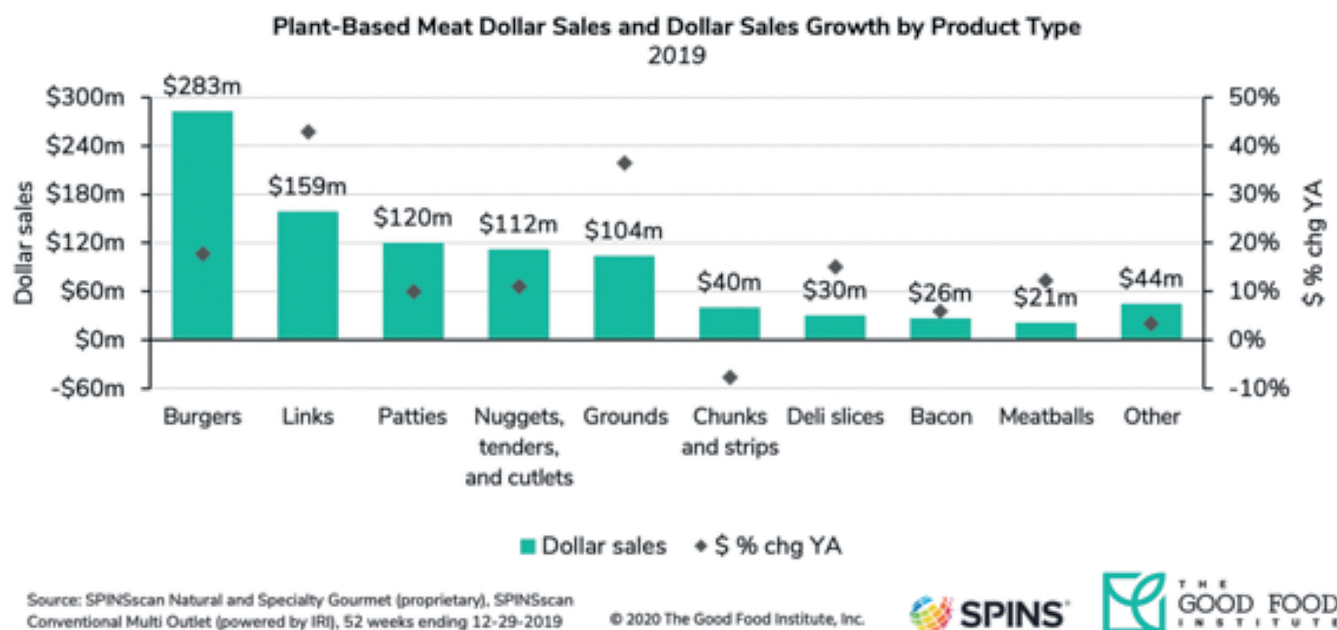
人造肉類市場的增長十分快速，經統計美國植物基底人造肉市場為 2019 年的 9.39 億美元，相較於 2017 年 6.82 億美元成長約 1.36 倍 (圖一)。全球市場將從 2018 年的 46 億美元增長到 2030 年的 850 億美元，到 2026 年時將達到 309 億美元。

2019 年，以美國市場為例銷售最佳的為漢堡肉排約 2.83 億美元，其次是香腸和熱狗約 1.59 億美元，然後是雞塊和早餐肉約 1.2 億美元 (如圖二)，而其中冷藏植物漢堡肉在過去一年中增長了 123%，在過去兩年中增長了 555%，在這些產品中植物性海鮮僅占植物性肉類美元總銷售額的 950 萬美元 (1%)，此為一新興市場，即具有發展



資料來源：SPINSscan Natural and Specialty Gourmet (proprietary), SPINSscan Conventional Multi Outlet (powered by IRI), 104 weeks ending 2019-Dec-29.

圖一：植物肉近年銷售金額



資料來源：SPINSscan Natural and Specialty Gourmet (proprietary), SPINSscan Conventional Multi Outlet (powered by IRI), 52 weeks ending 2019-Dec-29.

圖二：2019 年植物肉各商品銷售金額

潛力。

2019 年人造肉世界領先的業者如 Beyond Meat，以接近 15 億美金的價格上市，成為世界上最大的替代人造肉品牌之一。目前該公司正在進軍亞洲市場，並於 2020 年 4 月在中國星巴克提

供其無肉香腸。同年 11 月，Beyond Meat 宣布其新產品 Beyond Pork 將在中國上海餐廳進行販售，並開發適合亞洲人飲食習慣的人造肉產品。

另外，Beyond Meat 的主要競爭對手—Impossible Foods 也有大幅度的成長，也積極擴展



其產業版圖，並與漢堡王、Qdoba、White Castle 和 Red Robin 等連鎖店進行結合將其產品擴展到速食產業中。截至 2020 年 3 月，Impossible Foods 的價值為 40 億美金，2021 年將與美國最大超市 Kroger 結成合作夥伴關係，在全美 1,700 家雜貨店中出售其植物性漢堡排。另外，星巴克也宣布，將在美國菜單上添加 Impossible Foods 三明治。這些商業鏈結導致了許多其他快餐連鎖店對非肉類產品進行新產品開發測試 (CB Insights, 2019 年)，並且這種新興市場在未來幾年中還將繼續增加。

## 貳、不同種類替代性肉品 (Meat alternatives)

人造肉又稱仿生模似食品，常見技術可分為植物蛋白粉經由擠壓等工程製成的植物肉 (Plant-based meat, PBM)、利用生物工程抽取動物的肌肉幹細胞，進行培養使其產生肌肉組織培植肉 (Cell-based meat, CBM) 以及利用真菌發酵所產生的真菌肉 (Fungi-based meat, FBM)。

### 一、植物肉 (Plant-based meat, PBM)

植物肉是指以植物原料製作，模仿動物肉品的口感、味道或外觀的食物製品。最早的植物肉可以追溯到一千多年前的梁武帝時代，相傳當年梁武帝信佛便以素雞替代肉食，此後在民間流傳，而在宋代時期更記載於陶谷的「清異記」中豆腐作為素肉的現象，至今仍為素食者的主要蛋白質來源 (Shurtleff 等人, 2014 年)。隨著食品科技的蓬勃發展，1960 年代科學家從脫脂大豆粉、大豆濃縮蛋白或小麥蛋白中，以擠壓技術獲得組織類似於肉類的植物組織蛋白 (Textured Vegetable Protein, TVP)，20 世紀中後期開始應用於植物肉的製程 (King 等人, 2019 年)，現今植物肉所使用的原料大多為大豆蛋白、小麥蛋白、卵蛋白或

牛奶蛋白，並以拉伸、捏合、剪力、壓榨、折疊、擠壓等技術形成組織蛋白後，再加工形成各式各樣的植物肉 (Kyriakopoulou 等人, 2019 年)。在台灣的传统加工中，會將植物蛋白透過擠壓的技術製成絲狀植物組織蛋白，做成植物肉的主要材料之一，後續加工製成其他的植物肉製品，如素火腿、肉丸、雞塊等加工成品。

美國 Beyond Meat 公司以大豆蛋白、小麥蛋白、米穀粉等作為原料，運用濕式擠壓的技術打造出美味的碎肉，添加甜菜根汁增添肉類的顏色 (Egbert 和 Borders, 2006 年)，並使用擁有熱誘導凝膠特性且與大豆分離蛋白相似乳化特性的豌豆球蛋白，使植物肉多汁有彈性，形成美味又仿真的漢堡肉 (Vose, 1980 年)。

美國 Impossible Foods 公司的「人造肉」是採用大豆根部的血紅蛋白去模擬牛肉的顏色、質地與口感，不僅具有模仿牛肉切開時充滿肉汁的效果，還可以賦予植物肉相似於肉類的風味，讓該產品的纖維結構、外觀都更加接近真實的牛肉漢堡，甚至在烘烤時，肉質顏色也像牛肉一樣變深，同時會發出嘶嘶聲並散發出肉香味 (Fraser 等人, 2018 年)。

植物性海鮮方面，大多使用大豆蛋白、小麥蛋白或豌豆蛋白作為其主要蛋白質來源，與植物性陸生肉類替代品相似，而市場上的某些植物性的海鮮替代品並非旨在精確還原海鮮的質地與口味，而是以蔬果模擬方式，例如由胡蘿蔔、茄子和番茄製成的產品，未能成為蛋白質的替代來源 (Raychel 等人, 2020 年)。

### 二、組織培植肉 (Cell-based meat, CBM)

組織培植肉這類產品的生產原理是從活體動物身上提取肌肉幹細胞，透過生物工程培養，進行分裂生長，最終產生肌肉而成。目前國際間投入相關產品概念的新創公司或團隊非常眾多，美國 Memphis Meat、Mosa Meat、Future Meat、



Meatable、Finless Foods、Wild Type、Aleph Farm，甚至包括 NASA 都有資助相關的研發計畫，也有不少創投公司以資金支持這些新創公司，美國培養肉大廠 Eat Just. 則與日本合作，投入日本和牛培養肉的研發。投入的其他國家包括荷蘭、中國大陸、新加坡、日本、以色列、西班牙、澳洲等等，例如 2013 年，荷蘭研究團隊首次在實驗室培養出一塊漢堡肉，成本約台幣 873 萬元。2018 年 12 月，以色列科學家在實驗室裡，從細胞開始培養出了一塊牛排，一小塊肉成本約台幣 1,537 元，研究團隊表示，肉的風味還有待加強。

過去的二十年，科學家通過生物技術方法

發現了由骨骼肌衛星細胞產生的生物人工肌肉 (BAM)，2012 年有學者發明 BAM 組織培養肉 (Post，2012 年)，儘管從衛星細胞開發 BAM 的技術尚未成熟，但這些 BAM 可以成為人造蛋白的寶貴來源，應用於未來的食品開發 (Ismail 等人，2020 年)。有關幹細胞生產組織培植肉的文獻內容摘要，請參見表一。

培養肉在法規上也是挑戰之一，畢竟非傳統的肉食品原料，例如美國農業部 (USDA) 會審核其從細胞來源 (cell collection)、細胞儲存 (cell bank)、細胞培養 (cell growth) 到細胞分化 (cell differentiation) 等流程，美國企業希望政府部門調

表一：幹細胞生產組織培植肉的文獻內容摘要 (Kadim 等人，2015 年)

研究內容	參考文獻
對提高體外組織培植肉生產可行性的綜述。最大的挑戰是如何找到合適的幹細胞來源，並使其生長、增殖和分化，對此提供觀點與見解。	Langelaan 等人，2010 年
討論無活體動物的實驗室中肉類的開發以及此技術出現引起社會爭議、道德倫理和法規問題的影響。	Stephens，2010 年
作者指出，體外組織培植肉具有健康和環境優勢。這項技術面臨的巨大挑戰是生產系統結構化建立及工業環境上的配合。	Bhat & Fayaz，2011 年
組織培植肉與正常肉類相比，可減少能源使用 (7%-45%)、降低溫室氣體排放 (78%-96%)、減少土地使用 (99%) 和水的使用 (82%-96%) 來有效地保護環境。	Tuomisto & de Mattos，2011 年
作者研究脂肪組織作為幹細胞來源的潛力，可應用於未來臨床實驗。脂肪組織有助於增加組織培植肉的適口性。	Langelaan 等人，2013 年
組織培植肉的培養為肉類生產的一種替代方法。這種生物人工肌肉是動物性蛋白質的重要來源。面臨的挑戰是要確保組織培植肉在外觀、氣味、質地和味道等物性感覺方面能模擬真實肉類。	Post，2012 年
關於組織培植肉的道德問題之評論。作者得出結論：「要得到社會支持還需要很長的時間才能適應。」	Welin 等人，2012 年
作者研究了組織培植肉中促進健康的化合物，他們強調了組織培植肉中的必需胺基酸、植酸、共軛亞油酸和抗氧化劑的可用性與高品質，這些胺基酸對人類飲食至關重要。	Young 等人，2013 年
在一些國家中與組織培植肉有關的新聞文章研究。通過這次討論，可以幫助科學家瞭解消費者對組織培植肉發展的看法和策略。	Goodwin & Shoulders，2013 年
作者介紹可在實驗室中培養的組織培植肉的概念，為今後不需飼養動物且有益於環境的肉類生產研究，開啓了新的大門。	Post，2014 年

整法規，以免落後失去競爭力；而日本方面就擬鬆綁法規，讓企業可以合法使用基因編輯食物。此外，其他新創公司仍未能解決培養肉技術要如何大規模商業生產的問題，成本將是最大的上市障礙。

### 三、真菌肉 (Fungi-based meat, FBM)

真菌肉，主要以真菌、藻類及微生物等方式產生蛋白質，透過真菌培育方式，產生菌絲體，而菌絲體的質地口感與肉相似，且真菌蛋白含有 50% 以上蛋白質含量，具有低膽固醇高纖維質等營養特性，因此逐漸發展替代。

真菌蛋白最早被應用於印尼傳統食品天貝 (tempeh) 中，主要以脫殼煮過之大豆，接種根霉屬 (*Rhizopus* spp.) 真菌發酵 1-2 天後形成塊狀，含有豐富的  $\gamma$ -胺基丁酸 ( $\gamma$ -Aminobutyric acid, GABA)、類黃酮及多肽等活性物質，因蛋白質含量豐富，是素食者攝取蛋白質的主要食品之一。近年來發掘真菌蛋白有替代動物性蛋白質的潛力，絲狀真菌蛋白質可以被加工並用作食物，自 2002 年以來，真菌蛋白已被美國食品藥物管理局 (FDA) 指定為公認安全食物 (Generally Recognized as Safe, GRAS) (Denny 等人, 2008 年)。

英國於 1985 年推出 Quorn 肉，該食品利用土壤中鐮刀菌 (*Fusarium venenatum*) 來進行發酵，將碳水化合物轉化為蛋白質，並產生絲狀的真菌蛋白來生產植物性肉，並賦予植物肉有像肉一樣的纖維質感 (Wiebe, 2002 年)，絲狀真菌蛋白在生物反應器中嚴格控管，使其在 RNA 含量降低的條件下進行生產，再進一步加工成型，添加了蛋清、顏色與風味，並以蒸煮和膨化等技術來排列絲狀真菌並使其外觀及質地更接近肉類 (Dekkers 等人, 2018 年)，且真菌蛋白的飽和脂肪含量低，富有纖維及高品質的蛋白質，且不含膽固醇，是肉類替代品的優質選擇。

美國舊金山灣區的「Prime Roots」，運用製

作日本清酒所使用的米麴菌 (koji) 以發酵桶培養真菌蛋白，培植方法跟釀造啤酒或日本清酒相似，運用椰子油、芋類、米和豌豆為原料，米麴菌的孢子營養的環境下，幾天內就能長出豐富的纖維，且與雞胸肉的纖維非常相似，並取其加入植物性脂肪，加工調味後便成為最終產品。真菌肉的製造昂貴，降低生產中的成本是鼓勵消費真菌蛋白的挑戰之一 (Ritchie 等人, 2017 年)。

### 參、人造肉製作及加工製程 (Processing)

替代蛋白產生來源可分三方向：植物蛋白、微生物或藻類蛋白、組織培養肉蛋白，目前生產製造技術則以前兩者來源發展較為成熟與快速，而後者則開發較為新，還存許多問題挑戰，產業如何量化及投入成本高等皆需待進一步克服，此尚屬初期階段，產業規模化及商業模式的形成，還需努力開發。

近年，植物肉市場呈指數成長，市場的策略與趨勢則大部分焦點集中於植物蛋白的重組及形成擬真肉的植物肉。這類產品或許可稱素肉產品，過去我們熟悉的素肉主要是豆製品透過機械壓制對物理形態進行改變質地，新概念是將植物蛋白分子展開重新排列，並根據真實肉類所含有的氨基酸營養成分進行配比，再經過加熱/冷卻/擠壓等製作工藝，可能涉及合成生物學、生物化學、微生物發酵學及食品科學等。例如 Beyond meat 的技術背後 (原本也是跟台灣進口素肉原料)，其是以 90 年代擠壓技術為基礎，改良成為有肌肉紋理的技術升級。所以，台灣的業者已具良好的基礎可進軍國際市場，缺的只是好的營運模式與積極投入產品精進的研發。食品所在 2018 年也研發出多維纖維素肉批次連續製程技術 (Semi-continuous Simple Shear Technology)，生產可供直接調理、食用的全素植物蛋白肉產品。不僅更富有營養價值，也讓產品更仿真，具有仿肉肌纖維

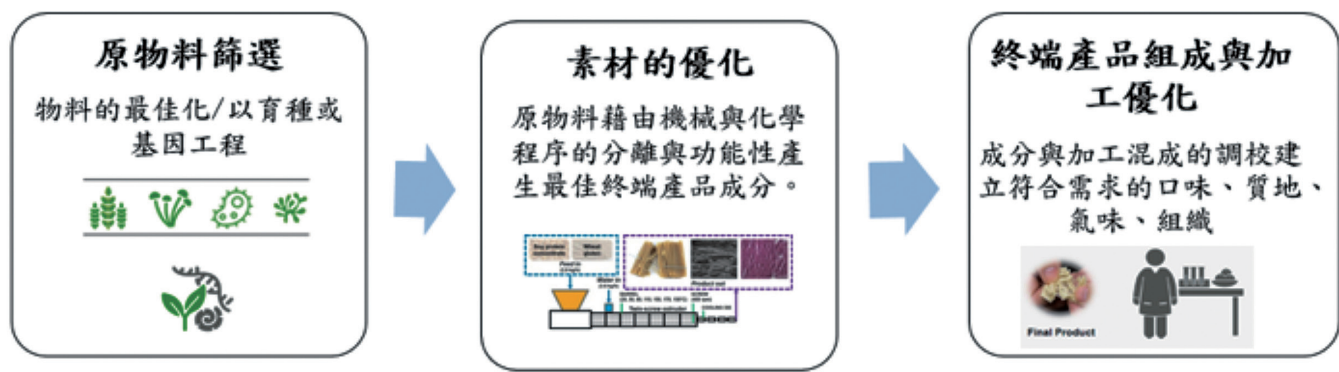
的質地與口感。

一、植物肉生產加工製作流程

植物肉的開發及生產製造主要掌握三個程序與原則，如圖三所示：

(一) 原物料篩選

實際上，所有植物蛋白都可以作為製備候選的蛋白肉類類似物和其他替代產品。但是，考慮到廣泛可用性、成本和加工功能性，大豆、豌豆之蛋白與小麥麵筋(穀物)被廣泛用作替代產品的組成部分，如表二所示。為了建立營養均衡的



資料來源：David Welch, The Good Food Institute, 2019 整理

圖三：植物肉的製造程序及產品優化原則

表二：商用植物肉所使用常見蛋白質種類及功能

蛋白質	結構特性	功能	參考文獻
Soy protein 大豆蛋白	分離和濃縮；存儲球蛋白主要是大豆球蛋白 (11S，六聚體，分子量 320-380 kDa) 和 $\beta$ - 伴大豆球蛋白 (7S，三聚體，分子量 150-220 kDa)；甘氨酸中的鹼性和酸性亞基通過二硫鍵連接。	通過加熱和擠壓形成集聚、膠凝和纖維；結合油和乳化。	Utsumi 等人，1997 年
Pea protein 豌豆蛋白	分離和濃縮；佔優勢的球蛋白：豆蛋白 (11S，六聚體，分子量 320-380 kDa)，豌豆球蛋白 (7S)，三聚體，分子量 150-170 kDa，缺少半胱氨酸殘基；小含量的弓形素 (分子量 290 kDa)。	功能類似於大豆蛋白	Lam 等人，2018 年
Wheat protein 小麥蛋白	麵筋呈拉長結構，具有兩個成分：麥醇溶蛋白 (醇溶性，分子量為 25-100 kDa 的多肽通過分子內二硫鍵連接的多肽) 和谷蛋白 (鹼溶性高分子大分子 MW66-88 kDa 和小的亞基 MW 32-45 kDa 相連，150-1500 kDa 的聚合物)。	與豆類蛋白質一起使用以提供纖維質地彈性和可擴展性。	Shimoni & Galili，1996 年
Potato protein 馬鈴薯蛋白	分為三類：patatins (抑菌素) (40-60%，MW 40-43 kDa)，蛋白酶抑制劑 (20-30%，MW 16-25 kDa) 和其他 (高分子量) 蛋白。	用於補充豆類蛋白質以改善質地。	Alting 等人，2011 年
Mung bean protein 綠豆蛋白	球蛋白 (60%)，Vicilin (豌豆素) 型 8S，分子量 (26-60 kDa)，白蛋白 (25%，分子量 24 kDa)；其他球蛋白包括基本型 7S 和豆類型 11S。	良好的膠凝潛力，有助於形成顆粒綁定和保水。	Yi-She 等人，2018 年

資料來源：Sha & Xiong，2020 年。



氨基酸分佈，通常將大米蛋白和綠豆蛋白與主要的豆類蛋白進行結合使用(Migala 等人，2019 年)。然而，豆類蛋白質的天然球形結構不利於構建類似肉的纖維質地結構。因此，需破壞性加工過程(例如熱擠壓和纖維紡絲)將天然蛋白小球轉變成絲狀聚集體或相互作用的纖維。

大豆和豌豆蛋白質由於其極富可用性和低成本，為目前非肉類產品製造中使用的兩種主要蛋白質來源。而兩者佔總蛋白質的 90% 的貯藏球蛋白部分根據其沉降係數可知由兩種類型組成：7S 球蛋白和 11S 球蛋白。 $\beta$ - 伴大豆球蛋白和豌豆球蛋白是 7S 的主要成分，大豆和豌豆中的大豆球蛋白和豆球蛋白分別是 11S 的主要成分。 $\beta$ - 伴大豆球蛋白和豌豆球蛋白在結構上相似，它是三聚體，其分子量約為 150-200 kDa (Lam 等人，2018 年)。

## (二) 素材的優化

在食品加工中具適當的離子強度和加熱條件下，7S 和 11S 球蛋白中的單個亞基將經歷解離、展開和重新聚集，並與通過鹼的提取和等電沉澱法從大豆(SPI)、豌豆(PPI) 和其他豆類中分離蛋白質的提供是使其在溶解度、凝膠化、乳化和起泡等方面之重要功能的呈現(Nishinari 等人，2018 年)。然而，關鍵的是形成凝膠的能力，因為粘彈性凝膠主要具有粘附顆粒、固定化脂肪，並會將水截留在乳液型替代蛋白質產品的基質中。分子豆類球狀蛋白與肌肉組織中存在的肌球蛋白或肌動球蛋白不同，分子豆類球狀蛋白的締合和結構比對其於天然形式並不賦有纖維質地的型式和肌肉細胞中水結合的能力。因此，緻密過程(諸如熱擠壓和攪促交聯的過程)是組裝成肉樣纖維結構、構象和咀嚼性所需的程序。

組織化植物蛋白(Textured vegetable protein; TVP) 主要通過水性酒精洗滌製備的大豆濃縮蛋白製成，是替代肉類的極好材料(Chajuss, 2004 年)。

包含有小麥麵筋的大豆或豌豆蛋白的產品，有助於產生類似肉的咀嚼感。彈性和可延伸性的特性則歸因於兩個主要蛋白質部分：麵筋和麥醇溶蛋白(Chiang 等人，2019 年)。另其他幾種植物蛋白的結構，如馬鈴薯蛋白(Alting 等人，2011 年)，綠豆蛋白(Yi-Shen 等人，2018 年)和大米蛋白(Amagliani 等人，2017 年)，則為開發複合產品的次要材料，通過與主要成分蛋白質的物理相互作用，可形成紋理特徵(Wang 等人，2018 年)。儘管根據肌肉肌絲之間自然存在適合捕集水分的間隙，通過這些配方策略下，對植物蛋白進行工程改造仍然很困難。

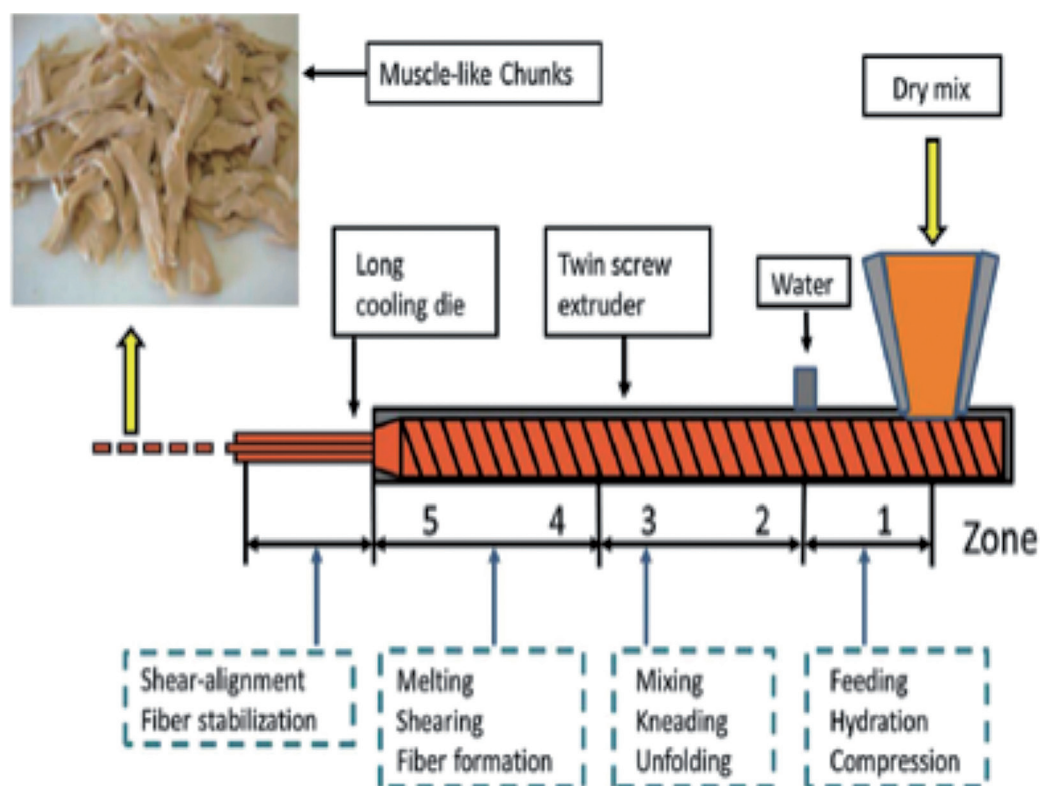
在植物肉製造方面，已開發了許多處理技術，無論是全肌肉之類似物還是重組替代品，主要在於紋理質地的模擬，而熱擠壓是一種相對成熟且研究最多的技術，被廣泛使用。但是，也有幾種替代方法引入以構建肌肉纖維類似物，例如濕紡絲、靜電紡絲和錐形剪切。Mattice 等人從玉米醇溶蛋白產生纖維網絡或單蛋白質纖維與靜電紡絲比較，其有抗溶劑沉澱和機械伸長的特性。對此結果，機械伸長式展延似乎有利於構建類似全組織肉的纖維結構(Mattice 等人，2020 年)。然而，熱擠壓技術具高生產率、低成本、多功能性和能源效率等優勢，是目前用於植物蛋白轉化為結構化的聚集體或原纖維用於隨後製成肉類替代產品的主要加工技術(Dekkers 等人，2018 年)。擠壓機是具有向前流動的牽引流裝置單或雙旋轉螺桿的泵送作用；單螺桿擠出則是取決於機筒之間的摩擦和熔體。在雙螺桿擠出，物料是從一個螺桿批量轉移到另一個螺桿，使物料前進傳送效率更高。因此，對於高水分的蛋白質混合物，選擇雙螺桿擠出摩擦係數和粘性耗散則較低。

熱擠壓可分為低水分擠出、中水分擠出和高水分擠出(Akdogan, 1999 年)。低水分含量(< 30% 水分)用於 TVP 製備，並且產品具有聚集的或多或少的蛋白質擴展構象。水合後變性和聚集

的蛋白質使 TVP 具有類似肉粒的質地，因此被用作非肉類產品的主要成分 (Chajuss, 2004 年)。由濃縮的大豆蛋白和豌豆蛋白製得的 TVP 可以進一步加工，以製造重構的高蛋白塊狀、條狀和任意形的碎屑 (可作為章魚燒餡料和比薩餡料)。另水分含量大於 50% 的蛋白質混合物的擠壓，也稱為濕擠壓，此操作是使植物蛋白形成類似肉的纖維質感，因此適合全肌肉食用類似物 (Cheftel 等人, 1992 年)。蛋白質多肽的重排、層流和強擠出機的長縫冷卻模頭內的可分層漸進式則有利形成纖維結構 (Liu 等人, 2008 年)。一個典型的擠壓法製備植物肉，混合豆類蛋白 (主要是大豆和豌豆蛋白)，通常與麵筋一起使用，澱粉和難消化的多醣作為增稠劑，在高溫下被擠壓成複合纖維狀肉質質地，製備中依據所使用的特定蛋白質，擠出物的結構以及形成纖維質地則以二硫鍵結形成在保持剛性方面比非共價鍵形成更為重要 (Chiang 等人, 2019 年)。

製造擠壓過程是一項多功能操作過程，涉及混合、水合、剪切、均質化、壓縮、脫氣、加熱、整形和膨脹。在中等至高水分含量 (40–80%) 和高溫下進行擠出時 (140–180°C)，纖維和層結構是通過複雜剪切過程中的蛋白質組織化產生 (Wild 等人, 2014 年)。儘管未折疊的蛋白質分子的排列可以很容易地交聯成纖維，但在顯微鏡下，這種纖維是各向異性的，並且在結構上不像天然肌肉組織的纖維 (Lin 等人, 2002 年)。天然肌肉纖維的層次結構是相當複雜且獨特，這也賦予肉類其獨特的感官特性。

在熱擠壓過程中，通常將料源蛋白引入以乾混形式導入擠壓機被加工成纖維狀。為了獲得能夠吸收水的纖維結構，此至關重要的是原料混合物中的水分含量必須高於 40%，使用雙螺桿擠壓則可將高水份的蛋白質類物質製成纖維狀 (圖四)。Lin 等人在研究開發時，比較了三種水分含量 (60%、65% 和 70%) 和三種擠壓溫度 (138°C、



資料來源：Liu & Hsieh, 2008 年

圖四：雙螺桿擠壓機的示意圖



149°C 和 160°C)。對於產品的感官特性，發現水分含量比蒸煮溫度更為重要。適中至較高含水量則是有利形成可接受的質地和咀嚼性三維構象的重要關鍵(Lin 等人，2002 年)。

### (三) 終端產品組成與加工優化

為了創造類似於肉的感官屬性和營養輪廓，廣泛的添加劑被加入植物肉產品配方中。一般動物脂肪是肉製品中味道、質地、多汁和口感的主要成分(Calkins 等人，2007 年)，為了形成類似於動物脂肪的口感，使用從熱帶水果(例如椰子和可可豆)中提取的固體脂肪與含有更多不飽和脂肪酸的液體油(例如葵花籽油和低芥酸菜籽油)混合。為了給予植物基材的「漢堡」和「香腸」呈現普通牛肉和豬肉香腸餡餅的大理石花紋，將飽和油和不飽和油的混合物攪打成小球狀的白色脂肪(Moskin，2019 年)。為了植物肉的營養和風味，還使用了芝麻油和酪梨油。另一方面，植物油大部不含膽固醇，因此被認為比動物脂肪更健康。

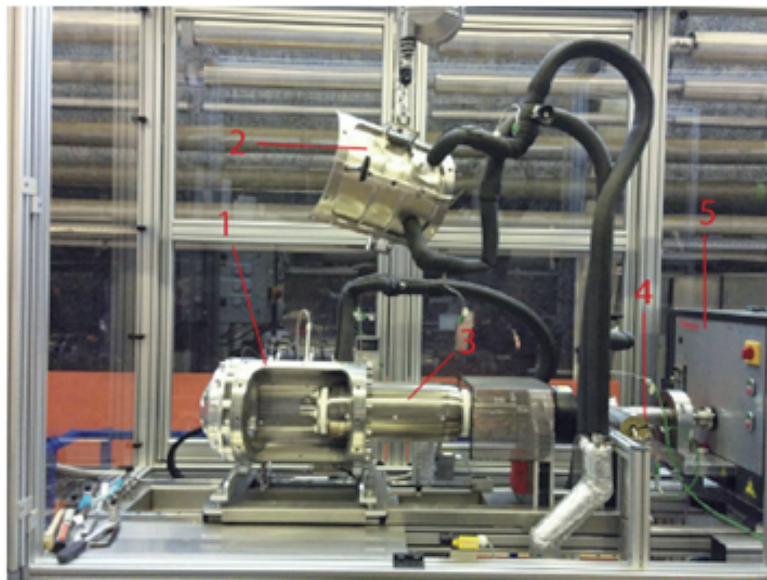
在植物肉加工中，蛋白質通常在結構形成和水的固定為主要作用，通常需要碳水化合物聚合物來改善結構的一致性，能結合水並減少協同作用。這些必需的植物生物聚合物則分為三類：1、由小麥、燕麥、蘋果和其他可食用植物製成的植物細胞壁材料的粗纖維，2、可消化的澱粉，3、純化的多醣及其衍生物。果膠化合物是水果纖維中主要的碳水化合物，而直鏈澱粉和支鏈澱粉構成各種澱粉。多醣膠可從海藻如鹿角菜角之提取，樹木中提取如豆角膠和阿拉伯樹膠，或者是通過微生物發酵製成，如三仙膠。這些物質能夠通過氫鍵和離子-偶極相互作用牢固地結合水，改善產品的厚度和稠度並減少蒸煮時的變化。由微生物轉麩醯胺酸攜可交聯來自不同多肽的麩醯胺酸攜和離氨酸殘基，可提供牢固的蛋白質結合，可改善質地細密的植物蛋白產品的可切片性。

Leghemoglobin (血紅蛋白)，一種來自大豆植物的血紅素色素，已使用生物技術成功生產，它依產品重量的 0.8% 的最大添加量用於碎肉植物肉中，作為顏色添加劑(FDA，2019 年)。因大豆血紅蛋白能夠複製肉血紅素蛋白(血紅蛋白和肌紅蛋白)的「血腥」外觀。紅甜菜、紅捲心菜、紅色漿果、辣椒粉和胡蘿蔔中的色素提取物可作為著色劑，嵌入於高度加工的替代肉餅和香腸中，以呈現紅色外觀。植物性雞肉產品中則用二氧化鈦(TiO<sub>2</sub>)來增強和增亮發白的顏色，因它還具有抗菌活性，可以提高產品的保質期(Liao 等人，2020 年)。

酵母提取物、核苷酸、糖和其他引起味道的成分通常用於植物肉產品，可彌補風味的不足。通過混合香料和草藥(如黑胡椒、牛至葉、鼠尾草、迷迭香和丁香等)的添加使擁有強烈而複雜的香氣，進行對煮熟的香腸、肉餅和其他加工肉製品的模仿。這些調味品不僅產生複雜肉類風味，且掩蓋某些豆類蛋白質的豆腥味，也加入精選礦物質和維生素以彌補營養不足，使營養成分接近普通肉。為防止植物性產品易受脂質和蛋白質氧化，則摻入抗氧化劑以抑制氧化反應和酸敗。有機酸、香料提取物和磷酸鹽化合物的加入這些調味品不僅產生加工後的肉類複雜的風味，也助於改善由植物原料製成植物肉的微生物穩定性和保質。

## 二、新興人造肉製造技術

一種稱為高溫錐形剪切池(HTSC)的新技術也用來製備基於植物肉(Krintiras 等人，2016 年)。HTSC 是一種 couette cell 技術(圖五)，底部圓錐體是可旋轉的。兩個錐體之間的腔是封閉的，以防止在 95-140°C 的溫度下加熱時蒸汽逸出。Schreuders 等人應用該設備技術將大豆蛋白-小麥麵筋和豌豆蛋白-小麥麵筋混合加工成各向異性纖維。將混合物進行 15 分鐘的恆定剪切和加熱，



Applying shear forces to create fibrous plant-based meat



WAGENINGEN  
UNIVERSITY & RESEARCH

資料來源：Krintiras 等人，2016 年

圖五：Actual picture of the up-scaled Couette Cell. 1. Housing; 2. Lid; 3. Inner cylinder; 4. Shaft; 5. Rheodrive unit.

然後冷卻至 25°C。將產品密封在塑料袋中後，在室溫下放置至少 1 小時，以獲得結構穩定的纖維。發現在 140°C 下生產的豌豆蛋白-麵筋纖維的強度與大豆蛋白-麵筋纖維的強度相似，而在 110 和 120°C 下加工的豌豆蛋白混合物與加工的雞肉具有相似的機械強度 (Schreuders 等人，2019 年)。

另一新興的 3D 列印技術，也稱為「添加劑製造」，這是一個新穎的概念，通過精確控制植物蛋白質的添加來形成類似肌肉的結構，然後通過逐層模仿肌肉纖維結構的方式形成結構 (Dankar 等人，2018 年)。西班牙初創 Novameat 公司應用 3D 技術生產牛排和其他類似肉類，並使用植物來源的成分來模擬動物肉產品的質地、味道、外觀和營養特性 (Lamb，2020 年)。

#### 肆、未來發展及技術挑戰

##### (Challenges and opportunities)

近年世界人口的持續增長、消費水準普遍的提高，對動物性蛋白質食品需求旺盛。然而近年來有關動物疫病等事件的頻繁發生與相關生產成

本上漲，加劇了國際肉類供應的緊張態勢。因環境多變和資源漸趨缺乏，使得傳統肉品生產的發展受到嚴峻挑戰。在全球需求的潮流下，各國民間企業的積極參與未來替代性產品的開發與消費，其中所謂人造肉引發了生產食品與消費市場的高度關注。

#### 一、植物肉風潮下台灣市場趨勢

這波植物肉風潮下也迅速進入台灣市場，momo 富邦媒體也引進未來肉 (Beyond Meat)。未來肉鎖定的客群中，素食者只是其中之一，重點則在於如何讓肉食主義者嘗試素食。

根據食品工業研究所的調查顯示，台灣的素食人口約有 230 萬人，占總人口 10%，其占比與歐美國家相當，坐擁龐大的素食消費市場，為植物肉的研發、銷售產業鏈帶來更多的商機與基底，是台灣產業的一大優勢。近年來觀察到消費者更注重養生概念，同時考量到銀髮族的需求後，針對人造肉的製程技術也要更求精進。就產業趨勢，建議台灣業者除了精進原本的大豆蛋白素肉、素雞、素魚和素肉乾等技術，讓產品質地可以更像



肉類之外，應該也可以投入其他植物蛋白的研發，包括豌豆蛋白、菇類蛋白、米蛋白、扁豆蛋白等等的應用，或這些植物蛋白的結合，或者與原已有的蒟蒻技術結合。就以豌豆蛋白來說，國際公司因認知消費者擔憂黃豆原料可能不利身體健康，紛紛轉以黃豌豆製造植物肉，造成豌豆市場價格變動就是明顯案例，顯見各國企業的企圖心。同樣，台灣企業也應具有國際佈局的思維，可喜的是台灣知名食品廠商鈺統食品公司，也於三年前投入以豌豆蛋白為主的植物肉研發，也於2020年後期創立自有品牌開始切入植物肉市場，對國內未來植物肉產業的國際競爭力，將可漸趨提升與強化。

## 二、工業技術研究院參與的動機與目的

工研院2021年三月宣布全院將在2050年達到二氧化碳淨零排放的目標，更成立「淨零永續策略辦公室」作為推動零碳排平台，運用跨領域整合產業的創新研究和科技研發，規劃出臺灣2050淨零碳排策略藍圖，協助臺灣產業朝向淨零永續發展，以提升全球競爭力，掌握全球零碳排放的新商機。工業技術研究院中分院的生化應用技術團隊在農食原料及生技產品的開發技術已琢磨多年，團隊內具跨領域專業人才，近年人造肉或是所謂的未來肉，2021年相繼國內外廠商投入產品研發的趨勢，以及全球減碳或零排放要求驅動下，人造肉對人類飲食的選擇將產生巨大的改變潮流下，工研院中分院秉持著既往技術領域成果，以前瞻角度參與，著眼於國內外業者較少參與的區塊，從終端產品發想，考量國內原材料資源掌控與永續性，朝結合微生物發酵技術產生蛋白原料及新型海鮮人造蝦肉加工技術開發為主，以區隔市場與技術，並鏈接目前國內已布局的廠商技術與具潛力廠商共同開發，進一步強化產業於國際競爭力，擴展符合國際糧食環境永續發展終極目標。

## 伍、結論 (Conclusions)

在全球肉類市場需求量增長及環保意識推動的日益關注下，研究人員和企業家將目光轉向了替代肉類生產方法，在食品工業的傳統技術和新興技術都有相當大的提升。在原物料部分如大豆、豌豆、小麥、米與綠豆蛋白以及菌類、藻類蛋白等原料被廣泛作為替代產品的主要成分，再經過加工製程後，蛋白質經展開和重新聚合以使其產生凝膠、乳化等物性變化，產生類似肉的多汁與咀嚼感，並通過香料與風味添加劑，可更貼近真實肉品的質地與口味。而即便加工技術日新月異的進步，人造肉口感擬真性上仍必須通過進一步的研究，來改善相似度不高等問題。而尚未上市的組織培養肉技術，也需再經過多年的研究和開發，才能確保獲得與常規肉類相當的品質。目前在植物肉、組織培養肉及真菌肉的技術上尚未完善，未來對於添加劑的使用、產品安全性、營養相關因素仍存在著挑戰，而質地口感相關的特性也是產品開發和應用研究的主要目標，須通過提高蛋白質的利用率和產品的整體品質，從而增加消費者的接受度，擴大人造肉的國際市場與經濟價值。

## 參考文獻

- Akdogan, H. (1999). High moisture food extrusion. *International Journal of Food Science & Technology*, 34, 195-207.
- Alting, A. C., Pouvreau, L., Giuseppin, M. L. F., & van Nieuwenhuijzen, N. H. (2011). Potato proteins. In G. O. Phillips, & P. A. Williams (Eds.). *Handbook of food proteins* (pp. 316-334).
- Amagliani, L., O'Regan, J., Kelly, A. L., & O'Mahony, J. A. (2017). The composition,

- extraction, functionality and applications of rice proteins: A review. *Trends in Food Science & Technology*, 64, 1-12.
- Bhat ZF, Fayaz H. (2011). Prospectus of cultured meat: advancing meat alternatives. *J Food Sci Technol*. 2011;48:125-40. doi: 10.1007/s13197-010-0198-7.
- Chajuss, D. (2004). Soy protein concentrate: Technology, properties, and applications. In K. Liu (Ed.). *Soy proteins as functional foods and ingredients* (pp. 121-133). Champaign, Illinois, USA: AOCS Press.
- Cheftel, J. C., Kitagawa, M., & Queguiner, C. (1992). New protein texturization processes by extrusion cooking at high moisture levels. *Food Reviews International*, 8, 235-275.
- Chiang, J. H., Loveday, S. M., Hardacre, A. K., & Parker, M. E. (2019). Effects of soy protein to wheat gluten ratio on the physicochemical properties of extruded meat analogues. *Food Structure*, 19, 100102.
- Dankar, I., Haddarah, A., Omar, F. E., Sepulcre, F., & Pujolà, M. (2018). 3D printing technology: The new era for food customization and elaboration. *Trends in Food Science & Technology*, 75, 231-242.
- David Welch. (2019). The Science Behind Plant based Proteins, *The Good Food Institute*.
- Dekkers BL, Boom RM, van der Goot AJ. (2018) Structuring processes for meat analogues. *Trends Food Sci Technol*. 2018;81:25-36.
- Denny A, Aisbitt B, Lunn J. (2008). Mycoprotein and health nutrition. *Bulletin*. 2008;33:298-310. doi: 10.1111/j.1467-3010.2008.00730.x.
- Egbert R, Borders C. (2006). Achieving success with meat analogs. *Food Technol*. 2006;60:28-34.
- FDA (2019). Food and Drug Administration. Listing of color additives exempt from certification; soy leghemoglobin. *Federal Register* 84 FR 37573.
- Fraser RZ, Shitut M, Agrawal P, Mendes O, Klapholz S. (2018). Safety evaluation of soy leghemoglobin protein preparation derived from pichia pastoris, intended for use as a flavor catalyst in plant-based meat. *Int J Toxicol*. 2018;37:241-62.
- Goodwin JN, Shoulders CW. (2013). The future of meat: a qualitative analysis of cultured meat media coverage. *Meat Sci*. 2013;95:445-50. doi: 10.1016/j.meatsci.2013.05.027.
- Ismail, I., Hwang, Y. H., & Joo, S. T. (2020). Meat analog as future food: a review. *Journal of animal science and technology*, 62(2), 111-120. <https://doi.org/10.5187/jast.2020.62.2.111>.
- Kadim IT, Mahgoub O, Baqir S, Faye B, Purchas R. (2015). Cultured meat from muscle stem cells: a review of challenges and prospects. *J Integr Agric*. 2015;14:222-33. doi: 10.1016/S2095-3119(14)60881-9.
- King T, Lawrence S. [Accessed 08 Mar 2021]; Meat the alternative-Australia's \$3 billion opportunity [Internet] 2019 [https://www.foodfrontier.org/wp-content/uploads/2019/09/Meat\\_the\\_Alternative\\_FoodFrontier.pdf](https://www.foodfrontier.org/wp-content/uploads/2019/09/Meat_the_Alternative_FoodFrontier.pdf).
- Krintiras, G. A., Diaz, J. G., van der Goot, A. J., Stankiewicz, A. I., & Stefanidis, G. D. (2016). On the use of the Couette Cell technology for large scale production of textured soy-based meat replacers. *Journal of Food Engineering*, 169, 205-213.
- Kyriakopoulou K, Dekkers B, van der Goot AJ. (2019). Plant-based meat analogues. In: Galanakis CM, editor. Sustainable meat



- production and processing. *London: Academic Press; 2019*. pp. 103-26. editor. p.
- Lam, A. C. Y., Can Karaca, A., Tyler, R. T., & Nickerson, M. T. (2018). Pea protein isolates: Structure, extraction, and functionality. *Food Reviews International*, 34, 126-147.
- Lamb, C. (2020). NovaMeat unveils version 2.0 of its 3D-printed meatless steak. The spoon. Accessed <https://thespoon.tech/novameat-unveils-version-2-0-of-its-3d-printedmeatless-steak/>, Accessed date: 2 February 2020.
- Langelan MLP, Boonen KJM, Polak RB, Baaijens FPT, Post MJ, van der Schaft DWJ. (2010). Meet the new meat: tissue engineered skeletal muscle. *Trends Food Sci Technol*. 2010;21:59-66. doi: 10.1016/j.tifs.2009.11.001.
- Liao, C., Li, Y., & Tjong, S. C. (2020). Visible-light active titanium dioxide nanomaterials with bactericidal properties. *Nanomaterials*, 10, 124.
- Lin, S., Huff, H. E., & Hsieh, F. (2002). Extrusion process parameters, sensory characteristics, and structural properties of a high moisture soy protein meat analog. *Journal of Food Science*, 67, 1066-1072.
- Liu, K., & Hsieh, F. H. (2008). Protein-protein interactions during high-moisture extrusion for fibrous meat analogues and comparison of protein solubility methods using different solvent systems. *Journal of Agricultural and Food Chemistry*, 56, 2681-2687.
- Mattice, K. D., & Marangoni, A. G. (2020). Comparing methods to produce fibrous material from zein. *Food Research International*, 128, 108804.
- Megido, R. C., Gierts, C., Blecker, C., Brostaux, Y., Haubruge, É., Alabi, T., & Francis, F. (2016). Consumer acceptance of insect-based alternative meat products in Western countries. *Food Quality and Preference*, 52, 237-243.
- Migala, J., Nied, J., Miller K. (2019). What is the beyond burger and is it healthy? Women's health. Accessed: <https://www.womenshealthmag.com/food/a-21566428/beyond-meatburger-ingredients/>, Accessed date: 5 Nov. 2020.
- Moskin, J. (2019). How do the new plant-based burgers stack up? The New York times. Accessed <https://www.nytimes.com/2019/10/22/dining/veggie-burger-taste-test.html/>, Accessed date: 15 November 2019.
- Nishinari, K., Fang, Y., Nagano, T., Guo, S., & Wang, R. (2018). Soy as a food ingredient. In R. Yada (Ed.). *Proteins in food processing* (pp. 149-186). Duxford, UK: Woodhead Publishing.
- Post MJ. (2012). Cultured meat from stem cells: challenges and prospects. *Meat Sci*. 2012;92:297-301. doi: 10.1016/j.meatsci.2012.04.008.
- Post MJ. (2014). Cultured beef: medical technology to produce food. *J Sci Food Agric*. 2014;94:1039-41. doi: 10.1002/jsfa.6474.
- Raychel E. Santo, Brent F. Kim, Sarah E. Goldman, Jan Dutkiewicz, Erin M. B. Biehl, Martin W. Bloem, Roni A. Neffl, and Kieve E. (2020). NachmanConsidering Plant-Based Meat Substitutes and Cell-Based Meats: A Public Health and Food Systems Perspective Front. Sustain. *Food Syst.*, 31 August 2020.
- Ritchie H, Laird J, Ritchie D. 3f bio. (2017). Halving the cost of mycoprotein through integrated fermentation processes. *Ind Biotechnol*. 2017;13:29-31.



- Schreuders, F. K. G., Dekkers, B. L., Bodnár, I., Erni, P., Boom, R. M., & van der Goot, A. J. (2019). Comparing structuring potential of pea and soy protein with gluten for meat analogue preparation. *Journal of Food Engineering*, 261, 32-39.
- Sha, L., & Xiong, Y. L. (2020). Plant protein-based alternatives of reconstructed meat: Science, technology, and challenges. *Trends in Food Science & Technology*.
- Shimoni, Y., & Galili, G. (1996). Intramolecular disulfide bonds between conserved cysteines in wheat gliadins control their deposition into protein bodies. *Journal of Biological Chemistry*, 271, 18869-18874.
- Shurtleff W, Huang HT, Aoyagi A. [Accessed 08 Mar 2021]; History of soybeans and soyfoods in China and Taiwan, and in Chinese cookbooks, restaurants, and Chinese work with soyfoods outside China (1024 BCE to 2014) [Internet] 2014 <http://www.soyinfocenter.com/pdf/176/Chin.pdf>.
- Stephens N. (2010). In vitro meat: zombies on the menu. *Scripted*. 2010;7:394-401.
- Tuomisto HL, de Mattos MJT. (2011). Environmental impacts of cultured meat production. *Environ Sci Technol*. 2011;45:6117-23. doi: 10.1021/es200130u.
- Utsumi, S., Matsumura, Y., & Mori, T. (1997). Structure-function relationships of soy proteins. In S. Damodaran, & A. Paraf S (Eds.). *Food proteins and their applications* (pp.257-291). New York: Marcel Dekker Inc.
- Vose JR. (1980). Production and functionality of starches and protein isolates from legume seeds (field peas and horsebeans) *Cereal Chem*.1980;57:406-10.
- Wang, T., Xu, P., Chen, Z., Zhou, X., & Wang, R. (2018). Alteration of the structure of rice proteins by their interaction with soy protein isolates to design novel protein composites. *Food & Function*, 9, 4282-4291.
- Welin S, Gold J, Berlin J. (2012). In vitro meat: what are the moral issues? In: Kaplan DM, editor. The philosophy of food. *Berkeley, CA: University of California Press; 2012*. pp. 292-394. editor. p.
- Wiebe M. (2002). Myco-protein from *Fusarium venenatum*: a well-established product for human consumption. *Appl Microbiol Biotechnol*. 2002;58:421-7. doi: 10.1007/s00253-002-0931-x.
- Yi-Shen, Z., Shuai, S., & FitzGerald, R. (2018). Mung bean proteins and peptides: Nutritional, functional and bioactive properties. *Food & Nutrition Research*, 62, 1-11.
- Young JF, Therkildsen M, Ekstrand B, Che BN, Larsen MK, Oksbjerg N, et al. (2013). Novel aspects of health promoting compounds in meat. *Meat Sci*. 2013;95:904-11. doi: 10.1016/j.meatsci.2013.04.036.

## Article

# Anti-Inflammatory, Antiallergic, and COVID-19 Main Protease (M<sup>Pro</sup>) Inhibitory Activities of Butenolides from a Marine-Derived Fungus *Aspergillus terreus*

Ibrahim Seyda Uras <sup>1,2,†</sup>, Sherif S. Ebada <sup>3,4,\*,†</sup> , Michal Korinek <sup>5,6,7,8</sup> , Amgad Albohy <sup>9</sup> ,  
Basma S. Abdulrazik <sup>9</sup>, Yi-Hsuan Wang <sup>7</sup>, Bing-Hung Chen <sup>6,10,11</sup> , Jim-Tong Horng <sup>12</sup>, Wenhan Lin <sup>13,\*</sup> ,  
Tsong-Long Hwang <sup>7,8,14,15,\*</sup>  and Belma Konuklugil <sup>1,16,\*</sup>

- <sup>1</sup> Department of Pharmacognosy, Faculty of Pharmacy, Ankara University, Ankara 06560, Turkey; isuras@ankara.edu.tr
- <sup>2</sup> Department of Pharmacognosy, Faculty of Pharmacy, Agri Ibrahim Cecen University, Agri 04100, Turkey
- <sup>3</sup> Department of Pharmacognosy, Faculty of Pharmacy, Ain Shams University, Abbasia, Cairo 11566, Egypt
- <sup>4</sup> Department of Pharmacognosy, Faculty of Pharmacy, Sinai University, Kantara, Ismailia 41511, Egypt
- <sup>5</sup> Graduate Institute of Natural Products, College of Pharmacy, Kaohsiung Medical University, Kaohsiung 80708, Taiwan; mickorinek@hotmail.com
- <sup>6</sup> Department of Biotechnology, College of Life Science, Kaohsiung Medical University, Kaohsiung 80708, Taiwan; bhchen@kmu.edu.tw
- <sup>7</sup> Graduate Institute of Natural Products, College of Medicine, Chang Gung University, Taoyuan 33302, Taiwan; d0901501@cgu.edu.tw
- <sup>8</sup> Research Center for Chinese Herbal Medicine, Research Center for Food and Cosmetic Safety, and Graduate Institute of Health Industry Technology, College of Human Ecology, Chang Gung University of Science and Technology, Taoyuan 33302, Taiwan
- <sup>9</sup> Department of Pharmaceutical Chemistry, Faculty of Pharmacy, The British University in Egypt (BUE), El-Sherouk City, Suez Desert Road, Cairo 11837, Egypt; amgad.albohy@bue.edu.eg (A.A.); basma.sabry@bue.edu.eg (B.S.A.)
- <sup>10</sup> Department of Medical Research, Kaohsiung Medical University Hospital, Kaohsiung 80708, Taiwan
- <sup>11</sup> The Institute of Biomedical Sciences, National Sun Yat-sen University, Kaohsiung 80424, Taiwan
- <sup>12</sup> Department of Biochemistry and Molecular Biology, College of Medicine, Chang Gung University, Taoyuan 33302, Taiwan; jimtung@mail.cgu.edu.tw
- <sup>13</sup> State Key Laboratory of Natural and Biomimetic Drugs, Peking University, Beijing 100083, China
- <sup>14</sup> Department of Anesthesiology, Chang Gung Memorial Hospital, Taoyuan 33302, Taiwan
- <sup>15</sup> Department of Chemical Engineering, Ming Chi University of Technology, New Taipei City 24301, Taiwan
- <sup>16</sup> Department of Pharmacognosy, Faculty of Pharmacy, Lokman Hekim University, Çankaya, Ankara 06510, Turkey
- \* Correspondence: sherif\_elsayed@pharma.asu.edu.eg (S.S.E.); whlin@bjmu.edu.cn (W.L.); htl@mail.cgu.edu.tw (T.-L.H.); konuklugil@pharmacy.ankara.edu.tr (B.K.); Tel.: +20-2405-1180 (S.S.E.); Fax: +20-2405-1107 (S.S.E.)
- † These authors equally contributed to this work.



**Citation:** Uras, I.S.; Ebada, S.S.; Korinek, M.; Albohy, A.; Abdulrazik, B.S.; Wang, Y.-H.; Chen, B.-H.; Horng, J.-T.; Lin, W.; Hwang, T.-L.; et al. Anti-Inflammatory, Antiallergic, and COVID-19 Main Protease (M<sup>Pro</sup>) Inhibitory Activities of Butenolides from a Marine-Derived Fungus *Aspergillus terreus*. *Molecules* **2021**, *26*, 3354. <https://doi.org/10.3390/molecules26113354>

Academic Editor: Enrique Barrajon

Received: 14 May 2021

Accepted: 28 May 2021

Published: 2 June 2021

**Publisher's Note:** MDPI stays neutral with regard to jurisdictional claims in published maps and institutional affiliations.



**Copyright:** © 2021 by the authors. Licensee MDPI, Basel, Switzerland. This article is an open access article distributed under the terms and conditions of the Creative Commons Attribution (CC BY) license (<https://creativecommons.org/licenses/by/4.0/>).

**Abstract:** In December 2020, the U.K. authorities reported to the World Health Organization (WHO) that a new COVID-19 variant, considered to be a variant under investigation from December 2020 (VUI-202012/01), was identified through viral genomic sequencing. Although several other mutants were previously reported, VUI-202012/01 proved to be about 70% more transmissible. Hence, the usefulness and effectiveness of the newly U.S. Food and Drug Administration (FDA)-approved COVID-19 vaccines against these new variants are doubtfully questioned. As a result of these unexpected mutants from COVID-19 and due to lack of time, much research interest is directed toward assessing secondary metabolites as potential candidates for developing lead pharmaceuticals. In this study, a marine-derived fungus *Aspergillus terreus* was investigated, affording two butenolide derivatives, butyrolactones I (1) and III (2), a meroterpenoid, terretonin (3), and 4-hydroxy-3-(3-methylbut-2-enyl)benzaldehyde (4). Chemical structures were unambiguously determined based on mass spectrometry and extensive 1D/2D NMR analyses experiments. Compounds (1–4) were assessed for their in vitro anti-inflammatory, antiallergic, and in silico COVID-19 main protease (M<sup>Pro</sup>) and elastase inhibitory activities. Among the tested compounds, only 1 revealed significant activities comparable to or even more potent than respective standard drugs, which makes butyrolactone I (1)

a potential lead entity for developing a new remedy to treat and/or control the currently devastating and deadly effects of COVID-19 pandemic and elastase-related inflammatory complications.

**Keywords:** *Aspergillus terreus*; butenolides; antiallergic; COVID-19 M<sup>Pro</sup>; elastase

## 1. Introduction

For more than a year now, since 2019, the whole world has been faced with the Coronavirus Disease 2019 (COVID-19) pandemic, believed to be caused by severe acute respiratory syndrome coronavirus 2 (SARS-CoV 2), a zoonotic viral infection that first emerged and was reported in Wuhan, China in December 2019 [1,2]. During this year, scientists from all around the globe set new horizons for collaborations to race against time to produce a dependable and a reliable vaccine. This mission was accomplished in December 2020 when the U.S. Food and Drug Administration (FDA) issued the first Emergency Use Authorization (EUA) for the Pfizer–BioNTech vaccine [3] and the United Kingdom approved the emergency use of the Oxford–AstraZeneca vaccine for the prevention of the COVID-19 in individuals 16 years of age or older [4]. However, simultaneously, two new viral variants were identified at two widely spaced localities in London, United Kingdom, designated as a variant under investigation of December 2020 (VUI-202012/01) and in Cape Town, South Africa, named 501.V2, that both shared a common worrying feature of being up to 70% more transmissible [5]. New variants are not the only ones evolved by SARS-CoV-2, but they are the ones that succeeded in adopting uncontrolled transmission among humans, forcing several countries to move back to strict lockdowns, social distancing and other infection control measures [5]. These two new variants also raised questions about the efficacy and effectiveness of the approved vaccines against them, which will take more time to figure out.

In other domains, more research efforts have been directed toward finding out other treatment alternatives to ease COVID-19 severity in vulnerable patients, especially acute respiratory distress symptoms mainly caused by neutrophil elastase (NE) enzyme, an intracellular enzyme stored in azurophilic granules of polymorphonuclear neutrophils (PMNs) that are a major component of human innate immunity [6,7]. Although NE's main function is to devastate functional proteins of xenobiotics and/or pathogens of various origins, it has also been found to induce deleterious effects on the lungs as elastin-rich connective tissue affording pathologic edematous symptoms such as acute lung injury (ALI), acute respiratory distress syndrome (ARDS), or chronic obstructive pulmonary disorder (COPD) [7,8]. Moreover, NE contributes to the invasion of SARS-CoV-2 into host cells and plays a role in the COVID-associated ARDS, developed usually in the late stage of the COVID disease. Currently, sivelestat is the only approved NE inhibitor for the treatment of ARDS (in Korea and Japan) [9].

Fungi from various environments proved to be a prolific source producing a plethora of secondary metabolites with intriguing spectrum of biological activities and/or industrial applications [10]. The *Aspergillus* genus is among the most abundant fungal genera, comprising about 250 species, and is a major source contributing to the discovery of bioactive fungal metabolites [11]. *Aspergillus terreus* is a widely distributed fungus in diverse environments including extreme living conditions of high salinity [12], high temperature [13], high alkalinity [14], and drought [15]. Its ability to accommodate these extreme conditions stressed its probable evolution of gene clusters or regulatory mechanism to acclimatize these environments that may also induce the biosynthesis of a wide variety of fungal secondary metabolites including alkaloids, polyketides, peptides, terpenes, and lignans [11,16–19]. Butenolides (a rare type of lignans) and terretonins (meroterpenoids) are considered as typical metabolites of the genus *Aspergillus* that have exhibited a wide range of bioactivities such as antibacterial [20], cytotoxic [21], anti-inflammatory [22], antioxidant [23], and antiviral activities [24].

As part of our ongoing research directed toward exploring secondary metabolites for their relevant bioactivities, we investigated those obtained from a marine-derived fungus *Aspergillus terreus* for their in vitro anti-inflammatory, antiallergic, and in silico molecular modeling against the COVID-19 main protease ( $M^{pro}$ ) as a potential target for developing an antiviral drug. In this study, we report the isolation and identification of four different fungal metabolites (1–4) (Figure 1), their in vitro bioactivity assessment, and their in silico docking study results.

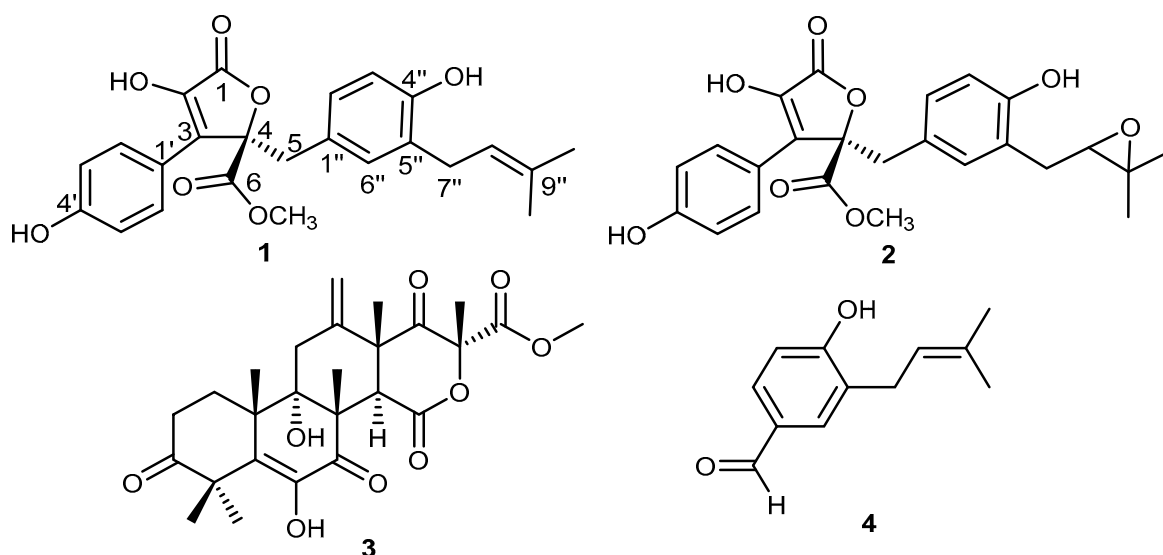


Figure 1. Chemical structures of 1–4.

## 2. Results and Discussion

### 2.1. Isolation and Characterization of Main Secondary Metabolites in the Fungal Extract

A detailed chromatographic investigation of the solid rice culture extract from the cultivated fungal strain *Aspergillus terreus* derived from the marine annelide *Spirorbis* sp. was performed by applying different chromatographic procedures; that is, MS, 1D and 2D NMR spectral analyses, and comparing the obtained results with the reported literature. The obtained results afforded four different compounds.

Compound 1 was isolated as an orange-coloured amorphous solid. Its UV spectrum revealed two absorption maxima ( $\lambda_{max}$ ) at 210 and 307 nm. The HRESIMS revealed the presence of two pseudomolecular ion peaks at  $m/z$  447.12980  $[M + Na]^+$  (calcd. for  $C_{24}H_{24}O_7Na$ , 447.13092) and at  $m/z$  423.12077  $[M - H]^-$  (calcd. for  $C_{24}H_{23}O_7$ , 423.12201). Hence, the molecular formula was established to be  $C_{24}H_{24}O_7$ , indicating the existence of 13 degrees of unsaturation. The  $^{13}C$  NMR, DEPT, and HMQC spectra of 1 differentiated the presence of 11 quaternary carbons including two carbonyl groups ( $\delta_C$  170.1 and  $\delta_C$  169.8), three oxygenated olefinic carbons ( $\delta_C$  157.2,  $\delta_C$  153.2, and  $\delta_C$  144.9), five olefinic carbons ( $\delta_C$  137.7, 133.9, 128.8, 124.6, and 121.8), and one aliphatic quaternary carbon ( $\delta_C$  86.2). In addition, eight tertiary, two secondary, and three primary carbons were also distinguished. The  $^1H$  NMR spectrum of 1 clearly revealed the existence of two different aromatic systems, one recognized as 1,4-disubstituted phenyl and illustrated by two proton resonances each integrated for two protons at  $\delta_H$  6.90 (2H, d,  $J$  = 8.8 Hz) and at  $\delta_H$  7.61 (2H, d,  $J$  = 8.8 Hz). The second aromatic spin system was shown to be an 1,3,4-trisubstituted aromatic moiety as represented by three different proton resonances at  $\delta_H$  6.59 (1H, dd,  $J$  = 8.1, 2.0 Hz),  $\delta_H$  6.52 (1H, d,  $J$  = 8.1 Hz), and  $\delta_H$  6.51 (1H, d,  $J$  = 2.0 Hz). Moreover, the  $^1H$  NMR spectrum displayed three singlet methyl groups including one oxygenated methoxy group ( $\delta_H$  3.75/ $\delta_C$  53.7) and two olefinic methyl groups at  $\delta_H$  1.65 and  $\delta_H$  1.59 ppm directly connected to carbon peaks at  $\delta_C$  25.7 and  $\delta_C$  17.7 ppm, respectively. By comparing the obtained data with the reported fungal metabolites in the literature, they revealed a great

agreement to butyrolactone I, a butenolide fungal metabolite first reported from *Aspergillus terreus* var. *Africans* IFO8355 [25–27].

Compound **2** was purified as a yellow-coloured amorphous solid showing absorption maxima ( $\lambda_{\max}$ ) in its UV spectrum at 225 and 308 nm similar to those shown by **1**. The HRESIMS of **2** exhibited two pseudomolecular ion peaks at  $m/z$  463.12586  $[M + Na]^+$  (calcd. for  $C_{24}H_{24}O_8Na$ , 463.12691) and at  $m/z$  439.11538  $[M - H]^-$  (calcd. for  $C_{24}H_{23}O_8$ , 439.11654), indicating the molecular formula to be  $C_{24}H_{24}O_8$ , differing by an additional oxygen atom compared with butyrolactone I (**1**) and similarly having 13 degrees of unsaturation. The  $^1H$  and  $^{13}C$  NMR spectra of **2** revealed a close similarity to **1**, except for the disappearance of the characteristic isoprenyl peaks and the existence of two oxygenated  $sp^3$  carbons differentiated into one methine ( $\delta_C$  69.7) and one aliphatic quaternary carbon ( $\delta_C$  76.8) together with two singlet methyl groups at  $\delta_H$  1.21 ( $\delta_C$  24.8) and  $\delta_H$  1.24 ( $\delta_C$  22.0). The HMBC spectrum of **2** exhibited clear long-range correlations from the two singlet methyl groups to two carbons at  $\delta_C$  69.7 and  $\delta_C$  76.8, suggesting the replacement of isoprenyl moiety by an epoxy ring. By searching the reported literature, compound **2** was confirmed to be butyrolactone III [28,29].

Compound **3** was obtained as a creamy-coloured amorphous solid, with its UV spectrum showing two absorption maxima ( $\lambda_{\max}$ ) at 220 and 278 nm. The molecular formula was determined to be  $C_{26}H_{32}O_9$  based on its HRESIMS spectrum, which disclosed the presence of two pseudomolecular ion peaks at  $m/z$  489.2070  $[M + H]^+$  (calcd. for  $C_{26}H_{33}O_9$ , 489.2125), at  $m/z$  511.1887  $[M + Na]^+$  (calcd. for  $C_{26}H_{32}O_9Na$ , 511.1944), and at  $m/z$  487.1971  $[M - H]^-$  (calcd. for  $C_{26}H_{31}O_9$ , 487.1968), indicating the existence of 11 degrees of unsaturation. Both 1D and 2D NMR spectra of **3** revealed a similar pattern to those presented by terretonin, a meroterpenoid previously reported from *A. terreus* fungus [30,31].

Compound **4** was obtained as a red-coloured solid powder. Its  $^{13}C$  NMR spectrum revealed twelve distinct carbon resonances that can be differentiated through  $^1H$  NMR and HMQC experiment into four quaternary ( $\delta_C$  161.1, 132.2, 128.5, and 128.4), five tertiary including one aldehyde carbon at  $\delta_C$  191.1 s, together with three aromatic carbons ( $\delta_C$  130.7,  $\delta_C$  130.1, and  $\delta_C$  115.1) and an olefinic carbon at  $\delta_C$  121.9 [ $\delta_H$  5.29 (1H, td,  $J = 7.4$ , 1.5 Hz)]; one secondary carbon at  $\delta_C$  27.7 [ $\delta_H$  3.26 (2H, d,  $J = 7.4$  Hz)]; in addition to two primary carbons at  $\delta_C$  25.5 [ $\delta_H$  1.71 (3H, d,  $J = 1.5$  Hz)], and  $\delta_C$  17.6 [ $\delta_H$  1.68 (3H, d,  $J = 1.5$  Hz)]. The  $^1H$  NMR spectrum in DMSO- $d_6$  revealed a clear 1,3,4-trisubstituted aromatic moiety through three proton resonances at  $\delta_H$  7.60 (1H, d,  $J = 8.2$ , 2.2 Hz),  $\delta_H$  7.58 (1H, d,  $J = 2.2$  Hz), and  $\delta_H$  6.95 (1H, d,  $J = 8.2$  Hz). In addition, it also showed two deshielded protons at  $\delta_H$  10.58 and  $\delta_H$  9.75 ppm ascribed for an aromatic hydroxyl group and an aldehyde moiety, respectively. By comparing the obtained 1D and 2D NMR data of **4** with the reported literature, it turned out to be identical to those reported for 4-hydroxy-3-(3-methylbut-2-enyl)benzaldehyde, a fungal metabolite first reported in 2012 from the root rotting pathogen *Heterobasidion occidentale* [32] and later reported from the fruits of *Narthecium ossifragum* [33].

Based on the previous reports about the activity of butyrolactones, they have been distinguished as potent inhibitors of cyclin-dependent kinases (CDKs) that play an important role in the occurrence of various diseases such as cancer, Alzheimer's disease, Parkinson's disease, stroke, diabetes, glomerulonephritis, and inflammation. Isolated butyrolactones (**1** and **2**) along with terretonin (**3**) and 4-hydroxy-3-(3-methylbut-2-enyl)benzaldehyde (**4**) were subjected to in vitro antiallergic, anti-inflammatory, anti-HCoV-229, and neutrophil elastase enzymatic assays. The viability assays towards the cells used in the tests were also performed.

## 2.2. Degranulation Assay in Mast Cells

The toxicity of isolated compounds was tested on RBL-2H3 cells up to 100  $\mu M$ . The results revealed that all tested compounds were non-toxic as illustrated by the viability rate exceeding 90%. Isolated compounds (**1–4**) were then tested for their antiallergic



activity via determining their inhibitory activities against A23187- and antigen-induced  $\beta$ -hexosaminidase release in RBL-2H3 cells. Calcium ionophore A23187 induces calcium transport into the mast cell membrane, whereas antigen (IgE plus DNP-BSA) acts via the Fc $\epsilon$ RI receptor, resembling a physiological condition. The attained results (Table 1) displayed that only butyrolactone I (1), among the tested compounds, showed moderate antiallergic activity, illustrated via inhibiting A23187- and antigen-induced degranulation with IC<sub>50</sub> values of 39.7 and 41.6  $\mu$ M, respectively, compared with azelastine as a standard antiallergic drug (34.5 and 35.5% at 10  $\mu$ M, respectively). The obtained results are in accordance with and supported by the previously reported activity of 1 in alleviating ovalbumin-induced allergy symptoms via reducing the levels of histamine and mouse mast cell proteinases [34].

**Table 1.** Inhibitory activity of butyrolactone I (1) on A23187- and antigen-induced degranulation.

Compound.	Cell Viability, RBL-2H3 <sup>a</sup>	Inhibition of A23187-Induced Degranulation <sup>b</sup>	Inhibition of Antigen-Induced Degranulation <sup>c</sup>
	% (100 $\mu$ M)	IC <sub>50</sub> ( $\mu$ M) <sup>d</sup>	IC <sub>50</sub> ( $\mu$ M) <sup>d</sup>
Butyrolactone I (1)	>90%	39.7 <sup>e</sup>	41.6 <sup>f</sup>
Butyrolactone III (2)	>90%	>100	>100
Terretonin (3)	>90%	>100	>100
4-Hydroxy-3-(3-methylbut-2-enyl)benzaldehyde (4)	>90%	>100	>100

<sup>a</sup> The cytotoxicity of samples to RBL-2H3 was evaluated using MTT viability assay. The results are presented as mean ( $n = 3$ ) compared with untreated control (DMSO). All samples were nontoxic towards RBL-2H3 cells. <sup>b</sup> Azelastine (10  $\mu$ M) was used as a positive control and inhibited  $34.5 \pm 2.5\%$  of A23187-induced degranulation. The inhibition of degranulation was assessed by A23187-induced  $\beta$ -hexosaminidase release in RBL-2H3 cells. The results are presented as mean  $\pm$  S.E.M. ( $n = 3$ ). <sup>c</sup> Azelastine (10  $\mu$ M) was used as a positive control and inhibited  $35.5 \pm 8.1\%$  of antigen-induced degranulation. The inhibition of degranulation was assessed by antigen-induced  $\beta$ -hexosaminidase release in RBL-2H3 cells. The results are presented as mean  $\pm$  S.E.M. ( $n = 3$ ). <sup>d</sup> Concentration necessary for 50% inhibition (IC<sub>50</sub>). <sup>e</sup> Butyrolactone I (1) showed dose-dependent inhibition of A23187-induced degranulation with  $26.0 \pm 2.4\%$  (10  $\mu$ M) and  $98.7 \pm 0.7\%$  inhibition at 100  $\mu$ M. <sup>f</sup> Butyrolactone I (1) showed dose-dependent inhibition of antigen-induced degranulation with  $30.0 \pm 3.3\%$  (10  $\mu$ M) and  $87.0 \pm 2.4\%$  inhibition at 100  $\mu$ M. >100, not active (insignificant inhibition of degranulation at 100  $\mu$ M, below 20%).

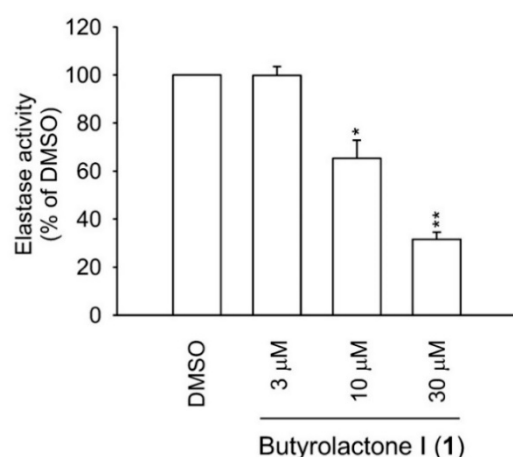
### 2.3. Human Neutrophil Viability, Elastase Release, and Elastase Enzymatic Assays

The results of an in vitro anti-inflammatory assay of compounds 1–4 (Table 2) revealed that only butyrolactone I (1) featured potent inhibitory activities against neutrophil elastase release (IC<sub>50</sub> = 2.30  $\mu$ M). Interestingly, butyrolactone I (1) rather than III (2) exhibited significant activities more potent than genistein used as a standard drug (IC<sub>50</sub> = 32.67  $\mu$ M). Further, the cell viability assay based on lactate dehydrogenase release was performed to exclude toxic effects of 1 on human neutrophils. Both butyrolactone I (1) and III (2) were non-toxic to neutrophils (Table 2). Human neutrophil elastase plays a pivotal role in the development of several inflammatory symptoms including respiratory harmful effects accompanying several acute and chronic respiratory disorders [8]. In the cell-free system, butyrolactone I (1) revealed a dose-dependent direct inhibitory effect on the enzymatic activity of elastase (Figure 2) with an IC<sub>50</sub> value of 16.70  $\mu$ M (Table 2). Based on these results, the anti-inflammatory effects of 1 were, at least partly, attributed to its interaction with elastase enzyme. Therefore, we performed the following in silico molecular modeling experiment to simulate and identify the interaction sites.

**Table 2.** Effects of the isolated compounds from the marine-derived fungus *Aspergillus terreus* on elastase release, viability, and elastase enzymatic activity in vitro.

Compound	Elastase Release in Human Neutrophils <sup>a</sup>	Cell viability, Human Neutrophils <sup>c</sup>	Elastase Enzymatic Activity (Cell-Free) <sup>d</sup>
	IC <sub>50</sub> (μM) <sup>b</sup>	% (10 μM)	IC <sub>50</sub> (μM) <sup>b</sup>
Butyrolactone I (1)	2.30 ± 0.27	94.13 ± 2.31	16.70 ± 2.64
Butyrolactone III (2)	>10	98.25 ± 1.77	>30
Terretonin (3)	>10	n.t.	n.t.
4-Hydroxy-3-(3-methylbut-2-enyl)benzaldehyde (4)	>10	n.t.	n.t.

<sup>a</sup> Inhibition of elastase release in fMLF/cytochalasin B (CB)-induced human neutrophils. Genistein inhibited elastase release with an IC<sub>50</sub> value 32.67 ± 1.45. <sup>b</sup> Concentration necessary for 50% inhibition (IC<sub>50</sub>). The results are presented as mean ± S.E.M. (*n* = 3). \* *p* < 0.05, \*\* *p* < 0.01, \*\*\* *p* < 0.001 compared with the control (0.1% DMSO). <sup>c</sup> Percentage of cell viability (%) at 10 μM. The results are based on the lactate dehydrogenase release and presented as mean ± S.E.M. (*n* = 3). <sup>d</sup> Sivelestat was used as a positive control and inhibited elastase enzyme with an IC<sub>50</sub> value 17.92 ± 4.66 nM. n.t.: not tested.

**Figure 2.** In vitro elastase inhibitory activity of butyrolactone I (1) in the cell-free system. The results are presented as mean ± S.E.M. (*n* = 3). \* *p* < 0.05, \*\* *p* < 0.01 compared with the control (0.1% DMSO).

#### 2.4. Molecular Docking Studies

Docking studies were used to investigate the affinity of isolated compounds to the human neutrophil elastase (NE). The crystal structure of NE is available in the protein data bank (PDB) with the ID 1H1B co-crystallized with GW475151. Validation of the docking procedure was reported earlier, where the co-crystallized ligand was redocked in the active site with a docking score of −6.9 kcal/mol, and an RMSD of 1.317 between docked, and crystallized structures [35]. The co-crystallized ligand is known to form a hydrogen bond with Ser195 that is important for binding [36]. In this study, we have docked the isolated compounds (1–4) in the active site of the human NE. Out of the tested compounds, only butyrolactone I (1) has shown a docking score superior to that of the co-crystallized ligand (Table 3). All of tested compounds were found to form a hydrogen bond with Ser195 similar to GW475151, the co-crystallized ligand. It is worth mentioning here that 1 was found to inhibit human elastase in vitro with an IC<sub>50</sub> of 16.70 μM (Table 2). The binding mode of compound 1 as well as its interaction with amino acids in the active site is shown in Figure 3. Butyrolactone III (2), which is a very similar structure, did not show similar results in either elastase assays (Table 3, no noticed inhibition at concentration up to 10 μM) or docking study. This might be attributed to the fact that the isoprene part of butyrolactone I (1) is docked in a hydrophobic side pocket, forming hydrophobic interactions with Phe21 and Leu99, as can be seen in Figure 3. This binding mode will not be favored for the epoxide ring of butyrolactone III (2), leading to a flipped alternative binding mode that is missing the key interaction with Ser195.

**Table 3.** Docking results of tested compounds in the active sites of human NE (1H1B) and SARS-CoV-2 main protease (6LU7). Amino acids' interactions with both the co-crystallized ligands and tested ligands are shown bold.

Ligand	1H1B (Elastase)		6LU7 (M <sup>Pro</sup> )	
	Binding Affinity (kcal/mol)	Interacting Residues	Binding Affinity (kcal/mol)	Interacting Residues
Butyrolactone I (1)	−7.3	<b>Ser195</b> -Arg147	−7.3	<b>Gly143</b> -Ser144- <b>His163</b> - <b>Glu166</b>
Butyrolactone III (2)	−6.7	<b>Ser195</b> -Arg147	−7.8	Thr26- Leu141- <b>Gly143</b> - Ser144- Cys145- <b>His163</b> - <b>Glu166</b>
Terretonin (3)	−6.7	<b>Ser195</b> - Val216	−7.8	Asn142- <b>Gly143</b> - <b>His163</b>
4-Hydroxy-3-(3-methylbut-2-enyl)benzaldehyde (4)	−5.1	<b>Ser195</b> - Cyc191	−5.6	Leu141- <b>Gly143</b> -Ser144-Cys145- <b>Glu166</b>
1H1B-Ligand	−6.9	<b>Ser195</b>	–	–
6lu7-Ligand	–	–	−7.1 (3rd pose)	Phe140, Gly143, His163, His164, Glu166, Gln189, Thr190

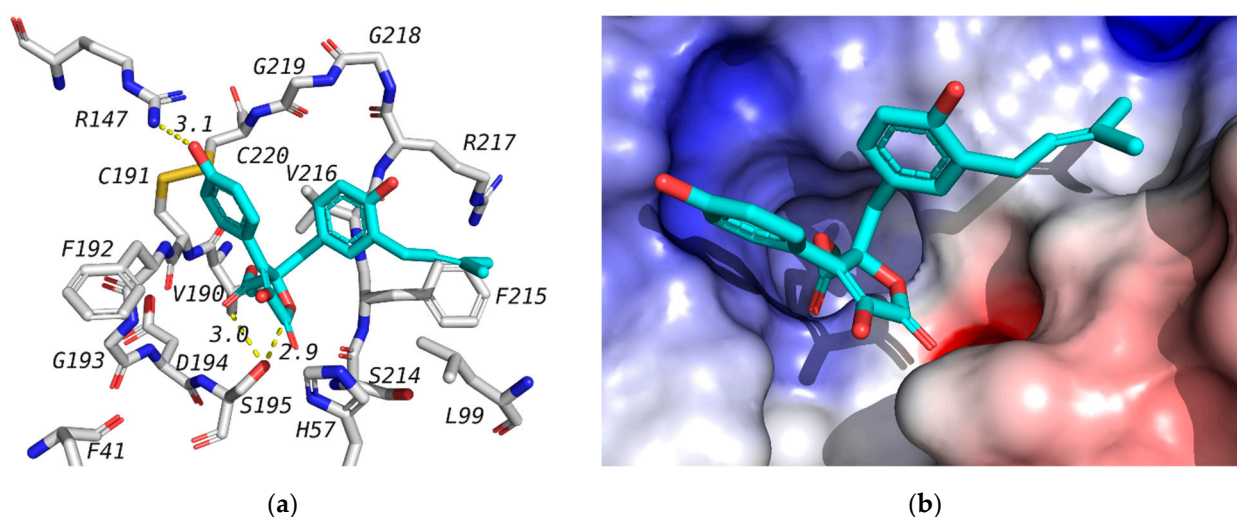


**Figure 3.** Docking of compound butyrolactone I (1) (blue) in the active site of human NE. (a) Interactions of 1 with amino acids in the active site. (b) Docking pose of 1.

In addition to the human NE, we were also interested in investigating the potential binding and inhibitory activities of isolated compounds against SARS-CoV-2 main protease (M<sup>Pro</sup>) owing to the current pandemic situation. The viral main protease is a key enzyme in the virus life cycle that has been the target for several investigations since the beginning of last year. The target crystal structure is available under PDB ID of 6LU7 co-crystallized with a peptide-like inhibitor called N3 [35]. It was found to interact with several amino acids in the active site, including Phe140, Gly143, His163, His164, Glu166, Gln189, and Thr190. Several research groups investigated synthetic and natural products for their inhibition of this target among other SARS-CoV-2 targets [36–38]. We have previously used the same target to investigate the potential inhibition of phytochemicals from the Jordanian hawksbeard [39]. We also reported validation of the same docking procedure through the docking of N3 co-crystallized ligand in the active site of 6LU7 [39]. The docking score of the co-crystallized ligand was found to be −7.1 kcal/mol.

Among the tested compounds, butyrolactone III (2) and terretonin (3) have shown the best scores (−7.8 kcal/mol) compared with the co-crystallized ligand N3 (−7.1 kcal/mol), as shown in Table 3. Both compounds were found to bind in the same pocket where N3 binds, but each overlaps with slightly different parts of N3, as shown in Figure 4. In addition, both compounds were able to maintain two of the hydrogen bonds seen with N3, which include hydrogen bonds with Gly143 and His163.

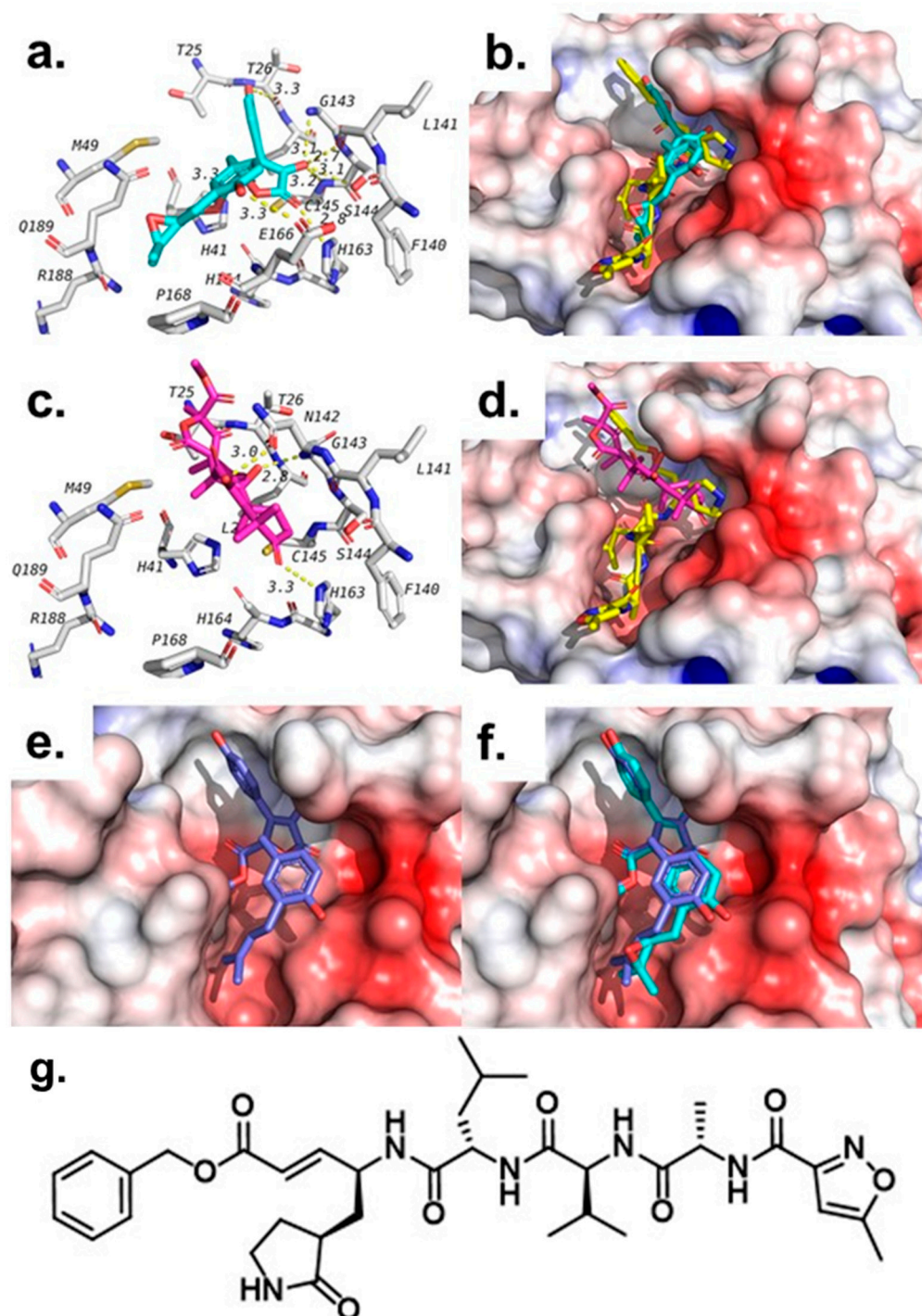


**Figure 4.** Poses and interactions of tested compounds in the active site of SARS-CoV-2 main protease (6LU7). (a) Interactions of butyrolactone III (2) (Cyan) in the active site. (b) Overlapping of butyrolactone III (2) with co-crystallized ligand N3 (yellow). (c) Interactions of terretinin (3) (pink) in the active site. (d) Overlapping of terretinin (3) with co-crystallized ligand N3 (yellow). (e) Binding pose of butyrolactone I (1). (f) Overlapping of the binding poses of butyrolactone I (1) and butyrolactone III (2). (g) Structure of the co-crystallized ligand (N3) in 6LU7 pdb file.

Beside these two hydrogen bonds, both compounds were found to form other hydrogen bonds and hydrophobic interactions with residues in the active site of the SARS-CoV-2 main protease, as shown in Table 3 and Figure 4. In addition to these two compounds, butyrolactone I (1) has also shown a docking score that is better than that of the co-crystallized



ligand (N3), but weaker than 2 and 3. The docking pose of butyrolactone I (1) in the active site of the main protease is shown in Figure 4e. This docking pose is very similar, as expected, to the proposed binding pose of butyrolactone III (2), as seen in Figure 4f. Compound 4, on the other hand, showed the lowest binding affinity (-5.6 kcal/mol) to SARS-CoV-2 main protease compared with the co-crystallized ligand N3. Furthermore, we performed an in vitro human coronavirus 229E (HCoV-229) assay to determine possible protective effects of compounds 1–4 (10  $\mu$ M) against the HCoV-229 infection in Huh7 cells; however, none of the compounds exerted effects (see supplementary materials, Figure S1).

These results suggest a potential role of these isolated compounds in the inhibition of the SARS-CoV-2 main protease with a possible role in controlling the new virus and late stage of coronavirus-associated ARDS inflammation. The results also support the need for further investigation of these compounds as well as the natural products reservoir for new leads that could help us with our battle against the COVID-19 virus.

### 3. Materials and Methods

#### 3.1. General Experimental Procedures

A Perkin-Elmer-241 MC polarimeter was used for determining optical rotation. Chromatographic separation procedures were performed applying column chromatography with different stationary phases such as silica gel 60 M (0.04–0.063 mm) and Sephadex LH20. For screening purposes, ready-made silica gel 60 F<sub>254</sub> TLC plates (Merck, Darmstadt, Germany) were used. For visualization purposes of TLC plates, UV light at 254 and 365 nm wavelengths was applied as a non-destructive technique or after spraying with anisaldehyde reagent and heating. Final purification of fractions was achieved using preparative HPLC (Agilent, Santa Clara, CA, U.S.A.) on Zorbax Eclipse XDB-C18 (Agilent technologies, Santa Clara, CA, U.S.A.) preparative column (9.4 mm  $\times$  250 mm, L  $\times$  ID; 5  $\mu$ m particle size) at a flow rate of 2 mL/min and UV screening detection at 210 to 330 nm. A standard gradient elution was applied using (MeOH, in Water): 0 min, 10% MeOH; 5 min, 10% MeOH; 40 min, 90% MeOH, with a flow rate of 1 mL/min. Each solvent ratio/flow timetable will be present for the compounds purified by HPLC. Preparative TLC separation was done using Flat Bottom TLC Chamber (Camag®, Muttentz, Switzerland). Silica gel 60 (0.04–0.063, Merck, Darmstadt, Germany) and Sephadex® LH-20 (Sigma-Aldrich, St. Louis, MO, USA) were used for column chromatography and separation was monitored using normal phase silica gel precoated plates F<sub>254</sub> (Merck, Darmstadt, Germany). An Agilent 600 MHz spectrometer (Santa Clara, CA, USA) was used for 1D (<sup>1</sup>H and <sup>13</sup>C NMR) and 2D NMR spectra (chemical shifts in ppm). Chloroform-*d*, DMSO-*d*<sub>6</sub> and methanol-*d*<sub>4</sub> NMR solvents (Sigma Aldrich, Munich, Germany) were used to dissolve the isolated compounds. Supplementary materials of this study includes HPLC chromatograms, Mass, 1D, and 2D NMR spectra of isolated compounds along with NMR data for each compound in a tabulated form.

#### 3.2. Sponge and Fungal Strain Material

The fungus *Aspergillus terreus* was separated from the annelide *Spirorbis* sp., which was collected by one of our co-authors (B.G.) from Marmara Sea, İstanbul, Turkey in July, 2018. For identification, this fungus was cultured on Sabouraud 4% dextrose agar (SDA, Merck, Germany) at room temperature for a week in an incubator (Nüve, Turkey). The fungus was identified as *Aspergillus terreus* (GenBank accession number MT273950) based on DNA amplification and ITS (internal transcribed spacer) sequencing data analysis, as reported previously in the literature. This fungal strain was deposited in the laboratory of the Department of Pharmacognosy, Faculty of Pharmacy, Ankara University (B.K.).

#### 3.3. Fermentation, Extraction, and Isolation

The fungal strain was cultivated on a 100 mL solid rice medium prepared by autoclaving (100 g of rice and 100 mL of distilled water containing 3.5% artificial sea salt



in a 60-piece 2000 mL Erlenmeyer flask). Fermentation continued for 30 days at room temperature away from light under static conditions.

To discontinue the fermentation process, ethyl acetate (EtOAc) ( $3 \times 350$  mL) was added to each flask to stop the growth of cells. After adding EtOAc, flasks were shaken for 12 h, then filtered, and EtOAc filtrate was pooled and evaporated under reduced pressure until yielding a solid residue (3.7 g). The crude extract was then partitioned between *n*-hexane and 90% aqueous MeOH by liquid–liquid fractionation, where both fractions were collected and dried up under vacuum. The aqueous 90% MeOH phase (1.3 g) was subjected to vacuum liquid chromatography (VLC) using silica gel 60 as a stationary phase and the mobile phase started with *n*-hexane/EtOAc (30:70) followed by a gradient elution development of DCM/MeOH (100:0, 90:10, 80:20, 70:30, 60:40, 50:50, 30:70, 10:90, 0:100), respectively, affording ten fractions (AT-1~AT-10).

All obtained fractions were subjected to TLC and analytical HPLC procedures. Fraction AT-2 was chosen for further preparative TLC and HPLC purification procedures. Fraction AT-2 (272 mg), eluted with DCM/MeOH (100:0), was applied on column chromatography using silica gel (Qingdao Haiyang Chemical HG/T2354-92) as stationary phase and petroleum ether/EtOAc as mobile phase at ratios of 4:1, 3:1, 2:1, and 1:1, each 300 mL, respectively, yielding **1** (4.4 mg), **2** (5.3 mg), and **4** (1.8 mg). The subfraction of AT-4 (78 mg) from silica column application was applied on column chromatography using silica gel as the stationary phase and petroleum ether/EtOAc as the mobile phase at ratios of 4:1, 3:1, 2:1, and 1:1, each 200 mL, followed by preparative HPLC for final purification to yield **3** (2.0 mg).

**Butyrolactone I (1).** Orange-coloured amorphous solid;  $[\alpha]_D^{20} +91.0^\circ$  (*c* 0.02, MeOH); UV (MeOH)  $\lambda_{\max}$  210 and 307 nm;  $^1\text{H}$  and  $^{13}\text{C}$  NMR, see supplementary material Table S1; HRESIMS  $m/z$  447.12980  $[\text{M} + \text{Na}]^+$  (calcd. for  $\text{C}_{24}\text{H}_{24}\text{O}_7\text{Na}$ , 447.13092) and at  $m/z$  423.12077  $[\text{M} - \text{H}]^-$  (calcd. for  $\text{C}_{24}\text{H}_{23}\text{O}_7$ , 423.12201).

**Butyrolactone III (2).** Yellow-coloured amorphous solid;  $[\alpha]_D^{20} +76.0^\circ$  (*c* 0.02, MeOH); UV (MeOH)  $\lambda_{\max}$  225 and 308 nm;  $^1\text{H}$  and  $^{13}\text{C}$  NMR, see supplementary material Table S2; HRESIMS  $m/z$  463.12586  $[\text{M} + \text{Na}]^+$  (calcd. for  $\text{C}_{24}\text{H}_{24}\text{O}_8\text{Na}$ , 463.12691) and at  $m/z$  439.11538  $[\text{M} - \text{H}]^-$  (calcd. for  $\text{C}_{24}\text{H}_{23}\text{O}_8$ , 423.11654).

**Terretonin (3).** Creamy-coloured amorphous solid;  $[\alpha]_D^{20} -112.4^\circ$  (*c* 0.02, MeOH); UV (MeOH)  $\lambda_{\max}$  220 and 278 nm;  $^1\text{H}$  and  $^{13}\text{C}$  NMR, see supplementary material Table S3; HRESIMS  $m/z$  489.2070  $[\text{M} + \text{H}]^+$  (calcd. for  $\text{C}_{26}\text{H}_{33}\text{O}_9$ , 489.2125),  $m/z$  511.1887  $[\text{M} + \text{Na}]^+$  (calcd. for  $\text{C}_{26}\text{H}_{32}\text{O}_9\text{Na}$ , 511.1944), and  $m/z$  487.1971  $[\text{M} - \text{H}]^-$  (calcd. for  $\text{C}_{26}\text{H}_{31}\text{O}_9$ , 487.1968).

**4-Hydroxy-3-(3-methylbut-2-enyl)benzaldehyde (4).** Red-coloured solid powder;  $^1\text{H}$  and  $^{13}\text{C}$  NMR, see supplementary material Table S4.

### 3.4. Degranulation Assay and MTT Cell Viability Assay in Mast Cells

The mucosal mast-cell-derived rat basophilic leukemia cells (RBL-2H3) were purchased from Bioresource Collection and Research Center (Hsin-Chu, Taiwan). The cells were cultured in DMEM containing 10% FBS, 100 U/mL penicillin, and 100  $\mu\text{g}/\text{mL}$  streptomycin in 10 cm cell culture dishes at  $37^\circ\text{C}$  in a humidified chamber with 5%  $\text{CO}_2$  in air. The level of degranulation in RBL-2H3 cells was evaluated using  $\beta$ -hexosaminidase release assay induced by A23187 or antigen as reported before with some modifications [40]. Briefly, the cells were seeded in a 96-well plate ( $2 \times 10^4$  cells/well, for the A23187-induced assay) or a 48-well plate ( $3 \times 10^4$  cells/well, for the antigen-induced assay) overnight. The cells for the antigen-induced assay were sensitized with anti-DNP IgE (0.5  $\mu\text{g}/\text{mL}$ ; Sigma) during seeding overnight. RBL-2H3 cells were then treated with the samples (0.5, 5, and 50  $\mu\text{M}$ ) for 30 min in Tyrode's buffer with a maximal DMSO dose of 0.5%. For the A23187-induced assay, the cells were activated by addition of A23187 (final concentration 0.5  $\mu\text{M}$ ), while cells for the antigen-induced assay were activated by the addition of DNP-BSA (final

concentration 100 ng/mL) for 30 min. Azelastine (10  $\mu$ M) served as the positive control. The amount of  $\beta$ -hexosaminidase was detected using the method utilizing p-NAG as the substrate according to the procedure described before [41].

The viability of the RBL-2H3 cells in the presence of the samples (10 and 100  $\mu$ M) was determined using the methylthiazole tetrazolium (MTT) assay according to a previous method [41].

### 3.5. Elastase Release Assay and Lactate Dehydrogenase (LDH) Viability Assay by Human Neutrophils

The human neutrophils were obtained from venous blood of healthy adult volunteers (20–30 years old) following the reported procedure [42]. Elastase release by the activated neutrophils was determined using elastase substrate (*N*-methoxysuccinyl-Ala-Ala-Pro-Val-*p*-nitroanilide) according to the previous methodology [42]. The tested samples' concentration was 1 to 10  $\mu$ M and the total incubation time in fMLF/CB-induced cells was 15 min. Genistein was used as the positive control. Cytotoxicity test was performed based on the release of LDH stored in the cytoplasm out of the cells [43]. Briefly, preheated (37 °C, 5 min, 1 mM  $\text{CaCl}_2$ ) human neutrophils ( $6 \times 10^5$  cells  $\text{mL}^{-1}$ ) were incubated with test compounds for 15 min. Total LDH release control was represented as completely lysed cells by 0.1% of Triton X-100 solution incubated with cells for 30 min. The cells were centrifuged at 4 °C for  $200 \times g$  for 8 min, and LDH reagent was added to supernatant and reacted at room temperature for 30 min in the dark. The absorbance was then measured at 492 nm, and the LDH release was calculated and compared to the total LDH release set as 100%.

### 3.6. Determination of Elastase Enzymatic Activity

The compounds were further tested for direct inhibition of elastase enzymatic activity [43]. The neutrophil suspension ( $6 \times 10^5$  cells  $\text{mL}^{-1}$ ) was preheated for 5 min in the presence of  $\text{CaCl}_2$  (1 mM) at 37 °C. Priming agent CB (1.5  $\mu\text{g mL}^{-1}$ ) was added for 2 min, followed by fMLF (0.1  $\mu$ M) for 20 min to release the elastase from the cells. After centrifugation at 1000  $g$  for 5 min at 4 °C, the supernatant containing elastase was preheated at 37 °C for 5 min, and the test compounds were added. Then, 0.1 mM of substrate methoxysuccinyl-Ala-Ala-Pro-Val-*p*-nitroanilide was added for 10 min. The effect of the compounds on elastase enzymatic activity was quantified by measuring the absorbance at 405 nm.

### 3.7. Molecular Modeling Studies

Docking study was done using the procedure we reported and validated earlier [39]. Tested compounds were downloaded from Pubchem ([www.pubchem.ncbi.nlm.nih.gov](http://www.pubchem.ncbi.nlm.nih.gov), accessed on 10 May 2021) or built from the 2D structures. Ligands and proteins were prepared as reported earlier [44]. Docking analysis and image preparation were done using PyMol. The proposed binding mode of the isolated compounds with neutrophil elastase (NE) and SARS-CoV-2 main protease ( $\text{M}^{\text{Pro}}$ ) was studied using Autodock Vina and a method similar to what we reported earlier [39]. Here, crystal structures of NE (PDB ID:1H1B) and SARS-CoV-2  $\text{M}^{\text{Pro}}$  (PDB ID: 6LU7) were used. Prepared and co-crystallized ligands were docked in a grid box in the active site ( $25 \times 25 \times 25 \text{ \AA}^3$ , centered on co-crystallized ligand) using exhaustiveness of 16. For each ligand, the top nine binding poses were ranked according to their binding affinities and the predicted binding interactions were analyzed. The pose with the best binding affinity and binding mode similar to co-crystallized ligand was reported.

### 3.8. Coronavirus 229E Assay

The protective effects of the samples against human coronavirus 229E (HCoV-229) were determined similarly to the previously described method [45]. Huh7 cells (human liver carcinoma cell line) were infected with 9TCID50 (median tissue culture infectious dose) of each coronavirus 229E in the presence or absence of the compounds or vehicle. After incubation at 33 °C for 6 days, the surviving cells were then stained with MTT (3-[4,5-

dimethylthiazol-2-yl]-2,5-diphenyl tetrazolium bromide). The percentage of surviving cells was then calculated.

#### 4. Conclusions

Two butenolides, butyrolactons I (1) and III (2), along with one meroterpenoid, teretonin (3), and a prenylated hydroxybenzaldehyde derivative (4) were isolated from a marine-derived fungus *Aspergillus terreus*. Interestingly, butyrolactone I (1) revealed significant in vitro antiallergic, anti-inflammatory, and antielastase activity. These results were supported by molecular docking studies that also exhibited a possible potential role of 1 for inhibiting SARS-CoV-2 main protease, an essential enzyme for producing the viral functional proteins. These results shed more light on butyrolactone I (1) and other butenolide derivatives as potential candidates for developing lead compounds that may pave the way for producing new pharmaceuticals against SARS-CoV-2 and/or its pathological effects, in particular, ARDS, granting additional time for the immune system to fight for the patient's life.

**Supplementary Materials:** The following are available online, Figure S1: Human coronavirus 229E (HCoV-229E) protective activity, Table S1: <sup>1</sup>H and <sup>13</sup>C NMR Data of butyrolactone I (1), Table S2: <sup>1</sup>H and <sup>13</sup>C NMR Data of butyrolactone III (2), Table S3: <sup>1</sup>H and <sup>13</sup>C NMR Data of teretonin (3), Table S4: <sup>1</sup>H and <sup>13</sup>C NMR Data of 4-hydroxy-3-(3-methylbut-2-enyl)benzaldehyde (4).

**Author Contributions:** S.S.E., W.L. and B.K.: conceptualization, writing, reviewing and editing the manuscript; I.S.U., S.S.E. and B.K.: methodology, purification and isolation of pure metabolites; I.S.U., S.S.E. and B.K.: NMR analysis and data curation; A.A. and B.S.A.: molecular modeling; M.K. and B.-H.C.: antiallergy assay; Y.-H.W. and T.-L.H.: anti-inflammatory assay; J.-T.H.: coronavirus 229E assay. All authors have read and agreed to the published version of the manuscript.

**Funding:** This research was funded by TÜBİTAK-BMBF Project No: 114S916. This research was supported by the grants from the Ministry of Science and Technology (MOST 106-2320-B-255-003-MY3 and MOST 108-2320-B-255-003-MY3, MOST 109-2327-B-255-001, and MOST 109-2327-B-182-002), Chang Gung Memorial Hospital (CMRPF1G0241~3, CMRPF1J0051~3, and BMRP450), and Chang Gung University (104-6576A3), Taiwan. The funders had no role in the study design, data collection and analysis, decision to publish, or preparation of the manuscript.

**Institutional Review Board Statement:** Not applicable.

**Informed Consent Statement:** Not applicable.

**Data Availability Statement:** Data are available upon request from authors.

**Acknowledgments:** S.S.E. acknowledges The Scientific and Technological Research Council of Turkey (TÜBİTAK) for a financially supported visiting scientist fellowship.

**Conflicts of Interest:** The authors declare no conflict of interest.

**Sample Availability:** Samples of compounds (1 and 2) are available from the authors upon request.

#### References

1. Rothan, H.A.; Byrareddy, S.N. The epidemiology and pathogenesis of coronavirus disease (COVID-19) outbreak. *J. Autoimmun.* **2020**, *108*, 102433. [CrossRef]
2. da Silva, P.G.; Mesquita, J.R.; Nascimento, M.D.J.; Ferriera, V.A.M. Viral, host and environmental factors that favour anthropozoonotic spillover of coronaviruses: An opinionated review, focusing on SARS-CoV, MERS-CoV and SARS-CoV-2. *Sci. Total Environ.* **2021**, *750*, 141483. [CrossRef]
3. Pfizer-BioNtech COVID-19 Vaccine. Available online: <https://www.fda.gov/emergency-preparedness-and-response/coronavirus-disease-2019-covid-19/pfizer-biontech-covid-19-vaccine> (accessed on 4 January 2021).
4. COVID-19: Oxford-AstraZeneca Vaccine Approved for Use in UK. Available online: <https://www.bbc.com/news/health-55280671> (accessed on 4 January 2021).
5. Risk Assessment: Risk related to Spread of New SARS-CoV-2 Variants of Concern in the EU/EEA. Available online: <https://www.ecdc.europa.eu/en/publications-data/covid-19-risk-assessment-spread-new-sars-cov-2-variants-eueea> (accessed on 4 January 2021).

6. Henriksen, P.A. The potential of neutrophil elastase inhibitors as anti-inflammatory therapies. *Curr. Opin. Hematol.* **2014**, *21*, 23–28. [\[CrossRef\]](#)
7. Hoenderdos, K.; Condliffe, A. The neutrophil in chronic obstructive pulmonary disease. *Am. J. Respir. Cell. Mol. Biol.* **2013**, *48*, 531–539. [\[CrossRef\]](#)
8. Moraes, T.J.; Chow, C.W.; Downey, G.P. Proteases and lung injury. *Crit. Care Med.* **2003**, *31*, S189–S194. [\[CrossRef\]](#)
9. Chiang, C.-C.; Korinek, M.; Cheng, W.-J.; Hwang, T.-L. Targeting neutrophils to treat acute respiratory distress syndrome in coronavirus disease. *Front. Pharmacol.* **2020**, *11*, 572009. [\[CrossRef\]](#)
10. Zhang, Y.L.; Zhang, J.; Jiang, N.; Lu, Y.H.; Wang, L.; Xu, S.H.; Wang, W.; Zhang, G.F.; Xu, Q.; Ge, H.M.; et al. Immunosuppressive polyketides from mantis-associated *Daldinia eschscholzii*. *J. Am. Chem. Soc.* **2011**, *133*, 5931–5940. [\[CrossRef\]](#)
11. Ebada, S.S.; El-Neketi, M.; Ebrahim, W.; Mándi, A.; Kurtán, T.; Kalscheuer, R.; Müller, W.E.G.; Proksch, P. Cytotoxic secondary metabolites from the endophytic fungus *Aspergillus versicolor* KU258497. *Phytochem. Lett.* **2018**, *24*, 88–93. [\[CrossRef\]](#)
12. Wang, Y.; Zheng, J.K.; Liu, P.P.; Wang, W.; Zhu, W.M. Three new compounds from *Aspergillus terreus* PT06-2 grown in a high salt medium. *Mar. Drugs* **2011**, *9*, 1368–1378. [\[CrossRef\]](#)
13. Liao, W.Y.; Shen, C.N.; Lin, L.H.; Yang, Y.L.; Han, H.Y.; Chen, J.W.; Kuo, S.C.; Wu, S.H.; Liaw, C.C. Asperjinone, a Nor-Neolignan, and terrein, a suppressor of ABCG2-expressing breast cancer cells, from thermophilic *Aspergillus terreus*. *J. Nat. Prod.* **2012**, *75*, 630–635. [\[CrossRef\]](#)
14. Deng, C.M.; Huang, C.H.; Wu, Q.L.; Pang, J.Y.; Lin, Y.C. A new sesquiterpene from the mangrove endophytic fungus *Aspergillus terreus* (No. GX7-3B). *Nat. Prod. Res.* **2013**, *27*, 1882–1887. [\[CrossRef\]](#)
15. Wijeratne, E.M.K.; Turbyville, T.J.; Zhang, Z.G.; Bigelow, D.; Pierson, L.S.; VanEtten, H.D.; Whitesell, L.; Canfield, L.M.; Gunatilaka, A.A.L. Cytotoxic constituents of *Aspergillus terreus* from the rhizosphere of *Opuntia versicolor* of the Sonoran Desert. *J. Nat. Prod.* **2003**, *66*, 1567–1573. [\[CrossRef\]](#) [\[PubMed\]](#)
16. Ebada, S.S.; Ebrahim, W. A new antibacterial quinolone derivative from the endophytic fungus *Aspergillus versicolor* strain Eich.5.2.2. *S. Afr. J. Bot.* **2020**, *134*, 151–155. [\[CrossRef\]](#)
17. Zhou, M.; Miao, M.M.; Du, G.; Li, X.N.; Shang, S.Z.; Zhao, W.; Liu, Z.H.; Yang, G.Y.; Che, C.T.; Hu, Q.F.; et al. Aspergillines A-E, highly oxygenated hexacyclic indole-tetrahydrofuran-tetramic acid derivatives from *Aspergillus versicolor*. *Org. Lett.* **2014**, *16*, 5016–5019. [\[CrossRef\]](#)
18. Gao, H.Q.; Zhou, L.N.; Cai, S.X.; Zhang, G.J.; Zhu, T.J.; Gu, Q.Q.; Li, D.H. Diorcinols B-E, new prenylated diphenyl ethers from the marine-derived fungus *Aspergillus versicolor* ZLN-60. *J. Antibiot.* **2013**, *66*, 539–542. [\[CrossRef\]](#) [\[PubMed\]](#)
19. Ji, N.Y.; Liu, X.H.; Miao, F.P.; Qiao, M.F. Aspeverin, a new alkaloid from an algicolous strain of *Aspergillus versicolor*. *Org. Lett.* **2013**, *15*, 2327–2329. [\[CrossRef\]](#)
20. Wang, W.; Kim, H.; Nam, S.J.; Rho, B.J.; Kang, H. Antibacterial butenolides from the Korean tunicate *Pseudodistoma antinboja*. *J. Nat. Prod.* **2012**, *75*, 2049–2054. [\[CrossRef\]](#)
21. Bai, Z.Q.; Lin, X.P.; Wang, Y.Z.; Wang, J.F.; Zhou, X.F.; Yang, B.; Liu, J.; Yang, X.W.; Wang, Y.; Liu, Y.H. New phenyl derivatives from endophytic fungus *Aspergillus flavipes* AIL8 derived of mangrove plant *Acanthus ilicifolius*. *Fitoterapia* **2014**, *95*, 194–202. [\[CrossRef\]](#)
22. Qin, J.J.; Zhu, J.X.; Zeng, Q.; Cheng, X.R.; Zhu, Y.; Zhang, S.D.; Shan, L.; Jin, H.Z.; Zhang, W.D. Pseudoguaianolides and guaianolides from *Inula hupehensis* as potential anti-inflammatory agents. *J. Nat. Prod.* **2011**, *74*, 1881–1887. [\[CrossRef\]](#)
23. Dewi, R.T.; Tachibana, S.; Darmawan, A. Effect on  $\alpha$ -glucosidase inhibition and antioxidant activities of butyrolactone derivatives from *Aspergillus terreus* MC751. *Med. Chem. Res.* **2014**, *23*, 454–460. [\[CrossRef\]](#)
24. Lin, X.; Li, K.; Yang, L.; Peng, X.; Fang, W.; Tian, X.; Liu, Y.; Zhou, X. Dereplication and targeted isolation of bioactive Sulphur compounds from bacteria isolated from a hydrothermal field. *Nat. Prod. Res.* **2019**, *33*, 494–499. [\[CrossRef\]](#) [\[PubMed\]](#)
25. Kiriya, N.; Nitta, K.; Sakaguchi, Y.; Taguchi, Y.; Yamamoto, Y. Studies on the metabolic products of *Aspergillus terreus*. III. Metabolites of the strain IFO 8835. *Chem. Pharm. Bull.* **1977**, *25*, 2593–2601. [\[CrossRef\]](#)
26. Rao, K.V.; Sadhukhan, A.K.; Veerender, M.; Ravikumar, V.; Mohan, E.V.S.; Dhanvantri, S.D.; Sitaramkumar, M.; Babu, J.M.; Vyas, K.; Reddy, G.O. Butyrolactones from *Aspergillus terreus*. *Chem. Pharm. Bull.* **2000**, *48*, 559–562. [\[CrossRef\]](#)
27. Niu, X.; Dahse, H.-M.; Menzel, K.-D.; Lozach, O.; Walther, G.; Meijer, L.; Grabley, S.; Sattler, I. Butyrolactone I derivatives from *Aspergillus terreus* carrying an unusual sulfate moiety. *J. Nat. Prod.* **2008**, *71*, 689–692. [\[CrossRef\]](#)
28. Nitta, K.; Fujita, N.; Yoshimura, T.; Arai, K.; Yamamoto, Y. Metabolic products of *Aspergillus terreus*. IX. Biosynthesis of butyrolactone derivatives isolated from strains IFO 8835 and 4100. *Chem. Pharm. Bull.* **1983**, *31*, 1528–1533. [\[CrossRef\]](#)
29. Chen, M.; Wang, K.-L.; Liu, M.; She, Z.-G.; Wang, C.-Y. Bioactive steroid derivatives and butyrolactone derivatives from a gorgonian-derived fungus *Aspergillus* sp. fungus. *Chem. Biodivers.* **2015**, *12*, 1398–1406. [\[CrossRef\]](#)
30. Springer, J.P.; Dorner, J.W.; Cole, R.J.; Cox, R.H. Terretonin, a toxic compound from *Aspergillus terreus*. *J. Org. Chem.* **1979**, *44*, 4852–4854. [\[CrossRef\]](#)
31. Li, G.-Y.; Li, B.-G.; Yang, T.; Yin, J.-H.; Qi, H.-Y.; Liu, G.-Y.; Zhang, G.-L. Sesterterpenoids, terretonins A-D, and an alkaloid, asterrelenin, from *Aspergillus terreus*. *J. Nat. Prod.* **2006**, *68*, 1243–1246. [\[CrossRef\]](#)
32. Hansson, D.; Menkis, A.; Olson, A.; Stenlid, J.; Broberg, A.; Karlsson, M. Biosynthesis of fomannoxin in the root rotting pathogen. *Heterobasidion occidentale*. *Phytochemistry* **2012**, *84*, 31–39. [\[CrossRef\]](#)
33. Vu, M.; Herfindal, L.; Juvik, O.J.; Vedeler, A.; Haavik, S. Toxic aromatic compounds from fruits of *Nartheceum ossifragum* L. *Phytochemistry* **2016**, *132*, 76–85. [\[CrossRef\]](#)



34. Liu, Q.-M.; Xie, C.-L.; Gao, Y.-Y.; Liu, B.; Lin, W.-X.; Liu, H.; Cao, M.-J.; Su, W.-J.; Yang, X.-W.; Liu, G.-M. Deep-sea-derived butyrolactone I suppresses ovalbumin-induced anaphylaxis by regulating mast cell function in a murine model. *J. Agric. Food Chem.* **2018**, *66*, 5581–5592. [[CrossRef](#)] [[PubMed](#)]
35. Jin, Z.; Du, X.; Xu, Y.; Deng, Y.; Liu, M.; Zaho, Y.; Zhang, B.; Li, X.; Zhang, L.; Peng, C.; et al. Structure of M<sup>Pro</sup> from SARS-CoV-2 and discovery of its inhibitors. *Nature* **2020**, *582*, 289–293. [[CrossRef](#)]
36. Sacco, M.D.; Ma, C.; Lagarias, P.; Gao, A.; Townsend, J.A.; Meng, X.; Dube, P.; Zhang, X.; Hu, Y.; Kitamura, N.; et al. Structure and inhibition of the SARS-CoV-2 main protease reveal strategy for developing dual inhibitors against M<sup>Pro</sup> and cathepsin L. *Sci. Adv.* **2020**, *6*, eabe0751. [[CrossRef](#)]
37. Zahran, E.M.; Albohy, A.; Khalil, A.; Ibrahim, A.H.; Ahmed, H.A.; El-hossary, E.M.; Bringmann, G.; Abdelmohsen, U.R. Bioactivity potential of marine natural products from scleractinia-associated microbes and in silico anti-SARS-CoV-2 evaluation. *Mar. Drugs* **2020**, *18*, 645. [[CrossRef](#)] [[PubMed](#)]
38. Said, M.A.; Albohy, A.; Abdelrahman, M.A.; Ibrahim, H.S. Importance of glutamine 189 flexibility in SARS-CoV-2 main protease: Lesson learned from in silico virtual screening of ChEMBL database and molecular dynamics. *Eur. J. Pharm. Sci.* **2021**, *160*, 105744. [[CrossRef](#)] [[PubMed](#)]
39. Ebada, S.S.; Al-Jawabri, N.A.; Youssef, F.S.; El-Kashef, D.H.; Knedel, T.-O.; Albohy, A.; Korinek, M.; Hwang, T.-L.; Chen, B.-H.; Lin, G.-H.; et al. Anti-inflammatory, antiallergic and COVID-19 protease inhibitory activities of phytochemicals from the Jordanian hawksbeard: Identification, structure-activity relationships, molecular modeling and impact on its folk medicinal uses. *RSC Adv.* **2020**, *10*, 38128–38141. [[CrossRef](#)]
40. Macdonald, S.J.F.; Dowle, M.D.; Harrison, L.A.; Clarke, G.D.F.; Inglis, G.G.A.; Johnson, M.R.; Shah, P.; Smith, R.A.; Amour, A.; Fleetwood, G.; et al. Discovery of further pyrrolidine *trans*-lactams as inhibitors of human neutrophil elastase (HNE) with potential as development candidates and the crystal structure of HNE complexed with an inhibitor (GW475151). *J. Med. Chem.* **2002**, *45*, 3878–3890. [[CrossRef](#)] [[PubMed](#)]
41. Korinek, M.; Wagh, V.D.; Lo, I.-W.; Hsu, Y.-M.; Hsu, H.-Y.; Hwang, T.-L.; Wu, Y.-C.; Cheng, Y.-B.; Chen, B.-H.; Chang, F.-R. Antiallergic phorbol ester from the seeds of *Aquilaria malaccensis*. *Int. J. Mol. Med.* **2016**, *17*, 398. [[CrossRef](#)]
42. Korinek, M.; Tsai, Y.H.; El-Shazly, M.; Lai, K.H.; Backlund, A.; Wu, S.F.; Lai, W.C.; Wu, T.Y.; Chen, S.L.; Wu, Y.C.; et al. Antiallergic hydroxy fatty acids from *Typhonium blumei* explored through ChemGPS-NP. *Front. Pharmacol.* **2017**, *8*, 356. [[CrossRef](#)] [[PubMed](#)]
43. Tsai, Y.F.; Yu, H.P.; Chang, W.Y.; Liu, F.C.; Huang, Z.C.; Hwang, T.L. Sirtinol inhibits neutrophil elastase activity and attenuates lipopolysaccharide-mediated acute lung injury in mice. *Sci. Rep.* **2015**, *5*, 8347. [[CrossRef](#)]
44. Ebada, S.S.; Al-Jawabri, N.A.; Youssef, F.S.; Albohy, A.; Aldalaien, S.M.; Disi, A.M.; Proksch, P. In vivo antiulcer activity, phytochemical exploration, and molecular modelling of the polyphenolic-rich fraction of *Crepis sancta* extract. *Inflammopharmacology* **2020**, *28*, 321–331. [[CrossRef](#)]
45. Hsieh, C.-F.; Jheng, J.-R.; Lin, G.-H.; Chen, Y.-L.; Ho, J.Y.; Liu, C.-J.; Hsu, K.-Y.; Chen, Y.-S.; Chan, Y.F.; Yu, H.-M.; et al. Rosmarinic acid exhibits broad anti-enterovirus A71 activity by inhibiting the interaction between the five-fold axis of capsid VP1 and cognate sulfated receptors. *Emerg. Microbes Infect.* **2020**, *9*, 1194–1205. [[CrossRef](#)]





Article

# Identification of Fucosylated SERPINA1 as a Novel Plasma Marker for Pancreatic Cancer Using Lectin Affinity Capture Coupled with iTRAQ-Based Quantitative Glycoproteomics

Chia-Chun Wu <sup>1,†</sup> , Yu-Ting Lu <sup>1,†</sup>, Ta-Sen Yeh <sup>2,3,†</sup>, Yun-Hsin Chan <sup>2</sup>, Srinivas Dash <sup>4</sup> and Jau-Song Yu <sup>1,4,5,6,\*</sup>

<sup>1</sup> Molecular Medicine Research Center, Chang Gung University, Taoyuan 33302, Taiwan; wuchiachun9@gmail.com (C.-C.W.); judy1143039@gmail.com (Y.-T.L.)

<sup>2</sup> Department of General Surgery, Chang Gung Memorial Hospital, Linkou 33305, Taiwan; tsy471027@cgmh.org.tw (T.-S.Y.); fm423344@gmail.com (Y.-H.C.)

<sup>3</sup> College of Medicine, Chang Gung University, Taoyuan 33302, Taiwan

<sup>4</sup> Graduate Institute of Biomedical Sciences, College of Medicine, Chang Gung University, Taoyuan 33302, Taiwan; srinivasdash26@gmail.com

<sup>5</sup> Liver Research Center, Chang Gung Memorial Hospital, Linkou 33305, Taiwan

<sup>6</sup> Research Center for Food and Cosmetic Safety, College of Human Ecology, Chang Gung University of Science and Technology, Taoyuan 33302, Taiwan

\* Correspondence: yusong@mail.cgu.edu.tw; Tel.: +886-3-211-8800 (ext. 5171); Fax: +886-3-211-8891

† These authors contribute equally to this study.



**Citation:** Wu, C.-C.; Lu, Y.-T.; Yeh, T.-S.; Chan, Y.-H.; Dash, S.; Yu, J.-S. Identification of Fucosylated SERPINA1 as a Novel Plasma Marker for Pancreatic Cancer Using Lectin Affinity Capture Coupled with iTRAQ-Based Quantitative Glycoproteomics. *Int. J. Mol. Sci.* **2021**, *22*, 6079. <https://doi.org/10.3390/ijms22116079>

Academic Editor: Daniela Basso

Received: 2 April 2021

Accepted: 31 May 2021

Published: 4 June 2021

**Publisher's Note:** MDPI stays neutral with regard to jurisdictional claims in published maps and institutional affiliations.



**Copyright:** © 2021 by the authors. Licensee MDPI, Basel, Switzerland. This article is an open access article distributed under the terms and conditions of the Creative Commons Attribution (CC BY) license (<https://creativecommons.org/licenses/by/4.0/>).

**Abstract:** Pancreatic cancer (PC) is an aggressive cancer with a high mortality rate, necessitating the development of effective diagnostic, prognostic and predictive biomarkers for disease management. Aberrantly fucosylated proteins in PC are considered a valuable resource of clinically useful biomarkers. The main objective of the present study was to identify novel plasma glycoproteins of PC using the iTRAQ quantitative proteomics approach coupled with *Aleuria aurantia* lectin (AAL)-based glycopeptide enrichment and isotope-coded glycosylation site-specific tagging, with a view to analyzing the glycoproteome profiles of plasma samples from patients with non-metastatic and metastatic PC and gallstones (GS). As a result, 22 glycopeptides with significantly elevated levels in plasma samples of PC were identified. Fucosylated SERPINA1 (fuco-SERPINA1) was selected for further validation in 121 plasma samples (50 GS and 71 PC) using an AAL-based reverse lectin ELISA technique developed in-house. Our analyses revealed significantly higher plasma levels of fuco-SERPINA1 in PC than GS subjects (310.7 ng/mL v.s. 153.6 ng/mL,  $p = 0.0114$ ). Elevated fuco-SERPINA1 levels were associated with higher TNM stage ( $p = 0.024$ ) and poorer prognosis for overall survival (log-rank test,  $p = 0.0083$ ). The increased plasma fuco-SERPINA1 levels support the utility of this protein as a novel prognosticator for PC.

**Keywords:** pancreatic cancer; plasma; glycoprotein; AAL; iTRAQ-based quantitative proteome; reverse lectin-based ELISA; fucosylated SERPINA1

## 1. Introduction

Pancreatic cancer (PC) is the most lethal malignant disease associated with a high mortality rate. The 5-year survival rates of PC are reported as ~8% and 9% in the United States [1] and European Union [2], respectively. In 2016, PC was ranked the eighth leading cause of cancer-related mortality in Taiwan. Since the majority of early-stage (stage I or II) PC cases are asymptomatic, ~80% patients present at later stages (stage III or IV) of disease progression with metastatic spread and unresectable tumors at the time of diagnosis [3,4]. For patients with locally resectable non-metastatic disease, surgical resection followed by adjuvant chemotherapy is the main treatment modality. Chemotherapy administered to patients with advanced disease is frequently associated with treatment resistance and unfavorable side effects. Effective management of PC thus remains a major challenge [5].

Reliable diagnostic, prognostic and predictive biomarkers of PC for better patient stratification and guidance of therapy choices remain an urgent medical requirement. Among the currently available tumor biomarkers, CA19-9 is commonly used to monitor PC. However, CA19-9 is not an effective biomarker for early detection in view of its false-positive results in chronic pancreatitis, biliary tract inflammation and cancers in other organs, including stomach, colon, ovary, uterus and liver [6,7].

Protein glycosylation, the most abundant posttranslational modification, plays fundamental roles in protein function. Aberrant protein glycosylation is known to regulate numerous disease processes including malignant transformation [8]. For example, previous studies have reported significant involvement of aberrant protein fucosylation in tumorigenesis of PC [9,10]. To facilitate systematic identification of glycoproteins involved in the regulation of normal biological functions and/or disease processes, the lectin-based approach has been employed to enrich glycopeptides for proteomic analysis [11,12]. Glycoproteomic analysis of *N*-linked glycopeptides using lectin-affinity capture coupled with isotope-coded glycosylation site-specific tagging (IGOT) and isobaric tag for relative and absolute quantitation (iTRAQ) labeling has also been developed to quantify and identify glycopeptides with accurate glycosylated sites [11,12]. In 2014, Nie et al. [13] used a microarray of 16 lectins to identify *Aleuria aurantia* lectin (AAL), which recognizes terminal  $\alpha$ -linked fucose, as a useful tool to distinguish PC. The group further applied AAL-affinity capture coupled with TMT labeling and label-free approaches to identify three serum proteins ( $\alpha$ -1 antichymotrypsin, thrombospondin-1 and haptoglobin) as a potential marker panel for PC detection [13].

Following the initial discovery of dysregulated glycoproteins in biological samples, researchers often need to develop methods to quantify glycosylation changes of specific target glycoproteins in a large number of samples, such as serum/plasma, in a high-throughput manner. For example, lectin-based antibody microarrays and lectin-based immunosorbent assays (lectin-ELISA) have been developed, both of which are based on coating antibodies to slides or 96-well plates followed by capture of antigens in samples and subsequent detection of captured antigens by lectin [14–16]. However, glycans on the antibodies used for coating to slides or plates may interfere with the assays, and further experimental designs to diminish this type of interference are required [17,18]. To circumvent this issue, a reverse lectin-based ELISA system whereby specific lectins are coated to slides or plates followed by capture of glycoproteins in samples and their detection with specific antibodies has been applied successfully to quantify different glycoproteins in serum/plasma samples [19,20].

In the present study, AAL was used as a glycopeptide enrichment tool for identifying novel biomarkers from abundant protein-depleted plasma samples collected from PC patients and subjects with gallstones (GS) by application of IGOT coupled with MS analysis. Numerous plasma glycopeptides upregulated in PC patients compared to controls and predicted to harbor core or antennary fucose were identified. Among them, fucosylated SERPINA1 (fuco-SERPINA1) displaying the highest fold change between the metastatic PC and GS groups was selected for further verification. Furthermore, a reverse lectin-based ELISA assay was developed in-house to evaluate the biomarker potential of fuco-SERPINA1.

## 2. Results

### 2.1. Study Population and Experimental Design

We recruited 30 subjects (10 metastasis-free PC patients (M0), 10 PC patients with distant metastasis (M1) and 10 subjects with gallstones (GS)) for the discovery experiment and an additional 91 subjects (40 GS and 51 PC) for verification experiments. The clinicopathological characteristics of the enrolled subjects are shown in Table 1. Plasma samples were collected from all subjects for measurement of proteins and glycoproteins. To establish useful plasma glycobiomarkers for PC, three groups of pooled plasma samples from GS, M0 and M1 groups (10 cases per group) were subjected to depletion of the top 14 high-abundance proteins followed by iTRAQ labeling (with three plex 114, 115 and 116)

and 2D-LC-MS/MS analysis for systemic comparison of differential expression of proteins and glycoproteins. For glycoproteomic analysis, *Aleuria aurantia* lectin (AAL), identified as an ideal lectin for discrimination of PC from normal and other pancreatitis cases [13], was applied to enrich glycopeptides and *N*-glycosidase (PNGase F) used to eliminate glycan from asparagine (Asn) in H<sub>2</sub><sup>18</sup>O-containing solution for transferring Asn to aspartic acid (Asp) with <sup>18</sup>O labeling to enhance the accuracy of identifying glycopeptides in MS analysis. <sup>18</sup>O-labeled glycopeptides containing fucose and upregulated in PC were selected as targets for verification. Glyco-SERPINA1, one of the candidate targets in plasma samples of PC and GS, was further validated using reverse AAL-based ELISA. The workflow of our study design is presented in Figure 1.

**Table 1.** Clinicopathological characteristics of the enrolled subjects used in this study.

Characteristics		Gallstones (GS)	Non-Metastatic PC (M0)	Metastatic PC (M1)
<b>(For Discovery Experiment, <i>n</i> = 30)</b>		-	-	-
Gender	Female	6	5	1
	Male	4	5	9
Age (years) <sup>a</sup>		62.9 ± 11.0	61.5 ± 9.8	59.9 ± 9.3
Tumor size (T)	T3	-	4	4
	T4	-	6	6
Lymph node metastasis (N)	Yes	-	8	8
	No	-	2	2
Distant metastasis (M)	Yes	-	0	10
	No	-	10	0
Stage	I–II	-	4	0
	III–IV	-	6	10
<b>(Total enrolled subjects, <i>n</i> = 121)</b>		-	-	-
Gender	Female	29	12	12
	Male	21	15	32
Age (years)		54.4 ± 13.2	61.3 ± 12.2	62.4 ± 9.9
Tumor size (T)	T1	-	1	0
	T2	-	1	4
	T3	-	15	23
	T4	-	10	16
Lymph node metastasis (N)	Yes	-	21	37
	No	-	6	7
Distant metastasis (M)	Yes	-	0	44
	No	-	27	0
Stage	I–II	-	17	0
	III–IV	-	10	44

<sup>a</sup> Data are shown in mean ± standard deviation (SD).

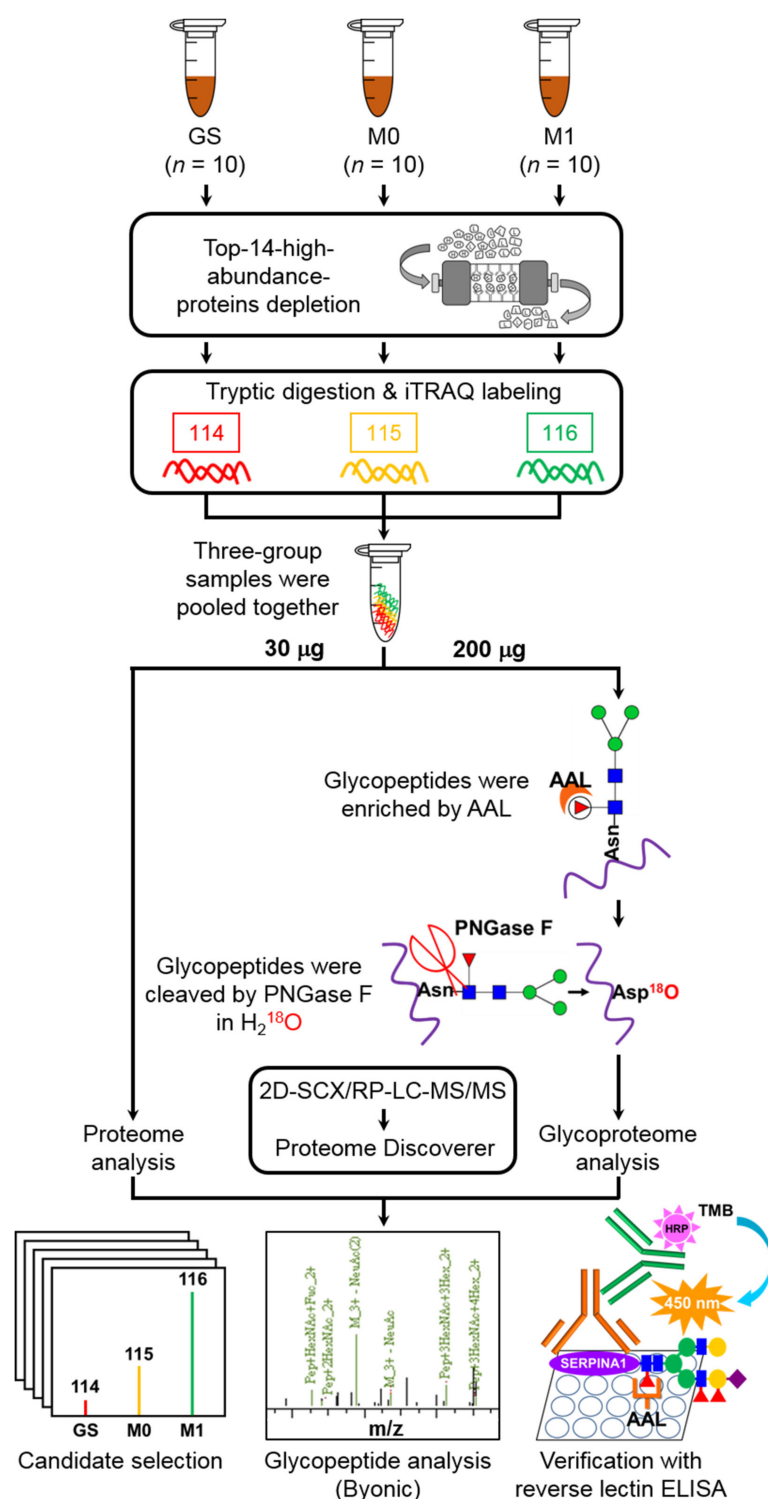


**Figure 1.** Schematic representation of the experimental design of this study. iTRAQ labeling coupled with 2D-SCX/RP-LC-MS/MS was applied for comprehensive analysis of the proteome profile of plasma samples from patients with PC, including non-metastatic (M0) and metastatic (M1) pancreatic cancers and subjects with gallstone lesions (GS). AAL was employed to enrich glycopeptides with specific glycan and  $H_2^{18}O$  to label glycosylated sites via PNGase F-mediated reaction for glycoproteome profiling analysis. We selected  $^{18}O$ -labeled fucose-containing glycopeptides upregulated in PC plasma samples as candidate targets. Fuco-SERPINA1, one of the candidate proteins, was selected for validation in plasma samples of PC and GS using reverse AAL-based ELISA.

## 2.2. iTRAQ-Based Quantitative Glycoproteomics Coupled with Glycopeptide Enrichment via AAL-Affinity Capture Technique for Identification of Plasma Glycobiomarkers

Using the strategy shown in Figure 1, a total of 1707 proteins (10,302 peptides) and 2160 proteins (10,572 peptides) were respectively identified in the plasma proteome and glycoproteome profiles of the three groups (GS, M0 and M1) in the discovery experiment (Table 2). Detailed identification and quantification of peptides/proteins and glycopeptides/glycoproteins are presented in Tables S1 and S2. Quantitative proteome profiling facilitated the quantification of 1489 and 1472 proteins in M0/GS and M1/GS groups, respectively. For glycoproteome analysis, 281 and 267 <sup>18</sup>O-labeled peptides containing the N to D modification (N to D-<sup>18</sup>O peptides) were quantified in M0/GS and M1/GS groups, corresponding to 133 and 130 N to D-<sup>18</sup>O proteins, respectively. The ratio of N to D-<sup>18</sup>O peptides to total identified peptides was 3.01–3.32%. Among the N to D-<sup>18</sup>O peptides identified, ~87% (244 of 281 in the M0/GS group, 232 of 267 in M1/GS group) possessed the consensus N-glycosylation motif (NXS/T/C, X represents any amino acid except proline) (Table 2).

**Table 2.** Numbers of identified proteins, peptides and glycopeptides in plasma proteome and glycoproteome.

Identified Proteins, Peptides and Glycopeptides	Quantitative Proteome Profiling			Quantitative Glycoproteome Profiling		
	GS + M0 + M1	M0/GS	M1/GS	GS + M0 + M1	M0/GS	M1/GS
Total proteins	1707	1489	1472	2160	1749	1953
N to D- <sup>18</sup> O proteins	-	-	-	145	133	130
Total peptides	10,102	8621	8304	10,572	8453	8872
N to D- <sup>18</sup> O peptides	-	-	-	333	281	267
Ratio (N to D- <sup>18</sup> O peptides/total peptides)	-	-	-	3.15%	3.32%	3.01%
N to D- <sup>18</sup> O and NXS/T/C peptides	-	-	-	284	244	232
Ratio (N to D- <sup>18</sup> O and NXS/T/C peptides/N to D- <sup>18</sup> O peptides)	-	-	-	85.29%	86.83%	86.89%

N to D-<sup>18</sup>O, asparagine (N) was transferred to aspartate (D) by replacing -NH<sub>2</sub> with -<sup>18</sup>OH via glycosidase treatment (PNGase F) in H<sub>2</sub><sup>18</sup>O-containing buffer. NXS/T/C, consensus sequence of N-linkage glycosylation, where X represents any amino acid except proline.

## 2.3. Selection of Candidate Plasma Glycomarkers of PC through Integrating Expression of Glycopeptides and Their Glycan Compositions

The flowchart of candidate glycopeptide selection is depicted in Figure 2. To identify candidate glycopeptides, we first selected 441 peptides displaying upregulation ( $\geq$ mean + S.D. 1.36 for M0/GS group, 2.01 for M1/GS group) in both M0 and M1 compared to the GS group and further identified 27 peptides with N to D-<sup>18</sup>O modification. After removal of redundant peptides, 22 peptides derived from 19 proteins were selected as candidates and their protein ratios (determined via quantitative proteome analysis) were applied to normalize the glycopeptide ratio for measuring changes in their glycosylation levels (Table 3). The representative MS/MS spectra of the 22 peptides are shown in Supplementary Figure S1. In total, 15 of the 22 target peptides were identified with glycan modifications, among which 12 were detected with fucose decoration (Table 3 and Table S3).



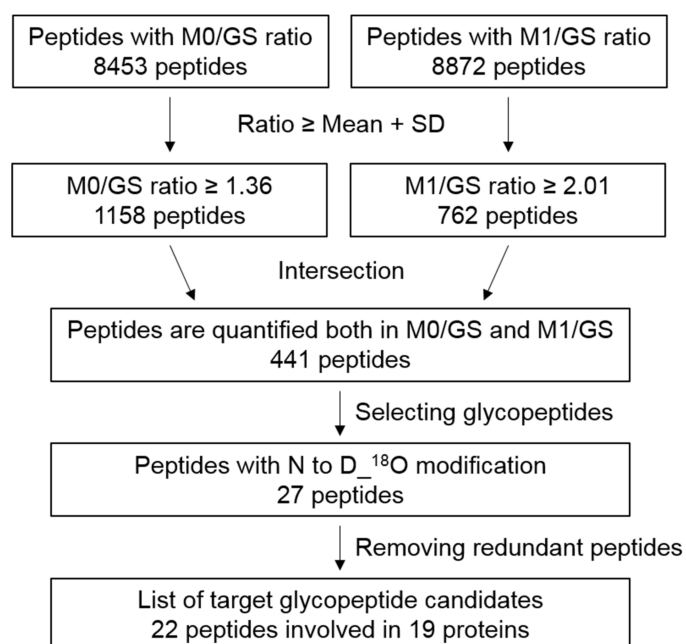


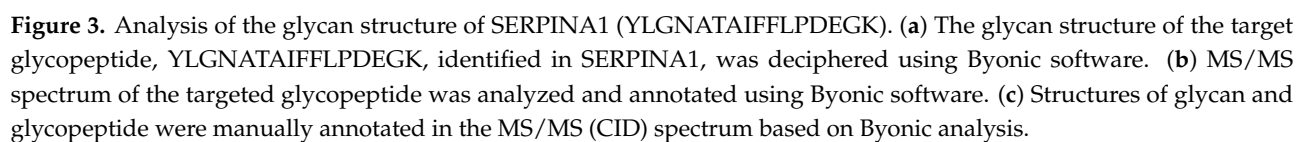
**Figure 2.** Flowchart for selecting candidate glycopeptides from glycoproteome analysis. From glycoproteome analysis, 8453 and 8872 peptides with quantified ratios in M0/GS and M1/GS groups were subjected to statistical analysis to determine mean and SD values. Peptides with ratios smaller than mean + SD were initially filtered out. The remaining 1158 and 762 peptides were intersected, leading to the identification of 441 peptides from which 27 harboring the modification of N to D- $^{18}\text{O}$  were further selected. After removing redundant peptides, 22 peptides representing 19 proteins were selected as target candidates.

Among the 12 fucose-containing peptide candidates, SERPINA1 was selected for further validation since the glycopeptide (YLGNATAIFFLPDEGK) displayed significantly elevated levels in PC (including both M0 and M1 groups) versus GS samples, with the highest fold change between the M1 and GS groups (5.22) among the fucose-containing peptides. Figure 3 depicts the in-depth resolved glycan structure of SERPINA1 (YLGNATAIFFLPDEGK) based on analysis using Byonic software (Figure 3a,b) as well as the indicated peaks with fucosylated glycan in the collision-induced dissociation fragment spectrum (Figure 3c).

**Table 3.** List of 22 glycopeptides showing significantly elevated levels in plasma samples of PC patients compared to GS controls.

Gene Name	Protein Name	Sequence [N(n) to D- <sup>18</sup> O] <sup>a</sup>	Modified Site	M0/GS		M1/GS				Glycan Occu-pancy	Fucosylated Glycan
				Gp <sub>b</sub>	p <sup>c</sup>	Gp/p <sub>d</sub>	Gp	p	Gp/p		
APOH	Beta-2-glycoprotein 1	R.VYKPSAGnNSLYR.D	N162	1.97	1.18	1.66	3.21	1.70	1.89	V	V
ATRN	Attractin	R.nHSCSEGQISIFR.Y	N731	1.89	1.20	1.57	2.35	1.54	1.53	V	V
AZGP1	Zinc-alpha-2-glycoprotein	R.FGCEIEEnNR.S	N127	1.36	1.20	1.14	2.28	2.00	1.14		
CD14	Monocyte differentiation antigen CD14	R.nVSWATGR.S	N151	1.88	1.38	1.37	2.65	1.60	1.66	V	V
CD163	Scavenger receptor cysteine-rich type 1 protein M130	K.APGWAnSSAGSGR.I	N105	2.13	1.78	1.20	3.00	2.46	1.22	V	V
CD163	Scavenger receptor cysteine-rich type 1 protein M130	K.EDAAVnCTDISVQK.T	N1027	1.64	1.78	0.92	2.41	2.46	0.98		
CTSD	Cathepsin D	K.GSLSYLnVTR.K	N263	3.15	2.61	1.20	2.51	2.23	1.12	V	
ICAM1	Intercellular adhesion molecule 1	R.LNPTVTYnGnDSFSAK.A	N267	3.05	2.48	1.23	3.16	2.42	1.30	V	V
IL18BP	Interleukin-18-binding protein	K.ALVLQLTPALHSTnFSC VLVDPEQVVQR.H	N147	2.87	1.99	1.44	4.12	1.95	2.11		
IL6ST	Interleukin-6 receptor subunit beta	K.EQYTIInR.T	N83	1.47	1.39	1.06	2.10	1.87	1.12	V	V
LEPR	Leptin receptor	K.YSEnSTTVIR.E	N276	2.41	1.64	1.47	2.28	2.00	1.14		
LRG1	Leucine-rich alpha-2-glycoprotein	K.MFSQnDTR.C	N325	1.61	1.30	1.24	3.39	2.32	1.46	V	
LRG1	Leucine-rich alpha-2-glycoprotein	R.KLPPGLLAnFTLLR.T	N186	1.57	1.30	1.21	2.96	2.32	1.28	V	V
LRG1	Leucine-rich alpha-2-glycoprotein	K.LPPGLLAnFTLLR.T	N186	1.43	1.30	1.10	2.15	2.32	0.93	V	V
LUM	Lumican	R.LSHNELADSGIPGnSFNV SLVELDLSYNK.L	N249	2.51	1.17	2.14	4.04	1.74	2.32		
MMRN1	Multimerin-1	K.FNPGAESVVLsnSTLK.F	N136	2.61	0.68	3.82	3.32	0.84	3.93	V	V
ORM1	Alpha-1-acid glycoprotein 1	R.QDQCIYnTTYLNVR.E	N93	2.34	2.02	1.16	5.39	4.73	1.14		
OSMR	Oncostatin-M-specific receptor subunit beta	R.SVNILFnLTHR.V	N326	1.54	1.31	1.18	2.14	1.43	1.49	V	V
PRNP	Major prion protein	K.GEnFTETDVK.M	N197	1.42	N/A <sup>e</sup>	N/A	2.70	N/A	N/A		
SERPINA1	Alpha-1-antitrypsin	K.YLGnATAIFLPDEGK.L	N271	1.87	1.57	1.19	5.22	3.74	1.40	V	V
SERPINC1	Antithrombin-III	K.SLTFnETYQ DISELVYGAK.L	N187	1.95	1.18	1.66	2.58	1.46	1.77	V	V
VASN	Vasorin	R.LHEITnETFR.G	N117	1.46	1.49	0.98	2.21	1.71	1.29	V	

<sup>a</sup> Sites with N-glycosylation of N to D-<sup>18</sup>O modification are presented in bold and lower case. <sup>b</sup> Gp, ratio of glycopeptide obtained from glycoproteome analysis. <sup>c</sup> p, ratio of protein obtained from proteome analysis. <sup>d</sup> Gp/p, level changes of glycosylation. <sup>e</sup> N/A, protein not identified in proteome analysis.



#### 2.4. Removal of Glycans from SERPINA1 Protein by PNGase F Blocks Its AAL Lectin Binding Activity

To examine potential glycosylation on SERPINA1, we treated plasma proteins obtained from PC patients and a commercially available recombinant human SERPINA1 protein (derived from a mouse myeloma cell line NS0) with PNGase F to eliminate glycan. SERPINA1 was subsequently detected via Western and AAL lectin blots. As shown in Figure 4, Western blot using an anti-SERPINA1 antibody led to the detection of a major 60 kDa protein band in both PC plasma and recombinant human SERPINA1 protein samples prior to PNGase F treatment. Another protein band with lower apparent molecular weight (~57 kDa) emerged clearly after PNGase F treatment. AAL lectin blot analysis showed strong lectin binding signal of the 60 kDa recombinant human SERPINA1, which was significantly diminished after PNGase F treatment (Figure 4b, middle panel). Importantly, the ~57 kDa SERPINA1 protein band completely lacked the AAL binding signal. The results collectively suggest that SERPINA1 is modified via glycosylation and its glycan structures are accessible for recognition by AAL.

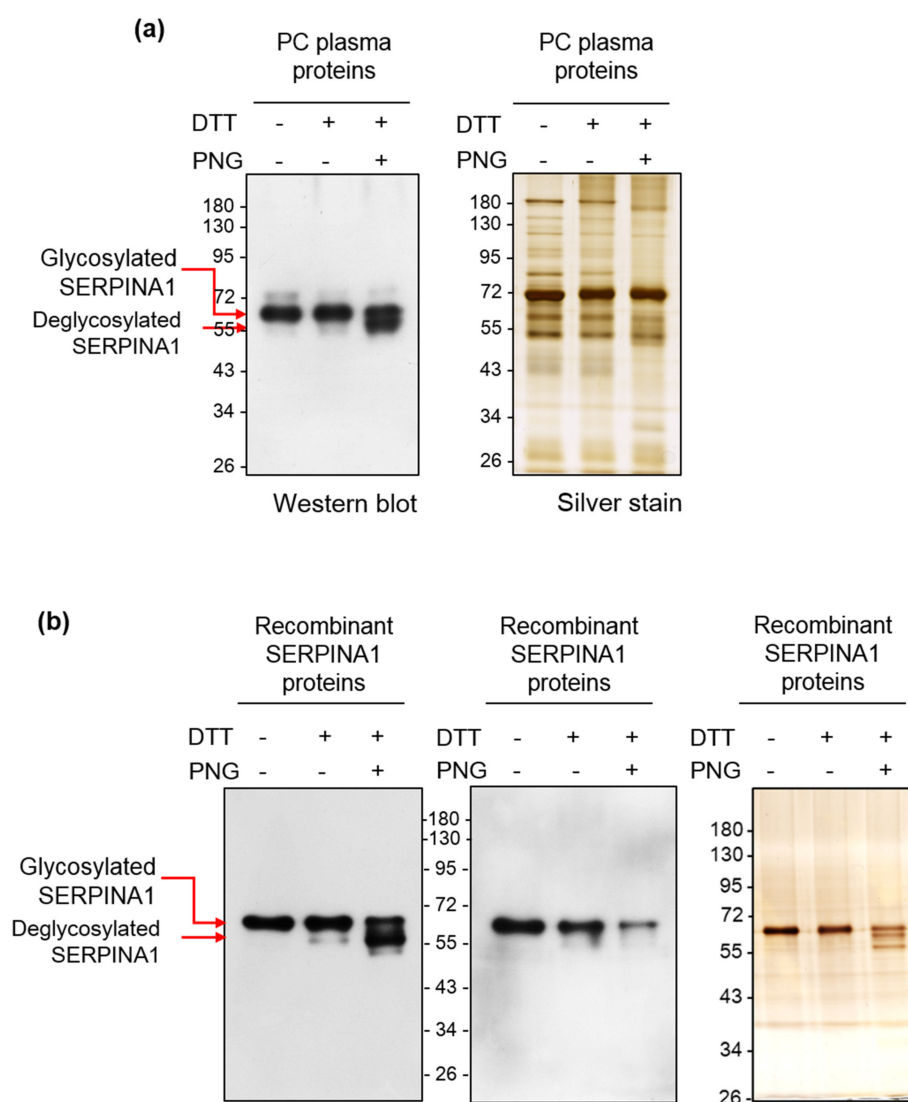


**Figure 4.** Deglycosylation of SERPINA1 protein by PNGase F alters its apparent molecular weight and AAL lectin-binding activity. (a,b) PC plasma proteins (2 µg) and recombinant SERPINA1 protein (200 ng) were treated with or without PNGase F (PNG) (protein/PNGase F = 10 µg/1U and 1 µg/1U, respectively) at 37 °C for 20 h and subjected to Western blot (for SERPINA1) or AAL blot analysis. Protein pattern revealed by silver staining is shown as loading control.

### 2.5. Development of AAL-Based Reverse Lectin ELISA for Measuring Glycosylated SERPINA1 Levels

To measure the levels of glycosylated SERPINA1 in individual samples, we developed an AAL-based reverse lectin ELISA technique and evaluated its specificity for glycosylated SERPINA1. Recombinant SERPINA1 protein harboring AAL-specific glycan was used as a standard. Dynamic range of detecting glycosylated SERPINA1 was determined from 1.563 to 800 ng/mL based on the standard curve generated using linear dilutions of recombinant SERPINA1 proteins (Figure S2a). To evaluate the specificity of AAL binding to glycosylated SERPINA1 via recognition of fucose in this system, we initially examined the effect of PNGase F treatment on the AAL binding capability of recombinant SERPINA1. PNGase F-catalyzed deglycosylation of SERPINA1 completely abolished recognition of AAL (Figure 5a). Next, we investigated the effect of addition of different sugar types in reverse lectin ELISA. The ELISA signal was suppressed by L-fucose but not lactose in a dose-dependent manner (Figure 5b). The collective results suggest that fucose is a pivotal component of glycan for AAL binding to glycosylated SERPINA1 and validate the effective application of our newly developed AAL-based reverse lectin ELISA assay to detect fuco-SERPINA1 in clinical plasma samples.

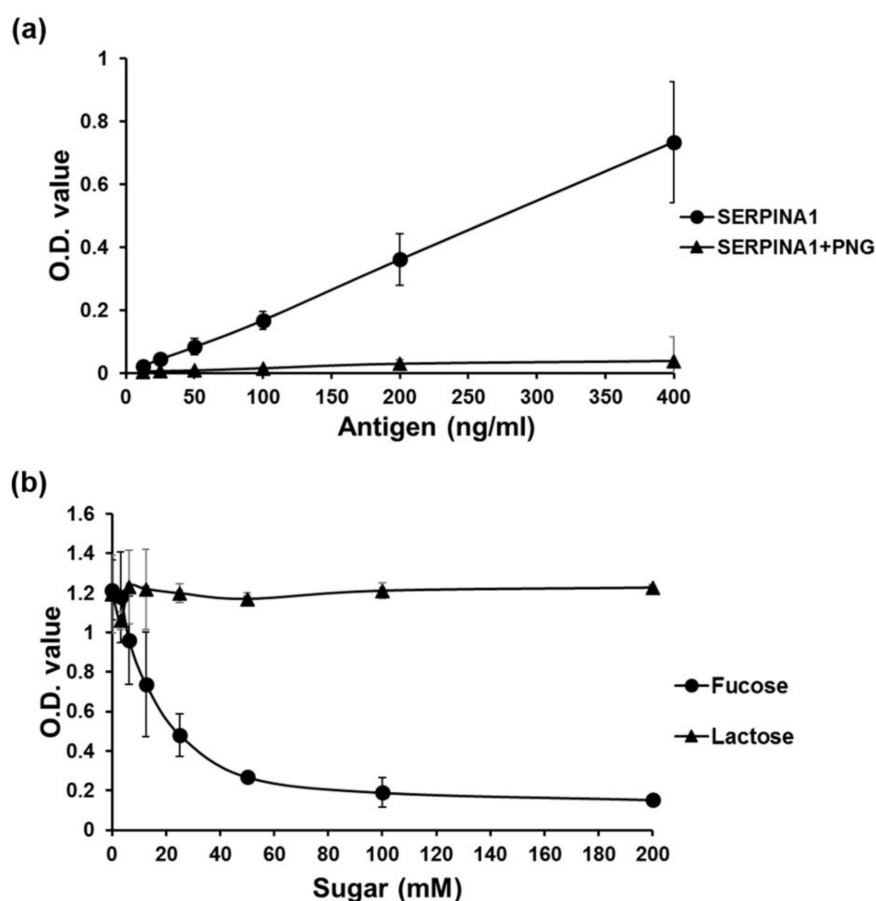


**Figure 5.** Evaluation of the specificity of AAL binding to fuco-SERPINA1 in reverse lectin ELISA. (a) Different amounts of recombinant SERPINA1 protein were treated with or without PNGase F (PNG) (protein:PNGase F = 1 µg:1U, 37 °C for 20 h) and subjected to AAL-based reverse lectin ELISA. (b) AAL was pre-incubated with different doses of L-fucose or lactose at room temperature for 0.5 h and coated onto ELISA plates. Plates were subjected to reverse lectin ELISA for detecting fixed amounts of fuco-SERPINA1. OD values were measured at 450 nm and each data point was examined in duplicate. Data expressed as mean ± S.D. are presented as a black solid line.



## 2.6. Changes in SERPINA1 and Fuco-SERPINA1 Levels in Individual Plasma Samples

The AAL-based reverse lectin ELISA system was applied to determine the levels of fuco-SERPINA1 in plasma samples of 121 subjects (50 GS and 71 PC) enrolled in this study. Levels of fuco-SERPINA1 were significantly higher in PC than GS patients (310.7 ng/mL v.s. 153.6 ng/mL,  $p = 0.0114$ ) (Figure 6a). Notably, levels of fuco-SERPINA1 were also significantly higher in PC patients with distant metastasis (M1) than the metastasis-free (M0) PC group (M0: 228.6 ng/mL; M1: 361.1 ng/mL,  $p = 0.043$ ) (Figure 6b). We additionally measured the levels of SERPINA1 protein in the same sample set using a commercial ELISA kit with a detection range of 7.813 to 8000 µg/mL (Figure S2b). The results consistently revealed significant elevation of SERPINA1 protein in PC compared to GS (139.9 µg/mL v.s. 106.1 µg/mL,  $p < 0.0001$ ), but the extent of change (1.32-fold) was lower than that of fuco-SERPINA1 (2.02-fold) (Figure 6c). Moreover, patients with distant metastasis of PC had slightly higher SERPINA1 levels compared to metastasis-free patients (129.7 µg/mL v.s. 146.1 µg/mL,  $p = 0.017$ ) (Figure 6d). Levels of CA19-9 in the 50 GS and 71 PC subjects were additionally determined. The results showed dramatic elevation of CA19-9 levels in PC patients relative to GS subjects (Figure 6e,f). Taken together, these results confirmed our findings from the quantitative glycoproteomics study, demonstrating that (i) both plasma SERPINA1 and fuco-SERPINA1 levels are significantly elevated in PC compared to GS patients, and (ii) the observed increase in plasma fuco-SERPINA1 levels is mainly due to significant elevation in cases of PC with distant metastasis.

## 2.7. Associations of Plasma Levels of Fuco-SERPINA1, SERPINA1 and CA19-9 with Clinicopathological Characteristics of PC Patients

Next, we explored the potential association of plasma levels of fuco-SERPINA1, SERPINA1 and CA19-9 with different clinicopathological characteristics (gender, age, TNM stage, tumor stage, lymph node metastasis and distant metastasis) of enrolled PC patients (Table 4 and Table S4). The results showed that (i) all three measurements (fuco-SERPINA1, SERPINA1 and CA19-9) are not significantly associated with gender or age, (ii) higher levels of fuco-SERPINA1 are significantly correlated with higher TNM stage ( $p = 0.024$ ) and distant metastatic PC (M1) ( $p = 0.043$ ), (iii) SERPINA1 protein levels are significantly correlated with distant metastasis at diagnosis ( $p = 0.017$ ), and (iv) plasma levels of CA19-9 do not show a significant correlation with the clinical characteristics, although subjects with distant metastatic PC (M1) at diagnosis tend to have higher CA19-9 levels ( $p = 0.097$ ).

## 2.8. Receiver Operating Characteristic (ROC) Curve Analysis of Fuco-SERPINA1, SERPINA1 and CA19-9

The efficacy of fuco-SERPINA1, SERPINA1 or CA19-9 for discriminating between PC patients and GS controls was assessed via ROC curve analysis. AUC (Area Under ROC Curve) values of fuco-SERPINA1, SERPINA1 and CA19-9 were determined as 0.652, 0.836 and 0.914, respectively (Figure 7a). The plasma levels of CA19-9 displayed outstanding performance in discriminating PC patients from GS controls. Discriminatory power was also high for SERPINA1 protein but poor for fuco-SERPINA1. Combination of fuco-SERPINA1 with SERPINA1 protein or CA19-9 did not enhance the discriminating power of CA19-9 or SERPINA1 protein alone. On the other hand, the discriminatory power of the combination of SERPINA1 protein and CA19-9 was greater than that of either marker alone (AUC = 0.956) (Figure 7b).

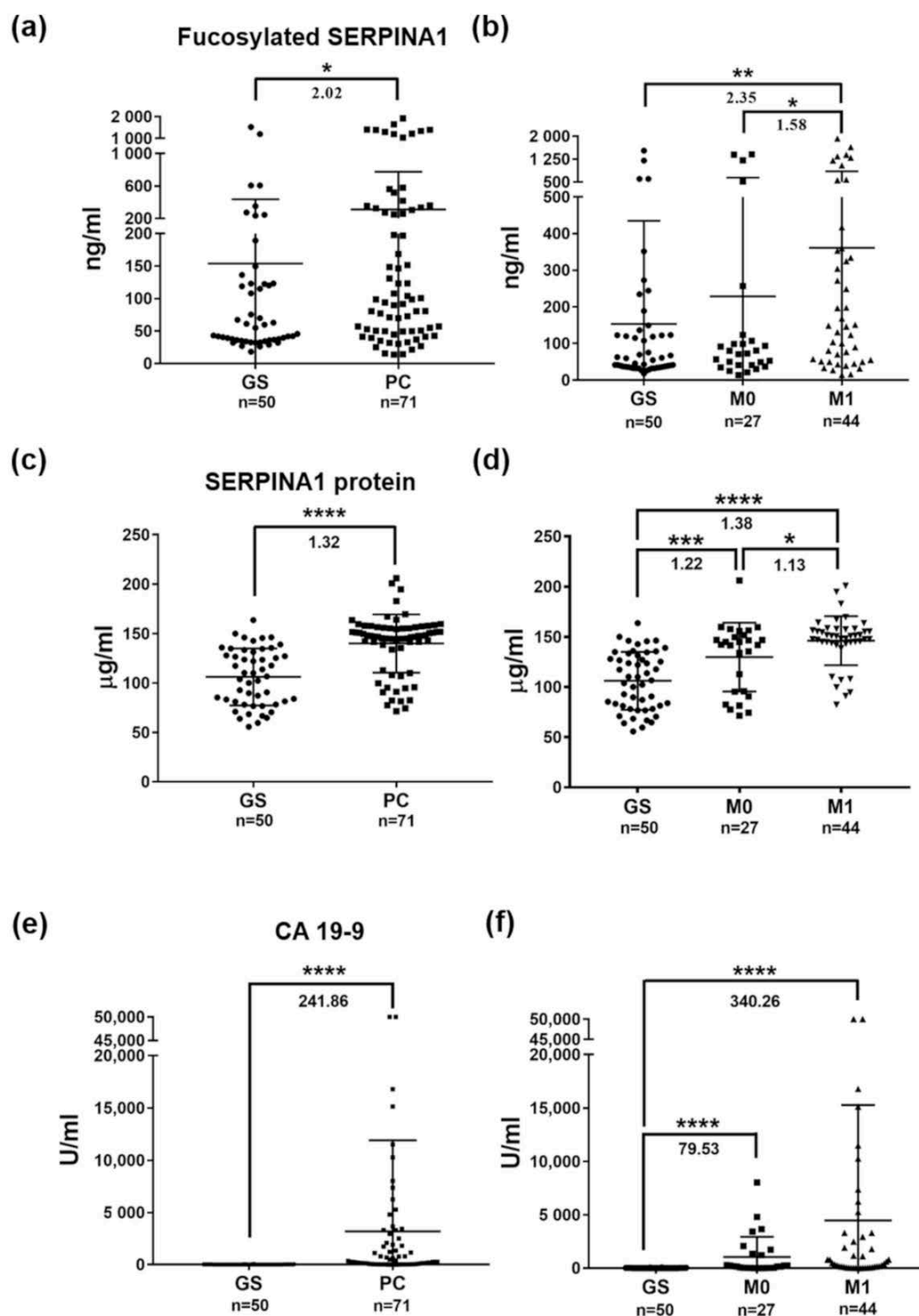


**Figure 6.** Plasma levels of fuco-SERPINA1, SERPINA1 and CA19-9 measured in enrolled subjects. (a,b) Levels of fuco-SERPINA1 measured in plasma specimens from GS and PC patients using AAL-based reverse lectin ELISA. (c,d) Levels of SERPINA1 protein measured in plasma specimens from GS and PC patients using commercial ELISA kits. (e,f) Levels of CA19-9 measured in plasma specimens from GS and PC patients using ECLIA. The horizontal lines indicate mean  $\pm$  S.D. \*,  $p \leq 0.05$ ; \*\*,  $p \leq 0.01$ ; \*\*\*,  $p \leq 0.001$ ; \*\*\*\*,  $p \leq 0.0001$ .

**Table 4.** Correlations of plasma fucosylated SERPINA1, SERPINA1, and CA19-9 levels with clinicopathological characteristics of PC patients.

Characteristics	Number	Fucosylated SERPINA1 (ng/mL)	<i>p</i> -Value	SERPINA1 protein (µg/mL)	<i>p</i> -Value	CA19-9 (U/mL)	<i>p</i> -Value
Gender <sup>a</sup>	-	-	-	-	-	-	-
Male	47	332.6 ± 482.1	0.949	142.1 ± 28.5	0.450	3329 ± 10,192	0.693
Female	24	267.8 ± 438.8	-	135.6 ± 31.4	-	2854 ± 4884	-
Age (years) <sup>a</sup>	-	-	-	-	-	-	-
<62 <sup>c</sup>	35	302.5 ± 422.2	0.862	140.8 ± 29.8	0.905	4572 ± 11,843	0.844
≥62	36	318.7 ± 509.3	-	139 ± 29.5	-	1804 ± 3488	-
TNM stage <sup>b</sup>	-	-	-	-	-	-	-
Stage I and II	17	201.1.7 ± 418.4	0.024 <sup>d</sup>	130.2 ± 36.5	0.060	781.1 ± 1191	0.222
Stage III	10	275.3 ± 423.2	-	129 ± 31.7	-	1495 ± 2753	-
Stage IV	44	361.1 ± 491.8	-	146.1 ± 24.5	-	4471 ± 10,827	-
Tumor stage <sup>b</sup>	-	-	-	-	-	-	-
T1 and T2	6	267.0 ± 508.0	0.300	137.2 ± 32.6	0.774	319 ± 371	0.336
T3	38	281.3 ± 444.2	-	141.7 ± 30.7	-	4516 ± 11,447	-
T4	26	301.8 ± 395.7	-	137.8 ± 28.4	-	1976 ± 3565	-
Lymph node metastasis <sup>a</sup>	-	-	-	-	-	-	-
N0	13	327.2 ± 573.2	0.610	136.4 ± 36.9	0.994	5447 ± 13,704	0.799
N1	58	307 ± 443.2	-	140.7 ± 27.8	-	2658 ± 7248	-
Distant metastasis <sup>a</sup>	-	-	-	-	-	-	-
M0	27	228.6 ± 413.6	0.043 <sup>d</sup>	129.7 ± 34.2	0.017 <sup>d</sup>	1045 ± 1903	0.097
M1	44	361.1 ± 491.8	-	146.1 ± 24.5	-	4471 ± 10,827	-

*p*-values were evaluated using <sup>a</sup> Mann–Whitney test (mean ± SD) or <sup>b</sup> Kruskal–Wallis test (mean ± SD). <sup>c</sup> Threshold of age was determined based on the median of patient ages. <sup>d</sup> Statistically significant, *p*-value ≤ 0.05.

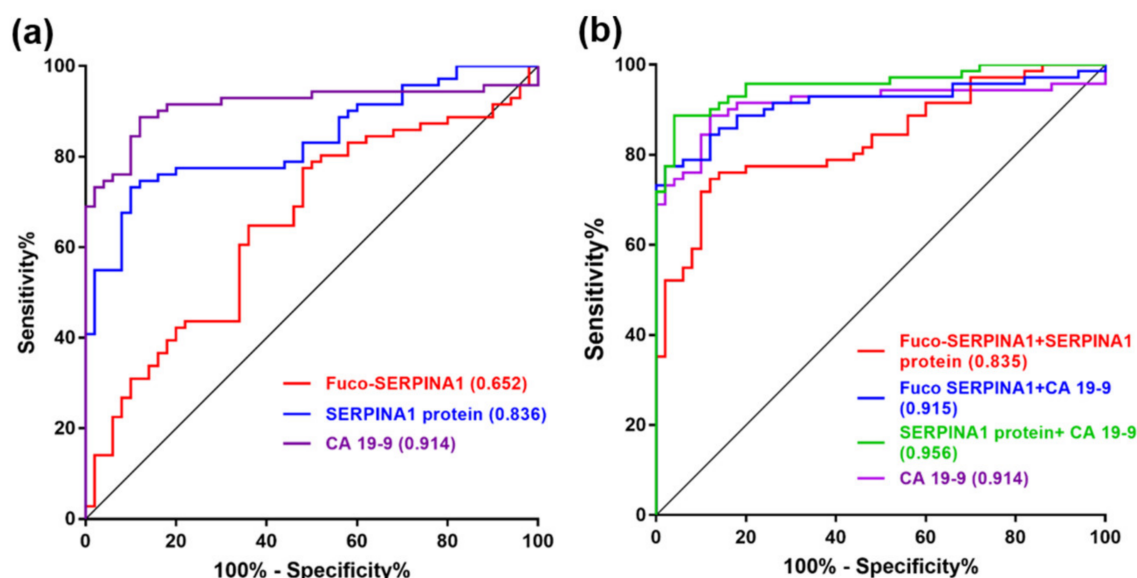


**Figure 7.** ROC curve analysis of fuco-SERPINA1, SERPINA1 protein and CA19-9 in discriminating PC patients from GS subjects. (a) The discriminatory power of plasma fuco-SERPINA1, SERPINA1 and CA19-9 was evaluated via ROC curve analysis. (b) The discriminatory power of combined fuco-SERPINA1 with SERPINA1 or CA19-9 was further evaluated. AUC values are presented in brackets.

### 2.9. Association of Overall Survival (OS) with Fuco-SERPINA1, SERPINA1 and CA19-9

To investigate the association of patient survival with plasma levels of fuco-SERPINA1 and SERPINA1, their median levels were used as cut-off values (98.7 ng/mL for fuco-SERPINA1; 147.1 µg/mL for SERPINA1 protein). Patients were stratified into high- and low-level groups and Kaplan–Meier plots generated to estimate OS rates. The cut-off value for CA19-9 was set at 37 U/mL. OS rates were determined in 70 of the 71 PC patients. PC patients with high fuco-SERPINA1 levels ( $n = 35$ ) had significantly lower survival rate than those with low fuco-SERPINA1 levels ( $n = 35$ ;  $p = 0.0083$ ). Similarly, higher SERPINA1 protein and CA19-9 levels were respectively associated with poorer survival rates ( $p < 0.0001$ ;  $p = 0.0109$ ) (Figure 8). Our results suggest that plasma levels of both fuco-SERPINA1 and SERPINA1 protein may serve as effective novel prognosticators of PC.

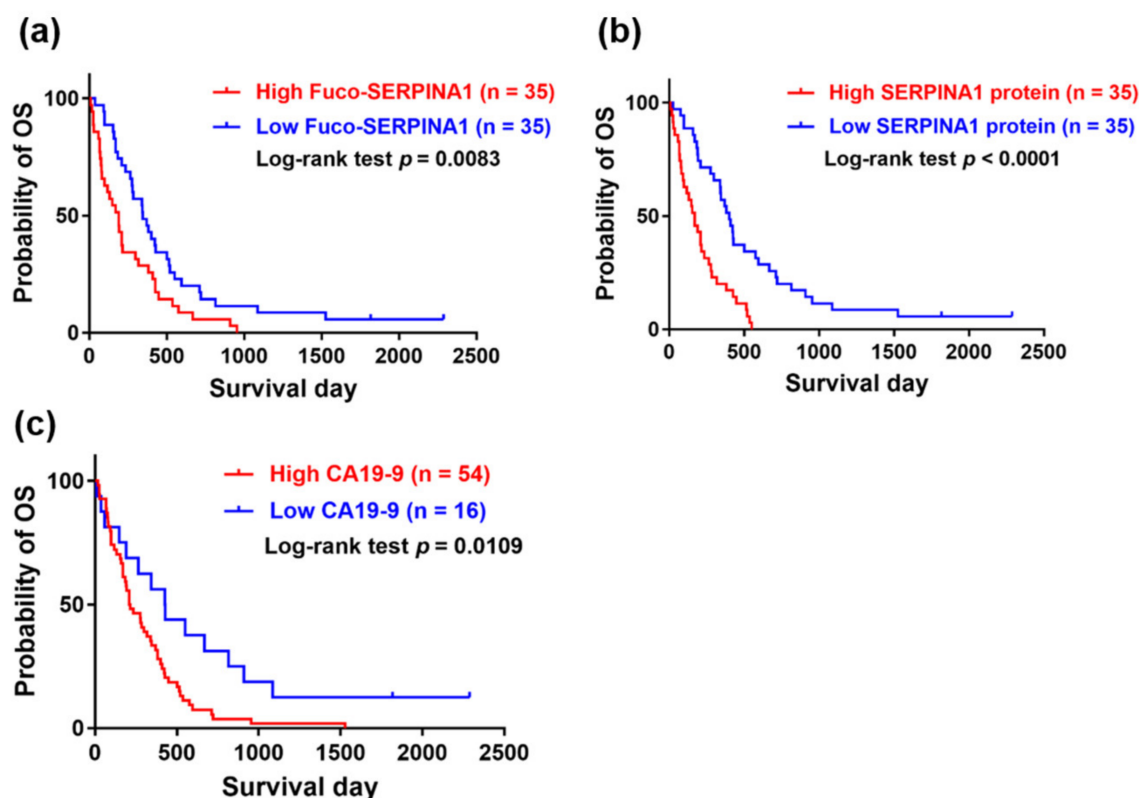


**Figure 8.** Association between overall survival of PC patients and plasma levels of fuco-SERPINA1 (a), SERPINA1 (b) and CA19-9 (c) analyzed using Kaplan–Meier plot. The time of survival was assessed in 68 of 71 PC patients enrolled in this study. The log-rank test  $p$ -value is denoted in each plot.

### 3. Discussion

Abnormal glycosylation is considered a hallmark associated with cancer [8]. Specific glycoproteins incorporating aberrant glycans have been uncovered with significantly higher specificity for cancers than the proteins themselves, such as glycosylated alpha-fetoprotein (AFP), which serves as a more reliable marker for hepatocellular carcinoma (HCC) than AFP protein [21,22]. Several studies have reported abnormal fucosylation in colorectal and prostate cancer types [23,24] and increase in haptoglobin decorated with glycan of core fucosylation ( $\alpha$ -1-6 linked fucose on  $N$ -acetylglucosamine at the reducing end) in serum samples of PC patients [10,25].

Previously, a lectin-based quantitative proteomics approach was applied to identify potential serum glycomarkers for PC. Six candidate proteins were verified using ELISA (alpha-1-antichymotrypsin (AACT), alpha-1-antitrypsin (A1AT), leucine-rich alpha-2-glycoprotein (LRG), thrombospondin-1 (THBS1) and haptoglobin (HPT)) or AAL lectin-ELISA (HPT and lumican (LUM)) in serum samples from 34 PC patients and 142 non-PC controls, which

yielded a three-marker panel (AACT, THBS1 and HPT) with higher diagnostic potency for PC than the single biomarker CA19-9 [13]. Interestingly, the group observed elevated serum levels of  $\alpha$ -1-antitrypsin (A1AT, also known as SERPINA1) in PC patients compared to non-PC controls. In the present study, we adopted a different experimental design by incorporating isotope-coded glycosylation-site-specific tagging (IGOT) into the lectin-based quantitative proteomics approach [26], which facilitated the identification of 22 glycopeptides with definite glycosylation sites that were significantly elevated in plasma samples of PC compared to non-PC subjects (Table 3). The majority of glycosylation sites, except Asn 325, Asn 186 and Asn 186 for LRG1, Asn 136 for MMRN1 and Asn 117 for VASN, have been reported in UniPept, a database of human N-linked glycosites (<http://www.unipept.org> accessed on 31 March 2021) [27], validating the robustness of our assay platform for accurate identification of glycosylation sites. Moreover, analysis using Byonic software led to successful elucidation of the glycan structures of 12 fucose-containing glycopeptides, including <sup>268</sup>YLGNATAIFFLPDEGK<sup>283</sup> derived from SERPINA1. To our knowledge, the majority of differentially expressed glycopeptides identified in our experiments have not been reported in earlier PC studies.

SERPINA1 (alpha-1-antitrypsin) is an inducible gene mainly expressed in hepatocytes, monocytes and macrophages. It encodes for AAT, a serine protease inhibitor mainly synthesized by the liver, and a highly expressed glycoprotein released into the bloodstream [28]. It acts as an inhibitor of neutrophil elastase, trypsin, chymotrypsin, thrombin, plasmin and cathepsin G. Deficiency of this protein mainly causes chronic obstructive pulmonary disease [29,30]. Several studies have reported an increase in serum SERPINA1 protein levels in the pregnancy, inflammatory response and different malignancy types derived from lung, liver, stomach, colon, prostate and pancreas [31–37]. However, little is known about glycosylation in PC although an increased level of serum fucosylated SERPINA1 has been reported in patients with lung cancer or hepatocellular carcinoma [38,39]. Previous LC-MS/MS analyses have led to the identification of three N-glycosylation sites of standard serum protein SERPINA1: Asn 70 (decorated with di-antennary glycan without fucose), Asn 107 (decorated with core and peripheral fucose linked to di-, tri- and tetra-antennary glycans) and Asn 271 (decorated with core and peripheral fucose linked to di- and tri-antennary glycans) [40]. Among the three sites, glycosylation of SERPINA1 at Asn 271 was significantly higher in plasma samples of PC patients (especially for the distant metastatic PC subgroup) (Table 3), with the deduced structure containing di-antennary glycans displaying both core and antennary fucosylation (Figure 3). Importantly, we successfully developed sensitive AAL-based reverse lectin ELISA in this study for measurement of fuco-SERPINA1 levels in plasma specimens, and reported for the first time that both plasma fuco-SERPINA1 and SERPINA1 protein levels are significantly elevated in patients with distant metastatic PC (Figure 6) in association with poor prognosis in OS (Figure 8). However, the PC sample used in this study was relatively small and the utility of fuco-SERPINA1 and SERPINA1 proteins as novel prognosticators for PC should be examined with larger sample numbers in the future.

Except SERPINA1, 10 targets, including beta-2-glycoprotein 1 (APOH), attractin (ATRN), monocyte differentiation antigen CD14 (CD14), scavenger receptor cysteine-rich type 1 protein M130 (CD163), intercellular adhesion molecule 1 (ICAM1), interleukin-6 receptor subunit beta (IL6ST), leucine-rich alpha-2-glycoprotein (LRG1), multimerin-1 (MMRN1), oncostatin-M-specific receptor subunit beta (OSMR) and antithrombin-III (SERPINC1), were also identified with fucosylation on their glycans. Among them, five targets (APOH, CD14, ICAM1, LRG1 and SERPINC1) were reported to be associated with other cancers or prognostic significance. For example, fucosylated APOH, CD14 and ICAM1 were detected with a high level in plasma of patients with human hepatocellular carcinoma (HCC) and fucosylated ICAM1 may represent a good prognostic marker for HCC [41–43]. In addition, fucosylated ICAM1 was identified as a potential biomarker for distinguishing Hodgkin's lymphoma from other lymphocytic cancers [44]. Higher serum levels of SERPINC1 with sialylation and fucosylation in PC patients as compared



to normal or chronic pancreatitis subjects has been reported [45]. The plasma levels of core-fucosylated LRG1 were found to be elevated in oral cancer patients relative to normal cases; moreover, the serum levels of LRG1 with fucosylated triantennary *N*-glycan was identified as a new marker to distinguish colorectal cancer patients from healthy, with a sensitivity and specificity exceeding CA19-9 [46,47].

In addition, the plasma levels of five glycopeptides derived from fructose-bisphosphate aldolase A (ALDOA), HPT, hemopexin (HPX), SERPINA1 and 14-3-3 protein theta (YWHAQ) were found to be significantly elevated in the M1 group compared with the M0 group ( $\geq$ mean + S.D. 2.57) (Table S2c). Among them, two proteins (HPT and HPX) in their sialylated and fucosylated forms have been reported as potential biomarkers for PC [13,45]. Notably, studies have unraveled core and peripheral fucose linked to di- and tri-antennary glycans as the glycoconjugate structures of HPT, and patients with late-stage PC showed significantly higher serum fucosylated HPT (fuco-HPT) levels than those of early-stage PC patients and healthy subjects [10,48]. Therefore, it may be worth to examine the potential of combining fuco-SERPINA1 and fuco-HPT as biomarker panel to improve the detection of metastatic PC.

We used an AAL affinity column to enrich iTRAQ-labeled glycopeptides from plasma samples. This peptide level-based protocol is more efficient for enrichment of glycopeptides than the protein level-based protocol owing to lower-level contamination of non-glycosylated proteins or peptides during the enrichment process [49,50]. Currently, shaving *N*-glycan from Asn with PNGase F in heavy water ( $\text{H}_2^{18}\text{O}$ ) to generate converted Asp with  $^{18}\text{O}$  labeling (+3 Da) is a feasible method in glycoproteomic analysis shown to enhance identifiable accuracy by eliminating the false glycosylated identification of chemical-inducible deamidation (−0.984 Da) during sample preparation [49–52]. In total, 10,572 peptides from AAL-affinity captured samples were identified. However, fewer peptides with  $^{18}\text{O}$  labeling (3.15%, 333/10,572) were acquired (Table 2), implicating significant non-specific retention of non-glycopeptides on the AAL affinity column prior to elution using 10% acetic acid (AA)/30% acetonitrile (ACN) in our study design. Replacement of elution buffer (10% AA/30% ACN) with PNGase F as a strategy for isotopic glycosidase elution and labeling on lectin column chromatography (IGEL), originally developed by the group of Ueda [49], may improve our design.

## 4. Materials and Methods

### 4.1. Plasma Samples

Peripheral blood samples were drawn from participants with standardized phlebotomy procedures and collected into an EDTA tube. After blood samples were centrifuged at  $2000 \times g$ , plasma was isolated from the supernatants and then immediately aliquoted, transferred into plain polypropylene tubes, and stored in a dedicated freezer at  $-80^\circ\text{C}$  until use. A total of 121 plasma samples from patients were obtained from Chang Gung Memorial Hospital (Linkou, Taiwan) after informed consent had been acquired from all subjects. Of them, those with distant metastasis when the blood was drawn and tested for targeted molecules were designated as M1 ( $n = 44$ ); while those without distant metastasis were designated as M0 ( $n = 27$ ). Meanwhile, a cohort of 50 patients with gallstones (GS) subjected for elective cholecystectomy served as controls. Pathological staging of pancreatic cancer was based on AJCC edition 8. The detailed clinicopathological features are shown in Supplementary Table S4. The concentration of CA19-9 was measured by electrochemiluminescence immunoassay (ECLIA) with Roche cobas® 8000 e602 analyzer (Roche Diagnostics, Rotkreuz, Switzerland).

### 4.2. Depletion of High-Abundance Plasma Proteins

Three plasma samples pooled from 10 GS controls, non-metastatic PC (M0) and metastatic PC (M1) patients were subjected to depletion of 14 highly abundant proteins using the Agilent Human 14 Multiple Affinity Removal System (MARS) column ( $4.6 \times 100$  mm; Agilent, Palo Alto, CA, USA), according to the procedure as previously

described [53]. Briefly, each pooled sample (40  $\mu$ L) was diluted 3-fold with 120  $\mu$ L buffer A of the MARS column system. Diluted samples were processed with AKTA purifier 10 fast protein liquid chromatography (FPLC) (GE Healthcare Life Sciences, Piscataway, NJ, USA). Depleted fractions were desalted, concentrated, quantified and stored at  $-80^{\circ}\text{C}$  for further analysis.

#### 4.3. Tryptic Digestion of Plasma Proteins and iTRAQ Labeling

Tryptic digestion of depleted plasma samples and iTRAQ labeling of digested peptides were performed as previously described [54]. Briefly, lyophilized depleted plasma samples (80  $\mu$ g protein) were reduced, alkylated, and digested with 8  $\mu$ g sequencing-grade modified porcine trypsin (1  $\mu$ g/ $\mu$ L in trypsin resuspension buffer; Promega, Fitchburg, WI, USA) at  $37^{\circ}\text{C}$  for 16 h. The resulting tryptic peptides of GS, M0, and M1 groups were labeled with iTRAQ tags 114, 115 and 116, respectively. Finally, iTRAQ-labeled products were pooled, separated into two fractions (30  $\mu$ g and 200  $\mu$ g) and desalted with solid-phase extraction Oasis HLB (30  $\mu$ m) cartridges (Waters, Milford, MA, USA).

#### 4.4. Glycopeptide Purification and Enzymatic Deglycosylation Integrated with $^{18}\text{O}$ Labeling on Glycosylated Sites

Lyophilized, iTRAQ-labeled samples (200  $\mu$ g peptide) were reconstituted with 1 mL lectin binding buffer (20 mM Tris, 0.3 M NaCl, 1 mM  $\text{CaCl}_2$ , 1 mM  $\text{MgCl}_2$ , pH 7.4) and incubated with 2 mg AAL agarose beads (Vector Laboratories, Burlingame, CA, USA) via rotation at room temperature for 1 h. After washing with lectin binding buffer three times and 500  $\mu$ L ddH $_2\text{O}$  twice, AAL pull-down peptides were transferred to a new tube and eluted using 10% AA/30% ACN with shaking at room temperature for 10 min. Eluted peptides were re-lyophilized and dissolved in 50 mM sodium phosphate buffer, pH 7.5, supplemented with 90% H $_2^{18}\text{O}$  and 40 U (1 unit/ $\mu$ L) N-glycosidase F (PNGase F; Roche Applied Science, Mannheim, Germany) and incubated at  $37^{\circ}\text{C}$  with slight shaking for 20 h. Deglycosylated peptides were desalted with 40  $\mu$ L C18 resin (source 15RPC, GE Healthcare, Björksgatan, Sweden) and lyophilized for further analysis using 2D-SCX/RP-LC-MS/MS.

#### 4.5. Two-Dimension LC-MS/MS Analysis

Dried peptides including total plasma peptides (36  $\mu$ g) and AAL-enrichment peptides were reconstituted in 30% ACN/0.1% formic acid (FA) and loaded onto home-made SCX column of two different sizes (0.5  $\times$  200 mm and 0.5  $\times$  100 mm; Luna SCX 5  $\mu$ m, Phenomenex, Torrance, CA, USA) at flow rate of 3  $\mu$ L/minute for 30 min. Peptides were eluted with 0–95% HPLC mobile phase (1 M ammonium nitrate/25% ACN/0.1% FA) and separated into 72 and 48 fractions using online 2D-HPLC (Dionex Ultimate 3000, Thermo Fisher, San Jose, CA, USA). Each SCX fraction was further 40-fold diluted in-line using 0.1% FA prior to trapping columns (Zorbax 300SB-C18 5  $\mu$ m, 0.3  $\times$  5 mm; Agilent Technologies, Wilmington, DE, USA) and diluted peptides resolved on an analytical C18 column (Synergi Hydro-RP 2.5  $\mu$ m, 0.075  $\times$  200 mm with a 15  $\mu$ m tip; Phenomenex, Torrance, CA, USA), with 0–95% HPLC mobile phase (100% ACN/0.1% FA) at a flow rate of 0.25  $\mu$ L/min. The LC apparatus was coupled to a two-dimensional linear ion trap mass spectrometer (LTQ-Orbitrap ELITE; Thermo Fisher, San Jose, CA, USA) controlled using Xcalibur 2.2 software (Thermo Fisher, San Jose, CA, USA), as previously described [54].

#### 4.6. Mass Spectrometric Data Analysis

RAW files of resulting MS/MS spectra obtained from LTQ-Orbitrap MS were searched against the database containing 20,316 entries of *Homo sapiens* in SwissProt released on 4 March 2018 (<https://www.uniprot.org/uniprot/?query=%&fil=reviewed%3Ayes+AND+organism%3A%28Homo+sapiens+%29+%5B9606%5D>) accessed on 31 March 2021) and commercial Proteome Discoverer 1.4 software (Thermo Fisher, San Jose, CA, USA) employed for data processing. The cleaved enzyme was set to “trypsin” with a maximum of one missed cleavage site. The precursor mass tolerance was set to 10 ppm and fragment

ions mass tolerance to 0.5 Da for CID mode via ion trap analysis and 0.05 Da for HCD mode via Orbitrap analysis. The fixed modification was set to methylthiolation at cysteine (+45.99 Da) and variable modifications set to acetylation at protein N-terminus (+42.01 Da), oxidation at methionine (+15.99 Da), pyroglutamate conversion at N-terminal glutamine (−17.03 Da) and iTRAQ 4plex labeling at lysine and peptide N-terminal (+144.10 Da). Moreover, variable modifications of deamination at asparagine (N to D) and deamination with  $^{18}\text{O}$  labeling at asparagine (N to D- $^{18}\text{O}$ ) were set for glycosylated site identification. Based on Mascot search results, the score threshold of peptide identification was set to “1% false discovery rate (FDR)” in the processing workflow and Peptide Validator algorithm was applied in calculation of FDR for peptide sequence analysis to distinguish true positives from random matches (decoy database). The decoy database was generated with Mascot and the size, including the number of amino acids and proteins, was the same as the original normal database [55]. In iTRAQ quantification, each reporter ion was integrated by the mode of most confident centroid at 20 ppm tolerance and iTRAQplex of 114 (114.11 Da) set as a denominator to compare other iTRAQplex of 115 (115.11 Da), 116 (116.11 Da) and 117 (117.11 Da) to generate a quantifiable ratio. Glycopeptides were processed using Byonic software (v2.12.0) (Protein Metrics Inc., Cupertino, CA, USA) in RAW files obtained from PC proteome analysis. The digested enzyme was set to “trypsin” with a maximum of one missed cleavage site. Mass tolerance and modification were the same as the above values. The library of 390 mammalian N-glycans was additionally set to the modified list for searching N-glycosylated peptides. Manual inspection was applied to confirm the confidence of identified glycopeptides and detect mass peaks of oxonium ion and glycan loss using Symbol Nomenclature for Glycans (SNFG). The mass spectrometry proteomics data were deposited to the ProteomeXchange Consortium via the PRIDE [56] partner repository (<https://www.ebi.ac.uk/pride/login>; Username: reviewer\_pxd025150@ebi.ac.uk; Password: tE4tQjpe; Accessed date: 1 April 2021) with the dataset identifier PXD025150.

#### 4.7. Reverse AAL-Based ELISA

AAL (100  $\mu\text{L}$ ; Vector Laboratories, Burlingame, CA, USA) (2.5  $\mu\text{g}/\text{mL}$ , diluted in PBS buffer, pH 7.4) was added to wells of a 96-well plate (Corning Incorporated, Corning, NY, USA) and incubated at 4 °C overnight. After removal of unbound AAL, the plate was rinsed with washing buffer (0.1% Tween-20 in PBS, pH 7.4) (300  $\mu\text{L}/\text{well}$ ) six times and blocked with blocking buffer (T-Pro Biotechnology, New Taipei County, Taiwan) (150  $\mu\text{L}/\text{well}$ ) at room temperature for 2 h. Next, the plate was rinsed with washing buffer (350  $\mu\text{L}/\text{well}$ ) four times, and 100  $\mu\text{L}$  serially diluted recombinant SERPINA1 protein (Research and Diagnostic Systems, Minneapolis, MN, USA) or plasma samples with 5-fold dilution (3% BSA/PBS) added to the wells and incubated at room temperature for 1 h. The plate was rinsed with washing buffer (300  $\mu\text{L}/\text{well}$ ) six times, and 100  $\mu\text{L}$  Serpin A1 antibodies (Research and Diagnostic Systems, Minneapolis, MN, USA) (1  $\mu\text{g}/\text{mL}$ ) diluted in blocking buffer) added to each well and incubated at room temperature for 1 h, followed by six rinses with washing buffer (300  $\mu\text{L}/\text{well}$ ). Horseradish peroxidase conjugated-secondary antibody (100  $\mu\text{L}$ ; anti-mouse IgG HRP; Jackson ImmunoResearch Laboratories, West Grove, PA, USA) (1:3000, diluted in blocking buffer) was added to each well and incubated at room temperature for 40 min, followed by rinsing with washing buffer (300  $\mu\text{L}/\text{well}$ ) six times. Finally, 100  $\mu\text{L}$  NeA-Blue Tetramethylbenzidine (TMB) solution (Clinical Science Products, Mansfield, MA, USA) was added to each well and incubated at room temperature for 30 min. The reaction terminated with 50  $\mu\text{L}$  2 N  $\text{H}_2\text{SO}_4$  solution. Reaction products were measured with SpectraMax M5 Microplate Reader (MDS Inc., Toronto, ON, Canada) at an absorbance wavelength of 450 nm.

#### 4.8. ELISA for SERPINA1 Protein

Plasma levels of SERPINA1 protein were measured using a commercially available ELISA kit (Sino Biological Inc., Beijing, China). Briefly, 100  $\mu\text{L}$  mouse anti-SERPINA1 monoclonal

antibodies, serving as capture antibodies (1 µg/mL, diluted in PBS buffer, pH 7.4), were coated onto a 96-well plate (Corning Incorporated, Corning, NY, USA) and incubated at 4 °C overnight. The plate was patted dry, rinsed with washing buffer (20 mM Tris, 150 mM NaCl and 0.05 % Tween-20, pH 7.2–7.4) (300 µL/well) three times, and blocked with blocking buffer (2% BSA in washing buffer) (300 µL/well) for 2 h. After rinsing the plate with washing buffer (350 µL/well) three times, 100 µL serially diluted recombinant SERPINA1 protein (as a standard curve) or plasma samples with 50,000-fold dilution in 0.1% BSA/washing buffer were added to wells and incubated at room temperature for 2 h. The plate was rinsed with washing buffer (300 µL/well) six times, and 100 µL rabbit anti-SERPINA1 monoclonal antibodies conjugated to horseradish peroxidase (detection antibodies; 0.4 µL/mL, diluted in 0.5% BSA/washing buffer) added to each well and incubated at room temperature for 1 h, followed by six rinses with washing buffer (300 µL/well). Finally, 100 µL TMB solution was added to each well and incubated for 20 min, and the reaction terminated with 50 µL 2 N H<sub>2</sub>SO<sub>4</sub> solution. Reaction products were measured using a SpectraMax M5 Microplate Reader at an absorbance wavelength of 450 nm.

#### 4.9. Statistical Analysis

The Mann–Whitney test was used to compare the differences in plasma levels of fuco-SERPINA1 and SERPINA1 proteins between GS and PC groups. Mann–Whitney and Kruskal–Wallis tests were used to evaluate the association of plasma fuco-SERPINA1, SERPINA1 and CA19-9 with various clinicopathological parameters of PC patients. Overall survival (OS) analysis was performed using the Kaplan–Meier method and differences in OS assessed via log-rank test. The diagnostic power of fuco-SERPINA1, SERPINA1 and CA19-9 was analyzed by constructing a receiver operating characteristic (ROC) curve with sensitivity versus 1-specificity and calculating area under the ROC curve (AUC). For all statistical analyses, a two-tailed *p*-value ≤ 0.05 was considered significant. Calculations and diagrams were generated using GraphPad Prism 7.0 (GraphPad Software, Inc., San Diego, CA, USA).

## 5. Conclusions

Our results demonstrated significant elevation of plasma fuco-SERPINA1 in PC patients compared to GS subjects, which was significantly associated with TNM stage and poor prognosis. Plasma fuco-SERPINA1 may therefore serve as a novel prognosticator for PC, which should be further examined on a larger scale in the future. The differentially expressed glycopeptides with definite glycosylation sites identified in this study present a valuable reservoir to explore novel biomarkers for PC.

**Supplementary Materials:** The following are available online at <https://www.mdpi.com/article/10.3390/ijms22116079/s1>.

**Author Contributions:** Conceptualization, C.-C.W. and J.-S.Y.; methodology, C.-C.W. and Y.-T.L.; formal analysis, C.-C.W. and Y.-T.L.; investigation, C.-C.W., Y.-T.L., Y.-H.C. and T.-S.Y.; resources, T.-S.Y.; data curation, T.-S.Y. and Y.-H.C.; writing—original draft preparation, C.-C.W., Y.-T.L. and S.D.; writing—review and editing, T.-S.Y. and J.-S.Y.; visualization, C.-C.W. and Y.-T.L.; supervision, J.-S.Y.; project administration, C.-C.W. and J.-S.Y.; funding acquisition, J.-S.Y. All authors have read and agreed to the published version of the manuscript.

**Funding:** This research was funded by the Ministry of Science and Technology, Taiwan, grant number MOST 109-2320-B-182-009-MY3 and by Chang Gung Memorial Hospital, Taiwan, grant number CLRPD1J0012 and CMRPD1H0253. This research was also supported by the “Molecular Medicine Research Center, Chang Gung University” from The Featured Areas Research Center Program within the framework of the Higher Education Sprout Project by the Ministry of Education in Taiwan. The APC was funded by the Ministry of Science and Technology, Taiwan.

**Institutional Review Board Statement:** The study was conducted according to the guidelines of the Declaration of Helsinki, and approved by the Institutional Review Board of Chang Gung Memorial Hospital (protocol code 102-3393B, 1 October 2013).



**Informed Consent Statement:** Informed consent was obtained from all subjects involved in the study. Written informed consent was obtained from the patients to publish this paper.

**Data Availability Statement:** The data that support the findings of this study are available from the corresponding author upon reasonable request.

**Acknowledgments:** We would like to thank Kun-Yi Chien from the Chang Gung University Proteomics Core Laboratory for the excellent assistance with the LC-MS/MS analysis of plasma glycoproteome presented in this investigation.

**Conflicts of Interest:** The authors declare no conflict of interest. The funders had no role in the design of the study; in the collection, analyses, or interpretation of data; in the writing of the manuscript, or in the decision to publish the results.

## References

1. Siegel, R.L.; Miller, K.D.; Jemal, A. Cancer statistics, 2017. *CA Cancer J. Clin.* **2017**, *67*, 7–30. [\[CrossRef\]](#) [\[PubMed\]](#)
2. Rawla, P.; Sunkara, T.; Gaduputi, V. Epidemiology of pancreatic cancer: Global trends, etiology and risk factors. *World J. Oncol.* **2019**, *10*, 10–27. [\[CrossRef\]](#) [\[PubMed\]](#)
3. Bond-Smith, G.; Banga, N.; Hammond, T.M.; Imber, C.J. Pancreatic adenocarcinoma. *BMJ* **2012**, *344*, e2476. [\[CrossRef\]](#) [\[PubMed\]](#)
4. Bramhall, S.R.; Allum, W.H.; Jones, A.G.; Allwood, A.; Cummins, C.; Neoptolemos, J.P. Treatment and survival in 13,560 patients with pancreatic cancer, and incidence of the disease, in the West Midlands: An epidemiological study. *Br. J. Surg.* **1995**, *82*, 111–115. [\[CrossRef\]](#) [\[PubMed\]](#)
5. Ryan, D.P.; Hong, T.S.; Bardeesy, N. Pancreatic adenocarcinoma. *N. Engl. J. Med.* **2014**, *371*, 1039–1049. [\[CrossRef\]](#) [\[PubMed\]](#)
6. Locker, G.Y.; Hamilton, S.; Harris, J.; Jessup, J.M.; Kemeny, N.; Macdonald, J.S.; Somerfield, M.R.; Hayes, D.F.; Bast, R.C., Jr. ASCO 2006 update of recommendations for the use of tumor markers in gastrointestinal cancer. *J. Clin. Oncol.* **2006**, *24*, 5313–5327. [\[CrossRef\]](#) [\[PubMed\]](#)
7. Kunovsky, L.; Tesarikova, P.; Kala, Z.; Kroupa, R.; Kysela, P.; Dolina, J.; Trna, J. The use of biomarkers in early diagnostics of pancreatic cancer. *Can. J. Gastroenterol. Hepatol.* **2018**, *2018*, 5389820. [\[CrossRef\]](#) [\[PubMed\]](#)
8. Munkley, J.; Elliott, D.J. Hallmarks of glycosylation in cancer. *Oncotarget* **2016**, *7*, 35478–35489. [\[CrossRef\]](#)
9. Terao, N.; Takamatsu, S.; Minehira, T.; Sobajima, T.; Nakayama, K.; Kamada, Y.; Miyoshi, E. Fucosylation is a common glycosylation type in pancreatic cancer stem cell-like phenotypes. *World J. Gastroenterol.* **2015**, *21*, 3876–3887. [\[CrossRef\]](#)
10. Okuyama, N.; Ide, Y.; Nakano, M.; Nakagawa, T.; Yamanaka, K.; Moriwaki, K.; Murata, K.; Ohigashi, H.; Yokoyama, S.; Eguchi, H.; et al. Fucosylated haptoglobin is a novel marker for pancreatic cancer: A detailed analysis of the oligosaccharide structure and a possible mechanism for fucosylation. *Int. J. Cancer* **2006**, *118*, 2803–2808. [\[CrossRef\]](#)
11. Geng, M.; Zhang, X.; Bina, M.; Regnier, F. Proteomics of glycoproteins based on affinity selection of glycopeptides from tryptic digests. *J. Chromatogr. B Biomed. Sci. Appl.* **2001**, *752*, 293–306. [\[CrossRef\]](#)
12. Xiong, L.; Regnier, F.E. Use of a lectin affinity selector in the search for unusual glycosylation in proteomics. *J. Chromatogr. B Analyt. Technol. Biomed. Life Sci.* **2002**, *782*, 405–418. [\[CrossRef\]](#)
13. Nie, S.; Lo, A.; Wu, J.; Zhu, J.; Tan, Z.; Simeone, D.M.; Anderson, M.A.; Shedden, K.A.; Ruffin, M.T.; Lubman, D.M. Glycoprotein biomarker panel for pancreatic cancer discovered by quantitative proteomics analysis. *J. Proteome Res.* **2014**, *13*, 1873–1884. [\[CrossRef\]](#)
14. Chen, S.; LaRoche, T.; Hamelinck, D.; Bergsma, D.; Brenner, D.; Simeone, D.; Brand, R.E.; Haab, B.B. Multiplexed analysis of glycan variation on native proteins captured by antibody microarrays. *Nat. Methods* **2007**, *4*, 437–444. [\[CrossRef\]](#)
15. Li, Y.; Tao, S.C.; Bova, G.S.; Liu, A.Y.; Chan, D.W.; Zhu, H.; Zhang, H. Detection and verification of glycosylation patterns of glycoproteins from clinical specimens using lectin microarrays and lectin-based immunosorbent assays. *Anal. Chem.* **2011**, *83*, 8509–8516. [\[CrossRef\]](#)
16. Wu, J.; Xie, X.; Liu, Y.; He, J.; Benitez, R.; Buckanovich, R.J.; Lubman, D.M. Identification and confirmation of differentially expressed fucosylated glycoproteins in the serum of ovarian cancer patients using a lectin array and LC-MS/MS. *J. Proteome Res.* **2012**, *11*, 4541–4552. [\[CrossRef\]](#)
17. Abraham, R.; Moller, D.; Gabel, D.; Senter, P.; Hellstrom, I.; Hellstrom, K.E. The influence of periodate oxidation on monoclonal antibody avidity and immunoreactivity. *J. Immunol. Methods* **1991**, *144*, 77–86. [\[CrossRef\]](#)
18. Wu, J.; Xie, X.; Nie, S.; Buckanovich, R.J.; Lubman, D.M. Altered expression of sialylated glycoproteins in ovarian cancer sera using lectin-based ELISA assay and quantitative glycoproteomics analysis. *J. Proteome Res.* **2013**, *12*, 3342–3352. [\[CrossRef\]](#)
19. Wu, J.; Zhu, J.; Yin, H.; Buckanovich, R.J.; Lubman, D.M. Analysis of glycan variation on glycoproteins from serum by the reverse lectin-based ELISA assay. *J. Proteome Res.* **2014**, *13*, 2197–2204. [\[CrossRef\]](#)
20. Astrom, E.; Stal, P.; Zenlander, R.; Edenvik, P.; Alexandersson, C.; Haglund, M.; Ryden, I.; Pahlsson, P. Reverse lectin ELISA for detecting fucosylated forms of alpha1-acid glycoprotein associated with hepatocellular carcinoma. *PLoS ONE* **2017**, *12*, e0173897. [\[CrossRef\]](#)
21. Li, D.; Mallory, T.; Satomura, S. AFP-L3: A new generation of tumor marker for hepatocellular carcinoma. *Clin. Chim. Acta* **2001**, *313*, 15–19. [\[CrossRef\]](#)



22. Kim, H.; Sohn, A.; Yeo, I.; Yu, S.J.; Yoon, J.H.; Kim, Y. Clinical assay for AFP-L3 by Using Multiple Reaction Monitoring-mass spectrometry for diagnosing hepatocellular carcinoma. *Clin. Chem.* **2018**, *64*, 1230–1238. [\[CrossRef\]](#)
23. Muinelo-Romay, L.; Villar-Portela, S.; Cuevas, E.; Gil-Martin, E.; Fernandez-Briera, A. Identification of alpha(1,6)fucosylated proteins differentially expressed in human colorectal cancer. *BMC Cancer* **2011**, *11*, 508. [\[CrossRef\]](#)
24. Saldova, R.; Fan, Y.; Fitzpatrick, J.M.; Watson, R.W.; Rudd, P.M. Core fucosylation and alpha2-3 sialylation in serum N-glycome is significantly increased in prostate cancer comparing to benign prostate hyperplasia. *Glycobiology* **2011**, *21*, 195–205. [\[CrossRef\]](#)
25. Lin, Z.; Simeone, D.M.; Anderson, M.A.; Brand, R.E.; Xie, X.; Shedden, K.A.; Ruffin, M.T.; Lubman, D.M. Mass spectrometric assay for analysis of haptoglobin fucosylation in pancreatic cancer. *J. Proteome Res.* **2011**, *10*, 2602–2611. [\[CrossRef\]](#)
26. Kaji, H.; Yamauchi, Y.; Takahashi, N.; Isobe, T. Mass spectrometric identification of N-linked glycopeptides using lectin-mediated affinity capture and glycosylation site-specific stable isotope tagging. *Nat. Protoc.* **2006**, *1*, 3019–3027. [\[CrossRef\]](#)
27. Zhang, H.; Loriaux, P.; Eng, J.; Campbell, D.; Keller, A.; Moss, P.; Bonneau, R.; Zhang, N.; Zhou, Y.; Wollscheid, B.; et al. UniPep—a database for human N-linked glycosites: A resource for biomarker discovery. *Genome Biol.* **2006**, *7*, R73. [\[CrossRef\]](#)
28. Miravittles, M. Alpha-1-antitrypsin and other proteinase inhibitors. *Curr. Opin. Pharmacol.* **2012**, *12*, 309–314. [\[CrossRef\]](#)
29. Gettins, P.G. Serpin structure, mechanism, and function. *Chem. Rev.* **2002**, *102*, 4751–4804. [\[CrossRef\]](#)
30. DeMeo, D.L.; Silverman, E.K. Alpha1-antitrypsin deficiency. 2: Genetic aspects of alpha(1)-antitrypsin deficiency: Phenotypes and genetic modifiers of emphysema risk. *Thorax* **2004**, *59*, 259–264. [\[CrossRef\]](#)
31. Stockley, R.A. The multiple facets of alpha-1-antitrypsin. *Ann. Transl. Med.* **2015**, *3*, 130. [\[CrossRef\]](#) [\[PubMed\]](#)
32. El-Akawi, Z.J.; Abu-Awad, A.M.; Sharara, A.M.; Khader, Y. The importance of alpha-1 antitrypsin (alpha1-AT) and neopterin serum levels in the evaluation of non-small cell lung and prostate cancer patients. *Neuro Endocrinol. Lett.* **2010**, *31*, 113–116. [\[PubMed\]](#)
33. Hong, W.S.; Hong, S.I. Clinical usefulness of alpha-1-antitrypsin in the diagnosis of hepatocellular carcinoma. *J. Korean Med. Sci.* **1991**, *6*, 206–213. [\[CrossRef\]](#) [\[PubMed\]](#)
34. Hsu, P.I.; Chen, C.H.; Hsiao, M.; Wu, D.C.; Lin, C.Y.; Lai, K.H.; Lu, P.J. Diagnosis of gastric malignancy using gastric juice alpha1-antitrypsin. *Cancer Epidemiol. Biomarkers Prev.* **2010**, *19*, 405–411. [\[CrossRef\]](#)
35. Perez-Holanda, S.; Blanco, I.; Menendez, M.; Rodrigo, L. Serum concentration of alpha-1 antitrypsin is significantly higher in colorectal cancer patients than in healthy controls. *BMC Cancer* **2014**, *14*, 355. [\[CrossRef\]](#)
36. Tountas, Y.; Sparos, L.; Theodoropoulos, C.; Trichopoulos, D. Alpha 1-antitrypsin and cancer of the pancreas. *Digestion* **1985**, *31*, 37–40. [\[CrossRef\]](#)
37. Rotondo, J.C.; Oton-Gonzalez, L.; Selvatici, R.; Rizzo, P.; Pavasini, R.; Campo, G.C.; Lanzillotti, C.; Mazziotta, C.; De Mattei, M.; Tognon, M.; et al. SERPINA1 gene promoter is differentially methylated in peripheral blood mononuclear cells of pregnant women. *Front. Cell Dev. Biol.* **2020**, *8*, 550543. [\[CrossRef\]](#)
38. Liang, Y.; Ma, T.; Thakur, A.; Yu, H.; Gao, L.; Shi, P.; Li, X.; Ren, H.; Jia, L.; Zhang, S.; et al. Differentially expressed glycosylated patterns of alpha-1-antitrypsin as serum biomarkers for the diagnosis of lung cancer. *Glycobiology* **2015**, *25*, 331–340. [\[CrossRef\]](#)
39. Comunale, M.A.; Wang, M.; Anbarasan, N.; Betesh, L.; Karabudak, A.; Moritz, E.; Devarajan, K.; Marrero, J.; Block, T.M.; Mehta, A. Total serum glycan analysis is superior to lectin-FLISA for the early detection of hepatocellular carcinoma. *Proteomics Clin. Appl.* **2013**, *7*, 690–700. [\[CrossRef\]](#)
40. Yin, H.; An, M.; So, P.K.; Wong, M.Y.; Lubman, D.M.; Yao, Z. The analysis of alpha-1-antitrypsin glycosylation with direct LC-MS/MS. *Electrophoresis* **2018**, *39*, 2351–2361. [\[CrossRef\]](#)
41. Ji, E.S.; Hwang, H.; Park, G.W.; Lee, J.Y.; Lee, H.K.; Choi, N.Y.; Jeong, H.K.; Kim, K.H.; Kim, J.Y.; Lee, S.; et al. Analysis of fucosylation in liver-secreted N-glycoproteins from human hepatocellular carcinoma plasma using liquid chromatography with tandem mass spectrometry. *Anal. Bioanal. Chem.* **2016**, *408*, 7761–7774. [\[CrossRef\]](#)
42. Liu, Y.; He, J.; Li, C.; Benitez, R.; Fu, S.; Marrero, J.; Lubman, D.M. Identification and confirmation of biomarkers using an integrated platform for quantitative analysis of glycoproteins and their glycosylations. *J. Proteome Res.* **2010**, *9*, 798–805. [\[CrossRef\]](#)
43. Loong, J.H.; Wong, T.L.; Tong, M.; Sharma, R.; Zhou, L.; Ng, K.Y.; Yu, H.J.; Li, C.H.; Man, K.; Lo, C.M.; et al. Glucose deprivation induced aberrant FUT1-mediated fucosylation drives cancer stemness in hepatocellular carcinoma. *J. Clin. Investig.* **2021**, *131*, e143377. [\[CrossRef\]](#)
44. Powlesland, A.S.; Barrio, M.M.; Mordoh, J.; Hitchen, P.G.; Dell, A.; Drickamer, K.; Taylor, M.E. Glycoproteomic characterization of carriers of the CD15/Lewisx epitope on Hodgkin's Reed-Sternberg cells. *BMC Biochem.* **2011**, *12*, 13. [\[CrossRef\]](#)
45. Zhao, J.; Patwa, T.H.; Qiu, W.; Shedden, K.; Hinderer, R.; Misek, D.E.; Anderson, M.A.; Simeone, D.M.; Lubman, D.M. Glycoprotein microarrays with multi-lectin detection: Unique lectin binding patterns as a tool for classifying normal, chronic pancreatitis and pancreatic cancer sera. *J. Proteome Res.* **2007**, *6*, 1864–1874. [\[CrossRef\]](#)
46. Chang, S.C.; Lin, W.L.; Chang, Y.F.; Lee, C.T.; Wu, J.S.; Hsu, P.H.; Chang, C.F. Glycoproteomic identification of novel plasma biomarkers for oral cancer. *J. Food Drug Anal.* **2019**, *27*, 483–493. [\[CrossRef\]](#)
47. Shinozaki, E.; Tanabe, K.; Akiyoshi, T.; Tsuchida, T.; Miyazaki, Y.; Kojima, N.; Igarashi, M.; Ueno, M.; Suenaga, M.; Mizunuma, N.; et al. Serum leucine-rich alpha-2-glycoprotein-1 with fucosylated triantennary N-glycan: A novel colorectal cancer marker. *BMC Cancer* **2018**, *18*, 406. [\[CrossRef\]](#)
48. Matsumoto, H.; Shinzaki, S.; Narisada, M.; Kawamoto, S.; Kuwamoto, K.; Moriwaki, K.; Kanke, F.; Satomura, S.; Kumada, T.; Miyoshi, E. Clinical application of a lectin-antibody ELISA to measure fucosylated haptoglobin in sera of patients with pancreatic cancer. *Clin. Chem. Lab. Med.* **2010**, *48*, 505–512. [\[CrossRef\]](#)

49. Ueda, K.; Takami, S.; Saichi, N.; Daigo, Y.; Ishikawa, N.; Kohno, N.; Katsumata, M.; Yamane, A.; Ota, M.; Sato, T.A.; et al. Development of serum glycoproteomic profiling technique; Simultaneous identification of glycosylation sites and site-specific quantification of glycan structure changes. *Mol. Cell Proteom.* **2010**, *9*, 1819–1828. [[CrossRef](#)]
50. Kaji, H.; Saito, H.; Yamauchi, Y.; Shinkawa, T.; Taoka, M.; Hirabayashi, J.; Kasai, K.; Takahashi, N.; Isobe, T. Lectin affinity capture, isotope-coded tagging and mass spectrometry to identify N-linked glycoproteins. *Nat. Biotechnol.* **2003**, *21*, 667–672. [[CrossRef](#)]
51. Kuster, B.; Mann, M. 18O-labeling of N-glycosylation sites to improve the identification of gel-separated glycoproteins using peptide mass mapping and database searching. *Anal. Chem.* **1999**, *71*, 1431–1440. [[CrossRef](#)] [[PubMed](#)]
52. Narimatsu, H.; Sawaki, H.; Kuno, A.; Kaji, H.; Ito, H.; Ikehara, Y. A strategy for discovery of cancer glyco-biomarkers in serum using newly developed technologies for glycoproteomics. *FEBS J.* **2010**, *277*, 95–105. [[CrossRef](#)]
53. Wu, C.C.; Lin, J.D.; Chen, J.T.; Chang, C.M.; Weng, H.F.; Hsueh, C.; Chien, H.P.; Yu, J.S. Integrated analysis of fine-needle-aspiration cystic fluid proteome, cancer cell secretome, and public transcriptome datasets for papillary thyroid cancer biomarker discovery. *Oncotarget* **2018**, *9*, 12079–12100. [[CrossRef](#)]
54. Liu, J.C.; Chen, Y.T.; Hsieh, Y.J.; Wu, C.C.; Huang, M.C.; Hsu, Y.C.; Wu, C.T.; Chen, C.K.; Dash, S.; Yu, J.S. Association of urinary ketamine and APOA1 levels with bladder dysfunction in ketamine abusers revealed via proteomics and targeted metabolite analyses. *Sci. Rep.* **2021**, *11*, 9583. [[CrossRef](#)]
55. Wang, G.; Wu, W.W.; Zhang, Z.; Masilamani, S.; Shen, R.F. Decoy methods for assessing false positives and false discovery rates in shotgun proteomics. *Anal. Chem.* **2009**, *81*, 146–159. [[CrossRef](#)]
56. Perez-Riverol, Y.; Csordas, A.; Bai, J.; Bernal-Llinares, M.; Hewapathirana, S.; Kundu, D.J.; Inuganti, A.; Griss, J.; Mayer, G.; Eisenacher, M.; et al. The PRIDE database and related tools and resources in 2019: Improving support for quantification data. *Nucleic Acids Res.* **2019**, *47*, D442–D450. [[CrossRef](#)]



# Electrochemical immunoassay for serum parathyroid hormone using screen-printed carbon electrode and magnetic beads

Pravanjan Malla<sup>a</sup>, Hao-Ping Liao<sup>a</sup>, Chi-Hsien Liu<sup>a,b,c,d,\*</sup>, Wei-Chi Wu<sup>d,e</sup>

<sup>a</sup> Department of Chemical and Materials Engineering, Chang Gung University, 259, Wen-Hwa First Road, Kwei-Shan, Tao-Yuan 333, Taiwan

<sup>b</sup> Research Center for Chinese Herbal Medicine and Research Center for Food and Cosmetic Safety, College of Human Ecology, Chang Gung University of Science and Technology, 261, Wen-Hwa First Road, Taoyuan, Taiwan

<sup>c</sup> Department of Chemical Engineering, Ming Chi University of Technology, 84, Gung-Juan Road, New Taipei City, Taiwan

<sup>d</sup> Department of Ophthalmology, Chang Gung Memorial Hospital, Linkou, 5, Fu-Hsing Street, Taoyuan, Taiwan

<sup>e</sup> College of Medicine, Chang Gung University, 259, Wen-Hwa First Road, Taoyuan, Taiwan

## ARTICLE INFO

### Keywords:

Magnetic beads  
Screen-printed electrode  
Parathyroid hormone

## ABSTRACT

Using magnetic beads (MBs) in electrochemical immunosensors has been shown to improve their sensitivity, reduce analysis time, and minimize reaction volume. The antigen–antibody interaction can be improved with the correct orientation of the antibody using aminophenyl boronic acid (APBA) as the immobilized ligand. In this work, a highly sensitive magneto immunosensor to detect parathyroid hormone (PTH) was reported. The analysis was based on the immobilization of anti-PTH antibodies onto MBs followed by immunocapture, voltammetric and impedimetric assay. We introduce a facile two-step method to detect PTH by using MBs modified by APBA and antibody-peroxidase complex. Immunocapture of PTH by the antibodies takes place on the modified MBs, and the immunocomplexes are separated by a magnet on a screen-printed electrode. Electrochemical detection was performed by measuring the catalytic current and impedance. The APBA coating, antibody-peroxidase ratio, MB characterization, and electrochemical parameters were systematically investigated in this study. The PTH immunosensor exhibited a linear range between 10 and 300 pg mL<sup>-1</sup>, with a limit of detection of 11.56 pg mL<sup>-1</sup> by voltammetry and 49.30 pg mL<sup>-1</sup> by impedance spectroscopy. A magneto immunosensor was successfully prepared by using modified MBs and a disposable electrode, which can be applied to analyze PTH quickly as a point of care device.

## 1. Introduction

Parathyroid hormone (PTH) is an important biomolecule for maintaining calcium and phosphate homeostasis [1]. Radioimmunoassay and immunological assays have been applied to detect PTH using different polyclonal antibodies directed against epitopes within the middle, N-, or C-terminal portion of the intact protein [2]. Such assays have been improved by utilizing two antibodies directed against distinct sequences in PTH because of the cross reactivity with digested hormonal fragments and insufficient sensitivity. However, intact PTH and its truncated fragments have different activities for mineral homeostasis and different clearance rates in patients with cardiovascular disease, chronic kidney diseases, hypoparathyroidism, and hyperparathyroidism [3]. Rapid measurement of PTH levels is frequently needed to confirm that parathyroid adenoma has been successfully removed during surgery [4]. Point-of-care and fragment-specific PTH

assays pave the way for analyzing the concentrations of PTH and its fragments in patients.

Magnetic beads (MBs) have been incorporated in electrochemical sensors for environment [5], biomedical [6], and enzyme assays [7] to improve the detection performance through capture and concentration of the targets. Furthermore, MBs functionalized by antibody, enzyme, or one of their conjugates can directly participate in signal generation, increase the electron transfer rate, and improve the sensitivity, selectivity, and limits of detection. For instance, antibody-modified MBs combined with carbon electrodes have recently been used to detect lactate dehydrogenase from malaria protozoa in blood cells [8]. An immunosensor comprising neutravidin-functionalized MBs and screen-printed carbon electrodes can determine two biomarkers of breast cancer at the same time [9]. However, the orientation of immobilized antibodies on the beads affects their detection capability and sensitivity [10]. Aminophenyl boronic acid (APBA) forms cyclic boro-

\* Corresponding author at: Department of Chemical and Materials Engineering, Chang Gung University, 259, Wen-Hwa First Road, Kwei-Shan, Tao-Yuan 333, Taiwan.  
E-mail address: [CHL@mail.cgu.edu.tw](mailto:CHL@mail.cgu.edu.tw) (C.-H. Liu).

nated esters with 1,2- and 1,3-diols on the carbohydrate moiety of glycoproteins. APBA modified on the nanoparticles has been reported to maintain the correct orientation of antibodies and improve the sensing performance during immunological assays [11]. Screen-printed electrodes (SPEs) have advantages such as mass production, low cost, disposability, sensitivity, and miniaturization [12]. SPEs have been successfully used for quick detection of antibodies and biomarkers in human serum [13,14]. MBs integrated with SPEs enable the rapid detection of biomolecules using only a small volume of sample, minor washing steps, and low detection limits [15].

In this study, antibody-modified MBs were used to capture PTH using the specific affinities. The immunocomplex and MBs can be attracted onto the working electrode of the SPE via an external magnet. Finally, the analytical signal is generated by peroxidase using hydrogen peroxide and hydroquinone as the substrates. We systematically characterized the MBs and SPEs by scanning electron microscopy (SEM), thermogravimetric analysis, and Fourier-transform infrared spectroscopy (FTIR). The performance of these immunosensors was evaluated using electrochemical impedance spectroscopy (EIS) and square wave voltammetry (SWV) to detect serum PTH.

## 2. Experimental

### 2.1. Reagents and materials

Carboxylated MB having size 2–10  $\mu\text{m}$  was purchased from TAN Bead (U-120, Toayuan, Taiwan). Hydroquinone (HQ), 1-Ethyl-3-(3-dimethyl aminopropyl) carbodiimide hydrochloride (EDC), *N*-hydroxy succinimide (NHS), potassium ferricyanide ( $\text{K}_3\text{Fe}(\text{CN})_6$ ), sodium phosphate dibasic ( $\text{Na}_2\text{HPO}_4$ , 99%), sodium phosphate monobasic ( $\text{NaH}_2\text{PO}_4$ ), 3-aminophenyl boronic acid hemisulfate salt (APBA, 95%), polyethylene glycol (PEG, mw:3350), bovine serum albumin, insulin, human immunoglobulin, lysozyme, and L-ascorbic acid were purchased from Sigma-Aldrich (St. Louis, MO, USA). Polyclonal rabbit anti-human PTH antibody (AB51516), and human PTH (AB51234) were from Abcam (MA, USA). Human PTH ELISA kit (SEK13192), anti-PTH capture antibody (Ab) (13192-MM02), anti-PTH detection Ab (13192-T08), and recombinant PTH (aa 32–65, 13192-H09E) were purchased from Sino Biological (Beijing, China). All the chemicals were dissolved in phosphate buffer solution (PBS, 0.1 M, and pH 7.0) in this study. The human serum was collected from male donors within the USA and purchased from Sigma-Aldrich (H4522). Streptavidin conjugated Horseradish peroxidase (HRP) was purchased from the R&D system (Minneapolis, USA). Hydrogen peroxide ( $\text{H}_2\text{O}_2$ , 30%) was purchased from Fluka (MI, USA). All other chemicals were of extra pure analytical grade and used without further purification. All aqueous solutions were prepared using the ultrapure water system (Sartorius Lab instruments GmbH & Co, Gottingen, Germany). Disposable SPEs (TE-100) were purchased from Zensor (Taichung, Taiwan). TE-100 (Fig S6) consists of carbon working electrode ( $0.071\text{ cm}^2$ ), silver pseudo reference electrode ( $0.01\text{ cm}^2$ ) and carbon counter electrode ( $0.05\text{ cm}^2$ ). The detailed information of SPE is available from Zensor website. <https://www.zensor.com.tw/assets/download/Zensor%20R&D%20Technology-4.1%20Screen%20printed%20carbon%20electrode.pdf>.

### 2.2. Apparatus

The modified MBs was investigated using a scanning electron microscope (HITACHI S-4700, Tokyo, Japan) and Zeta Sizer® Nano ZS 90 (Malvern, Worcestershire, UK). Surface functionalization of nanomaterials was characterization by using Fourier transform infrared spectroscopy (FTIR, Alpha, Bruker, Germany). The IR spectra were recorded in the range of  $500\text{--}4000\text{ cm}^{-1}$  with a resolution of  $2\text{ cm}^{-1}$  at room temperature using an attenuated total reflection device. The

spectra of the samples were then processed by Bruker Opus software. Thermogravimetric analysis (TGA) experiments were carried out using a TA Q50 analyser (TA instruments) in nitrogen environment at various heating rates. The electrochemical properties of the SPE were analysed using ECAS 100 Electrochemical Simulator purchased from Zensor. The impedance data were regressed by Zsimpwin software (Amertek, TN, USA) to obtain the charge transfer resistance ( $R_{ct}$ ), the uncompensated solution resistance, and the double-layer capacitance using the equivalent circuit.

### 2.3. Preparation of APBA modified MBs

Following a typical procedure, 200  $\mu\text{L}$  of carboxyl-functionalized MBs ( $0.5\text{ mg mL}^{-1}$ ) was added to a solution containing EDC ( $200\text{ }\mu\text{L}$ ,  $64\text{ mg mL}^{-1}$ ) and NHS ( $200\text{ }\mu\text{L}$ ,  $128\text{ mg mL}^{-1}$ ). It was allowed to vortex for 1 h at room temperature. Then, they were washed twice with 1 mL of 0.1 M PBS and the supernatant was discarded. After that, 200  $\mu\text{L}$  of 0.1% APBA solution was added to the above solution and vortexed for 1 h at room temperature. Separately,  $500\text{ ng mL}^{-1}$  Ab and  $200\times$  of streptavidin-HRP were mixed and incubated for 30 min at  $4^\circ\text{C}$ . The MB-APBA were washed twice with 0.1 M PBS, then 200  $\mu\text{L}$  HRP-Ab solution was added to the MB-APBA and incubated for 30 min at  $4^\circ\text{C}$  to form MB-APBA-HRP-Ab. Then, the MB-APBA-HRP-Ab was further treated in a 5% PEG solution for 30 min to block nonspecific binding sites. The mixture was vortexed for 30 min at room temperature. Subsequently, the MB-APBA-HRP-Ab-PEG was washed twice with 0.1 M PBS (pH 7.0). After the wash and separation, 200  $\mu\text{L}$  serum PTH was added to MB-APBA-HRP-Ab-PEG and incubated for 30 min at room temperature. The separation of modified MBs after each treatment was performed using an external magnet.

### 2.4. Fabrication of the electrochemical immunosensor

The fabrication of the immunosensor is outlined in Fig. 1. First, an SPE was cleaned by sonication with DDW (10 sec), and a magnet was pasted to the backside of the SPE. The magnetic field caused the adsorption of MB-APBA-HRP-Ab-PEG on the surface of the electrode. Then, 5  $\mu\text{L}$  of MB solution was dropped into 200  $\mu\text{L}$  serum PTH for 30 min. After washing with PBS, 95  $\mu\text{L}$  of 5.0 mM of  $\text{H}_2\text{O}_2$  + HQ was added. The SWV and EIS signals were obtained using  $100\text{ pg mL}^{-1}$  serum PTH. The SWV was obtained by applying a potential range of 0.2–0.4 V to the MB-APBA-HRP-Ab-PEG in a deoxygenated 0.1 M PBS containing 5.0 mM of  $\text{H}_2\text{O}_2$  + HQ (optimized) to obtain the catalytic response [16]. After every scan, the electrode was washed with PBS to remove nonspecific conjugation. Finally, the electrochemical signals of the immunosensor were recorded, and PTH was detected based on redox response signals of  $\text{K}_3\text{Fe}(\text{CN})_6$  as the electroactive agent.

### 2.5. Optimization of HRP dilution and antibody concentration

To optimize HRP, different dilutions ( $50\times$ ,  $200\times$ ,  $400\times$ , and  $800\times$ ) were selected to perform the test. The antibody concentration was fixed at  $250\text{ ng mL}^{-1}$ . Then HRP was added to MB-APBA solution and allowed to vortex for 30 min at room temperature. The MB-APBA-HRP-Ab was further incubated in a 5% PEG solution for 30 min to block nonspecific binding sites. After being washed, the MB-APBA-HRP-Ab-PEG resuspended in 100  $\mu\text{L}$  0.1 M PBS. Similarly, to optimize antibodies, different concentrations (100, 250, 500 and  $1000\text{ ng mL}^{-1}$ ) were selected, and optimized HRP dilution from the above test was used. The SWV was obtained using  $100\text{ pg mL}^{-1}$  Serum PTH in this experiment. Each signal was repeated three times ( $n = 3$ ). Based on the signal/blank (S/B) ratio, the optimal concentration was selected. The S/B ratio was calculated using the following formula [17]:

$$\text{S/B ratio} = \Delta I_{100} / \Delta I_0$$



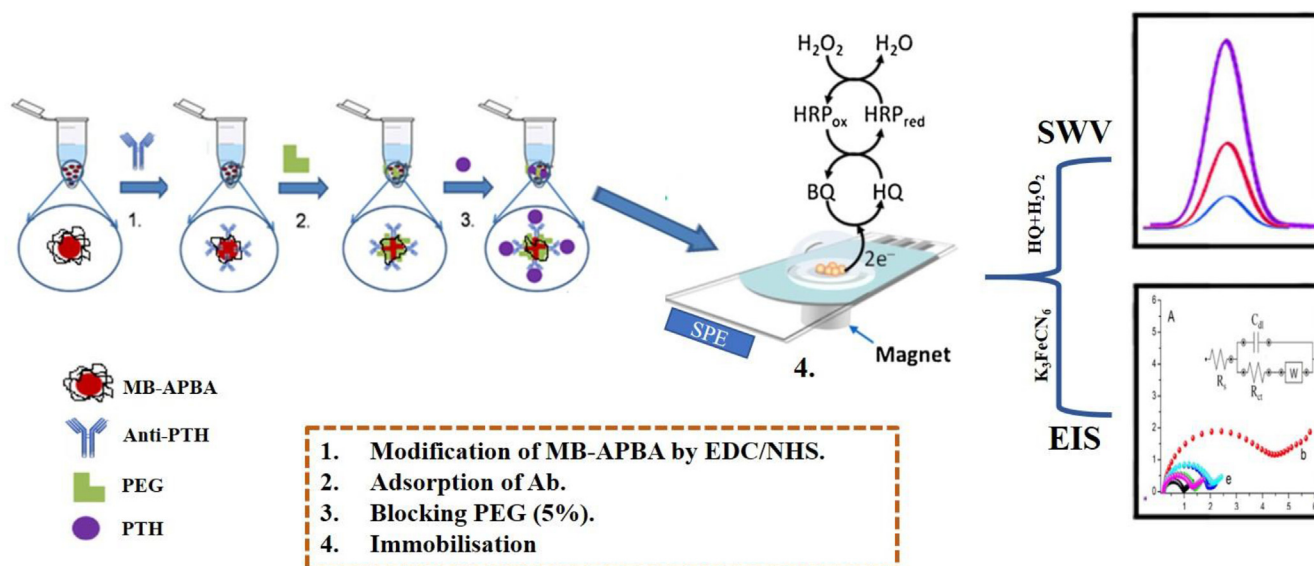


Fig. 1. Schematic diagram showing the fabrication process and the immuno-electrochemical reaction of magneto immunosensor.

$$\Delta I_0 = I_{\text{PBS}} - I_0$$

$$\Delta I_{100} = I_{\text{PBS}} - I_{100}$$

Where  $I_{100}$  is a signal from a serum sample contains 100  $\text{pg mL}^{-1}$  PTH,  $I_0$  is from a serum sample contains no PTH, and  $I_{\text{PBS}}$  is a signal from PBS (control) using MB-APBA-HRP-Ab-PEG.

## 2.6. Optimization of analytical procedure and signal recording

For optimization of HQ and  $\text{H}_2\text{O}_2$ , different concentrations (2, 5, 8, 10 mM) were tested for the experiment. The prepared MB-APBA-HRP-Ab-PEG and MB-APBA-HRP-Ab-PEG-PTH run SWV by using different HQ +  $\text{H}_2\text{O}_2$  concentration. SWV techniques were applied to determine the effects of the PTH dosage on electrochemical signals by using 95  $\mu\text{L}$  of 5 mM HQ +  $\text{H}_2\text{O}_2$  mixture in pH 7.0 PBS. SWV was carried out using the following parameters: initial potential = 200 mV, end potential = -400 mV, increment time = 5 ms, amplitude = 75 mV, sample width = 6 ms, pulse period = 100 ms, pre-potential = 200 mV, pre-time = 5 s, sensitivity =  $10^{-6}$ . EIS was run by 3 mM ferricyanide in PBS with amplitude 100 mV, frequency range 1–1000 Hz, initial potential 50 mV. Histogram of charge transfer resistance of different MBs were studied. Human serum spiked with 100  $\text{pg mL}^{-1}$  of PTH was used. Assays were performed in triplicate and the error bar represented the standard deviation of three repeats. An enzyme-linked immunosorbent assay (ELISA) assay was performed according to the Sino's protocol. The claimed detection range was between 0.3  $\text{ng mL}^{-1}$  and 20  $\text{ng mL}^{-1}$ .

## 2.7. Statistical analysis

The mean and standard deviation (SD) of measurements were calculated by Analysis Toolpak in Microsoft Excel to evaluate the reproducibility of the biosensor. The data are expressed as mean  $\pm$  standard deviation from three repeats ( $n = 3$ ). Limit of detection (LOD) was calculated using the following equation:  $\text{LOD} = 3 \times \text{SD}/m$ ; where  $m$  is the slope of the calibration curve, and SD is from the peak currents of lowest PTH concentration (three runs). Similarly, LOQ was calculated by equation:  $\text{LOQ} = 10 \times \text{SD}/m$  [18].

## 3. Results and discussion

### 3.1. Characterization of modified MBs

The modified MBs were carefully characterized after each modification by SEM imaging. The microscopic images of the modified MBs revealed topological and morphological characteristics. Fig. 2 (A–C) show the micro-scale images of the pure APBA, MB, and MB-APBA. Pure APBA have a typical flake-like surface, seen in Fig. 2(A) MB had an aggregated cluster-like structure as in Fig. 2(B), and MB-APBA had a round shape, as shown in Fig. 2(C). Also, the various sizes and surface charge of the MBs were characterized using Zetasizer. An increased size with a decrease in negative charge indicated conjugation of APBA on the MB surface. The sizes and potential charges of modified MBs are summarized in Table 1. The diameter of MBs increased from 2.3  $\mu\text{m}$  to 4.3  $\mu\text{m}$  after the APBA modification. The zeta potential increased slightly since carboxylic acid was replaced by boronic acid.

To determine the amount of APBA conjugated with MBs, the kinetics of APBA in the EDC/NHS conjugation was analyzed by UV spectroscopy at 233 nm. The APBA standard curve was used to evaluate the amount of APBA reacted. After 60 min, the concentration of APBA declined from 0.69 ppm to 0.19 ppm (Table S1). This indicated that 72.46% of APBA addition (0.73 nmol) reacted with MBs, as shown in Fig. 3(A). The average APBA loading was 0.29 nmol APBA/ $\mu\text{g}$  MBs. The thermal decomposition of MBs modified with APBA was also investigated using TGA. The immobilization of APBA on the magnetic nanoparticles was confirmed, and the oxidation of the APBA on MBs is shown in Fig. 4 (B). The conjugated APBA on MBs had lower initial decomposition temperatures than the original carboxylic acid. TGA results suggested APBA was conjugated on the MBs.

MB-APBA conjugates were characterized by FTIR spectra. The characteristic peak of the B = O stretching mode ( $1340 \text{ cm}^{-1}$ ) and C – N stretching at  $1243 \text{ cm}^{-1}$  gave direct evidence of the successful grafting of boronic acid onto MB surfaces [19]. An absorption band appeared around  $1692 \text{ cm}^{-1}$ , assignable to the C=O symmetric stretching vibration in the carboxyl groups. The significant stretching vibration of the aromatic C=C bond was observed at  $1644 \text{ cm}^{-1}$ , indicating the addition of aromatic compounds. The broad peak at  $3362 \text{ cm}^{-1}$  seen in Fig. 4(A) can be assigned to the OH stretching vibration from the carboxylic acid group [20]. FTIR spectra confirmed that our MB-APBA conjugation was successful.



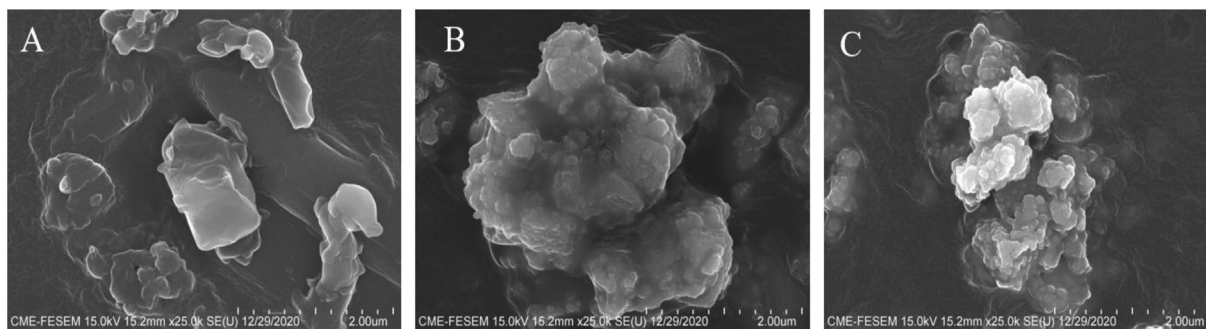


Fig. 2. SEM images of (A) pure APBA, (B) MB, (C) MB-APBA conjugate, with 2.0  $\mu\text{m}$  scale bar.

Table 1

Summary of zeta potential and size of modified magnetic beads.

Sample	Zeta potential (mV)	Size (nm)
MB	$-18.73 \pm 0.61$	$2330 \pm 372$
MB-APBA	$-15.43 \pm 0.11$	$3461 \pm 346$
MB-APBA-HRP-Ab	$-18.40 \pm 0.36$	$4397 \pm 520$

We also performed a tetramethylbenzidine (TMB, HRP substrate) assay to evaluate the capability of MB-APBA for HRP immobilization. Dilution ratios from  $50 \times$  to  $1000 \times$  of HRP were used to test their adsorption on MB-APBA. The standard curve results are shown in Fig. 3(B). The activity was high in the  $50 \times$  dilution, but it gradually decreased as the HRP dosage decreased. The results of HRP activity implied that APBA moiety on MBs was a good ligand for glycoprotein immobilization. Previously, boronic acid has been applied to immobilize antibody on the electrode [21].

### 3.2. Parameter optimization of SWV measurement

SWV alters the electrode potential by using a specific waveform to adjust the decay rates of the charging and faradaic currents. This increased ratio of faradaic to non-faradaic current allows for a lower detection limit and higher sensitivity in reversible and irreversible reactions [17]. The main parameters related to SWV assay were the increment time and pulse period. The S/B ratio was used as the indicator of optimization. Several increment periods of 5, 10, 15, and 20 ms with a fixed pulse period of 100 ms, were evaluated. The antibody ( $250 \text{ ng mL}^{-1}$ ) and  $200 \times$  HRP dilution were fixed for the test. The serum PTH was  $100 \text{ pg mL}^{-1}$  for this experiment. The S/B ratio decreased with increases in increment time, as shown in Fig. 5(A). Based on the S/B ratio, the 5-ms increment was selected for further

experiments. Similarly, several pulse periods (100, 200, 300, 400 ms) were evaluated for SWV assay. The S/B ratio decreased with increases in the pulse period (Fig. 5(B)). The optimization results are summarized in Table S2. Finally, increment time of 5-ms and pulse period of 100-ms were selected for further experiments.

### 3.3. Optimization of antibody and HRP concentration using SWV

A crucial step in signal amplification and detection was the ratio of antibodies to HRP on the MB platform [22]. The orientation and density of the immobilized antibodies on the biosensors impact their assay performance [10]. Thus, the HRP dose and the antibody concentration on APBA modified MBs were both optimized. To optimize HRP, different dilutions ( $50$ ,  $200$ ,  $400$ ,  $800 \times$ ) were used, while the antibody concentration was fixed at  $250 \text{ ng mL}^{-1}$ . The signal current of SWV increased with increases in the HRP fold, as shown in Fig. 6(A). After  $200 \times$  the S/B ratio decreased.  $200 \times$  had higher S/B ratio (1.21), as seen in Table S3. So the optimal concentration  $200 \times$  of HRP was selected for further experiment. Similarly, to optimize the antibody concentration,  $100$ ,  $250$ ,  $500$ , and  $1000 \text{ ng mL}^{-1}$  were used, and the optimal HRP ( $200 \times$ ) was fixed. The S/B ratio of SWV increased with increased antibody concentration, as shown in Fig. 6(B). Based on the S/B ratio, the optimal concentration of antibody ( $250 \text{ ng mL}^{-1}$ ) was selected as it had the highest S/B ratio (Table S3). To improve the total assay time, the incubation times of HRP-Ab were tested. For optimization of incubation time  $10$ ,  $20$ ,  $30$ ,  $60 \text{ min}$  were considered for this test. The optimized HRP-Ab was selected for this test. The SWV signal indicates  $30 \text{ min}$  has higher S/B (1.23) ratio as seen in Fig. S1(A). The optimization process led to an incubation period of  $30 \text{ min}$  for the  $200 \times$  dilution HRP and  $250 \text{ ng mL}^{-1}$  Ab concentration. Similarly, for the optimization of  $\text{HQ} + \text{H}_2\text{O}_2$  concentration  $2$ ,  $5$ ,  $8$ ,  $10 \text{ mM}$  were selected. The current signal increased with  $\text{HQ} + \text{H}_2\text{O}_2$  concentration as seen in Fig. S1(B).  $5 \text{ mM}$  of  $\text{HQ} + \text{H}_2\text{O}$  has high S/B ratio (1.21) as

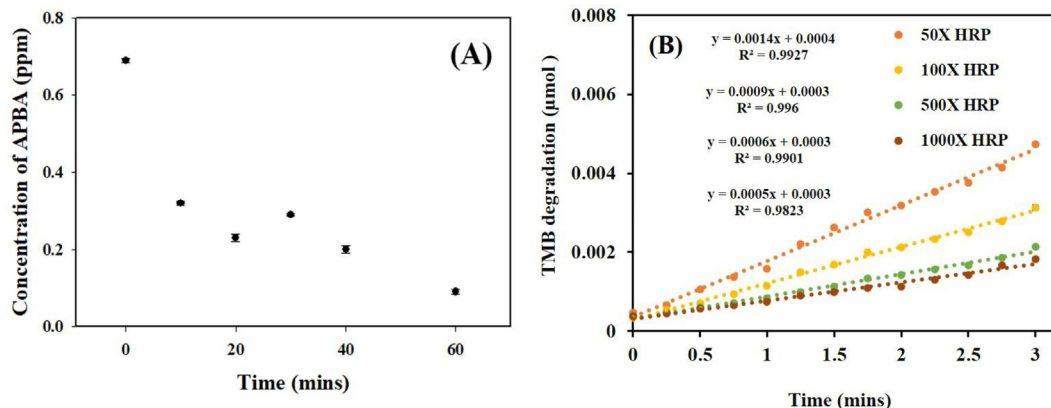


Fig. 3. (A) Amount of APBA adsorbed during conjugation of MB and APBA, (B) TMB assay of different dilution of HRP with MB-APBA.

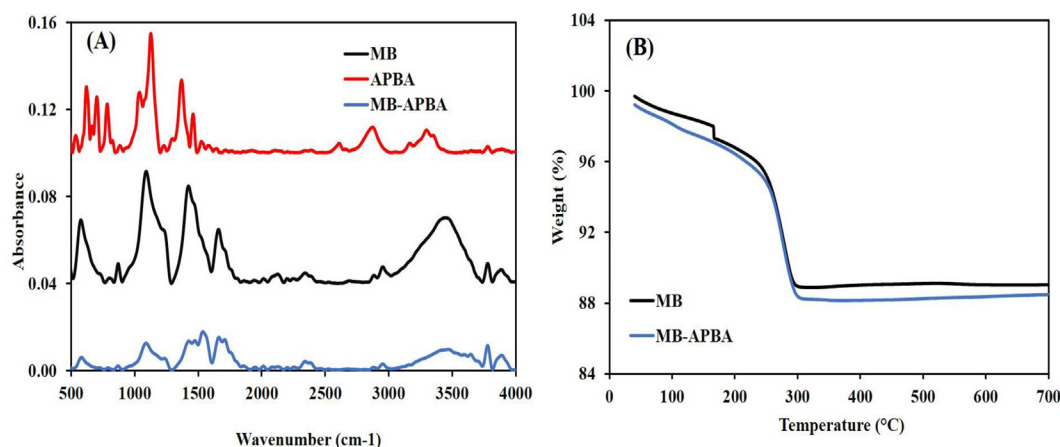


Fig. 4. (A) FTIR characterization, (B) TGA analysis of MB, and MB-APBA.

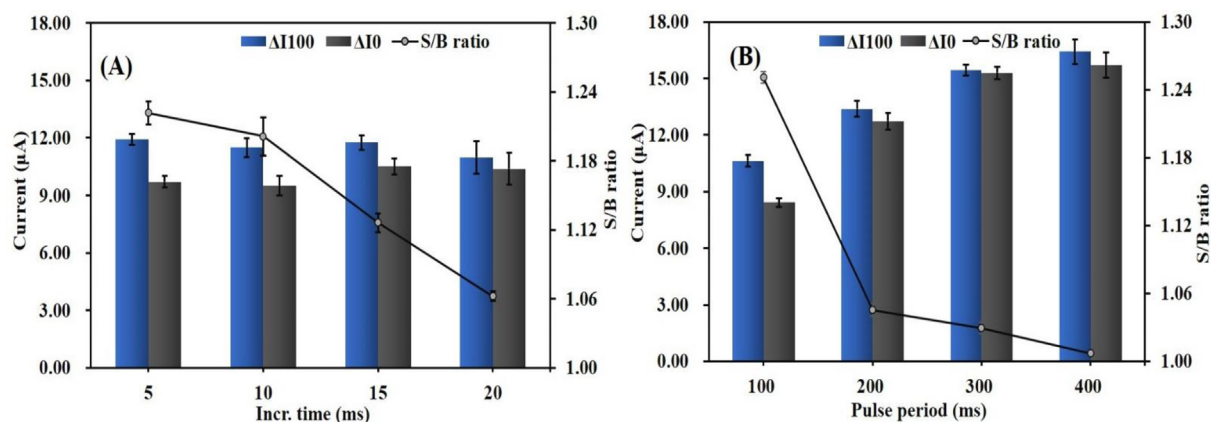


Fig. 5. Parameter optimization of SWV (A) increment time (B) pulse period. The increment range (5–20 ms) and pulse range (100–500 ms) were tested. The SWV signals were obtained using 0 and 100 pg mL<sup>-1</sup> PTH concentrations. ΔI<sub>100</sub> was considered as signal and ΔI<sub>0</sub> was blank. S/B ratio = ΔI<sub>100</sub>/ΔI<sub>0</sub>, n = 3.

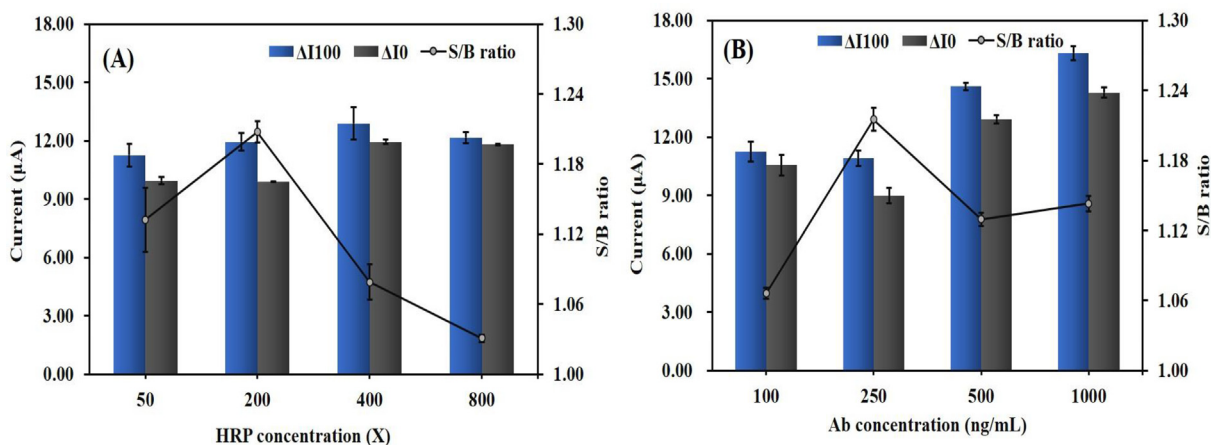


Fig. 6. Optimization of (A) HRP dilution, (B) antibody loading on MB-APBA. SWV was run with amplitude 75 mV, pulse period 100 mV, and potential range (200 mV ~ -400 mV). The antibody concentration 250 ng mL<sup>-1</sup> was selected during the HRP test (6A) and 200 × HRP was selected for Ab-HRP optimization (6B). The SWV signals were obtained using 0 and 100 pg mL<sup>-1</sup> PTH concentrations. ΔI<sub>100</sub> was considered as signal and ΔI<sub>0</sub> was blank. S/B ratio = ΔI<sub>100</sub>/ΔI<sub>0</sub>, n = 3.

mentioned in Table S4. So, 5 mM of HQ + H<sub>2</sub>O<sub>2</sub> was selected as for further test. Amount of MNP loading on SPE play an important role. For this test different volume of MB from 1 to 7 μL were selected. Michaelis Menton equation was used to calculate the K<sub>m</sub> and K<sub>cat</sub> of MBs. The obtained results indicate K<sub>m</sub> and K<sub>cat</sub> value increased with

MNP volume and finally saturate at 5 μL as seen in Fig. S2. The lowest amount of MBs (1 μL) led to the lowest K<sub>m</sub> and K<sub>cat</sub> due to the reduced amount of HRP [23]. The optimized volume of MBs was 5 μL.

Furthermore, in immunoassay protocols where enzyme conjugates are used, the addition of a blocking agent is usually advantageous to

improve the S/B ratio. It also protects the immobilized antibodies, and it avoids nonspecific binding of impurities to MBs. Efficient blocking reagents exhibited lower steric barriers and allowed the recognition of a specific recognition of an analyte at an extremely low concentration [17]. For this purpose, 6 blocking agents were selected for their ability to prevent the nonspecific binding from serum proteins. The chemicals tested included 5% Dextran sulfate, glucose, bovine serum albumin, polyethylene glycol (MW-3350  $\text{g mol}^{-1}$ ), polystyrene sulfonate and polyvinylpyrrolidone. The S/B ratios from SWV and DPV were 6.7 and 5.14 (Fig. S3) using the PTH-spiked human serum. The PEG provided the largest signal (S/B ratio), which was validated by both DPV and SWV methods.

For incubation time of MB with PTH, MBs were incubated with PTH for 10, 20, 30, 60 min. SWV was run with 0 and 100  $\text{pg mL}^{-1}$  of serum PTH. Highest S/B ratio (1.21) was seen in case of 30 min (Fig. S4). So, 30-minute incubation time was selected for adsorption of MB with PTH.

### 3.4. Electrochemical characterization of modified MBs

We characterized the charge transfer process of modified MBs on the SPE using the EIS. The Nyquist plot derived from EIS spectra can be used to investigate the change in resistance and capacitance of the interface, thus providing insights into the effects of surface modification. The results were evaluated by using EIS tests in 3 mM ferricyanide solution in 0.1 M PBS, pH 7.0. Moreover, SWV tests in 5 mM HQ and  $\text{H}_2\text{O}_2$  in 0.1 M PBS, pH 7.0, were performed to test the PTH signal of different MBs in an open circuit. The current modification in the SWVs and the changes in Rct in EIS data after each modification of MBs confirmed the changes effected by that step. Therefore, the SWV showed passivation of the MBs after each modification because of the isolating character of the immobilized molecules (see Fig. 7(A)(B)). The EIS spectra of different modified MBs are shown in Fig. 7(C). The EIS spectra were recorded at an equilibrium potential without external biasing in the frequency range of  $1 \sim 1 \times 10^3$  Hz with a 100 mV amplitude [24]. Bare SPE exhibited the smallest semicircle, with a diameter of 1406  $\Omega$  (blue curve in Fig. 7(C)). This suggested high electron transfer and small impedance. After MB was introduced, the charge resistance increased to 2670  $\Omega$  (orange curve in Fig. 7(C)). This means that the introduction of MB elevated the electron transfer resistance to the redox probe. The Rct of MB-APBA increased significantly, indicating high electron transfer resistance after immobilization with the HRP-Ab complex. The Rct of MB-APBA-HRP-Ab-PEG increased significantly to 7365  $\Omega$  (yellow curve in Fig. 7(C)). This suggests that the rebinding of antibodies occupied the imprinted cavities and hindered the arrival of the redox mediator ferricyanide to the electrode surface [19]. Finally, the MB-APBA-HRP-Ab-PEG combined with SPE was used to analyze the serum PTH in the following sections.

### 3.5. PTH detection using SWV and EIS methods

SWV was the electroanalytical technique applied because of its greater sensitivity [19]. Under optimized conditions, the developed sensor was tested with different concentrations of PTH to direct electrochemical detection, using SWV and the EIS method. The analytical performances of the immunosensor also were determined. The overlapped voltammograms registered in 5 mM HQ and  $\text{H}_2\text{O}_2$  in 0.1 M PBS, pH 7.0, after contacting the MB-APBA-HRP-Ab-PEG for 30 min with PTH solutions of different concentrations, are shown in Fig. 8(A). Each test was performed using the same immunosensor, and a minimum of three tests were effectuated for each PTH concentration. Fig. 8(A) shows that the current peak intensity decreased linearly with the increase in PTH concentration within the dynamic range of  $10 \sim 300 \text{ pg mL}^{-1}$ .

When the concentration of PTH increased, the thickness of immuno-complexes on MBs increased. The non-electroactive complex

was a blocking layer against electron- and mass-transfer to insulate the electron transfer of the redox mediator. The antigen has been proved to decrease the activity of the HRP-labelled antibody on the immunosensor and reduce the current signal [25,26]. The LOD was determined to be  $11.56 \text{ pg mL}^{-1}$ , according to  $3 \times \text{SD/m}$ . The linear regression was expressed ( $I = 5.071 - 0.0117(\text{PTH})$ ,  $R^2 = 0.9912$ ) with a relative standard deviation (RSD) of 5% and a sensitivity of  $0.0117 \mu\text{A pg}^{-1} \text{ mL}$ . A minimum of three tests were performed for each concentration included in the calibration plot, and the average current intensity was used to plot the calibration chart (Fig. 8(B)). RSD and LOD values were calculated based on a previous report [22].

EIS, an effective method for probing the features of a surface-modified electrode, was employed to monitor the stepwise construction of magneto immunosensors. Fig. 8(C) illustrates the Nyquist diagrams of different concentrations of PTH, which were conducted in pH 7.0 PBS containing 3 mM ferricyanide at frequencies from 1 to  $1 \times 10^3$  Hz. In this study, the dose-dependent EIS responses from the serum PTH were recorded using the modified beads and SPE, where an increase in the Rct values was observed on an increase in PTH concentrations. This can be ascribed to the formation of the antigen-antibody complex, which insulated HRP from the contact of the redox probe and hindered the transfer of electrons to the electrode [25,26]. The Rct of the immunosensors had a linear relationship with the PTH dosage ( $10\text{--}300 \text{ pg mL}^{-1}$ ) spiked in the serum (Fig. 8(D)). The recovery rates are indicated in Table 2. The linear regression was expressed as  $R_{\text{ct}} = 26.357 \text{ PTH} + 8225.6$ ,  $R^2 = 0.9949$ . The LOD also was determined to be  $49.30 \text{ pg mL}^{-1}$ , according to  $3 \times \text{SD/m}$ . The developed immunosensor can be considered a versatile, reliable, and accurate tool for screening PTH in clinical samples.

### 3.6. Interference test

To study the selectivity of the fabricated immunosensors, human serum spiked with  $100 \text{ pg mL}^{-1}$  of PTH was evaluated in the presence of potentially interfering compounds such as insulin, lysozyme, vitamin C, immunoglobulin, serum albumin, lactic acid and ovalbumin at a concentration of  $1 \text{ mg mL}^{-1}$  [6,17]. These potentially interfering species had almost no influence on the current response of PTH (the signal change was below 5%). This indicated that the immunosensor possesses excellent selectivity toward PTH. PTH sensing was not affected by the tested proteins or small molecules. Only upon incubation of the immunosensor with PTH-containing samples did the S/B signal of the sensor present a distinct increase (Fig. 9).

### 3.7. Storage and stability test

The storage of immunosensors has been report to affect their precision and electrochemical response [34]. The modified MBs were stored at  $4^\circ\text{C}$  for 35 days, and the PTH sensing activity was assessed every 7 days. The storage stability of the fabricated immunosensors was evaluated based on the peak current of SWV using  $100 \text{ pg mL}^{-1}$  of PTH on the first day as 100%. Under  $4^\circ\text{C}$  storage after 35 days, the PTH sensing ability was maintained, as indicated in Fig. 10. Most of the results after storage were similar to the day-1 measurements. The relative standard deviations of all measurements were within 8%. After being stored in a refrigerator for four weeks, the MBs retained about 95% of their original response, meaning good storage stability. The activity and targeting of antibody-peroxidase on MBs could be retained after a 35-day storage for PTH measurements, suggesting that the sensor had good stability.

The comparison of the published immunosensors for PTH is summarized in Table 3, as reported in the literature. These reported immunosensors adopt the electrochemiluminescence (ECL), EIS, DPV, SWV, and CV methods to quantify the PTH concentration. For instance, the polydopamine modified nanoparticles integrated with the carbon electrode were designed for PTH detection, which having

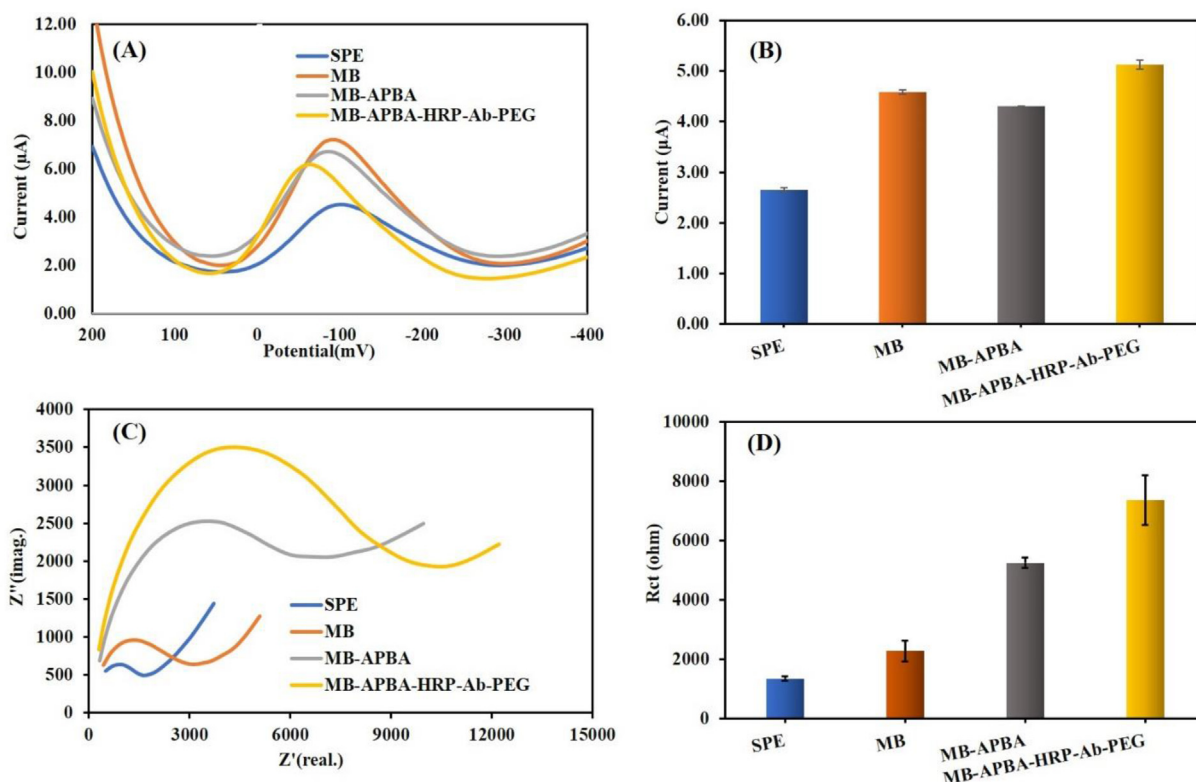


**Fig. 7.** (A) SWV currents of different MBs in the potential range (200 mV ~ -400 mV), (B) histogram of SWV peak current using different MBs, (C) Impedance spectra of different MBs on bare SPEs (D) histogram of charge transfer resistance using different MBs. SWV was run with amplitude 75 mV, pulse period 100 mV, and potential range (200 mV ~ -400 mV) using 5 mM HQ + H<sub>2</sub>O<sub>2</sub>. Nyquist plots recorded on bare SPEs by 3 mM ferricyanide in PBS with amplitude 100 mV, frequency range 1 ~ 1000 Hz, initial potential 50 mV. Human serum spiked with 100 pg mL<sup>-1</sup> of PTH was used. n = 3.

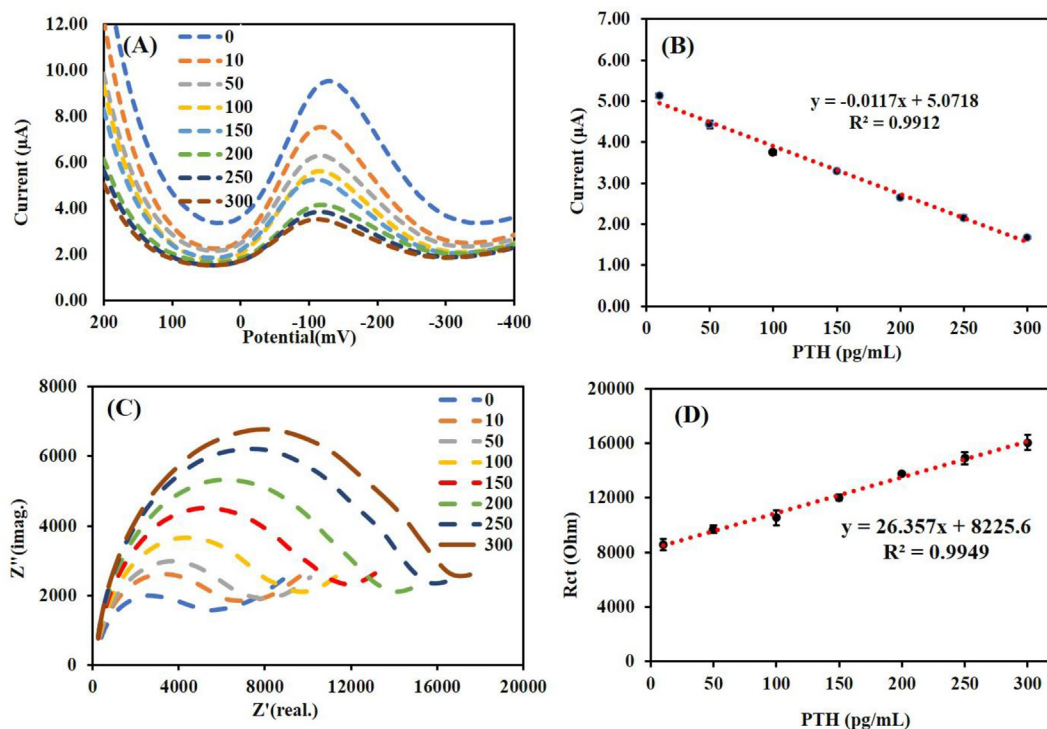


**Fig. 8.** (A) SWV responses of the proposed immunosensor in different concentrations of PTH in 0.1 M pH 7.0 PBS containing 5 mM HQ + H<sub>2</sub>O<sub>2</sub>, scanning from 200 mV to -400 mV with an amplitude of 75 mV s<sup>-1</sup>, pulse period of 100 ms and (B) Calibration curve for PTH determination. (C) Nyquist curves recorded in a solution of 0.1 M PBS containing 3 mM ferricyanide with applied potential was 0.05 V at the frequency range of 1–1000 Hz and (D) EIS standard curve of PTH. n = 3.



**Table 2**

Comparison of recovery of PTH by ELISA, SWV, and EIS methods.

PTH(pg mL <sup>-1</sup> )	ELISA found (pg mL <sup>-1</sup> )	Recovery (%)	SWV found(pg mL <sup>-1</sup> )	Recovery (%)	EIS found(pg mL <sup>-1</sup> )	Recovery (%)
50	42.82	85.64	54.85	109.71	55.61	111.22
100	89.49	89.49	112.69	112.69	87.81	87.81
150	158.60	105.73	151.72	101.15	143.46	95.64
200	207.04	103.52	206.42	103.21	209.73	104.86
250	242.16	96.86	248.30	99.32	253.23	101.29
300	306.16	102.05	290.18	96.73	297.12	99.04

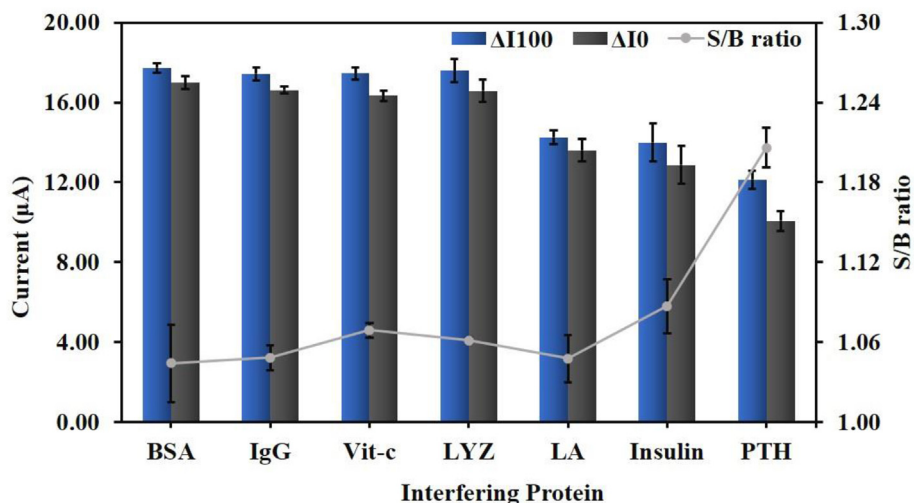


**Fig. 9.** SWV histogram of the fabricated immunosensor (MB-APBA-HRP-Ab-PEG) under the interfering compounds at 1 mg mL<sup>-1</sup>. The tested PTH concentration in human serum was 100 pg mL<sup>-1</sup>. n = 3.

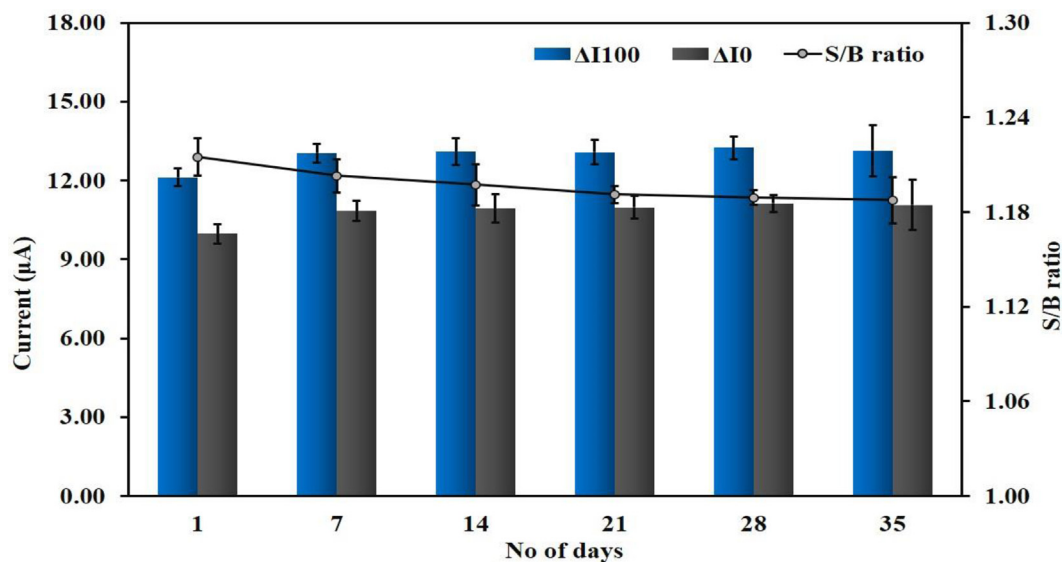


**Fig. 10.** Stability test of the immunosensor after a 28-day storage at 4 °C. SWV was run with amplitude 75 mV, pulse period 100 mV, and initial potential (200 mV ~ -400 mV) using 5 mM HQ + H<sub>2</sub>O<sub>2</sub>. The tested PTH concentration was 100 pg mL<sup>-1</sup>.

a linear response within 0.05–8 ng/mL by ECL technique [30]. The Au-Pt hybrid disk electrode maintains its performance of PTH detection for only a 10-day storage [35]. Dittmer et al. choose the magneto-resistive silicon chips and MBs combined the magnetic actuation technique to detect PTH. They measure the lowest PTH concentration (10 pM) using magnetic forces of MBs induced by electromagnets above and

below the sensor chip in a 15-minute assay [33]. In this study, we reported for the first time that the antibody-modified MBs combined with SPE to electrochemically analyze serum PTH (2.4 pM) with high efficiency in 30 min. The proposed immunosensor could detect PTH in serum using both SWV and EIS methods, in performance that was fast and precise. The specificity and sensitivity of detection of this



**Table 3**

Comparison different PTH immunosensors in literature.

Nanomaterials/Electrode used	Method*	Linear range(pg mL <sup>-1</sup> )	LOD(pg mL <sup>-1</sup> )	Reference
Ag, avidin, BSA-modified ITO electrode	Chronocoulogram	0.1–100	0.1	[27]
Au-Pt hybrid disk electrode	DPV	1–10000	0.36	[28]
AuNP/MWCNT/SPE	SWV, DPV	1–1000	0.065, 0.886	[17]
MoS <sub>2</sub> -graphene composite	EIS	1–50	5	[29]
MWCNT-AuNP Nanocomposite	CV, EIS	1–100000	0.092, 0.033	[6]
Glassy carbon electrode	ECL	50–8000	17	[30]
Au/MOH/APTES/Anti-PTH/BSA	EIS	10–50	7.65	[31]
disposable ITO-PET	CV, EIS	0.001–2.5	0.89	[32]
MB/ silicon chip	Magnetic actuation	94–9400	–	[33]
MB-APBA-HRP-Ab-PE-PTH/SPE	SWV, EIS	10 ~ 300	11.56, 49.30	This work

\*Cyclic voltammetry (CV), Differential pulse voltammetry (DPV), Electrochemiluminescence(ECL)

immunosensor could apply to physiological conditions, and it has good repeatability. This biosensor has advantages such as being fast, low-cost, sensitive, and suitable for on-site testing.

### 3.8. Electron transfer rate constant of MB-APBA-HRP-Ab

Cyclic voltammograms (CV) of MB-APBA-HRP-Ab on SPE and the plain SPE using different scan rates are shown in Fig. S5(A). The symmetric peaks of CV Fig. S5 (A) (B) indicated a reversible electrochemical reaction. The scan rate of voltammetry can be used to evaluate the charge transfer process involved in the electrode electrolyte interface. The square root of the scan rate was plotted against the peak current in Fig. S5 (C) based on Randles-Sevcik equation  $I_p = [0.4463 (n^3 F^3 D_0 / RT)^{1/2} A C] v^{1/2}$ . The addition of MBs could increase the slope from 69.5 to 83.4, which might be due to the increase of surface area (A). This reversible behaviour indicated the fast kinetics of electron transfer using redox-active ferricyanide on the electrode [17].

To investigate the charge transfer process, the electron transfer rate constant (Ks, cm s<sup>-1</sup>) of the quasi-reversible system was estimated by the Nicholson method [36]. CV scanning was performed over a potential range from - 500 to + 600 mV at different scan rates varying from 10 to 100 mV s<sup>-1</sup> using 3 mM ferricyanide in PBS. The calculation of Ks by CV data was based on the Nicholson equation:  $\Psi = Ks [\pi D n v F / (RT)]^{-1/2}$

where  $\Psi$ , a dynamic parameter, is a function of potential difference ( $\Delta E_p$ ); D is the diffusion coefficient; n is the number of electrons transferred in the reaction; F is the Faraday constant; v is the scanning rate; R is the gas constant; and T is the temperature in Kelvin. As known, the variations in oxidation and reduction peak currents in CV related with different electrode surfaces can be theoretically attributed to electron transfer rates or charge transfer resistances [37,38]. The Ks of plane SPE (without MB) was 0.0025 cm s<sup>-1</sup> whereas in presence of MB on SPE surface the Ks slightly reduced to 0.0022 cm s<sup>-1</sup>. These data including the linear relationship of (scan rate<sup>1/2</sup>) versus current and the symmetric CV indicated the improvement and robustness of the developed immunosensors.

## 4. Conclusion

A magneto immunosensor was successfully prepared by using modified MBs and SPEs. Both voltammetric and impedimetric methods were performed, and their assays using spiked serum PTH were evaluated. We provided evidence of the rapid analysis of serum PTH, which has the potential to be applied for clinical assays. The advantages of the developed PTH immunosensor include easy immobilization, low cost, a disposable electrode, label-free detection, and detection within a few minutes in contrast to the expensive instruments used in hospitals. The developed immunosensors showed good stability and reproducibility, and the detection limits of serum PTH were 11.56 pg mL<sup>-1</sup> and 49.30 pg mL<sup>-1</sup>, using the SWV and EIS methods.

## CRediT authorship contribution statement

**Pravanjan Malla:** Data curation, Formal analysis, Software, Writing - original draft, Validation, Visualization. **Hao-Ping Liao:** Data curation, Formal analysis, Software. **Chi-Hsien Liu:** Conceptualization, Funding acquisition, Investigation, Methodology, Project administration, Resources, Supervision, Writing - original draft, Writing - review & editing. **Wei-Chi Wu:** Funding acquisition, Resources, Writing - review & editing.

## Declaration of Competing Interest

The authors declare that they have no known competing financial interests or personal relationships that could have appeared to influence the work reported in this paper.

## Acknowledgements

We express gratitude to Ministry of Science and Technology (MOST 108-2221-E-182-039), Chang Gung University (BMRP 758) and Chang Gung Memorial Hospital (2 J0161, 2 J0162, 2H0072, 2H0073) for funding and supporting this research. We appreciate the critical comments from Prof. Purnendu Parhi at Ravenshaw University, India.

## Appendix A. Supplementary data

Supplementary data to this article can be found online at <https://doi.org/10.1016/j.jelechem.2021.115463>.

## References

- [1] C. Goettsch, H. Iwata, E. Aikawa, Parathyroid hormone: Critical bridge between bone metabolism and cardiovascular disease, *Arterioscler. Thromb. Vasc. Biol.* 34 (7) (2014) 1333–1335.
- [2] S.E. Rodgers, J.I. Lew, The Parathyroid Hormone Assay, *Endocrine Practice* 17 (2011) 2–6.
- [3] J.-C. Souberbielle, F. Brazier, M.-L. Piketty, C. Cormier, S. Minisola, E. Cavalier, How the reference values for serum parathyroid hormone concentration are (or should be) established?, *J. Endocrinol. Invest.* 40 (3) (2017) 241–256.
- [4] L.J. Sokoll, F.H. Wians Jr, A.T. Remaley, Rapid intraoperative immunoassay of parathyroid hormone and other hormones: A new paradigm for point-of-care testing, *Clin. Chem.* 50 (7) (2004) 1126–1135.
- [5] F.L. Rivera, F.J. Recio, F.J. Palomares, J. Sánchez-Marcos, N. Menéndez, E. Mazarío, P. Herrasti, Fenton-like degradation enhancement of methylene blue dye with magnetic heating induction, *J. Electroanal. Chem.* 879 (2020) 114773.
- [6] P. Malla, G.C. Chen, H.P. Liao, C.H. Liu, W.C. Wu, Label-free parathyroid hormone immunosensor using nanocomposite modified carbon electrode, *J. Electroanal. Chem.* 880 (2021) 114917.
- [7] R.H. Xu, X.J. Chen, J. Chen, R.P. Liang, J.D. Qiu, Electrochemical assay of protein kinase activity based on the Fe3O4@PNE-Ti4+ functionalized PDMS microchip, *J. Electroanal. Chem.* 877 (2020) 114645.
- [8] G. Ruiz-Vega, K. Arias-Alpizar, E. de la Serna, L.N. Borgheti-Cardoso, E. Sulleiro, I. Molina, X. Fernández-Busquets, A. Sánchez-Montalvá, F.J. del Campo, E. Baldrich, Electrochemical POC device for fast malaria quantitative diagnosis in whole blood by using magnetic beads, Poly-HRP and microfluidic paper electrodes, *Biosensors and Bioelectronics* 150 (2020) 111925.

- [9] A. Valverde, V. Serafin, J. Garoz, A. Montero-Calle, A. González-Cortés, M. Arenas, J. Camps, R. Barderas, P. Yáñez-Sedeño, S. Campuzano, J.M. Pingarrón, Electrochemical immunoplatfrom to improve the reliability of breast cancer diagnosis through the simultaneous determination of RANKL and TNF in serum, *Sens. Actuators, B* 314 (2020) 128096, <https://doi.org/10.1016/j.snb.2020.128096>.
- [10] A.K. Trilling, J. Beekwilder, H. Zuilhof, Antibody orientation on biosensor surfaces: A minireview, *Analyst* 138 (6) (2013) 1619–1627.
- [11] E.A. Andreev, M.A. Komkova, V.N. Nikitina, A.A. Karyakin, Reagentless Impedimetric Sensors Based on Aminophenylboronic Acids, *J. Anal. Chem.* 74 (2) (2019) 153–171.
- [12] N.-B. Mincu, V. Lazar, D. Stan, C.M. Mihailescu, R. Iosub, A.L. Mateescu, Screen-Printed Electrodes (SPE) for In Vitro Diagnostic Purpose, *Diagnostics* 10 (8) (2020) 517.
- [13] H. Ehzari, M. Samimi, M. Safari, M.B. Gholivand, Label-free electrochemical immunosensor for sensitive HER2 biomarker detection using the core-shell magnetic metal-organic frameworks, *J. Electroanal. Chem.* 877 (2020) 114722.
- [14] S. Wei, H. Xiao, M. Gu, Z. Chen, L. Cao, Ultrasensitive label-free electrochemical immunosensor based on core-shell Au@PtNPs functionalized rGO-TEPA/PB nanocomposite for HBsAg detection, *J. Electroanal. Chem.* 890 (2021) 115216.
- [15] Z. Farka, T. Jurófk, D. Kováro, L. Trnková, P. Skládal, Nanoparticle-Based Immunochemical Biosensors and Assays: Recent Advances and Challenges, *Chem. Rev.* 117 (15) (2017) 9973–10042.
- [16] P. Chandra, H.-B. Noh, R. Pallela, Y.-B. Shim, Ultrasensitive detection of drug resistant cancer cells in biological matrixes using an amperometric nanobiosensor, *Biosens. Bioelectron.* 70 (2015) 418–425.
- [17] G.-C. Chen, C.-H. Liu, W.-C. Wu, Electrochemical immunosensor for serum parathyroid hormone using voltammetric techniques and a portable simulator, *Anal. Chim. Acta* 1143 (2021) 84–92.
- [18] Ü. Şengül, Comparing determination methods of detection and quantification limits for aflatoxin analysis in hazelnut, *J. Food Drug Anal.* 24 (1) (2016) 56–62.
- [19] J. Huang, Y. Wu, J. Cong, J. Luo, X. Liu, Selective and sensitive glycoprotein detection via a biomimetic electrochemical sensor based on surface molecular imprinting and boronate-modified reduced graphene oxide, *Sens. Actuators, B* 259 (2018) 1–9.
- [20] F. Mollarasouli, V. Serafin, S. Campuzano, P. Yáñez-Sedeño, J.M. Pingarrón, K. Asadpour-Zeynali, Ultrasensitive determination of receptor tyrosine kinase with a label-free electrochemical immunosensor using graphene quantum dots-modified screen-printed electrodes, *Anal. Chim. Acta* 1011 (2018) 28–34.
- [21] J.-A. Ho, W.-L. Hsu, W.-C. Liao, J.-K. Chiu, M.-L. Chen, H.-C. Chang, C.-C. Li, Ultrasensitive electrochemical detection of biotin using electrically addressable site-oriented antibody immobilization approach via aminophenyl boronic acid, *Biosens. Bioelectron.* 26 (3) (2010) 1021–1027.
- [22] A. Adumitrăchioaie, M. Tertiş, M. Suci, F. Graur, C. Cristea, A novel immunosensing platform for serotonin detection in complex real samples based on graphene oxide and chitosan, *Electrochim. Acta* 311 (2019) 50–61.
- [23] M. Freitas, H.P.A. Nouws, E. Keating, C. Delerue-Matos, High-performance electrochemical immunomagnetic assay for breast cancer analysis, *Sens. Actuators, B* 308 (2020) 127667.
- [24] X. Li, M. Yu, Z. Chen, X. Lin, Q. Wu, A sensor for detection of carcinoembryonic antigen based on the polyaniline-Au nanoparticles and gap-based interdigitated electrode, *Sens. Actuators, B* 239 (2017) 874–882.
- [25] J. Chen, J. Tang, F. Yan, H. Ju, A gold nanoparticles/sol-gel composite architecture for encapsulation of immunoconjugate for reagentless electrochemical immunoassay, *Biomaterials* 27 (10) (2006) 2313–2321.
- [26] F. Zhu, G. Zhao, W. Dou, Voltammetric sandwich immunoassay for Cronobacter sakazakii using a screen-printed carbon electrode modified with horseradish peroxidase, reduced graphene oxide, thionine and gold nanoparticles, *Mikrochim Acta* 185 (1) (2017) 45.
- [27] A. Bhatia, P. Nandhakumar, G. Kim, J. Kim, N.-S. Lee, Y.H. Yoon, H. Yang, Ultrasensitive Detection of Parathyroid Hormone through Fast Silver Deposition Induced by Enzymatic Nitroso Reduction and Redox Cycling, *ACS Sensors* 4 (6) (2019) 1641–1647.
- [28] H.M. Özcan, K. Yildiz, C. Çakar, T. Aydin, E. Asav, A. Sağiroğlu, M.K. Sezgintürk, Ultrasensitive impedimetric biosensor fabricated by a new immobilisation technique for parathyroid hormone, *Appl. Biochem. Biotechnol.* 176 (5) (2015) 1251–1262.
- [29] H.U. Kim, H.Y. Kim, A. Kulkarni, C. Ahn, Y. Jin, Y. Kim, K.N. Lee, M.H. Lee, T. Kim, A sensitive electrochemical sensor for in vitro detection of parathyroid hormone based on a MoS<sub>2</sub>-graphene composite, *Sci. Rep.* 6 (2016) 34587.
- [30] S. Li, Y. Liu, Q. Ma, A novel polydopamine electrochemiluminescence organic nanoparticle-based biosensor for parathyroid hormone detection, *Talanta* 202 (2019) 540–545.
- [31] Ç. Sayıklı Şimşek, M. Nur Sonuç Karaboğa, M.K. Sezgintürk, A new immobilization procedure for development of an electrochemical immunosensor for parathyroid hormone detection based on gold electrodes modified with 6-mercaptohexanol and silane, *Talanta* 144 (2015) 210–218.
- [32] B. Özcan, M.A. Hanbaba, M. Kemal Sezgintürk, Ultra-sensitive detection of parathyroid hormone in human serum: a cheap and practical biosensing platform modified by an epoxy ended-silane agent, *Int. J. Environ. Anal. Chem.* 100 (4) (2020) 393–407.
- [33] W.U. Dittmer, P. de Kievit, M.W.J. Prins, J.L.M. Vissers, M.E.C. Mersch, M.F.W.C. Martens, Sensitive and rapid immunoassay for parathyroid hormone using magnetic particle labels and magnetic actuation, *J. Immunol. Methods* 338 (1–2) (2008) 40–46.
- [34] M. Pohanka, Screen Printed Electrodes in Biosensors and Bioassays, A Review, *International Journal of Electrochemical Science* 15 (11) (2020) 11024–11035.
- [35] A.K. Yagati, A. Go, S.G. Chavan, C. Baek, M.-H. Lee, J. Min, Nanostructured Au-Pt hybrid disk electrodes for enhanced parathyroid hormone detection in human serum, *Bioelectrochemistry* 128 (2019) 165–174.
- [36] P. Malla, G.-C. Chen, H.-P. Liao, C.-H. Liu, W.-C. Wu, Label-free parathyroid hormone immunosensor using nanocomposite modified carbon electrode, *J. Electroanal. Chem.* 880 (2021) 114917, <https://doi.org/10.1016/j.jelechem.2020.114917>.
- [37] I.-S. Park N. Kim 13 10 1998 1091 1097
- [38] I. Markovich, D. Mandler, The effect of an alkylsilane monolayer on an indium tin oxide surface on the electrochemistry of hexacyanoferrate, *J. Electroanal. Chem.* 484 (2) (2000) 194–202.



Review

# Photosensitizer-Functionalized Nanocomposites for Light-Activated Cancer Theranostics

Banendu Sunder Dash <sup>1</sup> , Suprava Das <sup>1</sup> and Jyh-Ping Chen <sup>1,2,3,4,\*</sup>

<sup>1</sup> Department of Chemical and Materials Engineering, Chang Gung University, Kwei-San, Taoyuan 33302, Taiwan; banendusunder@gmail.com (B.S.D.); supravadas0603@gmail.com (S.D.)

<sup>2</sup> Craniofacial Research Center, Department of Plastic and Reconstructive Surgery, Chang Gung Memorial Hospital, Linkou, Kwei-San, Taoyuan 33305, Taiwan

<sup>3</sup> Research Center for Food and Cosmetic Safety, Research Center for Chinese Herbal Medicine, College of Human Ecology, Chang Gung University of Science and Technology, Taoyuan 33305, Taiwan

<sup>4</sup> Department of Materials Engineering, Ming Chi University of Technology, Tai-Shan, New Taipei City 24301, Taiwan

\* Correspondence: jpchen@mail.cgu.edu.tw; Tel.: +886-3-2118800

**Abstract:** Photosensitizers (PSs) have received significant attention recently in cancer treatment due to its theranostic capability for imaging and phototherapy. These PSs are highly responsive to light source of a suitable wavelength for image-guided cancer therapy from generated singlet oxygen and/or thermal heat. Various organic dye PSs show tremendous attenuation of tumor cells during cancer treatment. Among them, porphyrin and chlorophyll-based ultraviolet-visible (UV-Vis) dyes are employed for photodynamic therapy (PDT) by reactive oxygen species (ROS) and free radicals generated with 400–700 nm laser lights, which have poor tissue penetration depth. To enhance the efficacy of PDT, other light sources such as red light laser and X-ray have been suggested; nonetheless, it is still a challenging task to improve the light penetration depth for deep tumor treatment. To overcome this deficiency, near infrared (NIR) (700–900 nm) PSs, indocyanine green (ICG), and its derivatives like IR780, IR806 and IR820, have been introduced for imaging and phototherapy. These NIR PSs have been used in various cancer treatment modality by combining photothermal therapy (PTT) and/or PDT with chemotherapy or immunotherapy. In this review, we will focus on the use of different PSs showing photothermal/photodynamic response to UV-Vis or NIR-Vis light. The emphasis is a comprehensive review of recent smart design of PS-loaded nanocomposites for targeted delivery of PSs in light-activated combination cancer therapy.

**Keywords:** photosensitizer; cancer therapy; nanocomposite; photodynamic therapy; photothermal therapy



**Citation:** Dash, B.S.; Das, S.; Chen, J.-P. Photosensitizer-Functionalized Nanocomposites for Light-Activated Cancer Theranostics. *Int. J. Mol. Sci.* **2021**, *22*, 6658. <https://doi.org/10.3390/ijms22136658>

Academic Editors: M. Sheikh Mohamed and Toru Maekawa

Received: 2 June 2021

Accepted: 17 June 2021

Published: 22 June 2021

**Publisher's Note:** MDPI stays neutral with regard to jurisdictional claims in published maps and institutional affiliations.



**Copyright:** © 2021 by the authors. Licensee MDPI, Basel, Switzerland. This article is an open access article distributed under the terms and conditions of the Creative Commons Attribution (CC BY) license (<https://creativecommons.org/licenses/by/4.0/>).

## 1. Introduction

Photosensitizers (PSs) have been used as light-responsive drugs with their imaging capabilities, easy synthesis, tunable energy levels, and biocompatibility, which make them an innovative tool for therapeutic approaches in treatment of various cancers [1–7]. Among different methods for cancer therapy, photodynamic therapy (PDT) using a PS can take advantage of penetrated light into a targeted tissue for improving tumor control. The PDT comprises of three major components; PS, oxygen, and light source of appropriate wavelength [8], which when act together, generate a photochemical reaction. Depending on the part of the body being treated, the photosensitizing agent is either administered into the bloodstream through a vein or placed directly on the skin. By irradiation light on the targeted area, the excited PS emits energy in the form of heat and exhibits intersystem crossing (ISC), leading to the formation of reactive oxygen species (ROS) in triplet state [9].

The mechanism of killing cancer cells by activating PS with light has been revealed to be composed of three major mechanisms, apoptotic, autophagy, and necrotic cell death.

The PSs for PDT could be classified into two categories, non-porphyrinoid based PSs (first generation PSs) and porphyrinoid based PSs (second generation PSs). The non-porphyrinoid PSs were limited by requiring the use of shorter wavelength (<630 nm) light source [10]. A complex mixtures of PSs may demand confinement of the treated patient in the dark to avoid skin photosensitization [11]. Photofrin is the most commonly used commercially available PS approved by the U.S. Food and Drug Administration (FDA), a hematoporphyrin derivative belonging to the porphyrin family. In 1841, Scherer introduced hematoporphyrin [12] and the observation of porphyrin fluorescence from treated tumors was published by Policard in 1924 [13]. The first generation compounds also have the demerits of suboptimal tumor selectivity, tumoricidal depth [14], and being a complex mixture of uncertain compounds [15]. The second generation PSs is purer in a chemical sense and offer high quantum yields for the triplet state generation and ROS formation. A group led by Hasan has done a significant number of studies relating to the combination of PDT with other forms of cancer treatment methods [16,17]. Though it is very hard to anticipate the efficacy of both types of PSs, the second generation PSs have still been found to be more reliable in complex biological environments.

For effective implementation, the uptake of PSs in cancer cells and their retention in cancer cells have been studied, including mechanism of tumor response and temperature sensitivity throughout the treatment period. Two of the main advantages of second generation PSs are the intense absorption in the red light wavelength and limited skin photosensitization. Graphene-based nanomaterials are good photothermal agents for photothermal therapy (PTT) [18]. However, for intracellular imaging, they need to be labeled with various fluorescein dyes like fluorescein isothiocyanate (FITC), quantum dots, and cyanine 5 (Cy 5) [19,20]. As PSs, near infrared (NIR) dyes not only could be used for fluorescence imaging but also could be a suitable tool for PDT/PTT. Various NIR organic dyes are endowed with photodynamic properties and show promising results in PDT-based cancer treatment [21–23]. Compared with ultraviolet-visible (UV-Vis) dyes for imaging and PDT, the ICG derivatives show deep tissue penetration depth, useful for imaging as well as for PTT/PDT with their good photothermal conversion upon NIR light activation [24–27]. This review provides up-to-date discussion about applications of different types of UV-Vis and NIR-activated PSs in a nanocomposite form for cancer therapy. The advantages and disadvantages of using these PSs for tumor destruction, which is directly related to their cancer treatment efficacy, are described. In addition, we aim to discuss the benefits of using PSs for PTT and/or PDT, while combining with other cancer therapeutic agents for combination cancer therapy.

## 2. Functions of Photosensitizers (PSs)

### 2.1. Imaging

Through multimodal imaging techniques to determine the response during PDT, signals recorded during light irradiation can be easily depicted and monitored. A PS can thus be used both as an imaging agent in addition to a light-activated therapeutic agent, as shown in Figure 1. After delivery of a PS into the targeted tissue, it can act as an imaging moiety upon light exposure by emitting fluorescence signal. The PS 5-aminolevulinic acid (5-ALA) has been deployed as an intraoperative optical imaging agent for direct visualization of tumor tissue during fluorescence guided surgery [28]. The fluorescence emitted by 5-ALA is useful for diagnose of cancers in pre-malignancy and different malignancy stages [29]. As a PS, Chlorin e6 (Ce6) has the tendency to aggregate at room temperature. Hence, Ce6 was embedded within polyvinylpyrrolidone (PVP) for interfaced with a fluorescence endoscope system directly for photodynamic diagnosis of nasopharyngeal carcinoma [30]. The fluorescence properties of the NIR PS ICG were studied in aqueous solutions, from which concentration-dependent quenching effect was found to directly impact its fluorescence property [31]. By accumulation of an imaging-guided PS in tumor tissues, it can help to increase fluorescence intensity over time. Using NIR emission-centered PSs will give higher fluorescence quantum yield, rendering better performance as imaging agents.

## 2.2. Photodynamic Therapy (PDT)/Photothermal Therapy (PTT)

In molecular spectroscopy, a Jablonski diagram represents the energy diagram accompanied by a molecule's electronic states and the transitions between them (Figure 1). The energy dissipation involves the movement of electrons upon excitation from the ground state to a higher energy state when UV-Vis or NIR light absorption occurs. In accordance with the transition between different spin states (denoted by transition between  $S_1$  to  $T_1$ ), intersystem crossing (ISC) of states are arranged vertically by energy, and grouped horizontally by spin multiplicity. Non-radiative vibration relaxation that leads to photothermal effects is shown by dotted arrow. The radiative transition is shown by straight solid arrow. The transition of triplet oxygen to singlet oxygen leads to formation of reactive oxygen species (ROS), leading to photodynamic effects. Radical formation from the excited state can also cause damage to cancer tissue for phototherapy in the NIR region. In order to avoid redundant interference of drugs in whole organism, the PDT is well pronounced for treatment of targeted tissue only. For PDT in cancer treatment, a light-sensitive PS was administered intravenously, orally, or topically, depending on the location of tumor, followed by accumulation of the PS at the desired targeted site. A light source of appropriate wavelength is applied to the targeted site to generate ROS for killing the cancer cells without affecting healthy tissues. The cell death triggered by PDT can occur through apoptosis and necrosis; the apoptotic pathway is referred to as programmed cell death, whereas necrotic pathway is designated as non-programmed cell death. An apoptotic pathway can shift into the necrotic pathway over decrease in the availability of caspases and intracellular adenosine triphosphate (ATP) concentration [32]. In addition, another cell mechanism called paraptosis can also lead to cell death with photo damage to the endoplasmic reticulum during PDT, by initiating impaired apoptotic pathways [33].

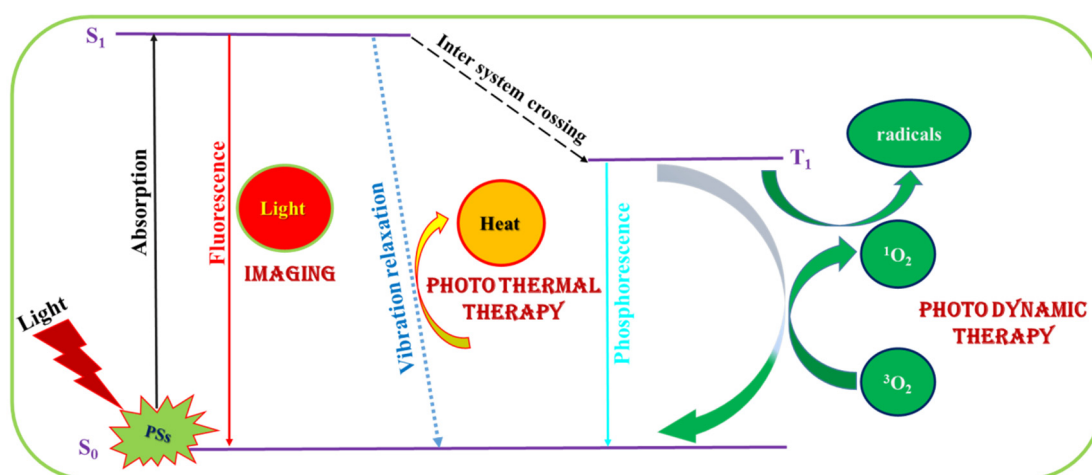


**Figure 1.** The Jablonski diagram showing the process of fluorescence imaging as well as photothermal therapy and photodynamic therapy when a photosensitizers (PS) is irradiated with light.

## 3. Photosensitizers (PSs) for Cancer Theranostics

In order to implement PDT for cancer therapy, various PSs have been developed. These PSs could be classified into two types. The lower wavelength based PSs (e.g., Photofrin, Chlorin e6, Rose Bengal and 5-aminolevulinic acid) (Figure 2) are efficiently activated by light sources in the UV-Vis range (400–700 nm), which show limited penetration into the tissue. On the other hand, the longer wavelength-based PS (e.g., ICG and IR780) (Figure 2) are mostly activated by light in the higher NIR wavelength range (700–900 nm), which show intense penetration ability with excellent anti-cancer efficacy. However, these PSs are still limited by factors like agglomeration and insolubility in aqueous solutions, leading to limited generation of ROS. To overcome these problems, new NIR PSs (e.g., IR806 and IR820), showing better aqueous suspension ability and better imaging properties, were



developed recently for in vitro and in vivo use (Figure 2). From a comprehensive literature search, we find out more than 1000 research articles published within the last decade on UV-Vis PSs for cancer therapy, within which more than half are using Photofrin and 5-aminolevulinic acid. For NIR PSs, the number is more than 700, with ICG accounting for ~60% of them. For clinical trials, 5-aminolevulinic acid is used for basal cell carcinoma (phase I and 2); Photofrin is used for brain tumor (phase 1 and 2) and esophageal adenocarcinoma (phase 3); Rose Bengal is used for melanoma (phase 1 and 2); ICG is used for head and neck cancer (phase 2) and breast cancer (phase 2).

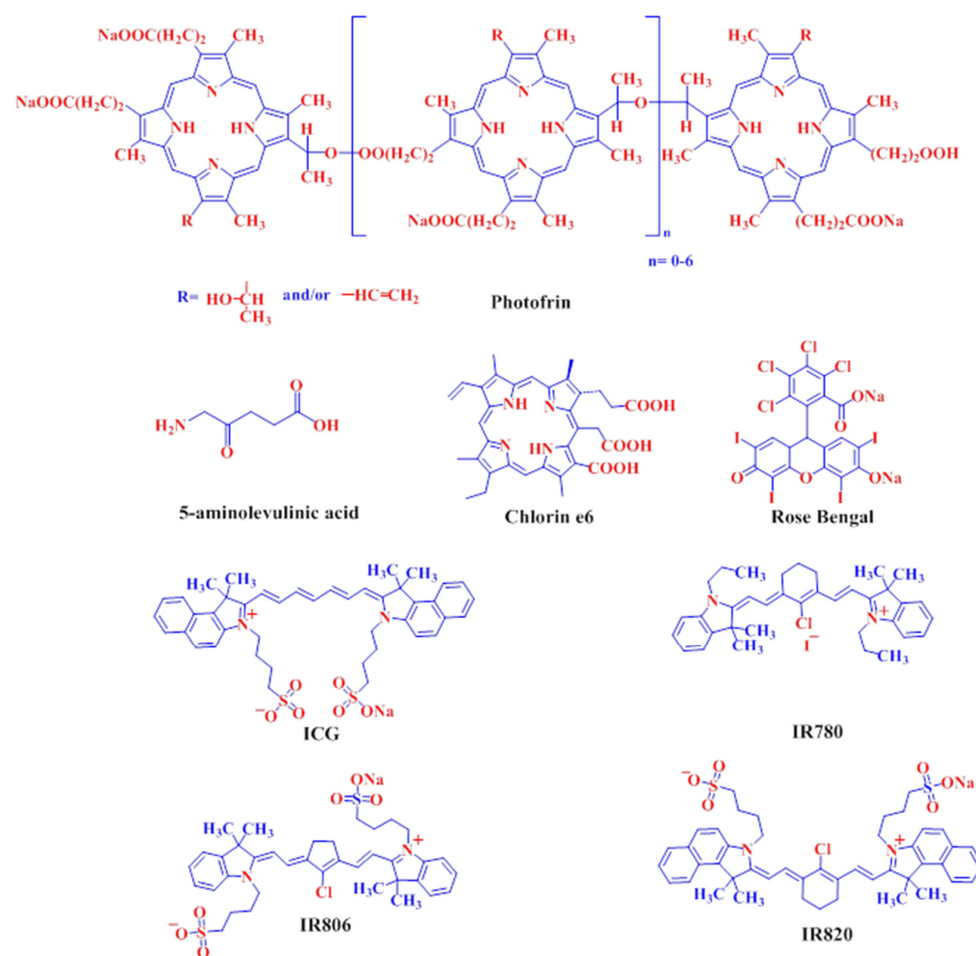


**Figure 2.** The chemical structure of ultraviolet-visible (UV-Vis) photosensitizers (top row) and near infrared (NIR) photosensitizers (bottom row).

### 3.1. UV-Vis Photosensitizers

The UV-Vis PSs are dyes excited by blue, green, and red light within 400–700 nm. Herein, we discussed the advances in incorporating these PSs in a nanocomposite for treating different types of cancer in vitro and in vivo.

#### 3.1.1. Porfimer Sodium (Photofrin)

In the past, porfimer sodium was widely used as a PS for cancer treatment as Photofrin, which was approved by the U.S. FDA for treatment of specific kinds of cancer like esophagus and lung cancer. In 1995, Tsukagoshi combined porfimer sodium with laser as a new method for cancer therapy by selective accumulation of the PS, Photofrin II, in cancer tissues and further irradiation with light to cause tumor cell death [34]. Tumor selectivity of porfimer sodium is based on the following reasons, high affinity for lipoprotein, especially low-density lipoprotein (LDL); elevation of LDL receptor activity in cancer tissue; lack or incompleteness of lymphatic system in cancer tissue. By stimulation with 630 nm light, highly

reactive excited singlet oxygen ( $^1\text{O}_2$ ) was produced, which can kill tumor cells through mitochondrial apoptosis due to the release of cytochrome c triggering photodamage in the cytoplasm. Somers et al. carried out a comparative study using Photofrin-mediated PDT on squamous cell carcinoma (SqCCa) of the larynx [35]. In their experiments, 26 patients were taken with early stage of SqCCa, who have failed prior to surgery and/or radiation therapy. Outcomes of this study demonstrated potential treatment of early-stage laryngeal malignancies from multiple Photofrin administration and laser retreatment. The Photofrin mainly interacted with mitochondrial membranes, endoplasmic reticulum, and Golgi complexes of cancer cells. Under the irradiation process, singlet oxygen species and other ROS are produced, causing photo-oxidative damage to proteins and lipids of cancer cells that reside within a few nanometers of the PS. Cai et al. used Photofrin for PDT, in combination with glycated chitosan (GC) as an immunomodulatory agent for laser immunotherapy (LIT), in treating mice bearing EMT6 breast tumors and 4T1 metastatic breast tumors [36]. The long-term effects of LIT help to improve the survival rate of mice as well as minimizing the growth of the tumor.

In another study, Betsy et al. used modified Photofrin for breast cancer treatment. They modified the PS with picolylamine groups and its zinc complex compound to kill MDA-MB-231 cancer cells, finding that picoly Photofrin can enhance singlet oxygen production [37]. Choi and co-workers studied the effectiveness of generated ROS in cancer treatment with HeLa cells using Photofrin for PDT, together with a chemotherapeutic drug (carboplatin) [38]. Combination of Photofrin with carboplatin results in better cancer treatment outcomes than using Photofrin alone. Zhu et al. studied sinoporphyrin sodium and Photofrin-mediated PDT against HCT116 cells [39]. They observed that sinoporphyrin sodium-based PDT shows better anti-tumor efficiency both in vitro and in vivo as compared to Photofrin-based PDT, suggesting that sinoporphyrin sodium can be also used as an effective UV-Vis PS. Kano and co-worker introduced a new approach in which Photofrin was complexed with tumor-localizing polyethylene glycol-grafted poly(L-lysine) (PLL-g-PEG) for accumulating the PS at the tumor [40]. During the complexation process, Photofrin could be strongly bound to PLL-g-PEG due to both ionic and hydrophobic interactions, and the nanocomposite comprising Photofrin and PLL-g-PEG provides better anti-cancer performance tested with 4T1 and CT26 cancer cells over pristine Photofrin. Crescenzi et al. carried out comparative study between monotherapy (PDT or chemotherapy) and combination therapy (PDT plus chemotherapy) using Photofrin as the PS, as well as cisplatin and gemcitabine as cytotoxic drugs [41]. Using lung cancer cell line (H1299), they concluded that combination chemo-photodynamic therapy results in a better synergistic effect than monotherapy. From the above studies, it could be concluded about the incompetence of using Photofrin alone for cancer treatment, which further underlines the importance of using a targeted nanocomposite formulation or by combining Photofrin-based PDT with other cancer therapeutic agents for effective cancer treatment.

### 3.1.2. 5-Aminolevulinic Acid (5-ALA)

5-Aminolevulinic acid (5-ALA) is a naturally occurring amino acid, and biosynthesized ALA can be found in mammals from the Shemin pathway that occurs in mitochondria. The ALA is a precursor of porphyrin, heme, and bile pigments, and it is metabolized into protoporphyrin IX (PpIX) during the course of heme synthesis. PpIX preferentially accumulates in tumor cells, resulting in red fluorescence following irradiation with UV-Vis light and the formation of singlet oxygen, for ALA-induced photodynamic diagnosis and therapy [42]. Babic and co-workers used 5-ALA modified squalene (SQ) in the detection and treatment of tumors using prostate cancer cells PC3 and human glioblastoma cells U87MG [43]. As a natural precursor of cholesterol for targeting tumors, the 5-ALA modified SQ nanocomposite showed promising anti-cancer effects for both cancer cell lines compared to using pristine 5-ALA. Ma and co-workers provided a new strategy for skin cancer treatment by loading 5-ALA within hollow mesoporous silica nanoparticles (HMSNPs) to kill B16F10 skin cancer cells [44]. By using folic acid (FA) as a targeting

ligand, 5-ALA loaded nanocomposite shows excellent cytotoxicity towards cancer cells for PDT in vitro. Choi et al. used liposomes to encapsulate 5-ALA for in vitro PDT of human cholangiocarcinoma cells (HuCC-T1) [45]. The 5-ALA encapsulated liposomes showed enhanced phototoxicity due to better intracellular uptake by cancer cells than free 5-ALA. Wang and co-workers used 5-ALA loaded mesoporous organosilica coated Prussian blue nanoparticles (PS@PMOs) for glioma treatment against a malignant glioma cell line (U87MG) [46]. They found effective phototoxicity of 5-ALA after loading in the nanoparticles to show photodynamic therapeutic effects. In a different study, Wang et al. used poly(lactic-co-glycolic acid) (PLGA) nanoparticles (NPs) to deliver 5-ALA for PDT in skin cancer treatment [47]. From in vivo studies, they found that PS-loaded NPs showed more cytotoxicity toward the squamous cell carcinoma (SCC) cell line. To improve PDT, Chen et al. used nanoethosomes (ES) to load 5-ALA, followed by conjugating with hyaluronic acid (HA) as a targeting ligand for synergistic transdermal delivery [48]. The hypertrophic scar fibroblasts (HSFs) cell line was used for in vivo and in vitro studies. Embedding 5-ALA within ES and conjugating the nanocomposite with HA provides effective targeted transdermal delivery to significantly elevating PDT efficacy.

In recent years, combination cancer therapy has received significant attention. For this reason, Kang and co-workers developed a combination cancer therapy approach (chemotherapy plus PDT) using glutathione-responsive multifunctional nanogel for cancer treatment (Figure 3) [49]. With 5-ALA for PDT and doxorubicin (DOX) as a chemo drug, the “Trojan Horse” nanogel shows effective response against the 4T1 cancer cell line. For glutathione depletion, Li et al. used dual-targeted 5-ALA for enhanced PDT [50]. By using ALA methyl ester (OMe), which can be metabolized to PpIX inside the cells, the combination of dual targeting with PDT provides enhanced cancer therapeutic efficacy.

### 3.1.3. Chlorin e6 (Ce6)

Chlorin e6 (Ce6) was considered one of the most efficient first-generation PSs due to its low dark toxicity and excellent anticancer properties. In 1993, Goff and co-workers introduced immune-conjugate by binding a monoclonal antibody (OC125) with Ce6 for anticancer treatment, which shows excellent in vivo phototoxicity in an animal model created with antigen CA 125-overexpressing ovarian cancer cells [51]. After multiple low-dose treatments, the number of cancer cells was significantly reduced with no treatment-related deaths. In another research, Feng et al. employed a new approach by using diselenide (Se-Se) bonds to link hyaluronic acid (HA) and Ce6, followed by self-assembly into HA-Se-Se-Ce6 micelles [52]. The HA was used as hydrophilic shell to target cluster of differentiation 44 (CD44) receptors overexpressed on 4T1 cancer cells, while PS could be released from the Ce6-containing core after disassembling of micelles in an intracellular redox environment. The targeted delivery of Ce6 to 4T1 tumors was proved in an orthotopic mammary fat pad tumor model for enhanced PDT of breast cancer. Liu and co-workers combined chemotherapy, PDT, and PTT for cancer treatment using reduced graphene oxide (rGO) as a drug carrier, doxorubicin (DOX) as a chemotherapy drug, and Ce6 as PS [53]. In vitro studies showed that Ce6-based combination treatment results in better results than using free Ce6 alone. Xu et al. used polyethylene glycol (PEG)-Ce6 chelated gadolinium ion nanoparticles (PEG-Ce6-Gd NPs) for cancer diagnosis and treatment, which were synthesized via a self-assembly approach [54]. In pre-clinical studies, PEG-Ce6-Gd NPs were verified as promising non-toxic nano-agents for PDT and for contrast-enhanced MRI diagnosis. The synthesized NPs were able to significantly increase their phototoxicity under laser irradiation, inducing the death of cancer cells. Using C6 cell line in vitro and in vivo, the nanotheranostic agent PEG-Ce6-Gd NPs could facilitate diagnosis and PDT treatment of glioma xenografts in mice. To enhance PDT, Liu and his research team doped graphene oxide nanosheet with MnO<sub>2</sub> for chemo-photodynamic combinatorial therapy after loading cisplatin and Ce6 and surface conjugation with HA targeting ligand [55]. Since a tumor shows extreme hypoxia pathologically, MnO<sub>2</sub> doping can catalyze the decomposition of

$\text{H}_2\text{O}_2$  into oxygen to alleviate tumor hypoxia and fortify ROS generation from Ce6 after 635 nm laser irradiation.

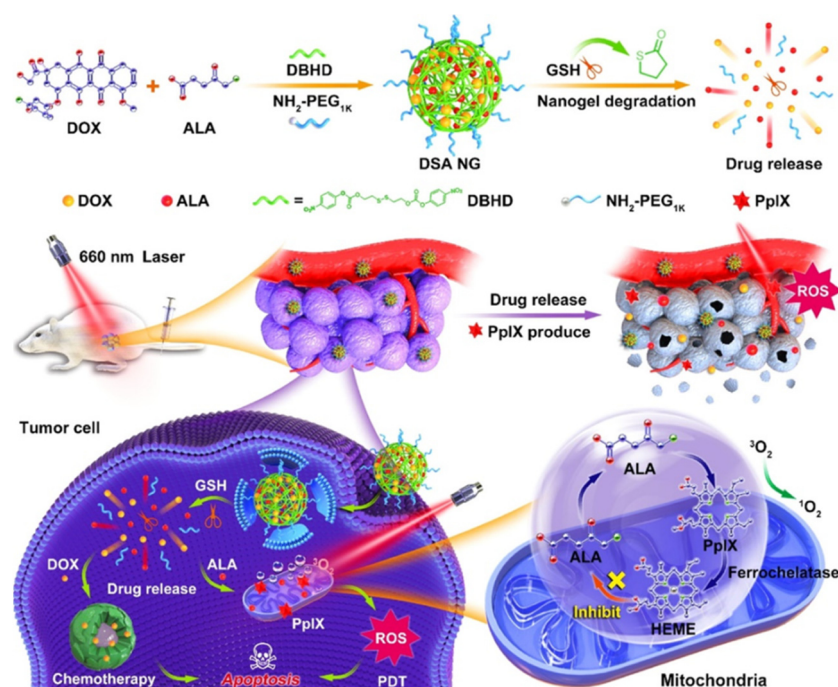


**Figure 3.** A glutathione-responsive multifunctional nanogel loaded with 5-aminolevulinic acid (5-ALA) photosensitizer and doxorubicin (DOX) for chemo/photodynamic combination cancer therapy. Reproduced with permission from [49]. Copyright 2010. American Chemical Society.

Hu et al. conjugated IR820 with d- $\alpha$ -tocopheryl polyethylene glycol 1000 succinate (TPGS) for encapsulation of Ce6 in TPGS-IR820/Ce6 micelles [56]. The TPGS-IR820/Ce6 micelles are endowed with multiple theranostic properties, including fluorescence imaging, PTT, and PDT. The stable micelles have a high singlet oxygen production capability as well as remarkable photothermal conversion efficiency. Following effective cellular internalization, a single NIR laser irradiation of the micelles leads to remarkable anticancer activity in vitro and in vivo. As it is important not to damage surrounding healthy tissues during PDT in cancer treatment, Kaščáková and co-workers employed targeted PDT through vascular and cellular targeting, with the overexpressed neuropeptide somatostatin receptor (sst<sub>2</sub>) on tumor cells and neovascular-endothelial cells [57]. They synthesized two Ce6 derivatives, Ce6-K<sub>3</sub>-[Tyr3]-octreotate and Ce6-[Tyr3]-octreotate-K<sub>3</sub>-[Tyr3]-octreotate for PDT treatment, using human erythroleukemic K562 cells. The first derivative was demonstrated to show better anticancer properties than the second one due to the difference in hydrophobicity. Lee and co-workers used Er-doped NaYF<sub>4</sub>:Yb,Er,Nd@NaYF<sub>4</sub>:Nd up conversion nanoparticles (UCNPs), emitting dual red and green signals upon NIR laser irradiation, for enhanced PDT against B16BL6 melanoma cells [58]. By incorporating dual PSs (Ce6 and Rose Bengal), both PSs received red and green emissions from Er-doped UCNPs and generated abundant cytotoxic ROS to destroy cancer cells using an 808 nm wavelength excitation light source. Most importantly, their study revealed the use of dual PS is preferred over single PS, with higher ROS generation rates, to improve the efficacy of PDT.

### 3.1.4. Rose Bengal (RB)

Rose Bengal (RB), a xanthine dye-based PS with incorporated halogen atoms chlorine and iodine to increase anticancer properties, is widely used as a fluorescein in biological applications. In particular, the heavy atoms in the xanthene rings enhances spin-orbit coupling and promotes intersystem crossing in an excited state of the PS, leading to in-



creased triplet state population and ROS generation. This PS is mainly excited at longer wavelengths (>640 nm), which allows deep light penetration to cause phototoxicity. Furthermore, the short tissue accumulation durations of RB, usually less than two weeks, allows early patient release from the dark. However, like most second generation PSs that are hydrophobic with poor water solubility, RB is prone to aggregation under physiological settings, lowering the quantum yields of ROS generation significantly. Multiple cell death mechanism, including apoptosis, autophagy, and necrosis, are efficiently triggered by this PS, all of which occur independently of one another. Because of its photo-bleaching feature, RB is generally accepted as a PS with few adverse effects [59,60].

Sun et al. developed a cancer treatment modality by combining radiation therapy (RT) with X-ray-induced photodynamic therapy (X-PDT) for clinical deep penetrating cancer therapy. They used RB-doped silica for PDT, together with arginylglycylaspartic acid (RGD) peptide, as a targeting agent for treating U87 malignant glioma cell line in vitro and in animal studies [61]. The results show that low dose X-ray irradiation, as well as using RB as a PS and RGD as a targeting ligand, can overcome the limitation of RT and PDT in cancer treatment. Gianotti and co-workers developed a modified nanosystem with mesoporous silica (MSNs) as a nanocarrier for RB for treating skin cancer [62]. After green light irradiation, RB loaded within MSNs function as a PDT agent and generated ROS to reduce the proliferation of human melanoma SK-MEL-28 cells. Wang and co-workers developed novel nanoplatforms for phototherapy of oral cancer with RB as a photodynamic agent and gold nanorods (GNRs) as a photothermal agent [63]. Green laser light was used to activate RB and red laser light for GNRs during in vitro study with Cal-27 cells. In vivo study with hamster cheek pouches, an animal model found RB-GNRs with combined PDT/PTT, can provide enhanced anti-cancer efficacy against oral cancer.

For the controlled release of RB by light irradiation, Yeh et al. developed a nanoplatform by encapsulating RB within nanocomposites of chitosan (CTS)/poly (vinyl alcohol) (PVA)/branched polyethylenimine (bPEI)/hydrophobic magnetic nanoparticle through electrostatic interaction [64]. Release of the PS and a chemo drug (paclitaxel) from the nanoclusters could be achieved simultaneously after laser light irradiation through a ROS-responsive photo-oxidation mechanism sensitized by RB (Figure 4). They demonstrated highly effective PDT or PDT-combined therapy against MCF-7 breast cancer cells, SKOV-3 ovarian cancer cells, and Tramp-C1 prostate cancer cell lines in vitro, as well as enhanced PDT efficacy against multidrug-resistant MCF-7/MDR tumors in xenograft animal model. Jain et al. synthesized GAG@mSiO<sub>2</sub>@RB nanocomposite by loading RB in mesoporous silica (mSiO<sub>2</sub>)-coated magnetic luminescent Gd<sub>2.98</sub>Ce<sub>0.02</sub>Al<sub>5</sub>O<sub>12</sub> nanoparticles (GAG) for X-rays PDT (X-PDT) [65]. The GAG@mSiO<sub>2</sub>@RB nanocomposite produced four times more singlet oxygen when exposed to low-energy X-rays and showed excellent PDT effect upon irradiation with blue light laser against MDA-MB-231 cells, as compared to RB alone. Combining X-PDT with imaging property, the GAG@mSiO<sub>2</sub>@RB nanocomposite is suitable for the theranostic application of deep tumors without the limitation of restricted light penetration depth.

Liu and co-workers used self-assembled RB-loaded peptido-nanomicelles (RBNs) for cancer treatment [66]. The nanocomposite exhibited excellent synergistic effect towards nasopharyngeal carcinoma (NPC) cells from combination sonodynamic therapy (SDT), PDT and chemotherapy (CT). In vitro and in vivo studies in nude mice verified RBNs deliver effective payloads for NPC-targeted cell killing. The combination therapy demonstrated an overwhelming tumor inhibition and lesion elimination capability due to the synergy-enhanced approach. Overall, RBN-mediated combination SDT/PDT/CT provides a promising approach for clinical NPC treatments in a non-invasive, efficacious, and precise manner. Additional efforts by Zhang et al. used carboxymethyl chitosan (CMCS)-RB-DOX nanoparticles for co-delivery of RB and DOX [67]. The combination of PDT with chemotherapy leads to better inhibition effects on Cal-27 oral cancer cells with a sustained intracellular release of RB and DOX. Aside from those reports, other studies also support the use of RB-loaded nanocomposites in combination cancer therapy, which can



synergistically improve cytotoxicity against cancer cells and exhibit better cancer treatment outcomes than using PDT alone [68–70].

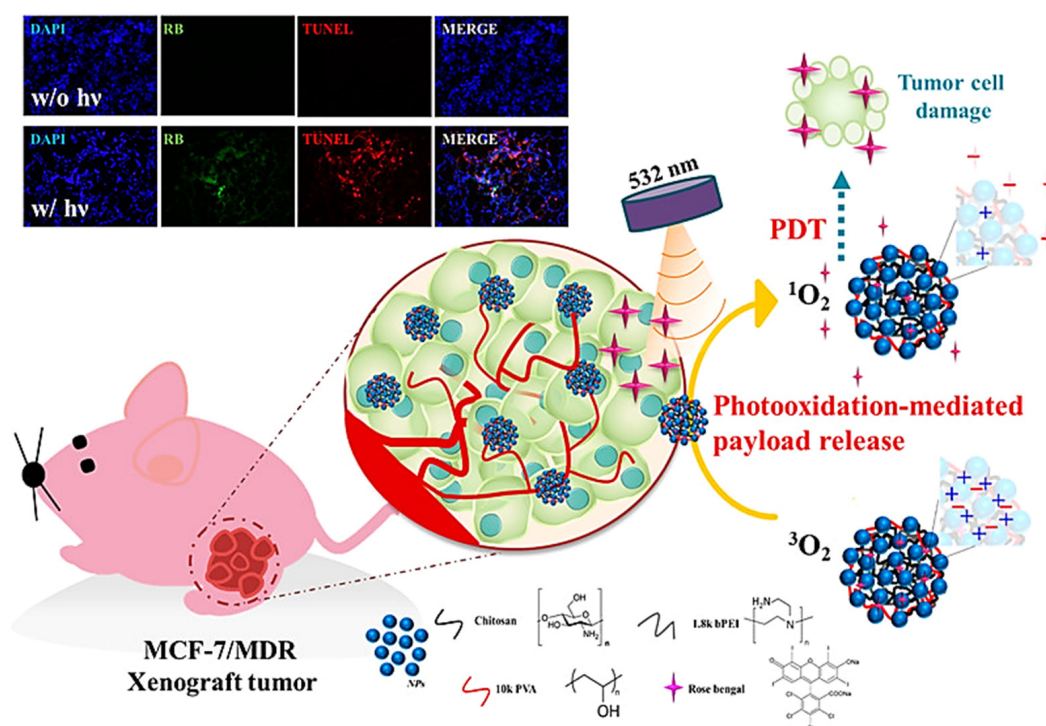


**Figure 4.** Encapsulation of Rose Bengal (RB) photosensitizer within chitosan/poly (vinyl alcohol) (PVA)/branched polyethylenimine (bPEI)/hydrophobic magnetic nanoparticles nanocomposites through electrostatic interaction provide a ROS-responsive photo-oxidation-responsive nanoplatform for controlled paclitaxel release and photodynamic therapy. Reproduced with permission from [64]. Copyright 2018. American Chemical Society.

### 3.2. NIR Photosensitizers

The near infrared-based PSs are employed more frequently due to their higher ROS production when induced by longer wavelengths light sources that are endowed with deeper tumor penetration depth. Due to the lack of a long-wavelength absorption band, lower wavelength PSs are limited by their inability to penetrate tissue and elicit abundant photo-induced damage to tumor tissues [71,72]. Thus, near-infrared (NIR)-activated PDT technology has recently been recognized as a promising method for improving cancer treatment [73]. Among the NIR dyes, ICG is the earliest PS with U.S FDA approval status for both PDT and PTT. However, ICG has several limitations that could be resolved with newly developed NIR PSs (IR780, IR806, and IR820) for cancer treatment.

#### 3.2.1. Indocyanine Green (ICG)

Indocyanine green (ICG) is considered an active dye that finds many applications in cancer theranostics by functioning as a photothermal agent (PA), a photosensitizer (PS), or a fluorescence imaging probe. During photothermal treatment of cancer, ICG could convert the optical energy into thermal energy in the presence of NIR light and effectively destroy the tumor. Additionally, ICG also generates ROS to further integrate with their anti-tumor properties, from which dual phototherapy (PTT/PDT) works better than single phototherapy (PTT or PDT) [74]. Sheng et al. used human serum albumin (HAS) and ICG to prepare HSA-ICG NPs by intermolecular disulfide bonds [75]. This nanocomposite shows excellent accumulation and long-term retention in 4T1 tumor-bearing mice from ICG-based NIR fluorescence and photoacoustic dual-modal imaging in vivo, providing image-guided cancer phototherapy with 808 nm laser light to exhibit PDT/PTT synergistic effects. Zhu et al. synthesized a nanocomposite by binding ICG with tumor-targeting ligand holo-

transferrin (holo-Tf) through hydrophobic interaction and hydrogen bonds [76]. The holo-Tf-ICG assembly was used for PTT as well as dual-mode (fluorescence and photoacoustic) imaging of U87 orthotopic glioma in nude mice, providing excellent diagnostics and tumor ablation abilities (Figure 5).

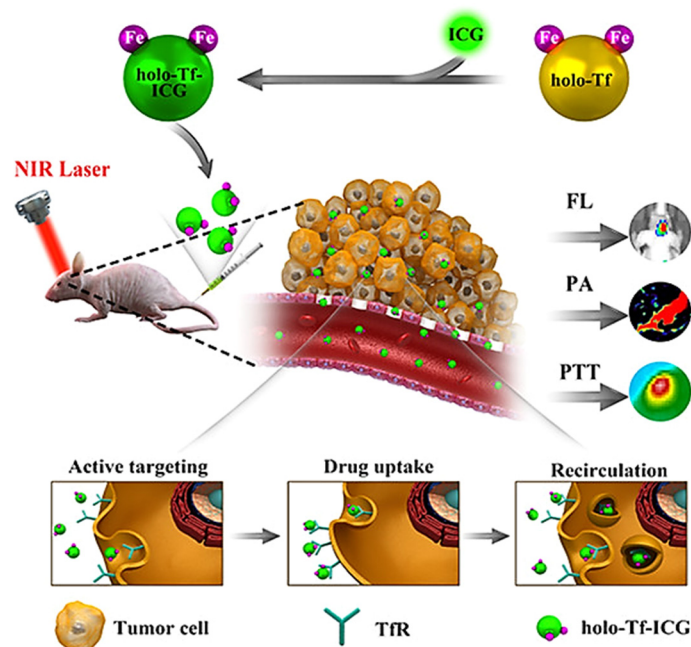


**Figure 5.** Conjugation of ICG to holo-transferrin (holo-Tf), followed by self-assembly into holo-Tf-ICG nanoparticles for tumor-targeted photoacoustic (PA) and fluorescence (FL) imaging-guided photothermal therapy (PTT) of glioma. Reproduced with permission from [76]. Copyright 2017. American Chemical Society.

Sherien and co-workers carried out a comparative study about using ICG-entrapped polymeric nanoparticles (ICG-ormosil) and free ICG for PDT treatment against adenocarcinoma cells (MCF-7) and hepatocellular carcinoma cells (HepG2) [77]. Both forms of PS (ICG-ormosil and free ICG) showed similar cytotoxic and phototoxic impacts on MCF-7 and HepG2 cell lines. Nonetheless, the entrapment of ICG in polymeric nanoparticles was found to enhance its water stability over free ICG with improved photodynamic activity. Following the same line, Tamai et al. used ICG-loaded super carbonate apatite (sCA) for PDT treatment against HT29 cancer cells [78]. The sCA-ICG outperforms free ICG in cancer treatment in vitro and in vivo. Other than a good carrier for ICG for PDT, sCA was also found to help the quick removal of ICG from other organs, making this nanocomposite a novel tool for cancer research.

As the high concentration of glutathione (GSH) inside tumor cells can consume generated ROS during PDT and lead to insufficient therapeutic effect. Realizing this limitation, Hu and co-workers combined the use of a GSH-depletion agent, phenethyl isothiocyanate (PEITC), with ICG-encapsulated hydroxyethyl starch-oleic acid (HES-OA) NPs to increase the impact of PDT [79]. The HES-OA NPs exhibited excellent stability, promoting cellular uptake and enhancing tumor accumulation, and generated effective singlet oxygen with laser light exposure. Using the ICG-loaded NPs together with PEITC was shown to result in better cancer cell killing both in vitro and in vivo by enhancing the photodynamic effect. In a different study, Hu et al. used ICG-loaded polydopamine-reduced graphene oxide nanocomposites (ICG-PDA-rGO) as a theranostic agent for amplifying photoacoustic (PA) imaging and PTT [80]. The PDA layer coated on rGO surface was shown to promote loading of ICG molecules, quench ICG fluorescence, and enhance optical absorption at 780 nm. Together, the ICG-PDA-rGO nanocomposite showed a stronger PTT effect and better PA contrast than pure GO and PDA-rGO, as well as suppressing 4T1 tumor com-

pletely in vivo. Our group developed a novel carrier for ICG in dual-targeted (magnetic and HA ligand) PTT/PDT [81]. From in vitro and in vivo experiments, magnetic liposome (MPLs) encapsulating ICG was coated with hyaluronic acid-polyethylene glycol (HA-PEG) for targeting the U87MG cell line. Intravenous administration of HA-PEG-MPLs prevents tumor growth after successive short-term NIR laser irradiation in vivo.

With encouraging results shown from the combination of chemotherapy (CT) and PTT for improving cancer therapeutic efficacy, a dual-responsive, folic acid (FA)-decorated polymeric micelles (FA Co-PMs) was developed by Zhang et al. for targeted NIR imaging and combination PTT/CT by encapsulating DOX and ICG [82]. The nanocomposite showed triggered DOX release in response to intracellular acidic pH/reduction environments as well as good photothermal response to NIR laser. With significant targeting of BEL-7404 cells and laser-induced hyperthermia, FA Co-PMs synergistically induced death of BEL-7404 cells by apoptosis in vitro and suppressed tumor growth in BEL-7404 xenograft in vivo. A tumor-targeted mesoporous silica nanoparticle (MSN) was designed by Lei and co-workers to load ICG and DOX for NIR-induced photothermal drug release in combined CT/PTT [83]. The nanocomposite was smartly modified with a thermal-cleavable gatekeeper, which can be de-capped by ICG-generated hyperthermia under NIR illumination to trigger DOX release after intracellular uptake for combined cancer therapy. Finally, a similar system for combination therapy was designed based upon poly( $\gamma$ -glutamic acid)-*g*-poly(lactic-co-glycolic acid) ( $\gamma$ -PGA-*g*-PLGA) nanoparticles for loading DOX and ICG [84]. After coating with cholesterol-PEG for alleviating multidrug resistance (MDR), the nanocomposite could effectively treat human MDR breast cancer with combined CT/PTT.

### 3.2.2. IR780 Iodide

The lipophilic dye IR780 iodide accumulates specifically in breast cancer cells as well as human lung cancer cells, with peak emission at 780 nm to be easily detected from NIR fluorescence imaging. The use of IR780 for prostate cancer imaging has been intensively researched to increase its therapeutic efficacy [85]. With considerable optical absorption and emission in the NIR region, IR780 has attracted the attention of researchers working in the fields of cancer treatments and imaging modalities. When IR780 is exposed to NIR light, it generates a significant amount of ROS and shows good photothermal conversion, making it an active agent for use in cancer photodynamic and photothermal treatment [27]. Several deficiencies shown by ICG, including poor stability, concentration-dependent aggregation, short circulation half-life, and off-target effects, prompts the use of different NIR-based dyes as improved PSs [86]. Among them, IR780, a lipophilic cationic heptamethine dye, presents a relatively new NIR dye showing more stability than ICG as well as higher fluorescence intensity than ICG [87–89]. When IR780 iodide is exposed to light at 808 nm wavelength, it produces singlet oxygen for PDT. On the other hand, because of the heat generated by laser irradiation, IR780 may also be employed as a photothermal agent for PTT. To overcome the weak water solubility and low tumor-targeting effectiveness of IR780 iodide, Wang et al. conjugated IR780 to transferrin (Tf), followed by self-assembly into IR780-loaded Tf nanoparticles (NPs) for targeted imaging and PDT/PTT, with photothermal response as well as singlet oxygen generation under 808 nm laser irradiation [90]. In vitro and in vivo studies demonstrated that loading IR780 in Tf NPs could destroy cancer cells more effectively. Xing and co-workers developed a photo-responsive nanocluster (NC) system, by the combination of polydopamine (PDA) with TPGS micelles for loading IR780 and DOX, for combined chemo-phototherapy against breast cancer cells [91]. Their study confirms the use of DOX as a chemo drug to amplify the efficiency of PTT/PDT in suppressing multidrug resistance (MDR) breast cancer.

As stated earlier, the efficacy of PDT is largely limited by oxygen deficiency in the hypoxic tumor microenvironment, even with IR780. To solve this problem, Yang and co-workers fabricated a NIR-responsive nanocomposite for co-delivery of oxygen and DOX, by loading DOX in an oxygenated amphiphile (F-IR780-PEG) to form F/DOX nanoparti-

cles [92]. The intrinsic fluorescent features of IR780 make F/DOX nanoparticles suitable for the imaging-guided treatment of hypoxic tumors with synergistic CT/PDT. Yue et al. developed a nanoplatform based on thermosensitive liposomes for loading IR780 as well as Lonidamine as an anti-cancer drug [93]. By releasing ROS for PDT in mitochondria using an 808 nm light source, the IR-780-entrapped liposomal formulation increased anti-cancer efficacy for lung cancer treatment with effects from combination cancer therapy. Yuan et al. loaded IR-780 in PEG-C13 micelle as a targeted photothermal and imaging agent for cancer therapy [94]. The self-assembled micelle showed good phototherapy efficacy both in vitro and in vivo.

As IR780 exhibits insoluble properties in all clinically used solvents, Li and co-workers used folic acid-conjugated graphene quantum dots (GQDs-FA) for loading IR780 (Figure 6) [95]. With an improved loading capacity of IR780 through strong  $\pi$ - $\pi$  stacking, over 2400-fold higher aqueous concentration of IR780 could be achieved using IR780/GQDs-FA. Loading IR-780 by non-covalent interaction further enhances its photostability, which upon laser treatment, produces efficient hyperthermia to kill HeLa cancer cells. Wang et al. employed IR780 as a PDT agent for combination with immunotherapy using anti-PD-L1 peptide [96]. Their innovative design provides an IR780-loaded nanocomposite for effectively eradicating metastatic and invasive tumors as well. Under laser light irradiation, IR780 destroys tumor cells by creating ROS, while PDT-induced immunogenic cell death exposes tumor-associated antigens and damage-associated molecular patterns, allowing dendritic cells to mature and cytotoxic T lymphocytes to activate cytotoxic T lymphocytes for immunotherapy.

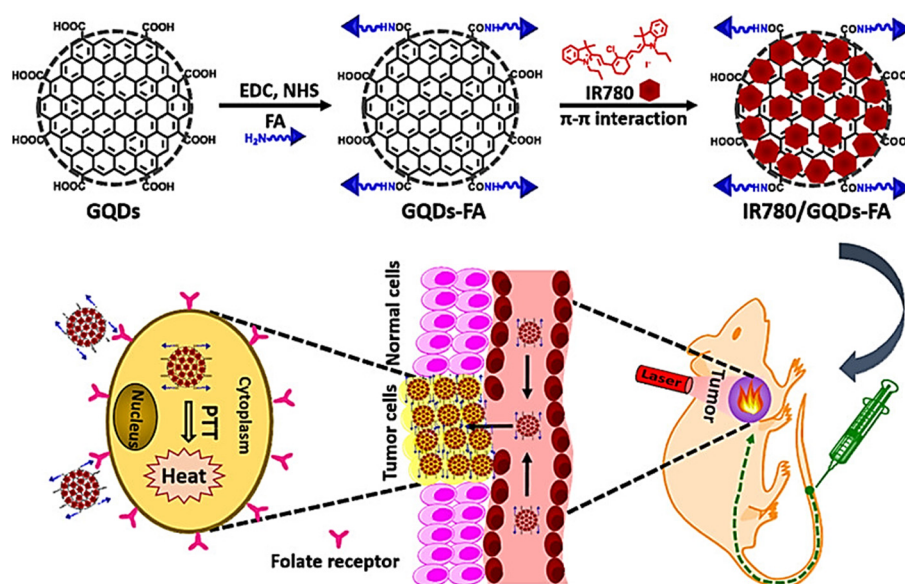


**Figure 6.** Loading IR780 iodide on folic acid (FA)-functionalized graphene quantum dots (GQDs) for targeted photothermal therapy (PTT). Reproduced with permission from [95]. Copyright 2017. American Chemical Society.

### 3.2.3. IR806

The IR806 is a negatively charged hydrophilic PS with a sulfonate functional group that enhances its hydrophilicity, which is missing in IR780. This difference also prevents agglomeration and less toxicity associated with IR806 in comparison to hydrophobic IR780 [97,98]. Chang et al. synthesized a nanocomposite based on IR806 for dual (fluorescence and magnetic resonance) image-guided PTT [24]. After functionalizing IR780-iron oxide complex with mPEG-PCL-G2.0PAMAM-Cit for tumor targeting, the enhanced photothermal conversion efficiency originated from both the PS and iron oxide nanoparticles provide effective PTT with low-power ( $0.25 \text{ W/cm}^2$ ) 808 nm lasers. Similarly, for magnetic targeting as well as image-guided PTT/PDT using 808 nm laser, Deng et al. developed a



nanocomposite with IR806 and  $\text{MnFe}_2\text{O}_4$  (MFO-IR) for magnetic-targeted/MRI-guided synergistic PTT/PDT [99]. After derivatization with carboxyl groups, IR806 was conjugated to  $\text{MnFe}_2\text{O}_4$  nanoparticles, showing multi-functionality as PS carriers, targeting ligands, MRI contrast agents, and photothermal agents. In vitro experiments show NIR light-responsive ROS generation for cell apoptosis and hyperthermia with HeLa cells. After guidance with an external magnetic field and followed by 808 nm laser irradiation, the nanocomposite could completely eradicate subcutaneous tumors in vivo.

Using 793 nm NIR laser for improving tissue penetration and reducing overheating by water absorption, Lin et al. synthesized IR806-loaded neodymium up-conversion nanoparticles (UCNPs) for heat generation and luminescence imaging [100]. From in vitro and in vivo studies performed against MDA-MB-231 cancer cells using polyethylene glycol-folic acid (PEG-FA) as a tumor targeting agent, potential theranostic cancer treatment was successfully demonstrated from this IR806-loaded nanocomposite. Jogdand and co-workers entrapped IR806 in chitosan-coated niosome (NioIR-C) to enhance the photothermal conversion efficacy of IR806 by chitosan [101]. The mucoadhesive nature of NioIR-C and its intracellular uptake by cancer cells enhanced the PTT therapeutic effect against MCF-7 and MDA-MB-231 breast cancer cells. Using the additive nature of PTT/PDT in the central nervous system, Wang et al. used self-assembled  $\text{Fe}_3\text{O}_4$ -IR806 as a nanocomposite for treating malignant glioma [102]. By complexing with IR806, the nanoplateform shows a 3.5-fold increase of photothermal conversion efficiency over that of  $\text{Fe}_3\text{O}_4$  nanoparticles for PTT, which also generates ROS for PDT with NIR light irradiation. The nanocomposite suppressed the growth of glioma cells by photothermal ablation and generated ROS cytotoxicity in vitro, in addition to inhibiting tumor growth in vivo with NIR light induction. A limiting factor in PDT is the short-life and restricted diffusion distance of ROS generated by a PS. Therefore, Yu et al. used IR806 to develop a mitochondria-targeted NIR-responsive  $\text{TiO}_2$ -coated UCNPs nanocomposite for PDT [103]. By localizing into mitochondria through intracellular trafficking followed by NIR laser irradiation, the nanocomposite could produce ROS in mitochondria and induce the domino effect on ROS burst, which leads to mitochondria collapse and cell apoptosis with overproduced ROS accumulated in mitochondria. This enhanced PDT strategy was proved to be effective for the complete removal of the tumor in vivo. Using gel matrix as a scaffold for the administration of PS has rarely been reported. For this purpose, Asadian-Birjand and co-workers conjugate IR806 into a nanogel of dendritic polyglycerol (dPG) and oligo ethylene glycol (OEG) [104]. Improved phototoxicity of the dye-nanogel nanocomposite against a human carcinoma cell line after NIR laser irradiation in vitro implicates its potential use as a photothermal and photodynamic agent in cancer therapy.

#### 3.2.4. IR820

The scientific community has shown extensive interest in NIR-based fluorophores due to their combined molecular imaging and hyperthermia properties. The cyanine dye IR820 exhibits optical and thermal properties similar to those of ICG, albeit conferred with excellent in vitro and in vivo stability over ICG. Although IR820 shows a lower quantum yield as compared to ICG in fluorescent emission study; however, it shows less dependence of the emission peak location on concentration. Under all temperature and light conditions, IR820 provides a half-life nearly twice that of ICG in aqueous solutions. After 3-min laser irradiation, IR820 produced slightly lower peak temperatures (less than 10%) than ICG in hyperthermia applications [105]. When comparing the heat-generating capacity and imaging properties between ICG and IR820, IR820 showed enhanced stability with nearly doubled degradation half-time and prolonged image collection time, in addition to similar heat generation property with ICG [106]. The negative charge of IR820 can provide stable static interaction with amine groups, although its absorption in the NIR region was weakened [107]. It was shown that IR820 might act both as a PS and a photothermal agent (PA), transferring energy to  $^3\text{O}_2$  to produce  $^1\text{O}_2$  and generating heat by laser irradiation at 808 nm [108].



In an interesting work by Xia and co-authors, IR820 was conjugated to porous silicon nanoparticles (PSiNPs) for the controlled release of DOX in cancer therapy [109]. A high drug release percentage (98%) of DOX was noted using NIR-triggered DOX release in acidic endosomal environments. The combination of IR820 and DOX enhanced the chemo-photothermal combination therapy towards HeLa cancer cells in vitro. Consider tumor imaging only, Zhou et al. conjugated IR820 to chitosan quaternary ammonium salt capped ferroferric oxide (CSQ-Fe) nanoparticles. The IR820-CSQ-Fe nanocomposite was used for multimodal MRI, NIR fluorescence imaging as well as multispectral optoacoustic tomography of MDA-MB-231 cancer cells [110]. For solving the poor solubility of paclitaxel (PTX) and short life-time of IR820, an “all-in-one” approach for dual photo-chemo therapy/imaging was suggested by Zhang et al., who prepared IR820-PTX nanocomposite with very high drug content (96% IR820 and PTX) [111]. This enzyme and pH-sensitive conjugates show good stability in the blood stream for NIR fluorescence image-guided CT/PTT. A “triple-punch” strategy of cancer PTT, PDT, and immunotherapy was used by Wu et al., who designed a mitochondria-targeted and NIR-activated multifunctional graphene nanocomposite after modification with triphenylphosphonium (Figure 7) [112]. By generating abundant ROS and photothermal heat for cell apoptosis, this photo-active nanocomposite is confirmed for PTT/PDT in vitro. With the conjugation of lipophilic DP-CpG cytosine-guanosine oligonucleotides to graphene surface by hydrophobic interaction for promoting secretion of pro-inflammatory cytokines and improves tumor immunogenicity, the GT/IR820/DP-CpG is also effective for immunotherapy. From photo-immunotherapy in vivo, an 88% tumor inhibition rate was obtained, implicating PTT/PDT effect from IR820 could be combined with DP-CpG immunostimulation for multimodal cancer therapy.

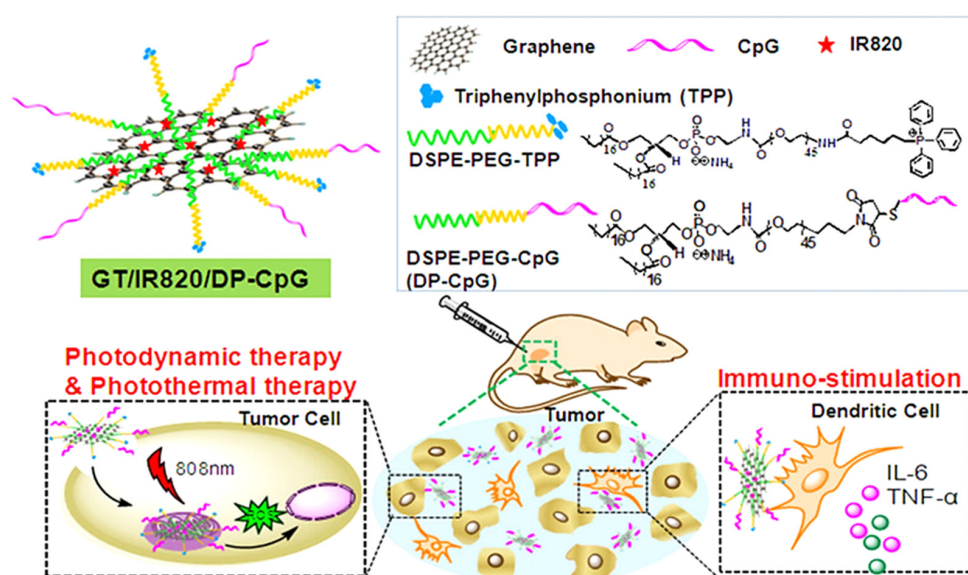


**Figure 7.** The “triple-punch” anticancer strategy mediated by NIR photosensitizer IR820/CpG oligonucleotides and mitochondria-targeted TPP-modified nanographene for photodynamic/photothermal/immunotherapy. Reproduced with permission from [112]. Copyright 2018. American Chemical Society.

Zaharie-Butucel et al. developed hybrid nanomaterials by using chitosan-reduced graphene oxide (chit-rGO) as a carrier for delivery of IR820 and DOX in vitro against murine colon carcinoma cells (C26) [113]. In their study, the anticancer activity against C26 cancer cells could be improved by the combination of the photodynamic effect of IR820, the photothermal effect of IR820 and chit-rGO, as well as the chemotherapeutic effect of DOX. Using microneedle (MN) patches to deliver IR820 and cisplatin, Fu and co-workers fabricated a nanodevice for breast cancer therapy by delivery of the PDT and

chemotherapy agents from the drug-carrying needle tips, with inserted MN in the skin for local cancer treatment [114]. The developed MN patch was shown to be with low toxicity for controllable synergistic chemo-photodynamic therapy efficacy. Combining PTT with an indoleamine 2,3-dioxygenase (IDO) inhibitor is an attractive approach for immunotherapy. For this purpose, Zhang and co-workers conjugated IR820 with the IDO inhibitor 1-methyl-tryptophan (1MT) to induce immunogenic cell death (ICD), followed by self-assembly into IR820-1MT nanoparticles [115]. This nanocomposite not only showed 90% loading of both therapeutic agents but also solved the poor water solubility of 1MT and the short lifetime of IR820. After triggering by NIR laser, IR820-1MT nanoparticles showed excellent photothermal-assisted immunotherapy against tumor recurrence and metastasis. The heme oxygenase-1 (HO-1) is an antioxidant protein, which is overexpressed in response to the stress experienced by cancer cells during anticancer therapy for regulating cell apoptosis. It is conceivable that reducing the anti-oxidative ability of cancer cells by inhibition of HO-1 activity will make cancer cells more vulnerable to damage caused by photothermal heating during PTT. Following this reasoning, Noh et al. developed a multifunctional nanocomposite by conjugating amphiphilic polymers with zinc protoporphyrin (ZnPP) for inhibition of HO-1, together with IR820 for PTT [116]. The nanocomposite showed enhanced oxidative-photothermal combination anticancer therapy upon NIR laser irradiation by elevating cytotoxicity against cancer cells. An in vivo study with a mouse xenograft model revealed that dual image-guided enhanced PTT could lead to thermal ablation of the tumor without side-effects and tumor recurrence.

A summary of PS/wavelength, the delivery and functionalization agents in the nanocomposites, the cancer cell lines used for the study, as well as the types of study are provided in Table 1.

**Table 1.** Summary of photosensitizer-containing nanocomposites for cancer therapy.

Photosensitizer /Wavelength	Delivery/Functionalization Agents	Cancer Cells	Types of Study	Reference
<b>Ultraviolet-Visible (UV-Vis) Photosensitizers (PSs)</b>				
Porphyrin sodium (Photofrin) /510–630 nm	GC	EMT6, 4T1	In vitro, In vivo	[36]
	Zn	MDA-MB-231	In vitro	[37]
	Carboplatin	HeLa	In vitro	[38]
	Chloroquine	HCT116	In vitro, In vivo	[39]
	PLL-g-PEG	4T1, CT26	In vitro, In vivo	[40]
5-aminolevulinic acid (5-ALA) /400–660 nm	Cisplatin, Gemcitabine	H1299	In vitro	[41]
	SQ	PC3, U87MG	In vitro	[43]
	FA, HMSNPs	B16F10	In vitro	[44]
	Liposomes	HuCC-T1	In vitro	[45]
	PB@PMOs	U87MG	In vitro, In vivo	[46]
	PLGA	SCC	In vivo	[47]
	ES, HA	HSFs	In vitro, In vivo	[48]
	DOX	4T1	In vitro, In vivo	[49]
Chlorin e6 (Ce6) /635–808 nm	OMe	HeLa	In vitro, In vivo	[50]
	HA	4T1	In vitro, In vivo	[52]
	DOX, rGO	U87	In vitro, In vivo	[53]
	PEG, Gd	C6	In vitro, In vivo	[54]
	Cisplatin, HA, MnO <sub>2</sub>	MDA-MB-231	In vitro, In vivo	[55]
	TPGS, IR820	B16	In vitro, In vivo	[56]
	K3-[Tyr3]-octreotate	K562	In vitro, In vivo	[57]
Rose Bengal (RB) /532–808 nm	RB, UCNPs	B16BL6	In vitro	[58]
	Silica, RGD	U87	In vitro, In vivo	[61]
	MSNs	SK-MEL-28	In vitro	[62]
	GNRs	Cal-27	In vitro, In vivo	[63]
	CTS, PVA, bPEI	MCF-7	In vitro, In vivo	[64]
	GAG, mSiO <sub>2</sub>	MDA-MB-231	In vitro	[65]
	RBNs	CNE-2Z	In vitro, In vivo	[66]
	CMCS, DOX	Cal-27	In vitro	[67]

Table 1. Cont.

Photosensitizer /Wavelength	Delivery/Functionalization Agents	Cancer Cells	Types of Study	Reference
Near infrared (NIR) Photosensitizers (PSs)				
Indocyanine green (ICG) /807–808 nm	HSA	4T1	In vitro, In vivo	[75]
	Holo-Tf	U87	In vitro, In vivo	[76]
	Ormosil	MCF-7, HepG2	In vitro	[77]
	sCA	HT29	In vitro, In vivo	[78]
	HES-OA	HepG2	In vitro, In vivo	[79]
	PDA-rGO	4T1	In vitro, In vivo	[80]
	MPLs, HA-PEG	U87MG	In vitro, In vivo	[81]
	FA, DOX, Co-PMs	BEL-7404	In vitro, In vivo	[82]
	DOX, MSN, RGD	4T1	In vitro, In vivo	[83]
	$\gamma$ -PGA-g-PLGA, DOX	MCF-7, MCF-7/MDR	In vitro, In vivo	[84]
Infrared 780 iodide (IR780) /808 nm	Transferrin	CT26	In vitro, In vivo	[90]
	PDA, DOX	MCF-7	In vitro, In vivo	[91]
	Oxygenated amphiphiles, DOX	MCF-7	In vitro, In vivo	[92]
	Liposomes, Lonidamine	LL/2	In vitro, In vivo	[93]
	Micelles, PEG	CT26	In vitro, In vivo	[94]
	FA, GQD	HeLa	In vitro, In vivo	[95]
	Anti-PD-L1 peptide	B16F10	In vitro, In vivo	[96]
Infrared 806 (IR806) /785–980 nm	Iron oxide, mPEG-PCL-G2-Cit	A549	In vitro, In vivo	[24]
	MnFe <sub>2</sub> O <sub>4</sub>	HeLa	In vitro, In vivo	[99]
	Neodymium UCNPs, PEG-FA	MDA-MB-231	In vitro	[100]
	Niosome, chitosan	MCF-7, MDA-MB-231	In vitro	[101]
	Fe <sub>3</sub> O <sub>4</sub>	U87MG	In vitro, In vivo	[102]
	TiO <sub>2</sub> -UCNPs	MCF-7	In vitro, In vivo	[103]
	dPG, OEG	A2780	In vitro	[104]
Infrared 820 (IR820) /785–808 nm	PSiNPs, DOX	HeLa	In vitro	[109]
	CSQ-Fe	MDA-MB-231	In vitro	[110]
	PTX	MCF-7, HeLa	In vitro, In vivo	[111]
	Graphene, DP-CpG	EMT6	In vitro, In vivo	[112]
	Chit-rGO, DOX	C26	In vitro	[113]
	Microneedles, Cisplatin	4T1	In vitro, In vivo	[114]
	1MT	B16F10	In vitro, In vivo	[115]
	ZnPP-conjugated micelles	A549	In vitro, In vivo	[116]

#### 4. Conclusions and Outlook

In this review, the most important and commonly used PSs for delivery by different nanocomposites are discussed in the context of cancer theranostics. While perfect PSs with responsiveness to deep tissue penetration light and high solubility in physiological buffers are still elusive, advances in nanomaterial design by complexing PSs with smartly designed nanocomposites have provided encouraging results in combination cancer therapy based on PS-mediated PTT and/or PDT. Although the second generation PSs has limitations like their first-generation counterparts, their numerous usages in a clinical setting have proven their multi-functionality and efficacy in phototherapy-based cancer treatments guided by different imaging modalities. Among all PSs, the long-wavelength PSs (IR806 and IR820) should provide a better solution to the issues faced during phototherapy if their half-lives could be further extended. Contemporaneous research is still ongoing to develop better PSs that may enhance the photodynamic effect, and more research is warranted for new PSs that could be used for dual PDT/PTT with high efficiency. This could be complemented through the unique design of a nanocomposite that can incorporate PSs with moieties alleviating hypoxia and inhibiting thermal stress protein activity in a single nanopatform for enhanced PTT/PDT. A better treatment outcome in a clinical setting may be possible if more PSs could be used for detection during cancer treatment to realize new multitasking nanotheranostic tools. Advances in the development of more specific technologies for delivery of PS and/or light source are also urgently needed to achieve the best clinical approach towards cancer treatment.

**Author Contributions:** Conceptualization, B.S.D. and J.-P.C.; writing—original draft preparation, B.S.D.; writing—review and editing, S.D. and J.-P.C.; visualization, B.S.D.; supervision, J.-P.C.; funding acquisition, J.-P.C. All authors have read and agreed to the published version of the manuscript.

**Funding:** This research was funded by the Ministry of Science and Technology, Taiwan, ROC (MOST 109-2314-B-182-013-MY3) and Chang Gung Memorial Hospital, Taiwan, ROC (BMRP249, CMRPD2K0131 and CMRPD2I0042). The APC was funded by Chang Gung University.

**Institutional Review Board Statement:** Not applicable.

**Informed Consent Statement:** Not applicable.

**Acknowledgments:** We acknowledge the technical support by the Imaging Core Laboratories of the Institute for Radiological Research, Chang Gung Memorial Hospital, Linkou, and the Instrumentation Center, Chang Gung University.

**Conflicts of Interest:** The authors declare no conflict of interest. The funders had no role in the design of the study; in the collection, analyses, or interpretation of data; in the writing of the manuscript, or in the decision to publish the results.

## References

- Hosokawa, S.; Takahashi, G.; Sugiyama, K.I.; Takebayashi, S.; Okamura, J.; Takizawa, Y.; Mineta, H. Porfimer sodium-mediated photodynamic therapy in patients with head and neck squamous cell carcinoma. *Photodiagn. Photodyn. Ther.* **2020**, *29*, 101627. [\[CrossRef\]](#)
- Schipmann, S.; Müther, M.; Stögbauer, L.; Zimmer, S.; Brokinkel, B.; Holling, M.; Grauer, O.; Molina, E.S.; Warneke, N.; Stummer, W. Combination of ALA-induced fluorescence-guided resection and intraoperative open photodynamic therapy for recurrent glioblastoma: Case series on a promising dual strategy for local tumor control. *J. Neurosurg.* **2021**, *134*, 426. [\[CrossRef\]](#)
- Cao, W.; Liu, B.; Xia, F.; Duan, M.; Hong, Y.; Niu, J.; Wang, L.; Liu, Y.; Li, C.; Cui, D. MnO<sub>2</sub>@Ce6-loaded mesenchymal stem cells as an “oxygen-laden guided-missile” for the enhanced photodynamic therapy on lung cancer. *Nanoscale* **2020**, *12*, 3090–3102. [\[CrossRef\]](#)
- Qin, J.; Kunda, N.; Qiao, G.; Calata, J.F.; Pardiwala, K.; Prabhakar, B.S.; Maker, A.V. Colon cancer cell treatment with rose bengal generates a protective immune response via immunogenic cell death. *Cell Death Dis.* **2017**, *8*, e2584. [\[CrossRef\]](#)
- Lin, J.; Lin, L.S.; Chen, D.R.; Lin, K.J.; Wang, Y.F.; Chang, Y.J. Indocyanine green fluorescence method for sentinel lymph node biopsy in breast cancer. *Asian J. Surg.* **2020**, *43*, 1149–1153. [\[CrossRef\]](#)
- He, B.; Hu, H.Y.; Tan, T.; Wang, H.; Sun, K.X.; Li, Y.P.; Zhang, Z.W. IR-780-loaded polymeric micelles enhance the efficacy of photothermal therapy in treating breast cancer lymphatic metastasis in mice. *Acta Pharmacol. Sin.* **2018**, *39*, 132–139. [\[CrossRef\]](#) [\[PubMed\]](#)
- Feng, Z.; Yu, X.; Jiang, M.; Zhu, L.; Zhang, Y.; Yang, W.; Xi, W.; Li, G.; Qian, J. Excretable IR-820 for in vivo NIR-II fluorescence cerebrovascular imaging and photothermal therapy of subcutaneous tumor. *Theranostics* **2019**, *9*, 5706–5719. [\[CrossRef\]](#) [\[PubMed\]](#)
- Sibata, C.H.; Colussi, V.C.; Oleinick, N.L.; Kinsella, T.J. Photodynamic therapy: A new concept in medical treatment. *Braz. J. Med. Biol. Res.* **2000**, *33*, 869–880. [\[CrossRef\]](#)
- Shibu, E.S.; Hamada, M.; Murase, N.; Biju, V. Nanomaterials formulations for photothermal and photodynamic therapy of cancer. *J. Photochem. Photobiol. C Photochem. Rev.* **2013**, *15*, 53–72. [\[CrossRef\]](#)
- Spikes, J.D. New trends in photobiology: Chlorins as photosensitizers in biology and medicine. *J. Photochem. Photobiol. B Biol.* **1990**, *6*, 259–274. [\[CrossRef\]](#)
- Baas, P.; van Mansom, I.; van Tinteren, H.; Stewart, F.A.; van Zandwijk, N. Effect of N-acetylcysteine on photofrin-induced skin photosensitivity in patients. *Lasers Surg. Med.* **1995**, *16*, 359–367. [\[CrossRef\]](#)
- Patrice, T.; Moan, J.; Peng, Q. An outline of the history of PDT. In *Photodynamic Therapy*; Patrice, T., Ed.; The Royal Society of Chemistry: London, UK, 2003; pp. 1–18.
- Inaguma, M.; Hashimoto, K. Porphyrin-like fluorescence in oral cancer: In vivo fluorescence spectral characterization of lesions by use of a near-ultraviolet excited autofluorescence diagnosis system and separation of fluorescent extracts by capillary electrophoresis. *Cancer* **1999**, *86*, 2201–2211. [\[CrossRef\]](#)
- Orenstein, A.; Kostenich, G.; Roitman, L.; Shechtman, Y.; Kopolovic, Y.; Ehrenberg, B.; Malik, Z. A comparative study of tissue distribution and photodynamic therapy selectivity of chlorin e6, Photofrin II and ALA-induced protoporphyrin IX in a colon carcinoma model. *Br. J. Cancer* **1996**, *73*, 937–944. [\[CrossRef\]](#) [\[PubMed\]](#)
- Kessel, D.; Thompson, P. Purification and analysis of hematoporphyrin and hematoporphyrin derivative by gel exclusion and reverse-phase chromatography. *Photochem. Photobiol.* **1987**, *46*, 1023–1025. [\[CrossRef\]](#) [\[PubMed\]](#)
- De Silva, P.; Saad, M.A.; Thomsen, H.C.; Bano, S.; Ashraf, S.; Hasan, T. Photodynamic therapy, priming and optical imaging: Potential co-conspirators in treatment design and optimization—A Thomas Dougherty Award for Excellence in PDT paper. *J. Porphyr. Phthalocyanines* **2020**, *24*, 1320–1360. [\[CrossRef\]](#)



17. Bano, S.; Obaid, G.; Swain, J.W.; Yamada, M.; Pogue, B.W.; Wang, K.; Hasan, T. NIR Photodynamic Destruction of PDAC and HNSCC Nodules Using Triple-Receptor-Targeted Photoimmuno-Nanoconjugates: Targeting Heterogeneity in Cancer. *J. Clin. Med.* **2020**, *9*, 2390. [\[CrossRef\]](#)
18. Dash, B.S.; Jose, G.; Lu, Y.J.; Chen, J.P. Functionalized Reduced Graphene Oxide as a Versatile Tool for Cancer Therapy. *Int. J. Mol. Sci.* **2021**, *22*, 2989. [\[CrossRef\]](#) [\[PubMed\]](#)
19. Lu, Y.J.; Lin, P.Y.; Huang, P.H.; Kuo, C.Y.; Shalumon, K.T.; Chen, M.Y.; Chen, J.P. Magnetic Graphene Oxide for Dual Targeted Delivery of Doxorubicin and Photothermal Therapy. *Nanomaterials* **2018**, *8*, 193. [\[CrossRef\]](#)
20. Robinson, J.T.; Tabakman, S.M.; Liang, Y.; Wang, H.; Sanchez Casalongue, H.; Vinh, D.; Dai, H. Ultrasmall Reduced Graphene Oxide with High Near-Infrared Absorbance for Photothermal Therapy. *J. Am. Chem. Soc.* **2011**, *133*, 6825–6831. [\[CrossRef\]](#)
21. Swamy, P.C.A.; Sivaraman, G.; Priyanka, R.N.; Raja, S.O.; Ponnuvel, K.; Shanmugpriya, J.; Gulyani, A. Near Infrared (NIR) absorbing dyes as promising photosensitizer for photo dynamic therapy. *Coord. Chem. Rev.* **2020**, *411*, 213233. [\[CrossRef\]](#)
22. Sheng, Z.; Hu, D.; Xue, M.; He, M.; Gong, P.; Cai, L. Indocyanine Green Nanoparticles for Theranostic Applications. *Nano Micro Lett.* **2013**, *5*, 145–150. [\[CrossRef\]](#)
23. Kirchherr, A.K.; Briel, A.; Mäder, K. Stabilization of Indocyanine Green by Encapsulation within Micellar Systems. *Mol. Pharm.* **2009**, *6*, 480–491. [\[CrossRef\]](#) [\[PubMed\]](#)
24. Chang, Y.; Li, X.; Kong, X.; Li, Y.; Liu, X.; Zhang, Y.; Tu, L.; Xue, B.; Wu, F.; Cao, D.; et al. A highly effective in vivo photothermal nanoplatfrom with dual imaging-guided therapy of cancer based on the charge reversal complex of dye and iron oxide. *J. Mater. Chem. B* **2015**, *3*, 8321–8327. [\[CrossRef\]](#) [\[PubMed\]](#)
25. Valcourt, D.M.; Dang, M.N.; Day, E.S. IR820-loaded PLGA nanoparticles for photothermal therapy of triple-negative breast cancer. *J. Biomed. Mater. Res. Part A* **2019**, *107*, 1702–1712. [\[CrossRef\]](#) [\[PubMed\]](#)
26. Jiang, X.; Du, B.; Huang, Y.; Yu, M.; Zheng, J. Cancer Photothermal Therapy with ICG-Conjugated Gold Nanoclusters. *Bioconjug. Chem.* **2020**, *31*, 1522–1528. [\[CrossRef\]](#)
27. Alves, C.G.; Lima-Sousa, R.; de Melo-Diogo, D.; Louro, R.O.; Correia, I.J. IR780 based nanomaterials for cancer imaging and photothermal, photodynamic and combinatorial therapies. *Int. J. Pharm.* **2018**, *542*, 164–175. [\[CrossRef\]](#)
28. Stummer, W.; Pichlmeier, U.; Meinel, T.; Wiestler, O.D.; Zanella, F.; Reulen, H.J.; ALA-Glioma Study Group. Fluorescence-guided surgery with 5-aminolevulinic acid for resection of malignant glioma: A randomised controlled multicentre phase III trial. *Lancet Oncol.* **2006**, *7*, 392–401. [\[CrossRef\]](#)
29. Ebihara, A.; Krasieva, T.B.; Liaw, L.H.L.; Fago, S.; Messadi, D.; Osann, K.; Wilder-Smith, P. Detection and diagnosis of oral cancer by light-induced fluorescence. *Lasers Surg. Med.* **2003**, *32*, 17–24. [\[CrossRef\]](#) [\[PubMed\]](#)
30. Ramaswamy, B.; Manivasager, V.; Chin, W.W.; Soo, K.C.; Olivo, M. Photodynamic diagnosis of a human nasopharyngeal carcinoma xenograft model using the novel Chlorin e6 photosensitizer Fotolon®. *Int. J. Oncol.* **2005**, *26*, 1501–1506. [\[CrossRef\]](#)
31. Saxena, V.; Sadoqi, M.; Shao, J. Degradation Kinetics of Indocyanine Green in Aqueous Solution. *J. Pharm. Sci.* **2003**, *92*, 2090–2097. [\[CrossRef\]](#)
32. Leist, M.; Single, B.; Castoldi, A.F.; Kühnle, S.; Nicotera, P. Intracellular Adenosine Triphosphate (ATP) Concentration: A Switch in the Decision Between Apoptosis and Necrosis. *J. Exp. Med.* **1997**, *185*, 1481–1486. [\[CrossRef\]](#)
33. Kessel, D. Paraptosis and Photodynamic Therapy: A Progress Report. *Photochem. Photobiol.* **2020**, *96*, 1096–1100. [\[CrossRef\]](#) [\[PubMed\]](#)
34. Tsukagoshi, S. Porfimer sodium (Photofrin-II). *Cancer Chemother.* **1995**, *22*, 1271–1278.
35. Schweitzer, V.G.; Somers, M.L. Photofrin-mediated photodynamic therapy for treatment of early stage laryngeal malignancies. *Oncol. Rev.* **2010**, *4*, 203–209. [\[CrossRef\]](#)
36. Cai, X.; Feng, J.; Chen, F.; Guo, C.; Sun, L.; Li, L. Synergistic effect of glycated chitosan and photofrin photodynamic therapy on different breast tumor model. *Photodiagn. Photodyn. Ther.* **2020**, *31*, 101842. [\[CrossRef\]](#) [\[PubMed\]](#)
37. Marydasan, B.; Nair, R.R.; Babu, P.S.; Ramaiah, D.; Nair, S.A. Picolyl Porphyrin Nanostructures as a Functional Drug Entrant for Photodynamic Therapy in Human Breast Cancers. *ACS Omega* **2019**, *4*, 12808–12816. [\[CrossRef\]](#)
38. Choi, Y.; Chang, J.E.; Jheon, S.; Han, S.J.; Kim, J.K. Enhanced production of reactive oxygen species in HeLa cells under concurrent low-dose carboplatin and Photofrin® photodynamic therapy. *Oncol. Rep.* **2018**, *40*, 339–345.
39. Zhu, B.; Li, S.; Yu, L.; Hu, W.; Sheng, D.; Hou, J.; Zhao, N.; Hou, X.; Wu, Y.; Han, Z.; et al. Inhibition of Autophagy with Chloroquine Enhanced Sinoporphyrin Sodium Mediated Photodynamic Therapy-induced Apoptosis in Human Colorectal Cancer Cells. *Int. J. Biol. Sci.* **2019**, *15*, 12–23. [\[CrossRef\]](#) [\[PubMed\]](#)
40. Kano, A.; Taniwaki, Y.; Nakamura, I.; Shimada, N.; Moriyama, K.; Maruyama, A. Tumor delivery of Photofrin® by PLL-g-PEG for photodynamic therapy. *J. Control. Release* **2013**, *167*, 315–321. [\[CrossRef\]](#)
41. Crescenzi, E.; Chiaviello, A.; Cinti, G.; Reddi, E.; Veneziani, B.M.; Palumbo, G. Low doses of cisplatin or gemcitabine plus Photofrin/photodynamic therapy: Disjointed cell cycle phase-related activity accounts for synergistic outcome in metastatic non-small cell lung cancer cells (H1299). *Mol. Cancer Ther.* **2006**, *5*, 776–785. [\[CrossRef\]](#)
42. Ishizuka, M.; Abe, F.; Sano, Y.; Takahashi, K.; Inoue, K.; Nakajima, M.; Kohda, T.; Komatsu, N.; Ogura, S.I.; Tanaka, T. Novel development of 5-aminolevulinic acid (ALA) in cancer diagnoses and therapy. *Int. Immunopharmacol.* **2011**, *11*, 358–365. [\[CrossRef\]](#) [\[PubMed\]](#)
43. Babic, A.; Herceg, V.; Bastien, E.; Lassalle, H.P.; Bezdetnaya, L.; Lange, N. 5-Aminolevulinic Acid-Squalene Nanoassemblies for Tumor Photodetection and Therapy: In Vitro Studies. *Nanoscale Res. Lett.* **2018**, *13*. [\[CrossRef\]](#)



44. Ma, X.; Qu, Q.; Zhao, Y. Targeted Delivery of 5-Aminolevulinic Acid by Multifunctional Hollow Mesoporous Silica Nanoparticles for Photodynamic Skin Cancer Therapy. *ACS Appl. Mater. Interfaces* **2015**, *7*, 10671–10676. [\[CrossRef\]](#)
45. Choi, K.H.; Chung, C.W.; Kim, C.H.; Kim, D.H.; Jeong, Y.I.; Kang, D.H. Effect of 5-Aminolevulinic Acid-Encapsulate Liposomes on Photodynamic Therapy in Human Cholangiocarcinoma Cells. *J. Nanosci. Nanotechnol.* **2014**, *14*, 5628–5632. [\[CrossRef\]](#) [\[PubMed\]](#)
46. Wang, X.; Tian, Y.; Liao, X.; Tang, Y.; Ni, Q.; Sun, J.; Zhao, Y.; Zhang, J.; Teng, Z.; Lu, G. Enhancing selective photosensitizer accumulation and oxygen supply for high-efficacy photodynamic therapy toward glioma by 5-aminolevulinic acid loaded nanoplatfrom. *J. Colloid Interface Sci.* **2020**, *565*, 483–493. [\[CrossRef\]](#) [\[PubMed\]](#)
47. Wang, X.; Shi, L.; Tu, Q.; Wang, H.; Zhang, H.; Wang, P.; Zhang, L.; Huang, Z.; Zhao, F.; Luan, H.; et al. Treating cutaneous squamous cell carcinoma using 5-aminolevulinic acid polylactic-co-glycolic acid nanoparticle-mediated photodynamic therapy in a mouse model. *Int. J. Nanomed.* **2015**, *10*, 347–355.
48. Chen, Y.; Zhang, Z.; Xin, Y.; Zhou, R.; Jiang, K.; Sun, X.; He, D.; Song, J.; Zhang, Y. Synergistic transdermal delivery of nanoethosomes embedded in hyaluronic acid nanogels for enhancing photodynamic therapy. *Nanoscale* **2020**, *12*, 15435–15442. [\[CrossRef\]](#) [\[PubMed\]](#)
49. Wang, Y.; Zu, M.; Ma, X.; Jia, D.; Lu, Y.; Zhang, T.; Xue, P.; Kang, Y.; Xu, Z. Glutathione-Responsive Multifunctional “Trojan Horse” Nanogel as a Nanotheranostic for Combined Chemotherapy and Photodynamic Anticancer Therapy. *ACS Appl. Mater. Interfaces* **2020**, *12*, 50896–50908. [\[CrossRef\]](#)
50. Li, K.; Dong, W.; Miao, Y.; Liu, Q.; Qiu, L.; Lin, J. Dual-targeted 5-aminolevulinic acid derivatives with glutathione depletion function for enhanced photodynamic therapy. *J. Photochem. Photobiol. B Biol.* **2021**, *215*, 112107. [\[CrossRef\]](#)
51. Goff, B.A.; Hermanto, U.; Rumbaugh, J.; Blake, J.; Bamberg, M.; Hasan, T. Photoimmunotherapy and biodistribution with an OC125-chlorin immunoconjugate in an in vivo murine ovarian cancer model. *Br. J. Cancer* **1994**, *70*, 474–480. [\[CrossRef\]](#)
52. Feng, C.; Zhu, D.; Chen, L.; Lu, Y.; Liu, J.; Kim, N.Y.; Liang, S.; Zhang, X.; Lin, Y.; Ma, Y.; et al. Targeted Delivery of Chlorin e6 via Redox Sensitive Diselenide-Containing Micelles for Improved Photodynamic Therapy in Cluster of Differentiation 44-Overexpressing Breast Cancer. *Front. Pharmacol.* **2019**, *10*, 369. [\[CrossRef\]](#) [\[PubMed\]](#)
53. Liu, J.; Liu, K.; Feng, L.; Liu, Z.; Xu, L. Comparison of nanomedicine-based chemotherapy, photodynamic therapy and photothermal therapy using reduced graphene oxide for the model system. *Biomater. Sci.* **2017**, *5*, 331–340. [\[CrossRef\]](#) [\[PubMed\]](#)
54. Xu, D.; Baidya, A.; Deng, K.; Li, Y.S.; Wu, B.; Xu, H.B. Multifunctional nanoparticle PEG-Ce6-Gd for MRI-guided photodynamic therapy. *Oncol. Rep.* **2021**, *45*, 547–556. [\[CrossRef\]](#)
55. Liu, P.; Xie, X.; Liu, M.; Hu, S.; Ding, J.; Zhou, W. A smart MnO<sub>2</sub>-doped graphene oxide nanosheet for enhanced chemophotodynamic combinatorial therapy via simultaneous oxygenation and glutathione depletion. *Acta Pharm. Sin. B* **2020**, *11*, 823–834. [\[CrossRef\]](#) [\[PubMed\]](#)
56. Hu, X.; Tian, H.; Jiang, W.; Song, A.; Li, Z.; Luan, Y. Rational Design of IR820- and Ce6-Based Versatile Micelle for Single NIR Laser-Induced Imaging and Dual-Modal Phototherapy. *Small* **2018**, *14*, 1802994. [\[CrossRef\]](#) [\[PubMed\]](#)
57. Kaščáková, S.; Hofland, L.J.; De Bruijn, H.S.; Ye, Y.; Achilefu, S.; Van Der Wansem, K.; van Koetsveld, P.M.; Brugts, M.P.; van der Lelij, A.J.; Sterenborg, H.J.; et al. Somatostatin Analogues for Receptor Targeted Photodynamic Therapy. *PLoS ONE* **2014**, *9*, e104448. [\[CrossRef\]](#)
58. Lee, S.Y.; Lee, R.; Kim, E.; Lee, S.; Park, Y.I. Near-Infrared Light-Triggered Photodynamic Therapy and Apoptosis Using Upconversion Nanoparticles With Dual Photosensitizers. *Front. Bioeng. Biotechnol.* **2020**, *8*, 275. [\[CrossRef\]](#)
59. Panzarini, E.; Inguscio, V.; Dini, L. Overview of Cell Death Mechanisms Induced by Rose Bengal Acetate-Photodynamic Therapy. *Int. J. Photoenergy* **2011**, *2011*, 713726. [\[CrossRef\]](#)
60. Bottiroli, G.; Croce, A.C.; Balzarini, P.; Locatelli, D.; Baglioni, P.; Nostro, P.L.; Monici, M.; Pratesi, R. Enzyme-assisted Cell Photosensitization: A Proposal for an Efficient Approach to Tumor Therapy and Diagnosis. The Rose Bengal Fluorogenic Substrate. *Photochem. Photobiol.* **1997**, *66*, 374–383. [\[CrossRef\]](#)
61. Sun, W.; Shi, T.; Luo, L.; Chen, X.; Lv, P.; Lv, Y.; Zhuang, Y.; Zhu, J.; Liu, G.; Chen, X.; et al. Monodisperse and Uniform Mesoporous Silicate Nanosensitizers Achieve Low-Dose X-Ray-Induced Deep-Penetrating Photodynamic Therapy. *Adv. Mater.* **2019**, *31*, 1808024. [\[CrossRef\]](#) [\[PubMed\]](#)
62. Gianotti, E.; Martins Estevão, B.; Cucinotta, F.; Hioka, N.; Rizzi, M.; Renò, F.; Marchese, L. An Efficient Rose Bengal Based Nanoplatfrom for Photodynamic Therapy. *Chem. Eur. J.* **2014**, *20*, 10921–10925. [\[CrossRef\]](#)
63. Wang, B.; Wang, J.H.; Liu, Q.; Huang, H.; Chen, M.; Li, K.; Li, C.; Yu, X.F.; Chu, P.K. Rose-bengal-conjugated gold nanorods for in vivo photodynamic and photothermal oral cancer therapies. *Biomaterials* **2014**, *35*, 1954–1966. [\[CrossRef\]](#)
64. Yeh, H.P.; Del Valle, A.C.; Syu, M.C.; Qian, Y.; Chang, Y.C.; Huang, Y.F. A New Photosensitized Oxidation-Responsive Nanoplatfrom for Controlled Drug Release and Photodynamic Cancer Therapy. *ACS Appl. Mater. Interfaces* **2018**, *10*, 21160–21172. [\[CrossRef\]](#)
65. Jain, A.; Koyani, R.; Muñoz, C.; Sengar, P.; Contreras, O.E.; Juárez, P.; Hirata, G.A. Magnetic-luminescent cerium-doped gadolinium aluminum garnet nanoparticles for simultaneous imaging and photodynamic therapy of cancer cells. *J. Colloid Interface Sci.* **2018**, *526*, 220–229. [\[CrossRef\]](#) [\[PubMed\]](#)
66. Liu, Z.; Wang, D.; Li, J.; Jiang, Y. Self-assembled peptido-nanomicelles as an engineered formulation for synergy-enhanced combinational SDT, PDT and chemotherapy to nasopharyngeal carcinoma. *Chem. Commun.* **2019**, *55*, 10226–10229. [\[CrossRef\]](#) [\[PubMed\]](#)

67. Zhang, X.; Li, L.; Liu, Q.; Wang, Y.; Yang, J.; Qiu, T.; Zhou, G. Co-Delivery of Rose Bengal and Doxorubicin Nanoparticles for Combination Photodynamic and Chemo-Therapy. *J. Biomed. Nanotechnol.* **2019**, *15*, 184–195. [\[CrossRef\]](#)
68. Wang, H.Y.; Hou, L.; Li, H.L.; Wang, X.; Cao, Y.; Zhang, B.Y.; Wang, J.T.; Wei, S.J.; Dang, H.W.; Ran, H.T. A nanosystem loaded with perfluorohexane and rose bengal coupled upconversion nanoparticles for multimodal imaging and synergetic chemo-photodynamic therapy of cancer. *Biomater. Sci.* **2020**, *8*, 2488–2506. [\[CrossRef\]](#) [\[PubMed\]](#)
69. Li, X.; Wang, J.; Cui, R.; Xu, D.; Zhu, L.; Li, Z.; Chen, H.; Gao, Y.; Jia, L. Hypoxia/pH dual-responsive nitroimidazole-modified chitosan/rose bengal derivative nanoparticles for enhanced photodynamic anticancer therapy. *Dyes Pigments* **2020**, *179*, 108395. [\[CrossRef\]](#)
70. Borodziuk, A.; Kowalik, P.; Duda, M.; Wojciechowski, T.; Minikayev, R.; Kalinowska, D.; Klepka, M.; Sobczak, K.; Kłopotowski, Ł.; Sikora, B. Unmodified Rose Bengal photosensitizer conjugated with NaYF<sub>4</sub>:Yb,Er upconverting nanoparticles for efficient photodynamic therapy. *Nanotechnology* **2020**, *31*, 465101. [\[CrossRef\]](#) [\[PubMed\]](#)
71. Long, R.; Mao, K.; Ye, X.; Yan, W.; Huang, Y.; Wang, J.; Fu, Y.; Wang, X.; Wu, X.; Xie, Y.; et al. Surface Facet of Palladium Nanocrystals: A Key Parameter to the Activation of Molecular Oxygen for Organic Catalysis and Cancer Treatment. *J. Am. Chem. Soc.* **2013**, *135*, 3200–3207. [\[CrossRef\]](#)
72. Hou, L.; Zhang, X.; Pijper, T.C.; Browne, W.R.; Feringa, B.L. Reversible Photochemical Control of Singlet Oxygen Generation Using Diarylethene Photochromic Switches. *J. Am. Chem. Soc.* **2014**, *136*, 910–913. [\[CrossRef\]](#)
73. Gao, R.; Mei, X.; Yan, D.; Liang, R.; Wei, M. Nano-photosensitizer based on layered double hydroxide and isophthalic acid for singlet oxygenation and photodynamic therapy. *Nat. Commun.* **2018**, *9*, 2798. [\[CrossRef\]](#)
74. Shirata, C.; Kaneko, J.; Inagaki, Y.; Kokudo, T.; Sato, M.; Kiritani, S.; Akamatsu, N.; Arita, J.; Sakamoto, Y.; Hasegawa, K.; et al. Near-infrared photothermal/photodynamic therapy with indocyanine green induces apoptosis of hepatocellular carcinoma cells through oxidative stress. *Sci. Rep.* **2017**, *7*, 13958. [\[CrossRef\]](#) [\[PubMed\]](#)
75. Sheng, Z.; Hu, D.; Zheng, M.; Zhao, P.; Liu, H.; Gao, D.; Gong, P.; Gao, G.; Zhang, P.; Ma, Y.; et al. Smart Human Serum Albumin-Indocyanine Green Nanoparticles Generated by Programmed Assembly for Dual-Modal Imaging-Guided Cancer Synergistic Phototherapy. *ACS Nano* **2014**, *8*, 12310–12322. [\[CrossRef\]](#)
76. Zhu, M.; Sheng, Z.; Jia, Y.; Hu, D.; Liu, X.; Xia, X.; Liu, C.; Wang, P.; Wang, X.; Zheng, H. Indocyanine Green-holo-Transferrin Nanoassemblies for Tumor-Targeted Dual-Modal Imaging and Photothermal Therapy of Glioma. *ACS Appl. Mater. Interfaces* **2017**, *9*, 39249–39258. [\[CrossRef\]](#) [\[PubMed\]](#)
77. El-Daly, S.M.; Gamal-Eldeen, A.M.; Abo-Zeid, M.A.; Borai, I.H.; Wafay, H.A.; Abdel-Ghaffar, A.R.B. Photodynamic therapeutic activity of indocyanine green entrapped in polymeric nanoparticles. *Photodiagn. Photodyn. Ther.* **2013**, *10*, 173–185. [\[CrossRef\]](#)
78. Tamai, K.; Mizushima, T.; Wu, X.; Inoue, A.; Ota, M.; Yokoyama, Y.; Miyoshi, N.; Haraguchi, N.; Takahashi, H.; Nishimura, J.; et al. Photodynamic Therapy Using Indocyanine Green Loaded on Super Carbonate Apatite as Minimally Invasive Cancer Treatment. *Mol. Cancer Ther.* **2018**, *17*, 1613–1622. [\[CrossRef\]](#) [\[PubMed\]](#)
79. Hu, H.; Chen, J.; Yang, H.; Huang, X.; Wu, H.; Wu, Y.; Li, F.; Yi, Y.; Xiao, C.; Li, Y.; et al. Potentiating photodynamic therapy of ICG-loaded nanoparticles by depleting GSH with PEITC. *Nanoscale* **2019**, *11*, 6384–6393. [\[CrossRef\]](#)
80. Hu, D.; Zhang, J.; Gao, G.; Sheng, Z.; Cui, H.; Cai, L. Indocyanine Green-Loaded Polydopamine-Reduced Graphene Oxide Nanocomposites with Amplifying Photoacoustic and Photothermal Effects for Cancer Theranostics. *Theranostics* **2016**, *6*, 1043–1052. [\[CrossRef\]](#) [\[PubMed\]](#)
81. Anilkumar, T.S.; Lu, Y.J.; Chen, H.A.; Hsu, H.L.; Jose, G.; Chen, J.P. Dual targeted magnetic photosensitive liposomes for photothermal/photodynamic tumor therapy. *J. Magn. Magn. Mater.* **2019**, *473*, 241–252. [\[CrossRef\]](#)
82. Zhang, L.; Qin, Y.; Zhang, Z.; Fan, F.; Huang, C.; Lu, L.; Wang, H.; Jin, X.; Zhao, H.; Kong, D.; et al. Dual pH/reduction-responsive hybrid polymeric micelles for targeted chemo-photothermal combination therapy. *Acta Biomater.* **2018**, *75*, 371–385. [\[CrossRef\]](#) [\[PubMed\]](#)
83. Lei, Q.; Qiu, W.X.; Hu, J.J.; Cao, P.X.; Zhu, C.H.; Cheng, H.; Zhang, X.Z. Multifunctional Mesoporous Silica Nanoparticles with Thermal-Responsive Gatekeeper for NIR Light-Triggered Chemo/Photothermal-Therapy. *Small* **2016**, *12*, 4286–4298. [\[CrossRef\]](#) [\[PubMed\]](#)
84. Chen, H.H.; Lu, I.L.; Liu, T.I.; Tsai, Y.C.; Chiang, W.H.; Lin, S.C.; Chiu, H.C. Indocyanine green/doxorubicin-encapsulated functionalized nanoparticles for effective combination therapy against human MDR breast cancer. *Colloids Surf. B Biointerfaces* **2019**, *177*, 294–305. [\[CrossRef\]](#) [\[PubMed\]](#)
85. Yi, X.; Yan, F.; Wang, F.; Qin, W.; Wu, G.; Yang, X.; Shao, C.; Chung, L.W.; Yuan, J. IR-780 dye for near-infrared fluorescence imaging in prostate cancer. *Med. Sci. Monit.* **2015**, *21*, 511–517.
86. Bahmani, B.; Bacon, D.; Anvari, B. Erythrocyte-derived photo-theranostic agents: Hybrid nano-vesicles containing indocyanine green for near infrared imaging and therapeutic applications. *Sci. Rep.* **2013**, *3*, 2180. [\[CrossRef\]](#) [\[PubMed\]](#)
87. Wang, Y.; Liu, T.; Zhang, E.; Luo, S.; Tan, X.; Shi, C. Preferential accumulation of the near infrared heptamethine dye IR-780 in the mitochondria of drug-resistant lung cancer cells. *Biomaterials* **2014**, *35*, 4116–4124. [\[CrossRef\]](#) [\[PubMed\]](#)
88. Yue, C.; Liu, P.; Zheng, M.; Zhao, P.; Wang, Y.; Ma, Y.; Cai, L. IR-780 dye loaded tumor targeting theranostic nanoparticles for NIR imaging and photothermal therapy. *Biomaterials* **2013**, *34*, 6853–6861. [\[CrossRef\]](#)
89. Zhang, C.; Wang, S.; Xiao, J.; Tan, X.; Zhu, Y.; Su, Y.; Cheng, T.; Shi, C. Sentinel lymph node mapping by a near-infrared fluorescent heptamethine dye. *Biomaterials* **2010**, *31*, 1911–1917. [\[CrossRef\]](#) [\[PubMed\]](#)

90. Wang, K.; Zhang, Y.; Wang, J.; Yuan, A.; Sun, M.; Wu, J.; Hu, Y. Self-assembled IR780-loaded transferrin nanoparticles as an imaging, targeting and PDT/PTT agent for cancer therapy. *Sci. Rep.* **2016**, *6*, 27421. [\[CrossRef\]](#)
91. Xing, Y.; Ding, T.; Wang, Z.; Wang, L.; Guan, H.; Tang, J.; Mo, D.; Zhang, J. Temporally Controlled Photothermal/Photodynamic and Combined Therapy for Overcoming Multidrug Resistance of Cancer by Polydopamine Nanoclustered Micelles. *ACS Appl. Mater. Interfaces* **2019**, *11*, 13945–13953. [\[CrossRef\]](#)
92. Yang, G.; Tian, J.; Chen, C.; Jiang, D.; Xue, Y.; Wang, C.; Gao, Y.; Zhang, W. An oxygen self-sufficient NIR-responsive nanosystem for enhanced PDT and chemotherapy against hypoxic tumors. *Chem. Sci.* **2019**, *10*, 5766–5772. [\[CrossRef\]](#)
93. Yue, C.; Yang, Y.; Song, J.; Alfranca, G.; Zhang, C.; Zhang, Q.; Yin, T.; Pan, F.; Jesús, M.; Cui, D. Mitochondria-targeting near-infrared light-triggered thermosensitive liposomes for localized photothermal and photodynamic ablation of tumors combined with chemotherapy. *Nanoscale* **2017**, *9*, 11103–11118. [\[CrossRef\]](#)
94. Yuan, A.; Qiu, X.; Tang, X.; Liu, W.; Wu, J.; Hu, Y. Self-assembled PEG-IR-780-C13 micelle as a targeting, safe and highly-effective photothermal agent for in vivo imaging and cancer therapy. *Biomaterials* **2015**, *51*, 184–193. [\[CrossRef\]](#)
95. Li, S.; Zhou, S.; Li, Y.; Li, X.; Zhu, J.; Fan, L.; Yang, S. Exceptionally High Payload of the IR780 Iodide on Folic Acid-Functionalized Graphene Quantum Dots for Targeted Photothermal Therapy. *ACS Appl. Mater. Interfaces* **2017**, *9*, 22332–22341. [\[CrossRef\]](#) [\[PubMed\]](#)
96. Wang, N.; Zhou, Y.; Xu, Y.; Ren, X.; Zhou, S.; Shang, Q.; Jiang, Y.; Luan, Y. Molecular engineering of anti-PD-L1 peptide and photosensitizer for immune checkpoint blockade photodynamic-immunotherapy. *Chem. Eng. J.* **2020**, *400*, 125995. [\[CrossRef\]](#)
97. Yuan, A.; Wu, J.; Tang, X.; Zhao, L.; Xu, F.; Hu, Y. Application of Near-Infrared Dyes for Tumor Imaging, Photothermal, and Photodynamic Therapies. *J. Pharm. Sci.* **2013**, *102*, 6–28. [\[CrossRef\]](#)
98. Lacroix, A.; Vengut-Climent, E.; De Rochambeau, D.; Sleiman, H.F. Uptake and Fate of Fluorescently Labeled DNA Nanostructures in Cellular Environments: A Cautionary Tale. *ACS Cent. Sci.* **2019**, *5*, 882–891. [\[CrossRef\]](#) [\[PubMed\]](#)
99. Deng, K.; Chen, Y.; Li, C.; Deng, X.; Hou, Z.; Cheng, Z.; Han, Y.; Xing, B.; Lin, J. 808 nm light responsive nanotheranostic agents based on near-infrared dye functionalized manganese ferrite for magnetic-targeted and imaging-guided photodynamic/photothermal therapy. *J. Mater. Chem. B* **2017**, *5*, 1803–1814. [\[CrossRef\]](#)
100. Lin, S.L.; Chen, Z.R.; Chang, C.A. Nd<sup>3+</sup> sensitized core-shell-shell nanocomposites loaded with IR806 dye for photothermal therapy and up-conversion luminescence imaging by a single wavelength NIR light irradiation. *Nanotheranostics* **2018**, *2*, 243–257. [\[CrossRef\]](#)
101. Jogdand, A.; Alvi, S.B.; Rajalakshmi, P.S.; Rengan, A.K. NIR-dye based mucoadhesive nanosystem for photothermal therapy in breast cancer cells. *J. Photochem. Photobiol. B Biol.* **2020**, *208*, 111901. [\[CrossRef\]](#)
102. Wang, X.; Li, Z.; Ding, Y.; Wang, K.; Xing, Z.; Sun, X.; Guo, W.; Hong, X.; Zhu, X.; Liu, Y. Enhanced photothermal-photodynamic therapy for glioma based on near-infrared dye functionalized Fe<sub>3</sub>O<sub>4</sub> superparticles. *Chem. Eng. J.* **2020**, *381*, 122693. [\[CrossRef\]](#)
103. Yu, Z.; Sun, Q.; Pan, W.; Li, N.; Tang, B. A Near-Infrared Triggered Nanophotosensitizer Inducing Domino Effect on Mitochondrial Reactive Oxygen Species Burst for Cancer Therapy. *ACS Nano* **2015**, *9*, 11064–11074. [\[CrossRef\]](#)
104. Asadian-Birjand, M.; Bergueiro, J.; Wedepohl, S.; Calderón, M. Near Infrared Dye Conjugated Nanogels for Combined Photodynamic and Photothermal Therapies. *Macromol. Biosci.* **2016**, *16*, 1432–1441. [\[CrossRef\]](#)
105. Fernandez-Fernandez, A.; Manchanda, R.; Lei, T.; Carvajal, D.A.; Tang, Y.; Kazmi, S.Z.R.; McGoron, A.J. Comparative Study of the Optical and Heat Generation Properties of IR820 and Indocyanine Green. *Mol. Imaging* **2012**, *11*. [\[CrossRef\]](#)
106. Le Zhou, M.Z.; Fu, Q.; Li, J.; Sun, H. Targeted near infrared hyperthermia combined with immune stimulation for optimized therapeutic efficacy in thyroid cancer treatment. *Oncotarget* **2016**, *7*, 6878. [\[CrossRef\]](#)
107. Li, W.; Peng, J.; Tan, L.; Wu, J.; Shi, K.; Qu, Y.; Wei, X.; Qian, Z. Mild photothermal therapy/photodynamic therapy/chemotherapy of breast cancer by Lyp-1 modified Docetaxel/IR820 Co-loaded micelles. *Biomaterials* **2016**, *106*, 119–133. [\[CrossRef\]](#)
108. Liu, R.; Zhang, L.; Zhao, J.; Luo, Z.; Huang, Y.; Zhao, S. Aptamer and IR820 Dual-Functionalized Carbon Dots for Targeted Cancer Therapy against Hypoxic Tumors Based on an 808 nm Laser-Triggered Three-Pathway Strategy. *Adv. Ther.* **2018**, *1*, 1800041. [\[CrossRef\]](#)
109. Xia, B.; Wang, B.; Chen, Z.; Zhang, Q.; Shi, J. Near-Infrared Light-Triggered Intracellular Delivery of Anticancer Drugs Using Porous Silicon Nanoparticles Conjugated with IR820 Dyes. *Adv. Mater. Interfaces* **2016**, *3*, 1500715. [\[CrossRef\]](#)
110. Zhou, H.; Hou, X.; Liu, Y.; Zhao, T.; Shang, Q.; Tang, J.; Liu, J.; Wang, Y.; Wu, Q.; Luo, Z.; et al. Superstable Magnetic Nanoparticles in Conjugation with Near-Infrared Dye as a Multimodal Theranostic Platform. *ACS Appl. Mater. Interfaces* **2016**, *8*, 4424–4433. [\[CrossRef\]](#) [\[PubMed\]](#)
111. Zhang, D.; Zhang, J.; Li, Q.; Tian, H.; Zhang, N.; Li, Z.; Luan, Y. pH- and Enzyme-Sensitive IR820–Paclitaxel Conjugate Self-Assembled Nanovehicles for Near-Infrared Fluorescence Imaging-Guided Chemo–Photothermal Therapy. *ACS Appl. Mater. Interfaces* **2018**, *10*, 30092–30102. [\[CrossRef\]](#) [\[PubMed\]](#)
112. Wu, C.; Wang, L.; Tian, Y.; Guan, X.; Liu, Q.; Li, S.; Qin, X.; Yang, H.; Liu, Y. “Triple-Punch” Anticancer Strategy Mediated by Near-Infrared Photosensitizer/CpG Oligonucleotides Dual-Dressed and Mitochondria-Targeted Nanographene. *ACS Appl. Mater. Interfaces* **2018**, *10*, 6942–6955. [\[CrossRef\]](#)
113. Zaharie-Butucel, D.; Potara, M.; Suarasan, S.; Licarete, E.; Astilean, S. Efficient combined near-infrared-triggered therapy: Phototherapy over chemotherapy in chitosan-reduced graphene oxide-IR820 dye-doxorubicin nanoplateforms. *J. Colloid Interface Sci.* **2019**, *552*, 218–229. [\[CrossRef\]](#)

- 
114. Fu, J.J.; Li, C.W.; Liu, Y.; Chen, M.Y.; Zhang, Q.; Yu, X.Y.; Wu, B.; Li, J.X.; Du, L.R.; Dang, Y.Y.; et al. The microneedles carrying cisplatin and IR820 to perform synergistic chemo-photodynamic therapy against breast cancer. *J. Nanobiotechnol.* **2020**, *18*, 146. [[CrossRef](#)]
  115. Zhang, D.; Zhang, J.; Li, Q.; Song, A.; Li, Z.; Luan, Y. Cold to Hot: Rational Design of a Minimalist Multifunctional Photo-immunotherapy Nanoplatfrom toward Boosting Immunotherapy Capability. *ACS Appl. Mater. Interfaces* **2019**, *11*, 32633–32646. [[CrossRef](#)] [[PubMed](#)]
  116. Noh, J.; Jung, E.; Yoo, D.; Kang, C.; Kim, C.; Park, S.; Khang, G.; Lee, D. Dual Imaging-Guided Oxidative–Photothermal Combination Anticancer Therapeutics. *ACS Appl. Mater. Interfaces* **2018**, *10*, 40424–40433. [[CrossRef](#)]





Article

# GMI, an Immunomodulatory Peptide from *Ganoderma microsporum*, Restrains Periprosthetic Joint Infections via Modulating the Functions of Myeloid-Derived Suppressor Cells and Effector T Cells

Kuo-Ti Peng <sup>1,2,\*</sup>, Jiun-Liang Chen <sup>1</sup>, Liang-Tseng Kuo <sup>1,2</sup> , Pei-An Yu <sup>1</sup>, Wei-Hsiu Hsu <sup>1,2</sup>, Chiang-Wen Lee <sup>3,4,5</sup>, Pey-Jium Chang <sup>6,7</sup> and Tsung-Yu Huang <sup>2,8,9,\*</sup>

- <sup>1</sup> Department of Orthopedic Surgery, Chang Gung Memorial Hospital, Puzi 61363, Taiwan; yq0139@cgmh.org.tw (J.-L.C.); light71829@gmail.com (L.-T.K.); b9002065@cgmh.org.tw (P.-A.Y.); 7572@cgmh.org.tw (W.-H.H.)
- <sup>2</sup> College of Medicine, Chang Gung University, Taoyuan 33303, Taiwan
- <sup>3</sup> Division of Basic Medical Sciences and Recurrent Diseases, Health Promotion Research Center, Department of Nursing, Chang Gung University of Science and Technology, Puzi 61363, Taiwan; cwlee@mail.cgu.edu.tw
- <sup>4</sup> Research Center for Industry of Human Ecology, Research Center for Chinese Herbal Medicine, Chang Gung University of Science and Technology, Taoyuan 33303, Taiwan
- <sup>5</sup> Department of Rehabilitation, Chang Gung Memorial Hospital, Puzi 61363, Taiwan
- <sup>6</sup> Graduate Institute of Clinical Medical Sciences, College of Medicine, Chang-Gung University, Taoyuan 33302, Taiwan; peyjium@mail.cgu.edu.tw
- <sup>7</sup> Department of Nephrology, Chang-Gung Memorial Hospital, Chiayi 61363, Taiwan
- <sup>8</sup> Division of Infectious Diseases, Department of Internal Medicine, Chang Gung Memorial Hospital, Chiayi 61363, Taiwan
- <sup>9</sup> Department of Nursing, Chiayi Campus, Chang Gung University of Science and Technology, Chiayi 61363, Taiwan
- \* Correspondence: mr3497@cgmh.org.tw (K.-T.P.); r12045@cgmh.org.tw (T.-Y.H.); Tel.: +886-(536)-21000 (ext. 2004) (T.-Y.H.)



**Citation:** Peng, K.-T.; Chen, J.-L.; Kuo, L.-T.; Yu, P.-A.; Hsu, W.-H.; Lee, C.-W.; Chang, P.-J.; Huang, T.-Y. GMI, an Immunomodulatory Peptide from *Ganoderma microsporum*, Restrains Periprosthetic Joint Infections via Modulating the Functions of Myeloid-Derived Suppressor Cells and Effector T Cells. *Int. J. Mol. Sci.* **2021**, *22*, 6854. <https://doi.org/10.3390/ijms22136854>

Academic Editor: Luigi Casella

Received: 14 May 2021

Accepted: 22 June 2021

Published: 25 June 2021

**Publisher's Note:** MDPI stays neutral with regard to jurisdictional claims in published maps and institutional affiliations.



**Copyright:** © 2021 by the authors. Licensee MDPI, Basel, Switzerland. This article is an open access article distributed under the terms and conditions of the Creative Commons Attribution (CC BY) license (<https://creativecommons.org/licenses/by/4.0/>).

**Abstract:** Periprosthetic joint infections (PJIs) caused by *Staphylococcus aureus* infection are difficult to treat due to antibiotic resistance. It is known that the biofilms from methicillin-resistant *S. aureus* (MRSA) promote expansion of myeloid-derived suppressor cells (MDSCs) to suppress T-cell proliferation and benefit bacterial infections. This study finds that GMI, a fungal immunomodulatory peptide isolated from *Ganoderma microsporum*, suppresses MDSC expansion to promote the proliferation of cytotoxic T cells. The enhancement is likely attributed to increased expression of IL-6 and TNF- $\alpha$  and reduction in ROS expression. Similar beneficial effects of GMI on the suppression of MDSC expansion and IL-6 expression are also observed in the whole blood and reduces the accumulation of MDSCs in the infected bone region in a mouse PJI infection model. This study shows that GMI is potentially useful for treating *S. aureus*-induced PJIs.

**Keywords:** periprosthetic joint infections; GMI; T cells; myeloid-derived suppressor cells

## 1. Introduction

*Staphylococcus aureus* is a Gram-positive bacterium causing periprosthetic joint infections (PJIs) [1,2]. In primary total joint arthroplasties, the PJI incidence is 1–2%, although 2–6% was observed in revision joint arthroplasties [3]. Although many strategies have been developed to improve PJI treatments [4,5], including debridement with prosthesis retention, one-stage or two-stage reimplantation, and antibiotic therapy, high treatment failure rates of 10–30% during follow-ups [1,6–8] cause a huge financial burden on patients [9,10]. PJI caused by *S. aureus* infection is particularly difficult to treat as this pathogen produces biofilms and is highly resistant to many antibiotics [11–16]. Furthermore, *S. aureus* often



contaminates surgical instruments and implants, making the treatment of PJI challenging [17,18]. Therefore, this study seeks a treatment method that improves antibiotic therapy of PJIs caused by MRSA infection.

Myeloid-derived suppressor cells (MDSCs), an innate immune cell subset, are known to decrease immune-mediated pathology of the hosts to prevent the collateral damage caused by host immune responses [19]. However, the decreased immunity often provides advantages to bacterial infection [19]. For instance, *S. aureus* promotes the expansion of MDSCs from bone marrow cells (BMCs) to suppress T-cell proliferation, resulting in decreased host immunity [20]. Therefore, compounds that prevent or reverse the expansion of MDSCs may be beneficial to the treatments of PJI.

Many natural compounds have been reported to have immunomodulatory and overall health-benefiting effects to people. These compounds are considered safer and less toxic than the synthetic drugs [21,22]. Fungal immunomodulatory proteins (FIPs) are a group of peptides, which are known to modulate immunity [23,24]. So far, 38 types of FIPs have been identified, which are classified into five subgroups [24]. It is well known that FIPs have anti-inflammatory, anti-cancer, and anti-allergic activities. FIPs also inhibit replication of respiratory syncytial virus and microglia [23–26]. *Ganoderma* spp., also called Lingzhi or Reishi, is a popular chemoprevention mushroom. GMI (GenBank AGU04723.1), the FIP from *Ganoderma microsporum*, is a 111-amino acid peptide and one of the active components in the mushroom. The gene encoding GMI, *Pichia pastoris*, has been cloned and can be produced by yeast and is widely used in biochemical research and biotech industries [24,27]. The recombinant GMI was demonstrated to regulate cytokine expression, inhibit lung cancer cells [28–31], and have anti-inflammatory and neuroprotective activities [26]. This study finds that both in vitro and in an *S. aureus*-induced mouse PJI model, GMI promotes T cell proliferation via suppression of MDSC expansion, increases cytokine expression, and reduces ROS, showing that GMI is an attractive candidate for PJI treatment.

## 2. Materials and Methods

### 2.1. Animals

Male C57BL/6J mice that were 8–12 weeks old with weights from 22–25 g were purchased from National Laboratory Animal Center (Taiwan). The mice were acclimated to a room with controlled temperature (25 °C) and humidity (50 ± 10%) with a 12-h day-night cycle. The studies were approved by the Institutional Animal Care and Use Committee of the Chang Gung Memorial Hospital (IACUC permit number: 2019122309) and were performed in accordance with the Animal Protection Law by the Council of Agriculture, Executive Yuan (Taiwan) and the guidelines of National Research Council (USA) for the care and use of laboratory animals.

### 2.2. GMI, *S. aureus* and Biofilm Preparation

GMI is a fungal immunomodulatory protein from *Ganoderma microsporum* (NCBI protein ID AGU04723.1) and was provided by MycoMagic Biotechnology Co, Ltd. (Taipei, Taiwan).

*S. aureus* ATCC43300, a MRSA strain, was purchased from the Bioresource Collection and Research Center (BCRC, Hsinchu, Taiwan). The bacteria were cultured in brain heart infusion (BHI) media (Bacto, Sydney, Australia). After culturing for 4 days, *S. aureus* biofilms were then prepared by autoclaving and centrifugation according to a method reported elsewhere [20]. The biofilms were suspended in RPMI 1640 medium; the number of proteins in the biofilms was quantified using a BCA protein assay kit (Pierce) and was adjusted to 0.2 mg/mL with RPMI 1640 medium. For experiments using live bacteria, *S. aureus* was harvested by centrifugation and enumerated spectrophotometrically by measuring the turbidity at 600 nm ( $A_{600}$ ) and by viable cell counts.

### 2.3. Isolating MDSCs from Mouse Bone Marrow by Cell Sorting

Bone marrow cells (BMCs) in mouse femur were collected and treated with anti-CD11b antibody conjugated with FITC and anti-Gr1 antibody conjugated with PE according to

the methods described earlier [20]. MDSCs, which were stained by both antibodies, were sorted with a FACS Aria Fusion cell sorter (BD). The purity of the isolated cell population was then verified by flow cytometry.

#### 2.4. Analysis of MDSC Expansion

Transwell plates with 0.4- $\mu$ m pore size inserts were used to examine how biofilms and GMI influenced MDSC expansion. BMCs were cultured in the lower compartment in RPMI 1640 medium containing 10% fetal calf serum with different concentrations of GMI; *S. aureus* biofilms (0.2 mg/mL) were added to the inserts. The membrane in the inserts prevented the presence of biofilm debris in the lower compartment to interfere with flow cytometry analysis of BMCs and MDSCs. After culturing for 48 h, cells stained with anti-CD11b-FITC and anti-Gr1-PE antibodies were analyzed using flow cytometry (BD FACSCanto II) to determine the numbers of MDSC proportion. Acquisition of flow cytometry data from the flow cytometer was performed using FACSDiva software (BD Biosciences, Franklin Lakes, NJ, USA). The number of events analyzed was 10,000 per sample. Analysis was performed using FlowJo software (Tree Star, Ashland, OR, USA).

#### 2.5. Analysis of Tc, T<sub>H</sub>, Treg Cells by Flow Cytometry

After treating BMCs with biofilms for 48 h, MDSCs were isolated by sorting as described above. MDSCs ( $1 \times 10^5$  cells) were then treated with GMI, washed with PBS, and cocultured for 48 h with CFSE-labeled spleen T cells ( $2 \times 10^5$  cells) that were stimulated by Dynabeads Mouse T-Activator CD3/CD28 (Gibco). The mouse spleen T cells were purified and labeled with CFSE according to a method described elsewhere [20]. Cells were then stained with anti-CD3-PerCP-Cy5.5 (BD Bioscience), anti-CD4-APC-H7 (BD Bioscience), anti-CD8-PE-Cy7 (BD Bioscience), anti-CD25-PE (BD Bioscience), and anti-FoxP3-Alexa Fluor 647 (BD Bioscience) to analyze Tc, T<sub>H</sub>, and Treg cells by flow cytometry.

#### 2.6. Preparation of Blood Samples for Flow Cytometry Analysis

For determining the effect of GMI on the dynamic changes of the immune cell populations in the peripheral blood of mice, 100  $\mu$ L blood samples were collected. After lysing red blood cells with ACK Lysing buffer (Thermo Fisher, Waltham, MA USA), leukocytes were suspended in PBS containing 2% FBS. T cells were then analyzed by flow cytometry as described above.

#### 2.7. Analysis of IL-6 and TNF- $\alpha$ in Culture Medium and Plasma

A Cytometric Bead Array (CBA) Mouse Inflammation kit was used to quantify IL-6 and TNF- $\alpha$  in culture medium and blood. After mixing 50  $\mu$ L cell culture medium or 50  $\mu$ L blood with the beads, IL-6 and TNF- $\alpha$  captured by the beads were reacted with mouse inflammation PE detection reagent for two hours and analyzed by flow cytometry.

#### 2.8. Measurement of ROS

ROS was measured with 10  $\mu$ M 2',7'-dichlorofluorescein diacetate (DCFDA) (Sigma-Aldrich, St. Louis, MO, USA) according to a method described by Evgeniy et al. and analyzed by flow cytometry [32].

#### 2.9. GMI Treatment of Mice Infected by *S. aureus*

Orthopedic implantation was performed in male C57BL/6J mice according to a method described previously [20] and infected with  $2 \times 10^6$  CFU of *S. aureus* at the intramedullary canal containing the implant. The mice were divided into five groups, including the control group and four different treatment groups ( $n = 4$  for each group), which include (i) the group that received GMI (8 mg/kg) only; (ii) the group that was infected with *S. aureus* only; (iii–v) the groups that were injected intraperitoneally with different concentrations of GMI (2 and 8 mg/kg) three times a week after the infection with *S. aureus* for 3 days. Mice that received implants but without *S. aureus* inoculation served

as the control-operated group. After injection for 2 weeks, the mice were sacrificed, and the femurs were fixed in 10% formalin.

### 2.10. Fluorescence Molecular Tomography

The PJI mice were divided into four groups, including the control group and three different treatment groups with various concentrations of GMI injection (0, 2, and 8 mg/kg) ( $n = 4$  for each group). After GMI injection for 24 h, DilC18 (7)—labeled MDSCs ( $5 \times 10^6$  cells), were injected via tail vein. The infection sites were observed by fluorescence molecular tomography (FMT) at Days 1, 4, and 7. Fluorescence of MDSCs were quantitatively assessed with TrueQuan software.

### 2.11. Statistical Analysis

Results were expressed as mean  $\pm$  standard deviation (SD) and analyzed statistically by Student's *t*-test with GraphPad Prism software (GraphPad, San Diego, CA, USA). A *p*-value less than 0.05 was considered significant.

## 3. Results

### 3.1. Influence of GMI on *S. aureus* Biofilm-Mediated MDSC Expansion

In this study, we investigated whether GMI treatments affected MDSC expansion that was stimulated by *S. aureus* biofilms [20]. We found that in the absence of GMI, 27% of BMCs were expanded to MDSCs (Figure 1A). After treating BMCs with *S. aureus* biofilms, a 1.5-fold increase in MDSC expansion was observed (Figure 1B). The results were consistent with the results of an earlier study which reported that *S. aureus* biofilms activates MDSC proliferation [20]. We also found that although GMI did not seem to promote MDSC expansion from BMCs that were untreated with *S. aureus* biofilms (Figure 1A), GMI treatments impacted the expansion that was stimulated by *S. aureus* biofilms. We found that GMI at 1 and 2.5  $\mu\text{g}$  reduced the expansion from 1.5-fold to 1.2- and 1.1-fold, respectively (Figure 1B).

### 3.2. Activation of IL-6 and TNF- $\alpha$ Expression by GMI

*S. aureus* biofilms are known to stimulate the production of inflammatory cytokines, including IL-6 and TNF- $\alpha$  [33]. In this study, we found that little IL-6 was released into the culture medium by MDSCs that were untreated with biofilms and GMI (Figure 1C). When the cells were treated with 0.5  $\mu\text{g}/\text{mL}$  GMI, the amounts of IL-6 increased only a little. However, if the concentration of GMI increased to 1 and 2.5  $\mu\text{g}/\text{mL}$ , the amounts of IL-6 increased to 10 ng/mL and 50 ng/mL, respectively (Figure 1C), showing that GMI activates the expression of IL-6 from MDSCs untreated with biofilms. We also found that MDSCs that were treated with biofilms produced 27 ng/mL IL-6, an amount substantially higher than that produced by MDSCs untreated with biofilms (Figure 1C), verifying our earlier findings that *S. aureus* biofilms stimulates IL-6 expression [20]. When biofilm-treated MDSCs were incubated with 0.5 to 2.5  $\mu\text{g}/\text{mL}$  GMI, the amounts of IL-6 increased from 25 to 225 ng/mL in a dose-dependent manner (Figure 1C), showing that GMI promotes the expression of IL-6 by the cells treated with biofilms. We also found that MDSCs untreated with biofilms produced little TNF- $\alpha$  even when the cells were incubated with GMI (Figure 1D). However, we found that GMI stimulated TNF- $\alpha$  expression by the cells treated with biofilms. The results showed that the cells untreated with GMI produced 2700 ng/mL TNF- $\alpha$ ; the concentration increased from 2800 to 4800 ng/mL in a dose-dependent manner when the cells were treated with 0.5 to 2.5  $\mu\text{g}/\text{mL}$  GMI (Figure 1D). These results showed that GMI promotes TNF- $\alpha$  expression by the MDSCs treated with biofilms.

### 3.3. Reduction in ROS Expression by GMI

MDSCs are known to release ROS to suppress T cell responses [34]. We found that although GMI did not seem to affect the release of ROS after the cells were treated with 0.5 and 1  $\mu\text{g}$  GMI (Figure 1E), a reduction in ROS expression by 40% from 3000 to 1800 units DCF fluorescence was observed when compared with the ROS from cells untreated with

GMI (Figure 1E). These results showed that GMI reduces the amounts of ROS produced by the cells that are treated with biofilms.

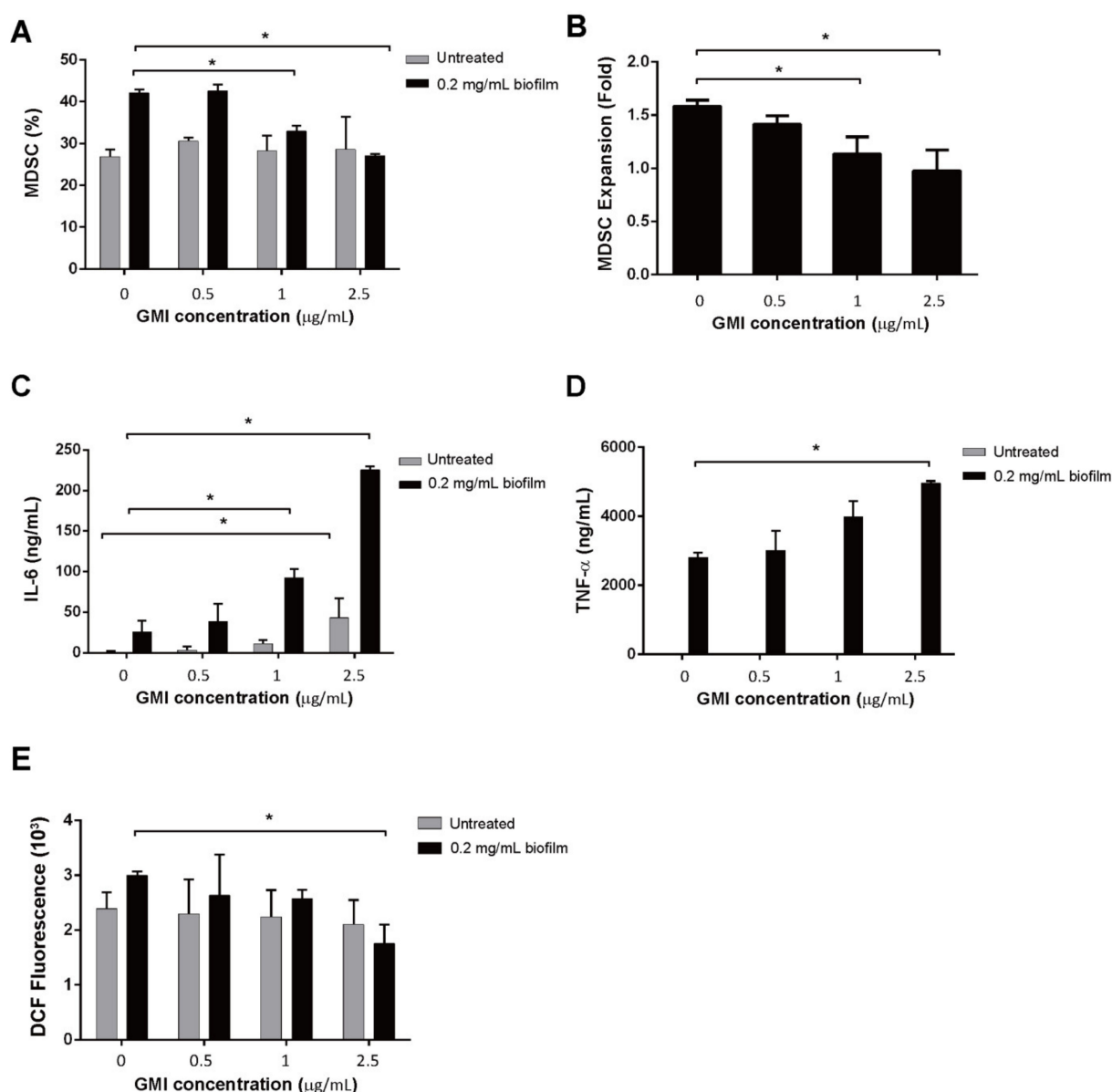


**Figure 1.** Influence of GMI on MDSC expansion and IL-6, TNF- $\alpha$ , and ROS production. BMCs were treated with *S. aureus* biofilms GMI for 48 h. BMCs were also untreated with the biofilm but treated with GMI for the purpose of comparison. The number of MDSCs, which were CD11b-FITC and Gr1-PE positive, were determined by cell sorting with a cell sorter. The percentage of MDSCs in the whole cell population was presented (A). The number of MDSCs from BMCs treated with biofilms was divided by those untreated with biofilms to show the fold increase in the enhancement of MDSC expansion by biofilms (B). The amounts of IL-6 and TNF- $\alpha$  produced by the cells were determined using a CBA kit followed by flow cytometry. (C,D). Cells were treated with 10  $\mu$ M DCFDA, cell population with ROS production was determined by flow cytometry (E). The results were analyzed statistically with Student's *t*-test. \*:  $p < 0.05$ .

### 3.4. Effects of GMI on the Suppression of T Cell Proliferation by MDSCs

MDSCs were prepared using a cell sorter from BMCs that were treated or untreated with biofilms. MDSCs were then treated with GMI for 24 h and then cocultured with CFSE-labeled T cells treated with anti-CD3/CD28 antibodies that were conjugated to magnetic beads for 48 h at a ratio of 1:2 ( $1 \times 10^5$ : $2 \times 10^5$ ) to test how GMI treatment affected MDSC's ability to suppress T cell proliferation. We found that in the case of MDSCs from BMCs

that were untreated with biofilms, the number of T cells increased by 30% if GMI was not added to the culture. The number of T cells increased from 30% to 34%, 46%, 61% after 0.5, 1, and 2.5  $\mu\text{g}$  GMI was added, respectively (Figure 2), showing the promotion of T cell proliferation by GMI. GMI also promoted T cell proliferation that was suppressed by MDSCs from BMCs treated with biofilms. In the absence of GMI, an increase of 20% of T cells was observed (Figure 2), however, the percentage increased to 25%, 50%, 61.5% after 0.5, 1, and 2.5  $\mu\text{g}$  GMI was added, showing that GMI inhibits the suppression of T cell proliferation by MDSCs.

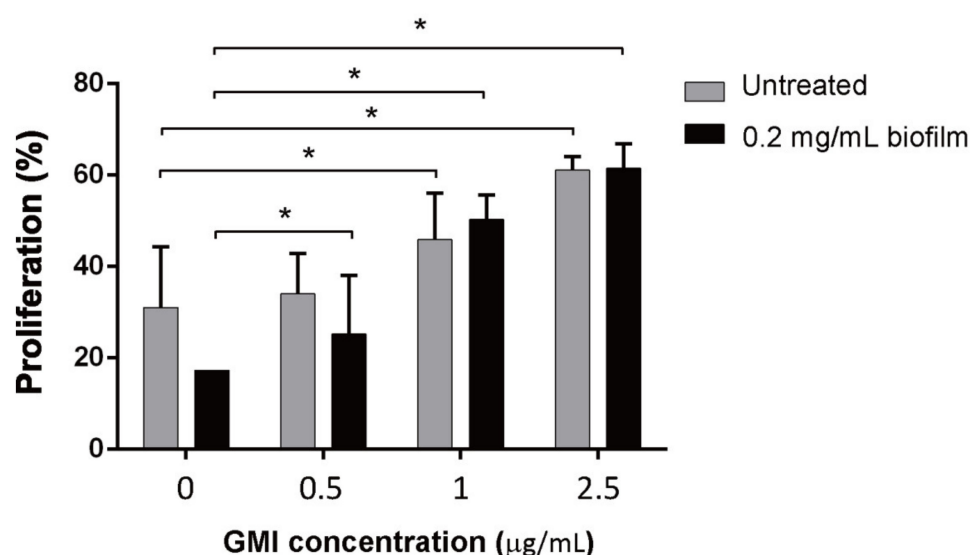


**Figure 2.** Influence of GMI on the suppression of T cell proliferation by MDSCs. Freshly isolated mouse BMCs were untreated or treated with 0.2 mg/mL *S. aureus* biofilms for 48 h. MDSCs expanded from BMCs were treated with anti-CD11b antibody conjugated with FITC and anti-Gr1 antibody conjugated with PE. The cells that were bound to both antibodies were separated using a cell sorter. MDSCs were treated with different concentrations of GMI for 24 h and then cocultured with activated CFSE-labeled T cells at a ratio of 0.5:1. The results were analyzed statistically with Student's *t*-test. \*:  $p < 0.05$ .

We further investigated the specific T cell subtypes that were affected by GMI treatment. We cocultured MDSCs and T cells for 48 h then treated the cells with anti-CD3 antibody conjugate to PerCP-Cy5.5 and anti-CD8 antibody conjugated with PE-Cy7 to label Tc cells. T<sub>H</sub> cells in the T cell population were similarly labeled with anti-CD3 antibody conjugated with PerCP-Cy5 and anti-CD4 antibody conjugated with APC-H7; Treg, anti-CD3 antibody conjugate with PerCP-Cy5.5, anti-CD4 antibody conjugated with APC-H7, anti-CD25 antibody conjugated with PE, and FoxP3 conjugated with Alexa fluor 647. After flow cytometry analysis, we found that few Tc cells proliferated if the cells were untreated with GMI (Figure 3). However, when 0.5  $\mu\text{g}$  GMI was added to the culture, regardless of whether MDSCs were treated or untreated with biofilms, enhancement of Tc cell proliferation became evident (Figure 3). When T cells were cocultured with MDSCs that were untreated with biofilm, 1  $\mu\text{g}$  GMI increased the Tc cells by 27.5% (Figure 3). If Tc cells were cocultured with MDSCs that were treated with biofilms, a 58% increase was observed (Figure 3). GMI at 1  $\mu\text{g}$  seemed to yield the maximum enhancement as 2.5  $\mu\text{g}$  did not further enhance the proliferation. Unlike Tc cells, the proliferation of T<sub>H</sub> cells did not increase much after treatment with GMI. When T cells were cocultured with MDSCs that were untreated with biofilms, the number of T<sub>H</sub> cells increased by 4%; the proliferation increased to only 6% when they were cultured in the medium containing 1 or 2.5  $\mu\text{g/mL}$  GMI (Figure 3). When T cells were incubated with MDSCs that were treated with biofilms, GMI treatment increased proliferation of T<sub>H</sub> cells by 8% (Figure 3). We also found that after coculturing T cells with MDSCs or biofilm-treated MDSCs, Treg cells increased only by 0.5% and 1%, respectively (Figure 3). When the cells were cocultured in the presence



of 0.5  $\mu\text{g}$  GMI, GMI enhanced the proliferation of Treg cells that were cocultured with biofilm-treated MDSCs to 1.5% while the percent of proliferation was unchanged for the Treg cells when the cells were cocultured with MDSCs untreated with biofilm. In the presence of 1 or 2.5  $\mu\text{g}$  GMI, proliferation of Treg increased to about 1%; when the cells were treated with biofilm, the percentages increased to 2 and 3%, respectively (Figure 3). The results showed that among the three subtypes of T cells, GMI preferentially promotes the proliferation of Tc cells that is suppressed by MDSCs.

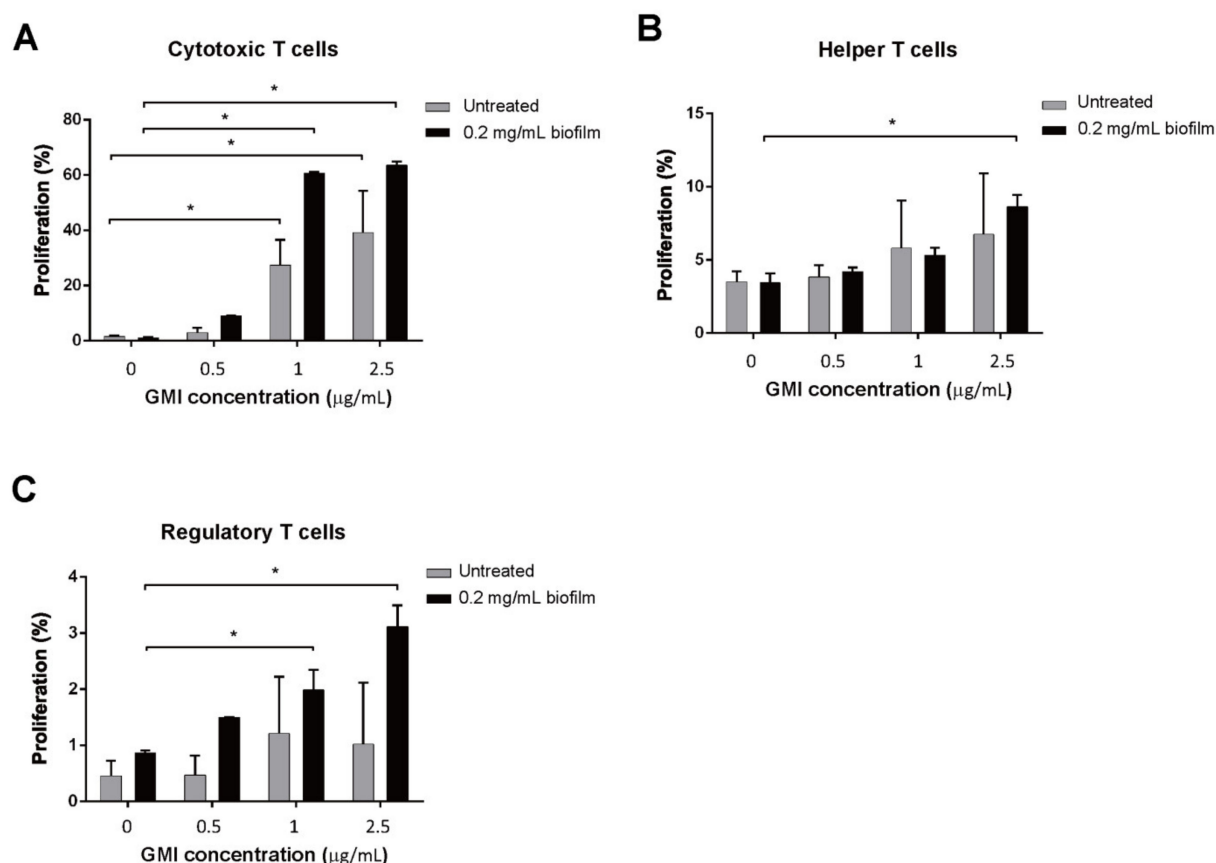


**Figure 3.** Activation of T cell proliferation that was suppressed by MDSCs. MDSCs that were treated or untreated with biofilm were incubated with GMI. At 24 h after incubation, the cells were cocultured for 48 h with activated CFSE-labeled T cells at a ratio of 0.5:1, and proliferation of Tc (A), T<sub>H</sub> (B), and Treg (C) cells were examined and enumerated by flow cytometry. The results were analyzed statistically with Student's *t*-test. \*:  $p < 0.05$ .

### 3.5. Promotion of T Cell Proliferation by GMI

After demonstrating that GMI promotes T cell proliferation that is suppressed by MDSCs, we further investigated whether GMI directly promoted T cell proliferation in the absence of MDSCs. We found that GMI promoted T cell proliferation in a dose-dependent manner. After adding 0.5, 1, and 2.5  $\mu\text{g}$  GMI, T cell proliferation increased from 1% to 37%, 42%, and 70%, respectively (Figure 4). The results indicated that GMI can either indirectly promote T cell proliferation by reducing MDSCs' suppression or directly enhance T cell proliferation.

### 3.6. Effects of GMI on the Production of Cytokines

As it is commonly known that IL-6 promotes proliferation and activation of T cells [35], we further evaluated whether GMI treatment increased IL-6 production. After treating the cells with GMI for 48 h, IL-6 in the culture medium was captured with CBA beads and quantified by flow cytometry. We found that in the absence of GMI, little IL-6 was expressed. However, 6, 8, 9 ng/mL IL-6 were detected in the medium when cells were

treated with 0.5, 1, and 2.5  $\mu\text{g}$  GMI, respectively (Figure 5), showing that GMI promotes the synthesis of IL-6, from T cells.

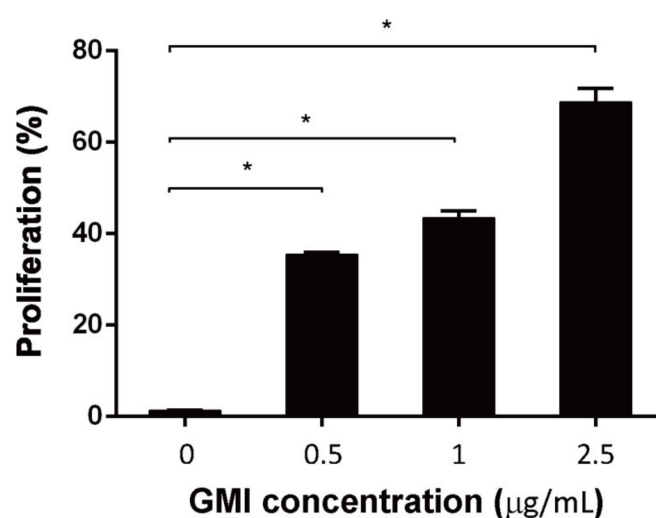


**Figure 4.** Enhancement of T cell proliferation by GMI. T cells were incubated with GMI for 48 h. T cells were then enumerated by flow cytometry. The results were analyzed statistically with Student's *t*-test. \*:  $p < 0.05$ .

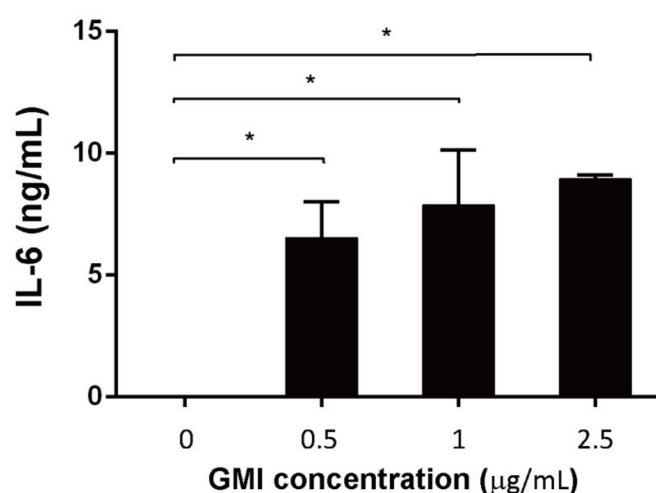


**Figure 5.** Expression of IL-6 by T cells after GMI treatment. T cells were cultured in the presence of GMI for 48 h. IL-6 in the culture medium was assayed by a CBA kit. The results were analyzed statistically with Student's *t*-test. \*:  $p < 0.05$ .

### 3.7. Effects of GMI on *S. aureus*-Induced Mouse PJI Model

This study used an *S. aureus* induced mouse PJI model [20,36] to evaluate whether GMI is useful for treating PJI. As shown in Figure 6A, the X-ray image showed that the bone had severe permeated pathologic fractal after *S. aureus* infection. We also observed that treatment with 8 mg/kg GMI reduced osteolytic destructions (Figure 6). We also studied whether GMI-suppressed MDSC expansion and cytokine changes could be observed in the mouse PJI model. *S. aureus* infection increased MDSCs levels in PBMCs by 21-fold as compared to the control group (Figure 6). We found that MDSC expansion was reduced in GMI treatment groups in a dose-dependent manner; the groups treated with 2 mg/kg and 8 mg/kg GMI decreased the number of MDSCs by 30.7% and 61.9%, respectively (Figure 6B). A similar pattern was obtained for the IL-6 in blood (Figure 6C). *S. aureus* infection caused a 10.4-fold

increase in IL-6. The level decreased to 41% and 60.9% after the mice were injected with 2 mg/kg GMI and 8 mg/kg GMI, respectively (Figure 6). The results showed that GMI not only reduces MDSC expansion but also increases expression of IL-6 in mice.

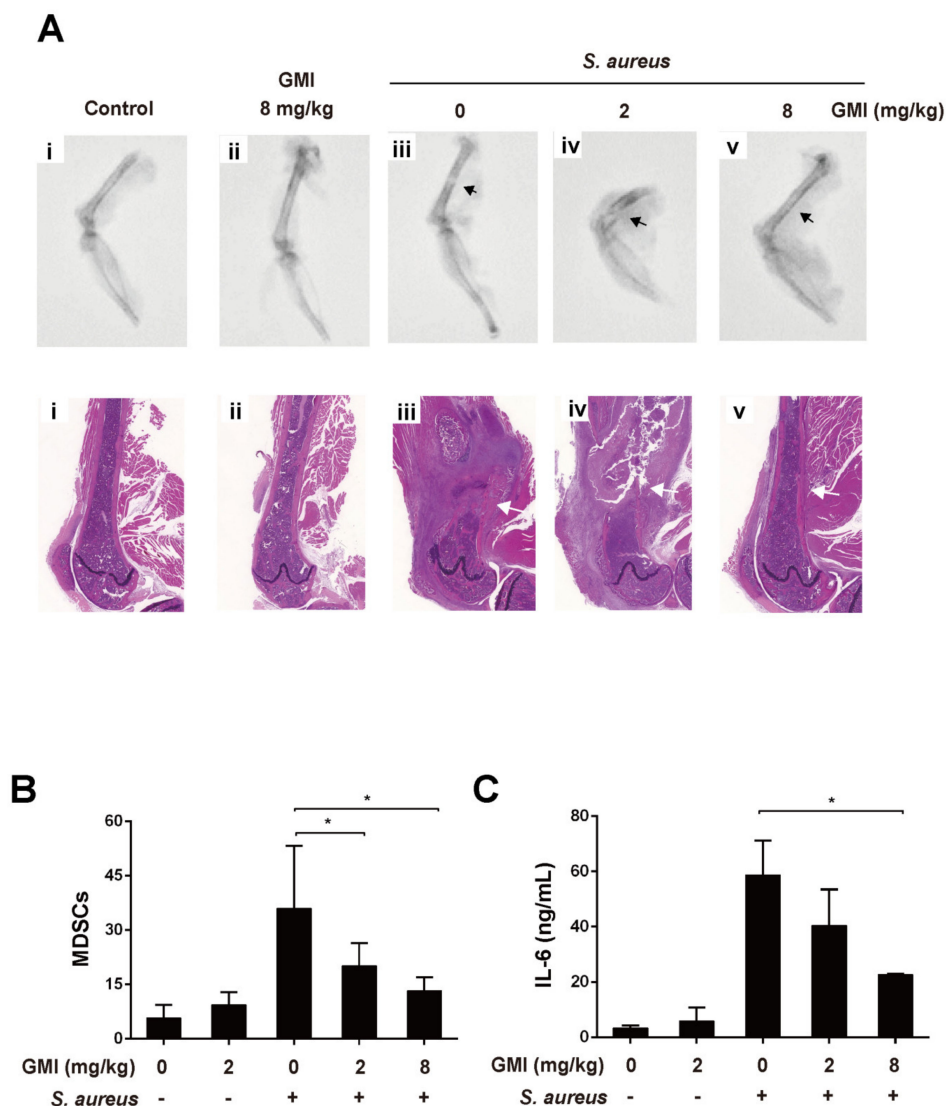


**Figure 6.** Influence of GMI treatment on *S. aureus* infection in a mouse PJI model. Mice were divided into five groups ( $n = 4$ ): (i) control group (ii) GMI (8 mg/kg) only; (iii) infected with *S. aureus* only; (iv,v) infected with *S. aureus* and injecting 2 and 8 mg/kg GMI. (A) X-ray images (upper) and histological staining (lower) of femur in mice infected with *S. aureus* are shown. Black arrow indicates *S. aureus* infection site and bone destruction; White arrow showed infiltrating mononuclear immune cells. (B) MDSCs in PBMCs were enumerated by flow cytometry. (C) The concentration of IL-6 in GMI-treated mice that were uninfected or infected with *S. aureus* was determined using a CBA kit. The results were analyzed statistically with Student's *t*-test. \*:  $p < 0.05$ .

It is known that *S. aureus* promotes local MDSC accumulation in the infected regions [37–40]. To demonstrate how GMI affected the accumulation of MDSC in a prosthesis, we injected mice with  $5 \times 10^6$  MDSCs that were labeled with a near-IR fluorescent lipophilic cyanine dye DiI18 (7) ('DiR') via tail veins, and the infected site was observed by fluorescence molecular tomography (FMT) at Days 1, 4, and 7. We found that introducing GMI decreased the aggregation of MDSC-DiR in the lesion region with a notably decrease during the studying period; MDSCs-DiR signals decreased in group injected with 8 mg/kg

GMI compared to the control PJI group. The signal intensity decreased by 25.2%, 58.1%, and 74.3% at Days 1, 4, and 7, respectively (Figure 7). The results showed that GMI reduces the accumulation of MDSCs at the injection sites.

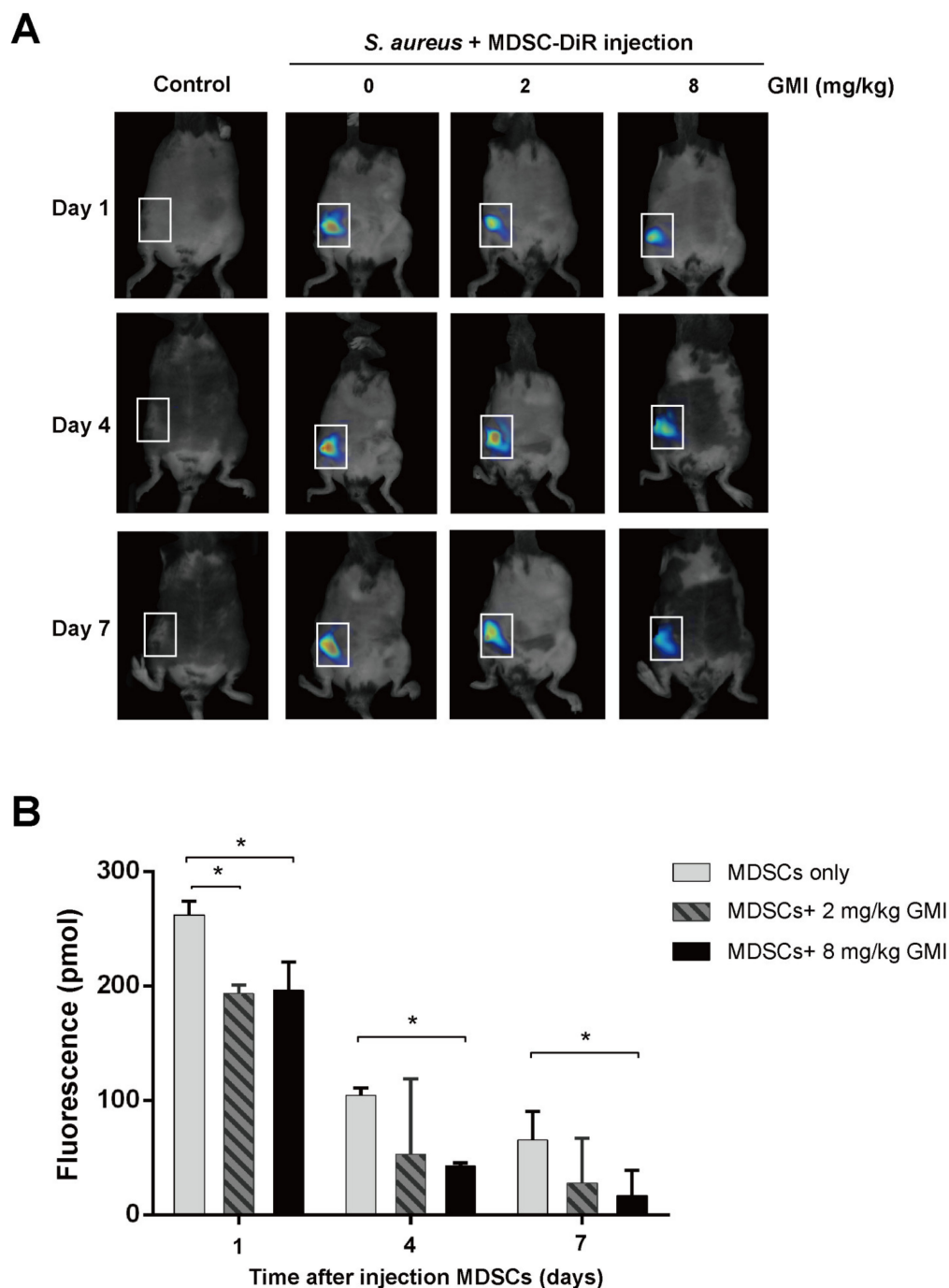


**Figure 7.** Effects of GMI on the recruitment and accumulation of local MDSCs in the infected regions after *S. aureus* infection. (A) The FMT images obtained on day 1, 4, and 7 after injection. (B) Fluorescence of MDSCs were quantitatively assessed with TrueQuan software. The results were analyzed statistically with Student's *t*-test. \*:  $p < 0.05$ .

#### 4. Discussion

PJI is a disaster after total joint arthroplasty. Treatment of the disease requires surgical intervention and a prolonged antibiotic course. As the failure rate of PJI treatment is

high and the disease is often associated with high morbidity and functional loss, effective treatment methods are urgently needed [6]. It is commonly known that PJI caused by *S. aureus* infection is particularly troublesome as *S. aureus* biofilms often persist on the surface of the implants and are difficult to remove [1]. Additionally, the biofilms are known to reduce host's immunity and increase resistance to antibiotics [41], causing the treatment of *S. aureus* infection extremely difficult. This study finds that GMI is an effective agent which promotes T cell proliferation that is suppressed by *S. aureus*, making this compound potentially useful for treating PJI.

MDSC is an innate immune cell subset that decreases immune-mediated pathology of the hosts to prevent the collateral damage caused by robust host immune responses [19]. However, the decreased immunity often provides advantages to bacterial infection [19]. In an earlier study, we demonstrated that the biofilms formed by *S. aureus* strains USA300 and Col induce the expansion of MDSC, indicating that *S. aureus* exploits the expansion of MDSCs and reduced T cell proliferation to benefit their infection. We also demonstrated that curcumin inhibits MDSC expansion [36], showing that natural compounds may be useful for treating PJI. As *G. microsporum* has been widely used as a new dietary ingredient to modulate immunity, this study evaluates a peptide, GMI, isolated from this fungus, to determine whether this compound has similar effects as curcumin on inhibiting MDSC expansion. We found that GMI at 2.5 µg substantially reduces the MDSC expansion that is induced by *S. aureus* biofilms (Figure 1A,B), showing that GMI is potentially useful for treatment PJI caused by *S. aureus*.

In this study, we cocultured MDSCs and T cells to examine how GMI influences the suppression of T cell proliferation by MDSCs. We found that when coculturing T cells with MDSCs, a 30% T proliferation was observed; a 20% proliferation was observed when T cells were cocultured with MDSCs from BMCs treated with *S. aureus* biofilms (Figure 2). This finding is consistent with results that *S. aureus* biofilms stimulate MDSC expansion to inhibit T cell proliferation [20]. This study also showed that GMI promoted T cell proliferation that is suppressed by both types of MDSCs. At 2.5 µg/mL of GMI, the suppression of T cell proliferation by MDSCs and the MDSCs from biofilm-treated BMCs was reduced and a 60% proliferation was observed (Figure 2), showing that GMI significantly reduced the suppression of T cell proliferation by MDSCs from biofilm-treated BMCs. More importantly, Tc cells were more responsive to GMI treatment than T<sub>H</sub> and Treg cells, showing that GMI specifically reduced the suppression of Tc proliferation by MDSCs. The stimulation of T cell proliferation by GMI may be attributed to its ability to promote the expression of IL-6 and TNF-α (Figure 1). GMI is an FIP with a sequence and structure similar to Lingzhi 8 (LZ8) from *Ganoderma microsporum*. LZ-8 is known to induce mouse splenocytes, human peripheral blood lymphocytes, PBMC, and T cell proliferation and activation [22,24,42]. LZ-8 also upregulates the expression of IL-2, TNF-α, IFN-γ, and IL-1β [43,44]. It is well known that IL-6, TNF-α, and IL-1, influence MDSC expansion [40,45,46] and promote the T cell proliferation [35]. Meanwhile, the expression of IL-6 reduces apoptosis of CD4 T cells [47], increases activated T cells migration [48], and regulates Th1/Th2 balance toward Th2 differentiation [49]. Importantly, IL-6 promotes differentiation of naïve CD8 T cell into a unique population of effector CD8+ T cells for antagonizing the viral infection [50]. It is also known that TNF-α promotes T cell activation and proliferation [51]. The increases in TNF-α and IL-6 levels may explain how GMI promotes proliferation T<sub>c</sub> cells.

Finally, we examined how the administration of GMI benefits the treatment of PJI in an *S. aureus*-induced PJI mouse model. We found that GMI treatment reduced osteolytic destructions (Figure 6). We also found that MDSC expansion was reduced in GMI treatment groups but increased IL-6 and TNF-α expression, which were consistent with the in vitro results (Figures 1–4). It is known that *S. aureus* promotes local MDSC accumulation in the infected regions [37–40]. To demonstrate how GMI affected the accumulation of MDSC in prosthesis, we injected mice MDSCs and observed by fluorescence molecular tomography (FMT), the aggregation of MDSC in the lesion reduced significantly during



the studying period, showing that GMI reduces accumulation of MDSCs at the injection sites. This study demonstrates that GMI is an attractive compound potentially beneficial to the treatment of PJI.

**Author Contributions:** Conceived and designed the experiments: K.-T.P., T.-Y.H., P.-J.C. Performed the experiments: K.-T.P., J.-L.C., L.-T.K., C.-W.L. Analyzed and interpreted the data: K.-T.P., P.-A.Y., W.-H.H. Contributed reagents/materials/analysis tools: T.-Y.H., C.-W.L. Contributed to the writing of the manuscript: K.-T.P., T.-Y.H., P.-J.C., J.-L.C. All authors have read and agreed to the published version of the manuscript.

**Funding:** This work was supported by the Chang Gung Medical Research Program Foundation (grants CMRPG6J0231-0232 and CMRPG6H0402 from the Chang Gung Memorial Hospital Taiwan), and the Ministry of Science and Technology (R.O.C.) (grants NMRPG6K6011-6012) [MOST 109-2314-B-182A-024-MY3].

**Institutional Review Board Statement:** The studies were approved by the Institutional Animal Care and Use Committee of the Chang Gung Memorial Hospital (IACUC permit number: 2019122309).

**Informed Consent Statement:** Not applicable.

**Data Availability Statement:** Not applicable.

**Acknowledgments:** We thank Pei-Chun Chen for the excellent technical assistance.

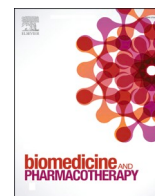
**Conflicts of Interest:** The authors declare no conflict of interest.

## References

1. Ricciardi, B.F.; Muthukrishnan, G.; Masters, E.; Ninomiya, M.; Lee, C.C.; Schwarz, E.M. *Staphylococcus aureus* Evasion of Host Immunity in the Setting of Prosthetic Joint Infection: Biofilm and Beyond. *Curr. Rev. Musculoskelet. Med.* **2018**, *11*, 389–400. [[CrossRef](#)] [[PubMed](#)]
2. Gbejuade, H.O.; Lovering, A.M.; Webb, J.C. The role of microbial biofilms in prosthetic joint infections. *Acta Orthop.* **2015**, *86*, 147–158. [[CrossRef](#)]
3. Gallo, J.; Kolar, M.; Novotny, R.; Rihakova, P.; Ticha, V. Pathogenesis of prosthesis-related infection. *Biomed. Pap.* **2003**, *147*, 27–35. [[CrossRef](#)]
4. Rao, N.; Ziran, B.H.; Lipsky, B.A. Treating osteomyelitis: Antibiotics and surgery. *Plast. Reconstr. Surg.* **2011**, *127* (Suppl. S1), S177–S187. [[CrossRef](#)]
5. Fagotti, L.; Tatka, J.; Salles, M.J.C.; Queiroz, M.C. Risk Factors and Treatment Options for Failure of a Two-Stage Exchange. *Curr. Rev. Musculoskelet. Med.* **2018**, *11*, 420–427. [[CrossRef](#)]
6. Vilchez, F.; Martinez-Pastor, J.C.; Garcia-Ramiro, S.; Bori, G.; Macule, F.; Sierra, J.; Font, L.; Mensa, J.; Soriano, A. Outcome and predictors of treatment failure in early post-surgical prosthetic joint infections due to *Staphylococcus aureus* treated with debridement. *Clin. Microbiol. Infect.* **2011**, *17*, 439–444. [[CrossRef](#)] [[PubMed](#)]
7. Bryan, A.J.; Abdel, M.P.; Sanders, T.L.; Fitzgerald, S.F.; Hanssen, A.D.; Berry, D.J. Irrigation and Debridement with Component Retention for Acute Infection After Hip Arthroplasty: Improved Results with Contemporary Management. *J. Bone Jt. Surg. Am.* **2017**, *99*, 2011–2018. [[CrossRef](#)] [[PubMed](#)]
8. Nodzo, S.R.; Boyle, K.K.; Spiro, S.; Nocon, A.A.; Miller, A.O.; Westrich, G.H. Success rates, characteristics, and costs of articulating antibiotic spacers for total knee periprosthetic joint infection. *Knee* **2017**, *24*, 1175–1181. [[CrossRef](#)] [[PubMed](#)]
9. Kurtz, S.M.; Lau, E.; Watson, H.; Schmier, J.K.; Parvizi, J. Economic burden of periprosthetic joint infection in the United States. *J. Arthroplast.* **2012**, *27* (Suppl. S8), 61.e1–65.e1. [[CrossRef](#)] [[PubMed](#)]
10. Peel, T.N.; Dowsey, M.M.; Buising, K.L.; Liew, D.; Choong, P.F. Cost analysis of debridement and retention for management of prosthetic joint infection. *Clin. Microbiol. Infect.* **2013**, *19*, 181–186. [[CrossRef](#)]
11. Darbani, R.; Farshadfar, C.; Tavana, S.; Saljoughi, H.; Zonouri, S.S.; Branch, S.; Zonouri, S.S. Identification of DNA gyrase Subunit a Mutations Associated with Ciprofloxacin Resistance in *Staphylococcus aureus* Isolated from Nasal Infection in Kurdistan, Iran. *J. Mol. Biol. Res.* **2017**, *7*, 186–193. [[CrossRef](#)]
12. Yilmaz, E.S.; Aslantas, O. Antimicrobial resistance and underlying mechanisms in *Staphylococcus aureus* isolates. *Asian Pac. J. Trop. Med.* **2017**, *10*, 1059–1064. [[CrossRef](#)] [[PubMed](#)]
13. Foster, T.J. Antibiotic resistance in *Staphylococcus aureus*: Current status and future prospects. *FEMS Microbiol. Rev.* **2017**, *41*, 430–449. [[CrossRef](#)] [[PubMed](#)]
14. Drago, L.; De Vecchi, E.; Nicola, L.; Gismondo, M.R. In vitro evaluation of antibiotics' combinations for empirical therapy of suspected methicillin resistant *Staphylococcus aureus* severe respiratory infections. *BMC Infect. Dis.* **2007**, *7*, 111. [[CrossRef](#)] [[PubMed](#)]
15. Grundmann, H.; Aires-de-Sousa, M.; Boyce, J.; Tiemersma, E. Emergence and resurgence of methicillin-resistant *Staphylococcus aureus* as a public-health threat. *Lancet* **2006**, *368*, 874–885. [[CrossRef](#)]

16. Hiramatsu, K.; Katayama, Y.; Yuzawa, H.; Ito, T. Molecular genetics of methicillin-resistant *Staphylococcus aureus*. *Int. J. Med. Microbiol.* **2002**, *292*, 67–74. [[CrossRef](#)]
17. Ciofu, O.; Rojo-Moliner, E.; Macia, M.D.; Oliver, A. Antibiotic treatment of biofilm infections. *APMIS* **2017**, *125*, 304–319. [[CrossRef](#)] [[PubMed](#)]
18. Flemming, H.C.; Wingender, J. The biofilm matrix. *Nat. Rev. Microbiol.* **2010**, *8*, 623–633. [[CrossRef](#)]
19. Medina, E.; Hartl, D. Myeloid-Derived Suppressor Cells in Infection: A General Overview. *J. Innate Immun.* **2018**, *10*, 407–413. [[CrossRef](#)]
20. Peng, K.T.; Hsieh, C.C.; Huang, T.Y.; Chen, P.C.; Shih, H.N.; Lee, M.S.; Chang, P.J. *Staphylococcus aureus* biofilm elicits the expansion, activation and polarization of myeloid-derived suppressor cells in vivo and in vitro. *PLoS ONE* **2017**, *12*, e0183271. [[CrossRef](#)] [[PubMed](#)]
21. Labrecque, J.; Charlebois, S. Functional foods: An empirical study on perceived health benefits in relation to pre-purchase intentions. *Nutr. Food Sci.* **2011**, *41*, 308–318. [[CrossRef](#)]
22. Zhao, S.; Gao, Q.; Rong, C.; Wang, S.; Zhao, Z.; Liu, Y.; Xu, J. Immunomodulatory Effects of Edible and Medicinal Mushrooms and Their Bioactive Immunoregulatory Products. *J. Fungi* **2020**, *6*, 269. [[CrossRef](#)]
23. Li, Q.Z.; Wang, X.F.; Zhou, X.W. Recent status and prospects of the fungal immunomodulatory protein family. *Crit. Rev. Biotechnol.* **2011**, *31*, 365–375. [[CrossRef](#)]
24. Liu, Y.; Bastiaan-Net, S.; Wichers, H.J. Current Understanding of the Structure and Function of Fungal Immunomodulatory Proteins. *Front. Nutr.* **2020**, *7*, 132. [[CrossRef](#)]
25. Chang, Y.C.; Chow, Y.H.; Sun, H.L.; Liu, Y.F.; Lee, Y.T.; Lue, K.H.; Ko, J.L. Alleviation of respiratory syncytial virus replication and inflammation by fungal immunomodulatory protein FIP-fve from *Flammulina velutipes*. *Antivir. Res.* **2014**, *110*, 124–131. [[CrossRef](#)]
26. Chen, W.Y.; Chang, C.Y.; Li, J.R.; Wang, J.D.; Wu, C.C.; Kuan, Y.H.; Liao, S.L.; Wang, W.Y.; Chen, C.J. Anti-inflammatory and Neuroprotective Effects of Fungal Immunomodulatory Protein Involving Microglial Inhibition. *Int. J. Mol. Sci.* **2018**, *19*, 3678. [[CrossRef](#)]
27. Wu, M.-y.; Hsu, M.-F.; Huang, C.-S.; Fu, H.-Y.; Wang, A.; Hseu, R.-S.; Huang, C.-T.; Yang, C.-S. A 2.0 Å Structure of the Fungal Immunomodulatory Protein GMI from *Ganoderma microsporum*. In Proceedings of the 2nd Asia-Oceania Forum for Synchrotron Radiation Research, Hsinchu, Taiwan, 2–3 November 2007.
28. Hsin, I.L.; Sheu, G.T.; Jan, M.S.; Sun, H.L.; Wu, T.C.; Chiu, L.Y.; Lue, K.H.; Ko, J.L. Inhibition of lysosome degradation on autophagosome formation and responses to GMI, an immunomodulatory protein from *Ganoderma microsporum*. *Br. J. Pharm.* **2012**, *167*, 1287–1300. [[CrossRef](#)] [[PubMed](#)]
29. Hsin, I.L.; Ou, C.C.; Wu, T.C.; Jan, M.S.; Wu, M.F.; Chiu, L.Y.; Lue, K.H.; Ko, J.L. GMI, an immunomodulatory protein from *Ganoderma microsporum*, induces autophagy in non-small cell lung cancer cells. *Autophagy* **2011**, *7*, 873–882. [[CrossRef](#)] [[PubMed](#)]
30. Lin, C.H.; Hsiao, Y.M.; Ou, C.C.; Lin, Y.W.; Chiu, Y.L.; Lue, K.H.; Chang, J.G.; Ko, J.L. GMI, a *Ganoderma* immunomodulatory protein, down-regulates tumor necrosis factor alpha-induced expression of matrix metalloproteinase 9 via NF-κB pathway in human alveolar epithelial A549 cells. *J. Agric. Food Chem.* **2010**, *58*, 12014–12021. [[CrossRef](#)] [[PubMed](#)]
31. Lin, C.-H.; Sheu, G.-T.; Lin, Y.-W.; Yeh, C.-S.; Huang, Y.-H.; Lai, Y.-C.; Chang, J.-G.; Ko, J.-L. A new immunomodulatory protein from *Ganoderma microsporum* inhibits epidermal growth factor mediated migration and invasion in A549 lung cancer cells. *Process. Biochem.* **2010**, *45*, 1537–1542. [[CrossRef](#)]
32. Eruslanov, E.; Kusmartsev, S. Identification of ROS using oxidized DCFDA and flow-cytometry. *Methods Mol. Biol.* **2010**, *594*, 57–72. [[PubMed](#)]
33. Tankersley, A.; Frank, M.B.; Bebak, M.; Brennan, R. Early effects of *Staphylococcus aureus* biofilm secreted products on inflammatory responses of human epithelial keratinocytes. *J. Inflamm.* **2014**, *11*, 17. [[CrossRef](#)] [[PubMed](#)]
34. Ohl, K.; Tenbrock, K. Reactive Oxygen Species as Regulators of MDSC-Mediated Immune Suppression. *Front. Immunol.* **2018**, *9*, 2499. [[CrossRef](#)]
35. Dienz, O.; Rincon, M. The effects of IL-6 on CD4 T cell responses. *Clin. Immunol.* **2009**, *130*, 27–33. [[CrossRef](#)]
36. Peng, K.T.; Chiang, Y.C.; Huang, T.Y.; Chen, P.C.; Chang, P.J.; Lee, C.W. Curcumin nanoparticles are a promising anti-bacterial and anti-inflammatory agent for treating periprosthetic joint infections. *Int. J. Nanomed.* **2019**, *14*, 469–481. [[CrossRef](#)] [[PubMed](#)]
37. Skabytska, Y.; Wolbing, F.; Gunther, C.; Koberle, M.; Kaesler, S.; Chen, K.M.; Guenova, E.; Demircioglu, D.; Kempf, W.E.; Volz, T.; et al. Cutaneous innate immune sensing of Toll-like receptor 2–6 ligands suppresses T cell immunity by inducing myeloid-derived suppressor cells. *Immunity* **2014**, *41*, 762–775. [[CrossRef](#)]
38. Heim, C.E.; Vidlak, D.; Kielian, T. Interleukin-10 production by myeloid-derived suppressor cells contributes to bacterial persistence during *Staphylococcus aureus* orthopedic biofilm infection. *J. Leukoc. Biol.* **2015**, *98*, 1003–1013. [[CrossRef](#)] [[PubMed](#)]
39. Heim, C.E.; Vidlak, D.; Scherr, T.D.; Hartman, C.W.; Garvin, K.L.; Kielian, T. IL-12 promotes myeloid-derived suppressor cell recruitment and bacterial persistence during *Staphylococcus aureus* orthopedic implant infection. *J. Immunol.* **2015**, *194*, 3861–3872. [[CrossRef](#)] [[PubMed](#)]
40. Dorhoi, A.; Du Plessis, N. Monocytic Myeloid-Derived Suppressor Cells in Chronic Infections. *Front. Immunol.* **2017**, *8*, 1895. [[CrossRef](#)] [[PubMed](#)]
41. Singh, S.; Singh, S.K.; Chowdhury, I.; Singh, R. Understanding the Mechanism of Bacterial Biofilms Resistance to Antimicrobial Agents. *Open Microbiol. J.* **2017**, *11*, 53–62. [[CrossRef](#)] [[PubMed](#)]

42. Lin, T.Y.; Hua, W.J.; Yeh, H.; Tseng, A.J. Functional proteomic analysis reveals that fungal immunomodulatory protein reduced expressions of heat shock proteins correlates to apoptosis in lung cancer cells. *Phytomedicine* **2021**, *80*, 153384. [[CrossRef](#)] [[PubMed](#)]
43. Haak-Frendscho, M.; Kino, K.; Sone, T.; Jardieu, P. Ling Zhi-8: A novel T cell mitogen induces cytokine production and upregulation of ICAM-1 expression. *Cell Immunol.* **1993**, *150*, 101–113. [[CrossRef](#)]
44. Hsu, H.Y.; Hua, K.F.; Wu, W.C.; Hsu, J.; Weng, S.T.; Lin, T.L.; Liu, C.Y.; Hseu, R.S.; Huang, C.T. Reishi immuno-modulation protein induces interleukin-2 expression via protein kinase-dependent signaling pathways within human T cells. *J. Cell Physiol.* **2008**, *215*, 15–26. [[CrossRef](#)] [[PubMed](#)]
45. Fang, Z.; Li, J.; Yu, X.; Zhang, D.; Ren, G.; Shi, B.; Wang, C.; Kosinska, A.D.; Wang, S.; Zhou, X.; et al. Polarization of Monocytic Myeloid-Derived Suppressor Cells by Hepatitis B Surface Antigen Is Mediated via ERK/IL-6/STAT3 Signaling Feedback and Restrains the Activation of T Cells in Chronic Hepatitis B Virus Infection. *J. Immunol.* **2015**, *195*, 4873–4883. [[CrossRef](#)]
46. Garg, A.; Spector, S.A. HIV type 1 gp120-induced expansion of myeloid derived suppressor cells is dependent on interleukin 6 and suppresses immunity. *J. Infect. Dis.* **2014**, *209*, 441–451. [[CrossRef](#)]
47. Rochman, I.; Paul, W.E.; Ben-Sasson, S.Z. IL-6 increases primed cell expansion and survival. *J. Immunol* **2005**, *174*, 4761–4767. [[CrossRef](#)] [[PubMed](#)]
48. Weissenbach, M.; Clahsen, T.; Weber, C.; Spitzer, D.; Wirth, D.; Vestweber, D.; Heinrich, P.C.; Schaper, F. Interleukin-6 is a direct mediator of T cell migration. *Eur. J. Immunol.* **2004**, *34*, 2895–2906. [[CrossRef](#)]
49. Diehl, S.; Rincon, M. The two faces of IL-6 on Th1/Th2 differentiation. *Mol. Immunol.* **2002**, *39*, 531–536. [[CrossRef](#)]
50. Neumann, J.; Prezzemolo, T.; Vanderbeke, L.; Roca, C.P.; Gerbaux, M.; Janssens, S.; Willemsen, M.; Burton, O.; van Mol, P.; van Herck, Y.; et al. Increased IL-10-producing regulatory T cells are characteristic of severe cases of COVID-19. *Clin. Transl. Immunol.* **2020**, *9*, e1204. [[CrossRef](#)]
51. Mehta, A.K.; Gracias, D.T.; Croft, M. TNF activity and T cells. *Cytokine* **2018**, *101*, 14–18. [[CrossRef](#)]



# Precisely adjusting the hepatic clearance of highly extracted drugs using the modified well-stirred model

Shu-Hao Hsu<sup>a</sup>, An-Chun Cheng<sup>a</sup>, Tien-Yu Chang<sup>a</sup>, Li-Heng Pao<sup>b,c</sup>, Cheng-Huei Hsiong<sup>d</sup>, Hong-Jaan Wang<sup>e,f,\*</sup>

<sup>a</sup> School of Pharmacy, National Defense Medical Center, Taipei, Taiwan, Republic of China

<sup>b</sup> Graduate Institute of Health Industry Technology, Research Center for Food and Cosmetic Safety, and Research Center for Chinese Herbal Medicine, College of Human Ecology, Chang Gung University of Science and Technology, Taoyuan, Taiwan, Republic of China

<sup>c</sup> Department of Gastroenterology and Hepatology, Chang Gung Memorial Hospital, Taoyuan, Taiwan, Republic of China

<sup>d</sup> Sinew Pharma Inc., Taipei, Taiwan, Republic of China

<sup>e</sup> Graduate Institute of Pharmacy, National Defense Medical Center, Taipei, Taiwan, Republic of China

<sup>f</sup> Graduate Institute of Life Science, National Defense Medical Center, Taipei, Taiwan, Republic of China

## ARTICLE INFO

### Keywords:

Well-stirred model  
Modified well-stirred model  
Hepatic clearance  
Diazepam  
In vitro to in vivo extrapolation

## ABSTRACT

Hepatic clearance has been widely studied for over 50 yr. Many models have been developed using either theoretical or empirical tests to predict drug metabolism. The well-stirred, parallel-tube, and dispersion metabolic models have been extensively discussed. However, to our knowledge, these models cannot fully describe all relevant scenarios in hepatic clearance. We addressed this issue using the isolated perfused rat liver technique with minor modifications. Diazepam was selected to illustrate different levels of drug plasma-protein binding by changing the added concentration of human serum albumin. The free fractions of diazepam at different albumin concentrations were assayed by rapid equilibrium dialysis. The experimental data provide new insights concerning an accepted formula used to describe hepatic clearance. Regarding drug concentrations passing through the liver, the driving force concentration ( $C_{H,ss}$ ) in terms of  $C_{in}$  (influx in the liver) or  $C_{out}$  (efflux from the liver) needs to be carefully considered when determining drug hepatic and intrinsic clearances. The newly established model, termed the modified well-stirred model, which was derived from the original formula, successfully estimated hepatic drug metabolism. Using the modified well-stirred model, a theoretical driving force concentration of diazepam passing through the liver was evaluated. The model was further used to assess the predictability of in vitro to in vivo extrapolation. This study was not intended to refute the existing models, but rather to augment them using experimental data. The results stress the importance of proper calculation of dose when the drug clearance deviates from the prediction of the well-stirred model.

## 1. Introduction

The concept of clearance was first introduced into pharmacy by Möller et al. in 1928, where it was used as a pharmacodynamics term to describe the excretion of drugs by the kidneys [1,2]. The same authors

defined renal clearance as the volume of body fluid perfusing the kidneys that is completely cleared of the drug per unit time. After two decades, Lewis extended the concept of clearance to liver metabolism or excretion [3]. In 1972 and 1973, hepatic clearance ( $CL_H$ ) was eventually defined as the product of hepatic blood flow ( $Q_H$ ) and liver extraction

**Abbreviations:**  $C_{H,ss}$ , steady-state concentration of drug within the liver that is driving elimination;  $C_{H,ss,u}$ , steady-state concentration of unbound drug within the liver that is driving elimination;  $C_{in}$ , drug concentration entering liver;  $CL_H$ , hepatic clearance;  $CL_{int}$ , intrinsic clearance;  $C_{out}$ , drug concentration exiting liver;  $C_{PTM}$ , logarithmic mean drug concentration in PTM;  $C_H$ , total drug concentration in the liver;  $C_{H,u}$ , free drug concentration that diffuses into the cell; DM, dispersion model;  $D_N$ , dispersion number;  $ER_H$ , hepatic extraction ratio;  $F_H$ , hepatic availability;  $f_u$ , fraction of unbound drug intravascularly;  $f_{u,e}$ , fraction of unbound drug extracellularly; HSA, human serum albumin; IPRL, isolated perfused rat liver; IVIVE, in vitro to in vivo extrapolation; MWSM, modified well-stirred model; PTM, parallel-tube model;  $Q_H$ , hepatic blood flow; WSM, well-stirred model.

\* Corresponding author at: School of Pharmacy, National Defense Medical Center, R9304, No.161, Section 6, Min-Chuan E. Rd., Neihs District, Taipei, Taiwan, Republic of China.

E-mail address: [hongjaan@mail.ndmctsg.edu.tw](mailto:hongjaan@mail.ndmctsg.edu.tw) (H.-J. Wang).

<https://doi.org/10.1016/j.bioph.2021.111855>

Received 27 April 2021; Received in revised form 11 June 2021; Accepted 24 June 2021

Available online 3 July 2021

0753-3322/© 2021 The Authors. Published by Elsevier Masson SAS. This is an open access article under the CC BY-NC-ND license

(<http://creativecommons.org/licenses/by-nc-nd/4.0/>).

ratio ( $ER_H$ ) (Eq. 1) [4,5], which was believed to be the beginning of its widespread use in the pharmacokinetic field.

$$CL_H = Q_H \cdot ER_H \quad (1)$$

In 1977, Pang and Rowland further interpreted Eq. (1), requiring that the following three conditions are met [6]. First, the rate change in the amount of drug ( $v$ ) transferred to the liver when passing through it can be expressed as a product of the  $Q_H$  and the difference in drug concentration before and after hepatic perfusion (Eq. 2). Second, when the drug reaches steady state in the liver, the rate of drug loss due to binding or distribution ( $v_{eq}$ ) approaches zero, i.e.,  $v$  is equal to enzymatic metabolism ( $v_{met}$ ) when ignoring biliary excretion ( $v_{bile}$ ) and is also represented as  $v_{ss}$  (Eq. 3). Third, at steady state,  $CL_H$  can be defined as the ratio of the drug's metabolic rate to the concentration of drug entering the liver (Eq. 4). Accordingly, the relationship between the  $CL_H$  and the blood drug concentration at steady state can be obtained sequentially from Eqs. (1)–(4), yielding Eq. (5).

$$v = Q_H(C_{in} - C_{out}) = v_{eq} + v_{met} + v_{bile} \quad (2)$$

$$v = v_{ss} = v_{met} \text{ (at steady state)} \quad (3)$$

$$CL_H = \frac{v_{met}}{C_{in}} \quad (4)$$

$$CL_H = \frac{v_{met}}{C_{in}} = \frac{v_{ss}}{C_{in}} = \frac{Q_H(C_{in} - C_{out})}{C_{in}} = Q_H \cdot ER_H \quad (5)$$

Besides using  $CL_H$  to describe drug metabolism in the liver, intrinsic clearance ( $CL_{int}$ ) is used to define the metabolic capacity of intracellular enzymes. Empirically, when a drug enters the liver via the bloodstream, only the unbound portion of the drug is available for intracellular metabolism. The concentration of free drug that diffuses into the liver cell ( $C_{H,u}$ ) can be expressed as the product of the unbound fraction ( $f_u$ )

and the total drug concentration ( $C_H$ ), while the relationship between  $CL_{int}$  and  $v_{met}$  can be expressed by Eq. (6). Then, Eq. (2) can be rearranged and substituted with Eq. (6) to obtain Eq. (7) ( $v_{eq}$  and  $v_{bile}$  are assumed to be zero).

$$CL_{int} = \frac{v_{met}}{f_u \cdot C_H} \quad (6)$$

$$Q_H \cdot C_{in} - Q_H \cdot C_{out} = CL_{int} \cdot f_u \cdot C_H \quad (7)$$

Many hepatic perfusion models have been proposed in the last 50 years based on Eq. (7) (Table A1). Among them, the well-stirred model (WSM) [6], parallel-tube model (PTM) [7], and dispersion model (DM) [8] related to  $CL_H$  have been widely discussed [9]. The definition of each model is briefly described in the appendix material (pp. A1) and the model patterns are indicated in Fig. 1. In the past, scientists have established these three models based on the concept of clearance. From the derivation of  $CL_H$  in Eq. (5), the hepatic drug concentration is defined as  $C_{in}$ , which can also represent the driving concentration of drug metabolism in the liver [10]. However, derived from Eq. (6), it can be seen that when calculating  $v_{met}$  from  $CL_{int}$  (or vice versa), the elimination driving concentrations of the drug in WSM, PTM, and DM are expressed as  $f_u \cdot C_{out}$ ,  $f_u \cdot C_{PTM}$ , and  $f_u \cdot C_{DM}$  (Table 1), respectively. The concentrations defined in the above models are significantly different from the concentration defined in Eq. (5). Therefore, when calculating  $CL_{int}$  of a drug, a consistent definition of the driving concentration for drug metabolism in hepatic or intrinsic clearance is obtained if the metabolic concentration of the denominator is defined as  $f_u \cdot C_{in}$ .

Previous reports, which aimed to compare the suitability of WSM, PTM, and DM in describing the process of hepatic drug metabolism, have not been able to reach a harmonious conclusion [10–12]. The major difference in the three models lies in the different “reference” concentrations [11] used when defining intrinsic clearance. In view of this, Prof. Benet and colleagues provided detailed comments on the

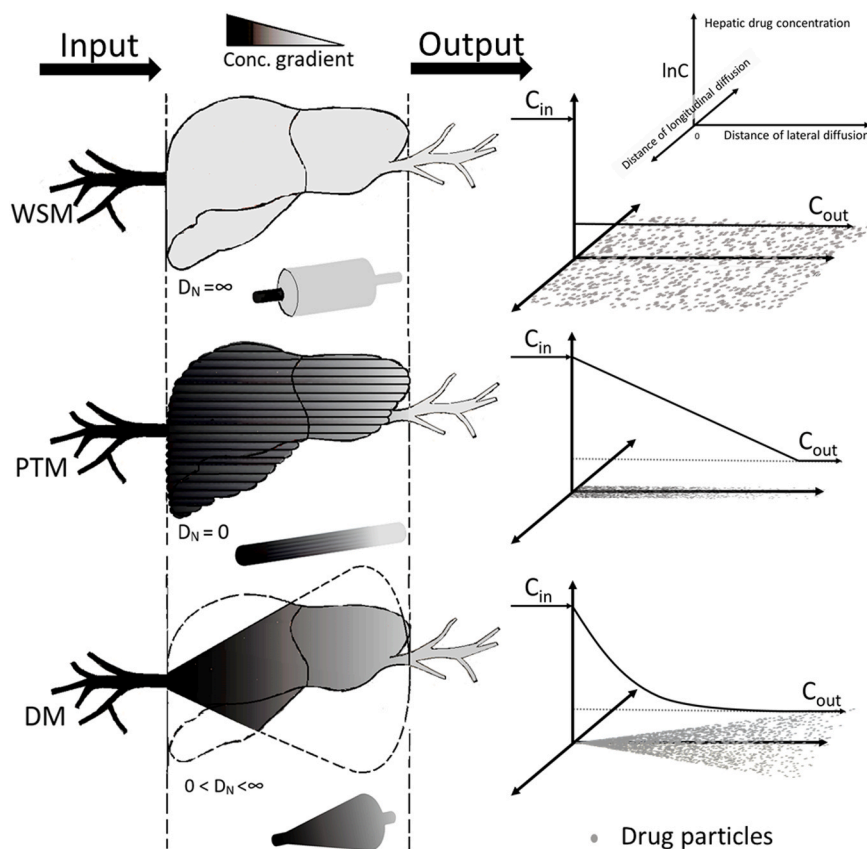


**Fig. 1.** Schematic diagram of three main hepatic clearance models illustrating drug distribution and metabolism in the liver. (A) Well-stirred model: drug distributed and metabolized instantly while entering the liver with an infinite longitudinal diffusion coefficient ( $D_N$ ); (B) parallel tube model: unidirectional drug flow through the liver with no longitudinal diffusion ( $D_N = 0$ ). The concentration changes in the liver follow first-order elimination; (C) dispersion model: the concentration changes in this model are dependent on  $D_N$  ( $0-\infty$ ). The concentration levels as the drug passes through the liver are indicated as gradients from dark to light. The right plots indicate the corresponding decline in drug concentration as the drug passes through the liver.



**Table 1**

Drug elimination-driving concentrations and corresponding calculation methods of hepatic clearance for newly established and commonly discussed models.

Models	Represented elimination driving concentration in the model	$CL_H^a$
Well-stirred (equilibrium venous)	$C_{WSM} = C_{out}$	$\frac{Q_H \cdot f_u \cdot CL_{int}}{Q_H + f_u \cdot CL_{int}}$ (Eq. 8)
Parallel tube (plug flow)	$C_{PTM} = \frac{C_{in} - C_{out}}{\ln C_{in} - \ln C_{out}}$	$\frac{f_u \cdot CL_{int}}{Q_H \cdot (1 - e^{-\frac{f_u \cdot CL_{int}}{Q_H}})}$ (Eq. 9)
Dispersion	$C_{DM} = \frac{C_{in}}{R_N} \left( 1 - \frac{4a}{(1+a)^2 \cdot e^{2D_N} - (1-a)^2 \cdot e^{-\left(\frac{a+1}{2D_N}\right)}} \right)$ $R_N = \frac{f_u \cdot CL_{int}}{Q_H}, a = \sqrt{1 + 4 \cdot D_N \cdot R_N}, D_N = 0 \sim \infty$	$Q_H \left( 1 - \frac{4a}{(1+a)^2 \cdot e^{2D_N} - (1-a)^2 \cdot e^{-\left(\frac{a+1}{2D_N}\right)}} \right)$ (Eq. 10)
Modified well-stirred	$C_{MWSM} = C_{in}$	$f_u \cdot CL_{int}$ (Eq. 11)

<sup>a</sup> Equations represent the calculation of hepatic clearance ( $CL_H$ ) in each model under steady state metabolism. Modified well-stirred model (MWSM) and well-stirred model (WSM) presume the drug to be evenly distributed and metabolized once it enters the liver. The difference between these two models is that MWSM assumes that the concentration of drug reaching the cells is the same as the concentration of drug entering the liver, both of which are represented by  $C_{in}$ . By comparison, WSM assumes that the drug concentration reaching the cells for metabolism is similar to  $C_{out}$ . Parallel tube model (PTM) assumes that the drug is gradually metabolized in the liver in a single direction and the changes in concentration follow first-order kinetics. In PTM,  $C_H$  is represented by the logarithmic mean ( $C_{PTM}$ ) of the drug concentration entering and leaving the liver. Dispersion model (DM) assumes that, in addition to being gradually metabolized after entering the liver, the drug may undergo longitudinal diffusion. Thus, the concentration of drug reaching the cells ( $C_{DM}$ ) must take into consideration  $D_N$ ,  $CL_{int}$  and  $C_{in}$ .

forementioned controversy using experimental data [13] and literature searches [14]. However, some of the experimental data still did not match the predicted results of the WSM, particularly when the drug remained unbound during liver metabolism. In the present study, we developed a modified well-stirred model (MWSM) and described the rate of drug metabolism in the liver by substituting  $C_{in}$  with  $C_H$  in Eq. (7). As with the steady-state assumption that  $v_{ss}$  is equal to  $v_{met}$ , the substituted equation can be rearranged and incorporated into Eq. (5) to derive a very simple formula for calculating  $CL_H$  (eq. 11 in Table 1). In addition, the experimental data from a published report [15] were reevaluated by MWSM to assess the predictability of in vitro to in vivo extrapolation (IVIVE) and to partially explain the reason why  $CL_H$  is often underestimated from in vitro predictions.

## 2. Methods

### 2.1. Chemicals

Diazepam was purchased from Thermo Fisher Scientific (Bellefonte, PA, USA); its internal standard diazepam-d5 was obtained from Cerilant (Round Rock, TX, USA). The perfusion buffer used in the isolated perfused rat liver (IPRL) study was composed of taurocholate, sodium bicarbonate, and commercialized Krebs-Ringer powder, which were obtained from Acros Organics (Geel, Belgium), Merck (Taipei, ROC), and Sigma-Aldrich (St. Louis, MO, USA), respectively. Fatty acid-free human serum albumin (HSA) was obtained from SeraCare (Milford, MA, USA). The rapid equilibrium dialysis (RED) apparatus and testing inserts were purchased from Thermo Fisher Scientific (Rockford, IL, USA). All other chemicals used in the study were analytical or LC-MS grade.

### 2.2. Diazepam protein-binding determination

Diazepam is a typical drug possessing high plasma protein binding (>98%), low hepatic extraction ratio (<0.3), high intrinsic clearance (>36 mL/min/kg) [16], and rapid passive diffusion across cell membranes [17]. The main pathway of diazepam metabolism is mediated by cytochrome P450 in the liver and with almost no transporter effect [18, 19]. Diazepam has been used for model discrimination in IPRL studies since 1983 [20] and was therefore selected as a model compound in a previous report [13] as well as in this study.

The protein binding of diazepam to HSA was determined by RED assay [21]. Briefly, diazepam was prepared at 1 µg/mL in Krebs buffer containing varied HSA concentrations of 0%, 0.025%, 0.04%, 0.05%,

0.075%, 0.1%, or 2% (w/v). Five hundred microliters of diazepam testing solution was added to the sample chamber of the insert and 750 µL of blank buffer was added to the adjacent chamber. The loaded inserts were assembled in a Teflon-based plate. The plate was sealed with a self-adhesive lid and agitated at 20 rpm and  $37 \pm 1$  °C on an oscillating shaker (Genepure Rocking Shaker, OSR205-01) for the required experimental time of 8 h.

### 2.3. Surgery and liver perfusion

Male Sprague-Dawley rats (350–450 g; BioLASCO Co., Ltd, Taipei, ROC) were housed in the Laboratory Animal Center of National Defense Medical Center with a 12-h light/dark cycle and allowed free access to water and food. Approval for their use in experiments was obtained from our Institutional Animal Care and Use Committee (IACUC-20-164). Prior to surgery, anesthesia was achieved by intraperitoneal injection of 20 mg/kg tiletamine and zolazepam (Zoletil, Virbac Taiwan, Taipei, ROC), and 8 mg/kg xylazine (Rompun, Bayer Taiwan, Taipei, ROC). Livers were isolated for perfusion as described previously [13]. The perfusate containing 1 µg/mL diazepam with 0%, 0.025%, 0.04%, 0.05%, 0.075%, 0.1%, or 2% HSA was freshly prepared, and remained at 4 °C after mixing until all foam disappeared. The oxygenated (95% O<sub>2</sub>/5% CO<sub>2</sub>) perfusate was warmed to  $37 \pm 0.2$  °C and was pumped through the liver at a flow rate of 15 mL/min via a catheter inserted in the portal vein. Perfusion was performed in a single-pass manner from a reservoir containing 500 mL of perfusate, through a Teflon tube and bubble trap placed before the liver. The metabolized perfusion fluid ( $C_{out}$ ) was collected via a catheter at the inferior vena cava, and an adjustable opening was placed at the front of the hepatic portal vein to collect the prehepatic perfusion fluid ( $C_{in}$ ). Liver viability was assessed on the basis of its appearance (uniformly pink to brown), portal vein pressure (8–10 mm Hg), perfusate pH (7.35–7.45), and metabolic capability. The entire experiment consisted of 7 cycles of 20 min/cycle. During each cycle, 2 mL of  $C_{in}$  was collected at 20 min, and 2 mL of  $C_{out}$  was collected at 16, 17, 18, 19, and 20 min. Bile elimination was not considered because it accounts for < 0.2% of the total metabolism [6].

### 2.4. Sample preparation and analysis

The liquid-liquid extraction method was selected for sample preparation. A 400 µL perfusate sample was combined with 80 µL (1 µg/mL) of diazepam-d5, 150 µL 1 N Na<sub>2</sub>CO<sub>3</sub>, and 2 mL extraction solvent (n-hexane: isoamyl alcohol, 9:1). The mixture was extracted by vortexing for 5 min and the upper organic phase was collected, dried,

reconstituted with 85% acetonitrile, and injected for analysis.

Diazepam and diazepam-d5 were analyzed on an Agilent Technologies 1200 series high-performance liquid chromatograph (Böblingen, Germany) connected to the ionization interface of an Applied Biosystems-Sciex API 3000 series triple-quadrupole mass spectrometer (Foster City, CA, USA). A Thermo Hypersil BDS C18 column (4.6 × 100 mm, 5 mm; Thermo Fisher Scientific, Waltham, MA, USA) was used for compound separation in the study. Isocratic elution (water: methanol, 1:9, in 2 mM ammonium acetate and 0.1% formic acid) was carried out for 5 min for each injected sample at a flow rate of 0.4 mL/min. The mass spectrometry conditions were described previously [13]. The data were processed using Analyst 1.4.2 software (Applied Biosystems-Sciex, Framingham, MA, USA).

## 2.5. Data analysis

The formula parameters and experimental data were imported into Prism 6.0 software (GraphPad Software, Inc). According to the observed  $C_{in}$  and  $C_{out}$  at 0.04% or 0.05% HSA in the IPRL, Eqs. (8)–(10) (Table 1) were utilized to calculate the  $CL_{int}$  of diazepam in WSM, PTM, and DM, respectively. Then, based on the results, a curve representing the hepatic availability ( $F_H$ ) versus  $f_u$  of the drug for each model was simulated. The blood flow velocity in each equation was fixed at 15 mL/min and the dispersion number ( $D_N$ ) in Eq. (10) was set to 0.34 [22]. The  $f_u$  of diazepam was considered to be the x-axis in order to generate the corresponding  $F_H$  ( $C_{out}/C_{in}$ ), which was plotted on the y-axis. Each model was then compared to determine which more closely represented the observed experimental data from the IPRL studies [13,22]. The coefficient of determination ( $R^2$ ) calculated by Prism was used to help make this decision. The closer  $R^2$  was to 1, the closer the point distribution was to the nonlinear regression curve [23].

## 2.6. Data reevaluation

To compare the IVIVE power between WSM and MWSM, we reanalyzed the reported data that have been broadly discussed in model discriminations. All drug metabolism data were collected from a previous report (101 drugs for human hepatocytes, 83 drugs for human microsome incubations, 128 drugs for rat hepatocytes, and 71 drugs for rat microsome incubations) [15]. The observed  $CL_{int}$  ( $CL_{int,obs}$ ) of each drug was then back-calculated from in vivo  $CL_H$ ,  $f_u$  (herein referred to as unbound fraction in blood), and  $Q_H$  according to the representative equations for WSM (Eq. 12) and MWSM (Eq. 13). In contrast, the human and rat in vitro  $CL_{int}$  as well as their predicted  $CL_{int}$  ( $CL_{int,pred}$ ) for each drug were obtained from the literature report [15].

$$CL_{int,obs,WSM} = \frac{CL_H}{f_u \cdot (1 - \frac{CL_H}{Q_H})} \quad (12)$$

$$CL_{int,obs,MWSM} = \frac{CL_H}{f_u} \quad (13)$$

To demonstrate the impact of the use of WSM and MWSM in IVIVE for drugs with different  $ER_H$ , level of improvement (LoI) was employed in this study to indicate the degree of improvement in IVIVE when using MWSM versus WSM. Specifically, the values of  $|CL_{int,obs,MWSM} - CL_{int,pred}|$  and  $|CL_{int,obs,WSM} - CL_{int,pred}|$  of all drugs were compared. A drug with a smaller value in the former equation indicated that the calculation of  $CL_{int,obs}$  resulted in a value closer to  $CL_{int,pred}$  when using MWSM than when using WSM, and LoI could be calculated from Eq. (14). A drug with a smaller value in the latter equation indicated the opposite, and LoI could be calculated from Eq. (15) instead. The detailed LoI calculations are provided in the appendix material (pp. A2–A3). A graph was plotted using calculated LoI as the y-axis and  $ER_H$  as the x-axis. A trend line was drawn from all data points that fit the conditions of Eq. (14) (i.e., all data points with  $LoI > 0$ ) to indicate the correlation between  $ER_H$  and LoI for

all drugs that exhibited improvement in IVIVE due to the use of MWSM.

$$LoI(\%) = \left( 1 - \frac{|CL_{int,obs,MWSM} - CL_{int,pred}|}{|CL_{int,obs,WSM} - CL_{int,pred}|} \right) \cdot 100\% \quad (14)$$

$$LoI(\%) = - \left( 1 - \frac{|CL_{int,obs,WSM} - CL_{int,pred}|}{|CL_{int,obs,MWSM} - CL_{int,pred}|} \right) \cdot 100\% \quad (15)$$

## 3. Results

### 3.1. Equilibrium dialysis

The unbound fraction of diazepam at each HSA concentration was determined by RED and was compared to the corresponding value in a previous report [13]. We noted from previous reports that the unbound fraction of diazepam showed a steep change when HSA concentrations were between 0% and 0.1%. Therefore, to advance the accuracy of IPRL studies, HSA concentrations of 0.075% and 0.04% were added in the present analysis. The corresponding fractions of drugs not bound to protein at different HSA concentrations are listed in Table A2. Fig. 2 also shows that the  $f_u$  of diazepam decreased as HSA concentration increased. In addition, the coefficient of variation (CV%) of  $f_u$  at each concentration was <5% (data not shown), which indicated that the intra-variability was low in all experimental groups. The parameter  $f_u$  was the most sensitive to changes in protein concentration between 0.04% and 0.05% HSA. This implies that within this concentration interval, a slight change in the amount of albumin would lead to a substantial change in the drug-albumin binding ratio.

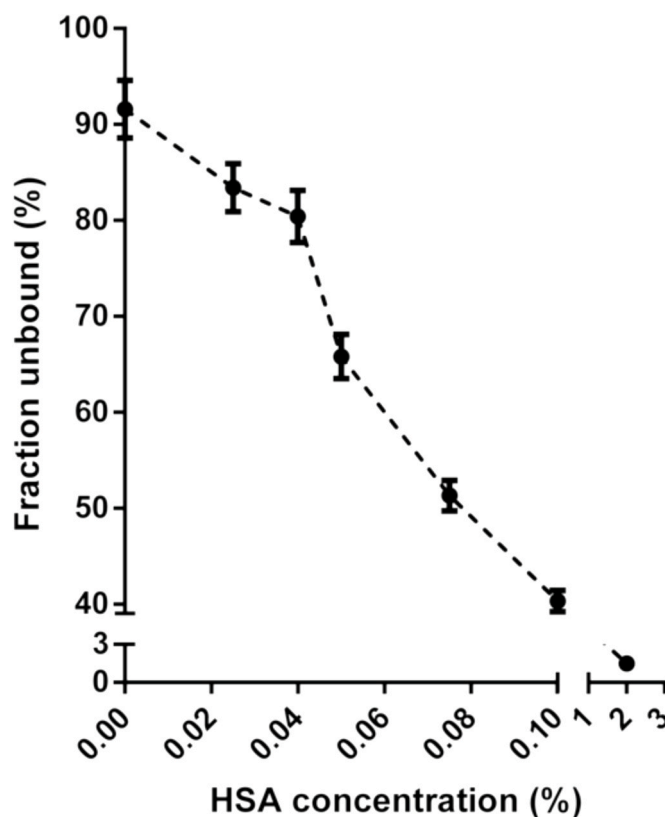


Fig. 2. Different protein concentrations correspond to specific protein-binding rates using the fast equilibrium dialysis method. The parameter  $f_u$  was the most sensitive to changes in HSA concentration between 0.04% and 0.05% HSA. HSA: human serum albumin;  $f_u$ : fraction of unbound drug in blood.

### 3.2. Diazepam metabolism in IPRL

Perfusion was performed in two different sequences in the study, as shown in Fig. A1. Both sequences were based on the experimental methods and conditions of this study, where no significant decrease in liver drug metabolic activity was shown after seven cycles of perfusion (Fig. 3 and Table A2). Under these perfusion sequences, the mean  $F_H$  of diazepam perfused at the seventh cycle was 8.92%. Therefore, the data generated using a seven-cycle experimental design were reliable. In the second perfusion sequence, the impact of high protein concentration on the perfusion of proteins at low concentration was considered. Therefore, the sequence of protein perfusion occurred from low to high concentration to minimize cross-contamination. Furthermore, perfusion of 0% protein was added to the final cycle, and only the perfusates with an  $F_H$  value < 15% in that cycle were included to ensure that the hepatic activity did not decrease significantly during a single experiment. In addition to the newly added HSA test concentrations of 0.075% and 0.04%, the metabolism of diazepam at high protein concentrations (0.5% and 2%) was assessed based on previously reported data [13]. The above data were used to calculate the mean, standard deviation, and CV % of  $F_H$  at each protein concentration (Table A2). As the unbound fraction of drug decreased, the amount of free drug gradually decreased, and hepatic metabolism of the drug became more difficult. Thus, the hepatic availability of the drug gradually increased. The trend of the impact of albumin changes on the metabolic ratio of diazepam was consistent with that of previous reports [13].

### 3.3. Fitting the model-simulated curves

As shown in Fig. 2, changes in the fraction of diazepam bound to protein were greatest at HSA concentrations between 0.04% and 0.05%. Since the protein-binding status of a drug intensely influences its metabolism [12], the diazepam metabolism in this range could have been changed from one model to another. Considering this, we utilized 0.04% and 0.05% HSA to calculate the reference points for  $CL_{int}$  in each model. Each of these two points was used as a cutoff to examine which model was suitable for the two populations. The degree of curve-fitting between  $f_u$  and  $F_H$  was best when using 0.04% HSA ( $f_u = 0.8$ ) as a cutoff point (Table 2).

Based on the coefficient of determination, MWSM displayed higher

**Table 2**

Degree of fitting in various models and HSA subgroups illustrated by  $R^2$  values.

Concentration of HSA (%)	Modified WSM	WSM	PTM	DM
0–0.04	0.6343	0.1451	0.3196	0.2367
0.04–2	0.5414	0.9450	0.8676	0.9158

WSM: well-stirred model; PTM: parallel-tube model; DM: dispersion model; HSA: human serum albumin

accuracy in predicting changes in diazepam liver metabolism at a lower concentration range of 0–0.04% HSA (Fig. 4). The product of drug concentration entering the liver and the fraction not bound to protein can represent the driving concentration in intrinsic clearance ( $C_{H,ss,u} = f_u \cdot f_{u,E} \cdot C_{in}$ ). Because of the high degree of unbound drug ( $f_u \cdot f_{u,E} \approx 1$ ), the driving concentration of the drug entering cells and undergoing metabolism is thereby close to  $C_{in}$ . In contrast, WSM could be used to describe hepatic drug metabolism at higher albumin concentrations (Fig. 4). At high albumin concentration (0.04–2%, i.e., the protein level in the blood vessels is high), the interstitial and intracellular albumin concentrations are also elevated. This renders the value of  $f_{u,E} \cdot C_{in}$  closer to that of  $C_{out}$ . In this case, driving concentration can be expressed as the unbound fraction of the drug in the blood vessels multiplied by the liver drug concentration ( $C_{H,ss,u} = f_u \cdot C_{out}$ ). Thus, the observed experimental values are closer to the WSM predictions.

### 3.4. Reevaluation of IVIVE by MWSM

The results of the reanalysis of Wood's data [15] are shown in Fig. 5. These results show that more drugs exhibited improved results in IVIVE when using MWSM, irrespective of the materials used in the in vitro experiments (84.16% of drugs for human hepatocytes, 74.70% of drugs for human microsomes, 82.81% of drugs for rat hepatocytes, and 66.20% of drugs for rat microsomes). Specifically, drugs with a lower percentage were more suitable for WSM prediction ( $LoI < -0.2$ ) when using hepatocytes than when using microsomes. This indicates that when hepatocytes are used as the experimental material to predict in vivo clearances, the use of MWSM would lead to a higher probability of a more accurate prediction. Excluding the drugs that showed improved IVIVE using WSM (red dots in Fig. 5 and categorized in Table A3), the relationships between  $LoI$  and  $ER_H$  in the remaining drugs were

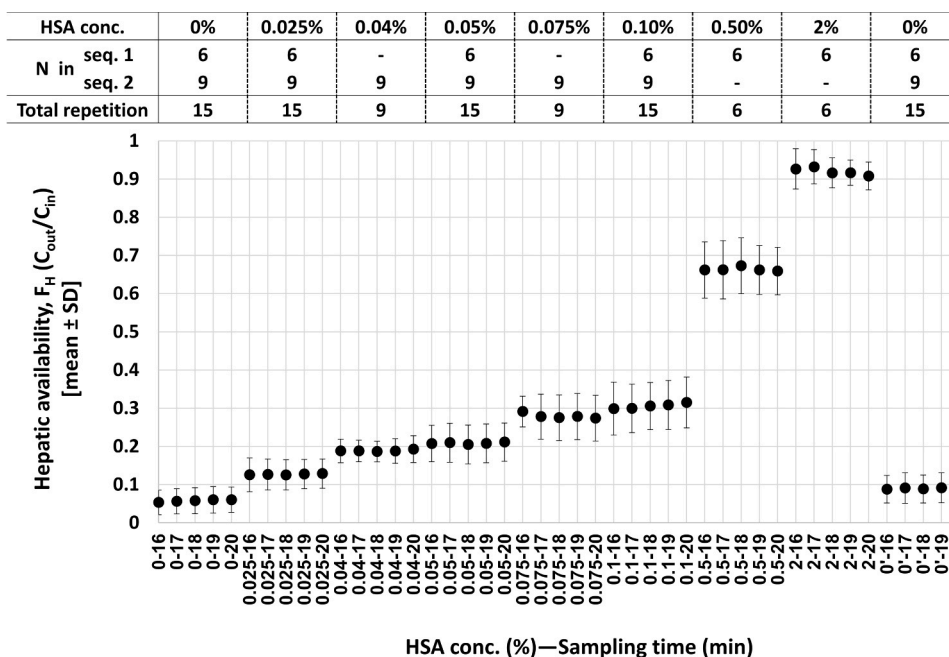


**Fig. 3.** Every point plotted in the graph represents the hepatic availability ( $F_H$ ) of diazepam after isolated rat liver perfusion. After equilibrating for 16 min with single-pass perfusion, the samples were collected one per minute until completion of the 20-min cycle. Each cycle was performed at 1  $\mu\text{g/mL}$  diazepam in Krebs buffer with different HSA concentrations of 0–2%. Except when 0% HSA was employed in cycle 7 to reassess liver activity, different HSA concentrations were used in each testing cycle. The observed data are derived from the combined experimental results, which were performed in two different sequences ( $n = 6$  for seq. 1 and  $n = 9$  for seq. 2). HSA, human serum albumin.

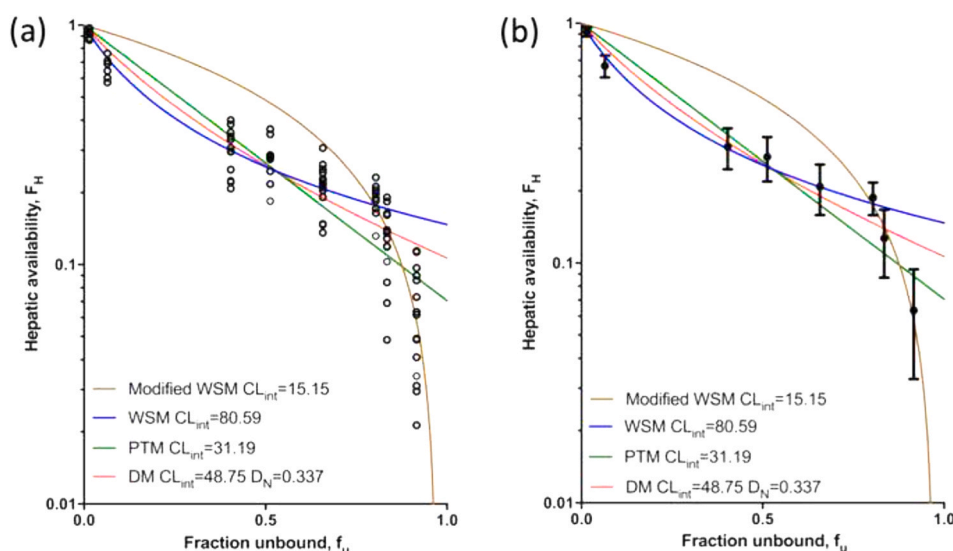


**Fig. 4.** Differences in hepatic availability ( $F_H$ ) of diazepam at specific protein binding rates. For the sample size ( $N$ ) of each observed data point in the plot, please refer to Fig. 3. According to an average value of  $f_u$  at the cutoff point, the simulated curves indicated in different colors were obtained from MWSM (brown), WSM (blue), PTM (green), and DM (red). The  $CL_{int}$  of diazepam calculated from each model is shown in the insert in each plot. All points in the figure represent the individual (a) and average (b) IPRL values in specific protein-binding with the cutoff point being 0.80. IPRL: isolated perfused rat liver; HSA: human serum albumin;  $f_u$ : fraction of unbound drug in blood;  $D_N$ : dispersion number;  $CL_{int}$ : intrinsic clearance; WSM: well-stirred model; PTM: parallel-tube model; DM: dispersion model. (For interpretation of the references to color in this figure legend, the reader is referred to the web version of this article.)

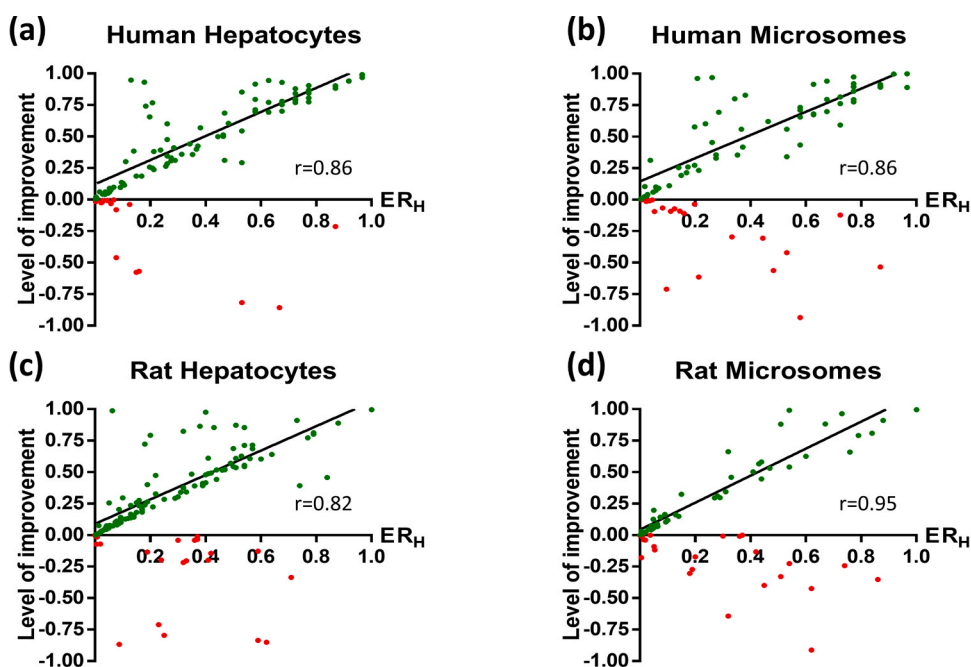


**Fig. 5.** Relationship between hepatic extraction ratio ( $ER_H$ ) and level of improvement in hepatocytes (a and c) and microsomes (b and d) from humans (a and b) and rats (c and d) by reanalyzing the Wood et al. dataset [15]. Drugs are predicted to be better with MWSM than with WSM when the level of improvement is higher than zero (green dots) and vice versa when the level of improvement is lower than zero (red dots). The trend in the data of all drugs shown as green dots is visually depicted with a linear regression line with the correlation coefficient ( $r$ ) for each plot given. WSM: well-stirred model; MWSM: modified well-stirred model. (For interpretation of the references to color in this figure legend, the reader is referred to the web version of this article.)

quantified via linear trend lines. The results indicated that, irrespective of the materials used,  $LoI$  increased with increasing  $ER_H$ , and the correlation coefficients ( $r$ ) were greater than 0.8 in all cases. These findings demonstrate a significant correlation between  $LoI$  and  $ER_H$ , which also implies that MWSM should be used in the future as the standard model when predicting the clearance of drugs with high  $ER_H$ . The results also validated our hypothesis that the MWSM prediction is closer to the actual metabolic status of high  $ER_H$  drugs.

#### 4. Discussion

The hepatic clearance of a drug can reflect the overall drug metabolizing capacity of the liver. Based on the well-stirred concept, drug clearance in the elimination organ is simply described by Eq. (1) and the extraction ratio is defined as the difference between organ-entering ( $C_{in}$ ) and organ-exiting ( $C_{out}$ ) drug concentrations divided by  $C_{in}$  [4,5]. However, it is uncertain why the so-called reference concentration is

represented by the concentration of drug that leaves the liver ( $C_{out}$ ). In 2018, therefore, Benet et al. evoked a new concept of steady-state driving force concentration ( $C_{H,ss}$ ) that drives drug metabolism in the liver and substantially explains hepatic clearance (Eq. 16) [10]. Actually, driving force concentration refers to the drug concentration during drug disposition in the liver, and it changes with time. However, even under steady state, accurately determining the concentration of a drug at the time of elimination remains difficult. Therefore, the influx drug concentration  $C_{in}$ , which is also the denominator of the extraction ratio, is used to represent the driving concentration. Under the well-stirred concept, this can be regarded as ideal for predicting hepatic clearance. On the contrary, the use of  $C_{out}$  to represent the driving concentration of a drug undergoing metabolism seems to violate Eq. (1) and Eq. (5) [10].

$$CL_H = \frac{\text{elimination rate}}{C_{H,ss}} \quad (16)$$

Nonetheless, under the well-stirred concept, Eq. (8) directed by  $C_{out}$



has been well-established for calculating drug hepatic clearance for nearly half a century (Table 1). Therefore, we sought to explain this seemingly irrational phenomenon from a protein-binding perspective. The distribution of drug-binding proteins is not limited to the blood vessels. Proteins with drug-binding capacity, such as albumin or tissue proteins, also exist in interstitial spaces or even within cells and can circulate across compartments [24]. Therefore, there is a definite possibility that interstitial or intracellular binding proteins would affect the availability of free drugs [25,26]. The free drug that is released from protein binding in the blood and crosses the capillary wall may also encounter and bind to extravascular proteins, and the bound fraction at this time is represented by  $f_{u,E}$ . Under such circumstances, one can rationally extrapolate that the concentration of drug being metabolized by intracellular enzymes ( $f_u f_{u,E} C_{in}$ ) will be lower than  $f_u C_{in}$  and closer to  $f_u C_{out}$ . Therefore, the  $C_{H,ss}$  in Eq. (16) will be close to  $C_{out}$ , thereby aligning with the WSM prediction. For drugs that display low  $ER_H$ , high protein-binding capacity, or difficulty passing through cell membranes,  $C_{H,ss}$  in the liver may be close to  $C_{out}$  due to the above factors. This hypothesis can also be confirmed by the present study. When the  $f_u$  of diazepam in the IPRL was lower than 0.8, the observed experimental values roughly matched the WSM predictions. In contrast, once the albumin concentration decreased ( $<0.04\%$ ) and led to an increased fraction of unbound drug ( $f_u > 0.8$ ), the concentration driving diazepam metabolism was close to  $C_{in}$ . This caused the observed experimental values to deviate from the WSM prediction and more closely match the MWSM prediction (right side of Fig. 4a and b). In previous results [13], the  $F_H$  of highly unbound diazepam also deviated from the predicted values of WSM in IPRL experiments, particularly in the absence of albumin. Based on the aforementioned theories, the main reason for the discrepancy may be that the concentration driving drug metabolism at the time was closer to  $C_{in}$ , and thus MWSM was more suitable than WSM for fitting and prediction.

Intrinsic clearance refers to the sum of the metabolic capacity of hepatic enzymes. In view of pharmacokinetics and enzyme kinetics, excluding transporter and protein-facilitating effects, only free drugs not bound to proteins can enter cells and be metabolized by enzymes. Therefore, the product of drug concentration exposed to metabolic enzymes and the unbound fraction of the drug equals the concentration driving the intrinsic clearance ( $C_{H,ss,u} = f_u C_H$ ). In MWSM, WSM, PTM, and DM,  $C_H$  is thereby expressed as  $C_{in}$ ,  $C_{out}$ ,  $C_{PTM}$ , and  $C_{DM}$ , respectively (Table 1). It has been assumed that when only  $C_{in}$ ,  $C_{out}$ , and  $Q_H$  are available from the elimination organ, drug metabolism in the liver conforms to WSM. However, in comparison with MWSM, we must consider the concentration driving hepatic drug metabolism, and we believe that a more precise representation should be  $C_{H,ss,u} = f_u f_{u,E} C_{in}$ . A reduction in the value of  $f_{u,E}$  indicates that the decreased concentration of free drug causes  $f_{u,E} C_{in}$  to deviate from  $C_{in}$  and become closer to  $C_{out}$ , thereby aligning with the WSM prediction. On the contrary, an  $f_{u,E}$  value closer to 1 indicates that the concentration driving metabolism will be close to  $f_u C_{in}$ , which will align with the MWSM prediction. In PTM and DM,  $C_H$  is not established based on a well-stirred concept of rapid distribution and metabolism, but the concept of  $Q$ -ER is applied to the equations to connect  $CL_H$ . Therefore, using diazepam with a high  $CL_{int}$  in the IPRL study as an example, the observed experimental values would not meet the predictions of the PTM and DM regardless of whether the changes in  $f_u$  drive  $C_H$  toward  $C_{in}$  or  $C_{out}$ . On the contrary, even if both WSM and MWSM are not ideal physiologic models, the concept of  $CL_H$  ( $Q_H ER_H$ ) will enable the observed experimental values from IPRL to preferentially meet the data simulated by WSM [27] or MWSM.

Recently, the topic of the inaccuracy of IVIVE predictions has been widely discussed [11,14,15,28]. The data published by Wood et al. clearly illustrate that the intrinsic clearance obtained from most in vitro metabolic experiments using hepatocytes or microsomes significantly underestimated the drug metabolic capacity of the liver [15]. The proportion of predictions that fell more than 2-fold outside the measured

values reached 66.5% [14], and the causes that render IVIVE unpredictable are multifactorial [29–31]. However, a key factor may actually stem from the use of inappropriate models that result in prediction bias. We reevaluated the experimental results in the literature using MWSM and found that drugs with higher  $ER_H$  exhibited better fitting when evaluated by MWSM than when evaluated by WSM. In addition,  $Lol$  increases with the  $ER_H$  of the drug (Fig. 5), indicating that the in vitro measurements of a drug's intrinsic clearance interpreted by MWSM can lead to better IVIVE, especially for drugs with a high extraction ratio. In fact, the results of this analysis also corroborate our observations in IPRL. Thus, when a low liver-extracted but high intrinsic cleared drug exhibits a high degree of freeness such as under a low  $f_u$ , the  $F_H$  of this drug can be accurately predicted by MWSM instead of WSM. Therefore, if WSM is used to explain all in vitro properties of a drug, there will be a considerable risk of inaccurate predictions. However, it must be noted that drugs approved for market after 2012 are not included in Wood's analysis. Based on the free drug hypothesis, the strategy suggested for new drug development was to focus on optimizing drug clearance, permeability, or protein binding [32,33]. We believed that when a drug possesses both high permeability and low protein binding, the tendency is to use MWSM to predict drug hepatic clearance. In contrast, once a drug with high permeability and high protein binding is developed, MWSM may be better to assess its hepatic clearance than WSM when it is influenced by disease status (as described below).

Clearance is a common parameter used for clinical assessment of drug metabolism. For drugs with high first-pass metabolism,  $CL_H$  is an important parameter to support this assessment. Therefore, accurate IVIVE is a useful tool for drug dose predictions. However, existing in vitro measurements generally underestimate the  $CL_H$  of drugs, which will severely impact drug dose assessment and reduce treatment effectiveness. In summary, assuming that only free drugs can enter and exit hepatocytes to undergo metabolism and that this process is not affected by other factors such as transporter proteins, the results of our diazepam-based IPRL experiments can establish three scenarios for the selection of drug  $CL_H$  assessment models. First, when the protein-binding ratio of the drug is high, it is more difficult for free drug to diffuse into cells at high protein concentrations. Accordingly,  $C_{H,ss,u}$  is close to  $f_u C_{out}$ , and hepatic drug metabolism aligns with the WSM prediction. Second, when protein binding of the drug is high, the free drug concentration increases when the concentration of intravascular and extravascular proteins lowers, which allows the drug to cross cell membranes easily and diffuse into cells. In this situation,  $C_{H,ss,u}$  may be close to  $f_u C_{in}$ , and hepatic drug metabolism should be described by MWSM. In clinical practice, this scenario may apply to patients with low plasma protein levels, such as those with poor hepatic function, massive blood loss, drug interactions, or other conditions that alter protein concentrations in bodily fluids [34,35]. Third, an extremely low protein-binding ratio of a drug allows the free drug to diffuse easily from the blood vessel to the interstitial spaces and further into the hepatocytes. In this case, hepatic drug metabolism should be described by MWSM.

## 5. Conclusion

We learned that when only  $C_{in}$ ,  $C_{out}$ , and  $Q_H$  are available to calculate drug elimination in the liver, WSM is the best model to describe drug hepatic clearance. Similar to the aphorism from the 1965 Nobel physicist Dr. Richard Feynman quoted in a previous paper [27], for the truth rather than the beauty, we aimed to find a reasonable explanation for the deviation from the WSM prediction in the last experimental point of the previous IPRL study. For the past half-century, Eq. (8) was commonly used to calculate drug hepatic clearance based on the well-stirred concept, and it assumed that the output concentration drove drug metabolism in the liver. Here, we utilized a new model, namely MWSM, to describe an extreme situation in which all drug molecules exist in free form and liver-input concentration drives drug metabolism.



We believe that extravascular protein binding is a critical factor influencing drug metabolism, particularly in hepatocytes. The product of  $f_u f_{u,E} C_{in}$  can explain the situation when  $C_{H,ss}$  is close to  $f_u C_{out}$  and allows Eq. (8) to predict most cases of drug metabolism in IPRL studies. The underestimation of in vivo  $CL_H$  from in vitro data was common in previous reports, and research to determine the cause of IVIVE inaccuracy is still ongoing. Based on the level of hepatic extraction, appropriate model selection between WSM and MWSM may be an efficient method to accurately predict drug hepatic clearance.

### CRedit authorship contribution statement

Designed Research: HJ Wang, SH Hsu. Performed Research: SH Hsu, AC Cheng. Analyzed Data: SH Hsu, TY Chang, HJ Wang. Wrote Manuscript: HJ Wang drafted first and all authors revised.

### Declaration of Competing Interest

All authors declare no conflict of interest.

### Acknowledgements

The brilliant findings related to the clearance concept derived from Dr. Benet and colleagues (University of California, San Francisco) inspired this work and allowed the study to proceed. The study was financially supported by the grants (MOST-109-2320-B-016-011 & MOST-110-2320-B-016-007) from the Ministry of Science and Technology, Taipei, Taiwan.

### Appendix A. Supporting information

Supplementary data associated with this article can be found in the online version at doi:10.1016/j.biopha.2021.111855.

### References

- [1] E. Möller, J.F. McIntosh, D.D. Van Slyke, Studies of urea excretion. II: Relationship between urine volume and the rate of urea excretion by normal adults, *J. Clin. Invest.* 6 (3) (1928) 427–465, <https://doi.org/10.1172/JCI100206>.
- [2] J. Dong, M.S. Park, Discussions on the hepatic well-stirred model: re-derivation from the dispersion model and re-analysis of the lidocaine data, *Eur. J. Pharm. Sci.* 124 (2018) 46–60, <https://doi.org/10.1016/j.ejps.2018.08.011>.
- [3] A.E. Lewis, The concept of hepatic clearance, *Am. J. Clin. Pathol.* 18 (10) (1948) 789–795, <https://doi.org/10.1093/ajcp/18.10.789>.
- [4] M. Rowland, Influence of route of administration on drug availability, *J. Pharm. Sci.* 61 (1) (1972) 70–74, <https://doi.org/10.1002/jps.2600610111>.
- [5] M. Rowland, L.Z. Benet, G.G. Graham, Clearance concepts in pharmacokinetics, *J. Pharm. Biopharm.* 1 (2) (1973) 123–136, <https://doi.org/10.1007/bf01059626>.
- [6] K.S. Pang, M. Rowland, Hepatic clearance of drugs. I. Theoretical considerations of a “well-stirred” model and a “parallel tube” model. Influence of hepatic blood flow, plasma and blood cell binding, and the hepatocellular enzymatic activity on hepatic drug clearance, *J. Pharm. Biopharm.* 5 (6) (1977) 625–653, <https://doi.org/10.1007/bf01059688>.
- [7] K. Winkler, S. Keiding, N. Tytgstrup, Clearance as a Quantitative Measure of Liver Function. The Liver. Quantitative Aspects of Structure and Function, Karger, Basel, 1973, pp. 144–155, <https://doi.org/10.1159/000394804>.
- [8] M.S. Roberts, M. Rowland, Hepatic elimination–dispersion model, *J. Pharm. Sci.* 74 (5) (1985) 585–587, <https://doi.org/10.1002/jps.2600740522>.
- [9] K. Ito, J.B. Houston, Comparison of the use of liver models for predicting drug clearance using in vitro kinetic data from hepatic microsomes and isolated hepatocytes, *Pharm. Res.* 21 (5) (2004) 785–792, <https://doi.org/10.1023/B:PHAM.0000026429.12114.7d>.
- [10] L.Z. Benet, S. Liu, A.R. Wolfe, The universally unrecognized assumption in predicting drug clearance and organ extraction ratio, *Clin. Pharm. Ther.* 103 (3) (2018) 521–525, <https://doi.org/10.1002/cpt.802>.
- [11] M. Rowland, K.S. Pang, Commentary on “the universally unrecognized assumption in predicting drug clearance and organ extraction ratio”, *Clin. Pharm. Ther.* 103 (3) (2018) 386–388, <https://doi.org/10.1002/cpt.921>.
- [12] K.S. Pang, Y. Han, K. Noh, P. Lee, M. Rowland, Hepatic clearance concepts and misconceptions: why the well-stirred model is still used even though it is not physiologic reality? *Biochem. Pharm.* 169 (6) (2019), 113596 <https://doi.org/10.1016/j.bcp.2019.07.025>.
- [13] H.J. Wang, L.Z. Benet, Protein binding and hepatic clearance: re-examining the discrimination between models of hepatic clearance with diazepam in the isolated perfused rat liver preparation, *Drug Metab. Dispos.* 47 (12) (2019) 1397–1402, <https://doi.org/10.1124/dmd.119.088872>.
- [14] L.Z. Benet, J.K. Sodhi, Investigating the theoretical basis for in vitro–in vivo extrapolation (IVIVE) in predicting drug metabolic clearance and proposing future experimental pathways, *AAPS J.* 22 (5) (2020) 120, <https://doi.org/10.1208/s12248-020-00501-9>.
- [15] F.L. Wood, J.B. Houston, D. Hallifax, Clearance prediction methodology needs fundamental improvement: trends common to rat and human hepatocytes/microsomes and implications for experimental methodology, *Drug Metab. Dispos.* 45 (11) (2017) 1178–1188, <https://doi.org/10.1124/dmd.117.077040>.
- [16] M. Rowland, D. Leitch, G. Fleming, B. Smith, Protein binding and hepatic clearance: discrimination between models of hepatic clearance with diazepam, a drug of high intrinsic clearance, in the isolated perfused rat liver preparation, *J. Pharm. Biopharm.* 12 (2) (1984) 129–147, <https://doi.org/10.1007/bf01059274>.
- [17] N.W. Norman Calvey, *Drug Absorption, Distribution and Elimination, Principles and Practice of Pharmacology for Anaesthetists* (New Jersey), Wiley-Blackwell, Hoboken, New Jersey, 2008, pp. 1–22, <https://doi.org/10.1097/ALN.0b013e3181a5a4a2> (New Jersey).
- [18] R. Mandrioli, L. Mercolini, M.A. Raggi, Benzodiazepine metabolism: an analytical perspective, *Curr. Drug Metab.* 9 (8) (2008) 827–844, <https://doi.org/10.2174/138920008786049258>.
- [19] S. Gustafsson, V. Lindström, M. Ingelsson, M. Hammarlund-Udenaes, S. Syvänen, Intact blood-brain barrier transport of small molecular drugs in animal models of amyloid beta and alpha-synuclein pathology, *Neuropharmacology* 128 (2018) 482–491, <https://doi.org/10.1016/j.neuropharm.2017.08.002>.
- [20] M. Rowland, D. Leitch, G. Fleming, B. Smith, Protein binding and hepatic extraction of diazepam across the rat liver, *J. Pharm. Pharmacol.* 35 (6) (1983) 383–384, <https://doi.org/10.1111/j.2042-7158.1983.tb02961.x>.
- [21] N.J. Waters, R. Jones, G. Williams, B. Sohal, Validation of a rapid equilibrium dialysis approach for the measurement of plasma protein binding, *J. Pharm. Sci.* 97 (10) (2008) 4586–4595, <https://doi.org/10.1002/jps.21317>.
- [22] J.M. Diaz-Garcia, A.M. Evans, M. Rowland, Application of the axial dispersion model of hepatic drug elimination to the kinetics of diazepam in the isolated perfused rat liver, *J. Pharm. Biopharm.* 20 (2) (1992) 171–193, <https://doi.org/10.1007/bf01071000>.
- [23] T.O. Kvalseth, Cautionary Note about R<sup>2</sup>, *Am. Stat.* 39 (4) (1985) 279–285, <https://doi.org/10.2307/2683704>.
- [24] N. Rossing, Intra- and extravascular distribution of albumin and immunoglobulin in man, *Lymphology* 11 (4) (1978) 138–142. PMID: 739785.
- [25] M.P. Margaron, N. Soni, Serum albumin: touchstone or totem? *Anaesthesia* 53 (8) (1998) 789–803, <https://doi.org/10.1046/j.1365-2044.1998.00438.x>.
- [26] G.L. Francis, Albumin and mammalian cell culture: implications for biotechnology applications, *Cytotechnology* 62 (1) (2010) 1–16, <https://dx.doi.org/10.1007/s10616-010-9263-3>.
- [27] J.K. Sodhi, H.J. Wang, L.Z. Benet, Are there any experimental perfusion data that preferentially support the dispersion and parallel-tube models over the well-stirred model of organ elimination? *Drug Metab. Dispos.* 48 (7) (2020) 537–543, <https://doi.org/10.1124/dmd.120.090530>.
- [28] D. Hallifax, J.A. Foster, J.B. Houston, Prediction of human metabolic clearance from in vitro systems: retrospective analysis and prospective view, *Pharm. Res.* 27 (10) (2010) 2150–2161, <https://doi.org/10.1007/s11095-010-0218-3>.
- [29] H. Cubitt, K. Yeo, E. Howgate, A. Rostami-Hodjegan, Z. Barter, Sources of interindividual variability in IVIVE of clearance: an investigation into the prediction of benzodiazepine clearance using a mechanistic population-based pharmacokinetic model, *Xenobiotica* 41 (8) (2011) 623–638, <https://doi.org/10.3109/00498254.2011.560294>.
- [30] J. Gao, J. Zhou, X.P. He, Y.F. Zhang, N. Gao, X. Tian, Y. Fang, Q. Wen, L.J. Jia, H. Jin, H.L. Qiao, Changes in cytochrome P450s-mediated drug clearance in patients with hepatocellular carcinoma in vitro and in vivo: a bottom-up approach, *Oncotarget* 7 (19) (2016) 28612–28623, <https://dx.doi.org/10.18632/oncotarget.8704>.
- [31] C.M. Bowman, L.Z. Benet, An examination of protein binding and protein-facilitated uptake relating to in vitro–in vivo extrapolation, *Eur. J. Pharm. Sci.* 123 (2018) 502–514, <https://doi.org/10.1016/j.ejps.2018.08.008>.
- [32] S.A. Smith, N.J. Waters, Pharmacokinetic and pharmacodynamic considerations for drugs binding to alpha-1-acid glycoprotein, *Pharm. Res.* 36 (2) (2018) 30, <https://doi.org/10.1007/s11095-018-2551-x>.
- [33] P. Gardiner, R.J. Cox, K. Grime, Plasma protein binding as an optimizable parameter for acidic drugs, *Drug Metab. Dispos.* 47 (8) (2019) 865–873, <https://doi.org/10.1124/dmd.119.087163>.
- [34] P.B. Soeters, R.R. Wolfe, A. Shenkin, Hypoalbuminemia: pathogenesis and clinical significance, *J. Parent. Enter. Nutr.* 43 (2) (2019) 181–193, <https://doi.org/10.1002/jpen.1451>.
- [35] M. Ulldemolins, J.A. Roberts, J. Rello, D.L. Paterson, J. Lipman, The effects of hypoalbuminemia on optimizing antibacterial dosing in critically ill patients, *Clin. Pharmacol.* 50 (2) (2011) 99–110, <https://doi.org/10.2165/11539220-000000000-00000>.



# Vitamin D<sub>3</sub> decreases TNF- $\alpha$ -induced inflammation in lung epithelial cells through a reduction in mitochondrial fission and mitophagy

Yu-Chen Chen · Hsin-Ching Sung ·  
Tzu-Yi Chuang · Tsai-Chun Lai · Tzu-Lin Lee ·  
Chiang-Wen Lee · I-Ta Lee · Yuh-Lien Chen

Received: 8 February 2021 / Accepted: 24 June 2021  
© Springer Nature B.V. 2021

**Abstract** Previous work has shown an association between vitamin D<sub>3</sub> deficiency and an increased risk for acquiring various inflammatory diseases. Vitamin D<sub>3</sub> can reduce morbidity and mortality in these patients via different mechanisms. Lung inflammation is an important event in the initiation and development of respiratory disorders. However, the anti-inflammatory effects of vitamin D<sub>3</sub> and the underlying mechanisms remained to be determined. The purpose of this study was to examine the effects

and mechanisms of action of vitamin D<sub>3</sub> (Vit. D) on the expression of intercellular adhesion molecule-1 (ICAM-1) in vitro and in vivo with or without tumor necrosis factor  $\alpha$  (TNF- $\alpha$ ) treatment. Pretreatment with Vit. D reduced the expression of ICAM-1 and leukocyte adhesion in TNF- $\alpha$ -treated A549 cells. TNF- $\alpha$  increased the accumulation of mitochondrial reactive oxygen species (mtROS), while Vit. D reduced this effect. Pretreatment with Vit. D attenuated TNF- $\alpha$ -induced mitochondrial fission, as shown

Y.-C. Chen · T.-C. Lai · T.-L. Lee · Y.-L. Chen (✉)  
Department of Anatomy and Cell Biology, College  
of Medicine, National Taiwan University, No. 1, Sec 1,  
Ren-Ai Road, Taipei, Taiwan  
e-mail: ylchenv@ntu.edu.tw

H.-C. Sung (✉)  
Department of Anatomy, Graduate Institute of Biomedical  
Sciences, College of Medicine, Chang Gung University,  
No. 259, Wenhua 1st Rd., Guishan Dist., Taoyuan City,  
Taiwan  
e-mail: hcs@mail.cgu.edu.tw

H.-C. Sung  
Department of Dermatology, Aesthetic Medical Center,  
Chang Gung Memorial Hospital, Linkou, Taoyuan, Taiwan

T.-Y. Chuang (✉)  
Division of Pulmonary Medicine, Department of Internal  
Medicine, Min-Sheng General Hospital, No. 168 Jin-Kuo  
Road, Taoyuan City, Taiwan  
e-mail: revival\_chuang@yahoo.com

T.-Y. Chuang  
Department of Internal Medicine, College of Medicine  
and National Taiwan University Hospital, Taipei, Taiwan

C.-W. Lee  
Department of Nursing, Division of Basic Medical  
Sciences, and Chronic Diseases and Health Promotion  
Research Center, Chang Gung University of Science  
and Technology, Chiayi, Taiwan

C.-W. Lee  
Research Center for Industry of Human Ecology  
and Research Center for Chinese Herbal Medicine, Chang  
Gung University of Science and Technology, Taoyuan,  
Taiwan

C.-W. Lee  
Department of Orthopaedic Surgery, Chang Gung  
Memorial Hospital, Chiayi, Taiwan

I.-T. Lee  
School of Dentistry, College of Oral Medicine, Taipei  
Medical University, Taipei, Taiwan

by the increased expression of mitochondrial fission factor (Mff), phosphorylated dynamin-related protein 1 (p-DRP1), and mitophagy-related proteins (BCL2/adenovirus E1B 19 kDa protein-interacting protein 3, Bnip3) in A549 cells. Inhibition of DRP1 or Mff significantly decreased ICAM-1 expression. In addition, we found that Vit. D decreased TNF- $\alpha$ -induced ICAM-1 expression, mitochondrial fission, and mitophagy via the AKT and NF- $\kappa$ B pathways. Moreover, ICAM-1 expression, mitochondrial fission, and mitophagy were increased in the lung tissues of TNF- $\alpha$ -treated mice, while Vit. D supplementation reduced these effects. In this study, we elucidated the mechanisms by which Vit. D reduces the expression of adhesion molecules in models of airway inflammation. Vit. D might be served as a novel therapeutic agent for the targeting of epithelial activation in lung inflammation.

**Keywords** Adhesion molecules · ROS · Inflammation · Vitamin D<sub>3</sub> · Mitochondrial fission · Mitophagy

### Abbreviations

Vit. D	Vitamin D <sub>3</sub>
ROS	Reactive oxygen species
mtROS	Mitochondrial reactive oxygen species
ATP	Adenosine triphosphate
DRP1	Dynamin-related protein 1
Mff	Mitochondrial fission factor
Bnip3	BCL2/adenovirus E1B 19kDa protein-interacting protein 3
COPD	Chronic obstructive pulmonary disease
BSA	Bovine serum albumin
DMEM	Dulbecco's Modified Eagle Medium
FBS	Fetal bovine serum
SDS	Sodium dodecyl sulfate

### Introduction

Inflammatory lung diseases display high morbidity and mortality and pose a significant socio-economic burden to society (Scherer and Chen 2016). In the lung, inflammation is caused by pathogens or exposure to irritants, air pollutants, and allergens (Moldoveanu et al. 2009). Inflammation is an important factor in the occurrence and progression

of respiratory diseases, such as asthma and chronic obstructive pulmonary disease (Lee and Yang 2013). The complicated interactions between circulating polymorphonuclear leukocytes and constituent cells in lung tissues were involved in these inflammatory responses. During inflammation, intercellular adhesion molecule 1 (ICAM-1), a member of the immunoglobulin supergene family, which is upregulated in respiratory epithelial cells (Lee and Yang 2013; Roebuck and Finnegan 1999). Therefore, it is important to both mechanistically understand and attempt to inhibit the known inflammatory cascade that induces and amplifies lung inflammation.

Oxidative stress is a predictor and indicator of tissue damage and is involved in many biological and pathological diseases, such as inflammation and carcinogenesis (Cachon et al. 2014). Reactive oxygen species (ROS) are mainly produced by nicotinamide adenine dinucleotide phosphate (NADPH) oxidase family members in the plasma membrane and mitochondria (Forrester et al. 2018). An increasing body of evidence has shown that excessive ROS plays an important role in the pathogenesis of airway inflammation and tissue damage, so the neutralization of ROS or inhibition of the redox pathway may reduce inflammation (Babbar and Casero 2006; Kim et al. 2008, 2014; Liu et al. 2018). However, the role of excessive mitochondrial ROS (mtROS) production in driving lung inflammation and ICAM-1 expression has not been fully elucidated.

Under physiological conditions, mitochondria are not only the “powerhouses” of cells, producing large amounts of adenosine triphosphate (ATP) necessary for cells to live, but are also a hub for sensing inflammatory signals and the starting point for inflammatory responses (Ng Kee Kwong et al. 2017). Mitochondria undergo balanced membrane remodeling through fusion and fission and form a dynamic interconnected intracellular network (Park et al. 2013). When stressed, healthy and damaged mitochondria are separated through a fission mechanism, which is regulated by dynamin-related protein 1 (DRP1) and mitochondrial fission factor (Mff) (Westermann 2010). Damaged mitochondria are mainly degraded by mitophagy, a selective form of autophagy (Harris et al. 2018). Mitophagy can preserve energy metabolism and reduce damage caused by external stimuli, thereby protecting the body. However, excessive mitophagy can lead to cell death (Ravikumar

et al. 2010). Bcl2/adenovirus E1B 19 kDa protein-interacting protein 3 (Bnip3) is a receptor-mediated mitophagy-related factor located on the outer mitochondrial membrane that recruits LC3 interacting region (LIR) motifs and triggers mitophagy (Harris et al. 2018). However, the role of the mitophagy-associated proteins Bnip3 and LC3B in TNF- $\alpha$ -induced lung inflammation is still unclear.

Vitamin D<sub>3</sub> regulates adaptive and innate immune functions, proliferation and differentiation of many cell types, and airway remodeling (Hutchinson et al. 2018). Vitamin D<sub>3</sub> is primarily synthesized by 7-dehydrocholesterol in the skin upon exposure to ultraviolet B (UVB) radiation present in sunlight (Christakos et al. 2016; Dusso et al. 2005) but can also be obtained from the diet. Vitamin D<sub>3</sub> is not biologically active. The first metabolite of vitamin D<sub>3</sub>, 25(OH)D<sub>3</sub>, is the major circulating form of vitamin D<sub>3</sub> and the second metabolite of vitamin D<sub>3</sub>, 1,25(OH)<sub>2</sub>D<sub>3</sub>, is the biologically active form of vitamin D<sub>3</sub>. 25(OH)D<sub>3</sub> level in serum has become a reliable biomarker of vitamin D<sub>3</sub> status (Cashman et al. 2017). Vitamin D<sub>3</sub> deficiency is also closely related to the level of inflammatory biomarkers such as vascular cell adhesion molecule-1 (VCAM-1), ICAM-1, and interleukin-6 (IL-6) (Dobnig et al. 2008). In addition, vitamin D<sub>3</sub> extensively modulates both innate and adaptive immune responses and could reduce systemic inflammation in patients (Dusso et al. 2005). Vitamin D<sub>3</sub> administration reduced ICAM-1 and VCAM-1 levels in hemodialysis patients in a placebo-controlled, double-blind clinical trial (Naeini et al. 2017). It has been reported that vitamin D<sub>3</sub> deficiency is associated with the occurrence of bronchiectasis, which is linked to disorders such as asthma and chronic obstructive pulmonary disease (COPD) (Ferri et al. 2019). Vitamin D<sub>3</sub> treatment could reduce morbidity and mortality of patients with chronic kidney disease and end-stage kidney disease by reducing inflammatory mechanisms (Assimon et al. 2012). However, the role of vitamin D<sub>3</sub> in inflammatory diseases is not fully understood. Herein, we studied the effects and mechanisms of action of vitamin D<sub>3</sub> on the expression of adhesion molecules. A better understanding of these processes may provide important insights for preventing airway inflammation.

## Materials and methods

### Cell culture

A549 cells (tumor transformed human type II epithelial alveolar cells) and THP-1 cells (human monocytic cells) were bought from the American Type Culture Collection (VA, USA). A549 cells were cultured in Dulbecco's modified Eagle's medium (DMEM) (Biological Industries, BI, CT, USA) containing 10% fetal bovine serum (FBS, BI) and 1% penicillin/streptomycin (BI). THP-1 cells were cultured in RPMI-1640 medium (BI) containing 10% FBS and 1% penicillin/streptomycin/amphotericin B. Both types of cells were cultivated in a humidified, 5% CO<sub>2</sub> atmosphere at 37 °C.

### Western blot

Cells were pretreated with 25-hydroxy vitamin D<sub>3</sub> (25(OH)D<sub>3</sub>, 25VD<sub>3</sub>, Vit. D; Cayman, NY, USA) or 1,25-dihydroxyvitamin D<sub>3</sub> (1-25(OH)<sub>2</sub>D<sub>3</sub>; 1-25VD<sub>3</sub>; Cayman, NY, USA) for 24 h and then treated with 10 ng/mL TNF- $\alpha$  (PeproTech, NJ, USA). A uniform amount of protein samples (30  $\mu$ g) was subjected to sodium dodecyl sulfate–polyacrylamide gel electrophoresis, and then transferred to polyvinylidene fluoride membranes (Millipore, Germany). The membranes were blocked with Tris-buffered saline containing 0.1% Tween-20 and 5% nonfat dry milk for 1 h. Then, membranes were treated with primary antibodies against ICAM-1 (Santa Cruz, TX, USA; 1:2000 dilution); phospho-ERK, phospho-JNK, phospho-p38, phospho-AKT, phospho-p65, phospho-DRP1 (Ser616), DRP1, Mff, LC3B, Bnip3 (Cell Signaling, MA, USA; 1:2000 dilution); or HIF-1 $\alpha$  (GeneTex, CA, USA; 1:2000 dilution) overnight at 4 °C. Anti-GAPDH or anti- $\beta$ -actin antibodies (BIOTOOLS, Taiwan, 1:10,000 dilution) were used as loading controls. Furthermore, the membranes were incubated with horseradish peroxidase (HRP)-conjugated goat anti-rabbit IgG or goat anti-mouse IgG antibodies (Jackson ImmunoResearch Laboratories, PA, USA; 1:2000 dilution) for 1 h at room temperature (RT). Protein levels were detected using Immobilon Western Chemiluminescent HRP substrate (Merck, Germany). Images were visualized on a UVP ChemStudio PLUS Touch imaging system (Analytik Jena, Germany). The intensity of each band

was quantified using ImageJ and normalized to that of GAPDH or  $\beta$ -actin.

#### Immunofluorescent staining

To detect the in situ expression of ICAM-1, confluent A549 cells (control cells or cells treated with Vit. D for 24 h) on sterile coverslips were treated with the absence or presence of 10 ng/mL TNF- $\alpha$  at 37 °C for 4 h. Then, the medium was removed and the cells were rinsed with PBS, fixed in 4% paraformaldehyde for 15 min at RT, and permeabilized with 0.01% Triton X-100 at RT for 1 min. The cells were further blocked with 1% bovine serum albumin (BSA) in PBS at RT for 1 h. Then, cells were treated with anti-ICAM-1 (diluted 1:50 in PBS containing 1% BSA, Jackson ImmunoResearch Laboratories) overnight at 4 °C. After washing off the unbound antibody, the cells were treated with Alexa Fluor 488-conjugated secondary antibody (diluted 1:200 in PBS containing 1% BSA) for 1 h. Nuclei were labeled with 1  $\mu$ g/mL DAPI for 3 min, to observe and photograph these results with a fluorescence microscope (Leica, Germany). Further, to examine the expression of mitochondrial DRP1, Bnip3 or LC3B, control cells or 24 h Vit. D-treated cells on sterilized coverslips were incubated with 1  $\mu$ M MitoTracker (Invitrogen, CA, USA) or with LysoTracker (Invitrogen) for 30 min and then treated with or without 10 ng/mL TNF- $\alpha$  at 37 °C for 1–2 h. The cells were then fixed and permeabilized by the same method as described above. Then, the cells were incubated with primary antibodies against DRP1, Bnip3, or LC3B (1:200 dilution in PBS containing 1% BSA) overnight at 4 °C. Then, the subsequent experimental steps are the same as above.

#### Leukocyte-epithelial cell adhesion assay

A549 cells cultured in 12-well plates were pretreated with or without Vit. D for 24 h and treated with 10 ng/mL TNF- $\alpha$  for 4 h. 2',7'-bis-(2-carboxyethyl)-5-(and-6)-carboxyfluorescein acetoxymethyl ester (BCECF-AM, Invitrogen) labeled THP-1 cells were incubated with A549 cells for 1 h. Nonadherent THP-1 cells were removed by gentle washing with PBS. For each experiment, three randomly selected images were captured under a fluorescence microscope and the number of THP-1 cells adhered to A549 cells was counted in each image.

#### Detection of mitochondrial ROS

A549 cells were pretreated with Vit. D for 24 h and then stimulated with 10 ng/mL TNF- $\alpha$  for 4 h. MitoSOX Red (Invitrogen), a mitochondrial superoxide indicator, was used to detect mitochondrial ROS levels. A549 cells were incubated with 1.5  $\mu$ M MitoSOX Red at 37 °C for 15 min. Fluorescence intensity was examined using a fluorescence microscope and a FACSCalibur flow cytometer (Becton, Dickinson and Company, BD, NJ, USA).

#### Mitochondrial membrane potential ( $\Delta\psi$ M) determination

The change in mitochondrial transmembrane potential was analyzed using 5,5',6,6'-Tetrachloro-1,1',3,3'-tetraethylbenzimidazolyl-carbocyanine iodide (JC-1, Invitrogen). Cells were pretreated with Vit. D for 24 h and then stimulated with 10 ng/mL TNF- $\alpha$ . JC-1 (1  $\mu$ g/mL) was added to the culture media prior to TNF- $\alpha$  stimulation. At high  $\Delta\psi$ M, JC-1 forms aggregates and emits red fluorescence; at low  $\Delta\psi$ M, JC-1 exists as a monomer and emits green fluorescence. The fluorescence was measured by a fluorescence microscope and an LSRFortessa flow cytometer (BD).

#### Determination of adenosine triphosphate (ATP) levels

A Molecular Probes® ATP determination kit was used to examine the levels of cellular ATP (Invitrogen). The cells were collected in lysis buffer and centrifuged (14,500 $\times$ g) for 20 min at 4 °C. Subsequently, the supernatants were collected and twenty micrograms of each sample was added to a 96-well plate. Then, the reaction solution was added to the 96-well plate. ATP level was measured using a microplate luminometer (Berthold, Bad Wildbad, Germany) and calculated it based on the standard ATP curve.

#### Mitochondrial imaging

Confluent A549 cells (control cells or 24 h Vit. D-treated cells) on sterilized coverslips were incubated with 1  $\mu$ M MitoTracker (Invitrogen) at 37 °C



for 30 min and then stimulated with or without 10 ng/ml TNF- $\alpha$  for 0–4 h at 37 °C. Mitochondria were observed and imaged using a Zeiss ApoTome (Zeiss, Germany). ImageJ software was used to measure mitochondrial length from 20 cells and at least 10 mitochondria per cell. Three replicates were performed for each biological sample.

#### Transmission electron microscopy

After pretreatment with Vit. D for 24 h, the cells were treated with 10 ng/mL TNF- $\alpha$ . After centrifugation, the cells were collected, washed with PBS, fixed with 2% paraformaldehyde and 2% glutaraldehyde in PBS at 4 °C for 24 h, and then post-fixed with 1% osmic acid at RT for 1 h. The cells were further dehydrated in graded ethanol, washed with propylene oxide, and embedded in epoxy resin. The ultrathin sections were cut by using a Reichert ultramicrotome, stained with aqueous uranyl acetate and lead citrate, and viewed using a HITACHI H-7100 at 100 kV.

#### Mitochondrial isolation assay

Whole A549 cell lysates were collected in trypsin–EDTA and then the mitochondrial and cytoplasmic parts were prepared using a mitochondria isolation kit (Thermo Scientific, CA, USA). The experimental procedure was carried out in accordance with the manufacturer's instructions. The mitochondrial and cytoplasmic parts were stored at –20 °C for immunoblot analysis.

#### Acridine Orange (AO) staining

A549 cells were seeded on sterilized coverslips, preincubated with Vit. D for 24 h and then treated with TNF- $\alpha$  (10 ng/mL) for 2 h. AO reagent (1  $\mu$ g/mL, Cayman) was added to the culture media prior to TNF- $\alpha$  stimulation. Cells were washed with PBS and then observed and photographed under a fluorescence microscope. Red fluorescence indicated acidic autophagic vesicles, while green fluorescence was observed in the cytoplasm and nucleus.

#### Coimmunoprecipitation assay

For coimmunoprecipitation, cells were collected in lysis buffer and centrifuged at 12,000 $\times$ g for 10 min. Then, the supernatant was collected, incubated with 1  $\mu$ g of the appropriate antibody against protein of interest, and precipitated with GammaBind Plus-Sepharose beads (GE Healthcare, IL, USA) overnight at 4 °C. Wash the beads 3 times with PBS, and then centrifuge at 2500 $\times$ g for 5 min to collect the precipitated protein. The immunoprecipitated proteins were separated by SDS-PAGE and subjected to Western blot. *Primary antibodies* used for immunoblot were as follows: *DRP1* and *Snip3*. In addition, *Mff* and *LC3B* antibodies were used to check the purity of the precipitate.

#### Animal model

Male C57BL6/J wild-type mice were bought from National Taiwan University (Taipei, Taiwan). This study uses mice aged 8–12 weeks, weighing between 25 and 35 g. The mice were orally fed vitamin D<sub>3</sub> (10,000 IU/kg/day) for 14 days and then anesthetized by inhalation of 2% isoflurane. The neck of the mouse was shaved, and the surgical site was disinfected with 75% alcohol. Make a vertical 5 mm incision to expose the trachea. Use an insulin syringe to puncture the anterior wall of the trachea between the second and third tracheal cartilage rings at a 45° angle to avoid damage to the posterior wall. TNF- $\alpha$  (10  $\mu$ g/kg) in sterile PBS was slowly infused into the trachea. Then suture the skin incision. After returning to normal behavior, the mouse was placed back into the cage. The next day, the mice were anesthetized via inhalation of isoflurane and sacrificed.

Part of lung tissue was fixed in 4% buffered paraformaldehyde and embedded in paraffin for immunohistochemical analysis and hematoxylin–eosin staining. The remaining part was quickly frozen in liquid nitrogen for protein separation to examine the levels of ICAM-1, *DRP1*, *Mff*, *Snip3*, and *LC3B* expression by Western blot. In short, lung tissue was lysed in lysis buffer supplemented with phosphatase inhibitors and protease. The lysate was then centrifuged at 14,500 $\times$ g at 4 °C for 20 min. The supernatant was stored at –80 °C for further study.

## Immunohistochemistry

Five-micrometer-thick sections were cut from the paraffin blocks. The sections were placed in a 60 °C oven for 1 h for deparaffinization and then gradually rehydrated through graded alcohol: 100%, 95%, 85%, and 75% for 5 min each. After antigen retrieval using 10 mM sodium citrate, endogenous peroxidases were inactivated with 3% hydrogen peroxide for 10 min at RT. To check the ICAM-1 expression in lung tissues, the sections were incubated overnight with ICAM-1 antibody (1:200 dilution) at 4 °C. Subsequently, they were incubated with biotin-conjugated goat anti-mouse IgG (1:200 dilution, Jackson ImmunoResearch Laboratories) at RT for 1 h. After washing with PBS, the sections were incubated with avidin–biotin peroxidase complex (VECTASTAIN® ABC-HRP Kit, Vector Laboratories, CA, USA) for 1 h at RT. The sections were then stained with 3′3-diaminobenzidine tetrahydrochloride (DAB; Vector, CA, USA) and H<sub>2</sub>O<sub>2</sub>, counterstained with hematoxylin, and examined by light microscopy.

In order to check whether ICAM-1 is related to type II alveolar epithelial cells, the sections were double stained with ICAM-1 and SP-D (a marker for type II alveolar epithelial cells, 1:100, Bioss, Beijing, China) antibodies. After washing with PBS, the sections were incubated with Alexa Fluor 488 (1:200 dilution) for ICAM-1 and Alexa Fluor 594 (1:100 dilution) for SP-D. Subsequently, the slides were counterstained with DAPI solution and detected by fluorescence microscopy.

## Statistical analysis

Data are expressed as the fold change compared to the control value and expressed as the mean ± SEM. Statistical significance was determined through one-way analysis of variance (one-way ANOVA) using the Statistical Package for the Social Sciences (SPSS) with Fisher's least significant difference (LSD) test. Statistical analyses were performed using GraphPad Prism software (CA, USA). \* $p < 0.05$  compared with the control group; † $p < 0.05$  compared with the TNF- $\alpha$ -stimulated cells.

## Results

### Vit. D reduces TNF- $\alpha$ -induced ICAM-1 expression in A549 cells

Vit. D is reported to have anti-inflammatory effects (Brito et al. 2020). Therefore, we investigated whether Vit. D suppressed the inflammatory response by affecting TNF- $\alpha$ -induced adhesion molecules. To analyze the effect of Vit. D on ICAM-1 expression under inflammatory conditions, A549 cells were preincubated with 0.1, 0.5, 1, 5, or 10  $\mu$ M Vit. D for 24 h and then treated with 10 ng/mL TNF- $\alpha$  for 4 h. As shown in Fig. 1a, TNF- $\alpha$  significantly increased ICAM-1 expression, while 10  $\mu$ M Vit. D reduced this effect. In addition, TNF- $\alpha$  induced ICAM-1 expression in a time-dependent manner, while 10  $\mu$ M Vit. D reduced this expression (Fig. 1b). Based on this result, Vit. D was used at 10  $\mu$ M in all following experiments evaluating the anti-inflammatory effect and molecular mechanism of Vit. D treatment. 1,25-dihydroxyvitamin D<sub>3</sub> (1-25(OH)<sub>2</sub>D<sub>3</sub>; 1-25VD<sub>3</sub>) is an active, hormonal metabolite of vitamin D<sub>3</sub> (Dusso et al. 2005). To examine whether the protective effect of Vit. D (25VD<sub>3</sub>) is similar to that of 1-25VD<sub>3</sub>, A549 cells were pretreated with 0.1 or 10  $\mu$ M 1-25VD<sub>3</sub> for 24 h and then treated with TNF- $\alpha$  for 4 h. As shown in Fig. 1c, the low dose of 1-25VD<sub>3</sub> had no significant effect on ICAM-1 reduction, while the high dose of 1-25VD<sub>3</sub> significantly decreased TNF- $\alpha$ -induced ICAM-1 expression. Similarly, ICAM-1 was strongly present in the cytoplasm of TNF- $\alpha$ -treated A549 cells (T) by fluorescence microscopy. In contrast, pretreatment with Vit. D reduced ICAM-1 expression in TNF- $\alpha$ -treated A549 cells (Vit. D/T) (Fig. 1d). Because cell adhesion molecules are essential for monocyte binding, the subsequent step was to check the effects of Vit. D about the adhesion of monocytes to epithelial cells. TNF- $\alpha$ -treated A549 cells (T) exhibited increased monocyte adhesion compared with confluent control cells (C). Pretreatment with Vit. D reduced the number of monocytes adhered to TNF- $\alpha$ -treated A549 cells (Fig. 1e). In addition, pretreatment with an ICAM-1 neutralizing antibody significantly reduced the monocyte binding to TNF- $\alpha$ -treated A549 cells (ICAM-1 Ab/T) (Fig. 1e). These results suggested that Vit. D reduces TNF- $\alpha$ -induced inflammatory responses in A549 cells.

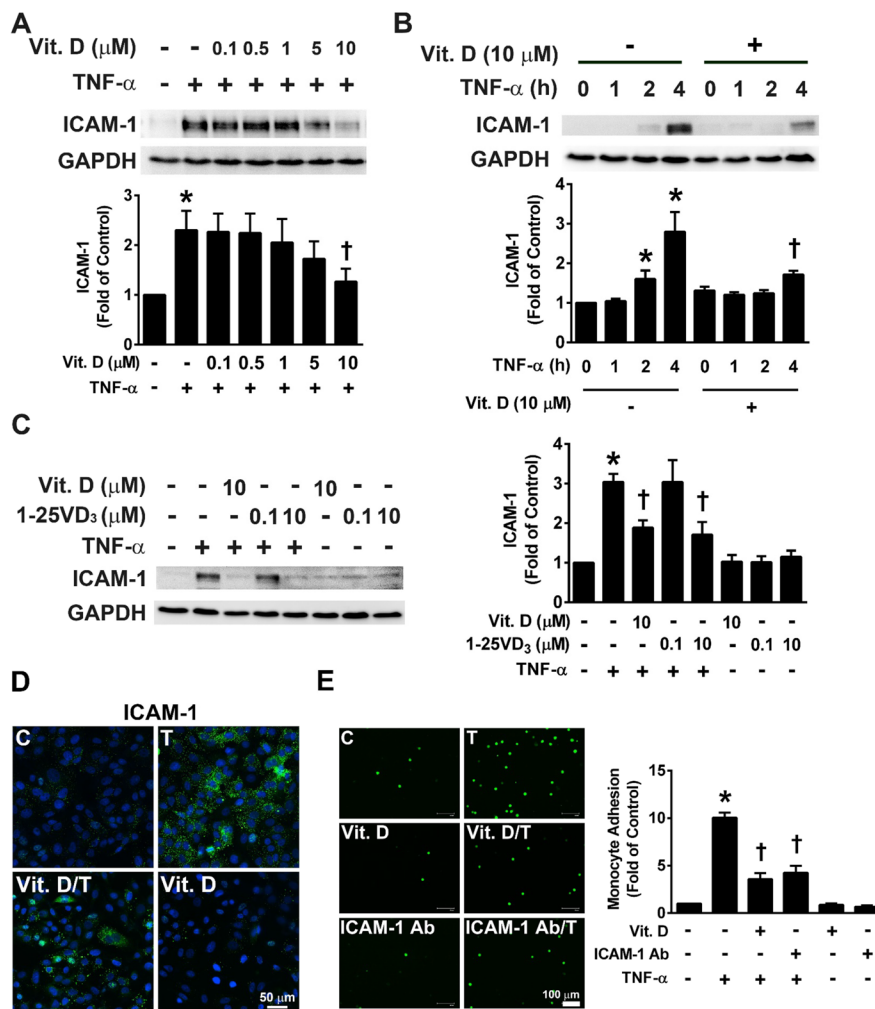


**Fig. 1** Vit. D reduces TNF- $\alpha$ -induced ICAM-1 expression in A549 cells. **a** A549 cells were pretreated with Vit. D (0–10  $\mu$ M) for 24 h and stimulated with TNF- $\alpha$  (10 ng/mL) for 4 h. Then, the expression of ICAM-1 was detected by Western blot. **b** A549 cells were pretreated with 10  $\mu$ M Vit. D for 24 h and then treated with TNF- $\alpha$  for the indicated times. Then, ICAM-1 levels were measured by Western blot. **c** A549 cells were pretreated with Vit. D (10  $\mu$ M) or 1-25VD<sub>3</sub> (0.1, 10  $\mu$ M) for 24 h and then stimulated with TNF- $\alpha$  (10 ng/mL) for 4 h. Then, expression of ICAM-1 was detected by Western blot. **d** The distribution of ICAM-1 expression was detected

by immunofluorescent staining. The nuclei were stained with DAPI. Bar=50  $\mu$ m. **e** Representative images and quantitative analysis of fluorescein-labeled THP-1 cells adhering to A549 cells. A549 cells were left untreated or were pretreated with 10  $\mu$ M Vit. D or 2  $\mu$ g/mL anti-ICAM-1 antibody for 24 h and then stimulated with TNF- $\alpha$  for 4 h. Then, a fluorescence microscope was used to photograph and count adherent cells. Bar=100  $\mu$ m. Data are reported as the mean  $\pm$  SEM (n=9). \* $p$  < 0.05 compared to untreated cells; † $p$  < 0.05 compared to TNF- $\alpha$ -treated cells

#### Vit. D reduces TNF- $\alpha$ -induced mitochondrial ROS (mtROS) production in A549 cells

We next wanted to examine whether Vit. D reduces TNF- $\alpha$ -induced inflammatory responses by decreasing mitochondrial oxidative stress. The production of ROS, which are predominantly derived from

mitochondria, is a key event in the progression of many inflammatory disorders (Liu et al. 2018; Park et al. 2013). Hypoxia-inducible factor-1 $\alpha$  (HIF-1 $\alpha$ ) has been recognized as a transcription factor that can act as a major regulator of oxygen homeostasis (Semenza 2014). Hypoxia-inducible factor-1 $\alpha$  (HIF-1 $\alpha$ ) has been recognized as a transcription

factor that can act as a major regulator of oxygen homeostasis. However, Haddad and Land reported that TNF- $\alpha$  plays a major role in mediating HIF-1 $\alpha$  regulation under normoxia (Haddad and Land 2001). In this study, we examined the effect of Vit. D on TNF- $\alpha$ -induced HIF-1 $\alpha$  expression. The data showed that TNF- $\alpha$  treatment significantly increased the expression of HIF-1 $\alpha$  in a time-dependent manner, while pretreatment with Vit. D reduced TNF- $\alpha$ -induced HIF-1 $\alpha$  expression (Fig. 2a). The levels of mtROS were evaluated using the MitoSOX Red assay. Cells treated with TNF- $\alpha$  for 4 h displayed significantly increased mtROS levels, as shown by both fluorescence microscopy (Fig. 2b) and flow cytometry (Fig. 2c). As shown in Fig. 2b, pretreatment with Vit. D significantly decreased TNF- $\alpha$ -induced mtROS production. MitoTEMPO, a mitochondrial-targeted antioxidant, was used to examine whether Vit. D affects ROS production in mitochondria. Pretreatment with MitoTEMPO significantly decreased TNF- $\alpha$ -induced mtROS production, as shown by fluorescence microscopy. The flow cytometry results were consistent with the fluorescence microscopy findings (Fig. 2c). TNF- $\alpha$ -induced HIF-1 $\alpha$  expression was suppressed by mitoquinol (MitoQ), a mitochondrial-targeted antioxidant (Fig. 2d). We next evaluated whether the expression of ICAM-1 in TNF- $\alpha$ -treated A549 cells was caused by the production of mtROS. The data showed that pretreatment with MitoQ reduced the expression of ICAM-1 in TNF- $\alpha$ -treated A549 cells (Fig. 2e). Taken together, these data indicate that TNF- $\alpha$ -induced ICAM-1 expression is related to mtROS production in A549 cells.

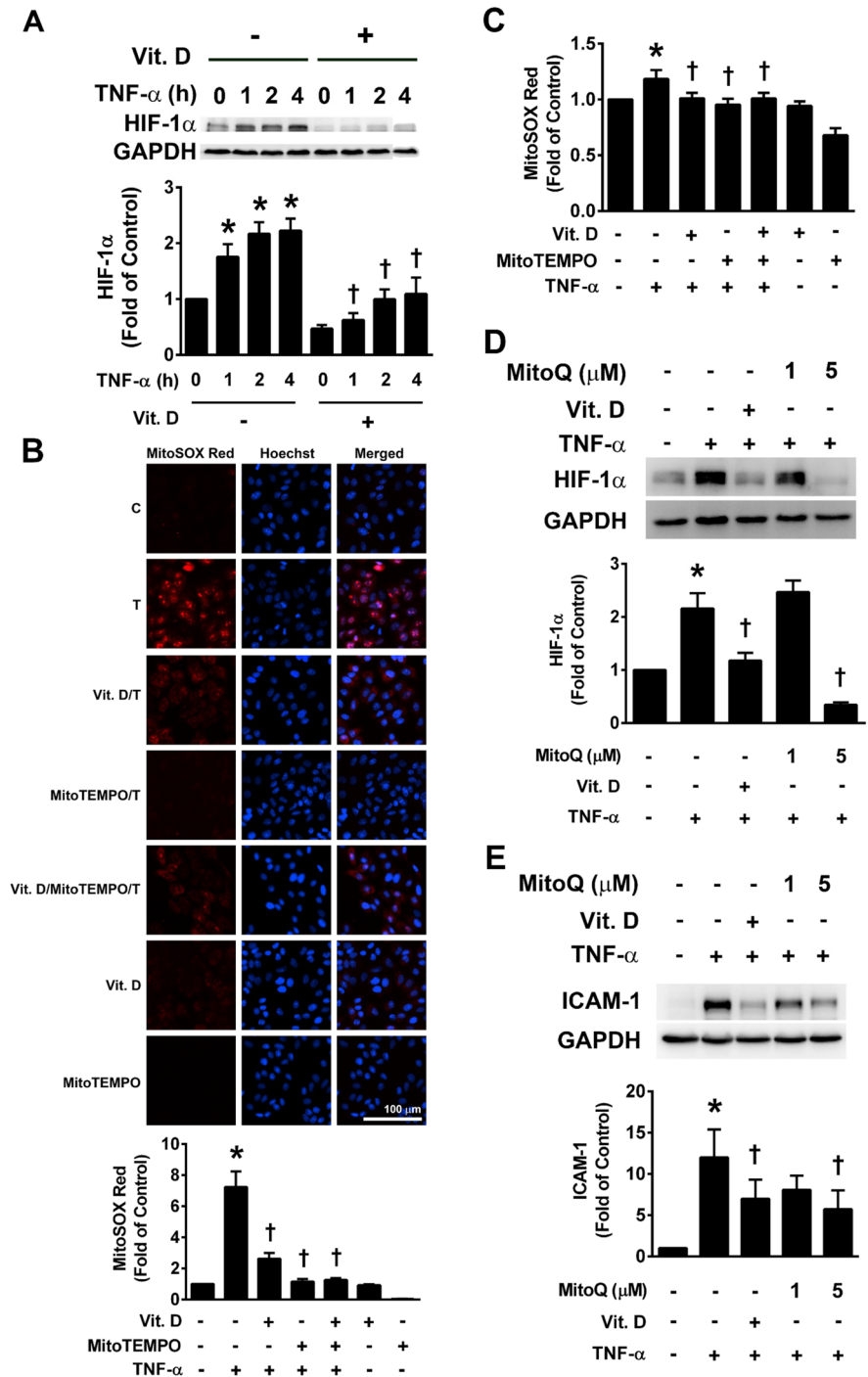
Vit. D attenuates the TNF- $\alpha$ -induced decrease in mitochondrial membrane potential ( $\Delta\Psi_m$ ) and increase in mitochondrial fission

Under normal conditions, mitochondria undergo dynamic and balanced membrane remodeling through cycles of fusion and fission. Once stimulated, healthy and damaged mitochondria are separated through a fission mechanism. Imbalances in mitochondrial fission and fusion play an important role in the progression of many diseases (Park et al. 2013; Westermann 2010). Due to the production of mtROS in TNF- $\alpha$ -stimulated A549 cells, we examined several mitochondrial functions, such as changes in membrane potential, ATP production and expression of

mitochondrial dynamics-related proteins. The levels of  $\Delta\Psi_m$  and ATP are key parameters for cell and mitochondrial function. Cells treated with TNF- $\alpha$  for 1 and 2 h (T1h, T2h) displayed a marked change in fluorescence shift from red to green, as shown by the JC-1 analysis; this change indicates the collapse of  $\Delta\Psi_m$ . Cells pretreated with Vit. D displayed reduced green fluorescence emission, with a distribution type is similar to that of the control group (Fig. 3a). Moreover, JC-1 analysis of flow cytometry showed that TNF- $\alpha$  stimulation increased the ratios of green to red MFI (mean fluorescence intensity), while Vit. D pretreatment reversed this effect (Fig. 3b and Supplementary Fig. 1). ATP level was decreased after TNF- $\alpha$  treatment, while Vit. D treatment protected cells from this TNF- $\alpha$ -induced influence (Fig. 3c).

Mitochondria are highly dynamic cellular organelles with the ability to undergo fission and fusion. Mitochondrial dynamics play the important role in cellular and mitochondrial function (Scott and Youle 2010). As shown in Fig. 3d, DRP1 phosphorylation at residue Ser616 was significantly increased after 1 and 2 h TNF- $\alpha$  stimulation, while pretreatment with Vit. D reduced this activation. The expression of Mff, an adaptor of DRP1, was also decreased in TNF- $\alpha$ -treated A549 cells pretreated with Vit. D. Next, MitoTracker was used to monitor changes in mitochondrial morphology in A549 cells incubated with Vit. D for 24 h and then treated with TNF- $\alpha$  for 0–4 h. We found that mitochondrial length was significantly reduced in TNF- $\alpha$ -treated cells as compared to cells pretreated with Vit. D before TNF- $\alpha$  stimulation (Fig. 3e). TEM images also showed that mitochondrial length was reduced in TNF- $\alpha$ -treated cells, while pretreatment with Vit. D reversed these effects (Fig. 3f). We also found that there was increased expression of mitochondrial DRP1 and Mff in TNF- $\alpha$ -treated cells. These data showed that cells pretreated with Vit. D displayed reduced mitochondrial DRP1 and Mff levels after 1 h TNF- $\alpha$  stimulation (Fig. 3g). Consistently, immunostaining showed that TNF- $\alpha$  stimulation increased DRP1 expression, while the mitochondrial marker MitoTracker was used to demonstrate that the expression of DRP1 was localized to the mitochondria (Fig. 3h). These data indicate that TNF- $\alpha$  increases DRP1 expression in the mitochondria. The mitochondrial fission inhibitor Mdivi-1 was used to investigate whether the inflammatory responses are caused by TNF- $\alpha$ -induced

**Fig. 2** The effect of Vit. D on TNF- $\alpha$ -induced mitochondrial ROS production in A549 cells. **a** A549 cells were pretreated with 10  $\mu$ M Vit. D for 24 h and then treated with TNF- $\alpha$  for the indicated times. HIF-1 $\alpha$  expression levels were measured by Western blot. **b, c** A549 cells were pretreated with 10  $\mu$ M Vit. D or with 100  $\mu$ M MitoTEMPO (a mitochondria-targeted antioxidant) for 24 h and then treated with TNF- $\alpha$  for 4 h. Mitochondrial ROS levels were detected using 1.5  $\mu$ M MitoSox Red (a mitochondrial ROS indicator) by fluorescence microscopy (**b**) and flow cytometry (**c**). Bar = 100  $\mu$ m. **d, e** A549 cells were incubated with 10  $\mu$ M Vit. D or 1 or 5  $\mu$ M mitoquinol (MitoQ, a mitochondria-targeted antioxidant) for 24 h and then stimulated with TNF- $\alpha$  for 4 h. Expression levels of HIF-1 $\alpha$  and ICAM-1 were measured by Western blot. Data are reported as the mean  $\pm$  SEM ( $n=9$ ). \* $p < 0.05$  compared to untreated cells; † $p < 0.05$  compared to TNF- $\alpha$ -treated cells



mitochondrial fission. Western blot analysis revealed that TNF- $\alpha$ -induced ICAM-1 expression was decreased following Mdivi-1 pretreatment (Fig. 3i). Pretreatment with Mdivi-1 also reduced the number of adherent monocytes (Fig. 3j). The efficiently

reduced endogenous levels of DRP1 and Mff were indicated by Western blot (Fig. 3k). Knockdown of DRP1 or Mff significantly reduced TNF- $\alpha$ -induced ICAM-1 expression (Fig. 3l). These results suggested



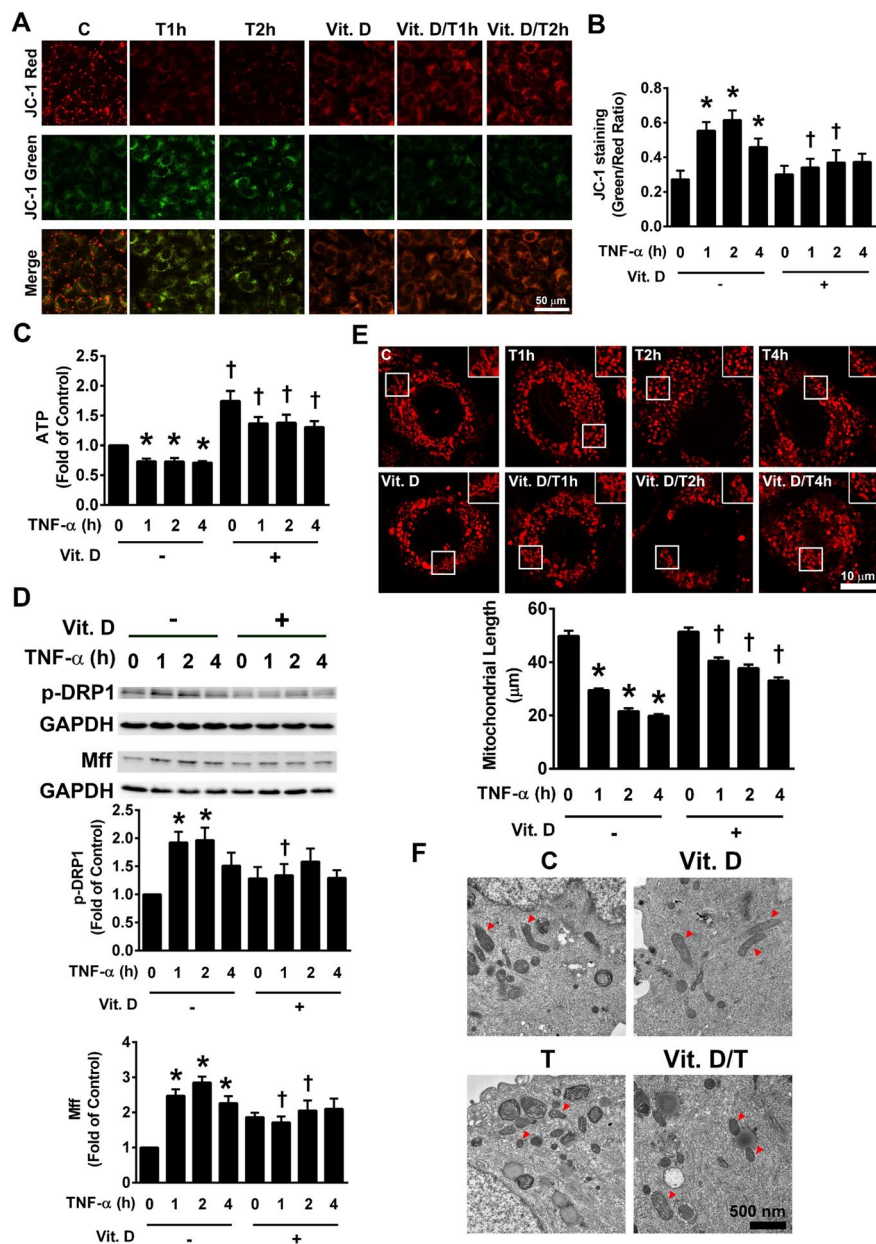
that Vit. D reduces ICAM-1 expression by decreasing TNF- $\alpha$ -induced mitochondrial fission in A549 cells.

### Vit. D reduces TNF- $\alpha$ -induced mitophagy

Mitochondrial dysfunction has been demonstrated to play a key role in several diseases, and the accumulation of dysfunctional mitochondria leads to oxidative stress and impairment of cellular functions (Bhatti et al. 2017). Mitochondrial dynamics and mitophagy have been identified as important mediators that control mitochondrial quality. Mitophagy appears to be an autophagic mechanism for the degradation of dysfunctional mitochondria (Harris et al. 2018). To investigate the involvement of mitophagy in A549 cells pretreated with Vit. D and then stimulated with TNF- $\alpha$  for the indicated times, we examined expression of the mitophagy-related protein Bnip3 by Western blot. As shown in Fig. 4a, TNF- $\alpha$  significantly increased both Bnip3 and LC3B expression in a time-dependent manner, while pretreatment with Vit. D reduced these TNF- $\alpha$ -induced effects. Interestingly, expression of the autophagy-related protein LC3B was significantly increased in the Vit. D pretreated cells. After 2 h of TNF- $\alpha$  stimulation, cells showed more acidic vesicular organelles by AO staining, which were detected as red-stained dots by fluorescence microscopy, compared with the 0 h group. Cells pretreated with Vit. D showed fewer red-stained dots (Fig. 4b). We then investigated whether Vit. D affected mitochondrial translocation of Bnip3 and LC3B in TNF- $\alpha$ -treated A549 cells. Vit. D pretreatment reduced mitochondrial translocation of Bnip3 when compared to that of TNF- $\alpha$ -treated cells, while mitochondrial fractions of LC3B expression showed no difference between TNF- $\alpha$  stimulation and Vit. D pretreatment with TNF- $\alpha$  stimulation (Fig. 4c). In addition, fluorescent staining revealed increased Bnip3 localization to mitochondria in TNF- $\alpha$ -treated cells, while Vit. D pretreatment reduced this effect (Fig. 4d). Coimmunoprecipitation was used to investigate interactions between Bnip3 and LC3B. As shown in Fig. 4e, Vit. D reduced TNF- $\alpha$ -induced Bnip3-LC3B interactions in A549 cells. These data suggested that Vit. D reduces TNF- $\alpha$ -induced Bnip3-mediated mitophagy. Mitophagy was identified in TNF- $\alpha$ -treated A549 cells with or without Vit. D pretreatment. Therefore, we next used bafilomycin A1 (Baf. A1) and chloroquine (CQ) to examine whether Vit. D reduced inflammation via inhibition

**Fig. 3** Vit. D reduces excessive TNF- $\alpha$ -induced mitochondrial fission in A549 cells. **a** A549 cells were pretreated with 10  $\mu$ M Vit. D for 24 h and then treated with TNF- $\alpha$  for the indicated times. Changes in mitochondrial membrane potential were detected using JC-1 staining and fluorescence microscopy. Bar=50  $\mu$ m. **b** Cells were incubated with 10  $\mu$ M Vit. D for 24 h and then stimulated with TNF- $\alpha$  for the indicated times. Changes in mitochondrial membrane potential were examined using JC-1 staining and flow cytometry. **c** ATP production was measured using an ATP assay. **d** The levels of mitochondrial fission-related proteins, phosphorylated DRP1 (Ser 616) and Mff, were examined by Western blot. **e** Mitochondrial morphology was observed using a Zeiss ApoTome. The right panel shows a larger magnification of the indicated area in the left panel. Bar=10  $\mu$ m. The bar graph shows mitochondrial lengths in A549 cells as measured using ImageJ software. **f** A549 cells were pretreated with 10  $\mu$ M Vit. D for 24 h and then stimulated with TNF- $\alpha$  for 2 h. Mitochondrial morphology (arrowhead) was examined using TEM. Scale bar=500 nm. **g** A549 cells were pretreated with Vit. D and then stimulated with TNF- $\alpha$  for 1 h. The mitochondrial fraction was analyzed by Western blot. **h** Immunofluorescence was used to assess colocalization of DRP-1 (green) and MitoTracker (mitochondria, red) Bar=10  $\mu$ m. **i** The cells were pretreated with mitochondrial division inhibitor 1 (Mdivi-1) for 1 h and then stimulated with TNF- $\alpha$  for 4 h. The expression of ICAM-1 was detected by Western blot. **j** Photographs and quantitative analysis of fluorescein-labeled THP-1 cells adhered to A549 cells after Mdivi-1 pretreatment and TNF- $\alpha$  stimulation. Bar=100  $\mu$ m. **k** A549 cells were transfected with 50 nM DRP1 siRNA or 25 nM Mff siRNA for 48 h and then DRP1 and Mff expression was determined by Western blot. **l** A549 cells were transfected with 50 nM DRP1 siRNA or 25 nM Mff siRNA for 48 h and then stimulated with TNF- $\alpha$  for 4 h. The expression of ICAM-1 was determined by Western blot. Data are reported as the mean  $\pm$  SEM ( $n=9$ ). \* $p < 0.05$  compared to untreated cells; † $p < 0.05$  compared to TNF- $\alpha$ -treated cells

of TNF- $\alpha$ -induced mitophagy (Fig. 4f). CQ inhibits autophagy because it raises the lysosomal pH, which results in the inhibition of autophagosome-lysosome fusion and lysosomal protein degradation whereas Baf. A1 inhibits the fusion between autophagosomes and lysosomes by inhibiting vacuolar H<sup>+</sup>-ATPase, thereby preventing the maturation of autophagosomes (Mauthe et al. 2018; Mauvezin and Neufeld 2015). Baf. A1 pretreatment did not affect TNF- $\alpha$ -induced monocyte adhesion, however, CQ pretreatment significantly increased TNF- $\alpha$ -induced monocyte adhesion (Fig. 4g). Mdivi-1 was used to assess rates of mitophagy and revealed that increased mitophagy was correlated with excess TNF- $\alpha$ -induced mitochondrial fission. As shown in the results, pretreatment with Mdivi-1 reduced TNF- $\alpha$ -induced Bnip3 expression in A549 cells (Fig. 4h). These data suggested that



mitophagy in A549 cells is caused by TNF- $\alpha$ -induced mitochondrial fission and that Vit. D could reduce these effects.

Vit. D reduces TNF- $\alpha$ -induced the expression of ICAM-1 in A549 cells through the AKT/p65 pathways

The inflammatory cytokines-induced ICAM-1 expression is mediated through multiple signaling

pathways, including MAPKs, AKT, and p65 (Lee and Yang 2013). We first examined whether TNF- $\alpha$ -induced ICAM-1 expression was mediated by activation of MAPKs. ERK1/2, p38 and JNK phosphorylation was significantly increased in A549 cells after 5 and 15 min of TNF- $\alpha$  stimulation but declined beginning at 30 min. In order to determine the impact of Vit. D, cells were pretreated with Vit. D for 24 h, then treated with TNF- $\alpha$  for 5, 15, and 30 min. As shown in Fig. 5a, Vit. D treatment

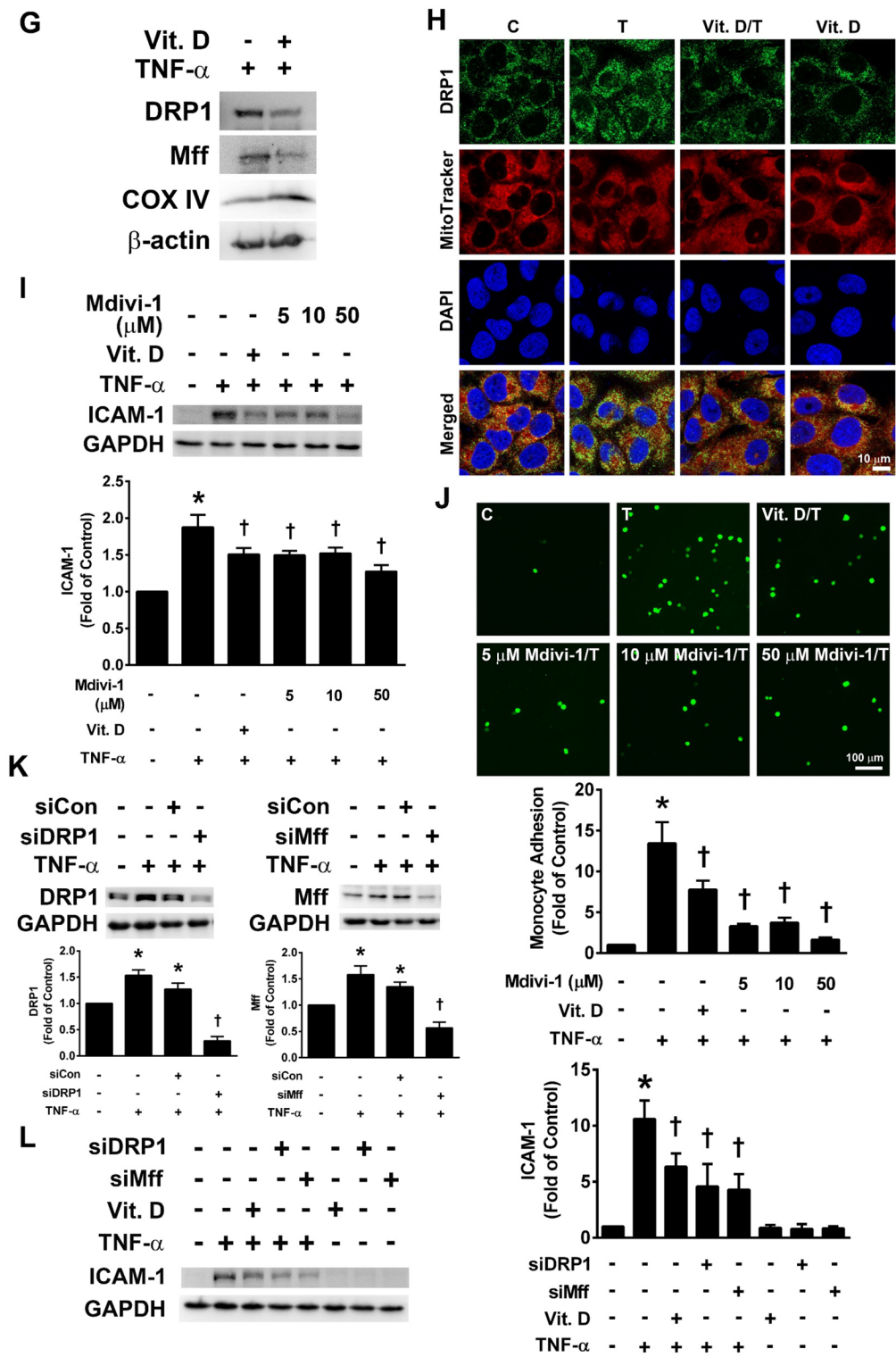
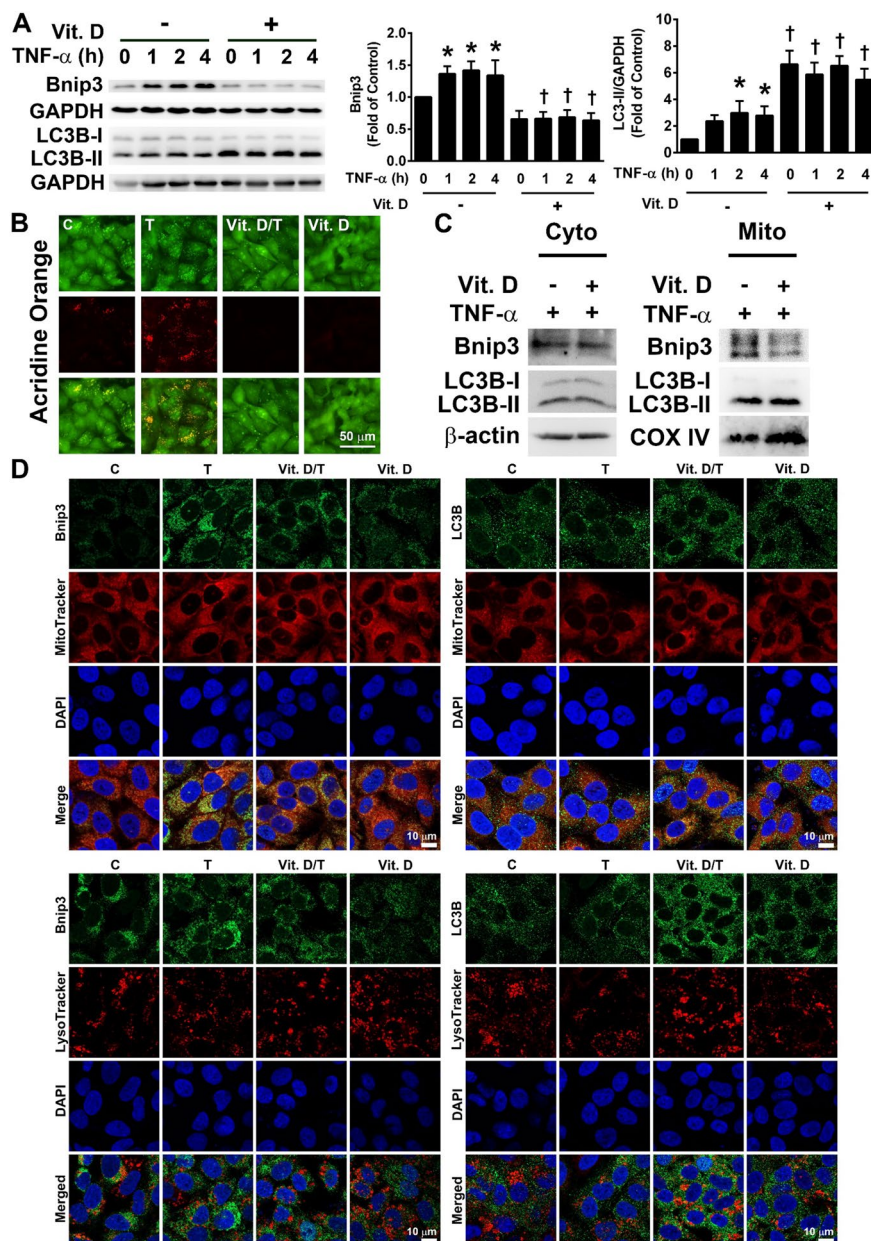


Fig. 3 (continued)





**Fig. 4** Vit. D reduces TNF- $\alpha$ -induced mitophagy in A549 cells. **a** A549 cells were pretreated with Vit. D for 24 h and then treated with TNF- $\alpha$  for the indicated times. Bnip3 and LC3B expression levels in cell lysates were examined by Western blot. **b** A549 cells were pretreated with Vit. D for 24 h and then treated with TNF- $\alpha$  for 2 h. The formation of autophagosomes was examined via Acridine Orange (AO) staining and fluorescence microscopy. Bar = 50  $\mu$ m. **c** A549 cells were pretreated with Vit. D for 24 h and then treated with TNF- $\alpha$  for 2 h. The cytoplasmic and mitochondrial fractions were examined for Bnip3 and LC3B expression by Western blot. **d** Immunofluorescence was used to assess colocalization of Bnip3 (green) or LC3B (green) and MitoTracker (mitochondria, red) or LysoTracker (lysosome, red). Bar = 10  $\mu$ m. **e** Coimmunoprecipitation of Bnip3 and LC3B in A549 cells pretreated with Vit. D for 24 h and stim-

ulated with TNF- $\alpha$  for 2 h. The left panel shows the Western blot analysis of whole cell lysates, and the right panel shows the analysis of immunoprecipitated samples. **f** A549 cells were pretreated with 100 nM bafilomycin A1 (Baf, A1) or 10  $\mu$ M chloroquine (CQ) for 6 h, treated with or without Vit. D for 24 h, and then stimulated with TNF- $\alpha$  for 4 h. The expression of ICAM-1 was examined by Western blot. **g** Representative images and quantitative analysis of fluorescein-labeled THP-1 cells adhered to A549 cells. The adherent cells were photographed and counted under a fluorescence microscope. Bar = 100  $\mu$ m. **h** A549 cells were pretreated with Mdivi-1 for 1 h and then stimulated with TNF- $\alpha$  for 2 h. Bnip3 and LC3B expression levels were analyzed by Western blot. Data are reported as the mean  $\pm$  SEM ( $n=9$ ). \* $p < 0.05$  compared to untreated cells; † $p < 0.05$  compared to TNF- $\alpha$ -treated cells

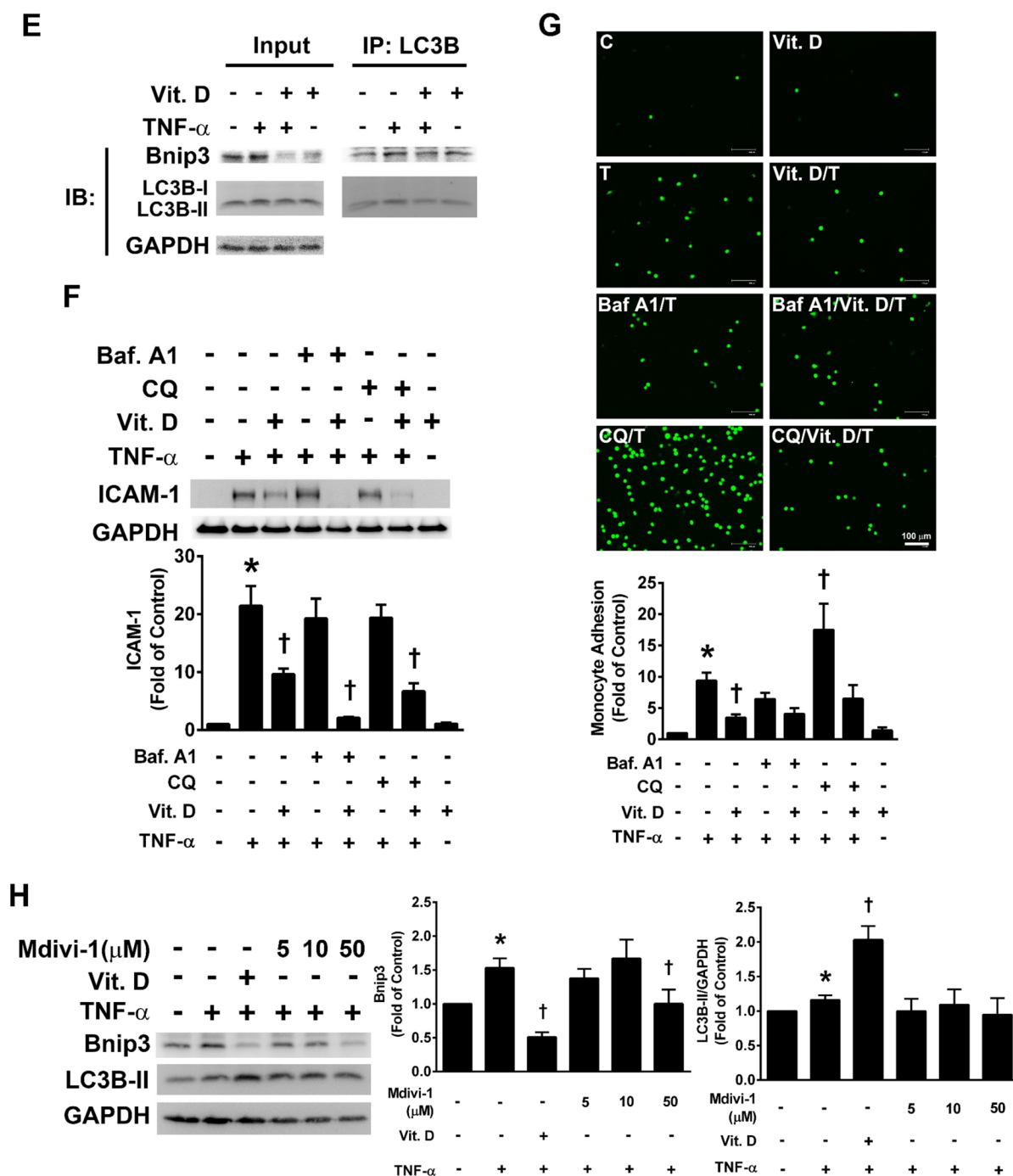
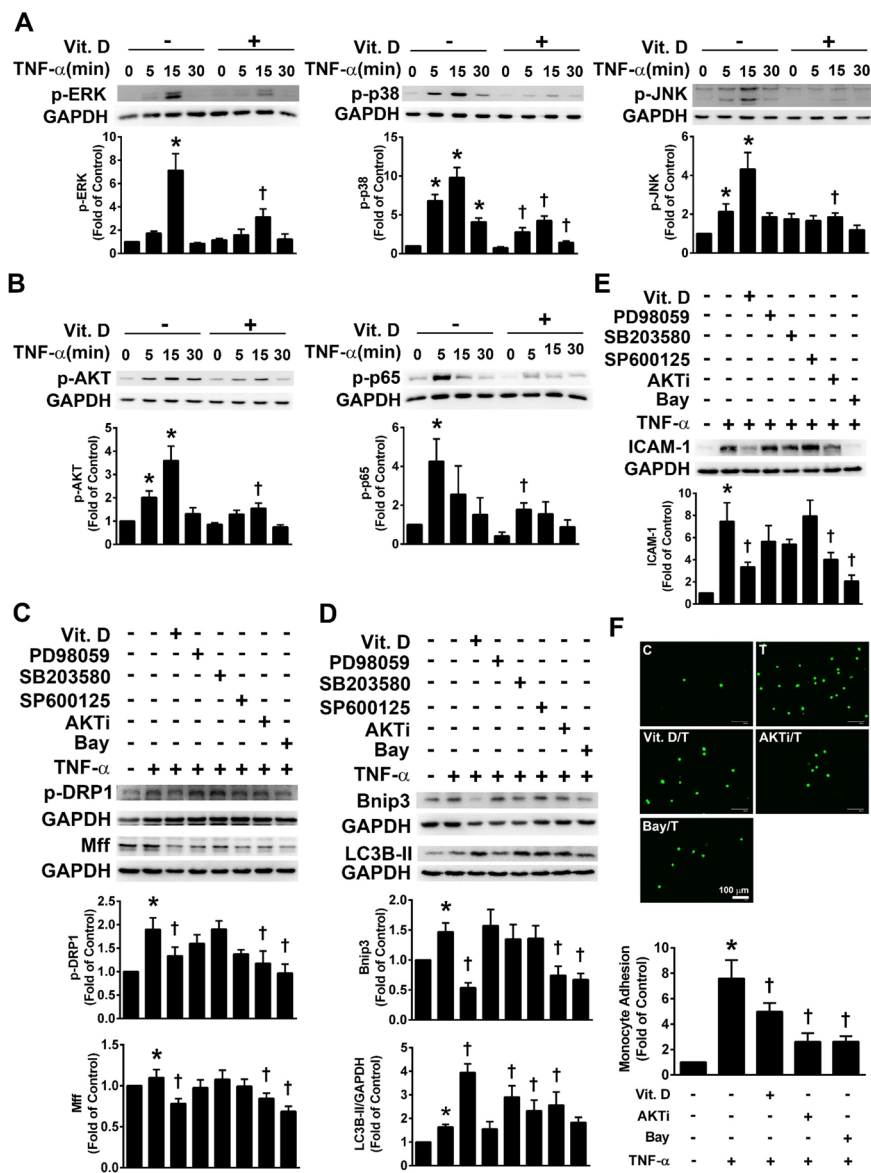


Fig. 4 (continued)

significantly decreased ERK, p38 and JNK phosphorylation levels. In addition, the levels of phosphorylated AKT and p65 expression were significantly induced after TNF- $\alpha$  stimulation, while Vit.

D pretreatment remarkably reduced these effects (Fig. 5b). To further confirm the involvement of MAPKs, AKT, and p65 in TNF- $\alpha$ -induced mitochondrial fission and mitophagy, we used inhibitors





**Fig. 5** Vit. D reduces TNF- $\alpha$ -induced mitochondrial fission, mitophagy, and ICAM-1 expression in A549 cells through the AKT/p53 pathways. **a**, **b** The effect of Vit. D treatment on TNF- $\alpha$ -induced phosphorylation of **a** ERK1/2, p38, JNK, **b** AKT and p65 in A549 cells. A549 cells were pretreated with 10  $\mu$ M Vit. D for 24 h and then stimulated with TNF- $\alpha$  for 0–30 min. The levels of phosphorylated ERK1/2, p38, JNK, AKT and p65 were analyzed by Western blot. **c** A549 cells were pretreated with 50  $\mu$ M PD98059 (an ERK1/2 inhibitor), 50  $\mu$ M SB203580 (a p38 inhibitor), 50  $\mu$ M SP600125 (a JNK inhibitor), 15  $\mu$ M AKTi (an AKT inhibitor), or 15  $\mu$ M Bay (a p65 inhibitor) for 1 h and then treated with TNF- $\alpha$  for 1 h. The expression of Ser616-phosphorylated DRP1 and Mff was analyzed by Western blot. **d** The effects of MAPKs, AKT, and

p65 on the expression of Bnip3 and LC3B after 2 h of TNF- $\alpha$  stimulation were detected by Western blot. **e** A549 cells were pretreated with PD98059, SB203580, SP600125, AKTi, or Bay for 1 h and then treated with TNF- $\alpha$  for 4 h. Then, expression of ICAM-1 was examined by Western blot. **f** The effects of AKT/p65 inhibitors on TNF- $\alpha$ -induced adhesion of fluorescein-labeled THP-1 cells to A549 cells. The cells were left untreated or pretreated with AKTi or Bay for 1 h. Then, they were treated with TNF- $\alpha$  in the continued presence of the inhibitors for 4 h. Bar = 100  $\mu$ m. **g**, **h** The effects of AKT/p65 inhibitors on mitochondrial length (**g**) and JC-1 staining (**h**). Bar = 10 or 50  $\mu$ m as panel indicated. Data are reported as the mean  $\pm$  SEM ( $n=9$ ). \* $p < 0.05$  compared to untreated cells; † $p < 0.05$  compared to TNF- $\alpha$ -treated cells

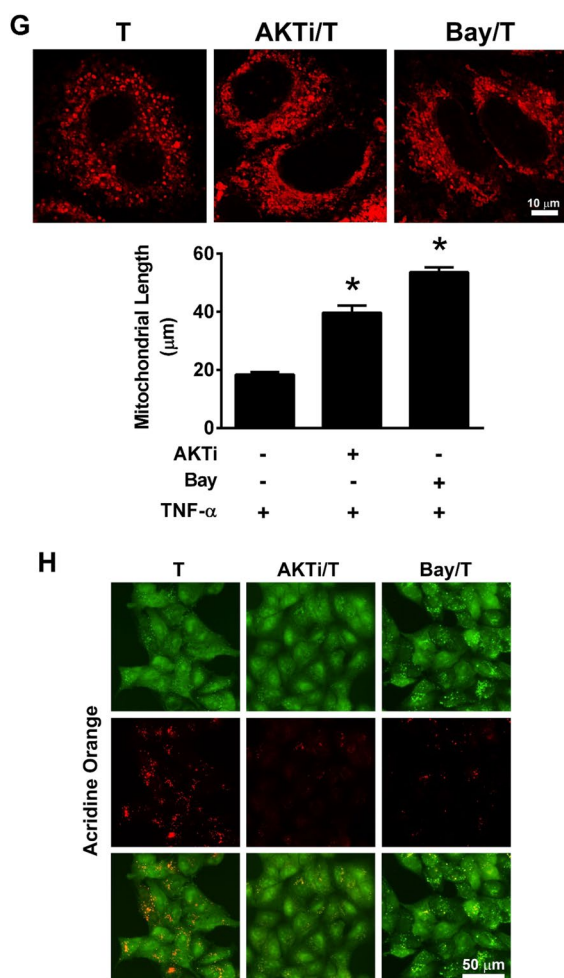


Fig. 5 (continued)

for specific signal transduction pathways. TNF- $\alpha$ -induced increases in p-DRP1, Mff, and Bnip3 expression was inhibited by pretreatment with AKTi (an AKT inhibitor) and Bay (an NF- $\kappa$ B inhibitor) but not with PD98059 (an ERK 1/2 inhibitor), SB203580 (a p38 inhibitor), or SP600125 (a JNK inhibitor), as demonstrated by Western blot (Fig. 5c, d). Furthermore, we assessed whether the activation of MAPKs/AKT/p65 was related to the inhibition of TNF- $\alpha$ -induced ICAM-1 expression by Vit. D. TNF- $\alpha$ -induced ICAM-1 expression was inhibited by pretreatment with AKTi and Bay but not with PD98059, SB203580, or SP600125, as shown by Western blot analysis (Fig. 5e). Moreover, AKT and p65 specific inhibitors reduced TNF- $\alpha$ -increased

monocyte binding (Fig. 5f), which further corroborated that sequential activation of the AKT/p65 pathway lead to the upregulation of ICAM-1 and subsequent monocyte binding. We also demonstrated that inhibitors specific for AKT and p65 enhanced TNF- $\alpha$ -induced reductions in mitochondrial length (Fig. 5g) and JC-1 staining (Fig. 5h). These data suggested that Vit. D decreased TNF- $\alpha$ -induced ICAM-1 expression, mitochondrial fission, and mitophagy via AKT and NF- $\kappa$ B pathways.

Vit. D reduces lung inflammation, mitochondrial fission, and mitophagy in TNF- $\alpha$ -treated mice

In order to examine the impact of Vit. D on the expression of ICAM-1 under inflammatory conditions *in vivo*, mice were orally fed Vit. D for 14 days and then stimulated for 24 h via intratracheal injection of TNF- $\alpha$ . At the light microscopic level, airspaces were inflated in healthy controls, and fewer blood cells were observed in the septal walls. 24 h of TNF- $\alpha$  stimulation caused thickening of distal airspaces and infiltration of many inflammatory cells, while preadministration of Vit. D reduced these effects (Fig. 6a). Western blot and immunohistochemical staining were performed to detect ICAM-1 expression levels in lung tissues. As shown in Fig. 6b, TNF- $\alpha$  significantly induced ICAM-1 expression in lung tissues, and pre-treatment with Vit. D diminished these effects. Consistent with the Western blot results, stronger ICAM-1 staining was observed on epithelial cells in the TNF- $\alpha$ -treated group; in contrast, preadministration of Vit. D followed by 24 h of TNF- $\alpha$  stimulation resulted in weaker ICAM-1 staining and weak ICAM-1 expression in the control and Vit. D-treated groups (Fig. 6c). The expression of ICAM-1 was colocalized with type II epithelial cell marker SP-D (Fig. 6d). Expression of the mitochondrial fission-related proteins DRP1 and Mff and the mitophagy-related protein Bnip3 was significantly increased after TNF- $\alpha$  treatment, while Vit. D preadministration reduced mitochondrial fission and mitophagy (Fig. 6e). Furthermore, inhibitors specific for AKT and p65 reduced TNF- $\alpha$ -induced the expression of ICAM-1, Mff, and Bnip3, while did not affect the expression DRP1 and LC3B in lung tissues (Fig. 6f).

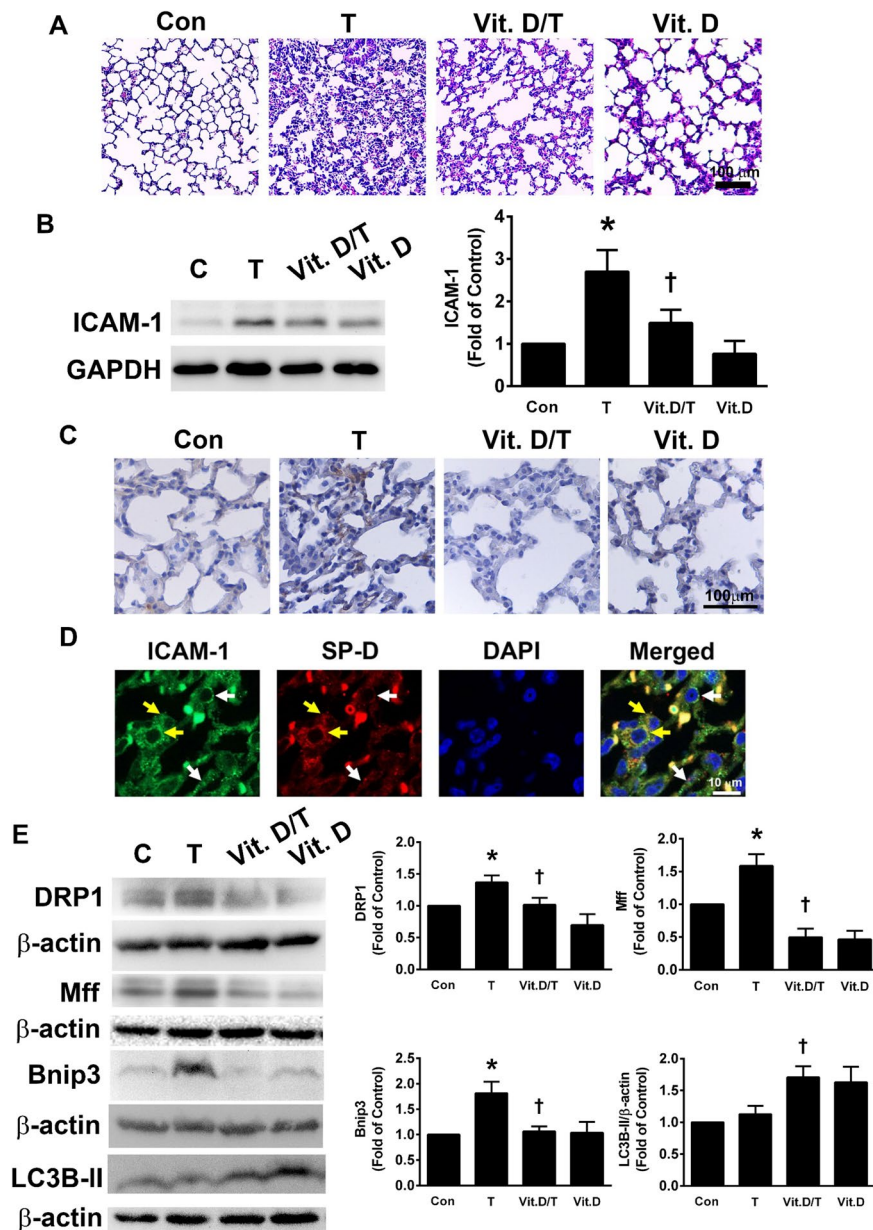


**Fig. 6** Vit. D reduces lung inflammation, mitochondrial fission, and mitophagy in TNF- $\alpha$ -treated mice. C57BL/6 J mice were orally administered vitamin D<sub>3</sub> (10,000 IU/kg/day) for 14 days, and then TNF- $\alpha$  (10  $\mu$ g/kg) was administered intratracheally. Mice were sacrificed 24 h after TNF- $\alpha$  treatment. **a** Representative light microscopic images of control (Con), TNF- $\alpha$  stimulated (T), Vit. D pre-administered and TNF- $\alpha$  stimulated (Vit. D/T), and Vit. D pre-administered (Vit. D) lung tissues. Bar=100  $\mu$ m. **b** The expression of ICAM-1 in lung tissues was examined by Western blot. **c** The localization of ICAM-1 expression in lung tissues was examined by immu-

nohistochemistry. Bar=100  $\mu$ m. **d** ICAM-1 expression (white arrow) was localized to type II epithelial cells (yellow arrow) in lung tissues, as demonstrated by immunohistochemistry. Bar=10  $\mu$ m. **e** The expression levels of mitochondrial fission-related proteins (DRP1 and Mff), mitophagy-related protein (Bnip3), and autophagy-related protein (LC3B) in lung tissues were examined by Western blot. **f** The effects of AKT/p65 inhibitors on the expression of ICAM-1, Mff, Bnip3, DRP1, and LC3B were examined by Western blot. Data are reported as the mean  $\pm$  SEM ( $n=5$ ). \* $p < 0.05$  compared to the control group; † $p < 0.05$  compared to TNF- $\alpha$ -treated group

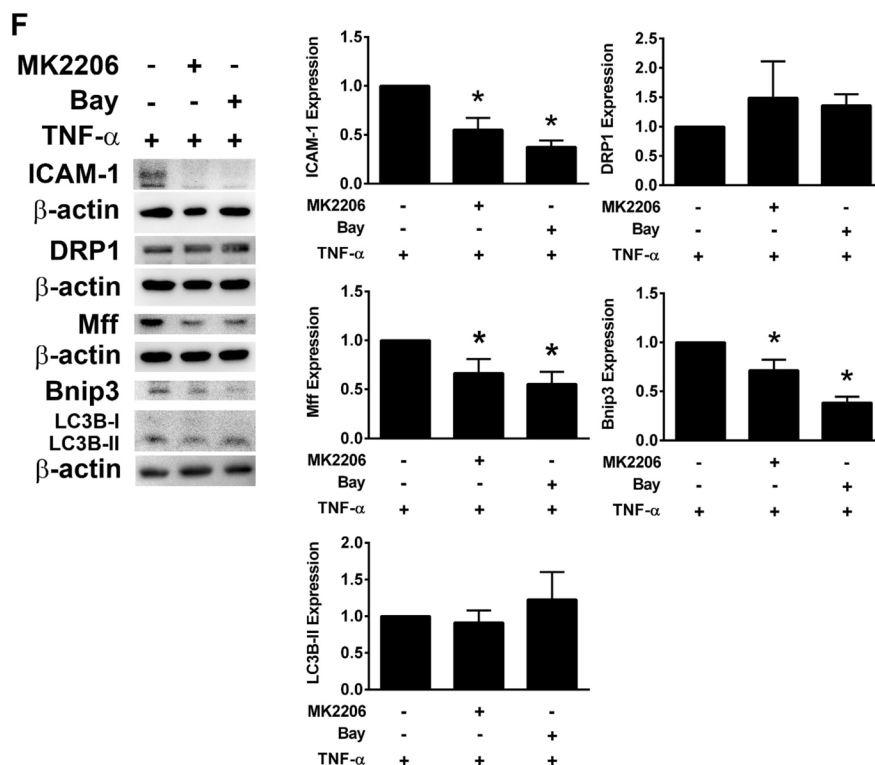


Fig. 6 (continued)

## Discussion

Inflammation is considered a key factor in lung injury that leads to respiratory system failure. Therefore, novel research related to lung injury is urgently needed to generate novel insights into potential lung injury treatments. Our data showed that Vit. D treatment remarkably attenuated ICAM-1 expression and monocyte binding to TNF- $\alpha$ -treated A549 cells. This effect was mediated by inhibiting AKT/NF- $\kappa$ B phosphorylation. Moreover, pretreatment with Vit. D significantly reduced TNF- $\alpha$ -induced mitochondrial fission and mitophagy. Furthermore, Vit. D treatment attenuated ICAM-1 expression, mitochondrial fission and mitophagy in murine lung tissues following TNF- $\alpha$  stimulation. Therefore, the protection of pulmonary epithelial cells by Vit. D is due to the AKT/NF- $\kappa$ B-mediated reduction of ICAM-1 expression, mitochondrial fission and mitophagy.

Vit. D has been found to be an essential nutrient necessary for the optimal absorption of dietary calcium and phosphate. Recently, due to the adverse

effects of vitamin deficiency on health, Vit. D has received more and more attention worldwide. Vit. D deficiency impairs lung function and aggravates hypertension and inflammatory diseases, including COPD, asthma, tuberculosis, acute lung injury and its more severe form, acute respiratory distress syndrome (Andersen et al. 2015; Shi et al. 2016). 1 $\alpha$ ,25-Dihydroxyvitamin D<sub>3</sub> treatment increased mitochondrial volume and mitochondrial oxygen consumption rate, which are likely to influence muscle strength in human skeletal muscle cells (Ryan et al. 2016). In addition, Vit. D extensively modulates both innate and adaptive immune responses and could reduce systemic inflammation in patients. Vit. D reduced inflammatory responses in both endothelial cells and db/db mice exposed to a diabetes-like environment (Einbinder et al. 2016). The addition of 1,25-dihydroxyvitamin D<sub>3</sub> reduced TNF- $\alpha$ -induced inflammation in human chondrocytes (Avcioglu et al. 2020). In this study, TNF- $\alpha$  treatment increased tumor necrosis factor receptor-2 (TNFR2) expression in A549 cells, while Vit. D pretreatment did not affect this

expression (Supplementary Fig. 2). Vit. D treatment reduces the morbidity and mortality of patients with chronic kidney failure and end-stage renal disease by reducing inflammatory mechanisms (Assimon et al. 2012). Our previous studies and other reports demonstrated that the inflammatory cytokines TNF- $\alpha$  and IL-1 $\beta$  increased ICAM-1 expression and monocyte adhesion in human lung epithelial cells and lung tissues (Oh and Kwon 2009; Sung et al. 2015, 2018; Peng et al. 2018). Furthermore, this study shows for the first time to show that Vit. D reduces the ICAM-1 expression in TNF- $\alpha$ -treated A549 cells and mouse lung tissue. In addition, Vit. D inhibits the adhesion of monocytes to A549 cells treated with TNF- $\alpha$ . ICAM-1 is an important regulator of respiratory epithelial cell inflammation (Lee and Yang 2013). Our experiments provide evidence that Vit. D can reduce ICAM-1 expression and monocyte adhesion; therefore Vit. D may be an effective therapeutic agent for lung inflammation.

Cell survival or death is closely tied to mitochondrial function (Reddy 2014). Healthy mitochondria produce ATP which is needed by cells, but damaged mitochondria produce pathological and excessive ROS (Tang et al. 2015). In this study, we demonstrated that TNF- $\alpha$ -treated A549 cells experienced mitochondrial dysfunction, as demonstrated by decreased ATP production and mitochondrial membrane potential, while Vit. D reversed these effects. In order to prohibit cell death and sustain mitochondrial function, harmful mitochondria may enter into degradation and fission. Oxidative stress affects mitochondrial fission (Kroemer et al. 2007) but may also cause excessive mitochondrial fission, leading to the changes of mitochondrial structure and function, and cell damage (Reddy 2014). Using MitoTracker and TEM, we observed shorter mitochondria, indicating upregulation of mitochondrial fission, in TNF- $\alpha$ -treated A549 cells, while Vit. D reduced this change. Mitochondrial fission is regulated by DRP1 and Mff (Westermann 2010). DRP1, a member of the conserved dynamin GTPase superfamily, is necessary for mitochondrial fission (Shen et al. 2018) and is mainly present in the cytosol, however activated DRP1 migrates from the cytosol to the outer mitochondrial membrane, where it interacts with adaptors after external stimulation (Zhou et al. 2019a). It has been suggested that the function of DRP1 is related

to various cellular processes, including autophagy, apoptosis and necrosis (Kim et al. 2018). The activity of DRP1 is controlled by phosphorylation by various kinases at three different sites, including Ser 616, Ser 637 and Ser 693 (van der Bliek et al. 2013). Phosphorylation of Ser616 promotes mitochondrial fission, leading to inflammation and apoptosis (Deng et al. 2020a, 2020b). High levels of DRP1 have been detected in RAW264.7 cells and mouse models of lipopolysaccharide (LPS)-induced acute lung injury (Deng et al. 2020b). TNF- $\alpha$  induces cardiomyocyte death by increasing the level of p-DRP1 Ser616 and mitochondrial translocation (Shen et al. 2018). It is well known that inhibiting DRP1 can prevent mucosal damage (Mazumder et al. 2019). Our data showed that TNF- $\alpha$  treatment upregulated the levels of p-DRP1 and Mff expression, while Vit. D reduced these effects. Importantly, we demonstrated that TNF- $\alpha$ -induced increases in ICAM-1 expression and monocyte adhesion could be reversed by Vit. D or by Mdivi-1, a mitochondrial fission inhibitor. Our study showed that Vit. D can be used as a mitochondrial fission inhibitor to reduce ICAM-1 expression and monocyte adhesion in TNF- $\alpha$ -treated A549 cells. Furthermore, in this study, stimulation with TNF- $\alpha$  increased the levels of mitochondrial fission-related proteins and ICAM-1 in the lung tissues of mice, while Vit. D treatment significantly decreased these levels. The previous study showed that Vit. D deficiency is associated with increased COVID-19 risk via altered mitochondrial dynamics, oxidative stress, and inflammatory states (de Las Heras et al. 2020). Based on the findings and our results, we suggest that the therapeutic effects of vitamin D<sub>3</sub> are mediated through the downregulation of ROS production and the improvement of mitochondrial function.

Healthy mitochondria sustain the mitochondrial life cycle to generate energy and participate in cell signal transduction, while deleterious mitochondria are cleared mainly through the mitochondrial autophagy (mitophagy) pathway, which is a lysosomal catabolic process accompanied by the expression of LC3B and Bnip3 (Yang and Klionsky 2010; Novak 2012). The effects of autophagy on lung inflammation are controversial (Zhang et al. 2019a; Qu et al. 2019; Li et al. 2016, 2019). In our study, TNF- $\alpha$  treatment significantly increased mitophagy by increasing Bnip3 expression. Additionally,



we used AO staining to demonstrate that TNF- $\alpha$  increased autophagolysosome. Furthermore, we used fluorescence microscopy to show that MitoTracker-labeled mitochondria colocalized with Bnip3, indicating the presence of mitophagy in TNF- $\alpha$ -treated A549 cells. Finally, interactions between Bnip3 and LC3B were increased in TNF- $\alpha$ -treated A549 cells. These results indicate that mitophagy is significantly activated by TNF- $\alpha$  stimulation in pulmonary epithelial cells, while Vit. D treatment can attenuate this effect. ROS have been suggested to be involved in the activation of HIF-1 $\alpha$  (Qutub and Popel 2008). It has been reported that the Bnip3 promoter contains a functional hypoxia response element (HRE) and can be activated under hypoxic environment (Chen et al. 2016; Zhang et al. 2019b; Fu et al. 2020). Thus, HIF-1 $\alpha$  activates the downstream protein Bnip3 and induces mitophagy. In our study, the expression of HIF-1 $\alpha$  and Bnip3 was significantly increased in TNF- $\alpha$ -treated A549 cells, while Vit. D reduced this effect. These results indicate that Vit. D attenuates TNF- $\alpha$ -induced HIF-1 $\alpha$  expression and further reduces the occurrence of mitophagy. Interestingly, Vit. D treatment decreased the expression of the mitophagy-related protein Bnip3 but increased the expression of LC3B in A549 cells with or without TNF- $\alpha$  stimulation. Previous study indicated that Vit. D modulates autophagy via VDR by directly upregulating transcription (Hoyer-Hansen et al. 2010). This discrepancy may be caused by VDR-driven transcriptional activation of LC3B under Vit. D treatment (Tavera-Mendoza et al. 2017). Therefore, Vit. D attenuated the mitophagy through the downregulation of Bnip3, while Vit. D sustained the autophagy probably via transcriptional activation of LC3B. In this study, VDR expression was present in A549 cells and 10  $\mu$ M of Vit. D significantly increased VDR expression (Supplementary Fig. 3). Vit. D significantly increased the expression of 25(OH)D 1 $\alpha$ -hydroxylase (CYP27B1, Supplementary Fig. 4). The present study suggested that the function of Vit. D used in the present study may be mediated by the increased VDR expression and converted to 1,25(OH)<sub>2</sub>D<sub>3</sub> via the increased 25(OH)D 1 $\alpha$ -hydroxylase expression. In addition, to comprehend the mechanism of Vit. D effect on TNF- $\alpha$ -induced mitophagy, we also examined another pathway about PINK1-Parkin. TNF- $\alpha$  significantly increased the expression of PINK1 and

Vit. D reduced the effect. However, TNF- $\alpha$  did not affect the expression of Parkin and even with Vit. D pretreatment (Supplementary Fig. 5). The expression of PINK1 and Parkin was not consistent, and further study is needed. Furthermore, the levels of mitophagy-related proteins were also decreased in lung tissues of mice, showing the same trend as in vitro study. In conclusion, our data indicated that the reduction of mitophagy is related to the protective impact of Vit. D on TNF- $\alpha$ -induced lung inflammation.

MAPK, PI3K/AKT and NF- $\kappa$ B pathways play vital roles in regulating the expression of pro-inflammatory cytokines, leading to the occurrence and development of lung inflammation (Lee and Yang 2013; Sung et al. 2015, 2018). In our study, as reported in previous studies, MAPK, AKT and NF- $\kappa$ B were strongly phosphorylated in A549 cells treated with TNF- $\alpha$  (Lee and Yang 2013; Oh and Kwon 2009). It has been reported that Vit. D attenuates inflammatory responses by reducing NF- $\kappa$ B activity (Mousa et al. 2017). Vit. D attenuated the LPS-induced inflammatory response in endothelial cells by inhibiting the PI3K/AKT/NF- $\kappa$ B signaling pathway (Zhou et al. 2019b). However, the detailed protective mechanism of Vit. D has not yet been determined. Our results showed that Vit. D significantly reduced the TNF- $\alpha$ -induced phosphorylation of MAPKs, AKT, and NF- $\kappa$ B. In addition, the TNF- $\alpha$ -induced increase in ICAM-1 expression and monocyte adhesion was markedly suppressed in the presence of inhibitors of either AKT or NF- $\kappa$ B. In addition, there is increasing evidence that the activation of MAPKs, AKT, or NF- $\kappa$ B is involved in mitochondrial fission and mitophagy (Aravamudan et al. 2014; Feng et al. 2018; Mao and Klionsky 2011). In this study, we demonstrated that TNF- $\alpha$  induces mitochondrial fission and mitophagy in A549 cells through the activation of NF- $\kappa$ B, while Vit. D reduces this effect.

Taken together, our current study shows that Vit. D prevents TNF- $\alpha$ -induced inflammation by the regulation of mitochondrial function. Vit. D inhibits TNF- $\alpha$ -induced mitochondrial fission and mitophagy by the inhibition of the expression of DRP1, Mff and Bnip3. This effect is mediated through the AKT/NF- $\kappa$ B pathway. Due to these findings, Vit. D should be considered a new and novel therapeutic agent for the targeting epithelial activation in lung inflammation.

**Supplementary Information** The online version contains supplementary material available at <https://doi.org/10.1007/s10565-021-09629-6>.

**Author contribution** Yuh-Lien Chen, Tzu-Yi Chuang, and Hsin-Ching Sung has full access to all data in the study and are responsible for the integrity of the data and the accuracy of data analysis. Yu-Chen Chen contributed to the research design, conducted experiments, assisted the analysis of samples, and participated in the interpretation of the results and the writing of the manuscript. Tsai-Chun Lai, Tzu-Lin Lee, Chiang-Wen Lee, and I-Ta Lee participated in the discussion of the results.

**Funding** This study was supported, in part, by grants from Chang Gung Memorial Hospital, Taiwan (CMRPD1H0311, CMRPD1J0181), Ministry of Health and Welfare, Executive Yuan, Taiwan (11008), and from the Ministry of Science and Technology of Taiwan (MOST 108–2320-B002-065-MY3).

**Data availability** All the data and materials are available. These are all openly available.

## Declarations

**Ethics approval and consent to participate** All animal procedures described in this study were conducted in accordance with the guidelines for the care and use of laboratory animals approved by National Taiwan University (IACUC: CGU108-33).

**Consent for publication** No personal information is included in this study.

**Conflict of interest** The authors declare no competing interests.

## References

- Andersen LB, Przybyl L, Haase N, von Versen-Hoynck F, Qadri F, Jorgensen JS, Sorensen GL, Fruekilde P, Poglitsch M, Szijarto I, Gollasch M, Peters J, Muller DN, Christesen HT and Dechend R. Vitamin D depletion aggravates hypertension and target-organ damage. *J Am Heart Assoc.* 2015;4(2). <https://doi.org/10.1161/JAHA.114.001417>
- Aravamudan B, Kiel A, Freeman M, Delmotte P, Thompson M, Vassallo R, Sieck GC, Pabelick CM, Prakash YS. Cigarette smoke-induced mitochondrial fragmentation and dysfunction in human airway smooth muscle. *Am J Physiol Lung Cell Mol Physiol.* 2014;306(9):L840–54. <https://doi.org/10.1152/ajplung.00155.2013>.
- Assimon MM, Salenger PV, El-Fawal HA, Mason DL. Nutritional vitamin D supplementation in haemodialysis: a potential vascular benefit? *Nephrology (carlton).* 2012;17(3):237–42. <https://doi.org/10.1111/j.1440-1797.2011.01555.x>.
- Avcioglu G, Ozbeklptec B, Akcan G, Gorgun B, Fidan K, Carhan A, Yilmaz G, Kozaci LD. Effects of 1,25-dihydroxy vitamin D3 on TNF-alpha induced inflammation in human chondrocytes and SW1353 cells: a possible role for toll-like receptors. *Mol Cell Biochem.* 2020;464(1–2):131–42. <https://doi.org/10.1007/s11010-019-03655-z>.
- Babbar N, Casero RA Jr. Tumor necrosis factor- $\alpha$  increases reactive oxygen species by inducing spermine oxidase in human lung epithelial cells: a potential mechanism for inflammation-induced carcinogenesis. *Cancer Res.* 2006;66(23):11125–30. <https://doi.org/10.1158/0008-5472.CAN-06-3174>.
- Bhatti JS, Bhatti GK, Reddy PH. Mitochondrial dysfunction and oxidative stress in metabolic disorders-a step towards mitochondria based therapeutic strategies. *Biochim Biophys Acta Mol Basis Dis.* 2017;1863(5):1066–77. <https://doi.org/10.1016/j.bbadis.2016.11.010>.
- Brito RBO, Rebello JF, Grabulosa CC, Pinto W, Morales A Jr, Elias RM, Moyses RMA, Dalboni MA. 25-vitamin D reduces inflammation in uremic environment. *Sci Rep.* 2020;10(1):128. <https://doi.org/10.1038/s41598-019-56874-1>.
- Cachon BF, Firmin S, Verdin A, Ayi-Fanou L, Billet S, Cazier F, Martin PJ, Aissi F, Courcot D, Sanni A, Shirali P. Pro-inflammatory effects and oxidative stress within human bronchial epithelial cells exposed to atmospheric particulate matter (PM(2.5) and PM(>2.5)) collected from Cotonou. *Benin Environ Pollut.* 2014;185:340–51. <https://doi.org/10.1016/j.envpol.2013.10.026>.
- Cashman KD, van den Heuvel EG, Schoemaker RJ, Preveraud DP, Macdonald HM, Arcot J. 25-Hydroxyvitamin D as a biomarker of vitamin D status and its modeling to inform strategies for prevention of vitamin D deficiency within the population. *Adv Nutr.* 2017;8(6):947–57. <https://doi.org/10.3945/an.117.015578>.
- Chen J, Bai M, Ning C, Xie B, Zhang J, Liao H, Xiong J, Tao X, Yan D, Xi X, Chen X, Yu Y, Bast RC, Zhang Z, Feng Y, Zheng W. Gankyrin facilitates follicle-stimulating hormone-driven ovarian cancer cell proliferation through the PI3K/AKT/HIF-1 $\alpha$ /cyclin D1 pathway. *Oncogene.* 2016;35(19):2506–17. <https://doi.org/10.1038/nc.2015.316>.
- Christakos S, Dhawan P, Verstuyf A, Verlinden L, Carmeliet G. Vitamin D: metabolism, molecular mechanism of action, and pleiotropic effects. *Physiol Rev.* 2016;96(1):365–408. <https://doi.org/10.1152/physrev.00014.2015>.
- de Las Heras N, Martin Gimenez VM, Ferder L, Manucha W and Lahera V. Implications of oxidative stress and potential role of mitochondrial dysfunction in COVID-19: therapeutic effects of vitamin D. *Antioxidants (Basel).* 2020;9(9). <https://doi.org/10.3390/antiox9090897>
- Deng S, Zhang L, Mo Y, Huang Y, Li W, Peng Q, Huang L and Ai Y. Mdivi-1 attenuates lipopolysaccharide-induced acute lung injury by inhibiting MAPKs, oxidative stress and apoptosis. *Pulm Pharmacol Ther.* 2020a;62:101918. <https://doi.org/10.1016/j.pupt.2020.101918>
- Deng X, Liu J, Liu L, Sun X, Huang J, Dong J. Drp1-mediated mitochondrial fission contributes to baicalein-induced apoptosis and autophagy in lung cancer via

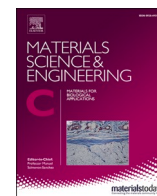
- activation of AMPK signaling pathway. *Int J Biol Sci*. 2020b;16(8):1403–16. <https://doi.org/10.7150/ijbs.41768>.
- Dobnig H, Pilz S, Scharnagl H, Renner W, Seelhorst U, Wellnitz B, Kinkeldei J, Boehm B, Weihrauch G, Maerz W. Independent association of low serum 25-hydroxyvitamin D and 1,25-dihydroxyvitamin D levels with all-cause and cardiovascular mortality. *Arch Intern Med*. 2008;168(12):1340–9. <https://doi.org/10.1001/archinte.168.12.1340>.
- Dusso AS, Brown AJ, Slatopolsky E. Vitamin D. *Am J Physiol Renal Physiol*. 2005;289(1):F8–28. <https://doi.org/10.1152/ajprenal.00336.2004>.
- Einbinder Y, Ohana M, Benchetrit S, Zehavi T, Nacasch N, Bernheim J, Zitman-Gal T. Glucagon-like peptide-1 and vitamin D: anti-inflammatory response in diabetic kidney disease in db/db mice and in cultured endothelial cells. *Diabetes Metab Res Rev*. 2016;32(8):805–15. <https://doi.org/10.1002/dmrr.2801>.
- Feng M, Wang L, Chang S, Yuan P. Penethylidine hydrochloride regulates mitochondrial dynamics and apoptosis through p38MAPK and JNK signal pathways and provides cardioprotection in rats with myocardial ischemia-reperfusion injury. *Eur J Pharm Sci*. 2018;121:243–50. <https://doi.org/10.1016/j.ejps.2018.05.023>.
- Ferri S, Crimi C, Heffler E, Campisi R, Noto A, Crimi N. Vitamin D and disease severity in bronchiectasis. *Respir Med*. 2019;148:1–5. <https://doi.org/10.1016/j.rmed.2019.01.009>.
- Forrester SJ, Kikuchi DS, Hernandez MS, Xu Q, Griendling KK. Reactive oxygen species in metabolic and inflammatory signaling. *Circ Res*. 2018;122(6):877–902. <https://doi.org/10.1161/CIRCRESAHA.117.311401>.
- Fu ZJ, Wang ZY, Xu L, Chen XH, Li XX, Liao WT, Ma HK, Jiang MD, Xu TT, Xu J, Shen Y, Song B, Gao PJ, Han WQ and Zhang W. HIF-1 $\alpha$ -BNIP3-mediated mitophagy in tubular cells protects against renal ischemia/reperfusion injury. *Redox Biol*. 2020;36:101671. <https://doi.org/10.1016/j.redox.2020.101671>.
- Haddad JJ, Land SC. A non-hypoxic, ROS-sensitive pathway mediates TNF- $\alpha$ -dependent regulation of HIF-1 $\alpha$ . *FEBS Lett*. 2001;505(2):269–74. [https://doi.org/10.1016/s0014-5793\(01\)02833-2](https://doi.org/10.1016/s0014-5793(01)02833-2).
- Harris J, Deen N, Zamani S, Hasnat MA. Mitophagy and the release of inflammatory cytokines. *Mitochondrion*. 2018;41:2–8. <https://doi.org/10.1016/j.mito.2017.10.009>.
- Hoyer-Hansen M, Nordbrandt SP, Jaattela M. Autophagy as a basis for the health-promoting effects of vitamin D. *Trends Mol Med*. 2010;16(7):295–302. <https://doi.org/10.1016/j.molmed.2010.04.005>.
- Hutchinson K, Kerley CP, Faul J, Grealley P, Coghlan D, Louw M, Elnazir B, Rochev Y. Vitamin D receptor variants and uncontrolled asthma. *Eur Ann Allergy Clin Immunol*. 2018;50(3):108–16. <https://doi.org/10.23822/EurAnnACI.1764-1489.46>.
- Kim H, Hwang J, Woo C, Kim E, Kim T, Cho K, Seo J, Lee S, Kim J. TNF- $\alpha$ -induced up-regulation of intercellular adhesion molecule-1 is regulated by a Rac-ROS-dependent cascade in human airway epithelial cells. *Exp Mol Med*. 2008;40(2):167–75. <https://doi.org/10.3858/emmm.2008.40.2.167>.
- Kim SR, Kim DI, Kim SH, Lee H, Lee KS, Cho SH and Lee YC. NLRP3 Inflammasome activation by mitochondrial ROS in bronchial epithelial cells is required for allergic inflammation. *Cell Death Dis*. 2014;5:e1498. <https://doi.org/10.1038/cddis.2014.460>.
- Kim YY, Yun SH, Yun J. Downregulation of Drp1, a fission regulator, is associated with human lung and colon cancers. *Acta Biochim Biophys Sin (shanghai)*. 2018;50(2):209–15. <https://doi.org/10.1093/abbs/gmx137>.
- Kroemer G, Galluzzi L, Brenner C. Mitochondrial membrane permeabilization in cell death. *Physiol Rev*. 2007;87(1):99–163. <https://doi.org/10.1152/physrev.00013.2006>.
- Lee IT, Yang CM. Inflammatory signalings involved in airway and pulmonary diseases. *Mediators Inflamm*. 2013;2013:791231. <https://doi.org/10.1155/2013/791231>.
- Li G, Li Y, Zheng SF, Han YB, Bai QL, Zhao T. Autophagy in pulmonary macrophages mediates lung inflammatory injury via c-Src tyrosine kinase pathway activation during mechanical ventilation. *Eur Rev Med Pharmacol Sci*. 2019;23(4):1674–80.
- Li Y, Yu G, Yuan S, Tan C, Xie J, Ding Y, Lian P, Fu L, Hou Q, Xu B, Wang H. 14,15-Epoxyeicosatrienoic acid suppresses cigarette smoke condensate-induced inflammation in lung epithelial cells by inhibiting autophagy. *Am J Physiol Lung Cell Mol Physiol*. 2016;311(5):L970–80. <https://doi.org/10.1152/ajplung.00161.2016>.
- Liu CW, Lee TL, Chen YC, Liang CJ, Wang SH, Lue JH, Tsai JS, Lee SW, Chen SH, Yang YF, Chuang TY and Chen YL. PM<sub>2.5</sub>-induced oxidative stress increases intercellular adhesion molecule-1 expression in lung epithelial cells through the IL-6/AKT/STAT3/NF- $\kappa$ B-dependent pathway. *Part Fibre Toxicol*. 2018;15(1):4. <https://doi.org/10.1186/s12989-018-0240-x>.
- Mao K, Klionsky DJ. MAPKs regulate mitophagy in *Saccharomyces cerevisiae*. *Autophagy*. 2011;7(12):1564–5. <https://doi.org/10.4161/auto.7.12.17971>.
- Mauthe M, Orhon I, Rocchi C, Zhou X, Luhr M, Hijlkema KJ, Coppes RP, Engedal N, Mari M, Reggiori F. Chloroquine inhibits autophagic flux by decreasing autophagosome-lysosome fusion. *Autophagy*. 2018;14(8):1435–55. <https://doi.org/10.1080/15548627.2018.1474314>.
- Mauvezin C, Neufeld TP. Bafilomycin A1 disrupts autophagic flux by inhibiting both V-ATPase-dependent acidification and Ca-P60A/SERCA-dependent autophagosome-lysosome fusion. *Autophagy*. 2015;11(8):1437–8. <https://doi.org/10.1080/15548627.2015.1066957>.
- Mazumder S, De R, Debsharma S, Bindu S, Maity P, Sarkar S, Saha SJ, Siddiqui AA, Banerjee C, Nag S, Saha D, Pramanik S, Mitra K, Bandyopadhyay U. Indomethacin impairs mitochondrial dynamics by activating the PKC $\zeta$ -p38-DRP1 pathway and inducing apoptosis in gastric cancer and normal mucosal cells. *J Biol Chem*. 2019;294(20):8238–58. <https://doi.org/10.1074/jbc.RA118.004415>.
- Moldoveanu B, Otmishi P, Jani P, Walker J, Sarmiento X, Guardiola J, Saad M, Yu J. Inflammatory mechanisms in the lung. *J Inflamm Res*. 2009;2:1–11.
- Mousa A, Naderpoor N, Johnson J, Sourris K, de Courten MPI, Wilson K, Scragg R, Plebanski M, de Courten

- B. Effect of vitamin D supplementation on inflammation and nuclear factor kappa-B activity in overweight/obese adults: a randomized placebo-controlled trial. *Sci Rep.* 2017;7(1):15154. <https://doi.org/10.1038/s41598-017-15264-1>.
- Naeini AE, Moieinzadeh F, Vahdat S, Ahmadi A, Hedayati ZP, Shahzeidi S. The effect of vitamin D administration on intracellular adhesion molecule-1 and vascular cell adhesion molecule-1 levels in hemodialysis patients: a placebo-controlled, double-blinded clinical trial. *J Res Pharm Pract.* 2017;6(1):16–20. <https://doi.org/10.4103/2279-042X.200994>.
- Ng Kee Kwong F, Nicholson AG, Harrison CL, Hansbro PM, Adcock IM and Chung KF. Is mitochondrial dysfunction a driving mechanism linking COPD to nonsmall cell lung carcinoma? *Eur Respir Rev.* 2017;26(146). <https://doi.org/10.1183/16000617.0040-2017>
- Novak I. Mitophagy: a complex mechanism of mitochondrial removal. *Antioxidants & Redox Signaling.* 2012;17(5):794–802. <https://doi.org/10.1089/ars.2011.4407>.
- Oh JH, Kwon TK. Withaferin A inhibits tumor necrosis factor- $\alpha$ -induced expression of cell adhesion molecules by inactivation of Akt and NF- $\kappa$ B in human pulmonary epithelial cells. *Int Immunopharmacol.* 2009;9(5):614–9. <https://doi.org/10.1016/j.intimp.2009.02.002>.
- Park J, Choi H, Min JS, Park SJ, Kim JH, Park HJ, Kim B, Chae JI, Yim M, Lee DS. Mitochondrial dynamics modulate the expression of pro-inflammatory mediators in microglial cells. *J Neurochem.* 2013;127(2):221–32. <https://doi.org/10.1111/jnc.12361>.
- Peng HL, Huang WC, Cheng SC, Liou CJ. Fisetin inhibits the generation of inflammatory mediators in interleukin-1 $\beta$ -induced human lung epithelial cells by suppressing the NF- $\kappa$ B and ERK1/2 pathways. *Int Immunopharmacol.* 2018;60:202–10. <https://doi.org/10.1016/j.intimp.2018.05.004>.
- Qu L, Chen C, He W, Chen Y, Li Y, Wen Y, Zhou S, Jiang Y, Yang X, Zhang R, Shen L. Glycyrrhizic acid ameliorates LPS-induced acute lung injury by regulating autophagy through the PI3K/AKT/mTOR pathway. *Am J Transl Res.* 2019;11(4):2042–55.
- Qutub AA, Popel AS. Reactive oxygen species regulate hypoxia-inducible factor 1 $\alpha$  differentially in cancer and ischemia. *Mol Cell Biol.* 2008;28(16):5106–19. <https://doi.org/10.1128/MCB.00060-08>.
- Ravikumar B, Sarkar S, Davies JE, Futter M, Garcia-Arencibia M, Green-Thompson ZW, Jimenez-Sanchez M, Korolchuk VI, Lichtenberg M, Luo S, Massey DC, Menzies FM, Moreau K, Narayanan U, Renna M, Siddiqi FH, Underwood BR, Winslow AR, Rubinshtein DC. Regulation of mammalian autophagy in physiology and pathophysiology. *Physiol Rev.* 2010;90(4):1383–435. <https://doi.org/10.1152/physrev.00030.2009>.
- Reddy PH. Inhibitors of mitochondrial fission as a therapeutic strategy for diseases with oxidative stress and mitochondrial dysfunction. *J Alzheimers Dis.* 2014;40(2):245–56. <https://doi.org/10.3233/JAD-132060>.
- Roebuck KA, Finnegan A. Regulation of intercellular adhesion molecule-1 (CD54) gene expression. *J Leukoc Biol.* 1999;66(6):876–88.
- Ryan ZC, Craig TA, Folmes CD, Wang X, Lanza IR, Schaible NS, Salisbury JL, Nair KS, Terzic A, Sieck GC, Kumar R. 1 $\alpha$ ,25-Dihydroxyvitamin D3 regulates mitochondrial oxygen consumption and dynamics in human skeletal muscle cells. *J Biol Chem.* 2016;291(3):1514–28. <https://doi.org/10.1074/jbc.M115.684399>.
- Scherer PM, Chen DL. Imaging pulmonary inflammation. *J Nucl Med.* 2016;57(11):1764–70. <https://doi.org/10.2967/jnumed.115.157438>.
- Scott I, Youle RJ. Mitochondrial fission and fusion. *Essays Biochem.* 2010;47:85–98. <https://doi.org/10.1042/bse0470085>.
- Semenza GL. Oxygen sensing, hypoxia-inducible factors, and disease pathophysiology. *Annu Rev Pathol.* 2014;9:47–71. <https://doi.org/10.1146/annurev-pathol-012513-104720>.
- Shen YL, Shi YZ, Chen GG, Wang LL, Zheng MZ, Jin HF, Chen YY. TNF- $\alpha$  induces Drp1-mediated mitochondrial fragmentation during inflammatory cardiomyocyte injury. *Int J Mol Med.* 2018;41(4):2317–27. <https://doi.org/10.3892/ijmm.2018.3385>.
- Shi YY, Liu TJ, Fu JH, Xu W, Wu LL, Hou AN, Xue XD. Vitamin D/VDR signaling attenuates lipopolysaccharide-induced acute lung injury by maintaining the integrity of the pulmonary epithelial barrier. *Mol Med Rep.* 2016;13(2):1186–94. <https://doi.org/10.3892/mmr.2015.4685>.
- Sung HC, Liang CJ, Lee CW, Yen FL, Hsiao CY, Wang SH, Jiang-Shieh YF, Tsai JS, Chen YL. The protective effect of eupafolin against TNF- $\alpha$ -induced lung inflammation via the reduction of intercellular cell adhesion molecule-1 expression. *J Ethnopharmacol.* 2015;170:136–47. <https://doi.org/10.1016/j.jep.2015.04.058>.
- Sung HC, Liu CW, Hsiao CY, Lin SR, Yu IS, Lin SW, Chiang MH, Liang CJ, Pu CM, Chen YC, Lin MS, Chen YL. The effects of wild bitter melon fruit extracts on ICAM-1 expression in pulmonary epithelial cells of C57BL/6J mice and MicroRNA-221/222 knockout mice: involvement of the MiR-221/-222/PI3K/AKT/NF- $\kappa$ B pathway. *Phytomedicine.* 2018;42:90–9. <https://doi.org/10.1016/j.phymed.2018.03.023>.
- Tang Y, Liu J, Long J. Phosphatase and tensin homolog-induced putative kinase 1 and Parkin in diabetic heart: role of mitophagy. *J Diabetes Investig.* 2015;6(3):250–5. <https://doi.org/10.1111/jdi.12302>.
- Tavera-Mendoza LE, Westerling T, Libby E, Marusyk A, Cato L, Cassani R, Cameron LA, Ficarro SB, Marto JA, Klawitter J, Brown M. Vitamin D receptor regulates autophagy in the normal mammary gland and in luminal breast cancer cells. *Proc Natl Acad Sci U S A.* 2017;114(11):E2186–94. <https://doi.org/10.1073/pnas.1615015114>.
- van der Bliek AM, Shen Q and Kawajiri S. Mechanisms of mitochondrial fission and fusion. *Cold Spring Harb Perspect Biol.* 2013;5(6). <https://doi.org/10.1101/cshperspect.a011072>
- Westermann B. Mitochondrial fusion and fission in cell life and death. *Nat Rev Mol Cell Biol.* 2010;11(12):872–84. <https://doi.org/10.1038/nrm3013>.
- Yang Z, Klionsky DJ. Mammalian autophagy: core molecular machinery and signaling regulation. *Curr Opin Cell Biol.* 2010;22(2):124–31. <https://doi.org/10.1016/j.ceb.2009.11.014>.

- Zhang L, Huang J, Dong R, Feng Y, Zhou M. Therapeutic potential of BLT1 antagonist for COPD: involvement of inducing autophagy and ameliorating inflammation. *Drug Des Devel Ther.* 2019a;13:3105–16. <https://doi.org/10.2147/DDDT.S215433>.
- Zhang Y, Liu D, Hu H, Zhang P, Xie R, Cui W. HIF-1 $\alpha$ /BNIP3 signaling pathway-induced-autophagy plays protective role during myocardial ischemia-reperfusion injury. *Biomed Pharmacother.* 2019b;120: 109464. <https://doi.org/10.1016/j.biopha.2019.109464>.
- Zhou K, Wu J, Chen J, Zhou Y, Chen X, Wu Q, Xu Y, Tu W, Lou X, Yang G, Jiang S. Schaftoside ameliorates oxygen glucose deprivation-induced inflammation associated with the TLR4/Myd88/Drp1-related mitochondrial fission in BV2 microglia cells. *J Pharmacol Sci.* 2019a;139(1):15–22. <https://doi.org/10.1016/j.jphs.2018.10.012>.
- Zhou W, Yuan G, Wang Q. Vitamin D attenuates lipopolysaccharide-induced inflammatory response in endothelial cells through inhibition of PI3K/Akt/NF-kappaB signaling pathway. *Pharmazie.* 2019b;74(7):412–7. <https://doi.org/10.1691/ph.2019.9373>.

**Publisher's note** Springer Nature remains neutral with regard to jurisdictional claims in published maps and institutional affiliations.





# Magnetic and GRPR-targeted reduced graphene oxide/doxorubicin nanocomposite for dual-targeted chemo-photothermal cancer therapy

Banendu Sunder Dash<sup>a</sup>, Yu-Jen Lu<sup>b,c</sup>, Huai-An Chen<sup>a</sup>, Chi-Cheng Chuang<sup>b,c</sup>,  
Jyh-Ping Chen<sup>a,d,e,f,\*</sup>

<sup>a</sup> Department of Chemical and Materials Engineering, Chang Gung University, Kwei-San, Taoyuan 33302, Taiwan

<sup>b</sup> Department of Neurosurgery, Chang Gung Memorial Hospital, Linkou, Kwei-San, Taoyuan 33305, Taiwan

<sup>c</sup> College of Medicine, Chang Gung University, Kwei-San, Taoyuan 33302, Taiwan

<sup>d</sup> Department of Plastic and Reconstructive Surgery and Craniofacial Research Center, Chang Gung Memorial Hospital, Linkou, Kwei-San, Taoyuan 33305, Taiwan

<sup>e</sup> Research Center for Food and Cosmetic Safety, Research Center for Chinese Herbal Medicine, College of Human Ecology, Chang Gung University of Science and Technology, Taoyuan 33302, Taiwan

<sup>f</sup> Department of Materials Engineering, Ming Chi University of Technology, Tai-Shan, New Taipei City 24301, Taiwan

## ARTICLE INFO

### Keywords:

Reduced graphene oxide  
Magnetic nanoparticles  
Nanomedicine  
Drug delivery  
Chemotherapy  
Photothermal therapy

## ABSTRACT

Herein, we design a rGO-based magnetic nanocomposite by decorating rGO with citrate-coated magnetic nanoparticles (CMNP). The magnetic rGO (mrGO) was modified by phospholipid-polyethylene glycol to prepare PEGylated mrGO, for conjugating with gastrin-releasing peptide receptor (GRPR)-binding peptide (mrGOG). The anticancer drug doxorubicin (DOX) was bound to mrGO (mrGOG) by  $\pi$ - $\pi$  stacking for drug delivery triggered by the low pH value in the endosome. The mrGOG showed enhanced photothermal effect under NIR irradiation, endorsing its role for dual targeted DOX delivery. With efficient DOX release in the endosomal environment and heat generation from light absorption in the NIR range, mrGOG/DOX could be used for combination chemo-photothermal therapy after intracellular uptake by cancer cells. We characterized the physico-chemical as well as biological properties of the synthesized nanocomposites. The mrGOG is stable in biological buffer solution, showing high biocompatibility and minimum hemolytic properties. Using U87 glioblastoma cells, we confirmed the magnetic drug targeting effect in vitro for selective cancer cell killing. The peptide ligand-mediated targeted delivery increases the efficiency of intracellular uptake of both nanocomposite and DOX up to  $\sim 3$  times due to the over-expressed GRPR on U87 surface, leading to higher cytotoxicity. The increased cytotoxicity using mrGOG over mrGO was shown from a decreased  $IC_{50}$  value (0.70 to 0.48  $\mu\text{g/mL}$ ) and an increased cell apoptosis rate (19.8% to 47.1%). The  $IC_{50}$  and apoptosis rate changed further to 0.19  $\mu\text{g/mL}$  and 76.8% in combination with NIR laser irradiation, with the photothermal effect supported from upregulation of heat shock protein HSP70 expression. Using U87 tumor xenograft model created in nude mice, we demonstrated that magnetic guidance after intravenous delivery of mrGOG/DOX could significantly reduce tumor size and prolong animal survival over free DOX and non-magnetic guided groups. Augmented with NIR laser treatment for 5 min, the anti-cancer efficacy significantly improves with elevated cell apoptosis and reduced cell proliferation. Together with safety profiles from hematological as well as major organ histological analysis of treated animals, the mrGOG nanocomposite is an effective nanomaterial for combination chemo-photothermal cancer therapy.

## 1. Introduction

Cancer is causing serious damage to human society and taking many lives everyday worldwide [1]. Nowadays, many cancer treatment modalities exist, such as chemotherapy, photothermal therapy and

radiation therapy [2]. To reduce associated side effects from these treatments, targeted therapy using nanomaterials carrying therapeutics could elicit higher cytotoxic effects [3]. Nonetheless, passive targeting with the enhanced permeability and retention (EPR) effect is less effective than ligand-mediated active targeting [4]. For active targeting,

\* Corresponding author at: Department of Chemical and Materials Engineering, Chang Gung University, Kwei-San, Taoyuan 33302, Taiwan.

E-mail address: [jpchen@mail.cgu.edu.tw](mailto:jpchen@mail.cgu.edu.tw) (J.-P. Chen).

<https://doi.org/10.1016/j.msec.2021.112311>

Received 13 April 2021; Received in revised form 17 June 2021; Accepted 4 July 2021

Available online 14 July 2021

0928-4931/© 2021 Elsevier B.V. All rights reserved.

ligands such as hyaluronic acid, folic acid, antibodies, peptides, which have high affinity toward a specific receptor molecule over-expressed on cancer cell surface, could be used [5–7]. Alternatively, magnetic targeting using a superparamagnetic nanomaterial guided under an external magnetic field could complement active targeting to offer dual targeted drug delivery for better therapeutic outcomes with fewer side effects [8].

The gastrin-releasing peptide (GRP) is a mammalian homolog of the peptide bombesin, a peptide with 14 amino acid residues isolated from the skin of frog [9]. Both GRP and bombesin exhibit binding affinity to gastrin-releasing peptide receptor (GRPR) [10] with a common amino acid sequence in the C-terminal region [11]. Evidence suggested that bombesin-like peptides and GRP are associated with development of many types of cancer due to their role as a growth factor [12,13]. The overexpression of GRPR has been reported in many tumors found in human, including high level expression of GRPR in glioblastoma cell lines [14]. The GRPR antagonists are good anticancer candidate compounds, which have shown impressive antitumor activity [15]. Nonetheless, with abundant expression on cancer cell surface, GRPR is also considered as an idea molecular target for targeted delivery of anticancer therapeutics [16,17]. Indeed, GRPR-targeted copolymers showed good active targeting of and internalization by the GRPR-overexpressing cancer cells [18]. For glioblastoma treatment, GRPR is a good therapeutic target with 100% of glioma samples being GRPR-positive while GRPR-positive cells are not detected in normal brain tissue [19]. Nonetheless, almost all studies used GRPR as a therapeutic target aims at inhibiting growth of human glioblastoma, such as interfering RNA (RNAi) for GRPR knockdown [20], a GRPR antagonist [21], and a GRPR antagonist combined with chemotherapeutic temozolomide [22]. Few studies used GRPR-binding peptide for targeted cancer therapy in glioblastoma treatment [23].

The photothermal therapy involves local temperature rise mediated by a photothermal agent upon exposure to an electromagnetic radiation. By converting energy from light into heat, a photothermal agent can induce death of cancer cells upon near infrared (NIR) laser irradiation for effective cancer treatment [24]. Many nanomaterials are effective photothermal agents, leading to cancer cell apoptosis/necrosis upon local hyperthermia induced by NIR light [25]. Combining photothermal therapy with chemotherapy has attracted attention recently by taking advantage of the synergistic effects from both modalities [26]. Specifically, gold (Au) nanostructure and doxorubicin (DOX) are the mostly widely used combination for chemo-photothermal therapy, with Au nanorod used as a photothermal agent whereas DOX employed as an anticancer drug [27]. Undoubtedly, the combination chemo-photothermal therapy will be more effective if a chemo drug-loaded photothermal agent could be guided to the tumor area for alleviating side effects from damage to normal cells [28].

Graphene-based carbon nanomaterials, like graphene oxide (GO) and reduced graphene oxide (rGO), are good candidates for delivery of chemotherapeutic drugs due to good biocompatibility and high water dispersibility [29,30]. Their tunable surface functionalization ability and high surface area for loading high amount of hydrophobic anticancer drugs via  $\pi$ - $\pi$  interaction; have empowered their application in cancer nanomedicine. Their pH-responsive drug release behavior also facilitates drug release in the low pH environment encountered in the endosomes after intracellular uptake. On the other hand, graphene-based nanomaterials are good photothermal agents for cancer treatment as well. Although GO is a promising nanomaterial for chemo-photothermal applications with good photothermal conversion efficiency and high drug loading [31,32], rGO offers even stronger photothermal effect in the NIR-I (700–950 nm) range in addition to provides better drug release efficiency, compared to GO [33,34]. Indeed, rGO functionalized by non-covalent PEGylation can improve colloidal stability as well as enhance NIR absorption over PEGylated GO [35]. With its unique properties, rGO was used not only as a drug carrier but also as a photothermal agent for cancer treatment in vitro and in vivo [36].

On the other hand, iron oxide magnetic nanoparticles could be synthesized by various methods such as co-precipitation, sol-gel synthesis, pyrolysis or sonochemical synthesis with different particle size and shape as well as surface chemistry and size distribution [37]. These nanoparticles find many biomedical application, such as a magnetic resonance imaging (MRI) contrast agent, in drug delivery and hyperthermia [38]. The magnetically separable properties of  $\text{Fe}_3\text{O}_4$ -containing composites make the development of reusable magnetic catalysts with high stability possible [39,40]. Specifically, by combination of GO with  $\text{Fe}_3\text{O}_4$ , magnetic GO could be used for enzymatic hydrolysis [41], degradation of antibiotics [42], or synthesis of indazolophthalazine-triones [43]. For biomedical applications, magnetic nanocomposites with  $\text{Fe}_3\text{O}_4$  with a strong magnetic moment could be synthesized for magnetic drug delivery to enhance the imaging-guided delivery and the therapeutic action in cancer therapy [44]. To enhance the functionality of GO, iron oxide nanoparticles could be combined with GO for therapeutic applications in MRI and drug delivery [45]. Other than MRI, the iron oxide functionalized GO nanocomposites could be used in magnetically targeted drug delivery and photothermal therapy [46,47]. By anchoring iron oxide to rGO nanosheets, a rGO/ $\text{Fe}_3\text{O}_4$  nanocomposite showed efficient tumor targeting as well as with multimodality imaging capability [48]. Recently, superparamagnetic rGO- $\text{Fe}_3\text{O}_4$  nanocomposite that can be guided by external magnetic fields was used as a drug carrier or targeted drug delivery [49].

In this study, we intend to design a rGO-based magnetic nanocomposite for combination chemo-photothermal cancer therapy. Using overexpressed GRPR on U87 human glioblastoma cells, we decorated rGO with bombesin-like GRPR-binding peptide together with magnetic nanoparticles, followed by DOX loading for dual-targeted drug delivery. After efficient intracellular uptake of the nanocomposites and pH-responsive drug release in the endosomes, concurrent NIR laser irradiation could induce cancer cell hyperthermia and elicit cell death. This nanocomposite for glioblastoma chemo-photothermal therapy was studied in vitro and in vivo with U87 tumor xenografts.

## 2. Materials and methods

### 2.1. Materials

The GO was purchased from Angstrom Materials. Branched polyethyleneimine (PEI, molecular weight = 25,000 Da), N-hydroxysuccinimide (NHS), 1-ethyl-3-(3-dimethylaminopropyl) carbodiimide (EDC) and L-cysteine were obtained from Sigma-Aldrich. Fe (III) chloride hexahydrate and Fe(II) chloride tetrahydrate were acquired from Acros Organics. 1,2-distearoyl-sn-glycero-3-phosphoethanolamine-N-[maleimide (polyethylene glycol)-2000] ammonium salt (DSPE-PEG<sub>2000</sub>-MAL) was provide by NOF Co. and bombesin-like GRPR-binding peptide with the amino acid sequence (Cys-Gly-Gly-Asn-Gln-Trp-Ala-Val-Gly-His-Leu-Met-NH<sub>2</sub>) was synthesized by Yao-Hong Biotechnology Inc. Pierce Immobilized TCEP Disulfide Reducing Gel and doxorubicin (HCl salt) were obtained from Thermo Fisher Scientific and LC Laboratories, respectively. The U87 human primary glioblastoma cell line modified with firefly luciferase gene was used in the study. For cell culture, the Dulbecco's Modified Eagle's Medium (DMEM) medium was used after supplemented with 10% fetal bovine serum (Thermo Fisher Scientific).

### 2.2. Synthesis of rGO by reduction/modification with polyethyleneimine (PEI)

Forty milliliter aqueous dispersion of GO (0.2 mg/mL) was mixed with 40 mL of PEI (0.5%) and heated to 80 °C for 2 h, with constant stirring under nitrogen atmosphere. The PEI reduced and modified GO through nucleophilic substitution reaction after changing brown-colored GO solution to black-colored rGO solution. After centrifugation at 30,000g to remove unreacted PEI, rGO was dispersed in deionized

(DI) water and stored at room temperature.

### 2.3. Synthesis of citric acid-coated magnetic nanoparticles (CMNP)

Following previous reports, we used co-precipitation method to synthesize citric acid-coated magnetic nanoparticles (CMNP), with some modification [50,51]. A three-necked flat bottom flask was filled with 2.15 g  $\text{FeCl}_3 \cdot 6\text{H}_2\text{O}$  and 0.79 g  $\text{FeCl}_2 \cdot 0.4 \text{H}_2\text{O}$  in 100 mL  $\text{H}_2\text{O}$ . After purging with nitrogen for 10 min, 5 mL of 25–30%  $\text{NH}_4\text{OH}$  solution and 50 mL of citric acid (5 mg/mL) were added for reaction at 90 °C. After stirring at 500 rpm using an overhead stirrer for 30 min under nitrogen atmosphere, the solution was cooled to room temperature to recover CMNP by magnetic separation. After washing twice with 50% acetone, CMNP was purified by ultrafiltration and dialysis for storage at 4 °C.

### 2.4. Preparation of magnetic reduced graphene oxide (mrGO)

The carbodiimide-catalyzed covalent bond formation between CMNP and rGO was used for preparation of mrGO. After mixing 10 mL of rGO solution (0.5 mg/mL) with 10 mL of CMNP solution (1 mg/mL), we added 30 mg of NHS and 30 mg of EDC for overnight reaction at room temperature by stirring at 500 rpm. The mrGO was purified by magnetic decantation and dialysis with a 12–14 kD dialysis tube against DI water for storage in DI water at 4 °C.

### 2.5. Preparation of GRPR-binding peptide conjugated magnetic reduced graphene oxide (mrGOG)

To conjugate GRPR-binding peptide to mrGO, we used maleimide groups associated with mrGO to react specifically with thiol groups in the peptide via thiol–maleimide “click” chemistry. To introduce maleimide groups together with polyethylene glycol (PEG) as a spacer, we mixed mrGO with DSPE-PEG<sub>2000</sub>-MAL at 2:1 mass ratio and sonicated the solution for 30 min to attach the DSPE moiety in DSPE-PEG<sub>2000</sub>-MAL to mrGO surface by physical absorption. After recovery by centrifugation, PEGylated mrGO was dispersed in water for conjugation with –SH group in cysteine residue in the peptide. To reduce possible disulfide bonds formed between peptide molecules, 750  $\mu\text{L}$  Immobilized TCEP Disulfide Reducing Resin was reacted with an equal volume of peptide (2 mg/mL) for 1 h at 4 °C and recovered by centrifugation. The GRPR-binding peptide containing a single -SH end group was recovered in the supernatant and reacted with maleimide-containing PEGylated mrGO prepared above at 1:5 mass ratio for 1 h at 4 °C. After magnetic separation, we added Immobilized TCEP Disulfide Reducing Resin-treated L-cysteine (100:1 mass ratio) to block any unreacted maleimide groups. The final GRPR-binding peptide conjugated mrGO (mrGOG) was recovered by centrifugation and stored in phosphate buffered saline (PBS) for drug loading.

### 2.6. Physical and chemical properties characterization

Transmission electron microscopy (TEM, JEOL JEM-2000EII) was used for characterization of particle morphology. Dynamic light scattering (DLS, Zetasizer Nano ZS 90) was used for measurement of particle size. A Bruker D2 PHASER X-ray diffractometer was used for X-ray diffraction (XRD) analysis with a  $\text{Cu-K}\alpha$  X-ray source ( $\lambda = 1.5406 \text{ \AA}$ ) from 10° to 70°. For Fourier transformed infrared (FTIR) spectroscopy analysis, a Bruker Tensor 27 spectrophotometer was used after blending sample with KBr. Raman spectroscopy was carried out with a Raman spectrometer (UniDRON, UniNanoTech) with 532 nm wavelength at 25 mW laser energy. For thermogravimetric analysis (TGA), we used TGA Q50 from TA Instruments with a platinum pan. For analysis of superparamagnetic properties, we used superconducting quantum interference device (SQUID, Quantum Design MPMS-3) from 0 to 300 K at 100 Oe. For quantification of iron oxide from the Fe content, we used a Varian 710-ES inductively coupled plasma optical emission

spectrometer (ICP-OES) after digesting CMNP with 36.5% HCl.

### 2.7. Loading and release of DOX

To load DOX to mrGOG by  $\pi$ - $\pi$  interaction, we mixed 0.1 mg mrGOG with DOX in 1 mL of PBS (pH 7.4) and mixed the solution at 100 rpm for 24 h at 4 °C. By separating mrGOG/DOX with centrifugation, the concentration of DOX in the supernatant was determined from solution absorbance at 490 nm. The loading efficiency (LE) and loading content (LC) were calculated from Eqs. (1) and (2).

$$\text{Loading efficiency (\%)} = \frac{\text{Weight of loaded DOX (mg)}}{\text{Total weight of DOX (mg)}} \times 100 \quad (1)$$

$$\text{Loading content} = \frac{\text{Weight of loaded DOX (mg)}}{\text{Total weight of mrGOG (mg)}} \quad (2)$$

To study pH-dependent drug release, mrGOG/DOX solution was prepared in 1 mL pH 7.4 or pH 5 PBS and shaken at 100 rpm at 37 °C in dark. At pre-determined time, the concentration of released DOX was obtained from solution absorbance using an UV-VIS spectrometer at 490 nm, after centrifugation to recover mrGOG/DOX in the precipitate. By re-suspending the precipitate in pH 7.4 or pH 5 PBS, the drug release experiment continued. We calculated the cumulative drug release from Eq. (3) by adding the total amount of drug released up to a certain time.

$$\text{Cumulative drug release (\%)} = \frac{\text{Weight of released DOX (mg)}}{\text{Weight of loaded DOX (mg)}} \times 100 \quad (3)$$

### 2.8. Laser induced heating effect in vitro

We placed 100  $\mu\text{L}$  of GO, rGO, mrGO or mrGOG solution (0.5 mg/mL) prepared with DI water in an Eppendorf tube, followed by irradiating the tube with 808 nm NIR laser (Shanghai Dream Lasers Technology) from the top at 1.5  $\text{W}/\text{cm}^2$ . From side of a tube, we used a Thermo GEAR G100EX infrared camera (Nippon Avionics) to acquire thermal images at different times and plotted time-lapsed peak temperature profiles.

### 2.9. In vitro studies

#### 2.9.1. Intracellular uptake (confocal microscopy)

After seeding  $2 \times 10^4$  U87 cells on a confocal cell imaging  $\mu$ -dish (ibidi polymer coverslip), we added 5(6)-carboxyfluorescein N-hydroxysuccinimide (fluorescein-NHS)-labelled mrGO (or mrGOG) and incubated for 24 h to study intracellular uptake. The cell nuclei were labelled with Hoechst 33342 (1  $\mu\text{g}/\text{mL}$ ) to show blue fluorescence. To block GRPR on U87 surface, excess GRPR-binding peptide (10 folds) was added before adding mrGOG. After fixing with paraformaldehyde and Triton X-100, cells were observed under a Zeiss LSM Meta confocal laser scanning microscope at 405 nm/460 nm excitation/emission wavelengths for blue fluorescence and 495 nm/520 nm excitation/emission wavelengths for green fluorescence. To visualize DOX and mrGOG after intracellular uptake, DOX-loaded fluorescein-labelled mrGOG was used. The red fluorescence of DOX was observed at 488 nm/560 nm excitation/emission wavelengths.

#### 2.9.2. Intracellular uptake and cell apoptosis (flow cytometry)

For quantitative analysis of intracellular nanocomposite uptake efficiency, we seeded  $3 \times 10^5$  U87 cells in a T25 flask and added fluorescein-labelled mrGO (or mrGOG) to 5  $\mu\text{g}/\text{mL}$  concentration. After 24 h, cells were detached and analyzed by flow cytometry (Attune NxT Flow cytometer, Life Technologies). For analysis of drug uptake efficiency, we incubated DOX, mrGO/DOX or mrGOG/DOX (5  $\mu\text{g}/\text{mL}$  DOX) with U87 cells for 24 h before analysis by flow cytometry. For apoptotic analysis, the dead cell apoptosis kit containing annexin V-FITC and propidium iodide (PI) (Thermo Fisher) was used, after incubating the test sample with U87 cells for 24 h before flow cytometry analysis.

### 2.9.3. Magnetic guidance (live/dead cell viability assay)

For DOX delivery under magnetic guidance, U87 cells ( $5 \times 10^4$  cells/well) were incubated with mrGOG/DOX at  $5 \mu\text{g/mL}$  in a 24-well culture dish for 24 h. An 1800 gauss magnet (diameter = 2 mm) was glued to the bottom of each well for magnetic guidance during cell culture. After washing cells with PBS, we used the Live/Dead cell viability assay kit for mammalian cells (Thermo Fisher Scientific) with calcein-AM and ethidium homodimer for cell staining. The live cell showing green fluorescence and dead cell showing red fluorescence were observed under a fluorescent inverted microscope.

### 2.9.4. In vitro cytotoxicity (MTT assay)

After placing U87 or 3 T3 cells in a 96-well culture plate ( $5 \times 10^3$  cells/well) for 24 h, we replenished spent culture medium with fresh medium containing the test sample. The laser group was subject to NIR irradiation (808 nm,  $1.5 \text{ W/cm}^2$ , 150 s) after adding the sample. The culture medium was removed at pre-determined times and replenished with 0.1 ml MTT solution (0.5 mg/mL) for incubation at  $37^\circ\text{C}$  for 3 h. The MTT solution was removed and replenished with 0.1 ml DMSO to dissolve the formed purple crystal. The solution absorbance (optical density, OD) was determined from an ELISA plate reader at 570 nm ( $\text{OD}_{570}$ ) and the relative cell viability (%) was determined from Eq. (4). Cells cultured in cell culture medium were taken as a control at 100%.

$$\text{Relative cell viability (\%)} = \frac{\text{OD}_{570} \text{ of sample}}{\text{OD}_{570} \text{ of control}} \times 100 \quad (4)$$

### 2.9.5. In vitro hemocompatibility

To assess the hemocompatibility of mrGOG, we took blood samples from rats and diluted the washed red blood cells (RBC) 4 times with PBS. The diluted RBC was incubated with the test sample at  $37^\circ\text{C}$  for 1 h, which includes negative control (PBS), positive control (DI water) or mrGOG diluted in PBS [52]. The solution absorbance of the supernatant was determined at 540 nm ( $\text{OD}_{540}$ ) after centrifugation and the extent of hemolysis was calculated from Eq. (5) for hemocompatibility.

$$\text{Hemolysis (\%)} = \frac{\text{OD}_{540} \text{ of mrGOG} - \text{OD}_{540} \text{ of PBS}}{\text{OD}_{540} \text{ of water} - \text{OD}_{540} \text{ of PBS}} \times 100 \quad (5)$$

### 2.9.6. Western blotting

The molecular mechanism of apoptosis due to DOX was determined by Western blotting to analyze expression of apoptotic marker proteins, phospho-ERK (p-ERK) and cleaved caspase 3. After incubating U87 cells in a 6-well cell culture plate ( $2 \times 10^5$  cell/well) with the test sample (mrGOG, DOX, mrGO/DOX or mrGOG/DOX) at  $37^\circ\text{C}$  for 24 h, we washed cells with PBS and detached cells with 0.05% trypsin/EDTA. After treating cells with lysis buffer for 30 min on ice and centrifugation, we removed cell debris and determined total protein concentration in the supernatant. The protein was heat-denatured in boiling water for 10 min, followed by separation with sodium dodecyl sulfate polyacrylamide gel electrophoresis. After transferring to a polyvinylidene fluoride membrane and blocked for nonspecific binding, the proteins were blotted with primary antibodies at  $4^\circ\text{C}$  for 12 h. With treatment from HRP-conjugated secondary antibody for 1 h and ECL Western blotting substrate for 5 min, the immune complexes were detected with a MultiGel-21 imaging system. For quantitative analysis of protein band density from Western blotting, we used the ImageJ software. For expression of heat shock protein 70 (HSP70) due to photothermal effect, we followed the same protocol using mrGOG as the test sample, with or without NIR laser irradiation (808 nm,  $1.5 \text{ W/cm}^2$ ).

### 2.10. In vivo anti-tumor efficacy

All animal experiments were approved by Chang Gung University's Institutional Animal Care and Use Committee. We created a xenograft tumor model from BALB/c nude mice (6 to 8 weeks old) by

subcutaneous injection of  $1 \times 10^6$  U87 cells to its right flank with a 25-gauge needle. The tumor size ( $\text{mm}^3$ ) was calculated from  $\text{length} \times \text{width}^2 \div 2$  using a caliper. Five days later when tumor size reached  $30 \text{ mm}^3$ , the mice were divided into 5 groups ( $n = 4$ , each group). On day 6 when the first treatment started, we injected  $100 \mu\text{l}$  of PBS (control), DOX or mrGOG/DOX into each mouse through its tail vein (5 mg DOX/kg body weight). For mice in the mrGOG/DOX + magnet group, an 1800 gauss magnet (diameter = 2 mm) was placed on top of the tumor for 1 h after administering mrGOG/DOX (5 mg/kg DOX). For the mrGOG/DOX + magnet + laser group, we irradiated the tumor with NIR laser (808 nm,  $1.5 \text{ W/cm}^2$ ) for 5 min after magnetic guidance. The mouse was subject to additional treatments on day 9, 13 and 16. The body weight as well as tumor size were monitored on day 8, 12, 15 and 19 and every other day thereafter. Since the U87 cell line has been genetically modified with luciferase gene, bioluminescence imaging (BLI) was employed for monitoring tumor size by Xenogen IVIS-200 non-invasive in vivo imaging [52]. For BLI normalization, the total bioluminescent signal intensity on day 19 was divided by that on day 5. Once the tumor volume grew to above  $1000 \text{ mm}^3$ , the mouse was sacrificed to determine the animal survival time curve.

Tumors tissues retrieved on day 19 were fixed in formalin and embedded in paraffin. After sectioning the tumor sample into  $5\text{-}\mu\text{m}$  thickness, we carried out hematoxylin and eosin (H&E) stain, immunohistochemical (IHC) stain and Prussian blue stain. For IHC analysis, we incubated a tissue slice with rabbit primary antibody for p-ERK, cleaved caspase 3 or Ki-67 overnight at  $4^\circ\text{C}$ , and followed by incubating with anti-rabbit secondary antibody. After counterstaining cell nuclei with hematoxylin, the tissue slice was examined under Aperio ScanScope XT slide scanner and immunoreactivity in each sample was quantified by image analysis (PAX-it software). The protein expression was obtained from area percentage containing the immunoreactivity in the region of interest (ROI) using four different areas for quantification. For Prussian blue staining to detected iron nanoparticles in tissue slices, the tissue sections were placed in a  $65^\circ\text{C}$  oven for 20 min, immersed in xylene for 10 min twice, immersed in gradient concentrations of ethanol (99%, 95%, 70%, and 50%, 3 min each), and washed with distilled water. The washed slide was incubated in a working iron stain solution for 20 min, soaked in a working pararosaniline solution for 10 min, and finally washed with distilled water. After re-immersing in gradient concentrations of ethanol (50%, 70%, 95% and 99%, 1 min each), the slide was immersed in xylene for 3 min and mounted for observation under an inverted microscope. For evaluation of the safety of the treatment, we collected blood samples with blood collection tubes after sacrificing the animal and subject the samples to hematological analysis. The major organs from sacrificed mouse were harvested for H&E histological examination.

### 2.11. Statistical analysis

We present the data as mean  $\pm$  standard deviation (SD) and carry out statistical analysis by one-way analysis of variance (ANOVA) analysis. The Tukey HSD test was used to compare subgroups using the SPSS software. The  $p < 0.05$  was considered to be significant statistically.

## 3. Results and discussion

### 3.1. Preparation and characterization of mrGOG/DOX

Fig. 1 depicts the flow diagram during the preparation of mrGOG/DOX. We first used branched PEI to reduce/modify GO at  $80^\circ\text{C}$ . The citrate-coated magnetic nanoparticles (CMNP) were conjugated to rGO through carbodiimide-mediated covalent bond formation between the -COOH groups in CMNP and the  $-\text{NH}_2$  groups in rGO to prepare mrGO. To prepare PEGylated mrGO, mrGO was physically modified with DSPE-PEG<sub>2000</sub>-maleimide through hydrophobic interaction of its hydrophobic tails with mrGO surface, to improve the colloidal stability. This step also



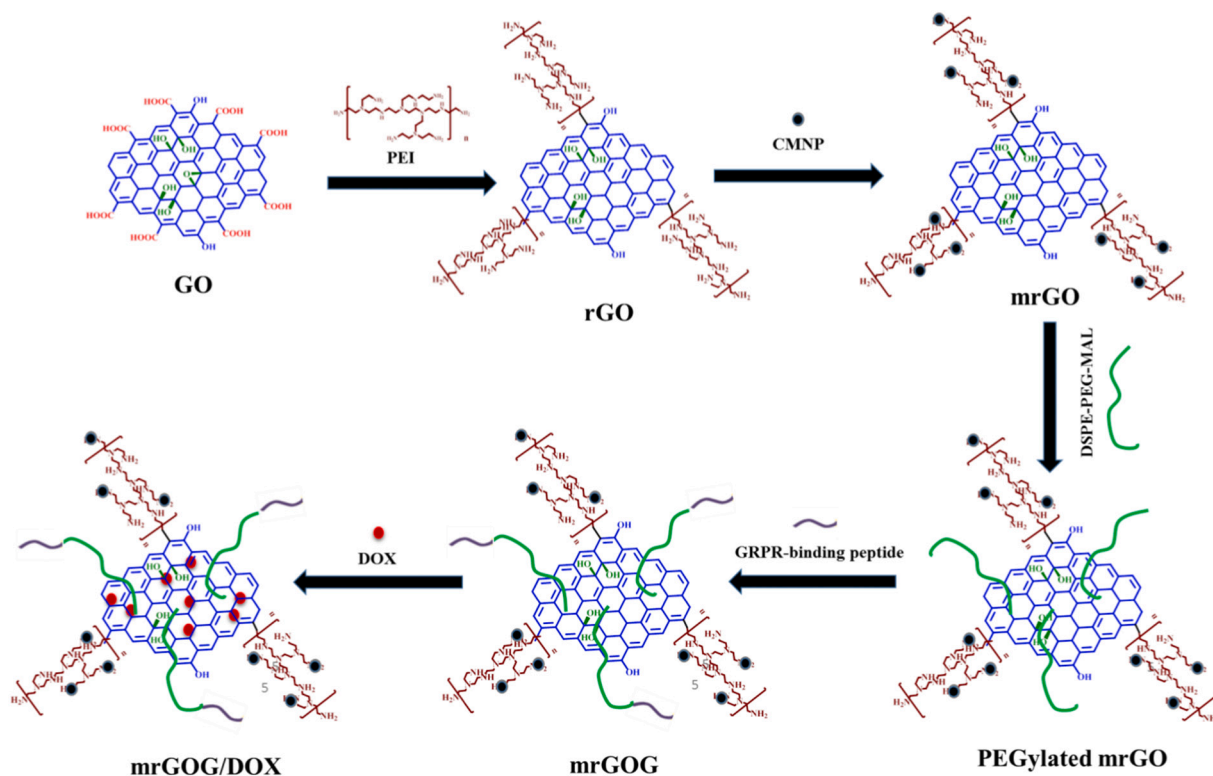


Fig. 1. A flow diagram denotes the preparation of mrGOG/DOX.

introduces a reactive maleimide function group for conjugation with GRPR-binding peptide, taking advantage of spontaneous covalent bond formation between maleimide and the sulfhydryl (–SH) group in the N-terminal cysteine residue, for mrGOG synthesis. Using  $\pi$ - $\pi$  stacking between mrGOG and DOX, the drug was loaded to mrGOG to obtain the dual targeted mrGOG/DOX nanocomposite.

The morphology of GO, rGO, mrGO, and mrGOG from TEM are

shown in Fig. 2A. A thin and transparent well-defined structure is shown for GO with  $\sim 150$  nm size. After PEI reduction/modification, the dense surface coating by PEI decreases the transparency and smoothness of rGO. After decorating with CMNP, both mrGO and mrGOG exhibit similar morphology, showing electron-dense black iron oxide nanoparticles in CMNP. As shown in Fig. 2B, the particle-size distribution curve from DLS shifted to the right for rGO after grafting PEI polymer.

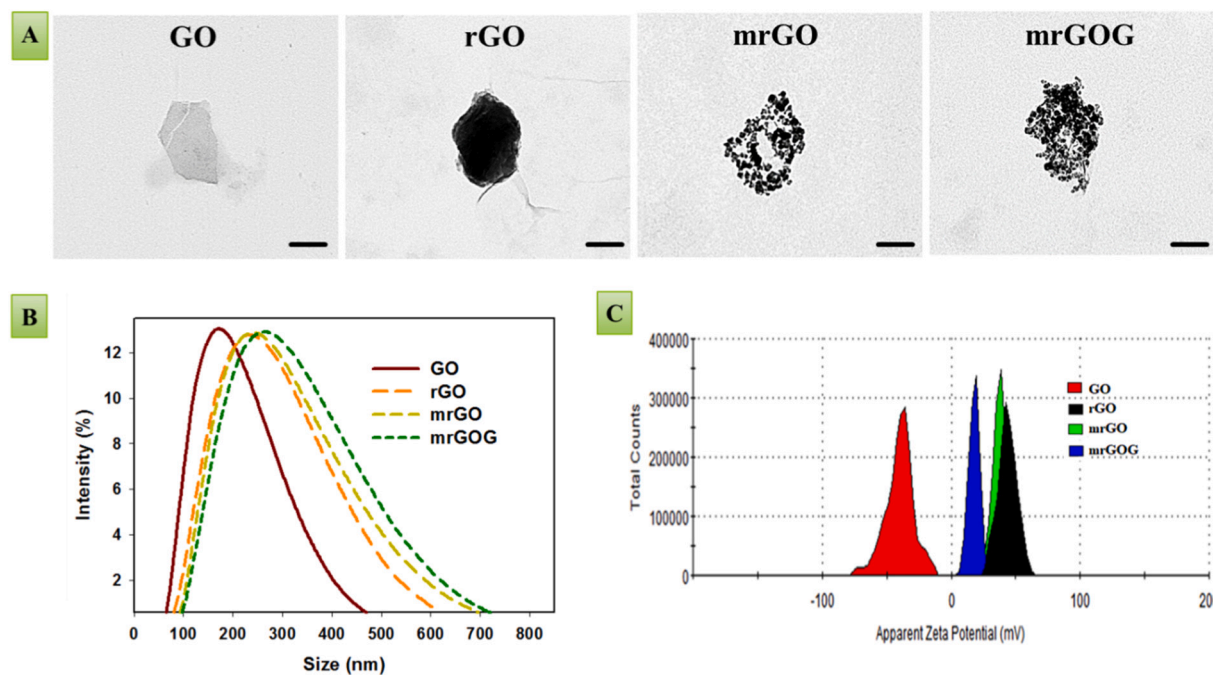


Fig. 2. The transmission electron microscopy (TEM) images (A, bar = 100 nm), particle size distribution curves from dynamic light scattering (DLS) (B), and zeta potential distribution curves (C) of GO, rGO, mrGO and mrGOG.



Nonetheless, CMNP decoration or peptide conjugation did not lead to large shift of the distribution curve. Therefore, the average hydrodynamic diameter significantly increased after reducing GO to rGO, but no significant difference was noted during the following steps (Table 1). The unimodal particle-size distribution curves also result in a polydispersity index less than 0.3 for all samples (Table 1). The zeta potential distribution curve in Fig. 2C indicates all samples other than GO have positive zeta potentials. The negative average zeta potential ( $-41.3$  mV) associated with GO changes dramatically to positive ( $44.3$  mV) for rGO after grafting with cationic PEI polymer (Table 1). After CMNP decoration, the average zeta potential of mrGO decreases to  $36.2$  mV due to anionic citrate groups in CMNP. The average zeta potential decreases again to  $15.2$  mV for mrGOG due to the negative charges associated with DSPE-PEG and peptide ligand, but still maintains at a value high enough for colloidal stability.

From FTIR spectra in Fig. 3A, GO displays characteristic peaks at  $1734$ ,  $1410$  and  $1067$   $\text{cm}^{-1}$  corresponding to the C=O stretching of carboxyl group, C=C stretching and C-O-C stretching, respectively. For rGO, the weaker C-O-C and the stronger C=C stretching vibrations indicate the restoration of the  $\pi$ - $\pi$  structure and successful reduction of GO by PEI. The two new peaks at  $2927$  and  $2845$   $\text{cm}^{-1}$  could be assigned to stretching modes of  $\text{CH}_2$  (asymmetric and symmetric) in PEI chains after reduction/conjugation of GO by PEI. The dramatic decrease of  $1734$   $\text{cm}^{-1}$  peak intensity also strongly suggests chemical modification of GO by PEI [53]. Due to stretching vibration of Fe-O bond, mrGO shows a new characteristic peak at  $570$   $\text{cm}^{-1}$  whereas a broad peak at  $1650$   $\text{cm}^{-1}$  supports covalent bond formation between PEI and CMNP. The modification with PEG leads to two additional peaks,  $1250$   $\text{cm}^{-1}$  from C-OH and  $945$   $\text{cm}^{-1}$  from P-O-C, in mrGOG. The imidazole groups in histidine residues of the GRPR-binding peptide also show an additional peak at  $1097$   $\text{cm}^{-1}$ , confirming successful peptide ligand conjugation.

The XRD analysis reveals a peak centered around  $2\theta = 11.3^\circ$  for GO, representing the (001) plane (Fig. 3B) [54]. After reduction with PEI, this peak disappears for rGO but a new peak appears at  $22.7^\circ$  due to the loss of crystal structure order to the (002) crystalline plane [55]. CMNP has six characteristic peaks, due to the (220), (311), (400), (422), (511) and (440) planes of  $\text{Fe}_3\text{O}_4$ . The crystalline size of iron oxide calculated from the highest peak at  $35.7^\circ$  from the Debye-Scherrer equation is  $13.2$  nm for CMNP, which maintains at  $13.0$  nm for mrGOG. After conjugation rGO with CMNP, the mrGOG displays all peaks from rGO and CMNP as expected.

The Raman spectra show D and G bands from  $\text{sp}^2$  vibration of C=C double bond disorder (Fig. 3C). The  $I_D/I_G$  value, which is the intensity ratio of D band ( $1347$   $\text{cm}^{-1}$ ) to G band ( $1597$   $\text{cm}^{-1}$ ), is  $0.98$  for GO. The CMNP has distinct peak profile from GO, showing peaks at  $500$   $\text{cm}^{-1}$  and lower, which also appear in mrGO and mrGOG. The  $I_D/I_G$  value increases to  $1.08$ ,  $1.07$  and  $1.06$  for rGO, mrGO and mrGOG, respectively, regardless of CMNP and peptide conjugation. Indeed, the change is due to the reduction of GO into rGO by PEI with higher intensity of the C=C double bond and formation of more  $\text{sp}^3$  carbon [56]. The change in  $I_D/I_G$  value is comparable to that found in other reports [57]. Taken together, the Raman spectroscopy provides additional information that GO has

been successfully reduced to rGO by PEI, which could be conjugated with CMNP for synthesis of magnetic nanocomposites.

From SQUID analysis, the value of saturation magnetization for CMNP is at  $57.3$  emu/g, whereas the values for mrGO and mrGOG are  $20.7$  emu/g and  $11.8$  emu/g (Fig. 3D). Reduction in saturation magnetization may arise from decreased weight percentage of CMNP in mrGO (or mrGOG), with the magnetic force being determined from unit weight of a sample. Considering all components other than CMNP are diamagnetic in mrGO (or mrGOG), the iron oxide contents are  $36.1\%$  and  $20.6\%$  in mrGO and mrGOG, respectively. They are comparable with values obtained by ICP-OES analysis, which are  $93.1 \pm 1.9\%$ ,  $40.6 \pm 1.9\%$  and  $20.2 \pm 0.8\%$  iron oxide in CMNP, mrGO and mrGOG, respectively ( $n = 3$ ). In addition, the SQUID analysis confirms the superparamagnetic properties of all samples, with the remnant magnetization being  $0.14$ ,  $0.04$  and  $0.03$  emu/g for CMNP, mrGO, mrGOG.

The thermal stability was investigated by TGA (Fig. S1A). The weight loss occurred at  $200$   $^\circ\text{C}$  due to decomposition of organic functional groups in GO. Additional thermal decomposition peak appears at  $500$   $^\circ\text{C}$  with sublimation of the carbon backbone. For rGO, significant weight loss appears between  $300$  and  $450$   $^\circ\text{C}$  with peak decomposition at  $350$   $^\circ\text{C}$ , due to pyrolysis of covalently bound PEI molecules in rGO [58,59]. From the  $\sim 7\%$  weight loss of CMNP at  $600$   $^\circ\text{C}$  due to citrate, the iron oxide content could be estimated to be  $\sim 40\%$  in mrGO and  $\sim 20\%$  in mrGOG, which are in line with those from ICP-OES analysis. The GO and rGO exhibit distinctive absorbance peaks at  $230$  and  $263$  nm from UV-VIS spectroscopy (Fig. S1B). The GO shows the peak absorbance at lower wavelength with the  $\pi \rightarrow \pi^*$  transition in C=C bond, which shows shifting to higher wavelength after removing the oxygen-containing groups and restoring the  $\pi$  electron conjugation [60–62].

Fig. S2A shows the magnetic responsiveness of mrGOG in PBS, with complete separation of opaque magnetic nanocomposite within 2 min under the influence of a magnet placing at tube side. Undoubtedly, such fast magnetic response will be important for magnetic targeting in vivo. Nonetheless, for application in nanomedicine, mrGOG should be stable in biological solution as well. Therefore, we checked the stability of mrGOG in PBS. As shown in Fig. S2B, the appearance and absorbance measurements of the solution endorse the colloidal stability of mrGOG.

### 3.2. Photothermal effect

The photothermal effect in vitro was determined from the time-dependent temperature change of a nanocomposite-containing solution after irradiation with NIR laser ( $808$  nm,  $1.5$  W/ $\text{cm}^2$ ), shown in Fig. 4A. The peak temperature rise for rGO solution is faster than GO with higher photothermal conversion efficiency associated with the restored  $\text{sp}^2$  structure in rGO (Fig. 4B). Furthermore, mrGO shows even higher photothermal response than rGO, which is supported from a previous report where iron oxide nanoparticles (or CMNP) was shown to have photothermal response after NIR irradiation [63]. Most importantly, PEGylation or ligand conjugation did not influence the photothermal effect of mrGO as mrGOG shows similar photothermal response with mrGO (Fig. 4B).

### 3.3. Drug loading and drug release

For DOX loading, mrGOG ( $0.1$  mg) was mixed separately with DOX ( $0.1$  to  $0.8$  mg) in  $1$  mL PBS to determine the loading efficiency (LE) and the loading content (LC) of drug (Fig. 4C). With increasing DOX concentration, the LE decreases from  $65\%$  to  $26\%$  with concomitant increase of LC from  $0.3$  to  $1.86$  mg/mg. We chose the intersection of LE and LC curves, where  $0.1$  mg mrGOG reacted with  $0.3$  mg DOX, as the condition for drug loading. For DOX release from mrGOG/DOX, the cumulative drug release profiles at pH 5 (the endosomal pH value) or pH 7.4 (the physiologic pH value) at  $37$   $^\circ\text{C}$  is shown in Fig. 4D. A sustained drug release behavior is observed, with the percentage of DOX released at pH 5 ( $\sim 78\%$ ) being about two times that at pH 7.4 ( $38\%$ ) in

**Table 1**

The results from analysis of average particle size by DLS and analysis of average zeta potential ( $n = 4$ ).

Sample	Average particle size (nm)	Polydispersity index (PDI)	Average zeta potential (mV)
GO	$156 \pm 7.1$	$0.21 \pm 0.02$	$-41.3 \pm 1.3$
rGO	$218 \pm 10.1^a$	$0.17 \pm 0.01^a$	$44.3 \pm 4.8^a$
mrGO	$233.5 \pm 11.2^a$	$0.19 \pm 0.02^a$	$36.2 \pm 1.9^{a,\beta}$
mrGOG	$253.4 \pm 14.3^a$	$0.20 \pm 0.01$	$15.2 \pm 2.4^{a,\beta,\gamma}$

<sup>a</sup>  $p < 0.05$  compared with GO

<sup>β</sup>  $p < 0.05$  compared with rGO.

<sup>γ</sup>  $p < 0.05$  compared with mrGO.

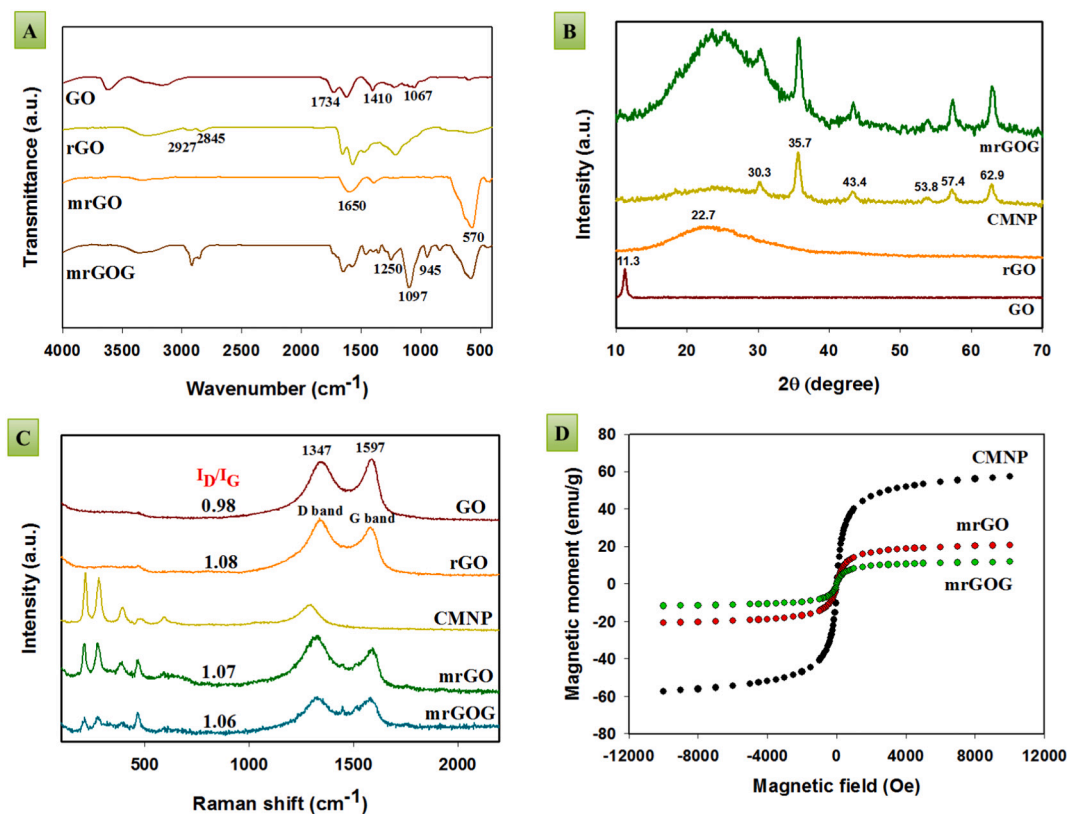


**Fig. 3.** The characterization of properties of GO, rGO, mrGO and mrGOG. (A) Fourier transformed infrared (FTIR) spectroscopy; (B) X-ray diffraction (XRD); (C) Raman spectroscopy; (D) superconducting quantum interference device (SQUID).

24 h. This pH-sensitive DOX release property meets the requirement for a fast release rate of DOX in an acidic endosomal environment after intracellular uptake of mrGOG/DOX [64,65]. The  $\pi$ - $\pi$  stacking for DOX loading is mainly from the interaction of aromatic rings in rGO and in DOX [66]. By weakening these interactions as well as hydrogen bonding, the release of DOX will be promoted in the acidic environment of endosomes after intracellular uptake of mrGOG/DOX. In addition, minimizing drug loss outside cancer cells at physiologic pH can increase intracellular drug concentration and exert higher cytotoxicity.

### 3.4. Intracellular uptake

To ensure the GRPR-binding peptide ligand designed in this study could target U87 cells with overexpressed GRPR, we used fluorescein-labelled peptide for interaction with U87 cells, and observed the expression of green fluorescence on cell surface. As shown in Fig. 5A, specific binding of peptide ligand to U87 is evident from the green fluorescence signal observed from U87 surface, supporting the use of GRPR-binding peptide as a ligand for active targeting of U87 cells. As active targeting should lead to enhanced internalization, we studied the intracellular uptake of nanocomposites by confocal microscopy for visualization of endocytosis of fluorescein-labelled mrGO and mrGOG. The confocal images in Fig. 5B demonstrates enhanced intracellular uptake of mrGOG in comparison with mrGO by comparing the green fluorescence signal intensity in U87 cells. The mrGO still shows limited intracellular uptake by U87 due to clathrin-mediated endocytosis [67]. For mrGOG, pretreating U87 beforehand with excess peptide ligand leads to restricted intracellular uptake, as the free peptide can bind with GRPR on U87 surface and impede targeting by mrGOG. This can down-regulate recognition of mrGOG by U87 and hamper its intracellular uptake. The confocal microscopy analysis therefore underlines the use of bombesin-like GRPR-binding peptide, for the first time, as a ligand for active targeting of U87 cancer cells.

The mrGOG/DOX should release DOX in the endosomes of cancer cells, which enters the nucleus and chelates DNA molecules to promote cell apoptosis. As shown in Fig. S3, we could observe the confinement of red fluorescence signal from DOX within the cell nucleus after contacting U87 with mrGOG/DOX, whereas the green fluorescence from fluorescein-labelled mrGOG appears only in cell cytoplasm after endocytosis [68]. This facilitated DOX delivery by mrGOG/DOX is expected to exert high cytotoxicity for chemotherapy, which can be combined with photothermal therapy after exposing mrGOG in the cell cytoplasm to NIR laser irradiation.

The uptake of nanocomposite by U87 was studied from intracellular fluorescence intensity of fluorescein-labelled mrGO and mrGOG with flow cytometry. As shown in Fig. 6A, the mean fluorescence intensity of mrGO and mrGOG is 898 and 2926. Consistent with results from confocal microscopy (Fig. 5B), mrGOG shows more than 3-fold higher intracellular uptake efficiency than mrGO, mediated by cellular trafficking with GRPR-binding peptide. As cytotoxicity elicited by DOX is related to its intracellular concentration, the intracellular uptake efficiency of DOX by U87 after treating with free DOX, mrGO/DOX or mrGOG/DOX was shown in Fig. 6 after flow cytometry analysis. Like uptake of nanocomposite, we find 2.8-fold increase of intracellular DOX uptake for mrGOG/DOX over mrGO/DOX, with the geometric mean fluorescence intensity being 8571 and 3076. The drug uptake efficacy is slightly lower than the nanocomposite uptake efficacy, which may arise from premature drug release before intracellular uptake. Although DOX uptake is more efficient for mrGO/DOX than free DOX (geometric mean = 1750), active drug targeting from mrGOG/DOX results in the highest accumulation of DOX intracellularly, which can concomitantly elevate the cytotoxicity. Taken together, we successfully synthesized mrGOG as an efficient nano-carrier for active targeting GRPR-overexpressing U87 for DOX delivery.

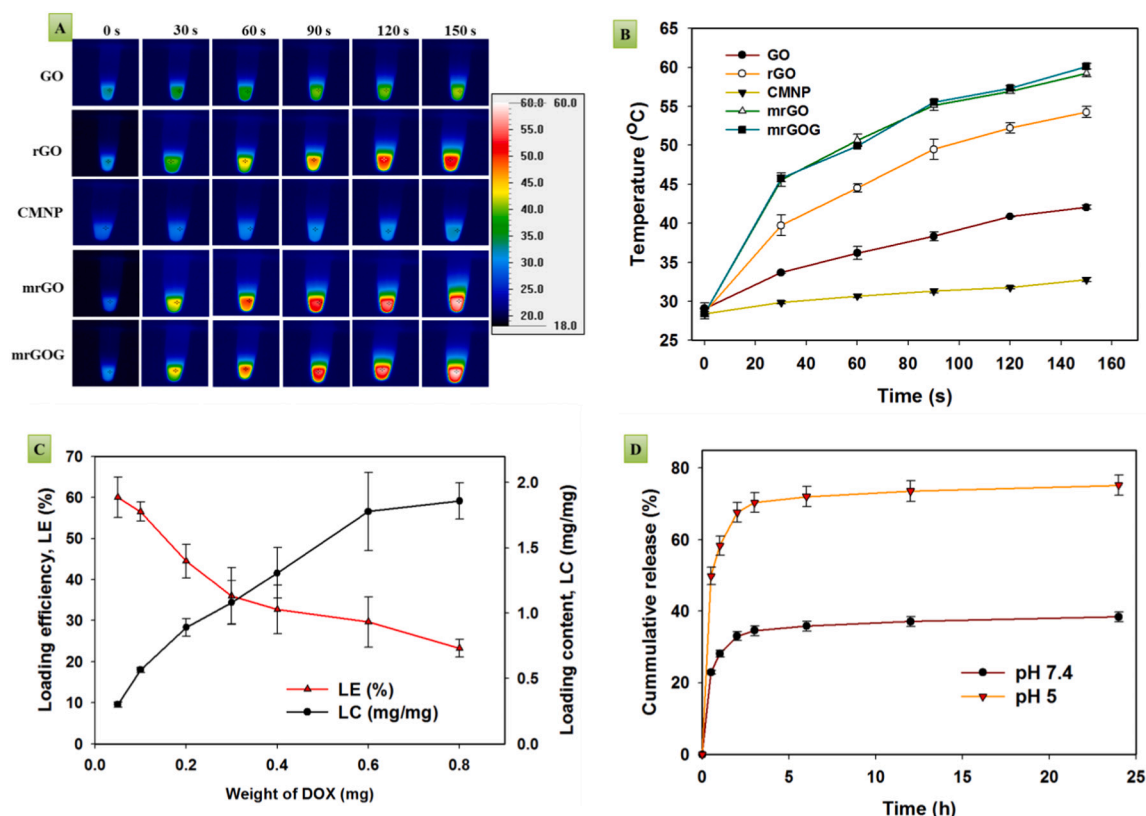


**Fig. 4.** (A) The thermal images and (B) the time-dependent peak temperature profiles after laser irradiation of 100  $\mu\text{L}$  sample solution with NIR laser (808 nm, 1.5  $\text{W}/\text{cm}^2$ ). The concentration is 0.5 mg/mL nanoparticles. (C) The loading efficiency and the loading content of DOX to mrGOG (0.1 mg). (D) The release curve of DOX from mrGOG/DOX in pH 5 and pH 7.4 PBS at 37  $^{\circ}\text{C}$ .

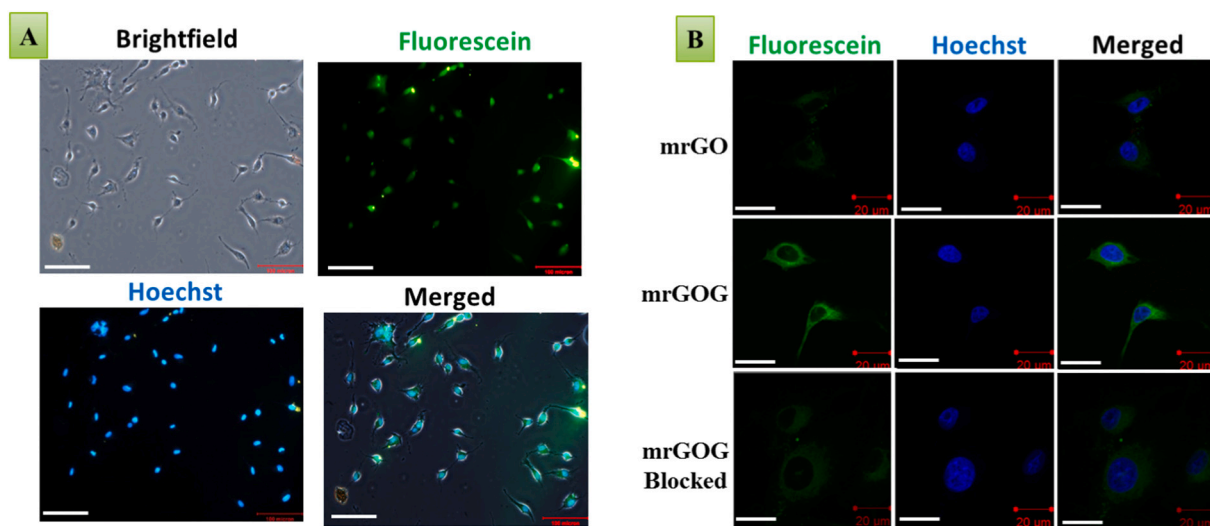


**Fig. 5.** (A) The cell surface binding of fluorescein-labelled GRPR-binding peptide to U87 glioblastoma cells was observed under an inverted fluorescent microscope. The cell nuclei were counterstained with Hoechst dye (bar = 100  $\mu\text{m}$ ). (B) The confocal microscopy analysis of in vitro uptake and inhibition studies of fluorescein-labelled mrGO and mrGOG by U87 cells. The blocking study used 10-fold excess of free GRPR-binding peptide before adding mrGOG. The cell nuclei labelled with Hoechst dye show blue fluorescence. Bar = 20  $\mu\text{m}$ .

### 3.5. In vitro cytotoxicity

The nano-carrier mrGOG was tested for in vitro cytotoxicity with both mouse fibroblast 3 T3 and human glioblastoma U87 cell lines for biocompatibility. As shown in Fig. 7A and B, mrGOG did not elicit pronounced cytotoxicity toward 3 T3 and U87 (from 0.01 to 100  $\mu\text{g}/\text{mL}$ )

at different cell culture times. Indeed, at the highest concentration, the cell survival rate is still more than 85% for both cell lines, underlining the high biocompatibility of mrGOG. After confirming mrGOG is not harmful to cancer cells, DOX-loaded mrGOG was studied for chemophotothermal therapy of U87 in vitro (mrGOG/DOX + laser). The cell viability was compared with those of free DOX, mrGO/DOX and

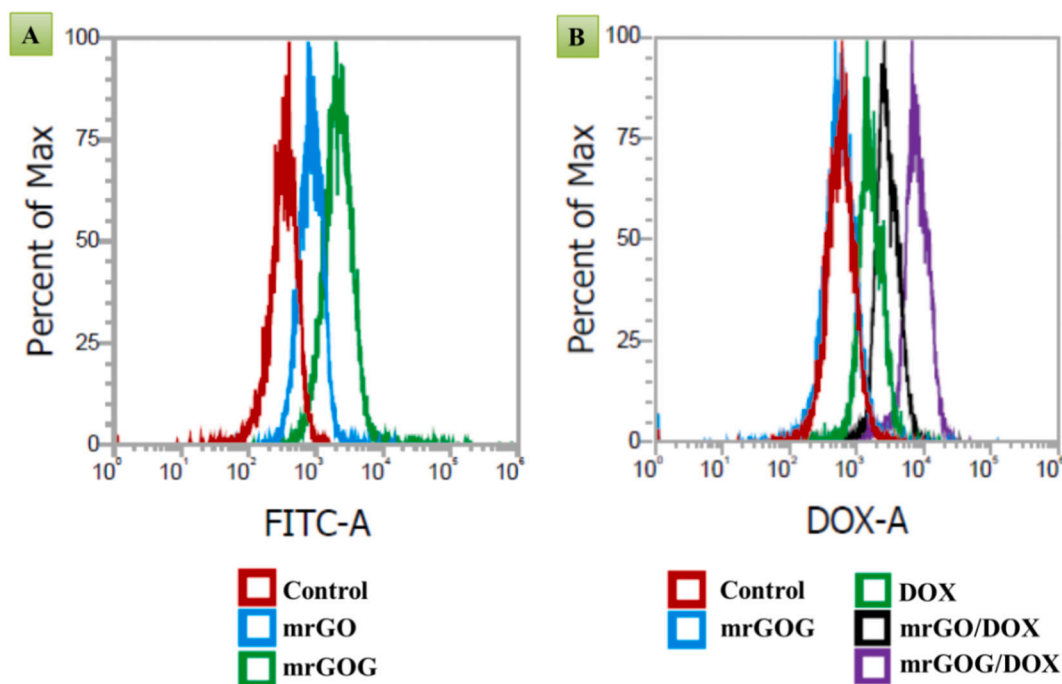


**Fig. 6.** (A) The flow cytometry analysis of U87 uptake efficiency of fluorescein-labelled mrGO and mrGOG after 24 h. (B) The flow cytometry analysis of U87 uptake efficiency of DOX by incubating cells with DOX, mrGO/DOX, or mrGOG/DOX for 24 h.

mrGOG/DOX. As shown in Fig. 7C, the cell viability after 48 h culture time is dependent on DOX concentration within 0.1 and 10  $\mu\text{g/mL}$ . The drug concentrations achieving 50% cytotoxicity ( $\text{IC}_{50}$ ) are 0.99, 0.70, 0.48, and 0.19  $\mu\text{g/mL}$  for DOX, mrGO/DOX, mrGOG/DOX and mrGOG + laser, respectively. Comparing mrGO/DOX and DOX, the passive accumulation of the positively charged mrGOG in U87 leads to higher cytotoxicity and 29% decrease of  $\text{IC}_{50}$  [69]. Active targeting of mrGOG/DOX raises intracellular DOX concentration (Fig. 6B), resulting in another 31% decrease of  $\text{IC}_{50}$ . Nonetheless, with NIR irradiation, the  $\text{IC}_{50}$  drastically reduces to 40% of that without laser treatment, endorsing the combination of photothermal therapy with chemotherapy in vitro.

As the major advantage offered by a magnetic nano-carrier is to offer magnet-guided drug delivery, we confirm this effect by incubating mrGOG/DOX with U87 under the guidance of a magnet glued to the bottom of well surface. As shown from the Live/Dead cell viability staining assay, dead cells with red fluorescence locates in the magnetically targeted zone, as mrGOG/DOX was attracted by the magnetic force and concentrated within the targeted zone to induce cell death (Fig. 7D). However, as most dead cells detached from well surface after death, the density of dead cells is less than expected. In contrast, live cells showing green fluorescence mainly exist outside the targeted zone without magnetic guidance. An external magnetic field therefore is expected to guide mrGOG/DOX to the tumor site and to increase local drug concentration, offering the possibility for dual targeted anti-cancer therapy in vivo.

### 3.6. The molecular mechanism of chemo-photothermal therapy

The cytotoxicity from chemo-photothermal therapy was investigated by flow cytometry for cell death due to apoptosis/necrosis. After co-culture for 24 h, U87 cells were analyzed by a flow cytometer where Q3 is the percentage of live cells, Q4 is early apoptosis, Q2 is late apoptosis and Q1 is necrosis. From Fig. 8, cell survival in the control (cell culture medium) group is 97.2% and close to mrGOG (96.7%), which is in line with the non-toxic nature of the mrGOG from MTT assays (Fig. 7B). The total apoptosis rates (early + late) are 15.3%, 19.8%,

47.1%, and 76.8% for DOX, mrGO/DOX, mrGOG/DOX, and mrGOG/DOX + laser, respectively, as noted from the trend of the cytotoxicity shown in Fig. 7C. Also noted is the increased necrosis rate in the mrGOG/DOX + laser group, as temperature rise from the photothermal effect induced by NIR laser can promote cell necrosis [70]. Taken together, the minimum percentage of live cells in the mrGOG/DOX + laser group (14.4%) endorse the use of targeted chemotherapy (from DOX delivery) in combination with photothermal therapy (from NIR laser irradiation).

Cell apoptosis involves cleavage of pro-caspase, rendering cleaved caspase 3 a reliable cell apoptosis indicator [71]. On the other hand, the activation of extracellular-signal-regulated kinase (ERK) protein by increasing its phosphorylation level is another signaling pathway during cell apoptosis [72]. Thus, the protein expression of intracellular cleaved caspase 3 and phosphorylated-ERK (p-ERK) was analyzed by Western blotting, followed by quantitative analysis for elucidating the molecular mechanism of cell apoptosis. As shown in Fig. 9A, U87 treated with mrGOG shows minimum cleaved caspase 3 and p-ERK protein expression similar to the control (PBS), announcing its high biocompatibility as noted before. In contrast, the DOX-loaded groups showed significant difference in cleaved caspase 3 and p-ERK protein expression, in the order of mrGOG/DOX > mrGO/DOX > DOX, supporting the cytotoxicity observed from MTT assays (Fig. 7C).

The heat shock proteins are stress-inducible chaperone proteins with significant induction at temperatures above 43  $^{\circ}\text{C}$  threshold, allowing their use as endogenous cellular markers after a thermal stress [73]. Specifically, induction of heat shock protein 70 (HSP70) expression can serve as an outcome predictor after thermal therapy [74]. As shown in Fig. 9B, exposure of mrGOG-treated U87 in PBS to NIR laser for 3 min results in significant increase of HSP70 production from Western blotting. The upregulation of HSP expression correlates well with laser exposure time, where significant increase of HSP production by U87 is found 5 min after laser irradiation. The upregulation of HSP70 expression also correlates well with the thermal stress experienced by the cells, shown from time-dependent temperature rise from thermal images [75].



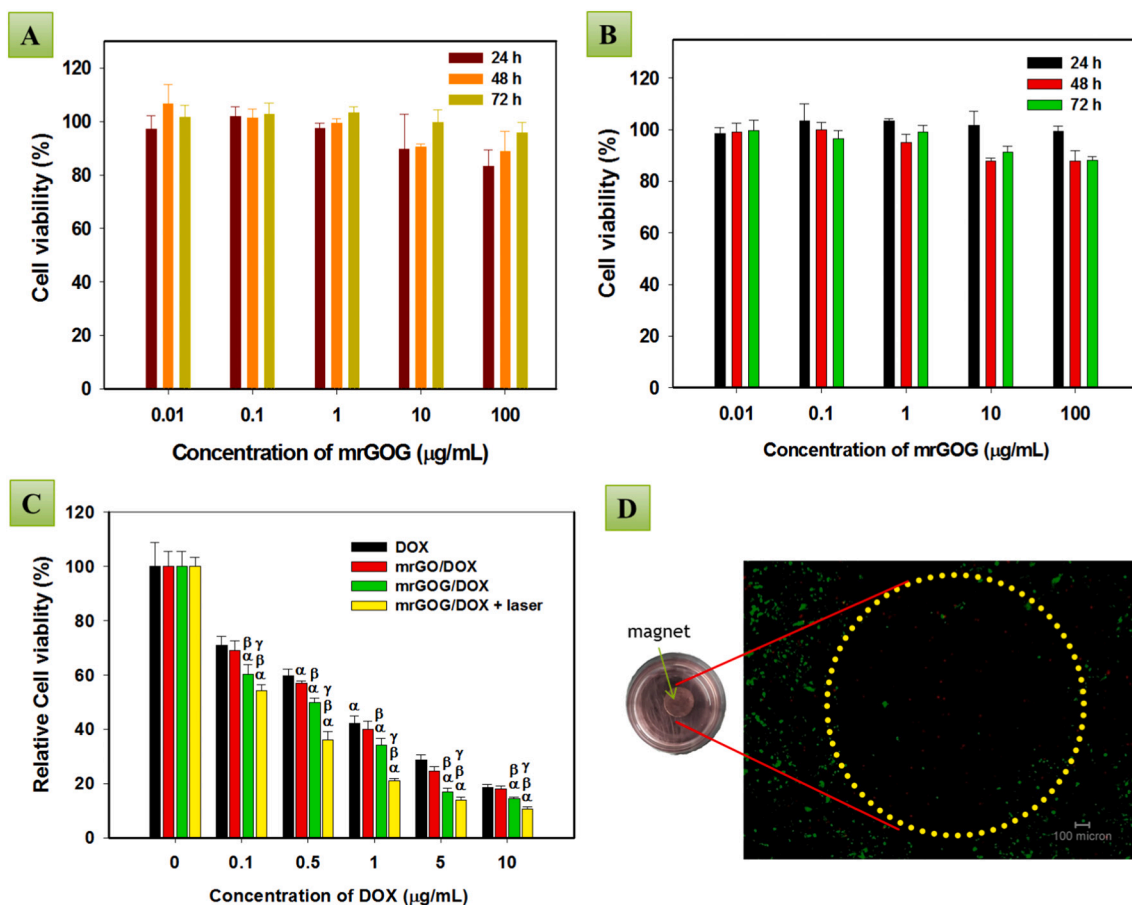


**Fig. 7.** The biocompatibility of mrGOG toward 3 T3 fibroblasts (A) and U87 glioblastoma cells (B). (C) In vitro cytotoxicity toward U87 by treating with DOX, mrGO/DOX, mrGOG/DOX, or mrGOG/DOX + laser. The laser group was subject to NIR laser irradiation (808 nm,  $1.5 \text{ W/cm}^2$ ) for 150 s. The cytotoxicity was measured by MTT assays.  $^{\alpha} p < 0.05$  compared with DOX,  $^{\beta} p < 0.05$  compared to mrGO/DOX,  $^{\gamma} p < 0.05$  compared to mrGOG/DOX. (D) The Live/Dead cell viability staining assay of U87 after incubating cells with mrGOG/DOX in a culture plate under magnetic guidance. A magnet was glued to the bottom of a well for magnetic guidance during cell culture. The dotted line in the image indicates the boundary of the magnet.

### 3.7. In vitro hemolysis

To investigate the potential risk associated with systemic administration of mrGOG in vivo, we tested its hemocompatibility from hemolysis experiments in vitro [76]. For this purpose, we incubated diluted red blood cells (RBC) with mrGOG of different concentrations (in PBS) at  $37^\circ\text{C}$  for 1 h. The damage to RBC was evaluated from the gross appearance and the absorption spectra of the supernatant (Fig. S4A). The PBS serves as the negative control while DI water is the positive control. At increasing mrGOG concentration, no difference in the color of the supernatant solution was detected by comparing with that of PBS, confirming that mrGOG will not damage RBC. However, DI water leads to red-colored solution due to rupture of RBC from difference in osmotic pressure. The absorption spectra of mrGOG were close to that of that of PBS, while DI water shows two absorption peaks, with the release of oxyhemoglobin from ruptured RBC. The hemolysis ratio calculated from Eq. (5) indicates that although slight change of hemolysis is noted at higher mrGOG concentrations, it is still well below the 2% threshold up to  $0.8 \text{ mg/mL}$  for negligible hemolysis (Fig. S4B). On the contrary, we can observe more than 95% hemolysis after incubating RBC with water, validating the assay accuracy. With the excellent hemocompatibility and biocompatibility, mrGOG/DOX will be used in the following animal experiments to evaluate combination chemo-photothermal therapy of xenograft U87 tumors [49].

### 3.8. In vivo study

In the xenograft tumor model by implanting U87 cells in nude mice, we grouped the mice into 5 using mice have tumor size higher than  $30 \text{ mm}^3$  ( $n = 4$  in each group). The first treatment started on day 6 with intravenous administration of  $100 \mu\text{L}$  of PBS (PBS), free DOX (DOX), or DOX-loaded mrGOG (mrGOG/DOX). The other two groups also administered mrGOG/DOX; one subject to magnetic guidance with a magnet on top of the tumor (mrGOG/DOX + magnet) and the other with NIR laser ( $808 \text{ nm}$ ,  $1.5 \text{ W/cm}^2$ ) irradiation for 5 min after magnetic guidance (mrGOG + magnet + laser). We repeated the same treatment again on day 9, 13 and 16 and sacrificed the animal when tumor size is over  $1000 \text{ mm}^3$ . To confirm the in vivo photothermal effect from mrGOG + magnet + laser treatment, we acquired the time-lapsed thermal images using an infrared thermal camera on day 6 (Fig. S5A) and plotted the peak temperature (mean  $\pm$  SD) of the tumor as a function of laser exposure time (Fig. S5B). That tumor peak temperature increases with time and reaches  $44.5^\circ\text{C}$  after 5 min (time used for in vivo study), strongly supporting the feasibility to use mrGOG/DOX for photothermal therapy with NIR laser in vivo.

Considering adverse effects after treatment, we did not notice any significant difference in body weight change among all groups, which points out minimum systemic toxicity associated with chemo-photothermal therapy after NIR laser exposure up to 4 times (Fig. 10A). The distribution of tumor size on day 15 (Fig. 10B) and on day 19 (Fig. 10C), when all mice are still alive, indicates the mrGOG/DOX + magnet + laser group provides the most pronounced treatment



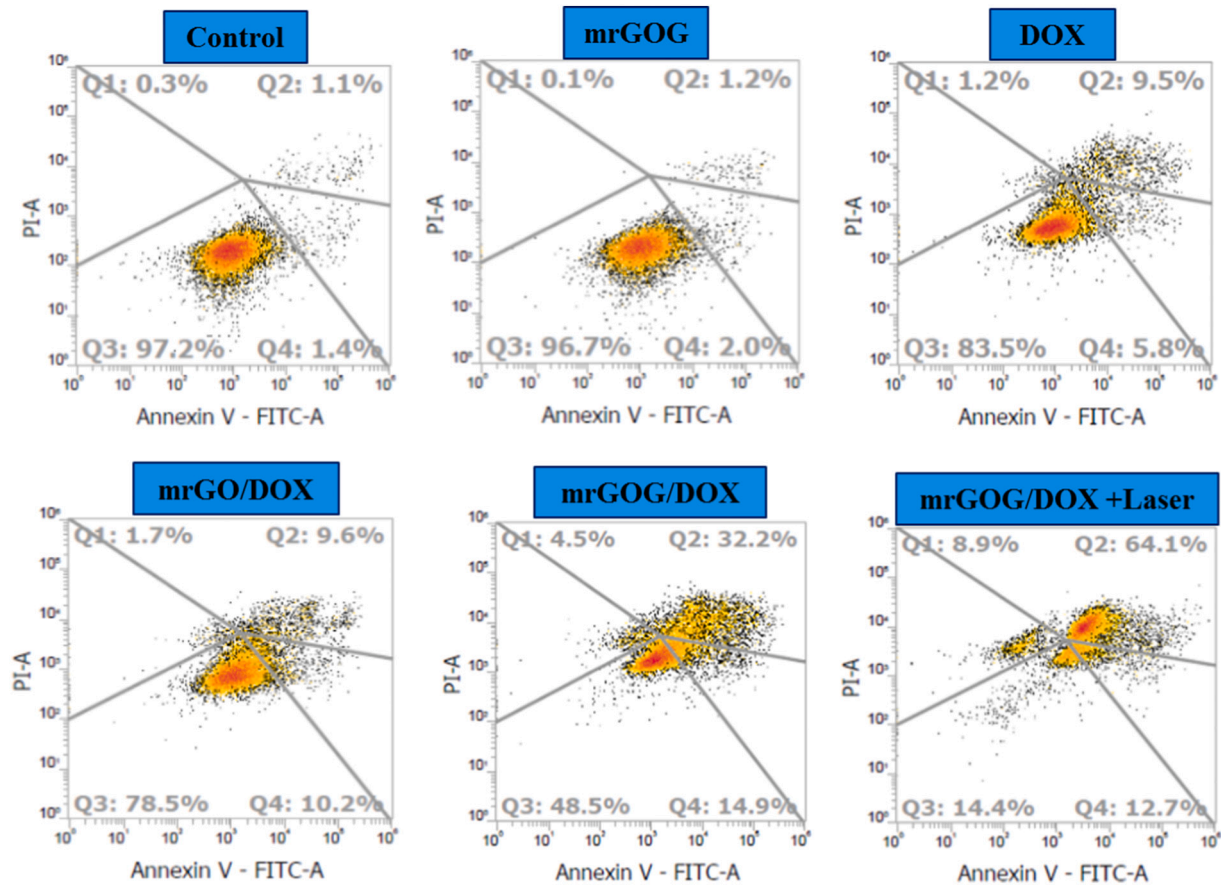


**Fig. 8.** The quantification of cell apoptosis and necrosis by flow cytometry with Annexin V-FITC/PI staining (5  $\mu$ g/mL DOX). Q3: live cells; Q4: early apoptosis; Q2: late apoptosis; Q1: necrosis.

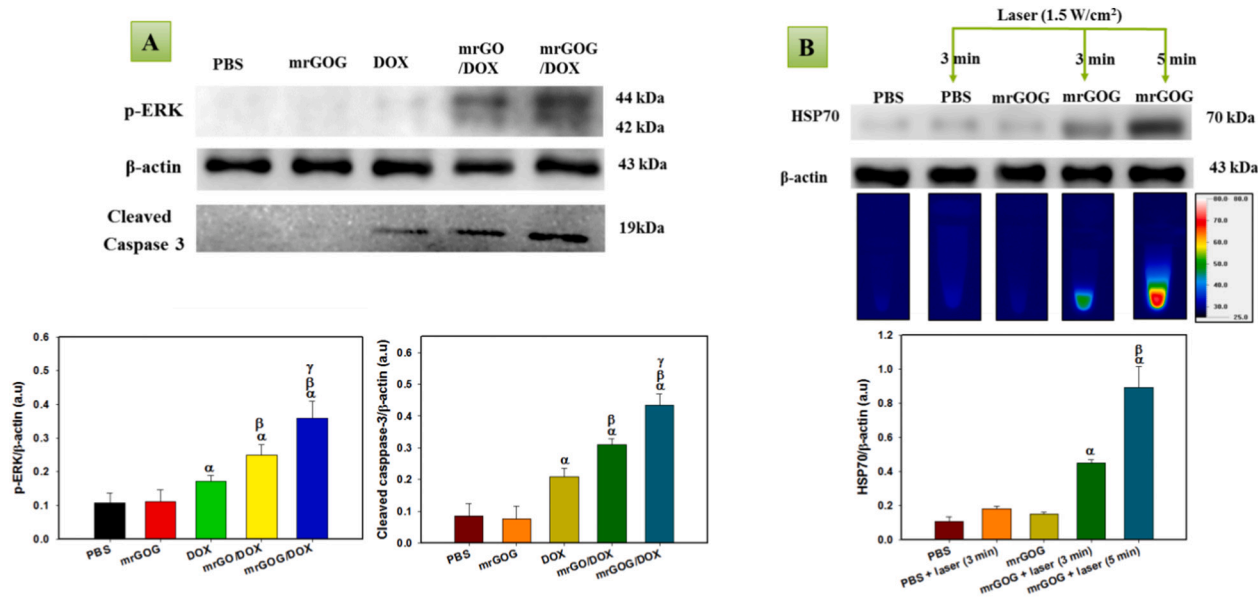


**Fig. 9.** (A) Western blotting of apoptosis marker protein p-ERK and cleaved caspase 3 after chemotherapy.  <sup>$\alpha$</sup>   $p < 0.05$  compared to mrGOG,  <sup>$\beta$</sup>   $p < 0.05$  compared to DOX,  <sup>$\gamma$</sup>   $p < 0.05$  compared with mrGO/DOX. (B) Western blotting of heat shock protein 70 (HSP70) after photothermal therapy with NIR laser irradiation (808 nm, 1.5 W/cm<sup>2</sup>) for 3 min or 5 min.  <sup>$\alpha$</sup>   $p < 0.05$  compared to mrGOG,  <sup>$\beta$</sup>   $p < 0.05$  compared to mrGOG/DOX (3 min). The thermal images are included below the gel images for each group.

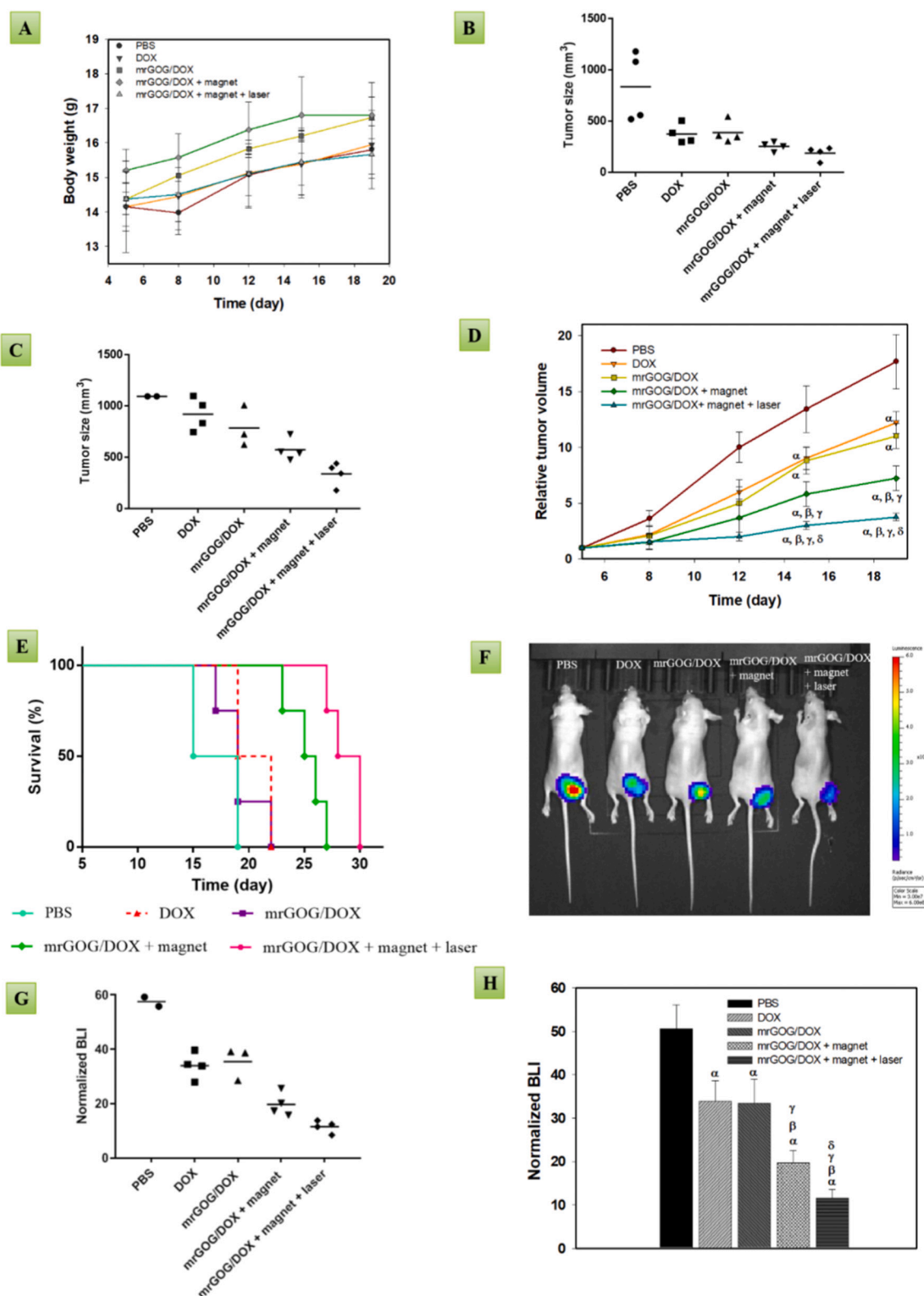


**Fig. 10.** The treatment of U87 xenograft tumor in nude mice was followed by the change of animal body weight (A); the tumor size on day 15 (B) and day 19 (C); the change of tumor size (mean  $\pm$  SD) (D); the survival curve (E). The treatment efficacy was also followed on day 19 from bioluminescence imaging (BLI) by an in vivo imaging system (IVIS) (F); the distribution of normalized BLI intensity (G); the comparison of normalized BLI intensity (mean  $\pm$  SD) (H).  $^{\alpha}$   $p < 0.05$  compared to PBS,  $^{\beta}$   $p < 0.05$  compared to DOX,  $^{\gamma}$   $p < 0.05$  compared to mrGOG/DOX,  $^{\delta}$   $p < 0.05$  compared to mrGOG/DOX + magnet.

efficacy compared with other groups with reduced tumor size. As shown from the tumor growth curve in Fig. 10D, the relative tumor volume (relative to day 5) increases rapidly for the PBS (control) group. Some treatment efficacy was evident from DOX or mrGOG/DOX treatment, which was further improved by employing magnetic guidance as shown from mrGOG/DOX + magnet treatment. Most importantly, the mrGOG + magnet + laser group reveals the slowest increase of tumor volume with significantly smaller tumor size compared with all other groups on day 15 and 19. It should be noted that magnetic targeting can successfully reduce tumor growth, as shown from the significantly reduced tumor size of mrGOG/DOX + magnet vs. mrGOG/DOX on day 15 and 19, by attenuating accumulation of mrGOG at the tumor site to improve the treatment outcome.

From survival curves shown in Fig. 10E, the median survival time increases from 17 days for the PBS control to ~20 days for the DOX (or mrGOG/DOX) group, which increases further to 25.5 days for the mrGOG/DOX + magnet group (Table 2). The mrGOG + magnet + laser group shows the longest survival time at 29 days. Most importantly, statistical analysis of the mean survival time shows the same trend, with mrGOG + magnet + laser showing the longest animal survival, followed by mrGOG + magnet. The trend in animal survival after different treatment is supported by that from tumor volume, supporting the use of magnetically guided mrGOG/DOX plus laser irradiation for dual targeted chemo-photothermal in glioblastoma treatment.

Considering accuracy of tumor size measurement with a caliber, we also re-confirm anti-tumor efficacy with bioluminescence imaging (BLI). The most pronounced anti-tumor efficacy with mrGOG + magnet + laser treatment is shown from representative IVIS images of tumor-bearing mice on day 19 (Fig. 10F). The comparison of normalized BLI value, after dividing the total bioluminescent signal intensity with the corresponding value on day 5, consistently shows the lowest value after mrGOG + magnet + laser treatment from other groups (Fig. 10G). This remarkable treatment benefit leads to significantly reduced normalized BLI value (Fig. 10H), as shown from tumor volume change in Fig. 10D.

After collecting blood samples of sacrificed mice, we carried out hematological analysis to assess the in vivo toxicities of each treatment. As shown in Table S1, no treatment significantly alters the level of blood counts when compared with the PBS control group ( $p > 0.05$ ). Thereby, together with body weight change shown in Fig. 10A, significant adverse effects were ruled out for all treatments, which has been a prime concern of chemotherapy.

The tumor sample retrieved on day 19 was subject to histological analysis. From H&E staining, the tumor in the PBS group shows the highest cell intensity. Comparison of the cell density within treatment groups confirms the trend observed from tumor size, with the mrGOG/DOX + magnet + laser group showing the lowest cell density. Increasing cell density is evident from mrGOG/DOX + magnet to mrGOG/DOX (or DOX). The immunohistochemical (IHC) staining of the Ki-67 in tumor samples, a marker protein for cell proliferation, further confirms the finding regarding cell density, as the tissue sample from the PBS control

group shows actively proliferating cells after staining with the anti-Ki-67 antibody (Fig. 11A). Indeed, treating tumor-bearing mice with DOX could arrest proliferation of U87 cells and result in less Ki-67 protein expression due to cell apoptosis. Treatment with DOX or mrGOG/DOX obviously leads to lower cell proliferation rate due to cellular apoptosis induced by the chemotherapeutic action of DOX. Magnetic targeted delivery of mrGOG/DOX further down-regulates the expression of Ki-67, with less cell proliferation due to higher DOX concentration delivered to the tumor. Most importantly, treating tumor-bearing mice with mrGOG + magnet + laser can provide the most effective inhibition of U87 proliferation as shown from the weakest Ki-67 immunoreactivity, which could be suggested to arise from abundant cellular apoptosis due to the additional photothermal therapy in vivo.

The observed cell death mechanism was further delineated by staining p-ERK and cleaved caspase 3 proteins in the tumor tissue samples, which are hallmark indicators of cell apoptosis. Caspases are a large family of enzymes crucial for initiation of cell apoptosis while cellular signals triggering the initiation of the programmed cell death cascade through proteolytic activation of the enzymes [77]. Caspase 3 is a member of the large caspase enzyme family found in the cytoplasm, which is cleaved in apoptotic cells. Thus, detection of the level of cleaved caspase 3 is a strong indicator of cell death induction, making it an important biomarker to evaluate cancer cell apoptosis [78]. On the other hand, p-ERK protein is activated in stress-related signaling pathways related to cell death [79]. Indeed, we could observe the highest expression of p-ERK and cleaved caspase 3, with the most intense brown color in the apoptotic area, in the mrGOG/DOX + magnet + laser treated tumor (Fig. 11A).

From quantitative analysis of IHC staining results, the means of the percentage of the positively stained area for Ki-67 in the region of interest (ROI) are 72.1%, 40.0%, 38.7%, 20.7% and 4.4% for mice treated with PBS, DOX, mrGOG, mrGOG/DOX + magnet and mrGOG/DOX + magnet + laser, respectively (Fig. 11B). The close to half reduction of Ki-67-positive area identified from the mrGOG/DOX + magnet group compared with the DOX (or mrGOG/DOX) group strongly supports the use of dual targeting for DOX delivery in arresting tumor cell proliferation. Furthermore, the ~90% decrease of Ki-67-positive area for mrGOG/DOX + magnet + laser group leads to the most pronounced anti-tumor efficacy with the combined chemo-photothermal treatment. The positively stained area shows a reverse trend for both apoptosis marker proteins, i.e., p-ERK and cleaved caspase 3, with the same significance levels found for Ki-67. The mean value of percent ROI for p-ERK (or cleaved caspase 3) increases significantly from 23.1% (or 27.8%) for mrGOG/DOX to 41.1% (or 36.1%) for mrGOG + magnet. This value continued increase to 56.8% (or 58.0%) for mrGOG + magnet + laser due to accelerated cell apoptosis rate.

To elucidate effectiveness of magnetic guidance of mrGOG/DOX, the tumor section was also stained with Prussian blue iron staining to identify ferric irons (corresponding to CMNP in mrGOG). As shown in Fig. S6A, the PBS group does not show any mrGOG as expected. In comparison, more iron ions (or mrGOG) exist in tissue slice of the mrGOG/DOX + magnet group, supporting the improved anti-tumor efficacy observed before. For assessment of possible systemic toxicity, H&E-stained sections from major organs of sacrificed mice were compared for morphologic changes. As shown in Fig. S6B, no observable differences between the PBS control group and all treatment groups is observed from the histological examination of tissue sections from heart, spleen, liver, kidney and lung. Overall, this supports the use of mrGOG/DOX + magnet + laser as a safe modality for combination chemo-photothermal cancer therapy.

#### 4. Conclusion

In this research, we successfully prepared a dual targeted magnetic nanocomposite based on rGO and demonstrated its efficacy as DOX carrier for combination chemo-photothermal cancer therapy. With the

**Table 2**

The survival times (days) and median survival times (days) calculated from survival curves after different treatments.

Treatment	Median survival time	Survival time (mean $\pm$ SD)
PBS	17	18 $\pm$ 1.7
DOX	20.5	20.5 $\pm$ 1.5 <sup>a</sup>
mrGOG/DOX	19	19.3 $\pm$ 2.1
mrGOG/DOX + magnet	25.5	24.5 $\pm$ 1.9 <sup>a,b,7</sup>
mrGOG/DOX + magnet + laser	29	28.5 $\pm$ 1.9 <sup>a,b,7,8</sup>

<sup>a</sup>  $p < 0.05$  compared to PBS.

<sup>b</sup>  $p < 0.05$  compared to DOX.

<sup>7</sup>  $p < 0.05$  compared to mrGOG/DOX.

<sup>8</sup>  $p < 0.05$  compared to mrGOG/DOX + magnet.



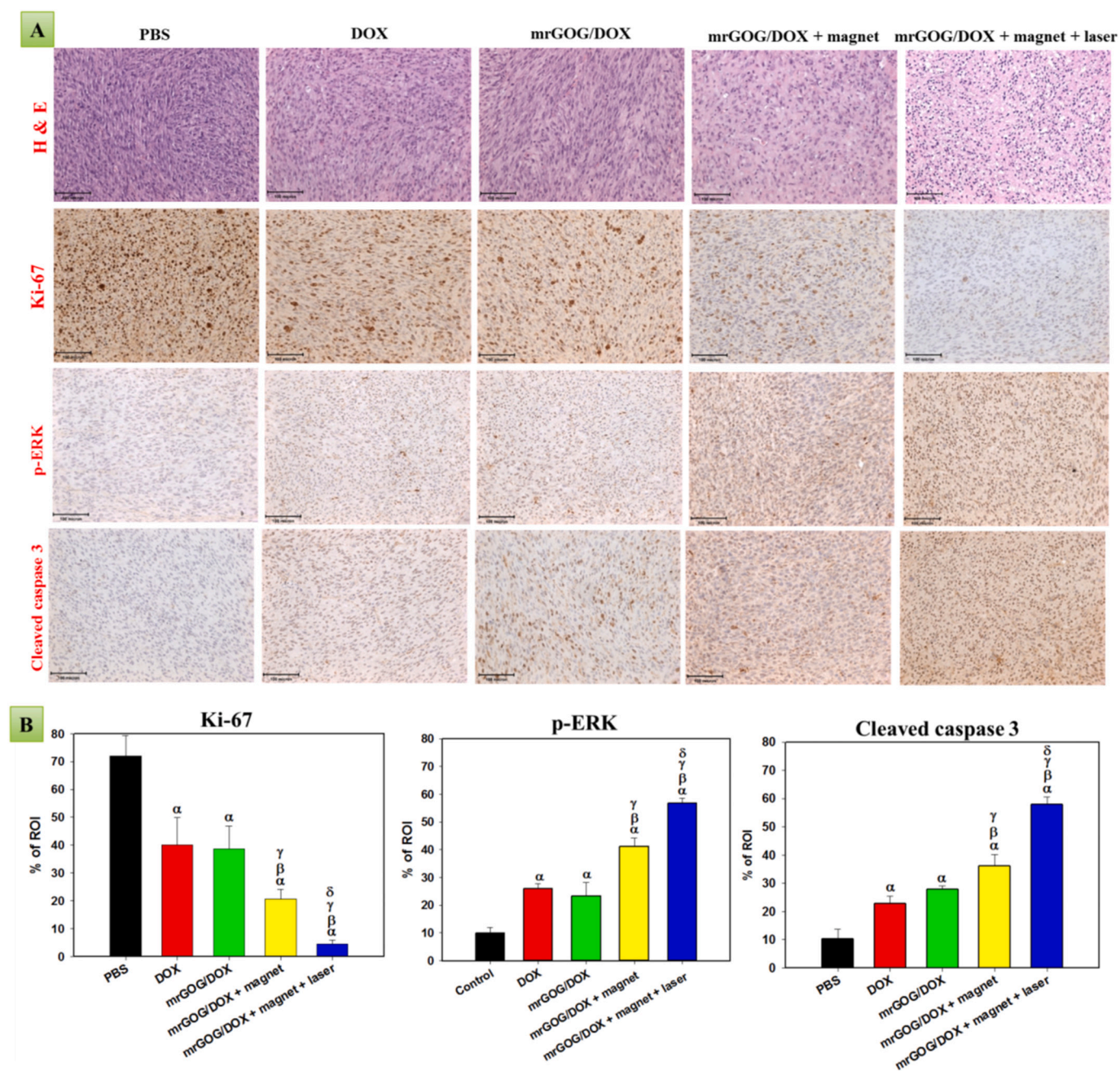


**Fig. 11.** The H&E staining and the immunohistochemical (IHC) staining of Ki-67, p-ERK and cleaved caspase 3 after different treatments (bar = 100  $\mu$ m) (A) and the quantitative analysis of IHC staining results (B).

dual targeting ability from GRPR-binding peptide-mediated active targeting as well as CMNP-mediated magnetic targeting, mrGOG offers the best outcomes in chemotherapy, which when combined with NIR laser for photothermal therapy can induce the highest cytotoxicity for cell apoptosis of GRPR-overexpressing U87 glioblastoma cells. For translation into combination cancer therapy in vivo, the xenograft tumor model strongly supports the in vitro anti-tumor efficacy. The diminished cancer cell proliferation, retarded tumor size increase and upregulated expression of apoptosis maker proteins with mrGOG/DOX + magnet + laser treatment announces successful treatment of U87 tumors. Supported by the biocompatibility in vitro and the safety in vivo, mrGOG will be a potential nanocomposite for combination chemo-photothermal cancer therapy.

#### Declaration of competing interest

The authors declare that they have no known competing financial interests or personal relationships that could have appeared to influence the work reported in this paper.

#### Acknowledgments

The authors would like to thank the Ministry of Science and Technology of Taiwan (ROC) (MOST106-2314-B-182-013-MY2) and Chang Gung Memorial Hospital (CMRPD2L0101, CMRPD2I0042 and CORPG3K0081) for financial supports.

## Appendix A. Supplementary data

Supplementary data to this article can be found online at <https://doi.org/10.1016/j.msec.2021.112311>.

## References

- [1] P. Anand, A.B. Kunnumakkara, C. Sundaram, K.B. Harikumar, S.T. Tharakan, O. S. Lai, B. Sung, B.B. Aggarwal, Cancer is a preventable disease that requires major lifestyle changes, *Pharm. Res.* 25 (9) (2008) 2097–2116.
- [2] S. Kruger, M. Ilmer, S. Kobold, B.L. Cadilha, S. Endres, S. Ormanns, G. Schuebbe, B. W. Renz, J.G. D'Haese, H. Schloesser, V. Heinemann, M. Subklewe, S. Boeck, J. Werner, M. von Bergwelt-Baildon, Advances in cancer immunotherapy 2019 – latest trends, *J. Exp. Clin. Cancer Res.* 38 (1) (2019) 268.
- [3] M. Goldberg, R. Langer, X. Jia, Nanostructured materials for applications in drug delivery and tissue engineering, *J. Biomater. Sci. Polym. Ed.* 18 (3) (2007) 241–268.
- [4] R. Duncan, The dawning era of polymer therapeutics, *Nat. Rev. Drug Discov.* 2 (5) (2003) 347–360.
- [5] R.K. Thapa, Y. Choi, J.-H. Jeong, Y.S. Youn, H.-G. Choi, C.S. Yong, J.O. Kim, Folate-mediated targeted delivery of combination chemotherapeutics loaded reduced graphene oxide for synergistic chemo-photothermal therapy of cancers, *Pharm. Res.* 33 (11) (2016) 2815–2827.
- [6] W. Miao, G. Shim, C.M. Kang, S. Lee, Y.S. Choe, H.-G. Choi, Y.-K. Oh, Cholesteryl hyaluronic acid-coated, reduced graphene oxide nanosheets for anti-cancer drug delivery, *Biomaterials* 34 (37) (2013) 9638–9647.
- [7] Y.-J. Lu, P.-Y. Lin, P.-H. Huang, C.-Y. Kuo, K.T. Shalumon, M.-Y. Chen, J.-P. Chen, Magnetic graphene oxide for dual targeted delivery of doxorubicin and photothermal therapy, *Nanomaterials* 8 (4) (2018) 193.
- [8] C. Liang, J. Song, Y. Zhang, Y. Guo, M. Deng, W. Gao, J. Zhang, Facile approach to prepare rGO@Fe<sub>3</sub>O<sub>4</sub> microspheres for the magnetically targeted and NIR-responsive chemo-photothermal combination therapy, *Nanoscale Res. Lett.* 15 (1) (2020) 86.
- [9] E.R. Spindel, E. Giladi, P. Brehm, R.H. Goodman, T.P. Segerson, Cloning and functional characterization of a complementary DNA encoding the murine fibroblast bombesin/gastrin-releasing peptide receptor, *Mol. Endocrinol.* (Baltimore, Md.) 4 (12) (1990) 1956–1963.
- [10] A. Varvarigou, P. Bouziotis, C. Zikos, F. Scopinaro, G. De Vincentis, Gastrin-releasing peptide (GRP) analogues for cancer imaging, *Cancer Biother. Radiopharm.* 19 (2) (2004) 219–229.
- [11] J.B. Dietrich, Neuropeptides, antagonists and cell proliferation: bombesin as an example, *Cell. Mol. Biol. (Noisy-le-Grand)* 40 (6) (1994) 731–746.
- [12] S. Narayan, Y.-S. Guo, C.M. Townsend, P. Singh, Specific binding and growth effects of bombesin-related peptides on mouse colon cancer cells in vitro, *Cancer Res.* 50 (21) (1990) 6772–6778.
- [13] F. Cuttitta, D.N. Carney, J. Mulshine, T.W. Moody, J. Fedorko, A. Fischler, J. D. Minna, Bombesin-like peptides can function as autocrine growth factors in human small-cell lung cancer, *Nature* 316 (6031) (1985) 823–826.
- [14] C.B. Farias, R.C. Lima, L.O. Lima, D.G. Flores, L. Meurer, A.L. Brunetto, G. Schwartzmann, R. Roesler, Stimulation of proliferation of U138-MG glioblastoma cells by gastrin-releasing peptide in combination with agents that enhance cAMP signaling, *Oncology* 75 (1–2) (2008) 27–31.
- [15] A.M. Bajo, A.V. Schally, K. Groot, K. Szepeshazi, Bombesin antagonists inhibit proangiogenic factors in human experimental breast cancers, *Br. J. Cancer* 90 (1) (2004) 245–252.
- [16] D. Pooja, A. Gunukula, N. Gupta, D.J. Adams, H. Kulhari, Bombesin receptors as potential targets for anticancer drug delivery and imaging, *Int. J. Biochem. Cell Biol.* 114 (2019), 105567.
- [17] P. Moreno, I. Ramos-Álvarez, T.W. Moody, R.T. Jensen, Bombesin related peptides/receptors and their promising therapeutic roles in cancer imaging, targeting and treatment, *Expert Opin. Ther. Targets* 20 (9) (2016) 1055–1073.
- [18] S. Alshehri, W. Fan, W. Zhang, J.C. Garrison, In vitro evaluation and biodistribution studies of HPMA copolymers targeting the gastrin releasing peptide receptor in prostate cancer, *Pharm. Res.* 37 (11) (2020) 229.
- [19] D.G. Flores, L. Meurer, A.F. Uberti, B.R. Macedo, G. Lenz, A.L. Brunetto, G. Schwartzmann, R. Roesler, Gastrin-releasing peptide receptor content in human glioma and normal brain, *Brain Res. Bull.* 82 (1–2) (2010) 95–98.
- [20] P.R. Menegotto, P.L. da Costa Lopez, B.K. Souza, C.B. de Farias, E.C. Filippi-Chiela, I.A. Vieira, G. Schwartzmann, G. Lenz, R. Roesler, Gastrin-releasing peptide receptor knockdown induces senescence in glioblastoma cells, *Mol. Neurobiol.* 54 (2) (2017) 888–894.
- [21] Z. Szereday, A.V. Schally, A. Nagy, A. Plonowski, A.M. Bajo, G. Halmos, K. Szepeshazi, K. Groot, Effective treatment of experimental U-87MG human glioblastoma in nude mice with a targeted cytotoxic bombesin analogue, AN-215, *Br. J. Cancer* 86 (8) (2002) 1322–1327.
- [22] M.S. de Oliveira, G. Cechim, E. Braganhol, D.G. Santos, L. Meurer, C.G. de Castro, A.L. Brunetto, G. Schwartzmann, A.M.O. Battastini, G. Lenz, R. Roesler, Anti-proliferative effect of the gastrin-release peptide receptor antagonist RC-3095 plus temozolomide in experimental glioblastoma models, *J. Neuro-Oncol.* 93 (2) (2009) 191–201.
- [23] L. Hosta-Rigau, I. Olmedo, J. Arbiol, L.J. Cruz, M.J. Kogan, F. Albericio, Multifunctionalized gold nanoparticles with peptides targeted to gastrin-releasing peptide receptor of a tumor cell line, *Bioconjug. Chem.* 21 (6) (2010) 1070–1078.
- [24] S. Nomura, Y. Morimoto, H. Tsujimoto, M. Arake, M. Harada, D. Saitoh, I. Hara, E. Ozeki, A. Satoh, E. Takayama, K. Hase, Y. Kishi, H. Ueno, Highly reliable, targeted photothermal cancer therapy combined with thermal dosimetry using a near-infrared absorbent, *Sci. Rep.* 10 (1) (2020) 9765.
- [25] A.C.V. Doughty, A.R. Hoover, E. Layton, C.K. Murray, E.W. Howard, W.R. Chen, Nanomaterial applications in photothermal therapy for cancer, *Materials (Basel, Switzerland)* 12 (5) (2019) 779.
- [26] X. Cai, X. Jia, W. Gao, K. Zhang, M. Ma, S. Wang, Y. Zheng, J. Shi, H. Chen, A versatile nanotheranostic agent for efficient dual-mode imaging guided synergistic chemo-thermal tumor therapy, *Adv. Funct. Mater.* 25 (17) (2015) 2520–2529.
- [27] D. Wang, Z. Xu, H. Yu, X. Chen, B. Feng, Z. Cui, B. Lin, Q. Yin, Z. Zhang, C. Chen, J. Wang, W. Zhang, Y. Li, Treatment of metastatic breast cancer by combination of chemotherapy and photothermal ablation using doxorubicin-loaded DNA wrapped gold nanorods, *Biomaterials* 35 (22) (2014) 8374–8384.
- [28] Z. Li, Y. Chen, Y. Yang, Y. Yu, Y. Zhang, D. Zhu, X. Yu, X. Ouyang, Z. Xie, Y. Zhao, L. Li, Recent advances in nanomaterials-based chemo-photothermal combination therapy for improving cancer treatment, *Front. Bioeng. Biotechnol.* 7 (2019) 293.
- [29] T.P. Dasari Shareena, D. McShan, A.K. Dasmahapatra, P.B. Tchounwou, A review on graphene-based nanomaterials in biomedical applications and risks in environment and health, *Nano-Micro Lett.* 10 (3) (2018) 53.
- [30] J. Liu, J. Dong, T. Zhang, Q. Peng, Graphene-based nanomaterials and their potentials in advanced drug delivery and cancer therapy, *J. Control. Release* 286 (2018) 64–73.
- [31] J. Bai, Y. Liu, X. Jiang, Multifunctional PEG-GO/CuS nanocomposites for near-infrared chemo-photothermal therapy, *Biomaterials* 35 (22) (2014) 5805–5813.
- [32] X. Wang, Q. Han, N. Yu, J. Li, L. Yang, R. Yang, C. Wang, Aptamer-conjugated graphene oxide-gold nanocomposites for targeted chemo-photothermal therapy of cancer cells, *J. Mater. Chem. B* 3 (19) (2015) 4036–4042.
- [33] H. Kim, D. Lee, J. Kim, T.-i. Kim, W.J. Kim, Photothermally triggered cytosolic drug delivery via endosome disruption using a functionalized reduced graphene oxide, *ACS Nano* 7 (8) (2013) 6735–6746.
- [34] J. Chen, H. Liu, C. Zhao, G. Qin, G. Xi, T. Li, X. Wang, T. Chen, One-step reduction and PEGylation of graphene oxide for photothermally controlled drug delivery, *Biomaterials* 35 (18) (2014) 4986–4995.
- [35] J.T. Robinson, S.M. Tabakman, Y. Liang, H. Wang, H. Sanchez Casalongue, D. Vinh, H. Dai, Ultrasmall reduced graphene oxide with high near-infrared absorbance for photothermal therapy, *J. Am. Chem. Soc.* 133 (17) (2011) 6825–6831.
- [36] B.S. Dash, G. Jose, Y.-J. Lu, J.-P. Chen, Functionalized reduced graphene oxide as a versatile tool for cancer therapy, *Int. J. Mol. Sci.* 22 (6) (2021) 2989.
- [37] M. Neamt, C. Nadejde, V.-D. Hodoroaba, R.J. Schneider, L. Verestiuc, U. Panne, Functionalized magnetic nanoparticles: synthesis, characterization, catalytic application and assessment of toxicity, *Sci. Rep.* 8 (1) (2018) 6278.
- [38] W. Wu, Z. Wu, T. Yu, C. Jiang, W.-S. Kim, Recent progress on magnetic iron oxide nanoparticles: synthesis, surface functional strategies and biomedical applications, *Sci. Technol. Adv. Mater.* 16 (2) (2015), 023501.
- [39] S. Rostamnia, E. Doustkhah, Synthesis of water-dispersed magnetic nanoparticles (H2O-DMNPs) of  $\beta$ -cyclodextrin modified Fe<sub>3</sub>O<sub>4</sub> and its catalytic application in Kabachnik–Fields multicomponent reaction, *J. Magn. Magn. Mater.* 386 (2015) 111–116.
- [40] S. Rostamnia, B. Gholipour, X. Liu, Y. Wang, H. Arandiyani, NH<sub>2</sub>-coordinately immobilized tris(8-quinolinolato)iron onto the silica coated magnetite nanoparticle: Fe<sub>3</sub>O<sub>4</sub>@SiO<sub>2</sub>-Fe<sub>3</sub>O<sub>4</sub> as a selective Fenton-like catalyst for clean oxidation of sulfides, *J. Colloid Interface Sci.* 511 (2018) 447–455.
- [41] M. Heidarizadeh, E. Doustkhah, S. Rostamnia, P.F. Rezaei, F.D. Harzevili, B. Zeynizadeh, Dithiocarbamate to modify magnetic graphene oxide nanocomposite (Fe<sub>3</sub>O<sub>4</sub>-GO): a new strategy for covalent enzyme (lipase) immobilization to fabrication a new nanobiocatalyst for enzymatic hydrolysis of PNPD, *Int. J. Biol. Macromol.* 101 (2017) 696–702.
- [42] H. Alamgholiloo, N.N. Pesyan, R. Mohammadi, S. Rostamnia, M. Shokouhimehr, Synergistic advanced oxidation process for the fast degradation of ciprofloxacin antibiotics using a GO/CuMOF-magnetic ternary nanocomposite, *J. Environ. Chem. Eng.* 9 (4) (2021), 105486.
- [43] E. Doustkhah, S. Rostamnia, Covalently bonded sulfonic acid magnetic graphene oxide: Fe<sub>3</sub>O<sub>4</sub>@GO-Pr-SO<sub>3</sub>H as a powerful hybrid catalyst for synthesis of indazolophthalazinetriones, *J. Colloid Interface Sci.* 478 (2016) 280–287.
- [44] P.M. Price, W.E. Mahmoud, A.A. Al-Ghamdi, L.M. Bronstein, Magnetic drug delivery: where the field is going, *Front. Chem.* 6 (619) (2018).
- [45] R. Gonzalez-Rodriguez, E. Campbell, A. Naumov, Multifunctional graphene oxide/iron oxide nanoparticles for magnetic targeted drug delivery dual magnetic resonance/fluorescence imaging and cancer sensing, *PLoS One* 14 (6) (2019), e0217072.
- [46] X. Ma, H. Tao, K. Yang, L. Feng, L. Cheng, X. Shi, Y. Li, L. Guo, Z. Liu, A functionalized graphene oxide-iron oxide nanocomposite for magnetically targeted drug delivery, photothermal therapy, and magnetic resonance imaging, *Nano Res.* 5 (3) (2012) 199–212.
- [47] C. Barrera, H. Groot, W. Vargas, D. Narváez, Efficacy and molecular effects of a reduced graphene oxide/Fe<sub>3</sub>O<sub>4</sub> nanocomposite in photothermal therapy against cancer, *Int. J. Nanomedicine* 15 (2020) 6421–6432.
- [48] C. Xu, S. Shi, L. Feng, F. Chen, S.A. Graves, E.B. Ehlerding, S. Goel, H. Sun, C. G. England, R.J. Nickles, Z. Liu, T. Wang, W. Cai, Long circulating reduced graphene oxide-iron oxide nanoparticles for efficient tumor targeting and multimodality imaging, *Nanoscale* 8 (25) (2016) 12683–12692.
- [49] X.J. Lee, H.N. Lim, N.S.K. Gowthaman, M.B.A. Rahman, C.A. Che Abdullah, K. Muthoosamy, In-situ surface functionalization of superparamagnetic reduced



- graphene oxide – Fe<sub>3</sub>O<sub>4</sub> nanocomposite via *Ganoderma lucidum* extract for targeted cancer therapy application, *Appl. Surf. Sci.* 512 (2020), 145738.
- [50] M. Răcuciu, D.E. Creangă, A. Airinei, Citric-acid-coated magnetite nanoparticles for biological applications, *Eur. Phys. J. E* 21 (2) (2006) 117–121.
- [51] G. Jose, Y.-J. Lu, H.-A. Chen, H.-L. Hsu, J.-T. Hung, T.S. Anilkumar, J.-P. Chen, Hyaluronic acid modified bubble-generating magnetic liposomes for targeted delivery of doxorubicin, *J. Magn. Magn. Mater.* 474 (2019) 355–364.
- [52] G. Jose, Y.J. Lu, J.T. Hung, A.L. Yu, J.P. Chen, Co-delivery of CPT-11 and panobinostat with anti-GD2 antibody conjugated immunoliposomes for targeted combination chemotherapy, *Cancers* 12 (11) (2020).
- [53] Y. Zhang, B. Chen, L. Zhang, J. Huang, F. Chen, Z. Yang, J. Yao, Z. Zhang, Controlled assembly of Fe<sub>3</sub>O<sub>4</sub> magnetic nanoparticles on graphene oxide, *Nanoscale* 3 (4) (2011) 1446–1450.
- [54] H. Liu, T. Kuila, N.H. Kim, B.-C. Ku, J.H. Lee, In situ synthesis of the reduced graphene oxide–polyethyleneimine composite and its gas barrier properties, *J. Mater. Chem. A* 1 (11) (2013) 3739–3746.
- [55] X. Cai, M. Lin, S. Tan, W. Mai, Y. Zhang, Z. Liang, Z. Lin, X. Zhang, The use of polyethyleneimine-modified reduced graphene oxide as a substrate for silver nanoparticles to produce a material with lower cytotoxicity and long-term antibacterial activity, *Carbon* 50 (10) (2012) 3407–3415.
- [56] S. Roy, X. Tang, T. Das, L. Zhang, Y. Li, S. Ting, X. Hu, C.Y. Yue, Enhanced molecular level dispersion and interface bonding at low loading of modified graphene oxide to fabricate super nylon 12, *Composites* 7 (5) (2015) 3142–3151.
- [57] D. Zaharie-Butucel, M. Potara, A.M. Craciun, R. Boukherroub, S. Szunerits, S. Astlean, Revealing the structure and functionality of graphene oxide and reduced graphene oxide/pyrene carboxylic acid interfaces by correlative spectral and imaging analysis, *Phys. Chem. Chem. Phys.* 19 (24) (2017) 16038–16046.
- [58] P. Chithaiah, M.M. Raju, G.U. Kulkarni, C.N.R. Rao, Simple synthesis of nanosheets of rGO and nitrogenated rGO, *Beilstein J. Nanotechnol.* 11 (2020) 68–75.
- [59] J. Porwal, N. Karanwal, S. Kaul, S.L. Jain, Carbocatalysis: N-doped reduced graphene oxide catalyzed esterification of fatty acids with long chain alcohols, *New J. Chem.* 40 (2) (2016) 1547–1553.
- [60] O. Akhavan, E. Ghaderi, S. Aghayee, Y. Fereydooni, A. Talebi, The use of a glucose-reduced graphene oxide suspension for photothermal cancer therapy, *J. Mater. Chem.* 22 (27) (2012) 13773.
- [61] L.Q. Xu, W.J. Yang, K.-G. Neoh, E.-T. Kang, G.D. Fu, Dopamine-induced reduction and functionalization of graphene oxide nanosheets 43 (20) (2010) 8336–8339.
- [62] D. Li, M.B. Müller, S. Gilje, R.B. Kaner, G.G. Wallace, Processable aqueous dispersions of graphene nanosheets, *Nat. Nanotechnol.* 3 (2) (2008) 101–105.
- [63] M. Chu, Y. Shao, J. Peng, X. Dai, H. Li, Q. Wu, D. Shi, Near-infrared laser light mediated cancer therapy by photothermal effect of Fe<sub>3</sub>O<sub>4</sub> magnetic nanoparticles, *Biomaterials* 34 (16) (2013) 4078–4088.
- [64] M. Oishi, H. Hayashi, M. Iijima, Y. Nagasaki, Endosomal release and intracellular delivery of anticancer drugs using pH-sensitive PEGylated nanogels, *J. Mater. Chem.* 17 (35) (2007) 3720–3725.
- [65] M. Lee, J. Jeong, D. Kim, Intracellular uptake and pH-dependent release of doxorubicin from the self-assembled micelles based on amphiphilic polyaspartamide graft copolymers, *Biomacromolecules* 16 (1) (2015) 136–144.
- [66] K. Ryu, J. Park, T.-I. Kim, Effect of pH-responsive charge-conversional polymer coating to cationic reduced graphene oxide nanostructures for tumor microenvironment-targeted drug delivery systems, *Nanomaterials (Basel)* 9 (9) (2019) 1289.
- [67] Q. Mu, G. Su, L. Li, B.O. Gilbertson, L.H. Yu, Q. Zhang, Y.-P. Sun, B. Yan, Size-dependent cell uptake of protein-coated graphene oxide nanosheets, *ACS Appl. Mater. Interfaces* 4 (4) (2012) 2259–2266.
- [68] Y.-J. Lu, K.-C. Wei, C.-C.M. Ma, S.-Y. Yang, J.-P. Chen, Dual targeted delivery of doxorubicin to cancer cells using folate-conjugated magnetic multi-walled carbon nanotubes, *Colloids Surf. B: Biointerfaces* 89 (2012) 1–9.
- [69] C. Fang, F.M. Kievit, Y.C. Cho, H. Mok, O.W. Press, M. Zhang, Effect of cationic side-chains on intracellular delivery and cytotoxicity of pH sensitive polymer-doxorubicin nanocarriers, *Nanoscale* 4 (22) (2012) 7012–7020.
- [70] Y. Zhang, X. Zhan, J. Xiong, S. Peng, W. Huang, R. Joshi, Y. Cai, Y. Liu, R. Li, K. Yuan, N. Zhou, W. Min, Temperature-dependent cell death patterns induced by functionalized gold nanoparticle photothermal therapy in melanoma cells, *Sci. Rep.* 8 (1) (2018) 8720.
- [71] V. Kaushal, C. Herzog, R.S. Haun, G.P. Kaushal, Caspase protocols in mice, *Methods Mol. Biol.* 1133 (2014) 141–154.
- [72] S. Cagnol, J.-C. Chambard, ERK and cell death: mechanisms of ERK-induced cell death – apoptosis, autophagy and senescence, *FEBS J.* 277 (1) (2010) 2–21.
- [73] L. Dubrez, S. Causse, N. Borges Bonan, B. Dumétier, C. Garrido, Heat-shock proteins: chaperoning DNA repair, *Oncogene* 39 (3) (2020) 516–529.
- [74] Z. Wang, S. Li, M. Zhang, Y. Ma, Y. Liu, W. Gao, J. Zhang, Y. Gu, Laser-triggered small interfering RNA releasing gold nanoshells against heat shock protein for sensitized photothermal therapy, *Adv. Sci. (Weinheim, Baden-Württemberg, Germany)* 4 (2) (2017), 1600327.
- [75] K.A. Court, H. Hatakeyama, S.Y. Wu, M.S. Lingegowda, C. Rodríguez-Aguayo, G. López-Berestein, L. Ju-Seog, C. Rinaldi, E.J. Juan, A.K. Sood, M. Torres-Lugo, <em>HSP70</em> inhibition synergistically enhances the effects of magnetic fluid hyperthermia in ovarian cancer, *Mol. Cancer Ther.* 16 (5) (2017) 966.
- [76] K. Amin, R.-M. Dannenfels, In vitro hemolysis: guidance for the pharmaceutical scientist, *J. Pharm. Sci.* 95 (6) (2006) 1173–1176.
- [77] A. Strasser, S. Cory, J.M. Adams, Deciphering the rules of programmed cell death to improve therapy of cancer and other diseases, *EMBO J.* 30 (18) (2011) 3667–3683.
- [78] M. Jelínek, K. Balušíková, M. Schmiedlová, V. Němcová-Fürstová, J. Sránek, J. Stancíková, I. Zanardi, I. Ojima, J. Kovár, The role of individual caspases in cell death induction by taxanes in breast cancer cells, *Cancer Cell Int.* 15 (1) (2015) 8.
- [79] R. Iurlaro, C. Muñoz-Pinedo, Cell death induced by endoplasmic reticulum stress, *FEBS J.* 283 (14) (2016) 2640–2652.

## Article

# The Demethoxy Derivatives of Curcumin Exhibit Greater Differentiation Suppression in 3T3-L1 Adipocytes than Curcumin: A Mechanistic Study of Adipogenesis and Molecular Docking

Ahmed Alalaiwe <sup>1</sup> , Jia-You Fang <sup>2,3,4</sup> , Hsien-Ju Lee <sup>2</sup>, Chun-Hui Chiu <sup>3,5</sup>  and Ching-Yun Hsu <sup>3,6,\*</sup>

<sup>1</sup> Department of Pharmaceutics, College of Pharmacy, Prince Sattam Bin Abdulaziz University, Al Kharj 11942, Saudi Arabia; alalaiwe@gmail.com

<sup>2</sup> Pharmaceutics Laboratory, Graduate Institute of Natural Products, Chang Gung University, Kweishan, Taoyuan 333, Taiwan; fajy@mail.cgu.edu.tw (J.-Y.F.); daxialeetw@gmail.com (H.-J.L.)

<sup>3</sup> Research Center for Food and Cosmetic Safety and Research Center for Chinese Herbal Medicine, Chang Gung University of Science and Technology, Kweishan, Taoyuan 333, Taiwan; chchiu@mail.cgu.edu.tw

<sup>4</sup> Department of Anesthesiology, Chang Gung Memorial Hospital, Kweishan, Taoyuan 333, Taiwan

<sup>5</sup> Graduate Institute of Health Industry Technology, Chang Gung University of Science and Technology, Kweishan, Taoyuan 333, Taiwan

<sup>6</sup> Department of Nutrition and Health Sciences, Chang Gung University of Science and Technology, Kweishan, Taoyuan 333, Taiwan

\* Correspondence: cyhsu@mail.cgu.edu.tw



**Citation:** Alalaiwe, A.; Fang, J.-Y.; Lee, H.-J.; Chiu, C.-H.; Hsu, C.-Y. The Demethoxy Derivatives of Curcumin Exhibit Greater Differentiation Suppression in 3T3-L1 Adipocytes than Curcumin: A Mechanistic Study of Adipogenesis and Molecular Docking. *Biomolecules* **2021**, *11*, 1025. <https://doi.org/10.3390/biom11071025>

Academic Editor: Chi-Feng Hung

Received: 21 June 2021

Accepted: 12 July 2021

Published: 14 July 2021

**Publisher's Note:** MDPI stays neutral with regard to jurisdictional claims in published maps and institutional affiliations.



**Copyright:** © 2021 by the authors. Licensee MDPI, Basel, Switzerland. This article is an open access article distributed under the terms and conditions of the Creative Commons Attribution (CC BY) license (<https://creativecommons.org/licenses/by/4.0/>).

**Abstract:** Curcumin is a known anti-adipogenic agent for alleviating obesity and related disorders. Comprehensive comparisons of the anti-adipogenic activity of curcumin with other curcuminoids is minimal. This study compared adipogenesis inhibition with curcumin, demethoxycurcumin (DMC), and bisdemethoxycurcumin (BDMC), and their underlying mechanisms. We differentiated 3T3-L1 cells in the presence of curcuminoids, to determine lipid accumulation and triglyceride (TG) production. The expression of adipogenic transcription factors and lipogenic proteins was analyzed by Western blot. A significant reduction in Oil red O (ORO) staining was observed in the cells treated with curcuminoids at 20  $\mu$ M. Inhibition was increased in the order of curcumin < DMC < BDMC. A similar trend was observed in the detection of intracellular TG. Curcuminoids suppressed differentiation by downregulating the expression of peroxisome proliferator-activated receptor  $\gamma$  (PPAR $\gamma$ ) and CCAAT/enhancer-binding protein  $\alpha$  (C/EBP $\alpha$ ), leading to the downregulation of the lipogenic enzymes acetyl-CoA carboxylase (ACC) and fatty acid synthase (FAS). AMP-activated protein kinase  $\alpha$  (AMPK $\alpha$ ) phosphorylation was also activated by BDMC. Curcuminoids reduced the release of proinflammatory cytokines and leptin in 3T3-L1 cells in a dose-dependent manner, with BDMC showing the greatest potency. BDMC at 20  $\mu$ M significantly decreased leptin by 72% compared with differentiated controls. Molecular docking computation indicated that curcuminoids, despite having structural similarity, had different interaction positions to PPAR $\gamma$ , C/EBP $\alpha$ , and ACC. The docking profiles suggested a possible interaction of curcuminoids with C/EBP $\alpha$  and ACC, to directly inhibit their expression.

**Keywords:** curcuminoid; demethoxycurcumin; bisdemethoxycurcumin; adipocyte; anti-adipogenesis; transcription factor

## 1. Introduction

Obesity influences one-third of adults globally, and represents a primary health problem [1]. The increasing prevalence of overweight children is also a concern. Obesity can shorten the life span and disrupt the function of many organs [2]. Collectively, this increases the risk of chronic obesity-related co-morbidities, including diabetes, hypertension, dyslipidemia, dyspnoea, fatty liver, cancer, and poor mental health [3]. The hyperplasia

and hypertrophy of adipocytes are important characteristics of obesity. Adipocytes are the primary constituent of adipose tissue and store triacylglycerol, which plays a crucial role in maintaining energy balance. In addition to storing fat, adipocytes are considered to influence endocrine cells, which secrete numerous bioactive peptides called adipokines, and has a profound impact on the metabolic homeostasis of other tissues [4]. The inhibition of adipogenesis, by reducing preadipocyte differentiation, is a promising therapeutic target to prevent or improve obesity and its associated comorbid conditions. Several anti-obesity drugs have been approved in the past ten years; however, most of them have been withdrawn due to adverse effects. For instance, amphetamine, rimonabant, and sibutramine have been shown to increase the risk of myocardial infarction and psychiatric disorder [5]. Their long-term success has also been questioned, considering weight regain after treatment discontinuation.

Natural products and phytochemicals are potential agents that ameliorate obesity via adipogenesis suppression, lipolysis enhancement, adipocyte hypertrophy inhibition, and fat cell apoptosis [6]. Herbal extracts, or their isolated compounds, can provide nutritional intervention for obesity management, due to their low cost and favorable side-effect profile. Among these phytochemicals, turmeric (*Curcuma longa*) has demonstrated beneficial activity in obesity and diabetes [7]. Curcumin is a linear diarylheptanoid that is primarily found in turmeric (Figure 1). Curcumin has been shown to have anti-inflammatory, antioxidant, neuroprotective, and chemopreventive properties [8], possibly by inhibiting preadipocyte differentiation and inflammation, as well as activating cellular antioxidants [9]. Clinical evidence supports the bioactivity of curcumin in promoting weight loss and reducing the triglyceride (TG) levels in patients with diabetes [10,11]. The pharmacological activity of turmeric is primarily derived from curcuminoids, which are a mixture of curcumin and its demethoxy derivatives, including demethoxycurcumin (DMC) and bisdemethoxycurcumin (BDMC). These polyphenols share the same structure of two benzenemethoxyl rings connected by an unsaturated chain (Figure 1). DMC and BDMC lack one and two methoxy moieties in the aromatic rings of curcumin, respectively. Antioxidant, anticancer, and neuroprotective potential of the demethoxy analogs of curcumin have been reported [11]. Although curcumin has been shown to improve obesity and the related syndromes, there is a paucity of data regarding the anti-obesity activity of DMC and BDMC. Lai et al. [12] demonstrated that BDMC inhibited the development of obesity in high-fat diet-fed mice. We aimed to systematically compare the inhibitory activity of curcumin and its demethoxy analogs against adipogenesis. The underlying mechanisms of the adipogenesis suppression by these compounds were also explored, using a cell-based study and computational molecular docking. Adipogenesis is a process that is involved in the differentiation of preadipocytes into mature adipocytes via intracellular lipid deposition. We employed an in vitro model with 3T3-L1 preadipocytes, to elucidate the molecular mechanisms of adipogenesis regulation by curcuminoids. Differentiation of the 3T3-L1 preadipocyte fibroblast cell line into mature adipocytes is one of the most commonly used in vitro models to study adipose tissue biology. Adipogenesis is controlled by the family of peroxisome proliferator-activated receptors (PPARs) and CCAAT/enhancer-binding proteins (C/EBPs). In addition, lipogenic enzymes such as acetyl-CoA carboxylase (ACC) and fatty acid synthase (FAS) are essential for anabolic lipogenesis [13]. These pathways offer the potential of therapeutic targets for combating obesity. An understanding of the underlying mechanisms regulating adipogenesis is helpful for examining obesity prevention and therapy with curcuminoids.

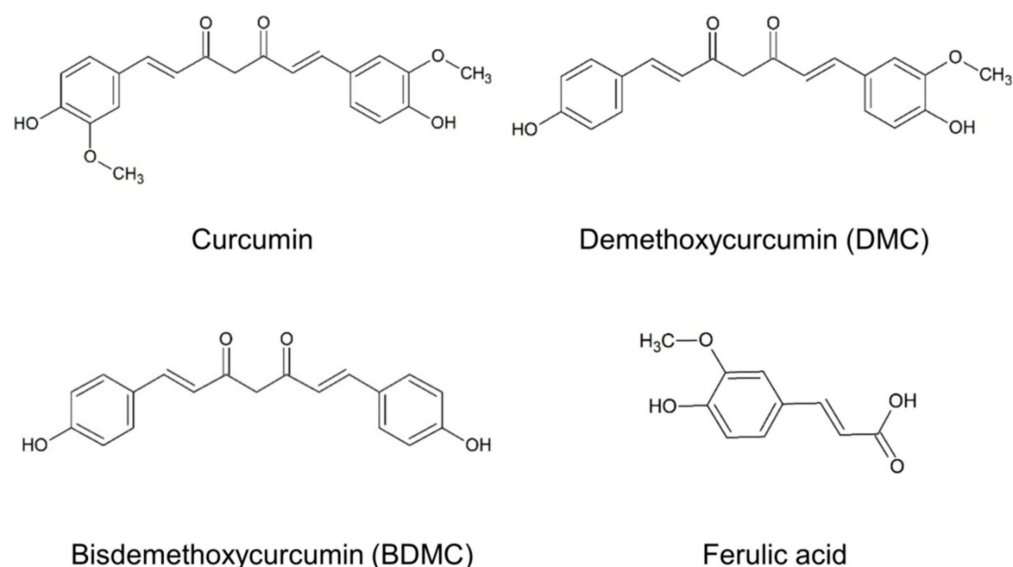


**Figure 1.** The chemical structures of curcumin, demethoxycurcumin (DMC), bisdemethoxycurcumin (BDMC), and ferulic acid.

## 2. Materials and Methods

### 2.1. Analysis of Curcuminoids in Turmeric Extract

The extract from turmeric rhizome (BCM-95) was supplied by Arjuna Natural (Kerala, India) and dissolved in ethanol. High-performance liquid chromatography (HPLC) was used to determine the amounts of curcumin, DMC, and BDMC in the extract. The HPLC system was from Hitachi Primaide (Tokyo, Japan) with an Agilent Zorbax SB-C18 column (Santa Clara, CA, USA). The mobile phase consisted of a mixture of acetonitrile and water containing 2% acetic acid (6:4). The flow rate and detection wavelength were set at 2 mL/min and 420 nm, respectively.

### 2.2. Molecular Modeling and Docking

The structures of curcuminoids were sketched by Discovery Studio version 4.1 workstation (Accelrys, San Diego, CA, USA). The physicochemical characteristics of these molecules estimated by Discovery Studio included molecular volume, predicted oil/water partition coefficient (Alog *P*), total polarity surface, hydrogen bond acceptor number, and hydrogen bond donor number. The crystal structures of PPAR $\gamma$  (protein data bank PDB ID: 1ZGY), C/EBP $\alpha$  (PDB ID: 1NWQ), and ACC (PDB ID: 2DN8) were downloaded from the RCSB Protein Data Bank ([www.rcsb.org](http://www.rcsb.org)). The molecular docking between these proteins and curcuminoids was performed by Discovery Studio. The negative CDOCKER energy was computed after conducting the docking simulation of the curcuminoids with the proteins to assess possible interactions.

### 2.3. Cell Culture and Differentiation

The 3T3-L1 preadipocytes were purchased from Bioresource Collection and Research Center (Hsinchu, Taiwan). The cells were cultured in Dulbecco's modified Eagle's medium (DMEM) containing 10% fetal bovine serum (FBS), 1% penicillin/streptomycin, and 1 mM sodium pyruvate at 37 °C in 5% CO<sub>2</sub> incubator. Two days after confluence, the cells were cultured in FBS-containing DMEM with the incorporation of 500  $\mu$ M 3-isobutyl-1-methylxanthine, 0.25  $\mu$ M dexamethasone, and 10  $\mu$ g/mL bovine insulin. After 2 days, the medium was changed to DMEM supplemented with 10% FBS and 10  $\mu$ g/mL insulin. This was continued to day 8 when the preadipocytes had fully differentiated to adipocytes.

#### 2.4. 3T3-L1 Cell Viability Assay

The preadipocytes were seeded in 96-well plates at a density of  $1 \times 10^5$  cells/well in DMEM. After 24 h, turmeric extract or curcuminoids in DMSO (0–40  $\mu$ M) were added into the well for 24 h to examine the cytotoxicity. After this treatment, the cells were cultured with 3-(4,5-dimethylthiazol-2-yl)-2,5-diphenyltetrazolium bromide (MTT) at 5  $\mu$ g/mL for a 4 h incubation. The unreacted dye was removed, and the formazan crystal was dissolved by dimethyl sulfoxide (100  $\mu$ L). The absorbance was determined at 540 nm in an enzyme-linked immunosorbent assay (ELISA) reader. The differentiated 3T3-L1 cells were also used for detecting viability. The concentration of the differentiated cells for the viability assay was  $2 \times 10^4$  cells/well.

#### 2.5. Oil Red O (ORO) Staining

Intracellular lipid accumulation in 3T3-L1 cells was detected using ORO staining. The preadipocytes were seeded in 6-well plates at a concentration of  $8 \times 10^4$  cells/well. The cells were treated with turmeric extract or curcuminoids dissolved in DMSO for 8 days. On day 8, the medium was removed, and the cells were washed using 20% isopropanol. Next, 10% formaldehyde was used to fix the cells for 1 h. The fixed cells were stained using ORO working solution for 20 min. After rinsing with double-distilled water, ORO was extracted using isopropanol (absorbance at 520 nm was measured spectrophotometrically).

#### 2.6. Triglyceride (TG) Accumulation in Cells

The treatment and differentiation of 3T3-L1 cells were carried out using the same approach as for the ORO assay. Total amount of TG was quantified using a triglyceride quantification colorimetric/fluorometric kit (Biovision, Milpitas, CA, USA) based on the manufacturer's protocol.

#### 2.7. Protein Extraction and Western Blotting

The treatment and differentiation of 3T3-L1 cells were carried out using the same approach as for the ORO assay. The 3T3-L1 cells were collected and washed in PBS and lysed in a radioimmunoprecipitation assay buffer for 30 min on ice. The cell lysate was centrifuged at 12,000 rpm and 4 °C for 20 min. The supernatant was resolved in 12% sodium dodecyl sulfate polyacrylamide gel (SDS-PAGE), and then transferred to a nitrocellulose membrane. The blots were blocked in PBS containing 0.5% Tween 20 and 5% skim milk for 1 h, then incubated overnight at 4 °C with a polyclonal antibody against PPAR $\gamma$  (1:1000), C/EBP $\alpha$  (1:500), p-AMP-activated protein kinase  $\alpha$  (p-AMPK $\alpha$ ) (1:1000), ACC (1:1000), FAS (1:1000), or  $\beta$ -actin (1:10,000) (Abcam, Cambridge, UK). The membrane was incubated with horseradish peroxidase-conjugated secondary antibody (1:8000) and visualized using an enhanced chemiluminescence kit (PerkinElmer, Waltham, MA, USA).

#### 2.8. ELISA Assay

The protein expression of interleukin (IL)-1 $\beta$ , IL-6, tumor necrosis factor (TNF)- $\alpha$ , and leptin in the supernatant of the cell medium was measured using ELISA kits (BioLegend, San Diego, CA, USA) according to manufacturer's instructions. The absorbance was determined at 450 nm using a microplate spectrophotometer. The concentration of these adipokines was estimated based on the corresponding curves.

#### 2.9. Statistical Analysis

Statistical differences were measured using the one-way analysis of variance followed by Tukey's multiple comparison test. The data distribution was checked by Kolmogorov–Smirnov test. The  $p$  values of 0.05, 0.01, and 0.001 were considered statistically significant.



### 3. Results

#### 3.1. Determination of Turmeric Extract

HPLC analysis was conducted for curcuminoid quantification in turmeric extract prior to the cell-based study. We firstly confirmed the retention time of standard curcumin, DMC, and BDMC, at 8.4, 7.3, and 6.3 min, respectively (Figure 2A). This indicated the lower lipophilicity of BDMC compared with other curcuminoids, as the shorter retention time suggests a less lipophilic compound. The representative HPLC profile of the turmeric extract indicated three peaks of curcuminoids (Figure 2B). The curcuminoid concentration in the extract was estimated with the established calibration curve (Figure 2C). The most abundant compound in the extract was curcumin (465.2 mg/g), followed by DMC (84.4 mg/g) and BDMC (5.9 mg/g).

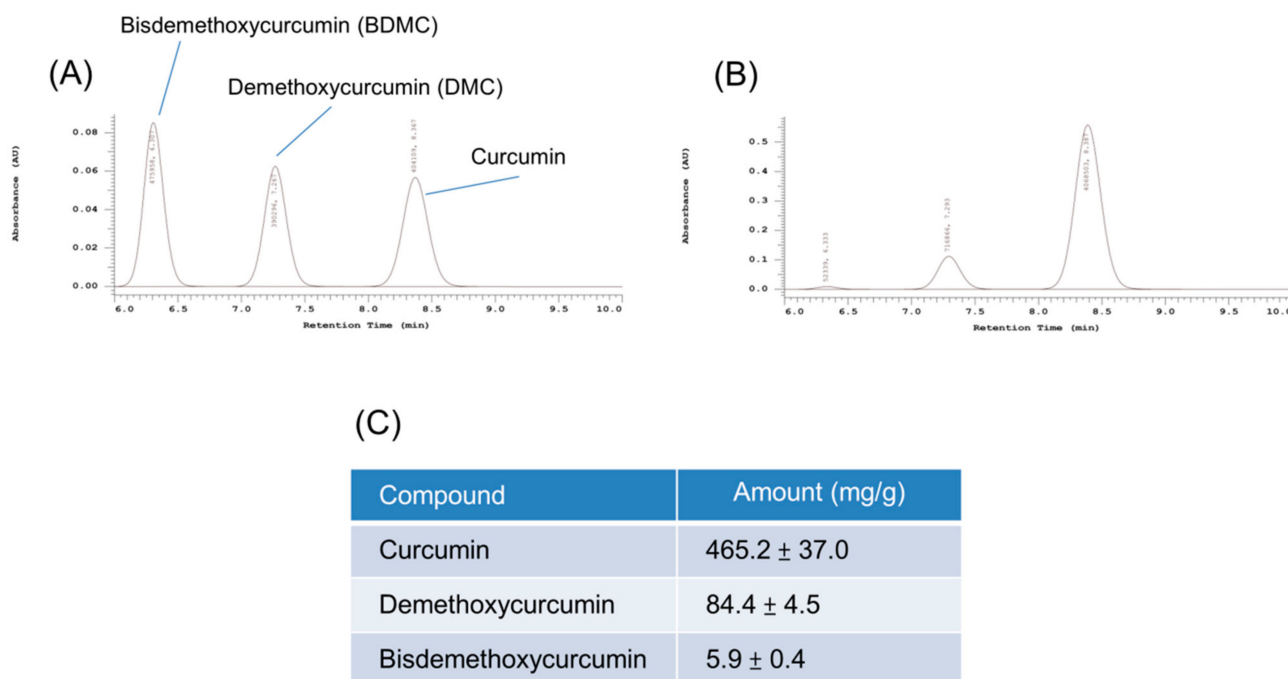


**Figure 2.** Quantitative analysis of curcumin, demethoxycurcumin (DMC), and bisdemethoxycurcumin (BDMC) in turmeric extract (BCM-95): (A) the HPLC chromatogram of the standards of three curcuminoids; (B) the HPLC chromatogram of three curcuminoids in turmeric extract; and (C) the amount (mg/g) of three curcuminoids in turmeric extract. All data are presented as the mean of three experiments ± S.E.M.

#### 3.2. Physicochemical Properties of Curcuminoids

The estimated physicochemical characteristics of curcumin, DMC, and BDMC were computed by molecular modeling, to understand the relationship with adipogenesis inhibition. Curcumin is relatively unstable in neutral or alkaline solution, and generates degradation products, such as ferulic acid. A dimer of ferulic acid is curcumin, in which two ferulates are linked through a methylene moiety (Figure 1). Thus, the physicochemical properties and anti-adipogenic effect of ferulic acid was also examined. The molecular weight of the four compounds ranged between 194 (ferulic acid) and 368 (curcumin) Da (Table 1). The molecular volume, which was predicted by molecular modeling, reflects molecular size. A correlation was found between molecular volume and molecular weight. Besides retention time, the tendency of lipophilicity can be assessed by Alog *P*. The trend of Alog *P* was as follows: ferulic acid (1.67) < curcumin (3.55) < DMC (3.57) < BDMC (3.59); however, the Alog *P* of the three curcuminoids was approximate. The H-bond acceptor number was decreased following the increase in dimethoxy. Both BDMC and ferulic acid

exhibited the H-bond acceptor number of four. All the compounds possessed two H-bond donor numbers.

**Table 1.** Physicochemical properties of curcumin and its derivatives determined by molecular modeling.

Physicochemical Property	Curcumin	DMC	BDMC	Ferulic Acid
Molecular formula	C <sub>21</sub> H <sub>20</sub> O <sub>6</sub>	C <sub>20</sub> H <sub>18</sub> O <sub>5</sub>	C <sub>19</sub> H <sub>16</sub> O <sub>4</sub>	C <sub>10</sub> H <sub>10</sub> O <sub>4</sub>
Molecular weight (Da)	368.38	338.35	308.33	194.18
Molecular volume (Å <sup>3</sup> )	295.66	267.88	241.27	151.60
Alog <i>P</i>	3.55	3.57	3.59	1.67
Hydrogen bond acceptor number	6	5	4	4
Hydrogen bond donor number	2	2	2	2

Alog *P*, predicted oil/water partition coefficient; BDMC, bisdemethoxycurcumin; DMC, demethoxycurcumin.

### 3.3. Adipocyte Viability Treated by Curcuminoids

MTT analysis was conducted in order to evaluate 3T3-L1 viability when treated with various concentrations of turmeric extract and the curcuminoids. The extract had negligible cytotoxicity within the range of 0–20 µM of the equivalent curcumin dose (Figure 3A). The adipocytes that were treated with 40 µM of the extract showed a significant decrease in viability compared with the controls. A similar result was observed for curcumin and BDMC. The cell viability following an intervention with 40 µM curcumin and BDMC was 68% and 76%, respectively. DMC and ferulic acid did not affect 3T3-L1 cell viability, even at the highest concentration of 40 µM. All the tested extracts or compounds, at doses of 0–20 µM, were considered non-cytotoxic to the cells. Concentrations of 5, 10, and 20 µM were employed for subsequent studies.

### 3.4. The Effect of Turmeric Extract and Curcuminoids on Lipid Accumulation

We next examined the effect of turmeric extract and curcuminoids on adipocyte differentiation, as determined by ORO staining and TG content. The preadipocytes differentiated into adipocytes for eight days, in the presence or absence of extract or curcuminoids. The intracellular lipids were stained by ORO. Based on the microscopic images (Figure 3B), the cells appeared to be round, with accumulated cytoplasmic lipid droplets. Lipid accumulation was estimated spectrophotometrically. Although the lipid accumulation was reduced following the extract treatment at higher concentrations, this inhibition did not achieve statistical significance (the right panel of Figure 3B). The number of intracellular lipid droplets was reduced when curcumin, DMC, or BDMC was present. The pure compounds arrested lipid deposition more profoundly than the corresponding concentration of the extract. Further, 5 µM of curcuminoid had no significant inhibitory effect on lipid accumulation. At 10 µM, a significant effect was observed with BDMC, but not curcumin and DMC. Concentrations up to 20 µM of all the curcuminoids resulted in a significant suppression of lipid accumulation compared with the controls. Lipid accumulation was decreased by 48%, 35%, and 27% with 20 µM curcumin, DMC, and BDMC, respectively. Ferulic acid did not inhibit adipocyte differentiation.

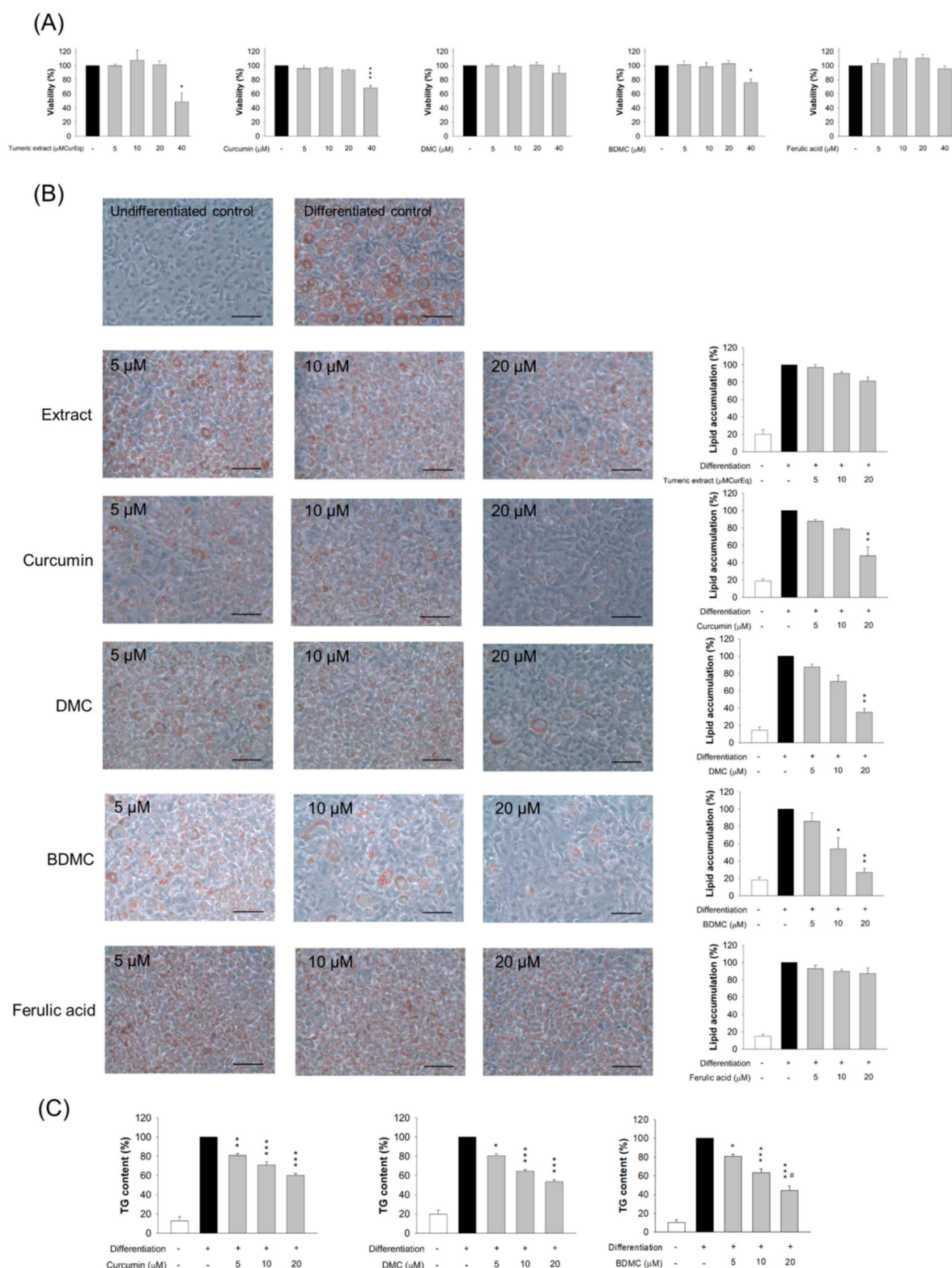


**Figure 3.** The 3T3-L1 cell viability and lipid accumulation after treatment of turmeric extract, curcuminoids, and ferulic acid. **(A)** The cell viability determined by MTT assay; **(B)** the ORO staining and the quantification of 3T3-LI cells; and **(C)** the intracellular TG content of 3T3-LI cells. All data are presented as the mean of three experiments  $\pm$  S.E.M. \*\*\*  $p < 0.001$ ; \*\*  $p < 0.01$ ; \*  $p < 0.05$  as compared to the differentiated control group. #  $p < 0.05$  as compared to the curcumin-treated group at the same dose.

We also exposed 3T3-L1 cells to the extract or compounds after the induction of differentiation. All the tested materials demonstrated no cytotoxicity against mature adipocytes at concentrations of 0–20  $\mu\text{M}$  (Figure S1A). It was found that 40  $\mu\text{M}$  of extract caused a cytotoxicity of nearly 100%. The compounds exhibited minor cytotoxicity compared with the extract in the mature 3T3-L1 cells. Lipid accumulation was unaffected when the mature adipocytes were treated with the extract and compounds (Figure S1B). This result demonstrates that the curcuminoids blocked lipid accumulation only when applied at the onset of differentiation. We then assessed whether a pretreatment of curcumin, DMC, or BDMC on preadipocytes reduced TG. The turmeric extract and ferulic acid were excluded in this experiment, because of the observed minimal effect on lipid accumulation inhibition. The TG amount was decreased following the increase in curcuminoid concentration (Figure 3C). Of the three compounds tested, BDMC displayed the greatest inhibition of TG. TG in 3T3-L1 cells was reduced by 40%, 46%, and 56% when curcumin, DMC, and BDMC were added to the differentiation medium at a concentration of 20  $\mu\text{M}$ , respectively.

### 3.5. The Effect of Curcuminoids on Expression of Adipogenic and Lipogenic Enzymes

We sought to investigate the pathways through which curcuminoids inhibited adipogenesis. To explore the impact of curcuminoids on 3T3-L1 differentiation, by downregulating the adipogenic transcription factors PPAR $\gamma$  and C/EBP $\alpha$ , the protein expression was determined. PPAR $\gamma$  is a nuclear hormone receptor that is expressed during adipocyte differentiation, prior to C/EBP $\alpha$ . PPAR $\gamma$  and C/EBP $\alpha$  were elevated during adipocyte differentiation in the absence of curcuminoids. PPAR $\gamma$  was decreased in differentiated 3T3-L1 cells that had been treated with curcuminoids at 20  $\mu\text{M}$ ; however, statistical significance was only reached in the BDMC-treated group (Figure 4A). Curcumin at 20  $\mu\text{M}$  considerably expressed less C/EBP $\alpha$  compared with the differentiated controls. DMC at 5  $\mu\text{M}$  showed higher potency to inhibit C/EBP $\alpha$  compared with curcumin. Nevertheless, this effect was not observed at concentrations of 10 and 20  $\mu\text{M}$ . BDMC at 5 and 10  $\mu\text{M}$  appeared to have no effect on C/EBP $\alpha$  inhibition. BDMC at 20  $\mu\text{M}$  significantly decreased the expression of C/EBP $\alpha$  by 55%. These results indicate that curcuminoids mediated adipocyte differentiation by suppressing adipogenic enzymes.

To verify the hypothesis that curcuminoids exerted anti-adipogenic activity through the modulation of transcription factors, a PPAR $\gamma$  inhibitor, GW9662, was used to treat the cells, in order to examine the TG levels. PPAR $\gamma$  inhibition by GW9662 markedly attenuated the TG content in the cells (Figure 4B). This result suggests the involvement of PPAR $\gamma$  regulation in the production of TG. We also found a significant decrease in TG, by nearly 50%, following the treatment of BDMC. The intervention of a PPAR $\gamma$  inhibitor in the BDMC-treated cells did not impact the TG levels, suggesting that factors other than transcription factors controlled adipogenesis inhibition by BDMC. AMPK $\alpha$  is a regulator of energy metabolism. The phosphorylation of AMPK $\alpha$  causes anti-adipogenesis by ACC suppression. We probed whether BDMC modulated AMPK phosphorylation. An increase in phospho-AMPK $\alpha$  after treatment of BDMC at 20  $\mu\text{M}$  was observed (Figure 4C), indicating that BDMC modulated lipid metabolism, in part due to AMPK $\alpha$  activation.

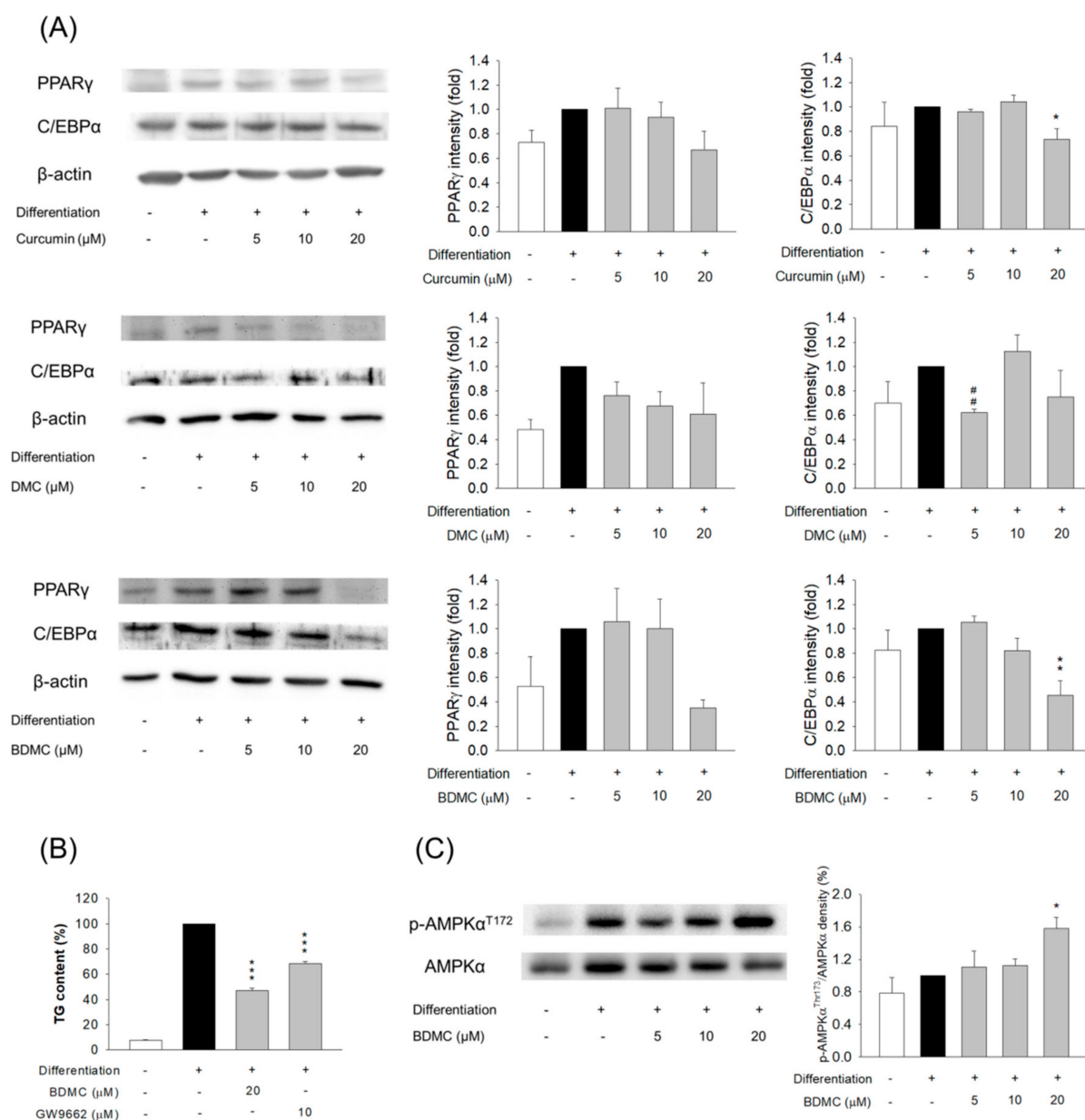


**Figure 4.** The effect of curcuminoids on transcription factors of 3T3-L1 cells. **(A)** The protein expression of PPAR $\gamma$  and C/EBP $\alpha$  after treatment of curcuminoids at 0–20  $\mu$ M; **(B)** the intracellular TG content of 3T3-L1 cells after the treatment of BDMC and/or GW9662; and **(C)** the protein expression and AMPK $\alpha$  after treatment of BDMC at 0–20  $\mu$ M. All data are presented as the mean of three experiments  $\pm$  S.E.M. \*\*\*  $p < 0.001$ ; \*\*  $p < 0.01$ ; \*  $p < 0.05$  as compared to the differentiated control group. <sup>#</sup>  $p < 0.01$  as compared to the curcumin-treated group at the same dose.

We next explored the protein level of lipogenic genes in the curcuminoid-treated 3T3-L1 cells. ACC is a rate-limiting enzyme in the synthesis of fatty acids. We found a notable increase in ACC after adipocyte differentiation (Figure 5A). Curcumin at 5 and 10  $\mu$ M did not significantly change the overexpression of ACC, whereas a 20  $\mu$ M dose lowered the ACC expression. A similar trend was observed for FAS downregulation by curcumin. DMC caused the inhibition of ACC and FAS in a dose-dependent manner (Figure 5B). BDMC showed greater inhibition on ACC than curcumin and DMC (Figure 5C). BDMC reduced ACC upregulation in differentiated cells by 92% at a 20  $\mu$ M dose. This result suggested the involvement of lipogenic pathways in reduced differentiation by curcuminoids.



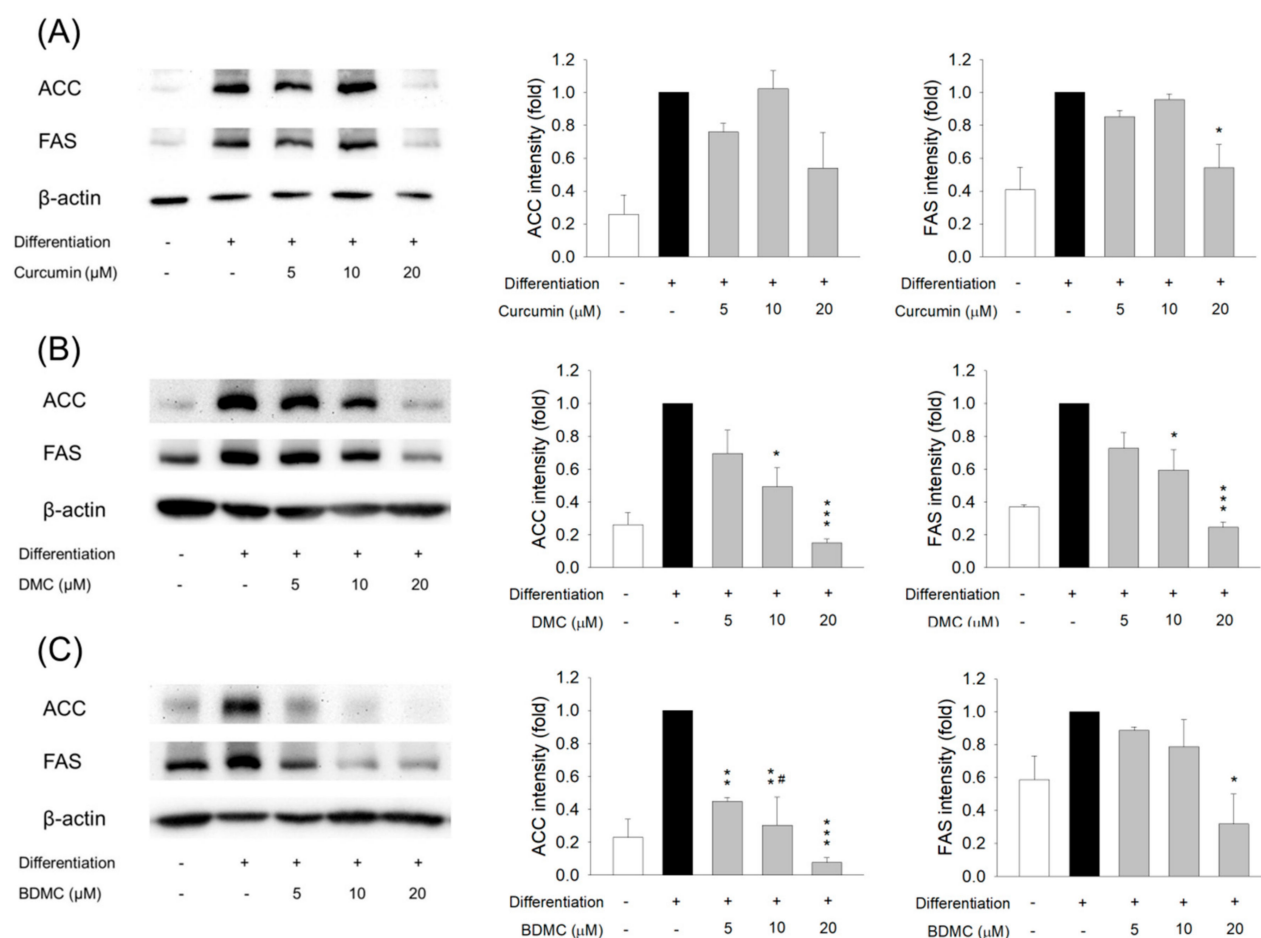


**Figure 5.** The effect of curcuminoids on lipogenic enzymes of 3T3-L1 cells. **(A)** The protein expression of ACC and FAS after treatment of curcumin at 0–20 μM; **(B)** the protein expression of ACC and FAS after treatment of DMC at 0–20 μM; and **(C)** the protein expression of ACC and FAS after treatment of BDMC at 0–20 μM. All data are presented as the mean of three experiments ± S.E.M. \*\*\*  $p < 0.001$ ; \*\*  $p < 0.01$ ; \*  $p < 0.05$  as compared to the differentiated control group. #  $p < 0.05$  as compared to the curcumin-treated group at the same dose.

### 3.6. The Effect of Curcuminoids on Expression of Adipokines

We evaluated whether adipokine expression by adipocytes was influenced by curcuminoids. These adipokines included IL-1β, IL-6, TNF-α, and leptin. Markedly increased protein levels of the adipokines were found in differentiated adipocytes (Figure 6), with 7-, 5-, 4-, and 40-fold increases in IL-1β, IL-6, TNF-α, and leptin, after differentiation, as compared to the non-differentiation control group, respectively. These increases were reduced by curcuminoids, at concentrations of 5–20 μM. A similar reduction in the protein level of the proinflammatory cytokine IL-1β was observed after the treatment of three compounds (Figure 6A). IL-6 inhibition was increased in the order of curcumin < DMC < BDMC (Figure 6B). The expression of IL-6 in the cells was decreased to 80%, 76%, and 66% by curcumin, DMC, and BDMC at a concentration of 20 μM, respectively. A similar trend was shown following the inhibition of TNF-α, although the difference in suppression by these curcuminoids did not attain statistical significance (Figure 6C). Leptin protein expression was arrested, in a concentration-dependent manner, by the curcuminoids, notably BDMC (Figure 6D). BDMC at 20 μM reduced leptin by 72% compared with differentiated cells without the treatment.

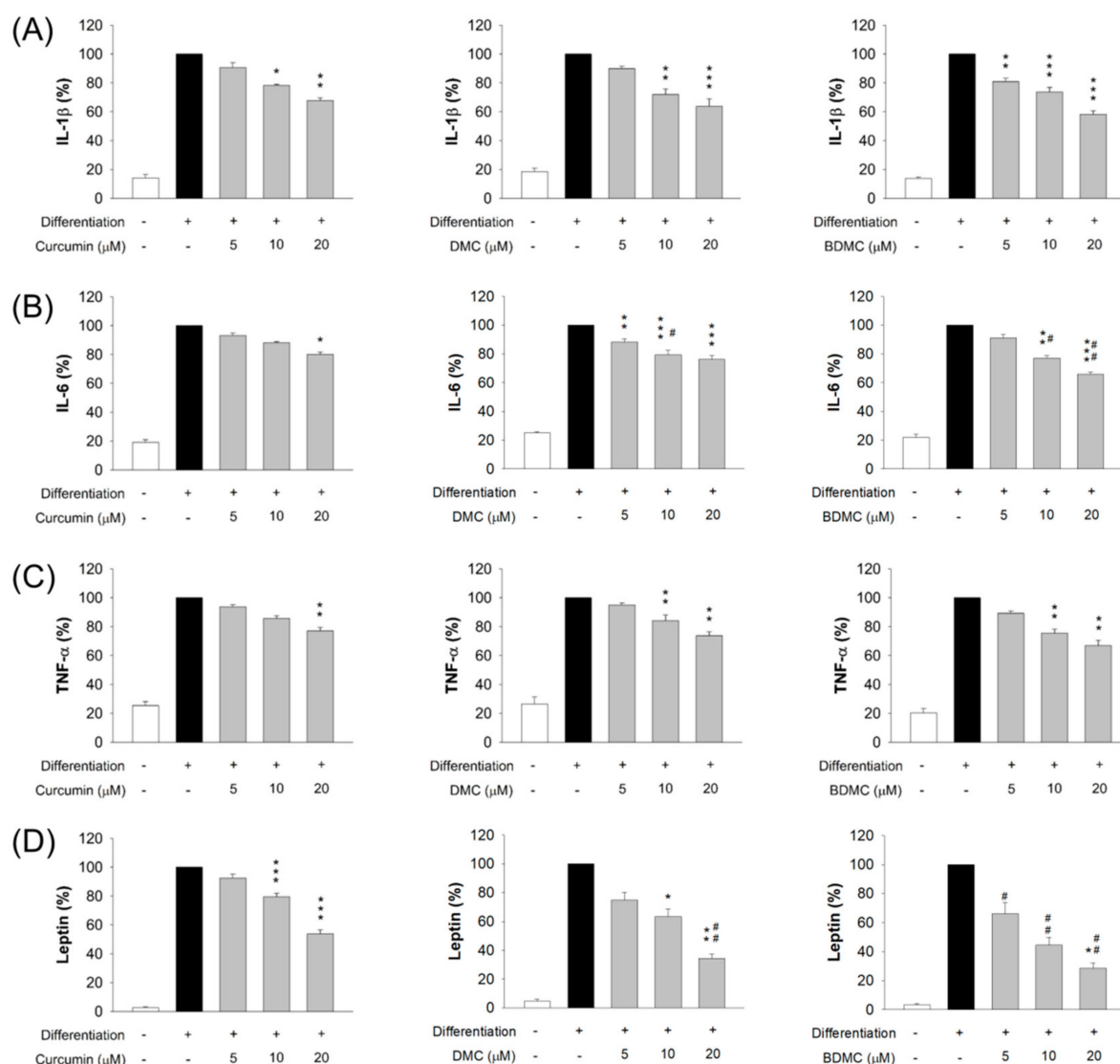


**Figure 6.** The effect of curcuminoids on adipokines of 3T3-L1 cells. (A) The protein expression of IL-1 $\beta$  after treatment of curcuminoids at 0–20  $\mu$ M; (B) the protein expression of IL-6 after treatment of DMC at 0–20  $\mu$ M; (C) the protein expression of IL-1 $\beta$  after treatment of BDMC at 0–20  $\mu$ M; and (D) the protein expression of leptin after treatment of curcuminoids at 0–20  $\mu$ M. All data are presented as the mean of three experiments  $\pm$  S.E.M. \*\*\*  $p < 0.001$ ; \*\*  $p < 0.01$ ; \*  $p < 0.05$  as compared to the differentiated control group. ##  $p < 0.01$ ; #  $p < 0.05$  as compared to the curcumin-treated group at the same dose.

### 3.7. Molecular Docking of Curcuminoids on PPAR $\gamma$ , C/EBP $\alpha$ , and ACC

We conducted molecular docking to elucidate the possible mechanism between curcuminoids and adipogenic or lipogenic markers, such as PPAR $\gamma$ , C/EBP $\alpha$ , and ACC. The three-dimensional model of these proteins was generated for their posterior use as the target structure in the in silico computation (the upper panel of Figure 7A–C). The possible interaction between compounds and proteins is illustrated in the lower panel of Figure 7A–C. The hydrogen bonding and van der Waals force were established by PPAR $\gamma$  and interacted with curcuminoids (Figure 7A). The docking result of PPAR $\gamma$  and curcumin showed that the Pi–Pi T-shaped interaction was stacked to Lys265. The Pi–anion and amide–Pi interactions were formed between the aromatic rings of DMC and PPAR $\gamma$ . However, these interactions were absent in BDMC. The lowest binding energy score (negative CDOCKER energy) of the curcuminoids interacting with proteins was calculated (Table 2). The greater negative energy indicates a stronger binding interaction. We demonstrated

that PPAR $\gamma$  interacted with DMC with the strongest force (-22), followed by BDMC (-18), and curcumin (-17).

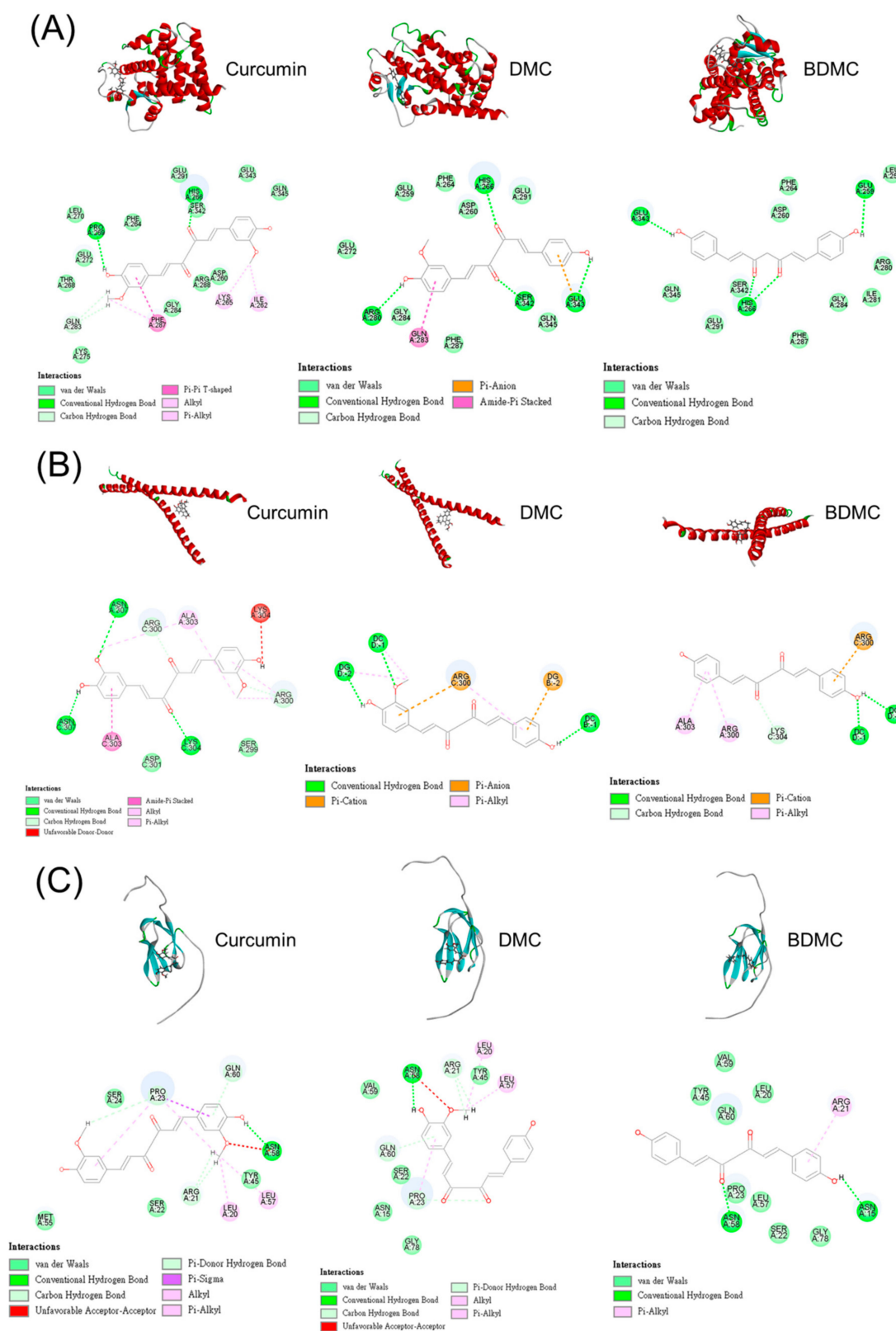


**Figure 7.** The docking poses of curcuminoids at the adipogenic or lipogenic factors. (A) The docking poses and the interaction of curcuminoids at PPAR $\gamma$ ; (B) the docking poses and the interaction of curcuminoids at C/EBP $\alpha$ ; and (C) the docking poses and the interaction of curcuminoids at ACC.

**Table 2.** The negative CDOCKER energy of curcumin and its derivatives with PPAR $\gamma$ , C/EBP $\alpha$ , and ACC.

Protein (PDB Code)	Curcumin	DMC	BDMC
PPAR $\gamma$ (1ZGY)	−16.757	−22.056	−18.371
C/EBP $\alpha$ (1NWQ)	−27.946	−31.258	−34.034
ACC (2DN8)	−12.264	−20.809	−22.749

BDMC, bisdemethoxycurcumin; DMC, demethoxycurcumin.

With respect to C/EBP $\alpha$ , the cooperativity of the interaction with curcuminoids included van der Waals, hydrogen bonding,  $\pi$ -anion,  $\pi$ -cation, and  $\pi$ -alkyl forces (Figure 7B). BDMC (−34) displayed the highest negative CDOCKER score with the interaction with C/EBP $\alpha$ , followed by DMC (−31), and curcumin (−28). This result demonstrated that BDMC could dock into a C/EBP $\alpha$  dimer in order to establish a stable complex. Although the interaction types between ACC and BDMC were fewer than those of curcumin and DMC (Figure 7C), BDMC demonstrated the greatest interaction with ACC (Table 2).

#### 4. Discussion

Obesity is a primary risk factor for diabetes, cardiovascular disorders, and cancers, contributing to a reduced life expectancy of 5–20 years [3]. The prevalence of obesity has tripled since 1975, and continues to increase. Some natural compounds have been found to have a beneficial effect on obesity. Curcumin from turmeric is an anti-obesity compound that has drawn attention as a therapeutic agent, due to evidence that supports its role in adipogenesis inhibition. We currently compare the ability of curcumin and its demethoxy derivatives to inhibit 3T3-L1 differentiation and adipogenesis. Among the curcuminoids that have been isolated from turmeric extract, BDMC showed a stronger anti-adipogenic potency in 3T3-L1 cells compared with curcumin and DMC. The curcuminoids inhibited adipogenesis and lipogenesis via control of the expression of PPAR $\gamma$ , C/EBP $\alpha$ , ACC, FAS, and AMPK $\alpha$ . The adipokines released from the 3T3-L1 differentiated cells were also downregulated by these compounds. We predicted a possible interaction of curcuminoids with C/EBP $\alpha$  and ACC, according to the molecular docking profiles. The curcuminoids in turmeric extract contained 83.7% curcumin, 15.2% DMC, and 1.1% BDMC. This percentage was similar to the turmeric extracts that were produced by the other investigators (70%–80% curcumin, 15%–20% DMC, and 3%–5% BDMC) [11,12,14]. Nevertheless, the percentage of curcuminoids from the turmeric extract only accounted for one-half of the proportion in our study. The other components in the extract could be carbohydrates, proteins, fats, minerals, and essential oils [11]. In our study, the extract had a minimal effect on 3T3-L1 cell differentiation. This result may indicate that components other than curcuminoids offset the anti-adipogenic activity of curcuminoids in the extract.

Energy balance and lipid homeostasis are regulated by adipocytes. Adipocyte differentiation determines the number of adipocytes that have formed in the development of obesity. We employed 3T3-L1 cells as a model to investigate the effect of curcuminoids on the inhibition of adipocyte differentiation. The 3T3-L1 cells can spontaneously differentiate into adipocytes, by exposing them to a hormonal cocktail and high concentration of insulin. The suppression of adipogenesis can be due to both biochemical mechanisms behind anti-adipogenic activity and the simple lysis of adipocyte membranes [15]. We found that adipocyte viability was not significantly affected by curcuminoids at concentrations  $\leq 20$   $\mu$ M, demonstrating that these compounds suppressed adipogenesis through means other than apoptosis induced by membrane lysis. Curcumin is reported to attenuate obesity-related disorders via different mechanisms, such as transcription factors, cellular receptors, growth factors, cytokines, and chemokines [16]. An increase in adipose tissue is generated by the increased size and number of lipid droplets in adipocytes [17]. Lipid droplets are dynamic cellular structures for transient stocks of lipids. An increase in lipid droplet size after adipocyte differentiation was observed. A large lipid droplet is associated with poor transport and metabolism of fatty acids in metabolically

inert organelles [18]. In this study, three curcuminoids inhibited lipid accumulation in lipid droplets without cytotoxicity. BDMC was associated with the greatest potency to inhibit lipid accumulation, followed by DMC and curcumin. Although ferulic acid, the degradation product of curcumin, is reported to have antioxidant and anti-inflammatory activities [19], no suppression of lipid accumulation was detected. This indicates the importance of dimer structure for inhibiting adipocyte differentiation. The curcuminoids had no significant effect on lipid accumulation on the differentiated adipocytes, suggesting that the inhibition by curcuminoids primarily occurred in the differentiative stage. Curcuminoids may demonstrate preventive, but not therapeutic, efficacy for the management of obesity. TGs are the primary form of fatty acid storage in adipocytes and other organs. Enhanced intracellular TG deposition can contribute to the development of obesity [20]. We also found improved performance of BDMC on the inhibition of TG production compared with curcumin and DMC.

The C/EBP family is vital for adipocyte differentiation. The early induction of C/EBP $\delta$  in conjunction with C/EBP $\beta$  has demonstrated a crucial role in promoting the expression of PPAR $\gamma$  and C/EBP $\alpha$ , which are both key regulators of adipocyte differentiation [21]. C/EBP $\alpha$  functions to sustain PPAR $\gamma$  expression in a positive feedback mechanism. Curcumin was found to decrease TG, through decreased PPAR $\gamma$  and C/EBP $\alpha$ , in the early stages of differentiation [22,23]. We observed that BDMC inhibited the expression of PPAR $\gamma$  and C/EBP $\alpha$  proteins to a greater extent than curcumin. It has been suggested that both the transcription factors were required to inhibit differentiation by curcuminoids. ACC and FAS are PPAR $\gamma$ -targeted lipogenic factors [24]. Lipogenesis is the process of fatty acid synthesis, and the subsequent production and storage of TG [25]. FAS is a lipogenic enzyme that is associated with adipocyte differentiation, obesity development, and insulin resistance [26]. The present study demonstrated that DMC and BDMC attenuated adipocyte differentiation through regulating ACC and FAS proteins in a concentration-dependent manner.

The PPAR $\gamma$  inhibitor GW9662 could not completely reverse TG inhibition by BDMC, supporting the hypothesis that signaling pathways other than PPAR $\gamma$  and C/EBP $\alpha$  controlled BDMC suppression of adipogenesis. AMPK is an energy regulator and sensor in adipocytes. The activation of AMPK leads to the phosphorylation of ACC and FAS, resulting in the direct inhibition of malonyl-CoA and de novo lipogenesis [13]. ACC is a downstream effector of AMPK for lipid biosynthesis; thus, AMPK activation may also be involved in the repression of adipogenesis by curcuminoids. Given that BDMC promoted AMPK phosphorylation in 3T3-L1 cells, the anti-adipogenic activity was further mediated by the activation of AMPK. The involvement of AMPK signaling is important for BDMC, since AMPK activation is regarded as a target in the prevention of obesity [27]. The collective mechanisms of action are associated with the strong anti-adipogenic effect of BDMC.

In addition to lipid substances, adipocytes release a series of cytokines, which are collectively named adipokines. Lipid accumulation is associated with a low-grade inflammatory condition in adipose tissue. A link between obesity and inflammation has been established, and specifically the secretion of proinflammatory adipokines such as IL-1 $\beta$ , IL-6, TNF- $\alpha$ , and MCP-1 is increased [28]. Obesity-induced adipokines can influence the function of adipocytes, through the infiltration of immune cells, including macrophages and neutrophils, to form a vicious cycle [29]. We had detected the change in IL-1 $\beta$ , IL-6, and TNF- $\alpha$  in 3T3-L1 cells after the treatment with curcuminoids. Adipocytes initially express IL-1 $\beta$  to elicit the proinflammatory cytokines IL-6 and TNF- $\alpha$  [30]. The first indication of increased adipokine release in obesity is provided by the identification of increased TNF- $\alpha$  [31]. This cytokine contributes to the adipokine dysregulation in adipocytes, to correlate with the degree of adiposity, body mass index, body fat percentage, and insulin resistance [32]. Similarly to TNF- $\alpha$ , IL-6 levels increase with obesity and body fat [33]. The recruitment of macrophages in adipose tissue is associated with increased IL-6 and TNF- $\alpha$  secretion, leading to insulin resistance [34]. Curcumin is known as an anti-inflammatory molecule that inhibits cytokines [35]. The anti-inflammatory effect of curcumin has been



demonstrated to be mediated by the downregulation of IL-1, IL-6, and TNF- $\alpha$  [36]. We showed that the demethoxy derivatives of curcumin were superior to the parent compound in the inhibition of adipokines, especially IL-6. Leptin is an adipose tissue hormone that regulates energy intake and balance. It can be categorized as a proinflammatory adipokine to stimulate the expression of IL-6 and TNF- $\alpha$  [37]. PPAR $\gamma$  and C/EBP $\alpha$  are the upstream actors that are necessary for the expression of leptin to regulate glucose and lipid metabolism [38]. Both DMC and BDMC had a greater impact on lessening leptin expression compared with curcumin. This result further supports the effect on adipogenesis inhibition, through PPAR $\gamma$  and C/EBP $\alpha$  modulation. Curcuminoids could counteract inflammation in adipocytes. It may be beneficial to attenuate the low-grade chronic inflammation that is associated with metabolic syndromes.

Our data showed greater anti-adipogenic activity of demethoxy derivatives compared with curcumin. This illustrated that the methoxy groups on the phenyl ring play an essential role in the control of adipocyte differentiation. The anti-adipogenic activity of curcuminoids was quite different than that of other bioactivities. The antioxidant activity of curcuminoids, determined by the linoleic acid peroxidation approach, represents a trend of BDMC < DMC < curcumin [39]. A similar tendency has been observed in the inhibitory capacity on supercoiled plasma DNA damage [40]. A previous study [41] has reported that curcuminoids suppress TNF- $\alpha$ -induced NF- $\kappa$ B activation in the order of BDMC < DMC < curcumin. The anti-breast cancer and anti-melanoma activities of BDMC were also less than curcumin and DMC in a cell-based study [42]. Although these investigations exhibited items to the contrary of our study, the superior chemical stability of BDMC over curcumin and DMC could be the reason for the observed stronger anti-adipogenic effect. Another possibility could be that the methoxy moieties in the curcumin structure might contribute a steric hindrance for cell membrane penetration and receptor binding. Matsuda et al. [43] reported that the flavonoids with methoxy groups are beneficial to enhance TG accumulation in 3T3-L1 cells. We may infer that curcumin and DMC containing methoxy groups were unfavorable to suppress adipogenesis, based on the case of flavonoids. The smaller molecular size of BDMC may also be favorable to penetrate across the adipocyte membrane, leading to cell uptake. Further work is needed to elucidate the correlation between the chemical features of curcuminoids and anti-adipogenic activity.

Curcumin can directly interact with a wide range of biomolecules, such as transcription factors, cellular receptors, and enzymes, for attenuating obesity-related disorders via different signaling mechanisms [16,44]. Curcumin is proved to inhibit the mRNA level of adipogenic transcription factors, particularly PPAR $\gamma$  and C/EBP $\alpha$ , in the early stage of adipocyte differentiation [45]. We employed molecular docking to predict possible interactions between curcuminoids and adipogenic factors, including PPAR $\gamma$ , C/EBP $\alpha$ , and ACC. Although the structures of the three curcuminoids exhibited similar backbones, the interaction with these proteins was quite different. The demethoxy derivatives showed stronger interactions with all the proteins that were tested, compared with curcumin. This confirmed the results from the cell-based study that showed DMC and BDMC usually possessed higher anti-adipogenic activity as compared to curcumin. A strongest interaction with C/EBP $\alpha$  and ACC was found between BDMC, followed by DMC and curcumin. A similar tendency was detectable in the Western blot assay of C/EBP $\alpha$  and ACC. The involvement of the C/EBP $\alpha$  and ACC pathways in curcuminoid-treated adipocytes was validated. This also suggested that curcuminoids might directly interact with C/EBP $\alpha$  and ACC, to inhibit adipocyte differentiation.

We currently demonstrated that BDMC inhibited 3T3-L1 differentiation, mainly through the downregulation of PPAR $\gamma$  and C/EBP $\alpha$ , leading to a subsequent downregulation of their target proteins ACC and FAS (Figure 8). Thus, lipid accumulation was inhibited by this pathway. BDMC also enhanced AMPK phosphorylation and reduced the expression of the downstream molecules ACC and FAS. Lipid accumulation was decreased by these pathways, resulting in a counteracting of proinflammatory adipokines. Given that humans can consume up to 8 g of curcumin per day, without experiencing adverse

effects [46], curcuminoids are an interesting preventive intervention against obesity and other related diseases. Due to the anti-adipogenic activity of BDMC in this study, we expect that BDMC will be a potential therapy for obesity management. Though curcumin is considered safe after administration in humans, some clinical studies have shown limited therapeutic effectiveness, due to its instability and poor oral bioavailability [47,48]. Since both DMC and BDMC are more chemically stable than curcumin in a physiological medium [49], the demethoxy derivatives may have applicability for preventing obesity.

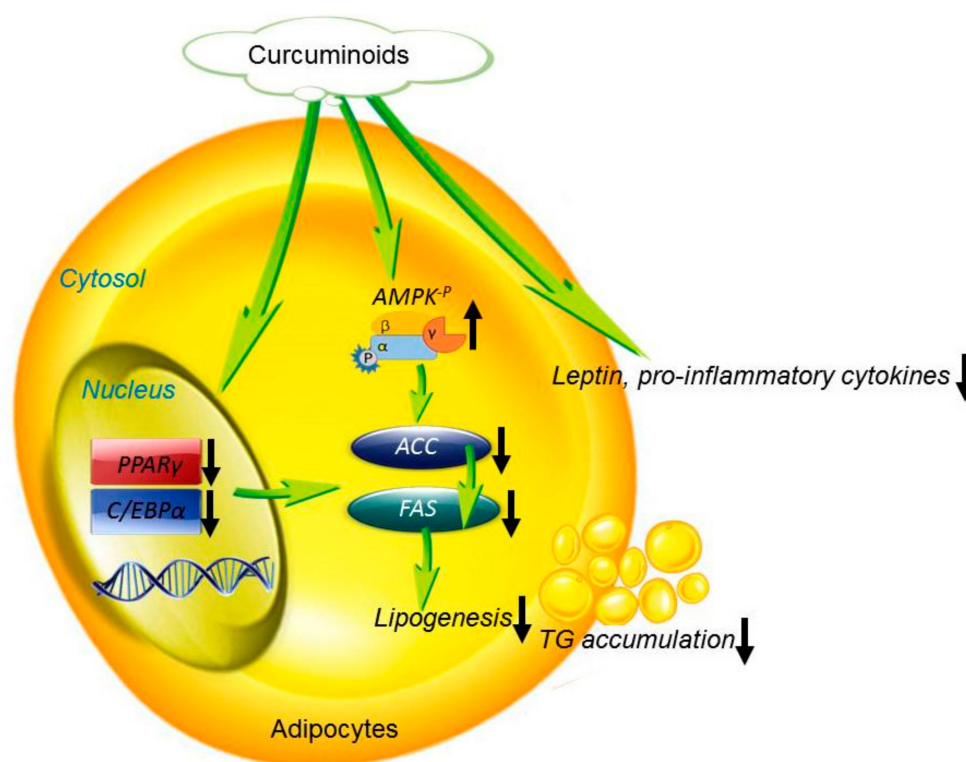


**Figure 8.** The proposed mechanisms of the anti-adipogenic activity of curcuminoids.

## 5. Conclusions

We demonstrated that curcuminoids inhibited 3T3-L1 cell differentiation, and that BDMC was the most active compound responsible for this effect. These compounds displayed anti-adipogenic activity, by reducing the expression of PPARγ and C/EBPα, which are the main transcription factors of adipogenesis in adipocyte differentiation. In addition, AMPKα phosphorylation was activated by curcuminoids, leading to the reduction in ACC and FAS expression. The subsequent TG generation and adipokine release were decreased. These results suggested that curcuminoids inhibit lipid accumulation via modulation of adipogenic transcription factors and lipogenic enzymes during differentiation for hindering preadipocyte maturation. Although BDMC revealed the greatest potential to inhibit adipogenesis among the three compounds tested, the inhibitory effect of the turmeric extract was insignificant, due to the very low amount of BDMC in the extract. It is important to select the turmeric products with abundant BDMC content for presenting considerable anti-adipogenic efficiency. The anti-adipogenic application of curcuminoids could be preventive. Our data suggest the potential of BDMC for improving obesity and the related chronic inflammation. Further studies are needed to further examine these expectations.

**Supplementary Materials:** The following are available online at <https://www.mdpi.com/article/10.3390/biom11071025/s1>, Figure S1: The viability and lipid accumulation of the 3T3-L1 cell exposed to the extract or compounds after the induction of differentiation. All the tested materials demonstrated no cytotoxicity against mature adipocytes at concentrations of 0–20 μM (Figure S1A). Lipid accumu-

lation was unaffected when the mature adipocytes were treated with the extract and compounds (Figure S1B).

**Author Contributions:** Conceptualization, C.-Y.H.; methodology, A.A., H.-J.L.; formal analysis, A.A., J.-Y.F.; investigation, A.A., H.-J.L., C.-H.C.; data curation, A.A.; C.-Y.H.; writing—original draft preparation, J.-Y.F., H.-J.L.; writing—review and editing, C.-Y.H.; funding acquisition, J.-Y.F., C.-Y.H. All authors have read and agreed to the published version of the manuscript.

**Funding:** This research was funded by the Ministry of Science and Technology of Taiwan (MOST-107-2320-B-182-016-MY3) and Chang Gung Memorial Hospital (CMRPD1K0051-2).

**Acknowledgments:** The authors are grateful for the financial support from the Ministry of Science and Technology of Taiwan (MOST-107-2320-B-182-016-MY3) and Chang Gung Memorial Hospital (CMRPD1K0051-2).

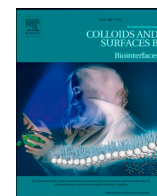
**Conflicts of Interest:** The authors declare no conflict of interest.

## References

- Chooi, Y.C.; Ding, C.; Magkos, F. The epidemiology of obesity. *Metab. Clin. Exp.* **2019**, *92*, 6–10. [\[CrossRef\]](#)
- Bray, G.A.; Frühbeck, G.; Ryan, D.H.; Wilding, J.P.H. Management of obesity. *Lancet* **2016**, *387*, 1947–1956. [\[CrossRef\]](#)
- Blüher, M. Obesity: Global epidemiology and pathogenesis. *Nat. Rev. Endocrinol.* **2019**, *15*, 288–298. [\[CrossRef\]](#)
- Longo, M.; Zatterale, F.; Naderi, J.; Parrillo, L.; Formisano, P.; Raciti, G.A.; Beguinot, F.; Miele, C. Adipose tissue dysfunction as determinant of obesity-associated metabolic complications. *Int. J. Mol. Sci.* **2019**, *20*, 2358. [\[CrossRef\]](#) [\[PubMed\]](#)
- Kang, J.G.; Park, C.Y. Anti-obesity drugs: A review about their effects and safety. *Diabetes Metab. J.* **2012**, *36*, 13–25. [\[CrossRef\]](#)
- Karri, S.; Sharma, S.; Hatware, K.; Patil, K. Natural anti-obesity agents and their therapeutic role in management of obesity: A future trend perspective. *Biomed. Pharmacol.* **2019**, *110*, 224–238. [\[CrossRef\]](#)
- Rolfe, V.; Mackonochie, M.; Mills, S.; MacLennan, E. Turmeric/curcumin and health outcomes: A meta-review of systematic reviews. *Eur. J. Integr. Med.* **2020**, *40*, 101252. [\[CrossRef\]](#)
- Tsuda, T. Curcumin as a functional food-derived factor: Degradation products, metabolites, bioactivity, and future perspectives. *Food Funct.* **2018**, *9*, 705. [\[CrossRef\]](#) [\[PubMed\]](#)
- Bradford, P.G. Curcumin and obesity. *BioFactors* **2013**, *39*, 78–87. [\[CrossRef\]](#) [\[PubMed\]](#)
- Mohammadi, A.; Sahebkar, A.; Iranshahi, M.; Amini, M.; Khojasteh, R.; Ghayour-Mobarhan, M.; Ferns, G.A. Effects of supplementation with curcuminoids on dyslipidemia in obese patients: A randomized crossover trial. *Phytother. Res.* **2013**, *27*, 374–379. [\[CrossRef\]](#)
- Panahi, Y.; Khalili, N.; Hosseini, M.S.; Abbasnazar, M.; Sahebkar, A. Lipid-modifying effects of adjunctive therapy with curcuminoids-piperine combination in patients with metabolic syndrome: Results of a randomized controlled trial. *Complent. Ther. Med.* **2014**, *22*, 851–857. [\[CrossRef\]](#)
- Lai, C.S.; Chen, Y.Y.; Lee, P.S.; Kalyanam, N.; Ho, C.T.; Liou, W.S.; Yu, R.C.; Pan, M.H. Bisdemethoxycurcumin inhibits adipogenesis in 3T3-L1 preadipocytes and suppresses obesity in high-fat diet-fed C57BL/6 mice. *J. Agric. Food Chem.* **2016**, *64*, 821–830. [\[CrossRef\]](#) [\[PubMed\]](#)
- Song, Z.; Xiaoli, A.M.; Yang, F. Regulation and metabolic significance of *de novo* lipogenesis in adipose tissues. *Nutrients* **2018**, *10*, 1383. [\[CrossRef\]](#) [\[PubMed\]](#)
- Gordon, O.N.; Luis, P.B.; Ashley, R.E.; Osheroff, N.; Schneider, C. Oxidative transformation of demethoxy- and bisdemethoxycurcumin: Products, mechanism of formation, and poisoning of human topoisomerase II $\alpha$ . *Chem. Res. Toxicol.* **2015**, *28*, 989–996. [\[CrossRef\]](#)
- Jakab, J.; Miškić, B.; Mikšić, Š.; Juranić, B.; Ćosić, V.; Schwarz, D.; Včev, A. Adipogenesis as a potential anti-obesity target: A review of pharmacological treatment and natural products. *Diabetes Metab. Syndr. Obes.* **2021**, *14*, 67–83. [\[CrossRef\]](#)
- Vari, R.; Scazzocchio, B.; Silenzi, A.; Giovannini, C.; Masella, R. Obesity-associated inflammation: Does curcumin exert a beneficial role? *Nutrients* **2021**, *13*, 1021. [\[CrossRef\]](#)
- Onal, G.; Kutlu, O.; Gozuacik, D.; Emre, S.D. Lipid droplets in health and disease. *Lipids Health Dis.* **2017**, *16*, 128. [\[CrossRef\]](#)
- Somwar, R.; Roberts, C.T.; Varlamov, O. Live-cell imaging demonstrates rapid cargo exchange between lipid droplets in adipocytes. *FEBS. Lett.* **2011**, *585*, 1946–1950. [\[CrossRef\]](#) [\[PubMed\]](#)
- De Oliveira Silva, E.; Batista, R. Ferulic acid and naturally occurring compounds bearing a feruloyl moiety: A review on their structures, occurrence, and potential health benefits. *Compr. Rev. Food Sci. Food Saf.* **2017**, *16*, 580–616. [\[CrossRef\]](#) [\[PubMed\]](#)
- Alves-Bezerra, M.; Cohen, D.E. Triglyceride metabolism in the liver. *Compr. Physiol.* **2018**, *8*, 1–22.
- Sarantopoulos, C.; Banyard, D.A.; Ziegler, M.E.; Sun, B.; Shaterian, A.; Widgerow, A.D. Elucidating the preadipocyte and its role in adipocyte formation: A comprehensive review. *Stem Cell Rev. Rep.* **2018**, *14*, 27–42. [\[CrossRef\]](#) [\[PubMed\]](#)
- Pan, Y.; Zhao, D.; Yu, N.; An, T.; Miao, J.; Mo, F.; Gu, Y.; Zhang, D.; Gao, S.; Jiang, G. Curcumin improves glycolipid metabolism through regulating peroxisome proliferator activated receptor  $\gamma$  signaling pathway in high-fat diet-induced obese mice and 3T3-L1 adipocytes. *R. Soc. Open Sci.* **2017**, *4*, 170917. [\[CrossRef\]](#) [\[PubMed\]](#)

23. Sakuma, S.; Sumida, M.; Endoh, Y.; Kurita, A.; Yamaguchi, A.; Watanabe, T.; Kohda, T.; Tsukiyama, Y.; Fujimoto, Y. Curcumin inhibits adipogenesis induced by benzyl butyl phthalate in 3T3-L1 cells. *Toxicol. Appl. Pharmacol.* **2017**, *329*, 158–164. [\[CrossRef\]](#) [\[PubMed\]](#)
24. Tung, Y.C.; Hsieh, P.H.; Pan, M.H.; Ho, C.T. Cellular models for the evaluation of the antiobesity effect of selected phytochemicals from food and herbs. *J. Food Drug Anal.* **2017**, *25*, 100–110. [\[CrossRef\]](#)
25. Wallace, M.; Metallo, C.M. Tracing insights into *de novo* lipogenesis in liver and adipose tissues. *Semin. Cell Dev. Biol.* **2020**, *108*, 65–71. [\[CrossRef\]](#) [\[PubMed\]](#)
26. Moseti, D.; Regassa, A.; Kim, W.K. Molecular regulation of adipogenesis and potential anti-adipogenic bioactive molecules. *Int. J. Mol. Sci.* **2016**, *17*, 124. [\[CrossRef\]](#)
27. Fang, C.; Kim, H.; Noratto, G.; Sun, Y.; Talcott, S.T.; Mertens-Talcott, S.U. Gallotanin derivatives from mango (*Mangifera indica* L.) suppress adipogenesis and increase thermogenesis in 3T3-L1 adipocytes in part through the AMPK pathway. *J. Funct. Foods* **2018**, *46*, 101–109. [\[CrossRef\]](#)
28. Taylor, E.B. The complex role of adipokines in obesity, inflammation, and autoimmunity. *Clin. Sci.* **2021**, *135*, 731–752. [\[CrossRef\]](#)
29. Francisco, V.; Pino, J.; Gonzalez-Gay, M.A.; Mera, A.; Lago, F.; Gómez, R.; Mobasheri, A.; Gualillo, O. Adipokines and inflammation: Is it a question of weight? *Br. J. Pharmacol.* **2018**, *175*, 1569–1579. [\[CrossRef\]](#)
30. Zieger, K.; Weiner, J.; Krause, K.; Schwarz, M.; Kohn, M.; Stumvoll, M.; Blüher, M.; Heiker, J.T. Vaspin suppresses cytokine-induced inflammation in 3T3-L1 adipocytes via inhibition of NFκB pathway. *Mol. Cell. Endocrinol.* **2018**, *460*, 181–188. [\[CrossRef\]](#)
31. Sung, J.H.; Chon, J.W.; Lee, M.A.; Park, J.K.; Woo, J.T.; Park, Y.K. The anti-obesity effect of *Lethariella dadonioides* in 3T3-L1 cells and obese mice. *Nutr. Res. Pract.* **2011**, *5*, 503–510. [\[CrossRef\]](#)
32. Bai, Y.; Sun, Q. Macrophage recruitment in obese adipose tissue. *Obes. Rev.* **2015**, *16*, 127–136. [\[CrossRef\]](#)
33. Wensveen, F.M.; Valentić, S.; Šestan, M.; Wensveen, T.T.; Polić, B. The “big bang” in obese fat: Events initiating obesity-induced adipose tissue inflammation. *Eur. J. Immunol.* **2015**, *45*, 2446–2456. [\[CrossRef\]](#) [\[PubMed\]](#)
34. Stolarczyk, E. Adipose tissue inflammation in obesity: A metabolic or immune response? *Curr. Opin. Pharmacol.* **2017**, *37*, 35–40. [\[CrossRef\]](#)
35. Marton, L.T.; Barbalho, S.M.; Sloan, K.P.; Sloan, L.A.; de Alvares Goulart, R.; Araújo, A.C.; Bechara, M.D. Curcumin, autoimmune and inflammatory diseases: Going beyond conventional therapy—a systematic review. *Crit. Rev. Food Sci. Nutr.* **2020**. [\[CrossRef\]](#) [\[PubMed\]](#)
36. Simental-Mendía, L.E.; Cicero, A.F.G.; Atkin, S.L.; Majeed, M.; Sahebkar, A. A systematic review and meta-analysis of the effect of curcuminoids on adiponectin levels. *Obes. Res. Clin. Pract.* **2019**, *13*, 340–344. [\[CrossRef\]](#) [\[PubMed\]](#)
37. Jayarathne, S.; Stull, A.J.; Miranda, A.; Scoggins, S.; Claycombe-Larson, K.; Kim, J.H.; Moustaid-Moussa, N. Tart cherry reduces inflammation in adipose tissue of Zucker fatty rats and cultured 3T3-L1 adipocytes. *Nutrients* **2018**, *10*, 1576. [\[CrossRef\]](#)
38. Lowe, C.E.; O’Rahilly, S.; Rochford, J.J. Adipogenesis at a glance. *J. Cell Sci.* **2011**, *124*, 2681–2686. [\[CrossRef\]](#) [\[PubMed\]](#)
39. Jayaprakasha, G.K.; Rao, L.J.; Sakariah, K.K. Antioxidant activities of curcumin, demethoxycurcumin and bisdemethoxycurcumin. *Food Chem.* **2006**, *98*, 720–724. [\[CrossRef\]](#)
40. Ahsan, H.; Parveen, N.; Khan, N.U.; Hadi, S.M. Pro-oxidant, anti-oxidant and cleavage activities on DNA of curcumin and its derivatives demethoxycurcumin and bisdemethoxycurcumin. *Chem.-Biol. Interact.* **1999**, *121*, 161–175. [\[CrossRef\]](#)
41. Sandur, S.K.; Pandey, M.K.; Sung, B.; Ahn, K.S.; Murakami, A.; Sethi, G.; Limtrakul, P.; Badmaev, V.; Aggarwal, B.B. Curcumin, demethoxycurcumin, bisdemethoxycurcumin, tetrahydrocurcumin and turmerones differentially regulate anti-inflammatory and anti-proliferative responses through a ROS-independent mechanism. *Carcinogenesis* **2007**, *28*, 1765–1773. [\[CrossRef\]](#)
42. Huang, C.; Lu, H.F.; Chen, Y.H.; Chen, J.C.; Chou, W.H.; Huang, H.C. Curcumin, demethoxycurcumin, and bisdemethoxycurcumin induced caspase-dependent and -independent apoptosis via Smad or Akt signaling pathways in HOS cells. *BMC Complement. Med. Ther.* **2020**, *20*, 68. [\[CrossRef\]](#) [\[PubMed\]](#)
43. Matsuda, H.; Kogami, Y.; Nakamura, S.; Sugiyama, T.; Ueno, T.; Yoshikawa, M. Structural requirements of flavonoids for the adipogenesis of 3T3-L1 cells. *Bioorg. Med. Chem.* **2011**, *19*, 2835–2841. [\[CrossRef\]](#)
44. Shehzad, A.; Ha, T.; Subhan, F.; Lee, Y.S. New mechanisms and anti-inflammatory role of curcumin in obesity and obesity-related metabolic diseases. *Eur. J. Nutr.* **2011**, *50*, 151–161. [\[CrossRef\]](#) [\[PubMed\]](#)
45. Kim, C.Y.; Young, C.; Le, T.T.; Chen, C.; Cheng, J.X.; Kim, K.H. Curcumin inhibits adipocyte differentiation through modulation of mitotic clonal expansion. *J. Nutr. Biochem.* **2011**, *22*, 910–920. [\[CrossRef\]](#) [\[PubMed\]](#)
46. Cheng, A.L.; Hsu, C.H.; Lin, J.K.; Hsu, M.M.; Ho, Y.F.; Shen, T.S.; Ko, J.Y.; Lin, J.T.; Lin, B.R.; Wu, M.S.; et al. Phase I clinical trial of curcumin, a chemopreventive agent, in patients with high-risk or pre-malignant lesions. *Anticancer Res.* **2001**, *21*, 2895–2900. [\[PubMed\]](#)
47. Wickenberg, J.; Ingemansson, S.L.; Hlebowicz, J. Effects of *Curcuma longa* (turmeric) on postprandial plasma glucose and insulin in healthy subjects. *Nutr. J.* **2010**, *9*, 43. [\[CrossRef\]](#)
48. Yang, Y.S.; Su, Y.F.; Yang, H.W.; Lee, Y.H.; Chou, J.I.; Ueng, K.C. Lipid-lowering effects of curcumin in patients with metabolic syndrome: A randomized, double-blind, placebo-controlled trial. *Phytother. Res.* **2014**, *28*, 1770–1777. [\[CrossRef\]](#) [\[PubMed\]](#)
49. Bettini, S.; Vergara, D.; Bonsegna, S.; Giotta, L.; Toto, C.; Chieppa, M.; Maffia, M.; Giovinazzo, G.; Valli, L.; Santino, A. Efficient stabilization of natural curcuminoids mediated by oil body encapsulation. *RSC Adv.* **2013**, *3*, 5422–5429. [\[CrossRef\]](#)





# Hydrogels: A potential platform for induced pluripotent stem cell culture and differentiation

M.R. Poorna<sup>a</sup>, R. Jayakumar<sup>a</sup>, Jyh-Ping Chen<sup>b,c,d,\*</sup>, Ullas Mony<sup>a,e,\*\*</sup>

<sup>a</sup> Centre for Nanosciences and Molecular Medicine, Amrita Vishwa Vidyapeetham, Kochi 682041, India

<sup>b</sup> Department of Chemical and Materials Engineering, Chang Gung University, Kwei-San, Taoyuan 33302, Taiwan, ROC

<sup>c</sup> Department of Plastic and Reconstructive Surgery and Craniofacial Research Center, Chang Gung Memorial Hospital, Linkou, Kwei-San, Taoyuan 33305, Taiwan, ROC

<sup>d</sup> Research Center for Food and Cosmetic Safety, Research Center for Chinese Herbal Medicine, College of Human Ecology, Chang Gung University of Science and Technology, Taoyuan 33305, Taiwan, ROC

<sup>e</sup> Department of Biochemistry, Centre of Molecular Medicine and Diagnostics (COMManD), Saveetha Dental College and Hospitals, Saveetha Institute of Medical and Technical Sciences, Saveetha University, Chennai, 600077, India

## ARTICLE INFO

### Keywords:

iPSC  
Scaffolds  
Hydrogel  
Tissue engineering  
Regenerative medicine

## ABSTRACT

Induced pluripotent stem cells (iPSCs) can be used to generate desired types of cells that belong to the three germ layers (*i.e.*, ectoderm, endoderm and mesoderm). These cells possess great potential in regenerative medicine. Before iPSCs are used in various biomedical applications, the existing xenogeneic culture methods must be improved to meet the technical standards of safety, cost effectiveness, and ease of handling. In addition to commonly used 2D substrates, a culture system that mimics the native cellular environment in tissues will be a good choice when culturing iPSC cells and differentiating them into different lineages. Hydrogels are potential candidates that recapitulate the native complex three-dimensional microenvironment. They possess mechanical properties similar to those of many soft tissues. Moreover, hydrogels support iPSC adhesion, proliferation and differentiation to various cell types. They are xeno-free and cost-effective. In addition to other substrates, such as mouse embryonic fibroblast (MEF), Matrigel, and vitronectin, the use of hydrogel-based substrates for iPSC culture and differentiation may help generate large numbers of clinical-grade cells that can be used in potential clinical applications. This review mainly focuses on the use of hydrogels for the culture and differentiation of iPSCs into various cell types and their potential applications in regenerative medicine.

## 1. Introduction

Induced pluripotent stem cells are reprogrammed somatic cells that maintain long-term proliferation and the ability to differentiate into any cells within the body (Fig. 1) [1]. These properties allow individual or patient-specific cells and tissues to be generated from iPSCs and makes them more appealing for clinical uses, as they bypass the hurdles associated with immune rejection [2]. Therefore, this reprogramming technology has countless prospective applications in disease modeling [3], regenerative medicine, drug screening for efficacy and toxicity [4] and in basic research on stem cells and differentiation processes. The commonly used method of generating iPSCs is the reprogramming of somatic cells with exogenous transcription factors such as Oct4, Sox2, Klf4, and c-Myc (OSKM) (Fig. 2) [1,5–8]. Integrating or nonintegrating methods are used to generate iPSCs. Clinical translation of iPSCs derived

by integrating methods is strictly limited due to safety concerns. Currently, several nonintegrating reprogramming methods are available; among those methods, mRNA reprogramming is perhaps best suited for clinical translation [9]. This excellent method of generating pluripotent stem cells from somatic cells helps to bypass ethical problems associated with embryonic stem cells (ESCs).

An appropriate culture condition that supports iPSC growth is crucial for the expansion of these cells. iPSCs are cultured as adhesion cultures and suspension cultures [10]. For adherence, iPSCs require very specific extracellular matrix (ECM) and/or other proteins or synthetic polymers as substrates that mimic the native cellular environment [11]. The conventional method of adhesion-based iPSC culture is a two-dimensional (2D) culture platform, and it does not completely recapitulate the native 3D environment [12]. Although these systems have successfully generated different types of cells that belong to the

\* Corresponding author at: Department of Chemical and Materials Engineering, Chang Gung University, Kwei-San, Taoyuan 33302, Taiwan, ROC.

\*\* Corresponding author.

E-mail addresses: [jpchen@mail.cgu.edu.tw](mailto:jpchen@mail.cgu.edu.tw) (J.-P. Chen), [ullasmony@gmail.com](mailto:ullasmony@gmail.com) (U. Mony).

<https://doi.org/10.1016/j.colsurfb.2021.111991>

Received 3 February 2021; Received in revised form 16 July 2021; Accepted 18 July 2021

Available online 20 July 2021

0927-7765/© 2021 Elsevier B.V. All rights reserved.



three germ layers, a few limitations remain to be addressed. 2D differentiation systems show critically limited clinical utility because of the lack of safety, scalability and efficiency [13]. Clinical and industrial applications of iPSCs require a large number of cells. This requirement cannot be fulfilled by conventional adherent culture. However, in suspension culture, iPSCs do not require any substrates for adherence, and they form spheroids in suspension. However, because of limited nutrient and oxygen supplies into the aggregates, a size limitation for spheroid formation exists [14,15]. The lack of ECM in these culture systems may lead to cell death and unstable spheroid formation [16]. Thus, an alternative approach to overcome these limitations is the use of biomaterials. Engineering a stem cell niche or an appropriate stem cell 3D microenvironment with both biophysical and biochemical signals using appropriate biomaterials influences the fate of stem cells [12]. Reports on the use of different biomaterials that are similar to ECM for the culture and differentiation of iPSCs have been published [17]. These materials provide stability and strength and facilitate the adhesion, proliferation and differentiation of iPSCs. In fact, substrate stiffness, topography and composition are reported to affect pluripotent stem cell differentiation [17]. As a potential strategy resembling the natural cell environment, a series of ECM-equivalent substrates, including elastomeric films, fibrillar foams [18], nanofibrous scaffolds [19], hydroxyapatite ceramics [18] and hydrogels [20], are available. Among the substrates developed, the most promising novel substrate is hydrogels. Hydrogels are hydrophilic 3D networks of water-soluble polymers with the ability to recapitulate the native complex 3D microenvironment [21]. The spatiotemporal manipulation of biophysical cues helps recapitulate the 3D microenvironment where stem cells reside. The stem cell niche consists of both biochemical and biophysical factors that direct the fate of stem cells, and many of these factors are provided by the

extracellular matrix (ECM). The stem cell ECM comprises adhesive proteins (e.g., vitronectin, fibronectin, and laminin), fibrous structural proteins (e.g., collagen and elastin) and polysaccharides forming a complex 3D network. This network of adhesive proteins promotes cell adhesion to the matrix through specific receptors such as selectins, integrins and syndecan. Fibrous structural proteins provide mechanical resistance to shear and tensile stress to resident cells, while polysaccharides contain hydrophilic groups that help absorb water. Apart from the microstructure of the ECM, direct cell-cell interactions and the interaction of stem cells with other supporting cell types through secreted soluble factors modulate the signaling pathways that are involved in regulating the maintenance of the stem cell pool and controlling the differentiation of stem cells. Therefore, while engineering biomaterials, controlling the fate of stem cells with the following two strategies must be considered: (a) strategies to maintain stemness and (b) strategies to differentiate stem cells into desired cell types [22]. Due to their desirable physical characteristics, biocompatibility, variable composition and flexibility in fabrication, hydrogels have proven useful in various applications, including cell culture, cell therapy and drug delivery [23]. For example, stimuli-responsive polymeric hydrogels have been widely used for controlled and targeted drug delivery. Polyvinyl amine, a pH-sensitive polymer, has been shown to have an effective drug release capability with changes in the external environmental pH [24]. Inspired by the native stem cell niche, hydrogel platforms were developed to regulate stem cell fate by controlling microenvironmental factors such as the microstructure of the ECM, degradability, mechanics, cell-cell interactions and cell-adhesive ligand presentation. Due to this level of control, engineered hydrogel niches have the capacity for better reproducibility in producing stem cells for clinical applications and for generating biomimetic tissue constructs [22]. In regenerative medicine,

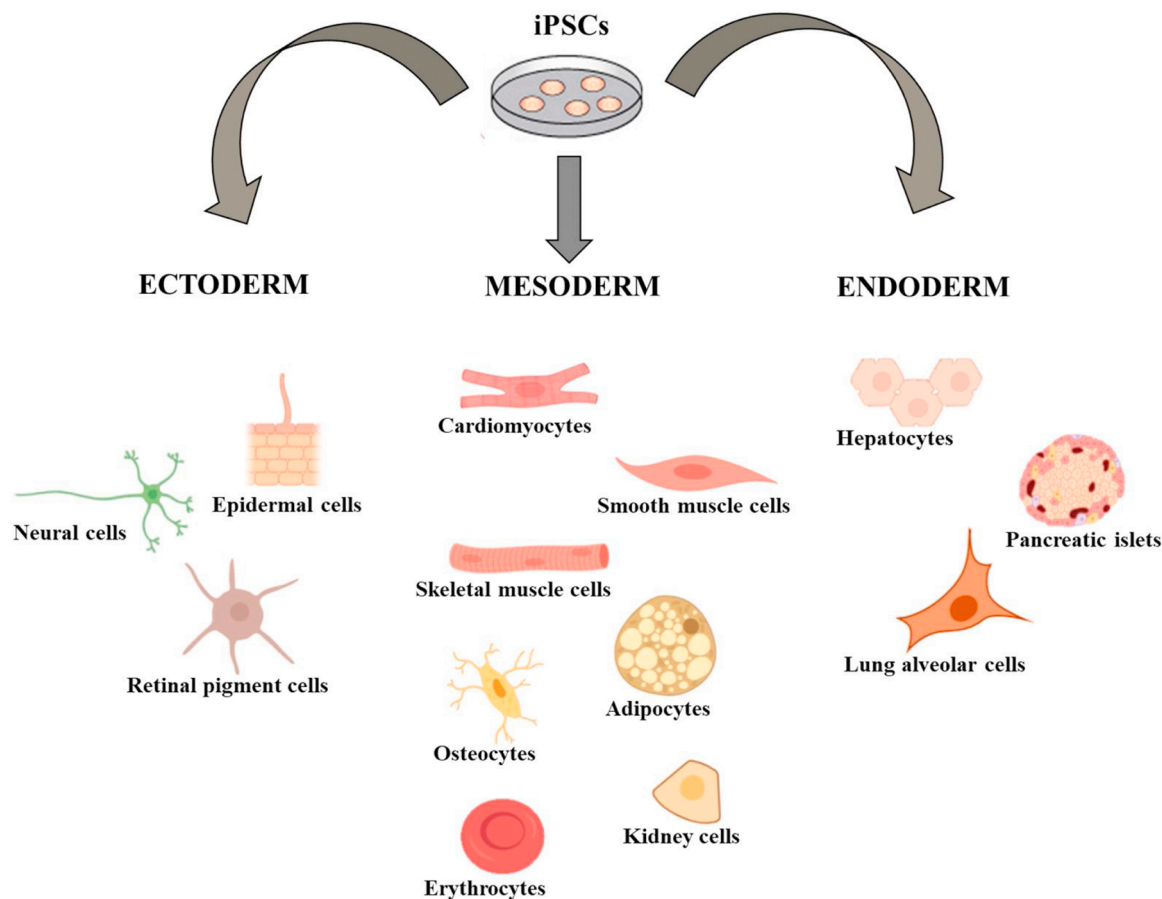


**Fig. 1.** iPSC differentiation into different lineages: iPSCs can be differentiated into different cell types that belong to the three germ layers: ectoderm, mesoderm and endoderm.

depending on the properties of various tissues in the body, hydrogels may be the material of choice for many applications. For example, hydrogels may not be the best material for extensive bone fracture regeneration in load-bearing areas, whereas they have been applied in nonload-bearing areas such as maxillofacial and cranial bones [25]. This review briefly discusses the uses of hydrogels in regenerative medicine and tissue engineering, and provides an update on various hydrogel-based substrates/matrices for iPSC culture and their differentiation toward different cells in the body.

## 2. *In vitro* culture systems of iPSCs: advantages and limitations

While iPSCs hold great promise for biomedical research, these cells must be maintained in an undifferentiated state *in vitro*. Over the past decade, scientists have gained knowledge in culturing stem cells, but the culture of stem cells remains a challenge. Different culture conditions are required for different types of stem cells. For example, human ESCs and iPSCs are cultured on a supporting layer of cells, such as human foreskin fibroblasts (HFFs) or MEFs, or on extracellular matrix [26]. Furthermore, ESCs and iPSCs must maintain pluripotency and avoid overgrowth while in culture. Different *in vitro* culture systems have been developed for the generation and culture of iPSCs.

### 2.1. Feeder cell-dependent culture systems

A standard culture method for the maintenance of iPSCs is to coculture these cells with fibroblasts. iPSCs are cultured on irradiated or mytomyocin-C-treated feeder layer cells such as MEFs. In this type of culture system, MEF-seeded plates are prepared in advance. The feeder layer acts as a supporting matrix for cell adhesion and proliferation and helps to maintain the self-renewal capacity of iPSCs by producing essential growth factors, cytokines and ECM proteins [27]. Since MEFs are animal-derived and have the risk of xenogenic contamination and cross-transfer of animal-derived pathogens to iPSCs cultured on top of them, the clinical translation of iPSCs or iPSC-derived cells from these feeder-dependent culture systems is a major challenge [28].

### 2.2. Feeder-free culture systems

Matrigel was used as an alternative substrate for iPSC expansion as a feeder-free culture condition that overcomes the limitation of the feeder cell layer. Matrigel is derived from Engelbreth-Holm-Swarm (EHS) mouse sarcoma cells and is composed of fibronectin, collagen IV, laminin, heparin sulfate proteoglycans, and enactin, among other growth factors [29]. A detailed proteomic analysis of Matrigel revealed many complex proteins, including growth factors, transcription factors,

structural proteins and binding proteins involved in biological processes and molecular functions of cells [29]. Matrigel substrate along with the appropriate media composition helps pluripotent stem cells (PSCs) remain in an undifferentiated state. However, as an animal-derived product with poorly defined matrix components, Matrigel is an inappropriate product for clinical use. Thus, ECM-specific proteins such as laminin, fibronectin and vitronectin have been used in recent years. For example, vitronectin, an ECM glycoprotein, is being used as a substrate for culturing iPSCs. Recombinant truncated vitronectin (VTN-N) is used for iPSC culture, as it supports the attachment and survival of iPSCs better than wild-type vitronectin. This protein is produced by the fermentation of recombinant *E. coli* [30]. However, the mass production of this protein is very expensive. For potential clinical applications, xeno-free and cost-effective products are essential. Hydrogels (both natural and synthetic) have recently been considered to overcome the limitations associated with safety, scalability and production cost involved in the derivation, expansion and differentiation of iPSCs [13]. Hydrogels overcome the limitations associated with the use of MEFs and Matrigel, such as the xenogenic origin, risk of cellular cross-contamination, cross-transfer of animal-derived pathogens, lack of reproducibility and inefficiency for application in clinics. Hydrogels are either natural or synthetic. Although some of the natural hydrogels are of animal origin, careful selection of xeno-free hydrogels for iPSC culture and differentiation can overcome the above-mentioned limitations associated with MEFs and Matrigel. Hydrogels also overcome the limitations associated with vitronectin, including long-term instability, cost-effectiveness, and scalability. Hydrogels have been explored for developing xeno-free, chemically defined culture platforms for the large-scale expansion of iPSCs to address the safety and efficiency issues associated with the aforementioned traditional expansion methods. In addition to these benefits, hydrogel-based platforms reduce safety concerns associated with viral vectors and enhance the efficiency of reprogramming with superior tunability [13]. Hydrogels have been used to create nanoparticle-based artificial reprogramming factors for cellular reprogramming [31] and to deliver reprogramming factors to targeted subcellular locations with accurate timing. In addition, hydrogels potentially create a stem cell-like microenvironment by incorporating key niche elements to regulate stem cell fate and function [32,33]. Moreover, cells reprogrammed on soft hydrogels [34] or hydrogels with aligned micropatterns [35] show better reprogramming efficiency than cells reprogrammed on traditional hydrogels. The advantages and limitations of *in vitro* culture substrates used for the expansion and differentiation of iPSCs are shown in Fig. 3.

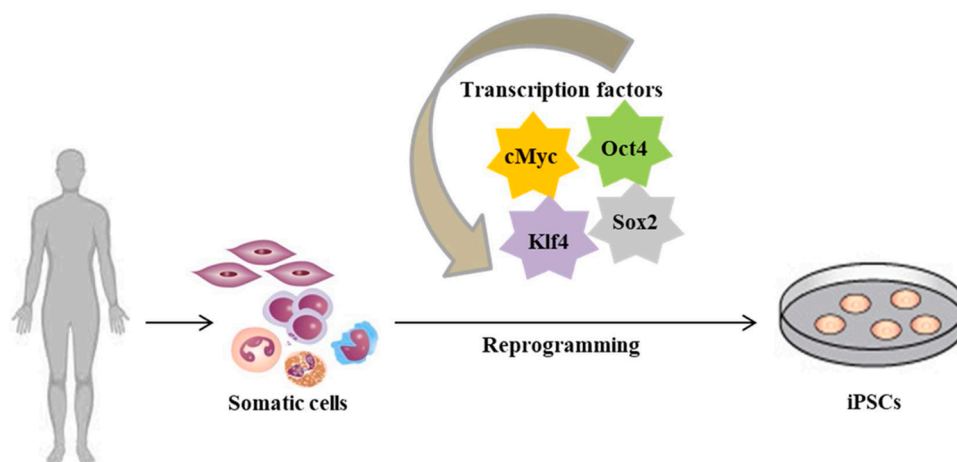


Fig. 2. Generation of induced pluripotent stem cells: iPSCs can be generated from somatic cells by reprogramming using the transcription factors OSKM.

<i>In vitro</i> culture substrates	Advantages	Limitations
<b>MEF</b>	<ul style="list-style-type: none"> <li>Act as a feeder layer by producing essential growth factors, cytokines and ECM proteins</li> <li>Helps maintain the self-renewal capacity of iPSCs</li> </ul>	<ul style="list-style-type: none"> <li>Animal origin</li> <li>Risk of xenogenic contamination</li> <li>Cross-transfer of animal derived pathogens</li> <li>Lack of reproducibility</li> <li>Inappropriate for clinical use</li> </ul>
<b>Matrigel</b>	<ul style="list-style-type: none"> <li>Used for iPSC expansion and differentiation</li> <li>Enables stable culture of PSCs</li> <li>Helps iPSCs remain in an undifferentiated state</li> </ul>	<ul style="list-style-type: none"> <li>Animal origin</li> <li>Poorly defined matrix components</li> <li>Inappropriate for clinical use</li> </ul>
<b>Vitronectin</b>	<ul style="list-style-type: none"> <li>Provides a defined surface for iPSC expansion</li> <li>Helps PSCs remain in an undifferentiated state</li> </ul>	<ul style="list-style-type: none"> <li>Inappropriate for large scale production</li> <li>Very expensive</li> <li>Unstable for long-term use</li> </ul>
<b>Hydrogel</b>	<ul style="list-style-type: none"> <li>Xeno-free</li> <li>Free from cellular cross-contamination and pathogens</li> <li>Good reproducibility</li> <li>Appropriate for clinical use</li> <li>Scalability</li> <li>Cost effective</li> <li>Stable and can recapitulate the native 3D environment</li> </ul>	<ul style="list-style-type: none"> <li>Some hydrogels are too weak to handle the stress needed for proper mechanotransduction</li> </ul>

Fig. 3. *In vitro* culture substrates used for the expansion and differentiation of iPSCs.

### 3. Hydrogel as a substrate for iPSC culture

Progressive development in the field of biomaterials and their properties supports cell survival, adhesion, proliferation and differentiation. Biomaterials such as nanofiber hydrogels have been shown to serve as substrates for the culture and differentiation of iPSCs by mimicking ECM stiffness and facilitating the diffusion of growth factors and nutrients [36]. A recent study used an alginate hydrogel functionalized with synthetic E-cadherin to study its role in promoting the attachment, viability, maintenance of pluripotency and the ability of PSCs to differentiate. The conjugated synthetic peptide mimicking E-cadherin in the ECM increased cell-to-cell contacts and promoted the

culture of PSCs as single cells by preventing apoptosis [37]. One of the advantages of using hydrogels for cell culture is that their stiffness can be changed depending on the origin of the tissue to be emulated. Additionally, the stiffness of the underlying culture substrate affects the cellular behavior [23]. Thus, stiffness is an important physical cue for the expansion and differentiation of pluripotent stem cells [26]. Polyacrylamide hydrogels with stiffnesses ranging from 3–25 kPa have been studied for the long-term maintenance of iPSCs. Based on the results of cell adhesion, viability, proliferation and gene expression analyses, a stiffness greater than 25 kPa was recommended to maintain the pluripotency and self-renewal capacity of iPSCs, whereas a stiffness less than 25 kPa will not support these properties [38]. Polyacrylamide

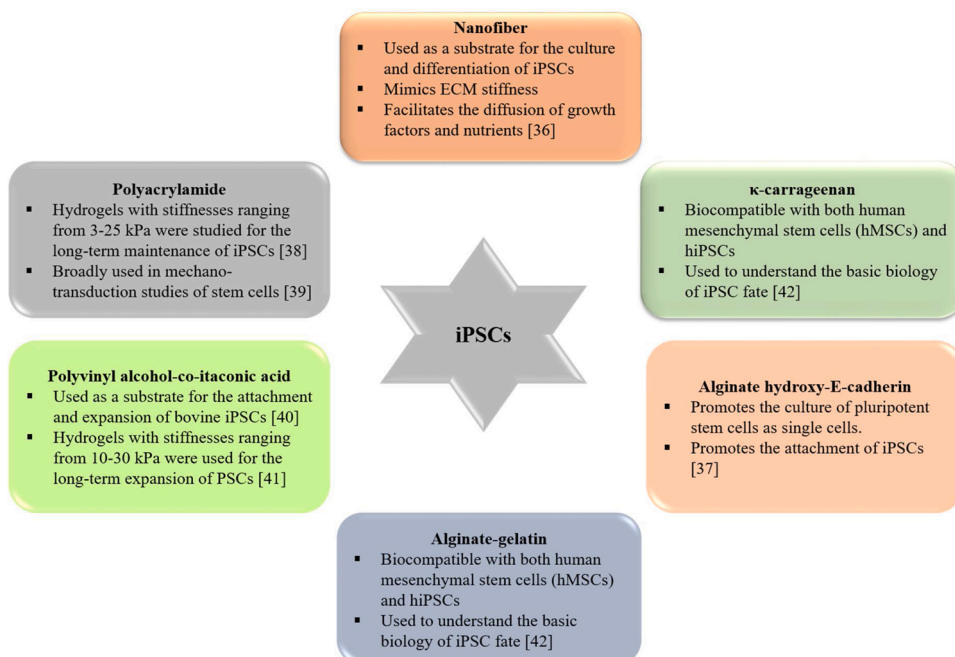


Fig. 4. Hydrogel substrates used for iPSC culture.

hydrogels are used broadly in mechanotransduction studies of stem cells [39]. Another synthetic hydrogel, poly(vinyl alcohol), was used as a substrate for the attachment and expansion of bovine iPSCs [40]. Poly(vinyl alcohol-co-itaconic acid) (P-IA) hydrogels with varying stiffnesses of 10–30 kPa were used for the long-term expansion of pluripotent stem cells [41]. Other hydrogel-based substrates, such as micropatterned  $\kappa$ -carrageenan hydrogels and alginate-gelatin hydrogels, are biocompatible with both human mesenchymal stem cells (hMSCs) and hiPSCs and have been used to understand the basic biology of iPSC fate [42]. All these studies indicate that hydrogels can be used as a xeno-free clinical grade culture system for extensive application in cell-based therapies. Fig. 4 shows different hydrogels used as substrates for iPSC culture.

#### 4. Hydrogels and their applications in tissue engineering and regenerative medicine

Over the years, research has defined hydrogels in different ways. The most common definition is that hydrogels are cross-linked polymers that are capable of swelling by absorbing water and retain water in their structures, but they are not dissolved in water. Hydrogels hold large quantities of water because of their hydrophilic structure. They contain 50–90 % water, depending on the type of hydrogel preparation and the degree of cross-linking. The presence of water in the hydrogel provides them with good biocompatibility and an excellent drug encapsulation capacity [43].

##### 4.1. Classification of hydrogels

Hydrogels are often classified into two categories: natural and synthetic hydrogels (Fig. 5). Natural hydrogels consist of collagen, hyaluronic acid, fibrin, chitin, gelatin, chitosan, carrageenan and alginate [44]. Generally, these polymers are either components of natural ECM or are extracted from natural sources such as brown algae, seaweed, and bacterial culture. In addition, hydrogel properties are similar to natural ECM and have desirable features such as biocompatibility and biodegradability. Moreover, most of the natural hydrogels except alginate possess natural binding sites that facilitate the interaction between cells and hydrogels [44]. Due to these characteristic properties, natural hydrogels promote the adhesion and proliferation of cells and enable tissue regeneration [23]. Since they possess features similar to the native cellular environment, these hydrogels are commonly used in tissue engineering applications [45]. For example, collagen is the most abundant protein in mammalian tissue ECM, comprising 25 % of the whole-body protein content. The properties of collagen, such as biocompatibility, biodegradability, weak antigenicity and cell adhesion, make it an attractive material for wound dressing and vascular applications [46]. Nevertheless, these materials are subject to breakage because of their

low mechanical strength and poor stability [44]. Poly(ethylene glycol) (PEG), poly(lactic acid) (PLA), poly(lactic-co-glycolic acid) (PLGA), poly(vinyl alcohol) (PVA) and polyacrylamide (PMA) are synthetic polymers that are used frequently in the fabrication of hydrogels [47]. They have a high strength with a tunable chemical composition and mechanical properties. However, their biocompatibility, degradability and availability of adhesion sites are some of the concerns associated with synthetic hydrogel use [48].

##### 4.2. Fabrication of hydrogels

Studies have proposed various fabrication methods for the preparation of hydrogels from different monomers and polymers based on the characteristics needed for the hydrogels [23]. Fabrication of hydrogels replicates the microenvironment and controls the spatial localization in the limits of the scaffolding material [49]. This process allows them to generate native cellular environments and synchronize cellular events similar to those in living tissues [50]. A vivid and vast variety of synthetic and natural polymer compositions and cross-linking methods have been adopted to fabricate and functionalize hydrogels with biological and chemical cues [51,52]. Hydrogels are fabricated by simply crosslinking hydrophilic polymeric chains or by polymerizing water-soluble monomers with multifunctional cross-linkers.

Initially, research on hydrogels was focused on chemically cross-linked polymeric networks to study their fundamental characteristics. With advances in hydrogel research, different types of hydrogels that respond to variations in environmental conditions, such as temperature, pH and magnetic and electric fields, have been developed [53]. Hydrogel formation is achieved through either a covalent crosslinking method such as photopolymerization and Michael-type addition or through physical interactions (e.g., self-assembly and ionic interactions), often for cell encapsulation [54]. For example, the osteogenic and hepatic differentiation of murine ESCs in suspension is supported by the self-assembling hydrogel RAD-161 [55,56], and the encapsulation of human ESCs in hyaluronic acid hydrogels supports their growth and survival [57].

Fabrication of hydrogels for cell culture experiments involves either encapsulating the cells within the substrate or seeding cells on substrates after substrate fabrication using molds [18]. Certain criteria must be considered when designing hydrogels for the encapsulation of cells. Prior to cell encapsulation, the cells must be suspended in a liquid precursor solution, and the structure and chemistry of the hydrogels must be suitable for tissue formation and cell survival. Moreover, the degradation products should not exert any adverse effects on the encapsulated cells. Radical chain polymerization and chemical cross-linking are the most common mechanisms used to create covalently crosslinked hydrogels for the encapsulation of cells. A unique set of

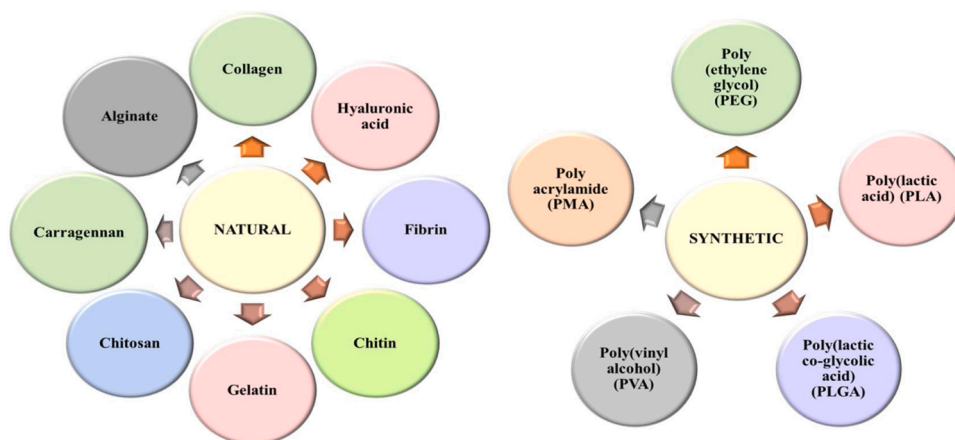


Fig. 5. Classification of hydrogels: Cartoon showing various types of naturally occurring hydrogels and synthetic polymers used for the fabrication of hydrogels.



liquid precursors with multifunctional macromers are utilized by each mechanism to enable crosslinking [58]. A study by Wang et al. used a biodegradable, injectable OPF hydrogel [oligo [poly(ethylene glycol) fumarate] as a mouse embryonic stem cell (mESC) carrier for treating myocardial infarction (MI) [59]. Under physiological conditions, OPF-based formulations are crosslinked in the presence of radical initiators to form hydrogels. The mESCs were encapsulated in OPF hydrogels and injected into a rat MI model. The encapsulated ESCs in the OPF hydrogel retained their ability to differentiate following ascorbic acid induction. Additionally, the combination of OPF hydrogels and mESCs improved cell retention and survival within the ischemic myocardium after transplantation [59].

#### 4.3. Mechanics of hydrogels

In recent years, hydrogels have attracted attention due to their versatile properties and the possibility of modifying their structure to tune their properties. Among the properties of hydrogels, mechanical properties are important for the stability of the material in culture and may also influence cellular mechanotransduction, which in turn influences cellular behaviors such as adhesion, spreading, migration and stem cell differentiation [46,23]. Substrate stiffness is considered a crucial tool determining stem cell fate, and this property can direct the differentiation of pluripotent stem cells, mesenchymal stem cells, osteoblasts, and neural and hepatic progenitor cells [17]. The elasticity of the tissues in the human body ranges from less than 1 kPa in the brain, breast, and lung 1–10 kPa in muscle and endothelial tissues, 100 kPa in precalcified bone, 1 MPa in cartilage and up to 2–4 GPa in bone [44,45,49,60]. Fine control over the mechanical properties of the hydrogels provides a key parameter for guiding stem cell fate, where its final differentiation can be tuned extensively. For example, hMSCs (human mesenchymal stem cells) cultured on poly(acrylamide) gels of different stiffnesses, 0.1–1, 8–17 and 25–40 kPa, enabled their differentiation into neural, muscle and bone lineages, respectively [47,61]. Similarly, neural stem cells cultured on collagen/hyaluronic acid matrices with a stiffness of  $\approx 1$  kPa (soft) and  $\approx 10$  kPa (stiffer) differentiate into neurons and glial cells, respectively [48,62]. Remarkable progress has been achieved in the synthesis and fabrication of hydrogels from natural and synthetic sources for various applications. The area of application includes stem cell research, substrates for stem cell culture, regenerative medicine, cell therapy, wound healing, and cancer research.

#### 4.4. Applications of hydrogels

Hydrogels possess structural and mechanical properties and an ECM that resembles those of natural tissues and support cell adhesion and the diffusion of proteins [21]. These properties allow the usage of hydrogels as a platform for iPSC-based tissue engineering and regenerative medicine, wound healing and cell therapy.

##### 4.4.1. iPSC-based tissue engineering and regenerative medicine

The use of a gelatin methacrylate (GelMA) hydrogel that encapsulated iPSC-derived neural stem cells was reported for spinal cord injury [63]. In mice, the encapsulated cells remain viable at the injury site and are effective at promoting neurite outgrowth and neuronal differentiation. Subsequently, the encapsulated neural stem cells in the GelMA hydrogel promote functional recovery of spinal cord injury in a mouse model [63]. For applications in neural tissue engineering, a natural polymer hydrogel system based on chitosan-alginate (Chi-Alg) promoted the proliferation of olfactory ensheathing cells (OECs) and neural stem cells (NSCs). This hydrogel has a highly interconnected porous structure that facilitates cell adhesion, proliferation and diffusion of nutrients. The combination of the chitosan-alginate hydrogel with OECs and NSCs shows good potential for application in stem cell-based neural tissue engineering [64].

##### 4.4.2. iPSC-based wound healing

Hydrogels have been used for iPSC-based wound healing and wound regeneration applications [65]. Human corneal keratocytes reprogram iPSCs together with an injectable amphiphatic carboxymethyl-hexanoyl chitosan (CHC) hydrogel to facilitate wound healing in damaged corneas [66]. This combined treatment enhances the reconstruction of the cornea by reducing oxidative stress. Additionally, it recruits epithelial cells toward the injured areas, thereby restoring the corneal epithelial thickness. This study concluded that iPSCs along with CHC hydrogels potentially represent an alternative cell-based therapeutic strategy for ocular diseases [66].

##### 4.4.3. For studying iPSC differentiation and for cell transplantation

Wu et al. (2017) used methacrylated hyaluronic acid (Me HA) hydrogels as a 3D *in vitro* model for the culture and differentiation of iPSC-derived neural progenitor cells (NPCs) toward a mature neural phenotype [67]. In this study, the effect of hydrogel stiffness on cellular behavior was studied by encapsulating NPCs in both soft and rigid Me HA hydrogels. The cells encapsulated in soft hydrogel showed neurite outgrowth and increased levels of neurite differentiation. Rigid hydrogels maintained the properties of NPCs. In the study, the softer hydrogel had a stiffness of  $0.51 \pm 0.20$  kPa, and the rigid hydrogel had a stiffness of  $1.41 \pm 0.27$  kPa [67]. Recently, a study by Goetzke and coworkers showed the differentiation of iPSCs to mesenchymal stem cells using a fibrin hydrogel in which iPSCs were embedded. However, the cells embedded in the hydrogel gave rise to small cells having a heterogeneous growth pattern with the lowest expression of MSC markers and displayed a low differentiation potential. However, differentiation performed on normal cell culture plastic and on the surface of fibrin hydrogel resulted in the typical phenotype of MSCs [68]. Folic acid (FA) hydrogel-encapsulated iPSCs transplanted into acute myocardial infarction mouse models showed significant improvements in iPS cell retention, survival, differentiation into cardiomyocytes and stimulation of neovascularization [69]. Chiang et al. (2015) showed that an injectable carboxymethyl-hexanoyl chitosan hydrogel (CHC) with sustained hepatocyte growth factor (HGF) release acted as an excellent vehicle for iPSC-derived hepatocyte engraftment in an iPSC-based therapy for acute hepatic failure in a mouse model [70]. In a periodontal rat defect model, chitosan/gelatin/glycerol phosphate hydrogel-encapsulated iPSCs with BMP-6 promoted the osteogenesis and differentiation of new connective tissue and periodontal ligament formation. This study revealed a better strategy to enhance periodontal regeneration [71]. A glycol chitosan/poly(EO-co-Gly) hydrogel loaded with iPSCs overexpressing growth differentiation factor 5 enhance the repair of intervertebral disc degeneration in rat models [72].

#### 5. Hydrogels as substrates for iPSC differentiation and for culturing iPSC-derived cells

Hydrogels have been used as substrates for the differentiation of iPSCs into ectoderm, endoderm and mesoderm lineages. The use of various hydrogels as substrates in the differentiation of iPSCs into various tissues, as well as the use of hydrogels as substrates for the proliferation of iPSC-derived tissues, is summarized in Fig. 6.

##### 5.1. Hydrogels for differentiation into the ectoderm lineage

###### 5.1.1. Neural cells

ECM properties such as stiffness and topographical cues along with soluble factors and biochemical signals from the microenvironment are important parameters that modulate the differentiation of stem cells toward specific lineages [73]. Culturing neural stem/progenitor cells on soft substrates with Young's moduli similar to those of the native brain results in increased differentiation [74,75]. Hydrogels based on the native ECM microenvironment have the potential to recapitulate the CNS microenvironment *in vitro* and have been used for culturing neural



Germ layers	Hydrogels	Uses of hydrogels	Cell types
<b>Ectoderm</b>	Hyaluronic acid	<ul style="list-style-type: none"> <li>For neural progenitor cell differentiation</li> <li>As potential carriers for delivering cells to patients in clinics</li> <li>As a physiological model for testing new drugs [77]</li> </ul>	Neural progenitor cells
	Alginate/collagen	<ul style="list-style-type: none"> <li>As a 3D cell culture platform for human iPSC-derived neurons</li> <li>Promotes neuronal development and maturation [78]</li> </ul>	Neurons
	Polyethylene glycol (PEG)	<ul style="list-style-type: none"> <li>For culturing iPSC-derived neural stem cells [79]</li> </ul>	Neural stem cells
	Gelatin/laminin	<ul style="list-style-type: none"> <li>Promotes rapid adhesion of human iPSC-derived spinal spheroids</li> <li>Promotes rapid axon elongation</li> <li>For neuromuscular tissue engineering applications [80]</li> </ul>	Spinal spheroids
	Collagen I	<ul style="list-style-type: none"> <li>For the differentiation of iPSCs into mammary-like organoids</li> <li>For the potential development of <i>in vitro</i> models</li> <li>For bioengineering mammary tissues [88]</li> </ul>	Mammary-like organoids
	Fibrin	<ul style="list-style-type: none"> <li>For the differentiation of iPSCs into oligodendrocytes</li> <li>Potential for tissue engineering of spinal cord injuries [81]</li> <li>For the differentiation of iPSCs into retinal pigment epithelium (RPE) cells</li> <li>Can support surgical implantation</li> <li>Possibly used for the transplantation of RPE cells [82, 84]</li> </ul>	Oligodendrocytes Retinal pigment epithelium (RPE) cells
<b>Endoderm</b>	Synthetic-nanofiber	<ul style="list-style-type: none"> <li>For the differentiation of human iPSCs into hepatocytes [36]</li> </ul>	Hepatocytes
	Nanofibrillar cellulose/Cellulose nanofibrils	<ul style="list-style-type: none"> <li>For 3D culture of human HepaRG cells and hepatocellular carcinoma HepG2 cells [90]</li> <li>As a thin film substrate for the differentiation of iPSCs into hepatocyte-like cells [91]</li> </ul>	Hepatocytes
	Alginate	<ul style="list-style-type: none"> <li>For culturing pluripotent stem cell-derived intestinal organoids [93]</li> </ul>	Intestinal organoids
	Polyethylene glycol (PEG)	<ul style="list-style-type: none"> <li>Supports the generation of intestinal organoids from human ESCs and iPSCs</li> <li>Can act as a delivery vehicle</li> <li>Potential applications in cell therapy for gastrointestinal diseases [94]</li> </ul>	Intestinal organoids
	Carboxymethyl-hexanoyl chitosan (CHC)	<ul style="list-style-type: none"> <li>For culturing iPSC-derived hepatocytes</li> <li>CHC along with HGF promoted recovery from liver injuries</li> <li>Serves as a delivery vehicle for iPSC-derived hepatocytes <i>in vivo</i> [92]</li> </ul>	Hepatocytes
	PVAMA-AlgMA-GelMA hydrogel	<ul style="list-style-type: none"> <li>For the differentiation of iPSCs into pancreatic islets [95]</li> </ul>	Pancreatic islets
<b>Mesoderm</b>	Collagen/Fibrin	<ul style="list-style-type: none"> <li>For culturing iPSC-derived cardiomyocytes</li> <li>Provides a basis for the development of a more sophisticated and customised matrix for tissue engineering applications [97]</li> </ul>	Cardiomyocytes
	Alginate	<ul style="list-style-type: none"> <li>For generating vascular smooth muscle cells from pluripotent stem cells</li> <li>Provides a 3D microenvironment and protects cells by reducing hydrodynamic stresses [100]</li> </ul>	Vascular smooth muscle cells
	PuraMatrix	<ul style="list-style-type: none"> <li>For encapsulating iPSC-derived osteoprogenitor cells [87]</li> <li>For bone regeneration [83]</li> </ul>	Osteoprogenitor cells

Fig. 6. Hydrogels used for the culture and differentiation of cells belonging to ectoderm, endoderm and mesoderm lineages.

stem/progenitor cells. These 3D *in vitro* culture systems have been used to study the development of neurons and differentiation of neural progenitor cells [76]. Hyaluronic acid (HA)-based hydrogels were used to induce the differentiation of neural progenitor cells (NPCs). Hyaluronic acid is a high molecular weight ECM component of native tissues that significantly affects the proliferation of neurons and their development. In a study, NPCs derived from the ventral midbrain were photo-encapsulated in HA hydrogel, and after three weeks, these cells encapsulated in hydrogel showed mechanical properties similar to those of a neonatal brain and subsequently differentiated into neurons. Additionally, tuning the mechanical properties of hydrogels influences the differentiation status, and hydrogels might be used as carriers for delivering cells to patients in clinics or as physiological models for testing new drugs [77].

In 2019, Moxon and coworkers showed that alginate, a component of the cell walls of brown algae, recapitulates some features of the brain ECM. Through chemical modification or blending alginate with a cell adhesive material such as collagen, they showed enhanced neural development [78]. In addition, by modulating the concentration of alginate ionic cross-linker, the stiffness of the hydrogel changed to a brain ECM-like microenvironment. This property facilitates cell adhesion, neuronal maturation and synapse formation. Thus, the alginate/collagen hydrogel serves as a 3D cell culture platform for human iPSC-derived neurons to promote neuronal development and

maturation [78]. In addition to natural hydrogels, one of the synthetic biomaterial polyethylene glycol (PEG) hydrogels is used for culturing iPSC-derived neural stem cells. The effects of the N-cadherin-derived peptide His-Ala-Val-Asp-Ile (HAVDI) on cell survival, extension of neurites and neural differentiation marker expression have been reported. N-cadherin is a cell adhesion molecule with important roles in homeostasis and the development of brain tissue. A PEG hydrogel containing a continuous gradient of the N-cadherin-derived peptide HAVDI exerts concentration-dependent effects on hiPSC-derived neural stem cell survival and differentiation [79]. Hydrogels have been applied in neuromuscular tissue engineering. For example, in one study, a hydrogel was fabricated by the enzymatic crosslinking of a gelatin hydrogel with laminin, an ECM protein. This hydrogel has a surface elastic modulus of  $4.29 \pm 2.35$  kPa to  $24.1 \pm 12.9$  kPa, while its bulk elastic modulus ranges from  $1.46 \pm 0.33$  kPa to  $8.40 \pm 0.73$  kPa. These ranges fall within the *in vivo* elastic moduli of various cellular ECMs, as well as muscular and neuronal tissues. Thus, the hydrogel combination prompted rapid adhesion of human iPSC-derived spinal spheroids and rapid axon elongation on the hydrogel. Additionally, these axons exhibited a more mature morphology and better electrophysiological properties. In addition to iPSC-derived spinal spheroids, Schwann and skeletal muscle cells have also been cultured on a gelatin-laminin hydrogel. These cells showed good adhesion, proliferation, a healthy morphology and expressed cell-specific markers. The study suggests the

use of this hybrid hydrogel for the generation of functional neuromuscular junctions and to produce associated organs on a chip [80]. For the differentiation of iPSCs to oligodendrocytes, a natural polymer, fibrin hydrogel, was used as a scaffold [81]. In this study, cells encapsulated in the hydrogel showed good viability, elongated morphology, and strong adhesion. Additionally, the differentiated cells expressed oligodendrocyte markers such as Oligo 2, O4, Sox 10, MBP and PDGFR $\alpha$ . This study suggests the use of fibrin hydrogels to provide a metabolically active cellular environment for the differentiation of iPSCs into preoligodendrocytes and has the potential for tissue engineering of spinal cord injuries [81].

### 5.1.2. Retinal pigment epithelium cells

Retinal pigment epithelial cells (RPE) comprise a simple layer of cuboidal cells that are located behind the photoreceptor (PR) cells. RPEs have many functions, such as phagocytosis of the shed PR outer segment membrane, conversion and storage of retinoids, absorption of scattered light, and ion and fluid transport. The clinical use of RPE cells has progressed, and the use of xeno-free materials has increased in importance. Gandhi and coworkers used an autologous human fibrin hydrogel to differentiate iPSCs into retinal pigment epithelium cells (RPE) [82]. They prepared fibrin gels by mixing 30 mg/mL fibrinogen with 50 U/mL thrombin and allowed the gel to polymerize prior to seeding iPSCs. Aprotinin (50 U/mL) was also supplemented in the culture media to improve hydrogel stability. In this study, the average thickness of the hydrogel used was  $200 \pm 30 \mu\text{m}$ , and the mechanical strength of the hydrogel was increased by increasing the concentration of fibrinogen [82]. Fibrin is an insoluble protein that forms a 3D mesh and prevents blood flow by forming clots. Fibrin forms a hydrogel when isolated. Fibrin gels are used in vascular engineering applications, and different approaches have confirmed the formation of vessel-like structures both *in vitro* and *in vivo*. Furthermore, fibrin hydrogels have been used for drug encapsulation and cell delivery [83]. Fibrin hydrogels can be formed in different sizes and shapes with stiffness and degradation properties suitable for RPE cells. This fibrin hydrogel serves as a long-lived substrate for differentiation into RPE cells by providing good mechanical strength and degradation properties, which may help in surgical implantation. Additionally, fibrin hydrogels can be used as scaffolds for the transplantation of RPE cells [82,84].

iPSC-derived organoid models of different tissues help to create an *in vitro* physiological system more precisely than classical culture techniques [85]. Organoids combine the pliability of *in vitro* systems with the three-dimensional architecture and differentiation of *in vivo* model systems. These novel model systems have been used to study the respective organ- or tissue-specific physiology and pathology at a greater depth, thereby having applications in cancer biology, clinical translation and precision or personalized medicine. For example, in cancer and chronic inflammatory disease research, patient iPSC-derived organoids may help predict therapeutic responses and provide insights into tumor biology and inflammatory disease processes, respectively [86]. In this context, a 3-D hydrogel-based iPSC-derived organoid culture system holds promise.

### 5.1.3. Mammary-like organoids

An organoid is a 3D cell aggregate derived from stem cells that is capable of self-renewal and self-organization [87]. Although iPSCs have been differentiated into various organoids/tissues, the generation of mammary organoids/cells from human iPSCs has not been established. A 3D culture system of a floating mixed gel composed of collagen I and Matrigel was used for iPSC differentiation into mammary-like organoids [88]. This mixed gel was prepared by mixing 3 portions of Matrigel (10.1 mg/mL) with 1 portion of collagen I (4 mg/mL) to form a final concentration of 2.5 mg/mL Matrigel and 1 mg/mL collagen I. Collagen I is the most abundant protein in the human body. Collagen fibrils are formed by the assembly of collagen I polymers, and these fibrils assemble to form large collagen fibers. The orientation and organization

of these fibers correlate with the invasion of breast cancer and the prognosis of patients [89]. Additionally, collagen I can yield a stiffness of 170 kPa, which is similar to the stiffness of the normal mammary gland [89]. Interestingly, the iPSCs that differentiated into organoids on this mixed hydrogel expressed breast tissue markers such as  $\alpha$ -lactalbumin, acetyl-CoA, milk protein, luminal epithelial markers such as EpCAM and CK18, and the basal markers CK14 and P63. These markers were also detected in normal human mammary gland tissue, which was used as a control. These iPSC-derived mammary-like organoids can be used for the development of *in vitro* models to identify the specific effects of different factors on breast cancer development and for the bioengineering of mammary tissues [88]. The findings of this study may reveal new method to develop iPSC-based approaches for solving captious questions in human breast cancer development.

## 5.2. Hydrogels for the endoderm lineage

### 5.2.1. Hepatocyte like-cells

According to different studies, 3D culture systems mimic the microenvironment that enhances hepatocyte differentiation. Synthetic nanofiber hydrogels were used for the differentiation of human iPSCs into hepatocytes [36]. These hydrogels are xeno-free synthetic biomaterials that support iPS cell adhesion and differentiation. The pore size of this gel ranges from 50–200 nm and can be synthesized by interweaving synthetic self-assembling polypeptides. This hydrogel generates hepatocyte-like cell (HLC) spheroids expressing hepatocyte markers and shows metabolic activity and functional maturity [36]. Nanofibrillar cellulose hydrogel (NFC) has been used as a 3D cell culture scaffold for human HepaRG cells and hepatocellular carcinoma HepG2 cells. In this study, the cells encapsulated in the scaffold formed 3D multicellular spheroids. NFC is a plant-derived biomaterial that mainly consists of  $\beta$ -D-(1/4) glucopyranose polysaccharide chains and is isolated from the wood and cell walls of plants. It is noncytotoxic and exhibits tunable chemical and physical properties. Hence, it has diverse biomedical and pharmaceutical applications [90]. A recent study from our group showed that cellulose nanofibrils (CNFs), also known as nanofibrillar cellulose, used as thin film substrates effectively differentiated iPSCs into hepatocyte-like cells (HLCs) [91]. The web-like structure of CNFs and their biocompatibility aid in the differentiation of iPSCs into HLCs. The differentiated cells on CNFs were compared with the cells differentiated on Matrigel in terms of surface marker expression, albumin secretion and lipid accumulation. Additionally, these differentiated cells showed functional maturity and expressed biomarkers similar to primary hepatocytes. Slightly higher expression of the mature hepatic marker ASGPR1 was observed in the HLCs growing on CNFs than in the HLCs growing on Matrigel. This difference in gene expression may be due to the clustering of cells on CNFs during proliferation that led to cell-cell interactions and cell-cell communication. CNF overcomes the limitations of Matrigel and is more cost-effective than Matrigel [91]. Chiang and coworkers developed an injectable carboxymethyl-hexanoyl chitosan (CHC) hydrogel containing hepatocyte growth factor (HGF) with sustained release. In this study, iPSCs were reprogrammed from human dental pulp fibroblasts and differentiated into hepatocytes. These differentiated hepatocytes were cultured in the HGF-CHC hydrogel. This hydrogel serves as a delivery vehicle for iPSC-derived hepatocytes *in vivo*. The authors also revealed that the antioxidant capacity of these differentiated hepatocytes was increased in the presence of HGF-CHC. HGF in hydrogels reduces apoptosis-related protein expression and levels of oxidative substances and eventually promotes the recovery of liver functions during injuries [92].

### 5.2.2. Intestinal organoids

Human intestinal organoids (HIOs) are considered an excellent tool to study intestinal development and possess the potential to provide a customized and scalable source of intestine in the area of regenerative therapies. Capeling et al. documented the use of nonadhesive alginate

hydrogels for culturing pluripotent stem cell-derived intestinal organoids [93]. Initially, iPSCs were induced to differentiate into the intestinal lineage on a 2D surface, and the generated spheroids were collected by detaching them from the 2D surface. These spheroids were embedded in alginate hydrogels. A 3D hydrogel network was formed by cross-linking calcium chloride with an alginate solution containing these spheroids. The HIOs grown on alginate were highly similar to the HIOs grown on Matrigel, which was used as a control. HIOs grown on both alginate and Matrigel had a similar engraftment and maturation status when transplanted *in vivo*. After transplantation, the cells closely resembled the human intestine. Collectively, these results showed the effectiveness of alginate as a supporting matrix for the culture and differentiation of iPSC-derived HIOs and as a substitute for cell-derived ECM. [93]. A different study used a synthetic PEG hydrogel for the generation of intestinal organoids from both human ESCs and iPSCs. These hydrogels served as a vehicle to deliver intestinal organoids to the injured murine intestinal mucosa. Transplantation resulted in HIO engraftment and improved colonic wound repair. This strategy might be a basis for the development of therapies using pluripotent stem cell-derived human intestinal organoids for gastrointestinal diseases [94].

### 5.2.3. Pancreatic islets

A recent study reported the use of a three-dimensional PVAMA-AlgMA-GelMA hydrogel scaffold for the differentiation of iPSCs into pancreatic islets [95]. Scaffolds were prepared from poly(vinyl alcohol) (PVA), alginate (Alg) and gelatin (Gel) conjugated with methacrylic anhydride (MA) to provide a 3D network for the encapsulation of iPSCs. The surface of PVAMA-AlgMA-GelMA scaffolds was grafted with activin A and BMP4 to induce the differentiation of iPSCs into definitive endoderm (DE). The resulting constructs were treated with retinoic acid-loaded solid lipid nanoparticles (RA-loaded SLNs) to regenerate insulin-producing cells. Many weight percentages of activin A and BMP4 were used for grafting on the surface of this hydrogel scaffold for the differentiation of iPSCs into the DE lineage. From DE, insulin-producing cells were generated. Immunofluorescence staining and flow cytometry analyses revealed that hydrogel scaffolds grafted with BMP4 and 75 % activin A followed by treatment with RA-loaded SLNs efficiently derive pancreatic islets from iPSCs [95].

## 5.3. Hydrogels for the mesoderm lineage

### 5.3.1. Cardiomyocytes

iPSCs can differentiate into cardiac lineages [96]. Highly functional cardiomyocytes for translational applications have been obtained by seeding iPSC-derived cardiomyocytes on collagen-fibrin hydrogels. Collagen is a structural protein that is present in cardiac muscles. Fibrin is involved in the cascade of wound healing and is used as a cardiac tissue scaffold component. This study helps elucidate how matrix components and hiPSC-derived cardiomyocytes interact to form functionally engineered tissue. Additionally, it provides a basis for the development of a more sophisticated and customized matrix for tissue engineering applications [97]. A stiffness of 9 kPa is ideal for the cardiac differentiation of iPSCs. Substrate stiffness contributes to cellular behaviors such as attachment, migration and differentiation [98].

### 5.3.2. Vascular smooth muscle cells (VSMCs)

VSMCs are the major cells in arteries that are important for maintaining the integrity of arterial walls [99]. They are critical and required in large numbers for applications in tissue engineering, disease modeling, drug discovery and cell therapy. In research labs, pluripotent stem cell-derived VSMCs have been produced on a small scale, but the production of these cells in larger quantities is very difficult. Alginate-based hydrogels have shown potential in mimicking the embryonic microenvironment due to their tunable flexibility, gelling behavior, nonadhesive property and reversible cross-linking [100]. These hydrogels have been fabricated into microbeads, macrobeads,

microfibers, microcapsules and microtubes. Alginate microcapsules and microbeads support the culture and differentiation of both mouse and human ESCs. In addition, alginate microtubes and microcapsules containing liquid cores provide a liquid-like microenvironment for the self-assembly of cells [101]. Recently, Lin et al. developed a method for culturing cells inside microscale alginate hydrogel tubes [102]. Alginate hydrogel tubes were prepared by pumping an HA solution containing cells and an alginate solution into the central area and side channels of a custom-made microextruder and extruding the sample into CaCl<sub>2</sub> buffer. Later, the CaCl<sub>2</sub> buffer was replaced with appropriate cell culture medium. iPSCs reprogrammed from both dermal fibroblasts and bone marrow mesenchymal stem cells were used in this study. Initially, the cells formed small clusters that subsequently grew into spheroids. Then, the hydrogel tubes were filled with these spheroids. Hydrogel microtubes provide a friendly microenvironment for cells and protect them from aggregation and hydrodynamic stresses. In this study, VSMCs grown in alginate tubes and VSMCs grown in 2D culture plates were compared. The results revealed a similar differentiation efficiency. Additionally, transplantation studies showed similar levels of blood vessel formation *in vivo* by VSMCs in alginate tubes and 2D cultured VSMCs. However, some differences were observed in global gene expression. Increased expression of genes associated with vasculature development, angiogenesis and cell migration was observed in VSMCs grown in alginate tubes. However, in 2D-cultured VSMCs, increased expression of genes associated with biosynthetic processes and cell death was observed. Only 10 days was required for the generation of stem cell-derived VSMCs with high purity, increased viability and high yield (approximately  $5.0 \times 10^8$  cells/mL) in this study. This manufacturing method provides VSMCs for different biomedical applications [102].

### 5.3.3. Osteoprogenitor cells

Bone tissue engineering is a novel remarkable method that is used to repair damaged bones [103]. This process involves the regeneration of tissues using stem cells, growth factors and scaffolds, with stem cells playing an important role in tissue regeneration. In bone tissue engineering, a microenvironment for the cells must be created to ensure the complete differentiation of bone tissue. For the successful regeneration of bone tissue, different types of materials have been explored for the fabrication of optimal scaffolds. Many biodegradable and biocompatible polymers have been investigated as bone scaffolds, and osteoinductive materials such as growth factors and metal ions were also incorporated into these scaffolds [104]. Hydrogels are widely used as scaffolds in bone tissue engineering for cell adhesion and the transport of growth factors [105]. Hydrogel scaffolds containing growth factors in which stem cells are encapsulated function as extracellular matrix and promote cell functioning [106]. Cells secrete the extracellular matrix needed for tissue regeneration, while the scaffolds serve as a temporary matrix. For bone regeneration, different hydrogel configurations have been formulated using various fabrication techniques. Ideally, for enhanced bone regeneration, the hydrogel formulations should meet the following criteria: 1) the hydrogel should be osteogenic, osteoconductive, osteoinductive and osteocompatible; 2) it should be nonimmunogenic and noncytotoxic to avoid an inflammatory response; 3) it should be biodegradable; 4) it should mimic the natural ECM to facilitate cell adhesion, proliferation and osteogenic differentiation; and 5) the porosity, mechanical strength and structural stability of the hydrogel should be optimized [107]. Human bone tissue has elastic moduli ranging from 1 to 20 GPa [104]. The ability of transplanted cells to regenerate bone *in vivo* was investigated by encapsulating iPSC-derived osteoprogenitor cells in PuraMatrix, a commercially available self-assembling synthetic peptide nanofiber hydrogel [108]. PuraMatrix has been used in calvarial bone defect models, where it showed acceptable regenerative properties [106]. PuraMatrix promotes the invasion of vascular endothelial cells from adjacent tissues and promotes new bone tissue formation [109]. In this study, encapsulated



osteoprogenitor cells transplanted in a calvarial bone defect rat model showed good vascularization and regeneration potential. The growth factors and cytokines secreted by the encapsulated iPSC-derived osteoprogenitors might explain this result [108]. Other than iPSC-derived osteoprogenitors, stem cells such as human dental pulp stem cells (hDPSCs), bone marrow stem cells (hBMSCs) and iPSC-derived mesenchymal stem cells (hiPSC-MSCs) are exciting cell sources in regenerative medicine [110]. In 2016, Wang et al. used injectable calcium phosphate together with alginate-fibrin hydrogel for the encapsulation of all three of these stem cell types. The injectable scaffold was highly porous and fast setting. Calcium phosphate is a promising enhancer of bone regeneration when used along with cell-encapsulating hydrogel fibers. In this study, the authors compared the osteogenic differentiation potential of hDPSCs, hBMSCs and hiPSC-MSCs of bone marrow origin and foreskin origin. The stem cells encapsulated in the hydrogel exhibited good proliferation. The hDPSCs showed a higher proliferative rate than other stem cells. hDPSCs, bone marrow-derived hiPSC-MSCs and hBMSCs differentiated into osteogenic lineages and expressed increased levels of osteogenic markers such as ALP, RUNX2, COL1A1 and OC. Over time, mineralization of hDPSCs, bone marrow-derived hiPSC-MSCs and hBMSCs in scaffolds was also increased. Based on the results of this study, hDPSCs, bone marrow-derived hiPSC-MSCs and hBMSCs were all promising cell sources for bone engineering; however, foreskin-derived hiPSC-MSCs were relatively inferior for osteogenic differentiation [89].

## 6. Current state of the field and future directions

Over the past decade, the discovery of iPSCs has provided opportunities for countless applications in personalized medicine, such as patient-specific disease modeling, drug screening and stem cell-mediated tissue repair [111]. Novel approaches are required to scale up the expansion of stem cells for translating stem cell therapies to the clinic [112]. Engineered microenvironments along with specific culture conditions promote the maintenance of stemness in various cell types, including iPSCs, thereby making these materials an attractive platform for the future scale-up of pluripotent stem cells [112]. Recently, a study reported the use of thermoresponsive 3D hydrogel platforms for scaling up the production of pluripotent stem cells. A fully defined and scalable synthetic hydrogel system for the expansion and differentiation of human pluripotent stem cells was developed by Lei and Schaffer. This 3D culture system allows higher-density cell culture than traditional 2D methods and supports easy release of the cells that are encapsulated, simplifying the processing steps that are needed to expand and collect the cells [113]. A minimal approach to material design is required to engineer stem cell niches for industrial-scale stem cell production. Alterations in microenvironmental cues through recently developed engineering approaches have resulted in significant improvements in the efficiency of iPSC generation [34,35]. Compared to traditional 2D culture, reprogramming was more efficient and more rapid in the engineered hydrogels, as nutrient transport was better in this system [114]. A recent study reported that a hyaluronic acid-based hydrogel with a low elastic modulus accelerates the reprogramming of iPSCs [115]. Additionally, significant progress has been achieved in generating a pure population of differentiated cells for therapeutic applications and for *in vitro* assays [13]. Many of the existing protocols for differentiation use poorly defined substrates and procedures, such as Matrigel and hanging-drop embryoid body formation, resulting in highly variable outcomes. Recent techniques, such as rotary suspension culture [116] and microwell aggregation [117], have been used to generate uniform-sized embryoid bodies with high differentiation potential.

With continued innovation, different types of hydrogel materials will be specially modified and functionalized to achieve better performance. Thus, for iPSC-based cell therapy, fabricating hydrogels by considering all the design principles observed from the native stem cell niche will be beneficial. Biomaterials may be helpful in delivering iPSCs by controlling the delivery time of reprogramming factors [118]. Moreover,

hydrogel-based platforms may reduce safety concerns associated with viral vectors, improve iPSC reprogramming efficiency and regulate the epigenetic state of iPSCs [11]. More research focused on developing engineered hydrogels for specific tissue types while maintaining their native microenvironment along with suitable soluble factors to direct stem cell proliferation and differentiation into functional tissue constructs for potential clinical translation is needed.

## 7. Conclusions

iPSCs hold great promise in the areas of tissue engineering and regenerative medicine. However, before reaching clinics, many hurdles must be overcome. Currently, iPSCs are expanded and differentiated on MEF, Matrigel or vitronectin substrates. Although these culture systems successfully generate cell types that belong to the three germ layers, some limitations exist in translating these cell types to clinics. The major limitations are non-xeno-free and non-resemblance to the native complex microenvironment of the tissues. Hydrogels that are xeno-free, cost effective and recapitulate the native niche will be ideal candidates to overcome these limitations. Thus, hydrogels, which are biomimetic matrices, have great potential for use in various biomedical applications.

## Declaration of Competing Interest

The authors have no conflicts of interest to declare.

## Acknowledgments

The authors are grateful for the support and infrastructure provided by the Centre for Nanosciences and Molecular Medicine, Amrita Vishwa Vidyapeetham. The financial support by Chang Gung Memorial Hospital (CMRPD2K0131) is acknowledged.

## References

- [1] K. Takahashi, S. Yamanaka, Induction of pluripotent stem cells from mouse embryonic and adult fibroblast cultures by defined factors, *Cell* 126 (2006) 663–676, <https://doi.org/10.1016/j.cell.2006.07.024>.
- [2] H. Okano, M. Nakamura, K. Yoshida, Y. Okada, O. Tsuji, S. Nori, E. Ikeda, S. Yamanaka, K. Miura, Steps toward safe cell therapy using induced pluripotent stem cells, *Circ. Res.* 112 (2013) 523–533, <https://doi.org/10.1161/CIRCRESAHA.111.256149>.
- [3] C.Y. Park, J. Kim, J. Kweon, J.S. Son, J.S. Lee, J.E. Yoo, S.R. Cho, J.H. Kim, J. S. Kim, D.W. Kim, Targeted inversion and reversion of the blood coagulation factor 8 gene in human iPS cells using TALENs, *Proc. Natl. Acad. Sci. U. S. A.* 111 (2014) 9253–9258, <https://doi.org/10.1073/pnas.1323941111>.
- [4] J. Lu, S. Einhorn, L. Venkatarangan, M. Miller, D.A. Mann, P.B. Watkins, E. Le Cluyse, Morphological and functional characterization and assessment of iPSC-derived hepatocytes for *in vitro* toxicity testing, *Toxicol. Sci.* 147 (2015) 39–54, <https://doi.org/10.1093/toxsci/kfv117>.
- [5] K. Takahashi, K. Tanabe, M. Ohnuki, M. Narita, T. Ichisaka, K. Tomoda, S. Yamanaka, Induction of pluripotent stem cells from adult human fibroblasts by defined factors, *Cell* 131 (2007) 861–872, <https://doi.org/10.1016/j.cell.2007.11.019>.
- [6] I.H. Park, R. Zhao, J.A. West, A. Yabuuchi, H. Huo, T.A. Ince, P.H. Lerou, M. W. Lensch, G.Q. Daley, Reprogramming of human somatic cells to pluripotency with defined factors, *Nature* 451 (2008) 141–146, <https://doi.org/10.1038/nature06534>.
- [7] F. Gonzalez, M.B. Monasterio, G. Tiscornia, N.M. Pulido, R. Vassena, L.B. Morera, I.R. Piza, J.C.I. Belmonte, Generation of mouse-induced pluripotent stem cells by transient expression of a single nonviral polycistronic vector, *PNAS* 106 (2009) 8918–8922, <https://doi.org/10.1073/pnas.0901471106>.
- [8] I. De Lazaro, G. Cossu, K. Kostarelou, Transient transcription factor (OSKM) expression is key towards clinical translation of *in vivo* cell reprogramming, *EMBO Mol. Med.* 9 (2017) 733–736, <https://doi.org/10.15252/emmm.201707650>.
- [9] L. Warren, C. Lin, mRNA-based genetic reprogramming, *Mol. Ther.* 27 (2019) 729–734, <https://doi.org/10.1016/j.ymthe.2018.12.009>.
- [10] I. Horiguchi, M. Kino-oka, Current developments in the stable production of human induced pluripotent stem cells, *Engineering* (2021), <https://doi.org/10.1016/j.eng.2021.01.001>.
- [11] Y. Hayashi, M.K. Furue, Biological effects of culture substrates on human pluripotent stem cells, *Stem Cells Int.* (2016), <https://doi.org/10.1155/2016/5380560>.

- [12] T.B. Bertucci, G. Dai, Biomaterial engineering for controlling pluripotent stem cell fate, *Stem Cells Int.* (2018), <https://doi.org/10.1155/2018/9068203>.
- [13] Z. Tong, A. Solanki, A. Hamilos, O. Levy, K. Wen, X. Yin, J.M. Karp, Application of biomaterials to advance induced pluripotent stem cell research and therapy, *EMBO J.* 34 (2015) 987–1008, <https://doi.org/10.15252/emj.201490756>.
- [14] R.M. Sutherland, B. Sordat, Ba J. mat, H. Gabbert, B. Bourrat, W. Mueller-Klieser, Oxygenation and differentiation in multicellular spheroids of human colon carcinoma, *Cancer Res.* 46 (1986) 5320–5329. PMID: 3756881.
- [15] A.P. Van Winkle, I.D. Gates, M.S. Kallos, Mass transfer limitations in embryoid bodies during human embryonic stem cell differentiation, *Cells Tissues Organs* (Print) 196 (2012) 34–47, <https://doi.org/10.1159/000330691>.
- [16] M.H. Kim, K. Takeuchi, M. Kino-Oka, Role of cell-secreted extracellular matrix formation in aggregate formation and stability of human induced pluripotent stem cells in suspension culture, *J. Biosci. Bioeng.* 127 (2019) 372–380, <https://doi.org/10.1016/j.jbiosc.2018.08.010>.
- [17] L. Macri-Pellizzeri, B. Pelacho, A. Sancho, O. glesias-Garcia, A.M. Simón-Yarza, M. Soriano-Navarro, S. González-Granero, J.M. García-Verdugo, E.M. De-Juan-Pardo, F. Prosper, Substrate stiffness and composition specifically direct differentiation of induced pluripotent stem cells, *Tissue Eng. Part A* 21 (2015) 1633–1641, <https://doi.org/10.1089/ten.tea.2014.0251>.
- [18] S.R. Caliali, J.A. Burdick, A practical guide to hydrogels for cell culture, *Nat. Methods* 13 (2016) 405, <https://doi.org/10.1038/nmeth.3839>.
- [19] K. Saha, J.F. Pollock, D.V. Schaffer, K.E. Healy, Designing synthetic materials to control stem cell phenotype, *Curr. Opin. Chem. Biol.* 11 (2007) 381–387, <https://doi.org/10.1016/j.cbpa.2007.05.030>.
- [20] A. Skardal, L. Smith, S. Bharadwaj, A. Atala, S. Soker, Y. Zhang, Tissue specific synthetic ECM hydrogels for 3-D in vitro maintenance of hepatocyte function, *Biomaterials* 33 (2012) 4565–4575, <https://doi.org/10.1016/j.biomaterials.2012.03.034>.
- [21] K.T. Nguyen, J.L. West, Photopolymerizable hydrogels for tissue engineering applications, *Biomaterials* 23 (2002) 4307–4314, [https://doi.org/10.1016/S0142-9612\(02\)00175-8](https://doi.org/10.1016/S0142-9612(02)00175-8).
- [22] C.M. Madl, S.C. Heilshorn, Engineering hydrogel microenvironments to recapitulate the stem cell niche, *Annu. Rev. Biomed. Eng.* 20 (2018) 21–47, <https://doi.org/10.1146/annurev-bioeng-062117-120954>.
- [23] G. Jose, K.T. Shalunon, J.P. Chen, Natural polymers based hydrogels for cell culture applications, *Curr. Med.* (2020), <https://doi.org/10.2174/0929867326666190903113004>.
- [24] L. Brannon-Peppas, N.A. Peppas, Equilibrium swelling behavior of pH-sensitive hydrogels, *Chem. Eng. Sci.* 46 (1991) 715–722, [https://doi.org/10.1016/0009-2509\(91\)80177-Z](https://doi.org/10.1016/0009-2509(91)80177-Z).
- [25] A.K. Shukla, U. Kandam, Three-dimensional macroporous materials for tissue engineering of craniofacial bone, *Br. J. Oral Maxillofac. Surg.* 55 (2017) 875–891, <https://doi.org/10.1016/j.bjoms.2017.09.007>.
- [26] A. Higuchi, Q.D. Ling, S.S. Kumar, Y. Chang, A.A. Alarfaj, M.A. Munusamy, K. Murugan, S.T. Hsu, A. Umezawa, Physical cues of cell culture materials lead the direction of differentiation lineages of pluripotent stem cells, *J. Mater. Chem. B Mater. Biol. Med.* 3 (2015) 8032–8058, <https://doi.org/10.1039/c5tb01276g>.
- [27] H. Hongisto, S. Vuoristo, A. Mikhailova, R. Suuronen, I. Virtanen, T. Otonkoski, H. Skottman, Laminin-511 expression is associated with the functionality of feeder cells in human embryonic stem cell culture, *Stem Cell Res.* 8 (2012) 97–108, <https://doi.org/10.1016/j.scr.2011.08.005>.
- [28] S. Llamas, E. García-Pérez, A. Meana, F. Larcher, M. del Río, Feeder layer cell actions and applications, *Tissue Eng. B Rev.* 21 (2015) 345–353, <https://doi.org/10.1089/ten.teb.2014.0547>.
- [29] C.S. Hughes, L.M. Postovit, G.A. Lajoie, Matrigel: a complex protein mixture required for optimal growth of cell culture, *Proteomics* 10 (2010) 1886–1890, <https://doi.org/10.1002/pmic.200900758>.
- [30] A.B. Prowse, M.R. Doran, J.J. Cooper-White, F. Chong, T.P. Munro, J. Fitzpatrick, T.L. Chung, D.N. Haylock, P.P. Gray, E.J. Wolvetang, Long term culture of human embryonic stem cells on recombinant vitronectin in ascorbate free media, *Biomaterials* 31 (2010) 8281–8288, <https://doi.org/10.1016/j.biomaterials.2010.07.037>.
- [31] S. Patel, D. Jung, P.T. Yin, P. Carlton, M. Yamamoto, T. Bando, H. Sugiyama, K. B. Lee, NanoScript: a nanoparticle-based artificial transcription factor for effective gene regulation, *ACS Nano* 8 (2014) 8959–8967, <https://doi.org/10.1021/nn501589f>.
- [32] M.P. Lutolf, P.M. Gilbert, H.M. Blau, Designing materials to direct stem-cell fate, *Nature* 462 (2009) 433–441, <https://doi.org/10.1038/nature08602>.
- [33] W.L. Murphy, T.C. McDevitt, A.J. Engler, Materials as stem cell regulators, *Nat. Mater.* 13 (2014) 547–557, <https://doi.org/10.1038/nmat3937>.
- [34] B. Choi, K.S. Park, J.H. Kim, K.W. Ko, J.S. Kim, D.K. Han, S.H. Lee, Stiffness of hydrogels regulates cellular reprogramming efficiency through mesenchymal-to-epithelial transition and stemness markers, *Macromol. Biosci.* 16 (2016) 199–206, <https://doi.org/10.1002/mabi.201500273>.
- [35] T.L. Downing, J. Soto, C. Morez, T. Houssin, A. Fritz, F. Yuan, J. Chu, S. Patel, D. V. Schaffer, S. Li, Biophysical regulation of epigenetic state and cell reprogramming, *Nat. Mater.* 12 (2013) 1154–1162, <https://doi.org/10.1038/nmat3777>.
- [36] Y. Luo, C. Lou, S. Zhang, Z. Zhu, Q. Xing, P. Wang, T. Liu, H. Liu, C. Li, W. Shi, Z. Du, Three-dimensional hydrogel culture conditions promote the differentiation of human induced pluripotent stem cells into hepatocytes, *Cytotherapy* 20 (2018) 95–107, <https://doi.org/10.1016/j.jcyt.2017.08.008>.
- [37] T. Richardson, C. Wiegand, F. Adisa, K. Ravikumar, J. Candiello, P. Kumta, I. Banerjee, Engineered peptide modified hydrogel platform for propagation of human pluripotent stem cells, *Acta Biomater.* 113 (2020) 228–239, <https://doi.org/10.1016/j.actbio.2020.06.034>.
- [38] S. Paiva, P. Joanne, C. Migdal, E.L. Soler, Y. Hovhannisyan, A. Nicolas, O. Agbulut, Polyacrylamide hydrogels with rigidity-independent surface chemistry show limited long-term maintenance of pluripotency of human induced pluripotent stem cells on soft substrates, *ACS Biomater. Sci. Eng.* 6 (2019) 340–351, <https://doi.org/10.1021/acsbomaterials.9b01189>.
- [39] S. Lee, A.E. Stanton, X. Tong, F. Yang, Hydrogels with enhanced protein conjugation efficiency reveal stiffness-induced YAP localization in stem cells depends on biochemical cues, *Biomaterials* 202 (2019) 26–34, <https://doi.org/10.1016/j.biomaterials.2019.02.021>.
- [40] E.D.O. Sanguinet, N.M. Siqueira, F.D. Menezes, G.M. Rasia, N. Lothhammer, R. M. Soares, F.V. Meirelles, F.F. Bressan, A. Bos-Mikich, Interaction of fibroblasts and induced pluripotent stem cells with poly (vinyl alcohol)-based hydrogel substrates, *J. Biomed. Mater. Res. Part B Appl. Biomater.* 108 (2020) 857–867, <https://doi.org/10.1002/jbm.b.34439>.
- [41] T.C. Sung, H.F. Li, A. Higuchi, Q.D. Ling, J.S. Yang, Y.C. Tseng, C.H. Pan, A. A. Alarfaj, M.A. Munusamy, S. Kumar, S.T. Hsu, Human pluripotent stem cell culture on polyvinyl alcohol-co-itaconic acid hydrogels with varying stiffness under xeno-free conditions, *JoVE* 132 (2018) e57314, <https://doi.org/10.3791/57314>.
- [42] S. Vignesh, A. Gopalakrishnan, M.R. Poorna, S.V. Nair, R. Jayakumar, U. Mony, Fabrication of micropatterned alginate-gelatin and k-carrageenan hydrogels of defined shapes using simple wax mould method as a platform for stem cell/ induced Pluripotent Stem Cells (iPSC) culture, *Int. J. Biol. Macromol.* 112 (2018) 737–744, <https://doi.org/10.1016/j.ijbiomac.2018.02.031>.
- [43] J. Li, D.J. Mooney, Designing hydrogels for controlled drug delivery, *Nat. Rev. Mater.* 1 (2016), <https://doi.org/10.1038/natrevmats.2016.71>.
- [44] Y.H. Tsou, J. Khoneisser, P.C. Huang, X. Xu, Hydrogel as a bioactive material to regulate stem cell fate, *Bioact. Mater.* 1 (2016) 39–55, <https://doi.org/10.1016/j.bioactmat.2016.05.001>.
- [45] J.L. Drury, D.J. Mooney, Hydrogels for tissue engineering: scaffold design variables and applications, *Biomaterials* 24 (2003) 4337–4351, [https://doi.org/10.1016/S0142-9612\(03\)00340-5](https://doi.org/10.1016/S0142-9612(03)00340-5).
- [46] F. Copes, N. Pien, S. Van Vlierberghe, F. Boccafroschi, D. Mantovani, Collagen-based tissue engineering strategies for vascular medicine, *Front. Bioeng. Biotechnol.* 7 (2019), <https://doi.org/10.3389/fbioe.2019.00166>.
- [47] P. Ghasemiyeh, S. Mohammadi-Samani, Hydrogels as drug delivery systems; pros and cons, *Trends Pharmacol. Sci.* 5 (2019) 7–24, <https://doi.org/10.30476/TIPS.2019.81604.1002>.
- [48] I.M. Garnica-Palafox, F.M. Sánchez-Arévalo, Influence of natural and synthetic crosslinking reagents on the structural and mechanical properties of chitosan-based hybrid hydrogels, *Carbohydr. Polym.* 151 (2016) 1073–1081, <https://doi.org/10.1016/j.carbpol.2016.06.036>.
- [49] D.E. Ingber, Cellular mechanotransduction: putting all the pieces together again, *FASEB J.* 20 (2006) 811–827, <https://doi.org/10.1096/fj.05-5424rev>.
- [50] A. Khademhosseini, J.P. Vacanti, R. Langer, Progress in tissue engineering, *Sci. Am.* 300 (2009) 64–71, <https://doi.org/10.1038/scientificamerican0509-64>.
- [51] D.S. Benoit, M.P. Schwartz, A.R. Durney, K.S. Anseth, Small functional groups for controlled differentiation of hydrogel-encapsulated human mesenchymal stem cells, *Nat. Mater.* 7 (2008) 816–823, <https://doi.org/10.1038/nmat2269>.
- [52] M.C. Cushing, K.S. Anseth, Hydrogel cell cultures, *Science* 316 (2007) 1133–1134, <https://doi.org/10.1126/science.1140171>.
- [53] H. Fan, J.P. Gong, Fabrication of bioinspired hydrogels: challenges and opportunities, *Macromolecules* 53 (2020), <https://doi.org/10.1021/acs.macromol.0c00238>.
- [54] G.D. Nicodemus, S.J. Bryant, Cell encapsulation in biodegradable hydrogels for tissue engineering applications, *Tissue Eng.* 14 (2008) 149–165, <https://doi.org/10.1089/ten.teb.2007.0332>.
- [55] E. Garreta, E. Genove, S. Borrós, C.E. Semino, Osteogenic differentiation of mouse embryonic stem cells and mouse embryonic fibroblasts in a three-dimensional self-assembling peptide scaffold, *Tissue Eng.* 12 (2006) 2215–2227, <https://doi.org/10.1089/ten.2006.12.2215>.
- [56] E. Genove, S. Schmitmeier, A. Sala, S. Borrós, A. Bader, L.G. Griffith, C.E. Semino, Functionalized Self-assembling Peptide Hydrogel Enhance Maintenance of Hepatocyte Activity In Vitro, *J. Cell. Mol. Med.* 13 (2009) 3387–3397, <https://doi.org/10.1111/j.1582-4934.2009.00970.x>.
- [57] S. Gerecht, J.A. Burdick, S. Ferreira, A. Townsend, R. Langer, G. Vunjak-Novakovic, Hyaluronic acid hydrogel for controlled self-renewal and differentiation of human embryonic stem cells, *Proc. Natl. Acad. Sci. U. S. A.* 104 (2007) 11298–11303, <https://doi.org/10.1073/pnas.0703723104>.
- [58] G.D. Nicodemus, S.J. Bryant, Cell encapsulation in biodegradable hydrogels for tissue engineering applications, *Tissue Eng. Part B Rev.* 14 (2008) 149–165, <https://doi.org/10.1089/ten.teb.2007.0332>.
- [59] H. Wang, Z. Liu, D. Li, X. Guo, F.K. Kasper, C. Duan, C. Wang, Injectable biodegradable hydrogels for embryonic stem cell transplantation: improved cardiac remodelling and function of myocardial infarction, *J. Cell. Mol. Med.* 16 (2012) 1310–1320, <https://doi.org/10.1111/j.1582-4934.2011.01409.x>.
- [60] T.R. Cox, J.T. Erler, Remodeling and homeostasis of the extracellular matrix: implications for fibrotic diseases and cancer, *DMM* 4 (2011) 165–178, <https://doi.org/10.1242/dmm.004077>.
- [61] A.J. Engler, S. Sen, H.L. Sweeney, D.E. Discher, Matrix elasticity directs stem cell lineage specification, *Cell* 126 (2006) 677–689, <https://doi.org/10.1016/j.cell.2006.06.044>.
- [62] G.J. Her, H.C. Wu, M.H. Chen, M.Y. Chen, S.C. Chang, T.W. Wang, Control of three-dimensional substrate stiffness to manipulate mesenchymal stem cell fate



- toward neuronal or glial lineages, *Acta Biomater.* 9 (2013) 5170–5180, <https://doi.org/10.1016/j.actbio.2012.10.012>.
- [63] L. Fan, C. Liu, X. Chen, Y. Zou, Z. Zhou, C. Lin, G. Tan, L. Zhou, C. Ning, Q. Wang, Directing induced pluripotent stem cell derived neural stem cell fate with a three-dimensional biomimetic hydrogel for spinal cord injury repair, *ACS Appl. Mater. Interfaces* 10 (2018) 17742–17755, <https://doi.org/10.1021/acsami.8b05293>.
- [64] G. Wang, X. Wang, L. Huang, Feasibility of chitosan-alginate (Chi-Alg) hydrogel used as scaffold for neural tissue engineering: a pilot study in vitro, *Biotechnol. Biotechnol. Equip.* 31 (2017) 766–773, <https://doi.org/10.1080/13102818.2017.1332493>.
- [65] N. Sood, A. Bhardwaj, S. Mehta, A. Mehta, Stimuli-responsive hydrogels in drug delivery and tissue engineering, *Drug Deliv.* (2014) 1–23, <https://doi.org/10.3109/10717544.2014.940091>.
- [66] S. Lee, A.E. Stanton, X. Tong, F. Yang, Hydrogels with enhanced protein conjugation efficiency reveal stiffness-induced YAP localization in stem cells depends on biochemical cues, *Biomaterials* 202 (2019) 26–34, <https://doi.org/10.1016/j.biomaterials.2019.02.021>.
- [67] S. Wu, R. Xu, B. Duan, P. Jiang, Three-dimensional hyaluronic acid hydrogel-based models for in vitro human iPSC-derived NPC culture and differentiation, *J. Mater. Chem. B Mater. Biol. Med.* 5 (2017) 3870–3878, <https://doi.org/10.1039/C7TB00721C>.
- [68] R. Goetzke, H. Keijderer, J. Franzen, A. Ostrowska, S. Nüchtern, P. Mela, W. Wagner, Differentiation of induced pluripotent stem cells towards mesenchymal stromal cells is hampered by culture in 3D hydrogels, *Sci. Rep.* 9 (2019) 1–12, <https://doi.org/10.1038/s41598-019-51911-5>.
- [69] H. Li, J. Gao, Y. Shang, Y. Hua, M. Ye, Z. Yang, C. Ou, M. Chen, Folic Acid Derived Hydrogel Enhances the Survival and Promotes Therapeutic Efficacy of iPS Cells for Acute Myocardial Infarction, *ACS Appl. Mater. Interfaces* 10 (2018) 24459–24468, <https://doi.org/10.1021/acsami.8b08659>.
- [70] C. Chiang, W. Wu, H. Li, Y. Chien, C. Sun, C. Peng, et al., Enhanced antioxidant capacity of dental pulp-derived iPSC-differentiated hepatocytes and liver regeneration by injectable HGF-releasing hydrogel in fulminant hepatic failure, *Cell Transplant.* 24 (2015) 541–559, <https://doi.org/10.3727/096368915X686986>.
- [71] K. H.Chien, Y. L.Chang, M. L.Wang, J.H. Chuang, Y. C.Yang, M. C.Tai, C.Y. Wang, H.Y.Li Y.Y.Liu, S.Y.Kao J.T.Chen, H. L.Chen, W.L. Lo, Promoting induced pluripotent stem cell-driven biomineralization and periodontal regeneration in rats with maxillary-molar defects using injectable BMP-6 hydrogel, *Sci. Rep.* 8 (2018) 114, <https://doi.org/10.1038/s41598-017-18415-6>.
- [72] A. Hu, R. Xing, L. Jiang, Z. Li, P. Liu, H. Wang, X. Li, J. Dong, Thermosensitive hydrogels loaded with human-induced pluripotent stem cells overexpressing growth differentiation factor-5 ameliorate intervertebral disc degeneration in rats, *J. Biomed. Mater. Res. B Appl. Biomater.* 108 (2020) 2005–2016, <https://doi.org/10.1002/jbm.b.34541>.
- [73] M.P. Lutolf, P.M. Gilbert, H.M. Blau, Designing materials to direct stem-cell fate, *Nature* 462 (2009) 433–441, <https://doi.org/10.1038/nature08602>.
- [74] K. Saha, A.J. Keung, E.F. Irwin, Y. Li, L. Little, D.V. Schaffer, K.E. Healy, Substrate modulus directs neural stem cell behavior, *Biophys. J.* 95 (2008) 4426–4438, <https://doi.org/10.1529/biophysj.108.132217>.
- [75] A.I. Teixeira, S. Ilkhanizadeh, J.A. Wigenius, J.K. Duckworth, O. Inganas, O. Hermanson, The promotion of neuronal maturation on soft substrates, *Biomaterials* 30 (2009) 4567–4572, <https://doi.org/10.1016/j.biomaterials.2009.05.013>.
- [76] A. Liedmann, S. Frech, P.J. Morgan, A. Rolfs, M.J. Frech, Differentiation of human neural progenitor cells in functionalized hydrogel matrices, *BioResearch* 1 (2012) 16–24, <https://doi.org/10.1089/biores.2012.0209>.
- [77] S.K. Seidlits, Z.Z. Khaing, R.R. Petersen, J.D. Nickels, J.E. Vanscoy, J.B. Shear, C. E. Schmidt, The effects of hyaluronic acid hydrogels with tunable mechanical properties on neural progenitor cell differentiation, *Biomaterials* 31 (2010) 3930–3940, <https://doi.org/10.1016/j.biomaterials.2010.01.125>.
- [78] S.R. Moxon, N.J. Corbett, K. Fisher, G. Potjewyd, M. Domingos, N.M. Hooper, Blended alginate/collagen hydrogels promote neurogenesis and neuronal maturation, *Mater. Sci. Eng.* 104 (2019) 109904, <https://doi.org/10.1016/j.msec.2019.109904>.
- [79] H.J. Lim, Z. Khan, T.S. Wilems, X. Lu, T.H. Perera, Y.E. Kurosu, K.T. Ravivarapu, M.C. Mosley, L.A. Smith Callahan, Human induced pluripotent stem cell derived neural stem cell survival and neural differentiation on polyethylene glycol dimethacrylate hydrogels containing a continuous concentration gradient of N-Cadherin derived peptide His-Ala-Val-Asp-Ile, *Acta Biomater.* 3 (2017) 776–781, <https://doi.org/10.1021/acsbiomaterials.6b00745>.
- [80] R.R. Besser, A.C. Bowles, A. Allassaf, D. Carbonero, I. Claure, E. Jones, J. Reda, L. Wubker, W. Batchelor, N. Ziebarth, R. Silvera, Enzymatically crosslinked gelatin–laminin hydrogels for applications in neuromuscular tissue engineering, *Biomater. Sci.* 8 (2020) 591–606, <https://doi.org/10.1039/C9BM01430F>.
- [81] B. Nazari, M. Kazemi, A. Kamyab, B. Nazari, S. Ebrahimi-Barough, M. Hadjighassem, A. Norouzi-Javidan, A. Ai, A. Ahmadi, J. Ai, Fibrin hydrogel as a scaffold for differentiation of induced pluripotent stem cells into oligodendrocytes, *J. Biomed. Mater. Res. Part B Appl. Biomater.* 108 (2020) 192–200, <https://doi.org/10.1002/jbm.b.34378>.
- [82] J.K. Gandhi, T. Knudsen, M. Hill, B. Roy, L. Bachman, C. Pfannkoch-Andrews, K. N. Schmidt, M.M. Metko, M.J. Ackerman, Z. Resch, J.S. Pulido, Human Fibrinogen for Maintenance and Differentiation of Induced Pluripotent Stem Cells in Two Dimensions and Three Dimensions, *Stem Cells Transl. Med.* 8 (2019) 512–521, <https://doi.org/10.1002/sctm.18-0189>.
- [83] K.T. Morin, R.T. Tranquillo, In vitro models of angiogenesis and vasculogenesis in fibrin gel, *Exp. Cell Res.* 319 (2013) 2409–2417, <https://doi.org/10.1016/j.yexcr.2013.06.006>.
- [84] J.K. Gandhi, Z. Manzar, L.A. Bachman, C. Andrews-Pfannkoch, T. Knudsen, M. Hill, H. Schmidt, R. Iezzi, J.S. Pulido, A.D. Marmorstein, Fibrin hydrogels as a xenofree and rapidly degradable support for transplantation of retinal pigment epithelium monolayers, *Acta Biomater.* 67 (2018) 134–146, <https://doi.org/10.1016/j.actbio.2017.11.058>.
- [85] K. Y.H.Lo, C.J.Kuo Karlsson, Applications of organoids for Cancer biology and precision medicine, *Nat. Cancer* 1 (2020) 761–773, <https://doi.org/10.1038/s43018-020-0102-y>.
- [86] F. Tran, C. Klein, A. Arlt, S. Imm, E. Knappe, A. Simmons, P. Rosenstiel, P. Seibler, Stem Cells and Organoid Technology in Precision Medicine in Inflammation: Are We There Yet? *Front. Immunol.* 11 (2020) <https://doi.org/10.3389/fimmu.2020.573562>.
- [87] M. Simian, M.J. Bissell, Organoids: a historical perspective of thinking in three dimensions, *J. Cell Biol.* 216 (2017) 31–40, <https://doi.org/10.1083/jcb.201610056>.
- [88] Y. Qu, B. Han, B. Gao, S. Bose, Y. Gong, K. Wawrowsky, A.E. Giuliano, D. Sareen, X. Cui, Differentiation of human induced pluripotent stem cells to mammary-like organoids, *Stem Cell Rep.* 8 (2017) 205–215, <https://doi.org/10.1016/j.stemcr.2016.12.023>.
- [89] K.V. Nguyen-Ngoc, A.J. Ewald, Mammary ductal elongation and myoepithelial migration are regulated by the composition of the extracellular matrix, *J. Microsc.* (2013) 212–223, <https://doi.org/10.1111/jmi.12017>.
- [90] M. Bhattacharya, M.M. Malinen, P. Lauren, Y.R. Lou, S.W. Kuisma, L. Kanninen, M. Lille, A. Corlu, C. Guguen-Guillouzo, O. Ikkala, A. Laukkanen, A. Urtti, M. Yliperttula, Nanofibrillar cellulose hydrogel promotes three-dimensional liver cell culture, *J. Control. Release* 164 (2012) 291–298, <https://doi.org/10.1016/j.jconrel.2012.06.039>.
- [91] M.R. Poorna, S. Sudhindran, M.V. Thampi, U. Mony, Differentiation of induced pluripotent stem cells to hepatocyte-like cells on cellulose nanofibril substrate, *Colloids Surf. B Biointerfaces* (2020) 111466, <https://doi.org/10.1016/j.colsurfb.2020.111466>.
- [92] C.H. Chiang, W.W. Wu, H.Y. Li, Y. Chien, C.C. Sun, C.H. Peng, A.T. Lin, C. S. Huang, Y.H. Lai, S.H. Chiou, S.I. Hung, Enhanced antioxidant capacity of dental pulp-derived iPSC-differentiated hepatocytes and liver regeneration by injectable HGF-releasing hydrogel in fulminant hepatic failure, *Cell Transplant.* 24 (2015) 541–559, <https://doi.org/10.3727/096368915X686986>.
- [93] M.M. Capeling, M. Czerwinski, S. Huang, Y.H. Tsai, A. Wu, M.S. Nagy, B. Juliar, N. Sundaram, Y. Song, W.M. Han, S. Takayama, Nonadhesive alginate hydrogels support growth of pluripotent stem cell-derived intestinal organoids, *Stem cell rep* 12 (2019) 381–394, <https://doi.org/10.1016/j.stemcr.2018.12.001>.
- [94] R. Cruz-Acuña, M. Quiros, A.E. Farkas, P.H. Dedhia, S. Huang, D. Siuda, V. García-Hernández, A.J. Miller, J.R. Spence, A. Nusrat, A.J. García, Synthetic hydrogels for human intestinal organoid generation and colonic wound repair, *Nat. Cell Biol.* 19 (2017) 1326–1335, <https://doi.org/10.1038/ncb3632>.
- [95] Y.C. Kuo, I.H. Lee, R. Rajesh, Self-assembled ternary poly (vinyl alcohol)-alginate-gelatin hydrogel with controlled-release nanoparticles for pancreatic differentiation of iPS cells, *J. Taiwan Inst. Chem. Eng.* 104 (2019) 27–39, <https://doi.org/10.1016/j.jtice.2019.09.010>.
- [96] W.E. Wang, X. Chen, S.R. Houser, C. Zeng, Potential of cardiac stem/progenitor cells and induced pluripotent stem cells for cardiac repair in ischaemic heart disease, *Clin. Sci.* 125 (2013) 319–327, <https://doi.org/10.1042/CS20130019>.
- [97] N.J. Kaiser, R.J. Kant, A.J. Minor, K.L. Coulombe, Optimizing blended collagen-fibrin hydrogels for cardiac tissue engineering with human iPSC-derived cardiomyocytes, *ACS Biomater-Sci eng.* 5 (2018) 887–899, <https://doi.org/10.1021/acsbiomaterials.8b01112>.
- [98] B. Wang, X. Tu, J. Wei, L. Wang, Y. Chen, Substrate elasticity dependent colony formation and cardiac differentiation of human induced pluripotent stem cells, *Biofabrication* 11 (2018) 015005, <https://doi.org/10.1088/1758-5090/aae0a5>.
- [99] G.K. Owens, M.S. Kumar, B.R. Wamhoff, Molecular regulation of vascular smooth muscle cell differentiation in development and disease, *Physiol. Rev.* 84 (2008) 767–801, <https://doi.org/10.1152/physrev.00041.2003>.
- [100] W. Wang, X. Liu, Y. Xie, H. Zhang, W. Yu, Y. Xiong, X. Ma, Microencapsulation using natural polysaccharides for drug delivery and cell implantation, *J. Mater. Chem* 16 (2006) 3252, <https://doi.org/10.1039/b603595g>.
- [101] N.A. Raof, M.R. Padgen, A.R. Gracías, M. Bergkvist, Y. Xie, One-dimensional self-assembly of mouse embryonic stem cells using an array of hydrogel microstrands, *Biomaterials* 32 (2011) 4498–4505, <https://doi.org/10.1016/j.biomaterials.2011.03.011>.
- [102] H. Lin, X. Qiu, Q. Du, Q. Li, O. Wang, L. Akert, Z. Wang, D. Anderson, K. Liu, L. Gu, C. Zhang, Engineered microenvironment for manufacturing human pluripotent stem cell-derived vascular smooth muscle cells, *Stem Cell Rep.* 12 (2019) 84–97, <https://doi.org/10.1016/j.stemcr.2018.11.009>.
- [103] H. Kagami, H. Agata, The potential of somatic stem cells for alveolar bone tissue engineering, *IJOMS* 9 (2010) 1–10, <https://doi.org/10.5466/ijoms.9.1>.
- [104] H.D. Kim, S. Amirthalingam, S.L. Kim, S.S. Lee, J. Rangasamy, N.S. Hwang, Biomimetic materials and fabrication approaches for bone tissue engineering, *Adv. Healthc. Mater.* 6 (23) (2017) 1700612, <https://doi.org/10.1002/adhm.201700612>.
- [105] S. Yue, H. He, B. Li, T. Hou, Hydrogel as a biomaterial for bone tissue engineering: a review, *Nanomaterials* 10 (2020) 1511, <https://doi.org/10.3390/nano10081511>.
- [106] H. Nakahara, H. Misawa, A. Yoshida, T. Hayashi, M. Tanaka, T. Furumatsu, N. Tanaka, N. Kobayashi, T. Ozaki, Bone repair using a hybrid scaffold of self-

- assembling peptide PuraMatrix and polyetheretherketone cage in rats, *Cell Transplant.* 19 (2010) 791–797, <https://doi.org/10.3727/096368910X508906>.
- [107] X. Bai, M. Gao, S. Syed, J. Zhuang, X. Xu, X.Q. Zhang, Bioactive hydrogels for bone regeneration, *Bioact. Mater.* 3 (2018) 401–417, <https://doi.org/10.1016/j.bioactmat.2018.05.006>.
- [108] K. Hayashi, H. Ochiai-Shino, T. Shiga, S. Onodera, A. Saito, T. Shibahara, T. Azuma, Transplantation of human-induced pluripotent stem cells carried by self-assembling peptide nanofiber hydrogel improves bone regeneration in rat calvarial bone defects, *BDJ Open* 2 (2016) 1–7, <https://doi.org/10.1038/bdjopen.2015.7>.
- [109] N. Kishimoto, Y. Momota, R. Mori, Y. Hashimoto, K. Imai, T. Omasa, J. Kotani, Bone regeneration using dedifferentiated fat cells with PuraMatrixTM, *J. Tissue Eng.* 6 (2008) 127–134, <https://doi.org/10.11223/jarde.6.127>.
- [110] L. Wang, C. Zhang, C. Li, M.D. Weir, P. Wang, M.A. Reynolds, L. Zhao, H.H. Xu, Injectable calcium phosphate with hydrogel fibers encapsulating induced pluripotent, dental pulp and bone marrow stem cells for bone repair, *Mater. Sci. Eng. C* 69 (2016) 1125–1136, <https://doi.org/10.1016/j.msec.2016.08.019>.
- [111] A. Trounson, N.D. DeWitt, Pluripotent stem cells progressing to the clinic, *Nat. Rev. Mol. Cell Biol.* 17 (2016) 194–200, <https://doi.org/10.1038/nrm.2016.10>.
- [112] T.C. McDevitt, Scalable culture of human pluripotent stem cells in 3D, *PNAS* (2013), <https://doi.org/10.1073/pnas.1320575111>.
- [113] Y. Lei, D.V. Schaffer, A fully defined and scalable 3D culture system for human pluripotent stem cell expansion and differentiation, *PNAS* 110 (2013) E5039–E5048, <https://doi.org/10.1073/pnas.1309408110>.
- [114] J. Sia, R. Sun, J. Chu, S. Li, Dynamic culture improves cell reprogramming efficiency, *Biomaterials* 92 (2016) 36–45, <https://doi.org/10.1016/j.biomaterials.2016.03.033>.
- [115] D. Kim, B.H. Cha, J. Ahn, Y. Arai, B. Choi, S.H. Lee, Physicochemical properties in 3D hydrogel modulate cellular reprogramming into induced pluripotent stem Cells *Adv. Funct. Mater.* 31 (2021) 2007041, <https://doi.org/10.1002/adfm.202007041>.
- [116] J.C. Mohr, J. Zhang, S.M. Azarin, A.G. Soerens, J.J. de Pablo, J.A. Thomson, T. J. Kamp, The microwell control of embryoid body size in order to regulate cardiac differentiation of human embryonic stem cells, *Biomaterials* 31 (2010) 1885–1893, <https://doi.org/10.1016/j.biomaterials.2009.11.033>.
- [117] R.L. Carpenedo, C.Y. Sargent, T.C. McDevitt, Rotary suspension culture enhances the efficiency, yield, and homogeneity of embryoid body differentiation, *Stem Cells* 25 (2007) 2224–2234, <https://doi.org/10.1634/stemcells.2006-0523>.
- [118] S. Moradi, H. Mahdizadeh, T. Šarić, J. Kim, J. Harati, H. Shahsavarani, B. Greber, J.B. Moore, Research and therapy with induced pluripotent stem cells (iPSCs): social, legal, and ethical considerations, *Stem Cell Res. Ther.* 10 (2019) 1–13, <https://doi.org/10.1186/s13287-019-1455-y>.

## Article

# Liposomal IR-780 as a Highly Stable Nanotheranostic Agent for Improved Photothermal/Photodynamic Therapy of Brain Tumors by Convection-Enhanced Delivery

Yu-Jen Lu <sup>1,2,3,†</sup>, Anilkumar T. S. <sup>1,4,†</sup>, Chi-Cheng Chuang <sup>1</sup>  and Jyh-Ping Chen <sup>4,5,6,7,\*</sup> 

<sup>1</sup> Department of Neurosurgery, Chang Gung Memorial Hospital, Linkou, Kwei-San, Taoyuan 33305, Taiwan; luyj@cgmh.org.tw (Y.-J.L.); kumar@cgmh.org.tw (A.T.S.); ccc2915@cgmh.org.tw (C.-C.C.)

<sup>2</sup> College of Medicine, Chang Gung University, Kwei-San, Taoyuan 33302, Taiwan

<sup>3</sup> Center for Biomedical Science and Engineering, National Tsing Hua University, Hsinchu 300044, Taiwan

<sup>4</sup> Department of Chemical and Materials Engineering, Chang Gung University, Kwei-San, Taoyuan 33302, Taiwan

<sup>5</sup> Department of Plastic and Reconstructive Surgery and Craniofacial Research Center, Chang Gung Memorial Hospital, Linkou, Kwei-San, Taoyuan 33305, Taiwan

<sup>6</sup> Research Center for Food and Cosmetic Safety, Research Center for Chinese Herbal Medicine, College of Human Ecology, Chang Gung University of Science and Technology, Taoyuan 33305, Taiwan

<sup>7</sup> Department of Materials Engineering, Ming Chi University of Technology, Tai-Shan, New Taipei City 24301, Taiwan

\* Correspondence: jpchen@mail.cgu.edu.tw; Tel.: +886-3-211-8800

† These authors contributed equally to this work.



**Citation:** Lu, Y.-J.; S., A.T.; Chuang, C.-C.; Chen, J.-P. Liposomal IR-780 as a Highly Stable Nanotheranostic Agent for Improved Photothermal/Photodynamic Therapy of Brain Tumors by Convection-Enhanced Delivery. *Cancers* **2021**, *13*, 3690. <https://doi.org/10.3390/cancers13153690>

Academic Editor: Clare Hoskins

Received: 21 May 2021

Accepted: 19 July 2021

Published: 22 July 2021

**Publisher's Note:** MDPI stays neutral with regard to jurisdictional claims in published maps and institutional affiliations.



**Copyright:** © 2021 by the authors. Licensee MDPI, Basel, Switzerland. This article is an open access article distributed under the terms and conditions of the Creative Commons Attribution (CC BY) license (<https://creativecommons.org/licenses/by/4.0/>).

**Simple Summary:** To improve the use of hydrophobic photosensitizer IR-780 in photothermal/photodynamic therapy (PTT/PDT), we entrap IR-780 within the lipid bilayer of liposomes (ILs). Compared to free IR-780, ILs showed well-preserved photothermal response by maintaining the photostability of IR-780 from repeated near infrared (NIR) laser exposure both in vitro and in vivo. Combined with fast endocytosis by human glioblastoma cells, ILs demonstrated enhanced cytotoxicity and induced higher cell apoptosis rate toward human glioblastoma cells over free IR-780, due to PTT with overexpression of heat shock protein and PDT with generation of intracellular reactive oxygen species. To overcome the blood–brain barrier, we used convection enhanced delivery (CED) for specific delivery of ILs to brain tumors in intracranial glioma xenograft. Upon three successive NIR laser irradiations, the liposomal IR-780 could significantly improve the anti-cancer efficacy in glioma treatment, leading to diminished intracranial tumor size and prolonged animal survival time.

**Abstract:** As a hydrophobic photosensitizer, IR-780 suffers from poor water solubility and low photostability under near infrared (NIR) light, which severely limits its use during successive NIR laser-assisted photothermal/photodynamic therapy (PTT/PDT). To solve this problem, we fabricate cationic IR-780-loaded liposomes (ILs) by entrapping IR-780 within the lipid bilayer of liposomes. We demonstrate enhanced photostability of IR-780 in ILs with well-preserved photothermal response after three repeated NIR laser exposures, in contrast to the rapid decomposition of free IR-780. The cationic nature of ILs promotes fast endocytosis of liposomal IR-780 by U87MG human glioblastoma cells within 30 min. For PTT/PDT in vitro, ILs treatment plus NIR laser irradiation leads to overexpression of heat shock protein 70 and generation of intracellular reactive oxygen species by U87MG cells, resulting in enhanced cytotoxicity and higher cell apoptosis rate. Using intracranial glioma xenograft in nude mice and administration of ILs by convection enhanced delivery (CED) to overcome blood–brain barrier, liposomal IR-780 could be specifically delivered to the brain tumor, as demonstrated from fluorescence imaging. By providing a highly stable liposomal IR-780, ILs significantly improved anti-cancer efficacy in glioma treatment, as revealed from various diagnostic imaging tools and histological examination. Overall, CED of ILs plus successive laser-assisted PTT/PDT may be an alternative approach for treating brain tumor, which can retard glioma growth and prolong animal survival times from orthotopic brain tumor models.

**Keywords:** nanomedicine; cancer therapy; brain tumor; photothermal therapy; photodynamic therapy; liposome; IR-780; convection enhanced delivery

## 1. Introduction

Photothermal therapy (PTT) is one of the least invasive therapeutic modalities for cancer treatment with minimum toxicity. It mainly uses light, usually in the near-infrared (NIR) range for maximum tissue penetration, to directly kill cancer cells while converting light energy into heat. The PTT occurs at higher temperatures than the basal body temperature, usually by achieving a coagulation-threshold temperature above 50 °C, although tumor cell-damaging starts at around 41 °C [1]. The traditional application of PTT does not involve administration of any exogenous photo-absorbing compounds till the use of indocyanine green (ICG) for chromophore-enhanced PTT [2]. Recently, many nanomaterials have been employed as thermal-enhancing agents or a photothermal agents (PAs), to increase the efficiency as well as the targeting ability of PTT [3]. One of major concerns of PTT is the drainage of generated heat into the tumor vicinity, which could lead to unintended damage to neighboring non-tumor cells [4]. This difficulty could be overcome by using a PA for locally induced heat generation upon NIR light irradiation, where selective cancer cell killing occurs only after the intracellular uptake of the PA [5]. Other than ICG, many inorganic nanomaterials such as magnetic nanoparticles, Au nanorods and carbon-based nanomaterials are good PAs [6].

Being a form of phototherapy other than PTT, photodynamic therapy (PDT) also involves the use of light, but it uses a photosensitizer (PS) in conjunction with molecular oxygen to elicit death of cancer cells. After activation by light of a specific wavelength, a PS can generate free radicals and/or reactive oxygen species (ROS) from endogenous molecular oxygen to induce therapeutic cytotoxicity toward cancer cells via either cell apoptosis or necrosis [7]. The PDT offers significant advantages for cancer treatment, with greatly reduced long-term morbidity and minimal normal tissue toxicity. The effectiveness of this treatment strongly depends on the type of PS used, its concentration, along with duration of irradiation time and tumor cell oxygen level [8]. The selected PS may offer a photodynamic effect simultaneously with a photothermal effect when exposed to NIR laser irradiation for concurrent PTT/PDT.

Integrating molecular imaging with therapies in image-guided diagnosis or theranostics has attracted increasing interest recently. The imaging methods include NIR fluorescence imaging, magnetic resonance imaging (MRI), positron emission tomography (PET), ultrasonic imaging and X-ray computed tomography (X-CT) [9]. The NIR fluorescence imaging technique is used for real-time observation under in vivo biological condition. Several NIR fluorescence nanomaterials are commercially available as nanotheranostic agents, among which NIR dyes such as ICG, IR-780, IR-783 and IR-820 are the most extensively used, not only for NIR fluorescence imaging but also for PTT/PDT [6,9–11]. The ICG is the only chromophore that is approved by the U.S. Food and Drug Administration (FDA) for clinical imaging and diagnosis and has been used extensively to test liver function as well as in surgical navigation and ophthalmic angiography [12]. Nonetheless, IR-780, a heptamethine dye, was found to be a more powerful and stable nanotheranostic agent than ICG, exhibiting several distinct advantages [12,13]. The hydrophobic nature of IR-780 enables its encapsulation into the bilayer of liposomes for better encapsulation efficiency than ICG-based liposomes [14]. Furthermore, the singlet oxygen ( $^1\text{O}_2$ ) quantum yield, photostability and fluorescence intensity of IR-780 are higher than those of ICG. For IR-780, the  $^1\text{O}_2$  quantum yield could reach 0.127 vs. 0.002 for ICG [15].

Convection-enhanced delivery (CED) can increase the transport of drug in brain tumors by promoting fluid flow throughout the tumor with a locally applied pressure difference, during which convective diffusion becomes the dominant mechanism of mass transport [16]. This method was first used by a research group at the National Institute of



Health in early 1990s [17]. For drug delivery to the brain, CED addresses one of the most difficult challenges faced, namely the blood–brain barrier (BBB), which presents difficulty for delivering drug above a therapeutic concentration window to the brain tumor without demanding administration of toxic quantities of drugs [18]. Another advantage offered by this technique for drug delivery to the brain is the increased tumor selectivity offered by CED for treating glioma. The principle behind CED follows Darcy’s law, where the bulk flow velocity is directly proportional to the pressure gradient. In contrary to conventional drug delivery by diffusive flow based on a concentration gradient, CED requires relatively lesser amounts of drug to achieve similar therapeutic levels [19]. Clinical application of CED involves one or more catheters placed stereotactically through a burr hole into the interstitial spaces of the brain using image guidance. An infusion pump is connected to the catheter(s), which induces a pressure gradient and drives the flow. The drug is directly infused into the extracellular space of the brain, while displacing the extracellular fluid [20]. The convective transport is achieved by interstitial pathways in the brain, which, unlike diffusive transport that occurs during intravenous (IV) drug administration, is driven by the fluid flow velocity and is independent of the size of the molecule to be transported. Indeed, the amount of drug that could be delivered through CED may be 1000- to 10,000-fold high than intravenous (IV) delivery [21].

Although CED of chemotherapeutic drugs to the brain has been reported in glioblastoma treatment, few studies have explored its application for PTT/PDT. On the other hand, as CED will be suitable for delivery of a nanotheranostic agent to the brain for PTT/PDT with unobstructed penetration of laser light through the created burr hole during CED, the stability of a PS during repeated laser irradiation poses another hurdle for clinical application. A prolonged photostability of IR-780 is therefore imperative to meet the need of successful PTT/PDT. Toward this end, we aim to prepare IR-780-loaded liposomes (ILs) and protect hydrophobic IR-780 in the lipid bilayer of liposomes. The ILs after CED will lead to rapid and massive uptake by U87MG human glioblastoma cells surrounding the injection site to improve the outcomes of PTT/PDT with consecutive NIR laser irradiation. The physico-chemical properties as well as the biological responses of liposomal IR-780 were characterized *in vitro*, followed by concurrent PTT/PDT of intracranial human glioma xenografts in nude mice by CED of ILs in combination with three successive NIR laser treatments.

## 2. Materials and Methods

### 2.1. Materials

Cholesterol (CH), didodecyldimethylammonium bromide (DDAB) and IR-780 were purchased from Sigma-Aldrich (St. Louis, MO, USA). 1,2-Distearoyl-sn-glycero-3-phosphocholine (DSPC) was purchased from Avanti Polar Lipids Inc. (Alabaster, AL, USA). N-(Carbonyl-methoxypolyethylenglycol 2000)-1,2-dipalmitoyl-sn-glycero-3-phosphoethanolamine sodium salt (DSPE-PEG2000) was purchased from NOF Co. (Tokyo, Japan). Cell culture reagents were purchased from Life Technologies (Carlsbad, CA, USA). Female BALB/c nude mice weighing approximately 15–20 g (4–6 weeks old) were procured from the National Laboratory Animal Center (Taipei, Taiwan).

### 2.2. Preparation of IR-780-Loaded Liposomes (ILs)

The IR-780-loaded liposomes (ILs) were prepared using the thin film hydration method with some modification [22,23]. In brief, lipids (DSPC, CH, DDAB and DSPE-PEG2000) in molar 64/30/4/2 were taken in a round bottom flask filled with chloroform/methanol (2:1, *v/v*) to prepare a 10 mM lipid solution. IR-780 dissolved in methanol was added to this mixture to reach a final weight ratio of IR-780:lipids = 3:100. The resultant solution was dried in a rotary evaporator (EYELA N-1200AVF, Tokyo, Japan) to form a thin lipid film after removing the organic solvents, followed by vacuum drying overnight to remove residual solvents. The dried lipid film was then hydrated with 10 mL phosphate buffer saline (PBS) at 55 °C in a water bath for 30 min, after which the solution was sonicated using a probe

type sonicator (Q700, Qsonica, Newtown, CT, USA) for 15 min (5 s/5 s on/off pulse cycle, amplitude = 5) followed by a bath type sonicator for 30 min (30 s/5 s on/off pulse cycle, amplitude = 30). The resulting ILs solution was processed with a commercial temperature-controlled barrel extruder (Lipex<sup>®</sup> Extruder, Transferra Nanosciences, Burnaby, CA, USA) for 10 cycles at 55 °C using double-stacked polycarbonate membranes with 0.2 µm pore size. Subsequently, free IR-780 was removed by dialysis (MWCO = 12–14 KDa) overnight in phosphate buffered saline (PBS) at 4 °C. The encapsulation efficiency (EE) and loading efficiency of IR-780 in ILs was calculated using the following equations [6]:

$$EE (\%) = \frac{\text{Weight of encapsulated IR} - 780}{\text{Weight of IR} - 780 \text{ initially added}} \times 100 \quad (1)$$

$$LE (\%) = \frac{\text{Weight of encapsulated IR} - 780}{\text{Weight of liposomes}} \times 100 \quad (2)$$

### 2.3. Characteristic of IR-780-Loaded Liposomes (ILs)

The particle size distribution and zeta potential of ILs were determined by dynamic light scattering (DLS) using a Zetasizer Nano ZS (Malvern Panalytical, Malvern, UK) at 25 °C and at a scattering angle of 173° in auto mode. Nanoparticle tracking analysis (NTA) was used to confirm the size distribution of ILs using NanoSight LM10 (Malvern Panalytical, Malvern, UK) equipped with a 405 nm laser. The stability of ILs was measured by statically incubating a 2 mg/mL ILs solution prepared in 95% PBS/5% fetal bovine serum (FBS) at 37 °C. At different time points, samples were removed and analyzed by NTA at room temperature. The samples were measured for 60 s with manual gain and shutter adjustments. The photostability was studied using an ultraviolet–visible (UV–Vis) spectrophotometer (Genesys 150, Thermo Fisher Scientific, Waltham, MA, USA) to monitor the change of solution absorbance of a free IR-780 or ILs (2 µg/mL IR-780) solution prepared in PBS after continuous exposure to day light at 25 °C. For Fourier transform infrared spectroscopy (FTIR) analysis, freeze dried ILs and blank liposomes (without IR-780) were combined with KBr, compressed to form a pellet and analyzed with a Bruker Tensor II FTIR spectrometer (Billerica, MA, USA) from 400 to 4000 cm<sup>−1</sup> with a 4 cm<sup>−1</sup> resolution at 2.5 mm/s.

### 2.4. Photothermal and Photodynamic Effects

The photothermal and photodynamic effects of free IR-780 and ILs were studied separately. For photothermal experiments, aqueous solutions of free IR-780, ILs and PBS in Eppendorf tubes (0.5 mL) were irradiated with 808 nm NIR laser for 5 min and temperature change was monitored using an infrared thermal camera (InfReC Thermo GEAR G100EX, Tokyo, Japan). The concentration of IR-780 in ILs was the same as free IR-780 in all studies. In one study, the IR-780 concentrations were varied from 10 to 50 µg/mL with fixed NIR laser intensity at 1.5 W/cm<sup>2</sup>. In the other study, the IR-780 concentration was fixed (30 µg/mL), while the NIR laser intensity was varied from 1 to 2 W/cm<sup>2</sup>. The photothermal response of free IR-780 and ILs was also studied with repeated on/off laser irradiation cycles. A 0.5 mL solution of free IR-780 or ILs in PBS (40 µg/mL IR-780) was irradiated with three successive NIR laser cycles (1 W/cm<sup>2</sup>, 3 min on/15 min off). The change in temperature was monitored with an infrared thermal camera, and gross change of solution color was captured with a digital camera.

The photodynamic effects of free IR-780 and ILs were determined from reactive oxygen species (ROS) generation using 1,3-diphenyl isobenzofuran (DPBF) as a chemical probe [24]. Ten microliters of DPBF (2 mg/mL in acetonitrile) was mixed with 1 mL of free IR-780 or ILs (5 µg/mL IR-780 in acetonitrile) and irradiated with 808 nm NIR laser (1 W/cm<sup>2</sup>). At predetermined time points, the solution absorbance was immediately measured at 410 nm using an UV–Vis spectrophotometer. A blank prepared in acetonitrile was irradiated similarly with NIR laser and used as a control.

Intracellular ROS detection was measured with a cell permeable non-fluorescent probe, 2',7'-dichlorofluorescein diacetate (DCFH2-DA) [25]. Briefly, U87MG cells ( $1 \times 10^4$ ) were seeded in a 24-well cell culture plate and cultured overnight. After washing with PBS, the cells were treated with free IR-780 or ILs ( $2 \mu\text{g/mL}$  IR-780 in cell culture medium) for 2 h. After washing with PBS, the cells were further incubated with DCFH2-DA ( $20 \mu\text{M}$ ) for 60 min at  $37^\circ\text{C}$ . After washing with PBS and replenishing with cell culture medium, the cells were treated with NIR laser for 3 min at  $1.5 \text{ W/cm}^2$ . Control was PBS treatment without NIR laser exposure. The fluorescence due to ROS generation was detected by observation under an inverted fluorescence microscope (Olympus IX-71, Tokyo, Japan). The quantitative intercellular ROS was determined from flow cytometry using DCFH2-DA [26]. After seeding  $3 \times 10^5$  cells/well U87MG in a 6-well cell culture plate overnight, the cells were washed with PBS and cultured in cell culture medium containing free IR-780 or ILs ( $2 \mu\text{g/mL}$  IR-780) for 2 h at  $37^\circ\text{C}$ . The cells were washed again with PBS and incubated with DCFH2-DA ( $20 \mu\text{M}$ ) for 60 min. After further washing with PBS, the cells were treated with NIR laser for 3 min ( $1.5 \text{ W/cm}^2$ ) in cell culture medium. The fluorescence (ROS) was detected by Thermo Attune NxT flow cytometer (Waltham, MA, USA) at 488 nm excitation and 530 nm emission wavelengths.

Western immunoblot was conducted to understand the anticancer molecular mechanism. The expression of heat shock protein 70 (HSP70) was determined in U87MG cells after exposing to free IR-780 or ILs with or without NIR laser irradiation ( $1.5 \text{ W/cm}^2$ ) for 3 min [27]. Briefly,  $1 \times 10^6$  cells were seeded in T-75 flask and culture overnight. After incubating with free IR-780 or ILs ( $5 \mu\text{g/mL}$  IR-780) for 2 h, the cells were trypsinized and treated with NIR laser in an Eppendorf tube. After incubation for another 10 h, cells were washed and lysed by radioimmunoprecipitation assay (RIPA) buffer containing protease inhibitors. The supernatant was recovered, and the protein concentration was measured with BCA protein assays after centrifugation to remove cell debris. The protein was heat-denatured for 10 min in a sample buffer at  $95^\circ\text{C}$ , followed by separating aliquots of lysate by polyacrylamide sodium dodecyl sulfate gel electrophoresis at 50 V for 30 min ( $\sim 25 \mu\text{g}$  total protein/lane) and at 110 V for 2 h. The gels were transferred to a polyvinylidene fluoride membrane, blocked for non-specific binding with 5% fat-free milk for 1 h and treated with primary antibodies for HSP70 (ab231637, Abcam, Cambridge, UK) and  $\beta$ -actin (13E5, Cell Signaling Technology, Danvers, MA, USA) overnight at  $4^\circ\text{C}$ . After washing with Tris-buffered saline and Tween 20 (TBST) 3 times, secondary antibody (anti-rabbit IgG-HRP, 1:2000) was added, followed by ECL Western blotting substrate for color development. The band densitometry analysis was carried out using ImageJ software (National Institute of Health Bethesda, MD, USA) for relative protein expression after detection with a MultiGel-21 gel image system (Top Bio Co., Taipei, Taiwan).

## 2.5. Intracellular Uptake and Cytotoxicity

For in vitro experiments, U87MG human primary glioblastoma cells (ATCC HTB1) were obtained from the American Type Culture Collection (Manassas, VA, USA). To study the in vitro cell cytotoxic effect of free IR-780 and ILs with or without NIR laser irradiation, U87MG cells were seeded in a 96-well cell culture plate at  $5 \times 10^3$  cell/well and cultured overnight in cell culture medium (90% high glucose Dulbecco's modified Eagle's medium (DMEM) and 10% FBS) in a humidified  $\text{CO}_2$  incubator at  $37^\circ\text{C}$  under 5%  $\text{CO}_2$ . The cell culture medium was replaced with cell culture medium containing different concentrations of IR-780 or ILs and incubated at  $37^\circ\text{C}$  for 12 h in a humidified  $\text{CO}_2$  incubator. Each well was treated with NIR laser for 4 min at  $1.5 \text{ W/cm}^2$ . The cell viability was determined from (3(4,5-dimethylthiazol-2-yl)-2,5-diphenyltetrazolium bromide) (MTT) assays by measuring the solution absorbance at 540 nm using a microplate reader [28].

The flow cytometry study for apoptotic and necrotic cell distribution assays was performed with fluorescein isothiocyanate-labeled Annexin V (FITC-Annexin V) and propidium iodide (PI). At a cell seeding density of  $4 \times 10^5$  cells/well, U87MG was used in a 6-well cell culture plate, and cell culture was carried out overnight in a humidified  $\text{CO}_2$

incubator at 37 °C under 5% CO<sub>2</sub>. The cells were washed with PBS and cultured in fresh cell culture medium containing IR-780 or ILs (4 µg/mL IR-780) for 6 h. After washing in PBS, cells were trypsinized and collected in a glass tube (500 µL in cell culture medium). The laser treatment groups received NIR laser treatments for 5 min at 1.5 W/cm<sup>2</sup>. The cell suspension was reacted for 30 min with FITC–Annexin V followed by PI for flow cytometry analysis (Attune NxT flow cytometer) after adding 500 µL fresh cell culture medium.

The intracellular uptake of free IR-780 and ILs was studied with U87MG cells. For this,  $4 \times 10^4$  cells were seeded on 15 mm coverslips placed in a 24-well cell culture plate and cultured overnight with cell culture medium in a humidified 5% CO<sub>2</sub> incubator at 37 °C. The cells were further washed with PBS and cultured in cell culture medium containing free IR-780 or ILs (2 µg/mL IR-780) for predetermined times. The lysosomes were labeled with LysoTracker Green DND-26 (1 µM) for 60 min at 37 °C after washing cells with PBS. Further, the labeled cells were washed with PBS, fixed with 4% paraformaldehyde and treated with Triton X-100 (0.1% in PBS). In the final step, the labeled cells were counterstained for cell nucleus with Hoechst 33342 (1 µg/mL) for 15 min. For confocal laser scanning microscopy analysis, the coverslips were carefully removed and fixed to a glass plate using mounting medium. Cellular internalization was measured by an inverted confocal microscope LSM 510 Meta (Zeiss, Oberkochen, Germany), with excitation/emission wavelengths of 350 nm/451 nm, 504 nm/511 nm and 684/784 nm, for blue, green and red fluorescence, respectively. The red fluorescence was used for the identification for IR-780 or ILs, green for lysosomal identification and blue for cell nuclei [29].

## 2.6. Intracranial Xenograft Tumor Model

All animal experiments protocols were approved by the Chang Gung University's Institutional Animal Care and Use Committee (IACUC Approval No.: CGU105-034). To establish a human glioma xenograft model in nude mice, U87MG human glioblastoma cell lines genetically engineered to express firefly luciferase genes were implanted intracranially in BALB/c nude mice [30]. Prior to implantation, the animals were anesthetized with 3% isoflurane gas, and a sagittal incision was made in the skin overlying the calvarium, followed by creating a burr hole on right side of the brain at the center region between the bregma and lambda using a 26-gauge needle. Three microliters of U87MG cell suspensions ( $1 \times 10^5$  cells/µL in cell culture medium) was injected using a 10 µL Hamilton syringe 3 mm below the brain surface, before extracting the needle in 100 s. The tumor development was confirmed by bioluminescence imaging (BLI) using a non-invasive in vivo imaging system (IVIS) (Xenogen IVIS-200, Caliper Life Sciences, Waltham, MA, USA). The timeline for establishing the intracranial xenograft tumor model, convention-enhanced delivery (CED) and assessment of anti-tumor efficacy is shown in Figure S1.

## 2.7. Convection-Enhanced Delivery (CED)

The CED infusion cannulas were fabricated by taking a 20 cm Polymicro capillary tube (inner diameter = ~98 µm; outer diameter = ~240 µm) at one end. For infusion, a 0.3 mm stepped-tip was created with a 2 cm Polymicro capillary tube (inner diameter = ~323 µm, outer diameter = ~430 µm) and fixed with resins and molded with Super Flangeless (P-259X) rings. The other end was connected to a connector (luer Adapter 1/4-28 female to female luer), which could be fitted into a 100 µL Hamilton syringe. The U87MG tumor-bearing mice were randomly divided into three groups, namely PBS + laser, free IR-780 + laser and ILs + laser ( $n = 4$ , each group), on day 6 post-implantation of U87MG cells. The tumor-bearing mice were anesthetized with liquid isoflurane (Zoletil/Rompum = 4/1, diluted with saline 1:1) and held in fixed position using a stereotactic holder, while a sagittal incision was made in the skin overlying the calvarium. The animal received CED of PBS, free IR-780 or ILs (0.8 µg/µL IR-780) from a Hamilton syringe connected to CED infusion cannulas and mounted in a two-channel laboratory syringe pump (Figure S2). A total volume of 10 µL sample was infused at a 0.5 µL/min flow rate, and the CED infusion



cannulas were withdrawn 2 min post-delivery. For laser light treatment, the light was delivered through the same burr hole created during CED.

### 2.8. Bio-Distribution and In Vivo Fluorescence Imaging

The bio-distribution and in vivo degradation of ILs was performed by administrating 10  $\mu$ L of ILs (0.5  $\mu$ g/ $\mu$ L IR-780) or PBS (control) via CED on day 6 post-implantation of U87MG cells. The brain plus other major organs from a mouse were explanted after euthanasia on day 6, 8, 10 and 12, for ex vivo NIR fluorescence imaging using Xenogen IVIS-200 at excitation/emission wavelengths of 745 nm/850 nm.

### 2.9. In Vivo Photothermal Effects

On day 7 post-implantation of U87MG cells (1 day post-CED), mice in all three groups received the first NIR laser irradiation (808 nm) for 5 min on top of the closed sagittal incision in their head. The laser power used was at 1 W/cm<sup>2</sup>, to maintain a temperature below 55 °C in the brain. The real-time temperature profiles in tumor-bearing mice during laser irradiation were monitored using an infrared thermal camera (InfReC Thermo GEAR G100EX, Tokyo, Japan). The distance between the NIR laser head and the tumor was 30 cm. The second and third laser treatment were performed on day 9 and day 11, respectively, following the same protocol as the first treatment.

### 2.10. In Vivo Anti-Tumor Efficacy

The in vivo antitumor efficiency was monitored from bioluminescence signal intensity from BLI. On day 5, 7, 9, 12, 14 and 16 post-implantation of tumor cells, 100  $\mu$ L of luciferase solution (15 mg/mL) was intraperitoneally injected into mice for BLI within 10 min. By using the Living Image<sup>®</sup> 4.0 program (PerkinElmer, Waltham, MA, USA), the BLI intensity was determined as baseline on day 5 (i.e., before treatment) and also at each time point after treatment by calculating the total BLI peak intensity within the standardized region of interest (ROI) in the tumor. The BLI signal intensities at each time point were normalized with the baseline value on day 5. All mice were observed regularly and euthanized after they had reached moribund condition due to body weight loss of more than 25% from the initial value, or showing back hunk, hemiparesis and seizures. In order to determine systemic toxicity, a blood sample was collected in a blood collection tube after sacrificing the animal and subjected to basic hematological as well as biochemical analysis of major organ function.

### 2.11. Magnetic Resonance Imaging (MRI) and Positron Emission Tomography/Computed Tomography (PET/CT) Study

For visualization of tumor in mice brain, magnetic resonance imaging (MRI) was carried out using a Siemens 3.0 Tesla scanner (Magnetom Trio, Siemens, Munich, Germany) equipped with a wrist coil to achieve the relaxation of MRI. During the MRI on day 7 (before laser treatments), 13 and 16 (after laser treatments), mice were anesthetized under isoflurane (2.5%) inhalant. For the T1\* series, the image parameters used were as follows: gradient echo, TR/TE: 230/3.81 ms; flip angle: 70; slice thickness: 0.5 mm. The tumor volume in mouse brain was determined from the ROI by multiplying the summed up areas traced on each coronal T2-weight image with the slice thickness [31]. For the positron emission tomography/computed tomography (PET/CT) study, a NanoScan PET (PET122S, Mediso, Budapest, Hungary) was used. Mice were anesthetized with 2% isoflurane on day 5 (before laser treatment), as well as on day 12 (after laser treatment), and intravenously administrated with two different tumor uptake markers, namely Ga68 RGD ( $0.3 \pm 10\%$  mCi) (1 Curie (Ci) =  $3.7 \times 10^{10}$  decays/sec) or Ga68 FAPI ( $0.4 \pm 10\%$  mCi). PET imaging parameters used were as follows: 360 projection; 50 kVp 980  $\mu$ A; 170 ms exposure time; 1:4 binning; helical acquisition; pitch 1; voxel size 250  $\times$  250  $\times$  250  $\mu$ m. Using the PMOD 4.004 software, images were analyzed, and tumor uptake was quantified from the maximum standardized uptake value (SUV<sub>max</sub>).

### 2.12. Histological Analysis

The brain and major organs were carefully removed and preserved in formaldehyde after sacrificing the animal. To conduct hematoxylin and eosin (H&E) staining of tumor tissue and explanted organs, the sample was treated with phosphate buffered formalin, followed by paraffin embedding for sectioning into 5- $\mu$ m thickness. For immunohistochemical (IHC) staining, the cell proliferation marker Ki-67 and cell apoptosis marker cleaved caspase 3 (CC3) in tumor tissue was detected with primary antibody, followed by the UltraVision™ Quanto Detection System HRP DAB (Thermal Fisher Scientific, Waltham, MA, USA), and counterstained with hematoxylin. The primary antibody used was anti-Ki-67 (1:200) and CC3 (1:100) monoclonal antibodies from rabbit. The slides were analyzed with a TissueFAXS inverted bright field scanning system (TissueGnostics GmbH, Vienna, Austria), and immunoreactivity was quantified using the PAX-it image analysis software within a ROI of 280  $\times$  200  $\mu$ m dimensions ( $n = 3$ ). To evaluate safety of the treatment, the major organs from sacrificed mice were examined after H&E staining.

### 2.13. Statistical Analysis

All data were reported as mean  $\pm$  standard deviation (SD). The one-way analysis of variance (ANOVA) analysis with Tukey honestly significant difference (HSD) test was used to compare subgroups and statistical significance was declared at  $p < 0.05$ .

## 3. Results and Discussion

### 3.1. Characterization of ILs

We prepared ILs from DSPC, CH, DDAB and DSPE-PEG2000 by the thin film hydration method for entrapment of hydrophobic IR-780 within the lipid bilayer (Figure 1A). The CH plays a role in stabilizing ILs [32]. By incorporating DDAB, cationic ILs is expected to be accumulated around cancer cells by binding to negatively charged cell membrane as well as fusion with cell membrane for facilitated intracellular uptake. Previously, the PEGylated positively charged liposome was shown to increase the survival time of tumor-bearing rats after CED of liposomal carboplatin [33]. From the distribution curve of hydrodynamic diameter measured by DLS (Figure 1B) and zeta potential (Figure 1C), the average size and zeta potential was  $136.6 \pm 5.5$  nm and  $33.3 \pm 5.1$  mV, with a polydispersity index (PDI) of  $0.21 \pm 0.03$  ( $n = 3$ ). Consistent with DLS, the diameter of ILs was  $145 \pm 26$  nm from NTA, shown as fairly monodispersed light scattering particles from the screenshot image due to its cationic nature (Figure 1D).

The UV–Vis absorption spectrum of free IR-780 showed a strong absorption peak at 780 nm, which shifted slightly to  $\sim$ 790 nm for ILs, indicating successful encapsulation of IR-780 within ILs (Figure 1E). The strong absorption peak shown by ILs in the NIR region supports its use as a PTT/PDT agent with NIR laser light [34]. The EE and LE of IR-780 in ILs were calculated to be  $82.0 \pm 3.4\%$  and  $1.10 \pm 0.14\%$  ( $n = 3$ ), respectively, from a linear calibration curve constructed at 780 nm. From FTIR analysis, blank liposomes (without IR-780) revealed the symmetric and asymmetric stretch modes of phosphate group (P=O) at  $1100\text{ cm}^{-1}$  and  $1224\text{ cm}^{-1}$  as well as  $\text{CH}_2$  symmetric and asymmetric stretch modes at  $2849\text{ cm}^{-1}$  and  $2920\text{ cm}^{-1}$  from the major lipid component DSPC (Figure 1F) [6]. The free IR-780 revealed the aliphatic chloro compounds' C–Cl stretch at  $720\text{ cm}^{-1}$ , CN stretch at  $1170\text{ cm}^{-1}$  and aromatic ring stretch of C=C at  $1550\text{ cm}^{-1}$ . The encapsulation of IR-780 resulted in additional peaks that were assigned to IR-780 in the FTIR spectrum of ILs as expected [35].

To study the photostability of IR-780, free IR-780 and ILs in PBS were exposed to natural daylight at room temperature, and the absorption spectra were recorded with an UV–Vis spectrophotometer. As shown in Figure 2A, the maximum solution absorbance of free IR-780 decreased continuously with time to nearly zero after 9 h, indicating free IR-780 is unstable under light exposure. On the other hand, the maximal solution absorbance of ILs remained almost constant within 9 h, followed by a minimum decrease in 24 h (Figure 2B). For better comparison of photostability, the maximum absorbance (A) at

different time points was normalized with its initial value at time 0 ( $A_0$ ). As shown in Figure 2C, no noticeable difference in  $A/A_0$  was found for ILs till 24 h, in contrast to free IR-780, which showed fast degradation with less than 10% initial absorbance value after 9 h. The enhancement of IR-780 stability could be due to entrapment of the PS within the lipid bilayer of ILs, which is consistent with other reports showing improved stability of entrapped IR-780 or nanoparticle-conjugated IR-780 [12,13,34,36].

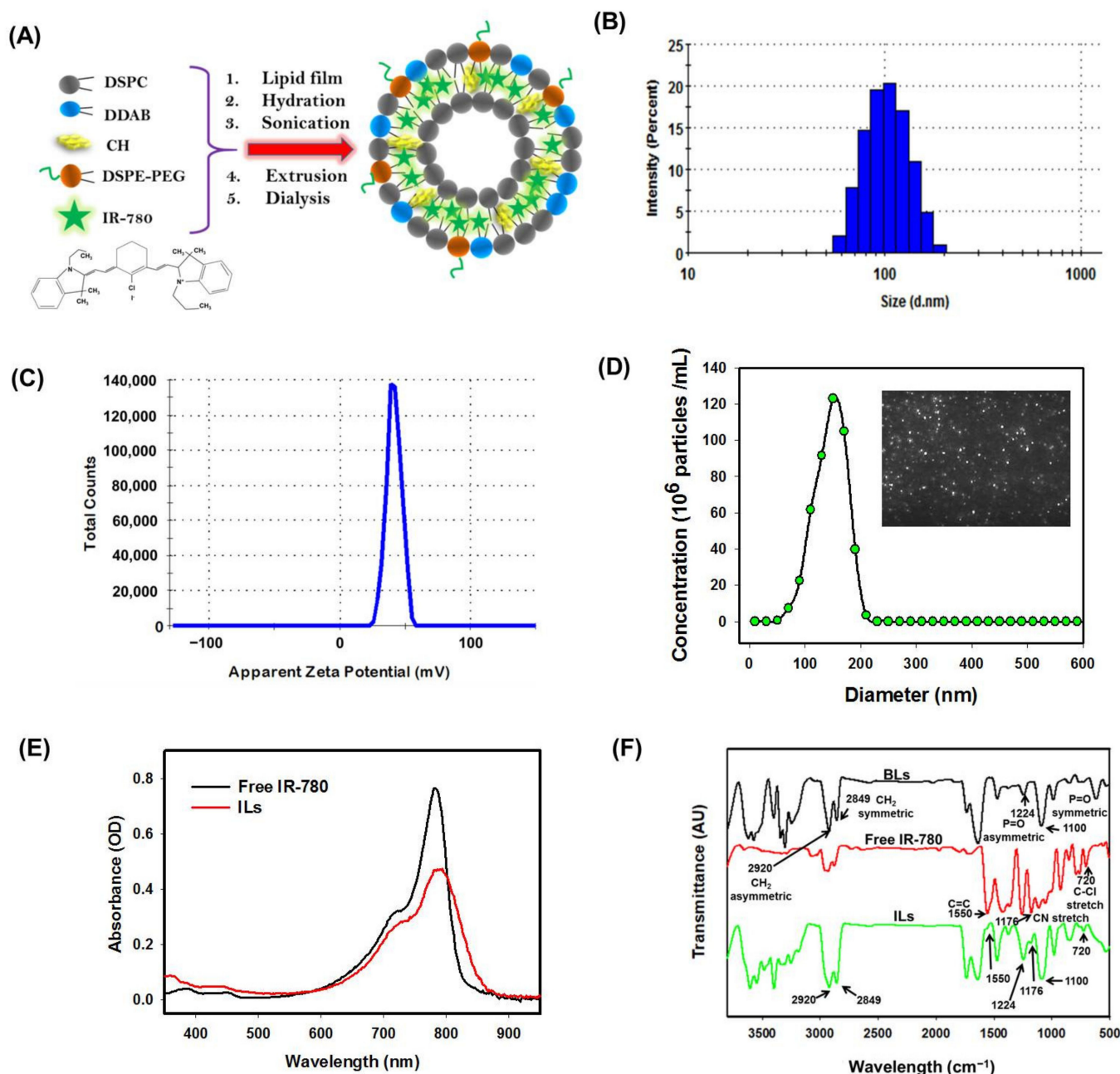


**Figure 1.** Preparation and characterization of IR-780-loaded liposomes (ILs). (A) The schematic diagram showing the structure of ILs. (B) The distribution curves of particle size from dynamic light scattering (DLS). (C) The distribution curves of zeta potential. (D) The particle size distribution from nanoparticle tracking analysis (NTA) with the insert showing light scattering particles taken from the screenshot of original video file. (E) The ultraviolet–visible (UV/Vis) absorption spectra of free IR-780 (4.5  $\mu\text{g/mL}$ ) and ILs (2.7  $\mu\text{g/mL}$  IR-780) in PBS. (F) The Fourier-transform infrared (FTIR) spectra of blank liposomes (BLs) (liposomes without IR-780), free IR-780 and ILs.

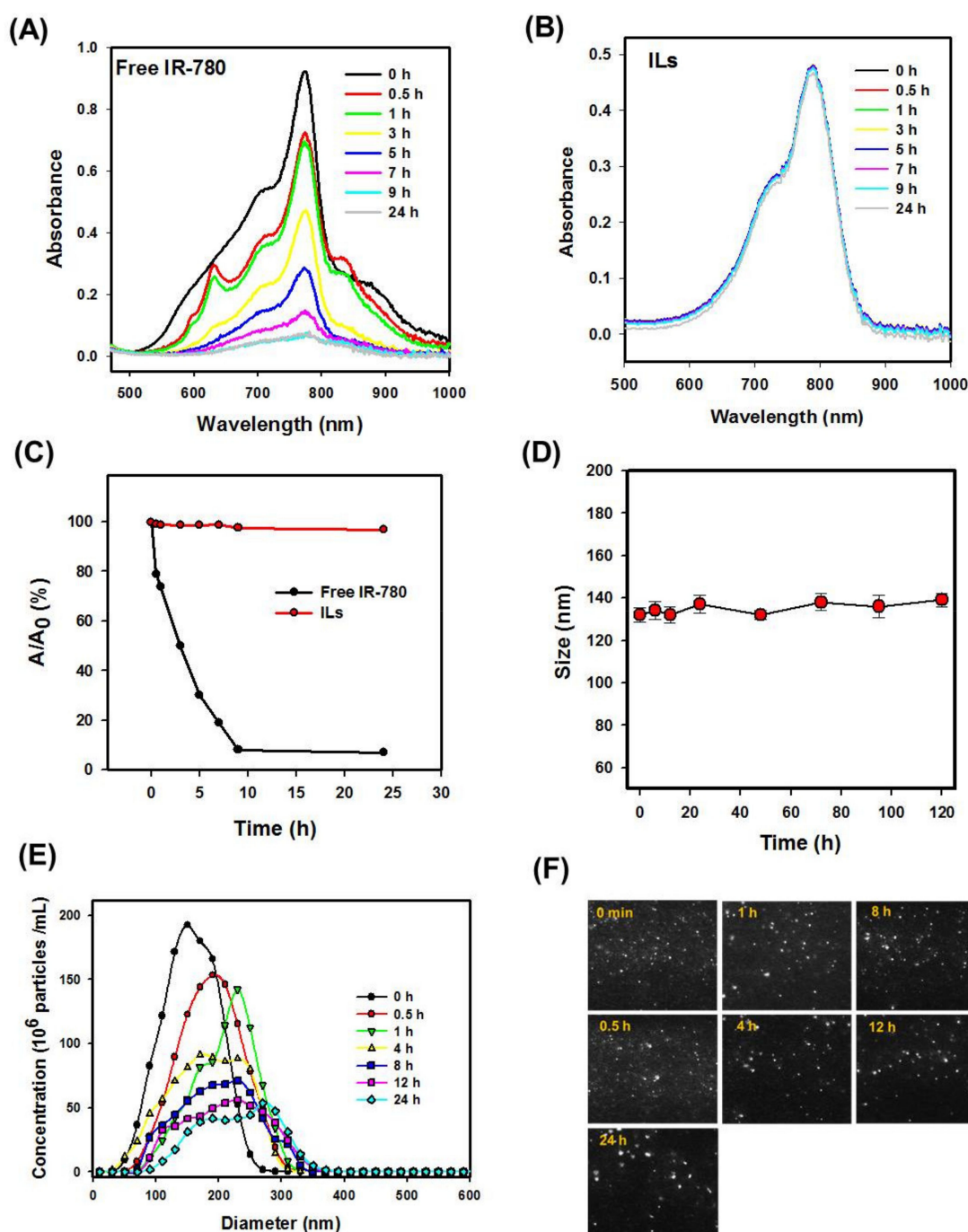


**Figure 2.** The stability of IR-780-loaded liposomes (ILs). The photostability of free IR-780 and ILs from ultraviolet–visible (UV/Vis) absorption spectra of free IR-780 (A) and ILs (B) in PBS under natural daylight exposure at room temperature was compared from normalized absorbance ( $A/A_0$ ) at different time points (C). The colloidal stability of ILs was determined from the change in average particle size in phosphate buffered saline (PBS) with dynamic light scattering (DLS) (D), the change in particle size distribution in 5% fetal bovine (FBS)/95% PBS with nanoparticle tracking analysis (NTA) (E) and the screen shots of light scattering particles from original NTA video files (F).

The colloidal stability of ILs was studied from the size (hydrodynamic diameter) change of ILs after incubating in PBS for different times. As shown in Figure 2D, the average particle size was within 132 to 140 nm, with no significant difference found up to 120 h. The stability of ILs in 5% serum/95% PBS was determined from NTA up to 24 h, shown as concentrations of ILs vs. particle diameter in Figure 2E. No noticeable difference in the size of the dispersing light was observed at any time from the screenshot images in



Figure 2F. The particle size shifted to a higher value with diminished particle concentration at longer incubation time, indicating time-dependent destruction of ILs. Many factors can influence the stability of liposomes, and the change in the concentration of ILs with time may be due to the destruction or aggregation of liposomes, leading to increased particle size and decreased particle concentration from NTA counts [37]. Unlike drug delivery by IV injection where long circulation time may be required before reaching the tumor site, CED could be completed within a much shorter period of time. Thus, ILs should be suitable for CED, considering their stability in vitro [38].

### 3.2. In Vitro Photothermal and Photodynamic Study

The in vitro photothermal effects of free IR-780 and ILs were studied after irradiating with NIR laser with real-time change in solution temperature monitored with an infrared (IR) thermal camera. The maximum temperature acquired from the IR camera image was used to plot the real-time temperature profile. When PBS was exposed to NIR laser at  $1 \text{ W/cm}^2$  intensity for 5 min, no substantial change in temperature was observed, although a minor temperature change from  $27^\circ\text{C}$  to  $30^\circ\text{C}$  was noted at  $1.5$  and  $2 \text{ W/cm}^2$  ( $450$  and  $600 \text{ J/cm}^2$ ) (Figure 3A,B). In contrast, when free IR-780 or ILs of the same IR-780 concentration was exposed to  $1 \text{ W/cm}^2$  laser irradiation, the temperature reached  $36^\circ\text{C}$  in 5 min. At  $1.5$  and  $2 \text{ W/cm}^2$  intensity, the temperature rose to  $38^\circ\text{C}$  and  $41^\circ\text{C}$  in 3 min for free IR-780 and ILs, with no significant difference found between them. Nonetheless, a distinctive temperature profile was found between free IR-780 and ILs after 3 min, with only free IR-780 showing a drop in temperature to  $37^\circ\text{C}$  (at  $1.5 \text{ W/cm}^2$ ) or  $38^\circ\text{C}$  (at  $2 \text{ W/cm}^2$ ) in 5 min. A temperature drop shown only by free IR-780 within 3 to 5 min, but not by ILs, underlines improved photostability of IR-780 in ILs with continuous decomposition of free IR-780 under NIR laser irradiation. This leads to retarded photothermal response with time, shown from a temperature drop at a longer time when the rate of heat dissipation is higher than the rate of heat generation. This difference is consistent with difference of decomposition rate between ILs and free IR-780 under daylight displayed in Figure 2C. Overall, ILs could be suggested as a preferred source for PTT over free IR-780 when exposed to NIR laser light.

The concentration-dependent photothermal effects at a fixed NIR laser intensity ( $1.5 \text{ W/cm}^2$ ) was examined next for free IR-780 and ILs with varying IR-780 concentrations. As shown in Figure 3C,D, the maximum temperature could be maintained at  $38$ ,  $40$  or  $44^\circ\text{C}$  after 3 min at  $30$ ,  $40$  or  $50 \mu\text{g/mL}$ , without significant difference found between free IR-780 and ILs. Nonetheless, at  $10$  and  $20 \mu\text{g/mL}$  concentrations, free IR-780 showed a temperature increase to  $32$  and  $35^\circ\text{C}$ , respectively, for the first 3 min, and a slight decrease to  $31$  and  $34^\circ\text{C}$ , respectively, in 5 min. In contrast, although the temperature of ILs increased similarly to  $32$  and  $35^\circ\text{C}$  in 3 min, it remained at this value thereafter till 5 min. From the in vitro photothermal study, we conclude that exposing  $30 \mu\text{g/mL}$  of free IR-780 to  $1.5$  or  $2 \text{ W/cm}^2$  NIR laser can result in a temperature rise suitable for PTT in 3 min. However, it fails to maintain this threshold PTT temperature for a longer duration. Only at a lower laser intensity ( $1 \text{ W/cm}^2$ ) and higher PS concentrations ( $30$ ,  $40$  or  $50 \mu\text{g/mL}$ ) could free IR-780 show comparable photothermal efficiency with ILs. The kinetics of peak temperature profiles are plotted using one-phase association fits and are shown in Figure 3E,F.

Other than continuous laser exposure, we compared the photostability between IR-780 and ILs after three repeated on/off laser cycles, consisting of 3 min on at  $1 \text{ W/cm}^2$  and 15 min off. As shown from the peak temperature profiles in Figure 4A, free IR-780 and ILs reached a maximum temperature ( $T_{\text{max}}$ ) of  $37^\circ\text{C}$  in 3 min and dropped to  $29^\circ\text{C}$  after turning off the laser in the first cycle. In second cycle, free IR-780 reached a  $T_{\text{max}}$  of  $35^\circ\text{C}$  while ILs reached  $38^\circ\text{C}$ . During the final cycle, free IR-780 only managed to reach a  $T_{\text{max}}$  of  $29^\circ\text{C}$ , in contrast to  $38^\circ\text{C}$  for ILs. The  $3^\circ\text{C}$  temperature difference between free IR-780 and ILs in the second cycle was due to the decomposition of IR-780 during the first cycle. Nonetheless, the drastic difference in photostability between IR-780 and ILs led to a  $9^\circ\text{C}$

temperature difference in  $T_{\max}$  during the third cycle, due to vast decomposition of IR-780 during the first two laser irradiation cycles. The ILs managed to reach similar  $T_{\max}$  within 3 min in all laser cycles due to protection of IR-780 by the lipid bilayer of ILs. The drastic change of thermal images at  $T_{\max}$  at 3 min (Figure 4B) and the pronounced change of solution color (Figure 4C) between free IR-780 and ILs support changes in photothermal and chemical properties of IR-780 under the influence of NIR laser and endorses the use of ILs for PTT/PDT. Using self-assembled IR-780 containing micelles for PTT, Yuan et al. found the temperature rise significantly reduced after the first laser cycle during repeated laser irradiation (808 nm, 1 W/cm<sup>2</sup>) [39]. In comparison, liposomes loaded with IR-780 are more stable after repeated laser irradiation, as temperature rise could be retained till three cycles, and lipid bilayers were suggested to offer protection of IR-780 against generated singlet oxygen [23].

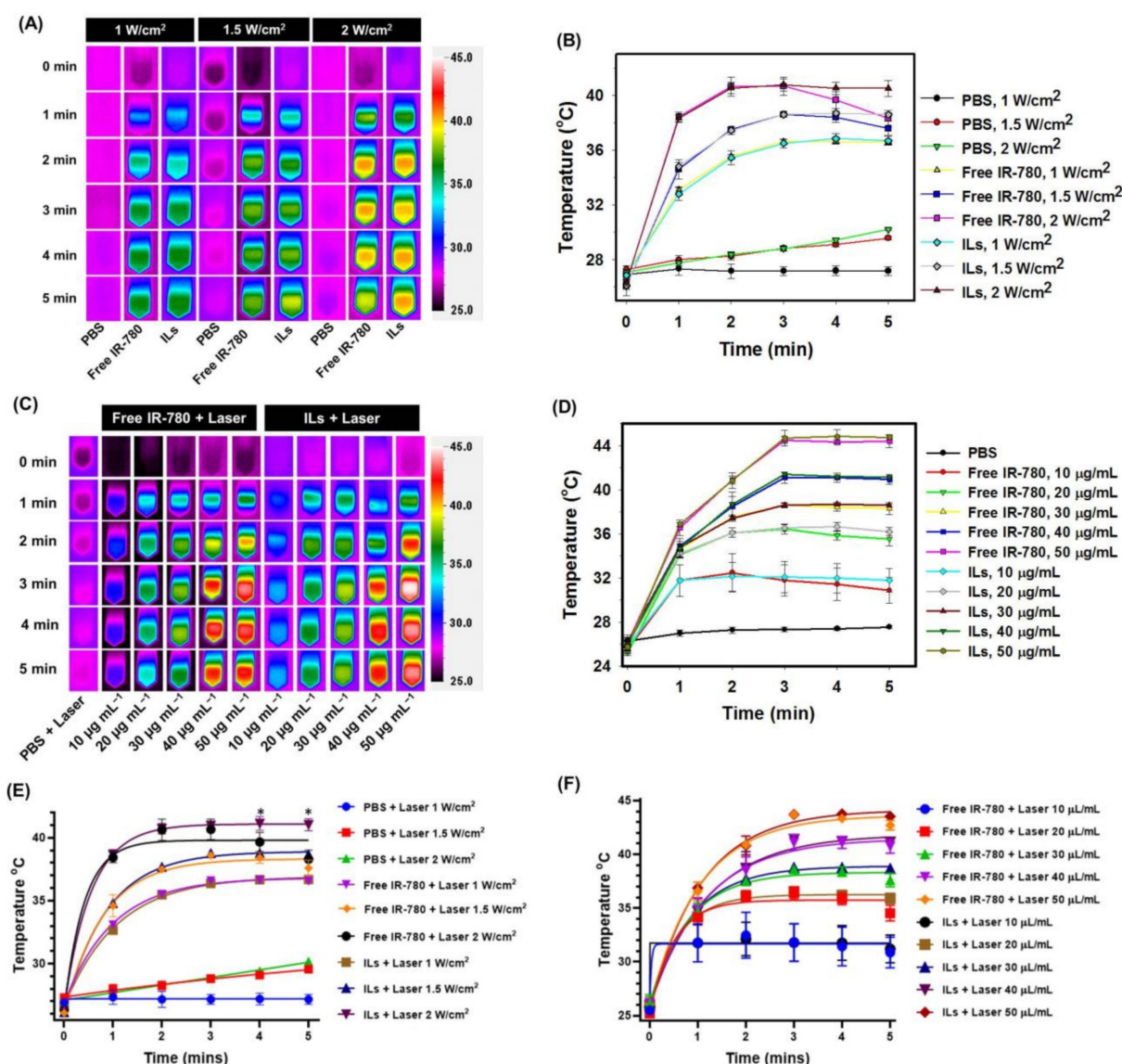


**Figure 3.** The in vitro photothermal effects with near infrared (NIR) laser irradiation. (A) The thermal images and (B) the peak temperature profiles of phosphate buffered saline (PBS), free IR-780 and IR-780-loaded liposomes (ILs) (30 µg/mL IR-780) after irradiating with 808 nm NIR laser at 1, 1.5 or 2 W/cm<sup>2</sup>. (C) The thermal images and (D) the peak temperature profiles of PBS, free IR-780 and ILs (10, 20, 30, 40 or 50 µg/mL IR-780) after irradiating with 808 nm NIR laser at 1.5 W/cm<sup>2</sup>. (E,F). The kinetics of peak temperature profiles are plotted using one-phase association fits. There is significant difference between Free IR-780 + laser and ILs + laser on 4 and 5 min at 2 W/cm<sup>2</sup> (\*  $p < 0.05$ ).

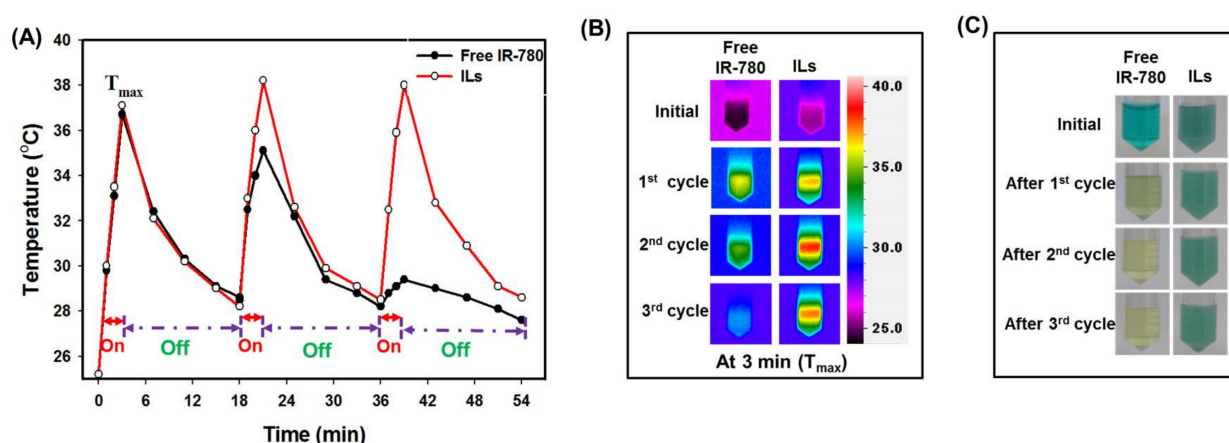


**Figure 4.** The photothermal stability of IR-780-loaded liposomes (ILs) and free IR-780. (A) The peak temperature profiles of free IR-780 and ILs (40  $\mu\text{g/mL}$  IR-780) during three on/off laser cycles. The near infrared (NIR) laser was used at 1  $\text{W}/\text{cm}^2$  with 3 min on and 15 min off. (B) The corresponding thermal images at  $T_{\text{max}}$  (3 min) for free IR-780 and ILs during each laser irradiation cycle. (C) The appearance of free IR-780 and ILs solution at the end of each laser irradiation cycle.

For PDT, the photodynamic effects of IR-780 were studied with DPBF as a chemical probe. The singlet oxygen ( $^1\text{O}_2$ ) or reactive oxygen species (ROS) produced from a PS after exposure to NIR laser is responsible for cytotoxicity in PDT [40–42]. The DPBF will react with  $^1\text{O}_2$  to give endoperoxides by 1,4-cycloaddition, which undergoes decomposition to generate o-dibenzoylbenzene at room temperature [43,44]. Although several other chemical methods could be used to detect  $^1\text{O}_2$ , the difference in absorption spectra between IR-780 and DPBF as well as the strong absorbance at 410 nm shown only by DPBF but not by its decomposed products from loss of the isobenzofuran  $\pi$  system, make facial detection of singlet oxygen possible [45]. As shown in Figure S3A and B, the decrease of solution absorbance at 410 nm after NIR laser irradiation for ROS generation is different for free IR-780 and ILs. The ability to generate ROS was compared by normalizing the maximum solution absorbance at different times (A) with its initial value at time 0 ( $A_0$ ) in Figure S3C. During the first 10 s, the  $A/A_0$  value was the same for IR-780 and ILs; nonetheless, free IR-780 showed much faster generation of ROS compared to ILs with comparatively smaller  $A/A_0$  values. The  $A/A_0$  values for free IR-780 and ILs decreased to 8% and 38%, respectively, 120 s after laser irradiation. This difference may have arisen as IR-780 was protected from NIR light within the lipid bilayer of ILs, consuming less energy and generating less ROS. You et al. also reported a similar behavior with a different PS (ICG) loaded in mesoporous silica-coated copper sulfide nanoparticles [24].

### 3.3. In Vitro Cell Culture Experiments

We first studied the intracellular uptake kinetics of free IR-780 and ILs by U87MG using confocal laser scanning microscopy. As shown in Figure 5A, there was no indication of red fluorescence signal after treating cells with free IR-780. The red fluorescence started to show after 1 h and continued to increase after 2 h. However, in case of ILs, strong red fluorescence intensity could be observed in cell cytoplasm as early as 0.5 h, which gradually increased with incubation time (Figure 5B). From merged images, high fluorescence intensity (yellow) corresponding to both IR-780 (red) and LysoTracker (green) was shown only for ILs but not for free IR-780, suggesting efficient uptake of ILs via endocytosis. That IR-780 shows much improved cellular trafficking rate upon entrapment in ILs could be related to the cationic nature of ILs (zeta potential = 33.3 mV), which could promote charge-mediated endocytosis of liposomes through passive accumulation and selective binding of ILs to the tumor cell surface, in contrast to free IR-780 that has negligible positive charge [29,46]. This is consistent with previous reports that cationic liposomes can fuse with anionic endosome membrane by electrostatic interaction [47], and cationic PEGylated liposomes had the most proficient cellular uptake in vitro [48].



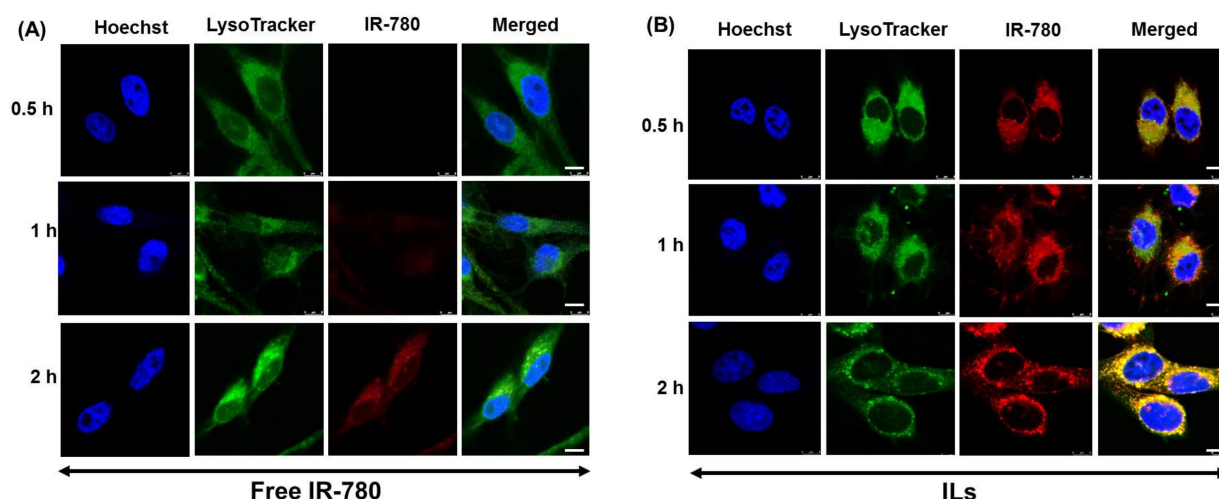


**Figure 5.** Intracellular uptake studies using confocal laser scanning microscopy. The intracellular uptake of free IR-780 (A) and IR-780-loaded liposomes (ILs) (B) by U87MG cells using free IR-780 or ILs (2  $\mu\text{g}/\text{mL}$  IR-780). Scale bar = 8  $\mu\text{m}$ .

For production of intracellular ROS, DCFH2-DA was chosen as an ROS probe. The DCFH2-DA can diffuse into U87MG cells and be deacetylated by cellular esterases to produce a non-fluorescent product, which is oxidized by ROS into a highly fluorescent product DCF for detection by fluorescence microscopy. To this end, U87MG cells were treated with free IR-780 or ILs for 2 h and washed to study intracellular uptake. The cells were incubated with DCFH2-DA for 1 h for permeation of DCFH2-DA into cells, followed by laser irradiation for 3 min at 1.5  $\text{W}/\text{cm}^2$ . As shown in Figure 6A, no green fluorescence signal could be observed for the PBS (control), free IR-780 and ILs groups without laser irradiation. In contrast, a strong green fluorescence signal was shown only in free IR-780 + laser and ILs + laser groups, indicating intracellular ROS was produced from endocytosed IR-780 after NIR irradiation [25]. Consistent with the ability to produce extracellular ROS, as shown in Figure S3, free IR-780 appeared to display a more intense green fluorescence signal than ILs, suggesting higher intracellular ROS production ability from free IR-780.

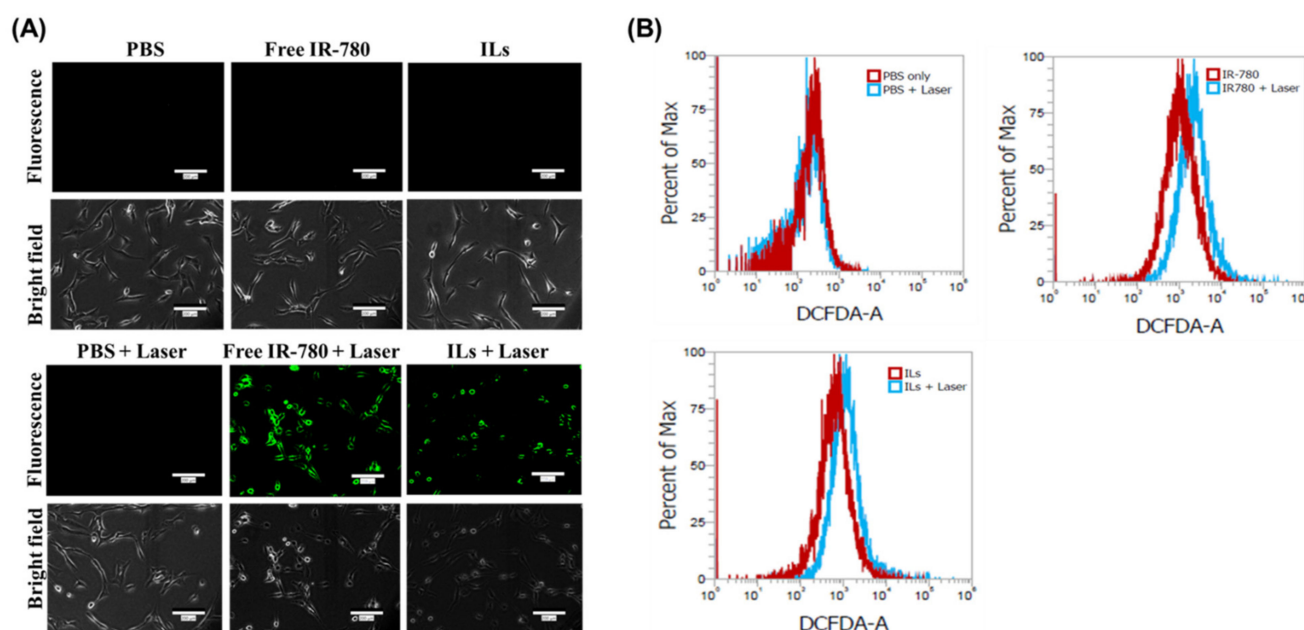


**Figure 6.** Intracellular ROS production by U87MG cells observed under an inverted fluorescence microscopy (bar = 200  $\mu\text{m}$ ) (A) and analysis by flow cytometry (B). The cells were treated with PBS, IR-780 or IR-780-loaded liposomes (ILs), followed by irradiation with 1.5  $\text{W}/\text{cm}^2$  near infrared (NIR) laser for 3 min.



The quantitative evaluation of intracellular ROS production was confirmed from flow cytometry analysis. As shown in Figure 6B, there was no peak shift in the PBS control group even with laser irradiation. In contrast, an obvious shift of peak fluorescence intensity was detected in free IR-780- and IL-treated cells upon laser exposure due to intracellular ROS production. The change of mean fluorescence intensity was 2.3-fold for free IR-780 (from 1375 to 3187) and 1.5-fold for ILs (from 1214 to 1840). These findings suggest that free IR-780 shows stronger ROS production ability than ILs upon NIR laser exposure, albeit with less photostability.

To understand the potential molecular mechanism of PTT/PDT after laser treatment of U87MG cells, we investigated the expression of a thermal stress-related protein, heat shock protein 70 (HSP70), which is typically overexpressed in most cancer cells or organelles, aiding cancer survival by preserving the protein homeostasis [49,50]. Increased HSP70 expression can also predict anti-tumor response [27,50], although decreased expression is associated with drug resisting cells in chemotherapy [50,51]. As shown in Figure S4, U87MG cells in free IR-780 + laser and ILs + laser groups show elevated expression of HSP70 from Western blotting, due to thermal stress experienced by the cells from the IR-780-induced photothermal response [27]. There was a significant difference in relative HSP70 protein expression by the action of NIR laser for free IR-780 and ILs, which was  $1.24 \pm 0.06$  and  $1.63 \pm 0.07$ , respectively. Comparing free IR-780 and ILs upon laser exposure, the less pronounced upregulation of HSP70 protein expression with free IR-780 may have been due to the higher rate of ROS generation, which resulted in reduced thermal stress experienced by U87MG cells.

After confirming the photothermal and photodynamic effects in vitro, concurrent PTT/PDT was studied by incubating U87MG cells with free IR-780 or ILs of different IR-780 concentrations for 12 h. The cells were irradiated with NIR laser at  $1.5 \text{ W/cm}^2$  for 4 min to induce cytotoxicity, followed by the determination of cell viability by MTT assays. As shown in Figure 7A, free IR-780 or ILs showed negligible cytotoxicity up to  $1.25 \mu\text{g/mL}$  concentration. Under laser exposure to induced PTT/PDT in vitro, free IR-780 or ILs showed drastically reduced cell viability, which was dose-dependent on IR-780 concentration. Most important, ILs exhibited significantly higher cytotoxicity toward U87MG compared to free IR-780, implicating differences in photostability between free and entrapped IR-780 upon continuous laser irradiation, as well as possible differences in their intracellular uptake, which may lead to significant differences in cancer cell killing effect with improved PTT/PDT by using ILs.

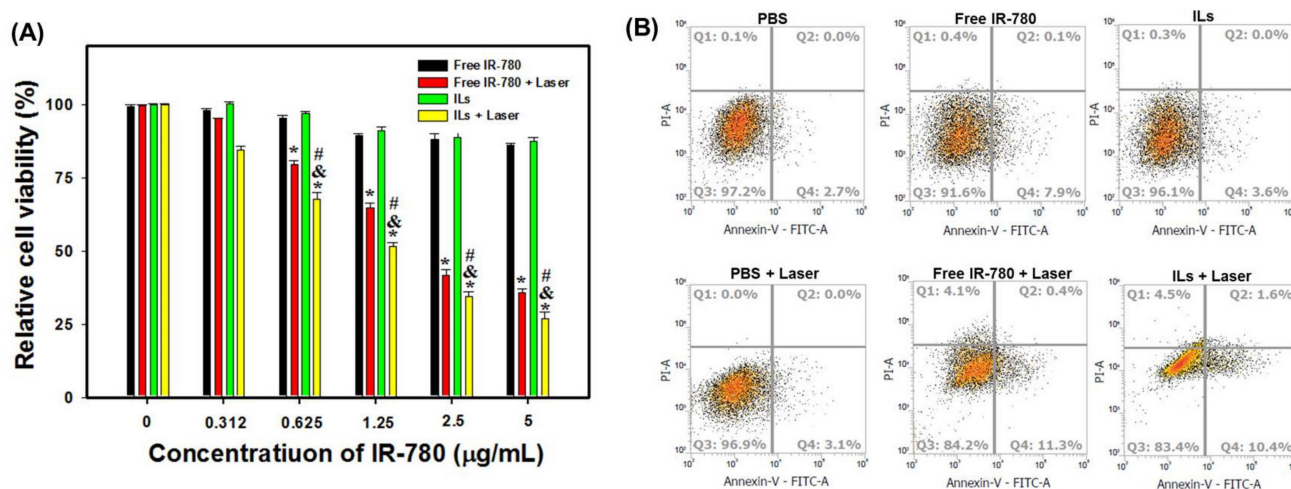


**Figure 7.** Cell cytotoxicity from MTT assays and flow cytometry. **(A)** In vitro cell cytotoxicity of free IR-780 and IR-780-loaded liposomes (ILs) with or without near infrared (NIR) laser treatment ( $1 \text{ W/cm}^2$  for 4 min) from MTT assays. \*  $p < 0.05$  compared with free IR-780, &  $p < 0.05$  compared with ILs, #  $p < 0.05$  compared with free IR-780 + laser. **(B)** The flow cytometry analysis of apoptotic and necrotic cells with fluorescein isothiocyanate-labeled Annexin V (FITC–Annexin V) and propidium iodide (PI).

The laser-induced cytotoxic due to free IR-780 and ILs (4 µg/mL IR-780) was further studied from flow cytometry analysis of cell apoptosis/necrosis (Figure 7B). To evaluate the percentage of live (Q3), early apoptotic (Q4), late apoptotic (Q2) and necrotic (Q1) cells based on variations in permeability and integrity of cell membranes, we used Annexin V/PI to stain the cells after different treatments in vitro. As shown in Figure 7B, cells in PBS control without NIR laser irradiation gave 97.2% live cells and a 3% apoptosis rate. A negligible change in cell viability (96.9%) was noted from the PBS + laser group. Without laser irradiation, free IR-780 resulted in an 8.0% apoptosis rate with 91.6% live cells. In contrast, ILs treatment showed a 3.6% apoptosis rate and 96.1% live cells. These findings further support the minimum cytotoxicity of ILs observed in Figure 7A, while entrapment in the lipid bilayer of ILs may even enhance the biocompatibility of IR-780. After laser irradiation, cells in free IR-780 showed an increase of necrosis rate, from 0.4% to 4.1%, while the apoptosis rate also increased to 11.7%. Similarly, laser irradiation of ILs also led to a vast increase of necrosis rate, from 0.3% to 4.5% and 12.0% cell apoptosis. Overall, a reduced percentage of viable cells with increased apoptotic and necrotic cells is consistent with the results from MTT assays of cell viability, which is based on mitochondria activity, and supports the use of ILs plus laser irradiation for concurrent PTT/PDT.

The laser fluence rate usually does not exceed 250 mW/cm<sup>2</sup> in PDT due to extensive photobleaching of the photosensitizer and thermal effects that predominate over the PDT effects at higher rates. However, it is difficult to completely rule out the contribution of PDT in the current study, as PTT and PDT are closely related by intersystem crossing of energy states, through energy dissipation during movement of electrons upon excitation from the ground state to a higher energy state [52]. Furthermore, we used 808 nm lasers at 1.5 to 2 W/cm<sup>2</sup> for PDT/PTT, which is within the range of laser fluence rates used in previous studies for PDT in vitro and in vivo with an 808 nm laser [13,53,54].

### 3.4. Bio-Distribution and In Vivo Photothermal Effects

The ex vivo IVIS fluorescence imaging shows a strong fluorescence signal found exclusively in the brain tumor area of a tumor-bearing mouse immediately after CED of ILs (6 days post-implantation of U87MG cells), in contrast to PBS administration (Figure S5). Most importantly, ILs could be specifically retained in the brain tumor, without distribution to other major organs, 6 days after CED (12 days post-implantation of U87MG cells). The fluorescence intensity within the ROI of the explanted brain at the end of the observation period (day 12) was 72% of its initial value (day 6). Combining with the photostability of IR-780 in ILs in vitro, the long-term retention of ILs after CED to the brain endorses its use for consecutive laser irradiation. In comparison to IV delivery [55], CED could specifically deliver liposomal IR-780 to the brain for alleviating associated toxicity from delivered therapeutics, while simultaneously facilitating NIR imaging and improved PTT/PDT of glioma [56].

Considering the penetration of NIR into tissue, as the animals used in this study were nude mice with very thin skulls (~0.32 mm from transverse view of MRI), the light can penetrate the skull and reach the tumor from the same burr hole created during CED. This may be translated to clinical practice, as CED has been used in preclinical and clinical studies for treating glioblastoma [57]. Furthermore, using an internal laser source, by implanting a laser catheter into the tumor as in laser interstitial thermal therapy (LITT) for treating glioblastoma, may also be applicable after CED in the future clinically [58].

To confirm the in vivo photostability of ILs, the photothermal response of ILs in vivo was judged from real-time thermal images when mice receiving CED of PBS, free IR-780 or ILs were treated with NIR laser (up to 5 min) on day 7, 9 and 11 post-implantation of tumor cells (Figure S6). During the first laser treatment, mice in ILs and free IR-780 groups showed identical peak temperature profiles, with temperatures rising from 37 °C to 54 °C within 1 min, which stayed constant thereafter (Figure S6A). Administration of PBS led to negligible temperature changes after laser treatment, as expected. The mice in the IL group during second laser treatment showed a similar temperature profile as the first treatment.

In contrast, mice in the free IR-780 group show reduced photothermal response with a drop of peak temperature from 54 °C to 44 °C (Figure S6B). During the third laser treatment, the IL group shows a slightly retarded rate of temperature rise but still manages to reach a peak temperature of 54 °C within 2 min. In contrast, the free IR-780 group showed drastically diminished photothermal effects, only to show a similar temperature profile as in the control PBS group (Figure S6C). Undoubtedly, such remarkable retention of *in vivo* photothermal responses of ILs over free IR-780 *in vivo* when exposed to successive laser treatment correlates well with the fast degradation and inferior photostability of IR-780 *in vitro*. Nonetheless, other than improved photostability, free drugs administered by CED showed early clearance from the central nerve system compared to drugs loaded within nanoparticles, which may also lead to rapid clearance of free IR-780 from the brain in contrast to long-term retention of ILs [59].

The anti-tumor efficiency was followed from bioluminescence imaging (BLI) signal intensity with IVIS. The first BLI was carried out before CED on day 5 post-implantation of tumor cells, where similar intensity levels were noted in all three groups (Figure 8A). On day 7, after the first laser treatment, reduction of the BLI signal intensity was noted in ILs + laser and free IR780 + laser groups, due to the concurrent PTT/PDT of brain tumor xenografts. Increased BLI signal intensity was noticed in the PBS + laser group at the same time point. On day 9 after the second laser treatment, the BLI intensities increased in the free IR-780 + laser group and the PBS + laser group, but no change in BLI intensity was observed from the ILs + laser group. A similar trend was observed on day 12 after the third laser treatment on day 11, although no significant difference in BLI intensity among groups could be observed (Figure 8B). Nonetheless, significance was shown on day 14 and 16 with the ILs + laser group showing a significantly lower normalized luminescence intensity than other groups, suggesting only ILs can inhibit the growth of glioma cells under repeated laser treatment *in vivo*. To confirm this hypothesis, that anti-cancer efficacy is associated with the photostability of free IR-780 *in vivo*, NIR fluorescence imaging of treated mice was carried out, where drastic changes of signal intensity were noted only for free IR-780, especially after day 12 (Figure 8C). From quantitative comparison of NIR imaging results, the *in vivo* fluorescence signal intensity decreased immediately after the laser treatment for both free IR-780 and ILs on day 7, with normalized fluorescence intensity (normalized to day 6) being less than 1 (Figure 8D). This trend could be also observed after the second and third laser treatment on day 9 and 11. Nonetheless, it is clear that ILs could substantially improve the degradation of IR-780 due to NIR laser irradiation, showing 52% normalized fluorescence intensity on day 12, in comparison with 13% for free IR-780. Taken together, we successfully proved our hypothesis, that liposomal IR-780 (ILs) can enhance photostability of IR-780 *in vivo*, for improved PTT/PDT of brain tumor, as revealed from the significant reduction of intracranial tumor size from normalized BLI intensity (Figure 8B).

From a safety perspective, the body weight of the mice was continuously monitored throughout the treatment period (Figure 8E). The body weight showed decreasing trends for all groups after day 6. Nonetheless, it is evident that mice in the ILs + laser group could better maintain their body weight than other groups to the end of the observation period, indicating fewer side effects from this treatment. To determine animal survival, we sacrificed the mouse when it lost more than 25% of the initial body weight or when it showed back hunk, hemiparesis or seizures. From the survival curve in Figure 8F, the median survival time of PBS + laser and free IR-780 + laser group was 16 days, while that for the ILs + laser group was 22 days. Furthermore, the survival time of the ILs + laser group ( $21.3 \pm 1.1$  days, mean  $\pm$  SD) significantly increased over that of the PBS + laser group ( $15.8 \pm 0.8$  days) and the free IR-780 + laser groups ( $15.8 \pm 0.3$  days), with no significant difference found between the latter two groups. The significantly prolonged survival times as well as the reduced tumor sizes (Figure 8B) endorse a highly efficient treatment modality of brain tumors by concurrent PTT/PDT via CED of ILs.

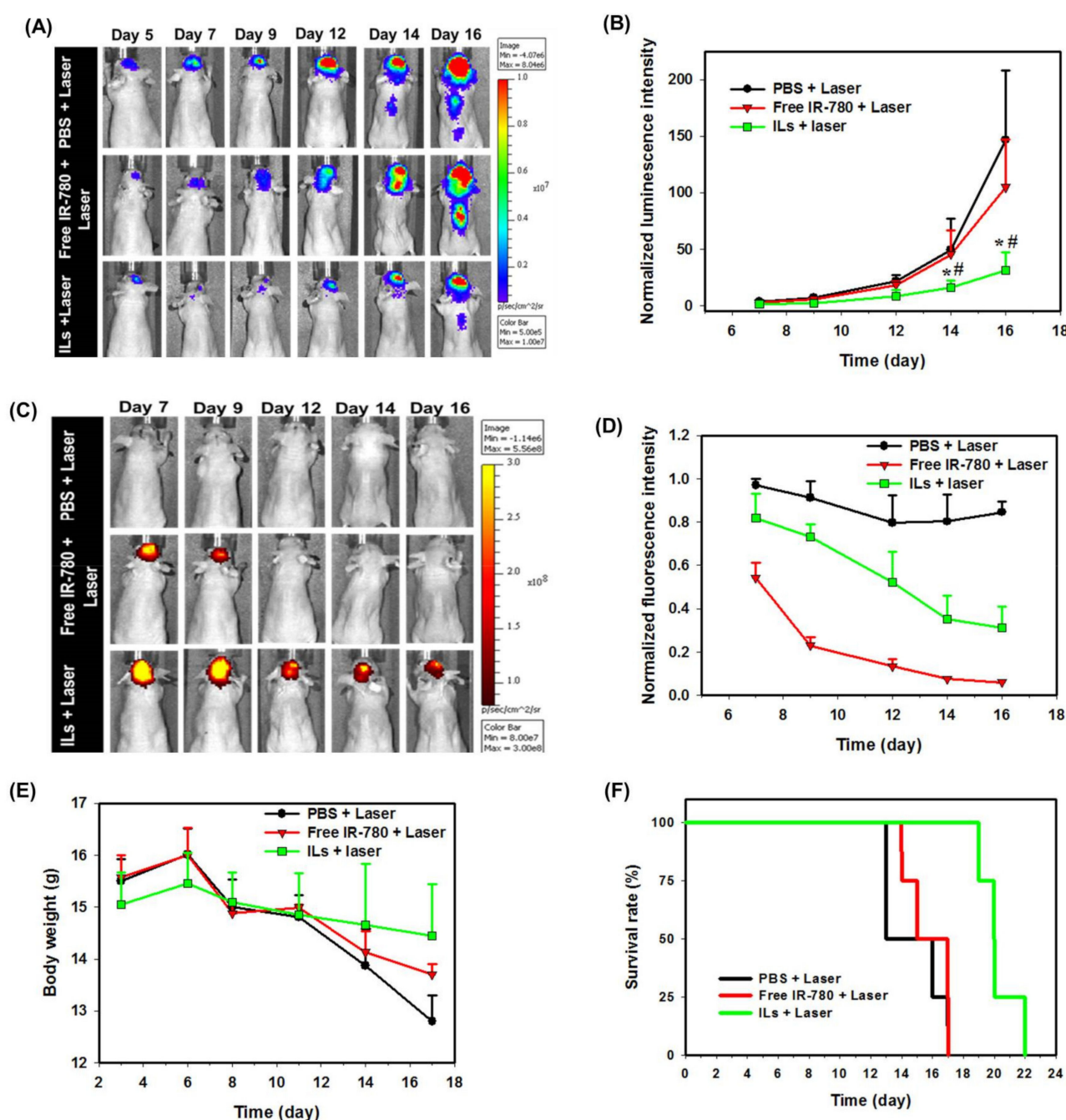


**Figure 8.** The representative images from bioluminescence imaging (BLI) (A) and the normalized bioluminescence intensity (normalized to day 5) (B) post-implantation of U87MG cells. The representative images from near infrared (NIR) fluorescence imaging (C) and the normalized fluorescence intensity (normalized to day 6) (D) post-implantation of U87MG cells. The change of body weight (E) and the animal survival rate (F) post-implantation of U87MG cells. \*  $p < 0.05$  compared with PBS + laser. #  $p < 0.05$  compared with free IR-780 + laser.

### 3.5. MRI and PET/CT Studies

As magnetic resonance (MR) imaging (MRI) is a paradigmatic method for diagnosis and identification of anatomical gliomas site [60], we used MRI at three different time points, i.e., on days 7, 13 and 16, for assessing the anti-tumor efficiency (Figure 9A). From ROI circled in yellow lines, no significant difference in tumor volume was found among all groups on day 7 (Figure 9B). However, differences in treatment efficacy were manifested on day 13 and 16 among all groups, with significantly reduced tumor volume shown from the ILs + laser group. The mean tumor volumes measured for the PBS + laser group were



49.5 mm<sup>3</sup> and 99 mm<sup>3</sup> on day 13 and 16, respectively. The free IR-780 + laser group showed some treatment benefits with 32.7 mm<sup>3</sup> and 90.6 mm<sup>3</sup> mean tumor volumes at the same time points. Most importantly, by retarding glioma growth to ~30% of the tumor size in the control, the ILs + laser treatment resulted in 14.8 mm<sup>3</sup> (day 13) and 34.6 mm<sup>3</sup> (day 16) mean tumor volume and provided the best anti-tumor outcomes, consistent with the prolonged survival time of glioma-bearing mice.

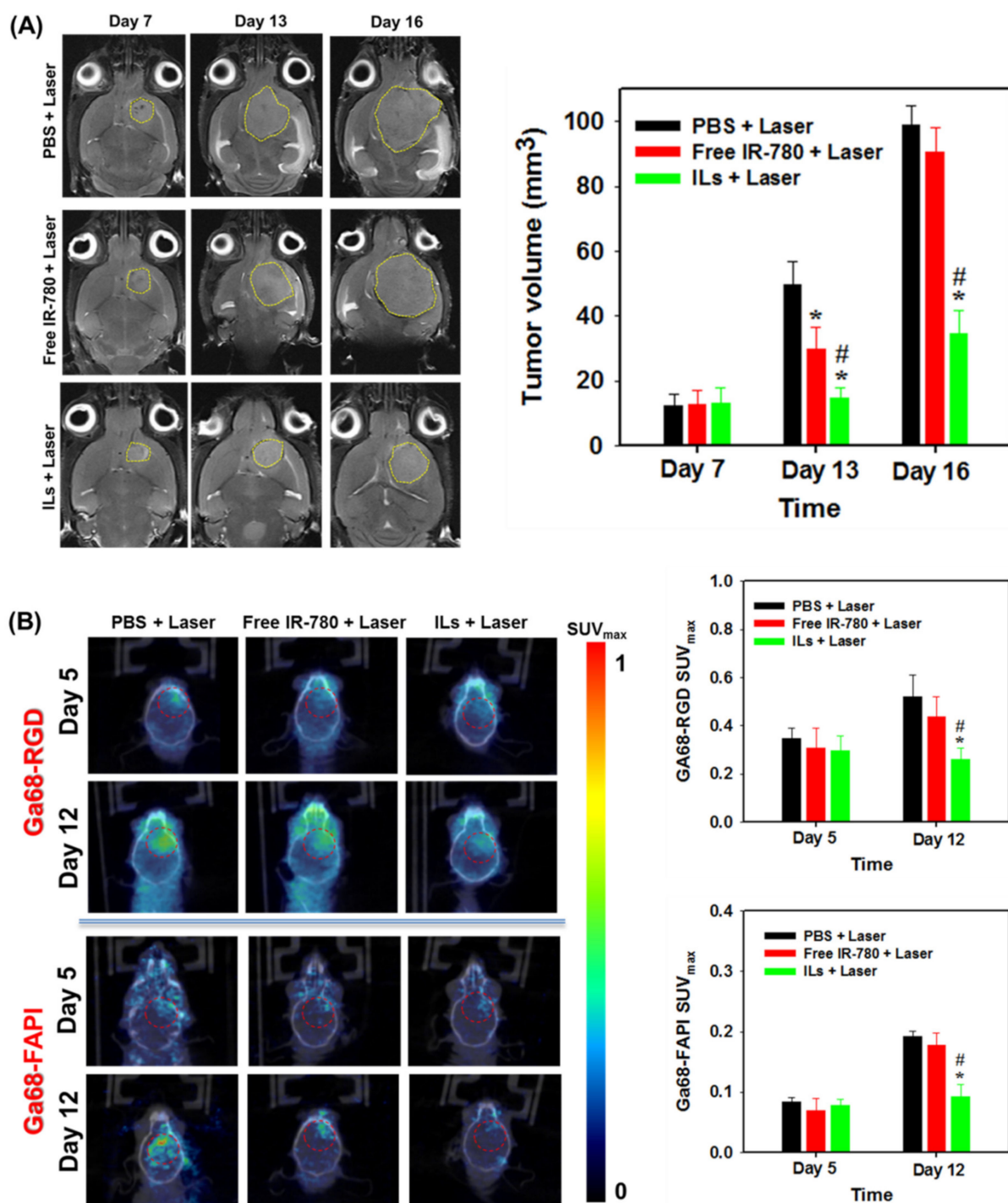


**Figure 9.** The representative coronal view images and the calculated tumor volumes from magnetic resonance imaging (MRI) (A), and Ga68-RGD and Ga68-FAPI positron emission tomography/computed tomography (PET/CT) (B) post-implantation of U87MG cells. \*  $p < 0.05$  compared with PBS + laser, #  $p < 0.05$  compared with free IR-780 + laser.

Angiogenesis is a naturally occurring physiological process that involves a complicated chemical process. This helps cancer cells for their growth and spread across various parts of the body or organ through chemical signals [61]. Angiogenesis is characterized by the expression of  $\alpha_v\beta_3$  integrin in neo-vessel endothelial cells that binds specifically to Arg–Gly–Asp (RGD) peptide [62]. The expression of  $\alpha_v\beta_3$  integrin is correlated with the malignancy of glioma, in conjunction with tumor-related angiogenic processes, to facilitate tumor progression [63]. Therefore, angiogenesis imaging with the help of radio-labelled RGD peptide may provide favorable results in locating tumors [64]. Among many radioisotopes, radionuclide  $^{68}\text{Ga}$  is a convenient option, as it is readily accessible and cost-effective. The  $^{68}\text{Ga}$ -based radiopharmaceuticals also display high spatial resolution compared to single-photon emission computed tomography, enabling more detailed quantification. In addition, with a 68 min half-life,  $^{68}\text{Ga}$  offers sufficient time for the preparation of small peptides or proteins [65]. The fibroblast activation protein (FAP) is overexpressed by many cancer-associated fibroblasts of several tumor entities, which are different from normal fibroblasts from the difference in their FAP specific expression. Therefore, targeting FAP with FAP-inhibitors (FAPI) is a new diagnostic approach allowing the visualization of tumor stroma, although they were first developed as anticancer drugs [66]. Radiolabeled FAPI ( $^{68}\text{Ga}$ -FAPI) has been used for PET/CT molecular imaging and diagnosis, demonstrating a favorable biodistribution and high uptake in xenograft tumors as well as in patients with various malignancies with activated stromal fibroblasts [67]. Moreover, the first PET studies in human with  $^{68}\text{Ga}$ -FAPI provided a high tumor-to-noise ratio imaging tool for identifying a broad range of tumors [68]. We therefore used PET/CT along with  $^{68}\text{Ga}$ -RGD or  $^{68}\text{Ga}$ -FAPI to study the treatment efficacy in the U87MG xenograft brain tumor model. As shown in Figure 9B, only the ILs + laser group showed a minimum change of signal intensity before treatment (day 5) and after treatment (day 12) from the coronal view PET/CT images. Most importantly, this group showed a significantly decreased maximum standardized uptake ( $\text{SUV}_{\text{max}}$ ) value obtained within the circled ROI for both  $^{68}\text{Ga}$ -labeled RGD and FAPI, confirming ILs + laser treatment provides improved PTT/PDT to delay tumor growth, as shown from MRI.

### 3.6. Histological Analysis

For histological analysis in Figure 10A, the brain tumor sections from H&E staining indicated that PBS + laser treatment does not develop detectable necrosis. Some necrosis areas were noted in the free IR-780 + laser group. In contrast, large areas of necrosis could be observed after ILs + laser treatment, as revealed from the excellent anti-tumor efficiency from BLI (Figure 8B). Follow-up image analysis using PAX-it software also showed significantly reduced cell nucleus area percentage within the ROI after ILs + laser treatment (Figure 10B). The IHC staining of cell proliferation marker (Ki-67) supports the H&E staining results. The area percentage of immunoreactive Ki-67 marker within ROI drastically reduced after ILs + laser treatment, to be ~26% (~22%) that of free IR-780 + laser (PBS + laser) treatment, indicating pronounced inhibition of growth of U87MG glioma cells (Figure 10B). Furthermore, a reverse trend of the immunoreactivity of the cell apoptotic marker, cleaved caspase-3 (CC-3), confirms that improved PTT/PDT could induce more cell apoptosis in the ILs + laser group. Indeed, the ILs + laser group showed 3.7-fold and 2.4-fold higher positively stained areas of CC3 compared to PBS + laser and free IR-780 + laser groups, due to the high cell apoptosis rate (Figure 10B).

To evaluate safety of the treatments, we conducted histology of major organs and blood analysis of sacrificed mice. We did not observe any apparent changes of the H&E staining results of major organs (Figure S7), revealing that IL delivery via CED as well as laser irradiation can avoid organ damage. From the results of hematological or biochemistry analysis of blood samples, we did not notice significant differences of all analyzed biochemical and hematological parameters in mice subject to ILs + laser treatment compared to PBS + laser as well as free IR-780 + laser groups, indicating no acute toxicity from the treatment (Table S1).

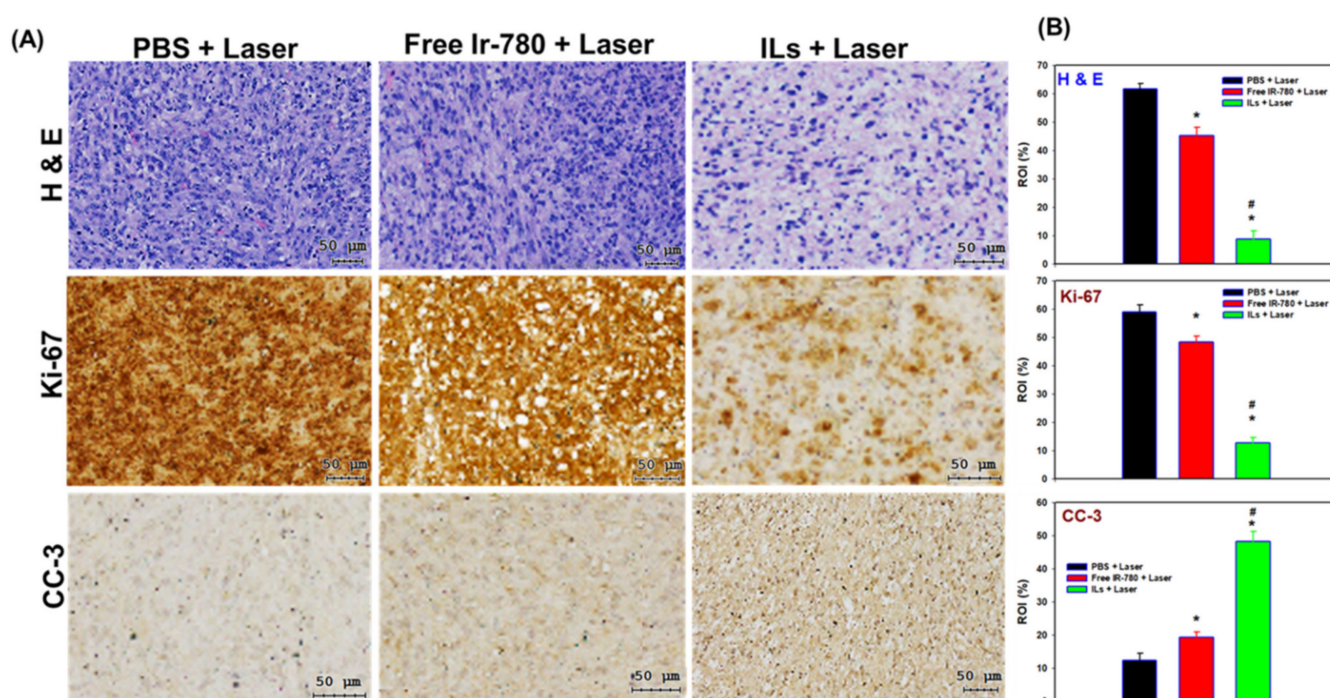


**Figure 10.** (A) The representative H&E staining, Ki-67 and cleaved caspase-3 (CC-3) immunohistochemical (IHC) staining images of paraffin-embedded tumor sections. (B) The corresponding positively stained area percentage within region of interest (ROI) (%) ( $n = 3$ ). \*  $p < 0.05$  compared with PBS + laser. #  $p < 0.05$  compared with free IR-780 + laser.

#### 4. Conclusions

By entrapping IR-780 within the lipid bilayer of cationic liposomes to maintain its photostability during successive NIR laser irradiation, we successfully prepared ILs in this study and demonstrated its improved PTT/PDT of intracranial glioma after CED. The application of ILs for PTT/PDT in vitro could be confirmed from real-time temperature change and ROS generation in vitro under NIR laser irradiation, which leads to cytotoxicity and apoptosis/necrosis of U87MG glioma cells. Compared to free IR-780, the intracellular uptake of ILs was substantially enhanced, and the IR-780 in ILs displayed enhanced photostability in vitro and in vivo after repeated laser irradiation for extending the PTT/PDT therapeutic efficacy. Using xenograft U87MG glioblastoma tumor models in mice brain, we demonstrate long-time retention of ILs in the brain tumor after CED, which facilitates PTT/PDT of intracranial glioma in vivo. Compared to free IR-780, ILs offers significant improvement of laser-assisted PTT/PDT in glioma treatment, judging from analysis with diagnostic imaging tools (BLI, MRI and PET/CT), as well as upregulation of apoptosis marker CC3 and downregulation of proliferation marker Ki-67 in tumor sections. Overall, the combination of CED of ILs with consecutive NIR laser treatment could provide an alternative approach for treating solid tumor in the brain.

**Supplementary Materials:** The following are available online at <https://www.mdpi.com/article/10.3390/cancers13153690/s1>, Figure S1: The timeline for establishing intracranial xenograft tumor model, convention-enhanced delivery (CED) and assessment of anti-tumor efficacy by bioluminescence imaging (BLI), magnetic resonance imaging (MRI), as well as positron emission tomography/computed tomography (PET/CT), Figure S2: The pictures showing the administration of samples into mouse brain via convention-enhanced delivery (CED), Figure S3: The ROS generation with DPBF probe due to NIR irradiation ( $1 \text{ W/cm}^2$ ) of free IR-780 (A) and ILs (B) solution for 120 s. (C) The change of relative absorbance ( $A/A_0$ ) at 410 nm of free IR-780, ILs and PBS (control), Figure S4: The expression of heat shock protein 70 (HSP70) by U87MG cells from Western blot analysis by treating with PBS (control), IR-780 or ILs with or without NIR laser irradiation, Figure S5: The ex vivo NIR fluorescence imaging of explanted brain and major organs from tumor-bearing mice after



CED of ILs or PBS (control) at different times post-implantation of U87MG cells. The fluorescence signal intensity within the ROI of the explanted brain is shown below the images, Figure S6: The representative real-time temperature distribution and the time-lapsed peak temperature profiles (mean  $\pm$  SD,  $n = 4$ ) of tumor-bearing nude mice. One, three and five days after convection-enhanced delivery (CED) of PBS, free IR-780 or ILs to tumor-bearing mice, the brain was irradiated with NIR laser ( $1 \text{ W/cm}^2$ ) for 5 min, and thermal images were captured with an infrared camera during the 1st (A), 2nd (B) and 3rd (C) laser treatment, Figure S7: The H&E staining results of tissue sections from major organs of tumor-bearing mice after different treatments. Bar = 100  $\mu\text{m}$ , Table S1: The hematological parameters and biochemistry analysis from treated mice.

**Author Contributions:** Conceptualization, Y.-J.L. and J.-P.C.; methodology, Y.-J.L., A.T.S. and J.-P.C.; formal analysis, Y.-J.L., A.T.S. and J.-P.C.; investigation, A.T.S.; resources, C.-C.C. and J.-P.C.; data curation, A.T.S. and Y.-J.L.; writing—original draft preparation, A.T.S.; writing—review and editing, J.-P.C.; supervision, C.-C.C. and J.-P.C.; project administration, Y.-J.L. and J.-P.C.; funding acquisition, Y.-J.L. and J.-P.C. All authors have read and agreed to the published version of the manuscript.

**Funding:** This research was funded by the Ministry of Science and Technology of Taiwan (ROC) (MOST106-2221-E-182-056-MY3) and Chang Gung Memorial Hospital (CMRPD2I0041, CMRPD2I0042 and CORPG3K0081) for financial support. The APC was funded by Chang Gung Memorial Hospital and Chang Gung University.

**Institutional Review Board Statement:** The study was conducted according to the guidelines of the Declaration of Helsinki and approved by the Institutional Animal Care and Use Committee of Chang Gung University (IACUC Approval No.: CGU105-034, date of approval: 25 April 2017).

**Informed Consent Statement:** Not applicable (no human subjects involved).

**Data Availability Statement:** The data presented in this study are available on request from the corresponding author.

**Acknowledgments:** The Microscope Core Laboratory and the Center for Advanced Molecular Imaging and Translation at Chang Gung Memorial Hospital, Linkou are acknowledged for providing IVIS, MRI and PET/CT analysis.

**Conflicts of Interest:** The authors declare no conflict of interest.

## References

1. Hsiao, C.W.; Chuang, E.Y.; Chen, H.L.; Wan, D.; Korupalli, C.; Liao, Z.X.; Chiu, Y.L.; Chia, W.T.; Lin, K.J.; Sung, H.W. Photothermal tumor ablation in mice with repeated therapy sessions using NIR-absorbing mi-cellar hydrogels formed in situ. *Biomaterials* **2015**, *56*, 26–35. [[CrossRef](#)] [[PubMed](#)]
2. Chen, W.R.; Adams, R.L.; Heaton, S.; Dickey, D.; Bartels, K.E.; Nordquist, R.E. Chromophore-enhanced laser-tumor tissue photothermal interaction using an 808-nm diode laser. *Cancer Lett.* **1995**, *88*, 15–19. [[CrossRef](#)]
3. Chitgupi, U.; Qin, Y.; Lovell, J.F. Targeted Nanomaterials for Phototherapy. *Nanotheranostics* **2017**, *1*, 38–58. [[CrossRef](#)]
4. Doughty, A.C.; Hoover, A.R.; Layton, E.; Murray, C.K.; Howard, E.W.; Chen, W.R. Nanomaterial Applications in Photothermal Therapy for Cancer. *Materials* **2019**, *12*, 779. [[CrossRef](#)]
5. Grosjes, T.; Barchiesi, D. Gold Nanoparticles as a Photothermal Agent in Cancer Therapy: The Thermal Ablation Characteristic Length. *Molecules* **2018**, *23*, 1316. [[CrossRef](#)] [[PubMed](#)]
6. Anilkumar, T.; Lu, Y.-J.; Chen, H.-A.; Hsu, H.-L.; Jose, G.; Chen, J.-P. Dual targeted magnetic photosensitive liposomes for photothermal/photodynamic tumor therapy. *J. Magn. Magn. Mater.* **2019**, *473*, 241–252. [[CrossRef](#)]
7. Zou, L.; Wang, H.; He, B.; Zeng, L.; Tan, T.; Cao, H.; He, X.; Zhang, Z.; Guo, S.; Li, Y. Current Approaches of Photothermal Therapy in Treating Cancer Metastasis with Nanotherapeutics. *Theranostics* **2016**, *6*, 762–772. [[CrossRef](#)]
8. Agostinis, P.; Berg, K.; Cengel, K.A.; Foster, T.H.; Girotti, A.W.; Gollnick, S.O.; Hahn, S.M.; Hamblin, M.R.; Juzeniene, A.; Kessel, D.; et al. Photodynamic therapy of cancer: An update. *CA A Cancer J. Clin.* **2011**, *61*, 250–281. [[CrossRef](#)]
9. Kuang, Y.; Zhang, K.; Cao, Y.; Chen, X.; Wang, K.; Liu, M.; Pei, R. Hydrophobic IR-780 Dye Encapsulated in cRGD-Conjugated Solid Lipid Nanoparticles for NIR Imaging-Guided Photothermal Therapy. *ACS Appl. Mater. Interfaces* **2017**, *9*, 12217–12226. [[CrossRef](#)]
10. Yang, Z.; Wang, J.; Ai, S.; Sun, J.; Mai, X.; Guan, W. Self-generating oxygen enhanced mitochondrion-targeted photodynamic therapy for tumor treatment with hypoxia scavenging. *Theranostics* **2019**, *9*, 6809–6823. [[CrossRef](#)]
11. Li, Y.; Zhou, Y.; Yue, X.; Dai, Z. Cyanine conjugates in cancer theranostics. *Bioact. Mater.* **2021**, *6*, 794–809. [[CrossRef](#)]
12. Li, S.; Zhou, S.; Li, Y.; Li, X.; Zhu, J.; Fan, L.; Yang, S. Exceptionally High Payload of the IR780 Iodide on Folic Acid-Functionalized Graphene Quantum Dots for Targeted Photothermal Therapy. *ACS Appl. Mater. Interfaces* **2017**, *9*, 22332–22341. [[CrossRef](#)] [[PubMed](#)]



13. Wang, K.; Zhang, Y.; Wang, J.; Yuan, A.; Sun, M.; Wu, J.; Hu, Y. Self-assembled IR780-loaded transferrin nanoparticles as an imaging, targeting and PDT/PTT agent for cancer therapy. *Sci. Rep.* **2016**, *6*, 27421. [\[CrossRef\]](#) [\[PubMed\]](#)
14. Zhang, L.; Wang, D.; Yang, K.; Sheng, D.; Tan, B.; Wang, Z.; Ran, H.; Yi, H.; Zhong, Y.; Lin, H.; et al. Mitochondria-Targeted Artificial “Nano-RBCs” for Amplified Synergistic Cancer Phototherapy by a Single NIR Irradiation. *Adv. Sci.* **2018**, *5*, 1800049. [\[CrossRef\]](#)
15. Ren, H.; Liu, J.; Su, F.; Ge, S.; Yuan, A.; Dai, W.; Wu, J.; Hu, Y. Relighting Photosensitizers by Synergistic Integration of Albumin and Perfluorocarbon for Enhanced Photodynamic Therapy. *ACS Appl. Mater. Interfaces* **2017**, *9*, 3463–3473. [\[CrossRef\]](#)
16. Stine, C.A.; Munson, J.M. Convection-Enhanced Delivery: Connection to and Impact of Interstitial Fluid Flow. *Front. Oncol.* **2019**, *9*, 966. [\[CrossRef\]](#)
17. Bobo, R.H.; Laske, D.W.; Akbasak, A.; Morrison, P.F.; Dedrick, R.L.; Oldfield, E.H. Convection-enhanced delivery of macromolecules in the brain. *Proc. Natl. Acad. Sci. USA* **1994**, *91*, 2076–2080. [\[CrossRef\]](#)
18. Lesniak, M.S.; Brem, H. Targeted therapy for brain tumours. *Nat. Rev. Drug Discov.* **2004**, *3*, 499–508. [\[CrossRef\]](#)
19. Lonser, R.R.; Sarntinoranont, M.; Morrison, P.F.; Oldfield, E.H. Convection-enhanced delivery to the central nervous system. *J. Neurosurg.* **2015**, *122*, 697–706. [\[CrossRef\]](#)
20. Souweidane, M.M.; Kramer, K.; Pandit-Taskar, N.; Zhou, Z.; Haque, S.; Zanzonico, P.; Carrasquillo, J.; Lyashchenko, S.K.; Thakur, S.; Donzelli, M.; et al. Convection-enhanced delivery for diffuse intrinsic pontine glioma: A single-centre, dose-escalation, phase 1 trial. *Lancet Oncol.* **2018**, *19*, 1040–1050. [\[CrossRef\]](#)
21. Pang, H.-H.; Chen, P.-Y.; Wei, K.-C.; Huang, C.-W.; Shiue, Y.-L.; Huang, C.-Y.; Yang, H.-W. Convection-Enhanced Delivery of a Virus-Like Nanotherapeutic Agent with Dual-Modal Imaging for Besiegement and Eradication of Brain Tumors. *Theranostics* **2019**, *9*, 1752–1763. [\[CrossRef\]](#)
22. Yan, F.; Duan, W.; Li, Y.; Wu, H.; Zhou, Y.; Pan, M.; Liu, H.; Liu, X.; Zheng, H. NIR-Laser-Controlled Drug Release from DOX/IR-780-Loaded Temperature-Sensitive-Liposomes for Chemo-Photothermal Synergistic Tumor Therapy. *Theranostics* **2016**, *6*, 2337–2351. [\[CrossRef\]](#)
23. Yang, X.; Li, H.; Qian, C.; Guo, Y.; Li, C.; Gao, F.; Yang, Y.; Wang, K.; Oupicky, D.; Sun, M. Near-infrared light-activated IR780-loaded liposomes for anti-tumor angiogenesis and Photothermal therapy. *Nanomed. Nanotechnol. Biol. Med.* **2018**, *14*, 2283–2294. [\[CrossRef\]](#)
24. You, Q.; Sun, Q.; Wang, J.; Tan, X.; Pang, X.; Liu, L.; Yu, M.; Tan, F.; Li, N. A single-light triggered and dual-imaging guided multifunctional platform for combined photothermal and photodynamic therapy based on TD-controlled and ICG-loaded CuS@mSiO<sub>2</sub>. *Nanoscale* **2016**, *9*, 3784–3796. [\[CrossRef\]](#)
25. Deng, K.; Chen, Y.; Li, C.; Deng, X.; Hou, Z.; Cheng, Z.; Han, Y.; Xing, B.; Lin, J. 808 nm light responsive nanotheranostic agents based on near-infrared dye functionalized manganese ferrite for magnetic-targeted and imaging-guided photodynamic/photothermal therapy. *J. Mater. Chem. B* **2017**, *5*, 1803–1814. [\[CrossRef\]](#)
26. Wang, N.; Zhou, Y.; Xu, Y.; Ren, X.; Zhou, S.; Shang, Q.; Jiang, Y.; Luan, Y. Molecular engineering of anti-PD-L1 peptide and photosensitizer for immune checkpoint blockade photodynamic-immunotherapy. *Chem. Eng. J.* **2020**, *400*, 125995. [\[CrossRef\]](#)
27. Tan, Y.; Zhu, Y.; Wen, L.; Yang, X.; Liu, X.; Meng, T.; Dai, S.; Ping, Y.; Yuan, H.; Hu, F. Mitochondria-Responsive Drug Release along with Heat Shock Mediated by Multifunctional Glycolipid Micelles for Precise Cancer Chemo-Phototherapy. *Theranostics* **2019**, *9*, 691–707. [\[CrossRef\]](#)
28. Rajendrakumar, S.K.; Chang, N.-C.; Mohapatra, A.; Uthaman, S.; Lee, B.-I.; Tsai, W.-B.; Park, I.-K. A Lipophilic IR-780 Dye-Encapsulated Zwitterionic Polymer-Lipid Micellar Nanoparticle for Enhanced Photothermal Therapy and NIR-Based Fluorescence Imaging in a Cervical Tumor Mouse Model. *Int. J. Mol. Sci.* **2018**, *19*, 1189. [\[CrossRef\]](#) [\[PubMed\]](#)
29. Anilkumar, T.S.; Lu, Y.-J.; Chen, J.-P. Optimization of the Preparation of Magnetic Liposomes for the Combined Use of Magnetic Hyperthermia and Photothermia in Dual Magneto-Photothermal Cancer Therapy. *Int. J. Mol. Sci.* **2020**, *21*, 5187. [\[CrossRef\]](#) [\[PubMed\]](#)
30. Jose, G.; Lu, Y.-J.; Hung, J.-T.; Yu, A.; Chen, J.-P. Co-Delivery of CPT-11 and Panobinostat with Anti-GD2 Antibody Conjugated Immunoliposomes for Targeted Combination Chemotherapy. *Cancers* **2020**, *12*, 3211. [\[CrossRef\]](#)
31. Kim, H.J.; Kim, W. Method of tumor volume evaluation using magnetic resonance imaging for outcome prediction in cervical cancer treated with concurrent chemotherapy and radiotherapy. *Radiat. Oncol. J.* **2012**, *30*, 70–77. [\[CrossRef\]](#) [\[PubMed\]](#)
32. Briuglia, M.-L.; Rotella, C.M.; McFarlane, A.; Lamprou, D.A. Influence of cholesterol on liposome stability and on in vitro drug release. *Drug Deliv. Transl. Res.* **2015**, *5*, 231–242. [\[CrossRef\]](#) [\[PubMed\]](#)
33. Shi, M.; Anantha, M.; Wehbe, M.; Bally, M.B.; Fortin, D.; Roy, L.-O.; Charest, G.; Richer, M.; Paquette, B.; Sanche, L. Liposomal formulations of carboplatin injected by convection-enhanced delivery increases the median survival time of F98 glioma bearing rats. *J. Nanobiotechnol.* **2018**, *16*, 1–12. [\[CrossRef\]](#)
34. Jiang, C.; Cheng, H.; Yuan, A.; Tang, X.; Wu, J.; Hu, Y. Hydrophobic IR780 encapsulated in biodegradable human serum albumin nanoparticles for photothermal and photodynamic therapy. *Acta Biomater.* **2015**, *14*, 61–69. [\[CrossRef\]](#) [\[PubMed\]](#)
35. Appidi, T.; Pemmaraju, D.B.; Khan, R.A.; Alvi, S.B.; Srivastava, R.; Pal, M.; Khan, N.; Rengan, A.K. Light-triggered selective ROS-dependent autophagy by bioactive nanoliposomes for efficient cancer theranostics. *Nanoscale* **2019**, *12*, 2028–2039. [\[CrossRef\]](#) [\[PubMed\]](#)

36. Peng, C.-L.; Shih, Y.-H.; Lee, P.-C.; Hsieh, T.M.-H.; Luo, T.-Y.; Shieh, M.-J. Multimodal Image-Guided Photothermal Therapy Mediated by 188Re-Labeled Micelles Containing a Cyanine-Type Photosensitizer. *ACS Nano* **2011**, *5*, 5594–5607. [[CrossRef](#)] [[PubMed](#)]
37. Song, J.; Zhang, N.; Zhang, L.; Yi, H.; Liu, Y.; Li, Y.; Li, X.; Wu, M.; Hao, L.; Yang, Z.; et al. IR780-loaded folate-targeted nanoparticles for near-infrared fluorescence image-guided surgery and photothermal therapy in ovarian cancer. *Int. J. Nanomed.* **2019**, *14*, 2757–2772. [[CrossRef](#)]
38. Lonser, R.R.; Walbridge, S.; Garmestani, K.; Butman, J.; Walters, H.A.; Vortmeyer, A.O.; Morrison, P.F.; Brechbiel, M.W.; Oldfield, E.H. Successful and safe perfusion of the primate brainstem: In vivo magnetic resonance imaging of macromolecular distribution during infusion. *J. Neurosurg.* **2002**, *97*, 905–913. [[CrossRef](#)]
39. Yuan, A.; Qiu, X.; Tang, X.; Liu, W.; Wu, J.; Hu, Y. Self-assembled PEG-IR-780-C13 micelle as a targeting, safe and highly-effective photothermal agent for in vivo imaging and cancer therapy. *Biomaterials* **2015**, *51*, 184–193. [[CrossRef](#)]
40. Lovell, J.; Liu, T.; Chen, J.; Zheng, G. Activatable Photosensitizers for Imaging and Therapy. *Chem. Rev.* **2010**, *110*, 2839–2857. [[CrossRef](#)]
41. DeRosa, M.C. Photosensitized singlet oxygen and its applications. *Co-ord. Chem. Rev.* **2002**, *233–234*, 351–371. [[CrossRef](#)]
42. Dąbrowski, J.M.; Arnaut, L.G. Photodynamic therapy (PDT) of cancer: From local to systemic treatment. *Photochem. Photobiol. Sci.* **2015**, *14*, 1765–1780. [[CrossRef](#)]
43. Howard, J.A.; Mendenhall, G.D. Autoxidation and Photooxidation of 1,3-Diphenylisobenzofuran: A Kinetic and Product Study. *Can. J. Chem.* **1975**, *53*, 2199–2201. [[CrossRef](#)]
44. Chadwick, S.J.; Salah, D.; Livesey, P.M.; Brust, M.; Volk, M. Singlet Oxygen Generation by Laser Irradiation of Gold Nanoparticles. *J. Phys. Chem. C* **2016**, *120*, 10647–10657. [[CrossRef](#)]
45. Zhang, X.-F.; Li, X. The photostability and fluorescence properties of diphenylisobenzofuran. *J. Lumin.* **2011**, *131*, 2263–2266. [[CrossRef](#)]
46. Li, S.; Johnson, J.; Peck, A.; Xie, Q. Near infrared fluorescent imaging of brain tumor with IR780 dye incorporated phospholipid nanoparticles. *J. Transl. Med.* **2017**, *15*, 1–12. [[CrossRef](#)]
47. Rayamajhi, S.; Marchitto, J.; Nguyen, T.D.T.; Marasini, R.; Celia, C.; Aryal, S. pH-responsive cationic liposome for endosomal escape mediated drug delivery. *Coll. Surf. B Biointerfaces* **2020**, *188*, 110804. [[CrossRef](#)]
48. Han, Y.; Park, J.-H. Convection-enhanced delivery of liposomal drugs for effective treatment of glioblastoma multiforme. *Drug Deliv. Transl. Res.* **2020**. [[CrossRef](#)] [[PubMed](#)]
49. Murphy, M.E. The HSP70 family and cancer. *Carcinogenesis* **2013**, *34*, 1181–1188. [[CrossRef](#)] [[PubMed](#)]
50. Ciocca, D.R.; Calderwood, S.K. Heat shock proteins in cancer: Diagnostic, prognostic, predictive, and treatment implications. *Cell Stress Chaperon* **2005**, *10*, 86–103. [[CrossRef](#)] [[PubMed](#)]
51. Wang, H.; Gao, Z.; Liu, X.; Agarwal, P.; Zhao, S.; Conroy, D.W.; Ji, G.; Yu, J.; Jaronec, C.P.; Liu, Z.; et al. Targeted production of reactive oxygen species in mitochondria to overcome cancer drug resistance. *Nat. Commun.* **2018**, *9*, 562. [[CrossRef](#)]
52. Dash, B.; Das, S.; Chen, J.-P. Photosensitizer-Functionalized Nanocomposites for Light-Activated Cancer Theranostics. *Int. J. Mol. Sci.* **2021**, *22*, 6658. [[CrossRef](#)]
53. Pais-Silva, C.; Diogo, D.M.D.M.; Correia, I.J. IR780-loaded TPGS-TOS micelles for breast cancer photodynamic therapy. *Eur. J. Pharm. Biopharm.* **2017**, *113*, 108–117. [[CrossRef](#)]
54. Cheng, Y.; Jiang, C.; Qiu, X.; Wang, K.; Huan, W.; Yuan, A.; Wu, J.; Hu, Y. Perfluorocarbon nanoparticles enhance reactive oxygen levels and tumour growth inhibition in photodynamic therapy. *Nat. Commun.* **2015**, *6*, 8785. [[CrossRef](#)] [[PubMed](#)]
55. Xu, Z.P.; Zeng, Q.; Lu, G.; Yu, A. Inorganic nanoparticles as carriers for efficient cellular delivery. *Chem. Eng. Sci.* **2006**, *61*, 1027–1040. [[CrossRef](#)]
56. Chen, P.-Y.; Ozawa, T.; Drummond, D.C.; Kalra, A.; Fitzgerald, J.B.; Kirpotin, D.B.; Wei, K.-C.; Butowski, N.; Prados, M.D.; Berger, M.S.; et al. Comparing routes of delivery for nanoliposomal irinotecan shows superior anti-tumor activity of local administration in treating intracranial glioblastoma xenografts. *Neuro-Oncology* **2012**, *15*, 189–197. [[CrossRef](#)] [[PubMed](#)]
57. Jahangiri, A.; Chin, A.; Flanagan, P.; Chen, R.; Bankiewicz, K.; Aghi, M.K. Convection-enhanced delivery in glioblastoma: A review of preclinical and clinical studies. *J. Neurosurg.* **2017**, *126*, 191–200. [[CrossRef](#)]
58. Salem, U.; Kumar, V.A.; Madewell, J.E.; Schomer, D.F.; Bastos, D.C.D.A.; Zinn, P.O.; Weinberg, J.S.; Rao, G.; Prabhu, S.S.; Colen, R.R. Neurosurgical applications of MRI guided laser interstitial thermal therapy (LITT). *Cancer Imaging* **2019**, *19*, 1–13. [[CrossRef](#)] [[PubMed](#)]
59. Krauze, M.T.; Noble, C.O.; Kawaguchi, T.; Drummond, D.; Kirpotin, D.B.; Yamashita, Y.; Kullberg, E.; Forsayeth, J.; Park, J.W.; Bankiewicz, K.S. Convection-enhanced delivery of nanoliposomal CPT-11 (irinotecan) and PEGylated liposomal doxorubicin (Doxil) in rodent intracranial brain tumor xenografts. *Neuro-Oncology* **2007**, *9*, 393–403. [[CrossRef](#)]
60. Lu, Y.-J.; Chuang, E.-Y.; Cheng, Y.-H.; Anilkumar, T.; Chen, H.-A.; Chen, J.-P. Thermosensitive magnetic liposomes for alternating magnetic field-inducible drug delivery in dual targeted brain tumor chemotherapy. *Chem. Eng. J.* **2019**, *373*, 720–733. [[CrossRef](#)]
61. Nishida, N.; Yano, H.; Nishida, T.; Kamura, T.; Kojiro, M. Angiogenesis in cancer. *Vasc. Heal. Risk Manag.* **2006**, *2*, 213–219. [[CrossRef](#)] [[PubMed](#)]
62. Eo, J.S.; Jeong, J.M. Angiogenesis Imaging Using 68Ga-RGD PET/CT: Therapeutic Implications. *Semin. Nucl. Med.* **2016**, *46*, 419–427. [[CrossRef](#)] [[PubMed](#)]

63. Provost, C.; Rozenblum-Beddok, L.; Nataf, V.; Merabtene, F.; Prignon, A.; Talbot, J.-N. [68Ga]RGD Versus [18F]FDG PET Imaging in Monitoring Treatment Response of a Mouse Model of Human Glioblastoma Tumor with Bevacizumab and/or Temozolomide. *Mol. Imaging Biol.* **2018**, *21*, 297–305. [[CrossRef](#)] [[PubMed](#)]
64. Isal, S.; Pierson, J.; Imbert, L.; Clement, A.; Collet, C.; Pinel, S.; Veran, N.; Reinhard, A.; Poussier, S.; Gauchotte, G.; et al. PET imaging of 68Ga-NODAGA-RGD, as compared with 18F-fluorodeoxyglucose, in experimental rodent models of engrafted glioblastoma. *EJNMMI Res.* **2018**, *8*, 51. [[CrossRef](#)]
65. Jung, K.-H.; Lee, Y.J.; Kim, J.Y.; Lee, K.C.; Park, J.-A.; Choi, J.Y. Preparing a 68Ga-labeled Arginine Glycine Aspartate (RGD)-peptide for Angiogenesis. *J. Vis. Exp.* **2019**, e58218. [[CrossRef](#)]
66. Giesel, F.L.; Kratochwil, C.; Lindner, T.; Marschalek, M.M.; Loktev, A.; Lehnert, W.; Debus, J.; Jäger, D.; Flechsig, P.; Altmann, A.; et al. 68Ga-FAPI PET/CT: Biodistribution and Preliminary Dosimetry Estimate of 2 DOTA-Containing FAP-Targeting Agents in Patients with Various Cancers. *J. Nucl. Med.* **2018**, *60*, 386–392. [[CrossRef](#)]
67. Varasteh, Z.; Mohanta, S.; Robu, S.; Braeuer, M.; Li, Y.; Omidvari, N.; Topping, G.; Sun, T.; Nekolla, S.G.; Richter, A.; et al. Molecular Imaging of Fibroblast Activity After Myocardial Infarction Using a 68Ga-Labeled Fibroblast Activation Protein Inhibitor, FAPI-04. *J. Nucl. Med.* **2019**, *60*, 1743–1749. [[CrossRef](#)]
68. Kratochwil, C.; Flechsig, P.; Lindner, T.; Abderrahim, L.; Altmann, A.; Mier, W.; Adeberg, S.; Rathke, H.; Röhrich, M.; Winter, H.; et al. 68Ga-FAPI PET/CT: Tracer Uptake in 28 Different Kinds of Cancer. *J. Nucl. Med.* **2019**, *60*, 801–805. [[CrossRef](#)] [[PubMed](#)]



# Higher Leptin-to-Adiponectin Ratio Strengthens the Association Between Body Measurements and Occurrence of Type 2 Diabetes Mellitus

Pei-Ju Liao<sup>1</sup>, Ming-Kuo Ting<sup>2</sup>, I-Wen Wu<sup>3</sup>, Shuo-Wei Chen<sup>4</sup>, Ning-I Yang<sup>5</sup> and Kuang-Hung Hsu<sup>6,7,8,9,10,11\*</sup>

<sup>1</sup> Master Degree Program in Healthcare Industry, Chang Gung University, Taoyuan, Taiwan, <sup>2</sup> Division of Endocrinology and Metabolism, Chang Gung Memorial Hospital, Keelung, Taiwan, <sup>3</sup> Division of Nephrology, Chang Gung Memorial Hospital, Keelung, Taiwan, <sup>4</sup> Division of Gastroenterology and Hepatology, Chang Gung Memorial Hospital, Keelung, Taiwan, <sup>5</sup> Division of Cardiology, Chang Gung Memorial Hospital, Keelung, Taiwan, <sup>6</sup> Healthy Aging Research Center, Chang Gung University, Taoyuan, Taiwan, <sup>7</sup> Laboratory for Epidemiology, Department of Healthcare Management, Chang Gung University, Taoyuan, Taiwan, <sup>8</sup> Department of Emergency Medicine, Chang Gung Memorial Hospital, Taoyuan, Taiwan, <sup>9</sup> Department of Urology, Chang Gung Memorial Hospital, Taoyuan, Taiwan, <sup>10</sup> Research Center for Food and Cosmetic Safety, College of Human Ecology, Chang Gung University of Science and Technology, Taoyuan, Taiwan, <sup>11</sup> Department of Safety, Health, and Environmental Engineering, Ming Chi University of Technology, Taipei, Taiwan

## OPEN ACCESS

### Edited by:

Chih-Yuan Wang,  
National Taiwan University Hospital,  
Taiwan

### Reviewed by:

Chien-Ning Huang,  
Chung Shan Medical  
University, Taiwan  
Ham-Shen Chen,  
Taipei Veterans General  
Hospital, Taiwan

### \*Correspondence:

Kuang-Hung Hsu  
khsu@mail.cgu.edu.tw

### Specialty section:

This article was submitted to  
Clinical Diabetes,  
a section of the journal  
Frontiers in Public Health

**Received:** 10 March 2021

**Accepted:** 23 June 2021

**Published:** 23 July 2021

### Citation:

Liao P-J, Ting M-K, Wu I-W,  
Chen S-W, Yang N-I and Hsu K-H  
(2021) Higher Leptin-to-Adiponectin  
Ratio Strengthens the Association  
Between Body Measurements and  
Occurrence of Type 2 Diabetes  
Mellitus.  
Front. Public Health 9:678681.  
doi: 10.3389/fpubh.2021.678681

**Aim:** This case-control study aimed to investigate the interrelations of body measurements and selected biomarkers in type 2 diabetes mellitus (T2DM).

**Methods:** We recruited 98 patients with T2DM and 98 controls from 2016 to 2018 in Taiwan. Body measurements were obtained using a three-dimensional body surface scanning system. Four biomarkers related to insulin resistance, adipokines, and inflammation were assayed. A multiple logistic regression model was used to perform multivariable analyses.

**Results:** Four body measurements, namely waist circumference (odds ratio, OR = 1.073; 95% confidence interval, CI = 1.017–1.133), forearm circumference (OR = 1.227; 95% CI = 1.002–1.501), thigh circumference (OR = 0.841; 95% CI = 0.73–0.969), and calf circumference (OR = 1.25; 95% CI = 1.076–1.451), were significantly associated with T2DM. Leptin (OR = 1.09; 95% CI = 1.036–1.146) and adiponectin (OR = 0.982; 95% CI = 0.967–0.997) were significantly associated with T2DM. Six body measurement combinations, namely body mass index, waist-to-hip ratio, waist-to-height ratio, waist-to-thigh ratio, forearm-to-thigh ratio, and calf-to-thigh ratio (CTR), were significantly associated with T2DM. CTR had the strongest linear association with T2DM. Moderating effects of significant biomarkers, namely leptin and adiponectin, were observed. Participants with high leptin-to-adiponectin ratios and in the fourth CTR quartile were 162.2 times more prone to develop T2DM.

**Conclusions:** We concluded that a combination of leptin and adiponectin modulated the strength of the association between body measurements and T2DM while providing clues for high-risk group identification and mechanistic conjectures of preventing T2DM.

**Keywords:** limbs measurements, body measurements, adiponectin, leptin, type 2 diabetes mellitus



## INTRODUCTION

Type 2 diabetes mellitus (T2DM) is a rapidly burgeoning chronic disease that causes complications resulting in increased healthcare burden and affecting patient quality of life (1, 2). Studies have demonstrated that central obesity, or abdominal visceral fat accumulation, predominantly indicates T2DM risk and is associated with inflammatory response mechanisms and insulin resistance (3). A meta-analysis indicated that body mass index (BMI), waist circumference (WC), and waist-to-hip ratio (WHR) are three major body shape markers associated with T2DM incidence (4). Another meta-analysis indicated that waist-to-height ratio (WHtR) was superior to BMI in predicting diabetes and several other cardiometabolic risk factors (5). Other studies have revealed that BMI, WC, WHR, and WHtR may predict diabetes occurrence. WC is an indicator of abdominal visceral fat accumulation and is associated with insulin resistance and cardiometabolic risk (6–9). In addition, researchers have reported that thigh circumference (TC) or waist-to-thigh ratio (WTR) was associated with T2DM (10–12). In particular, a small TC, such as low subcutaneous fat or low skeletal muscle in the thigh has been recognized as a risk factor for hyperlipidemia and hyperglycemia (13). Body measurements provide information related to adverse or protective effects of T2DM. Although studies have indicated associations between T2DM and selected body measurements, such as WC, BMI, and body weight, comprehensive whole body measurements have seldom been addressed. Therefore, the association among body measurements, T2DM, and biomarkers related to insulin resistance and inflammation requires clarification.

Several biomarkers related to insulin resistance and inflammation demonstrated correlations with T2DM. Most documented biomarkers were associated with adipocytokines secreted by adipocytes and macrophages and migrated to the adipose tissue. Leptin involves the regulation of satiety and body weight and is positively associated with obesity, fat mass, insulin resistance, triglyceride levels, and inflammatory cytokines (5, 14). Although an association between leptin and T2DM was reported in Caucasian populations (7, 8), its effect was less obvious when insulin resistance and other confounding variables were included into the analysis (8). Adiponectin is negatively associated with obesity and involved in lipid clearance (5, 14). A meta-analysis reported a relative risk of 0.72 in developing T2DM per 1-log mg/ml increments in adiponectin level (6). High serum levels of pro-inflammatory biomarkers, such as tumor necrosis factor- $\alpha$ , interleukin-6, and C-reactive protein (hsCRP), were associated with a high risk of T2DM. Insulin-like growth factor (IGF) shares a structural homology with insulin, and increased blood levels of IGF-I were observed to be associated with T2DM in epidemiological studies (15, 16).

Earlier studies have taken body measurements using non-invasive three-dimensional (3D) scanning technology and demonstrated their association with T2DM (11, 17, 18). However, associations between body measurements and selected biomarkers of T2DM have not been explored thoroughly to date. Based on previous studies (11, 13, 17, 19–21), limb measurements, in addition to WC, may represent a

feature for one's risk to T2DM. We hypothesize that selected biomarkers may strengthen the effect of a combination of body measurements, such as trunk and limb measurements, on T2DM. Therefore, this case-control study investigated the inter-relations between selected body measurements and recognized biomarkers on T2DM risk.

## MATERIALS AND METHODS

### Study Samples

In total, 196 participants (98 with T2DM and 98 non-DM controls) were recruited from the Department of Health Promotion and Examination of Chang Gung Memorial Hospital in Northern Taiwan, representing a normal Taiwanese population. A 1:1 matching was performed with the same sex and age ( $\pm 5$  years) for each case-control pair from a 3D cohort visiting the hospital from March 2016 to January 2018. A minimal sample size of 90 for each group was calculated based on the 1:1 case-control design ( $\alpha = 0.05$ ,  $1-\beta = 0.8$ , and odds ratio, OR = 2.5) according to previous publications (17, 22). Cases were ascertained by physicians of the endocrinology and metabolism department in the community hospital (Chang Gung Memorial Hospital). All T2DM cases included in this study were receiving treatment for blood sugar control for at least a year. The medication used for the treatment of T2DM included biguanides, alpha-glucosidase inhibitors, sulfonylureas, meglitinides, TZDs, DPP-4 inhibitors, SGLT-2 inhibitors, GLP-1 agonists, and insulin. Patients with comorbidities or complications, such as hypertension, cardiovascular disease, renal disease (chronic kidney disease, CKD, stages III, IV, V, and end-stage renal disease, ESRD), liver cirrhosis, chronic hepatitis, cancer, stroke, and disabilities, were excluded. The health status of controls was ascertained using questionnaires; data on medication and disease history and health check-up, such as fasting blood sugar (AC sugar), post-prandial sugar (PC sugar), and hemoglobin A1c (HbA<sub>1c</sub>) levels, were collected. Those who were not taking medications and without disease were included as healthy controls in this study. T2DM diagnosis was based on the following American Diabetes Association (ADA) guidelines: fasting for  $\geq 8$  h, AC sugar level  $\geq 126$  mg/dl, HbA<sub>1c</sub> level  $\geq 6.5\%$ , and PC sugar level ( $\geq 2$  h)  $\geq 200$  mg/dl for two consecutive examinations. As confirmed by their medical records, those with no major illness or complications, namely, hypertension, cardiovascular disease, heart disease, renal disease, liver cirrhosis, or chronic hepatitis, were recruited as participants. This study was approved by the Institutional Review Board of Chang Gung Medical Foundation (107-0011C).

### Anthropometric Parameters

3D body surface measurements were obtained through whole body 3D laser scanning according to previously published methods (17, 19). The 3D laser scanning machine (LT3DCam) was designed by Logistic Technology Company (LTC, Hsinchu, Taiwan) and was proved to have a high standard of accuracy because of objective and comprehensive methods of measuring the human body surface. The standard procedure of measurement requires a participant to remove all outer clothes

except for underclothing in preparation for scanning (women with bras in addition to pants). The participants were to stand still on the stage for scanning (total scanning time is ~10 s). In addition to body height and body weight, 22 one-dimensional measurements from four anatomical regions were obtained. The definition of each body measurement was adapted from previous research studies (17, 19) (**Supplementary Material**). The head and neck region included circumferences of the head and neck. The trunk region included chest circumference, chest width, WC, and waist width. The area from the hip to lower limbs included hip circumference, hip width, left leg length, right leg length, left TC, right TC, left calf circumference, and right calf circumference. The upper limb region included left arm length, right arm length, left upper arm circumference, right upper arm circumference, left forearm circumference, and right forearm circumference. In addition to frequently documented T2DM-related measurement combinations, such as BMI, WHR, WHtR, and WTR, we performed a backward selection from the 22 one-dimensional measurements, adjusting for age, sex, occupation, education, marriage, smoking, alcohol drinking, tea drinking, coffee drinking, betel nut chewing, and daily activity level. Combinations, such as forearm circumference to thigh circumference ratio (forearm to thigh ratio, FATR) and calf circumference to thigh circumference ratio (calf to thigh ratio, CTR), derived from significant body measurements by performing multivariable regression analysis, were used to evaluate their effects on T2DM and modulating effects of the selected biomarkers.

## Assays for Biomarkers

An enzyme-linked immunosorbent assay (ELISA) was used to quantify the concentration of serum biomarkers. The serum concentrations of leptin and adiponectin were assayed using commercial ELISA kits from Boster (Pleasanton, CA, United States). IGF-1 was determined using commercial ELISA kits from BioOcean (Shoreview, MN, United States). The hsCRP level was assayed using a commercial ELISA kit from Roche (Basel, Switzerland).

## Data Collection

A questionnaire was used to collect the following information: date of birth; sex; education; marital status; occupation; history of cigarette smoking, alcohol drinking, betel nut chewing, tea drinking, and coffee drinking; personal history of the disease (namely, diabetes, hypertension, heart disease, CKD, liver cirrhosis, and chronic hepatitis); and family history of T2DM. For those with no history of diabetes, a fasting blood glucose level was obtained. Diabetes was defined according to the ADA guidelines. For those with no history of hypertension, blood pressure was measured using a mercury sphygmomanometer on the left arm after a patient had rested for 20 min in a seated position. Hypertension was defined according to the guidelines of the Joint National Committee on Detection, Evaluation, and Treatment of High Blood Pressure (systolic blood pressure  $\geq 140$  mm Hg, diastolic blood pressure  $\geq 90$  mm Hg, or the use of antihypertensive medication) (23).

## Statistical Analyses

Two independent sample *t*-tests were performed to compare differences between continuous variables of the groups, and results are presented as the mean  $\pm$  SD. The  $\chi^2$ -test was performed to differentiate between the distribution of categorical variables, and the results are expressed as frequencies and percentages between groups. 3D body surface measurements were screened by a two-sample *t*-test by comparing differences between the patients and controls. To avoid collinearity in the regression analysis, one body measurement with the lowest *p*-value was selected from each anatomic dimension for subsequent multivariable analysis. A logistic regression model was used to determine the strength of the association between the selected body measurements and T2DM. In addition to the forced-in sociodemographic and lifestyle variables, a backward model selection with *p* < 0.2 was used to determine variables, namely, body measurements and biomarkers, to be retained in the regression model. The modulating effect was examined by comparing models with and without biomarkers while calculating the strength of association (OR) between the body measurement combinations and the T2DM. SPSS 22.0 statistical software (IBM Corporation, Armonk, NY, United States) was used for performing the analyses in this study.

## RESULTS

Patients with type 2 diabetes mellitus (T2DM) had a lower level of education than those in the non-DM controls. T2DM was associated with occupational categories in which farmers and laborers, self-employed workers, and service industry workers were observed to have a high risk. Among the lifestyle variables, cigarette smoking, betel nut chewing, and low to medium activity levels were associated with the high risk of T2DM (**Table 1**).

The results of most of the selected body measurements were statistically significant between the cases and controls. In general, the patients with T2DM had larger body measurements than those in the controls, except for body height, head circumference, hip width, arm length, and leg length. The results of the multivariable analysis indicated that WC (OR = 1.073; 95% CI = 1.017–1.133), left forearm circumference (OR = 1.227; 95% CI = 1.002–1.501), right TC (OR = 0.841; 95% CI = 0.73–0.969), and right calf circumference (OR = 1.25; 95% CI = 1.076–1.451) were significantly associated with T2DM after adjusting for age, sex, education, marital status, occupation, smoking, alcohol drinking, coffee drinking, betel nut chewing, and daily activity level. The following six selected combinations were significantly associated with T2DM in the multivariable logistic regression analysis: BMI (OR = 1.318; 95% CI = 1.171–1.483), WHR (OR = 1.109; 95% CI = 1.046–1.176), WHtR (OR = 1.162; 95% CI = 1.086–1.243), WTR (OR = 1.534; 95% CI = 1.229–1.913), FATR (OR = 1.12; 95% CI = 1.047–1.197), and CTR (OR = 1.142; 95% CI = 1.075–1.214) (**Table 2**).

The association between the four selected biomarkers and T2DM was examined, and the association between two biomarkers, namely, leptin and adiponectin, and T2DM was statistically significant in the univariate analysis. Leptin and

**TABLE 1 |** Sociodemographic and lifestyle variables of the study participants.

	Control participants (n = 98)	DM patients (n = 98)	p-value
<b>Demographics</b>			
Age	58.68 ± 11.01	56.40 ± 10.60	0.141
Gender			1.000
Female	41 (41.8%)	41 (41.8%)	
Male	57 (58.2%)	57 (58.2%)	
Education			<0.0001
Elementary and below	21 (21.4%)	38 (38.8%)	
Junior high school	9 (9.2%)	20 (20.4%)	
Senior high school	29 (29.6%)	28 (28.6%)	
College/university and above	39 (39.8%)	12 (12.2%)	
Marital status			0.830
Married or coupled	85 (86.7%)	86 (87.8%)	
Unmarried	13 (13.3%)	12 (12.2%)	
Occupation			<0.0001
Government	13 (13.3%)	5 (5.1%)	
Farmers and laborers	12 (12.2%)	20 (20.4%)	
Business	19 (19.4%)	2 (2.0%)	
Self-employment	17 (17.3%)	26 (26.5%)	
Service industry	12 (12.2%)	24 (24.5%)	
Others	25 (25.5%)	21 (21.4%)	
<b>Lifestyle variables</b>			
Cigarette smoking			0.046
No	73 (74.5%)	60 (61.2%)	
Yes	25 (25.5%)	38 (38.8%)	
Alcohol drinking			0.133
No	69 (70.4%)	59 (60.2%)	
Yes	29 (29.6%)	39 (39.8%)	
Tea drinking			0.381
No	42 (42.9%)	36 (36.7%)	
Yes	56 (57.1%)	62 (63.3%)	
Coffee drinking			0.368
No	31 (31.6%)	37 (37.8%)	
Yes	67 (68.4%)	61 (62.2%)	
Betel nut chewing			0.013
No	95 (96.9%)	86 (87.8%)	
Yes	3 (3.1%)	12 (12.2%)	
Activity level			0.023
Low	50 (51.0%)	48 (49.0%)	
Median	31 (31.6%)	44 (44.9%)	
High	17 (17.3%)	6 (6.1%)	

adiponectin were observed to be significantly associated with T2DM in backward selection modeling, with ORs of 1.09 (95% CI = 1.036–1.146) and 0.982 (95% CI = 0.967–0.997), respectively (Table 3).

Six body measurement combinations were tested accordingly and then further categorized into quartiles to determine the monotonic trend association with T2DM. The results demonstrated a monotonic trend in multivariable-adjusted ORs

for BMI (Q1 = 1, Q2 = 1.98, Q3 = 5.58, and Q4 = 7.3), WHR (Q1 = 1, Q2 = 2.07, Q3 = 4.36, and Q4 = 7.1), WHtR (Q1 = 1, Q2 = 2.5, Q3 = 4.62, and Q4 = 7.76), WTR (Q1 = 1, Q2 = 1.17, Q3 = 2.86, and Q4 = 4.15), FATR (Q1 = 1, Q2 = 0.9, Q3 = 2.3, and Q4 = 6.12), and CTR (Q1 = 1, Q2 = 4.3, Q3 = 10.72, and Q4 = 16.11). The highest strength of association was found between CTR and T2DM, followed by WHtR, BMI, and WHR (Figure 1). When leptin, adiponectin, and leptin-to-adiponectin ratios were stratified into median, high, and low, different moderating effects were found. The subgroup with higher leptin levels had multivariable-adjusted ORs of 1.03 (95% CI = 0.16–6.53), 3.94 (95% CI = 0.6–26), 19.86 (95% CI = 3.09–127.69), and 30.39 (95% CI = 4.43–208.71) with CTRs at Q1, Q2, Q3, and Q4, respectively, when compared with the subgroup with lower leptin and in the first CTR quartile (Q1) (Model 1, Table 4). The subgroup with lower adiponectin levels had multivariable-adjusted ORs of 3.09 (95% CI = 0.46–20.73), 8.82 (95% CI = 1.46–53.15), 27.74 (95% CI = 4.38–175.82), and 32.25 (95% CI = 4.37–237.9) with CTRs at Q1, Q2, Q3, and Q4, respectively, when compared with the subgroup with higher adiponectin and in the first CTR quartile (Q1) (Model 2, Table 4). The subgroup with higher leptin-to-adiponectin ratios had multivariable-adjusted ORs of 12.6 (95% CI = 1.78–89.27), 45.79 (95% CI = 6.28–333.69), 55.51 (95% CI = 7.83–393.53), and 162.2 (95% CI = 17.17–1534.37) with CTRs at Q1, Q2, Q3, and Q4, respectively, when compared with the subgroup with a lower leptin-to-adiponectin ratio and in the first CTR quartile (Q1) (Model 3, Table 4).

## DISCUSSION

The aim of this study was to investigate the interrelations of body measurements and selected biomarkers with T2DM. The results of this case–control study demonstrated that WC, left forearm circumference, right TC, and right calf circumference were associated with T2DM, whereas the biomarkers leptin and adiponectin were correlated with T2DM. In addition, the results indicated that CTR exhibited the highest strength of positive linear association with T2DM among the six selected body measurement combinations and was modulated by leptin, adiponectin, and the ratio of leptin to adiponectin in the multiple regression analysis. Although the literature indicated that TC is negatively associated with the incidence and prevalence of T2DM (20), this study indicated that calf circumference was another marker associated with T2DM and can interact with leptin and adiponectin mechanistically. Based on the findings of this study, a combination of WC or limb circumference measurements and leptin/adiponectin may be used to represent the risk of T2DM while providing evidence for intervention strategies to prevent the disease among high-risk groups. In future clinical or epidemiological practices, people with high values of the six selected body measurement combinations may be considered as high-risk groups for the occurrence and adverse progression of T2DM. Intensive interventions, such as exercise and nutrition, or examinations, such as leptin and adiponectin, are suggested for high-risk individuals.

**TABLE 2 |** Comparison of body measurements between the study groups.

Stage 1: body measurements	Control participants (n = 98)	DM patients (n = 98)	p-value	OR (95% CI)*
<b>Whole body</b>				
Height (cm)	163.1 ± 9	161.7 ± 8.6	0.249	
Weight (kg)	64.6 ± 13.1	72.6 ± 13.1	<0.0001	
<b>Head and neck</b>				
Head circumference (cm)	56.9 ± 2.9	57.3 ± 2.7	0.292	
Neck circumference (cm)	40.6 ± 4.3	42.8 ± 3.8	<0.0001	
<b>Trunk</b>				
Chest width (cm)	31.8 ± 3.3	33.6 ± 2.8	<0.0001	
Chest circumference (cm)	95.6 ± 9.6	102.9 ± 9.9	<0.0001	
Waist width (cm)	31 ± 3.2	33.1 ± 3.1	<0.0001	
Waist circumference (cm)	86.0 ± 11.4	95.6 ± 11.6	<0.0001	1.073 (1.017, 1.133)
<b>Hip</b>				
Hip width (cm)	34.6 ± 2.6	34.9 ± 2.4	0.510	
Hip circumference (cm)	94.4 ± 8.4	100.1 ± 9.1	<0.0001	
<b>Upper limbs</b>				
<b>Arm length (cm)</b>				
Left	52.9 ± 3.7	53.0 ± 4.1	0.893	
Right	53.1 ± 3.6	53.2 ± 4.0	0.878	
<b>Upper arm circumference (cm)</b>				
Left	30.5 ± 2.9	31.8 ± 3.3	0.002	
Right	30.5 ± 2.9	32.0 ± 3.2	0.001	
<b>Forearm circumference (cm)</b>				
Left	21.7 ± 2.9	24.2 ± 3.2	<0.0001	1.227 (1.002, 1.501)
Right	22.1 ± 3.0	24.5 ± 3.3	<0.0001	
<b>Lower limbs</b>				
<b>Leg length (cm)</b>				
Left	69.1 ± 5.1	68.0 ± 4.4	0.095	
Right	69.1 ± 5.0	68.0 ± 4.3	0.079	
<b>Thigh circumference (cm)</b>				
Left	50.6 ± 4.2	52.1 ± 5.1	0.020	
Right	50.6 ± 4.1	52.2 ± 5.1	0.013	0.841 (0.730, 0.969)
<b>Knee circumference (cm)</b>				
Left	38.5 ± 2.8	39.8 ± 3.7	0.005	
Right	38.6 ± 2.7	39.9 ± 3.7	0.006	
<b>Calf circumference (cm)</b>				
Left	30.7 ± 4.1	34.4 ± 4.4	<0.0001	1.250 (1.076, 1.451)
Right	30.8 ± 4.1	34.6 ± 4.5	<0.0001	
<b>Stage 2: measurement combinations</b>				
BMI	24.1 ± 3.3	27.8 ± 4.5	<0.0001	1.318 (1.171, 1.483)
WHR × 100	91.1 ± 8.0	95.3 ± 5.6	<0.0001	1.109 (1.046, 1.176)
WHtR × 100	52.7 ± 5.9	59.3 ± 8.0	<0.0001	1.162 (1.086, 1.243)
WTR × 10	17.0 ± 2.1	18.4 ± 1.8	<0.0001	1.534 (1.229, 1.913)
FATR × 100	43.4 ± 6.2	46.6 ± 6.7	0.001	1.120 (1.047, 1.197)
CTR × 100	61.2 ± 8.0	66.3 ± 6.3	<0.0001	1.142 (1.075, 1.214)

BMI, body mass index; WHR, waist-to-hip ratio; WHtR, waist-to-height ratio; WTR, waist-to-thigh ratio; FATR, forearm-to-thigh ratio; CTR, calf-to-thigh ratio.

\*ORs obtained from a multivariate model included age, sex, occupation, education, marriage, smoking, alcohol drinking, tea drinking, coffee drinking, betel nut chewing, daily activity level, and investigated variables (stage 1: included waist circumference, left forearm circumference, right thigh circumference, and right calf circumference; stage 2: only one combination was included in each model).

The associations between waist or limb measurement combinations and T2DM may be attributed to the secretion by adipocytes and macrophages that have migrated to the adipose

tissue, which activates adipocytokines such as adiponectin and leptin (3–5, 24). Among them, leptin is positively associated with obesity, fat mass, insulin resistance, triglyceride levels,



**TABLE 3 |** The distribution of biomarkers between the study groups.

	Control participants (n = 98)	DM patients (n = 98)	p-value	OR (95% CI)*	OR (95% CI)**
Leptin (ng/ml)	7.13 ± 7.26	12.88 ± 12.86	<0.0001	1.096(1.042,1.154)	1.090 (1.036, 1.146)
Adiponectin (μg/ml)	34.75 ± 36.25	22.13 ± 23.23	0.004	0.981 (0.968, 0.995)	0.982 (0.967, 0.997)
HSCRP (mg/l)	1.36 ± 1.78	1.79 ± 2.47	0.309	1.130 (0.946, 1.351)	
IGF (pg/ml)	28.39 ± 30.22	34.00 ± 45.36	0.162	1.001 (0.992, 1.011)	

\*Model includes age, sex, occupation, education, marriage, smoking, alcohol drinking, tea drinking, coffee drinking, betel nut chewing, daily activity level, and investigated variable (only one biomarker was included in each model).

\*\*Biomarkers were selected based on  $p < 0.2$  with backward model selection in which the model includes age, sex, occupation, education, marriage, smoking, alcohol drinking, tea drinking, coffee drinking, betel nut chewing, daily activity level, leptin, and adiponectin.

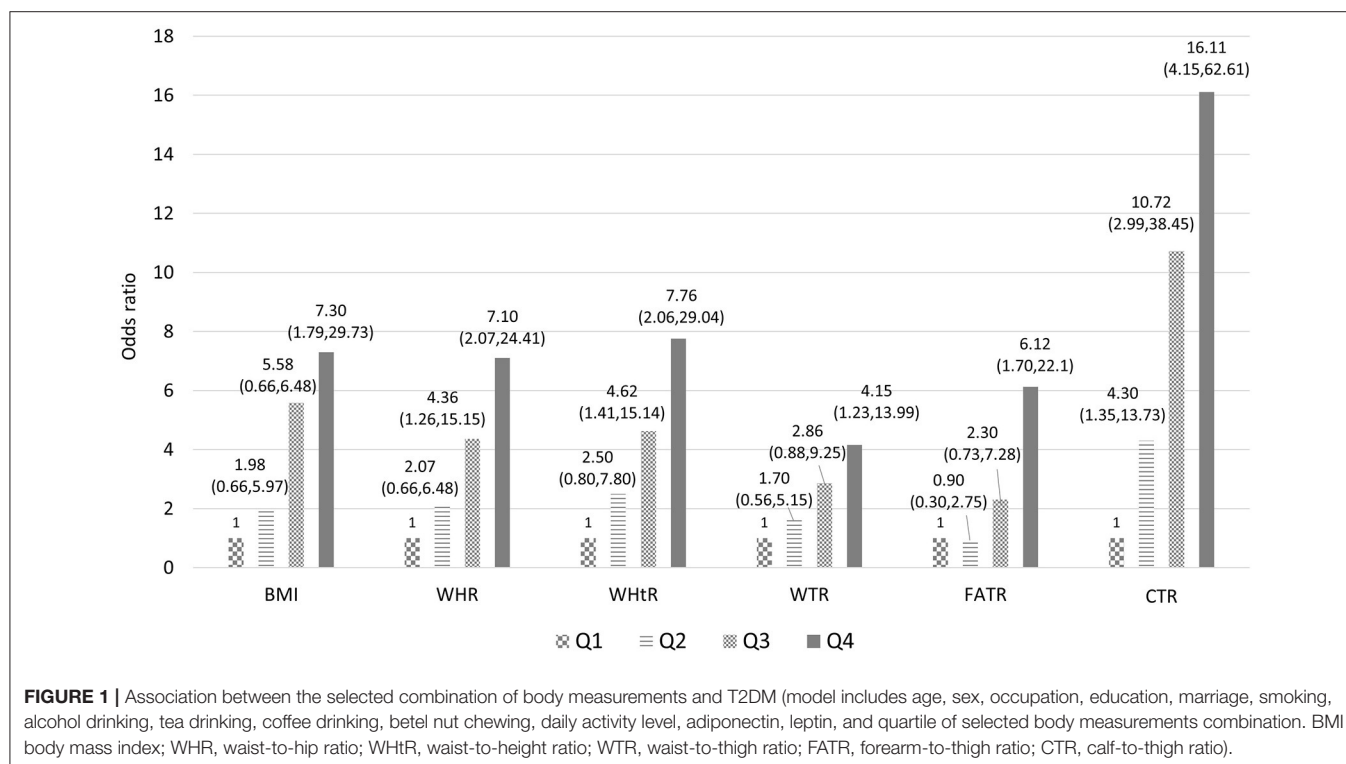


**FIGURE 1 |** Association between the selected combination of body measurements and T2DM (model includes age, sex, occupation, education, marriage, smoking, alcohol drinking, tea drinking, coffee drinking, betel nut chewing, daily activity level, adiponectin, leptin, and quartile of selected body measurements combination. BMI body mass index; WHR, waist-to-hip ratio; WHtR, waist-to-height ratio; WTR, waist-to-thigh ratio; FATR, forearm-to-thigh ratio; CTR, calf-to-thigh ratio).

and inflammatory cytokines and negatively associated with high-density lipoprotein cholesterol (5). Although a positive association of leptin with T2DM has been demonstrated in Caucasian populations (7, 8), its effect was unknown when body measurements and other confounders were taken into account. An earlier study demonstrated that high leptin levels were associated with a low risk of diabetes after adjusting for obesity, adiponectin, triglyceride, hypertension, and inflammation scores (8). Previous research demonstrated the association between central obesity and T2DM. However, in this study, limb measurements played an important role in the disease status, wherein a synergistic effect of adipokines on T2DM was observed. The thigh muscular tissue was observed to excrete proteins against insulin resistance and inflammation. An adverse combination of limb measurements may imply a lack of protective effects, especially in a state of leptin resistance, which is associated with high chance of insulin resistance and

T2DM (25). The results of this study showed a synergistically interactive effect of leptin levels and body measurements, such as central obesity and limbs measurements, on T2DM, providing an in-depth observation of future mechanistic and preventive methods.

The findings on the association between limb measurements and T2DM are the most notable, whereas levels of leptin and adipokines played a moderating role. A large TC is generally regarded as a protective factor for T2DM in both cross-sectional and longitudinal studies (20). As observed in the literature, thigh skeletal muscles are the key target organs for insulin action and sites of insulin resistance (21). A low muscle mass or less subcutaneous fat in the thighs is believed to be associated with hyperglycemia and diabetes by the action of insulin resistance (13). The association between the forearm/thigh or calf/thigh combination and T2DM is partly explained by a small TC, and the mechanism of

**TABLE 4 |** Stratified analysis between CTR quartile and leptin, adiponectin, and leptin-to-adiponectin ratio (high/low) on T2DM.

CTR Quartile	Model 1* Leptin						Model 2* Adiponectin						Model 3* Leptin-to-adiponectin ratio					
	Low			High			High			Low			Low			High		
	n	OR	95% CI	n	OR	95% CI	n	OR	95% CI	n	OR	95% CI	n	OR	95% CI	n	OR	95% CI
Q1	14	1.00	-	34	1.03	(0.16, 6.53)	29	1.00	-	19	3.09	(0.461, 20.73)	27	1.00	-	21	12.60	(1.78, 89.27)
Q2	31	3.56	(0.67, 18.95)	19	3.94	(0.60, 25.99)	23	8.54	(1.45, 50.19)	27	8.82	(1.46, 53.15)	24	6.22	(0.94, 41.05)	26	45.79	(6.28, 333.69)
Q3	24	7.20	(1.18, 43.99)	25	19.86	(3.09, 127.69)	21	11.99	(1.79, 80.49)	28	27.74	(4.38, 175.82)	21	66.37	(7.96, 553.75)	28	55.51	(7.83, 393.53)
Q4	28	8.52	(1.29, 56.49)	21	30.39	(4.43, 208.71)	24	26.80	(4.17, 172.27)	25	32.25	(1.02, 1.15)	25	39.85	(5.49, 289.27)	24	162.20	(17.15, 1534.37)

CTR, calf-to-thigh ratio.  
\*All the models are adjusted for age, sex, occupation, education, marital status, smoking, alcohol drinking, tea drinking, coffee drinking, betel nut chewing, daily activity level, leptin, and adiponectin excluding the investigated variable per se. Interactive effects between CTR and the biomarkers (leptin, adiponectin, and leptin-to-adiponectin ratio) were proved with significance level  $p < 0.001$ .

a large forearm or calf circumference in T2DM warrants further discussion.

Whether changes in plasma adipokines and/or inflammatory parameters observed in patients with T2DM are because of excessive adipose tissue and/or direct association with diabetes status is as yet unclear (21, 26). Earlier studies have demonstrated that circulating leptin levels were high in obese individuals and in patients with metabolic syndrome (27). Earlier reports have demonstrated that elevated leptin concentrations in obese participants were directly proportional to obesity and positively correlated with body fat mass. In contrast, hyperinsulinemia may, in turn, exacerbate obesity and further increase leptin levels, resulting in a positive feedback loop that promotes the development of diabetes (25, 28). Therefore, the results demonstrated a close relationship between T2DM and leptin levels and with adverse body measurements.

Leptin is assumed to be elevated by unfavorable body measurements, which indicate that fatty cells accumulate and, thus, reduce insulin sensitivity, possibly resulting in decreased glucose tolerance (29). These observations suggest that the independent role of high leptin levels in predicting the risk of diabetes can be because of the role of leptin in regulating insulin sensitivity and secretion. Moreover, adverse body measurements exacerbate the insulin resistance loop (30).

This study demonstrated an inverse relationship between adiponectin and T2DM in the multivariate regression analysis. The relationship between adiponectin and insulin sensitivity varies among ethnicities. In a multiethnic population-based study, adiponectin levels were negatively correlated with insulin resistance only in the Caucasian population, whereas no correlation was observed in Black and South Asian populations (31). This study demonstrated that the association between adiponectin and insulin sensitivity may be because of body shape differences. Adiponectin differs from other adipokines in that it is inversely proportional to obesity and even the distribution of body adipocytes (32, 33). We hypothesized that the discrepancy depends on the body shape distribution in the investigated population. Furthermore, the observations of the authors suggested that the role of adiponectin in T2DM can involve other biomarkers, such as leptin, as well as body measurements, such as limb circumference, in this Asian population. As per the results of this study, the ratio of leptin to adiponectin should be considered an important marker to estimate adverse body measurements of an individual as a risk for T2DM.

This study used a case-control design to explore the interrelations among body measurements, biomarkers, and T2DM. While relationships between T2DM and individual body measurements or biomarkers have been broadly explored, the interactive effect between body measurements and biomarkers in T2DM was rarely verified. Most notably, this study discloses the highest likelihood of T2DM among the participants with both higher CTR and leptin-to-adiponectin ratio, which provides a roomy discussion for the mechanistic pathway of T2DM in the future. To increase the accuracy and

comprehensiveness of body measurements, we used accurate measuring techniques such as 3D whole-body scanning, computer-based technology (which reduced measurement errors), biomarker analysis (which anchored biopathways and mechanisms), and multivariable model construction (which was more comprehensive). Nevertheless, this study has certain limitations. First are the limitations of a case-control design as opposed to a cohort study generally applied to this study, particularly on temporal ambiguity. Second, measurements of 3D whole body scanning were obtained only once; therefore, we did not count body measurement changes over time. Third, we selected one side with a lower  $p$ -value among the limb measurements for further combination analyses. We did not exercise the effects of choosing an alternative side for the combinations. Fourth, the study population was of Asian ethnicity; therefore, the findings may apply only to people in Asia (such as in China). Caution should be taken when generalizing the results to Western populations. Fifth, the DM vintage and treatment history were not included in the analysis, which may be confounded by disease progression or severity. Finally, this was a hospital-based sampling design that may need confirmation with community-based samples.

## CONCLUSIONS

In addition to body measurements, such as WC, TC, forearm circumference, and calf circumference, this study demonstrated leptin and adiponectin, and their combinations to be associated with T2DM. The CTR exhibited the strongest association with T2DM, whereas the ratio of leptin to adiponectin heightened the strength of the association with T2DM. The body measurements and significant biomarkers obtained in this study can provide mechanistic conjectures for high-risk group identification and prevention of T2DM in future practice.

## DATA AVAILABILITY STATEMENT

The datasets presented in this article are not readily available because Regulation of Ministry of Health and Welfare in Taiwan. Requests to access the datasets should be directed to Kuang-Hung Hsu (khsu@mail.cgu.edu.tw).

## REFERENCES

1. Wild SH, Roglic G, Green A, Sicree R, King H. Global prevalence of diabetes: estimates for the year 2000 and projections for 2030. Response to Rathman and Giani. *Diabetes Care*. (2004) 27:2569. doi: 10.2337/diacare.27.10.2569-a
2. Chan JC, Malik V, Jia W, Kadowaki T, Yajnik CS, Yoon K-H, et al. Diabetes in Asia: epidemiology, risk factors, and pathophysiology. *JAMA*. (2009) 301:2129–40. doi: 10.1001/jama.2009.726
3. Tchernof A, Després JP. Pathophysiology of human visceral obesity: an update. *Physiol Rev*. (2013) 93:359–404. doi: 10.1152/physrev.00033.2011
4. Vazquez G, Duval S, Jacobs DR, Jr., Silventoinen K. Comparison of body mass index, waist circumference, and waist/hip ratio in predicting incident diabetes: a meta-analysis. *Epidemiol Rev*. (2007) 29:115–28. doi: 10.1093/epirev/mxm008

## ETHICS STATEMENT

The studies involving human participants were reviewed and approved by Institutional Review Board of Chang Gung Medical Foundation. The patients/participants provided their written informed consent to participate in this study.

## AUTHOR CONTRIBUTIONS

P-JL and K-HH: study concept, design, statistical analysis, and drafting. M-KT, I-WW, S-WC, N-IY, and K-HH: acquisition of data, funding obtainment, administrative, technical, or material support. P-JL, M-KT, and K-HH: analysis and interpretation of data. K-HH: supervision. All authors contributed to the article and approved the submitted version.

## FUNDING

This study was supported by Ministry of Science and Technology (108-2410-H-182-008-MY2), the Chang Gung Medical Foundation (CMRPD3G0103 and CORPD3J0011), and the Healthy Aging Research Center of Chang Gung University (EMRPD1K0411, EMRPD1K0481, EMRPD1L0401, and EMRPD1L0451). The authors appreciate the partial support provided by the Wang Jhan-Yang Charitable Trust Fund (WJY 2020-HR-01, WJY 2021-HR-01, WJY 2020-AP-01, and WJY 2021-AP-01). All the funding bodies played no role in the study design; data collection, analysis, and interpretation; and in writing the manuscript.

## ACKNOWLEDGMENTS

The authors would like to acknowledge the support for data linkage provided by Health and Welfare Data Center, Ministry of Health and Welfare, Taiwan.

## SUPPLEMENTARY MATERIAL

The Supplementary Material for this article can be found online at: <https://www.frontiersin.org/articles/10.3389/fpubh.2021.678681/full#supplementary-material>

5. Savva SC, Lamnisos D, Kafatos AG. Predicting cardiometabolic risk: waist-to-height ratio or BMI. A meta-analysis. *Diabetes Metab Syndr Obesity Targets Ther*. (2013) 6:403–19. doi: 10.2147/DMSO.S34220
6. Preis SR, Massaro JM, Robins SJ, Hoffmann U, Vasan RS, Irlbeck T, et al. Abdominal subcutaneous and visceral adipose tissue and insulin resistance in the Framingham heart study. *Obesity*. (2010) 18:2191–8. doi: 10.1038/oby.2010.59
7. De Onis M, Habicht J-P. Anthropometric reference data for international use: recommendations from a World Health Organization Expert Committee. *Am J Clin Nutr*. (1996) 64:650–8. doi: 10.1093/ajcn/64.4.650
8. Pouliot M-C, Després J-P, Lemieux S, Moorjani S, Bouchard C, Tremblay A, et al. Waist circumference and abdominal sagittal diameter: best simple anthropometric indexes of abdominal visceral adipose tissue accumulation and related cardiovascular risk in men and women. *Am J Cardiol*. (1994) 73:460–8. doi: 10.1016/0002-9149(94)90676-9

9. Preis SR, Massaro JM, Hoffmann U, D'Agostino RB, Sr., Levy D, Robins SJ, et al. Neck circumference as a novel measure of cardiometabolic risk: the Framingham Heart study. *J Clin Endocrinol Metab.* (2010) 95:3701–10. doi: 10.1210/jc.2009-1779
10. Li C, Ford ES, Zhao G, Kahn HS, Mokdad AH. Waist-to-thigh ratio and diabetes among US adults: the third national health and nutrition examination survey. *Diab Res Clin Pract.* (2010) 89:79–87. doi: 10.1016/j.diabres.2010.02.014
11. Snijder MB, Dekker JM, Visser M, Bouter LM, Stehouwer CD, Kostense PJ, et al. Associations of hip and thigh circumferences independent of waist circumference with the incidence of type 2 diabetes: the Hoorn Study. *Am J Clin Nutr.* (2003) 77:1192–7. doi: 10.1093/ajcn/77.5.1192
12. Hsu K-H, Shih C-P, Liao P-J. Waist-to-thigh ratio is a predictor of internal organ cancers in humans: findings from a cohort study. *Ann Epidemiol.* (2013) 23:342–8. doi: 10.1016/j.annepidem.2013.04.004
13. Snijder M, Visser M, Dekker J, Goodpaster BH, Harris TB, Kritchevsky SB, et al. Low subcutaneous thigh fat is a risk factor for unfavourable glucose and lipid levels, independently of high abdominal fat. The Health ABC Study. *Diabetologia.* (2005) 48:301–8. doi: 10.1007/s00125-004-1637-7
14. Vinitha R, Ram J, Snehalatha C, Nanditha A, Shetty AS, Arun R, et al. Adiponectin, leptin, interleukin-6 and HbA1c in the prediction of incident type 2 diabetes: a nested case-control study in Asian Indian men with impaired glucose tolerance. *Diab Res Clin Pract.* (2015) 109:340–6. doi: 10.1016/j.diabres.2015.05.035
15. Rajpathak SN, He M, Sun Q, Kaplan RC, Muzumdar R, Rohan TE, et al. Insulin-like growth factor axis and risk of type 2 diabetes in women. *Diabetes.* (2012) 61:2248–54. doi: 10.2337/db11-1488
16. Burgers AMG, Biermasz NR, Schoones JW, Pereira AM, Renehan AG, Zwahlen M, et al. Meta-analysis and dose-response metaregression: circulating insulin-like growth factor I (IGF-I) and mortality. *J Clin Endocrinol Metab.* (2011) 96:2912–20. doi: 10.1210/jc.2011-1377
17. Chuang Y-C, Hsu K-H, Hwang C-J, Hu P-M, Lin T-M, Chiou W-K. Waist-to-thigh ratio can also be a better indicator associated with type 2 diabetes than traditional anthropometrical measurements in Taiwan population. *Ann Epidemiol.* (2006) 16:321–31. doi: 10.1016/j.annepidem.2005.04.014
18. Ben-Noun L, Sohar E, Laor A. Neck circumference as a simple screening measure for identifying overweight and obese patients. *Obes Res.* (2001) 9:470–7. doi: 10.1038/oby.2001.61
19. Lin J-D, Chiou W-K, Weng H-F, Tsai Y-H, Liu T-H. Comparison of three-dimensional anthropometric body surface scanning to waist-hip ratio and body mass index in correlation with metabolic risk factors. *J Clin Epidemiol.* (2002) 55:757–66. doi: 10.1016/S0895-4356(02)00433-X
20. Ting M-K, Liao P-J, Wu I-W, Chen S-W, Yang N-I, Lin T-Y, et al. Predicting type 2 diabetes mellitus occurrence using three-dimensional anthropometric body surface scanning measurements: a prospective cohort study. *J Diab Res.* (2018) 2018:1–11. doi: 10.1155/2018/6742384
21. Seidell J, Han T, Feskens EJ, Lean M. Narrow hips and broad waist circumferences independently contribute to increased risk of non-insulin-dependent diabetes mellitus. *J Intern Med.* (1997) 242:401–6. doi: 10.1046/j.1365-2796.1997.00235.x
22. Dupont WD. Power calculations for matched case-control studies. *Biometrics.* (1988) 44:1157–68. doi: 10.2307/2531743
23. Program NHBPE. The fifth report of the joint national committee on detection, evaluation and treatment of high blood pressure (JNC5). *Arch Int Med.* (1992) 153:154–83. doi: 10.1001/archinte.153.2.154
24. Laaksonen DE, Lakka HM, Niskanen LK, Kaplan GA, Salonen JT, Lakka TA. Metabolic syndrome and development of diabetes mellitus: application and validation of recently suggested definitions of the metabolic syndrome in a prospective cohort study. *Am J Epidemiol.* (2002) 156:1070–7. doi: 10.1093/aje/kwf145
25. Ramachandran A, Ma RCW, Snehalatha C. Diabetes in asia. *Lancet.* (2010) 375:408–18. doi: 10.1016/S0140-6736(09)60937-5
26. Larsen BA, Wassel CL, Kritchevsky SB, Strotmeyer ES, Criqui MH, Kanaya AM, et al. Association of muscle mass, area, and strength with incident diabetes in older adults: the health ABC study. *J Clin Endocrinol Metab.* (2016) 101:1847–55. doi: 10.1210/jc.2015-3643
27. Van der Kooy K, Seidell JC. Techniques for the measurement of visceral fat: a practical guide. *Int J Obes.* (1993) 17:187–96.
28. Cho NH, Oh TJ, Kim KM, Choi SH, Lee JH, Park KS, et al. Neck circumference and incidence of diabetes mellitus over 10 years in the Korean genome and epidemiology study (KoGES). *Sci Rep.* (2015) 5:18565. doi: 10.1038/srep18565
29. Kim JY, Bacha F, Tfayli H, Michaliszyn SF, Yousuf S, Arslanian S. Adipose tissue insulin resistance in youth on the spectrum from normal weight to obese and from normal glucose tolerance to impaired glucose tolerance to type 2 diabetes. *Diab Care.* (2019) 42:265–72. doi: 10.2337/dc18-1178
30. Sáinz N, Barrenetxe J, Moreno-Aliaga MJ, Martínez JA. Leptin resistance and diet-induced obesity: central and peripheral actions of leptin. *Metabolism.* (2015) 64:35–46. doi: 10.1016/j.metabol.2014.10.015
31. Dastani Z, Hivert M-F, Timpson N, Perry JR, Yuan X, Scott RA, et al. Novel loci for adiponectin levels and their influence on type 2 diabetes and metabolic traits: a multi-ethnic meta-analysis of 45,891 individuals. *PLoS Ggenet.* (2012) 8:e1002607. doi: 10.1371/journal.pgen.1002607
32. Gil-Campos M, Cañete R, Gil A. Adiponectin, the missing link in insulin resistance and obesity. *Clin Nutr.* (2004) 23:963–74. doi: 10.1016/j.clnu.2004.04.010
33. Hotta K, Funahashi T, Bodkin NL, Ortmeier HK, Arita Y, Hansen BC, et al. Circulating concentrations of the adipocyte protein adiponectin are decreased in parallel with reduced insulin sensitivity during the progression to type 2 diabetes in rhesus monkeys. *Diabetes.* (2001) 50:1126–33. doi: 10.2337/diabetes.50.5.1126

**Conflict of Interest:** The authors declare that the research was conducted in the absence of any commercial or financial relationships that could be construed as a potential conflict of interest.

**Publisher's Note:** All claims expressed in this article are solely those of the authors and do not necessarily represent those of their affiliated organizations, or those of the publisher, the editors and the reviewers. Any product that may be evaluated in this article, or claim that may be made by its manufacturer, is not guaranteed or endorsed by the publisher.

Copyright © 2021 Liao, Ting, Wu, Chen, Yang and Hsu. This is an open-access article distributed under the terms of the Creative Commons Attribution License (CC BY). The use, distribution or reproduction in other forums is permitted, provided the original author(s) and the copyright owner(s) are credited and that the original publication in this journal is cited, in accordance with accepted academic practice. No use, distribution or reproduction is permitted which does not comply with these terms.





# Cellular 5'-3' mRNA Exoribonuclease XRN1 Inhibits Interferon Beta Activation and Facilitates Influenza A Virus Replication

Yen-Chin Liu,<sup>a,b,c</sup> Bobo Wing-Yee Mok,<sup>a,b</sup> Pui Wang,<sup>a,b</sup>  Rei-Lin Kuo,<sup>c,d,e</sup>  Honglin Chen,<sup>a,b</sup>  Shin-Ru Shih<sup>c,e,f,g</sup>

<sup>a</sup>State Key Laboratory for Emerging Infectious Diseases, Department of Microbiology, The University of Hong Kong, Hong Kong SAR, People's Republic of China

<sup>b</sup>Collaborative Innovation Center for Diagnosis and Treatment of Infectious Diseases, The University of Hong Kong, Hong Kong SAR, People's Republic of China

<sup>c</sup>Research Center for Emerging Viral Infection, College of Medicine, Chang Gung University, Taoyuan, Taiwan

<sup>d</sup>Graduate Institute of Biomedical Sciences, College of Medicine, Chang Gung University, Taoyuan, Taiwan

<sup>e</sup>Department of Medical Biotechnology and Laboratory Science, College of Medicine, Chang Gung University, Taoyuan, Taiwan

<sup>f</sup>Department of Laboratory Medicine, Linkou Chang Gung Memorial Hospital, Taoyuan, Taiwan

<sup>g</sup>Research Center for Chinese Herbal Medicine, Research Center for Food and Cosmetic Safety, and Graduate Institute of Health Industry Technology, College of Human Ecology, Chang Gung University of Science and Technology, Taoyuan, Taiwan

**ABSTRACT** Cellular 5'-3' exoribonuclease 1 (XRN1) is best known for its role as a decay factor, which by degrading 5' monophosphate RNA after the decapping of DCP2 in P-bodies (PBs) in *Drosophila*, yeast, and mammals. XRN1 has been shown to degrade host antiviral mRNAs following the influenza A virus (IAV) PA-X-mediated exonucleolytic cleavage processes. However, the mechanistic details of how XRN1 facilitates influenza A virus replication remain unclear. In this study, we discovered that XRN1 and nonstructural protein 1 (NS1) of IAV are directly associated and colocalize in the PBs. Moreover, XRN1 downregulation impaired viral replication while the viral titers were significantly increased in cells overexpressing XRN1, which suggest that XRN1 is a positive regulator in IAV life cycle. We further demonstrated that the IAV growth curve could be suppressed by adenosine 3',5'-bisphosphate (pAp) treatment, an inhibitor of XRN1. In virus-infected *XRN1* knockout cells, the phosphorylated interferon regulatory factor 3 (p-IRF3) protein, interferon beta (*IFN-β*) mRNA, and interferon-stimulated genes (ISGs) were significantly increased, resulting in the enhancement of the host innate immune response and suppression of viral protein production. Our data suggest a novel mechanism by which the IAV hijacks the cellular XRN1 to suppress the host innate immune response and to facilitate viral replication.

**IMPORTANCE** A novel mechanistic discovery reveals that the host decay factor XRN1 contributes to influenza A virus replication, which exploits XRN1 activity to inhibit RIG-I-mediated innate immune response. Here, we identified a novel interaction between viral NS1 and host XRN1. Knockdown and knockout of XRN1 expression in human cell lines significantly decreased virus replication while boosting RIG-I-mediated interferon immune response, suggesting that XRN1 facilitates influenza A virus replication. The pAp effect as XRN1 inhibitor was evaluated; we found that pAp was capable of suppressing viral growth. To our knowledge, this study shows for the first time that a negative-strand and nucleus-replicating RNA virus, as influenza A virus, can hijack cellular XRN1 to suppress the host RIG-I-dependent innate immune response. These findings provide new insights suggesting that host XRN1 plays a positive role in influenza A virus replication and that the inhibitor pAp may be used in novel antiviral drug development.

**KEYWORDS** influenza virus, 5'-3' mRNA degradation, XRN1, nonstructural protein 1, NS1, interferon beta, *IFN-β*, viral replication, innate immune response

**Citation** Liu Y-C, Mok BW-Y, Wang P, Kuo R-L, Chen H, Shih S-R. 2021. Cellular 5'-3' mRNA exoribonuclease XRN1 inhibits interferon beta activation and facilitates influenza A virus replication. *mBio* 12:e00945-21. <https://doi.org/10.1128/mBio.00945-21>.

**Editor** Kanta Subbarao, The Peter Doherty Institute for Infection and Immunity

**Copyright** © 2021 Liu et al. This is an open-access article distributed under the terms of the [Creative Commons Attribution 4.0 International license](https://creativecommons.org/licenses/by/4.0/).

Address correspondence to Honglin Chen, [hichen@hku.hk](mailto:hichen@hku.hk), or Shin-Ru Shih, [srshih@mail.cgu.edu.tw](mailto:srshih@mail.cgu.edu.tw).

**Received** 6 April 2021

**Accepted** 25 June 2021

**Published** 27 July 2021

Influenza A virus (IAV) causes seasonal epidemics and occasional pandemics, leading to considerable mobility and mortality worldwide. The World Health Organization

(WHO) estimates that annual epidemics of influenza result in ~1 billion infections, 3 to 5 million cases of severe illness, and 300,000 to 500,000 deaths (1–3). The emergence of a novel influenza virus remains a worldwide threat, and effective antiviral drugs and universal influenza virus vaccines to protect against new viral pandemics are lacking (4–6). Therefore, research focusing on virus-host interactions may provide valuable insights into the identification of new therapeutic targets for influenza (7).

The IAV nonstructural protein 1 (NS1), which is encoded by the NS gene segment and expressed in the cytoplasm and nuclei of infected cells, has multiple functions and plays a central role in regulating viral replication mechanisms, inhibiting host innate/adaptive immune responses, and enhancing viral mRNA translation and regulation of virus replication through NS1-host RNA and protein interactions (8–11). NS1 downregulates interferon (IFN) production by inhibiting interferon regulatory factor 3 (IRF3) activity and IFN transcription, as well as through suppression of IFN pre-mRNA processing (9). The interaction between NS1 and the E3 ligase tripartite motif-containing protein 25 (TRIM25), which results in the suppressed ubiquitylation and activation of retinoic acid-inducible gene I (RIG-I) (12, 13). A mutation in position 171 of the NS1 protein decreases the expression of IFN and IFN-stimulated genes (ISGs) (14). The RNA-binding domain (RBD) of the NS1 protein is required for interaction with host splicing regulator SF2 in the nucleus that modulates splicing of NS mRNAs during influenza virus replication (15). Our previously reported results suggest that NS1 interacts with cellular P-bodies (PBs) and stress granules (SGs) through RNA-associated protein 55 (RAP55) during H5N1 infection (16). In this research, we further discovered that IAV NS1 can directly associate with 5′-3′ exoribonuclease XRN1, which is the critical factor for degrading 5′-3′ mRNA in PBs.

PBs functions as a site of mRNA decay, specifically that involving the 5′-to-3′ mRNA decay pathway, which carries out cytoplasmic mRNA degradation in *Drosophila*, yeast, and mammals (17–19). The 5′-to-3′ mRNA decay process occurs following 3′ deadenylation, consisting of mRNA decapped by mRNA-decapping enzyme 2 (DCP2), and mRNA-decapping enzyme 1A (DCP1A). EDC4 acts as a scaffold to provide binding sites for DCP1A trimers at its N-terminal WD40 domain and for DCP2 and XRN1 at its C-terminal  $\alpha$ -helical domain. The decapped and 5′ monophosphate RNA is then degraded from the 5′ end by exoribonuclease XRN1 (20–23).

The antiviral activity of XRN1 and DCP1/2 aggregation against cytoplasmic RNA viruses, such as Newcastle disease virus (NDV) and encephalomyocarditis virus (EMCV), effectively prevented cell death (24). In infection with flaviviruses such as Zika, dengue, and West Nile virus, XRN1 is stalled and blocked from continuing degradation at the site of the viral mRNA 3′ untranslated region (3′-UTR) due to the presence of pseudo-knots or stem loops, which are referred as XRN1-resistant structures (xrRNAs). The secondary structure of these viral mRNAs inhibits XRN1 function, which prevents the degradation of viral mRNA and leads to subgenomic flavivirus RNA (sfRNA) production. XRN1 is stalled at the 5′-UTR due to binding of hsa-miR-122 at the seed sequence site and the presence of stem loops during *Flaviviridae* hepatitis C virus (HCV) infection (25–28). However, XRN1 can regulate double-stranded RNA (dsRNA) accumulation and dsRNA-responsive innate immune effectors in vaccinia virus (VacV)-infected cells (29). In addition, XRN1 is also involved in completing the degradation of host antiviral mRNAs following virus-induced endonucleolytic cleavage processes, thereby suppressing cellular gene expression and evading host antiviral innate immune defenses in herpesvirus (HHV), severe acute respiratory syndrome (SARS) coronavirus (SCoV), and IAV infection (30, 31). Here, we further found that the phosphorylated IRF3 (p-IRF3) significantly increased in IAV-infected XRN1-depleted cells. Thus, we think that XRN1 is also involved in the upstream events of IFN gene transcription.

The three members of the RIG-I-like receptor (RLR) family that recognize RNA and are IFN inducible, are retinoic acid-inducible gene I (RIG-I), melanoma differentiation factor 5 (MDA5), and laboratory of genetics and physiology 2 (LGP-2) (32). RIG-I and MDA5 distinguish different RNA viruses and are critical for type I interferon responses.

RIG-I preferentially senses 5′ triphosphorylated ssRNA (pppRNA) and short dsRNA whereas MDA5 recognizes long dsRNA (33, 34). In addition, RIG-I is a key mediator of interferon beta (IFN- $\beta$ ) production in response to IAV RNA viruses and is activated by viral genomic single-stranded RNA (ssRNA) bearing 5′-phosphates (35), whereas MDA5 is a significant contributor to host defense against influenza A virus (36). Both RIG-I and MDA5 have the N-terminal tandem caspase activation recruitment domain (2CARD), which can interact with mitochondrial antiviral signaling protein (MAVS) on mitochondria or peroxisomes to activate the downstream TBK1 induction and IRF3 phosphorylation. The phosphorylated IRF3 forms a dimer and translocates to the nucleus, activating the transcription of *IFN- $\beta$* , and then triggering the downstream gene expression of ISGs with antiviral functions (37–39). Our findings showed that host XRN1 expression was positively correlated with IAV replication and negatively associated with the expression of immune-related genes, resulting in the shutdown of host *IFN- $\beta$*  expression and advancement of viral replication, thus contributing to the pathogenesis of viral infection.

## RESULTS

**NS1 directly associates with the host XRN1 in the PBs.** We previously reported that the NS1 protein of IAV interacts with cellular PBs and SGs through RAP55 during viral infection (16). In this study, we further confirmed that NS1 can interact with proteins of the 5′-to-3′ mRNA degradation pathway, including XRN1, EDC4, DCP1A, DCP2, DDX6, and RAP55, but not with AGO2, as it does not belong to the 5′-to-3′ mRNA degradation complex. However, AGO2 is present in the PBs and can establish AGO-microRNA (miRNA) interactions and target the mRNAs of these structures (40). These interactions without RNA intermediary were detected by overexpressing multiple GFP fusion proteins as well as V5-NS1 in HEK293T cells and analyzing the cell lysates following RNase A treatment using coimmunoprecipitation (Co-IP) and Western blotting (WB) assays. The input samples, whole-cell lysates at 8% concentration, were analyzed to evaluate the presence of NS1 and P-body components (Fig. 1A). Therefore, XRN1, which is a critical 5′-to-3′ mRNA-degrading enzyme in the PBs, was selected for further studies. The interaction between XRN1 and NS1 was further verified in WSN-infected A549 cell lysates following RNase A treatment by Co-IP and WB assays with antibodies against endogenous XRN1 and viral NS1, respectively. The results of these assays suggested that endogenous XRN1 interacts with WSN NS1 between 4 to 8 h postinfection (h.p.i.), without the presence of an RNA intermediary (Fig. 1B).

There are three functional domains within cellular XRN1, including the catalytic domain (amino acids 1 to 1173 [aa 1–1173]), C-terminal domain (aa 1174–1649), and EDC4-binding motif (EDC4-BM) domain (aa 1650–1706). To identify the interacting domains of XRN1 and NS1, we constructed tags that were fused with GFP, for various truncated forms of XRN1, and the fragments of XRN1 were cloned separately from each functional domain. Plasmids were transfected into HEK293T cells, followed by anti-GFP immunoprecipitation (IP) and WB assays. This mapping study revealed that the full-length XRN1 and the C-terminal region (aa 1174–1706) containing the C-terminal and EDC4-BM domains of XRN1 interacted with full-length NS1 in an RNA binding-independent manner (Fig. 1C). We next used an *in vitro* pulldown assay to assay whether the interaction between XRN1 and NS1 was direct. Purified His<sup>+</sup>-NS1 from various viruses WSN, PR8, CA04, and the GST-XRN1-C-terminal region fusion proteins were mixed and subjected to glutathione S-transferase (GST) pulldown and WB assays. The result revealed that the NS1 protein directly associates with the C-terminal region of XRN1 (Fig. 1D). These results suggest that NS1 directly associates with the C-terminal region of cellular XRN1 in the PBs.

**NS1 assembles and colocalizes with XRN1 in the cellular cytoplasm at 6 and 8 h.p.i.** We further examined the distribution of cellular XRN1 and viral NS1 in virus-infected cells. The localization of NS1 and XRN1 in A549 cells during a time course of WSN infection was studied using anti-XRN1 (green color), anti-NS1 (red color), and anti-DCP1A (purple color) antibodies in an immunofluorescence assay (IFA) by confocal

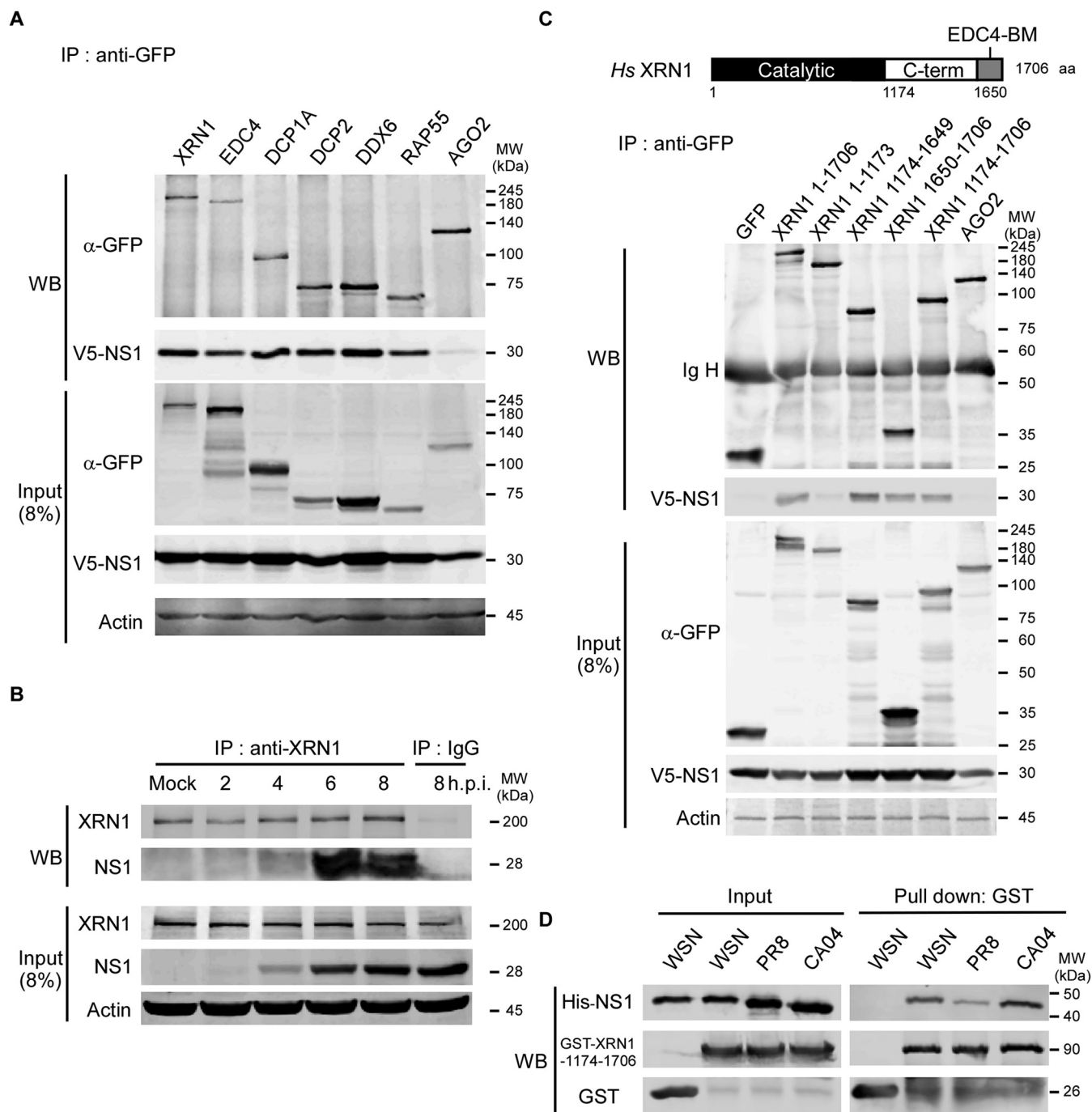


**FIG 1** NS1 directly associates with the cytoplasmic protein XRN1. (A) NS1 interacts with the components of 5'-to-3' mRNA decay factors in PBs, including XRN1, EDC4, DCP1A, DCP2, DDX6, and RAP55. HEK293T cells were transfected with plasmids encoding WSN V5-NS1, as well as cellular GFP-XRN1, EDC4, DCP1A, DDX6, RAP55, and AGO2. At 48 h after transfection, the lysates were treated with RNase A (10  $\mu$ g/ml) and immunoprecipitated (IP) with antibodies against GFP ( $\alpha$ -GFP). The components of P-bodies that interacted with NS1 were detected by Western blotting (WB) using an antibody against V5. The input samples were verified in the presence of NS1 and the components of the P-bodies in the lysates. Actin served as an internal control. The positions of molecular weight (MW) markers (in kilodaltons) are shown to the right of the gel. (B) Endogenous XRN1 associates with NS1 in virus-infected cells. The lysates harvested from A549 cells that were mock infected or infected with WSN at an MOI of 2 at various times postinfection (2 to 8 h.p.i.) were treated with RNase A (10  $\mu$ g/ml) and immunoprecipitated using an anti-XRN1 antibody and an anti-IgG antibody as a negative control. Then, the interacting NS1 constructs were detected by a WB assay. (C) NS1 associates with the C-terminal region of XRN1 containing the C-terminal domain (amino acids 1174 to 1649 [aa 1174–1649]) and EDC4-BM domain (aa 1650–1706). The functional domain architecture of human (*Homo sapiens* [Hs]) XRN1 is shown at the top of panel C. HEK293T cells were transfected with plasmids encoding V5-NS1, various truncated forms of GFP-XRN1, and GFP. At 48 h after transfection, the lysates were treated with RNase A (10  $\mu$ g/ml) and immunoprecipitated with antibodies against GFP. The bound NS1 was detected by WB using an antibody against V5. GFP served as a negative control. (D) The association between XRN1 and WSN NS1 is direct without RNA or protein intermediary. In the *in vitro* GST pull-down and WB assay, a total of 5  $\mu$ g of bacterially purified His<sup>+</sup>-NS1 from WSN, PR8, or CA04 was mixed with the GST-XRN1-C-terminal region (aa 1174–1706) fusion protein, followed by WB with anti-His and anti-GST.



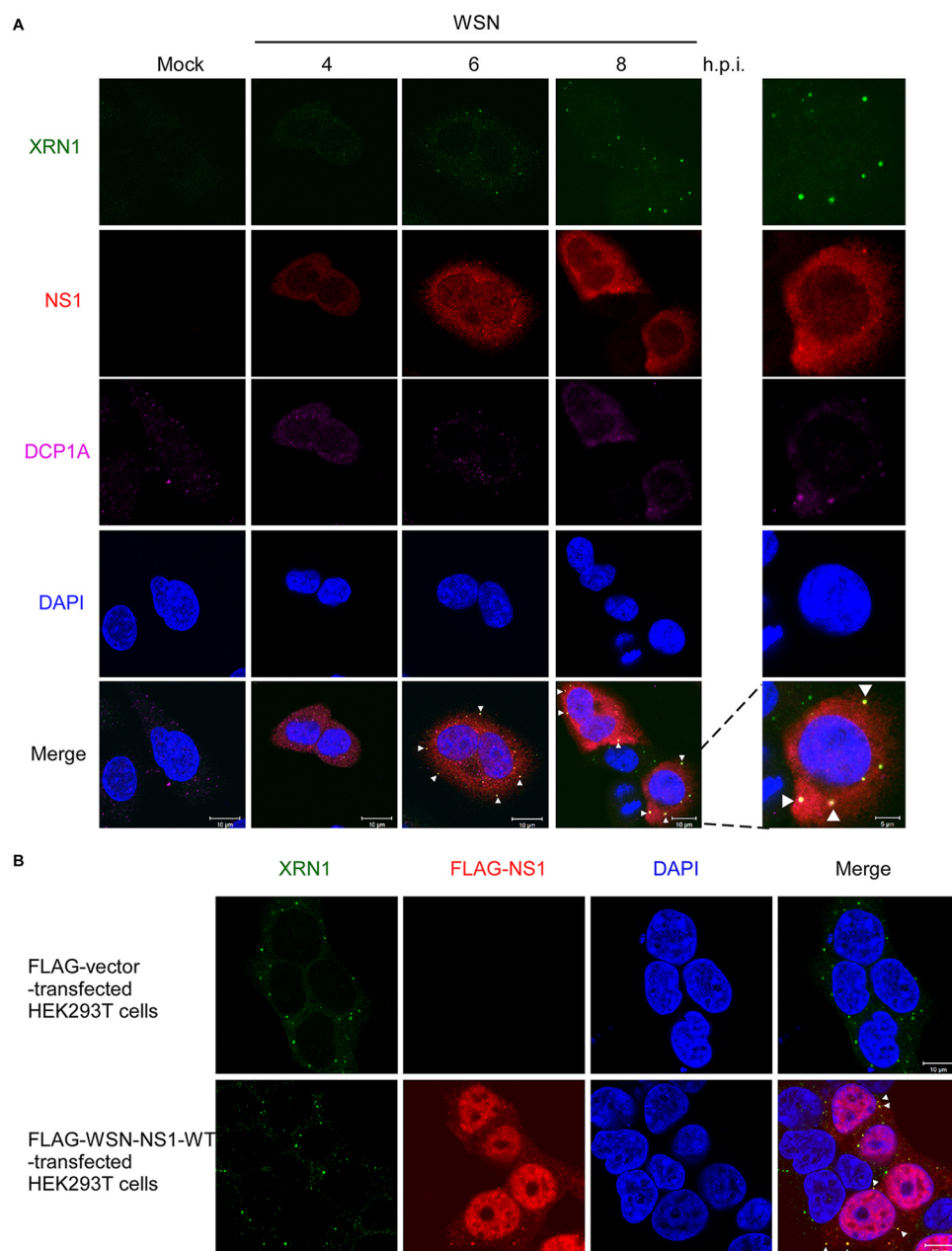


**FIG 2** WSN NS1 and XRN1 colocalize in the cytosol at 6 and 8 h.p.i. (A) The WSN NS1-XRN1 association is localized in the cytosol at 6 and 8 h.p.i. Mock-infected A549 cells or A549 cells infected with WSN at an MOI of 2 were fixed and stained using antibodies against XRN1 (green color), WSN NS1 (red color), and DCP1A (purple color) at 4, 6, and 8 h.p.i. The nuclei of A549 cells were stained with DAPI (blue color), and the merged images show the NS1 and XRN1 immunofluorescence signals. All immunofluorescence images were detected by confocal microscopy. Bars, 5 and 10  $\mu$ m. (B) Endogenous XRN1 colocalizes with FLAG-WSN-NS1 in the cytoplasm. HEK293T cells were transfected with a plasmid expressing FLAG-NS1 for 48 h and then stained using antibodies against FLAG (red color) and against endogenous XRN1 (green color). The nuclei were stained with DAPI dye (blue color). Bars, 10  $\mu$ m.

microscopy. DCP1A was used as a biomarker for the PBs (Fig. 2A). The confocal images showed that XRN1, NS1, and DCP1A were mostly located in the cytoplasm at 4, 6, and 8 h.p.i. In addition, XRN1 and NS1 accumulation and colocalization were detected in the merged images at 6 and 8 h.p.i as yellow dots (Fig. 2A, white arrowheads).

HEK293T cells were then transfected with FLAG-tagged NS1 (FLAG-NS1), and the resulting fluorescence was detected with an anti-FLAG antibody (green color) by IFA and confocal microscopy. The overexpressed FLAG-NS1 with the nuclear localization

sequence was partially expressed in the nucleus, whereas the FLAG-NS1 was also expressed and accumulated with the endogenous XRN1 in the cytoplasm (Fig. 2B). Colocalization of endogenous XRN1 and FLAG-NS1 was detected in the cytoplasm of HEK293T cells, it can be observed as yellow dots in the merged images of Fig. 2B (white arrowheads). These results indicated that cellular endogenous XRN1 colocalized with the IAV NS1 in infected cells and then assembled and accumulated in the cytoplasm to form the observed dots from 6 to 8 h.p.i.

**XRN1 contributes to IAV replication in human cells.** We sought to investigate the impact of XRN1 on the replication of influenza A viruses in human cells. Therefore, we used the CRISPR-Cas9 system to generate a stable human A549 XRN1 knockout cell line. The *XRN1* guide RNA (gRNA) sequence (GTATCCCTGTCTCAGCGAAG) targeted the complementary sequence of *XRN1* genomic DNA from 157 to 176 bp before the protospacer adjacent motif (TGG, 177 to 179 bp). *XRN1* genomic DNA with a five-nucleotide deletion (GAAGT, 173 to 177 bp) was expressed in A549 XRN1 knockout (KO) cells as well as A549 control cells (Fig. 3A). A549 XRN1 KO cells were used for viral growth kinetic studies and infected at a multiplicity of infection (MOI) of 0.01 in a multicycle experiment. The viral titer of A549 XRN1 KO cells decreased significantly compared with control cells at 24 to 72 h postinfection. Thus, XRN1 functions as a positive regulator in the WSN-infected A549 cells (Fig. 3B). Moreover, A549 cells were treated with negative-control (NC) small interfering RNA (siRNA) and XRN1 siRNA (siXRN1-1, siXRN1-2) to knock down *XRN1*, and then, the cells were infected with WSN at an MOI of 0.01. Consistent with the *XRN1* knockout results, the growth curves of siXRN1-1 and siXRN1-2 showed a decrease compared with A549 cells in multicycle experiments (Fig. 3C). HEK293T cells were treated with the FLAG-tagged vector or FLAG-tagged XRN1 (FLAG-XRN1) plasmid as a negative control as well as with full-length XRN1 expressed, then infected with WSN in a time course of 12, 24, 36, and 48 h. The data revealed that over-expressed FLAG-XRN1 resulted in a significant increase in viral titer compared with the FLAG-tagged vector (Fig. 3D).

We also measured the expression levels of viral proteins in A549 XRN1 knockdown and control cells. The siNC, siXRN1-1, and siXRN1-2 were transfected into A549 cells, followed by WSN infection. Viral NS1 and M1 protein expression yielded a lower signal in siXRN1-1 and siXRN1-2 infected cells at 8 h.p.i. (Fig. 3E). Therefore, our findings suggest that cellular XRN1 is essential for positive regulation of viral growth curves and viral protein expression.

**IAV titers decrease after inhibition of cellular XRN1 with adenosine 3', 5'-bisphosphate.** Since previous studies have revealed that adenosine 3',5'-bisphosphate (pAp) can inhibit the 5'-to-3' exonuclease activity of XRN1 (41, 42), we tested whether pAp was able to affect IAV replication by blocking the exonuclease function of XRN1. First, we evaluated the viability and cytotoxicity of pAp in A549 cells with the 3-(4,5-dimethylthiazol-2-yl)-2,5-diphenyltetrazolium bromide (MTT) assay. We found that 1 to 4 mM pAp treatment did not affect cellular viability and that the 50% cytotoxic concentration (CC50) was 6.06 mM (Fig. 4A). Then, we performed a time of addition assay to assess the effect of pAp on influenza virus replication. A549 cells were pretreated with pAp (4 mM) 2, 1, or 0 days before infection with WSN strain at an MOI of 0.01, and the viral supernatant was harvested at 48-h time points postinfection. The results revealed that pAp inhibited virus yields more effectively when it was applied 2 days before virus infection. XRN1 KO cells were treated with pAp to evaluate the occurrence of nonspecific effects on viral replication in the absence of XRN1 (Fig. 4B). We pretreated A549 cells with 1, 2, 3, or 4 mM pAp for 2 days and infected them with WSN (H1N1), PR8 (H1N1), CA04 (H1N1), or HK4801 (H3N2) during 48 h, and after incubation, the culture supernatants were harvested for plaque assay analysis. All conditions exhibited dose-dependent reductions in virus plaque formation after treatment with 3 and 4 mM concentrations of the XRN1 inhibitor pAp (Fig. 4C), indicating that the XRN1 inhibitor pAp can inhibit the replication of different influenza strains. In addition, A549 cells that had been pretreated with 4 mM pAp for 2 days were infected with WSN or exposed to synthetic polyinosinic-polycytidylic acid [poly(I:C)] dsRNA for 4, 6, and 8 h, and mRNA expression of *IFN-β* was detected by

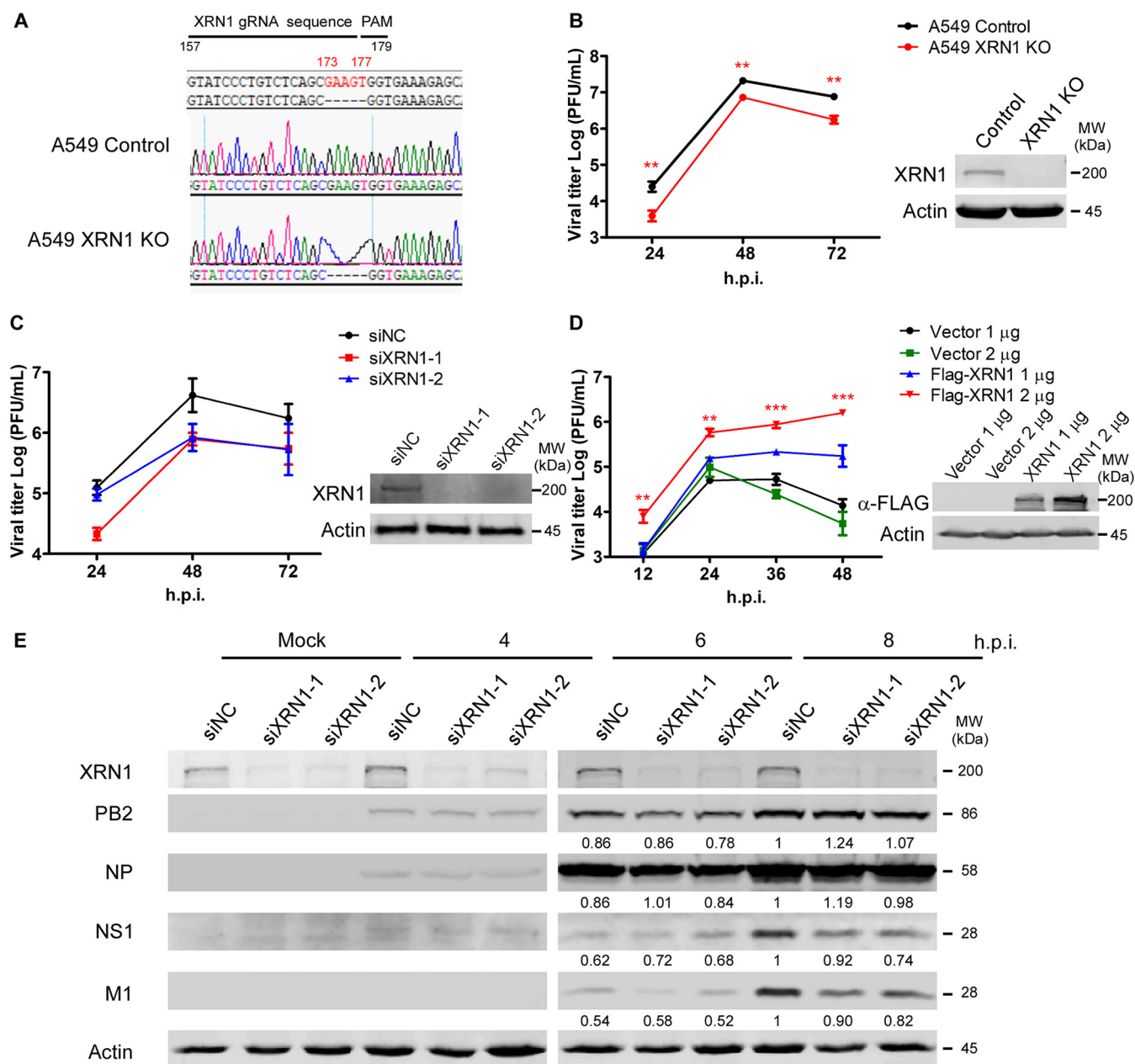


**FIG 3** XRN1 functions as a positive regulator of IAV replication. (A) The genomic DNA sequence of human A549 control cells and *XRN1* knockout cells. There are five genomic nucleotides (GAAGT, 173 to 177 bp) deleted in *XRN1* knockout A549 cells. PAM, protospacer adjacent motif. (B) The viral growth curve is decreased in *XRN1* knockout cells. The growth kinetics of WSN viruses were determined at an MOI of 0.01 for multicycle infections of human A549 control cells and *XRN1* knockout cells. The viral supernatants were harvested at 24, 48, and 72 h.p.i., and the viral titers were detected by plaque assay. Values are shown as means  $\pm$  standard deviations (SD) (error bars) ( $n=3$ ). Statistical significance was analyzed using a  $t$  test and indicated as follows: \*\*,  $P < 0.01$ . The XRN1 protein expression level was assessed by WB assay. (C) Viral titer is decreased in XRN1 knockdown cells. A549 cells were transfected with siRNA to knock down XRN1 for 72 h and then infected with WSN viruses at an MOI of 0.01 for multicycle infections. The viral titers were detected at 24, 48, and 72 h.p.i. by plaque assay, and the transfection efficiency was assessed by WB. The viral growth curve was constructed with data from two independent plaque assays ( $n=2$ ). (D) Overexpressed FLAG-full length-XRN1 protein in HEK293T cells enhances the viral growth curve. HEK293T cells were treated with various quantities of FLAG-tagged vector (FLAG-Vector) or FLAG-XRN1 for 48 h, then infected with WSN viruses at an MOI of 0.01. At 24, 48, and 72 h.p.i., the viral titers for the multicycle infections were detected by plaque assay, and the transfection efficiency was assessed by WB. Two micrograms of overexpressed FLAG-XRN1 was compared with 2  $\mu$ g of FLAG-Vector. Values are shown as means  $\pm$  standard deviations (SD) (error bars) ( $n=3$ ). Statistical significance was analyzed using a  $t$  test and indicated as follows: \*\*\*,  $P < 0.001$ ; \*\*,  $P < 0.01$ . (E) Viral NS1 and M1 proteins are reduced by XRN1 knockdown of A549 cells. A549 cells were transfected with siNC as a negative control and with XRN1-specific siRNA (siXRN1-1 and -2) on 3 days. After WSN infection at an MOI of 2 at 4, 6, and 8 h, the viral proteins were isolated and detected using specific antibodies. Virus protein levels were quantified with the AlphaEase FC software, and the values were normalized against actin expression.

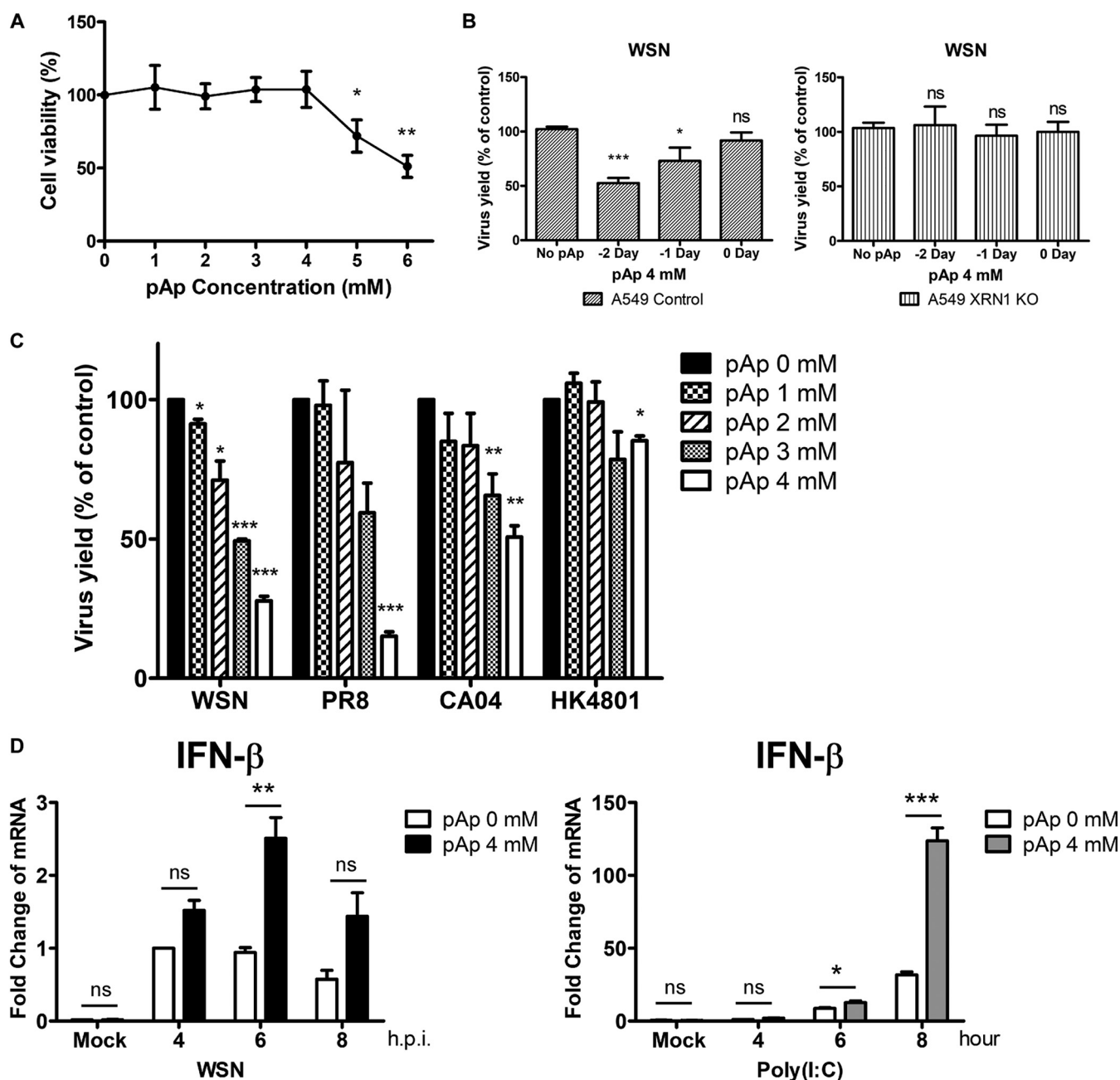


**FIG 4** The pAp inhibits viral replication in a broad range of influenza virus strains. (A) Viability of A549 cells after pAp treatment. A549 cells were treated with pAp in a dose-dependent manner for 3 days. We then used MTT assay to measure the cellular viability and cytotoxicity. (B) The pAp disrupts viral replication most effectively for 2 days treatment before viral infection. A549 cells or XRN1 KO cells were pretreated with 4 mM pAp 2, 1, and 0 days before WSN infection at an MOI of 0.01. The viral supernatants were harvested, and viral titers were determined by plaque assay. (C) The pAp reduces the IAV replication in a dose-dependent manner. A549 cells were pretreated with pAp for 2 days and then infected with the influenza virus strains A/WSN/33 (H1N1), A/Puerto Rico/8/34 (H1N1), A/California/04/2009 (H1N1), and A/Hong Kong/4801/2014 (H3N2). Virus yields were determined by plaque assay and reported as a percentage of the value for untreated controls. All exhibited dose-dependent reductions in virus plaque formation after treatment with 1, 2, 3, and 4 mM pAp. (D) A549 cells were pretreated with 4 mM pAp for 2 days and infected with WSN for 4, 6, and 8 h (left panel) or treated with poly(I:C) during 4, 6, and 8 h (right panel). The mRNAs levels of *IFN-β* were detected by RT-qPCR. Data represent the means  $\pm$  SD of three independent experiments. Statistical significance was determined by a *t* test and indicated as follows: \*\*\*,  $P < 0.001$ ; \*\*,  $P < 0.01$ ; \*,  $P < 0.05$ ; ns, not significant.

reverse transcription-quantitative PCR (RT-qPCR) (Fig. 4D). *IFN-β* levels significantly increased in pAp-treated A549 cells infected with WSN or exposed to poly(I:C), suggesting that pAp directly affects *IFN-β* induction, and not WSN infection *per se*. These results further demonstrate that loss of XRN1 activity in the pAp-treated cells results in the inhibition of IAV replication and upregulation of *IFN-β* mRNA levels.



### **XRN1 contributes to effective IAV inhibition of host immune responses.**

Considering that XRN1 inhibitor pAp contributes to the induction and upregulation of *IFN- $\beta$* , we further investigated the effect of *XRN1* KO cells on the induction of *IFN* and *ISGs*. A549 control and *XRN1* KO cells were infected with WSN at an MOI of 2 for 4, 6, and 8 h, and the mRNA expression levels of different cytokines, including *IFN- $\beta$* , *IFIT1*, *IFIT3*, *ISG15*, *IRF3*, *IRF7*, and *NF- $\kappa$ B* were measured by RT-qPCR. The A549 cells lacking the XRN1 protein showed increased *IFN- $\beta$* , *IFIT1*, *IFIT3*, and *ISG15* expression compared with the A549 control cells at 4 to 8 h after WSN infection (Fig. 5A). We found that mock-infected cells showed the lowest levels of *IFN* and *ISG* expression and that *IFN* and *ISG* basal levels did not increase in XRN1 knockout cells or pAp-treated cells (Fig. 5A and 4D). In addition, we transfected HEK293T cells with the FLAG-XRN1 plasmid and observed that XRN1 overexpression repressed the expression of innate response-related genes, such as *IFNB*, *IFIT1*, *IFIT3*, and *ISG15* in early stages of infection, 4 to 6 h.p.i. Moreover, at 8 h.p.i., the expression of these genes, in vector- or FLAG-XRN1-transfected cells was inhibited due to viral resistance (see Fig. S2A and B in the supplemental material).

We then investigated whether the increased mRNA expression levels of host innate immune cytokines were influenced by the virus. We detected the viral mRNA expression levels of PB2, NP, M, and NS1 in WSN-infected A549 control and *XRN1* KO cells at 4, 6, and 8 h. The levels of viral PB2, NP, M, and NS1 mRNA in A549 *XRN1* KO cells were not significantly different than those in A549 control cells after statistical analysis, but the fold change of M mRNA decreased from 87.87- to 54.69-fold, and that of NS1 mRNA decreased from 81.96- to 67.17-fold in XRN1 KO cells at 8 h postinfection (Fig. 5B). We used another A549 *XRN1* knockout cell line as well as a control cell line, which were gifts from the NIH (43). We obtained consistent results when using the NIH A549 control and NIH A549 *XRN1* KO cell lines, which showed that the levels of mRNAs of the innate immune response were increased (see Fig. S1A to C in the supplemental material). There was higher expression of *IFN- $\beta$* , *IFIT1*, *IFIT3*, *ISG15*, and *IRF7* mRNA in A549 *XRN1* KO cells after 8 h of infection with various virus strains, including WSN (H1N1), PR8 (H1N1), CA04 (H1N1), and HK4801 (H3N2). However, the mRNA levels of *IRF3* and *NF- $\kappa$ B* were similar to those observed in the control cells (Fig. 5C). We discovered that *IFN- $\beta$* , *IFIT1*, *IFIT3*, and *ISG15* mRNA expression is upregulated in XRN1-KO cells infected with various IAV strains.

**RIG-I-mediated signaling remains functional in XRN1-KO cells.** Since the expression of *IFN- $\beta$*  and downstream *ISG* genes was higher in XRN1-deficient cells than in A549 control cells after IAV infection, we now investigated whether XRN1 plays a role in the early steps of type I *IFN* (*IFN-I*) signaling cascade. We measured the protein levels of the upstream protein, phosphorylated *IRF3* (p-*IRF3*), which is a critical transcription factor promoting type I interferon expression. Significant upregulation was observed for p-*IRF3* in WSN-infected A549 *XRN1* KO cells compared with A549 control cells (Fig. 6A). To determine whether XRN1 affected *IRF3* phosphorylation and *IFN- $\beta$*  induction in IAV viral RNA (vRNA)-induced type I interferon immune system, the total WSN vRNA from supernatant of infected cells was prepared and transfected in XRN1-KO cells. The XRN1-KO cells were transfected with cellular RNA as a negative control, whereas poly(I:C), a synthetic analog of dsRNA, was used as a RIG-I and MDA5 agonist. The results showed that *IRF3* was activated by WSN vRNA and that p-*IRF3* was increased in WSN vRNA-transfected XRN1-KO cells compared to A549 controls, suggesting that XRN1 inhibits the vRNA-induced *IRF3* activation (Fig. 6B). It is known that the viral RNA sensors RIG-I and MDA5 are key mediators for *IFN- $\beta$*  production in response to RNA viruses. To verify whether RIG-I and MDA5 are still functional in XRN1-KO cells infected with IAV, *IFN- $\beta$*  mRNA levels were quantified in the XRN1-KO cells knocked down for RIG-I and MDA5 endogenous expression, respectively. We found that knockdown of RIG-I or MDA5 in XRN1-depleted cells does not induce *IFN- $\beta$*  mRNA production during IAV infection (Fig. 6C). These results suggest that IAV hijacks the cellular XRN1 to suppress host type I *IFN* signaling pathway.

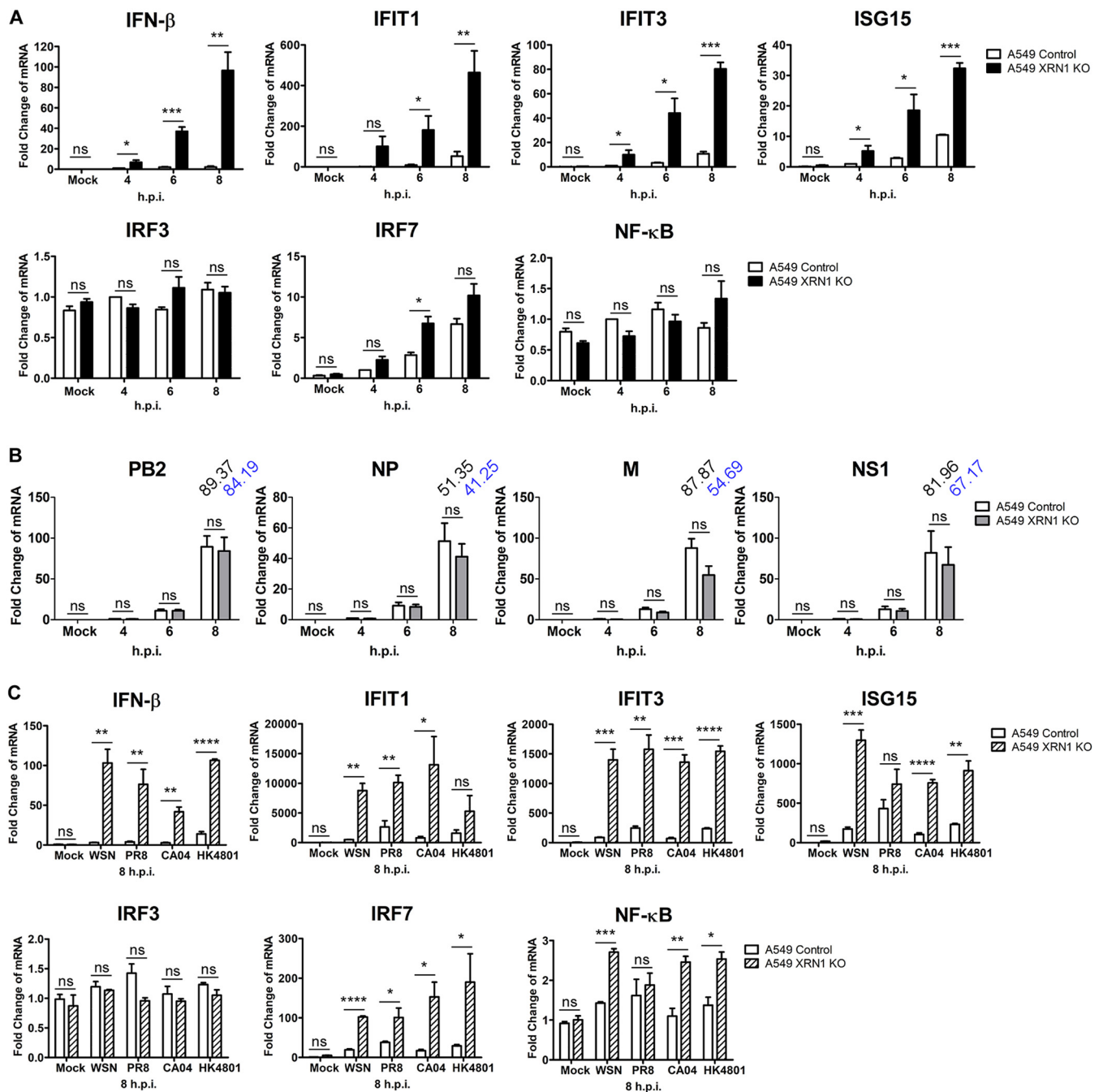


**FIG 5** XRN1 contributes to reducing the innate immune system. (A) Virus heavily elicits cellular mRNAs of the innate immune response in *XRN1* knockout A549 cells. RNAs were isolated from WSN-infected control and *XRN1* knockout A549 cells at 4 to 8 h.p.i. and evaluated using specific primers for *IFN- $\beta$* , *IFIT1*, *IFIT3*, *ISG15*, *IRF3*, *IRF7*, and *NF- $\kappa$ B* by RT-qPCR. All assays were performed and repeated three times. The fold changes in the amount of mRNA were calculated. (B) The level of viral mRNA in WSN-infected A549 control cells and *XRN1* knockout A549 cells. RNAs were isolated from WSN-infected control and *XRN1* knockout A549 cells at 4, 6, and 8 h and evaluated with specific primers for viral PB2, NP, M, and NS1 by RT-qPCR. The fold changes in the amount of mRNA were calculated. (C) There are significantly increased levels of *IFN- $\beta$* , *IFIT1*, *IFIT3*, and *ISG15* mRNA in *XRN1* KO cells infected with certain IAV constructs. The A549 control and *XRN1* knockout cells were infected with various IAV constructs, including A/WSN/33 (H1N1), A/Puerto Rico/8/34 (H1N1), A/California/04/2009 (H1N1), and A/Hong Kong/4801/2014 (H3N2), at an MOI of 2 for 8 h. Levels of cellular mRNAs were measured by RT-qPCR. Data represent means plus standard errors of the means of three independent experiments. Statistical significance was determined by a *t* test and indicated as follows: \*\*\*,  $P < 0.001$ ; \*\*,  $P < 0.01$ ; \*,  $P < 0.05$ ; ns, not significant.

**The coexistence of IAV NS1 and host XRN1 enhances the efficiency in inhibiting the antiviral immune response.** The NS1 protein of IAV inhibits host IFN responses by binding to viral vRNA, RIG-I, MAVS, and TBK1, which are required for RIG-I activation (9, 44). As the above results indicated that IAV NS1 directly associate with XRN1 (Fig. 1),

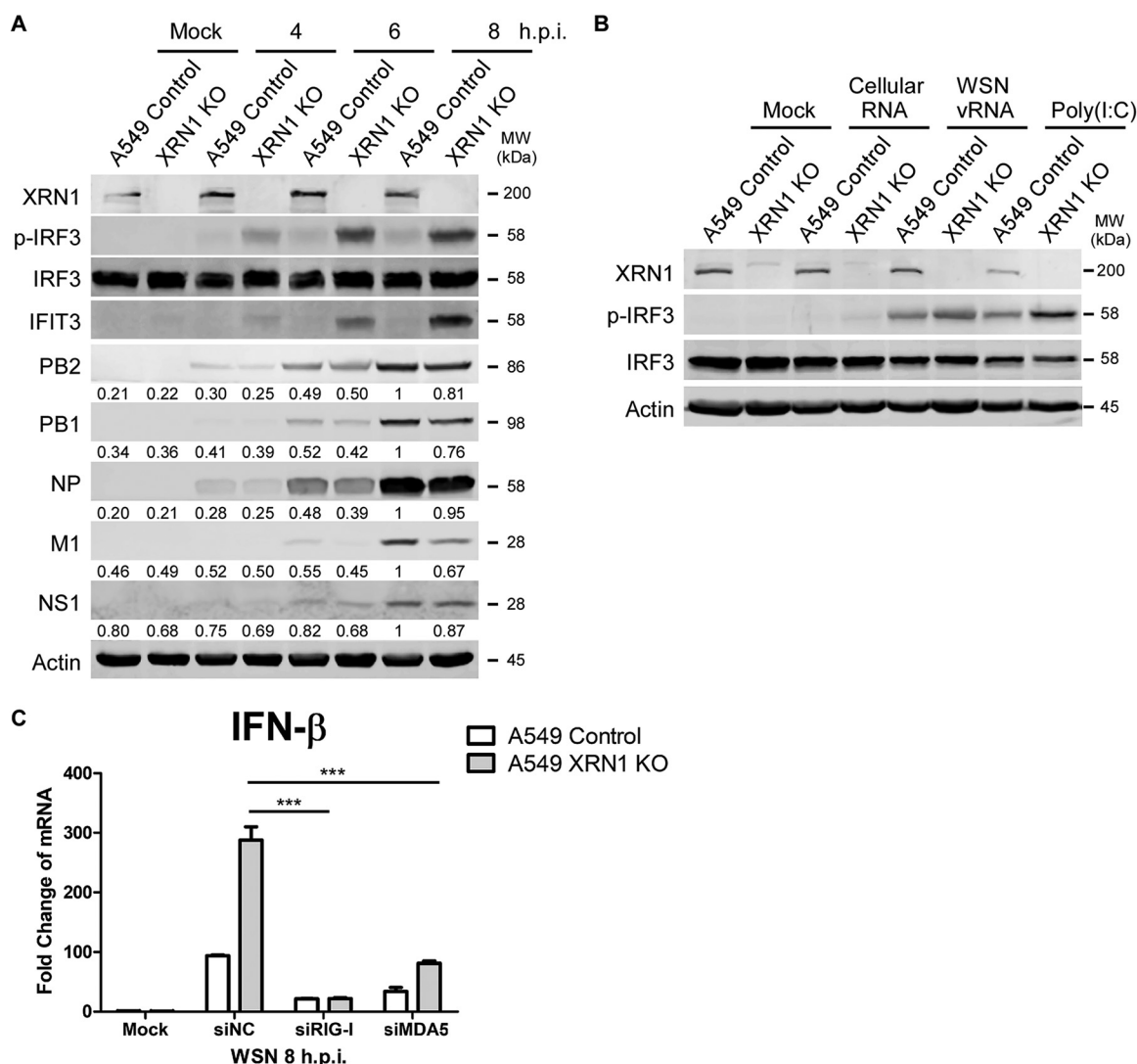


**FIG 6** Cellular XRN1 suppresses IAV vRNA-induced IRF3 activation and IFN- $\beta$  induction through RIG-I-mediated signaling pathway. (A) Host antiviral proteins activate and increase in A549 XRN1 knockout WSN-infected cells. Cellular and viral proteins were harvested from WSN-infected control and XRN1 knockout A549 cells at 4 to 8 h.p.i. and identified with the specific antibody for XRN1, p-IRF3, IRF3, IFIT3, PB2, PB1, NP, M, NS1, and actin by WB assay. Virus protein levels were quantified with the AlphaEase FC software, and the values were normalized against actin expression. (B) XRN1 has an impact on the influenza A virus vRNA-induced IRF3 activity and IFN- $\beta$  induction. A549 control or XRN1-KO cells were transfected with 2  $\mu$ g of total cellular RNAs, 2  $\mu$ g vRNAs, and 1  $\mu$ g poly(I:C) using Lipofectamine 2000 for 8 h. The cell lysates were harvested, and proteins were identified by WB assay. (C) A549 control and XRN1 KO cells were transfected with siRNA against RIG-I or MDA5 for 48 h, followed by infection with WSN for 8 h. The IFN- $\beta$  mRNA levels were detected through RT-qPCR. Statistical significance was determined by a *t* test and indicated as follows: \*\*\*, *P* < 0.001.

we investigated whether IAV NS1 is involved in XRN1-mediated suppression of the immune response. The A549 control and A549 XRN1 knockout cells were infected with Sendai virus. Phospho-IRF3 and the IFN- $\beta$  mRNA were detected at 4 h.p.i. We found that XRN1 knockout led to increased expression of p-IRF3 and the mRNA of IFN- $\beta$  compared with Sendai virus-infected A549 control cells (Fig. 7A and B). In a previous article, we reported that M-A14U substitution affects the splicing of M transcripts during viral replication and that M2 expression remains unchanged but M1 levels significantly decrease in DelNS1-M-A14U infection compared to wild-type WSN (WSN-WT) (45). We also determined that, despite lacking NS1, DelNS1-M-A14U viruses were able to replicate by modulating the alternative splicing of M mRNAs and that they cannot inhibit interferon expression in infected cells (45). Therefore, here we used the DelNS1-M-A14U viral model to study the innate immune response in the absence of the NS1

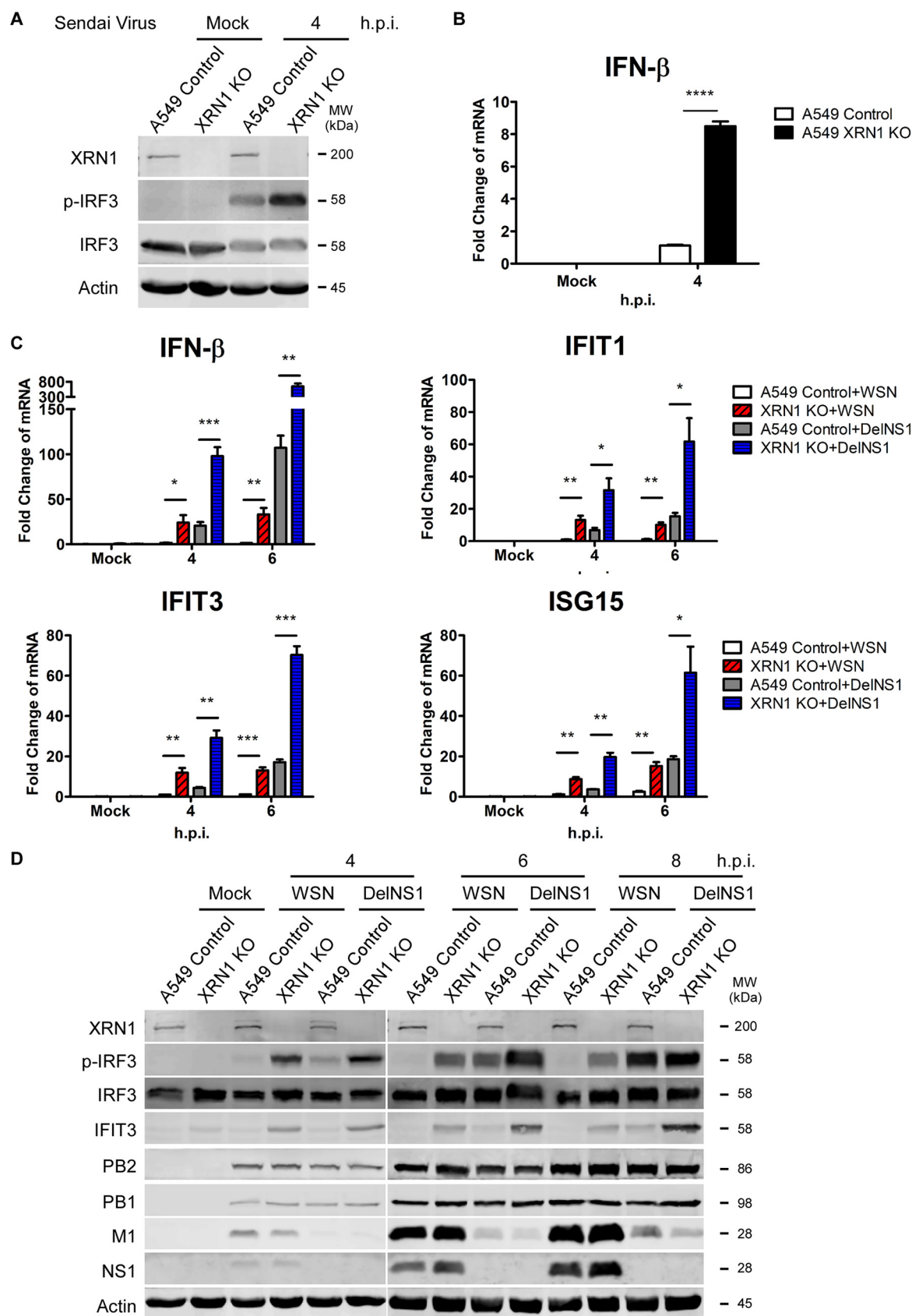


**FIG 7** The coexistence of IAV NS1 and host XRN1 enhances the efficiency in blocking type I IFN response. (A) The Sendai virus also induces IRF3 activity and a higher expression ratio in *XRN1* KO cells compared with A549 control cells. Cellular and viral proteins were (Continued on next page)



protein. We compared IFN- $\beta$ -related host antiviral response during infection of WSN and WSN DelNS1-M-A14U (WSN DelNS1) viruses in the A549 control and A549 XRN1-KO cells. The mRNA expression of *IFN- $\beta$* , *IFIT1*, *IFIT3*, and *ISG15* antiviral genes was significantly higher in WSN DelNS1-infected XRN1 KO cells at 4 and 6 h.p.i. (Fig. 7C). Consistently, the protein levels of p-IRF3 and IFIT3 showed significantly higher expression in WSN DelNS1-infected XRN1 KO cells at 6 and 8 h.p.i. (Fig. 7D). These data indicate that the coexistence of IAV NS1 and host XRN1 causes synergistic effects and enhances the efficiency in suppressing the RIG-I-mediated IRF3 activity and IFN- $\beta$  production.

## DISCUSSION

The NS1 protein of influenza virus plays an important role in viral replication, pathogenicity, and inhibition of innate immunity by multiple mechanisms. Notably, NS1 dramatically inhibits cellular gene expression and prevents the activation of key players in the IFN system through protein-protein interactions (44, 46). A schematic model is provided in Fig. 8. Our study uncovered a novel mechanism for influenza virus NS1 invasion of host cells involving its direct association with exoribonuclease XRN1 protein. The decay factor XRN1 contributes to influenza A virus replication and suppression of innate immune response, as this exoribonuclease inhibits IAV vRNA-induced type I interferon response, which results in the inhibition of IRF3 activation, IFN- $\beta$  induction, and downstream ISG gene expression. In this study, we identified six components of PBs, including XRN1, EDC4, DCP1A, DCP2, DDX6, and RAP55, that could associate with NS1 without the use of an RNA intermediary (Fig. 1A). Then, we selected the exoribonuclease protein XRN1, which occupies a central position in the 5'-to-3' mRNA decay complexes of PBs, for further analysis and confirmed the interaction between endogenous XRN1 and WSN NS1 without the intermediation of RNA (Fig. 1B and D). Furthermore, we further demonstrated that NS1 associates with the C-terminal region (aa 1174–1706) of XRN1 containing the C-terminal and EDC4-BM domains by overexpressing various truncated forms of XRN1 (Fig. 1C). Moreover, the assessment of NS1-XRN1 direct interaction was based on *in vitro* pulldown assays (Fig. 1D). We also observed that NS1 and XRN1 colocalized and accumulated with DCP1A in the PBs, which are distinct foci within the cytoplasm. This was easiest to observe at 6 and 8 h.p.i. in WSN-infected cells, as the NS1-XRN1 interaction was maintained between 4 and 8 h.p.i. (Fig. 2A and 1B). Moreover, the colocalization of endogenous XRN1 and FLAG-NS1 was detected in the cytoplasm of HEK293T cell through confocal microscopy (Fig. 2B), and the interaction without an RNA intermediary was detected using Co-IP (see Fig. S5A in the supplemental material). These results suggest that this interaction, aggregation, and accumulation between NS1 and XRN1 may provide advantages for the viral life cycle.

The data revealed that viral M1 and NS1 proteins decreased under knockdown of XRN1 (Fig. 3E) and knockout of XRN1 (Fig. 6A) at 8 h postinfection by using software normalized with the actin levels. In Fig. 5B, the decreased mRNA levels did not differ significantly after statistical analysis; however, the fold change of M mRNA decreased from 87.87- to 54.69-fold, and that of NS1 mRNA decreased from 81.96- to 67.17-fold in

### FIG 7 Legend (Continued)

harvested from Sendai virus-infected A549 control and XRN1 KO cells at 4 h.p.i. and identified with the specific antibody for XRN1, phospho-IRF3, IRF3, and actin by WB assay. (B) *IFN- $\beta$*  mRNA significantly increases in XRN1 knockout A549 cells infected with Sendai virus. RNA was isolated from Sendai virus-infected control and XRN1 knockout A549 cells at 4 h.p.i., and *IFN- $\beta$*  levels were determined by RT-qPCR. Gene expression was calculated as fold change comparing mRNA expression of XRN1 KO cells against that of A549 control cells. \*\*\*\*,  $P < 0.0001$ . (C) Gene expression of innate immunity-related genes in XRN1 knockout and control A549 cells after wild-type (WT) WSN or WSN DelNS1 infection. RNAs were isolated from WT WSN- or WSN DelNS1-infected A549 control and XRN1 KO cells at 4 to 6 h.p.i. and evaluated with specific primers for *IFN- $\beta$* , *IFIT1*, *IFIT3*, and *ISG15* by RT-qPCR. Data represent means plus standard errors of the means of three independent experiments. Statistical significance was determined by a *t* test and indicated as follows: \*\*\*,  $P < 0.001$ ; \*\*,  $P < 0.01$ ; \*,  $P < 0.05$ . (D) The protein expression of p-IRF3 and IFIT3 in WT WSN- and WSN DelNS1-infected cells. The cellular and viral proteins were harvested from WT WSN- or WSN DelNS1-infected control and XRN1 knockout A549 cells at 4 to 8 h.p.i. and identified with specific antibodies for XRN1, p-IRF3, IRF3, IFIT3, PB2, PB1, M1, NS1, and actin by WB assay.

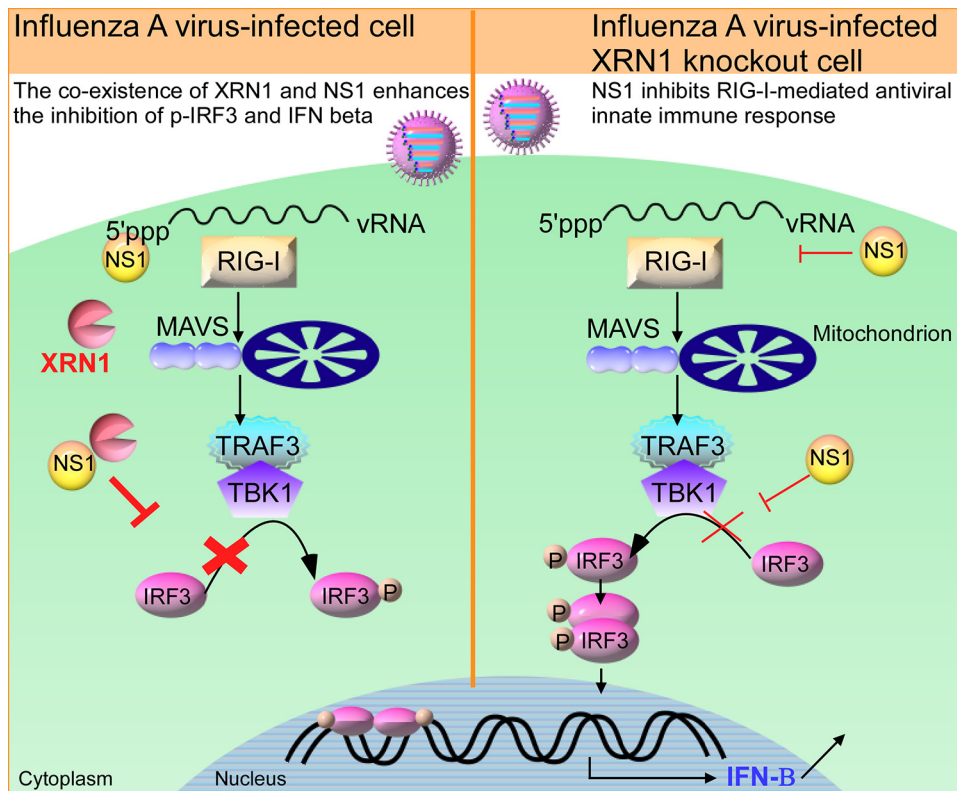


**FIG 8** Schematic model of influenza A virus hijacks cellular XRN1 to suppress the host RIG-I-mediated innate immune response and to facilitate viral replication. The decay factor XRN1 of PBs contributes to influenza A virus replication and participates in the IAV vRNA-induced and RIG-I-mediated type I interferon response, resulting in the inhibition of IRF3 activity, IFN- $\beta$  induction, and downstream ISG gene expression. The coexistence of IAV NS1 and host XRN1 enhances the inhibition of p-IRF3 and IFN- $\beta$  production.

XRN1 KO cells at 8 h postinfection. Therefore, both the mRNA and protein levels of M1 and NS1 were consistently reduced in IAV-infected XRN1-depleted cells. The results suggest that the XRN1 may affect viral replication at 8 h postinfection. These two approaches consistently demonstrate the important role of XRN1 in supporting IAV replication. In this study, we demonstrate that WSN viral growth decreased in XRN1 knockout and XRN1-deficient human lung cells. In contrast, the viral growth in WSN-infected HEK293T cells could be increased by the overexpression of FLAG-tagged XRN1 (Fig. 3). Furthermore, several mRNAs and proteins of the antiviral immune response, such as IFN- $\beta$ , IFIT1, IFIT3, and ISG15, were observed to significantly increase in IAV-infected XRN1 knockout A549 cells (Fig. 5). We have also measured IFN and ISG mRNA expression in A549 control cells and A549 XRN1 knockout cells, but after poly(I:C) treatment instead of WSN infection. We observed that the levels of IFN- $\beta$  and ISG genes increased in XRN1 knockout A549 cells exposed to poly(I:C) treatment (see Fig. S3A in the supplemental material). As we know poly(I:C) is a synthetic analog of dsRNA that can act as agonist of RIG-I and MDA5, leading to IFN- $\beta$  and ISG production. These results indicate that XRN1 can directly affect this innate immune response pathway under IAV infection. The H1N1 viruses tested (WSN, PR8, and CA04) showed similar infection levels in A549 control cells and A549 XRN1 KO cells at 8 h.p.i., based on viral NP protein expression (see Fig. S4A in the supplemental material). Moreover, we found that XRN1 KO cells infected with other IAV strains (see Fig. S4B in the supplemental material) also increased IFN- $\beta$ , IFIT1, IFIT3, and ISG15 mRNA expression. Here, we present evidence that the IRF3 mRNA of XRN1 KO cells upon WSN, PR8, CA04, and HK4801 infection are similar to that of A549 control (Fig. 5C). The expressive proteins of IRF3 are equal in virus-infected XRN1 KO cells and A549 control cells, but p-IRF3

significantly increases in XRN1 KO cells after viral infection (Fig. 6A and Fig. S4A). Therefore, XRN1 affects IFN- $\beta$  induction through the IRF3 phosphorylation, but not IRF3 protein expression. However, it remains unclear whether XRN1 affects the expression or activity of NF- $\kappa$ B, and this is worthy of further exploration. We therefore propose that XRN1 can be considered a host exoribonuclease factor for the positive regulation of influenza virus replication in human cells. This represents a strategy used by IAV NS1 to repress the host innate immune response through many pathways and allow efficient replication of virus (10, 44, 46).

Furthermore, we found that there was robust expression of IFN transcription factors and p-IRF3 in IAV-infected XRN1 KO cells (Fig. 6A). However, IRF3 phosphorylation by TBK1 was observed only in the IFN-producing pathways that use the adaptor protein MAVS to transduce signals from the cytosolic nucleic acid sensor RIG-I, which are activated by IAV viral RNA. Thus, we utilized purified IAV WSN vRNA to induce IRF3 activity in the type I IFN signaling pathway and found that XRN1 significantly affects the upstream of IFN- $\beta$  transcription (Fig. 6B). RIG-I-like receptors are a type of intracellular pattern recognition receptor involved in the recognition of viruses by the innate immune system. RIG-I is a key sensor of influenza A virus infection, mediating the transcriptional induction of cellular innate interferon immune response upon detection of viral 5' pppRNA. In addition to RIG-I, MDA5 is a significant contributor to the cellular defense against influenza A virus (36). Using siRNA against RIG-I and MDA5, we detected that the mRNA levels of IFN- $\beta$  failed to be induced in IAV-infected XRN1 knockout cells. XRN1 can inhibit the IFN- $\beta$  production through affecting the major RIG-I-mediated and minor MDA5-mediated IFN signaling pathways (Fig. 6C). XRN1 can inhibit p-IRF3, IFN- $\beta$ , and the downstream *ISG* gene production. The NS1 of IAV may enhance the efficiency in XRN1-mediated suppression of IRF3 phosphorylation (Fig. 7).

Our findings reveal a previously unexplored mechanism of virus attack to host immune pathways whereby influenza virus NS1 directly interacts with the cellular exoribonuclease XRN1. IAV utilizes XRN1 to inhibit IRF3 activity, repress cellular IFN- $\beta$  transcription, and then block IFN protein synthesis through RIG-I-mediated immune response. Our data indicate that host XRN1 has a strong impact on viral replication and the host innate immune responses to influenza A virus.

## MATERIALS AND METHODS

**Cell cultures and virus production.** Human lung adenocarcinoma cells (A549), human embryonic kidney cells (HEK293T), and Madin-Darby canine kidney (MDCK) cells were separately cultured in Dulbecco modified Eagle medium (DMEM) or minimal essential medium (MEM) containing 10% fetal bovine serum (FBS) and penicillin/streptomycin/glutamine (Gibco) at 37°C. H1N1 (A/WSN/1933), H1N1 (A/Puerto Rico/8/34), H1N1 (A/California/04/2009), and H3N2 (A/HK/4801/2014) were rescued using a DNA transfection system (15, 47, 48). Recombinant WSN viruses with deleted NS1 were prepared using eight pHW2000 plasmids containing mutant NS1-deleted gene segments, which were transfected into HEK293T cells and amplified in MDCK cells. The recombinant viruses were named DelNS1-M-A14U, as they adapted to gain an A14U substitution in the 3'-noncoding region of the M vRNA segment (45).

**Coimmunoprecipitation and Western blotting.** To map the interacting domains between XRN1 and NS1, the constructs of the various truncated forms of XRN1 and mutant NS1 were cotransfected into HEK293T cells using TransIT-LT1 reagent (Mirus) for 48 h. The cells were harvested and lysed with IP buffer (30 mM Tris-HCl [pH 7.4], 150 mM NaCl, 1% Triton X-100, and 1× proteinase inhibitor), the supernatant was treated with 10  $\mu$ l of anti-GFP Dynabeads protein A (Invitrogen) added at 4°C for 12 h, and then 10  $\mu$ g/ml RNase A was added at 30°C for 1 h. The coprecipitated proteins were collected with a magnet, followed by washing six times. The precipitated proteins were separated by 10% sodium dodecyl sulfate-polyacrylamide gel electrophoresis (SDS-PAGE) and subsequently identified using an anti-GFP antibody (diluted 1:5,000; Invitrogen), an anti-FLAG antibody (diluted 1:5,000; Sigma) or V5 antibody (diluted 1:5,000; Bio-Rad). Polyvinylidene difluoride (PVDF) membranes were analyzed by Odyssey scanner (LI-COR) using an IRDye 800CW or IRDye 680RD-linked secondary antibody.

**Protein purification and GST pulldown assay.** The pGEX-6P-XRN1-C-terminal region (aa 1174–1706) and pET32a-NS1 from various strains were transformed into BL21(DE3). Expression of the protein was induced by adding 1 mM or 0.1 mM isopropyl- $\beta$ -D-thiogalactopyranoside (IPTG) at 16°C for 16 h. The protein expressed from lysed cells was suspended in IP buffer (30 mM Tris [pH 7.4], 150 mM NaCl, 1% Triton X-100) and sonicated with a SonicPrep ultrasonic homogenizer (PolyScience). GST-tagged-XRN1 (aa 1174–1706) and His-tagged NS1 proteins were purified with glutathione Sepharose 4B (GE Healthcare) and nickel-nitrilotriacetic acid (Ni-NTA) beads (Qiagen), respectively. The purity of recombinant proteins was determined by SDS-PAGE. Five micrograms of recombinant NS1 protein was mixed

with GST-XRN1-bead or GST-bead (control) complexes at 4°C for 1 h. The targeted proteins were immunoprecipitated and analyzed by WB with an anti-GST antibody (diluted 1:1,000; ImmunoWay) and an anti-NS1 antibody (diluted 1:1,000; National University of Singapore [NUS]).

**Immunofluorescence microscopic analysis.** A549 cells grown on Millicell EZ glass slide (Millipore) at 80% confluence were infected with WSN at an MOI of 2 for 4 to 8 h.p.i. or were transfected with 2  $\mu$ g of the WSN NS1 clone. The cells were fixed in phosphate-buffered saline (PBS) containing 4% formaldehyde, permeated with 0.3% Triton X-100, blocked with 5% normal donkey serum for 1 h at 25°C, and then stained with anti-XRN1 (diluted 1:20; Santa Cruz), anti-WSN NS1 (diluted 1:100; NUS, anti-DCP1A (diluted 1:20; Santa Cruz), or anti-FLAG (diluted 1:100; Sigma) antibodies for 2 h at 37°C. Subsequently, the cells were stained with fluorescein isothiocyanate (FITC)-conjugated goat anti-mouse IgG (diluted 1:200; green, Invitrogen), goat anti-rabbit IgG (diluted 1:200; red, Invitrogen), or donkey anti-goat IgG (diluted 1:200; purple, Invitrogen) for 1 h at 25°C. The cells were washed three times with PBS and mounted in Vectashield antifade mounting medium with 4',6'-diamidino-2-phenylindole (DAPI) (Vector Laboratories). Confocal images were obtained with a confocal laser-scanning microscope (Zeiss; LSM 700).

**Generation of A549 CRISPR-Cas9 genetically modified cell lines.** The *XRN1* genes in A549 cells were inactivated using the CRISPR-Cas9 system using previously described methods (43, 49). The *XRN1* target sequence GTATCCTGTCTCAGCGAAG, along with plasmid vector pSpCas9(BB)-2A-Puro (PX459) v2.0 (Genscript), which drives expression of the *Streptococcus pyogenes* Cas9, a puromycin resistance cassette, and the chimeric guide RNA was introduced into mammalian cells. A549 cells ( $7 \times 10^4$  cells/well) seeded in 24-well plates were transfected with the recombinant plasmids using Lipofectamine 3000 (Life Technologies) for 1 day, after which 1 mg/ml of puromycin was added for a 3-day selection. Then, the cells were reseeded in 96-well plates (1 cell/well) without puromycin treatment. After 21 days, total protein was prepared from individual colonies, and the absence of proteins was confirmed by sequencing *XRN1* genomic DNA and Western blotting. The XRN1 knockout cells were generated from a single clone.

**Generation of XRN1-deficient cells.** A549 cells ( $1.5 \times 10^5$  cells/well) were transfected with 100  $\mu$ M *XRN1* small interfering RNA (siRNA) and AllStars negative-control siRNA (Qiagen) using Lipofectamine 3000 (Life Technologies). The *XRN1* siRNA-1 sequence is 5'-CAGGUCGUAAAUAUCAAUA-3' (Qiagen), and the *XRN1* siRNA-2 sequence is 5'-GGGAUCUGGAAAGAUGCAUACUUU-3' (Invitrogen). At 48 h post-transfection with siRNA, cells were reseeded at  $1 \times 10^5$  cells/well in a 24-well plate and were incubated for 24 h for further WSN infection and plaque assay.

**Viral growth kinetics and plaque assay.** A549 control cells or A549 *XRN1* knockout cells were seeded in 24-well plates ( $1 \times 10^5$  cells/well) and, after 24 h, were washed and infected with viruses at an MOI of 0.01. Following viral adsorption at 37°C for 1 h, the infected cells were washed twice with PBS and subsequently covered with MEM containing 1  $\mu$ g/ml tosylsulfonyl phenylalanyl chloromethyl ketone (TPCK) trypsin and incubated at 37°C. Supernatants were collected at different time points, and the titers of the virus were determined by plaque assay in MDCK cells. Monolayer MDCK cells in six-well plates ( $6 \times 10^5$  cells/well) were washed and infected with virus by performing 10-fold serial dilutions. After 1-h adsorption, the cells were washed twice with PBS and then overlaid with MEM containing 1  $\mu$ g/ml TPCK trypsin and 0.3% agarose gel at 37°C for 48 h. The plates were fixed in 10% formaldehyde and stained with 1% crystal violet. The viral titers are presented as the number of PFU per milliliter.

**RNA extraction and qRT-PCR.** Total RNA was extracted from mock-infected and IAV-infected A549 control cells or A549 *XRN1* knockout cells using RNAzol RT (Molecular Research Center), per the manufacturer's instructions. RNAs were converted into first-strand cDNAs using a PrimeScript RT reagent kit (TaKaRa) with oligo(dT) reverse primers. All PCRs were performed using specific primers (see Table S1 in the supplemental material), which were purchased from Integrated DNA Technologies (IDT). The qPCR analysis was performed using SYBR green reagents and the LightCycler 480 instrument (Roche).

**MTT assay.** A549 cells ( $2 \times 10^3$  cells/well) were seeded in 96-well plates for 24 h, and then the cells were treated with various concentrations of pAp (1 to 6 mM) (catalog no. A5763; Sigma). The viability of pAp-treated A549 cells was validated by MTT assay (Abcam) in accordance with the manufacturer's instructions.

## SUPPLEMENTAL MATERIAL

Supplemental material is available online only.

**FIG S1**, TIF file, 0.4 MB.

**FIG S2**, TIF file, 0.5 MB.

**FIG S3**, TIF file, 0.3 MB.

**FIG S4**, TIF file, 0.8 MB.

**FIG S5**, TIF file, 0.1 MB.

**TABLE S1**, DOCX file, 0.01 MB.

## ACKNOWLEDGMENTS

We thank Elisa Izaurralde (Department of Biochemistry, Max Planck Institute for Developmental Biology, Tübingen, Germany) for providing the pT7-EGFP-C1-HsXRN1 and pT7-EGFP-C1-HsXRN1\_1-1173 plasmids. We are grateful to Bernard Moss (Laboratory of



Viral Diseases, National Institute of Allergy and Infectious Diseases, National Institutes of Health, Bethesda, Maryland, USA) for providing the NIH A549 *XRN1* knockout and control cells. We also thank Yee-Joo Tan (Department of Microbiology and Immunology, Yong Loo Lin School of Medicine, National University Health System [NUHS], National University of Singapore, Singapore) for providing the antibody for IAV NS1 protein. We thank Yixin Chen (National Institute of Diagnostics and Vaccine Development in Infectious Diseases and State Key Laboratory of Molecular Vaccinology and Molecular Diagnostics, School of Public Health, Xiamen University, Xiamen, People's Republic of China) for providing the mouse antibody for IAV protein detection.

## REFERENCES

- Saunders-Hastings PR, Krewski D. 2016. Reviewing the history of pandemic influenza: understanding patterns of emergence and transmission. *Pathogens* 5:66. <https://doi.org/10.3390/pathogens5040066>.
- Krammer F, Smith GJD, Fouchier RAM, Peiris M, Kedzierska K, Doherty PC, Palese P, Shaw ML, Treanor J, Webster RG, Garcia-Sastre A. 2018. Influenza. *Nat Rev Dis Primers* 4:3. <https://doi.org/10.1038/s41572-018-0002-y>.
- Esposito S. 2018. 100 years since the 1918 influenza pandemic. *Hum Vaccin Immunother* 14:504–507. <https://doi.org/10.1080/21645515.2018.1446591>.
- Goneau LW, Mehta K, Wong J, L'Huillier AG, Gubbay JB. 2018. Zoonotic influenza and human health—Part 1. Virology and epidemiology of zoonotic influenzas. *Curr Infect Dis Rep* 20:37. <https://doi.org/10.1007/s11908-018-0642-9>.
- Mehta K, Goneau LW, Wong J, L'Huillier AG, Gubbay JB. 2018. Zoonotic influenza and human health—Part 2. Clinical features, diagnosis, treatment, and prevention strategies. *Curr Infect Dis Rep* 20:38. <https://doi.org/10.1007/s11908-018-0643-8>.
- Coughlan L, Palese P. 2018. Overcoming barriers in the path to a universal influenza virus vaccine. *Cell Host Microbe* 24:18–24. <https://doi.org/10.1016/j.chom.2018.06.016>.
- Hsu AC. 2018. Influenza virus: a master tactician in innate immune evasion and novel therapeutic interventions. *Front Immunol* 9:743. <https://doi.org/10.3389/fimmu.2018.00743>.
- Hale BG, Randall RE, Ortin J, Jackson D. 2008. The multifunctional NS1 protein of influenza A viruses. *J Gen Virol* 89:2359–2376. <https://doi.org/10.1099/vir.0.2008/004606-0>.
- Krug RM. 2015. Functions of the influenza A virus NS1 protein in antiviral defense. *Curr Opin Virol* 12:1–6. <https://doi.org/10.1016/j.coviro.2015.01.007>.
- Klemm C, Boergeling Y, Ludwig S, Ehrhardt C. 2018. Immunomodulatory nonstructural proteins of influenza A viruses. *Trends Microbiol* 26:624–636. <https://doi.org/10.1016/j.tim.2017.12.006>.
- Burgui I, Aragon T, Ortin J, Nieto A. 2003. PABP1 and eIF4G1 associate with influenza virus NS1 protein in viral mRNA translation initiation complexes. *J Gen Virol* 84:3263–3274. <https://doi.org/10.1099/vir.0.19487-0>.
- Gack MU, Albrecht RA, Urano T, Inn KS, Huang IC, Carnero E, Farzan M, Inoue S, Jung JU, Garcia-Sastre A. 2009. Influenza A virus NS1 targets the ubiquitin ligase TRIM25 to evade recognition by the host viral RNA sensor RIG-I. *Cell Host Microbe* 5:439–449. <https://doi.org/10.1016/j.chom.2009.04.006>.
- Koliopoulos MG, Lethier M, van der Veen AG, Haubrich K, Hennig J, Kowalinski E, Stevens RV, Martin SR, Reis e Sousa C, Cusack S, Rittinger K. 2018. Molecular mechanism of influenza A NS1-mediated TRIM25 recognition and inhibition. *Nat Commun* 9:1820. <https://doi.org/10.1038/s41467-018-04214-8>.
- Plant EP, Ilyushina NA, Sheikh F, Donnelly RP, Ye Z. 2017. Influenza virus NS1 protein mutations at position 171 impact innate interferon responses by respiratory epithelial cells. *Virus Res* 240:81–86. <https://doi.org/10.1016/j.virusres.2017.07.021>.
- Huang X, Zheng M, Wang P, Tai H, Chen Y, Zheng M, Wen X, Lau SY, Wu WL, Matsumoto K, Yuen KY, Chen H. 2017. An NS-segment exonic splicing enhancer regulates influenza A virus replication in mammalian cells. *Nat Commun* 8:14751. <https://doi.org/10.1038/ncomms14751>.
- Mok BW, Song W, Wang P, Tai H, Chen Y, Zheng M, Wen X, Lau SY, Wu WL, Matsumoto K, Yuen KY, Chen H. 2012. The NS1 protein of influenza A virus interacts with cellular processing bodies and stress granules through RNA-associated protein 55 (RAP55) during virus infection. *J Virol* 86:12695–12707. <https://doi.org/10.1128/JVI.00647-12>.
- Kulkarni M, Ozgur S, Stoecklin G. 2010. On track with P-bodies. *Biochem Soc Trans* 38:242–251. <https://doi.org/10.1042/BST0380242>.
- Jonas S, Izaurralde E. 2015. Towards a molecular understanding of micro-RNA-mediated gene silencing. *Nat Rev Genet* 16:421–433. <https://doi.org/10.1038/nrg3965>.
- Nagarajan VK, Jones CI, Newbury SF, Green PJ. 2013. XRN 5' → 3' exoribonucleases: structure, mechanisms and functions. *Biochim Biophys Acta* 1829:590–603. <https://doi.org/10.1016/j.bbaggm.2013.03.005>.
- Onomoto K, Yoneyama M, Fung G, Kato H, Fujita T. 2014. Antiviral innate immunity and stress granule responses. *Trends Immunol* 35:420–428. <https://doi.org/10.1016/j.it.2014.07.006>.
- Braun JE, Truffault V, Boland A, Huntzinger E, Chang CT, Haas G, Weichenrieder O, Coles M, Izaurralde E. 2012. A direct interaction between DCP1 and XRN1 couples mRNA decapping to 5' exonucleolytic degradation. *Nat Struct Mol Biol* 19:1324–1331. <https://doi.org/10.1038/nsmb.2413>.
- Jonas S, Izaurralde E. 2013. The role of disordered protein regions in the assembly of decapping complexes and RNP granules. *Genes Dev* 27:2628–2641. <https://doi.org/10.1101/gad.227843.113>.
- Chang CT, Bercovich N, Loh B, Jonas S, Izaurralde E. 2014. The activation of the decapping enzyme DCP2 by DCP1 occurs on the EDC4 scaffold and involves a conserved loop in DCP1. *Nucleic Acids Res* 42:5217–5233. <https://doi.org/10.1093/nar/gku129>.
- Ng CS, Kasumba DM, Fujita T, Luo H. 2020. Spatio-temporal characterization of the antiviral activity of the XRN1-DCP1/2 aggregation against cytoplasmic RNA viruses to prevent cell death. *Cell Death Differ* 27:2363–2382. <https://doi.org/10.1038/s41418-020-0509-0>.
- Akiyama BM, Laurence HM, Massey AR, Costantino DA, Xie X, Yang Y, Shi PY, Nix JC, Beckham JD, Kieft JS. 2016. Zika virus produces noncoding RNAs using a multi-pseudoknot structure that confounds a cellular exonuclease. *Science* 354:1148–1152. <https://doi.org/10.1126/science.aah3963>.
- Pashler AL, Towler BP, Jones CI, Newbury SF. 2016. The roles of the exoribonucleases DIS3L2 and XRN1 in human disease. *Biochem Soc Trans* 44:1377–1384. <https://doi.org/10.1042/BST20160107>.
- Gokhale NS, Horner SM. 2017. Knotty Zika virus blocks exonuclease to produce subgenomic flaviviral RNAs. *Cell Host Microbe* 21:1–2. <https://doi.org/10.1016/j.chom.2016.12.013>.
- Kieft JS, Rabe JL, Chapman EG. 2015. New hypotheses derived from the structure of a flaviviral Xrn1-resistant RNA: conservation, folding, and host adaptation. *RNA Biol* 12:1169–1177. <https://doi.org/10.1080/15476286.2015.1094599>.
- Burgess HM, Mohr I. 2015. Cellular 5'-3' mRNA exonuclease Xrn1 controls double-stranded RNA accumulation and anti-viral responses. *Cell Host Microbe* 17:332–344. <https://doi.org/10.1016/j.chom.2015.02.003>.
- Gaglia MM, Covarrubias S, Wong W, Glaunsinger BA. 2012. A common strategy for host RNA degradation by divergent viruses. *J Virol* 86:9527–9530. <https://doi.org/10.1128/JVI.01230-12>.
- Khapersky DA, Schmaling S, Larkins-Ford J, McCormick C, Gaglia MM. 2016. Selective degradation of host RNA polymerase II transcripts by influenza A virus PA-X host shutoff protein. *PLoS Pathog* 12:e1005427. <https://doi.org/10.1371/journal.ppat.1005427>.
- Yoneyama M, Fujita T. 2009. RNA recognition and signal transduction by RIG-I-like receptors. *Immunol Rev* 227:54–65. <https://doi.org/10.1111/j.1600-065X.2008.00727.x>.
- Rehwinkel J, Tan CP, Goubau D, Schulz O, Pichlmair A, Bier K, Robb N, Vreede F, Barclay W, Fodor E, Reis e Sousa C. 2010. RIG-I detects viral genomic RNA during negative-strand RNA virus infection. *Cell* 140:397–408. <https://doi.org/10.1016/j.cell.2010.01.020>.

34. Kato H, Takeuchi O, Sato S, Yoneyama M, Yamamoto M, Matsui K, Uematsu S, Jung A, Kawai T, Ishii KJ, Yamaguchi O, Otsu K, Tsujimura T, Koh CS, Reis e Sousa C, Matsuura Y, Fujita T, Akira S. 2006. Differential roles of MDA5 and RIG-I helicases in the recognition of RNA viruses. *Nature* 441:101–105. <https://doi.org/10.1038/nature04734>.
35. Pichlmair A, Schulz O, Tan CP, Naslund TI, Liljestrom P, Weber F, Reis e Sousa C. 2006. RIG-I-mediated antiviral responses to single-stranded RNA bearing 5'-phosphates. *Science* 314:997–1001. <https://doi.org/10.1126/science.1132998>.
36. Benitez AA, Panis M, Xue J, Varble A, Shim JV, Frick AL, Lopez CB, Sachs D, tenOever BR. 2015. In vivo RNAi screening identifies MDA5 as a significant contributor to the cellular defense against influenza A virus. *Cell Rep* 11:1714–1726. <https://doi.org/10.1016/j.celrep.2015.05.032>.
37. Wu B, Hur S. 2015. How RIG-I like receptors activate MAVS. *Curr Opin Virol* 12:91–98. <https://doi.org/10.1016/j.coviro.2015.04.004>.
38. Liu S, Cai X, Wu J, Cong Q, Chen X, Li T, Du F, Ren J, Wu YT, Grishin NV, Chen ZJ. 2015. Phosphorylation of innate immune adaptor proteins MAVS, STING, and TRIF induces IRF3 activation. *Science* 347:aaa2630. <https://doi.org/10.1126/science.aaa2630>.
39. Schneider WM, Chevillotte MD, Rice CM. 2014. Interferon-stimulated genes: a complex web of host defenses. *Annu Rev Immunol* 32:513–545. <https://doi.org/10.1146/annurev-immunol-032713-120231>.
40. Jabri E. 2005. P-bodies take a RISC. *Nat Struct Mol Biol* 12:564. <https://doi.org/10.1038/nsmb0705-564>.
41. Dichtl B, Stevens A, Tollervey D. 1997. Lithium toxicity in yeast is due to the inhibition of RNA processing enzymes. *EMBO J* 16:7184–7195. <https://doi.org/10.1093/emboj/16.23.7184>.
42. Yun JS, Yoon JH, Choi YJ, Son YJ, Kim S, Tong L, Chang JH. 2018. Molecular mechanism for the inhibition of DXO by adenosine 3',5'-bisphosphate. *Biochem Biophys Res Commun* 504:89–95. <https://doi.org/10.1016/j.bbrc.2018.08.135>.
43. Liu R, Moss B. 2016. Opposing roles of double-stranded RNA effector pathways and viral defense proteins revealed with CRISPR-Cas9 knockout cell lines and vaccinia virus mutants. *J Virol* 90:7864–7879. <https://doi.org/10.1128/JVI.00869-16>.
44. Nogales A, Martinez-Sobrido L, Topham DJ, DeDiego ML. 2018. Modulation of innate immune responses by the influenza A NS1 and PA-X proteins. *Viruses* 10:708. <https://doi.org/10.3390/v10120708>.
45. Zheng M, Wang P, Song W, Lau SY, Liu S, Huang X, Mok BW, Liu YC, Chen Y, Yuen KY, Chen H. 2015. An A14U substitution in the 3' noncoding region of the M segment of viral RNA supports replication of influenza virus with an NS1 deletion by modulating alternative splicing of M segment mRNAs. *J Virol* 89:10273–10285. <https://doi.org/10.1128/JVI.00919-15>.
46. Marc D. 2014. Influenza virus non-structural protein NS1: interferon antagonism and beyond. *J Gen Virol* 95:2594–2611. <https://doi.org/10.1099/vir.0.069542-0>.
47. Hoffmann E, Neumann G, Kawaoka Y, Hobom G, Webster RG. 2000. A DNA transfection system for generation of influenza A virus from eight plasmids. *Proc Natl Acad Sci U S A* 97:6108–6113. <https://doi.org/10.1073/pnas.100133697>.
48. Song W, Wang P, Mok BW, Lau SY, Huang X, Wu WL, Zheng M, Wen X, Yang S, Chen Y, Li L, Yuen KY, Chen H. 2014. The K526R substitution in viral protein PB2 enhances the effects of E627K on influenza virus replication. *Nat Commun* 5:5509. <https://doi.org/10.1038/ncomms6509>.
49. Cong L, Ran FA, Cox D, Lin S, Barretto R, Habib N, Hsu PD, Wu X, Jiang W, Marraffini LA, Zhang F. 2013. Multiplex genome engineering using CRISPR/Cas systems. *Science* 339:819–823. <https://doi.org/10.1126/science.1231143>.

# Combination of Thigh Circumference and Indices of Central Obesity Helps Predict Incident Chronic Kidney Disease: A 14-Year Prospective Cohort Study Using a Three-Dimensional Body Laser Scanner

I-Wen Wu, MD,\* Pei-Ju Liao, PhD,† Ming-Kuo Ting, MD,‡ Shuo-Wei Chen, MD,§  
Ning-I Yang, MD,¶ and Kuang-Hung Hsu, PhD\*\*††‡‡§§¶¶

**Objective:** Obesity, high body mass index, and visceral fat accumulation are associated with renal diseases. However, the association between body measurements and chronic kidney disease (CKD) is still unclear.

**Methods:** A cohort of 7,825 participants scheduled for follow-up of CKD was recruited from 2000 to 2008 in Taiwan. A questionnaire was developed to collect the basic demographics, lifestyle variables, personal disease history, and family disease history of the participants. A 3-dimensional body surface scanning system was used to take their body measurements. The participants underwent an average follow-up of 14.3 years for evaluation of the incidence of CKD. A multiple Cox regression model was built.

**Results:** Three body measurements, namely chest width (hazard ratio [HR] 1.059, 95% confidence interval [CI] 1.011-1.110), waist circumference (HR 1.017, 95% CI 1.006-1.029), and thigh circumference (HR 0.941, 95% CI 0.922-0.961), were significantly associated with CKD. Two combinations of body measurements, namely the waist-to-thigh ratio and chest-to-thigh ratio, were derived to predict the occurrence of CKD. Participants with the highest quartile of waist-to-thigh ratio and chest-to-thigh ratio had a 2.175-fold and 2.182-fold risk of developing CKD, respectively.

**Conclusions:** This study suggests that along with central obesity, body limb measurements can be used as an indicator to predict the occurrence of CKD. The effects of limb measurements on CKD could help provide an innovative perspective regarding the intervention to be developed for the treatment of CKD and a preventive medicine for high-risk individuals. The association of thigh circumference with CKD warrants further investigation.

© 2021 by the National Kidney Foundation, Inc. All rights reserved.

## Introduction

CHRONIC KIDNEY DISEASE (CKD) is one of the fast growing chronic diseases worldwide, along

with the increasing prevalence of obesity in the past 2 decades.<sup>1,2</sup> Obesity is a major cause of diabetes mellitus and hypertension, and an independent risk factor for

\*Department of Nephrology, Chang Gung Memorial Hospital, Keelung; College of Medicine, Chang Gung University, Taiwan.

†Master Degree Program in Healthcare Industry, Chang Gung University, Taoyuan, Taiwan.

‡Division of Endocrinology and Metabolism, Chang Gung Memorial Hospital, Keelung, Taiwan.

§Division of Gastroenterology and Hepatology, Chang Gung Memorial Hospital, Keelung, Taiwan.

¶Division of Cardiology, Chang Gung Memorial Hospital, Keelung, Taiwan.

\*\*Healthy Aging Research Center, Chang Gung University, Taoyuan, Taiwan.

††Laboratory for Epidemiology, Department of Health Care Management, Chang Gung University, Taoyuan, Taiwan.

‡‡Department of Emergency Medicine, Chang Gung Memorial Hospital, Taoyuan, Taiwan.

§§Research Center for Food and Cosmetic Safety, College of Human Ecology, Chang Gung University of Science and Technology, Taoyuan, Taiwan.

¶¶Department of Safety, Health and Environmental Engineering, Ming Chi University of Technology, Taipei, Taiwan.

Support and financial disclosure: This research was funded by research grants from the Chang Gung Memorial Hospital, Taiwan (CMRPG2F0072, CGRPG

2F0081, CMRPD3F0021, CMRPD3F0022, CMRPD3F0023, NARPD3J0021 and NARPD3J0022), the Healthy Aging Research Center of Chang Gung University, Taiwan (EMRPD1K0411, EMRPD1K0481, EMRPD1L0401, and EMRPD1L0451) and the Ministry of Science and Technology, Taiwan (108-2410-H-182-008-MY2). The authors appreciate the partial support provided by the Wang Jhan-Yang Charitable Trust Fund, Taiwan (WJY 2020-HR-01, WJY 2021-HR-01, WJY 2020-AP-01, and WJY 2021-AP-01). The authors would like to acknowledge the support for data linkage provided by Health and Welfare Data Science Center, Ministry of Health and Welfare, Taiwan. The authors have no conflicts of interest to declare.

Statement of Ethics: Approval of the present study was obtained from the Institutional Review Board of Chang Gung Memorial Hospital, and informed consents were waived (Approval No. 201802378A3C101, 104-1159, 104-5478B).

Address correspondence to Professor Kuang-Hung Hsu, Laboratory for Epidemiology, Department of Health Care Management, Chang Gung University, No. 259, Wen-Hua 1st Road, Kwei-Shan, Taoyuan 333, Taiwan. E-mail: [khsu@mail.cgu.edu.tw](mailto:khsu@mail.cgu.edu.tw)

© 2021 by the National Kidney Foundation, Inc. All rights reserved.

1051-2276/\$36.00

<https://doi.org/10.1053/j.jrn.2021.06.009>

CKD.<sup>3</sup> Studies have demonstrated that central obesity or abdominal visceral fat accumulation were associated with inflammatory response mechanisms and insulin resistance, and could indicate a high risk for CKD in the general population.<sup>4,5</sup>

Previous studies have indicated that obesity is paradoxically associated with better outcomes of patients undergoing hemodialysis but not of those with CKD.<sup>6,7</sup> In contrast, selected body measurements including body mass index (BMI), waist circumference (WC), waist-to-height ratio (WHtR), and waist-to-hip ratio were documented as major body shape markers associated with the incidence of CKD.<sup>8–10</sup> BMI is the most frequently used in epidemiological studies owing to its feasibility of measurement in varied settings. However, BMI can be influenced by muscle mass and bone density. The causal relationship between obesity and CKD was hampered by the limitations of BMI and considerably varied with age, sex, race, and disease severity. Studies have indicated that the WHtR was superior to BMI in predicting CKD and several other cardiometabolic conditions.<sup>11</sup> Studies have concluded that WC may play a common role in predicting the occurrence of CKD. Mechanistically, WC is an indicator of abdominal visceral fat accumulation and is associated with insulin resistance and inflammation, which increase the risk of developing CKD.<sup>12,13</sup>

Intersections between different body measurements and disease entities have been described in the literature. High thigh circumference (TC) or WTR was associated with the occurrence of various diseases including malignancies, type 2 diabetes mellitus (T2DM), and dementia.<sup>14–16</sup> Meanwhile, a small TC, with low subcutaneous fat or low skeletal muscle in the thigh, has been recognized as a risk factor for hyperlipidemia, hyperglycemia, and dementia.<sup>15,17</sup> The body measurements, predominantly limb measurements, can provide additional information for risk prognostication of various chronic diseases. However, the precise relationships between limb measurements and incident CKD remain unclear.

Previous studies have focused on the use of noninvasive three-dimensional (3D) scanning technology to collect body measurements and demonstrated the association of abnormal body estimates with different chronic disease statuses.<sup>14–16</sup> To comprehensively explore the different anthropomorphology indices linked to the occurrence of CKD, we conducted a 14-year prospective cohort study to investigate the association between selected body measurements derived from whole-body 3D laser scanning and renal outcomes.

## Materials and Methods

### Study Samples

A total of 7,825 individuals without CKD who underwent anthropometric measurements for a health examination in a medical center from 2000 to 2008 were

recruited. The personal and family history, lifestyle habits, and comorbidities of the participants were accurately recorded and followed up until December 2018 (average follow-up time of 14.24 years). This study was conducted in adherence with the principles of the Declaration of Helsinki after obtaining informed consent from all patients. The study was approved by the Institutional Review Board of the medical center.

### Anthropometrical Parameters

3D body surface measurements were collected using whole-body 3D laser scanning, according to previously published methods.<sup>18,19</sup>

In addition to body height, 36 measurements from 5 anatomical regions were recorded (Table S1). The head and neck region included head circumference, head surface area, head volume, and neck circumference. The trunk region consisted of chest width (ChW), chest circumference, chest sectional area, waist width, WC, waist sectional area, trunk surface area, and trunk volume. The hip region comprised hip circumference (HpC), hip width (HW), and hip sectional area (HSA). The lower limb region involved both the left and right leg length, TC, calf circumference, leg surface area, and leg volume. The upper limb region consisted of both the left and right arm length, upper arm circumference, forearm circumference, arm surface area, and arm volume. Backward selection was performed for the 36 measurements while adjusting for age, sex, occupation, education, marital status, smoking, alcohol consumption, betel nut chewing, personal underlying diseases, and family history of diseases. For preventing collinearity in the regression analysis, one significant measure of each dimension was selected into the model. ChW was selected in place of chest circumference for anatomic consideration of the effect of sex. Combinations of body measures derived from the significant body measurements performed by multivariable regression analysis were used to evaluate their effects on CKD.

### Data Collection

A questionnaire was administered to the participants to solicit the following information: birth date, sex, education level, marital status, occupation, and history of cigarette smoking, alcohol consumption, and betel nut chewing; personal history of diseases (including diabetes, hypertension, heart disease, CKD, liver cirrhosis, and chronic hepatitis); and family history of chronic diseases including hypertension, T2DM, stroke, heart diseases, liver cirrhosis, renal diseases, and cancer. The fasting blood glucose level and blood pressure history of patients without T2DM and hypertension were measured. T2DM was defined according to the guidelines of the American Diabetes Association, and hypertension was defined according to the guidelines of the Joint National Committee on Detection, Evaluation, and Treatment of



**Table 1.** The Association Between Baseline Characteristics and the Incidence of CKD

Variables	Total (%)	Person-Year	Number of CKD	Incidence Density	Univariate Analysis	
					HR	95% CI
Demographics						
Age						
≤49.92	3,916 (50.04)	56,918.86	193	0.0034	1	–
>49.92	3,909 (49.96)	55,024.1	437	0.0079	2.374	(2.004-2.812)
Sex						
Female	3,742 (47.82)	54,887.37	270	0.0049	1	
Male	4,083 (52.18)	57,055.59	360	0.0063	1.336	(1.14-1.564)
Education						
Junior high school and below	2,883 (36.84)	40,911.9	308	0.0075	2.184	(1.767-2.701)
High school	1,547 (19.77)	21,900.37	101	0.0046	1.359	(1.042-1.773)
College/university and above	2,427 (31.02)	34,626.2	118	0.0034	1	
Unknown	968 (12.37)	14,504.49	103	0.0071	1.975	(1.516-2.574)
Occupation						
Office workers	1,032 (13.19)	15,926.6	69	0.0043	1	
Farmers and labors	1,398 (17.87)	19,513.44	111	0.0057	1.43	(1.058-1.932)
Housekeeping, self-employment, students, and others	5,395 (68.95)	76,502.92	450	0.0059	1.466	(1.137-1.89)
Marriage						
Unmarried	320 (4.09)	4,509.34	17	0.0038	1	
Married or coupled	6,516 (83.27)	92,541.49	510	0.0055	1.428	(0.881-2.314)
Unknown	989 (12.64)	14,892.13	103	0.0069	1.701	(1.018-2.841)
Lifestyle variables						
Cigarette smoking						
No	5,899 (75.39)	85,079.55	455	0.0053	1	
Yes	1,926 (24.61)	26,863.4	175	0.0065	1.247	(1.047-1.485)
Alcohol drinking						
No	5,799 (74.11)	83,515.4	444	0.0053	1	
Yes	2,026 (25.89)	28,427.56	186	0.0065	1.262	(1.064-1.498)
Betel nut chewing						
No	7,311 (93.43)	104,675.71	576	0.0055	1	
Yes	514 (6.57)	7,267.25	54	0.0074	1.359	(1.028-1.796)
Personal underlying diseases						
Hypertension						
No	6,625 (84.66)	95,890.33	429	0.0045	1	
Yes	1,200 (15.34)	16,052.62	201	0.0125	2.941	(2.487-3.478)
T2DM						
No	7,335 (93.74)	105,762.44	504	0.0048	1	
Yes	490 (6.26)	6,180.51	126	0.0204	4.65	(3.824-5.655)
CVD						
No	6,882 (87.95)	99,340.81	504	0.0051	1	
Yes	943 (12.05)	12,602.14	126	0.0100	2.084	(1.714-2.534)
Chronic liver diseases and cirrhosis						
No	7,019 (89.7)	101,228.51	547	0.0054	1	
Yes	806 (10.3)	10,714.44	83	0.0077	1.539	(1.221-1.939)
Family disease history						
Hypertension						
No	5,143 (65.73)	73,991.67	412	0.0056	1	
Yes	2,682 (34.27)	37,951.29	218	0.0057	1.054	(0.894-1.242)
T2DM						
No	5,991 (76.56)	86,262.31	465	0.0054	1	
Yes	1,834 (23.44)	25,680.65	165	0.0064	1.223	(1.024,1.242)
Stroke						
No	6,762 (86.42)	96,779.42	538	0.0056	1	
Yes	1,063 (13.58)	15,163.54	92	0.0061	1.097	(0.88-1.369)
Heart diseases						
No	1,026 (13.11)	14,671.88	71	0.0048	1	
Yes	6,799 (86.89)	97,271.08	559	0.0057	0.846	(0.923-1.513)
Chronic liver diseases and cirrhosis						
No	482 (6.16)	6,824.41	37	0.0054	1	
Yes	7,343 (93.84)	105,118.55	593	0.0056	0.969	(0.74-1.437)

(Continued)

High Blood Pressure (systolic blood pressure  $\geq 140$  mm

**Table 1.** The Association Between Baseline Characteristics and the Incidence of CKD (*Continued*)

Variables	Total (%)	Person-Year	Number of CKD	Incidence Density	Univariate Analysis	
					HR	95% CI
Renal diseases						
No	270 (3.45)	3,857.72	15	0.0039	1	
Yes	7,555 (96.55)	108,085.23	615	0.0057	0.689	(0.87-2.421)
Cancer						
No	1,388 (17.74)	19,825.62	102	0.0051	1	
Yes	6,437 (82.26)	92,117.34	528	0.0057	0.907	(0.892-1.363)

CI, confidence interval; CKD, chronic kidney disease; CVD, cardiovascular disease; HR, hazard ratio; T2DM, type 2 diabetes mellitus.

Hg, diastolic blood pressure  $\geq 90$  mm Hg, or the use of antihypertensive medication).<sup>20</sup>

## Study Outcome

Serum creatinine and urinary protein were measured at baseline to confirm the status of CKD at participation. CKD was defined as having an eGFR  $< 60$  mL/min/1.73 m<sup>2</sup> or the presence of proteinuria at 2 separated occasions 3 months apart.<sup>21</sup> Only participants without CKD were enrolled and were followed up until the development of CKD or December 2018. To minimize possible misclassification of study end points owing to dropouts secondary to the extended observation period, all patients were linked with the National Health Insurance (NHI) claims database to ensure the reporting of CKD. Taiwan launched a single-payer NHI program in 1995, which covers almost 99% of the entire population of Taiwan. CKD was diagnosed according to the International Classification of Diseases, Ninth Revision codes of 580–588.<sup>22,23</sup>

## Statistical Analyses

The likelihood of developing CKD between the groups was represented by the incidence density, where Cox regression was applied to perform statistical tests and 3D body measurements were screened by comparing the differences between the patients and controls; the results were presented as the mean  $\pm$  standard deviation. To avoid collinearity in the regression analysis, one body measurement with the lowest *P* value was selected from each anatomic dimension, including the head and neck, trunk, hip, and upper and lower limbs, for the subsequent multivariable analysis. A Cox regression model was used to determine the strength of the association between the selected body estimates and CKD. In addition to the forced-in sociodemographic characteristics, lifestyle variables, and disease history, a backward model selection with *P*  $< .05$  was conducted to determine the variables, including body measurements from each anatomic part, to be reserved in the regression model. All statistical analyses were performed using SAS version 9.4 (SAS Inc., Cary, NC).

## Results

Older and male participants were the most likely to develop CKD. The analysis revealed that patients with

CKD had a lower level of education than did the controls without CKD. Farmers and laborers, homemakers, self-employed individuals, and service industry workers were at a higher risk of CKD than office workers were. Among the lifestyle variables, individuals who smoked, consumed alcohol, and chewed betel nut had a higher likelihood of developing CKD. Participants with underlying diseases including hypertension, T2DM, cardiovascular disease, and chronic hepatitis and liver cirrhosis had a higher risk of developing CKD (Table 1).

Most of the selected body measurements were significantly different between participants who did and did not develop CKD during the follow-up period, except for head volume, trunk surface area, HW and HpC, arm length and arm volume, and calf circumference. Overall, individuals prone to development of CKD had larger measurements of the neck, trunk, and upper limbs but smaller measurements of lower limbs compared with controls. Multivariable analyses indicated that ChW (hazard ratio [HR] 1.059, 95% confidential interval [CI] 1.011–1.110), WC (HR 1.017, 95% CI 1.006–1.029), and left TC (HR 0.941, 95% CI 0.922–0.961) were significantly associated with the development of CKD after adjusting for age, sex, education level, marital status, occupation, smoking, alcohol consumption, betel nut chewing, personal underlying diseases, and family disease history (Table 2).

Extensive analyses were performed to unveil the relationship between using a combination of significant body measurements and the development of CKD. ChW-left TC ratio (ChTR) and WC-left TC ratio (WTR) were applied and categorized into quartiles to explore their monotonic trend association with CKD. The results revealed a positive monotonic trend in multivariable-adjusted HRs for ChTR (Q1 = 1.00, Q2 = 1.329, Q3 = 1.568, Q4 = 2.182) and WTR (Q1 = 1.00, Q2 = 1.458, Q3 = 1.603, Q4 = 2.175) on the likelihood of CKD occurrence. Sensitivity analyses demonstrated that the trend effects of a combination of body measurements were similar among participants with different characteristics (Table 3).

## Discussion

Measurements of anthropometric indices represent simple and economical tools for diagnosing or predicting

**Table 2.** The Statistics of 3D Surface Body Measurements Between Subjects Who Develop CKD or Not

Body measurements	CKD (n = 630)	Non-CKD (n = 7195)	P Value	Univariate HR (95% CI)	Multiple HR* (95% CI)
<b>Head and neck</b>					
Head circumference (cm)	58.72 ± 1.81	58.95 ± 1.92	.006	0.956 (0.918-0.996)	
Head surface area (cm <sup>2</sup> )	1,313.30 ± 141.80	1,331.50 ± 205.70	.005	1.024 (0.99-1.059)	
Head volume (cm <sup>3</sup> )	4,775.70 ± 495.70	4,742.20 ± 531.40	.1	1.009 (0.993-1.026)	
Neck circumference (cm)	38.15 ± 3.78	37.11 ± 4.02	<.0001	1.071 (1.052-1.091)	
<b>Trunk</b>					1.059 (1.011-1.11)
Chest width (cm)	32.55 ± 2.81	32.10 ± 2.82	.0002	1.084 (1.055-1.113)	
Chest circumference (cm)	99.18 ± 9.19	96.59 ± 9.18	<.0001	1.028 (1.02-1.036)	
Chest sectional area (cm <sup>2</sup> )	695.20 ± 121.10	651.30 ± 123.30	<.0001	1.303 (1.219-1.392)	
Waist width (cm)	31.15 ± 3.03	30.49 ± 3.14	<.0001	1.098 (1.071-1.126)	
Waist circumference (cm)	90.38 ± 10.38	87.38 ± 10.42	<.0001	1.031 (1.024-1.039)	
Waist sectional area (cm <sup>2</sup> )	627.40 ± 144.40	582.90 ± 139.40	<.0001	1.281 (1.216-1.349)	
Trunk surface area (cm <sup>2</sup> )	6,713.60 ± 1,001.50	6,672.30 ± 1,665.80	.4	1.005 (1.002-1.007)	1.017 (1.006-1.029)
Trunk volume (cm <sup>3</sup> )	41,006.10 ± 8,258.00	38,643.30 ± 8,137.50	<.0001	1.003 (1.002-1.004)	
<b>Hip</b>					
Hip width (cm)	34.47 ± 2.49	34.43 ± 2.48	.7	1.011 (0.979-1.043)	
Hip circumference (cm)	97.60 ± 6.17	97.16 ± 6.24	.09	1.014 (1.002-1.027)	
Hip sectional area (cm <sup>2</sup> )	695.70 ± 107.00	685.40 ± 106.10	.02	1.103 (1.025-1.187)	
<b>Upper limbs</b>					
Upper arm circumference (cm)					
Left	30.85 ± 4.30	30.56 ± 3.95	.1	1.022 (1.003-1.042)	
Right	30.67 ± 4.11	30.12 ± 3.80	.001	1.028 (1.008-1.049)	
Forearm circumference (cm)					
Left	24.73 ± 2.74	24.58 ± 2.74	.2	1.049 (1.02-1.08)	
Right	24.66 ± 2.45	24.41 ± 2.55	.02	1.039 (1.008-1.071)	
Arm length (cm)					
Left	55.75 ± 3.29	55.67 ± 3.49	.6	1.013 (0.99-1.036)	
Right	56.42 ± 3.40	56.27 ± 3.52	.3	1.021 (0.998-1.045)	
Arm surface area (cm <sup>2</sup> )					
Left	1,488.80 ± 294.00	1,521.40 ± 313.00	.008	1.051 (1.022-1.08)	
Right	1,488.00 ± 253.80	1,509.50 ± 271.50	.04	1.056 (1.024-1.089)	
Arm volume (cm <sup>3</sup> )					
Left	2,399.60 ± 519.20	2,410.70 ± 545.10	.6	1.02 (1.005-1.035)	
Right	2,393.10 ± 457.10	2,362.80 ± 479.00	.1	1.018 (1.002-1.035)	
<b>Lower limbs</b>					
Thigh circumference (cm)					
Left	50.76 ± 5.12	51.21 ± 4.97	.03	0.952 (0.936-0.968)	0.941 (0.922-0.961)
Right	50.88 ± 5.08	51.27 ± 4.90	.05	0.953 (0.937-0.969)	
Calf circumference (cm)					
Left	33.68 ± 3.55	33.71 ± 3.43	.8	1 (0.976-1.024)	
Right	33.70 ± 3.46	33.74 ± 3.38	.8	1.005 (0.98-1.029)	
Leg length (cm)					
Left	67.73 ± 4.91	68.55 ± 4.99	.0001	0.989 (0.973-1.006)	
Right	67.70 ± 4.91	68.53 ± 5.02	.0001	0.989 (0.973-1.005)	
Leg surface area (cm <sup>2</sup> )					
Left	2,181.20 ± 353.60	2,242.30 ± 372.30	<.0001	0.969 (0.947-0.992)	
Right	2,212.50 ± 403.60	2,278.60 ± 413.00	.0001	0.979 (0.958-0.999)	
Leg volume (cm <sup>3</sup> )					
Left	5,933.20 ± 1,272.50	6,046.40 ± 1,365.90	.03	0.987 (0.981-0.993)	
Right	5,952.90 ± 1,283.30	6,078.50 ± 1,364.50	.02	0.987 (0.981-0.993)	

\*Performed by Cox proportional hazard model adjusted for age, sex, education, marriage, occupation, cigarette smoking, alcohol drinking, betel nut chewing, personal underlying diseases, and family disease history.

**Table 3.** Sensitivity Analysis of Body Measurement Combinations on the Likelihood of CKD Incidence

Categories	n	Chest Width/Left Thigh Circumference*				Waist Circumference/Left Thigh Circumference*			
		Q2	Q3	HR (95% CI)	HR† (95% CI)	Q2	Q3	HR (95% CI)	HR† (95% CI)
All	7,825	1.329 (1.024-1.724)	1.568 (1.196-2.056)	2.182 (1.642-2.900)	1.458 (1.104-1.926)	1.603 (1.206-2.132)	2.175 (1.630-2.902)		
Age	3,916	1.253 (0.794-1.976)	1.396 (0.847-2.302)	2.359 (1.424-3.908)	1.246 (0.771-2.012)	1.626 (1.002-2.637)	2.535 (1.566-4.106)		
Gender	3,909	1.492 (1.105-2.014)	1.351 (0.977-1.866)	2.096 (1.503-2.922)	1.024 (0.749-1.401)	1.454 (1.075-1.966)	1.697 (1.243-2.317)		
	3,742	1.354 (0.927-1.977)	1.558 (1.068-2.273)	1.985 (1.346-2.927)	1.569 (1.03-2.39)	1.76 (1.147-2.701)	2.508 (1.616-3.893)		
	4,083	0.974 (0.706-1.345)	1.29 (0.946-1.76)	1.795 (1.305-2.471)	1.461 (1.014-2.104)	1.611 (1.119-2.318)	2.285 (1.585-3.294)		
BMI	3,915	1.301 (0.836-2.024)	1.566 (0.991-2.475)	2.358 (1.472-3.776)	1.137 (0.722-1.791)	1.195 (0.747-1.914)	1.837 (1.152-2.928)		
	3,910	1.413 (1.026-1.946)	1.51 (1.083-2.107)	2.155 (1.515-3.064)	1.203 (0.862-1.678)	1.535 (1.103-2.137)	1.92 (1.366-2.700)		
Hypertension free	6,625	1.449 (1.063-1.976)	1.537 (1.103-2.142)	2.187 (1.547-3.093)	1.499 (1.085-2.07)	1.492 (1.064-2.093)	2.292 (1.640-3.203)		
Diabetes free	7,335	1.382 (1.044-1.829)	1.516 (1.118-2.055)	2.297 (1.679-3.143)	1.37 (1.017-1.845)	1.501 (1.102-2.042)	2.182 (1.600-2.976)		
Cardiovascular diseases free	6,882	1.431 (1.073-1.909)	1.617 (1.192-2.193)	2.267 (1.65-3.115)	1.469 (1.083-1.992)	1.579 (1.153-2.163)	2.067 (1.503-2.843)		
Free of the 3 diseases	5,482	1.625 (1.13-2.339)	1.792 (1.207-2.663)	2.667 (1.771-4.016)	1.735 (1.172-2.57)	2.087 (1.394-3.126)	2.919 (1.939-4.394)		

\*Q1 as the reference group, performed by Cox proportional hazard ratio model adjusted for age, sex, education, marriage, occupation, cigarette smoking, alcohol drinking, betel nut chewing, personal underlying diseases, and family disease history.

†All trend tests were statistically significant.



diseases in routine clinical examination. Traditionally, increased body weight, BMI, or WC has been associated with metabolic syndrome and CKD.<sup>12,14–18,20–24</sup> In this 14-year prospective cohort study, we found that high ChW, high WC, and low TC measurements were independent predictors of the development of CKD. A combination of ChTR and WTR can be used as an easy and feasible biomarker for predicting the incidence of CKD. The findings of our study have diagnostic as well as therapeutic implications. Further interventional studies to improve the size of these body estimates are warranted to determine the effect associated with these manipulations on the preservation of renal function.

The increased risk for incident CKD associated with high WC observed in our study was consistent with that reported in other studies. WC, which is a surrogate indicator of overweight and obesity, has been proposed to be a better predictor than BMI in several obesity-related health risk conditions, including CKD.<sup>25</sup> High WC reflects the accumulation of visceral fat, which results in insulin resistance, chronic inflammation, and oxidative stress. Similarly, a larger ChW also supplements WC by indicating visceral fat accumulation and may correlate to various components of metabolic syndrome, including hypertension, dyslipidemia, and hyperglycemia.<sup>26,27</sup> However, to the best of our knowledge, this is the first study to ascertain the relationship between ChW and incident CKD, which may represent an alternative surrogate of central obesity, with a significant predictive role for overweight and obesity. In addition, simultaneous measurements of ChW and WC may comprehensively assess central obesity or accumulation of abdominal fat by considering fat distribution in different parts of the trunk. Despite the significant association between anthropometric index indicative of central obesity and the risk of CKD,<sup>12,24</sup> the risk stratification derived from obesity may be misclassified in the presence of sarcopenia,<sup>28</sup> highlighting the importance of careful interpretation of a single body estimate with disease association.

Significant negative correlations between TC and CKD have not been reported to date. Investigations have reported that larger HC and TC were associated with a lower risk of T2DM independent of age, BMI, and WC.<sup>29,30</sup> The exact physiopathological mechanism of the association between low TC and CKD remains unclear. The thigh is mainly composed of muscle and subcutaneous fat, and it is one of the anatomic regions containing the highest proportion of skeletal muscle in the human body. Consequently, a low TC may be indicative of muscle wasting. The presence of abdominal visceral adipose tissue can predispose individuals to metabolic syndrome and cardiovascular disease, whereas the peripheral fat tissue and high muscle content have protective roles. Skeletal muscles are the key target organ for insulin action. Effective muscle function may have an important role in the

improvement of insulin resistance, oxygen consumption, and anti-inflammation actions.<sup>31</sup> An increase in femoral subcutaneous fat mass associated with large TC may also affect free fatty acid uptake and storage, lipid profile, and insulin sensitivity, thereby reducing the risk of renal damage.<sup>32,33</sup> In contrast, low muscle mass and less subcutaneous fat in the thighs may be associated with many risk factors of CKD, such as hyperlipidemia, hyperglycemia, hypertension, and systemic chronic inflammation.<sup>32</sup>

Considering the contribution of muscle mass in anthropomorphology and cautions in interpreting risk association using body indices, we proposed, for the first time, the use of a combination of chest, waist, and thigh measurements (ChTR and WTR) as a reliable biomarker for predicting the development of CKD. The use of body index ratio, such as the WHtR or waist-to-hip ratio, can enable accurate measurements of the relative accumulation of abdominal fat compared with the size of the body, and is more widely adopted than WC alone. These ratios were closely associated with many metabolic diseases, all-cause mortality, and the incidence of CKD.<sup>7,9–11</sup> Increase in ChTR or WTR is a strong predictor of CKD, with a monotonic trend. This close association between the two ratios and the development of CKD may be attributed to the imbalance of abdominal adipose tissue and peripheral muscle mass. The highest ratios represented extreme accumulation of abdominal adipose tissue or devastating muscle wasting. Both conditions involve dysregulation of numerous adipokines, inflammation, oxidative stress, increase in sympathetic activity, activation of angiotensin II, and hyperinsulinemia, consequently leading to glomerular hyperfiltration and increased proximal tubular sodium resorption.<sup>34–36</sup> All these conditions may cause multiple pathophysiologic processes that are implicated in CKD, such as insulin resistance, metabolic syndrome, and T2DM.<sup>37,38</sup>

Our findings have important implications for epidemiological studies and preventive medicine that entail the examination of anthropomorphological indices. The so-called “obesity paradox,” which uses BMI as a surrogate marker of body adiposity, may speculate the possible protective effect of body fat in scenarios of chronic illness; however, we advocate careful examination of the main components of body weight (fat and muscle) by using standardized body measurement ratios, such as ChTR or WTR, to draw conclusions regarding the effects of anthropometry in the prediction of disease. The ChTR and WTR can serve as reliable tools for use in clinical practice and epidemiological surveys of large population health screening activities to identify individuals at high risk of CKD. The use of these measurements also has certain clinical implications. Most of the current nutritional, physical, or lifestyle recommendations emphasize the reduction of body weight, WC, or BMI to improve

treatment outcomes. However, attention should be paid to measurements of ChW, TC, or more comprehensively ChTR and WTR by patients and clinicians to ensure appropriate body composition after such therapy. Further interventional trials designed to improve the measurement of ChTR and WTR should be conducted to elucidate the true clinical significance of these two body measurements in the renal outcomes of patients.

In this study, we employed accurate 3D laser measuring techniques with comprehensive whole body scanning, computer-based technology, unbiased outcome assessment by tracking the NHI database, and extended longitudinal cohort analysis to ensure research validity, reliability, and temporality; however, our study has certain limitations. First, we did not perform repeated measurements using the body surface scanner, and hence, could not determine the effects of temporal body changes on the incidence of CKD. Second, our findings were derived from a single ethnic population, which limits their generalizability to populations of different ethnicities. Third, the body composition was not measured using imaging methods such as dual-energy X-ray absorptiometry or computed tomography. However, extensive coverage of 36 body measurements may comprehensively assess the whole body composition by mapping with body tissue distribution in an indirect manner. Fluid component and edematous condition may have minimally affected the results of the present study, as the measurements of the dependent parts of the body were not used for analysis in these ambulatory patients. Surrogate markers of adiposity, such as leptin and adiponectin, were not available for this study sample. Finally, many confounders, such as environmental exposure, nutrition and food habits, health-seeking behaviors, and medication histories related to the development of CKD, were not determined. Although such variables can be assumed as nondifferential misclassification in this study, the multiple sensitivity analyses may have strengthened the conjecture of our supposition. Future studies with a detailed characterization of the physiology associated with the different anthropomorphologies, including adipokine/chemokine, pro-/anti-inflammatory markers, and others may help to delineate the mechanism of certain body phenotypes associated with the development of renal disease.

In conclusion, this 14-year prospective cohort study corroborates previous findings on the importance of surrogate anthropomorphological indices of central obesity, such as WC and ChW, in predicting the incidence of CKD. Our findings suggest that limb measurements, especially TC or a combination of ChTR and WTR, could serve as superior predictors of CKD. The effects of limb measurements on CKD provide an innovative insight into the development of interventions and preventive medicine for individuals at a high risk of developing CKD. The role of TC in preventing CKD warrants further investigation.

## Practical Applications

The findings of this study suggest that body limb measurements can be used as an indicator to predict the occurrence of CKD. The effects of limb measurements on CKD provide an innovative insight into the development of preventive medicine for individuals at high risk of developing CKD. In particular, the mechanism of enlarging the TC by exercises to prevent CKD warrants future investigations.

## Credit Authorship Contribution Statement

**I-Wen Wu:** Conceptualization, Methodology. **Pei-Ju Liao:** Data curation, Formal analysis. **Ming-Kuo Ting:** Formal analysis, Data curation. **Shuo-Wei Chen:** Formal analysis, Data curation. **Ning-I Yang:** Formal analysis, Data curation. **Kuang-Hung Hsu:** Conceptualization, Methodology, Data curation, Supervision.

## Supplementary Data

Supplementary data related to this article can be found at <https://doi.org/10.1053/j.jrn.2021.06.009>.

## References

1. Meguid El Nahas A, Bello AK. Chronic kidney disease: the global challenge. *Lancet*. 2005;365:331-340.
2. Parikh NI, Pencina MJ, Wang TJ, et al. Increasing trends in incidence of overweight and obesity over 5 decades. *Am J Med*. 2007;120:242-250.
3. Flegal KM, Graubard BI, Williamson DF, Gail MH. Cause-specific excess deaths associated with underweight, overweight, and obesity. *Jama*. 2007;298:2028-2037.
4. Fantuzzi G. Adipose tissue, adipokines, and inflammation. *J Allergy Clin Immunol*. 2005;115:911-919; quiz 920.
5. Sanches FM, Avesani CM, Kamimura MA, et al. Waist circumference and visceral fat in CKD: a cross-sectional study. *Am J Kidney Dis*. 2008;52:66-73.
6. Glanton CW, Hypolite IO, Hsieh PB, Agodoa LY, Yuan CM, Abbott KC. Factors associated with improved short term survival in obese end stage renal disease patients. *Ann Epidemiol*. 2003;13:136-143.
7. Kovesdy CP, Anderson JE, Kalantar-Zadeh K. Paradoxical association between body mass index and mortality in men with CKD not yet on dialysis. *Am J Kidney Dis*. 2007;49:581-591.
8. Elsayed EF, Sarnak MJ, Tighiouart H, et al. Waist-to-hip ratio, body mass index, and subsequent kidney disease and death. *Am J Kidney Dis*. 2008;52:29-38.
9. Elsayed EF, Tighiouart H, Weiner DE, et al. Waist-to-hip ratio and body mass index as risk factors for cardiovascular events in CKD. *Am J Kidney Dis*. 2008;52:49-57.
10. He Y, Li F, Wang F, Ma X, Zhao X, Zeng Q. The association of chronic kidney disease and waist circumference and waist-to-height ratio in Chinese urban adults. *Medicine (Baltimore)*. 2016;95:e3769.
11. Lin C-H, Chou C-Y, Lin C-C, Huang C-C, Liu C-S, Lai S-W. Waist-to-height ratio is the best index of obesity in association with chronic kidney disease. *Nutrition*. 2007;23:788-793.
12. Evans PD, McIntyre NJ, Fluck RJ, McIntyre CW, Taal MW. Anthropomorphic measurements that include central fat distribution are more closely related with key risk factors than BMI in CKD stage 3. *PLoS One*. 2012;7:e34699.
13. Madero M, Katz R, Murphy R, et al. Comparison between different measures of body fat with kidney function decline and incident CKD. *Clin J Am Soc Nephrol*. 2017;12:893-903.

14. Hsu K-H, Shih C-P, Liao P-J. Waist-to-thigh ratio is a predictor of internal organ cancers in humans: findings from a cohort study. *Ann Epidemiol.* 2013;23:342-348.
15. Liao PJ, Lin TY, Ting MK, et al. Chest width, waist circumference, and thigh circumference are predictors of dementia. *Int J Geriatr Psychiatry.* 2018;33:1019-1027.
16. Ting MK, Liao PJ, Wu IW, et al. Predicting type 2 diabetes mellitus occurrence using three-dimensional anthropometric body surface scanning measurements: a prospective cohort study. *J Diabetes Res.* 2018;2018:6742384.
17. Manolopoulos KN, Karpe F, Frayn KN. Gluteofemoral body fat as a determinant of metabolic health. *Int J Obes (Lond).* 2010;34:949-959.
18. Yu CY, Lo YH, Chiou WK. The 3D scanner for measuring body surface area: a simplified calculation in the Chinese adult. *Appl Ergon.* 2003;34:273-278.
19. Chuang YC, Hsu KH, Hwang CJ, Hu PM, Lin TM, Chiou WK. Waist-to-thigh ratio can also be a better indicator associated with type 2 diabetes than traditional anthropometrical measurements in Taiwan population. *Ann Epidemiol.* 2006;16:321-331.
20. The fifth report of the Joint National Committee on Detection, Evaluation, and Treatment of High Blood Pressure (JNC V). *Arch Intern Med.* 1993;153:154-183.
21. K/DOQI clinical practice guidelines for chronic kidney disease: evaluation, classification, and stratification. *Am J Kidney Dis.* 2002;39(2 Suppl 1):S1-S266.
22. Navaneethan SD, Jolly SE, Schold JD, et al. Development and validation of an electronic health record-based chronic kidney disease registry. *Clin J Am Soc Nephrol.* 2011;6:40-49.
23. Winkelmayer WC, Schneeweiss S, Mogun H, Patrick AR, Avorn J, Solomon DH. Identification of individuals with CKD from Medicare claims data: a validation study. *Am J Kidney Dis.* 2005;46:225-232.
24. Gelber RP, Kurth T, Kausz AT, et al. Association between body mass index and CKD in apparently healthy men. *Am J Kidney Dis.* 2005;46:871-880.
25. Kramer H, Shoham D, McClure LA, et al. Association of waist circumference and body mass index with all-cause mortality in CKD: the REGARDS (Reasons for Geographic and Racial Differences in Stroke) Study. *Am J Kidney Dis.* 2011;58:177-185.
26. Huang Z, Willett WC, Colditz GA, et al. Waist circumference, waist:hip ratio, and risk of breast cancer in the Nurses' Health Study. *Am J Epidemiol.* 1999;150:1316-1324.
27. Snijder MB, Dekker JM, Visser M, et al. Trunk fat and leg fat have independent and opposite associations with fasting and postload glucose levels: the Hoorn study. *Diabetes Care.* 2004;27:372-377.
28. Sharma D, Hawkins M, Abramowitz MK. Association of sarcopenia with eGFR and misclassification of obesity in adults with CKD in the United States. *Clin J Am Soc Nephrol.* 2014;9:2079-2088.
29. Joshipura K, Muñoz-Torres F, Vergara J, Palacios C, Pérez CM. Neck circumference may be a better alternative to standard anthropometric measures. *J Diabetes Res.* 2016;2016:6058916.
30. Jung KJ, Kimm H, Yun JE, Jee SH. Thigh circumference and diabetes: obesity as a potential effect modifier. *J Epidemiol.* 2013;23:329-336.
31. Seidell JC, Han TS, Feskens EJ, Lean ME. Narrow hips and broad waist circumferences independently contribute to increased risk of non-insulin-dependent diabetes mellitus. *J Intern Med.* 1997;242:401-406.
32. Snijder MB, Visser M, Dekker JM, et al. Low subcutaneous thigh fat is a risk factor for unfavourable glucose and lipid levels, independently of high abdominal fat. The Health ABC Study. *Diabetologia.* 2005;48:301-308.
33. Van Pelt RE, Evans EM, Schechtman KB, Ehsani AA, Kohrt WM. Contributions of total and regional fat mass to risk for cardiovascular disease in older women. *Am J Physiol Endocrinol Metab.* 2002;282:E1023-E1028.
34. *Recent Advances of Sarcopenia and Frailty in CKD.* Singapore: Springer; 2020.
35. Goodpaster BH, Krishnaswami S, Harris TB, et al. Obesity, regional body fat distribution, and the metabolic syndrome in older men and women. *Arch Intern Med.* 2005;165:777-783.
36. Vega GL, Adams-Huet B, Peshock R, Willett D, Shah B, Grundy SM. Influence of body fat content and distribution on variation in metabolic risk. *J Clin Endocrinol Metab.* 2006;91:4459-4466.
37. KDIGO 2012 clinical practice guideline for the evaluation and management of chronic kidney disease. *Kidney Int Suppl.* 2013;31:1-150.
38. Obermayr RP, Temml C, Knechtelsdorfer M, et al. Predictors of new-onset decline in kidney function in a general middle-european population. *Nephrol Dial Transplant.* 2008;23:1265-1273.

## CLINICAL AND POPULATION SCIENCES

## Increased Risk of Stroke in Patients With Obsessive-Compulsive Disorder

## A Nationwide Longitudinal Study

Mu-Hong Chen<sup>1</sup>, MD, PhD; Shih-Jen Tsai<sup>2</sup>, MD; Tung-Ping Su, MD; Cheng-Ta Li, MD, PhD; Wei-Chen Lin, MD; Tzeng-Ji Chen<sup>3</sup>, MD, PhD; Tai-Long Pan<sup>4</sup>, PhD; Ya-Mei Bai<sup>5</sup>, MD, PhD

**BACKGROUND AND PURPOSE:** Patients with obsessive-compulsive disorder (OCD) tend to be comorbid with stroke-related risk factors, including obesity, hypertension, and diabetes. However, the temporal association between OCD and subsequent stroke risk is unclear.

**METHODS:** Using data collected between 2001 and 2010 by Taiwan's National Health Insurance Research Database, 28 064 adult patients with OCD (International Classification of Diseases, Ninth Revision, Clinical Modification [ICD-9-CM] code: 300.3) and 28 064 age-, sex-, and comorbidity-matched controls were included in this study. Patients who developed ischemic (ICD-9-CM codes: 433, 434, and 435) and hemorrhagic (ICD-9-CM codes: 430, 431, and 432) stroke during follow-up (from enrollment to end of 2011) were identified. Moreover, medications used for treating OCD were assessed.

**RESULTS:** Patients with OCD (hazard ratio [HR], 3.02 [95% CI, 1.91–4.77]), especially middle-aged (HR, 2.66 [95% CI, 1.34–5.29]) and elderly adults (HR, 3.46 [95% CI, 1.70–7.05]), had an elevated risk of developing ischemic stroke during the follow-up period compared with non-OCD controls. The cumulative HR of hemorrhagic stroke did not differ (HR, 0.87 [95% CI, 0.42–1.80]) between the OCD and non-OCD groups. In patients with OCD, both short- (HR, 1.69 [95% CI, 0.74–3.88]; HR, 0.31 [95% CI, 0.05–1.95]) and long-term use (HR, 1.37 [95% CI, 0.60–3.16]; HR, 0.90 [95% CI, 0.22–3.76]) of OCD medications were not correlated with ischemic and hemorrhagic stroke compared with nonuse.

**CONCLUSIONS:** Clinicians should closely monitor cerebrovascular disease and related risks in patients with OCD. The pathomechanism of OCD with an increased risk of ischemic stroke warrants further investigation.

**GRAPHIC ABSTRACT:** An online [graphic abstract](#) is available for this article.

**Key Words:** comorbidity ■ hypertension ■ obesity ■ obsessive-compulsive disorder ■ risk factors

Obsessive-compulsive disorder (OCD), a severe and chronic mental disorder, manifests as recurrent intrusive obsessive thoughts, including fear of contamination, a need for symmetry, sexual obsession, and repetitive compulsive behaviors, including excessive cleaning and ordering as well as repeated checking, that an individual feels driven to perform.<sup>1</sup> The World Health Organization placed OCD in the ten most disabling conditions worldwide,<sup>1</sup> with a lifetime prevalence of 1% to

3%<sup>2</sup>; however, OCD is often missed in primary care settings and frequently undertreated.<sup>2</sup>

Mounting evidence has shown an association between OCD and stroke-related metabolic disorders, including obesity and diabetes.<sup>3,4</sup> Albert et al<sup>4</sup> evaluated metabolic syndrome in 104 patients with OCD and revealed that 36.5% had abdominal obesity, 42.3% had hypertension, 23.1% had high triglyceride levels, and 4.8% had fasting hyperglycemia. Moreover, comorbidity of bipolar disorder

Correspondence to: Tai-Long Pan, PhD, Liver Research Center, Chang Gung Memorial Hospital, Taoyuan 33375, Taiwan, Email [pan@mail.cgu.edu.tw](mailto:pan@mail.cgu.edu.tw) or Ya-Mei Bai, MD, PhD, Department of Psychiatry, Taipei Veterans General Hospital, No. 201, Shih-Pai Rd, Section 2, 11217 Taipei, Taiwan, Email [yambi@mail2000.com.tw](mailto:yambi@mail2000.com.tw)

The Data Supplement is available with this article at <https://www.ahajournals.org/doi/suppl/10.1161/STROKEAHA.120.032995>.

For Sources of Funding and Disclosures, see page 2607.

© 2021 American Heart Association, Inc.

Stroke is available at [www.ahajournals.org/journal/str](http://www.ahajournals.org/journal/str)



## Nonstandard Abbreviations and Acronyms

<b>CCI</b>	Charlson Comorbidity Index
<b>CRP</b>	C-reactive protein
<b>HR</b>	hazard ratio
<b>ICD-9-CM</b>	<i>International Classification of Diseases, Ninth Revision, Clinical Modification</i>
<b>IL</b>	interleukin
<b>NHIRD</b>	National Health Insurance Research Database
<b>OCD</b>	obsessive-compulsive disorder

with OCD further increased the risk of metabolic syndrome in patients with OCD.<sup>4</sup> Isomura compared the incidence of metabolic disorders between 25 415 patients with OCD and the general population and reported that patients with OCD were more likely to develop obesity, dyslipidemia, and type 2 diabetes later in life than the general population.<sup>3</sup> OCD following cerebrovascular accident has been commonly reported; however, the relationship between OCD and subsequent stroke has scarcely been investigated.<sup>3</sup> A Swedish study reported that OCD was related to an increased overall risk of cardiocerebrovascular diseases, including ischemic heart diseases, cerebrovascular diseases, and transient ischemic attack.<sup>3</sup> However, the study did not establish a correlation between OCD and certain cardiocerebrovascular diseases, especially stroke.<sup>3</sup>

We used Taiwan's National Health Insurance Research Database to include a large sample size and a longitudinal follow-up study design to investigate the temporal association between OCD and stroke, including ischemic and hemorrhagic stroke. We hypothesized that patients with OCD, especially elderly adults, would have an increased risk of developing new-onset stroke during the follow-up period compared with non-OCD controls.

## METHODS

### Data Source

In the current study, we used the Taiwan National Health Insurance Research Database (NHIRD), which was released and audited by the Department of Health and Bureau of the NHI Program for the purpose of scientific research, and contained comprehensive information about insured patients, such as demographic data (birth date, sex, residential location, and income) and clinical visits (visit dates and medical diagnoses). Every subject is assigned a unique and anonymous identifier by the National Health Research Institutes before releasing the data to researchers; thus, a subject can be followed anonymously and continuously using the unique identifier. A nationwide database with a large sample size can minimize selection bias. A specialized data set of mental disorders, including all psychiatric medical records of insured

individuals, was used to identify individuals with bipolar disorder in our study. The *International Classification of Diseases, Ninth Revision, Clinical Modification (ICD-9-CM)* was used to diagnosing diseases during the study period. The NHIRD has been used extensively in epidemiological studies in Taiwan.<sup>5–8</sup> This study was approved by the Institutional Review Board of Taipei Veterans General Hospital.

### Data Availability Statement

The NHIRD was released and audited by the Department of Health and Bureau of the NHI Program for the purpose of scientific research (<https://nhird.nhri.org.tw/>). NHIRD can be obtained through the formal application that is regulated by the Department of Health and Bureau of the NHI Program.

### Inclusion Criteria for Patients With OCD and the Control Group

The study flowchart was shown in Figure 1 in the [Data Supplement](#). Adult patients aged  $\geq 20$  years who were diagnosed as having OCD (*ICD-9-CM* code: 300.3) by board-certified psychiatrists between January 1, 2001, and December 31, 2010, based on the comprehensive interview and clinical judgment and who had no history of any stroke (*ICD-9-CM* codes: 430–438) before enrollment were included in the OCD cohort. The time of enrollment was defined as the time of OCD diagnosis. The age-, sex-, residence-, income-, and comorbidities-matched (1:1) control cohort was randomly identified after eliminating the study subjects, those who had been given a diagnosis of OCD at any time, and those with any stroke before enrollment. Income level (levels 1–3 per month:  $\leq 15840$  New Taiwanese Dollars or 528 US Dollars, 15841–25000 New Taiwanese Dollars or 528–833 US Dollars, and  $\geq 25000$  New Taiwanese Dollars or  $\geq 833$  US Dollars) and urbanization level of residence (levels 1–5, most to least urbanized) were regarded as the proxies for health care availability in Taiwan.<sup>9</sup> Medical and psychiatric comorbidities included traumatic brain injury, hypertension, dyslipidemia, diabetes, obesity, smoking, ischemic heart disease, schizophrenia, bipolar disorder, and major depressive disorder. Additionally, Charlson Comorbidity Index (CCI) and all-cause clinical visits were provided for the OCD and the matched-control cohorts. CCI consisting of 22 physical conditions was also assessed to determine the systemic health conditions of all enrolled subjects.<sup>10</sup> Finally, the use of OCD medications (antidepressants) during the follow-up was also examined, and the study cohort was divided into 3 subgroups: nonusers (cumulative defined daily dose during the follow-up  $< 30$ ), short-term users (cumulative defined daily dose  $= 30$ –364), and long-term users (cumulative defined daily dose  $\geq 365$ ). Antidepressants included selective serotonin reuptake inhibitors (fluoxetine, sertraline, paroxetine, fluvoxamine, citalopram, and escitalopram), serotonin-norepinephrine reuptake inhibitor (venlafaxine, duloxetine, and milnacipran), and norepinephrine-dopamine reuptake inhibitor (bupropion).

### Outcome Assessment

To ensure the diagnostic validity of stroke diagnosis, diagnoses of ischemic stroke (*ICD-9-CM* codes: 433, 434, and 435) and hemorrhagic stroke (*ICD-9-CM* codes: 430, 431, and 432) made by board-certified neurologists, neurosurgeons,

emergency room physicians, and internal medicine physicians after the brain imaging (computer tomography or magnetic resonance imaging) examination were recorded during the follow-up period (from enrollment to December 31, 2011, or until death). A positive predictive value for stroke diagnosis was 88.4% in the NHIRD.<sup>11</sup>

## Statistical Analysis

Regarding between-group comparisons, the *F* test was used for continuous variables and Pearson  $\chi^2$  test for nominal variables, where appropriate. The Cox regression model with adjustment of demographic data (age, sex, income, and residence), medical and psychiatric comorbidities (traumatic brain injury, hypertension, dyslipidemia, diabetes, obesity, smoking, ischemic heart disease, schizophrenia, bipolar disorder, and major depressive disorder), CCI scores, and all-cause clinical visits was used to investigate the hazard ratio (HR) with a 95% CI of ischemic stroke and hemorrhagic stroke among patients with OCD and the control group. Subanalysis stratified by age group (young adults [ $<40$  years] versus mid-adults [ $40\text{--}59$  years] versus the elderly [ $\geq 60$  years]) was further performed. Two types of sensitivity analysis were performed to validate the results. In the exclusion of enrollment period model, only patients diagnosed with OCD after the dates January 1, 2003, were included in the analysis; patients with OCD diagnosed before these time points were selectively excluded. In the exclusion of patients with psychiatric comorbidities model, patients with OCD only and the matched controls who had no schizophrenia, bipolar disorder, and major depressive disorder were included in the analysis. In this subanalysis, we can assess the independent effect of OCD in the risk of subsequent stroke. Furthermore, we assessed the OCD medication treatment and the stroke risk among patients with OCD. Analyses using the competing risk regression model were also performed with death as a competing risk. Finally, to reduce the matching (for stroke-related factors)-related bias, the aforementioned analyses were reperformed, and the study results were reconfirmed based on the nonmatching cohort (cases and controls). A 2-tailed  $P < 0.05$  was considered statistically significant. All data processing and statistical analyses were performed with Statistical Analysis Software version 9.1 (SAS Institute, Cary, NC).

## RESULTS

In all, 28064 patients with OCD and 28064 age-, sex-, and comorbidity-matched controls were included in current study, with an average age of 37 years and female predominance (Table 1). Patients with OCD had an increased incidence of new-onset ischemic stroke (0.29% versus 0.09%,  $P < 0.001$ ), but not hemorrhagic stroke (0.08% versus 0.05%,  $P = 0.188$ ), compared with the non-OCD controls (Table 1). In addition, patients with OCD had higher CCI scores ( $P < 0.001$ ) and all-cause clinical visits ( $P < 0.001$ ) than the non-OCD controls (Table 1).

The Kaplan-Meier survival analyses revealed that patients with OCD were more likely to develop ischemic stroke ( $P < 0.001$ ), but not hemorrhagic stroke

( $P = 0.700$ ), than the control group (Figure). The log minus log plots of the Cox regression analyses performed in current study met the proportional hazards assumption. The Cox regression analyses with the adjustment of demographic data, comorbidities, CCI scores, and all-cause clinical visits demonstrated that patients with OCD (HR, 3.02 [95% CI, 1.91–4.77]), especially the midlife adults (HR, 2.66 [95% CI, 1.34–5.29]) and the elderly (HR, 3.46 [95% CI, 1.70–7.05]), had an elevated risk of developing ischemic stroke during the follow-up period compared with the non-OCD controls (Table 2). The cumulative hazard of hemorrhagic stroke did not differ (HR, 0.87 [95% CI, 0.42–1.80]) between OCD and non-OCD groups (Table 2). In addition, the competing risk regression models with death as a competing risk showed the consistent findings that OCD was related to ischemic stroke (HR, 3.06 [95% CI, 1.93–4.84]), but not hemorrhagic stroke (HR, 0.87 [95% CI, 0.42–1.82]; Table 2). However, despite nonsignificance of hemorrhagic stroke between groups, there was a sudden drop of hemorrhagic stroke occurrence in the tenth year in the control group. We specifically checked the profiles of those 6 patients with hemorrhagic stroke and found that there were aged about 49-year-old, 3 had hypertension, 2 with diabetes, 3 with dyslipidemia, 5 with depression, and one with bipolar disorder.

Among patients with OCD, both short-term use (HR, 1.69 [95% CI, 0.74–3.88]; HR, 0.31 [95% CI, 0.05–1.95]) and long-term use (HR, 1.37 [95% CI, 0.60–3.16]; HR, 0.90 [95% CI, 0.22–3.76]) of OCD medications were not related to the ischemic and hemorrhagic stroke compared with the nonuse (Table 3). The sensitivity analyses of the exclusion of enrollment period model (HR, 2.87 [95% CI, 1.50–5.50]) and the exclusion of patients with psychiatric comorbidities model (HR, 8.15 [95% CI, 3.22–20.61]) confirmed the temporal association between OCD and ischemic stroke (Table 4). The competing risk regression models with death as a competing risk found the consistent findings (Tables 3 and 4).

Furthermore, the Cox regression analyses based on the unmatched sample with the adjustment of demographic data, comorbidities, CCI scores, and all-cause clinical visits confirmed the consistent findings that OCD was an independent risk factor of new-onset ischemic stroke (HR, 3.88 [95% CI, 2.26–6.68]), but not hemorrhagic stroke (HR, 1.44 [95% CI, 0.51–4.11]; Tables I and II in the [Data Supplement](#)). OCD medications were not related to any stroke (Table III in the [Data Supplement](#)). Finally, regarding the multiple testing burden in our analyses owing to the large number of models created as part of the analyses, *P* value of 0.05 was revised to 0.05/8 (0.00625) for the multiple comparison corrections. All statistical significance of our analyses was still existent because of all  $P \leq 0.001$  in current study.

**Table 1. Demographic Data and Incidence of Stroke Among Patients With OCD and the Control Group**

	Patients with OCD (n=28 064)	Controls (n=28 064)	P value
Age at diagnosis of enrollment, y, SD, n (%)	37.14 (12.62)	37.12 (12.71)	0.851
Female, n (%)	14 533 (51.8)	14 533 (51.8)	1.000
Ischemic stroke, n (%)	82 (0.29)	24 (0.09)	<0.001
Age at diagnosis, y (SD)	62.69 (13.28)	63.91 (14.56)	0.700
Duration between enrollment and diagnosis, y, SD; n (%)	4.63 (2.87)	6.44 (2.89)	0.008
<1 y	7 (8.5)	0 (0)	
1–2 y	10 (12.2)	1 (4.2)	
2–3 y	13 (15.9)	4 (16.7)	
3–4 y	10 (12.2)	0 (0)	
4–5 y	7 (8.5)	3 (12.5)	
5–6 y	8 (9.8)	1 (4.2)	
6–7 y	7 (8.5)	3 (12.5)	
7–8 y	6 (7.3)	5 (20.8)	
8–9 y	8 (9.8)	2 (8.3)	
9–10 y	5 (6.1)	1 (4.2)	
≥10 y	1 (1.2)	4 (16.7)	
Hemorrhagic stroke, n (%)	22 (0.08)	14 (0.05)	0.188
Age at diagnosis, y (SD)	49.33 (14.07)	53.90 (15.96)	0.373
Duration between enrollment and diagnosis, y, SD; n (%)	3.25 (2.37)	6.93 (3.44)	0.001
<1 y	6 (27.3)	0 (0)	
1–2 y	1 (4.5)	1 (7.1)	
2–3 y	3 (13.6)	1 (7.1)	
3–4 y	3 (13.6)	2 (14.3)	
4–5 y	4 (18.2)	1 (7.1)	
5–6 y	1 (4.5)	1 (7.1)	
6–7 y	3 (13.6)	1 (7.1)	
7–8 y	1 (4.5)	1 (7.1)	
8–9 y	0 (0)	0 (0)	
9–10 y	0 (0)	0 (0)	
≥10 y	0 (0)	6 (42.9)	
Medical and psychiatric comorbidities, n (%)			
Schizophrenia	3937 (14.0)	3937 (14.0)	1.000
Bipolar disorder	1788 (6.4)	1788 (6.4)	1.000
Major depressive disorder	6326 (22.5)	6326 (22.5)	1.000
Hypertension	3531 (12.6)	3531 (12.6)	1.000
Dyslipidemia	3086 (11.0)	3086 (11.0)	1.000
Diabetes	1613 (5.7)	1613 (5.7)	1.000
Ischemic heart disease	686 (2.4)	686 (2.4)	1.000
Obesity	690 (2.5)	690 (2.5)	1.000
Smoking	1126 (4.0)	1126 (4.0)	1.000
Traumatic brain injury	799 (2.8)	799 (2.8)	1.000
CCI score (SD)	1.32 (1.50)	1.09 (1.40)	<0.001
OCD medication treatment, n (%)			
<30 cDDD	3029 (10.8)	19518 (69.5)	

(Continued)

**Table 1. Continued**

	Patients with OCD (n=28 064)	Controls (n=28 064)	P value
30–364 cDDD	9541 (34.0)	4620 (16.5)	
≥365 cDDD	15 494 (55.2)	3926 (14.0)	
Level of urbanization, n (%)			
1 (most urbanized)	7596 (27.1)	7596 (27.1)	1.000
2	9747 (34.7)	9747 (34.7)	
3	3350 (11.9)	3350 (11.9)	
4	2844 (10.1)	2844 (10.1)	
5 (most rural)	4527 (16.1)	4527 (16.1)	
Income-related insured amount			
≤15 840 NTD/mo	11 552 (41.2)	11 552 (41.2)	
15 841–25 000 NTD/mo	8538 (30.4)	8538 (30.4)	
≥25 001 NTD/mo	7974 (28.4)	7974 (28.4)	
All-cause clinical visits (times per year, SD)	11.73 (14.23)	6.92 (8.27)	<0.001
All-cause mortality, n (%)	461 (1.6)	353 (1.3)	<0.001
Follow-up period, y (mean)	6.53 (3.02)	6.54 (3.02)	0.900

CCI indicates Charlson Comorbidity Index; cDDD, cumulative defined daily dose; NTD, New Taiwan Dollar; and OCD, obsessive-compulsive disorder.

## DISCUSSION

Our findings support the hypothesis that patients with OCD, especially middle-aged and elderly adults, were more likely to develop new-onset ischemic stroke later in life compared with non-OCD controls. However, the cumulative risk of hemorrhagic stroke did not differ between the OCD and non-OCD groups.

The association between OCD and subsequent stroke has not been investigated, although studies have suggested that patients with OCD have a higher prevalence of stroke-related metabolic disorders, including obesity, dyslipidemia, and type 2 diabetes, compared with non-OCD controls.<sup>3,4</sup> Abidin et al<sup>12</sup> performed 2 repeated nationally representative cross-sectional surveys in Singapore and determined that the prevalence of comorbid diabetes significantly increased from 4.1% in 2010 to 10.9% in 2016 in patients with OCD. An Italian study reported that the prevalence rates of hypertension, dyslipidemia, and type 2 diabetes were ≈40%, 20%, and 5%, respectively, in patients with OCD.<sup>4</sup> Isomura et al<sup>3</sup> revealed that patients with OCD were 45% more likely to have at least one metabolic or cardiovascular complication compared with non-OCD controls. Thus, patients with OCD were more likely to be exposed to stroke-related risk factors, especially metabolic syndrome, in this decade,<sup>3,4,12</sup> and consequently, they were associated with an increased risk of developing new-onset cerebrovascular disease. Our study revealed that ≈12%, 11%, and 6% of patients with OCD had comorbid hypertension, dyslipidemia, and diabetes, respectively. Furthermore, patients with OCD had a 3-fold increase in the

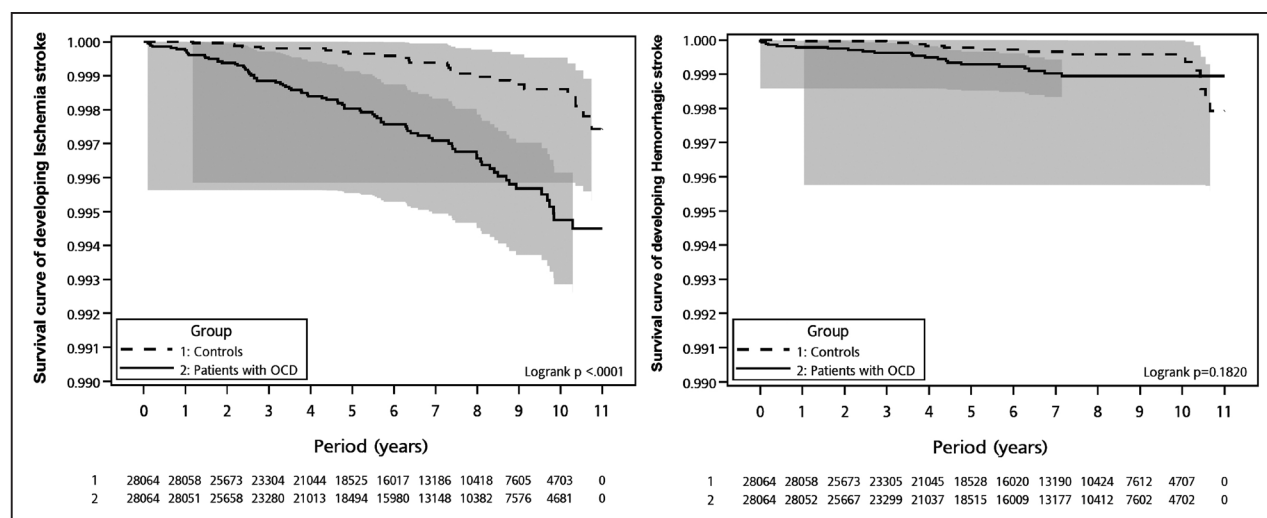


**Figure.** Survival curves of developing ischemic or hemorrhagic stroke between patients with obsessive-compulsive disorder (OCD) and control group.

incidence of ischemic stroke compared with non-OCD controls, independent of hypertension, dyslipidemia, diabetes, and other stroke-related comorbidities.

Isomura et al<sup>3</sup> reported that compared with patients who did not take serotonin reuptake inhibitors, patients who took higher doses (HR, 0.56 [95% CI, 0.32–0.99]) of serotonin reuptake inhibitors for a longer duration (HR, 0.14 [95% CI, 0.09–0.21]) had a significantly lower risk of metabolic and cardiovascular complications. However,

the association between serotonin reuptake inhibitors and stroke risk remains controversial.<sup>13,14</sup> Biffi et al<sup>13</sup> determined that those taking serotonin reuptake inhibitors and atypical antidepressants were at an increased risk of cerebrocardiovascular events, with odds ratios of 1.25 (95% CI, 1.21–1.29) and 1.31 (1.25–1.37), respectively. By contrast, Douros et al<sup>14</sup> reported that compared with the use of weak serotonin reuptake inhibitors, the use of strong inhibitors is associated

**Table 2.** Risk of Developing Ischemic Stroke and Hemorrhagic Stroke Among Patients With OCD and the Control Group\*

	<40 y	40–59 y	≥60 y	Total
	HR (95% CI)	HR (95% CI)	HR (95% CI)	HR (95% CI)
Cox regression model				
Ischemic stroke				
OCD				
Absence	1 (ref.)	1 (ref.)	1 (ref.)	1 (ref.)
Presence	2.42 (0.63–9.31)	2.66 (1.34–5.29)†	3.46 (1.70–7.05)†	3.02 (1.91–4.77)†
Hemorrhagic stroke				
OCD				
Absence	1 (ref.)	1 (ref.)	1 (ref.)	1 (ref.)
Presence	1.03 (0.31–3.43)	0.98 (0.33–2.90)	0.12 (0.01–1.74)	0.87 (0.42–1.80)
Competing risk regression model				
Ischemic stroke				
OCD				
Absence	1 (ref.)	1 (ref.)	1 (ref.)	1 (ref.)
Presence	2.41 (0.63–9.29)	2.67 (1.34–5.30)†	3.58 (1.76–7.28)†	3.06 (1.93–4.84)†
Hemorrhagic stroke				
OCD				
Absence	1 (ref.)	1 (ref.)	1 (ref.)	1 (ref.)
Presence	1.03 (0.31–3.44)	0.97 (0.33–2.88)	0.12 (0.01–1.70)	0.87 (0.42–1.82)

CCI indicates Charlson Comorbidity Index; HR, hazard ratio; and OCD, obsessive-compulsive disorder.

\*Adjusted by demographic data, medical and psychiatric comorbidities, all-cause clinical visits, and CCI scores and OCD as a binary variable.

†Statistical significance.



**Table 3. OCD Medication Treatment and Stroke Risk Among Patients With OCD\***

	Cox regression model	Competing risk regression model
	HR (95% CI)	
	Ischemic stroke	
OCD medication treatment		
<30 cDDD	1 (ref.)	1 (ref.)
30–364 cDDD	1.69 (0.74–3.88)	1.71 (0.74–3.92)
≥365 cDDD	1.37 (0.60–3.16)	1.35 (0.59–3.11)
	Hemorrhagic stroke	
OCD medication treatment		
<30 cDDD	1 (ref.)	1 (ref.)
30–364 cDDD	0.31 (0.05–1.95)	0.31 (0.05–1.92)
≥365 cDDD	0.90 (0.22–3.76)	0.89 (0.21–3.71)

CCI indicates Charlson Comorbidity Index; cDDD, cumulative defined daily dose; HR, hazard ratio; and OCD, obsessive-compulsive disorder.

\*Adjusted by demographic data, medical and psychiatric comorbidities, all-cause clinical visits, and CCI scores and OCD medication treatment as a binary variable.

with a decreased rate of ischemic stroke (relative risk: 0.88 [95% CI, 0.80–0.97]), although the effect size was smaller. Our study with a large sample size of 28 064 patients with OCD found no relationship between antidepressant exposure and subsequent risk of ischemic and hemorrhagic stroke. Further studies on the effect of antidepressants on the risk of cerebrocardiovascular disease, especially stroke, are warranted.

We propose several pathomechanisms to explain the temporal association between OCD and ischemic stroke. First, the presence of psychiatric comorbidities, especially schizophrenia, bipolar disorder, and major depressive disorder, in patients with OCD have been reported to be associated with stroke risk.<sup>15</sup> The comorbidities of severe mental health disorders further increased the likelihood of stroke-related risk factors, including obesity, smoking, and metabolic disorders, owing to hereditary and environmental factors.<sup>16,17</sup> The prevalence of severe mental health disorders being comorbid with OCD is high (≈10% in schizophrenia, 9%–35% in bipolar disorder, and up to 50% in depression).<sup>18</sup> However, severe mental health disorders comorbid with OCD were not adjusted for in the previous studies<sup>3</sup>; therefore, whether OCD is an independent risk factor of stroke remains unknown. In this study, we matched and adjusted for severe mental health disorders between patients with OCD and non-OCD controls and confirmed OCD as an independent risk factor for stroke, especially ischemic stroke. Second, mounting evidence suggests that OCD is a systemic inflammatory disease and that systemic inflammation, including elevated levels of CRP (C-reactive protein) and IL (interleukin)-6, increase the risk of cerebrocardiovascular events later in life.<sup>19,20</sup> Sekeryapan Gediz et al<sup>19</sup> reported a higher neutrophil-to-lymphocyte ratio and

**Table 4. Sensitivity Tests for the Risk of Developing Ischemic Stroke and Hemorrhagic Stroke Among Patients With OCD and the Control Group**

	Total*	Cohort 2003*	Excluding other psychiatric comorbidities†
	HR (95% CI)		
Cox regression model	Ischemic stroke		
OCD			
Absence	1 (ref.)	1 (ref.)	1 (ref.)
Presence	3.02 (1.91–4.77)‡	2.87 (1.50–5.50)‡	8.15 (3.22–20.61)‡
	Hemorrhagic stroke		
OCD			
Absence	1 (ref.)	1 (ref.)	1 (ref.)
Presence	0.87 (0.42–1.80)	0.80 (0.30–2.10)	2.55 (0.53–12.35)
Competing risk regression model	Ischemic stroke		
OCD			
Absence	1 (ref.)	1 (ref.)	1 (ref.)
Presence	3.06 (1.93–4.84)‡	2.85 (1.49–5.47)‡	8.28 (3.27–20.96)‡
	Hemorrhagic stroke		
OCD			
Absence	1 (ref.)	1 (ref.)	1 (ref.)
Presence	0.87 (0.42–1.82)	0.78 (0.30–2.08)	2.51 (0.52–12.16)

CCI indicates Charlson Comorbidity Index; HR, hazard ratio; and OCD, obsessive-compulsive disorder.

\*Adjusted by demographic data, medical and psychiatric comorbidities, all-cause clinical visits, and CCI scores and OCD as a binary variable.

†Adjusted by demographic data, medical comorbidities, all-cause clinical visits, and CCI scores and OCD as a binary variable.

‡Statistical significance.

choroidal vascularity index, which are 2 biomarkers of systemic inflammation, in patients with OCD compared with healthy controls. Turna et al<sup>20</sup> revealed that CRP level was elevated in patients with OCD compared with controls and that CRP had a moderate to strong association with psychiatric symptomatology. The Reasons for Geographical and Racial Differences in Stroke study used a large sample size of 30 239 community-dwelling participants to determine that low high-sensitivity CRP (<2 mg/L) is associated with a reduced risk of incident stroke and coronary heart disease.<sup>21</sup>

The limitations of our study are shared by other registry-based analyses. First, the incidence of stroke may be underestimated because only those who sought medical help would be identified by the database. However, the diagnostic validity of stroke was high based on the physician's diagnosis and confirmation by neuroimaging. Second, data on disease severity, family history, and environmental factors were unavailable in the National Health Insurance Research Database; thus, we could

not assess their impact. Third, our study emphasized the strong unidirectional association between OCD and subsequent ischemic stroke; no causal relationship could be established. Finally, cumulative defined daily dose of ODC medications indicates the cumulative treatment dose and treatment duration of ODC medications in the study period. The between-groups (nonmedication, short-term medication, long-term medication) analysis showed that OCD medications were not related to the stroke risk among patients with OCD in our study. However, the within-individual analysis may be applied in the future study to elucidate the stroke risk between medication and nonmedication periods in the individual level.

In conclusion, patients with OCD had an increased risk of developing new-onset ischemic stroke later in life compared with the non-OCD controls. OCD was an independent risk factor for ischemic stroke after adjustment for stroke-related comorbidities, including metabolic disorders and other severe mental diseases. Clinicians should closely monitor cerebrovascular disease and related risks in patients with OCD. The pathomechanism of OCD with an increased risk of ischemic stroke warrants further investigation.

## ARTICLE INFORMATION

Received October 7, 2020; final revision received March 23, 2021; accepted April 16, 2021.

## Affiliations

Department of Psychiatry (M.-H.C., S.-J.T., T.-P.S., C.-T.L., W.-C.L., Y.-M.B.) and Department of Family Medicine (T.-J.C.), Taipei Veterans General Hospital, Taiwan. Department of Psychiatry, College of Medicine (M.-H.C., S.-J.T., T.-P.S., C.-T.L., W.-C.L., Y.-M.B.) and Institute of Hospital and Health Care Administration (T.-J.C.), National Yang Ming Chiao Tung University, Taipei, Taiwan. Department of Psychiatry, Cheng Hsin General Hospital, Taipei, Taiwan (T.-P.S.). School of Traditional Chinese Medicine, Chang Gung University, Taoyuan, Taiwan (T.-L.P.). Research Center for Chinese Herbal Medicine and Research Center for Food and Cosmetic Safety, College of Human Ecology, Chang Gung University of Science and Technology, Taoyuan, Taiwan (T.-L.P.). Liver Research Center, Chang Gung Memorial Hospital, Taoyuan, Taiwan (T.-L.P.).

## Acknowledgments

We thank I-Fan Hu, MA (Courtauld Institute of Art, University of London; National Taiwan University) for his friendship and support in English editing. Drs Chen, Bai, and Pan designed the study, wrote the protocol, and draft the article. Dr Chen analyzed the data. Drs Su, Tsai, Li, and Lin performed the literature review and assisted with the preparation of the article. Drs Bai and Chen provided the advices on statistical analysis. All authors reviewed and edited the article. All authors proofed the final article and approved the submission.

## Sources of Funding

The study was supported by a grant from Taipei Veterans General Hospital (V106B-020, V107B-010, V107C-181, and V108B-012), Yen Tjing Ling Medical Foundation (CI-110-30), and Ministry of Science and Technology, Taiwan (107-2314-B-075-063-MY3, 108-2314-B-075-037).

## Disclosures

None.

## Supplemental Materials

Online Figure I  
Online Tables I–III  
STROBE Statement

## REFERENCES



- Murray CJ, Lopez AD. The incremental effect of age-weighting on YLLs, YLDs, and DALYs: a response. *Bull World Health Organ*. 1996;74:445–446.
- Kessler RC, Berglund P, Demler O, Jin R, Merikangas KR, Walters EE. Lifetime prevalence and age-of-onset distributions of DSM-IV disorders in the National Comorbidity Survey Replication. *Arch Gen Psychiatry*. 2005;62:593–602. doi: 10.1001/archpsyc.62.6.593
- Isomura K, Brander G, Chang Z, Kuja-Halkola R, Rück C, Hellner C, Lichtenstein P, Larsson H, Mataix-Cols D, Fernández de la Cruz L. Metabolic and cardiovascular complications in obsessive-compulsive disorder: a total population, sibling comparison study with long-term follow-up. *Biol Psychiatry*. 2018;84:324–331. doi: 10.1016/j.biopsych.2017.12.003
- Albert U, Aguglia A, Chiarle A, Bogetto F, Maina G. Metabolic syndrome and obsessive-compulsive disorder: a naturalistic Italian study. *Gen Hosp Psychiatry*. 2013;35:154–159. doi: 10.1016/j.genhosppsych.2012.10.004
- Chen MH, Pan TL, Li CT, Lin WC, Chen YS, Lee YC, Tsai SJ, Hsu JW, Huang KL, Tsai CF, et al. Risk of stroke among patients with post-traumatic stress disorder: nationwide longitudinal study. *Br J Psychiatry*. 2015;206:302–307. doi: 10.1192/bjp.bp.113.143610
- Chen MH, Su TP, Chen YS, Hsu JW, Huang KL, Chang WH, Bai YM. Attention deficit hyperactivity disorder, tic disorder, and allergy: is there a link? A nationwide population-based study. *J Child Psychol Psychiatry*. 2013;54:545–551. doi: 10.1111/jcpp.12018
- Cheng CM, Chang WH, Chen MH, Tsai CF, Su TP, Li CT, Tsai SJ, Hsu JW, Huang KL, Lin WC, et al. Co-aggregation of major psychiatric disorders in individuals with first-degree relatives with schizophrenia: a nationwide population-based study. *Mol Psychiatry*. 2018;23:1756–1763. doi: 10.1038/mp.2017.217
- Liang CS, Bai YM, Hsu JW, Huang KL, Ko NY, Chu HT, Yeh TC, Tsai SJ, Chen TJ, Chen MH. The risk of sexually transmitted infections following first-episode schizophrenia among adolescents and young adults: a Cohort Study of 220 545 Subjects. *Schizophr Bull*. 2020;46:795–803. doi: 10.1093/schbul/sbz126
- Liu CY, Hung YT, Chuang YL, Chen YJ, Weng WS, Liu JS. Incorporating development stratification of taiwan townships into sampling design of large scale health interview survey. *J Health Management (Chin)*. 2006;4:1–22
- Charlson ME, Pompei P, Ales KL, MacKenzie CR. A new method of classifying prognostic comorbidity in longitudinal studies: development and validation. *J Chronic Dis*. 1987;40:373–383. doi: 10.1016/0021-9681(87)90171-8
- Hsieh CY, Chen CH, Li CY, Lai ML. Validating the diagnosis of acute ischemic stroke in a National Health Insurance claims database. *J Formos Med Assoc*. 2015;114:254–259. doi: 10.1016/j.jfma.2013.09.009
- Abidin E, Chong SA, Vaingankar JA, Shafie S, Seah D, Chan CT, Ma S, James L, Heng D, Subramaniam M. Changes in the prevalence of comorbidity of mental and physical disorders in singapore between 2010 and 2016 [published online August 17, 2020]. *Singapore Med J*. doi: 10.11622/smedj.2020124
- Biffi A, Rea F, Scotti L, Lucenteforte E, Vannacci A, Lombardi N, Chinellato A, Onder G, Vitale C, Cascini S, et al. Italian Group for Appropriate Drug prescription in the Elderly (I-GrADE). Antidepressants and the risk of cardiovascular events in elderly affected by cardiovascular disease: a real-life investigation from Italy. *J Clin Psychopharmacol*. 2020;40:112–121. doi: 10.1097/JCP.0000000000001189
- Douros A, Dell'Aniello S, Dehghan G, Boivin JF, Renoux C. Degree of serotonin reuptake inhibition of antidepressants and ischemic risk: a cohort study. *Neurology*. 2019;93:e1010–e1020. doi: 10.1212/WNL.0000000000008060
- Osborn DP, Hardoon S, Omar RZ, Holt RI, King M, Larsen J, Marston L, Morris RW, Nazareth I, Walters K, et al. Cardiovascular risk prediction models for people with severe mental illness: results from the prediction and management of cardiovascular risk in people with severe mental illnesses (PRIMROSE) research program. *JAMA Psychiatry*. 2015;72:143–151. doi: 10.1001/jamapsychiatry.2014.2133
- Huang MH, Chen MH, Huang KL, Hsu JW, Bai YM, Cheng CM, Su TP, Li CT, Tsai SJ, Lin WC, et al. Increased risk of type 2 diabetes among the siblings of patients with schizophrenia. *CNS Spectr*. 2019;24:453–459. doi: 10.1017/S1092852918001396
- Tsao WY, Hsu JW, Huang KL, Bai YM, Su TP, Li CT, Tsai SJ, Lin WC, Chen TJ, Pan TL, et al. Risk of cardiometabolic diseases among siblings of patients with bipolar disorder. *J Affect Disord*. 2019;253:171–175. doi: 10.1016/j.jad.2019.04.094

18. Pallanti S, Grassi G, Sarrecchia ED, Cantisani A, Pellegrini M. Obsessive-compulsive disorder comorbidity: clinical assessment and therapeutic implications. *Front Psychiatry*. 2011;2:70. doi: 10.3389/fpsy.2011.00070
19. Sekeryapan Gediz B, Ozturk M, Kilinc Hekimsoy H, Yuksel EG, Ozdamar Erol Y. Choroidal vascularity index as a potential inflammatory biomarker for obsessive compulsive disorder [published online September 18, 2020]. *Ocul Immunol Inflamm*. doi: 10.1080/09273948.2020.1800052
20. Turna J, Grosman Kaplan K, Anglin R, Patterson B, Soreni N, Bercik P, Surette MG, Van Ameringen M. The gut microbiome and inflammation in obsessive-compulsive disorder patients compared to age- and sex-matched controls: a pilot study. *Acta Psychiatr Scand*. 2020;142:337–347. doi: 10.1111/acps.13175
21. Penson PE, Long DL, Howard G, Toth PP, Muntner P, Howard VJ, Safford MM, Jones SR, Martin SS, Mazidi M, et al. Associations between very low concentrations of low density lipoprotein cholesterol, high sensitivity C-reactive protein, and health outcomes in the Reasons for Geographical and Racial Differences in Stroke (REGARDS) study. *Eur Heart J*. 2018;39:3641–3653. doi: 10.1093/eurheartj/ehy533

REVIEW



## Recent advances in herbal combination nanomedicine for cancer: delivery technology and therapeutic outcomes

Doaa M. Anwar<sup>a,b,\*</sup>, Mousa El-Sayed<sup>c,d,\*</sup>, Asmaa Reda<sup>e,f</sup>, Jia-You Fang <sup>g,h,i</sup>, Sherine N. Khattab <sup>b,c</sup>  
and Ahmed O. Elzoghby <sup>b,j</sup>

<sup>a</sup>Department of Pharmaceutics and Pharmaceutical Technology, Faculty of Pharmacy, Arab Academy for Science Technology & Maritime Transport, Alexandria, Egypt; <sup>b</sup>Cancer Nanotechnology Research Laboratory (CNRL), Faculty of Pharmacy, Alexandria University, Alexandria, Egypt; <sup>c</sup>Chemistry Department, Faculty of Science, Alexandria University, Alexandria, Egypt; <sup>d</sup>Department of Chemistry, School of Sciences and Engineering, American University in Cairo, New Cairo, Egypt; <sup>e</sup>Nanomedicine Division, Center for Materials Science, University of Science and Technology (UST), Zewail City of Science and Technology, Giza, Egypt; <sup>f</sup>Molecular and Cellular Biology Department, Faculty of Science, Benha University, Benha, Egypt; <sup>g</sup>Pharmaceutics Laboratory, Graduate Institute of Natural Products, Chang Gung University, Taoyuan, Taiwan; <sup>h</sup>Research Center for Industry of Human Ecology, Research Center for Chinese Herbal Medicine, Chang Gung University of Science and Technology, Taoyuan, Taiwan; <sup>i</sup>Department of Anesthesiology Chang Gung Memorial Hospital, Taoyuan, Taiwan; <sup>j</sup>Department of Industrial Pharmacy, Faculty of Pharmacy, Alexandria University, Alexandria, Egypt

### ABSTRACT

**Introduction:** The use of herbal compounds in cancer therapy has great potential to promote the efficacy of current cancer therapeutic strategies. Herbal compounds were successfully reported to enhance tumor cells sensitization to the action of chemo-, hormonal- and gene-therapeutic agents *via* different mechanisms. Herbal ingredients can affect different signaling pathways, reduce the toxic side effects or inhibit the efflux of anticancer drugs.

**Areas covered:** This review will discuss the delivery of herbal compounds with other cancer treatments such as hormonal, small molecule inhibitors and inorganic hybrids to tumor cells. An overview of physicochemical properties of herbal components that require intelligent design of combo-nanomedicines for efficient co-delivery of those herbal-derived and other anticancer agents was discussed. Nanocarriers provide various benefits to overcome the shortcomings of the encapsulated herbal compounds including improved solubility, increased stability and enhanced tumor targeting. Different nanocarrier systems were the focus of this review.

**Expert opinion:** Multifunctional nanocarrier systems encapsulating herbal and different anticancer drugs showed to be a wonderful approach in the treatment of cancer enabling the co-delivery of anticancer drugs with versatile modes of action in an accurate manner in an attempt to enhance the efficacy, benefit from the synergism between the drugs as well as to minimize the development of multi-drug resistance. The main challenge point is the early detection and management of any developed adverse effect.

### ARTICLE HISTORY

Received 15 April 2021  
Accepted 12 July 2021

### KEYWORDS


Combo-nanomedicine; drug delivery; herbal compounds; anticancer drugs; combined cancer therapy

## 1. Introduction

Cancer is depicted as the worst monster subversive disease with the utmost cause of death worldwide [1]. It is characterized by ultra-expeditious proliferation, evasion of growth suppressors, replicative immortality, and evasion of the immune system [2]. Most cancer patients were treated with either surgery, radiotherapy, or conventional chemotherapy. In this systemic treatment, patients suffer from severe side effects like fatigue, hair loss, bruising, bleeding, anemia, Nausea, and vomiting [3]. Therefore, the envision model for cancer treatment is to eradicate cancer cells leaving normal cells healthy. Moreover, as chemoresistance has elevated in frequency, experiments have been developed in order to reveal how cancer cells can switch between different signaling pathways

to ensure their continued invasion as well as proliferation, leading to the induction of chemotherapy resistance. [4,5]

In this context, herbal compounds were considered as a powerful therapeutic tool as they contain thousands of components that work together against cancer [6]. Herbal medicines have been long utilized since ancient time, which is directly attributed to their therapeutic values and lower adverse side effects at the same time when compared to modern medicine [7]. Isolated and purified components of medicinal plants attracted attention as they have shown potential in combating various diseases including cancer [8], Alzheimer, and diabetes [9]. However, direct administration of herbal therapeutic agents suffers from bad bioavailability, poor permeability, and poor solubility for some herbal components, fast metabolism, and off-target effect, which means

**CONTACT** Sherine N. Khattab  [sh.n.khattab@gmail.com](mailto:sh.n.khattab@gmail.com)  Chemistry Department, Faculty of Science, Alexandria University, Alexandria 21321, Egypt; Ahmed O. Elzoghby  [aelzoghby@bwh.harvard.edu](mailto:aelzoghby@bwh.harvard.edu)  Department of Industrial Pharmacy, Faculty of Pharmacy, Alexandria University, Alexandria 21521, Egypt

\*These authors contributed equally



### Article highlights

- The most advantage in nano-drug delivery systems is co-administration of several therapeutic agents on the same carrier in a targeted controlled manner. This, in turn, will enhance pharmacokinetics and pharmacodynamics of these therapeutic agents.
- Various types of nanocarriers such as liposomes, nanoemulsions, nano-capsules, inorganic nanoparticles, and dendrimers, have been conjugated with antitumor herbal bioactives in order to overcome the problem of hydrophobicity.
- The mechanism of action for different herbal combination drug delivery systems in numerous types of cancer cells such as liver, breast, lung and colon cancer were deeply highlighted.
- The use of immunotherapy in combination with herbal compounds deserves extensive attention in order to discover the effect of these drugs on the immune system and the possibility of attacking healthy tissues.
- Despite all advantages of herbal combination therapy, there are still many issues that must be addressed and discussed to overcome all drawbacks and challenges of current therapeutics.

This box summarizes key points contained in the article.

that the therapeutic agents may bind to proteins or other molecules in the human body other than the target site for which the therapy was meant to bind. This may result in unexpected side effects [10]. Also, biologically active, water-soluble herbal components such as tannins, flavonoids, and terpenoids demonstrated low absorption across cell lipid membranes, resulting in reduced efficacy and bioavailability [11]. So, in order to increase their bio-efficacy, combination of herbal compounds with (chemo, hormonal, and gene therapy)

would promote a synergistic effect for cancer eradication. To achieve this depiction, the optimum design of nanoparticles was investigated [12]. Carrying potent herbal drug with a sensitizer, which acts in different ways to make cancer cells more susceptible to death by the targeted therapy in a biodegradable carrier or vehicle emerged on the marathon scene for cancer treatment [13,14]. Herein, this strategy could target multiple oncogenic pathways, reduce the effective dose, minimize toxicity to normal cells, achieve effective targeting (Figure 1), improve solubility of components, enhance drug action, achieve sustained controlled drug release and improve therapeutic accumulation in tumor tissue through passive and active targeting [15,16].

In this perspective, the novel approach in our review will highlight different herbal combination drug delivery systems that provide an improved design for combination therapy and their precise mechanism of action including synergistic, potentiation and additive effect with specific examples. We will also highlight the mechanism of action for combined drugs in the tumor cells. These novel insights provide new approaches for safe cancer treatment.

## 2. Optimum design for efficient combination therapy

Breakthrough in nanoparticle-mediated drug delivery is the principal mainstay in the cancer treatment arsenal, particularly targeted combination therapy [17]. The most flourishing advantage in nano drug delivery systems is the co-delivery

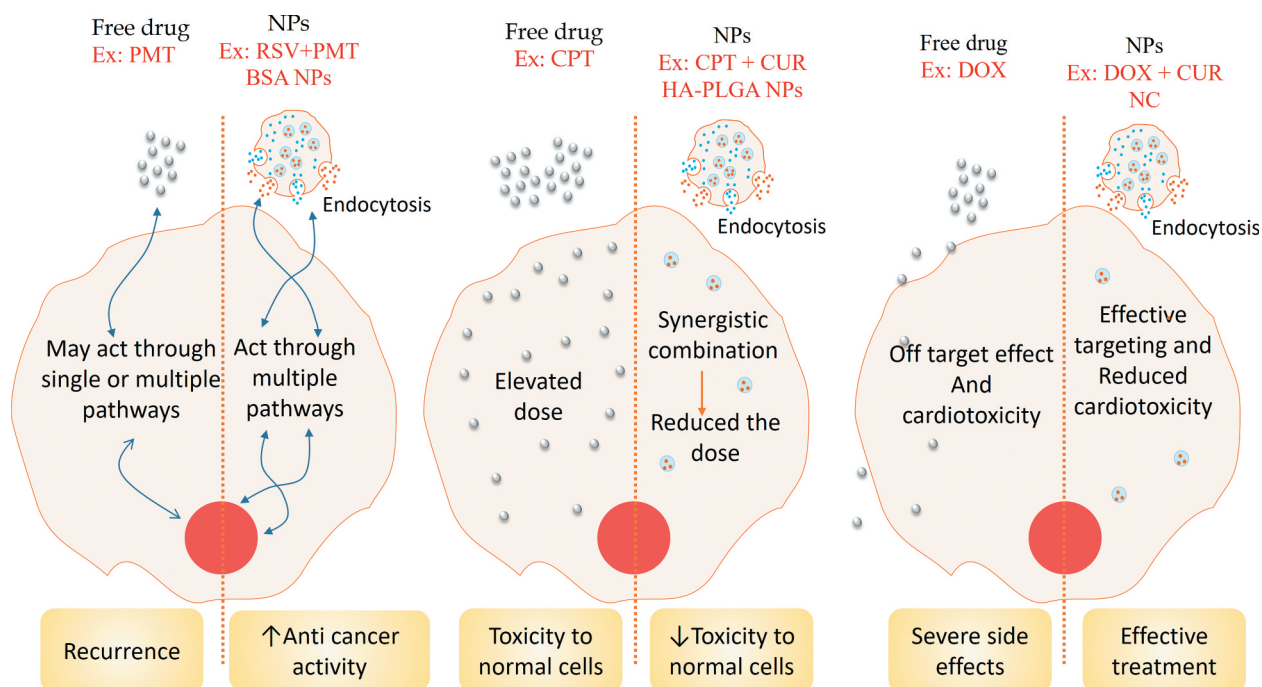


**Figure 1.** Schematic illustration of privileges of targeted combination therapy including high antitumor activity, minimum toxicity and effective treatment. Ex: example PMT: Pemetrexed, RSV: Resveratrol, BSA: Bovine serum albumin. CPT: Camptothecin. CUR: Curcumin. HA-PLGA: Hyaluronic Acid-Poly Lactic-co-Glycolic Acid. DOX: Doxorubicin. NC: Nano capsule.

of multiple therapeutic agents on the same carrier in a Spatio-temporal controlled manner. This, in turn, will improve the pharmacodynamics and pharmacokinetics of these therapeutic agents [18]. Compared to the 'Nano+free drug' approach where one drug can be encapsulated in nanoparticles (NPs) and the other is in free form or the 'Nano+Nano' approach where the two drugs are delivered in two separate NPs but this approach may lead to some drawbacks as the drugs may not reach to the targeted site at the same time, as a result decrease the synergism between the two drugs, so the optimum strategy is co-encapsulation of the two drugs in the same nanoparticle to ensure the maximum efficacy and synergism between the co-delivered drugs [19]. This approach maximizes the intracellular concentration of the drugs and confers drug synergism fighting the cancer [20].

Nowadays, because of the major role of natural products in cancer treatment, they are being widely targeted for drug discovery [21]. Plants are considered the main source of natural products, which are being utilized in medicine. Moreover, the presence of more than active molecule in the herbal compounds may lead to interaction, loss of activity and the possibility of observing new side effects. Hence, enormous types of nanocarriers such as nanoemulsions, phytosomes, dendrimers, nano-capsules, quantum dots, nanoparticles, and liposomes [22] have been conjugated with antitumor herbal bioactives to overcome the problem of hydrophobicity (Figure 2). Strikingly, biodegradable polymeric NPs especially those coated with hydrophilic polymers like PEG (polyethylene glycol) have shown prolonged plasma circulation and powerful ability to deliver genetic therapeutic tools [23]. Furthermore, their large surface area to volume ratio allows modification of NPs surface to be functionalized with targeting

moieties [24]. Herbal therapy shows severe limitation as their therapeutic effect could not be noticed except at the therapeutic concentration range [25,26].

### 3. Anticancer herbal combinatorial approach in nanomedicine

#### 3.1. Herbal and chemotherapeutic drugs encapsulated combinatorial approach

Chemotherapy is the treatment that is most widespread for cancer. This treatment uses drugs to put cancer cells to death or to stop the spreading and growth of cancer to other organs in the body. Unfortunately, chemotherapy not only affects cancer cells but also affects badly all cells growing and dividing quickly in the body such as the bone marrow that produces new blood cells or the cells in the hair, stomach, reproductive organs and skin [27,28]. Also radiation therapy has been used for many years for the treatment of many types of cancer but like other types of treatment it causes many side effects like skin problems, fatigue, lymphedema and nausea [29]. In addition, biological therapy which uses the immune system of the body to destroy the cancer cells cause mild side effects in comparison with other cancer therapies these adverse effects include flu-like symptoms such as fever, weakness, chills [30]. Moreover, drugs that block tumor blood vessels and prevent nutrients and oxygen from reaching to tumor is called angiogenic inhibitors [4]. This type of drugs may cause high blood pressure, rash, itchy skin. Herein, combination of herbal and chemo-therapy could lessen side effects associated with high doses of monotherapy [31]. Moreover it was recently found that Nrf2 activation may provide protection for cells against adverse effects of

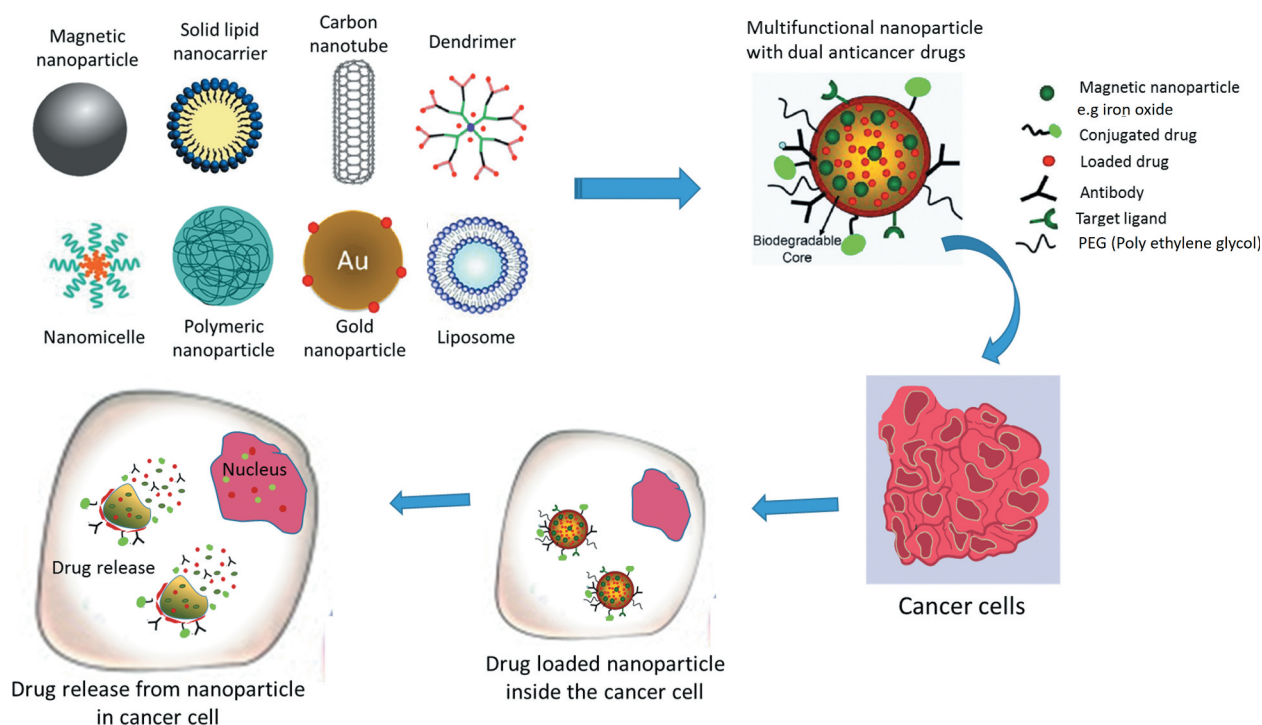


**Figure 2.** Schematic diagram illustrating different multifunctional nanoparticles with dual anticancer drugs targeted to cancer cells. Adapted with permission from reference 27 copyright (2019) Elsevier.

chemotherapeutic agents [32]. Further, it could restrain the multi-drug resistance of cancer through providing diverse mechanism of action [33,34]. But, piercing insight for this scenario lays a disaster which is therapeutic off target for healthy cells. To tackle this problem, drug delivery systems emerged as authentic solution that offer lots of advantages, Table 1. In particular, nanocarriers provide smart controlled release, maximum loading capacity, specific accumulation in target tissue and evading host defense mechanism [31,35].

Rastegar *et al* [36], have designed a co-delivery system for doxorubicin (DOX) and curcumin (CUR) that acted as a chemosensitizer for overcoming chemoresistance in breast cancer. The surface of magnetic NC was decorated by hydroxyapatite that was cross-linked with  $\beta$ -cyclodextrin. This design improved the bioavailability of CUR. DOX and CUR release was in a sustained pH-dependent manner. In addition, the antitumor efficacy revealed the reduction of tumor size. Further, downregulation of P-glycoprotein (P-gp) by western blot indicated the efficacy of drugs in targeting breast cancer multi-drug resistance.

Another drug delivery a 'Nano-in-Nano' approach, was developed to combine the delivery of berberine (BER) as the herbal drug and etoposide (ETP) *via* albumin nanoparticles. Plants that contain BER have been utilized for several years in the treatment of different diseases due to its anti-inflammatory, antimicrobial, antioxidant and anticancer activity. Co-encapsulation of BER was hypothesized to reduce the therapeutic dose of ETP, which as a result minimize its toxicity and overcome the problem of developing resistance, and moreover enhance its antitumor efficacy. The poorly soluble chemotherapeutic drug ETP was first preformulated into phospholipid complex (SPC) or water-soluble nanocrystals before the encapsulation into the hydrophilic albumin nanoparticles. On the other hand, different crosslinkers of albumin NPs (GA, genipin and  $Zn^{2+}$ ) were employed to sustain the release of BER as hydrophilic herbal drug, over several days. Upon administration into lung cancer-bearing mice, the mannose/phenylboronic acid (PBA) dual-targeted BER and ETP NPs showed a potential reduction of vascular endothelial growth factor (VEGF) expression level, triggered caspase activation with tumor cell apoptosis, and enhanced antiangiogenic effect that might refer to synergistic topoisomerase II inhibition and reduction of multidrug resistance (MDR) effect in A549 cells [37,38].

In a consequent study, to further enhance deep lung deposition of ETP and BER, PBA targeted-albumin NPs were incorporated into a spray dried inhalable nanocomposite (NC). The route of inhalation showed superiority over I.V. in reduction of the tumor angiogenesis [39].

Resveratrol (RSV), which is another herbal drug with potential anticancer activity, has also neuroprotective, antiviral, and antioxidant properties. In many studies, the synergism between Pemetrexed (PMX) and RSV was reported in the treatment of breast cancer, where the treatment with the combination therapy decreased the generation of ROS in cells more efficiently than cells treated only with PMX. Furthermore, the synergism between the two drugs, allow RSV to reduce the toxicity of PMX through the protection

against PMT induced apoptosis. Proposing the potential outcomes of co-administering PMX and RSV, lyotropic liquid crystalline nanoparticles (LCNPs) have been formulated for the lung cancer treatment through the combination of PMX and RSV. The results for the test of *in-vivo* in an animal model with urethane-induced lung cancer declared the best decrease in the average of lung weight with no significant difference to the group of the negative control, proving the synergistic effect of the two drugs in improving the therapeutic outcomes. Moreover, the nanocarriers demonstrated a supreme capacity in the suppression of induction of apoptosis and angiogenesis [40].

In another investigation, the herbal drug ellagic acid (EA) was reported to possess antioxidant and antifibrotic effects. In addition the promising antitumor effect of EA was exploited for synergistic combination with the chemotherapeutic drug DOX through induction of cell apoptosis *via* activation of different molecular signals from AMP-activated protein kinase to affect the Bcl-2/Bax apoptosis pathway, where EA can further inhibits NF- $\kappa$ B activation, in addition to its direct action on mitochondria [41]. Furthermore, EA was reported to eliminate drug resistance *via* inhibition of P-gp efflux pumps [5]. Taken together, a nanocarrier incorporating DOX and EA combination based on lactoferrin-chondroitin sulfate (LF-CS) electrostatic nanocomplex was developed by Abd Elwakil *et al* [42]. spray-dried inhalable NC were formulated to enable deep lung deposition and promote the drug delivery through the lung *via* combining the benefits of both nanoparticles (NPs) and microparticles (MPs) [43]. Through Tf and CD44 receptors overexpressed by lung cancer cells, the LF chondroitin nanocomplex showed enhanced entrapment into A549 lung carcinoma cells and subsequent superior cytotoxicity when tested in mice with lung carcinoma [44].

The chemotherapeutic drug, camptothecin (CPT), has showed an impressive anticancer activity in preclinical studies but due to its dose-limiting toxicity as well as limited antitumor efficacy it is always combined with other drugs. Therefore, its combination with CUR in HA-functionalized PLGA NPs showed an excellent targeting effect to colon cancer cells, and the synergistic effect against the cells of Colon-26 were very clear[45]. CPT was also co-administrated with CUR in Chitosan NPs. The results proved that CPT and CUR were simultaneously released and up-taken effectively by cells [46].

Recently docetaxel (DTX) and celastrol (CST) were conjugated to lactoferrin in an attempt for the treatment of breast cancer. The *in-vivo* result showed that the developed nanoconjugate has high *in vivo* anti-tumor efficacy, as expressed by decreasing in tumor volume, significant reduction of Ki-67 p65, COX-2 and NF- $\kappa$ B expression levels and extended survival rate in comparison with positive control and free combined drugs [47].

In this section, we reviewed some combination therapy for chemotherapeutics drugs. Unfortunately, there is some possible disadvantages for those combinations including the possibility of observing new side effects for chemotherapy other than the traditional side effects. This may result from the new combination with new active molecules. Moreover, it will be

**Table 1.** Combo-nanomedicines of herbal therapy with different antitumor remedies for cancer treatment.

Type of combo-nanomedicines	Delivery system	Drug Combination	Major Outcomes	Ref.
Herbal & chemo-therapy	TPGS-PAE polymeric NPs	Curcumin/ Doxorubicin	Synergistic effect in hepatocellular carcinoma	36
	Albumin nanoparticles	Berberine/ Etoposide	Induction of proapoptotic and antiangiogenic factors Synergistic effect in lung cancer Improved cellular internalization Elevated Caspase-3 and downregulate VEGF	39
	Lyotropic liquid crystalline nanoparticles	Resveratrol/ Pemetrexed	Supreme capacity in inhibition of angiogenesis Induction of apoptosis for the treatment of lung cancer.	40
	Lactoferrin-chondroitin sulfate electrostatic NPs	Ellagic acid/ Doxorubicin	Improved the anticancer efficacy of DOX Reduction in the DOX dose and side effects in lung carcinoma due to the synergistic effect.	42
	HA-PLGA NPs	Curcumin/ Camptothecin	Synergistic effect against Colon-26 cells excellent colon cancer cell-targeting ability.	46
Herbal & hormonal therapy	self-assembled lactoferrin conjugate	Docetaxel/ celastrol	high suppression of TNF- $\alpha$ , Ki-67 and COX-2 expression levels.	47
	Poly unsaturated fatty acid based nanomicelles	Naringenin/ Tamoxifen	Enhanced the reduction of tumor size. Improved animals' survival rate in breast cancer models.	55
	Diblock dendrosome	Curcumin/ Tamoxifen	Enhanced the anti-proliferation and apoptosis in both TS-MCF-7 and TR-MCF-7.	56
	Zein nanocapsules	Resveratrol/ Exemestane	Synergistic effect appeared on Ehrlich ascites mammary tumor	60
	Zein nanospheres	Luteolin/ Exemestane	Synergistic antitumor effect in breast cancer Reduction in tumor volume, growth biomarkers and histopathological studies.	61
	Albumin-shell oily-core nanocapsules	Exemestane/ Hesperetin	The percentage elevation was only 25 % of tumor volume in of breast cancer.	62
	Self-nano-emulsifying DDS (SNEDDS)	Bicalutamide/ Hesperetin	Elevation in the oral bioavailability of BCT. Diminishing the toxicity of BCT in the treatment of prostate cancer.	63
	PEG-PLA micelles	Bicalutamide/ Embelin	The co-administration of bicalutamide and embelin suppress prostate cancer tumors.	64
	DOTAP-based cationic liposomes	Curcumin/ Anti-STAT3 siRNA	Improvement in the nano- penetration to 160 $\mu$ m inside the skin High effectiveness in the treatment of skin cancer.	66
	Self-assembled cholesterol-modified low molecular weight chitosan	Curcumin/ Cy <sup>3</sup> labeled siRNA.	Enhancement of apoptosis Enhanced solubility and permeability of curcumin to lung carcinoma.	67
Herbal & genes therapy	Acidic milieu-sensitive multilamellar gold niosomes	thymoquinone (TQ)/ Akt-siRNA	Overcoming lack of cellular target specificity Inhibiting MDM2 expression in breast cancer cells.	68
	PLGA NPs-embedded hydrogel	Camptothecin/ CD98 siRNA	Enhanced internalization by Colon-26 cells. Synergistic effect appeared in the suppression of tumor growth.	69
	MD-UDCA micelles	Resveratrol/ Sulfasalazine	Elevated antitumor efficiency on mice bearing HCC due to the the synergistic effect.	70
	Self-assembled NPs of PEG derivative of vitamin E succinate Layer-by-layer lipid NPs)	Curcumin/ Sorafenib	Enhanced inhibitory effect on tumor progression Increased anti-angiogenesis and antiproliferation capability in HCC.	45
	Zein-Lf micelles	Berberine/ Rapamycin	Synergistic effect between BER/RAP therapy High cytotoxicity to lung cancer.	71, 72
Herbal & small molecule inhibitors therapy	LF-coated GL nanospheres	wogonin/ rapamycin	Reduction in p-AKT and MAPK expression levels Enhanced antitumor efficacy in breast cancer cells.	73
	PLGA/PEG NPs	Diosmin/ Celecoxib	Reduction in the evaluated tumor markers (TNF- $\alpha$ , NF- $\kappa$ B, COX-2, VEGF)	74
	Hybrid lipid protein shell nanoparticles	Curcumin/ Metformin	Massive decrease in hTERT gene expression Dose-dependent cytotoxicity against T47D breast cancer cells.	75, 76
	Phospholipid complex (SPC)	Genistein/ All-trans retinoic acid	Synergistic localized co-delivery of GNS and ATRA for lung cancer therapy.	77
	Spray-dried casein micelles	Quercetin/ Sorafenib	Superior cytotoxicity against liver cancer cell line and HCC-induced mice.	78
Herbal therapy & natural drugs	Succinyl-chitosan liposomes	Berberine/ Diosmin	The system enabled i.v. administration of DSN Controlled release of BRB	79
	PEGylated PLGA NPs	Quercetin/ Trans-resveratrol	Controlled release rate of the payload Prolonged therapeutic action at the target site for the treatment of cancerous intestinal conditions.	80
	Casein micelles	Curcumin/ Chrysin	Enhanced solubility and permeability of the co-delivered drugs for the treatment of melanoma cancer cells.	81
		Resveratrol/ monascus yellow pigments	Higher efficacy and reduction of tumor growth. Reduced toxicity and overcome the MDR in breast carcinoma.	82, 83

(Continued)



Table 1. (Continued).

Type of combo-nanomedicines	Delivery system	Drug Combination	Major Outcomes	Ref.
Herbal therapy & inorganic hybrids	Poly-SPIONs	Curcumin/ SPIONs	Excellent carrier for cancer specific imaging, targeting, and therapeutic application.	84
	SPIONs T7-modified magnetic PLGA nanoparticle	Curcumin & Paclitaxel/ SPIONs	Increase in the cellular uptake by >10-fold. Enhancement in brain delivery by >5-fold compared to the non-targeting NPs.	85
	SPIONs chondroitin sulfate- zein micelles	Celastrol/ Sulfasalazine	Enhanced antitumor efficacy and lowest percentage of tumor volume	127
	Liposome based gold nanoparticles	Curcumin/ GNPs	Irreversible cellular damage of cancer when tested in B16 F10 (melanoma) cell line.	86, 87
	Gold nanoparticles liposome-based gold nanoparticles	Curcumin/ GNPs	Enhanced cancer therapy when tested in C6 glioma cancer cells.	88
	Resveratrol capped Gold NPs (RSV-AuNPs)	Resveratrol/ GNPs	Synergistic effect appeared in diminishing the metastasis of breast cancer.	89
	lactoferrin conjugated mesoporous silica NPs	Pemetrexed/ ellagic acid	high cytotoxicity against MCF-7 cell lines and high uptake of the fabricated NPs	111
	Chondroitin sulfate-based nanocapsules	Celecoxib/ Honokiol/QDs	Increase in the uptake of LF-QDs-CS-NCs by breast cancer cells due to the receptor-mediated endocytosis (RME).	90
	Mannosylated BSA-NPs	Resveratrol/ Pemetrexed/ QDs	Increasing the apoptotic effect Decreased the level of angiogenic factor VEGF-1 in Ehrlich ascites bearing mice.	91
Herbal therapy & immunomodulator	CUR-PEG NPs	Curcumin/Trp2/ CpG ODN	Increased IFN- $\gamma$ production (7-fold). Reduction in the STAT3 pathway by (76%) in an advanced melanoma model.	92

TPGS-PAE: d- $\alpha$ -tocopheryl polyethylene glycol-block-poly( $\beta$ -amino ester) polymers; PEG-PLA: Polyethyleneglycol-b-poly(lactic acid).

difficult to figure out which of these medications is responsible for the new side effect. Furthermore, during the long period of treatment there is a chance for interaction between the components that may lead to a new adverse effect or the loss of activity [48]. Therefore, an intensive research should be focused on the study of those possible consequences of drug combinations *via* nanomedicines.

### 3.2. Herbal and hormone encapsulated combinatorial approach

Certain types of cancer are considered as hormone-dependent cancers such as breast, ovarian and prostate cancers. A lot of hormonal therapy have been approved by FDA for the treatment of these types of cancer such as Aromasin®, Femera®, which are considered as aromatase inhibitors for the treatment of breast cancer [49]. Also Altamofen® and Nolvadex® drugs which contain tamoxifen for the treatment of breast cancer, are estrogen receptor positive (ER+) [50]. Moreover, recently the FDA approved apalutamide®, as a drug that blocks the impact of testosterone and other similar hormones on the prostate cancer cells [51]. Hormone therapy mainly works by slowing or stopping the progression of cancer through administration of certain steroid hormones or drugs that would impede hormone production or alter its activity [52]. Interestingly, reports described that co-delivery of other therapeutic agents such as herbal anticancer drugs with lower toxicity and favorably higher potency alongside with hormonal drugs, results in dramatic reduction in the amount needed of both therapeutic agents with the same efficacy, Table 1. Regarding breast

cancer, patients are usually prescribed with hormonal medications that act by inhibiting the estrogen receptor or reduce the hormone concentration around tumor cells. More than 70% of all breast cancers are estrogen receptor positive (ER+), which is typically treated with the administration of tamoxifen to block the estrogen receptor [53]. While tamoxifen is considered as an effective therapeutic approach for ER+, its long-standing administration is associated with many complications and development of drug-resistant cancer cells [54].

The herbal drug naringenin (NAG) has been used for several years in the treatment of diseases due to its phytochemical properties which includes antiviral, antiadipogenic, anti-inflammatory and antitumor effects. Sandhu *et al* [55], investigated the role of co-delivering tamoxifen and NAG in polyunsaturated fatty acid-based (PUFA) nanomicelles. PUFA-rich lipids having combination of omega-6 and omega-3 fatty acids were found to enhance absorption of the drugs *via* intestinal lymphatic pathways and enhance their micellar solubilization. Co-administration of tamoxifen and NAG *via* nanomicelles resulted in enhanced cytotoxicity against MCF-7 and Caco-2 cells and this may be due to its own anti-proliferative activity and its inhibitory effect of P-gp efflux in synergistic way. In another investigation [56], dendrosomes co-loaded with tamoxifen and CUR showed dramatic increase in their anti-proliferative and apoptotic capability against both tamoxifen-sensitive (TS) and tamoxifen-resistant (TR) MCF-7 cells in and MCF-7 cancer while showed lower toxicity to normal fibroblast cells compared to tamoxifen alone.

The challenge point in cancer treatment using tamoxifen is studying the potential genetic and epigenetic changes within the cancer cells that could take a part in tamoxifen resistance appearing in alteration in ER expression and mutation of ER leading to ER activation instead of inhibition. Many studies that used tamoxifen in the treatment of cancer did not cover this point. A recognition of how the program of ER-controlled transcription is dysregulated in the breast cancer, and how it modifies the resistance development to this type of endocrine therapy will result in improving strategies for the use of current endocrine therapies and for developing novel and more efficacious agents for the treatment and prevention of breast cancer [57].

Aromatase is one of the most popular enzymes found in the breast tissues, which is responsible for the formation of the most potent endogenous estrogen, estradiol. In estrogen-dependent breast cancer, it is important to decrease the growth stimulatory effects of estrogens through the inhibition of aromatase. The herbal drug RSV showed bi-level suppression of aromatase at both enzyme and mRNA levels resulting in inhibition of estrogen biosynthesis [58,59]. Moreover, RSV has demonstrated a potent antagonism of estradiol-induced MCF-7 cell growth as well as powerful inhibition of P-gp activity and hence, RSV may overcome exemestane (EXM) resistance. Elzoghby *et al* [60] published a study in which zein nanocapsules were successfully fabricated to enhance the solubility and permeability of the aromatase inhibitor EXM and RSV, and hence inducing a synergistic cytotoxic effect against breast cancer cells. The NCs demonstrated enhanced cytotoxicity and reduction in tumor volume by 2.4-fold compared to free drugs in Ehrlich ascites mammary tumor models [60].

Similarly, the herbal tetrahydroxyflavone luteolin (LUT) that is characterized with multiple pharmacological activity, such as anti-allergy, antitumor and antioxidant was co-delivered with EXM *via* zein nanospheres to improve its anticancer efficacy and reduce the development of resistance *via* synergistic inhibition of aromatase. The nanospheres displayed enhanced antitumor activity in breast cancer bearing mice through inhibition of aromatase and down-regulation of Cyclin D1, VEGF, and up-regulation of apoptosis and necrosis markers [61].

Hesperetin (HES), a flavonoid that can be extracted from citrus fruits, has various biological properties, particularly anti-inflammatory, antioxidant and anticancer activity. Recently, by virtue of its strong aromatase suppression activity, the herbal drug HES was combined with EXM *via* albumin-shell oily-core NCs to diminish its bone detrimental effects and elevate its efficacy. Moreover, albumin as a protein give the opportunity for the conjugation of another targeting ligand through a carbodiimide reaction such as 3-aminophenylboronic acid (APBA) which was coupled to the shell of albumin to target sialic acid residues upregulated in many cancer cells (Figure 3). The authors reported that a significant decrease in both tumor Ki67 expression (3-folds) and volume (7-folds) was observed for the targeted nanocarriers in comparison with the positive control [62].

Androgens are one of the reasons of causing prostate cancer cells to grow. Decreasing levels of androgen or preventing them from going into the cells of prostate cancer

usually causes shrinkage of prostate cancers. Hesperetin was combined with bicalutamide (BCT) in self nano-emulsifying DDS (SNEDDS) to overcome the low bioavailability, solubility, and toxicity of BCT. HSP motivates apoptosis by utilizing the potential of mitochondrial membrane and suppresses cellular reproduction in PC-3 prostate cancer cells. The significant reduction in the biochemical markers of nephrotoxicity may be due to the increase for the concentration of HSP in SNEDDS [63]. In another investigation, codelivery of embelin and BCT in a PLGA-based micelles resulted in 60-fold elevation of the water solubility of BCT and embelin with improvement of drug bioavailability [64].

Despite the advantages of the combination of hormonal therapy, extensive clinical studies should be done to detect the possibilities of developing severe adverse effects due to the synergistic hormonal suppression on the other vital organs as this may interfere with the functionality of certain hormones in the human body. For example, women taking hormonal therapy for the treatment of breast cancer may develop side effects such as vaginal dryness and mood swings. Similarly, treating prostate cancer may impact on the erectile dysfunction and loss of libido. So cancer treatment using hormonal therapy needs more and more investigation to ensure its safety on other organs [65].

### 3.3. Herbal and gene therapy encapsulated combinatorial approach

One of the most stemming revolutions in combating cancer is gene therapy. Basically, the most common genetic therapeutic tools are; short hairpin RNA (shRNA) [66], small interfering RNA (siRNA) [67,68], micro RNA (miRNA) [69], and DNA. Their mechanism of action to eradicate cancer cells occurs *via* expression of pro-apoptotic proteins, substitution of mutant genes, production of anticancer cytokines, suppress MDR [70], silencing oncogenic pathways and activation of immune system for fighting cancer [71,72]. Although gene therapy holds great potential therapeutic effect, there are lots of difficulties that should be overcome. Basically, unmodified genetic tools have rapid clearance from the body being rapidly degraded by nucleases that limit serum half life time of siRNA to 5–60 min [73] and naked DNA to only 10 min [74,75]. Moreover, they lack specific target, perfect organ distribution and low cellular uptake. In this context, revolution in nanotechnology led to appearance of novel drug delivery carriers that are designed to surmount gene therapy challenges [70,76].

Piercing insight in mono-delivery of genetic therapy for cancer treatment showed that, only transient and partial anti-tumor effect appeared. To harness this emerged obstacle, nanoparticles co-encapsulating herbal and gene therapy hold promising potential effect for long lasting effect, overcoming multidrug resistance, promoting apoptosis and inhibition of angiogenesis by generating synergistic anticancer effect. Table 1 lists some examples of such promising combination therapy as an efficient way for cancer eradication.

Curcumin has been established as herbal anticancer. Anup *et al.* have designed a nano-combination for anti-STAT3 (signal

transducer and activator of transcription3) siRNA and CUR using DOTAP-based cationic liposomes for skin cancer treatment [77]. Moreover, Omkara *et al.* have developed a system for co-delivery of both CUR and Cy<sup>TM</sup>3 labeled siRNA through self-assembled cholesterol-modified low molecular weight chitosan (MW ~15 KDa). This co-delivery system enhanced apoptosis, decreased side effects, enhanced solubility and permeability of CUR [78].

Thymoquinone (TQ), the major component of the volatile oil of black seeds is considered nowadays, one of the most promising treatment options of cancer. TQ can act as both reactive oxygen species inducer (at a high concentration) and antioxidant (at low concentration) [79]. Shashi *et al.* have developed acidic milieu-sensitive multilamellar gold niosomes (Nio-Au) for the combination of TQ and Akt-siRNA. This system enables the delivery of TQ and Akt-siRNA for targeting MCF7 breast cancer cells overexpressing Akt.

Recently, CD98 siRNA (siCD98) was combined with one of the natural topoisomerase inhibitor CPT and co-loaded into CD98 Fab'-functionalized PLGA NPs, as an effective targeted DDS for the treatment of colon cancer [80].

Even though cancer is a genetic disorder, the genetic fluctuations between individuals or even between tumors at different positions in the same person are a fundamental issue. The major obstacles for the gene therapy are the clinical application, due to the financial, ethical and policy issues. Moreover, an argument that the genetic changes may transfer or pass to offspring is another limitation that need an extensive attention from the coming researchers. Furthermore, another challenge for the usage of cancer gene therapy either separate or in a combination is the inability to target metastatic cancer, due to the genetic as well as epigenetic heterogeneity, the development of resistance, and the difficulty in determining metastases location. Finally, efforts should be directed to design an ideal cancer gene therapy with the ability to treat primary as well as metastatic cancer with minimal adverse effect on normal cells and less effect on the coming generations [81].

### 3.4. Herbal and small molecule inhibitors encapsulated combinatorial approach

The co-delivery of small-molecule inhibitor drugs with other drugs are widespread in clinical practice and its encapsulation into macromolecular carriers is expected to help in the sustained and controlled drug release with balanced rates and ratios, and in targeting specific cancer cells.

It was reported that sulfasalazine (SSZ) would inhibit the proliferation of Huh-7 and SK-Hep-1 liver cancer cells *via* autophagy. Resveratrol (RSV) was reported to stimulate ROS generation, which as a result may induce autophagy for the apoptotic cell. Thus, RSV can decrease the effective dose of SSZ. Anwar *et al.* [82] have successfully fabricated amphiphilic maltodextrin-ursodeoxycholic acid (MD-UDCA) micelles for the dual targeted delivery of RSV and SSZ in an attempt to treat hepatocellular carcinoma. The developed micelles have overcome the RSV poor water solubility, low bioavailability and rapid metabolism by its incorporation into the micellar

lipophilic core. The maximum efficacy of the two drugs was achieved by decoration of the micelles surface by lactobionic acid (LA) and folic acid as targeting ligands, the dual targeted RSV-SSZ micelles had the superior antitumor efficacy, Table 1.

In another attempt to treat hepatocellular carcinoma (HCC), CUR was combined with sorafenib (SFB) as a tyrosine kinase inhibitor by self-assembled nanoparticles (SCN). These NPs were fabricated by utilizing the hydrophobic interactions between the hydrophobic moieties in sorafenib, CUR, and the lipophilic part of PEG derivative of alpha-tocopheryl succinate (PEG-VES). The concentration of CUR and SFB in the tissue was improved by 5.85-and 4.23-fold, respectively *via* SCN than free drug concentration, Table 1[45].

Through (AMP-Activated Protein Kinase) AMPK activation, BER was found to block the mTOR pathway. Consequently, co-administration of the mTOR inhibitor rapamycin (RAP) and BER on HepG2 cells, revealed the synergism between the two drugs as BER would preserve the cytotoxic effect of RAP at a smaller concentration. Thus, BER can decrease the immunosuppression associated with RAP allowing its dose to be minimized. Kabary *et al.* [83]. have recently fabricated polymeric shell-lipid core NPs for the co-administration of RAP and BER in an attempt to treat lung cancer. To increase their targeting to lung cancer cells, the NPs were covered with positive charged LF and negatively charged hyaluronic acid (HA) through layer-by-layer assembly which bind to transferrin (TfR), and CD44 receptors, respectively, overexpressed on lung cancer cells, (Figure 4, Table 1). The spray-dried lipid NC showed the best significant tumor growth suppression effect with 2.99-fold increase in caspase-3 level and a 3.6-fold decrease in the level of VEGF in lung tumor cells compared with the group of positive control [84].

Wogonin (WOG) a traditional Chinese medicinal herb was used for the treatment of allergic, inflammatory diseases and nowadays for the treatment of cancer. Recently WOG was combined with RAP for the treatment of breast cancer, Table 1. Self-assembled amphiphilic micelles were designed by Sabra *et al.* [85]. for the co-administration of the hydrophobic drugs WOG and RAP for treatment of breast cancer. Zein was utilized to form the hydrophobic micellar core, while LF was utilized to form the hydrophilic shell, which could attach to TfR and LDL receptors which are excessively found on cells of breast cancer. In order to improve the structural integrity of the micelles and prolong the release of the drug, glutaraldehyde was utilized as crosslinker. The newly fabricated micelles with WOG and RAP had the ability to inhibit Mitogen-activated protein kinase MAPK and p-AKT expression levels which as a result improve the antitumor efficacy [86].

The naturally occurring flavone glycoside Diosmin (DSN) was used for treating numerous disorders of blood vessels including varicose veins, hemorrhoids and poor circulation due to its healing properties, and recently it was proven to have anticancer properties. DSN and Celecoxib (CXB) as COX-2 inhibitors are expected to have anticancer synergistic effect and this may be attributed to their common inhibitory effects on TNF $\alpha$ , NF- $\kappa$ B and COX-2 [87]. Furthermore, both two drugs can suppress PI3K/AKT signaling pathway in tumor cells. Gliadin (GL) nanospheres were designed for the co-delivery

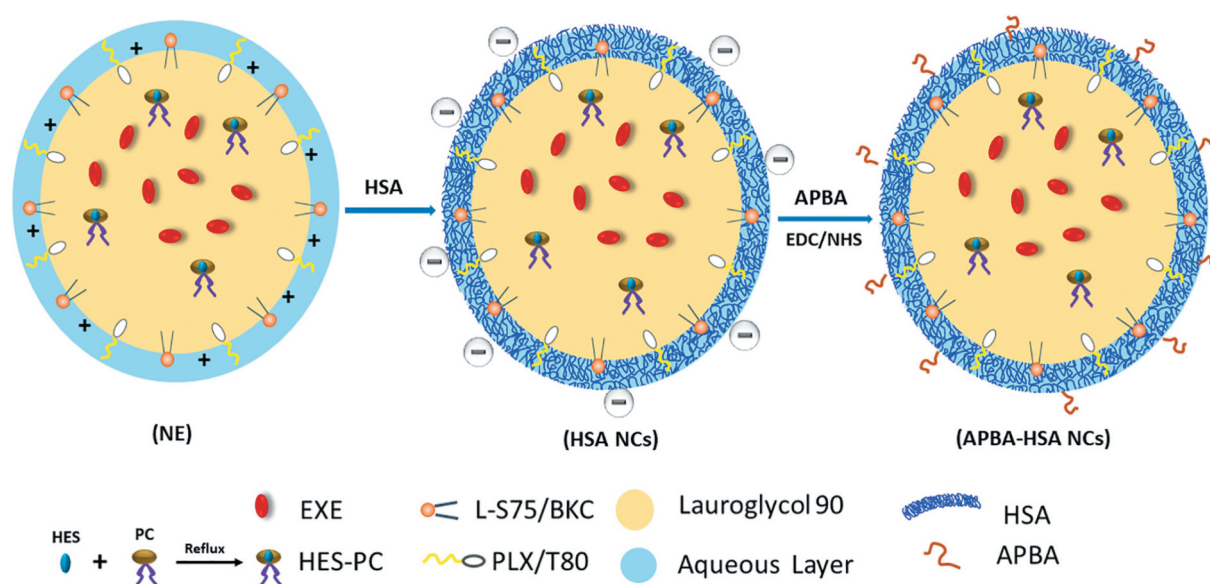


**Figure 3.** A Schematic diagram of dual EXE/HES-loaded APBA-targeted HSA NCs. Adapted with permission from reference 62 copyright (2019) Elsevier. HES: Hesperetin, HAS: Human serum albumin, APBA: 3-Aminophenylboronic acid, EXE: Exemestane, BKC: Benzalkonium chloride, PC: Phosphatidylcholine, PLX: Pluronic® F68.

of CXB and DSN to overcome their high lipophilicity and enhance their low bioavailability, Table 1. LF was used to coat the surface of GL *via* electrostatic interaction to improve the tumor targeting and enhance the GL nanospheres uptake by binding to TfR and LDL receptors which are excessively found on liver cancer cells. The antitumor efficacy showed that LF-targeted GL-NPs were superior in suppression of TNF- $\alpha$ , NF- $\kappa$ B and VEGF [88].

Metformin (MET) is an excessively used antidiabetic drug which reduces the resistance of insulin. Many epidemiological studies declared that many diabetic patients treated with MET have minimized incidence of cancer and cancer mortality [89]. Moreover, MET affects the development and retrogression of lung, breast and prostate cancer mouse xenografts *via* the consecutive modulation of c-MYC and DICER [90]. Farajzadeh *et al* [91] have optimized co-administration of CUR and MET into PLGA/PEG NPs to be specifically directed to hTERT gene in T47D breast tumor tissues, Table 1 [92].

The herbal drug Genistein (GNS), a tyrosine kinase suppressor can intervene with the G2/M phase of the cell cycle, suppress angiogenesis in tumor cells, and also stimulate autophagocytosis [93]. In a recent study, GNS was co-loaded with a metabolite of vitamin A, All-trans retinoic acid (ATRA), in hybrid lipid protein shell NPs (HLPNPs), for treatment of lung carcinoma, Table 1. In order to improve the deposition of these NPs deeply in the lung cells, the drug-loaded HLPNP NC with the dual-targeting ligands were modified into inhalable NC through spray-drying (Figure 5). The NC showed significant reduction in the tumor biomarkers, the weight of lung, and the metastatic foci diameters [94].

Medicinal plants that have antioxidant activities as Quercetin (QRC) play a vital role in exhibiting useful functions and is considered as an alternative resource of medicine to relieve the disease associated with oxidative stress like cancer. QRC as herbal drug was co-administrated with the SFB which was formulated as SPC as it is neither soluble in water nor in

oil medium, so its solubility and stability was increased through oily core-protein shell NCs. Lactoferrin as a targeting shell was electrostatically deposited onto the hydrophobic core loaded with the drug to form LF shell-oily core NCs. In order to, obtain dual targeting to the tumor cells, glycyrrhetic acid (GA) or LA were conjugated individually to LF shell for binding to GA as well as asialoglycoprotein receptors over-expressed on HCC. This study revealed the superiority of dual-targeted LF-NCs over the non-targeted formula. The results showed that LA/LF-NCs had high antitumor efficacy in mice bearing hepatocarcinoma, manifested as significant reduction in the mRNA expression levels of tumor necrosis factor  $\alpha$ , nuclear factor-kappa B and Ki-67 protein expression level in mice with liver cancer ( $P < 0.05$ ) [95].

In spite of the great success achieved due to the combination of small molecule inhibitors with herbal compounds, still there is a concern from developing new side effects due to the new combination and possibility of interaction between the released active molecules at the target site which may lead to loss of anticancer activity and developing new molecules causing severe adverse effects. From this point, we need further studies to ensure the safety of the new fabricated combinations [96].

### 3.5. Herbal and natural drugs encapsulated combinatorial approach

Several natural agents showed anticancer activity in many experimental systems. They could affect different targets, modulate the cell cycle proliferation, gene transduction, cell death and apoptosis. Recently, the use of green chemotherapy found to enhance the efficiency, overcome multidrug resistance (MDR) as well as many side effects of conventional therapy [97].

The synergism between DSN and BRB can be explained through decreasing the tumor growth *via* inhibiting the



expression for the markers of inflammation like COX2 and iNOS via knocking down the expression of NF $\kappa$ B in liver cancer induced rats. Moreover, BRB can inhibit the expression of Bcl-2, the anti-apoptotic factor, as well as suppressing mTOR-signaling causing autophagic death of HCC. A novel green nanomedicine for the treatment of liver cancer by synergistic phytotherapy was formulated by Abdelmoneem *et al*, Table 1 [98]. Spray-dried casein micelles (CAS MCs) were developed for the combination of two herbal nanomedicines, DSN and BRB for targeting liver cancer. To promote targeting of liver cancer cells, a dual targeting approach using lactobionic and folic acids was achieved through binding asialoglycoprotein and folate receptors overexpressed by cancer cells (Figure 6).

In addition, QRC and trans-RSV as natural polyphenols were combined in polymer-based liposomes designed for oral delivery by Caddeo *et al* [99] who utilized *N*-succinyl-chitosan for the formation of the protective shell on the liposome surface. The formulated liposomes can help in the treatment of pre-cancer and cancer of intestine that are combined with oxidative stress and inflammation.

PEGylated PLGA NPs have been designed for co-administration of CUR and chrysin to improved their absorption and permeability, Table 1 [100]. The concentration of drugs in the cell was enhanced showing synergistic effect between the CUR and chrysin on Caco-2 cell proliferation where the combination index (CI) value was  $<1$  [101]. A massive reduction in hTERT expression in Caco-2 cells was observed. After injection into C57/BL6 mice bearing B16F10 melanoma, CUR and Chrysin (Chr) co-loaded PLGA-PEG NPs resulted in a significant reduction in MMP-9, TERT as well as MMP-2 genes and elevation in expression of the tissue suppressors of metalloproteinase genes, TIMP-1 and TIMP-2 [102].

Recently, drugs isolated from microbial origin have gained a great attention because of the less side effects when compared to the cancer traditional treatment [103]. The

hydrophobic monascus yellow pigments (MYPs), ankaflavin, and monascin were separated from red mold rice, and were loaded with RSV into CAS MCs, Table 1. Combination of the RSV/MYPs into CAS MCs, has exploited high solubilizing power of the hydrophobic micellar core, the extraordinary cell membrane penetration potential of CAS MCs, the small-size-mediated EPR effect, and drug release of in a sustained manner [104]. Consequently, actively targeted folate-conjugated CAS micelles entrapping the lipophilic RSV/MYPs into their lipophilic core and passively targeted MYPs-loaded CAS MCs covered with a bilayer of PEGylated resveratrol-phytosomal complex were developed. In breast cancer bearing mice, FA-CAS MCs and PEG PC-CAS MCs successfully reduced NF- $\kappa$ B level and exhibited elevation in apoptotic caspase-3 level compared to free drugs [105].

Most herbal compounds and natural occurring remedies are considered safe and cause less side effects. However, many studies revealed the ability of these active molecules to interact with many other drugs and also with other active molecules causing unexpected adverse effects. The presence of more than herbal remedies in the same formula may increase the risk of loss of their activity due to the probability of interaction. Therefore, further investigation is needed to be directed to address this point [106].

### 3.6. Herbal and inorganic hybrids encapsulated combinatorial approach

The use of inorganic nanoparticles (INPs) for drug delivery comprises lots of advantages in the treatment process of cancer as therapeutic agents in addition to their capability to facilitate imaging and so monitoring cancer treatment progress [107]. Furthermore, INPs could be co-delivered with other chemotherapeutics in multifunctional NPs as nanotheranostic tools for cancer treatment and imaging [108,109].

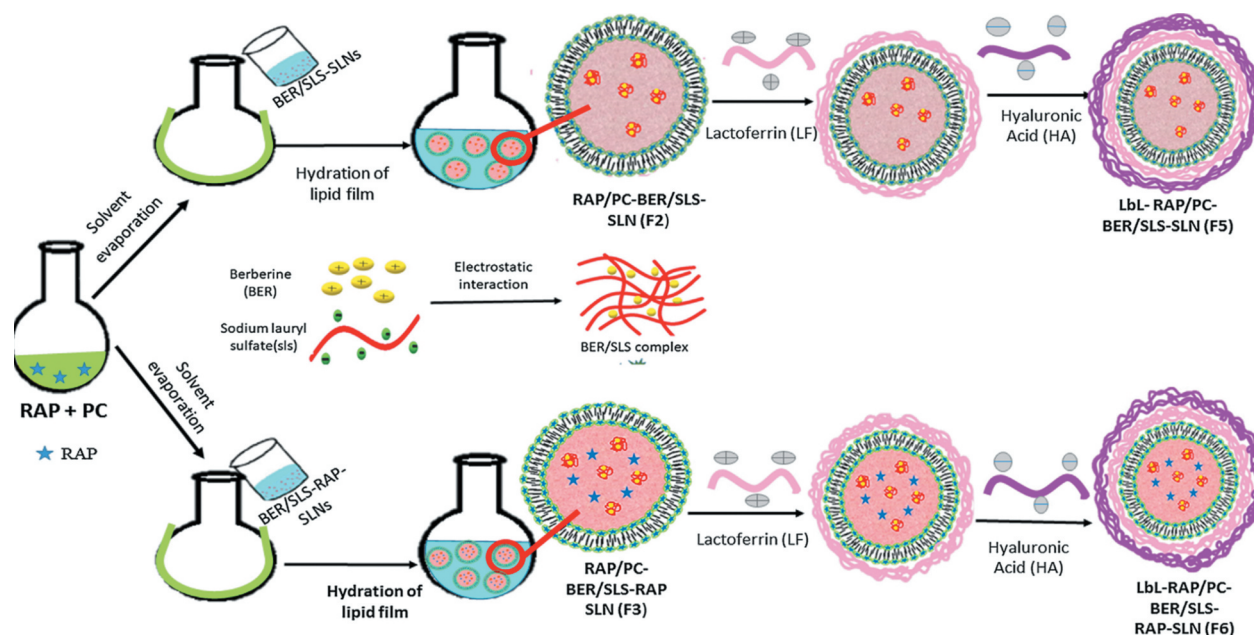


Figure 4. Schematic diagram illustrating the preparation steps of multi-compartmental nanocarriers; LbL-RAP/PC-BER/SLS-SLNs (F5) and LbL-RAP/PC-BER/SLS-RAP SLNs. Adapted with permission from reference 72 copyright (2018) Elsevier.

Theranostics refer to using nanomedicine to combine therapeutic and diagnostic agents in a single contemporary system [110].

Iron oxide nanoparticles have been extensively used for accurate imaging. They showed successful result in Magnetic Resonance Imaging (MRI) of cancer as well as soft tissues. They are considered safe as they are biodegradable and are not accumulated in the tissue [111]. As reported by Levy *et al* [112] iron species was found in both liver and spleen. At the sub-cellular level they observed the biotransformation of the iron oxide nanoparticles into (ferritin) iron storage species within lysosomes [112]. MRI have a lot of advantages over fluorescent probes as the signal localization within tissues is better and the image is deeper in the body [113]. Recently Chakraborty *et al* [114] designed SPIONs coated with glycine. The newly designed GSPIONs targeting specific immune cells in the lung, without causing any respiratory inflammation and noninvasive imaging was supported [114].

Superparamagnetic iron oxide nanoparticles (SPIONs), in addition to their high biocompatibility, could be targeted to the desired tumor sites by external magnet. Interestingly, they generate local heat for up to 43°C upon exposure to external alternative magnetic field (AMF) which induce apoptosis for cancer cells and nearby blood vessels [115,116]. Tumor cells are more liable to hyperthermia as compared to normal cells due to low pH, vascular disorganization, elevated hypoxia and poor regulation of temperature owing to limited transfer of fluid [117]. Although hyperthermia can kill cancer alone, they are usually combined with other types of therapies such as radiotherapy and chemotherapy for enhanced cancer

treatment, as well as monitoring the treatment process by magnetic resonance imaging (MRI) [117].

Dual responsive polymer was used to coat the designed aqueous-soluble SPIONs for the delivery of CUR to the target site, Table 1 [118]. Superparamagnetic mixed spinel ( $\text{MnFe}_2\text{O}_4$ ) NPs were modified with FA as a targeting ligand, poly-*N*-isopropyl acrylamide-co-poly-glutamic acid as a dual responsive polymer and carboxymethyl cellulose as water soluble component. The NPs successfully targeted breast cancer cells MCF7 and released the drug at pH 5.5 and 40°C. Cui *et al* [119], co-administrated CUR and paclitaxel with magnetic nanoparticle (MNPs) in poly(lactic-co-glycolic acid) (PLGA) NPs, Table 1. Dual brain targeting was accomplished by incorporation of magnetic targeting and TfR receptor-binding peptide T7. The combination of the two drugs lead to synergistic suppression of tumor growth through apoptosis induction and cell cycle arrest. The dual-targeted NPs yielded >5-fold increase in brain delivery compared to the non-targeted NPs. The NPs showed enhanced anticancer efficacy with 100% survival rate for mice with orthotopic glioma compared to only 62.5% for the groups which received free drugs.

SPIONs were utilized in another study for the treatment of breast cancer, in this study celastrol (CST) was combined with sulfasalazine (SFZ). The result proved that SPIONs targeted CST-loaded polymeric micelles showed the highest anti-tumor efficacy *in-vivo* via inhibition of VEGF and COX-2. Moreover, this formula was successful in decreasing the percentage of tumor volume in the tested mice [120].

Certain plasmonic nanomaterials, such as photothermal agents (PTAs), can convert NIR laser irradiation to local heat for thermal ablation of cancer [121–123]. Gold nanoparticles

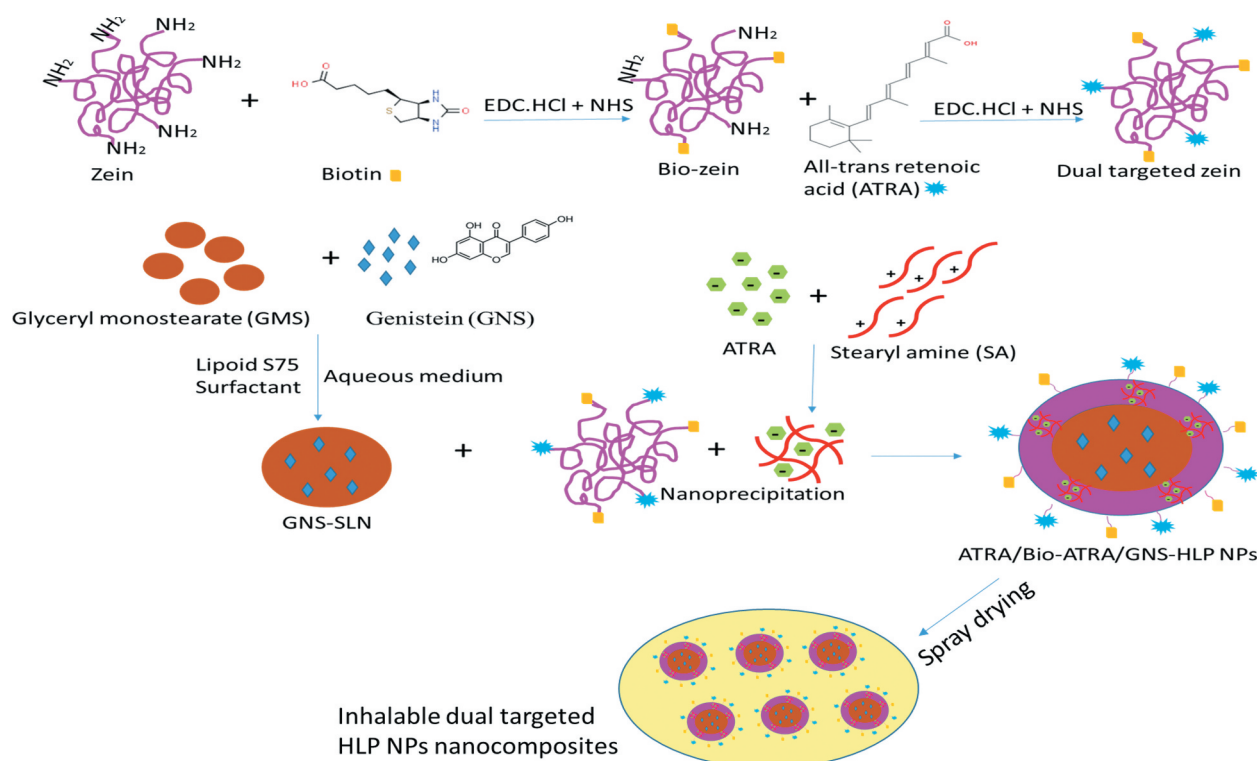


**Figure 5.** Schematic diagram for the formulation of ATRA/Bio-ATRA/GNS-HLPNPs. This diagram clarifies the co-loading of GNS and ATRA into HLPNPs and these NPs were decorated with biotin and ATRA for targeting lung cancer. Adapted with permission from reference 77 copyright (2020) American Chemical Society.

(GNPs), as an example of PTAs, exhibited encouraging therapeutic efficacy alone or synergistically in combination with other therapeutic agent as a contemporary approach, guided by their intrinsic imaging property [122,124]. CUR was encapsulated in liposome-based gold NPs with encapsulation efficiency around 70%, Table 1 [125]. These NPs specifically absorbed NIR light (780), converting the light energy to heat. The generated heat enhanced CUR release by destabilizing the liposomal core leading to irreversible damage of B16 F10 nanoparticles (Lipos Cur NPs) were around 12- and 10-folds increase, respectively when compared melanoma cells. Park *et al.* studied the effect of capping of RSV with GNPs (RSV-AuNPs) as anti-invasive therapy to human breast cancer cells in response to 12-O-tetradecanoylphorbol-13-acetate TPA stimulation, Table 3. The NPs exhibited suppression of COX-2, NF- $\kappa$ B and MMP-9 as well as the stimulation of HO-1 signaling cascades [126,127].

Another type of inorganic nanoparticles used for the delivery of anticancer drugs is mesoporous Silica, which it is widely used nowadays due to their attractive features such as biocompatibility, stability and high drug loading due to the large surface area. Recently lactoferrin conjugated mesoporous silica NPs were fabricated for the delivery of ellagic acid and pemetrexed for breast cancer treatment [128–130]. Furthermore, several reports highlighted the enhanced tumor combating by co-delivery of therapeutic agents alongside with Quantum dots (QDs). QDs are semiconductor-based crystals with a size range of 2–10 nm exhibiting tunable photoluminescence in a wide spectrum from visible to near IR wavelengths [131]. These distinctive physicochemical properties favored their usage in cell labeling and cancer imaging. Abdelhamid *et al.* [132], reported the co-delivery of CXB and the herbal alkaloid honokiol in the core of QDs-LF NCs, Table 1. Chondroitin sulfate (CS)-based NCs were used to improve the poor water

solubility of CXB and honokiol. Furthermore, a cationic layer of QD-LF conjugate was deposited electrostatically on the negatively charged CS-NCs. The antitumor efficacy of the nanocarriers revealed improved cytotoxicity against breast cancer cells. *In vivo* results revealed decrease in tumor volume, p-AKT and angiogenic marker VEGF-1 levels [133].

Similarly, mannosylated BSA-QDs nano-theranostics have been designed for targeted co-administration of RSV and PMT in an attempt to treat breast cancer, Table 1 [134]. QDs were conjugated through tumor-cleavable bond to BSA NPs to suppress their release into circulation. The combination of PMT with RSV improved the therapeutic efficacy for each of them through modifying different signaling pathways, leading to improved antitumor efficacy, decreased toxicity and multi-drug resistance.

Inorganic nanoparticles combination proved a great success in the treatment of cancer. However, there is still some concerns related to their biodistribution, accumulation in specific organs like liver and spleen, generation of free radicals and the need for biocompatibility studies to determine the immune response for various inorganic NPs [135].

### 3.7. Herbal and immunomodulatory drugs encapsulated combinatorial approach

In the recent decade, immunotherapy has a remarkable role in the treatment of many types of tumor. Cancer immunotherapy could stimulate immune responses against cancer cells in various ways. Some can stimulate the immune system of the body in a very general way. Others can motivate the attack of immune system to cancer cells specifically [136]. Recently Chakraborty *et al.* clarified that nanoparticles conjugated to amino acid are considered as immunomodulatory agents themselves which can be used for the treatment of different

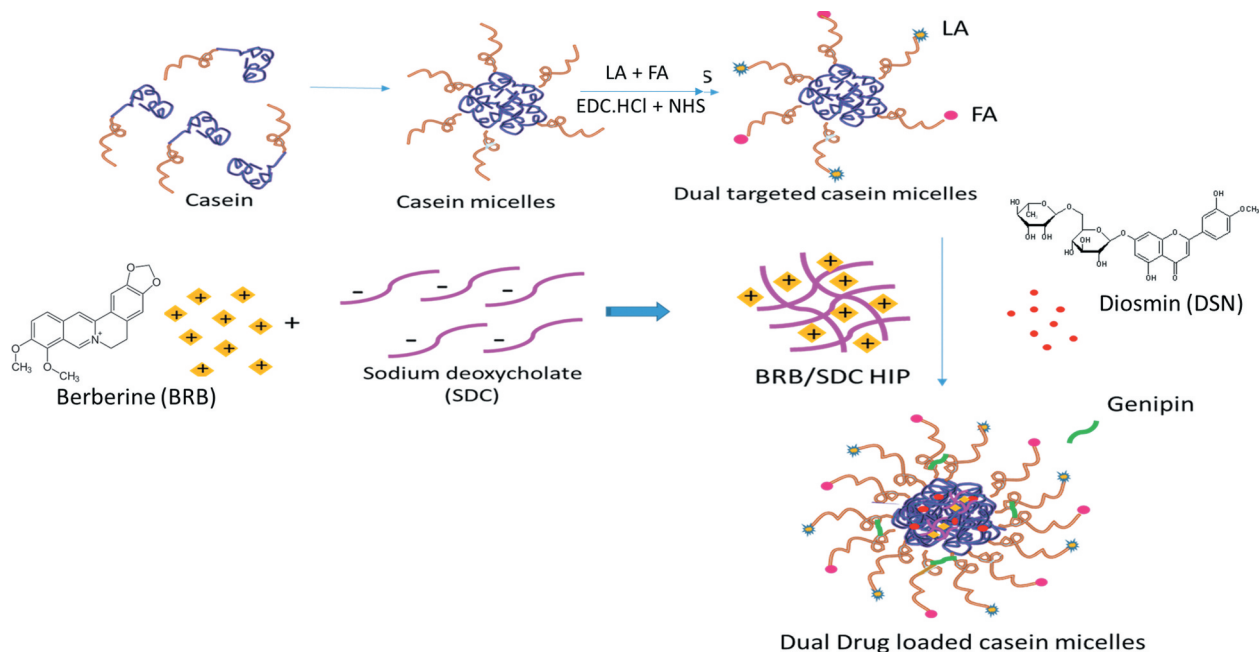


**Figure 6.** Schematic diagram illustrates the preparation steps of dual-targeted lactobionic acid-folic acid casein micelles (LA-FA-CAS MCs) for the co-loading of diosmin and berberine to liver cancer. Adapted with permission from reference 79 copyright (2018) Elsevier.

diseases [137]. One of the most immunogenic tumors is melanoma. An amphiphilic CUR-based micelle was delivered to the cancer cells to remodel the tumor microenvironment, in order to improve the vaccine activity [138], Table 1. The authors found that the combination of nano-vaccine and CUR-PEG micelles treatment led to a synergistic antitumor activity in B16F10 tumor-bearing mice [138]. In the tumor media, the combination resulted in a reduction in the levels of immunosuppressive factors, such as reduced numbers of Treg and MDSCs cells, decreased levels of CCL2 and IL-6; in correlation with elevated levels of pro-inflammatory cytokines, including IFN- $\gamma$  and TNF- $\alpha$ . Moreover, an increase in the tumor infiltration of CD8 + T cell and M1 macrophages in the treated tumors [139].

Immunotherapy nowadays is considered the most growing field for the treatment of cancer, researchers giving attention to discover the effect of these drugs on the immune system and the possibility of attacking healthy tissues and organs which may cause fatal adverse effects if targeted to vital organs, so the efforts should be directed to the preclinical and clinical studies to insure its safety to normal cells without any immune-related complications [140].

#### 4. Conclusion

Herbal multidrug-loaded nano-system presents a promising platform for targeting anticancer drug delivery. The flexibility in synthesis of nanoparticle systems has enabled unpredicted success in delivering an enormous range of anticancer therapeutics. All these novel strategies based on herbal-combinatorial NPs showed relative addressing for cancer drug resistance. This wonderful approach in the cancer treatment enables the co-administration of anticancer drugs with different modes of action in an accurate manner in order to benefit from the synergism between the drugs, to maximize the efficacy and to overcome the development of drug resistance. Despite all advances in the cancer treatment, there are still many issues that must be addressed to overcome all challenges and drawbacks of current therapeutics. Immunotherapy nowadays became an established support of cancer treatment. The main drivers behind this success are the checkpoint inhibitors. CTLA-4 and PD-L1 are gaining importance due to their potential of checkpoint blockade in clinical use as individual or combination treatment. Immunotherapies have many combination strategies, but toxicity could be the limiting factors when applying these combination strategies in the clinic. The critical point in the success of the treatment is the early detection as well as management of side effects. Another challenge is to maintain the reproducibility and manufacturability of the combination nanomedicine as well as to evaluate the safety of herbal nanoformulations and their interaction with cells.

#### 5. Expert opinion

One of the most researched area nowadays is the fabrication of drug delivery systems which can deliver the therapeutic drugs to the specific target site. Various types of cancer

treatment have been used such as chemotherapy, radiotherapy, hormonal therapy, immunotherapy, and gene therapy. Unfortunately, the treatment with each type of the mentioned therapies individually may cause many side effects and develop multidrug resistance. Herein most of researchers nowadays shifted toward the combination therapy especially combination with herbal therapy, to diminish many side effects associated with high doses of monotherapy. Herbal combination therapy because of its minimum toxicity to the normal cells has received growing attention over many years for the treatment of several cancer diseases. Herbal combinatorial approach refer to the combination of herbal compounds such as resveratrol, curcumin, ellagic acid, berberin, wogonin, diosmin, quercetin and honokiol with other types of anticancer drugs like doxorubicin, pemetrexed, camptothecin, tamoxifen, exemestane, Anti-STAT3 siRNA[141], sorafenib, sulfasalazine, and SPIONS. However, these combinations cannot success to reach to the targeted site without the presence of nano-carrier system. Several nano-drug delivery systems have been developed in order to incorporate the combination therapy with the addition of small target ligands to the surface for further targeting to the specific tumor site. All the fabricated nano-vehicles with the combination therapy aim to deliver the active therapy to the targeted tumor site with high drug concentration for prolonged period by the sustained release mechanism.

This review focus on several innovative nano delivery system that have been developed during the last decades for the delivery of herbal combination therapy to cancer cells in an attempt for the treatment of several cancer diseases. The delivery systems included in this review employ several nano-formulation strategies such as polymeric NPs, polymeric micelles, albumin NPs, diblock dendrosome, gold niosomes, and liposomes to overcome several limitation for the conventional therapy. Most research emphasis on improving the antitumor efficacy of the fabricated nano-delivery systems by the synergistic effect of the combination therapy. As a result the dose of both drugs decreased, sustaining the formula release time and enhancing the targeting ability of the nano-carrier to the active site.

Different mechanisms of action for the herbal combination therapy against the cancer cells were also highlighted in this review. The mechanism of action differs according to the type of antitumor remedies that combined with the herbal drug.

Despite the numerous advantages of herbal combination medicines, there are some limitations that may hinder their clinical applications such as the large scaling up of these formulations due to the experimental variables: stirring speed, sonication, drying method, concentration of the utilized components. In addition, optimization condition at the laboratory level may not produce the same result at the large scaling up. Also, the high cost and sterilization of the final product that may impact on their stability is considered as another challenge.

Finally, it can be deduced that by understanding the mechanism of action of the different anticancer remedies, choosing the suitable drug delivery system and studding the safety of these formulations on the human cells as well as



giving attention to the technologies that can be used for scaling up the developed formulation in an economic pathway, the development of an efficient and safe anticancer drug delivery system could be achieved.

## Funding

The paper was not funded.

## Declaration of interest

The authors have no relevant affiliations or financial involvement with any organization or entity with a financial interest in or financial conflict with the subject matter or materials discussed in the manuscript. This includes employment, consultancies, honoraria, stock ownership or options, expert testimony, grants or patents received or pending, or royalties.

## Reviewer disclosures

Peer reviewers on this manuscript have no relevant financial or other relationships to disclose.

## ORCID

Jia-You Fang  <http://orcid.org/0000-0003-2114-7709>

Sherine N. Khattab  <http://orcid.org/0000-0002-3162-6386>

Ahmed O. Elzoghby  <http://orcid.org/0000-0002-5193-7536>

## Reference

Papers of special note have been highlighted as either of interest (\*) or of considerable interest (\*\*) to readers.

- Klein CA. Parallel progression of primary tumours and metastases. *Nat Rev Cancer*. 2009;9(4):302.
- Hanahan D, Weinberg RA. Hallmarks of cancer: the next generation. *cell*. 2011;144(5):646–674.
- Hauner K, Maisch P, Retz M. Side effects of chemotherapy. *Urologe A*. 2017;56(4):472–479.
- Mashreghi M, Azarpara H, Bazaz MR, et al. Angiogenesis biomarkers and their targeting ligands as potential targets for tumor angiogenesis. *J Cell Physiol*. 2018;233:2949–2965.
- Ashrafizadeh S, Ashrafizadeh M, Zarrabi A, et al. Long non-coding RNAs in the doxorubicin resistance of cancer cells. *Cancer Lett*. 2021;508:104–114.
- Cragg GM, Grothaus PG, Newman DJ. Impact of natural products on developing new anti-cancer agents. *Chem Rev*. 2009;109(7):3012–3043.
- Sachan AK, Gupta A. A review on nanotized herbal drugs. *Int J Pharm Sci Res*. 2015;6:961.
- Ghosh S, Dutta S, Sarkar A, et al. Targeted delivery of curcumin in breast cancer cells via hyaluronic acid modified mesoporous silica nanoparticle to enhance anticancer efficiency. *Colloids Surf B*. 2021;197:111404.
- Shamsi-Goushki A, Mortazavi Z, Mirshekar MA, et al. <p>Comparative effects of curcumin versus nano-curcumin on insulin resistance, serum levels of apelin and lipid profile in type 2 diabetic rats. *Diabet metab syndr obes*. 2020;13:2337. .
- Khan J, Alexander A, Saraf S, et al. Recent advances and future prospects of phyto-phospholipid complexation technique for improving pharmacokinetic profile of plant actives. *J Control Release*. 2013;168(1):50–60. .
- Bonifácio BV, Da Silva PB, Dos Santos Ramos MA, et al. Nanotechnology-based drug delivery systems and herbal medicines: a review. *Int J Nanomedicine*. 2014;9:1.
- Farokhzad OC, Langer R. Impact of nanotechnology on drug delivery. *ACS Nano*. 2009;3(1):16–20.
- Ashrafizadeh M, Zarrabi A, Hashemi F, et al. Polychemotherapy with curcumin and doxorubicin via biological nanoplateforms: enhancing antitumor activity. *Pharmaceutics*. 2020;12(11):1084. .
- Ashrafizadeh M, Zarrabi A, Hushmandi K, et al. Progress in natural compounds/siRNA Co-delivery employing nanovehicles for cancer therapy. *ACS Comb Sci*. 2020;22(12):669–700. .
- Majumder P. Nanoparticle-assisted herbal synergism an effective therapeutic approach for the targeted treatment of breast cancer: a novel prospective. *Glob J Nanomed*. 2017;2:555–595.
- Ansari S, Farha Islam M, Islam F. Influence of nanotechnology on herbal drugs: a review. *J Adv Pharm Technol Res*. 2012;3(3):142. .
- importance of naocarrier system in the delivery of combination therapy**
- Hu C-MJ, Zhang L. Nanoparticle-based combination therapy toward overcoming drug resistance in cancer. *Biochem Pharmacol*. 2012;83(8):1104–1111.
- Liao L, Liu J, Dreaden EC, et al. A convergent synthetic platform for single-nanoparticle combination cancer therapy: ratiometric loading and controlled release of cisplatin, doxorubicin, and camptothecin. *J Am Chem Soc*. 2014;136(16):5896–5899. .
- Jain AK, Thanki K, Jain S. Co-encapsulation of tamoxifen and quercetin in polymeric nanoparticles: implications on oral bioavailability, antitumor efficacy, and drug-induced toxicity. *Mol Pharm*. 2013;10(9):3459–3474.
- Zhang RX, Wong HL, Xue HY, et al. Nanomedicine of synergistic drug combinations for cancer therapy – strategies and perspectives. *J Control Release*. 2016;240:489–503.
- Demain AL, Vaishnav P. Natural products for cancer chemotherapy. *Microbiol Biotechnol*. 2011;4(6):687–699.
- Khan H, Mirzaei HR, Amiri A, et al. Glyco-nanoparticles: new drug delivery systems in cancer therapy. *Semin Cancer Biol*. 2019;69:24–42.
- Langer R. Biomaterials in drug delivery and tissue engineering: one Laboratory's Experience. *Acc Chem Res*. 2000;33(2):94–101.
- Chen Y, Zhu X, Zhang X, et al. Nanoparticles modified with tumor-targeting scFv deliver siRNA and miRNA for cancer therapy. *Mol Ther*. 2010;18(9):1650–1656. .
- Verma H, Prasad SB, Yashwant SH. Herbal drug delivery system: a modern era prospective. *Int J Curr Pharm Res*. 2013;4:88–101.
- Gerber H-P, Ferrara N. Pharmacology and pharmacodynamics of bevacizumab as monotherapy or in combination with cytotoxic therapy in preclinical studies. *Cancer Res*. 2005;65:671–680.
- Hossen S, Hossain MK, Basher M, et al. Smart nanocarrier-based drug delivery systems for cancer therapy and toxicity studies: a review. *J. Adv. Res*. 2019;15:1–18.
- Drawbacksof chemotherapeutic drugs as a monotherapy.**
- Nurgali K, Jagoe RT, Abalo R. Adverse effects of cancer chemotherapy: anything new to improve tolerance and reduce sequelae? *Front. Pharmacol*. 2018;9:245.
- Ogama N, Suzuki S, Umeshita K, et al. Appetite and adverse effects associated with radiation therapy in patients with head and neck cancer. *Eur J Oncol Nurs*. 2010;14(1):3–10. .
- Williams J, Chen Y, Rubin P, et al. The biological basis of a comprehensive grading system for the adverse effects of cancer treatment. *Semin Radiat Oncol*. 2003;13(3):182–188. .
- Mirzaei HR, Sahebkar A, Salehi R, et al. Boron neutron capture therapy: moving toward targeted cancer therapy. *J Cancer Res Ther*. 2016;12(2):520. .
- Mirzaei S, Mohammadi AT, Gholami MH, et al. Nrf2 signaling pathway in cisplatin chemotherapy: potential involvement in organ protection and chemoresistance. *Pharmacol Res*. 2021;167:105575.
- Hu C-MJ, Aryal S, Zhang L. Nanoparticle-assisted combination therapies for effective cancer treatment. *Ther Deliv*. 2010;1(2):323–334.
- Moghadam ER, Ang HL, Asnaf SE, et al. Broad-spectrum preclinical antitumor activity of chrysin: current trends and future perspectives. *Biomolecules*. 2020;10(10):1374.

35. Kemp JA, Shim MS, Heo CY, et al. "Combo" nanomedicine: co-delivery of multi-modal therapeutics for efficient, targeted, and safe cancer therapy. *Adv. Drug Delivery Rev.* **2016**;98:3–18.
- **Mostrecent herbal-chemotherapeutic drugs combination therapy.**
36. Rastegar R, Akbari Javar H, Khoobi M, et al. Evaluation of a novel biocompatible magnetic nanomedicine based on beta-cyclodextrin, loaded doxorubicin-curcumin for overcoming chemoresistance in breast cancer. *Artif Cells Nanomed Biotechnol.* **2018**;46(sup2):207–216.
37. Mardani R, Hamblin MR, Taghizadeh M, et al. Nanomicellar-curcumin exerts its therapeutic effects via affecting angiogenesis, apoptosis, and T cells in a mouse model of melanoma lung metastasis. *Pathol Res Pract.* **2020**;216(9):153082.
38. Elgohary MM, Helmy MW, Mortada SM, et al. Dual-targeted nano-in-nano albumin carriers enhance the efficacy of combined chemo/herbal therapy of lung cancer. *Nanomedicine.* **2018**;13(17):2221–2224.
39. Elgohary MM, Helmy MW, Abdelfattah E-ZA, et al. Targeting sialic acid residues on lung cancer cells by inhalable boronic acid-decorated albumin nanocomposites for combined chemo/herbal therapy. *J Control Release.* **2018**;285:230–243.
40. Abdelaziz HM, Elzoghby AO, Helmy MW, et al. Liquid crystalline assembly for potential combinatorial chemo–herbal drug delivery to lung cancer cells. *Int J Nanomedicine.* **2019**;4:499.
41. Türk G, Ateşşahin A, Sönmez M, et al. Improvement of cisplatin-induced injuries to sperm quality, the oxidant-antioxidant system, and the histologic structure of the rat testis by ellagic acid. *Fertil Steril.* **2008**;89(5):1474–1481.
42. Abd Elwakil MM, Mabrouk MT, Helmy MW, et al. Inhalable lactoferrin–chondroitin nanocomposites for combined delivery of doxorubicin and ellagic acid to lung carcinoma. *Nanomedicine.* **2018**;13(16):2015–2035.
43. Muralidharan P, Malapit M, Mallory E, et al. Inhalable nanoparticulate powders for respiratory delivery. *Nanomedicine.* **2015**;11(5):1189–1199.
44. Sabra S, Abdelmoneem M, Abdelwakil M, et al. Self-assembled nanocarriers based on amphiphilic natural polymers for anti-cancer drug delivery applications. *Curr Pharm Des.* **2017**;23:5213–5229.
45. Cao H, Wang Y, He X, et al. Codelivery of sorafenib and curcumin by directed self-assembled nanoparticles enhances therapeutic effect on hepatocellular carcinoma. *Mol Pharm.* **2015**;12(3):922–931.
46. Xiao B, Si X, Han MK, et al. Co-delivery of camptothecin and curcumin by cationic polymeric nanoparticles for synergistic colon cancer combination chemotherapy. *J Mater Chem.* **2015**;3(39):7724–7733.
47. Abdelmoneem MA, Abd Elwakil MM, Khattab S, et al. Lactoferrin-dual drug nanoconjugate: synergistic anti-tumor efficacy of docetaxel and the NF- $\kappa$ B inhibitor celastrol. *Mater Sci Eng C.* **2020**;118:111422.
48. Senapati S, Mahanta AK, Kumar S, et al., Controlled drug delivery vehicles for cancer treatment and their performance. *Signal Transduct Target Ther.* **3**(1): 1–19. **2018**.
- **Different studies on herbal-hormonal combination therapy.**
49. Li JJ. Aromatase inhibitors for breast cancer: exemestane (Aromasin), anastrozole (Arimidex) and letrozole (Femara). Wiley Online Library; **2007**. p. 31–38.
50. Clemons M, Danson S, Howell A. Tamoxifen ('Nolvadex'): a review: antitumour treatment. *Cancer Treat Rev.* **2002**;28(4):165–180.
51. Chi KN, Agarwal N, Bjartell A, et al. Apalutamide for metastatic, castration-sensitive prostate cancer. *N Engl J Med.* **2019**;381(1):13–24.
52. Logman J, Heeg B, Botteman M, et al. Economic evaluation of zoledronic acid for the prevention of osteoporotic fractures in postmenopausal women with early-stage breast cancer receiving aromatase inhibitors in the UK. *Ann Oncol.* **2009**;21(7):1529–1536.
53. Abbasalipourkabir R, Salehzadeh A, Abdullah R. Tamoxifen-loaded solid lipid nanoparticles-induced apoptosis in breast cancer cell lines. *J Exp Nanosci.* **2016**;11(3):161–174.
54. Petinari L, Kohn LK, De Carvalho JE, et al. Cytotoxicity of tamoxifen in normal and tumoral cell lines and its ability to induce cellular transformation in vitro. *Cell Biol Int.* **2004**;28(7):531–539.
55. Sandhu PS, Kumar R, Beg S, et al. Natural lipids enriched self-nano-emulsifying systems for effective co-delivery of tamoxifen and naringenin: systematic approach for improved breast cancer therapeutics. *Nanomedicine.* **2017**;13(5):1703–1713.
56. Hajigholami S, Malekshahi ZV, Bodaghabadi N, et al. Nano packaged Tamoxifen and Curcumin; effective formulation against sensitive and resistant MCF-7 cells. *Iran J Pharm Res.* **2018**;17:1.
57. Shao W, Brown M. Advances in estrogen receptor biology: prospects for improvements in targeted breast cancer therapy. *Breast Cancer Res.* **2003**;6(1):1–14.
58. Hong Y, Chen S. Aromatase, estrone sulfatase, and 17 $\beta$ -hydroxysteroid dehydrogenase: structure–function studies and inhibitor development. *Mol Cell Endocrinol.* **2011**;340(2):120–126.
59. Wang Y, Lee KW, Chan FL, et al. The red wine polyphenol resveratrol displays bilevel inhibition on aromatase in breast cancer cells. *Toxicol Sci.* **2006**;92(1):71–77.
60. Elzoghby AO, El-Lakany SA, Helmy MW, et al. Shell-crosslinked zein nanocapsules for oral codelivery of exemestane and resveratrol in breast cancer therapy. *Nanomedicine.* **2017**;12(24):2785–2805.
61. El-Lakany SA, Elgindy NA, Helmy MW, et al. Lactoferrin-decorated vs PEGylated zein nanospheres for combined aromatase inhibitor and herbal therapy of breast cancer. *Expert Opin Drug Deliv.* **2018**;15(9):835–850.
62. Gaber M, Hany M, Mokhtar S, et al. Boronic-targeted albumin-shell oily-core nanocapsules for synergistic aromatase inhibitor/herbal breast cancer therapy. *Mater Sci Eng.* **2019**;105:110099.
63. Arya A, Ahmad H, Tulsankar S, et al. Bioflavonoid hesperetin overcome bicalutamide induced toxicity by co-delivery in novel SNEDDS formulations: optimization, in vivo evaluation and uptake mechanism. *Mater Sci Eng.* **2017**;71:954–964.
64. Danquah M, Li F, Duke CB, et al. Micellar delivery of bicalutamide and embelin for treating prostate cancer. *Pharm Res.* **2009**;26(9):2081.
65. Kumar RJ, Barqawi A, Crawford ED. Adverse events associated with hormonal therapy for prostate cancer. *Rev Urol.* **2005**; 7:S37.
- **herbal-gene therapy combination nanomedicine**
66. Oliver D, Ji H, Liu P, et al. Identification of novel cancer therapeutic targets using a designed and pooled shRNA library screen. *Sci Rep.* **2017**;7(1):43023.
67. Kim HJ, Kim A, Miyata K, et al. Recent progress in development of siRNA delivery vehicles for cancer therapy. *Adv Drug Deliv Rev.* **2016**;104:61–77.
68. Mirzaei S, Mahabady MK, Zabolian A, et al. Small interfering RNA (siRNA) to target genes and molecular pathways in glioblastoma therapy: current status with an emphasis on delivery systems. *Life Sci.* **2021**;275:119368.
69. Abdelfattah N, Rajamanickam S, Panneerdoss S, et al. MiR-584-5p potentiates vincristine and radiation response by inducing spindle defects and DNA damage in medulloblastoma. *Nature Communications.* **2018**;9(1):4541.
70. Ashrafzade M, Delfi M, Hashemi F, et al. Biomedical application of chitosan-based nanoscale delivery systems: potential usefulness in siRNA delivery for cancer therapy. *Carbohydr Polym.* **2021**;260:117809.
71. Zhong X, Zhang D, Xiong M, et al. Current strategies in cancer gene therapy. In: *Noncoding RNA for cancer gene therapy*. Springer, **2016**;209:51–60.
72. Salarinia R, Sahebkar A, Peyvandi M, et al. Epi-drugs and Epi-miRs: moving beyond current cancer therapies. *Curr Cancer Drug Targets.* **2016**;16(9):773–788. .
73. Soutschek J, Akinc A, Bramlage B, et al. Therapeutic silencing of an endogenous gene by systemic administration of modified siRNAs. *Nature.* **2004**;432(7014):173. .

74. Kawabata K, Takakura Y, Hashida M. The fate of plasmid DNA after intravenous injection in mice: involvement of scavenger receptors in its hepatic uptake. *Pharm Res.* 1995;12(6):825–830.
75. Takakura Y, Nishikawa M, Yamashita F, et al. Development of gene drug delivery systems based on pharmacokinetic studies. *Eur J Pharm Sci.* 2001;13(1):71–76.
76. Fessler AB, Dey A, Garmon CB, et al. Water-soluble isatoic anhydrides: a platform for RNA-SHAPE analysis and protein bioconjugation. *Bioconjug Chem.* 2018;29(9):3196–3202.
77. Jose A, Labala S, Ninave KM, et al. Effective skin cancer treatment by topical co-delivery of curcumin and STAT3 siRNA using cationic liposomes. *AAPS Pharm Sci Tech.* 2018;19(1):166–175.
78. Muddineti OS, Shah A, Rompicharla SVK, et al. Cholesterol-grafted chitosan micelles as a nanocarrier system for drug-siRNA co-delivery to the lung cancer cells. *Int J Biol Macromol.* 2018;118:857–863.
79. Mostofa AGM, Hossain MK, Basak D, et al. Thymoquinone as a potential adjuvant therapy for cancer treatment: evidence from preclinical studies. *Front Pharmacol.* 2017;8:295.
80. Xiao B, Viennois E, Chen Q, et al., Silencing of Intestinal Glycoprotein CD98 by orally targeted nanoparticles enhances chemosensitization of colon cancer. *ACS Nano.* 12(6): 5253–5265. 2018..
- **recent studies on Herbal & small molecule inhibitors nanomedicine.**
81. Das SK, Menezes ME, Bhatia S, et al. Gene therapies for cancer: strategies, challenges and successes. *J Cell Physiol.* 2015;230(2):259–271.
82. Anwar DM, Khattab S, Helmy MW, et al. Lactobionic/Folate dual-targeted Amphiphilic Maltodextrin-Based Micelles for Targeted Codelivery of Sulfasalazine and Resveratrol to Hepatocellular Carcinoma. *Bioconjugate Chem.* 2018;29(9):3026–3041.
83. Kabary DM, Helmy MW, Elkhodairy KA, et al. Hyaluronate/lactoferrin layer-by-layer-coated lipid nanocarriers for targeted co-delivery of rapamycin and berberine to lung carcinoma. *Colloids Surf B.* 2018;169:183–194.
84. Kabary DM, Helmy MW, Abdelfattah E-ZA, et al. Inhalable multi-compartmental phospholipid enveloped lipid core nanocomposites for localized mTOR inhibitor/herbal combined therapy of lung carcinoma. *Eur J Pharm Biopharm.* 2018;130:152–164.
85. Sabra SA, Elzoghby AO, Sheweita SA, et al. Self-assembled amphiphilic zein-lactoferrin micelles for tumor targeted co-delivery of rapamycin and wogonin to breast cancer. *Eur J Pharm Biopharm.* 2018;128:156–169.
86. Nakamura O, Hitora T, Yamagami Y, et al. The combination of rapamycin and MAPK inhibitors enhances the growth inhibitory effect on Nara-H cells. *Int J Mol Med.* 2014;33(6):1491–1497.
87. Gossiau A, Ho C-T, Li S. The role of rutin and diosmin, two citrus polyhydroxyflavones in disease prevention and treatment. *Journal of Food Bioactives.* 2019;5:43–56.
88. Abdelmoneem MA, Mahmoud M, Zaky A, et al. Decorating protein nanospheres with lactoferrin enhances oral COX-2 inhibitor/herbal therapy of hepatocellular carcinoma. *Nanomedicine.* 2018;13(19):2377–2395.
89. Parhi P, Mohanty C, Sahoo SK. Nanotechnology-based combinational drug delivery: an emerging approach for cancer therapy. *Drug Discov Today.* 2012;17(17–18):1044–1052.
90. Blandino G, Valerio M, Cioce M, et al. Metformin elicits anticancer effects through the sequential modulation of DICER and c-MYC. *Nat Commun.* 2012;3(1):865.
91. Farajzadeh R, Pilehvar-Soltanahmadi Y, Dadashpour M, et al. Nano-encapsulated metformin-curcumin in PLGA/PEG inhibits synergistically growth and hTERT gene expression in human breast cancer cells. *Artif Cells Nanomed Biotechnol.* 2018;46(5):917–925.
92. Afsharzadeh M, Hashemi M, Mokhtarzadeh A, et al. Recent advances in co-delivery systems based on polymeric nanoparticle for cancer treatment. *Artif Cells Nanomed Biotechnol.* 2018;46(6):1095–1110.
93. Hussain A, Harish G, Prabhu SA, et al. Inhibitory effect of genistein on the invasive potential of human cervical cancer cells via modulation of matrix metalloproteinase-9 and tissue inhibitors of matrix metalloproteinase-1 expression. *Cancer Epidemiol.* 2012;36(6):e387–e393.
94. Kamel NM, Helmy MW, Abdelfattah E-Z, et al. Inhalable dual-targeted hybrid lipid nanocore-protein shell composites for combined delivery of genistein and all-trans retinoic acid to lung cancer cells. *ACS Biomater Sci Eng.* 2020;6(1):71–87.
95. Abdelmoneem MA, Elnaggar MA, Hammady RS, et al. Dual-targeted Lactoferrin Shell-Oily Core Nanocapsules for synergistic targeted/Herbal Therapy of Hepatocellular Carcinoma. *ACS Biomater Sci Eng.* 2019;11:26731–26744.
- **combination of both Herbal therapy & natural drugs**
96. Lavanya V, Adil M, Ahmed N, et al. Small molecule inhibitors as emerging cancer therapeutics. *Integr Cancer Sci Ther.* 2014;1:39–46.
97. Hemalswarya S, Doble M. Potential synergism of natural products in the treatment of cancer. *Phytother Res.* 2006;20(4):239–249.
98. Abdelmoneem MA, Mahmoud M, Zaky A, et al. Dual-targeted casein micelles as green nanomedicine for synergistic phytotherapy of hepatocellular carcinoma. *J Control Release.* 2018;287:78–93.
99. Caddeo C, Pons R, Carbone C, et al. Physico-chemical characterization of succinyl chitosan-stabilized liposomes for the oral co-delivery of quercetin and resveratrol. *Carbohydr Polym.* 2017;157:1853–1861.
100. Lotfi-Attari J, Pilehvar-Soltanahmadi Y, Dadashpour M, et al. Co-delivery of curcumin and chrysin by polymeric nanoparticles inhibit synergistically growth and hTERT gene expression in human colorectal cancer cells. *Nutr Cancer.* 2017;69(8):1290–1299.
101. Bagherian A, Mardani R, Roudi B, et al. Combination therapy with nanomicellar-curcumin and temozolomide for in vitro therapy of glioblastoma multiforme via Wnt signaling pathways. *J Mol Neurosci.* 2020;70(10):1471–1483.
102. Tavakoli F, Jahanban-Esfahlan R, Seidi K, et al. Effects of nano-encapsulated curcumin-chrysin on telomerase, MMPs and TIMPs gene expression in mouse B16F10 melanoma tumour model. *Artif Cells Nanomed Biotechnol.* 2018;46(sup2):75–86.
103. Proksch P, Edrada R, Ebel R. Drugs from the seas - current status and microbiological implications. *Appl Microbiol Biotechnol.* 2002;59(2–3):125–134.
104. El-Far SW, Helmy MW, Khattab S, et al. Phytosomal bilayer-enveloped casein micelles for codelivery of monascus yellow pigments and resveratrol to breast cancer. *Nanomedicine.* 2018;13(5):481–499.
105. El-Far SW, Helmy MW, Khattab S, et al., Folate conjugated vs PEGylated phytosomal casein nanocarriers for codelivery of fungal- and herbal-derived anticancer drugs. *Nanomedicine.* 13(12): 1463–1480. 2018..
- **overview on the combination of herbal therapy & inorganic hybrids.**
106. Yeung KS, Gubili J, Mao JJ. Herb-drug interactions in Cancer care. *Oncology.* 2018;32:516–520.
107. Ulbrich K, Hola K, Subr V, et al. Targeted drug delivery with polymers and magnetic nanoparticles: covalent and noncovalent approaches, release control, and clinical studies. *Chem.rev* 2016;116(9):5338–5431.
108. Lammers T, Kiessling F, Hennink WE, et al. Nanotheranostics and image-guided drug delivery: current concepts and future directions. *Mol Pharm.* 2010;7(6):1899–1912.
109. Xie J, Lee S, Chen X. Nanoparticle-based theranostic agents. *Adv. Drug Deliv.* 2010;62(11):1064–1079.
110. Chakraborty A, Boer JC, Selomulya C, et al. Amino acid functionalized inorganic nanoparticles as cutting-edge therapeutic and diagnostic agents. *Bioconjug Chem.* 2018;29(3):657–671.
- **ironoxide nanoparticles for targeting cancer**
111. Yang H-M, Park CW, Woo M-A, et al. HER2/neu Antibody Conjugated Poly(amino acid)-coated iron oxide nanoparticles for breast cancer MR Imaging. *Biomacromolecules.* 2010;11(11):2866–2872.

112. Levy M, Luciani N, Alloyeau D, et al. Long term in vivo biotransformation of iron oxide nanoparticles. *Biomaterials*. 2011;32(16):3988–3999. .
113. Mazuel F, Espinosa A, Luciani N, et al. Massive intracellular biodegradation of iron oxide nanoparticles evidenced magnetically at single-endosome and tissue levels. *ACS Nano*. 2016;10(8):7627–7638. .
114. Chakraborty A, Royce SG, Selomulya C, et al. A novel approach for non-invasive lung imaging and targeting lung immune cells. *Int J Mol Sci*. 2020;21(5):1613. .
115. Harmon B, Takano Y, Winterford C, et al. The role of apoptosis in the response of cells and tumours to mild hyperthermia. *Int J Radiat Biol*. 1991;59(2):489–501. .
116. Vorotnikov E, Ivkov R, Foreman A, et al. The magnitude and time-dependence of the apoptotic response of normal and malignant cells subjected to ionizing radiation versus hyperthermia. *Int J Radiat Bio*. 2006;82(8):549–559.
117. Issels RD. Hyperthermia adds to chemotherapy. *Eur J Cancer*. 2008;44(17):2546–2554.
118. Patra S, Roy E, Karfa P, et al. Dual-responsive polymer coated superparamagnetic nanoparticle for targeted drug delivery and hyperthermia treatment. *ACS Appl Mater Interfaces*. 2015;7(17):9235–9246. .
119. Cui Y, Zhang M, Zeng F, et al. Dual-targeting magnetic PLGA nanoparticles for codelivery of paclitaxel and curcumin for brain tumor therapy. *ACS Appl Mater Interfaces*. 2016;8(47):32159–32169. .
120. Elhasany KA, Khattab S, Bekhit AA, et al. Combination of magnetic targeting with synergistic inhibition of NF- $\kappa$ B and glutathione via micellar drug nanomedicine enhances its anti-tumor efficacy. *Eur J Pharm Biopharm*. 2020;155:162–176.
121. Shanmugam V, Selvakumar S, Yeh C-S. Near-infrared light-responsive nanomaterials in cancer therapeutics. *Chem Soc Rev*. 2014;43(17):6254–6287.
122. Hu SH, Fang RH, Chen YW, et al. Photoresponsive Protein–Graphene–protein hybrid capsules with dual targeted heat-triggered drug delivery approach for enhanced tumor therapy. *Adv Funct Mater*. 2014;24(26):4144–4155. .
123. Alkilany AM, Thompson LB, Boulos SP, et al. Gold nanorods: their potential for photothermal therapeutics and drug delivery, tempered by the complexity of their biological interactions. *Adv Drug Deliv Rev*. 2012;64(2):190–199.
124. Wang Y, Yang T, Ke H, et al. Smart Albumin-Biomineralized nanocomposites for multimodal imaging and photothermal tumor ablation. *Adv Mater*. 2015;27(26):3874–3882. .
125. Singh SP, Alvi SB, Pemmaraju DB, et al. NIR triggered liposome gold nanoparticles entrapping curcumin as in situ adjuvant for photothermal treatment of skin cancer. *Int J Biol Macromol*. 2018;110:375–382.
126. Park SY, Chae SY, Park JO, et al. Gold-conjugated resveratrol nanoparticles attenuate the invasion and MMP-9 and COX-2 expression in breast cancer cells. *Oncol Rep*. 2016;35(6):3248–3256.
127. Davoodvandi A, Darvish M, Borran S, et al. The therapeutic potential of resveratrol in a mouse model of melanoma lung metastasis. *Int Immunopharmacol*. 2020;88:106905.
128. Ali OM, Bekhit AA, Khattab S, et al. Synthesis of lactoferrin mesoporous silica nanoparticles for pemetrexed/ellagic acid synergistic breast cancer therapy. *Colloids Surf*. 2020;188:110824.
129. Abdelmoneem MA, Abd Elwakil MM, Khattab SN, et al. Lactoferrin-dual drug nanoconjugate: synergistic anti-tumor efficacy of docetaxel and the NF- $\kappa$ B inhibitor celastrol. *Mater Sci Eng C*. 2021;118:111422.
130. Metawea OR, Abdelmoneem MA, Haiba NS, et al. A novel ‘smart’ PNIPAM-based copolymer for breast cancer targeted therapy: synthesis, and characterization of dual pH/temperature-responsive lactoferrin-targeted PNIPAM-co-AA. *Colloids Surf B*. 2021;202:111694.
131. Drbohlavova J, Adam V, Kizek R, et al. Quantum Dots — characterization, preparation and usage in biological systems. *Int J Mol Sci*. 2009;10(2):656–673.
132. AbdElhamid AS, Zayed DG, Helmy MW, et al. Lactoferrin-tagged quantum dots-based theranostic nanocapsules for combined COX-2 inhibitor/herbal therapy of breast cancer. *Nanomedicine*. 2018;13(20):2637–2656.
133. Hashemi Goradel N, Ghiyami-Hour F, Jahangiri S, et al. Nanoparticles as new tools for inhibition of cancer angiogenesis. *J Cell Physiol*. 2018;233(4):2902–2910.
134. Zayed DG, Ebrahim SM, Helmy MW, et al. Combining hydrophilic chemotherapy and hydrophobic phytotherapy via tumor-targeted albumin-QDs nano-hybrids: covalent coupling and phospholipid complexation approaches. *J Nanobiotechnology*. 2019;17(1):7.
135. Bhattacharyya S, Kudgus RA, Bhattacharya R, et al. Inorganic nanoparticles in cancer therapy. *Pharm Res*. 28(2): 237–259. 2011..
- **Immunotherapy as a novel strategy for cancer treatment.**
136. Helmy KY, Patel SA, Nahas GR, et al. Cancer immunotherapy: accomplishments to date and future promise. *Ther Deliv*. 2013;4(10):1307–1320.
137. Chakraborty A, Boer JC, Selomulya C, et al. Amino acid functionalized inorganic nanoparticles as cutting-edge therapeutic and diagnostic agents. *Bioconjugate Chem*. 2017;29(3):657–671.
138. Rana Shafabakhsh MH. Targeting regulatory T cells by Curcumin: a potential. *cell*. 2001;7:683–694.
139. Lu Y, Miao L, Wang Y, et al. Curcumin micelles remodel tumor microenvironment and enhance vaccine activity in an advanced melanoma model. *Mol Ther*. 2016;24(2):364–374.
140. Postow MA. Managing immune checkpoint-blocking antibody side effects. *ASCO Educational Book*. 2015;35(35):76–83.
141. Mirzaei S, Gholami MH, Hashemi F, et al. Employing siRNA tool and its delivery platforms in suppressing cisplatin resistance: approaching to a new era of cancer chemotherapy. *Life Sci*. 2021;277:119430.



RESEARCH ARTICLE

Open Access



# Critical role of triglycerides for adiponectin levels in hepatitis C: a joint study of human and HCV core transgenic mice

Ming-Ling Chang<sup>1,2\*</sup> , Jing-Hong Hu<sup>3</sup>, Li-Heng Pao<sup>4,5</sup>, Ming-Shyan Lin<sup>6</sup>, Chia-Jung Kuo<sup>1,2</sup>, Shiang-Chi Chen<sup>7</sup>, Chun-Ming Fan<sup>8</sup>, Ming-Yu Chang<sup>9,10</sup> and Rong-Nan Chien<sup>1,2,11\*</sup>

## Abstract

**Background:** Both hepatitis C virus (HCV) infection and adiponectin are critically involved in metabolism. The reversal and associations of altering adiponectin levels after sustained virological responses (SVRs) following direct-acting antivirals (DAA) in HCV-infected patients remained elusive.

**Methods:** A joint study was conducted in a prospective cohort of 427 HCV-infected patients and a line of HCV core transgenic mice.

**Results:** Of 427, 358 had completed a course of DAA therapy and 353 had SVRs. At baseline, male sex (95% CI  $\beta$ :  $-1.44$  to  $-0.417$ ), estimated glomerular filtration rate (eGFR) ( $-0.025$  to  $-0.008$ ), triglycerides ( $-0.015$  to  $-0.005$ ), and fibrosis-4 levels ( $0.08$ – $0.297$ ) were associated with adiponectin levels; BMI ( $0.029$ – $0.327$ ) and triglycerides levels ( $0.01$ – $0.03$ ) were associated with homeostatic model assessment for insulin resistance (HOMA-IR) in HCV-infected patients. At 24-week post-therapy, in SVR patients, male sex ( $-1.89$  to  $-0.5$ ) and eGFR ( $-0.02$  to  $-0.001$ ) levels were associated with adiponectin levels, levels of BMI ( $0.094$ – $0.335$ ) and alanine transaminase ( $0.018$ – $0.078$ ) were associated with HOMA-IR; compared with baseline levels, adiponectin levels decreased ( $6.53 \pm 2.77$  vs.  $5.45 \pm 2.56$   $\mu\text{g/mL}$ ,  $p < 0.001$ ). In 12-month-old HCV core transgenic mice with hepatic steatosis, triglyceride levels ( $0.021$ – $0.111$ ) were associated with adiponectin levels, and hepatic adiponectin expression was comparable with that of control mice.

**Conclusions:** Triglycerides and hepatic fibrosis are associated with HCV-specific alteration of adiponectin levels, and adiponectin may affect insulin sensitivity through triglycerides during HCV infection. In DAA-treated patients, after SVR, adiponectin levels decreased and the linking function of triglycerides between adiponectin and insulin sensitivity vanished. Moreover, HCV core with hepatic steatosis might affect extrahepatic adiponectin expression through triglycerides.

**Keywords:** HCV, Adiponectin, Triglycerides, HOMA-IR, SVR, DAA, HCV core

## Background

Hepatitis C virus (HCV) is a human pathogen responsible for acute and chronic liver disease, chronically infecting an estimated 71.1 million individuals worldwide [1], and classified into 8 genotypes [2]. In addition to hepatic complications including steatosis, liver cirrhosis and hepatocellular carcinoma (HCC), HCV infection induces several extrahepatic complications, such as

\*Correspondence: mlchang8210@gmail.com; ronald@cgmh.org.tw

<sup>1</sup> Division of Hepatology, Department of Gastroenterology and Hepatology, Chang Gung Memorial Hospital, No 5, Fu Hsing Street, Kuei Shan, Taoyuan, Taiwan

Full list of author information is available at the end of the article



© The Author(s) 2021. **Open Access** This article is licensed under a Creative Commons Attribution 4.0 International License, which permits use, sharing, adaptation, distribution and reproduction in any medium or format, as long as you give appropriate credit to the original author(s) and the source, provide a link to the Creative Commons licence, and indicate if changes were made. The images or other third party material in this article are included in the article's Creative Commons licence, unless indicated otherwise in a credit line to the material. If material is not included in the article's Creative Commons licence and your intended use is not permitted by statutory regulation or exceeds the permitted use, you will need to obtain permission directly from the copyright holder. To view a copy of this licence, visit <http://creativecommons.org/licenses/by/4.0/>. The Creative Commons Public Domain Dedication waiver (<http://creativecommons.org/publicdomain/zero/1.0/>) applies to the data made available in this article, unless otherwise stated in a credit line to the data.

hypolipidemia, insulin resistance (IR), diabetes and cardiovascular events [3, 4]. Thus, HCV is now considered to cause metabolic alterations instead of being simply a viral infection. The reversal of HCV-associated metabolic alterations after sustained virological response (SVR) following interferon-based studies had been well demonstrated [3, 5–10]. However, some HCV-associated cardiometabolic events cannot be reversed, and HCV-associated HCC is also not eradicable after SVR [3, 11]. Moreover, the reversal of metabolic alterations might be biased by interferon-based therapy, as interferon therapy has been associated with increases in lipid levels [12] and with immune modulation in the patients [13]. With the advent of direct-acting antivirals (DAAs), which target specific proteins of HCV during its life cycle [14], anti-HCV treatment has resulted in a high cure rate with a short treatment duration in patients with chronic HCV infection (CHC), and the reversal of HCV-associated metabolic alterations might not be biased by any interferon-related effects.

Adiponectin, a 30-kDa adipokine, is mainly expressed in adipocytes [15], while increased visceral adipose tissue stores reduce serum adiponectin [16]. It is the most abundantly secreted adipokine [17]. Several IR-associated hormones such as insulin and catecholamines dysregulate adiponectin expression [18]. Post-translational adiponectin modifications result in the secretion of oligomers of 90-kDa trimers, found in the circulation. Adiponectin might protect hepatocytes from triglyceride accumulation by increasing  $\beta$ -oxidation, decreasing fatty acid de novo synthesis, and promoting the uptake and inhibiting the production of glucose in the liver [19, 20]. Hepatic steatosis and hyperlipidemia are therefore usually associated with low adiponectin levels [20, 21]. Moreover, adiponectin possesses anti-inflammatory, anti-atherosclerotic and anti-apoptotic properties [22]. Paradoxically, circulating adiponectin levels have been associated with cardiovascular events and all-cause mortality [23–25]. Because both HCV infection and adiponectin are deeply involved in metabolism, their relationship might aid to probe the therapeutic targets for HCV-associated cardiometabolic complications. In CHC patients with SVRs following interferon-based therapy, adiponectin may affect insulin sensitivity through triglycerides. After viral clearance, adiponectin levels were directly associated with insulin sensitivity and decreased upon improved hepatic fibrosis [8]. However, how adiponectin levels evolve after SVR in CHC patients following DAA therapy remained unidentified and is crucial for the patients' prognosis, since interferon-based therapy had been replaced by DAA therapy as the standard of care treatment for CHC currently [26]. Being a HCV capsid protein, HCV core possesses the ability to interact with a

variety of cellular components [27] and is the least variable of the 10 HCV proteins in variant viruses emerging constantly in patients [28]. Our previous studies based on HCV core transgenic mice had shown that hepatic HCV core expression affects lipid metabolism genes [29], elicits mitochondrial stress [30], exhibits the topological and evolutionary relationships with hepatic lipid vesicles [31] and alters the serum adiponectin levels in the non-obese mice with hepatic steatosis [32]. By taking advantage of this HCV core transgenic mice, the associated basis for HCV-associated adiponectin level alteration might be uncovered.

Accordingly, we sought to elucidate the impact of HCV infection on adiponectin levels in a prospective study of CHC patients underwent DAA therapy. In parallel, the associated basis was elucidated via the serum biochemistry and immunohistochemistry (IHC) studies of the HCV core transgenic mice [29–32].

## Results

### Baseline characteristics of CHC patients

Of 427 CHC patients, 232 (54.3%) were female patients, the mean age was 61.3 years. The males had higher levels of body mass index (BMI), alanine aminotransferase (ALT), the homeostatic model assessment for insulin resistance (HOMA-IR), uric acid (UA), model for end-stage liver disease (MELD) score and ferritin and lower levels of total cholesterol (TC) and adiponectin than the females (Table 1).

### Baseline associations in CHC patients

At baseline, for all 427 CHC patients, male sex, estimated glomerular filtration rates (eGFRs) and levels of triglycerides (TG) were negatively, and levels of fibrosis-4 (FIB-4) were positively associated with adiponectin levels (Table 2); levels of BMI and TG and HCV genotype other than 1, 2 and 3 (non-HCV G123) were positively associated with HOMA-IR (Table 3). While we stratified the patients with baseline insulin resistance (IR), non-HCV G123 were positively associated with HOMA-IR among those with baseline IR (Additional file 1: Table S2); BMI levels were associated with HOMA-IR levels among those without baseline IR (Additional file 1: Table S3).

### Post-therapy associations in SVR patients

At 24 weeks post-therapy, among 353 SVR patients (Fig. 1), male sex and eGFRs were negatively associated with adiponectin levels (Table 4); levels of BMI and ALT were positively associated with HOMA-IR (Table 5). While we stratified the patients with baseline IR, among the SVR patients with baseline IR, levels of BMI were associated with HOMA-IR levels (Additional file 1: Table S4); levels of BMI, ALT and neutrophil

**Table 1** Baseline characteristics of the CHC patients

	All (n = 427)	Male (n = 195)	Female (n = 232)	p values *
Age (years)	61.3 ± 12.8	59.1 ± 12.1	61.3 ± 12.8	0.076
BMI (kg/m <sup>2</sup> )	24.6 ± 3.9	25.1 ± 3.46	24.2 ± 4.19	0.012
<i>HCV genotype</i>				
Genotype 1, n (%)	256 (59.9)	116 (59.4)	140 (60.3)	0.31
Genotype 2, n (%)	137 (32.0)	60 (30.7)	67 (28.8)	0.95
Genotype 3, n (%)	6 (1.7)	4 (2)	2 (0.8)	0.301
Log HCV RNA (logIU/mL)	5.98 ± 0.87	5.96 ± 0.92	5.98 ± 0.83	0.813
ALT (U/L)	79.8 ± 90.4	93.4 ± 108.4	68.5 ± 71.6	0.006
eGFR (mL/min/1.73 m <sup>2</sup> )	86.9 ± 41.7	89.1 ± 40.5	85.0 ± 42.8	0.326
TG (mg/dL)	102.6 ± 52.6	105.9 ± 58.5	99.8 ± 47.1	0.235
TC (mg/dL)	169.5 ± 35.3	163.7 ± 33.0	174.4 ± 36.5	0.002
Fasting glucose (mg/dL)	97.79 ± 31.41	100.10 ± 39.07	96.04 ± 23.96	0.066
Insulin (μIU/mL)	10.18 ± 30.01	10.53 ± 15.50	9.92 ± 37.29	0.793
HOMA-IR	3.17 ± 4.88	3.72 ± 6.61	2.77 ± 2.56	0.045
Uric acid (mg/dL)	5.71 ± 1.62	6.17 ± 1.69	5.28 ± 1.42	< 0.001
NLR	1.98 ± 1.24	2.06 ± 1.19	1.91 ± 1.29	0.248
Platelet (10 <sup>3</sup> /uL)	176.8 ± 71.7	176.8 ± 68.2	176.7 ± 74.8	0.996
Liver cirrhosis, n (%)	92 (21.5)	40 (20.9)	52 (22.4)	0.699
Fibrosis-4 score	3.53 ± 3.39	3.22 ± 3.23	3.79 ± 3.51	0.083
MELD score	9.08 ± 3.08	9.51 ± 4.00	8.69 ± 3.62	0.022
Ferritin (ng/mL)	376.1 ± 513.2	461.7 ± 448.9	298.1 ± 555.3	0.002
Adiponectin (μg/mL)	6.52 ± 2.71	5.87 ± 2.37	7.06 ± 2.85	< 0.001
IFNL3-rs12979860 CC genotype, n (%)	1018 (84.7)	166 (85.1)	195 (84.0)	0.829

CHC: chronic hepatitis C virus infection; DAA: direct-acting antivirals; BMI: body mass index; HCV: hepatitis C virus; RNA: ribonucleic acid; ALT: alanine transaminase; eGFR: estimated glomerular filtration rate; TG: triglycerides; TC: total cholesterol; HOMA-IR: homeostatic model assessment for insulin resistance; NLR: neutrophil lymphocyte ratio; IFNL3: interferon-λ3. \*, p values between male and female CHC patients

lymphocyte ratio (NLR) were associated with HOMA-IR levels among SVR patients without baseline IR (Additional file 1: Table S5).

#### Variable alterations in SVR patients

Compared with baseline levels, the SVR patients had decreased adiponectin levels, regardless of sex. Levels of ALT and eGFRs also decreased, while levels of BMI increased. By contrast, no differences were noted between pre- and post-therapy HOMA-IR levels among SVR patients. However, while we stratified the SVR patients by baseline IR, those with and without baseline IR had decreased and increased HOMA-IR levels, respectively (Table 6).

A summary of the associations and alterations of adiponectin and HOMA-IR levels was shown in Fig. 2.

#### Serum biochemistry of the mice

In 2-month-old tetracycline transactivator (tTA)-HCV core double transgenic FVB/N mice (DTM), sex was associated with adiponectin levels; in 12-month-old

DTM, sex and TG levels were independently associated with adiponectin levels (Table 7).

#### IHC studies of the mice

The livers of tTA-HCV core DTM showed extensive HCV core expressions (Fig. 3A) and intracellular lipid accumulations (Fig. 3C). By contrast, the livers of tTA DTM did not show any HCV core expression (Fig. 3B) and only exhibited negligible intrahepatic lipids (Fig. 3D). Comparable hepatic adiponectin expressions were noted between the livers of single transgenic mice (STM) and DTM (Fig. 3E, F) ( $p = 0.578$ ).

#### Discussion

The most compelling results of the current study are as follows:

(1) At baseline, male sex, eGFRs, levels of TG, and FIB-4 were associated with adiponectin levels; levels of BMI and TG and HCV genotype were associated with HOMA-IR levels in CHC patients. (2) At 24 weeks post-therapy, male sex and eGFRs were associated with adiponectin levels; levels of BMI and ALT were associated

**Table 2** Associations of adiponectin levels in CHC patients at baseline

Baseline factors	Univariate analyses		Multivariate analyses	
	95% CI of $\beta$ ( $\beta$ )	<i>p</i> values	95% CI of $\beta$ ( $\beta$ )	<i>p</i> values
Male, yes	− 1.74 to − 0.647 (− 1.194)	< 0.001	− 1.44 to − 0.417 (− 0.93)	< 0.001
Age (years)	0.026–0.068 (0.047)	< 0.001	− 0.039 to 0.015 (− 0.012)	0.394
BMI (kg/m <sup>2</sup> )	− 0.194 to − 0.159 (− 0.127)	< 0.001	− 0.098 to 0.052 (− 0.023)	0.545
HCV genotype	− 0.146 to 0.143 (0.014)	0.868		
Log HCV RNA (logIU/mL)	− 0.507 to 0.176 (− 0.165)	0.342		
ALT (U/L)	− 0.002 to 0.005 (0.001)	0.376		
eGFR (mL/min/1.73 m <sup>2</sup> )	− 0.025 to − 0.012 (− 0.019)	< 0.001	− 0.025 to − 0.008 (− 0.017)	< 0.001
TG (mg/dL)	− 0.018 to − 0.008 (− 0.013)	< 0.001	− 0.015 to − 0.005 (− 0.01)	< 0.001
TC (mg/dL)	− 0.004 to 0.013 (− 0.006)	0.183		
HOMA-IR	− 0.177 to − 0.005 (− 0.061)	0.034	− 0.052 to 0.053 (0.00)	0.99
Uric acid (mg/dL)	− 0.312 to 0.077 (− 0.117)	0.237		
NLR	− 0.321 to 0.203 (− 0.059)	0.659		
Platelet (10 <sup>3</sup> /uL)	− 0.013 to − 0.006 (− 0.009)	< 0.001	− 0.006 to 0.004 (− 0.001)	0.617
Liver cirrhosis, yes	− 0.391 to 0.948 (0.279)	0.414		
Fibrosis-4 score	0.17–0.324 (0.247)	< 0.001	0.08–0.297 (0.188)	0.001
Ferritin (ng/mL)	− 0.001 to 0.000 (0.000)	0.212		
IFNL3-rs12979860	− 0.471 to 0.421 (0.4752)	0.324		
CC genotype, yes				

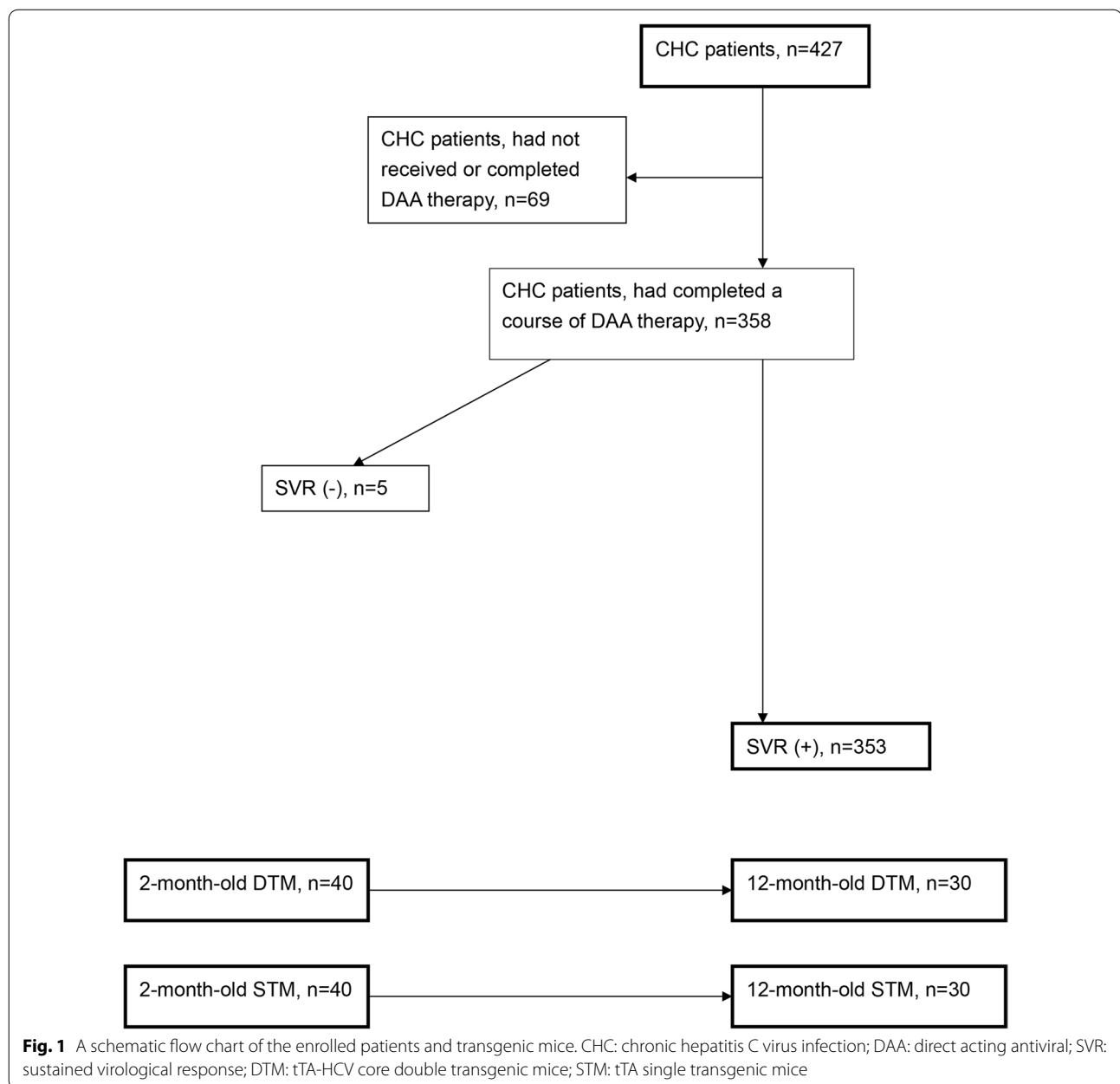
CHC: chronic hepatitis C virus infection; CI: confidence interval; BMI: body mass index; HCV: hepatitis C virus; RNA: ribonucleic acid; ALT: alanine transaminase; eGFR: estimated glomerular filtration rate; TG: triglycerides; TC: total cholesterol; HOMA-IR: homeostatic model assessment for insulin resistance; NLR: neutrophil lymphocyte ratio; IFNL3; interferon- $\lambda$ 3

**Table 3** Associations of HOMA-IR levels in CHC patients at baseline

Baseline factors	Univariate analyses		Multivariate analyses	
	95% CI of $\beta$ ( $\beta$ )	<i>p</i> values	95% CI of $\beta$ ( $\beta$ )	<i>p</i> values
Male, yes	0.081–1.964 (1.022)	0.033	− 1.44 to − 0.417 (− 0.93)	0.100
Age (years)	− 0.069 to 0.004 (− 0.032)	0.085	− 0.039 to 0.015 (− 0.012)	0.678
BMI (kg/m <sup>2</sup> )	0.142–0.378 (0.26)	< 0.001	0.029–0.327 (0.178)	0.02
HCV genotype	1.262–5.513 (3.387)	0.002	0.743–5.279 (3.011)	0.009
Log HCV RNA (logIU/mL)	0.001 to 1.072 (0.536)	0.05	− 0.343 to 0.868 (0.248)	0.433
ALT (U/L)	− 0.136 to 0.162 (0.013)	0.865		
eGFR (mL/min/1.73 m <sup>2</sup> )	0.000–0.023 (0.012)	0.043	− 0.013 to 0.023 (0.005)	0.575
TG (mg/dL)	0.015–0.033 (0.024)	< 0.001	0.01–0.03 (0.02)	< 0.001
TC (mg/dL)	− 0.015 to 0.012 (− 0.002)	0.812		
Adiponectin ( $\mu$ g/mL)	− 0.4 to − 0.016 (− 0.208)	0.034	− 0.197 to 0.215 (0.009)	0.932
Uric acid (mg/dL)	− 0.141 to 0.541 (0.2)	0.25		
NLR	− 0.275 to 0.573 (0.149)	0.491		
Platelet (10 <sup>3</sup> /uL)	− 0.004 to 0.009 (0.002)	0.489		
Liver cirrhosis, yes	− 0.692 to 1.595 (0.451)	0.438		
Fibrosis-4 score	− 0.183 to 0.188 (− 0.048)	0.49		
Ferritin (ng/mL)	0.000–0.002 (0.001)	0.027	0.000 to 0.002 (0.001)	0.134
IFNL3-rs12979860	− 1.695 to 1.849 (0.077)	0.932		
CC genotype, yes				

HOMA-IR: homeostatic model assessment for insulin resistance; CHC: chronic hepatitis C virus infection; CI: confidence interval; BMI: body mass index; HCV: hepatitis C virus; RNA: ribonucleic acid; ALT: alanine transaminase; eGFR: estimated glomerular filtration rate; TG: triglycerides; TC: total cholesterol; NLR: neutrophil lymphocyte ratio; IFNL3; interferon- $\lambda$ 3





with HOMA-IR levels in SVR patients; compared with baseline levels, adiponectin levels decreased, HOMA-IR levels decreased and increased in those with and without baseline IR, respectively. (3) TG levels were independently associated with adiponectin levels in 12-month-old HCV core mice. (4) Comparable hepatic adiponectin expression was noted between tTA-HCV core DTM and tTA STM.

The comparisons of the baseline variables between the female and male CHC patients showed sex dimorphism in metabolic profiles [33] and adiponectin levels [16]

and confirmed the reliability of the results of the current study. The factors consistently associated with adiponectin levels both pre-therapy in CHC patients and at 24 weeks post-therapy in SVR patients, such as sex and eGFR, disclosed their fundamental links of adiponectin, regardless of HCV infection. For example, higher adiponectin levels are usually noted in females than age-matched males [16], and circulating adiponectin level is elevated in chronic kidney disease patients [34]. By contrast, the pre-therapy only factors such as TG and FIB-4, suggested the potential links, direct or indirect, between

**Table 4** Associations of adiponectin levels in SVR patients at 24 weeks post-therapy

24-week post-therapy factors	Univariate analyses		Multivariate analyses	
	95% CI of $\beta$ ( $\beta$ )	<i>p</i> values	95% CI of $\beta$ ( $\beta$ )	<i>p</i> values
Male, yes	− 1.708 to − 0.548 (− 1.128)	< 0.001	− 1.89 to − 0.5 (− 1.195)	0.001
Age, (years)	− 0.01 to 0.037 (0.013)	0.252		
BMI (kg/m <sup>2</sup> )	− 0.183 to 0.136 (− 0.11)	0.004	− 0.139 to 0.16 (− 0.039)	0.443
ALT (U/L)	− 0.042 to − 0.003 (− 0.023)	0.024	− 0.04 to 0.004 (− 0.018)	0.112
eGFR (mL/min/1.73 m <sup>2</sup> )	− 0.024 to − 0.005 (− 0.015)	0.002	− 0.02 to − 0.001 (− 0.011)	0.034
TG (mg/dL)	− 0.008 to − 0.001 (− 0.005)	0.007	− 0.005 to 0.002 (− 0.002)	0.385
TC (mg/dL)	− 0.005 to 0.011 (0.003)	0.418		
HOMA-IR	− 0.153 to 0.045 (− 0.054)	0.283		
Uric acid (mg/dL)	− 0.326 to 0.047 (− 0.14)	0.141		
NLR	− 0.216 to 0.334 (0.059)	0.673		
Platelet (10 <sup>3</sup> /uL)	− 0.01 to 0.00 (− 0.005)	0.039		
Liver cirrhosis, yes	− 0.91 to 0.484 (− 0.213)	0.548		
Fibrosis-4 score	0.026 to 0.265 (0.146)	0.017	− 0.044 to 0.197 (21.72)	0.077
Ferritin (ng/mL)	− 0.001 to 0.001 (0.000)	0.904		
IFNL3-rs12979860	− 0.502 to 1.038 (0.268)	0.494		
CC genotype, yes				

SVR: sustained virological response; BMI: body mass index; HCV: hepatitis C virus; RNA: ribonucleic acid; ALT: alanine transaminase; eGFR: estimated glomerular filtration rate; TG: triglycerides; TC: total cholesterol; HOMA-IR: homeostatic model assessment for insulin resistance; NLR: neutrophil lymphocyte ratio; IFNL3; interferon- $\lambda$ 3

**Table 5** Associations of HOMA-IR levels in SVR patients at 24 weeks post-therapy

24-week post-therapy factors	Univariate analyses		Multivariate analyses	
	95% CI of $\beta$ ( $\beta$ )	<i>p</i> values	95% CI of $\beta$ ( $\beta$ )	<i>p</i> values
Male, yes	− 0.2028 to 1.232 (0.515)	0.158		
Age, (years)	− 0.041 to 0.015 (− 0.013)	0.354		
BMI (kg/m <sup>2</sup> )	0.184–0.358 (0.271)	< 0.001	0.094–0.335 (0.215)	0.001
ALT (U/L)	0.049–0.094 (0.071)	< 0.001	0.018–0.078 (0.048)	0.002
eGFR (mL/min/1.73 m <sup>2</sup> )	− 0.0024 to 0.025 (0.011)	0.102		
TG (mg/dL)	0.006–0.014 (0.01)	< 0.001	0.000–0.01 (0.005)	0.057
TC (mg/dL)	− 0.015 to 0.004 (− 0.005)	0.271		
Adiponectin ( $\mu$ g/mL)	− 0.22 to 0.064 (− 0.078)	0.283		
Uric acid (mg/dL)	− 0.1046 to 0.466 (0.181)	0.212		
NLR	− 6.116 to 4.889 (− 0.613)	0.391		
Platelet (10 <sup>3</sup> /uL)	− 0.013 to 0.00 (− 0.007)	0.059	− 0.013 to 0.002 (− 0.005)	0.145
Liver cirrhosis, yes	0.12–1.789 (0.954)	0.025	− 1.000 to 1.253 (0.126)	0.825
Fibrosis-4 score	− 0.069 to 0.263 (0.097)	0.252		
Ferritin (ng/mL)	0.001–0.004 (0.002)	0.001	0.000–0.003 (0.001)	0.092
IFNL3-rs12979860	− 1.875 to 0.318 (− 0.778)	0.163		
CC genotype, yes				

HOMA-IR: homeostatic model assessment for insulin resistance; SVR: sustained virological response; BMI: body mass index; HCV: hepatitis C virus; RNA: ribonucleic acid; ALT: alanine transaminase; eGFR: estimated glomerular filtration rate; TG: triglycerides; TC: total cholesterol; NLR: neutrophil lymphocyte ratio; IFNL3; interferon- $\lambda$ 3

HCV infection and adiponectin levels. Consistent with our previous studies based on CHC patients with interferon-based therapy [8, 17], both TG and hepatic fibrosis

(FIB-4) were involved in HCV-associated adiponectin alteration. In particular, during HCV infection, adiponectin might affect HOMA-IR levels through TG,

**Table 6** Comparisons between pre-therapy and 24-week post-therapy variables levels among CHC patients with SVRs

Therapy	Pre-therapy	24-week post-therapy	p values (pre- vs. post-)
<b>Adiponectin (µg/mL)</b>			
Total SVR patients	6.53 ± 2.77	5.45 ± 2.56	< 0.001
Male SVR patients	5.85 ± 2.35	4.85 ± 2.42	< 0.001
Female SVR patients	7.15 ± 2.98	5.98 ± 2.58	< 0.001
<b>HOMA-IR</b>			
Total SVR patients	3.25 ± 5.37	2.97 ± 3.09	0.417
Male SVR patients	3.92 ± 7.39	3.25 ± 3.70	0.491
Female SVR patients	2.62 ± 2.03	2.71 ± 2.37	0.327
Baseline IR (+)	1.63 ± 0.51	1.99 ± 1.49	0.001
Baseline IR (−)	5.40 ± 7.69	4.29 ± 4.04	0.01
<b>BMI</b>			
Total SVR patients	24.7 ± 3.9	24.9 ± 3.0	0.002
Male SVR patients	25.2 ± 3.4	25.5 ± 3.5	0.005
Female SVR patients	24.5 ± 4.38	24.4 ± 4.51	0.155
<b>ALT</b>			
Total SVR patients	85.0 ± 94.8	23.5 ± 16.0	< 0.001
Male SVR patients	100.7 ± 121.4	24.8 ± 15.0	< 0.001
Female SVR patients	71.9 ± 60.4	21.0 ± 14.6	< 0.001
<b>eGFR</b>			
Total SVR patients	92.4 ± 38.5	87.4 ± 36.4	< 0.001
Male SVR patients	94.8 ± 38.9	88.8 ± 35.8	< 0.001
Female SVR patients	90.2 ± 38.7	85.8 ± 37.6	0.045

CHC: chronic hepatitis C virus infection; SVR: sustained virological response; HOMA-IR: homeostatic model assessment for insulin resistance; BMI: body mass index; ALT: alanine transaminase; eGFR: estimated glomerular filtration rate

and the link was more evident among those with than those without baseline IR. Moreover, adiponectin levels consistently decreased after SVR, and HOMA-IR levels decreased and increased in those with and without baseline IR, respectively, in both interferon-treated [8] and DAA-treated CHC patients (Fig. 2). The HCV-associated factors for adiponectin might account for the decreasing trend of adiponectin levels, since low TG and high FIB-4 levels in CHC patients before viral clearance [8] lead to high baseline adiponectin levels; after viral clearance, reversal of hypotriglycemia and improved hepatic fibrosis [3, 8] cause decreased adiponectin levels. On the other hand, several pro-inflammatory cytokines such as tumor necrosis factor- $\alpha$  (TNF- $\alpha$ ) and interleukin 6, are reported to down-regulate the expression of adiponectin, resulting in decreased serum adiponectin levels [18, 35]. In particular, activation of the TNF- $\alpha$  system has a pivotal role in the inflammatory process of CHC, and TNF- $\alpha$  levels correlate with the degree of inflammation [36]. Anyhow, we trust that the inflammation was improved in CHC patients after viral clearance, evidenced by the decreased ALT and NLR levels in SVR patients. Thus, although TNF- $\alpha$  levels were not surveyed in the current study, TNF- $\alpha$  is less likely to be the culprit for decreased

adiponectin levels in SVR patients. Of note, the direct association between HOMA-IR and adiponectin levels in SVR patients following interferon-based therapy [8] vanished in SVR patients following DAA therapy (Fig. 2). The various metabolic or immune microenvironments following various therapeutic regimens might account for the discrepancies. For example, ferritin levels reflect the iron homeostasis [37] and are involved in a wide range of physiologic and pathologic processes [38]; the serum ferritin levels increased in SVR patients following interferon-based therapy [39] but decreased SVR patients following DAA therapy [40, 41]. Although the multivariate analyses in the current study did not show any independent role for ferritin levels in adiponectin and HOMA-IR levels, and the potential impact from ferritin on adiponectin and HOMA-IR levels, if any, might be indirect.

As the 12-month-old mice is equivalent to 58-year-old men [42], and the mean age of our human cohort is 61.3 years, the association of TG levels with adiponectin levels in 12-month-old HCV core transgenic mice echoes the crucial role of TG in affecting adiponectin levels in CHC patients and suggests the potential impact of HCV core on adiponectin levels. HCV core exhibits prominent topological relationship with intrahepatic lipid vesicles,

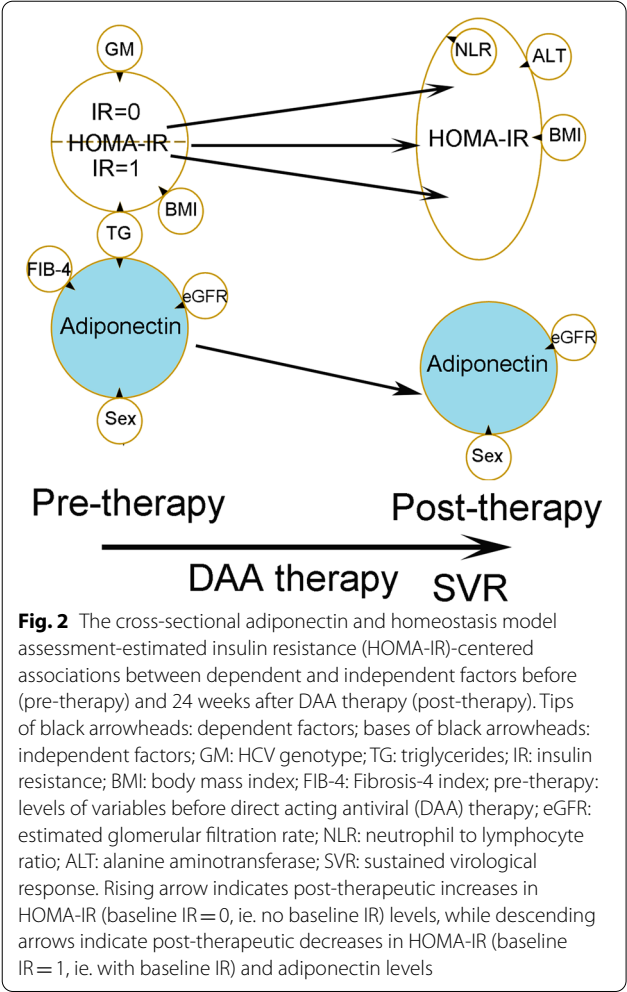


**Fig. 2** The cross-sectional adiponectin and homeostasis model assessment-estimated insulin resistance (HOMA-IR)-centered associations between dependent and independent factors before (pre-therapy) and 24 weeks after DAA therapy (post-therapy). Tips of black arrowheads: dependent factors; bases of black arrowheads: independent factors; GM: HCV genotype; TG: triglycerides; IR: insulin resistance; BMI: body mass index; FIB-4: Fibrosis-4 index; pre-therapy: levels of variables before direct acting antiviral (DAA) therapy; eGFR: estimated glomerular filtration rate; NLR: neutrophil to lymphocyte ratio; ALT: alanine aminotransferase; SVR: sustained virological response. Rising arrow indicates post-therapeutic increases in HOMA-IR (baseline IR = 0, ie. no baseline IR) levels, while descending arrows indicate post-therapeutic decreases in HOMA-IR (baseline IR = 1, ie. with baseline IR) and adiponectin levels

which are mainly composed of TG [31]. Interestingly, the association between TG and adiponectin levels was not significant in the 2-month-old mice, which are equivalent

to 20-year-old men [42]. Thus, the link between adiponectin and TG levels might not be evident until years of HCV infection in human. While that tTA-HCV core DTM (with hepatic steatosis) and tTA STM (without hepatic steatosis) had comparable hepatic adiponectin expression despite the different serum adiponectin levels [32] indicates that through interaction with TG, HCV core-related hepatic steatosis might alter adiponectin levels, via extrahepatic way.

**Conclusions**

Taken together, TG and fibrosis-4 levels are associated with HCV-specific alteration of adiponectin levels. Adiponectin may affect insulin sensitivity through TG during HCV infection. In DAA-treated CHC patients, after viral clearance, adiponectin levels decreased and the link function of TG between adiponectin and insulin sensitivity vanished. Additionally, HCV core with subsequent hepatic steatosis might affect extrahepatic adiponectin expression through TG. These findings might pave the way to probe the therapeutic target for cardiometabolic events in CHC patients after SVR following DAA therapy.

**Methods**

**Human study**

The study group comprised subjects aged 18 years or older with CHC. Subjects with human immunodeficiency virus, hepatitis B infection, hemochromatosis, primary biliary cholangitis, primary sclerosing cholangitis, autoimmune hepatitis or malignancy and recipients of solid organ transplants were excluded. CHC was defined as detectable HCV RNA for > 24 weeks.

A total of 427 CHC patients were consecutively recruited at a tertiary referral center between May 2015 and December 2019. Of the 427 patients, 358 (Fig. 1) had completed a course of anti-HCV therapy with

**Table 7** Associations of adiponectin levels in HCV core transgenic mice

	2-month-old DTM		12-month-old DTM					
	95% CI of $\beta$ ( $\beta$ )	<i>p</i> values	95% CI of $\beta$ ( $\beta$ )	<i>p</i> values	95% CI of $\beta$ ( $\beta$ )	<i>p</i> values	95% CI of $\beta$ ( $\beta$ )	<i>p</i> values
Male, yes	− 2.83 to − 1.07 (− 1.90)	< 0.001	− 6.954 to − 0.547 (− 3.75)	0.025	− 7.8 to − 2.5 (− 5.2)	0.001	− 5.616 to − 0.50 (− 3.059)	0.023
ALT (U/L)	0.000–0.007 (0.004)	0.041	− 2.37 to 0.039 (− 0.099)	0.144	− 0.035 to 0.025 (− 0.005)	0.29		
TG (mg/dL)	− 0.056 to 0.048 (− 0.004)	0.866			0.054–0.14 (0.097)	< 0.001	0.021–0.111 (0.066)	0.007
TC (mg/dL)	− 0.136 to 0.007 (− 0.065)	0.073	− 0.172 to 0.107 (− 0.032)	0.622	− 0.147 to 0.043 (− 0.052)	0.257		
HOMA-IR	− 0.343 to 0.221 (− 0.061)	0.662			− 0.891 to 0.493 (− 0.199)	0.536		

HCV: hepatitis C virus; DTM: tTA-HCV core double transgenic mice; ALT: alanine transaminase; eGFR: estimated glomerular filtration rate; TG: triglycerides; TC: total cholesterol; HOMA-IR: homeostatic model assessment for insulin resistance



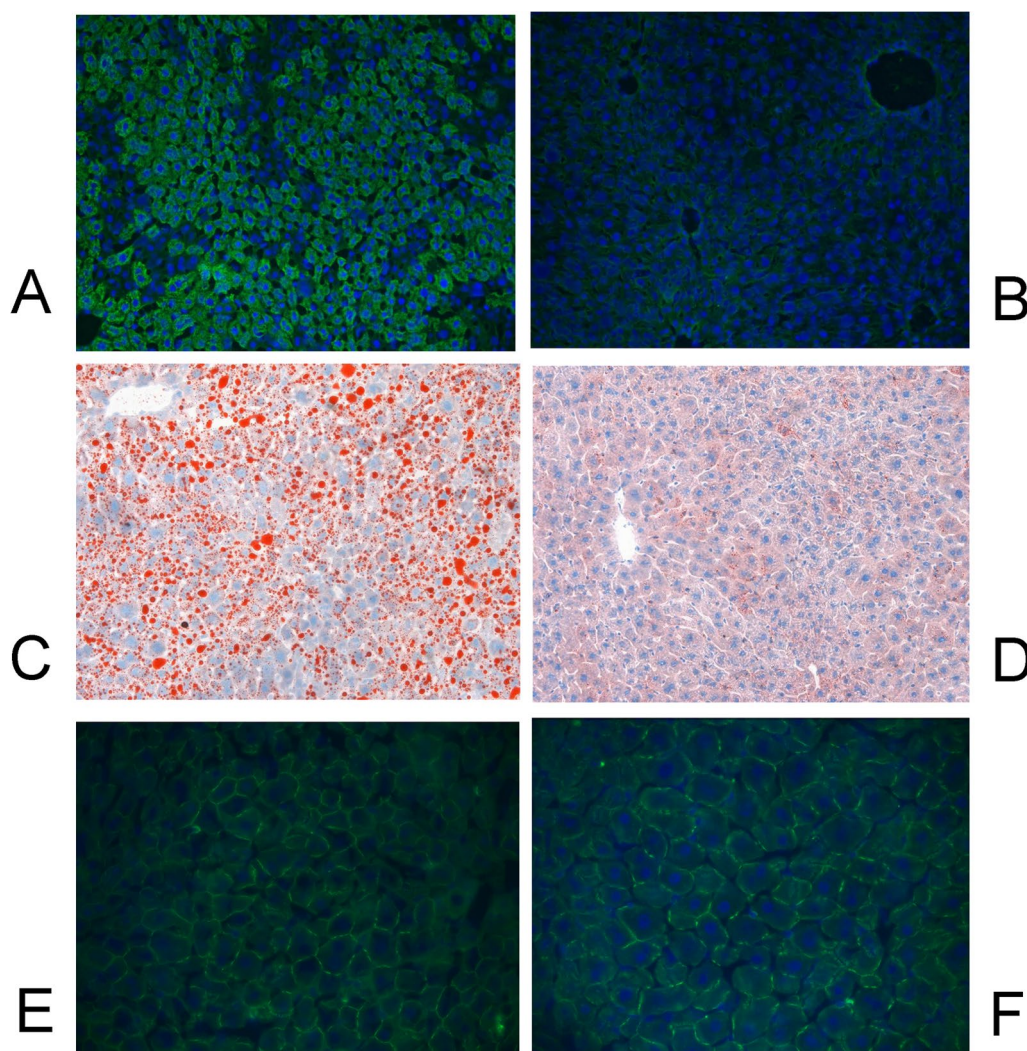


**Fig. 3** IHC studies for HCV core (**A** and **B**), lipid (**C** and **D**) and adiponectin (**E** and **F**) in the frozen liver samples of tTA-HCV core DTM (**A**, **C** and **E**) and tTA STM (**B**, **D** and **F**). The HCV core-positive cells were shown in green, the intracellular lipids were shown in red, the adiponectin was shown in green (in the cell borders)

various DAA combination (Additional file 1: Table S1) according to the reimburse policy of Bureau of National Health Insurance of the country and had been followed  $\geq 24$  weeks after completion of DAA therapy. HCV RNA levels, genotypes, and single-nucleotide polymorphisms of interferon- $\lambda 3$ -rs12979860 were assessed as previously described [5, 7, 21–25]. Several baseline factors including sex, age, body mass index, HCV genotype, levels of HCV RNA, eGFR, UA, TC, TG, fasting glucose, fasting insulin, HOMA-IR [fasting insulin ( $\mu\text{U/mL}$ )  $\times$  fasting glucose (mmol/L)/22.5], ALT and FIB-4 [(Age (years)  $\times$  aspartate transaminase (U/L)) / (Platelets ( $10^9/\text{L}$ )  $\times$  ( $\sqrt{\text{ALT (U/L)}}$ )] index, MELD score, ferritin, adiponectin (R&D Systems, MN, USA) and the presence

of hepatic cirrhosis were checked and recorded for all enrolled patients at baseline. Biochemical tests were performed at the clinical pathology laboratories of the hospital using routine automated techniques. An SVR was defined as undetectable levels of HCV RNA 12 weeks after the completion of therapy. In total, 353 had SVRs (Fig. 1). An IR was defined as  $\text{HOMA-IR} \geq 2.5$  [8]. The aforementioned variables were surveyed among the SVR patients at 24 weeks after the completion of therapy.

#### Animal study

tTA-HCV core DTM in which expression of the HCV core gene was suppressible by tetracycline were raised as previously described [29–32]. These mice were raised

and maintained in the specific-pathogen-free rooms of the animal center of the hospital, the experimental mice were acquired from the animal center of the hospital. For both the DTM and tTA STM, analyses of HCV core protein expression was performed by IHC staining as described previously [29–32], fat vesicles were identified by Oil Red O staining of frozen sections according to the manufacturer's protocol (BioGenex, Fremont, CA), and IHC studies of adiponectin (Novus Biologicals) were performed using frozen liver samples according to the manufacturer's protocols. Protein expression intensity was determined as described previously [10]. The fasting serum levels of adiponectin (R&D Systems, Minneapolis, MN) and insulin (Crystal Chem, Downers Grove, IL) were surveyed by using enzyme-linked immunosorbent assay bioassay kits according to manufacturer's protocols in 2-month-old (males,  $n=20$ , females,  $n=20$ ) and 12-month-old DTM (males,  $n=16$ , females,  $n=14$ ) and in 2-month-old (males,  $n=20$ , females,  $n=20$ ) and 12-month-old t-TA STM (males,  $n=15$ , females,  $n=15$ ). The assays for fasting serum glucose, TG, TC and ALT levels (Vitros DT60 II Chemistry System; Johnson & Johnson, Rochester, NY) were adopted for using tail blood according to the manufacturer's protocol in 2-month-old (males,  $n=20$ , females,  $n=20$ ) and 12-month-old DTM (males,  $n=16$ , females,  $n=14$ ). After the end of the experiments, all the mice were sacrificed with CO<sub>2</sub> euthanasia by using the home cages.

A schematic flow chart for the enrolled patients and transgenic mice was shown as Fig. 1.

## Statistics

All statistical analyses were performed using the Statistical Package for Social Science (SPSS package version 21, SPSS Inc., Chicago, IL, USA) or MedCalc (MedCalc ver. 12.4, MedCalc Software Corp., Acaciaaan, Ostend, Belgium) software. The continuous variables are summarized as means  $\pm$  standard deviations (SD), and the categorical variables are summarized as frequencies and percentages. The t-tests or Chi Square tests were applied for compared the variables between 2 groups while indicated. Multivariate linear regression models were used to assess the relationships between various dependent and independent factors by adjusting for all independent variables with  $p$  values  $<0.1$  in the univariate analyses. Repeated measures or Wilcoxon signed-rank tests were performed for the same variable measured in the same or matched subjects  $\geq 2$  time periods. Statistical significance was defined at the 5% level based on two-tailed tests.

## Abbreviations

HCV: Hepatitis C virus; SVRs: Sustained virological responses; DAA: Direct-acting antivirals; eGFR: Estimated glomerular filtration rate; HOMA-IR: Homeostatic model assessment for insulin resistance; HCC: Hepatocellular carcinoma; IR: Insulin resistance; CHC: Chronic HCV infection; IHC: Immunohistochemistry; BMI: Body mass index; TG: Triglycerides; tTA: Tetracycline transactivator; DTM: Double transgenic mice; STM: Single transgenic mice.

## Supplementary Information

The online version contains supplementary material available at <https://doi.org/10.1186/s12865-021-00445-5>.

**Additional file 1. Supplementary Table 1.** Various DAA combinations used in the study. **Supplementary Table 2.** Associations of HOMA-IR levels in CHC patients with baseline IR at baseline. **Supplementary Table 3.** Associations of HOMA-IR levels in CHC patients without baseline IR at baseline. **Supplementary Table 4.** Associations of HOMA-IR levels in SVR patients with baseline IR at 24 weeks post-therapy. **Supplementary Table 5.** Associations of HOMA-IR levels in SVR patients without baseline IR at 24 weeks post-therapy

## Acknowledgements

The authors thank Ms. Shu-Chun Chen, Ms. Chia-Hui Tsai, Mr. Chun-Kai Liang and Mr. Shuen-Shian Shiau from Division of Hepatology, Department of Gastroenterology, Chang Gung Memorial Hospital, Taiwan, for their assistance with data mining.

## Authors' contributions

LHP and MYC collected and analyzed the data and wrote the manuscript. JHH, MSL, CJK, SCC and CMF interpreted the data and wrote the manuscript. MLC and RNC designed and completed the study, drafted the article and critically revised it for intellectual content. All authors read and approved the final version of the article, including the authorship list.

## Funding

This study was supported by grants from the Chang Gung Medical Research Program (CMRPG3I0412, CMRPG3K0721 and CMRPG1K0111) and the National Science Council, Taiwan (MOST 110-2314-B-182-044-, 110-2629-B-182-001-, 109-2314-B-182-024- and 109-2629-B-182-002-). The funders had no role in study design, data collection and analysis, decision to publish, or preparation of the manuscript.

## Availability of data and materials

The datasets used and/or analyzed during the current study are available from the corresponding author on reasonable request. Because part of our data will be further analyzed for other study, we thus did not deposit the datasets in any publicly available repositories.

## Declarations

### Ethics approval and consent to participate

Written informed consent was obtained from each patient. The study protocols for human and animal studies conformed to the ethical guidelines of the 1975 Declaration of Helsinki and were approved by the Chang Gung Medical Foundation Institutional Review Board (IRB) (IRB No. 201801511B0) and Institutional Animal Care and Use Committee (IACUC) (IACUC No. 2018091701).

### Consent for publication

Not applicable.

### Informed consent

Written informed consent was obtained from each patient. The study protocols for human and animal studies conformed to the ethical guidelines of

the 1975 Declaration of Helsinki and were approved by the local institutional review board.

# Competing interests

The authors declare no competing interests.

# Author details

<sup>1</sup>Division of Hepatology, Department of Gastroenterology and Hepatology, Chang Gung Memorial Hospital, No 5, Fu Hsing Street, Kuei Shan, Taoyuan, Taiwan. <sup>2</sup>Department of Medicine, College of Medicine, Chang Gung University, Taoyuan, Taiwan. <sup>3</sup>Department of Internal Medicine, Chang Gung Memorial Hospital, Yunlin, Taiwan. <sup>4</sup>Graduate Institute of Health-Industry Technology, Chang Gung University of Science and Technology, Taoyuan, Taiwan. <sup>5</sup>Research Center for Industry of Human Ecology, Chang Gung University of Science and Technology, Taoyuan, Taiwan. <sup>6</sup>Department of Cardiology, Heart Failure Center, Chang Gung Memorial Hospital, Yunlin, Taiwan. <sup>7</sup>Department of Nursing, Taipei Medical University, Taipei, Taiwan. <sup>8</sup>Department of Biomedical Sciences, Chang Gung University, Taoyuan, Taiwan. <sup>9</sup>Division of Pediatric Neurologic Medicine, Chang Gung Children's Hospital, Taoyuan, Taiwan. <sup>10</sup>Division of Pediatrics, Chang Gung Memorial Hospital, Keelung, Taiwan. <sup>11</sup>Liver Research Unit, Department of Gastroenterology and Hepatology, Chang Gung Memorial Hospital, No 5, Fu Hsing Street, Kuei Shan, Taoyuan, Taiwan.

Received: 4 May 2020 Accepted: 29 July 2021

Published online: 11 August 2021

# References

1. Spearman CW, Dusheiko GM, Hellard M, Sonderup M. Hepatitis C. *Lancet*. 2019;394(10207):1451–66.
2. Borgia SM, Hedskog C, Parhy B, Hyland RH, Stamm LM, Brainard DM, et al. Identification of a Novel Hepatitis C Virus Genotype from Punjab, India: expanding classification of hepatitis c virus into 8 genotypes. *J Infect Dis*. 2018;218(11):1722–9.
3. Chang ML. Metabolic alterations and hepatitis C: from bench to bedside. *World J Gastroenterol*. 2016;22(4):1461–76.
4. Chang ML, Yang SS. Metabolic signature of hepatic fibrosis: from individual pathways to systems biology. *Cells*. 2019;8(11):1423.
5. Chang ML, Lin YS, Chang MY, Hsu CL, Chien RN, Fann CS. Accelerated cardiovascular risk after viral clearance in hepatitis C patients with the NAMPT-rs61330082 TT genotype: an 8-year prospective cohort study. *Virulence*. 2021;12(1):270–80.
6. Chang SW, Cheng ML, Shiao MS, Yeh CT, Wang CH, Fan CM, et al. Recovery of lipid metabolic alterations in hepatitis C patients after viral clearance: Incomplete restoration with accelerated  $\omega$ -oxidation. *J Clin Lipidol*. 2018;12(3):756–66.
7. Chang ML, Lin YS, Pao LH, Huang HC, Chiu CT. Link between plasminogen activator inhibitor-1 and cardiovascular risk in chronic hepatitis C after viral clearance. *Sci Rep*. 2017;7:42503.
8. Chang ML, Kuo CJ, Pao LH, Hsu CM, Chiu CT. The evolving relationship between adiponectin and insulin sensitivity in hepatitis C patients during viral clearance. *Virulence*. 2017;8(7):1255–64.
9. Chang ML, Chen WT, Hu JH, Chen SC, Gu PW, Chien RN. Altering retinol binding protein 4 levels in hepatitis C: Inflammation and steatosis matter. *Virulence*. 2020;11(1):1501–11.
10. Chang ML, Liang KH, Ku CL, Lo CC, Cheng YT, Hsu CM, et al. Resistin reinforces interferon  $\lambda$ -3 to eliminate hepatitis C virus with fine-tuning from RETN single-nucleotide polymorphisms. *Sci Rep*. 2016;6:30799.
11. Toyoda H, Kumada T, Tada T, Kiriyama S, Tanikawa M, Hisanaga Y, et al. Risk factors of hepatocellular carcinoma development in non-cirrhotic patients with sustained virologic response for chronic hepatitis C virus infection. *J Gastroenterol Hepatol*. 2015;30(7):1183–9.
12. Hamamoto S, Uchida Y, Wada T, Moritani M, Sato S, Hamamoto N, et al. Changes in serum lipid concentrations in patients with chronic hepatitis C virus positive hepatitis responsive or non-responsive to interferon therapy. *J Gastroenterol Hepatol*. 2005;20:204–8.
13. Teijaro JR. Pleiotropic roles of type 1 interferons in antiviral immune responses. *Adv Immunol*. 2016;132:135–58.
14. Halfon P, Locarnini S. Hepatitis C virus resistance to protease inhibitors. *J Hepatol*. 2011;55(1):192–206.
15. Yamauchi T, Kamon J, Ito Y, Tsuchida A, Yokomizo T, Kita S, et al. Cloning of adiponectin receptors that mediate antidiabetic metabolic effects. *Nature*. 2003;423(6941):762–9.
16. Chang ML, Hsu CM, Tseng JH, Tsou YK, Chen SC, Shiao SS, et al. Plasminogen activator inhibitor-1 is independently associated with non-alcoholic fatty liver disease whereas leptin and adiponectin vary between genders. *J Gastroenterol Hepatol*. 2015;30(2):329–36.
17. Chang ML, Hsu CM, Lin CH, Lin CY, Kuo CJ, Huang SW, et al. The Evolving Interplay among Abundant Adipokines in Patients with Hepatitis C during Viral Clearance. *Nutrients*. 2017;9(6):570.
18. Duntas LH, Popovic V, Panotopoulos G. Adiponectin: novelties in metabolism and hormonal regulation. *Nutr Neurosci*. 2004;7(4):195–200.
19. Stern JH, Rutkowski JM, Scherer PE. Adiponectin, leptin, and fatty acids in the maintenance of metabolic homeostasis through adipose tissue cross-talk. *Cell Metab*. 2016;23(5):770–84.
20. Guo R, Nair S, Zhang Y, Ren J. Adiponectin deficiency rescues high-fat diet-induced hepatic injury, apoptosis and autophagy loss despite persistent steatosis. *Int J Obes (Lond)*. 2017;41(9):1403–12.
21. Wanders D, Plaisance EP, Judd RL. Lipid-lowering drugs and circulating adiponectin. *Vitam Horm*. 2012;90:341–74.
22. Aprahamian TR, Sam F. Adiponectin in cardiovascular inflammation and obesity. *Int J Inflam*. 2011;2011:376909.
23. Wu ZJ, Cheng YJ, Gu WJ, Aung LH. Adiponectin is associated with increased mortality in patients with already established cardiovascular disease: a systematic review and meta-analysis. *Metabolism*. 2014;63(9):1157–66.
24. Karas MG, Benkeser D, Arnold AM, Bartz TM, Djousse L, Mukamal KJ, et al. Relations of plasma total and high-molecular-weight adiponectin to new-onset heart failure in adults  $\geq 65$  years of age (from the Cardiovascular Health study). *Am J Cardiol*. 2014;113(2):328–34.
25. Ye J, Liang Z, Liang Q, Zhang J, Mao S, Liang R. Adiponectin is associated with poor prognosis in carcinoma patients: evidence from a meta-analysis. *Lipids Health Dis*. 2015;14:154.
26. Chhatwal J, He T, Hur C, Lopez-Olivo MA. Direct-Acting Antiviral Agents for Patients With Hepatitis C Virus Genotype 1 Infection Are Cost-Saving. *Clin Gastroenterol Hepatol*. 2017;15(6):827–837.e8.
27. Gawlik K, Gallay PA. HCV core protein and virus assembly: what we know without structures. *Immunol Res*. 2014;60(1):1–10.
28. Cristina J, del Pilar MM, Moratorio G. Hepatitis C virus genetic variability in patients undergoing antiviral therapy. *Virus Res*. 2007;127(2):185–94.
29. Chang ML, Yeh CT, Chen JC, Huang CC, Lin SM, Sheen IS, et al. Altered expression patterns of lipid metabolism genes in an animal model of HCV core-related, nonobese, modest hepatic steatosis. *BMC Genomics*. 2008;9:109.
30. Chang ML, Chen JC, Chang MY, Yeh CT, Lin WP, Liang CK, et al. Acute expression of hepatitis C core protein in adult mouse liver: Mitochondrial stress and apoptosis. *Scand J Gastroenterol*. 2008;43(6):747–55.
31. Chang ML, Chen JC, Yeh CT, Sheen IS, Tai DI, Chang MY, et al. Topological and evolutionary relationships between HCV core protein and hepatic lipid vesicles: studies in vitro and in conditionally transgenic mice. *World J Gastroenterol*. 2007;13(25):3472–7.
32. Chang ML, Yeh HC, Tsou YK, Wang CJ, Cheng HY, Sung CM, et al. HCV core-induced nonobese hepatic steatosis is associated with hypoadiponectinemia and is ameliorated by adiponectin administration. *Obesity (Silver Spring)*. 2012;20(7):1474–80.
33. Li XD, Qiu BH, Su FC, Sun SX. Gender impacts on the correlations between nonalcoholic fatty liver disease and hypertension in a Chinese population aged 45–60 y. *Clin Exp Hypertens*. 2016;38(7):639–43.
34. Kim H, Yun HR, Park S, Jhee JH, Park JT, Yoo TH, et al. High serum adiponectin is associated with anemia development in chronic kidney disease: The results from the KNOW-CKD study. *Cytokine*. 2018;103:1–9.
35. Andrade-Oliveira V, Câmara NO, Moraes-Vieira PM. Adipokines as drug targets in diabetes and underlying disturbances. *J Diabetes Res*. 2015;2015:681612.
36. Knobler H, Schattner A. TNF- $\alpha$ , chronic hepatitis C and diabetes: a novel triad. *QJM*. 2005;98(1):1–6.
37. Fiorelli G. Serum ferritin and erythrocyte indices in iron overload. *Blood Transfus*. 2007;5(4):187–8.
38. Knovich MA, Storey JA, Coffman LG, Torti SV, Torti FM. Ferritin for the clinician. *Blood Rev*. 2009;23(3):95–104.

39. Mangia A, Sarli R, Gamberini R, Piga A, Cenderello G, Piazzolla V, et al. Randomised clinical trial: sofosbuvir and ledipasvir in patients with transfusion-dependent thalassaemia and HCV genotype 1 or 4 infection. *Aliment Pharmacol Ther.* 2017;46(4):424–31.
40. Origa R, Ponti ML, Filosa A, Galeota Lanza A, Piga A, Saracco GM, et al. Treatment of hepatitis C virus infection with direct-acting antiviral drugs is safe and effective in patients with hemoglobinopathies. *Am J Hematol.* 2017;92(12):1349–55.
41. Chang ML, Hu JH, Yen CH, Chen KH, Kuo CJ, Lin MS, et al. Evolution of ferritin levels in hepatitis C patients treated with antivirals. *Sci Rep.* 2020;10(1):19744.

42. <http://www.age-converter.com/mouse-age-calculator.html>

### Publisher's Note

Springer Nature remains neutral with regard to jurisdictional claims in published maps and institutional affiliations.

**Ready to submit your research? Choose BMC and benefit from:**

- fast, convenient online submission
- thorough peer review by experienced researchers in your field
- rapid publication on acceptance
- support for research data, including large and complex data types
- gold Open Access which fosters wider collaboration and increased citations
- maximum visibility for your research: over 100M website views per year

**At BMC, research is always in progress.**

Learn more [biomedcentral.com/submissions](https://biomedcentral.com/submissions)







# Roles of Neutrophils in Glioma and Brain Metastases

Ya-Jui Lin<sup>1,2,3</sup>, Kuo-Chen Wei<sup>1,4,5</sup>, Pin-Yuan Chen<sup>5,6</sup>, Michael Lim<sup>3\*</sup>  
and Tsong-Long Hwang<sup>2,7,8,9\*</sup>

<sup>1</sup> Department of Neurosurgery, Chang Gung Memorial Hospital, Linkou, Taiwan, <sup>2</sup> Graduate Institute of Natural Products, College of Medicine, Chang Gung University, Taoyuan, Taiwan, <sup>3</sup> Department of Neurosurgery, Stanford University School of Medicine, Stanford, CA, United States, <sup>4</sup> Department of Neurosurgery, New Taipei Municipal TuCheng Hospital, Chang Gung Medical Foundation, New Taipei, Taiwan, <sup>5</sup> School of Medicine, Chang Gung University, Taoyuan, Taiwan, <sup>6</sup> Department of Neurosurgery, Chang Gung Memorial Hospital, Keelung, Taiwan, <sup>7</sup> Research Center for Chinese Herbal Medicine, Research Center for Food and Cosmetic Safety, and Graduate Institute of Health Industry Technology, Chang Gung University of Science and Technology, Taoyuan, Taiwan, <sup>8</sup> Department of Anesthesiology, Chang Gung Memorial Hospital, Taoyuan, Taiwan, <sup>9</sup> Department of Chemical Engineering, Ming Chi University of Technology, New Taipei City, Taiwan

## OPEN ACCESS

### Edited by:

Susanna Mandruzzato,  
University Hospital of Padua, Italy

### Reviewed by:

Lisa Sevenich,  
Georg Speyer Haus, Germany  
Zachary J. Gerbec,  
British Columbia Cancer Research  
Centre, Canada

### \*Correspondence:

Michael Lim  
mklm@stanford.edu  
Tsong-Long Hwang  
htl@mail.cgu.edu.tw

### Specialty section:

This article was submitted to  
Cancer Immunity and Immunotherapy,  
a section of the journal  
Frontiers in Immunology

**Received:** 27 April 2021

**Accepted:** 19 July 2021

**Published:** 13 August 2021

### Citation:

Lin Y-J, Wei K-C, Chen P-Y,  
Lim M and Hwang T-L (2021)  
Roles of Neutrophils in Glioma  
and Brain Metastases.  
Front. Immunol. 12:701383.  
doi: 10.3389/fimmu.2021.701383

Neutrophils, which are the most abundant circulating leukocytes in humans, are the first line of defense against bacterial and fungal infections. Recent studies have reported the role and importance of neutrophils in cancers. Glioma and brain metastases are the most common malignant tumors of the brain. The tumor microenvironment (TME) in the brain is complex and unique owing to the brain-blood barrier or brain-tumor barrier, which may prevent drug penetration and decrease the efficacy of immunotherapy. However, there are limited studies on the correlation between brain cancer and neutrophils. This review discusses the origin and functions of neutrophils. Additionally, the current knowledge on the correlation between neutrophil-to-lymphocyte ratio and prognosis of glioma and brain metastases has been summarized. Furthermore, the implications of tumor-associated neutrophil (TAN) phenotypes and the functions of TANs have been discussed. Finally, the potential effects of various treatments on TANs and the ability of neutrophils to function as a nanocarrier of drugs to the brain TME have been summarized. However, further studies are needed to elucidate the complex interactions between neutrophils, other immune cells, and brain tumor cells.

**Keywords:** neutrophils, glioblastoma, brain metastases, neutrophil extracellular traps, nanocarrier

## INTRODUCTION

Paul Ehrlich coined the term neutrophils, which are also known as polymorphonuclear cells, in the late nineteenth century due to their preferential uptake of neutral pH dye and their inability to retain acidic or basic dyes (1, 2). Neutrophils, which are the most abundant circulating leukocytes in mammals, have a short life span and the neutrophil population is constantly replenished from the bone marrow (3). The first line of defense against bacterial and fungal infections is neutrophils. Additionally, neutrophils can modulate the adaptive immune response at the inflammation site through interaction with antigen-presenting cells and lymphocytes (4–6). Since the nineteenth century, inflammation has been correlated with the pathogenesis of cancer (7). Cancer-related inflammation, a hallmark of tumor biology, involves both stromal and inflammatory cells in the

tumor microenvironment (TME) (8, 9). The immune privilege of the central nervous system (CNS) can be attributed to the lack of dedicated lymphatic channels in the past (10). In 2015, a novel route of lymphatic channels from the brain that runs parallel to the dural venous sinuses and travel to the deep cervical lymph nodes was identified (11).

In the 1890s, William Coley first conceived the concept of cancer immunotherapy. Ehrlich and Thomas and Burnet further developed this concept in the 1950s and 1960s, respectively (12–15). Cancer immune surveillance involves the detection and elimination of the tumor cells by the immune system (12, 15). Thus, cancer immunotherapies, especially immune checkpoint inhibitors (ICIs), are an emerging therapeutic modality and have revolutionized cancer management (16, 17). In contrast to other immune cells, such as macrophages, neutrophils were not considered to be major players in the TME. However, recent developments in genetic tools have revealed the importance of neutrophils in the TME, especially in tumor progression and tumor resistance (2, 18). The presence and phenotype of neutrophils in the TME determine the efficacy of both traditional and novel cancer therapies (3, 19).

As neutrophils play an important role in the TME, they are potential targets to enhance the efficacy of immunotherapy. However, the role of neutrophils in brain cancer biology remains unclear. In this review, we focus on the role of neutrophils in glioma and brain metastases (BMs), which are the most common malignant brain tumors. This review proposes

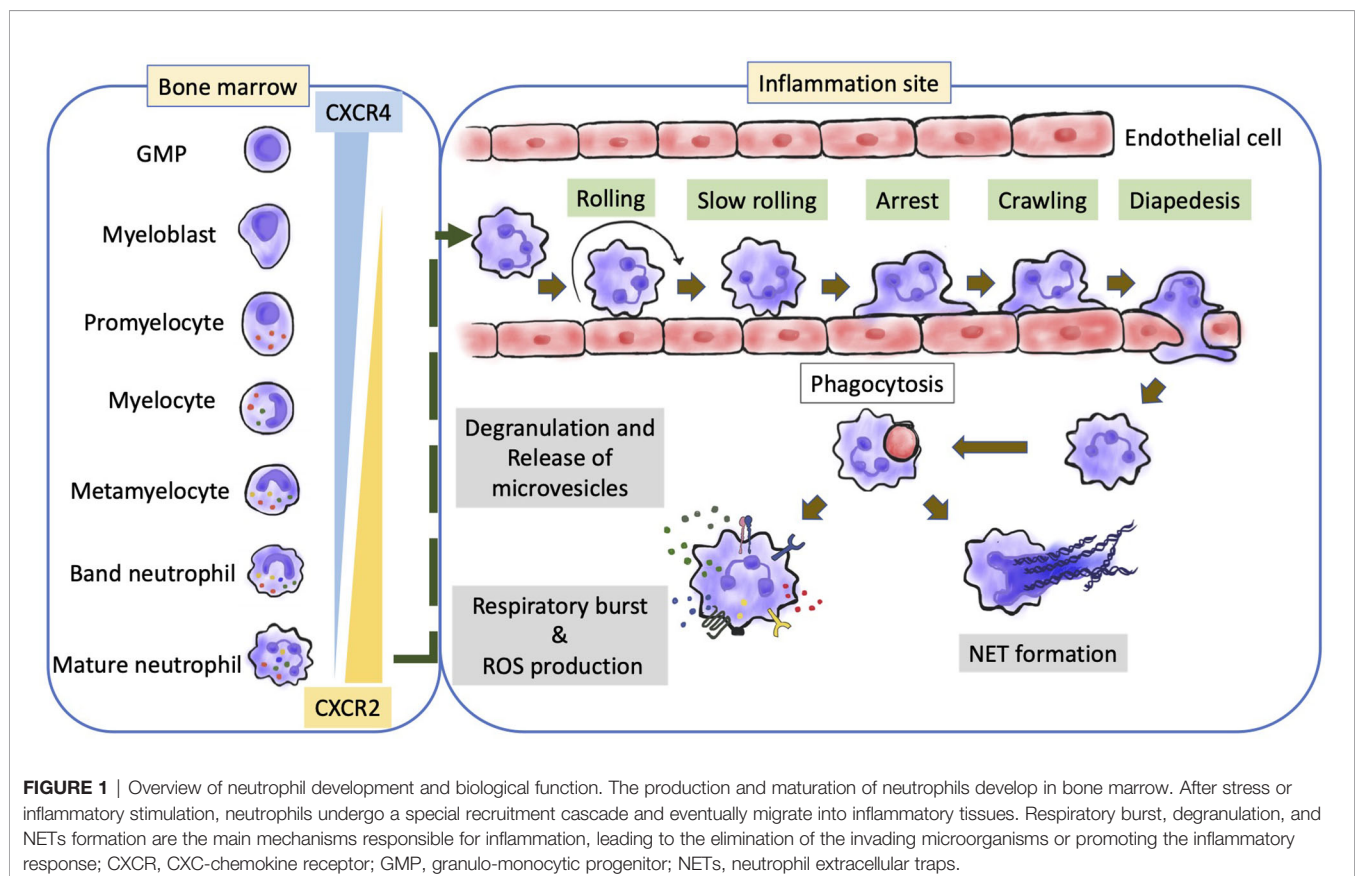
the neutrophil-to-lymphocyte ratio (NLR) as a biomarker for brain cancer. Additionally, this review discusses the heterogeneity of tumor-associated neutrophils (TANs). Furthermore, the current therapeutic modalities using neutrophils as targets or carriers to treat glioma and BM have been summarized.

## ORIGIN, LIFE CYCLE, AND BIOLOGICAL FUNCTIONS OF NEUTROPHILS

More than  $10^{11}$  neutrophils are produced every day under steady-state conditions (20, 21). Emergency granulopoiesis is a process in which the formation of neutrophils rapidly increases in response to infection or cancer (22).

### Granulopoiesis

Neutrophils are generated from lymphoid-primed multipotent progenitors (LMPPs) (23), which are derived from hematopoietic stem cells. LMPPs further differentiate into granulocyte-monocyte myeloid progenitors (24, 25). Neutrophils undergo maturation in the following steps: the formation of myeloblasts, followed by the formation of promyelocytes, myelocytes, metamyelocytes, band neutrophils, and segmented neutrophils (**Figure 1**) (22, 26, 27). The transitions from myeloblasts to promyelocytes, and from myelocytes to metamyelocytes are characterized by the



appearance of primary granules and secondary granules respectively. Meanwhile, the transition from the band neutrophils to the segmented neutrophils is characterized by the formation of tertiary granules (21, 28). These granules comprise various defensive factors and enzymes, such as myeloperoxidase (MPO), elastase, defensins, cathelicidins, and matrix metalloproteinases (MMPs), which protect against opportunistic infections and mediate the alleviation of inflammation (28, 29).

Granulocyte colony-stimulating factor (G-CSF), which is the master regulator of neutrophil generation and differentiation (30–32), can induce the proliferation and differentiation of myeloid progenitors. The expression of G-CSF receptor (G-CSFR) is detected in the myeloid lineage from the early stem and progenitor cells to fully differentiated neutrophils (33, 34). G-CSFR-signal transducer and activator of transcription 3 (STAT3) signaling regulates neutrophil formation (35). Other molecules, such as granulocyte-macrophage colony-stimulating factor (GM-CSF), interleukin 6 (IL-6), and KIT ligand (also known as KITLG) are reported to be involved in granulopoiesis (36–38). For example, these cytokines are upregulated in several animal models of cancer, which results in enhanced granulopoiesis and neutrophilia (39–45).

## Neutrophil Retention and Release From the Bone Marrow

In contrast to other immune cells, neutrophils are released from the bone marrow as terminally differentiated mature cells. Under homeostatic conditions, approximately 1%–2% of all neutrophils are mature neutrophils that circulate throughout the body (46). The immature cells are retained in the bone marrow due to the interaction between C-X-C chemokine receptor 4 (CXCR4) and CXCR2 (**Figure 1**). Osteoblasts and other bone marrow stromal cells constitutively express CXCL12 and tether CXCR4+ neutrophils (immature) in the bone marrow. Meanwhile, mature neutrophils exhibiting CXCR2 expression are released into the circulation through the interaction with CXCL1 and CXCL2 secreted by the endothelial cells and megakaryocytes (47–52). Several adhesion molecules, such as integrin subunit  $\alpha 4$  (ITG $\alpha 4$ ), vascular cell adhesion molecule 1 (VCAM1), and some proteases also play a critical role in neutrophil retention (52–55). G-CSF is reported to be a disruptor of neutrophil retention (56).

The molecules that regulate neutrophil release into the circulation are upregulated in tumors. These molecules override the neutrophil retention signals in the bone marrow to facilitate neutrophil egress and consequently increase neutrophil counts (39–42, 57). In addition to cytokines derived from tumor cells (41, 42, 57), stromal and immune cells can upregulate the expression of these molecules in tumor-bearing mice. The aberrant production of cytokines by the tumors or stromal cells can cause an imbalance in neutrophil retention and release from the bone marrow.

## Biological Functions

Neutrophils regulate immunity and inflammation by recognizing and responding to microbial and inflammatory stimuli (58, 59).

Phagocytosis and enzymatic processes (**Figure 1**), including the generation of reactive oxygen species (ROS) through the NADPH oxidase 2 (NOX2) and the release of granule-derived MPO, hydrolytic enzymes (such as elastase, lysozyme, and MMPs), and other antimicrobial proteins/peptides (such as lactoferrin and defensins) can eliminate the invading microorganisms after pathogen recognition (60, 61). Neutrophil granule-derived molecules can directly kill microorganisms, mediate positive feedback loops in neutrophils, or attract and activate monocytes (62, 63). Classical effector responses interact with each other at several levels, including the primary release of granules into the phagosome, processing of NOX2-derived superoxide and H<sub>2</sub>O<sub>2</sub> by granule-derived MPO, or NOX2-mediated activation of granule proteins (60–62, 64). Neutrophils also release their DNA into the extracellular space to form neutrophil extracellular traps (NETs), a complex of DNA and neutrophil-derived antimicrobial molecules (**Figure 1**) (65). In addition to trapping and killing bacteria (65), NETs are involved in various inflammatory diseases (66). NET formation (also called ‘NETosis’) is dependent on MPO, neutrophil elastase, peptidylarginine deiminase 4 (PAD4), and gasdermin D, which are potential therapeutic targets for NET-mediated pathologies (67–69). The genetic deficiency of NET-degrading DNases results in the development of NET-mediated vascular occlusion (70). However, previous studies have reported controversial findings on NETs generation and function.

Neutrophils can release various chemokines, cytokines, and lipid mediators through modulation of gene expression although they exhibit limited transcriptional activity (71–73). Therefore, neutrophils are involved in regulating the immune response and the interaction of various immune and non-immune cells (74–76). However, the functional relevance of these neutrophil-derived mediators is not completely understood. Neutrophils also release extracellular vesicles that exhibit antimicrobial functions (77), mediate the effects of neutrophil-derived LTB<sub>4</sub>, and contribute to the pathogenesis of inflammation and cancer (78–80).

## CURRENT THERAPEUTIC STRATEGIES FOR GLIOMA AND BMS

Brain tumors are a mixed group of primary and metastatic neoplasms that exhibit varying degrees of malignancy. Although malignant lesions are uncommon, their incidence has increased rapidly in highly developed and industrialized countries (81). Malignant brain tumors directly affect neurological function, psychological health, and quality of life (82). In the last few decades, advances in diagnostic methods, including the development of computed tomography in the mid-1970s and magnetic resonance imaging (MRI) in the mid-1980s, have revealed an increased incidence of brain tumors (83, 84).

Glioma is the most prevalent type of primary malignant brain tumor. Glioblastoma (GBM) is the worst grade of glioma with a median overall survival of 14 to 17 months and a five-year

survival rate of only 5.6% despite of the traditional triad of surgical excision, radiotherapy, and chemotherapy (85–88). Recently, tumor-treating fields, which involve the use of low-intensity alternating electric fields to interfere with cell division and organelle assembly, have been demonstrated to extend the OS of patients with glioma to 20.9 months (89). Besides, several studies have focused on immunotherapy as an effective treatment paradigm (90, 91). The results of phase I and II clinical trials on cancer vaccines were encouraging. The synergistic effects of anti-tumor vaccines and standard therapy have been previously demonstrated (92–96). Immunotherapy is believed to be a promising approach for enhancing the efficacy of the current chemoradiation regimen. However, phase III clinical studies have revealed the poor efficacy of ICIs and vaccine therapy for GBM. Nivolumab (monoclonal antibody to PD-1) of checkMate 143 (NCT02017717) (97) and Rindopepimut (EGFRvIII specific peptide and KLH conjugate) of ACT IV (NCT01480479) (98) both terminated early because no significant survival benefit. There are several obstacles to the success of GBM immunotherapy, such as the heterogeneity and low mutation burden of the tumors and local/systemic immunosuppression induced by GBM (99–103).

BM, which occurs in 10%–40% of patients with cancer, are the most common malignant brain tumors in adults (104, 105). The increased surveillance and improved control of primary cancer resulting in prolonged survival have increased the incidence of BMs (106). The most common primary sites of BMs are lung and breast carcinomas and melanoma (107). The management of BMs has been revolutionized by improved brain imaging and management of systemic diseases, distribution of stereotactic irradiation, and the development of less invasive surgical techniques that enable the removal of BMs even from eloquent brain areas with minimal morbidity (108). Although whole-brain radiation therapy (WBRT), stereotactic radiosurgery (SRS), and systemic therapies have improved the treatment outcomes, surgical resection is the major therapeutic strategy for large BMs. The indications for resection include a symptomatic mass, a mass with edema requiring high-dose steroids, a mass with a size more than 3 cm, and a mass with an unknown primary cancer (108). In addition, recent advances in immunotherapy have increased the therapeutic options for patients with metastatic melanoma. Ipilimumab (monoclonal antibody to CTLA-4) and nivolumab can stimulate T cell-mediated anti-tumor immune response. Previous studies have reported that ipilimumab treatment achieves CNS disease control in 24% of patients with melanoma exhibiting asymptomatic BM and 10% of patients with the symptomatic disease (109). Additionally, dual immune checkpoint blockade of ipilimumab and nivolumab has achieved higher intracranial responses (110). However, the efficacy of other ICIs for BMs has not been examined.

The understanding of the interaction of immune cells in the brain TME can aid in the development of effective immunotherapy strategies. Neutrophils, which are abundant in the circulation, are a potential therapeutic target for BMs as they have critical roles in immunity and inflammation. Therefore, many recent researches

focused on the analyses of brain immune TME landscape *via* flow cytometry, RNA sequencing, protein arrays, culture arrays, and spatial tissue characteristics in glioma and BMs (111, 112). Disease-specific immune cells enriched with pronounced differences in tissue-resident microglia, infiltrating monocyte-derived macrophages, neutrophils, and T cells between gliomas and BMs. Abundance of TAMs infiltrated in gliomas, whereas T cells were much fewer. However, lymphocytes and neutrophils accumulated obviously in BMs. This implies that tumors indeed shape their TME while growing within the brain. It is different from cancers that metastasize from extracranial sites. In addition, there were additional differences for BMs originated from distinct primary tumors. For example, abundance of CD4+ and CD8+ T cells represented the major immune compartment in melanoma BMs, whereas it showed the highest neutrophil infiltration in breast BMs. Therefore, defining the specific immunological signature of brain tumors can facilitate the rational design of targeted immunotherapy strategies.

## NLR AS A BIOMARKER

The local inflammatory process in the TME and systemic inflammation play important roles in cancer development and progression (113–115). The hallmarks of cancer-related inflammation include the presence of inflammatory cells and inflammatory mediators (for example, chemokines, cytokines and prostaglandins) in tumor tissues similar to that seen in chronic inflammatory responses (8). The upregulated levels of C-reactive protein, hypoalbuminemia, some cytokines, and leukocytes and their subtypes in the blood can be quantified to determine systemic inflammation (116, 117).

Inflammatory cytokines and chemokines, which can be produced by both tumor and stromal cells, contribute to the progression of malignancy (7). The increased NLR has been associated with increased peritumoral infiltration of macrophages and upregulation of several cytokines, such as IL-6, IL-7, IL-8, IL-9, IL-12, IL-17, and interferon- $\gamma$  (IFN $\gamma$ ) (118, 119). Neutrophils and macrophages are reported to secrete tumor growth-promoting factors, including vascular endothelial growth factor (120, 121), hepatocyte growth factor (122), IL-6 (123), IL-8 (124), MMPs (125), and elastases (126), which promote the development of pro-tumor TME. Nevertheless, IL-12 and IFN $\gamma$  are reported to enhance antitumor effect. IL-12 can be used as combinatorial immunotherapy and effective in preclinical glioblastoma model (127). On the other hand, cancer-related inflammation, like smoldering inflammation, in the TME has many pro-tumor effects. It exacerbates progression of malignant cells, promotes angiogenesis and metastasis, suppresses adaptive immune responses, and alters responses to hormones and chemotherapeutic agents (8). Therefore, the cons and pros of inflammation in cancer are still needed to be elucidated in the future.

Thus, biochemical markers of inflammation in patients with various cancers have been incorporated into prognostic scores (128). Neutrophilia, an inflammatory response, inhibits the



immune system by suppressing the cytolytic activity of immune cells, such as cytotoxic T cells and natural killer (NK) cells (129, 130). Several studies have reported the critical roles of tumor-infiltrating lymphocytes (TILs) in cancer. The upregulation of TILs has been associated with improved treatment response and prognosis (131–133). Therefore, an elevated NLR in peripheral blood was recognized as a poor prognostic indicator recently (134). The mechanisms underlying the correlation between high NLR and poor prognosis in patients with cancer have not been elucidated.

Recent studies have developed sensitive and accurate biomarkers for cancer. The changes in the blood NLR can be used to determine the optimal therapy for patients with advanced-stage cancer (135, 136). The prognostic value of NLR in early-stage cancer is lower than that in patients with advanced-stage cancer. However, NLR can aid in the evaluation of the early effects of systemic therapy (137–140). Some small-scale studies have reported that chemotherapy improved the clinical outcomes of patients with cancer through the alleviation of dysregulated NLR (135, 136).

Most patients with glioma exhibit neutrophilia (141) due to the increased production of G-CSF by tumor cells to promote growth (142, 143). G-CSF shifts bone marrow hematopoiesis toward the myeloid lineage and away from the lymphocyte lineage. This leads to a high NLR in patients with glioma. Several studies have demonstrated that the NLR of more than 4 is associated with poor prognosis when examined before treatment (144, 145), after the second surgery (146), and after TMZ and RT therapies (147). NLR of less than 4 is associated with improved prognosis in GBM with wild-type IDH1 (148). The baseline neutrophil count in the blood can also predict bevacizumab efficacy in patients with GBM (149). The upregulated surface expression of CD11b, a marker of neutrophil activation, can be used as an early predictor of tumor progression in patients with GBM (150). Arginase I produced by circulating neutrophils promotes tumor growth and induces immunosuppression (151).

The OS of patients with BMs is poor (152). Therefore, there is a need to develop multidisciplinary and individualized treatment approaches for BMs. Prognostic models with recursive partitioning analysis and graded prognostic assessment that incorporate multiple patient factors have been established to predict the treatment outcomes (153, 154). Although patients exhibit prolonged survival and undergo novel therapies, including targeted and immune therapy with SRS, novel factors must be incorporated into the predictive system to examine the survival benefits of novel therapies. Recently, NLR has been identified as one of the markers for predicting the outcomes of novel therapies (9, 155). The inflammatory cells are reported to cross into the brain (11). Hence, the association between NLR and OS in patients with BM was investigated. Several studies have investigated the optimal dichotomous cutoff values of NLR in various BMs. NLR values of more than 5, 3.3, and 6 are correlated with poor outcomes of post-resection, pre-SRS, post-SRS, respectively (156–158). There were no common optimal dichotomous cutoff values for NLR in all studies. The optimal NLR to predict OS in various malignancies

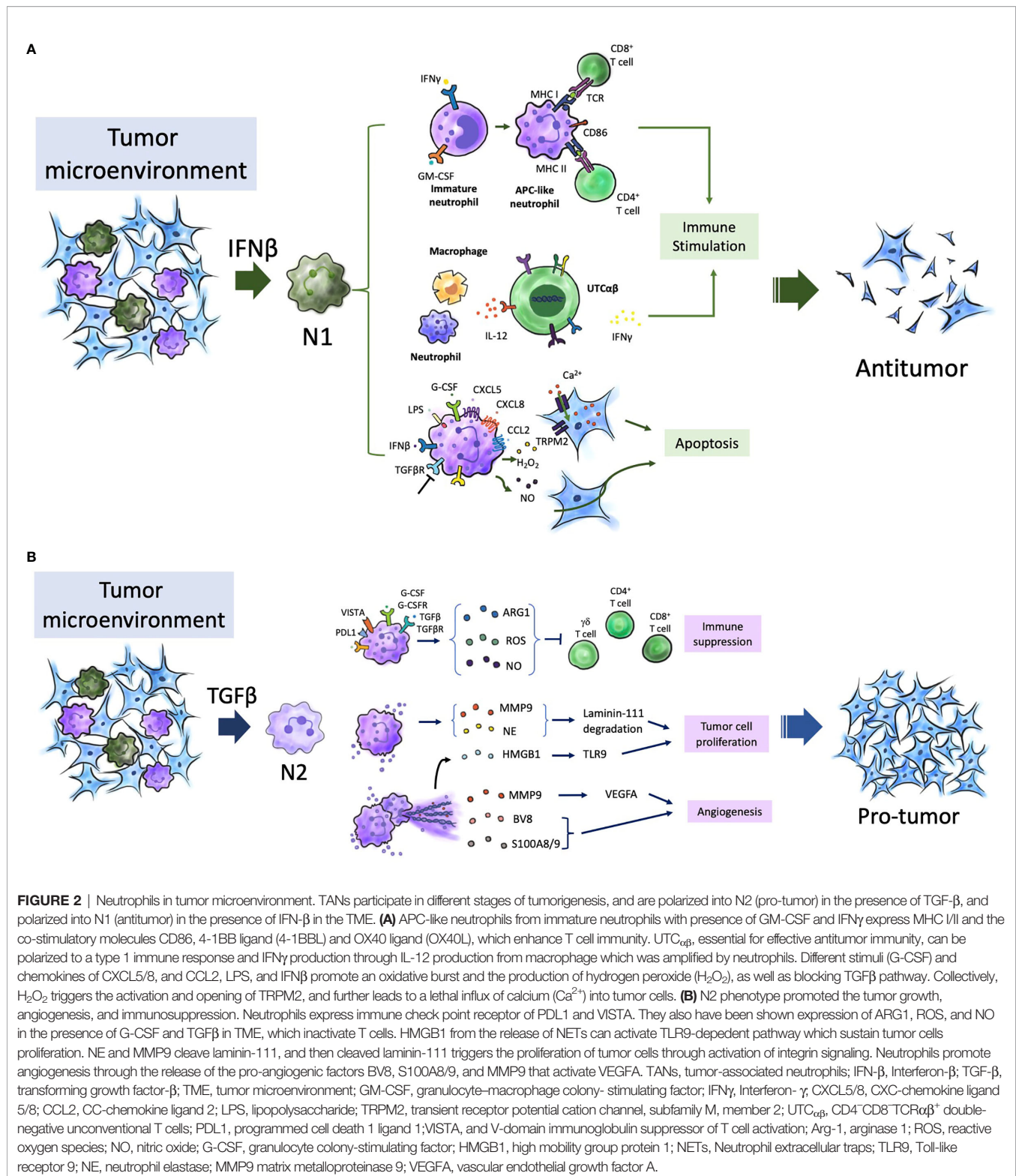
ranged from 2.18 to 7.5 (144, 147, 159–161). The increased NLR value is reported to be correlated with a high risk of local recurrence. Patients with elevated NLR are likely to exhibit neuronal death (157). Prospective validation must be performed to validate the simple and systemic marker NLR for determining if aggressive treatment is needed following initial treatment. Further studies are needed to examine the interaction between BMs and immunological environments.

Thus, NLR has been proposed as a surrogate marker for the prognosis of various cancers as lymphocyte and neutrophil counts can be easily determined based on the complete blood count. However, acute conditions, such as bacterial or viral infections or drug treatments may overlap chronic ongoing inflammation and affect the neutrophil and lymphocyte counts. Hypertension, diabetes mellitus, metabolic syndrome, left ventricular dysfunction and hypertrophy, acute coronary syndromes, cardiovascular diseases (162, 163), abnormal thyroid function tests, renal or hepatic dysfunction, previous history of infection (<3 months), inflammatory diseases (164), and some medications (e.g. steroids) can potentially affect the measurement of NLR. Therefore, NLR must be carefully validated.

## TAN HETEROGENEITY AND NETS

The complex roles of neutrophils in both tumor growth and metastasis have been reported. The role of neutrophils in cancer is dependent on various factors and may result in a pro-tumoral or an antitumoral effect (2). TANs in the TME and the functions of neutrophils, including circulating and bone marrow neutrophils and neutrophil lineage cells, determine their role in cancer. TANs are polarized to anti-tumor (N1) or pro-tumor (N2) phenotypes (**Figure 2**) (165). Since 2015, the functional plasticity of TANs and their ability to undergo alternative activation upon exposure to various cues in the TME have been demonstrated (166, 167). For example, the presence of transforming growth factor- $\beta$  (TGF $\beta$ ) promotes a pro-tumor phenotype (N2 TANs), whereas the presence of IFN $\beta$  or the inhibition of TGF $\beta$  signaling promotes the anti-tumor phenotype of TANs (N1 TANs) (165, 168). The binary N1/N2 phenotypes maybe an oversimple classification system to describe neutrophil polarization, as well as the M1/M2 phenotypes for TAMs (169–171). Neutrophil polarization may involve a spectrum of activation states. Multiple heterogeneous neutrophil subsets have been observed in the circulation of both tumor-bearing mouse models and patients with cancer. The following three distinct neutrophil populations have been identified in the circulation of both patients with cancer and mouse models: mature high-density neutrophils (HDNs), mature low-density neutrophils (LDNs), and immature LDNs (172–175). Mature HDNs exhibit an anti-tumor N1-like phenotype. However, mature LDNs, which are not cytotoxic, exhibited impaired functions and immunosuppressive properties (172–174).

The dual and opposite functions of neutrophils in tumor immunity may vary during the progression of cancer (173). Neutrophils can influence tumor development by modulating



the recruitment, profile and phenotype of other immune cells, especially TAMs and tumor-infiltrating lymphocytes (TIL) which are major components of the immune TME. Neutrophils are reported to exhibit growth-inhibitory activity

against early-stage cancers (176–178). Neutrophils are involved in networks of T cell-dependent antitumor immunity. In TME, with the contribution of IFN $\gamma$  and GM-CSF, immature neutrophils become mature and have the function of antigen-

presenting cells (APCs). Then, these APC-like neutrophils stimulate the proliferation of both CD4+ and CD8+ T cells through the major histocompatibility complex (MHC) class I and class II molecules and the co-stimulatory molecules CD86, 4-1BB ligand (4-1BBL) and OX40 ligand (OX40L) expression (177, 178). Furthermore, chemokine including CXCL10, CCL2, CCL3, CXCL1 and CXCL2 produced by TANs could recruit T cells as well as other leukocytes (74, 179, 180). Neutrophils are also able to kill tumor cells through direct contact and *via* ROS generation (165, 176, 181). The transient receptor potential cation channel, subfamily M, member 2 (TRPM2), a H<sub>2</sub>O<sub>2</sub>-dependent channel, can induce influx of calcium into tumor cells and further lead to cell death. In addition, TNF-related apoptosis inducing ligand (TRAIL) and TNF can induce the expression of the hepatocyte growth factor receptor (HGFR; also known as MET) on neutrophils (182). HGF present in the TME induce neutrophil recruitment and production of nitric oxide (NO), which results in killing of tumor cells (182). Neutrophils also engage in an interaction between macrophages and a subset of unconventional T cells (UTCs), known as CD4<sup>+</sup>CD8<sup>+</sup>TCR $\alpha\beta$ <sup>+</sup> double-negative UTCs (UTC $\alpha\beta$ ). The UTCs were essential for effective antitumor immunity (179). Neutrophils are able to enhance the production of IL-12 by macrophages, and then promote UTC $\alpha\beta$  polarize towards a type 1 immune response and IFN $\gamma$  production (179). However, the roles, mechanisms, significance of UTC $\alpha\beta$  in human tumors still need to be elucidated.

In contrast, the strong immunosuppressive activity of neutrophils is associated with polymorphonuclear myeloid-derived suppressor cells (MDSCs) in advanced-stage cancer. Polymorphonuclear MDSCs also share features with immature neutrophils. Recently, early neutrophil progenitor was reported to exhibit pro-tumor activity (173, 177, 183). The disease stage, the tumor type, and tissue context are all key determinants of neutrophils in promoting or restraining cancer. Neutrophils with intrinsic anti-tumor activity are recruited to the tumor, where they are reprogrammed to an immunosuppressive pro-tumor phenotype (from N1 to N2) (165, 173).

The ability of cancer-related neutrophils to release NETs has piqued the interest of the scientific community. NETs, which are released from neutrophils in response to extracellular pathogens, typically comprise fibrous decondensed chromatin with associated histones, MPO, and various cytoplasmic proteins, such as neutrophil elastase, cathepsin G, and lactoferrin. Although NETs are reported to be released in response to cancer cells, their role in cancer is not clear.

NETs, the release of ROS, and the trapping of cancer cells could theoretically promote a cytotoxic effect and inhibit the dissemination of cancer cells (184, 185). However, most studies have only described this phenomenon in circulating neutrophils (186–188). Some studies have also reported that NETs are spontaneously produced in samples from patients with cancer and that NETs promote metastatic dissemination after surgical stress (187). In mouse models, sustained lung inflammation caused by tobacco smoke exposure or nasal instillation of lipopolysaccharide leads to NETs formation (189). Neutrophil

elastase and matrix metalloproteinase 9 (NET-associated proteases) cleave the extracellular matrix protein laminin. The proteolytically remodeled laminin induced proliferation of dormant cancer cells by activating integrin  $\alpha 3 \beta 1$  signaling. Then, the dormant cancer cells are awakening to aggressively growing metastases. Therefore, NETs are hypothesized to act within the primary tumor to promote disease progression and dissemination. The enhanced release of NETs by the neutrophils has been suggested to promote tumor progression and metastatic dissemination. Thus, further studies are needed to clarify the pro-tumor and anti-tumor functions of NETs in glioma and BMs.

Macrophages are the major infiltrating immune cells (up to 30% tumor mass) in the brain TME (190). Thus, there was increased focus on macrophages in the brain TME in the past few years. However, one study reported that neutrophils infiltrate the human glioma and the degree of infiltration was markedly correlated with tumor grade (191). However, the mechanism of neutrophil recruitment and the role of neutrophils in tumor growth have not been elucidated. Most studies on neutrophils and brain tumors have focused on the impact of these cells on the response to anti-angiogenic therapy and vascularization (a hallmark of high-grade glioma). Enhanced neutrophil infiltration into tumor tissue is associated with acquired resistance to the vascular endothelial growth factor antibody (bevacizumab) and high glioma grade at advanced stages (191, 192). Preclinical studies have demonstrated that neutrophils contribute to glioblastoma progression by supporting the expansion of the glioma stem cell pool through S100 protein-dependent mechanism (192). S100 proteins are associated with secondary dissemination, especially the dissemination of breast cancer (193). S100A8 and S100A9, which are upregulated in the pre-metastatic brain, promote the recruitment of neutrophils and subsequently promote metastatic seeding (194). The brain may be aberrantly exposed to pathological inflammation associated with the tumor that influences disease progression. Therefore, future studies must focus on the mechanisms of neutrophil infiltration in the brain TME.

## NEUTROPHIL AS A THERAPEUTIC TARGET AND POTENTIAL COMBINATION OF NEUTROPHIL-TARGETING WITH OTHER CANCER THERAPIES

Traditionally, neutrophils were not considered to have a critical role in the TME. However, recent studies have demonstrated that (195–197) neutrophils play a major role in the pathogenesis of cancer, including tumor initiation, development, and progression. Furthermore, several studies have suggested that the presence and phenotype of neutrophils in the TME determine the outcomes of traditional and novel therapies, such as ICIs (198, 199). Most studies indicate that neutrophils promote tumorigenesis (167, 200). Therefore, neutrophils can be directly targeted to inhibit their recruitment, activation, or

phenotype reprogramming. Recently, the concept of targeting TANs has been proposed by several studies. The polarization of neutrophils (pro-tumor or anti-tumor) in cancers must be characterized to improve the efficacy of therapeutic modalities. Therefore, the development of next-generation immunotherapies is an important topic of research (201). Various approaches have been developed to therapeutically target neutrophils, including strategies to enhance, inhibit, or reprogram the neutrophil phenotype. Clinical trials on TGF $\beta$  pathway inhibitors and PDE5 inhibitors for glioma and BMs are ongoing. However, there are several challenges and controversies for using these strategies. For example, Galunisertib, a novel TGF $\beta$  receptor 1 kinase inhibitor, is currently undergoing clinical trials as a monotherapy or in combination with lomustine chemotherapy in two clinical trials involving patients with recurrent glioblastoma (NCT01582269 and NCT01682187) and those undergoing temozolomide-based chemoradiotherapy (NCT01220271). Here, we have listed some therapeutic mechanisms that potentially recruit, activate, inhibit, or modulate the phenotypes of neutrophils in the TME, which are currently being investigated in cancers of humans or animals (**Figure 3A**, **Table 1**).

## Combining Neutrophil-Targeting Therapy With Other Anticancer Therapies

Several chemotherapies are reported to cause neutropenia and consequently eliminate neutrophils from the TME. However, the effect of these chemotherapies on the neutrophil phenotype modulation and the subsequent implications in treatment efficacy are largely unknown. These patients are at an increased risk of opportunistic infections (211, 212). Furthermore, neutrophils are a key mediator of the efficacy, clinical value, and toxicity of these therapies in patients receiving ICIs (213).

However, limited studies have focused on the effects of drugs on cancer-related neutrophil phenotypes. A critical assessment of the most optimal combination therapy strategies is key for the successful clinical implementation of neutrophil-targeting approaches. Various mechanistic studies performed in clinically relevant mouse tumor models have addressed the impact of neutrophils on the efficacy of anticancer therapies.

## Chemotherapy

Neutropenia is a common “adverse effect” of chemotherapy (214). In the clinics, recombinant G-CSF and GM-CSF are commonly prescribed to increase neutrophil counts and reduce the risk of infection as they promote the release of neutrophils from the bone marrow (22, 215). However, the effects of G-CSF or GM-CSF on human neutrophil phenotypes are unclear. Contradictory findings have been reported for the pro-tumor and anti-tumor activities of the recruited neutrophils.

*In vitro* studies on neutrophils isolated from the peripheral blood of patients who received G-CSF have revealed contradictory findings on neutrophil function, including phagocytosis, oxidative burst, bacterial killing, and chemotaxis (216). Filgrastim (non-glycosylated G-CSF) and lenograstim (glycosylated G-CSF) exhibited differential effects on the chemotaxis and morphology of circulating neutrophils isolated from patients with non-Hodgkin lymphoma (217). Neutrophils from patients who received lenograstim exhibited impaired chemotaxis. In contrast, neutrophils isolated from patients who received filgrastim had a morphology that suggested enhanced activation and upregulated expression of integrin  $\beta$ 2. G-CSF and GM-CSF, which are reported to exert pro-tumor and anti-tumor effects, can affect both tumor and immune cells (218–222). Previous studies have reported that G-CSF induces the

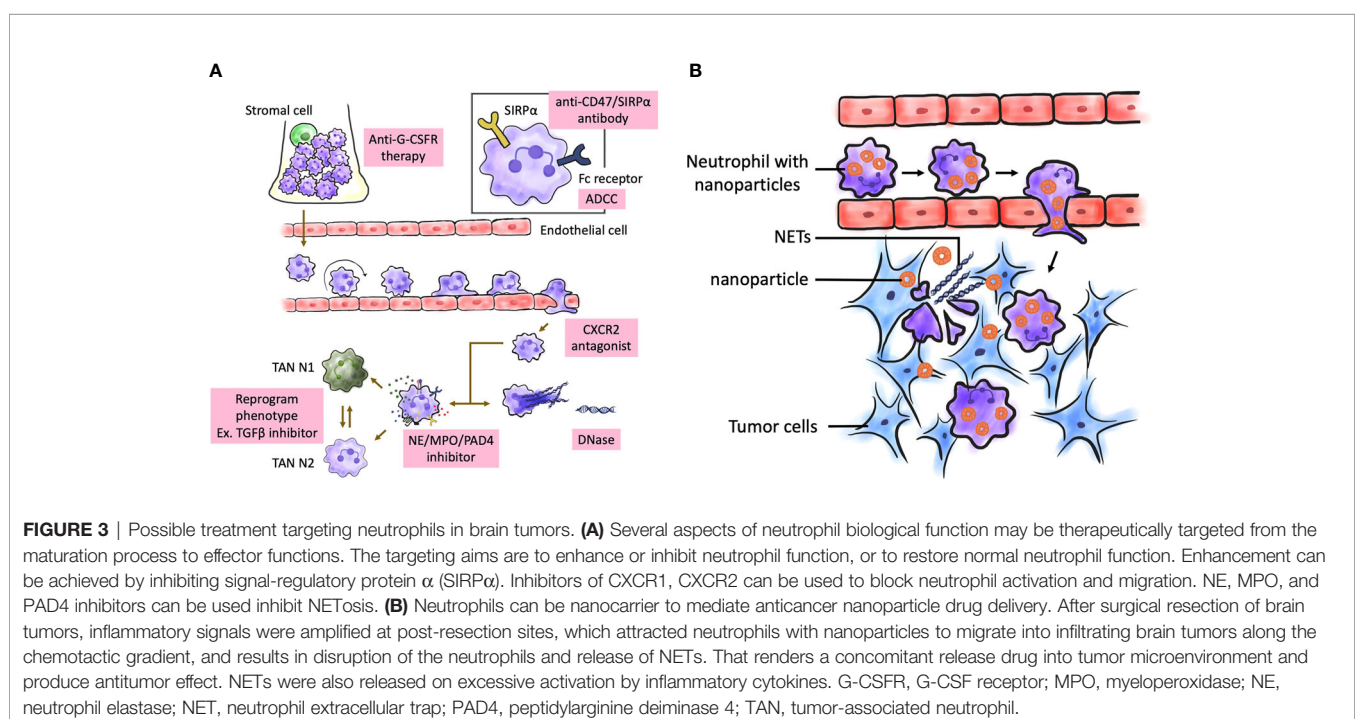




**TABLE 1 |** Agents with putative effects on neutrophils in patients with cancer.

Target	Effects on neutrophils	Agent	Study object
<b>TGFβ pathway inhibitor</b>	Promote the development of neutrophils with an antitumor phenotype (165)	Galunisertib (a TGFβR1 kinase inhibitor)	Humans (NCT02734160, NCT01582269, NCT01682187, NCT02452008)
		Fresolimumab (an anti- TGFβ monoclonal antibody)	Humans (NCT02581787)
<b>CD47-SIRPα inhibitor</b>	Delay the transmigration of neutrophils to tumor tissues, thus inducing macrophage-mediated phagocytosis of tumor cells (202, 203)	Hu5F9-G4 IBI188 CC-90002	Humans (NCT02216409) Humans (NCT03717103) Humans (NCT02367196)
<b>TRAIL-R agonist</b>	Triggers neutrophil apoptosis and clearance from tissues by targeting TRAIL-Rs expressed on neutrophils (204, 205)	Mapatumumab AMG 951 TRM-1	Humans (NCT01088347) Humans (NCT00508625) Humans (NCT00092924)
<b>ACKR2</b>	a novel immune checkpoint that regulates neutrophil differentiation, mobilization to tumor tissues and anti- metastatic activity in animal study (206)	–	–
<b>Chemokine signaling</b>			
CXCR1/ CXCR2	Inhibit neutrophil recruitment to the tumor; attenuate granulocytosis, neutrophil recruitment and vascular permeability by inhibiting the CXCR2 chemotactic axis (207, 208)	SX-682 Raparixin	Humans (NCT03161431) Humans (NCT02370238, NCT02001974)
CCR5	Inhibit both the release of immature neutrophils from bone marrow and their recruitment to the tumor (209, 210)	Maraviroc	Humans (NCT03274804, NCT01736813)

phagocytic and antibacterial activities of neutrophils (223) and promotes ROS production upon stimulation (224). However, the phenotypic modulation of TANs after treatment with G-CSF and GM-CSF is currently under investigation.

## Radiotherapy

Radiotherapy is one of the most important treatment modalities for cancer. Several studies on animal models have demonstrated that radiotherapy activates both the adaptive and innate immune responses through the release of antigens, Toll-like receptor ligands, and pro-inflammatory cytokines from tumor cells. This promotes the recruitment of myeloid cells, such as macrophages, dendritic cells, and neutrophils, and induces T cell-mediated immunogenic cell death (225–227). In preclinical models, radiotherapy induces sterile inflammation with rapid and transient infiltration of neutrophils into the tumors (228). These newly recruited neutrophils produce increased amounts of ROS and induce apoptosis in the tumor cells. Recent studies have suggested that the baseline blood neutrophil count is correlated with the survival of patients with different cancers after radiotherapy (229–232). However, limited studies have examined the effects of radiation on neutrophil phenotypes in patients with cancer. Clinical studies have demonstrated that radiotherapy can initiate a response outside the local radiation field (which is known as the “abscopal effect”) and this is correlated with enhanced recruitment of immune cells (233–236). Based on these observations, the combination of radiotherapy and immunotherapy or GM-CSF may improve the clinical outcomes of patients with cancer (237–239). The effects of radiotherapy on human neutrophils are unknown (229).

## ICIs

ICIs, such as anti-CTLA-4 and anti-PD-1 antibodies, exhibited satisfactory therapeutic efficacy in several patients with

advanced-stage cancers, especially in patients with melanoma. Although not all patients benefit from these agents, ICIs are frequently used as first-line therapies in patients with other cancers (240, 241) exhibiting upregulated expression of PD-1, PD-L1, and/or CTLA-4. Several studies have reported the effects of ICIs on the TME in mouse models (242) and patients with cancer (243–245). However, the effects of ICIs on intratumoral neutrophils remain unclear.

In a study published in 2017, changes in intratumoral immune cell subpopulations were investigated in patients with melanoma after treatment with the anti-PD-1 antibody nivolumab (243). The number of intratumoral neutrophils was not markedly different between patients who benefited from nivolumab and those who did not benefit from nivolumab although the intratumoral neutrophil counts varied between the two groups. Several studies have suggested a correlation between PD-L1 expression on neutrophils and an immunosuppressive phenotype. For example, PD-L1+ neutrophils are reported to suppress T cell function and promote disease progression in patients with gastric cancer (199). This suppressive effect may be reversed upon inhibition of PD-L1. The expression levels of PD-L1 in the intratumoral and peritumoral neutrophils were upregulated when compared with those in circulating neutrophils in patients with hepatocellular carcinoma (198). This suggested that TANs exert strong immunosuppressive effects in these patients and that PD-L1+ neutrophils are potential targets of anti-PD-1 and/or anti-PD-L1 antibodies.

## Targeting NETs

NETs, which are involved in antimicrobial immunity, autoimmune conditions, cardiovascular diseases, and tumor progression (66, 198, 246), are a potential therapeutic target for cancer. In several cases, NET formation is dependent on the

activity of NADPH oxidase. Thus, the inhibition of NADPH oxidase can alter NETosis (175). Superoxide can be transformed into hydrogen peroxide, which can activate azurophilic (primary) granule proteins, such as neutrophil elastase or MPO (175) and consequently promote the nuclear translocation of some molecules. In the nucleus, neutrophil elastase promotes nuclear decondensation. MPO upregulates the activity of neutrophil elastase. Hence, neutrophil elastase and MPO can serve as therapeutic targets for NET-associated disorders (247, 248). Neutrophil elastase inhibitors are effective in patients with bronchiectasis. Currently, studies on the therapeutic potential of neutrophil elastase inhibitors for bronchiolitis obliterans are ongoing (249). As PAD4 is critical for NET formation, it is a potential therapeutic target for NET-mediated diseases (250–252). The effect of PAD inhibitors on human patients has not been examined. Previous studies have targeted DNase I to alleviate NET-mediated pathology (253–256). Therefore, DNase I-mediated degradation of NETs can be a potential therapeutic strategy for cancers with NET involvement.

## NEUTROPHIL AS A NANOCARRIER

Surgical resection is the major therapeutic strategy for brain tumors (257). However, the infiltrating tumor cells near the eloquent brain area should not be completely removed to preserve neurological functions (258). Generally, adjuvant chemotherapy is necessary after surgery. However, the efficacy of adjuvant therapy is limited owing to poor drug penetration caused due to various physiological barriers, especially the blood-brain barrier (BBB) and blood-tumor barrier (BTB) (259–261), which contribute to tumor recurrence. Therefore, nanoparticle-based drug delivery systems (NDDSs) are used for enhanced targeting of the tumor (262–265). NDDSs utilize active targeting ligands or passive leakage of tumor vasculature (266–269). However, the efficacy of these NDDSs for postoperative glioma treatment is poor due to a low half-life of the nanoparticles in the circulation, insufficient intratumoral drug accumulation, and severe systemic toxicity.

Recently, cell-based drug delivery systems are considered powerful bioinspired drug delivery platforms for glioma (269–274). Vectorization of therapeutic agents using endogenous cells has been proposed as a potential strategy for targeted drug delivery to the brain (275–277). Neutrophils, which play a critical role in immune responses, can be activated within the vasculature. The activated neutrophils move along chemotactic gradients toward the inflammatory sites and eliminate the pathogens by phagocytosis (278–280). Additionally, neutrophils can cross the BBB/BTB and infiltrate the tumor mass (191, 281–283). TANs, which are distributed in the glioma region (284), promote the continuous recruitment of the circulating neutrophils (201). Surgical tumor excision leads to local brain inflammation with the release of inflammatory factors, such as IL-8 (285, 286) and TNF- $\alpha$  (287, 288) that activate the migration of neutrophils to the inflamed region of the brain (278). The amplification of inflammatory signals supports enhanced targeting of brain tumors.

Therefore, neutrophils could be explored as “Trojan horses” to carry concealed drug cargoes to diseased brain areas (**Figure 3B**). Zhang et al. demonstrated that the physiological activity of neutrophils carrying PTX liposomes was not affected and that these neutrophils migrate to the inflamed brain tumor. These neutrophils improved the survival of postsurgical glioma-bearing mice (289). Traditional nanoparticles passively target the tumor site [which is known as the enhanced permeability and retention effect (290)] or actively target the tumor site through ligand-receptor interactions (291). In contrast, the neutrophil-mediated drug delivery system can recognize postoperative inflammatory signals, such as IL-8 and CXCL1/KC (74, 292) and spontaneously deliver chemotherapeutics to infiltrating glioma cells. The aberrant activation of neutrophils by the upregulated inflammatory cytokines in the inflamed brain results in the disruption of neutrophils and promotes the release of NETs (293) with concomitant release of liposomes to deliver PTX into the remaining infiltrating tumor cells. We believe this strategy will offer new opportunities to explore endogenous immunocytes as drug delivery vehicles. In the future, neutrophils harvested from humans can be used to deliver drugs in clinics.

Several challenges associated with nanoparticle delivery systems must be addressed before translation into a human clinical model. The extraction of neutrophils from patients before intracranial implantation may pose an additional risk and delay surgery. The bioactivity of PTXCL within neutrophils *in vivo* remains unclear. The PTX resistance of glioma cells (as evidenced by the poor efficacy of PTX-CL/NE treatment) suggests that combination treatment must be considered to attain optimal therapeutic efficacy. However, neutrophil-mediated DDSs targeting the glioma-initiating stem cells in the perivascular niche can have potent therapeutic benefits (294, 295).

## CONCLUSION AND PERSPECTIVE

The role of neutrophils in cancer biology and their potential as therapeutic targets have been widely recognized. Recent studies have demonstrated the important biological roles of neutrophils. The complex roles of neutrophils in cancer include their ability to exert pro-tumor or anti-tumor activities and to exhibit various polarization phenotypes. The elucidation of the interaction of neutrophils in cancer can aid in the development of novel therapeutic interventions. For example, targeting TANs and/or circulating neutrophils can be potential next-generation immunotherapies. However, further studies are needed to examine the exact roles, recruitment pathways, subpopulations, and mechanisms of action of TANs to develop targeted therapeutic approaches. Additionally, the role of TANs in the brain TME is not clear although the extent of neutrophil infiltration is correlated with glioma grades. Thus, TANs in the brain TME are a potential therapeutic target for brain cancer. Additionally, TANs can improve the efficacy of chemotherapy or immunotherapy.

There are contradictory reports on several characteristics of neutrophils, including lifespan, transcriptional activity, roles in cancer, and subpopulation types. Additionally, neutrophils may escape therapeutic interventions because of their exceptional turnover and unexpected plasticity, especially in cancer. However, recent understanding of neutrophil biology has revealed that precise therapeutic interventions may provide therapeutic benefits without detrimental side effects. In particular, NETs are a key therapeutic target (296). Future studies must focus on small-molecule and biological therapeutics that can regulate the neutrophil compartment to promote the activation, inhibition, or depletion of neutrophils. Additionally, antibody-mediated delivery of small molecules can be a potential therapeutic strategy. Recent studies have suggested the potential applications of neutrophils as drug-trafficking cells (289, 297). Neutrophil-derived molecules, such as granule proteins and peptides may also be used as therapeutic agents under certain conditions. In summary, these findings indicate the potential of targeting neutrophils in human diseases.

## REFERENCES

- Ehrlich P. Methodologische Beiträge Zur Physiologie Und Pathologie Der Verschiedenen Formen Der Leukocyten. *Klin Med* (1880) 1:553–8.
- Coffelt SB, Wellenstein MD, de Visser KE. Neutrophils in Cancer: Neutral No More. *Nat Rev Cancer* (2016) 16:431–46. doi: 10.1038/nrc.2016.52
- Németh T, Sperandio M, Mócsai A. Neutrophils as Emerging Therapeutic Targets. *Nat Rev Drug Discovery* (2020) 19:253–75. doi: 10.1038/s41573-019-0054-z
- Leliefeld PH, Koenderman L, Pillay J. How Neutrophils Shape Adaptive Immune Responses. *Front Immunol* (2015) 6:471. doi: 10.3389/fimmu.2015.00471
- Rosales C, Lowell CA, Schnoor M, Uribe-Querol E. Neutrophils: Their Role in Innate and Adaptive Immunity 2017. *J Immunol Res* (2017) 2017:9748345. doi: 10.1155/2017/9748345
- Chiang CC, Cheng WJ, Korinek M, Lin CY, Hwang TL. Neutrophils in Psoriasis. *Front Immunol* (2019) 10:2376. doi: 10.3389/fimmu.2019.02376
- Balkwill F, Mantovani A. Inflammation and Cancer: Back to Virchow? *Lancet* (2001) 357:539–45. doi: 10.1016/S0140-6736(00)04046-0
- Mantovani A, Allavena P, Sica A, Balkwill F. Cancer-Related Inflammation. *Nature* (2008) 454:436–44. doi: 10.1038/nature07205
- Hanahan D, Weinberg RA. Hallmarks of Cancer: The Next Generation. *Cell* (2011) 144:646–74. doi: 10.1016/j.cell.2011.02.013
- Lim M, Xia Y, Bettgeowda C, Weller M. Current State of Immunotherapy for Glioblastoma. *Nat Rev Clin Oncol* (2018) 15:422–42. doi: 10.1038/s41571-018-0003-5
- Louveau A, Smirnov I, Keyes TJ, Eccles JD, Rouhani SJ, Peske JD, et al. Structural and Functional Features of Central Nervous System Lymphatic Vessels. *Nature* (2015) 523:337–41. doi: 10.1038/nature14432
- Burnet M. Cancer: A Biological Approach: III. Viruses Associated With Neoplastic Conditions: IV. Practical Applications. *Br Med J* (1957) 1:841–7. doi: 10.1136/bmj.1.5023.841
- Burnet FM. The Concept of Immunological Surveillance. *Prog Exp Tumor Res* (1970) 13:1–27. doi: 10.1159/000386035
- Thomas L. Cellular and Humoral Aspects of the Hypersensitive States. *Acta Med Scand* (1961) 170:128–8. doi: 10.1111/j.0954-6820.1961.tb00220.x
- Dunn GP, Old LJ, Schreiber RD. The Immunobiology of Cancer Immunosurveillance and Immunoeediting. *Immunity* (2004) 21:137–48. doi: 10.1016/j.immuni.2004.07.017
- Ribas A, Wolchok JD. Cancer Immunotherapy Using Checkpoint Blockade. *Science* (2018) 359:1350–5. doi: 10.1126/science.aar4060
- Medikonda R, Dunn G, Rahman M, Fecci P, Lim M. A Review of Glioblastoma Immunotherapy. *J Neurooncol* (2021) 151:41–53. doi: 10.1007/s11060-020-03448-1
- Ng LG, Ostuni R, Hidalgo A. Heterogeneity of Neutrophils. *Nat Rev Immunol* (2019) 19:255–65. doi: 10.1038/s41577-019-0141-8
- Shaul ME, Fridlender ZG. Tumour-Associated Neutrophils in Patients With Cancer. *Nat Rev Clin Oncol* (2019) 16:601–20. doi: 10.1038/s41571-019-0222-4
- Dancey JT, Deubelbeiss KA, Harker LA, Finch CA. Neutrophil Kinetics in Man. *J Clin Invest* (1976) 58:705–15. doi: 10.1172/JCI108517
- Borregaard N. Neutrophils, From Marrow to Microbes. *Immunity* (2010) 33:657–70. doi: 10.1016/j.immuni.2010.11.011
- Manz MG, Boettcher S. Emergency Granulopoiesis. *Nat Rev Immunol* (2014) 14:302–14. doi: 10.1038/nri3660
- Görgens A, Radtke S, Möllmann M, Cross M, Dürig J, Horn PA, et al. Revision of the Human Hematopoietic Tree: Granulocyte Subtypes Derive From Distinct Hematopoietic Lineages. *Cell Rep* (2013) 3:1539–52. doi: 10.1016/j.celrep.2013.04.025
- Friedman AD. Transcriptional Control of Granulocyte and Monocyte Development. *Oncogene* (2007) 26:6816–28. doi: 10.1038/sj.onc.1210764
- Fiedler K, Brunner C. The Role of Transcription Factors in the Guidance of Granulopoiesis. *Am J Blood Res* (2012) 2:57–65.
- Rosenbauer F, Tenen DG. Transcription Factors in Myeloid Development: Balancing Differentiation With Transformation. *Nat Rev Immunol* (2007) 7:105–17. doi: 10.1038/nri2024
- Pillay J, Tak T, Kamp VM, Koenderman L. Immune Suppression by Neutrophils and Granulocytic Myeloid-Derived Suppressor Cells: Similarities and Differences. *Cell Mol Life Sci* (2013) 70:3813–27. doi: 10.1007/s00018-013-1286-4
- Häger M, Cowland JB, Borregaard N. Neutrophil Granules in Health and Disease. *J Intern Med* (2010) 268:25–34. doi: 10.1111/j.1365-2796.2010.02237.x
- Borregaard N, Sørensen OE, Theilgaard-Mönch K. Neutrophil Granules: A Library of Innate Immunity Proteins. *Trends Immunol* (2007) 28:340–5. doi: 10.1016/j.it.2007.06.002
- Lieschke GJ, Grail D, Hodgson G, Metcalf D, Stanley E, Cheers C, et al. Mice Lacking Granulocyte Colony-Stimulating Factor Have Chronic Neutropenia, Granulocyte and Macrophage Progenitor Cell Deficiency, and Impaired Neutrophil Mobilization. *Blood* (1994) 84:1737–46. doi: 10.1182/blood.V84.6.1737.1737
- Liu F, Wu HY, Wesselschmidt R, Kornaga T, Link DC. Impaired Production and Increased Apoptosis of Neutrophils in Granulocyte Colony-Stimulating Factor Receptor-Deficient Mice. *Immunity* (1996) 5:491–501. doi: 10.1016/S1074-7613(00)80504-X
- Richards MK, Liu F, Iwasaki H, Akashi K, Link DC. Pivotal Role of Granulocyte Colony-Stimulating Factor in the Development of

## AUTHOR CONTRIBUTIONS

Y-JL, ML, and T-LH wrote and revised the manuscript. K-CW and P-YC consulted and revised the manuscript. Y-JL drew the figures. ML and T-LH initiated the concept and supervised the writing. All authors contributed to the article and approved the submitted version.

## FUNDING

This study is sponsored by Chang Gung Memorial Hospital (grants CMRPG3H1141). The sponsor had no role in the design or conduct of this research.

## ACKNOWLEDGMENTS

The authors thank Li-Ting Huang for drawing the figures.

- Progenitors in the Common Myeloid Pathway. *Blood* (2003) 102:3562–8. doi: 10.1182/blood-2003-02-0593
33. McKinstry WJ, Li CL, Rasko JE, Nicola NA, Johnson GR, Metcalf D. Cytokine Receptor Expression on Hematopoietic Stem and Progenitor Cells. *Blood* (1997) 89:65–71. doi: 10.1182/blood.V89.1.65.65\_71
  34. Adolfsson J, Månsson R, Buza-Vidas N, Hultquist A, Liuba K, Jensen CT, et al. Identification of Flt3+ Lymphomyeloid Stem Cells Lacking Erythro-Megakaryocytic Potential a Revised Road Map for Adult Blood Lineage Commitment. *Cell* (2005) 121:295–306. doi: 10.1016/j.cell.2005.02.013
  35. Panopoulos AD, Zhang L, Snow JW, Jones DM, Smith AM, El Kasmī KC, et al. STAT3 Governs Distinct Pathways in Emergency Granulopoiesis and Mature Neutrophils. *Blood* (2006) 108:3682–90. doi: 10.1182/blood-2006-02-003012
  36. Molinoux G, Migdalska A, Szmitskowski M, Zsebo K, Dexter TM. The Effects on Hematopoiesis of Recombinant Stem Cell Factor (Ligand for C-Kit) Administered *In Vivo* to Mice Either Alone or in Combination With Granulocyte Colony-Stimulating Factor. *Blood* (1991) 78:961–6. doi: 10.1182/blood.V78.4.961.bloodjournal784961
  37. Liu F, Poursine-Laurent J, Wu HY, Link DC. Interleukin-6 and the Granulocyte Colony-Stimulating Factor Receptor Are Major Independent Regulators of Granulopoiesis *In Vivo* But Are Not Required for Lineage Commitment or Terminal Differentiation. *Blood* (1997) 90:2583–90. doi: 10.1182/blood.V90.7.2583.2583\_2590
  38. Seymour JF, Lieschke GJ, Grail D, Quilici C, Hodgson G, Dunn AR. Mice Lacking Both Granulocyte Colony-Stimulating Factor (CSF) and Granulocyte-Macrophage CSF Have Impaired Reproductive Capacity, Perturbed Neonatal Granulopoiesis, Lung Disease, Amyloidosis, and Reduced Long-Term Survival. *Blood* (1997) 90:3037–49. doi: 10.1182/blood.V90.8.3037
  39. Casbon AJ, Reynaud D, Park C, Khuc E, Gan DD, Schepers K, et al. Invasive Breast Cancer Reprograms Early Myeloid Differentiation in the Bone Marrow to Generate Immunosuppressive Neutrophils. *Proc Natl Acad Sci USA* (2015) 112:E566–75. doi: 10.1073/pnas.1424927112
  40. Coffelt SB, Kersten K, Doornebal CW, Weiden J, Vrijland K, Hau CS, et al. IL-17-Producing Gammadelta T Cells and Neutrophils Conspire to Promote Breast Cancer Metastasis. *Nature* (2015) 522:345–8. doi: 10.1038/nature14282
  41. Waight JD, Hu Q, Miller A, Liu S, Abrams SI. Tumor-Derived G-CSF Facilitates Neoplastic Growth Through a Granulocytic Myeloid-Derived Suppressor Cell-Dependent Mechanism. *PLoS One* (2011) 6:e27690. doi: 10.1371/journal.pone.0027690
  42. Kowanetz M, Wu X, Lee J, Tan M, Hagenbeek T, Qu X, et al. Granulocyte-Colony Stimulating Factor Promotes Lung Metastasis Through Mobilization of Ly6G+Ly6C+ Granulocytes. *Proc Natl Acad Sci USA* (2010) 107:21248–55. doi: 10.1073/pnas.1015855107
  43. Bayne LJ, Beatty GL, Jhala N, Clark CE, Rhim AD, Stanger BZ, et al. Tumor-Derived Granulocyte-Macrophage Colony-Stimulating Factor Regulates Myeloid Inflammation and T Cell Immunity in Pancreatic Cancer. *Cancer Cell* (2012) 21:822–35. doi: 10.1016/j.ccr.2012.04.025
  44. Pylayeva-Gupta Y, Lee KE, Hajdu CH, Miller G, Bar-Sagi D. Oncogenic Kras-Induced GM-CSF Production Promotes the Development of Pancreatic Neoplasia. *Cancer Cell* (2012) 21:836–47. doi: 10.1016/j.ccr.2012.04.024
  45. Kuonen F, Laurent J, Secondini C, Lorusso G, Stehle JC, Rausch T, et al. Inhibition of the Kit Ligand/C-Kit Axis Attenuates Metastasis in a Mouse Model Mimicking Local Breast Cancer Relapse After Radiotherapy. *Clin Cancer Res* (2012) 18:4365–74. doi: 10.1158/1078-0432.CCR-11-3028
  46. Semerád CL, Liu F, Gregory AD, Stumpf K, Link DC. G-CSF Is an Essential Regulator of Neutrophil Trafficking From the Bone Marrow to the Blood. *Immunity* (2002) 17:413–23. doi: 10.1016/S1074-7613(02)00424-7
  47. Ma Q, Jones D, Springer TA. The Chemokine Receptor CXCR4 Is Required for the Retention of B Lineage and Granulocytic Precursors Within the Bone Marrow Microenvironment. *Immunity* (1999) 10:463–71. doi: 10.1016/S1074-7613(00)80046-1
  48. Martin C, Burdon PC, Bridger G, Gutierrez-Ramos JC, Williams TJ, Rankin SM. Chemokines Acting *via* CXCR2 and CXCR4 Control the Release of Neutrophils From the Bone Marrow and Their Return Following Senescence. *Immunity* (2003) 19:583–93. doi: 10.1016/S1074-7613(03)00263-2
  49. Suratt BT, Petty JM, Young SK, Malcolm KC, Lieber JG, Nick JA, et al. Role of the CXCR4/SDF-1 Chemokine Axis in Circulating Neutrophil Homeostasis. *Blood* (2004) 104:565–71. doi: 10.1182/blood-2003-10-3638
  50. Eash KJ, Means JM, White DW, Link DC. CXCR4 Is a Key Regulator of Neutrophil Release From the Bone Marrow Under Basal and Stress Granulopoiesis Conditions. *Blood* (2009) 113:4711–9. doi: 10.1182/blood-2008-09-177287
  51. Eash KJ, Greenbaum AM, Gopalan PK, Link DC. CXCR2 and CXCR4 Antagonistically Regulate Neutrophil Trafficking From Murine Bone Marrow. *J Clin Invest* (2010) 120:2423–31. doi: 10.1172/JCI41649
  52. Köhler A, De Filippo K, Hasenberg M, van den Brandt C, Nye E, Hosking MP, et al. G-CSF-Mediated Thrombopoietin Release Triggers Neutrophil Motility and Mobilization From Bone Marrow *via* Induction of Cxcr2 Ligands. *Blood* (2011) 117:4349–57. doi: 10.1182/blood-2010-09-308387
  53. Levesque JP, Liu F, Simmons PJ, Betsuyaku T, Senior RM, Pham C, et al. Characterization of Hematopoietic Progenitor Mobilization in Protease-Deficient Mice. *Blood* (2004) 104:65–72. doi: 10.1182/blood-2003-05-1589
  54. Burdon PC, Martin C, Rankin SM. The CXC Chemokine MIP-2 Stimulates Neutrophil Mobilization From the Rat Bone Marrow in a CD49d-Dependent Manner. *Blood* (2005) 105:2543–8. doi: 10.1182/blood-2004-08-3193
  55. Petty JM, Lenox CC, Weiss DJ, Poynter ME, Suratt BT. Crosstalk Between CXCR4/stromal Derived Factor-1 and VLA-4/VCAM-1 Pathways Regulates Neutrophil Retention in the Bone Marrow. *J Immunol* (2009) 182:604–12. doi: 10.4049/jimmunol.182.1.604
  56. Wengner AM, Pitchford SC, Furze RC, Rankin SM. The Coordinated Action of G-CSF and ELR + CXC Chemokines in Neutrophil Mobilization During Acute Inflammation. *Blood* (2008) 111:42–9. doi: 10.1182/blood-2007-07-099648
  57. Acharyya S, Oskarsson T, Vanharanta S, Malladi S, Kim J, Morris PG, et al. A CXCL1 Paracrine Network Links Cancer Chemoresistance and Metastasis. *Cell* (2012) 150:165–78. doi: 10.1016/j.cell.2012.04.042
  58. Mócsai A, Walzog B, Lowell CA. Intracellular Signalling During Neutrophil Recruitment. *Cardiovasc Res* (2015) 107:373–85. doi: 10.1093/cvr/cvv159
  59. Futosi K, Fodor S, Mócsai A. Neutrophil Cell Surface Receptors and Their Intracellular Signal Transduction Pathways. *Int Immunopharmacol* (2013) 17:638–50. doi: 10.1016/j.intimp.2013.06.034
  60. Winterbourn CC, Kettle AJ. Redox Reactions and Microbial Killing in the Neutrophil Phagosome. *Antioxid Redox Signal* (2013) 18:642–60. doi: 10.1089/ars.2012.4827
  61. Stapels DA, Geisbrecht BV, Rooijakkers SH. Neutrophil Serine Proteases in Antibacterial Defense. *Curr Opin Microbiol* (2015) 23:42–8. doi: 10.1016/j.mib.2014.11.002
  62. Cowland JB, Borregaard N. Granulopoiesis and Granules of Human Neutrophils. *Immunol Rev* (2016) 273:11–28. doi: 10.1111/imr.12440
  63. Németh T, Mócsai A. Feedback Amplification of Neutrophil Function. *Trends Immunol* (2016) 37:412–24. doi: 10.1016/j.it.2016.04.002
  64. Reeves EP, Lu H, Jacobs HL, Messina CG, Bolsover S, Gabella G, et al. Killing Activity of Neutrophils Is Mediated Through Activation of Proteases by K+ Flux. *Nature* (2002) 416:291–7. doi: 10.1038/416291a
  65. Brinkmann V, Reichard U, Goosmann C, Fauler B, Uhlemann Y, Weiss DS, et al. Neutrophil Extracellular Traps Kill Bacteria. *Science* (2004) 303:1532–5. doi: 10.1126/science.1092385
  66. Daniel C, Leppkes M, Muñoz LE, Schley G, Schett G, Herrmann M. Extracellular DNA Traps in Inflammation, Injury and Healing. *Nat Rev Nephrol* (2019) 15:559–75. doi: 10.1038/s41581-019-0163-2
  67. Porto BN, Stein RT. Neutrophil Extracellular Traps in Pulmonary Diseases: Too Much of a Good Thing? *Front Immunol* (2016) 7:311. doi: 10.3389/fimmu.2016.00311
  68. Sollberger G, Choidas A, Burn GL, Habenberger P, Di Lucrezia R, Kordes S, et al. Gasdermin D Plays a Vital Role in the Generation of Neutrophil Extracellular Traps. *Sci Immunol* (2018) 3:ear6689. doi: 10.1126/sciimmunol.ear6689
  69. Chen KW, Monteleone M, Boucher D, Sollberger G, Ramnath D, Condon ND, et al. Noncanonical Inflammasome Signaling Elicits Gasdermin D-



- Dependent Neutrophil Extracellular Traps. *Sci Immunol* (2018) 3:ear6676. doi: 10.1126/sciimmunol.aar6676
70. Jiménez-Alcázar M, Rangaswamy C, Panda R, Bitterling J, Simsek YJ, Long AT, et al. Host DNases Prevent Vascular Occlusion by Neutrophil Extracellular Traps. *Science* (2017) 358:1202–6. doi: 10.1126/science.aam8897
  71. Kovács M, Németh T, Jakus Z, Sitaru C, Simon E, Futosi K, et al. The Src Family Kinases Hck, Fgr, and Lyn Are Critical for the Generation of the *In Vivo* Inflammatory Environment Without a Direct Role in Leukocyte Recruitment. *J Exp Med* (2014) 211:1993–2011. doi: 10.1084/jem.20132496
  72. Tecchio C, Cassatella MA. Neutrophil-Derived Chemokines on the Road to Immunity. *Semin Immunol* (2016) 28:119–28. doi: 10.1016/j.smim.2016.04.003
  73. Weber FC, Németh T, Csepregi JZ, Dudeck A, Roers A, Oszvári B, et al. Neutrophils Are Required for Both the Sensitization and Elicitation Phase of Contact Hypersensitivity. *J Exp Med* (2015) 212:15–22. doi: 10.1084/jem.20130062
  74. Mantovani A, Cassatella MA, Costantini C, Jaillon S. Neutrophils in the Activation and Regulation of Innate and Adaptive Immunity. *Nat Rev Immunol* (2011) 11:519–31. doi: 10.1038/nri3024
  75. Mócsai A. Diverse Novel Functions of Neutrophils in Immunity, Inflammation, and Beyond. *J Exp Med* (2013) 210:1283–99. doi: 10.1084/jem.20122220
  76. Scapini P, Cassatella MA. Social Networking of Human Neutrophils Within the Immune System. *Blood* (2014) 124:710–9. doi: 10.1182/blood-2014-03-453217
  77. Timár CI, Lorincz AM, Csépanyi-Kömi R, Vályi-Nagy A, Nagy G, Buzás EI, et al. Antibacterial Effect of Microvesicles Released From Human Neutrophilic Granulocytes. *Blood* (2013) 121:510–8. doi: 10.1182/blood-2012-05-431114
  78. Majumdar R, Tavakoli Tameh A, Parent CA. Exosomes Mediate LTB4 Release During Neutrophil Chemotaxis. *PLoS Biol* (2016) 14:e1002336. doi: 10.1371/journal.pbio.1002336
  79. Benito-Martin A, Di Giannatale A, Ceder S, Peinado H. The New Deal: A Potential Role for Secreted Vesicles in Innate Immunity and Tumor Progression. *Front Immunol* (2015) 6:66. doi: 10.3389/fimmu.2015.00066
  80. Vargas A, Roux-Dalvai F, Droit A, Lavoie JP. Neutrophil-Derived Exosomes: A New Mechanism Contributing to Airway Smooth Muscle Remodeling. *Am J Respir Cell Mol Biol* (2016) 55:450–61. doi: 10.1165/rcmb.2016-0033OC
  81. Ostrom QT, Gittleman H, Fulop J, Liu M, Blanda R, Kromer C, et al. CBTRUS Statistical Report: Primary Brain and Central Nervous System Tumors Diagnosed in the United States in 2008–2012. *Neuro Oncol* (2015) 17(Suppl. 4):iv1–iv62. doi: 10.1093/neuonc/nov189
  82. Liu R, Page M, Solheim K, Fox S, Chang SM. Quality of Life in Adults With Brain Tumors: Current Knowledge and Future Directions. *Neuro Oncol* (2009) 11:330–9. doi: 10.1215/15228517-2008-093
  83. Hoffman S, Propp JM, McCarthy BJ. Temporal Trends in Incidence of Primary Brain Tumors in the United States, 1985–1999. *Neuro Oncol* (2006) 8:27–37. doi: 10.1215/S1522851705000323
  84. Deltour I, Johansen C, Auvinen A, Feychting M, Klaeboe L, Schüz J. Time Trends in Brain Tumor Incidence Rates in Denmark, Finland, Norway, and Sweden, 1974–2003. *J Natl Cancer Inst* (2009) 101:1721–4. doi: 10.1093/jnci/djp415
  85. Stupp R, Mason WP, van den Bent MJ, Weller M, Fisher B, Taphoorn MJ, et al. Radiotherapy Plus Concomitant and Adjuvant Temozolomide for Glioblastoma. *N Engl J Med* (2005) 352:987–96. doi: 10.1056/NEJMoa043330
  86. Ostrom QT, Gittleman H, Truitt G, Boscia A, Kruchko C, Barnholtz-Sloan JS. CBTRUS Statistical Report: Primary Brain and Other Central Nervous System Tumors Diagnosed in the United States in 2011–2015. *Neuro Oncol* (2018) 20:iv1–86. doi: 10.1093/neuonc/noy131
  87. Molinaro AM, Taylor JW, Wiencke JK, Wrensch MR. Genetic and Molecular Epidemiology of Adult Diffuse Glioma. *Nat Rev Neurol* (2019) 15:405–17. doi: 10.1038/s41582-019-0220-2
  88. Nagasawa DT, Chow F, Yew A, Kim W, Cremer N, Yang I. Temozolomide and Other Potential Agents for the Treatment of Glioblastoma Multiforme. *Neurosurg Clin N Am* (2012) 23:307–22, ix. doi: 10.1016/j.nec.2012.01.007
  89. Stupp R, Taillibert S, Kanner A, Read W, Steinberg D, Lhermitte B, et al. Effect of Tumor-Treating Fields Plus Maintenance Temozolomide vs Maintenance Temozolomide Alone on Survival in Patients With Glioblastoma: A Randomized Clinical Trial. *JAMA* (2017) 318:2306–16. doi: 10.1001/jama.2017.18718
  90. Sampson JH, Heimberger AB, Archer GE, Aldape KD, Friedman AH, Friedman HS, et al. Immunologic Escape After Prolonged Progression-Free Survival With Epidermal Growth Factor Receptor Variant III Peptide Vaccination in Patients With Newly Diagnosed Glioblastoma. *J Clin Oncol* (2010) 28:4722–9. doi: 10.1200/JCO.2010.28.6963
  91. Wheeler CJ, Das A, Liu G, Yu JS, Black KL. Clinical Responsiveness of Glioblastoma Multiforme to Chemotherapy After Vaccination. *Clin Cancer Res* (2004) 10:5316–26. doi: 10.1158/1078-0432.CCR-04-0497
  92. Newcomb EW, Demaria S, Lukyanov Y, Shao Y, Schnee T, Kawashima N, et al. The Combination of Ionizing Radiation and Peripheral Vaccination Produces Long-Term Survival of Mice Bearing Established Invasive GL261 Gliomas. *Clin Cancer Res* (2006) 12:4730–7. doi: 10.1158/1078-0432.CCR-06-0593
  93. Nowak AK, Robinson BW, Lake RA. Synergy Between Chemotherapy and Immunotherapy in the Treatment of Established Murine Solid Tumors. *Cancer Res* (2003) 63:4490–6.
  94. Liu G, Black KL, Yu JS. Sensitization of Malignant Glioma to Chemotherapy Through Dendritic Cell Vaccination. *Expert Rev Vaccines* (2006) 5:233–47. doi: 10.1586/14760584.5.2.233
  95. Patel AP, Tirosh I, Trombetta JJ, Shalek AK, Gillespie SM, Wakimoto H, et al. Single-Cell RNA-Seq Highlights Intratumoral Heterogeneity in Primary Glioblastoma. *Science* (2014) 344:1396–401. doi: 10.1126/science.1254257
  96. Mahlokoza T, Vellimana AK, Li T, Mao DD, Zohny ZS, Kim DH, et al. Biological and Therapeutic Implications of Multisector Sequencing in Newly Diagnosed Glioblastoma. *Neuro Oncol* (2018) 20:472–83. doi: 10.1093/neuonc/nox232
  97. Reardon DA, Brandes AA, Omuro A, Mulholland P, Lim M, Wick A, et al. Effect of Nivolumab vs Bevacizumab in Patients With Recurrent Glioblastoma: The CheckMate 143 Phase 3 Randomized Clinical Trial. *JAMA Oncol* (2020) 6(7):1003–10. doi: 10.1001/jamaoncol.2020.1024
  98. Weller M, Butowski N, Tran DD, Recht LD, Lim M, Hirte H, et al. Rindopepimut With Temozolomide for Patients With Newly Diagnosed, EGFRvIII- Expressing Glioblastoma (ACT IV): Results of a Randomized, Double-Blind, International Phase 3 Trial. *Lancet Oncol* (2017) 18:1373–85. doi: 10.1016/S1470-2045(17)30517-X
  99. Hodges TR, Ott M, Xiu J, Gatalica Z, Swensen J, Zhou S, et al. Mutational Burden, Immune Checkpoint Expression, and Mismatch Repair in Glioma: Implications for Immune Checkpoint Immunotherapy. *Neuro Oncol* (2017) 19:1047–57. doi: 10.1093/neuonc/nox026
  100. Zajac AJ, Blattman JN, Murali-Krishna K, Sourdiv DJ, Suresh M, Altman JD, et al. Viral Immune Evasion Due to Persistence of Activated T Cells Without Effector Function. *J Exp Med* (1998) 188:2205–13. doi: 10.1084/jem.188.12.2205
  101. Wherry EJ, Blattman JN, Murali-Krishna K, van der Most R, Ahmed R. Viral Persistence Alters CD8 T-Cell Immunodominance and Tissue Distribution and Results in Distinct Stages of Functional Impairment. *J Virol* (2003) 77:4911–27. doi: 10.1128/JVI.77.8.4911-4927.2003
  102. Woroniecka K, Chongsathidkiet P, Rhodin K, Kemeny H, Dechant C, Farber SH, et al. T-Cell Exhaustion Signatures Vary With Tumor Type and Are Severe in Glioblastoma. *Clin Cancer Res* (2018) 24:4175–86. doi: 10.1158/1078-0432.CCR-17-1846
  103. Sugihara AQ, Rolle CE, Lesniak MS. Regulatory T Cells Actively Infiltrate Metastatic Brain Tumors. *Int J Oncol* (2009) 34:1533–40. doi: 10.3892/ijo.00000282
  104. Soffietti R, Rudà R, Mutani R. Management of Brain Metastases. *J Neurol* (2002) 249:1357–69. doi: 10.1007/s00415-002-0870-6
  105. Wesseling P, von Deimling A, Aipape KD, Louis DN, Ohgaki H, Wiestler OD. *Metastatic tumours of the CNS. WHO Classification of Tumours of the Central Nervous System*. Lyon: IARC (2007) p. 248–51.
  106. Lin X, DeAngelis LM. Treatment of Brain Metastases. *J Clin Oncol* (2015) 33:3475–84. doi: 10.1200/JCO.2015.60.9503
  107. Nussbaum ES, Djalilian HR, Cho KH, Hall WA. Brain Metastases: Histology, Multiplicity, Surgery, and Survival. *Cancer* (1996) 78:1781–8. doi: 10.1002/(SICI)1097-0142(19961015)78:8<1781::AID-CNCR19>3.0.CO;2-U

108. Black PM, Johnson MD. Surgical Resection for Patients With Solid Brain Metastases: Current Status. *J Neurooncol* (2004) 69:119–24. doi: 10.1023/B:NEON.0000041875.09048.e7
109. Margolin K, Ernstoff MS, Hamid O, Lawrence D, McDermott D, Puzanov I, et al. Ipilimumab in Patients With Melanoma and Brain Metastases: An Open-Label, Phase 2 Trial. *Lancet Oncol* (2012) 13:459–65. doi: 10.1016/S1470-2045(12)70090-6
110. Long GV, Atkinson V, Lo S, Sandhu S, Guminski AD, Brown MP, et al. Combination Nivolumab and Ipilimumab or Nivolumab Alone in Melanoma Brain Metastases: A Multicenter Randomised Phase 2 Study. *Lancet Oncol* (2018) 19:672–81. doi: 10.1016/S1470-2045(18)30139-6
111. Friebe E, Kapoulou K, Unger S, Núñez NG, Utz S, Rushing EJ, et al. Single-Cell Mapping of Human Brain Cancer Reveals Tumor-Specific Instruction of Tissue-Invasive Leukocytes. *Cell* (2020) 181(7):1626–42.e20. doi: 10.1016/j.cell.2020.04.055
112. Klemm F, Maas RR, Bowman RL, Kornete M, Soukup K, Nassiri S, et al. Interrogation of the Microenvironmental Landscape in Brain Tumors Reveals Disease-Specific Alterations of Immune Cells. *Cell* (2020) 181(7):1643–60. doi: 10.1016/j.cell.2020.05.007
113. Grivennikov SI, Greten FR, Karin M. Immunity, Inflammation, and Cancer. *Cell* (2010) 140:883–99. doi: 10.1016/j.cell.2010.01.025
114. O'Callaghan DS, O'Donnell D, O'Connell F, O'Byrne KJ. The Role of Inflammation in the Pathogenesis of non-Small Cell Lung Cancer. *J Thorac Oncol* (2010) 5:2024–36. doi: 10.1097/JTO.0b013e3181f387e4
115. Aggarwal BB, Vijayalekshmi RV, Sung B. Targeting Inflammatory Pathways for Prevention and Therapy of Cancer: Short-Term Friend, Long-Term Foe. *Clin Cancer Res* (2009) 15:425–30. doi: 10.1158/1078-0432.CCR-08-0149
116. Roxburgh CS, McMillan DC. Role of Systemic Inflammatory Response in Predicting Survival in Patients With Primary Operable Cancer. *Future Oncol* (2010) 6:149–63. doi: 10.2217/fon.09.136
117. Viganó A, Bruera E, Jhangri GS, Newman SC, Fields AL, Suarez-Almazor ME, et al. Clinical Survival Predictors in Patients With Advanced Cancer. *Arch Intern Med* (2000) 160:861–8. doi: 10.1001/archinte.160.6.861
118. Motomura T, Shirabe K, Mano Y, Muto J, Toshima T, Umemoto Y, et al. Neutrophil-lymphocyte Ratio Reflects Hepatocellular Carcinoma Recurrence After Liver Transplantation via Inflammatory Microenvironment. *J Hepatol* (2013) 58:58–64. doi: 10.1016/j.jhep.2012.08.017
119. Kantola T, Klintrup K, Väyrynen JP, Vornanen J, Bloigu R, Karhu T, et al. Stage-Dependent Alterations of the Serum Cytokine Pattern in Colorectal Carcinoma. *Br J Cancer* (2012) 107:1729–36. doi: 10.1038/bjc.2012.456
120. McCourt M, Wang JH, Sookhai S, Redmond HP. Proinflammatory Mediators Stimulate Neutrophil-Directed Angiogenesis. *Arch Surg* (1999) 134:1325–31, discussion 1331–1322. doi: 10.1001/archsurg.134.12.1325
121. Di Carlo E, Forni G, Musiani P. Neutrophils in the Antitumoral Immune Response. *Chem Immunol Allergy* (2003) 83:182–203. doi: 10.1159/000071561
122. McCourt M, Wang JH, Sookhai S, Redmond HP. Activated Human Neutrophils Release Hepatocyte Growth Factor/Scatter Factor. *Eur J Surg Oncol* (2001) 27:396–403. doi: 10.1053/ejso.2001.1133
123. Jabłońska E, Kiluk M, Markiewicz W, Piotrowski L, Grabowska Z, Jabłoński J. TNF-Alpha, IL-6 and Their Soluble Receptor Serum Levels and Secretion by Neutrophils in Cancer Patients. *Arch Immunol Ther Exp (Warsz)* (2001) 49:63–9.
124. Schaidt H, Oka M, Bogenrieder T, Nesbit M, Satyamoorthy K, Berking C, et al. Differential Response of Primary and Metastatic Melanomas to Neutrophils Attracted by IL-8. *Int J Cancer* (2003) 103:335–43. doi: 10.1002/ijc.10775
125. Shamamian P, Schwartz JD, Pocock BJ, Monea S, Whiting D, Marcus SG, et al. Activation of Progelatinase A (MMP-2) by Neutrophil Elastase, Cathepsin G, and Proteinase-3: A Role for Inflammatory Cells in Tumor Invasion and Angiogenesis. *J Cell Physiol* (2001) 189:197–206. doi: 10.1002/jcp.10014
126. Scapini P, Nesi L, Morini M, Tanghetti E, Belleri M, Noonan D, et al. Generation of Biologically Active Angiostatin Kringle 1–3 by Activated Human Neutrophils. *J Immunol* (2002) 168:5798–804. doi: 10.4049/jimmunol.168.11.5798
127. Agliardi G, Liuzzi AR, Hotblack A, De Feo D, Núñez N, Stowe CL, et al. Intratumoral IL-12 Delivery Empowers CAR-T Cell Immunotherapy in a Pre-Clinical Model of Glioblastoma. *Nat Commun* (2021) 12(1):444. doi: 10.1038/s41467-020-20599-x
128. McMillan DC. The Systemic Inflammation-Based Glasgow Prognostic Score: A Decade of Experience in Patients With Cancer. *Cancer Treat Rev* (2013) 39:534–40. doi: 10.1016/j.ctrv.2012.08.003
129. Petrie HT, Klassen LW, Kay HD. Inhibition of Human Cytotoxic T Lymphocyte Activity *In Vitro* by Autologous Peripheral Blood Granulocytes. *J Immunol* (1985) 134:230–4.
130. el-Hag A, Clark RA. Immunosuppression by Activated Human Neutrophils. Dependence on the Myeloperoxidase System. *J Immunol* (1987) 139:2406–13.
131. Loi S, Sirtaine N, Piette F, Salgado R, Viale G, Van Eenoo F, et al. Prognostic and Predictive Value of Tumor-Infiltrating Lymphocytes in a Phase III Randomized Adjuvant Breast Cancer Trial in Node-Positive Breast Cancer Comparing the Addition of Docetaxel to Doxorubicin With Doxorubicin-Based Chemotherapy: BIG 02–98. *J Clin Oncol* (2013) 31:860–7. doi: 10.1200/JCO.2011.41.0902
132. Gooden MJ, de Bock GH, Leffers N, Daemen T, Nijman HW. The Prognostic Influence of Tumour-Infiltrating Lymphocytes in Cancer: A Systematic Review With Meta-Analysis. *Br J Cancer* (2011) 105:93–103. doi: 10.1038/bjc.2011.189
133. Denkert C, Loibl S, Noske A, Roller M, Müller BM, Komor M, et al. Tumor-Associated Lymphocytes as an Independent Predictor of Response to Neoadjuvant Chemotherapy in Breast Cancer. *J Clin Oncol* (2010) 28:105–13. doi: 10.1200/JCO.2009.23.7370
134. Guthrie GJ, Charles KA, Roxburgh CS, Horgan PG, McMillan DC, Clarke SJ. The Systemic Inflammation Based Neutrophil-Lymphocyte Ratio: Experience in Patients With Cancer. *Crit Rev Oncol Hematol* (2013) 88:218–30. doi: 10.1016/j.critrevonc.2013.03.010
135. Kao SC, Pavlakis N, Harvie R, Vardy JL, Boyer MJ, van Zandwijk N, et al. High Blood Neutrophil-to-Lymphocyte Ratio Is an Indicator of Poor Prognosis in Malignant Mesothelioma Patients Undergoing Systemic Therapy. *Clin Cancer Res* (2010) 16:5805–13. doi: 10.1158/1078-0432.CCR-10-2245
136. Chua W, Charles KA, Baracos VE, Clarke SJ. Neutrophil/lymphocyte Ratio Predicts Chemotherapy Outcomes in Patients With Advanced Colorectal Cancer. *Br J Cancer* (2011) 104:1288–95. doi: 10.1038/bjc.2011.100
137. Botta C, Mazzanti R, Guglielmo A, Cusi MG, Vincenzi B, Mantovani G, et al. Treatment-Related Changes in Systemic Inflammatory Status, Measured by Neutrophil-to-Lymphocyte Ratio, Is Predictive of Outcome in Metastatic Colorectal Cancer Patients. *Eur J Cancer* (2011) 47:S181. doi: 10.1016/S0959-8049(11)70932-7
138. Lee Y, Kim SH, Han JY, Kim HT, Yun T, Lee JS. Early Neutrophil-to-Lymphocyte Ratio Reduction as a Surrogate Marker of Prognosis in Never Smokers With Advanced Lung Adenocarcinoma Receiving Gefitinib or Standard Chemotherapy as First-Line Therapy. *J Cancer Res Clin Oncol* (2012) 138:2009–16. doi: 10.1007/s00432-012-1281-4
139. Leibowitz-Amit R, Templeton AJ, Atenafu EG, Vera-Badillo FE, Chlilamma M, Solow HL, et al. Novel Predictive Markers of PSA Response to Abiraterone Acetate in Men With Metastatic Castration-Resistant Prostate-Cancer (mCRPC). *J Clin Oncol* (2013) 31(Suppl.):5058. doi: 10.1200/jco.2013.31.15\_suppl.5058
140. Park YH, Lee YJ, Ku JH, Kwak C, Kim HH. Neutrophil-To-Lymphocyte Ratio Reduction as a Surrogate Marker of Prognosis in Patients With Metastatic Clear Cell Renal Cell Carcinoma Receiving Sunitinib as First-Line Therapy. *J Urol* (2013) 189:e787. doi: 10.1016/j.juro.2013.02.2338
141. Gabrusiewicz K, Rodriguez B, Wei J, Hashimoto Y, Healy LM, Maiti SN, et al. Glioblastoma-Infiltrated Innate Immune Cells Resemble M0 Macrophage Phenotype. *JCI Insight* (2016) 1(2):e85841. doi: 10.1172/jci.insight.85841
142. Nitta T, Sato K, Allegretta M, Brocke S, Lim M, Mitchell DJ, et al. Expression of Granulocyte Colony Stimulating Factor and Granulocyte-Macrophage Colony Stimulating Factor Genes in Human Astrocytoma Cell Lines and in Glioma Specimens. *Brain Res* (1992) 571:19–25. doi: 10.1016/0006-8993(92)90505-4

143. Albulescu R, Codrici E, Popescu ID, Mihai S, Necula LG, Petrescu D, et al. Cytokine Patterns in Brain Tumour Progression. *Mediators Inflamm* (2013) 2013:979748. doi: 10.1155/2013/979748
144. Bambury RM, Teo MY, Power DG, Yusuf A, Murray S, Battley JE, et al. The Association of Pre-Treatment Neutrophil to Lymphocyte Ratio With Overall Survival in Patients With Glioblastoma Multiforme. *J Neurooncol* (2013) 114:149–54. doi: 10.1007/s11060-013-1164-9
145. Wiencke JK, Koestler DC, Salas LA, Wiemels JL, Roy RP, Hansen HM, et al. Immunomethylomic Approach to Explore the Blood Neutrophil Lymphocyte Ratio (NLR) in Glioma Survival. *Clin Epigenet* (2017) 9:10. doi: 10.1186/s13148-017-0316-8
146. McNamara MG, Lwin Z, Jiang H, Templeton AJ, Zadeh G, Bernstein M, et al. Factors Impacting Survival Following Second Surgery in Patients With Glioblastoma in the Temozolomide Treatment Era, Incorporating Neutrophil/Lymphocyte Ratio and Time to First Progression. *J Neurooncol* (2014) 117:147–52. doi: 10.1007/s11060-014-1366-9
147. Mason M, Maurice C, McNamara MG, Tieu MT, Lwin Z, Millar BA, et al. Neutrophil-Lymphocyte Ratio Dynamics During Concurrent Chemoradiotherapy for Glioblastoma Is an Independent Predictor for Overall Survival. *J Neurooncol* (2017) 132:463–71. doi: 10.1007/s11060-017-2395-y
148. Wang PF, Song HW, Cai HQ, Kong LW, Yao K, Jiang T, et al. Preoperative Inflammation Markers and IDH Mutation Status Predict Glioblastoma Patient Survival. *Oncotarget* (2017) 8:50117–23. doi: 10.18632/oncotarget.15235
149. Bertaut A, Truntzer C, Madkouri R, Kaderbhai CG, Derangère V, Vincent J, et al. Blood Baseline Neutrophil Count Predicts Bevacizumab Efficacy in Glioblastoma. *Oncotarget* (2016) 7:70948–58. doi: 10.18632/oncotarget.10898
150. Rahbar A, Cederarv M, Wolmer-Solberg N, Tammik C, Stragliotto G, Peredo I, et al. Enhanced Neutrophil Activity Is Associated With Shorter Time to Tumor Progression in Glioblastoma Patients. *Oncoimmunology* (2016) 5:e1075693. doi: 10.1080/2162402X.2015.1075693
151. Sippel TR, White J, Nag K, Tsvankin V, Klaassen M, Kleinschmidt-DeMasters BK, et al. Neutrophil Degranulation and Immunosuppression in Patients With GBM: Restoration of Cellular Immune Function by Targeting Arginase I. *Clin Cancer Res* (2011) 17:6992–7002. doi: 10.1158/1078-0432.CCR-11-1107
152. Scoccianti S, Ricardi U. Treatment of Brain Metastases: Review of Phase III Randomized Controlled Trials. *Radiother Oncol* (2012) 102:168–79. doi: 10.1016/j.radonc.2011.08.041
153. Gaspar L, Scott C, Rotman M, Asbell S, Phillips T, Wasserman T, et al. Recursive Partitioning Analysis (RPA) of Prognostic Factors in Three Radiation Therapy Oncology Group (RTOG) Brain Metastases Trials. *Int J Radiat Oncol Biol Phys* (1997) 37:745–51. doi: 10.1016/S0360-3016(96)00619-0
154. Sperduto PW, Berkey B, Gaspar LE, Mehta M, Curran W. A New Prognostic Index and Comparison to Three Other Indices for Patients With Brain Metastases: An Analysis of 1,960 Patients in the RTOG Database. *Int J Radiat Oncol Biol Phys* (2008) 70:510–4. doi: 10.1016/j.ijrobp.2007.06.074
155. Hanahan D, Weinberg RA. The Hallmarks of Cancer. *Cell* (2000) 100:57–70. doi: 10.1016/S0092-8674(00)81683-9
156. Mitsuya K, Nakasu Y, Kurakane T, Hayashi N, Harada H, Nozaki K. Elevated Preoperative Neutrophil-to-Lymphocyte Ratio as a Predictor of Worse Survival After Resection in Patients With Brain Metastasis. *J Neurosurg* (2017) 127:433–7. doi: 10.3171/2016.8.JNS16899
157. Zhang L, Hu Y, Chen W, Tian Y, Xie Y, Chen J. Pre-Stereotactic Radiosurgery Neutrophil-to-Lymphocyte Ratio Is a Predictor of the Prognosis for Brain Metastases. *J Neurooncol* (2020) 147:691–700. doi: 10.1007/s11060-020-03477-w
158. Chowdhary M, Switchenko JM, Press RH, Jhaveri J, Buchwald ZS, Blumenfeld PA, et al. Post-Treatment Neutrophil-to-Lymphocyte Ratio Predicts for Overall Survival in Brain Metastases Treated With Stereotactic Radiosurgery. *J Neurooncol* (2018) 139:689–97. doi: 10.1007/s11060-018-2914-5
159. Alagappan M, Pollom EL, von Eyben R, Kozak MM, Aggarwal S, Poultides GA, et al. Albumin and Neutrophil-Lymphocyte Ratio (NLR) Predict Survival in Patients With Pancreatic Adenocarcinoma Treated With SBRT. *Am J Clin Oncol* (2018) 41:242–7. doi: 10.1097/COC.0000000000000263
160. Hyder J, Boggs DH, Hanna A, Suntharalingam M, Chuong MD. Changes in Neutrophil-to-Lymphocyte and Platelet-Tolymphocyte Ratios During Chemoradiation Predict for Survival and Pathologic Complete Response in Trimodality Esophageal Cancer Patients. *J Gastrointest Oncol* (2016) 7:189–95. doi: 10.3978/j.issn.2078-6891.2015.080
161. Shaverdian N, Veruttipong D, Wang J, Schae D, Kupelian P, Lee P. Pretreatment Immune Parameters Predict for Overall Survival and Toxicity in Early-Stage Non-Small-Cell Lung Cancer Patients Treated With Stereotactic Body Radiation Therapy. *Clin Lung Cancer* (2016) 17:39–46. doi: 10.1016/j.clcc.2015.07.007
162. Ulusoy R, Yokuşoğlu M, Kırılmaz A, Nevruz O, Baysan O, Kılıçaslan F. Mean Platelet Volume in ST Elevation and non-ST Elevation Myocardial Infarction. *Gulhane Med J* (2011) 53(2):114–8.
163. Bhat T, Teli S, Rijal J, Bhat H, Raza M, Khoeiry G, et al. Neutrophil to Lymphocyte Ratio and Cardiovascular Diseases: A Review. *Expert Rev Cardiovasc Ther* (2013) 11:55–9. doi: 10.1586/erc.12.159
164. Balta S, Demirkol S, Cakar M, Arslan Z, Unlu M, Celik T. Other Inflammatory Markers Should Not be Forgotten When Assessing the Neutrophil-to-Lymphocyte Ratio. *Clin Appl Thromb Hemost* (2013) 19:693–4. doi: 10.1177/1076029613486019
165. Fridlender ZG, Sun J, Kim S, Kapoor V, Cheng G, Ling L, et al. Polarization of Tumor-Associated Neutrophil Phenotype by TGF- $\beta$ : “N1” Versus “N2” TAN. *Cancer Cell* (2009) 16:183–94. doi: 10.1016/j.ccr.2009.06.017
166. Granot Z, Fridlender ZG. Plasticity Beyond Cancer Cells and the “Immunosuppressive Switch”. *Cancer Res* (2015) 75:4441–5. doi: 10.1158/0008-5472.CAN-15-1502
167. Sionov RV, Fridlender ZG, Granot Z. The Multifaceted Roles Neutrophils Play in the Tumor Microenvironment. *Cancer Microenviron* (2015) 8:125–58. doi: 10.1007/s12307-014-0147-5
168. Andzinski L, Kasnitz N, Stahnke S, Wu CF, Gereke M, von Köckritz-Blickwede M, et al. Type I IFNs Induce Anti-Tumor Polarization of Tumor Associated Neutrophils in Mice and Human. *Int J Cancer* (2016) 138:1982–93. doi: 10.1002/ijc.29945
169. Noy R, Pollard JW. Tumor-Associated Macrophages: From Mechanisms to Therapy. *Immunity* (2014) 41:49–61. doi: 10.1016/j.immuni.2014.06.010
170. Qian BZ, Pollard JW. Macrophage Diversity Enhances Tumor Progression and Metastasis. *Cell* (2010) 141:39–51. doi: 10.1016/j.cell.2010.03.014
171. Ruffell B, Affara NI, Coussens LM. Differential Macrophage Programming in the Tumor Microenvironment. *Trends Immunol* (2012) 33:119–26. doi: 10.1016/j.it.2011.12.001
172. Brandau S, Trellakis S, Bruderek K, Schmaltz D, Steller G, Elian M, et al. Myeloid-Derived Suppressor Cells in the Peripheral Blood of Cancer Patients Contain a Subset of Immature Neutrophils With Impaired Migratory Properties. *J Leukoc Biol* (2011) 89:311–7. doi: 10.1189/jlb.0310162
173. Sagiv JY, Michaeli J, Assi S, Mishalian I, Kisos H, Levy L, et al. Phenotypic Diversity and Plasticity in Circulating Neutrophil Subpopulations in Cancer. *Cell Rep* (2015) 10:562–73. doi: 10.1016/j.celrep.2014.12.039
174. Lang S, Bruderek K, Kaspar C, Höing B, Kanaan O, Dominas N, et al. Clinical Relevance and Suppressive Capacity of Human Myeloid-Derived Suppressor Cell Subsets. *Clin Cancer Res* (2018) 24:4834–44. doi: 10.1158/1078-0432.CCR-17-3726
175. Ley K, Hoffman HM, Kubes P, Cassatella MA, Zychlinsky A, Hedrick CC, et al. Neutrophils: New Insights and Open Questions. *Sci Immunol* (2018) 3:eat4579. doi: 10.1126/sciimmunol.aat4579
176. Blaisdell A, Crequer A, Columbus D, Daikoku T, Mittal K, Dey SK, et al. Neutrophils Oppose Uterine Epithelial Carcinogenesis via Debridement of Hypoxic Tumor Cells. *Cancer Cell* (2015) 28:785–99. doi: 10.1016/j.ccell.2015.11.005
177. Eruslanov EB, Bhojnagarwala PS, Quatromoni JG, Stephen TL, Ranganathan A, Deshpande C, et al. Tumor-Associated Neutrophils Stimulate T Cell Responses in Early-Stage Human Lung Cancer. *J Clin Invest* (2014) 124:5466–80. doi: 10.1172/JCI77053
178. Singhal S, Bhojnagarwala PS, O'Brien S, Moon EK, Garfall AL, Rao AS, Quatromoni JG, et al. Origin and Role of a Subset of Tumor-Associated Neutrophils With Antigen-Presenting Cell Features in Early-Stage Human Lung Cancer. *Cancer Cell* (2016) 30:120–35. doi: 10.1016/j.ccell.2016.06.001
179. Ponzetta A, Carriero R, Carnevale S, Barbagallo M, Molgora M, Perucchini C, et al. Neutrophils Driving Unconventional T Cells Mediate Resistance



- Against Murine Sarcomas and Selected Human Tumors. *Cell* (2019) 178:346–360.e24. doi: 10.1016/j.cell.2019.05.047
180. Fridlender ZG, Sun J, Mishalian I, Singhal S, Cheng G, Kapoor V, et al. Transcriptomic Analysis Comparing Tumor-Associated Neutrophils With Granulocytic Myeloid-Derived Suppressor Cells and Normal Neutrophils. *PLoS One* (2012) 7:e31524. doi: 10.1371/journal.pone.0031524
  181. Mahiddine K, Blaisdell A, Ma S, Cr  quer-Grandhomme A, Lowell CA, Erlebacher A. Relief of Tumor Hypoxia Unleashes the Tumoricidal Potential of Neutrophils. *J Clin Invest* (2020) 130:389–403. doi: 10.1172/JCI130952
  182. Finisguerra V, Di Conza G, Di Matteo M, Serneels J, Costa S, Thompson AA, et al. MET Is Required for the Recruitment of Anti-Tumoural Neutrophils. *Nature* (2015) 522:349–53. doi: 10.1038/nature14407
  183. Zhu YP, Padgett L, Dinh HQ, Marcovecchio P, Blatchley A, Wu R, et al. Identification of an Early Unipotent Neutrophil Progenitor With Pro-Tumoral Activity in Mouse and Human Bone Marrow. *Cell Rep* (2018) 24:2329–41.e8. doi: 10.1016/j.celrep.2018.07.097
  184. Gupta AK, Joshi MB, Philippova M, Erne P, Hasler P, Hahn S, et al. Activated Endothelial Cells Induce Neutrophil Extracellular Traps and Are Susceptible to NETosis-Mediated Cell Death. *FEBS Lett* (2010) 584:3193–7. doi: 10.1016/j.febslet.2010.06.006
  185. Saffarzadeh M, Juenemann C, Queisser MA, Lochnit G, Barreto G, Galuska SP, et al. Neutrophil Extracellular Traps Directly Induce Epithelial and Endothelial Cell Death: A Predominant Role of Histones. *PLoS One* (2012) 7:e32366. doi: 10.1371/journal.pone.0032366
  186. Demers M, Krause DS, Schatzberg D, Martinod K, Voorhees JR, Fuchs TA, et al. Cancers Predispose Neutrophils to Release Extracellular DNA Traps That Contribute to Cancer-Associated Thrombosis. *Proc Natl Acad Sci USA* (2012) 109:13076–81. doi: 10.1073/pnas.1200419109
  187. Tohme S, Yazdani HO, Al-Khafaji AB, Chidi AP, Loughran P, Mowen K, et al. Neutrophil Extracellular Traps Promote the Development and Progression of Liver Metastases After Surgical Stress. *Cancer Res* (2016) 76:1367–80. doi: 10.1158/0008-5472.CAN-15-1591
  188. Richardson JJR, Hendrickse C, Gao-Smith F, Thickett DR. Neutrophil Extracellular Trap Production in Patients With Colorectal Cancer In Vitro. *Int J Inflam* (2017) 2017:4915062. doi: 10.1155/2017/4915062
  189. Albregues J, Shields MA, Ng D, Park CG, Ambrico A, Poindexter ME, et al. Neutrophil Extracellular Traps Produced During Inflammation Awaken Dormant Cancer Cells in Mice. *Science* (2018) 361(6409):ea40227. doi: 10.1126/science.a40227
  190. Graeber MB, Scheithauer BW, Kreutzberg GW. Microglia in Brain Tumors. *Glia* (2002) 40:252–9. doi: 10.1002/glia.10147
  191. Fossati G, Ricevuti G, Edwards SW, Walker C, Dalton A, Rossi ML. Neutrophil Infiltration Into Human Gliomas. *Acta Neuropathol* (1999) 98:349–54. doi: 10.1007/s004010051093
  192. Liang J, Piao Y, Holmes L, Fuller GN, Henry V, Tiao N, et al. Neutrophils Promote the Malignant Glioma Phenotype Through S100A4. *Clin Cancer Res* (2014) 20:187–98. doi: 10.1158/1078-0432.CCR-13-1279
  193. Bresnick AR, Weber DJ, Zimmer DB. S100 Proteins in Cancer. *Nat Rev Cancer* (2015) 15:96–109. doi: 10.1038/nrc3893
  194. Liu Y, Kosaka A, Ikeura M, Kohanbash G, Fellows-Mayle W, Snyder LA, et al. Premetastatic Soil and Prevention of Breast Cancer Brain Metastasis. *Neuro Oncol* (2013) 15:891–903. doi: 10.1093/neuonc/not031
  195. Shaul ME, Fridlender ZG. Neutrophils as Active Regulators of the Immune System in the Tumor Microenvironment. *J Leukoc Biol* (2017) 102:343–9. doi: 10.1189/jlb.5MR1216-508R
  196. Piccard H, Muschel RJ, Opdenakker G. On the Dual Roles and Polarized Phenotypes of Neutrophils in Tumor Development and Progression. *Crit Rev Oncol Hematol* (2012) 82:296–309. doi: 10.1016/j.critrevonc.2011.06.004
  197. Kim J, Bae JS. Tumor-Associated Macrophages and Neutrophils in Tumor Microenvironment. *Mediators Inflammation* (2016) 2016:6058147. doi: 10.1155/2016/6058147
  198. He G, Zhang H, Zhou J, Wang B, Chen Y, Kong Y, et al. Peritumoral Neutrophils Negatively Regulate Adaptive Immunity via the PD-L1/PD-1 Signalling Pathway in Hepatocellular Carcinoma. *J Exp Clin Cancer Res* (2015) 34:141. doi: 10.1186/s13046-015-0256-0
  199. Wang TT, Zhao YL, Peng LS, Chen N, Chen W, Lv YP, et al. Tumour-Activated Neutrophils in Gastric Cancer Foster Immune Suppression and Disease Progression Through GM-CSF-PD-L1 Pathway. *Gut* (2017) 66:1900–11. doi: 10.1136/gutjnl-2016-313075
  200. Vols S, Sionov RV, Granot Z. Always Look on the Bright Side: Anti-Tumor Functions of Neutrophils. *Curr Pharm Des* (2017) 23:4862–92. doi: 10.2174/1381612823666170704125420
  201. Gregory AD, Houghton AM. Tumor-Associated Neutrophils: New Targets for Cancer Therapy. *Cancer Res* (2011) 71:2411–6. doi: 10.1158/0008-5472.CAN-10-2583
  202. Ring NG, Herndler-Brandstetter D, Weiskopf K, Shan L, Volkmer JP, George BM, et al. Anti-Sirp   Antibody Immunotherapy Enhances Neutrophil and Macrophage Antitumor Activity. *Proc Natl Acad Sci USA* (2017) 114:E10578–85. doi: 10.1073/pnas.1710877114
  203. Liu Y, B  hring HJ, Zen K, Burst SL, Schnell FJ, Williams IR, et al. Signal Regulatory Protein (Sirp  ), a Cellular Ligand for CD47, Regulates Neutrophil Transmigration. *J Biol Chem* (2002) 277:10028–36. doi: 10.1074/jbc.M109720200
  204. Condamine T, Kumar V, Ramachandran IR, Youn JI, Celis E, Finnberg N, et al. ER Stress Regulates Myeloid-Derived Suppressor Cell Fate Through TRAILR-Mediated Apoptosis. *J Clin Invest* (2014) 124:2626–39. doi: 10.1172/JCI74056
  205. Renshaw SA, Parmar JS, Singleton V, Rowe SJ, Dockrell DH, Dower SK, et al. Acceleration of Human Neutrophil Apoptosis by TRAIL. *J Immunol* (2003) 170:1027–33. doi: 10.4049/jimmunol.170.2.1027
  206. Massara M, Bonavita O, Savino B, Caronni N, Mollica Poeta V, Sironi M, et al. ACKR2 in Hematopoietic Precursors as a Checkpoint of Neutrophil Release and Antimetastatic Activity. *Nat Commun* (2018) 9:676. doi: 10.1038/s41467-018-03080-8
  207. Steele CW, Karim SA, Leach JDG, Bailey P, Upstill-Goddard R, Rishi L, et al. CXCR2 Inhibition Profoundly Suppresses Metastases and Augments Immunotherapy in Pancreatic Ductal Adenocarcinoma. *Cancer Cell* (2016) 29:832–45. doi: 10.1016/j.ccell.2016.04.014
  208. Highfill SL, Cui Y, Giles AJ, Smith JP, Zhang H, Morse E, et al. Disruption of CXCR2-Mediated MDSC Tumor Trafficking Enhances Anti-PD1 Efficacy. *Sci Transl Med* (2014) 6:237ra67. doi: 10.1126/scitranslmed.3007974
  209. Velasco-Vel  zquez M, Jiao X, De La Fuente M, Pestell TG, Ertel A, et al. CCR5 Antagonist Blocks Metastasis of Basal Breast Cancer Cells. *Cancer Res* (2012) 72:3839–50. doi: 10.1158/0008-5472.CAN-11-3917
  210. Hawila E, Razon H, Wildbaum G, Blattner C, Sapir Y, Shaked Y, et al. CCR5 Directs the Mobilization of CD11b+Gr1+Ly6C  low Polymorphonuclear Myeloid Cells From the Bone Marrow to the Blood to Support Tumor Development. *Cell Rep* (2017) 21:2212–22. doi: 10.1016/j.celrep.2017.10.104
  211. Sung L, Nathan PC, Alibhai SM, Tomlinson GA, Beyene J. Meta-Analysis: Effect of Prophylactic Hematopoietic Colony-Stimulating Factors on Mortality and Outcomes of Infection. *Ann Intern Med* (2007) 147:400–11. doi: 10.7326/0003-4819-147-6-200709180-00010
  212. Lyman GH, Kuderer NM, Crawford J, Wolff DA, Culakova E, Poniewierski MS, et al. Predicting Individual Risk of Neutropenic Complications in Patients Receiving Cancer Chemotherapy. *Cancer* (2011) 117:1917–27. doi: 10.1002/cncr.25691
  213. Weber R, Fleming V, Hu X, Nagibin V, Groth C, Altevogt P, et al. Myeloid-Derived Suppressor Cells Hinder the Anti-Cancer Activity of Immune Checkpoint Inhibitors. *Front Immunol* (2018) 9:1310. doi: 10.3389/fimmu.2018.01310
  214. Crawford J, Dale DC, Lyman GH. Chemotherapy-Induced Neutropenia: Risks, Consequences, and New Directions for its Management. *Cancer* (2004) 100:228–37. doi: 10.1002/cncr.11882
  215. Mehta HM, Malandra M, Corey SJ. G-CSF and GM-CSF in Neutropenia. *J Immunol* (2015) 195:1341–9. doi: 10.4049/jimmunol.1500861
  216. Spiekermann K, Roesler J, Emmendoerffer A, Elsner J, Welte K. Functional Features of Neutrophils Induced by G-CSF and GM-CSF Treatment: Differential Effects and Clinical Implications. *Leukemia* (1997) 11:466–78. doi: 10.1038/sj.leu.2400607
  217. Azzar   A, Carulli G, Rizzuti-Gullaci A, Capochiani E, Petrini M. Lenograstim and Filgrastim Effects on Neutrophil Motility in Patients Undergoing Chemotherapy: Evaluation by Computer-Assisted Image Analysis. *Am J Hematol* (2001) 66:306–7. doi: 10.1002/ajh.1064
  218. Berdel WE, Danhauser-Riedl S, Steinhilber G, Winton EF. Various Human Hematopoietic Growth Factors (Interleukin-3, GM-CSF, G-CSF) Stimulate



- Clonal Growth of Nonhematopoietic Tumor Cells. *Blood* (1989) 73:80–3. doi: 10.1182/blood.V73.1.80.bloodjournal73180
219. Yamashita Y, Nara N, Aoki N. Antiproliferative and Differentiative Effect of Granulocyte-Macrophage Colony-Stimulating Factor on a Variant Human Small Cell Lung Cancer Cell Line. *Cancer Res* (1989) 49:5334–8.
  220. Mach N, Gillessen S, Wilson SB, Sheehan C, Mihm M, Dranoff G. Differences in Dendritic Cells Stimulated *In Vivo* by Tumors Engineered to Secrete Granulocyte-Macrophage Colony-Stimulating Factor or Flt3-Ligand. *Cancer Res* (2000) 60:3239–46.
  221. Gillessen S, Naumov YN, Nieuwenhuis EE, Exley MA, Lee FS, Mach N, et al. CD1d-Restricted T Cells Regulate Dendritic Cell Function and Antitumor Immunity in a Granulocyte-Macrophage Colony-Stimulating Factor-Dependent Fashion. *Proc Natl Acad Sci USA* (2003) 100:8874–9. doi: 10.1073/pnas.1033098100
  222. Gutschalk CM, Herold-Mende CC, Fusenig NE, Mueller MM. Granulocyte Colony-Stimulating Factor and Granulocyte-Macrophage Colony-Stimulating Factor Promote Malignant Growth of Cells From Head and Neck Squamous Cell Carcinomas *In Vivo*. *Cancer Res* (2006) 66:8026–36. doi: 10.1158/0008-5472.CAN-06-0158
  223. Roilides E, Walsh TJ, Pizzo PA, Rubin M. Granulocyte Colony-Stimulating Factor Enhances the Phagocytic and Bactericidal Activity of Normal and Defective Human Neutrophils. *J Infect Dis* (1991) 163:579–83. doi: 10.1093/infdis/163.3.579
  224. Kitagawa S, Yuo A, Souza LM, Saito M, Miura Y, Takaku F. Recombinant Human Granulocyte Colony-Stimulating Factor Enhances Superoxide Release in Human Granulocytes Stimulated by the Chemotactic Peptide. *Biochem Biophys Res Commun* (1987) 144:1143–6. doi: 10.1016/0006-291X(87)91430-6
  225. Demaria S, Formenti SC. Radiation as an Immunological Adjuvant: Current Evidence on Dose and Fractionation. *Front Oncol* (2012) 2:153. doi: 10.3389/fonc.2012.00153
  226. Demaria S, Formenti SC. Role of T Lymphocytes in Tumor Response to Radiotherapy. *Front Oncol* (2012) 2:95. doi: 10.3389/fonc.2012.00095
  227. Golden EB, Frances D, Pellicciotti I, Demaria S, Helen Barcellos-Hoff M, Formenti SC. Radiation Fosters Dose-Dependent and Chemotherapy-Induced Immunogenic Cell Death. *Oncoimmunology* (2014) 3:e28518. doi: 10.4161/onci.28518
  228. Takeshima T, Pop LM, Laine A, Iyengar P, Vitetta ES, Hannan R. Key Role for Neutrophils in Radiation-Induced Antitumor Immune Responses: Potentiation With G-CSF. *Proc Natl Acad Sci USA* (2016) 113:11300–5. doi: 10.1073/pnas.1613187113
  229. Schernberg A, Blanchard P, Chargari C, Deutsch E. Neutrophils, a Candidate Biomarker and Target for Radiation Therapy? *Acta Oncol* (2017) 56:1522–30. doi: 10.1080/0284186X.2017.1348623
  230. Bahig H, Taussky D, Delouya G, Nadiri A, Gagnon-Jacques A, Bodson-Clermont P, et al. Neutrophil Count Is Associated With Survival in Localized Prostate Cancer. *BMC Cancer* (2015) 15:594. doi: 10.1186/s12885-015-1599-9
  231. Escande A, Haie-Meder C, Maroun P, Gouy S, Mazeron R, Leroy T, et al. Neutrophilia in Locally Advanced Cervical Cancer: A Novel Biomarker for Image-Guided Adaptive Brachytherapy? *Oncotarget* (2016) 7:74886–94. doi: 10.18632/oncotarget.12440
  232. Schernberg A, Moureau-Zabotto L, Rivin Del Campo E, Escande A, Ducreux M, Nguyen F, Goere D, et al. Leukocytosis and Neutrophilia Predict Outcome in Locally Advanced Esophageal Cancer Treated With Definitive Chemoradiation. *Oncotarget* (2017) 8:11579–88. doi: 10.18632/oncotarget.14584
  233. Teitz-Tennenbaum S, Li Q, Rynkiewicz S, Ito F, Davis MA, McGinn CJ, et al. Radiotherapy Potentiates the Therapeutic Efficacy of Intratumoral Dendritic Cell Administration. *Cancer Res* (2003) 63:8466–75.
  234. Demaria S, Ng B, Devitt ML, Babb JS, Kawashima N, Liebes L, et al. Ionizing Radiation Inhibition of Distant Untreated Tumors (Abscopal Effect) Is Immune Mediated. *Int J Radiat Oncol Biol Phys* (2004) 58:862–70. doi: 10.1016/j.ijrobp.2003.09.012
  235. Finkelstein SE, Iclozan C, Bui MM, Cotter MJ, Ramakrishnan R, Ahmed J, et al. Combination of External Beam Radiotherapy (EBRT) With Intratumoral Injection of Dendritic Cells as Neo-Adjuvant Treatment of High-Risk Soft Tissue Sarcoma Patients. *Int J Radiat Oncol Biol Phys* (2012) 82:924–32. doi: 10.1016/j.ijrobp.2010.12.068
  236. Golden EB, Chhabra A, Chachoua A, Adams S, Donach M, Fenton-Kerimian M, et al. Local Radiotherapy and Granulocyte-Macrophage Colony-Stimulating Factor to Generate Abscopal Responses in Patients With Metastatic Solid Tumours: A Proof-of-Principle Trial. *Lancet Oncol* (2015) 16:795–803. doi: 10.1016/S1470-2045(15)00054-6
  237. Hiniker SM, Chen DS, Reddy S, Chang DT, Jones JC, Mollick JA, et al. A Systemic Complete Response of Metastatic Melanoma to Local Radiation and Immunotherapy. *Transl Oncol* (2012) 5:404–7. doi: 10.1593/tlo.12280
  238. Golden EB, Demaria S, Schiff PB, Chachoua A, Formenti SC. An Abscopal Response to Radiation and Ipilimumab in a Patient With Metastatic Non-Small Cell Lung Cancer. *Cancer Immunol Res* (2013) 1:365–72. doi: 10.1158/2326-6066.CIR-13-0115
  239. Demaria S, Golden EB, Formenti SC. Role of Local Radiation Therapy in Cancer Immunotherapy. *JAMA Oncol* (2015) 1:1325–32. doi: 10.1001/jamaoncol.2015.2756
  240. Liu X, Cho WC. Precision Medicine in Immune Checkpoint Blockade Therapy for non-Small Cell Lung Cancer. *Clin Transl Med* (2017) 6:7. doi: 10.1186/s40169-017-0136-7
  241. Remon J, Besse B. Immune Checkpoint Inhibitors in First-Line Therapy of Advanced Non-Small Cell Lung Cancer. *Curr Opin Oncol* (2017) 29:97–104. doi: 10.1097/CCO.0000000000000351
  242. Gubin MM, Esaulova E, Ward JP, Malkova ON, Runci D, Wong P, et al. High-Dimensional Analysis Delineates Myeloid and Lymphoid Compartment Remodeling During Successful Immune-Checkpoint Cancer Therapy. *Cell* (2018) 175:1014–30.e19. doi: 10.1016/j.cell.2018.09.030
  243. Riaz N, Havel JJ, Makarov V, Desrichard A, Urba WJ, Sims JS, et al. Tumor and Microenvironment Evolution During Immunotherapy With Nivolumab. *Cell* (2017) 171:934–49.e16. doi: 10.1016/j.cell.2017.09.028
  244. Krieg C, Nowicka M, Guglietta S, Schindler S, Hartmann FJ, Weber LM, et al. High-Dimensional Single-Cell Analysis Predicts Response to Anti-PD-1 Immunotherapy. *Nat Med* (2018) 24:144–53. doi: 10.1038/nm.4466
  245. Madonna G, Ballesteros-Merino C, Feng Z, Bifulco C, Capone M, Giannarelli D, et al. PD-L1 Expression With Immune-Infiltrate Evaluation and Outcome Prediction in Melanoma Patients Treated With Ipilimumab. *Oncoimmunology* (2018) 7:e1405206. doi: 10.1080/2162402X.2017.1405206
  246. Apel F, Zychlinsky A, Kenny EF. The Role of Neutrophil Extracellular Traps in Rheumatic Diseases. *Nat Rev Rheumatol* (2018) 14:467–75. doi: 10.1038/s41584-018-0039-z
  247. Papayannopoulos V, Metzler KD, Hakkin A, Zychlinsky A. Neutrophil Elastase and Myeloperoxidase Regulate the Formation of Neutrophil Extracellular Traps. *J Cell Biol* (2010) 191:677–91. doi: 10.1083/jcb.201006052
  248. Bronze-da-Rocha E, Santos-Silva A. Neutrophil Elastase Inhibitors and Chronic Kidney Disease. *Int J Biol Sci* (2018) 14:1343–60. doi: 10.7150/ijbs.26111
  249. Stockley R, De Soyza A, Gunawardena K, Perrett J, Forsman-Semb K, Entwistle N, et al. Phase II Study of a Neutrophil Elastase Inhibitor (AZD9668) in Patients With Bronchiectasis. *Respir Med* (2013) 107:524–33. doi: 10.1016/j.rmed.2012.12.009
  250. Li P, Li M, Lindberg MR, Kennett MJ, Xiong N, Wang Y. PAD4 Is Essential for Antibacterial Innate Immunity Mediated by Neutrophil Extracellular Traps. *J Exp Med* (2010) 207:1853–62. doi: 10.1084/jem.20100239
  251. Lewis HD, Liddle J, Coote JE, Atkinson SJ, Barker MD, Bax BD, et al. Inhibition of PAD4 Activity Is Sufficient to Disrupt Mouse and Human NET Formation. *Nat Chem Biol* (2015) 11:189–91. doi: 10.1038/nchembio.1735
  252. Koushik S, Joshi N, Nagaraju S, Mahmood S, Mudeenahally K, Padmavathy R, et al. PAD4: Pathophysiology, Current Therapeutics and Future Perspective in Rheumatoid Arthritis. *Expert Opin Ther Targets* (2017) 21:433–47. doi: 10.1080/14728222.2017.1294160
  253. Brill A, Fuchs TA, Savchenko AS, Thomas GM, Martinod K, De Meyer SF, et al. Neutrophil Extracellular Traps Promote Deep Vein Thrombosis in Mice. *J Thromb Haemost* (2012) 10:136–44. doi: 10.1111/j.1538-7836.2011.04544.x
  254. Caudrillier A, Kessenbrock K, Gilliss BM, Nguyen JX, Marques MB, Monestier M, et al. Platelets Induce Neutrophil Extracellular Traps in Transfusion-Related Acute Lung Injury. *J Clin Invest* (2012) 122:2661–71. doi: 10.1172/JCI61303
  255. Thomas GM, Carbo C, Curtis BR, Martinod K, Mazo IB, Schatzberg D, et al. Extracellular DNA Traps Are Associated With the Pathogenesis of TRALI in

- Humans and Mice. *Blood* (2012) 119:6335–43. doi: 10.1182/blood-2012-01-405183
256. Cools-Lartigue J, Spicer J, McDonald B, Gowing S, Chow S, Giannias B, et al. Neutrophil Extracellular Traps Sequester Circulating Tumor Cells and Promote Metastasis. *J Clin Invest* (2013) 123:3446–58. doi: 10.1172/JCI67484
  257. Park JK, Hodges T, Arko L, Shen M, Dello Iacono D, McNabb A, et al. Scale to Predict Survival After Surgery for Recurrent Glioblastoma Multiforme. *J Clin Oncol* (2010) 28:3838–43. doi: 10.1200/JCO.2010.30.0582
  258. Lacroix M, Abi-Said D, Fourney DR, Gokaslan ZL, Shi W, DeMonte F, et al. A Multivariate Analysis of 416 Patients With Glioblastoma Multiforme: Prognosis, Extent of Resection, and Survival. *J Neurosurg* (2001) 95:190–8. doi: 10.3171/jns.2001.95.2.0190
  259. Groothuis DR. The Blood–Brain and Blood–Tumor Barriers: A Review of Strategies for Increasing Drug Delivery. *Neuro Oncol* (2000) 2:45–59. doi: 10.1215/15228517-2-1-45
  260. Neuwelt EA, Bauer B, Fahlke C, Fricker G, Iadecola C, Janigro D, et al. Engaging Neuroscience to Advance Translational Research in Brain Barrier Biology. *Nat Rev Neurosci* (2011) 12:169–82. doi: 10.1038/nrn2995
  261. Amoretti M, Amsler C, Bonomi G, Bouchta A, Bowe P, Carraro C, et al. Production and Detection of Cold Antihydrogen Atoms. *Nature* (2002) 419:456–9. doi: 10.1038/nature01096
  262. Peer D, Karp JM, Hong S, Farokhzad OC, Margalit R, Langer R. Nanocarriers as an Emerging Platform for Cancer Therapy. *Nat Nanotechnol* (2007) 2:751–60. doi: 10.1038/nnano.2007.387
  263. Mo R, Gu Z. Tumor Microenvironment and Intracellular Signal-Activated Nanomaterials for Anticancer Drug Delivery. *Mater Today* (2016) 19:274–83. doi: 10.1016/j.mattod.2015.11.025
  264. Lu Y, Aimetti AA, Langer R, Gu Z. Bioresponsive Materials. *Nat Mater Rev* (2016) 1:16075. doi: 10.1038/natrevmats.2016.75
  265. Mangraviti A, Gullotti D, Tyler B, Brem H. Nanobiotechnology-Based Delivery Strategies: New Frontiers in Brain Tumor Targeted Therapies. *J Control Release* (2016) 240:443–53. doi: 10.1016/j.jconrel.2016.03.031
  266. Cheng Y, Morshed RA, Auffinger B, Tobias AL, Lesniak MS. Multifunctional Nanoparticles for Brain Tumor Imaging and Therapy. *Adv Drug Deliv Rev* (2014) 66:42–57. doi: 10.1016/j.addr.2013.09.006
  267. Lee C, Hwang HS, Lee S, Kim B, Kim JO, Oh KT, et al. Rabies Virus-Inspired Silica-Coated Gold Nanorods as a Photothermal Therapeutic Platform for Treating Brain Tumors. *Adv Mater* (2017) 29:28134459. doi: 10.1002/adma.201605563
  268. Singh A, Kim W, Kim Y, Jeong K, Kang CS, Kim Y, et al. Multifunctional Photonics Nanoparticles for Crossing the Blood–Brain Barrier and Effecting Optically Trackable Brain Theranostics. *Adv Funct Mater* (2016) 26:7057–66. doi: 10.1002/adfm.201602808
  269. Zeng L, Zou L, Yu H, He X, Cao H, Zhan Z, et al. Treatment of Malignant Brain Tumor by Tumor-Triggered Programmed Wormlike Micelles With Precise Targeting and Deep Penetration. *Adv Funct Mater* (2016) 26:4201–12. doi: 10.1002/adfm.201600642
  270. Zhang X, Yao S, Liu C, Jiang Y. Tumor Tropic Delivery of Doxorubicin-Polymer Conjugates Using Mesenchymal Stem Cells for Glioma Therapy. *Biomaterials* (2015) 39:269–81. doi: 10.1016/j.biomaterials.2014.11.003
  271. Roger M, Clavreul A, Venier-Julienne MC, Passirani C, Sindji L, Schiller P, et al. Mesenchymal Stem Cells as Cellular Vehicles for Delivery of Nanoparticles to Brain Tumors. *Biomaterials* (2010) 31:8393–401. doi: 10.1016/j.biomaterials.2010.07.048
  272. Bexell D, Scheding S, Bengzon J. Toward Brain Tumor Gene Therapy Using Multipotent Mesenchymal Stromal Cell Vectors. *Mol Ther* (2010) 18:1067–75. doi: 10.1038/mt.2010.58
  273. Roger M, Clavreul A, Huynh NT, Passirani C, Schiller P, Vessi  res A, et al. Ferrociphenol Lipid Nanocapsule Delivery by Mesenchymal Stromal Cells in Brain Tumor Therapy. *Int J Pharm* (2012) 423:63–8. doi: 10.1016/j.jipharm.2011.04.058
  274. Kim SM, Lim JY, Park SI, Jeong CH, Oh JH, Jeong M, et al. Gene Therapy Using TRAIL-Secreting Human Umbilical Cord Blood-Derived Mesenchymal Stem Cells Against Intracranial Glioma. *Cancer Res* (2008) 68:9614–23. doi: 10.1158/0008-5472.CAN-08-0451
  275. Pierig   F, Serafini S, Rossi L, Magnani M. Cell-Based Drug Delivery. *Adv Drug Deliv Rev* (2008) 60(2):286–95. doi: 10.1016/j.addr.2007.08.029
  276. Batrakova EV, Gendelman HE, Kabanov AV. Cell-Mediated Drug Delivery. *Expert Opin Drug Deliv* (2011) 8:415–33. doi: 10.1517/17425247.2011.559457
  277. Gu L, Mooney DJ. Biomaterials and Emerging Anticancer Therapeutics: Engineering the Microenvironment. *Nat Rev Cancer* (2016) 16:56–66. doi: 10.1038/nrc.2015.3
  278. Kolaczowska E, Kubes P. Neutrophil Recruitment and Function in Health and Inflammation. *Nat Rev Immunol* (2013) 13:159–75. doi: 10.1038/nri3399
  279. Phillipson M, Kubes P. The Neutrophil in Vascular Inflammation. *Nat Med* (2011) 17:1381–90. doi: 10.1038/nm.2514
  280. Nathan C. Neutrophils and Immunity: Challenges and Opportunities. *Nat Rev Immunol* (2006) 6:173–82. doi: 10.1038/nri1785
  281. Inglis VI, Jones MPJ, Tse ADY, Easton AS. Neutrophils Both Reduce and Increase Permeability in a Cell Culture Model of the Blood–Brain Barrier. *Brain Res* (2004) 998:218–29. doi: 10.1016/j.brainres.2003.11.031
  282. Bernardes-Silva M, Anthony DC, Issekutz AC, Perry VH. Recruitment of Neutrophils Across the Blood–Brain Barrier: The Role of E- and P-Selectins. *J Cereb Blood Flow Metab* (2001) 21:1115–24. doi: 10.1097/00004647-200109000-00009
  283. Uehara T, Baba I, Nomura Y. Induction of Cytokine-Induced Neutrophil Chemoattractant in Response to Various Stresses in Rat C6 Glioma Cells. *Brain Res* (1998) 790:284–92. doi: 10.1016/S0006-8993(98)00080-8
  284. Mishalian I, Bayuh R, Levy L, Zolotarov L, Michaeli J, Fridlender ZG, et al. Tumor-Associated Neutrophils (TAN) Develop Pro-Tumorigenic Properties During Tumor Progression. *Cancer Immunol Immunother* (2013) 62:1745–56. doi: 10.1007/s00262-013-1476-9
  285. Salmaggi A, Eoli M, Frigerio S, Silvani A, Gelati M, Corsini E, et al. Intracavitary vEGF, bFGF, IL-8, IL-12 Levels in Primary and Recurrent Malignant Glioma. *J Neurooncol* (2003) 62:297–303. doi: 10.1023/a:1023367223575
  286. Brat DJ, Bellail AC, VanMeir EG. The Role of Interleukin-8 and Its Receptors in Gliomagenesis and Tumoral Angiogenesis. *Neuro Oncol* (2005) 7:122–33. doi: 10.1215/S1152851704001061
  287. Ryuto M, Ono M, Izumi H, Yoshida S, Weich HA, Kohno K, et al. Induction of Vascular Endothelial Growth Factor by Tumor Necrosis Factor Alpha in Human Glioma Cells. *Possible Roles SP-1 J Biol Chem* (1996) Nov 8271 (45):28220–8. doi: 10.1074/jbc.271.45.28220
  288. Nabors LB, Suswam E, Huang Y, Yang X, Johnson MJ, King PH. Tumor Necrosis Factor  $\alpha$  Induces Angiogenic Factor Up-Regulation in Malignant Glioma Cells: A Role for RNA Stabilization and HuR. *Cancer Res* (2003) 63:4181–7.
  289. Xue J, Zhao Z, Zhang L, Xue L, Shen S, Wen Y, et al. Neutrophil-Mediated Anticancer Drug Delivery for Suppression of Postoperative Malignant Glioma Recurrence. *Nat Nanotechnol* (2017) 12:692–700. doi: 10.1038/nnano.2017.54
  290. Iyer AK, Khaled G, Fang J, Maeda H. Exploiting the Enhanced Permeability and Retention Effect for Tumor Targeting. *Drug Discov Today* (2006) 11:812–8. doi: 10.1016/j.drudis.2006.07.005
  291. Bertrand N, Wu J, Xu X, Kamaly N, Farokhzad OC. Cancer Nanotechnology: The Impact of Passive and Active Targeting in the Era of Modern Cancer Biology. *Adv Drug Deliv Rev* (2014) 66:2–25. doi: 10.1016/j.addr.2013.11.009
  292. De Filippo K, Dudeck A, Hasenberg M, Nye E, van Rooijen N, Hartmann K, et al. Mast Cell and Macrophage Chemokines CXCL1/CXCL2 Control the Early Stage of Neutrophil Recruitment During Tissue Inflammation. *Blood* (2013) 121:4930–7. doi: 10.1182/blood-2013-02-486217
  293. Keshari RS, Jyoti A, Dubey M, Kothari N, Kohli M, Bogra J, et al. Cytokines Induced Neutrophil Extracellular Traps Formation: Implication for the Inflammatory Disease Condition. *PLoS One* (2012) 7:e48111. doi: 10.1371/journal.pone.0048111
  294. Schneider JR, Kwan BS, MD K, Boockvar J.A., MD. Neutrophil-Guided Drug Delivery for Targeting Residual Glioma Cells. *Neurosurgery* (2018) 82(1): N7–9. doi: 10.1093/neuros/nyx531
  295. Wu M, Zhang H, Tie C, Yan C, Deng Z, Wan Q, et al. MR Imaging Tracking of Inflammation-Activatable Engineered Neutrophils for Targeted Therapy of Surgically Treated Glioma. *Nat Commun* (2018) 9:4777. doi: 10.1038/s41467-018-07250-6
  296. Willis VC, Banda NK, Cordova KN, Chandra PE, Robinson WH, Cooper DC, et al. Protein Arginine Deiminase 4 Inhibition Is Sufficient for the Amelioration of Collagen-Induced Arthritis. *Clin Exp Immunol* (2017) 188:263–74. doi: 10.1111/cei.12932

297. Chu D, Gao J, Wang Z. Neutrophil-Mediated Delivery of Therapeutic Nanoparticles Across Blood Vessel Barrier for Treatment of Inflammation and Infection. *ACS Nano* (2015) 9:11800–11. doi: 10.1021/acs.nano.5b05583

**Conflict of Interest:** The authors declare that the research was conducted in the absence of any commercial or financial relationships that could be construed as a potential conflict of interest.

**Publisher's Note:** All claims expressed in this article are solely those of the authors and do not necessarily represent those of their affiliated organizations, or those of

the publisher, the editors and the reviewers. Any product that may be evaluated in this article, or claim that may be made by its manufacturer, is not guaranteed or endorsed by the publisher.

*Copyright © 2021 Lin, Wei, Chen, Lim and Hwang. This is an open-access article distributed under the terms of the Creative Commons Attribution License (CC BY). The use, distribution or reproduction in other forums is permitted, provided the original author(s) and the copyright owner(s) are credited and that the original publication in this journal is cited, in accordance with accepted academic practice. No use, distribution or reproduction is permitted which does not comply with these terms.*



Article

# Functional Hyaluronic Acid-Polylactic Acid/Silver Nanoparticles Core-Sheath Nanofiber Membranes for Prevention of Post-Operative Tendon Adhesion

Chih-Hao Chen <sup>1,2</sup> , Yuan-Hsun Cheng <sup>3</sup>, Shih-Heng Chen <sup>2</sup> , Andy Deng-Chi Chuang <sup>1</sup>  
and Jyh-Ping Chen <sup>2,3,4,5,\*</sup>

- <sup>1</sup> Department of Plastic and Reconstructive Surgery, Chang Gung Memorial Hospital at Keelung, Keelung 20401, Taiwan; chchen5027@gmail.com (C.-H.C.); andy.d.chuang@gmail.com (A.D.-C.C.)  
<sup>2</sup> Department of Plastic and Reconstructive Surgery, Chang Gung Memorial Hospital at Linkou, College of Medicine, Chang Gung University, Kwei-San, Taoyuan 33305, Taiwan; shihheng@mac.com  
<sup>3</sup> Department of Chemical and Materials Engineering, Chang Gung University, Kwei-San, Taoyuan 33302, Taiwan; cf30039@yahoo.com.tw  
<sup>4</sup> Research Center for Food and Cosmetic Safety, Research Center for Chinese Herbal Medicine, Linkou Campus, College of Human Ecology, Chang Gung University of Science and Technology, Taoyuan 33305, Taiwan  
<sup>5</sup> Department of Materials Engineering, Ming Chi University of Technology, Tai-Shan, New Taipei City 24301, Taiwan  
\* Correspondence: jpchen@mail.cgu.edu.tw; Tel.: +886-3-2118800



**Citation:** Chen, C.-H.; Cheng, Y.-H.; Chen, S.-H.; Chuang, A.D.-C.; Chen, J.-P. Functional Hyaluronic Acid-Polylactic Acid/Silver Nanoparticles Core-Sheath Nanofiber Membranes for Prevention of Post-Operative Tendon Adhesion. *Int. J. Mol. Sci.* **2021**, *22*, 8781. <https://doi.org/10.3390/ijms22168781>

Academic Editor: Vijay Kumar Thakur

Received: 30 June 2021

Accepted: 13 August 2021

Published: 16 August 2021

**Publisher's Note:** MDPI stays neutral with regard to jurisdictional claims in published maps and institutional affiliations.



**Copyright:** © 2021 by the authors. Licensee MDPI, Basel, Switzerland. This article is an open access article distributed under the terms and conditions of the Creative Commons Attribution (CC BY) license (<https://creativecommons.org/licenses/by/4.0/>).

**Abstract:** In this study, we prepared core-sheath nanofiber membranes (CSNFM) with silver nanoparticles (Ag NPs) embedding in the polylactic acid (PLA) nanofiber sheath and hyaluronic acid (HA) in the nanofiber core. The PLA/Ag NPs sheath provides mechanical support as well as anti-bacterial and anti-inflammatory properties. The controlled release of HA from the core could exert anti-adhesion effects to promote tendon sliding while reducing fibroblast attachment. From the microfibrillar structural nature of CSNFM, they function as barrier membranes to reduce fibroblast penetration without hampering nutrient transports to prevent post-operative peritendinous adhesion. As the anti-adhesion efficacy will depend on release rate of HA from the core as well as Ag NP from the sheath, we fabricated CSNFM of comparable fiber diameter, but with thick (Tk) or thin (Tn) sheath. Similar CSNFM with thick (Tk<sup>+</sup>) and thin (Tn<sup>+</sup>) sheath but with embedded Ag NPs in the sheath were also prepared. The physico-chemical properties of the barrier membranes were characterized in details, together with their biological response including cell penetration, cell attachment and proliferation, and cytotoxicity. Peritendinous anti-adhesion models in rabbits were used to test the efficacy of CSNFM as anti-adhesion barriers, from gross observation, histology, and biomechanical tests. Overall, the CSNFM with thin-sheath and Ag NPs (Tn<sup>+</sup>) shows antibacterial activity with low cytotoxicity, prevents fibroblast penetration, and exerts the highest efficacy in reducing fibroblast attachment in vitro. From in vivo studies, the Tn<sup>+</sup> membrane also shows significant improvement in preventing peritendinous adhesions as well as anti-inflammatory efficacy, compared with Tk and Tn CSNFM and a commercial adhesion barrier film (SurgiWrap<sup>®</sup>) made from PLA.

**Keywords:** electrospinning; core-sheath nanofibers; anti-adhesion; silver nanoparticles; polylactic acid; hyaluronic acid

## 1. Introduction

Postoperative tissue adhesion is a universal and critical clinical challenge. The inflammatory response after tissue injury prompts the surrounding fibroblasts to repair the injured tissue, yet excessive fibrous tissues not only hamper healing, but also result in tissue adhesion in the vicinity. The probability of such a phenomenon can reach 67–100%



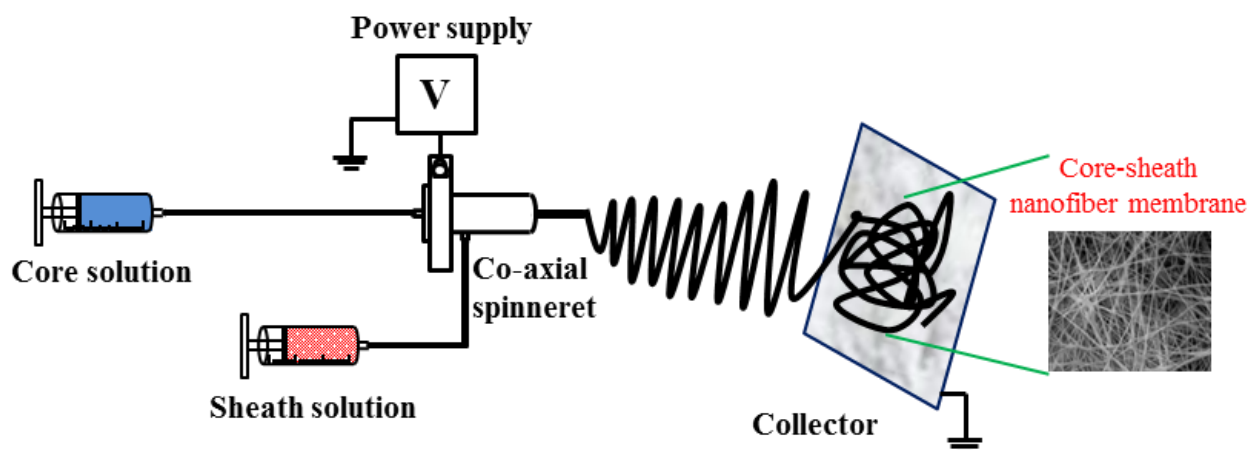
after gastrointestinal surgery and 4–30% after tendon injury and repair [1–3]. In the context of tendon injury, the surrounding fibroblasts aggregate to repair the injured tissue. Nonetheless, the excessive fibroblast proliferation and protein synthesis can lead to formation of a layer of dense connective tissue over the tendon and surrounding tissues, causing tendon adhesion. This in turn restricts joint movement and results in compromised tendon gliding and pain. In such cases, complex surgical intervention is required [4]. In these cases, prevention of peritendinous adhesion is desirable with an ideal biomimetic tendon sheath surrogates to allow free and smooth movement of the encased tendon, while simultaneously maintaining a permeable barrier between the tendon and the peritendinous tissue. Such a barrier would prevent infiltration of fibroblasts and decrease the incidence of unwanted tendon adhesion during the healing process, while the permeability of the barrier would allow diffusion of cytokines, nutrients, and wastes to and from the recovering tendon.

Poly(lactic acid) (PLA) is a biocompatible and biodegradable polymer with widespread applications in medicine and tissue engineering [5–8]. It is one of the most promising biodegradable polymers made from renewable sources to be used in nanocomposites [9,10]. PLA has shown excellent anti-adhesion properties both in the abdominal cavity and after tendon surgery, but its extensive application is limited by its hardness, hydrophobicity, and slow degradation rate [4,11,12]. Still, by making modifications of PLA scaffolds via coating, grafting, or blending with other materials, the intrinsic properties of PLA could be tuned to broaden the applicability of PLA-based scaffolds [11,13–17]. For tendon repair, electrospun PLA nanofiber membranes have shown promising results as an effective tendon sheath surrogate [18–20]. Such a design provides a desired mechanical barrier between the injured tendon and its surrounding, while taking advantage of the non-cytotoxic nature of the material and the permeability offered by the microfibrillar structure for nutrients exchange. By further modifying the fundamental polymeric nanofiber design through structural change or the coalescence of novel agents to the polymer fibers, desirable traits and improved functionality could be introduced [21–23].

For this purpose, modifying electrospun nanofiber structure and grafting or loading nanofibers with functional molecules can introduce different attributes into the final nanofiber design [22,24,25]. In particular, a core-sheath nanofiber structure produced via co-axial electrospinning allows fabrication of dual compartment nanofibers endowed with multi-functionality [26]. Such designs would allow controlled release of therapeutics within the core while maintaining the structural integrity of the fiber, which is supported through the outer sheath layer [27,28]. Additionally, by modulating the flow rate of spinning solutions fed to a co-axial spinneret, core-sheath nanofibers with varying core-to-sheath ratios but comparable fiber diameters may be produced with well controlled electrospinning conditions [29]. In these instances, a core-sheath nanofiber with a large core diameter and a thin sheath thickness may show faster release of the therapeutic molecules from the core, together with fast elution of embedded functional nanoparticles from the sheath to exert improved multi-functionality.

With its good biocompatibility and biodegradability as well as nonimmunogenic properties, hyaluronic acid (HA) has been used extensively for biomedical applications [30,31]. Previously, we designed core-sheath nanofiber membranes (CSNFMs) with hyaluronic acid (HA)-infused core and silver nanoparticles (Ag NPs)-imbedded polycaprolactone (PCL) sheath, to provide controlled release of HA and Ag NPs from the membranes [24]. Such a design was shown to be effective in providing anti-adhesion, anti-bacterial, and anti-inflammatory activities via a synergistic effect of HA and Ag NPs. Despite the advantages offered through design of such CSNFMs, we postulate that the overall efficacy of an anti-adhesion membrane would depend on the core-sheath ratio of the nanofiber, since varied release rate of HA and Ag NPs may affect the collective effects from both agents. Toward this end, we used co-axial electrospinning to prepare CSNFMs with comparable fiber diameter but different core-sheath ratios (Scheme 1). Considering the polymer used in a commercial anti-adhesion film SurgiWrap<sup>®</sup>, we also replaced PCL in the sheath with

polylactic acid (PLA) for its favorable mechanical properties and biocompatibility, to control the release of lubricating HA from the core. The Ag NPs were embedded in the PLA sheath for the anti-bacterial and anti-inflammatory activity. By modulating the release rate of HA and Ag NPs by changing the core-sheath ratio, we aim to determine the optimal design of such CSNFMs to prevent post-surgical tendon adhesion *in vivo*.



**Scheme 1.** The schematic diagram for preparation of core-sheath nanofiber membranes (CSNFMs). The sheath spinning solution contains polylactic acid in methylene chloride/*N,N'*-dimethylformamide. For silver nanoparticles (Ag NPs)-embedded CSNFMs, the sheath spinning solution contains  $\text{AgNO}_3$ , which is exposed to UV light beforehand to form Ag NPs. The core spinning solution contains hyaluronic acid and polyethylene oxide in formic acid.

## 2. Results and Discussion

### 2.1. Preparation and Characterization of Core-Sheath Nanofiber Membranes (CSNFMs)

We determined the morphology and the diameter of nanofibers by scanning electron microscopy (SEM). From Figure 1A, we can observe the four types of CSNFMs fabricated in this study, thick-sheath (Tk) and thin-sheath (Tn) without Ag NPs and thick-sheath ( $\text{Tk}^+$ ) and thin-sheath ( $\text{Tn}^+$ ) with Ag NPs, to comprise continuous and beadless nanofibers from co-axial electrospinning. Measurements by ImageJ software indicate the fiber diameter is  $643 \pm 119$  nm for Tk,  $680 \pm 167$  nm for Tn,  $692 \pm 165$  nm for  $\text{Tk}^+$ , and  $725 \pm 226$  nm for  $\text{Tn}^+$ , with no significant difference found among all membranes. The mean pore flow pore diameters measured by capillary flow porometry are  $1.89 \pm 0.40$ ,  $2.28 \pm 0.33$ ,  $1.80 \pm 0.62$ , and  $1.94 \pm 0.62$   $\mu\text{m}$  for Tk, Tn,  $\text{Tk}^+$ , and  $\text{Tn}^+$ , respectively. As with fiber diameter, there is no significant difference in pores size among all membranes, although all are associated with a pore size small enough to prevent fibroblast penetration. The transmission electron microscopy (TEM) images of the nanofibers show a distinct core-sheath structure (Figure 1B). Differences in nanofiber structure with thick sheath (Tk and  $\text{Tk}^+$ ) or thin sheath (Tn and  $\text{Tn}^+$ ) is clearly observed, depending on individual flow rates of the polymer solutions in the co-axial spinneret. Both spherical and rod-like Ag NPs with size ranging from 10 nm to 40 nm are observed to be embedded in the sheath of  $\text{Tn}^+$  and  $\text{Tk}^+$  CSNFMs after reducing the  $\text{AgNO}_3$ -containing sheath spinning solution with 254 nm UV light.

The core-sheath structure was further demonstrated from TEM images after immersing the CSNFMs in phosphate buffered saline (PBS) for 14 days to release HA and Ag NPs. As shown in Figure 2A, there is diminished color within the core area after eluting HA from the core, together with disappearance of dark spots (Ag NPs) for  $\text{Tk}^+$  and  $\text{Tn}^+$  after the release of Ag NPs from the sheath. Further proof of the core-sheath structure was provided by comparing the field-emission scanning electron microscopy (FE-SEM) images of the cross sections of the Tk and Tn nanofibers, before and after immersion in PBS. After losing HA from the core in PBS for 14 days, a clear hollow core is evident for both CSNFMs regardless of sheath thickness, supporting successful fabrication of CSNFMs (Figure 2B).

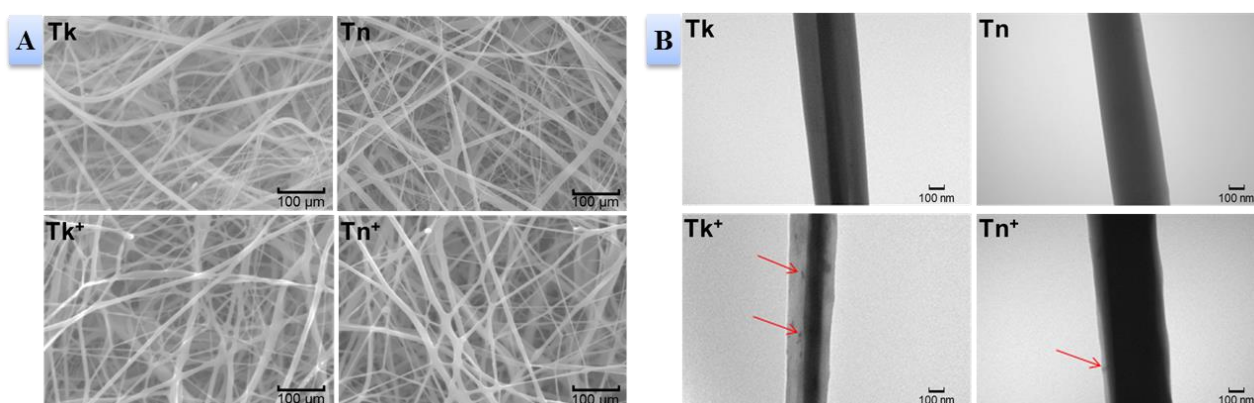


**Figure 1.** The scanning electron microscopy (SEM) (A, bar = 100  $\mu\text{m}$ ) and transmission electron microscopy (TEM) (B, bar = 100 nm) images of Tk, Tn, Tk<sup>+</sup>, and Tn<sup>+</sup> core-sheath nanofiber membranes (CSNFMs). The red arrows in (B) indicate Ag NPs in the sheath.

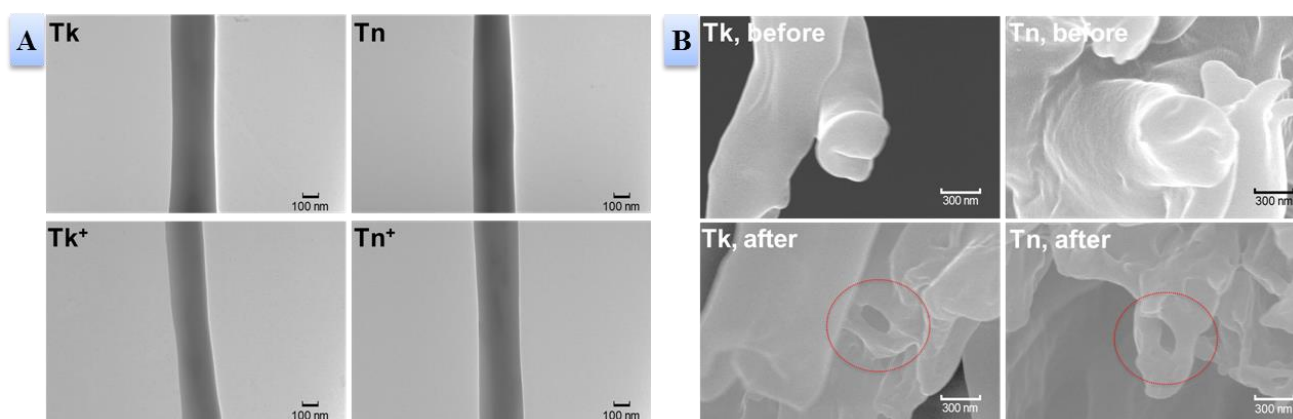


**Figure 2.** (A) The transmission electron microscopy (TEM) images of Tk, Tn, Tk<sup>+</sup>, and Tn<sup>+</sup> CSNFMs after immersion in PBS for two weeks (bar = 100 nm). (B) The field-emission scanning electron microscopy (FE-SEM) images of Tk and Tn core-sheath nanofiber membranes (CSNFMs) before and after immersion in PBS for two weeks (bar = 300 nm). The red circles indicate the hollow core structure after eluting HA from the core.

From X-ray diffraction (XRD) analysis, all CSNFMs display two broad peaks at  $2\theta = 16.8^\circ$  and  $22.6^\circ$  due to PLA (Figure 3A). A similar peak intensity for Tk (Tn) with Tk<sup>+</sup> (Tn<sup>+</sup>) indicates Ag NPs do not influence the crystallinity of PLA. Furthermore, the high-resolution XRD spectra of Tk<sup>+</sup> and Tn<sup>+</sup> in Figure 3B clearly display two additional Ag peaks at  $2\theta = 38.1^\circ$  and  $44.3^\circ$ , which correspond to the (111) and (200) crystalline planes of Ag. This confirms the formation of Ag NPs after UV-reduction of AgNO<sub>3</sub> in PLA solution prepared from methylene chloride/dimethylformamide (MC/DMF) [32]. This also coincides with JCPDS file No. 04-0783 for the face-centered cubic structure of Ag NPs [33].

From X-ray photoelectron spectroscopy (XPS) analysis, characteristic peaks assigned to Ag only appear for Tk<sup>+</sup> and Tn<sup>+</sup> (Figure 4A), indicating some Ag NPs are exposed on the surface of those nanofibers since the detection limit of XPS is only restricted to several nanometers from the surface. We could further confirm the existence of Ag NPs on the nanofiber surface from the high-resolution XPS spectra in Figure 4B, which shows Ag peaks at 366.9 eV (Ag<sub>3d3/2</sub>) and 372.9 eV (Ag<sub>3d5/2</sub>) for Tk<sup>+</sup> and Tn<sup>+</sup> (Figure 4B). The elemental compositions of different CSNFMs from XPS analysis are shown in Table 1. The approximate amounts of Ag NPs on fiber surface are estimated to be 0.03% and 0.01% for Tk<sup>+</sup> and Tn<sup>+</sup>, respectively. This low value is expected, as only few Ag NPs will be present on nanofiber surface with the electrostatic repulsion force generated from the positive voltage during electrospinning [34].

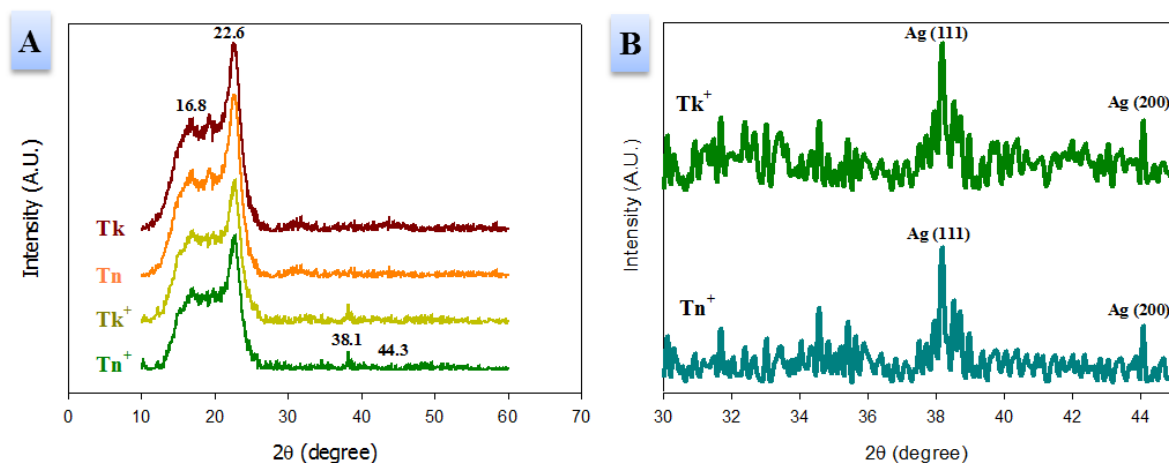


**Figure 3.** The X-ray diffraction (XRD) analysis of Tk, Tn, Tk<sup>+</sup>, and Tn<sup>+</sup> CSNFMs (A) and high resolution XRD spectra of Tk<sup>+</sup> and Tn<sup>+</sup> CSNFMs (B).

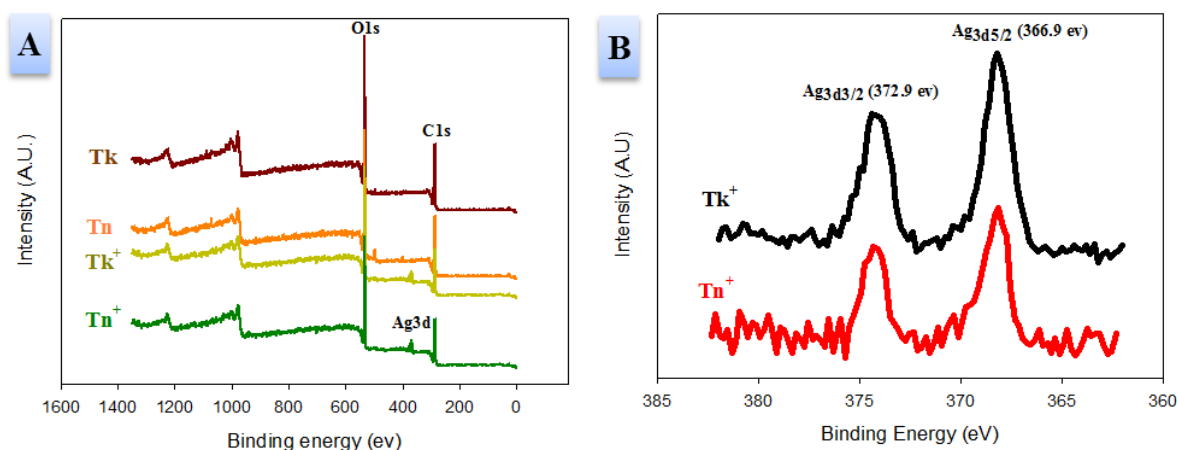


**Figure 4.** The X-ray photoelectron spectroscopy (XPS) analysis of Tk, Tn, Tk<sup>+</sup>, and Tn<sup>+</sup> CSNFMs (A) and high resolution XPS spectra of Tk<sup>+</sup> and Tn<sup>+</sup> CSNFMs (B).

**Table 1.** The elemental composition from X-ray photoelectron spectroscopy (XPS) analysis.

Sample	Elemental Composition (Atomic %)			
	C	N	O	Ag
Tk	79.01	0.56	20.43	0.00
Tn	81.35	0.84	17.81	0.00
Tk <sup>+</sup>	78.23	0.64	21.10	0.03
Tn <sup>+</sup>	78.81	0.63	20.55	0.01

## 2.2. Protein Permeability, Release Property and Anti-Bacterial Activity

For an anti-adhesion barrier membrane to be effective, the fibroblast penetration and migration should be prevented without impeding the permeation of nutrients that are important during tendon healing. To confirm the permeation properties, the permeation coefficient of a sample nutrient (bovine serum albumin, BSA) thorough the CSNFMs was determined at 37 °C in a side-by-side permeation cell and compared with that of a commercial anti-adhesion barrier film (SurgiWrap®). As shown in Table 2, there is no significant difference in permeability coefficient of BSA through all CSNFMs while the permeability coefficient of BSA was almost three orders lower in SurgiWrap®, reflecting the impermeable nature of SurgiWrap® to BSA. Indeed, the impermeability of SurgiWrap® to BSA. Indeed, the impermeability of SurgiWrap® to BSA.



could be related to its non-porous and dense membrane nature, which is expected to profoundly hamper nutrient transport across the barrier membrane. Despite that the same polymer (70:30 poly(L-lactide-co-D,L-lactide)) was used in SurgiWrap<sup>®</sup> and in the sheath of CSNFMs, the use of electrospinning to produce macroporous CSNFMs could drastically improve the membrane permeability of BSA. This suggests that despite that CSNFMs are associated with small pore size ( $\sim 2 \mu\text{m}$ ), they do not hamper the transport of nutrients through the barrier during tendon healing, announcing the advantage of using such macroporous membranes for anti-adhesion purposes over a dense polymer film such as SurgiWrap<sup>®</sup> [35].

**Table 2.** The permeability coefficient of BSA through different CSNFMs and SurgiWrap<sup>®</sup>.

Sample	Tk	Tn	Tk <sup>+</sup>	Tn <sup>+</sup>	SurgiWrap <sup>®</sup>
Permeability coefficient ( $10^{-5} \text{ cm/s}$ )	$5.66 \pm 1.05$	$5.89 \pm 1.07$	$5.00 \pm 0.92$	$5.26 \pm 0.67$	$5.39 \pm 0.81 \times 10^{-3}$

The individual release profiles of HA and Ag NPs were studied next. During the first week, all CSNFMs showed rapid and steady HA release, to reach  $\sim 90\%$  cumulative HA release percentage (calculated based on HA used for preparation of the CSNFMs) after 10 days (Figure 5A). Nonetheless, CSNFMs with thin sheath (Tn and Tn<sup>+</sup>) shows higher HA release rate than their thick-sheath counterparts (Tk and Tk<sup>+</sup>), as less diffusion length is required for diffusion of HA through the sheath. Considering the cumulative mass of HA released, which is directly related to its anti-adhesion functionality, it is similar for Tn and Tn<sup>+</sup>, but  $\sim 3$  times higher than that of Tk and Tk<sup>+</sup>, with higher loading of HA in the large core of thin-sheath nanofibers (Figure 5B). For release of Ag NPs, the quantity of embedded nanoparticles in the membranes was determined beforehand. From the amount of silver nitrate used for preparation of CSNFMs, the theoretical contents of Ag NPs are 0.76 and 0.49 mg/g membrane in Tk<sup>+</sup> and Tn<sup>+</sup>, respectively, assuming 100% reduction efficiency of Ag<sup>+</sup> to Ag NPs by photo-reduction of Ag<sup>+</sup> ions with UV light in MC/DMF. The actual amount Ag NPs embedded in CSNFMs from coupled plasma optical emission spectrometry (ICP-OES) analysis revealed 0.65 and 0.39 mg/g membrane for Tk<sup>+</sup> and Tn<sup>+</sup>, respectively. This high reduction efficiency ( $>80\%$ ) can facially produce dispersed Ag NPs in PLA polymer solution to be used as the sheath spinning solution. Indeed, a previous study confirmed the use of DMF to reduce Ag<sup>+</sup> to Ag in a mixed solvent system, where Ag NPs could be formed in situ without agglomeration during crystal growth for embedding in a polymer matrix [36]. Using the amount of Ag NPs loaded in Tn<sup>+</sup> and Tk<sup>+</sup>, the cumulative release percentage profiles of Ag NPs is similar for both CSNFMs, which is faster than HA and reached  $\sim 90\%$  within five days (Figure 5C). Although the release percentage is similar, the released mass of Ag NPs for Tk<sup>+</sup> is about two times that of Tn<sup>+</sup>, as more Ag NPs are embedded in Tk<sup>+</sup> with its thick sheath (Figure 5D). In an aqueous environment, Ag NPs on the surface of nanofibers are readily to react with water and mostly released into the solution in form of silver ions. After the initial release of surface Ag, the release process becomes diffusion limited. However, with the large surface area of nanofibers, it is difficult to have extended release of Ag. Since an inflammatory response after tendon surgery is expected to be more severe during the first few days, the fast release of Ag NPs from CSNFMs is deemed suitable to induce early anti-inflammatory and subsequent anti-adhesion effects during tendon healing [37].

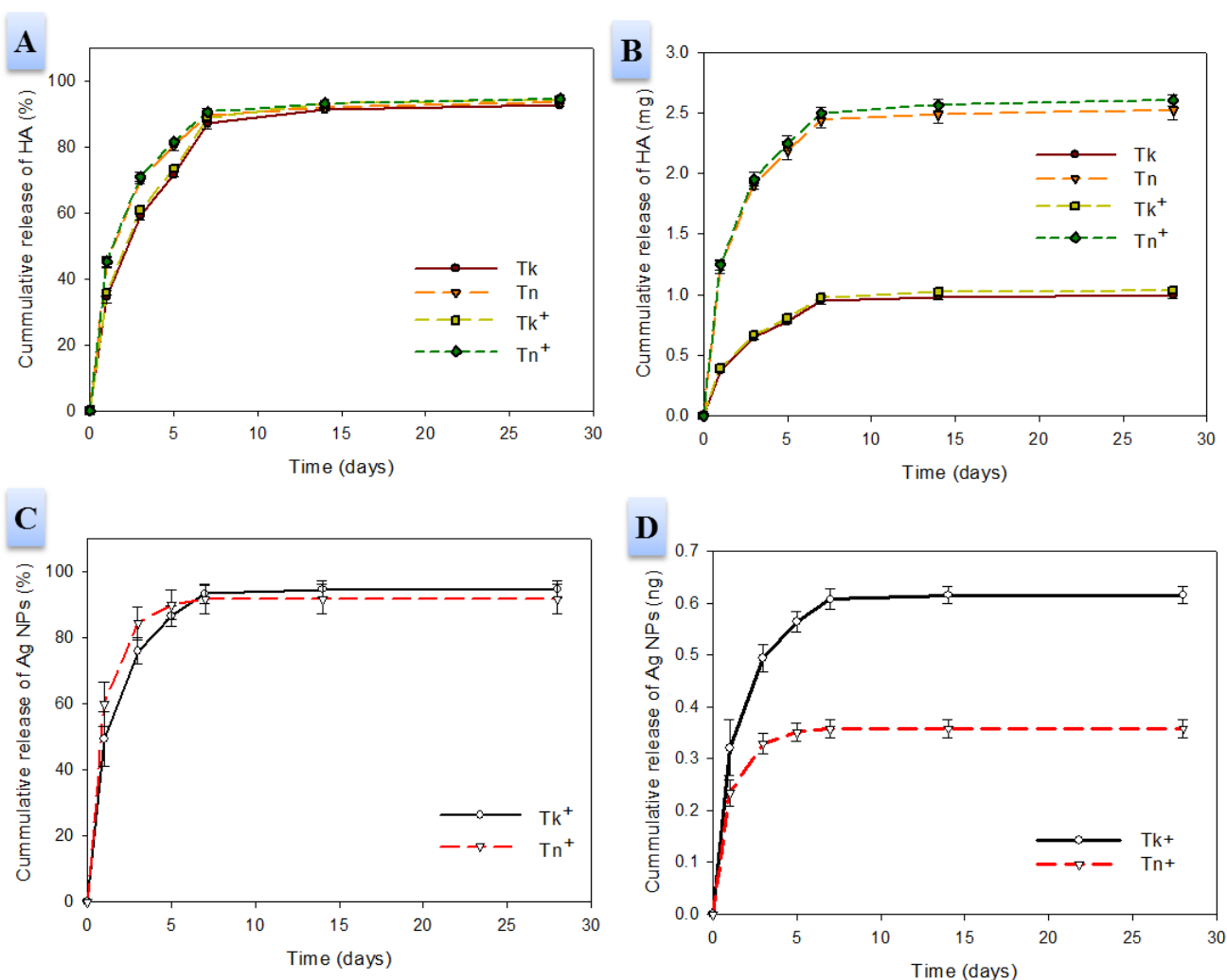


**Figure 5.** The cumulative release percentage (A) and cumulative released mass (B) of HA. The cumulative release percentage (C) and cumulative released mass (D) of Ag NPs.

For anti-bacteria activity of CSNFMs, we used two typical bacteria strains causing infection to determine the bacteriostatic efficacy against *S. aureus* and *E. coli* with released Ag NPs. As shown in Figure 6, bacteriostatic rings were readily observable around Tk<sup>+</sup> and Tn<sup>+</sup> membrane disks for both bacteria, while no zone of inhibition was observed for Tk and Tn. With diffusion of Ag NPs from the pre-wetted membrane to the surrounding test area on an agar plate, only Ag NPs-embedded CSNFMs can display anti-bacterial activity, by incorporating released Ag into the cell membrane and inducing cell death [38]. The corresponding zone of inhibition of Tk<sup>+</sup> is  $1.29 \pm 0.11 \text{ cm}^2$  for *E. coli* and  $0.97 \pm 0.15 \text{ cm}^2$  for *S. aureus* with difference in their wall structure. The *S. aureus* is a Gram-positive strain, which has thicker peptidoglycan layer in the cell wall than the Gram-negative *E. coli*, making the penetration of Ag NPs more difficult when interfering with the metabolic pathways [39]. In comparison, the inhibition zone of Tn<sup>+</sup> is  $1.04 \pm 0.14 \text{ cm}^2$  for *E. coli* and  $0.92 \pm 0.14 \text{ cm}^2$  for *S. aureus* as less Ag NPs were released from the membranes (Figure 5D).

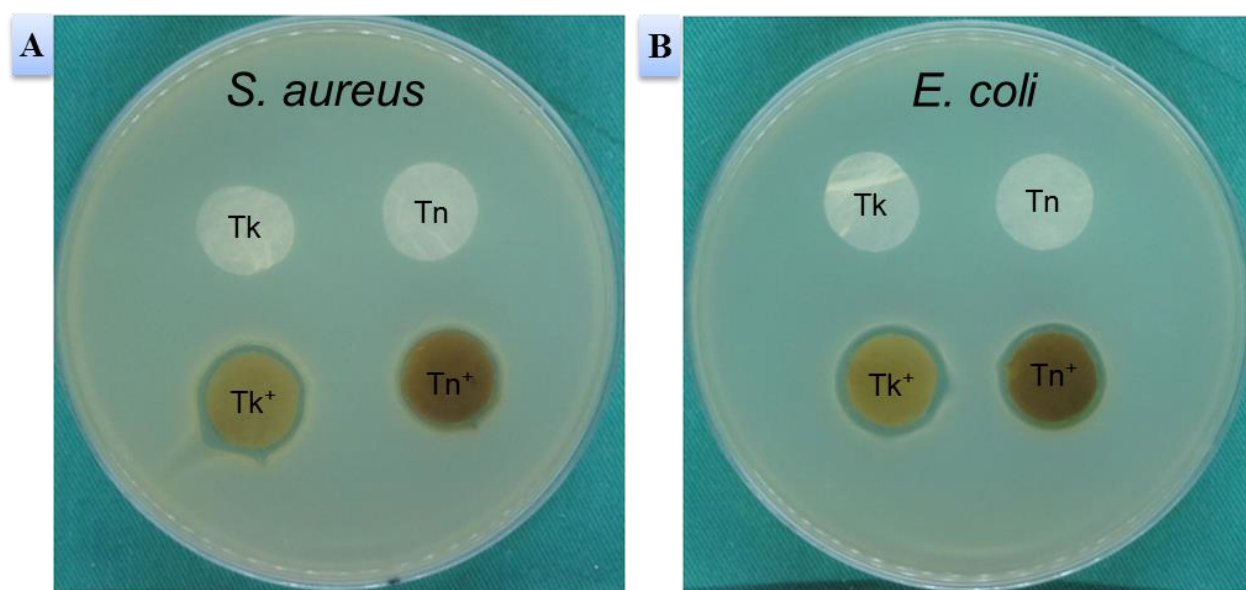


**Figure 6.** The antibacterial activity of CSNFMs determined from the bacteriostatic rings for *S. aureus* (A) and *E. coli* (B). A disk shaped membrane with 1.5 cm diameter is used in the study and the weight of Ag NPs in Tn<sup>+</sup> and TK<sup>+</sup> are ~0.0195 and ~0.0325 mg, respectively.

### 2.3. In Vitro Cell Culture

The penetration of 3T3 fibroblasts during in vitro cell culture was tested by serum concentration-induced cell migration to the lower chamber of a double chamber dish, by placing a CSNFM at the bottom of a cell insert fitted in the upper chamber. The control is without using a membrane in the cell culture insert. The amount of migrated 3T3 fibroblasts to the lower chamber was determined from the MTS assays. As shown in Figure 7, the penetrated cells in all CSNFMs were only ~10% that in the control group, with no significant difference found between different membranes. Microscopic observation of the bottom chamber surface also confirmed these findings, with minimal cells found on the bottom chamber surface using a CSNFM as a barrier, in contrast to abundant cells found in the control. These findings are consistent with the results from pore size analysis, as the pore size of all CSNFMs was much smaller than the size of fibroblasts to effectively block cell penetration. Taken together, the hindered cell migration through a CSNFM supports the choice of such a macroporous structured membrane to block fibroblast penetration, mitigate tendon adhesion, and ultimately achieve desirable anti-adhesion effects in vivo, pending evaluation of their effects on cell attachment and cytotoxicity.

The possible cytotoxicity of Tk and Tk<sup>+</sup> was determined using the indirect method by culturing fibroblasts with a 24-h extract of a CSNFM membrane, to realize whether any of the constituents of CSNFMs have cytotoxic effects. By normalizing the MTS absorbance of the sample (extract) with that of the control (fresh cell culture medium), the relative cell viability was  $93.3 \pm 2.7\%$  for Tk, indicating no cytotoxicity is associated with all constituents within this CSNFM, excluding Ag NPs. (Figure 8A). The relative cell viability decreased to  $78.8 \pm 3.4\%$  and  $74.5 \pm 3.8\%$  for Tk<sup>+</sup> prepared with 0.1% and 0.25% AgNO<sub>3</sub>, with no significant difference. Both samples also meet the requirement for a non-toxic medical device per ISO 10993-5 standard (>70% viability). However, for Tk<sup>+</sup> membranes prepared with 0.5% AgNO<sub>3</sub>, cell viability drastically decreased to  $49.0 \pm 2.3\%$ , implicating overdosing of AgNO<sub>3</sub> in the shell spinning solution could raise the cytotoxicity of CSNFMs. This may arise due to incomplete reduction of Ag<sup>+</sup>, with cytotoxicity induced by Ag NPs to be much lower than that caused by Ag<sup>+</sup> on mammalian cells [40]. Taken together, we confirm a 0.25% AgNO<sub>3</sub> dose in the sheath spinning solution would be ideal, considering both bacteriostatic effect and tolerable cytotoxicity, which was adopted for preparation of Tn<sup>+</sup> and Tk<sup>+</sup> CSNFMs.

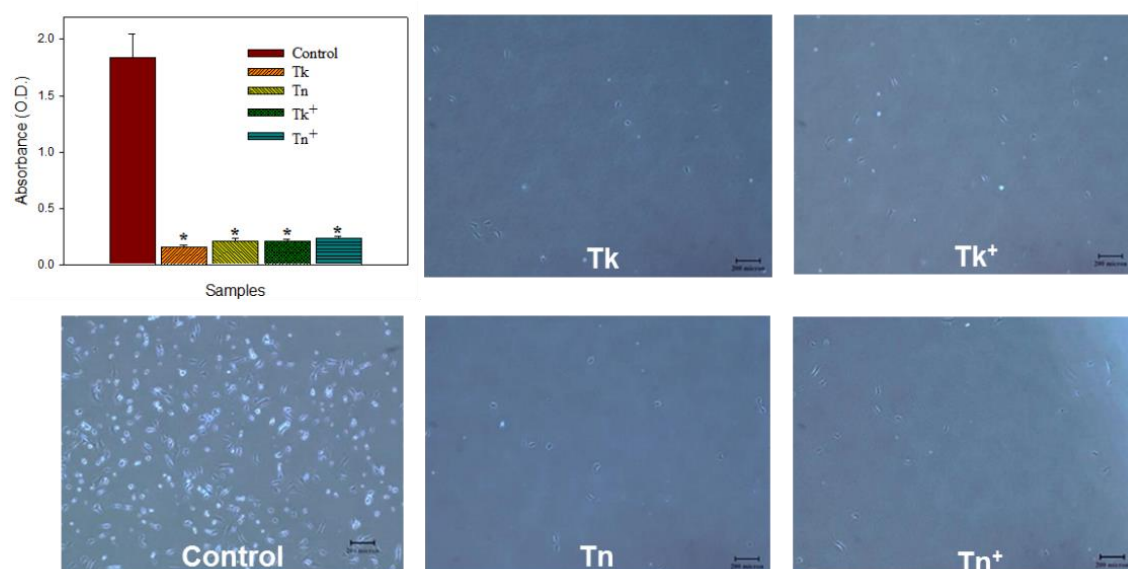


**Figure 7.** The penetration of 3T3 fibroblasts through a CSNFM in 24 h by determining penetrated cell number from solution absorbance with MTS assays, and direct microscopic observation of penetrated cells (bar = 200 μm). The control is without a CSNFM. \*  $p < 0.05$  compared with control.

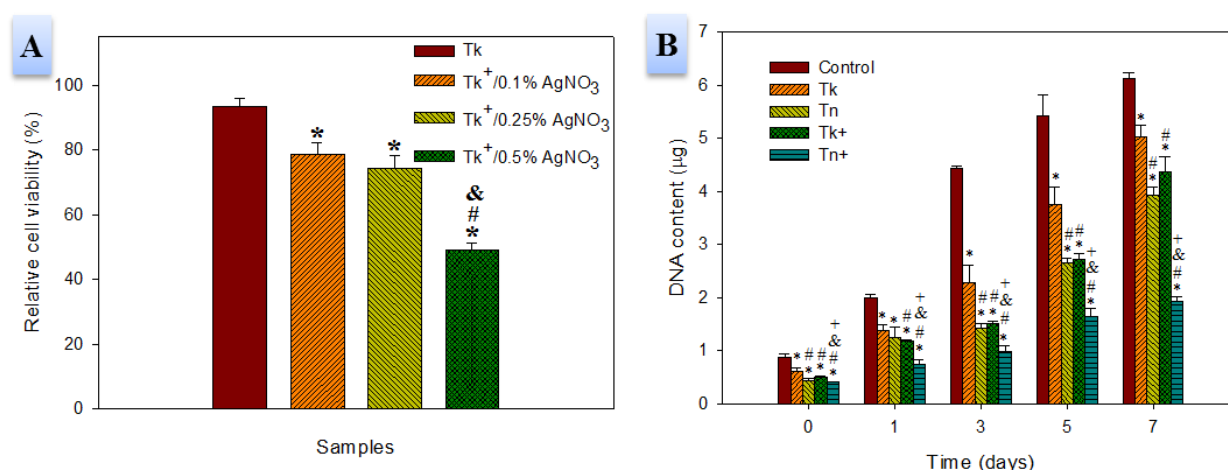


**Figure 8.** (A) The cytotoxicity tests of CSNFMs using the indirect contact method. \*  $p < 0.05$  compared with Tk; #  $p < 0.05$  compared with Tk<sup>+</sup>/0.1% AgNO<sub>3</sub>; &  $p < 0.05$  compared with Tk<sup>+</sup>/0.25% AgNO<sub>3</sub>. (B) The attachment and proliferation of 3T3 fibroblasts on control (TCPS) and CSNFMs from DNA assays. \*  $p < 0.05$  compared with control; #  $p < 0.05$  compared with Tk; &  $p < 0.05$  compared with Tn; +  $p < 0.05$  compared with Tk<sup>+</sup>.

The attachment and proliferation of fibroblasts was studied by seeding 3T3 cells on CSNFMs and cultured for seven days, before determining cell numbers with DNA assays. The cell attachment on all CSNFMs was much lower than that on a tissue culture polystyrene (TCPS) plate that is used as a control (Figure 8B), suggesting that all membranes developed in this study could reduce fibroblast attachment. Nonetheless, the Tn<sup>+</sup> shows significant reduction of adhered cell number from other membranes. The drastic drop in number of adhered cells in CSNFMs compared with the control is consistent with our previous studies and may be due to the synergistic effects of HA and Ag NPs as Tk<sup>+</sup> (Tn<sup>+</sup>) showed significant decrease of attached fibroblasts compared with Tk (Tn) [41]. Previously, HA was shown to have a strong influence on the adhesion of fetal fibroblasts [42], while Ag NPs are known to reduce fibroblast adhesion [43]. The membranes with thinner sheath (Tn and Tn<sup>+</sup>) also demonstrated lower cell attachment than Tk and Tk<sup>+</sup>, indicating more



HA released from thin-sheath membrane is beneficial in reducing cell attachment from combined lubrication and anti-adhesion effects [44].

For cell proliferation, the cell number on day 1, 3, 5, and 7 followed the same trend as day 0, with TCPS showing the maximum cell number and Tn<sup>+</sup> the minimum (Figure 8B). We can ascribe this effect on cell proliferation to released HA and Ag NPs, where previous reports found hindrance of fibroblast proliferation caused by high concentrations of HA [45,46], and reduction in fibroblasts proliferation reported for Ag NPs [47]. The Live/Dead staining images of fibroblasts on CSNFMs in Figure 9 support the trend observed in Figure 8B with more cells observed on Tk and Tk<sup>+</sup> relative to that on Tn on day 7, but the least number of viable cells were found on Tn<sup>+</sup>.

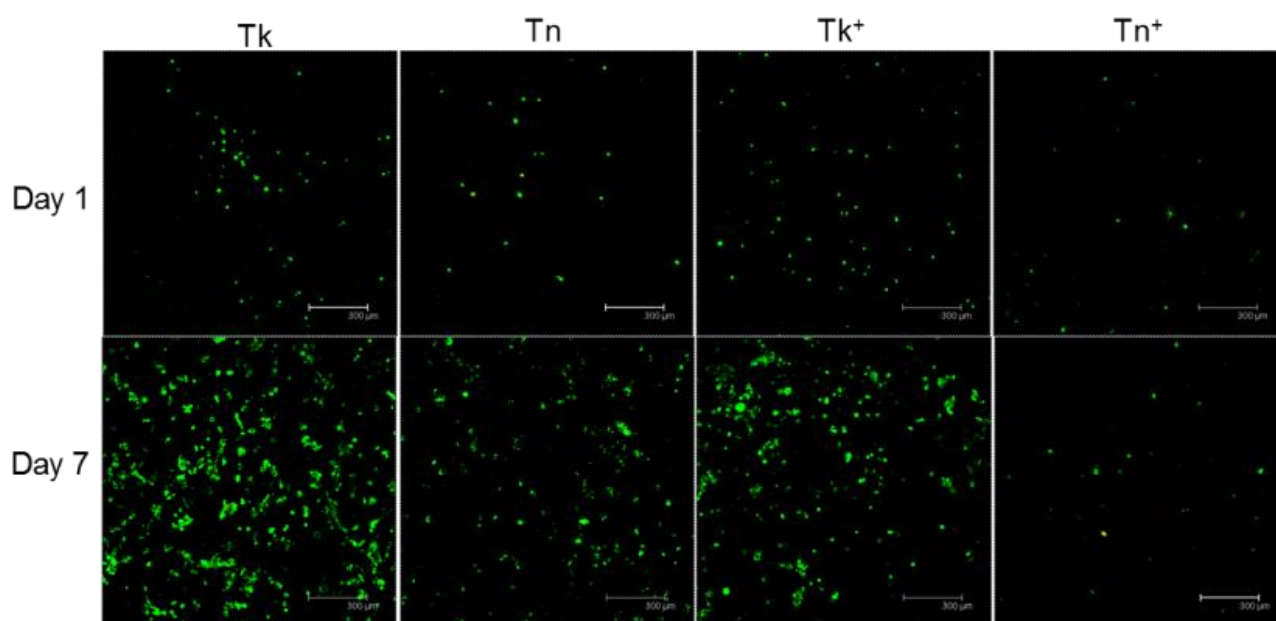


**Figure 9.** The Live/Dead staining of fibroblasts on CSNFMs by calcein AM and propidium iodide for live (green) and dead (red) cells after cultured for one and seven days and observed by confocal laser scanning microscopy. Bar = 300  $\mu$ m.

To elucidate the molecular mechanism of reduced fibroblast attachment on the membrane, the expression of a focal adhesion protein (vinculin) as well as cytoskeletal actin distribution in 3T3 fibroblasts were observed under a confocal microscope after cultured for 24 h. As shown in Figure 10, fibroblasts attached to TCPS showed distinctive cellular spreading with flattened cell morphology to result in enhanced vinculin (green fluorescence) expression and a well-distributed F-actin fibrous cytoskeleton (red fluorescence). By comparison, the fibroblasts found on CSNFMs were relatively round, showed minimal vinculin expression, and showed restricted cytoskeletal distribution without obvious stretching and cellular spreading, indicative of poor cell adhesion [48]. This may be supported from a previous report reporting the negative impact of HA on cellular adhesion and migration of skin dermal fibroblasts [49]. A synergistic effect was found by combining Ag NPs with HA as Tn<sup>+</sup>, with Ag NPs embedded in the thin sheath and the highest amount of released HA, which demonstrated the least staining of vinculin by inhibiting cell adhesion as well as suppressing cell spreading. Thus, we used Tn<sup>+</sup> membrane to compare with Tn in the animal study to elucidate the effects from Ag NPs in vivo.

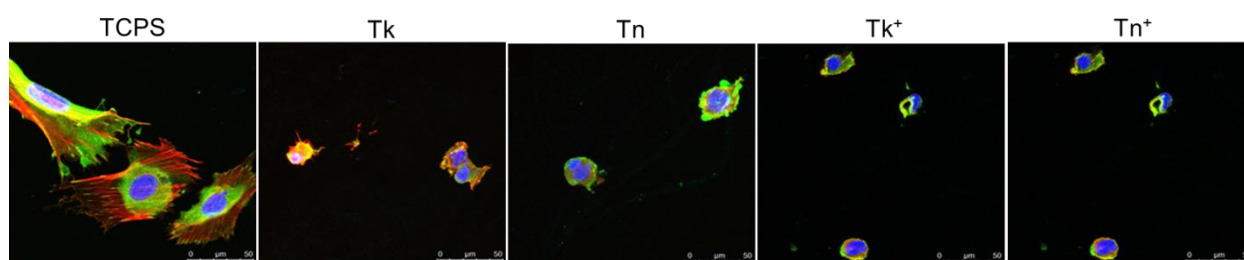


**Figure 10.** The cytoskeletal F-actin (red) distribution and vinculin focal adhesion protein (green) expression of fibroblasts after cultured on control (TCPS) and different CSNFMs for one day and examined under a confocal laser scanning microscope. The cell nuclei were counterstained with DAPI (blue). Bar = 50  $\mu$ m.

#### 2.4. In Vivo Studies

Using SurgiWrap<sup>®</sup> as a positive control, Tn vs Tk for the effect of HA, and Tn vs Tn<sup>+</sup> for the effect of Ag NPs, we carried out animal studies with a flexor digitorum profundus (FDP) tendon rupture model in rabbits. Direct visualization of the rabbit flexor tendons showed similar extents of peritendinous adhesions for the control (untreated) group and the Tk group, with the flexor tendon being firmly attached to the surrounding tissue with tight adhesions (Figure 11). These adhesions are composed of excessive fibrous tissues in which fibroblast aggregated in the process of wound repair. The adhesions also completely covered the injured tendon such that a strong force was required to separate the tendon from the surrounding tissues. In contrast to the control and Tk groups, mild degree of peritendinous adhesions with minimal adhesion bands were observed in the positive control (SurgiWrap<sup>®</sup>) and Tn groups, while the Tn<sup>+</sup> group showed a nearly complete lack of adhesion (Figure 11).

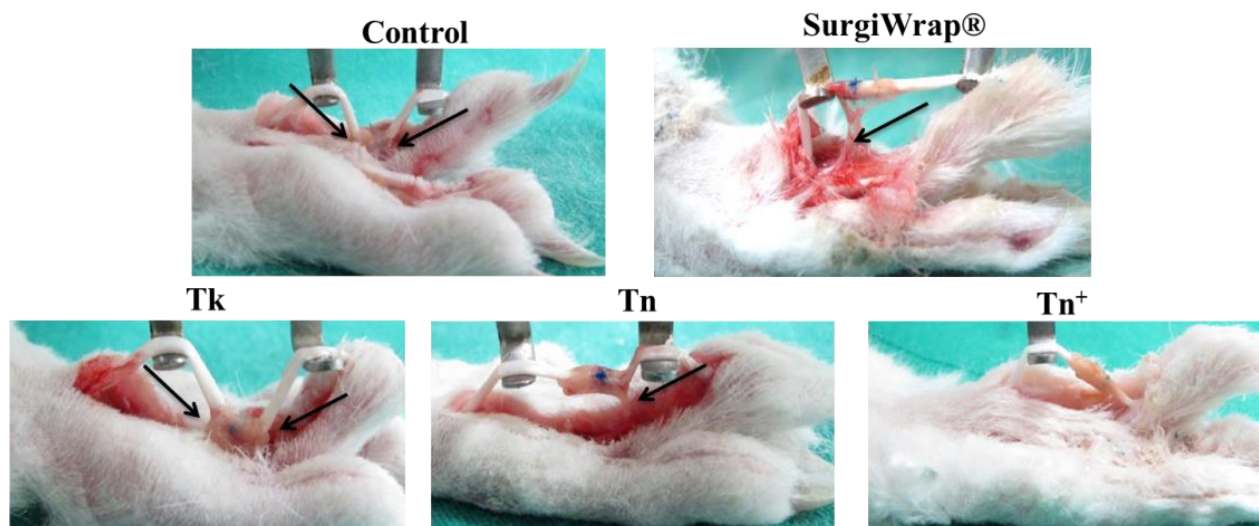


**Figure 11.** The rabbit flexor tendons observed three weeks post-operatively. Note the substantial peritendinous adhesions (black arrows) in the control and Tk groups, with fewer adhesions observed in the SurgiWrap<sup>®</sup> and Tn groups. Peritendinous adhesions are absent in the Tn<sup>+</sup> group.

From biomechanical analysis, the flexion angles of the distal interphalangeal (DIP) and proximal interphalangeal (PIP) joints show a comparable pattern to the gross examination of peritendinous adhesions, with the untreated control group performing similarly to the Tk group (Figure 12A,B). Though there are no significant differences between these two groups for the DIP joint flexion angles, the PIP joint flexion angles of the Tk group were significantly worse than the untreated control group. Findings for the SurgiWrap<sup>®</sup> and Tn groups were also alike without any significant differences between them but showed

improvement over control and Tk. Most importantly, the Tn<sup>+</sup> group performed significantly better than all other groups. A similar pattern is also observed for tendon gliding excursion and pull-out force (Figure 12C,D). These findings are directly compatible with the amount of peritendinous adhesions observed from gross examination. Mechanical testing for the force tolerated before rupture of healed tendon revealed no significant difference among all groups (Figure 12E). This supports the idea that neither CSNFMs or SurgiWrap® will affect the normal process of tendon healing [50]. Based on these findings, wrapping the injured tendon with a Tn<sup>+</sup> CSNFM is deemed the most effective treatment to exert the anti-adhesion effect while still allowing normal healing of the contained tendon.

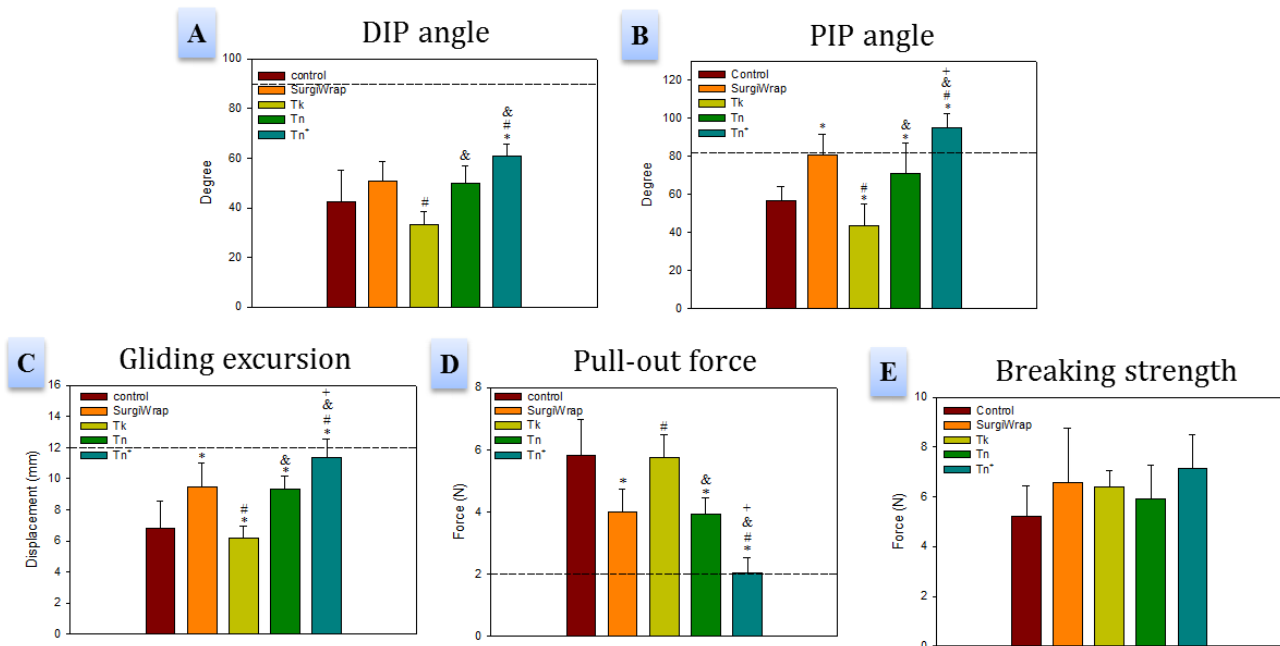


**Figure 12.** The assessment of peritendinous adhesions three weeks post-operation for distal interphalangeal (DIP) flexion angle (A), proximal interphalangeal (PIP) flexion angle (B), tendon gliding distance (C), and pull-out force (D). The dotted line represents the average value found for normal flexor digitorum profundus tendons. (E) Comparison of the breaking strength of healed tendons at three weeks. \*  $p < 0.05$  compared with control; #  $p < 0.05$  compared with SurgiWrap®; &  $p < 0.05$  compared with Tk; +  $p < 0.05$  compared with Tn. The data are expressed as mean  $\pm$  standard deviation ( $n = 8$ ).

Considering adverse effects from treatments, the blood samples taken from the animals one week post-operatively revealed no significant differences between the control and all experiment groups from complete blood count (Figure 13A), renal (Figure 13B), and liver (Figure 13C) function assessments. The results verify that wrapping CSNFMs around the injured tendons of the rabbits will not cause noticeable inflammatory responses or metabolic abnormalities in the liver and kidney. Hence, the materials did not directly influence the rabbits' physiological conditions.

From histological examination in Figure 14, the hematoxylin and eosin (H&E) stain of the tendon tissue sections revealed severe adhesions between the tendon and the surrounding tissues for the unwrapped control group, leading to the severe restriction of tendon movement. The Tk membrane treated tendon also exhibited postoperative adhesion between the tendon suture and its surrounding tissues. In the SurgiWrap® and Tn groups, loose fibrous tissues formed around the repaired tendon, resulting in mild adhesion. There is a noticeable gap between the membrane and the surrounding tissue, allowing better tendon sliding. Compared with other groups, the Tn<sup>+</sup> group exhibited excellent anti-adhesion effect with the least loose fibrous tissue formation while still retained a sizable interval between the tendon and its surrounding tissue. Masson trichrome staining was used to observe collagen fiber distribution and morphology (Figure 14). In the unwrapped control



group, collagen arrangement was relatively irregular. In contrast, the Tn<sup>+</sup> CSNFM group demonstrated the most regular collagen arrangement.

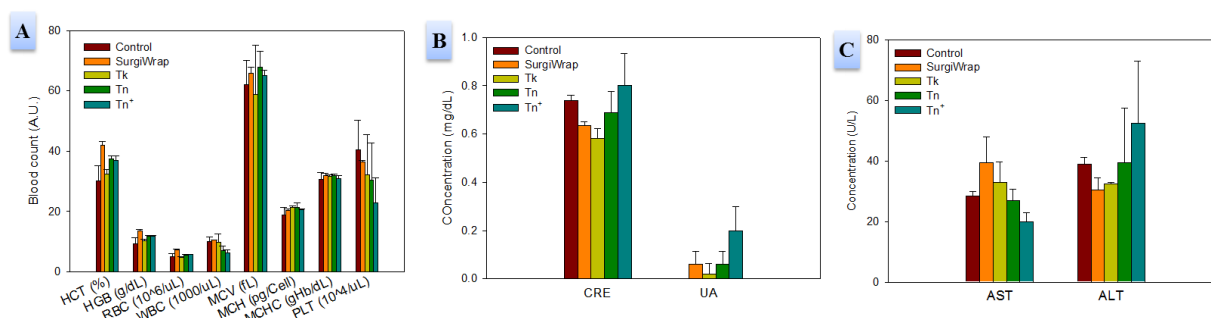


**Figure 13.** The blood testing results at one week postoperatively from complete blood count (A), renal (B), and liver (C) functions assessments. HCT, hematocrit; HGB, hemoglobin; RBC, red blood cell; WBC, white blood cell; MCV, mean corpuscular volume; MCH, mean corpuscular hemoglobin; MCHC: mean corpuscular hemoglobin concentration; PLT, platelet; CRE, creatinine; UA, uric acid; AST, aspartate aminotransferase; ALT, alanine aminotransferase. The data are expressed as mean  $\pm$  standard deviation ( $n = 8$ ).

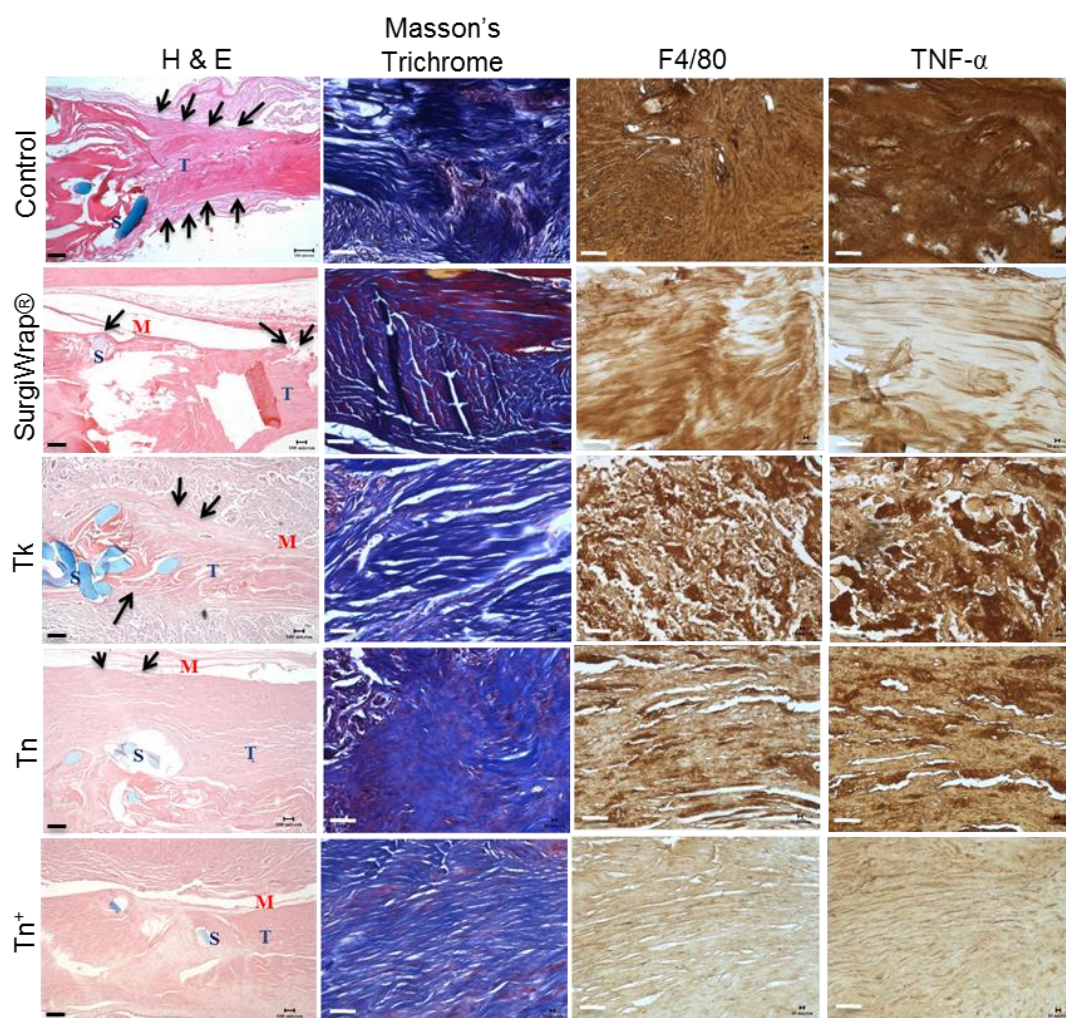


**Figure 14.** The histological analysis of untreated tendons (control group), tendons treated with SurgiWrap®, and tendons treated with Tk, Tn, or Tn<sup>+</sup> CSNFMs. The hematoxylin-eosin (H&E) staining shows adhesion tissues around repaired tendon (black arrows) as well the position of suture (S), tendon (T), and membrane (M) (bar = 200  $\mu$ m). The Masson's trichrome stain and immunohistochemical (IHC) staining of TNF- $\alpha$  and F4/80 are included (bar = 50  $\mu$ m).



When a tendon is injured or damaged during surgery, the body initiates an inflammatory response in response to the insult with macrophages aggregate in the wound, attaching to the damaged tissue. As a glycoprotein member of the epidermal growth factor-transmembrane 7 family, F4/80 is expressed on the majority of tissue macrophages as a widely used murine macrophage marker [51]. F4/80 immunohistochemical (IHC) staining can, thus, be used to determine the extent of postoperative tendon inflammation [52]. The F4/80 IHC staining image for the untreated control group exhibited deep staining (Figure 14), implying the abundance of F4/80 expression in the tendon arising from a more severe inflammatory response. The SurgiWrap<sup>®</sup>, Tk, and Tn groups also had marked staining for F4/80, though on a less severe level than the untreated control. Compared to other groups, the Tn<sup>+</sup> group exhibited considerably lighter staining, indicating a milder inflammation response. Because Ag NPs exerted an anti-inflammatory effect, postoperative inflammation was milder in the Tn<sup>+</sup>-wrapped group [53]. Tumor necrosis factor- $\alpha$  (TNF- $\alpha$ ) is a major pro-inflammatory cytokine that is expressed in the early stage of cell inflammation and induces apoptosis [54]. As TNF- $\alpha$  is produced by macrophages/monocytes during acute inflammation, we also used IHC staining to investigate the presence of this inflammatory cytokine around the site of repaired tendon. The staining intensity of the pro-inflammatory cytokine TNF- $\alpha$  in Tn<sup>+</sup> is much weaker than all the other groups, with light brown color, endorsing the anti-inflammation performance of this CSNFM due to Ag NPs (Figure 14). This effect is consistent with a recent study confirming the anti-inflammatory activity of Ag NPs originating from inhibition of production of pro-inflammatory cytokines (IL-1 $\beta$ , IL-6 and TNF- $\alpha$ ) in macrophages [55]. Using both TNF- $\alpha$  and F4/80 as macrophage markers, we confirm from IHC staining the dominance of the Ag NPs-embedded CSNFM (Tn<sup>+</sup>) over the commercially available barrier material (SurgiWrap<sup>®</sup>) as well as CSNFMs without Ag NPs (Tk and Tn) in preventing post-surgical tendon inflammation *in vivo*.

### 3. Materials and Methods

#### 3.1. Materials

Poly(L-lactide-co-D,L-lactide) (Resomer<sup>®</sup> LR704S, L-Lactide:D,L-Lactide = 70:30, intrinsic viscosity = 2.4 dL/g), polyethylene oxide (PEO, molecular weight = 2,000,000 Da), silver nitrate (AgNO<sub>3</sub>), Dulbecco's modified Eagle's medium (DMEM), and actin cytoskeleton/focal adhesion staining Kit (FAK100) were purchased from Sigma-Aldrich (St. Louis, MO, USA). Hyaluronic acid (HA, average molecular weight = 1,300,000 Da) was obtained from Shandong Freda Biochem Co., Ltd. (Jinan, China). Antibiotics, LIVE/DEAD<sup>®</sup> Viability/Cytotoxicity kit for mammalian cells, fetal bovine serum (FBS), and trypsin-EDTA were acquired from Life Technologies (Carlsbad, CA, USA). SurgiWrap<sup>®</sup> was purchased from MAST Biosurgery (San Diego, CA, USA). CellTiter 96<sup>®</sup> AQueous One Solution Cell Proliferation Assay was obtained from Promega (Madison, WI, USA).

#### 3.2. Preparation of Core-Sheath Nanofibrous Membrane (CSNFMs)

The CSNFMs were produced by co-axial electrospinning with two polymer solutions prepared separately for the core and sheath compartments. The sheath spinning solution was prepared by dissolving PLA in a 7:3 (*v/v*) methylene chloride (MC) and N,N'-dimethylformamide (DMF) solution to reach 5% (*w/v*) polymer concentration. For Ag NPs-embedded CSNFMs, the spinning solution contains 0.25% (*w/v*) AgNO<sub>3</sub> prepared in 7:3 (*v/v*) MC/DMF, which was exposed to 254 nm UV light exposure at 0.1 J/cm<sup>2</sup> for 3 h in a UV Crosslinker to form Ag NPs. For the core spinning solution, 0.2 g of HA and 0.05 g of PEO were dissolved in 10 mL of formic acid. A commercial electrospinning system (Falco Tech Enterprise, Co. Ltd., New Taipei City, Taiwan) was used, containing two syringe pumps connected to a high-voltage power supply and a co-axial spinneret for electrospinning. The solution flow rates for the core and sheath are 0.5 mL/h and 1 mL/h, respectively, for the CSNFMs with thick sheath (Tk) while they are 1 mL/h and 0.5 mL/h for the CSNFMs with thin sheath (Tn). The applied voltage was 25 kV and nanofibers were collected on an aluminum foil placed 15 cm from the needle tip. For Ag NPs-embedded

nanofibers, termed Tk<sup>+</sup> for the thick-sheath and Tn<sup>+</sup> for the thin-sheath, the CSNFMs were prepared following the same fabrication condition using the Ag NPs-containing sheath solution.

### 3.3. Characterization of Core-Sheath Nanofibrous Membrane (CSNFMs)

The morphology of nanofibers was observed under a scanning electron microscope (SEM, Hitachi S3000N, Tokyo, Japan) at 15 kV. The average fiber diameter was estimated from 100 randomly chosen nanofibers from five images (20 each) using the ImageJ software. A transmission electron microscope (TEM, Hitachi H-7500, Tokyo, Japan) was used to examine the core-sheath structure at 75 kV. The membrane pore size was measured by using a capillary flow porometer (CFRP-1500AE, Porous Materials Inc., Ithaca, NY, USA) using Galwick<sup>®</sup> with 15.9 dyne/cm surface tension. For X-ray diffraction (XRD) analysis, a Siemens D5005 X-ray diffractometer was used for scanning from  $2\theta = 10^\circ$  to  $60^\circ$  at  $1.2^\circ/\text{min}$  scanning speed. For surface chemical composition analysis, a PHI 1600 ESCA spectrometer from Physical Electronics (Chanhassen, MN, USA) was used for high-resolution X-ray photoelectron spectroscopy (XPS). The amount of Ag NPs in the membranes was determined from coupled plasma optical emission spectrometry (ICP-OES) analysis (Agilent 725, Santa Clara, CA, USA). A side-by-side permeation chamber was to determine the diffusion of bovine serum albumin (BSA) through a membrane at  $37^\circ\text{C}$ . By placing a CSNFM or SurgiWrap<sup>®</sup> firmly between the two half-cells, the permeability coefficient of BSA was calculated from the time-lapsed protein concentration change in the receptor cell [56].

### 3.4. Release of HA and Ag NPs

The release of HA and Ag NPs from a 1.5-cm disk-shaped CSNFM was determined in 3 mL of PBS (pH 7.4) placed in a 20 mL glass vial at  $37^\circ\text{C}$ . At predetermined times, all PBS was removed and replenished with equal volume of PBS to continue the experiment. The concentration of HA in the PBS was analyzed with an ELISA kit for HA and the amount of Ag released was analyzed using ICP-OES after digesting with 5% nitric acid. The cumulative weight of HA or Ag released from the membrane was determined by adding the total amount of HA or Ag released up to a certain time. The cumulative percentage HA or Ag released from the membrane was calculated by dividing the cumulative released weight with the weight initially loaded in the membrane. After the release experiments, the membranes were immersed in liquid nitrogen and broken to expose the cross section. Samples were examined for core-sheath morphology using FE-SEM (JSM-7500F, JEOL, Tokyo, Japan) and TEM (JEM-1230, JEOL, Tokyo, Japan).

### 3.5. In Vitro Cell Culture

#### 3.5.1. Anti-Bacterial Activity

The anti-bacterial activity CSNFMs was tested against Gram-positive (*Staphylococcus aureus*, BCRC 10451) and Gram-negative (*Escherichia coli*, BCRC 11634) bacteria. The strains were cultured in 10 mL of Luria-Bertani broth for inoculation on an agar plate. Disk-shaped CSNFMs (1.5-cm diameter) were pre-wetted with PBS and placed in the agar plate for incubation at  $37^\circ\text{C}$  for 24 h. The zone of inhibition was calculated from the area ( $\text{cm}^2$ ) of the bacteriostatic ring around the membrane.

#### 3.5.2. Cell Penetration

For cell penetration tests, a CSNFM was fitted to the bottom porous membrane of a cell insert (Transwell<sup>®</sup> cell culture inserts, Corning, Tewksbury, MA, USA), which is fitted in the upper chamber of a double-chamber dish. A cell insert without a CSNFM was used as the control. NIH/3T3 mouse embryonic fibroblasts (ATCC-CRL1658) ( $2.5 \times 10^5$  cells) diluted in DMEM/2% FBS were added to the upper chamber and the lower chamber was filled with DMEM/10% FBS. After incubated for 24 h at  $37^\circ\text{C}$ , cell penetration driven by FBS concentration gradient was determined from the number of viable cells in the lower chamber by using MTS assays (CellTiter 96<sup>®</sup> Aqueous Solution Cell Proliferation Assay)

at 492 nm with an ELISA plate reader. The direct microscopic observation of cells in the lower chamber was done using an inverted microscope (Olympus IX-71, Tokyo, Japan).

### 3.5.3. Cytotoxicity

The indirect contact method (ISO 10993-5:2009, biological evaluation of medical devices– Part 5: tests for in vitro cytotoxicity) was employed to test for in vitro cytotoxicity of CSNFMs. We cultured 3T3 fibroblasts ( $1.0 \times 10^4$  cells) at 37 °C with the extraction medium of membranes, which was prepared by incubating 15-mm diameter CSNFMs in 90% DMEM/10% FBS at 37 °C for 24 h. The MTS assay was used to measure the solution absorbance values at 492 nm and normalized to that from cells cultured with 90% DMEM/10% FBS.

### 3.5.4. Cell Attachment and Proliferation

We seeded 3T3 fibroblasts on a pre-wetted disc-shaped CSNFM of 15 mm diameter at  $1.0 \times 10^4$  seeding density and carried out cell culture at 37 °C with DMEM supplemented with 10% (v/v) FBS and 1% (v/v) antibiotic-antimycotic. A control was prepared by seeding the same amount of fibroblasts on tissue culture polystyrene (TCPS) plates. After 3 h, the membranes or TCPS plates were washed with DMEM to remove loosely attached cells for determination of cell attachment efficiency at day 0. The cell culture continued for up to seven days with medium change every other day. The cell proliferation rate was determined from number of cells attached to the CSNFMs (or TCPS plates) on day 1, 3, 5, and 7. The cell number was determined from the DNA content with Hoechst 33258 DNA assays. The distribution of live and dead fibroblasts on CSNFMs were assessed on day 1 and 7 using a LIVE/DEAD® Viability/Cytotoxicity kit containing the fluorescent molecular probe calcein AM and propidium iodide to visualize live cells (in green) and dead cells (in red) under a confocal laser scanning microscope (Zeiss LSM 510 Meta, Oberkochen, Germany).

### 3.5.5. Cytoskeletal and Vinculin Staining

Triple fluorescence staining of the cytoskeleton, vinculin, and nucleus were done for 3T3 cells cultured on the CSNFMs for 24 h. The membranes were washed with PBS and treated with 4% paraformaldehyde for 20 min; followed by permeabilizing cells with 0.1% Triton X-100 for 10 min. The cytoskeletal distribution was examined by incubating cultured cells with tetramethylrhodamine (TRITC)-conjugated phalloidin for 30 min to stain F-actin. Vinculin staining was accomplished by incubating the sample with mouse anti-vinculin primary antibody for 1 h, followed by incubating with FITC-conjugated goat anti-mouse IgG secondary antibody for 1 h. The visualization of nucleus was achieved by counter-staining with 4',6-diamidino-2-phenylindole (DAPI) for 5 min. The stained cells were observed under a confocal laser scanning microscope (Zeiss LSM 510 Meta, Oberkochen, Germany) for green, red and blue fluorescence originated from vinculin, actin cytoskeleton and nucleus in stained cells. A control with 3T3 cells seeded on TCPS plates was similarly stained and imaged.

## 3.6. In Vivo Studies

### 3.6.1. Animal Model

All animal experiment procedures carried out in this study were approved by the Institutional Animal Care and Use committee (IACUC) of Chang Gung University. A total of forty 3-month-old New Zealand white rabbits (National Laboratory Animal Breeding and Research Center, Taipei, Taiwan) were used in this study. The rabbits were grouped into three experimental groups (treated with Tk, Tn or Tn<sup>+</sup> CSNFMs), a positive control group (treated with SurgiWrap®), and a negative control group (untreated), with eight rabbits in each group. A flexor digitorum profundus (FDP) tendon rupture model of the hind paw similar to our previous study was used [22]. After the tendon sheaths were removed and the zone-II FDP tendons ruptured and repaired, each repair site is wrapped with an

8 × 10 mm strip of membrane (Tk, Tn or Tn<sup>+</sup>) for the experiment group and SurgiWrap™ for the positive control group. The negative control group was left untreated. Three weeks post-operatively, the rabbits were euthanized and the hind paws were removed at the ankle joints.

### 3.6.2. Gross Evaluation and Biomechanical Measurements

Three weeks post-operatively, each FDP tendon is photographed for gross evaluation to determine the severity of peritendinous adhesion. For biomechanical measurements, the range of motion for the distal interphalangeal (DIP) and proximal interphalangeal (PIP) joints were measured as the flexion angle. Tendon gliding is measured as the amount of tendon excursion observed when 1 N of pulling force is exerted on the FDP tendon. Post-operative tendon adhesion is evaluated by the pull-out force (maximum force required to fully remove a tendon from its sheath). The possible effect of treatment on the normal process of tendon healing is assessed by measuring the breaking force of healed tendon (the maximum tensile force that a tendon would withstand before its breakage).

### 3.6.3. Blood Test

To examine the possible adverse effect induced by the treatment, blood tests of the animals were conducted one week post-operatively. Complete blood count, and renal function (creatinine and uric acid) as well as liver function (alanine aminotransferase and aspartate aminotransferase) were assessed.

### 3.6.4. Histological Examination

The harvested samples were serially dehydrated in ethanol and the dehydrated specimens were then embedded in paraffin wax. The tissue block is shaved with a microtome knife to a thickness of 5 µm. The sections are mounted on glass slides that are heated to 70 °C and immersed in xylene for 5 min, repeating for three times before deparaffinizing the slides. The slides were then rehydrated for hematoxylin and eosin (H&E) and Masson's trichrome staining as well as immunohistochemical (IHC) staining of F4/80 and TNF-α.

### 3.7. Statistical Analysis

The mean and standard deviation were calculated for all data. The one-way analysis of variance (ANOVA) was used for statistical analysis with SPSS 10.0 (Chicago, USA). A p-value less than 0.05 were considered statistically significant. The post-hoc analysis was carried out with Fisher's Least Significant Difference (LSD) test.

## 4. Conclusions

In this study, we successfully prepared functional HA-PLA/Ag NPs CSNFMs with different sheath length scale and core diameter. By controlling the release rate of HA from the core and Ag NPs from the sheath, we demonstrate the best anti-adhesion outcomes offered by large-core/thin-sheath nanofibers with embedded Ag NPs (Tn<sup>+</sup>) in vivo. In vitro cell experiments confirm that the Tn<sup>+</sup> CSNFM can reduce attachment and prevent penetration of fibroblasts without exerting pronounced cytotoxicity in vitro. In addition, the Ag NPs-containing membranes are endowed with anti-bacterial activity by releasing Ag. In vivo studies with different CSNFMs and SurgiWrap® in a rabbit flexor tendon rupture model demonstrated that as a barrier membrane, the Tn<sup>+</sup> CSNFM can effectively reduce inflammation and prevent peritendinous adhesion after tendon surgery, based on gross observation, histological analysis, and functional assays.

**Author Contributions:** Conceptualization, C.-H.C. and J.-P.C.; methodology, C.-H.C. and J.-P.C.; formal analysis, Y.-H.C. and S.-H.C.; resources, J.-P.C.; data curation, Y.-H.C. and S.-H.C.; writing—original draft preparation, C.-H.C. and A.D.-C.C.; writing—review and editing, J.-P.C.; supervision, J.-P.C.; project administration, C.-H.C. and J.-P.C.; funding acquisition, C.-H.C. and J.-P.C. All authors have read and agreed to the published version of the manuscript.



**Funding:** This research was funded by the Ministry of Science and Technology, Taiwan, ROC (MOST109-2314-B-182-013-MY3) and Chang Gung Memorial Hospital, Taiwan, ROC (BMRP249, CMRPG3G1901 and CMRPD2J0113). The APC was funded by Chang Gung University.

**Institutional Review Board Statement:** The study was conducted according to the guidelines of the Declaration of Helsinki and approved by the Institutional Review Board of Chang Gung University.

**Informed Consent Statement:** Not applicable.

**Data Availability Statement:** The data presented in this study are available on request from the corresponding author.

**Acknowledgments:** We acknowledge the technical support by the Imaging Core Laboratories of the Institute for Radiological Research, Chang Gung Memorial Hospital, Linkou, and the Microscopy Center, Chang Gung University.

**Conflicts of Interest:** The authors declare no conflict of interest. The funders had no role in the design of the study; in the collection, analyses, or interpretation of data; in the writing of the manuscript, or in the decision to publish the results.

## References

1. Beyene, R.T.; Kavalukas, S.L.; Barbul, A. Intra-abdominal adhesions: Anatomy, physiology, pathophysiology, and treatment. *Curr. Probl. Surg.* **2015**, *52*, 271–319. [\[CrossRef\]](#) [\[PubMed\]](#)
2. Dy, C.J.; Hernandez-Soria, A.; Ma, Y.; Roberts, T.R.; Daluiski, A. Complications After Flexor Tendon Repair: A Systematic Review and Meta-Analysis. *J. Hand Surg.* **2012**, *37*, 543–551. [\[CrossRef\]](#) [\[PubMed\]](#)
3. Titan, A.L.; Foster, D.S.; Chang, J.; Longaker, M.T. Flexor Tendon: Development, Healing, Adhesion Formation, and Contributing Growth Factors. *Plast. Reconstr. Surg.* **2019**, *144*, 639e–647e. [\[CrossRef\]](#)
4. Evanko, S.P.; Potter-Perigo, S.; Petty, L.J.; Workman, G.A.; Wight, T.N. Hyaluronan Controls the Deposition of Fibronectin and Collagen and Modulates TGF- $\beta$ 1 Induction of Lung Myofibroblasts. *Matrix Biol.* **2015**, *42*, 74–92. [\[CrossRef\]](#)
5. de Melo, F.; Carrijo, A.; Hong, K.; Trumbic, B.; Vercesi, F.; Waldorf, H.A.; Zenker, S. Minimally Invasive Aesthetic Treatment of the Face and Neck Using Combinations of a PCL-Based Collagen Stimulator, PLLA/PLGA Suspension Sutures, and Cross-Linked Hyaluronic Acid. *Clin. Cosmet. Investig. Dermatol.* **2020**, *13*, 333–344. [\[CrossRef\]](#)
6. Narayanan, G.; Vernekar, V.N.; Kuyinu, E.; Laurencin, C.T. Poly (lactic acid)-based biomaterials for orthopaedic regenerative engineering. *Adv. Drug Deliv. Rev.* **2016**, *107*, 247–276. [\[CrossRef\]](#)
7. Peres, C.; Matos, A.I.; Connot, J.; Sainz, V.; Zupančič, E.; Silva, J.M.; Graça, L.; Sá Gaspar, R.; Préat, V.; Florindo, H.F. Poly(lactic acid)-based particulate systems are promising tools for immune modulation. *Acta Biomater.* **2017**, *48*, 41–57. [\[CrossRef\]](#) [\[PubMed\]](#)
8. Santoro, M.; Shah, S.R.; Walker, J.L.; Mikos, A.G. Poly(lactic acid) nanofibrous scaffolds for tissue engineering. *Adv. Drug Deliv. Rev.* **2016**, *107*, 206–212. [\[CrossRef\]](#)
9. Dubey, S.P.; Thakur, V.K.; Krishnaswamy, S.; Abhyankar, H.A.; Marchante, V.; Brighton, J.L. Progress in environmental-friendly polymer nanocomposite material from PLA: Synthesis, processing and applications. *Vacuum* **2017**, *146*, 655–663. [\[CrossRef\]](#)
10. Ates, B.; Koytepe, S.; Ulu, A.; Gurses, C.; Thakur, V.K. Chemistry, Structures, and Advanced Applications of Nanocomposites from Biorenewable Resources. *Chem. Rev.* **2020**, *120*, 9304–9362. [\[CrossRef\]](#)
11. Saini, P.; Arora, M.; Ravi Kumar, M.N.V. Poly(lactic acid) blends in biomedical applications. *Adv. Drug Deliv. Rev.* **2016**, *107*, 47–59. [\[CrossRef\]](#)
12. Komachi, T.; Sumiyoshi, H.; Inagaki, Y.; Takeoka, S.; Nagase, Y.; Okamura, Y. Adhesive and Robust Multilayered Poly(lactic acid) Nanosheets for Hemostatic Dressing in Liver Injury Model. *J. Biomed. Mater. Res. Part B Appl. Biomater.* **2016**, *105*, 1747–1757. [\[CrossRef\]](#)
13. Ospina-Orejarena, A.; Vera-Graziano, R.; Castillo-Ortega, M.M.; Hinestroza, J.P.; Rodriguez-Gonzalez, M.; Palomares-Aguilera, L.; Morales-Moctezuma, M.; Maciel-Cerda, A. Grafting collagen on poly (lactic acid) by a simple route to produce electrospun scaffolds, and their cell adhesion evaluation. *Tissue Eng. Regen. Med.* **2016**, *13*, 375–387. [\[CrossRef\]](#)
14. Zhang, C.; Wang, L.; Zhai, t.; Wang, X.; Dan, Y.; Turng, L.-S. The surface grafting of graphene oxide with poly(ethylene glycol) as a reinforcement for poly(lactic acid) nanocomposite scaffolds for potential tissue engineering applications. *J. Mech. Behav. Biomed. Mater.* **2016**, *53*, 403–413. [\[CrossRef\]](#) [\[PubMed\]](#)
15. Sensini, A.; Gualandi, C.; Cristofolini, L.; Tozzi, G.; Dicarlo, M.; Teti, G.; Mattioli-Belmonte, M.; Focarete, M.L. Biofabrication of bundles of poly(lactic acid)-collagen blends mimicking the fascicles of the human Achille tendon. *Biofabrication* **2017**, *9*, 015025. [\[CrossRef\]](#) [\[PubMed\]](#)
16. Zeng, S.; Ye, J.; Cui, Z.; Si, J.; Wang, Q.; Wang, X.; Peng, K.; Chen, W. Surface biofunctionalization of three-dimensional porous poly(lactic acid) scaffold using chitosan/OGP coating for bone tissue engineering. *Mater. Sci. Eng. C Mater. Biol. Appl.* **2017**, *77*, 92–101. [\[CrossRef\]](#)
17. Zhang, S.; Li, H.; Yuan, M.; Yuan, M.; Chen, H. Poly(Lactic Acid) Blends with Poly(Trimethylene Carbonate) as Biodegradable Medical Adhesive Material. *Int. J. Mol. Sci.* **2017**, *18*, 2041. [\[CrossRef\]](#) [\[PubMed\]](#)

18. Zou, J.; Lu, M.; Chen, S.; Cai, C.; Yao, Z.; Cui, W.; Fan, C.; Liu, S. Beeswax-inspired superhydrophobic electrospun membranes for peritendinous anti-adhesion. *Mater. Sci. Eng. C Mater. Biol. Appl.* **2020**, *116*, 111166. [\[CrossRef\]](#)
19. Liu, S.; Liu, S.; Liu, X.; Zhao, J.; Cui, W.; Fan, C. Antibacterial antiadhesion membranes from silver-nanoparticle-doped electrospun poly(L-lactide) nanofibers. *J. Appl. Polym. Sci.* **2013**, *129*, 3459–3465. [\[CrossRef\]](#)
20. Jiang, S.; Yan, H.; Fan, D.; Song, J.; Fan, C. Multi-Layer Electrospun Membrane Mimicking Tendon Sheath for Prevention of Tendon Adhesions. *Int. J. Mol. Sci.* **2015**, *16*, 6932–6944. [\[CrossRef\]](#) [\[PubMed\]](#)
21. Chen, S.-H.; Chen, C.-H.; Fong, Y.-T.; Chen, J.-P. Prevention of peritendinous adhesions with electrospun chitosan-grafted polycaprolactone nanofibrous membranes. *Acta Biomater.* **2014**, *10*, 4971–4982. [\[CrossRef\]](#)
22. Liu, S.; Hu, C.; Li, F.; Li, X.-j.; Cui, W.; Fan, C. Prevention of Peritendinous Adhesions with Electrospun Ibuprofen-Loaded Poly(l-Lactic Acid)-Polyethylene Glycol Fibrous Membranes. *Tissue Eng. Part A* **2012**, *19*, 529–537. [\[CrossRef\]](#) [\[PubMed\]](#)
23. Hu, C.; Liu, S.; Zhang, Y.; Li, B.; Yang, H.; Fan, C.; Cui, W. Long-term drug release from electrospun fibers for in vivo inflammation prevention in the prevention of peritendinous adhesions. *Acta Biomater.* **2013**, *9*, 7381–7388. [\[CrossRef\]](#) [\[PubMed\]](#)
24. Chen, C.-H.; Chen, S.-H.; Shalumon, K.T.; Chen, J.-P. Dual functional core-sheath electrospun hyaluronic acid/polycaprolactone nanofibrous membranes embedded with silver nanoparticles for prevention of peritendinous adhesion. *Acta Biomater.* **2015**, *26*, 225–235. [\[CrossRef\]](#)
25. Luo, D.; Zhang, X.; Shahid, S.; Cattell, M.J.; Gould, D.J.; Sukhorukov, G.B. Electrospun poly(lactic acid) fibers containing novel chlorhexidine particles with sustained antibacterial activity. *Biomater. Sci.* **2017**, *5*, 111–119. [\[CrossRef\]](#) [\[PubMed\]](#)
26. Moghe, A.K.; Gupta, B.S. Co-axial Electrospinning for Nanofiber Structures: Preparation and Applications. *Polym. Rev.* **2008**, *48*, 353–377. [\[CrossRef\]](#)
27. Yu, D.G.; Wang, X.; Li, X.Y.; Chian, W.; Li, Y.; Liao, Y.Z. Electrospun biphasic drug release polyvinylpyrrolidone/ethyl cellulose core/sheath nanofibers. *Acta Biomater.* **2013**, *9*, 5665–5672. [\[CrossRef\]](#)
28. Su, Y.; Su, Q.; Liu, W.; Lim, M.; Venugopal, J.R.; Mo, X.; Ramakrishna, S.; Al-Deyab, S.S.; El-newehy, M. Controlled release of bone morphogenetic protein 2 and dexamethasone loaded in core-shell PLLACL–collagen fibers for use in bone tissue engineering. *Acta Biomater.* **2012**, *8*, 763–771. [\[CrossRef\]](#)
29. Jiang, H.; Hu, Y.; Li, Y.; Zhao, P.; Zhu, K.; Chen, W. A facile technique to prepare biodegradable coaxial electrospun nanofibers for controlled release of bioactive agents. *J. Control. Release* **2005**, *108*, 237–243. [\[CrossRef\]](#)
30. Dubashynskaya, N.V.; Raik, S.V.; Dubrovskii, Y.A.; Demyanova, E.V.; Shcherbakova, E.S.; Poshina, D.N.; Shasherina, A.Y.; Anufrikov, Y.A.; Skorik, Y.A. Hyaluronan/Diethylaminoethyl Chitosan Polyelectrolyte Complexes as Carriers for Improved Colistin Delivery. *Int. J. Mol. Sci.* **2021**, *22*, 8381. [\[CrossRef\]](#)
31. Ashrafizadeh, M.; Mirzaei, S.; Gholami, M.H.; Hashemi, F.; Zabolian, A.; Raei, M.; Hushmandi, K.; Zarrabi, A.; Voelcker, N.H.; Aref, A.R.; et al. Hyaluronic acid-based nanoplatforms for Doxorubicin: A review of stimuli-responsive carriers, co-delivery and resistance suppression. *Carbohydr. Polym.* **2021**, *272*, 118491. [\[CrossRef\]](#)
32. Wu, J.; Zheng, Y.; Song, W.; Luan, J.; Wen, X.; Wu, Z.; Chen, X.; Wang, Q.; Guo, S. In situ synthesis of silver-nanoparticles/bacterial cellulose composites for slow-released antimicrobial wound dressing. *Carbohydr. Polym.* **2014**, *102*, 762–771. [\[CrossRef\]](#) [\[PubMed\]](#)
33. Chu, Z.; Zhao, T.; Li, L.; Fan, J.; Qin, Y. Characterization of Antimicrobial Poly(Lactic Acid)/Nano-Composite Films with Silver and Zinc Oxide Nanoparticles. *Materials* **2017**, *10*, 659. [\[CrossRef\]](#) [\[PubMed\]](#)
34. Cao, X.; Tang, M.; Liu, F.; Nie, Y.; Zhao, C. Immobilization of silver nanoparticles onto sulfonated polyethersulfone membranes as antibacterial materials. *Colloids Surf. B Biointerfaces* **2010**, *81*, 555–562. [\[CrossRef\]](#) [\[PubMed\]](#)
35. Chen, S.H.; Chen, C.H.; Shalumon, K.T.; Chen, J.P. Preparation and characterization of antiadhesion barrier film from hyaluronic acid-grafted electrospun poly(caprolactone) nanofibrous membranes for prevention of flexor tendon postoperative peritendinous adhesion. *Int. J. Nanomed.* **2014**, *9*, 4079–4092. [\[CrossRef\]](#)
36. Chen, J.-P.; Chiang, Y. Bioactive Electrospun Silver Nanoparticles-Containing Polyurethane Nanofibers as Wound Dressings. *J. Nanosci. Nanotechnol.* **2010**, *10*, 7560–7564. [\[CrossRef\]](#)
37. Wang, H.; Cheng, M.; Hu, J.; Wang, C.; Xu, S.; Han, C.C. Preparation and Optimization of Silver Nanoparticles Embedded Electrospun Membrane for Implant Associated Infections Prevention. *ACS Appl. Mater. Interfaces* **2013**, *5*, 11014–11021. [\[CrossRef\]](#)
38. Kim, J.S.; Kuk, E.; Yu, K.N.; Kim, J.-H.; Park, S.J.; Lee, H.J.; Kim, S.H.; Park, Y.K.; Park, Y.H.; Hwang, C.-Y.; et al. Antimicrobial effects of silver nanoparticles. *Nanomed. Nanotechnol. Biol. Med.* **2007**, *3*, 95–101. [\[CrossRef\]](#)
39. Joshi, A.S.; Singh, P.; Mijakovic, I. Interactions of Gold and Silver Nanoparticles with Bacterial Biofilms: Molecular Interactions behind Inhibition and Resistance. *Int. J. Mol. Sci.* **2020**, *21*, 7658. [\[CrossRef\]](#)
40. Vrček, I.V.; Žuntar, I.; Petlevski, R.; Pavičić, I.; Dutour Sikirić, M.; Ćurlin, M.; Goessler, W. Comparison of in vitro toxicity of silver ions and silver nanoparticles on human hepatoma cells. *Environ. Toxicol.* **2016**, *31*, 679–692. [\[CrossRef\]](#) [\[PubMed\]](#)
41. Shalumon, K.T.; Sheu, C.; Chen, C.-H.; Chen, S.-H.; Jose, G.; Kuo, C.-Y.; Chen, J.-P. Multi-functional electrospun antibacterial core-shell nanofibrous membranes for prolonged prevention of post-surgical tendon adhesion and inflammation. *Acta Biomater.* **2018**, *72*, 121–136. [\[CrossRef\]](#)
42. Morra, M. Engineering of Biomaterials Surfaces by Hyaluronan. *Biomacromolecules* **2005**, *6*, 1205–1223. [\[CrossRef\]](#)
43. Vieira, L.F.d.A.; Lins, M.P.; Viana, I.M.M.N.; dos Santos, J.E.; Smaniotto, S.; Reis, M.D.d.S. Metallic nanoparticles reduce the migration of human fibroblasts in vitro. *Nanoscale Res. Lett.* **2017**, *12*, 200. [\[CrossRef\]](#)
44. Yagi, M.; Sato, N.; Mitsui, Y.; Gotoh, M.; Hamada, T.; Nagata, K. Hyaluronan modulates proliferation and migration of rabbit fibroblasts derived from flexor tendon epitenon and endotenon. *J. Hand Surg. Am.* **2010**, *35*, 791–796. [\[CrossRef\]](#) [\[PubMed\]](#)

45. Zhao, N.; Wang, X.; Qin, L.; Guo, Z.; Li, D. Effect of molecular weight and concentration of hyaluronan on cell proliferation and osteogenic differentiation in vitro. *Biochem. Biophys. Res. Commun.* **2015**, *465*, 569–574. [[CrossRef](#)]
46. Yamada, T.; Gotoh, M.; Nakama, K.; Mitsui, Y.; Higuchi, F.; Nagata, K. Effects of hyaluronan on cell proliferation and mRNA expression of procollagens alpha 1 (I) and alpha 1 (III) in tendon-derived fibroblasts from patients with rotator cuff disease: An in vitro study. *Am. J. Sports Med.* **2007**, *35*, 1870–1876. [[CrossRef](#)] [[PubMed](#)]
47. Liu, X.; Lee, P.-y.; Ho, C.-m.; Lui, V.C.H.; Chen, Y.; Che, C.-m.; Tam, P.K.H.; Wong, K.K.Y. Silver Nanoparticles Mediate Differential Responses in Keratinocytes and Fibroblasts during Skin Wound Healing. *ChemMedChem* **2010**, *5*, 468–475. [[CrossRef](#)] [[PubMed](#)]
48. Peng, X.; Nelson, E.S.; Maiers, J.L.; DeMali, K.A. New Insights into Vinculin Function and Regulation. *Int. Rev. Cell Mol. Biol.* **2011**, *287*, 191–231. [[CrossRef](#)]
49. Qian, Y.; Li, L.; Jiang, C.; Xu, W.; Lv, Y.; Zhong, L.; Cai, K.; Yang, L. The effect of hyaluronan on the motility of skin dermal fibroblasts in nanofibrous scaffolds. *Int. J. Biol. Macromol.* **2015**, *79*, 133–143. [[CrossRef](#)] [[PubMed](#)]
50. Namba, J.; Shiamada, K.; Saito, M.; Murase, T.; Yamada, H.; Yoshikawa, H. Modulation of peritendinous adhesion formation by alginate solution in a rabbit flexor tendon model. *J. Biomed. Mater. Res. Part B Appl. Biomater.* **2007**, *80*, 273–279. [[CrossRef](#)]
51. Dos Anjos Cassado, A. F4/80 as a Major Macrophage Marker: The Case of the Peritoneum and Spleen. *Results Probl. Cell Differ.* **2017**, *62*, 161–179. [[CrossRef](#)] [[PubMed](#)]
52. Austyn, J.M.; Gordon, S. F4/80, a monoclonal antibody directed specifically against the mouse macrophage. *Eur. J. Immunol.* **1981**, *11*, 805–815. [[CrossRef](#)]
53. Kwan, K.H.L.; Yeung, K.W.K.; Liu, x.; Wong, K.K.Y.; Shum, H.C.; Lam, Y.W.; Cheng, S.H.; Cheung, K.M.C.; To, M.K.T. Silver nanoparticles alter proteoglycan expression in the promotion of tendon repair. *Nanomed. Nanotechnol. Biol. Med.* **2014**, *10*, 1375–1383. [[CrossRef](#)]
54. Fehaid, A.; Taniguchi, A. Silver nanoparticles reduce the apoptosis induced by tumor necrosis factor- $\alpha$ . *Sci. Technol. Adv. Mater.* **2018**, *19*, 526–534. [[CrossRef](#)] [[PubMed](#)]
55. Tyavambiza, C.; Elbagory, A.M.; Madihe, A.M.; Meyer, M.; Meyer, S. The Antimicrobial and Anti-Inflammatory Effects of Silver Nanoparticles Synthesised from Cotyledon orbiculata Aqueous Extract. *Nanomaterials* **2021**, *11*, 1343. [[CrossRef](#)] [[PubMed](#)]
56. Chen, J.-P.; Chang, F.-N. Preparation and characterization of hydroxyapatite/gelatin composite membranes for immunoisolation. *Appl. Surf. Sci.* **2012**, *262*, 176–183. [[CrossRef](#)]

## Article

# Identification of Two Novel CIL-102 Upregulations of ERP29 and FUMH to Inhibit the Migration and Invasiveness of Colorectal Cancer Cells by Using the Proteomic Approach

Kung-Chuan Cheng <sup>1</sup>, Hsing-Chun Kuo <sup>2,3,4,5</sup>, Meng-Chiao Hsieh <sup>6</sup>, Cheng-Yi Huang <sup>6</sup>, Chih-Chuan Teng <sup>2,3</sup>, Shui-Yi Tung <sup>7,8</sup>, Chien-Heng Shen <sup>7</sup>, Kam-Fai Lee <sup>9</sup>, Ya-Ling Yang <sup>10</sup> and Ko-Chao Lee <sup>11,\*</sup>

- <sup>1</sup> Division of Colorectal Surgery, Department of Surgery, Chang Gung Memorial Hospital, Kaohsiung Medical Center, Kaohsiung 83301, Taiwan; topguncheng@gmail.com
- <sup>2</sup> Division of Basic Medical Sciences, Department of Nursing, Chang Gung University of Science and Technology, Chiayi 61363, Taiwan; guscsi@gmail.com (H.-C.K.); ccteng@gw.cgust.edu.tw (C.-C.T.)
- <sup>3</sup> Research Fellow, Chang Gung Memorial Hospital, Chiayi 61363, Taiwan
- <sup>4</sup> Research Center for Food and Cosmetic Safety, College of Human Ecology, Chang Gung University of Science and Technology, Taoyuan 33303, Taiwan
- <sup>5</sup> Chronic Diseases and Health Promotion Research Center, Chang Gung University of Science and Technology, Chiayi 61363, Taiwan
- <sup>6</sup> Division of Colon and Rectal Surgery, Department of Surgery, Chang Gung Memorial Hospital, Chiayi 61363, Taiwan; mr8872@gmail.com (M.-C.H.); scorpievo@yahoo.com.tw (C.-Y.H.)
- <sup>7</sup> Department of Hepato-Gastroenterology, Chang Gung Memorial Hospital, Chiayi 61363, Taiwan; ma1898@yahoo.com (S.-Y.T.); gi2216@adm.cgmh.org.tw (C.-H.S.)
- <sup>8</sup> Graduate Institute of Clinical Medical Sciences, College of Medicine, Chang Gung University, Chiayi 61363, Taiwan
- <sup>9</sup> Department of Pathology, Chang Gung Memorial Hospital, Chiayi 61363, Taiwan; lkf2002@cgmh.org.tw
- <sup>10</sup> Department of Anesthesiology, Kaohsiung Chang Gung Memorial Hospital and Chang Gung University College of Medicine, Kaohsiung 83301, Taiwan; yaling453@yahoo.com.tw
- <sup>11</sup> Division of Colorectal Surgery, Department of Surgery, Chang Gung Memorial Hospital, Kaohsiung Medical Center, Chang Gung University College of Medicine, Kaohsiung 83301, Taiwan
- \* Correspondence: kmch4329@gmail.com; Tel.: +886-731-7123; Fax: +886-731-8762



**Citation:** Cheng, K.-C.; Kuo, H.-C.; Hsieh, M.-C.; Huang, C.-Y.; Teng, C.-C.; Tung, S.-Y.; Shen, C.-H.; Lee, K.-F.; Yang, Y.-L.; Lee, K.-C. Identification of Two Novel CIL-102 Upregulations of ERP29 and FUMH to Inhibit the Migration and Invasiveness of Colorectal Cancer Cells by Using the Proteomic Approach. *Biomolecules* **2021**, *11*, 1280. <https://doi.org/10.3390/biom11091280>

Academic Editor: Shih-Min Hsia

Received: 4 August 2021

Accepted: 21 August 2021

Published: 27 August 2021

**Publisher's Note:** MDPI stays neutral with regard to jurisdictional claims in published maps and institutional affiliations.



**Copyright:** © 2021 by the authors. Licensee MDPI, Basel, Switzerland. This article is an open access article distributed under the terms and conditions of the Creative Commons Attribution (CC BY) license (<https://creativecommons.org/licenses/by/4.0/>).

**Abstract:** CIL-102 (1-[4-(furo[2,3-b]quinolin-4-ylamino) phenyl]ethanone) is a major active agent of Camptotheca acuminata's alkaloid derivative, and its anti-tumorigenic activity, a valuable biological property of the agent, has been reported in many types of cancer. In this study, we researched the novel CIL-102-induced protein for either the induction of cell apoptosis or the inhibition of cell migration/invasiveness in colorectal cancer cells (CRC) and their molecular mechanism. Firstly, our data showed that CIL-102 treatment not only increased the cytotoxicity of cells and the production of Reactive Oxygen Species (ROS), but it also decreased cell migration and invasiveness in DLD-1 cells. In addition, many cellular death-related proteins (cleavage caspase 9, cleavage caspase 3, Bcl-2, and TNFR1 and TRAIL) and JNK MAPK/p300 pathways were increased in a time-dependent manner. Using the proteomic approach with a MALDI-TOF-TOF analysis, CIL-102-regulated differentially expressed proteins were identified, including eight downregulated and 11 upregulated proteins. Among them, upregulated Endoplasmic Reticulum resident Protein 29 (ERP29) and Fumarate Hydratase (FUMH) by CIL-102 were blocked by the inhibition of ROS production, JNK activity, and p300/CBP (CREB binding protein) signaling pathways. Importantly, the knockdown of ERP29 and FUMH expression by shRNA abolished the inhibition of cell migration and invasion by CIL-102 in DLD-1 cells. Together, our findings demonstrate that ERP29 and FUMH were upregulated by CIL102 via ROS production, JNK activity, and p300/CBP pathways, and that they were involved in the inhibition of the aggressive status of colorectal cancer cells.

**Keywords:** CIL-102; ROS; JNK; p300/CBP; ERP29; FUMH



## 1. Introduction

Colorectal cancer (CRC) is an aggressive, malignant disease with a poor prognosis [1]. A large body of evidence demonstrates the self-sufficiency of CRC cells by using growth signals to escape from apoptosis, along with the tendency for cancer invasion and metastasis to be the fourth leading cause of cancer-related deaths in the industrialized world [2]. In fact, cell apoptosis is an important physiological process of cell death that helps maintain our body homeostasis [3]. Under the intrinsic apoptotic stimulus, such as an abnormal ROS evaluation, the release of cytochrome c from the mitochondria sequentially increases the activity of caspase-9 and caspase-3 for the induction of cell apoptosis [4]. In addition, ROS functions as the second messenger that is sensitive to oxidative damage-mediated cell apoptosis, and it triggers the intrinsic or extrinsic apoptotic signaling pathways [5]. Therefore, with regard to cancer therapy, the induction of cancer cell apoptosis, or ROS, is a great therapeutic strategy for destroying cancer cells without excessive inflammation [6]. Due to the issue of intrinsic chemo-resistance, it is imperative and urgent to develop more effective drugs for CRC treatment rather than classical chemotherapy treatments [7].

Recently, phenolic phytochemicals and Camptothecin (CPT)—alkaloids originally isolated from the bark and stem of *Camptotheca acuminata*—were both capable of inhibiting cell proliferation [8,9] and inducing cell apoptosis in CRC. CPT interacts mechanically with the DNA to form a complex, and it reduces the synthesis of DNA, RNA, and protein [10]. A number of the synthesized furo[2,3-b]quinoline derivatives, such as CIL-102, have been recognized for their anti-cancer effects on many cancer types, including prostate and breast cancer, leukemia, and cervical carcinoma [11,12]. CIL-102 treatment not only inhibits the proliferation and invasiveness of cancer cells [13,14] but also induces cancer cell apoptosis [15]. Many intracellular signals, such as ERK1/2, Cdc25cSer216, p21, GADD45, and ROS production, participate in CIL-102-mediated anti-cancer action [15,16]. In gastric cancer, CIL-102 treatment has shown a strong anti-cancer effect. Furthermore, the treatment activates intracellular signals for the induction of cancer cell apoptosis. These signals were involved in the H3K4 trimethylation of TNFR1 and TRAIL proteins, including ROS derived and JNK/mTOR/p300 pathways in DLD-1 cells. CIL-102 treatment works well to induce cell apoptosis in other types of cancers, such as colorectal cancer; however, its mechanism related to the induced downstream protein, by means of CIL-102 treatment for its anti-invasiveness properties, remains unclear.

By using the proteomic approach with the MALDI-TOF-TOF analysis (2DE MS/MS), Endoplasmic Reticulum resident Protein 29 (ERP29) and Fumarate hydratase (FUMH) were identified as the novel upregulation proteins of CIL-102 treatment in DLD-1 cells. Furthermore, CIL-102 increases and produces ROS, JNK activity, and p300/CBP pathways. Both ERP29 and FUMH are required for the CIL-102-mediated inhibition of cell migration and the invasiveness of colorectal cancer cells. Taken together, this study demonstrates a novel anti-cancer mechanism for CIL-102 to inhibit cell migration and the invasiveness of colorectal cancer cells via the upregulation of ERP29 and FUMH.

## 2. Materials and Methods

### 2.1. Chemical Reagents, Antibodies, and Cell Culture

The chemical reagents, such as 1-[4-(Furo[2,3-b]quinolin-4-ylamino)phenyl] ethenone (CIL-102), 3-(4,5-dimethylthiazol-2-yl)-2,5-diphenyltetrazolium bromide (MTT), ROS scavenger (*N*-acetyl cysteine [NAC]), 2,7-dichlorodihydrofluorescein diacetate (H<sub>2</sub>DCFDA), dihydroethidium (DHE), ERK inhibitor (PD98059), c-Jun N-terminal kinase (JNK1/2) inhibitor (SP600125), p300/CBP inhibitor (C646), mTOR inhibitor (rapamycin), SDS, NP-40, sodium deoxycholate, and protease inhibitor cocktails, were obtained from Sigma (St. Louis, MO, USA). The antibodies were obtained from Santa Cruz Biotechnology (Santa Cruz, CA, USA), including anti-p300/CBP (sc-32244), anti-Bcl-2 (sc-7382), anti-Bcl-XL (sc-8392), anti-β-actin (sc-8432) antibodies (diluted 1:1000), and monoclonal secondary antibodies (sc-2357, diluted 1:5000). The purchased antibodies from Cell Signaling Technology (Beverly, MA, USA) were anti-cdk1, anti-ERK1/2Thr<sup>202</sup>Tyr<sup>204</sup> (#9101), anti-JNK1/2 Thr<sup>183</sup>Tyr<sup>185</sup>

(#9251), anti-cleavage caspase-3 (#9661), and caspase-9 (#9505) antibodies (diluted 1:1000). The purchased antibodies from Millipore (Millipore, CA, USA) were anti-Acetyl-Histone H3 (Lys9/14) (12-360) antibodies (diluted 1:1000). The purchased antibodies from Sigma-Aldrich (Sigma, Saint Louis, MO, USA) were anti-p300/CBP (P2859) and anti- $\beta$ -actin (A5441) antibodies (diluted 1:1000). All culture materials were from Gibco (Grand Island, NY, USA). Two human colon cancer cell line DLD-1 (BCRC Number: 60132) and the human colorectal carcinoma cell line HCT-116 (BCRC Number: 60349) were purchased from the Bioresources Collection and Research Center (BCRC) of the Food Industry Research and Development Institute (Hsinchu, Taiwan). The human DLD-1 and HCT-116 cells were grown in plastic tissue culture flasks or dishes or in microplates (Nunc, Naperville, Denmark) with the cell culture medium, including Dulbecco's Modified Eagle Medium (DMEM), and supplemented with 10% fetal calf serum (Gibco), non-essential amino acids, 1 mM sodium pyruvate, and 1% antibiotics (100 units/mL of penicillin and 100  $\mu$ g/mL of streptomycin), at 37 °C in a humidified atmosphere of 5% CO<sub>2</sub> and 95% air [17].

## 2.2. Cell Viability and Reactive Oxygen Species Detection

The 4',6-diamidino-2-phenylindole (DAPI) staining was used to check the morphological characteristics of the cells under fluorescence microscopy. After fixing with 4% paraformaldehyde for 30 min at room temperature, permeabilizing in 0.2% Triton X-100 in phosphate-buffered saline three times for 15 min, and then PBS washing, the cells were incubated with 1  $\mu$ g/mL of DAPI for 30 min. Using a fluorescent microscope with 340/380 nm, the apoptotic nuclei in the field of the 200–300 cells were observed. According to a previous report [18], the percentage of apoptotic cells was scored and calculated under a 200 $\times$  magnification excitation filter.

As previously described, after co-staining with Annexin V-FITC and propidium iodide (Biosource International, Camarillo, CA, USA), the cells were subjected to flow cytometer analysis (Attune NxT Flow Cytometer, Thermo Fisher Scientific Inc.) for measurement of cell apoptosis. Based on the fluorescent intensity, the number of the apoptotic cells (V+/PI−) can be calculated using the Attune NxT software 3.1 (Thermo Fisher Scientific Inc., Ramsey, MN, USA), and the data are represented as a percentage of the untreated control group with three independent experiments [19].

Using the fluorescent probes of H2DCFDA (2,7-dichlorodihydrofluorescein diacetate), it was possible to detect intracellular accumulation of ROS (O<sub>2</sub><sup>−</sup>) in the cells. After PBS washing, the cells were applied to Attune NxT Flow Cytometer analysis and analyzed with Attune NxT software. The data were analyzed and presented as a percentage of the fluorescent intensity with three independent experiments. The apoptotic cells (V+/PI−) were identified using the fluorescence-activated cell sorter analysis in an Attune NxT Flow Cytometer [20].

## 2.3. Matrigel Invasion and Scratch Analysis

Based on a chamber with two medium-filled compartments, the Boyden chamber assays were used to measure tumor cell invasion. As described above, the cells (1  $\times$  10<sup>5</sup>/mL cells (1  $\times$  10<sup>5</sup>/mL)) in a serum-free medium were collected and added to an inner cup of the 48-well transwell chamber (Corning Life Sciences, Corning, NY, USA). The transwell chamber was coated with 50  $\mu$ L of matrigel (BD Biosciences, Franklin Lakes, NJ, USA; 1:10 dilution in a serum-free medium). The outer cup had the medium that was supplemented with 10% serum or the indicated agent. After 24-h incubation at 37 °C in a humidified atmosphere with 5% CO<sub>2</sub>, the membrane containing the cells was fixed and stained with a modified Giemsa stain (Sigma, Saint Louis, MO, USA). Under a light microscope at a 200 $\times$  magnification, the cells on the lower side of the membrane were counted and analyzed [21].

Scratch assays of the plating cells in a six-well culture dish were performed. After the cells attached and reached confluence, a 4-mm scratch was made through the culture dish. After washing twice with phosphate-buffered saline (PBS, pH = 7), the cells were cultured in the culture medium with or without CIL-102. Using Openlab v3.0.2 image analysis software (Improvision, Coventry, UK), it was possible to quantify the area that was progressively filled with the cells in the period of the experimental time [21].

#### 2.4. Proteomic Dimensional Protein Electrophoresis Analysis

The chemical reagents and experimental procedure for 2D gel electrophoresis were described in our previous study [22]. After treatment, the total proteins of the cells were extracted and precipitated by 10% trichloroacetate in acetone. Their concentrations were measured by the Bradford assay with bovine serum albumin as the standard sample for normalization. Prior to the 2D-PAGE analysis, protein samples were suspended in a rehydration solution and then applied to Iso-Electric Focusing (IEF) in the pH 3–10 immobilized-gradient strips (Immobiline Dry Strips, Amersham Biosciences, Uppsala, Sweden) with an Ettan IPGphor II apparatus (Amersham Biosciences). Using 10% SDS-PAGE gels, it was possible to carry out the two-dimension electrophoresis.

#### 2.5. In-Gel Digestion and the Peptide Fingerprints' Identification with MALDI-TOF

The total cell proteins that were resolved in six pairs of silver-stained 2D SDS-PAGE gels were scanned using the ImageMaster 2D Platinum Software 6.0 (Amersham Biosciences). Therefore, the protein profiles of each pair of silver-stained gels were recorded and compared with other treated groups. Among all six pairs of 2D gels, the protein spots differentially expressed by at least three folds were subjected to the in-gel digestion for further mass spectrometric analysis of matrix-assisted laser desorption/ionization-time-of-flight (MALDI-TOF/TOF). After the gel pieces were then dehydrated, performed with trypsin digestion, the FlexAnalysis system (Bruker-Franzen Analytik, Bremen, Germany) was used to acquire mass spectra as the sum of the ion signals by the irradiation of the targets with a mean of 300 laser pulses. Peptide fingerprints (selected in the mass range of 700–4000 Daltons) were analyzed by the Mascot software (<http://www.matrixscience.com>, accessed on 5 February 2021). A Mascot score with  $p < 0.05$  was considered statistically significant, as described in our previous study [22]. The MALDI-TOF/TOF data were searched and analyzed by the in-house MASCOT software (version 2.2.04) to identify proteins that required the detection of unique peptides and proteins with more than two spectral counts. Then, by using MASCOT search engines, the peptide mass data of each spot were submitted to the SwissProt 100425 human species bio-information stations for further analysis. With a higher MASCOT score in the bovine database than in the human database, the proteins were considered as serum contamination and removed [23].

#### 2.6. Cell Extracts' Preparation and Immunoblot Analysis

To obtain the total cell lysate, the cells were lysed with a buffer (1% NP-40, 0.5% sodium deoxycholate, 0.1% Sodium Dodecyl Sulfate (SDS)) and a protease inhibitor mixture (phenylmethylsulfonyl fluoride, aprotinin, and sodium orthovanadate). As previously described [24], the total cell lysates (50 µg of protein) were separated by SDS-polyacrylamide gel electrophoresis (PAGE) (12% running, 4% stacking). After transferring the protein in gel on the membrane, the designated antibodies and Western light chemiluminescent detection system (Bio-Rad, Hercules, CA, USA) were used to detect the level of the specific proteins.

### 2.7. The shRNA Lentivirus Transfection

The methods of the shRNA Lentivirus transfection for applying the knockdown of genetic functions were established (Santa Cruz Biotechnology) [14]. Following the recommended protocol, the cells were infected with the designated Control shRNA Lentiviral Particles, ERP29 and PROF1 siRNA, and shRNA Plasmids using the shRNA expression of lentiviral particles (Santa Cruz, CA, USA).

### 2.8. Statistical Analysis

Data were reported as the means  $\pm$  standard deviation (means  $\pm$  SD) of three independent experiments, and the groups were compared using the one-way Analysis of Variance (ANOVA) with Tukey's Multiple Comparison Test by the SAS software statistical package "SigmaPlot" version 9.0 (SAS Institute Inc., Cary, NC, USA) [25]. Significant differences were established at  $p < 0.05$ .

## 3. Results

### 3.1. CIL-102 Reduces the Migration and Invasion of DLD-1 Cells

Our previous study demonstrated that there was an increase in the cellular levels of p21 and GADD45 by the 9-anilinofuroquinoline derivative, CIL-102, inhibiting DLD-1 proliferation and cell cycle distribution [15,16]. It remains unknown whether it can inhibit migration and invasion in the CRC. Its affecting proteins also remain unknown. Firstly, DAPI staining showed that treatment with CIL-102 at 1- $\mu$ M concentrations induced the early apoptotic chromatin condensation in DLD-1 cells (Figure 1A), but previously not in normal epithelial HCoEpiC cells [13]. Using the scratch-wound assay to observe the continuous rapid movement of DLD-1 cells for 24 h (Figure 1B), our data revealed that cells that did not receive the CIL-102 treatment control showed at a high confluence (90–100%) of the monolayer region, which gradually migrated into the cell-free "scratch" region (Figure 1D). In contrast, treatment with CIL-102 at 1- and 2- $\mu$ M concentrations for 24 h reduced the cell migration by 22% and 11%, compared to the treatment control group (Figure 1C). Furthermore, by using the Boyden chamber assay, we determined that CIL-102 at 1-, 2-, and 5- $\mu$ M concentrations also inhibited the invasiveness of DLD-1 cells. The quantification of revealed observations also exhibited a significant anti-invasive effect compared to the control group and was respectively shown as 65%, 35%, and 16%, which supported the results obtained with the scratch-wound assay in a dose-response relationship (Figure 1E). By using flow cytometry analysis for annexin-V and PI, our results revealed that an increased percentage of annexin V-positive cells was found in all untreated and CIL-102-treated DLD-1 cells in a dose-dependent manner and was shown as 8%, 23%, and 28%. (Figure 2A). In addition, CIL-102 initially increased the intracellular ROS production in DLD-1 cells after 24 h, by 1.2- and 1.5-fold (Figure 2B), compared to the control.



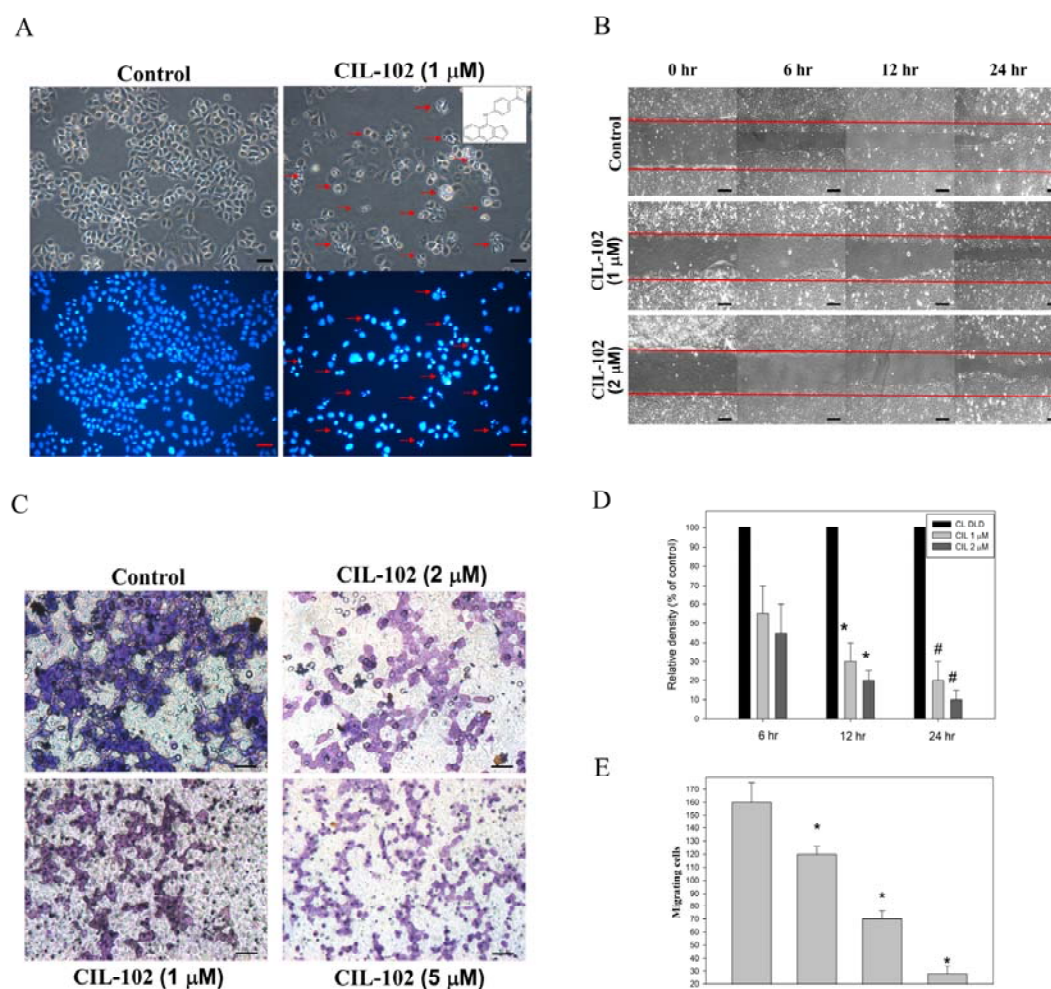


**Figure 1.** CIL-102 treatment impairs cell migration and the invasiveness of human colorectal cancer cells. **(A)** DLD-1 cells were treated with either 0.1% DMSO (as control) or CIL-102 (1  $\mu$ M) for 24 h. The morphological characteristics (nuclear condensation) of the apoptotic cells were measured by DAPI staining under fluorescence microscopy. The red arrow indicates the apoptotic cells. **(B,D)** The migration of treated DLD-1 cells, with or without CIL-102 (1 and 2  $\mu$ M), was performed for 6, 12, and 24 h and visualized by scratch-wound assay, as described in the Methods section. The quantification of the filled surface area with DLD-1 cells was done by using densitometric analyses. Data are presented as a percentage of the control group (means  $\pm$  SD), based on three independent experiments in triplicate. Control VS CIL-102, \*  $p < 0.05$ , compared with the control group for 12 h; #  $p < 0.01$ , compared with the control group for 24 h. **(C,E)** Invasiveness of DLD-1 cells treated with various concentrations (1, 2, 5  $\mu$ M) of CIL-102 for 24 h was detected by the Boyden Chamber method, as described in the Methods section. The lower and upper chemotaxis cells were separated by a polycarbonate membrane. The representative images of cell invasion were detected through a layer of matrigel into the inner membrane under microscopy. Magnification  $\times 200$ . The number of cell invasions into the inner membrane was quantified by manual counting and the data are presented as means  $\pm$  SD. Control cells indicate the cells with a saline treatment. The experiments were performed in triplicate. \*  $p < 0.05$ , compared to the untreated control cultures.

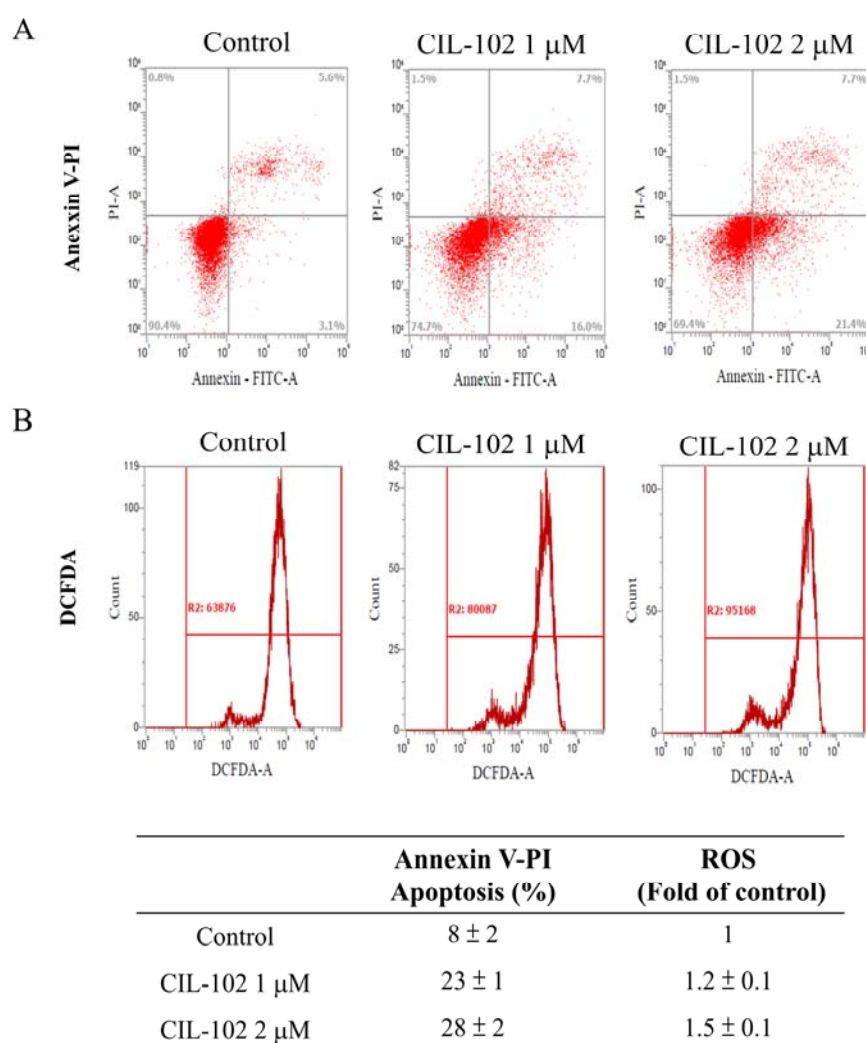


**Figure 2.** CIL-102 treatment induces cell apoptosis and the ROS production of DLD-1 cells. (A) FITC-conjugated Annexin-V and PI stainings of DLD-1 cells, with or without CIL-102 treatment, for 24 h were performed by flow cytometry analysis, as described in the Materials and Methods sections. The percentages of the apoptotic or neurosis cells in these treated cells are shown in each frame, as indicated. (B) Intracellular ROS of DLD-1 cells treated, with or without CIL-102, at 1- and 2-μM concentrations for 24 h was measured by a FACS analysis, as described in the Materials and Methods sections. Representative histograms of typical H2DCFDA profiles are shown. The production of ROS was expressed as the fold of the control group. Data are presented, based on three independent experiments, as mean ± S.D.

### 3.2. CIL-102 Treatment Triggers Apoptotic Signals in DLD-1 Cells

To determine which cell death-related proteins were involved in the CIL-102-induced cell apoptosis of DLD-1 cells, the protein levels of the hallmarks representing apoptotic cell death [26], such as the cleavage of caspase 9, caspase 3, and Bcl-2, were measured by Western blot. Our data showed that the CIL-102 treatment increased the active form of caspase-3 and -9 in a time-dependent manner in DLD-1 cells (Figure 3). In contrast, anti-apoptotic Bcl-2 and Bcl-XL proteins were decreased in the cells with the CIL-102 treatment (Figure 3A). Furthermore, in comparison to the untreated group, a time-dependent increase was found in the phosphorylation of JNK1/2 Thr183/Tyr185 and the level of p300/CBP in the CIL-102-treated DLD-1 (Figure 3B). Accordingly, our data showed that CIL-102 may activate multiple-protein kinases' pathways for the induction of intrinsic cell apoptosis.

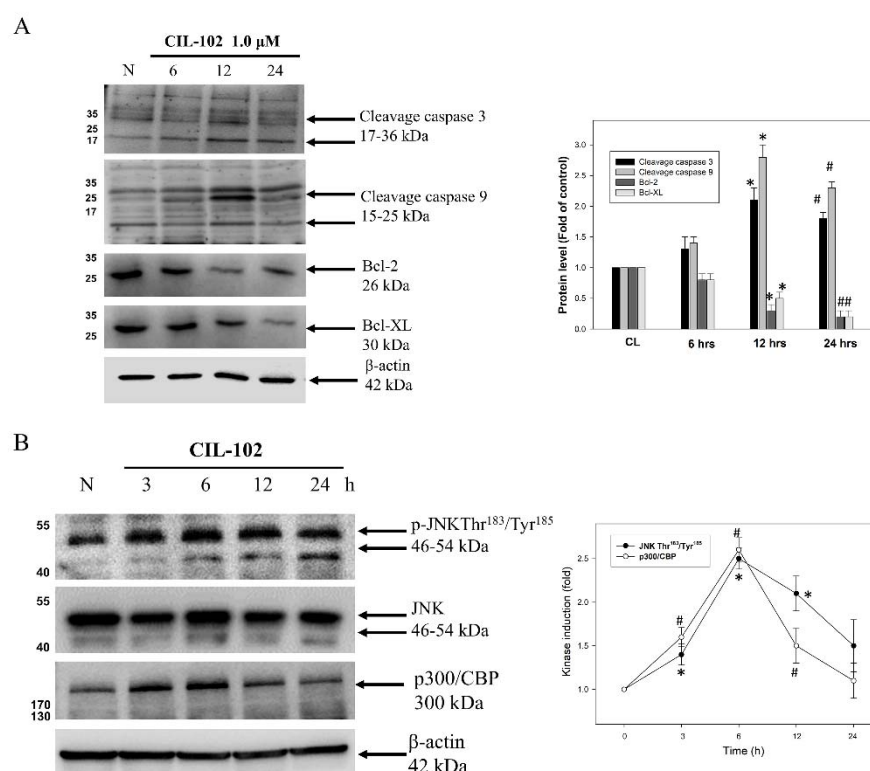


**Figure 3.** CIL-102 treatment activates the death-related signaling pathways in DLD-1 cells. The protein level of CIL-102 (1  $\mu$ M)-treated DLD-1 cell for 0–24 h were detected by Western blot, including cleavage caspase 3, cleavage caspase 9, Bcl-2, and Bcl-XL (A) and p-JNK and p300/CBP (B). Protein levels were quantified by a densitometric analysis and normalized by a loading control,  $\beta$ -actin. The data are presented as 100% of the control group (means  $\pm$  SD) from three independent experiments. \*  $p < 0.05$ , when compared with the untreated control group at 12 h. #  $p < 0.05$ , when compared with the untreated control group at 24 h. (B). \*  $p < 0.05$ , p-JNK when compared with the untreated control group at 12 h. #  $p < 0.05$ , p300/CBP when compared with the untreated control group at 24 h.

### 3.3. Proteomic Profiling of CIL-102-Treated DLD-1 Cells

By using the proteomic approach with the MALDI-TOF-TOF analysis, we wanted to investigate the novel CIL-102-upregulated protein [27,28]. More than 800 protein spots from cell lysates of DLD-1 cells, with or without the CIL-102 treatment, were visualized in the silver-stained 2D-PAGE analysis (Figure 4). The images of protein expression profile gels (i.e., the six pairs from the control and the CIL-102-treated groups) were analyzed by using the ImageMaster software. Our image analysis showed that 19 proteins were identified as differentially expressed proteins, where their protein level had more than a three-fold change compared to the untreated and CIL-102-treated groups (Figure 4). Among them, 11 protein spots showed a greater than three-fold change in the CIL-102 treatment (Figure 5, Table 1), including Fumarate Hydratase (FUMH) and Endoplasmic Reticulum Resident Protein 29 (ERP29). Compared to the untreated group, eight spots of 19 differential display proteins were downregulated consistently by the CIL-102-treated group (Figure 5). After the peptide fingerprint identification of these spots by MALDI-TOF MS, the full names of 19 proteins were listed in Table 1. It presents the zoomed views of a representative gel region and displays several differentially expressed, oxidative stress-related proteins on the effect of CIL-102, which inhibited invasive action in the DLD-1. Spots 9 and 10 were subsequently identified by using a 2D proteomic analysis, including Fumarate Hydratase (FUMH) and Endoplasmic Reticulum Resident Protein 29 (ERP29), which may mediate the oxidative stress and the aggressive effects of CIL-102 in DLD-1 cells (Table 1). From previous studies, one protein ERP29 was shown to be a tumor suppressor and a chaperone protein, which involves the regulation of primary tumor development

and the arrest of cell growth [27]. Another differential display protein, FUMH, also shows anti-tumor functions, including the inactivation of tumor metastasis, tumor aggressiveness, and EMT changes by epigenetic modification [28].

**Table 1.** Differentially expressed protein.

Spot	Protein Name	Mr/PI	Accession No	MASCOT Score	Matched Peptides
1	Stress-induced-phosphoprotein	63/6.4	STIP1_HUMAN	1200	95
2	X-ray repair cross-complementing protein 6	70/6.2	XRCC6_HUMAN	1230	55
3	Glucose-6-phosphate isomerase	63/9.1	G6PI_HUMAN	60	2
4	S-methyl-5'-thioadenosine phosphorylase	31/6.9	MTAP_HUMAN	261	10
5	Heterogeneous nuclear ribonucleoprotein L	64/9.2	HNRPL_HUMAN	310	17
6	Alcohol dehydrogenase [NADP(+)]	36/6.3	AK1A1_HUMAN	438	17
7	Glutamate dehydrogenase 1	61/5.8	DHE3_HUMAN	1000	49
8	GMP synthase	77/6.4	GUAA_HUMAN	592	20
9	Fumarate hydratase	54/9.4	FUMH_HUMAN	420	21
10	Histidine triad nucleotide-binding protein 1	13/6.4	HINT1_HUMAN	125	8
11	Endoplasmic reticulum resident protein 29	29/7.5	ERP29_HUMAN	430	23
12	WD repeat-containing protein 1	66/6.1	WDR1_HUMAN	625	39
13	GTP-binding nuclear protein	24/7.7	RAN_HUMAN	534	40
14	Heat shock protein beta-1	22/5.9	HSPB1_HUMAN	411	42
15	Mitochondrial import receptor subunit TOM40 homolog	38/6.9	TOM40_HUMAN	372	15
16	Peroxisome oxidoreductin-2	22/5.5	PRDX2_HUMAN	548	38
17	Heat shock protein 75 kDa	80/8.9	TRAP1_HUMAN	468	14
18	L-lactate dehydrogenase B chain	36/5.6	LDHB_HUMAN	491	26
19	UDP-glucose 6-dehydrogenase	55/6.8	UGDH_HUMAN	1049	60

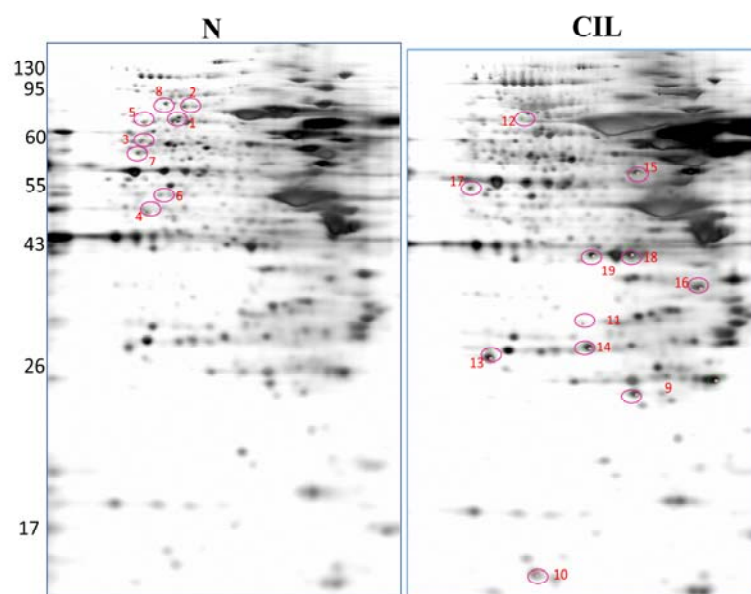


**Figure 4.** The representative two-dimensional gel electrophoretograms of DLD-1 cells, with or without the CIL-102 treatment. Six pairs of cell protein extracts from the CIL-102-treated and untreated DLD-1 cells were evaluated, and a representative pair of the proteomic gel images are shown. Nineteen protein spots (the upregulation of eight protein spots and the downregulation of 11 protein spots in the CIL-102-treated group) with a three-fold difference between both groups, were subjected to a MALDI-TOF-TOF analysis. The full names of these differentially displayed protein spots are encircled and annotated in Table 1, respectively.



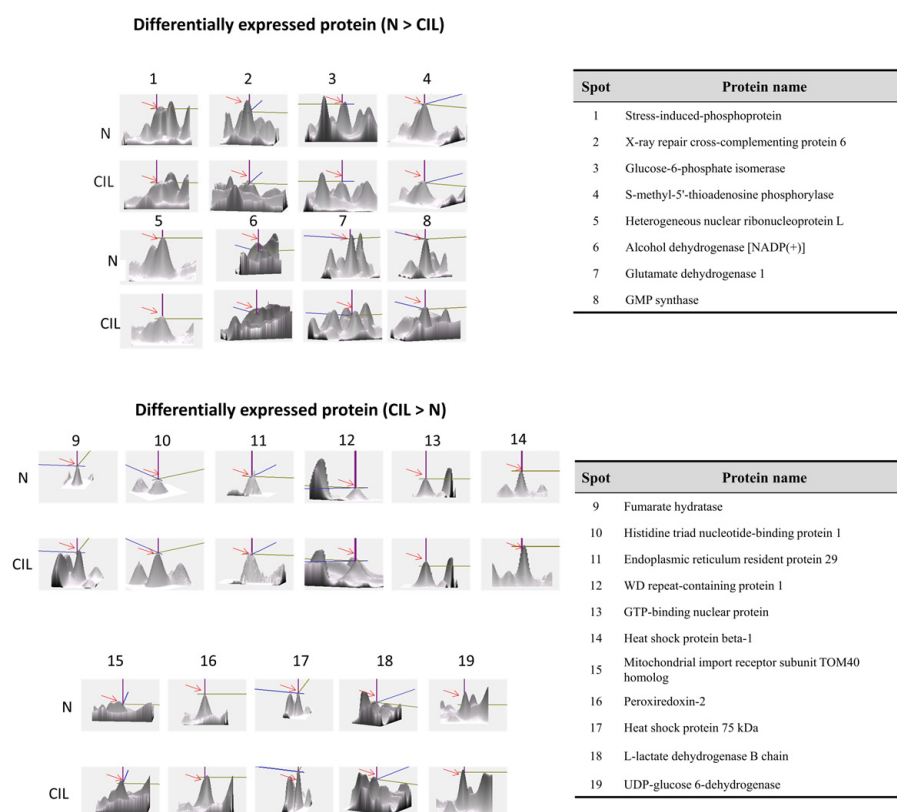


**Figure 5.** A representative close view of CIL-102-mediated differentially expressed proteins. The expression pattern of differentially expressed proteins (the number is the same as in Table 1) in DLD-1 cells, with or without CIL-102 treatment (one pair of experiments), are shown. Six pairs of cell protein extracts with four reproducible blots were performed in total.

### 3.4. Upregulation of FUMH and ERP29 by CIL-102 via the Signaling Pathways of ROS, JNK, and Histone Acetylation to Inhibit Cell Migration and Invasion

Next, we determined if FUMH and ERP29 play a role in the reduction of cancer cell migration and invasion by CIL-102. As shown in Table 2, the downregulation of both FUMH and ERP29 by shRNA significantly decreased the CIL-102-inhibited migration and invasion in DLD-1 cells at 24 h, respectively (\*  $p < 0.01$ ). In contrast, the addition of Lenti shRNA ERP29 and shRNA FUMH alone significantly increased cancer migration and invasion (Table 2), which implies that they have a tumor-suppressive effect. These data indicated that CIL-102 treatment reduced the migration and invasion of DLD-1 cells through the upregulated FUMH and ERP29.

To determine which signaling pathways are involved in the upregulation of FUMH and ERP29 by CIL-102, chemical inhibitors were used to block ROS production, JNK activation, and histone acetylation in CIL-102-treated DLD-1 cells. As shown in Figure 6, ROS scavenger NAC, JNK inhibitor SP600125, and P300 inhibitor C646 almost blocked the CIL-102-induced levels of the phospho-JNK, P300 CBP, and histone H3K9K14ac (acetyl Lys9/Lys14). Furthermore, our data showed that the increase of FUMH and ERP29 by CIL-102 was blocked by these chemical inhibitors (Figure 6), which suggests that the CIL-102 treatment increased FUMH and ERP29 expression through the production of ROS and the activation of JNK and P300. Taken together, our results demonstrated a novel mechanism for CIL-102 to reduce the migration and invasion of CRC cancer via the upregulation of FUMH and ERP29.

**Table 2.** Effects of the kinase inhibitor on the CIL-102 induction associated with cancer cell aggressive status in DLD-1 cells.

	Cell Invasion (%)	Migration (%)
Control	100	100
CIL-102	24 ± 2	42 ± 2
CIL-102	97 ± 2	98 ± 2
Lenti GFP		
CIL-102	55 ± 3	58 ± 3
Lenti ERP29		
CIL-102	45 ± 3	65 ± 2
Lenti FUMH		
Lenti ERP29	165 ± 2	140 ± 2
Lenti FUMH	150 ± 2	145 ± 2

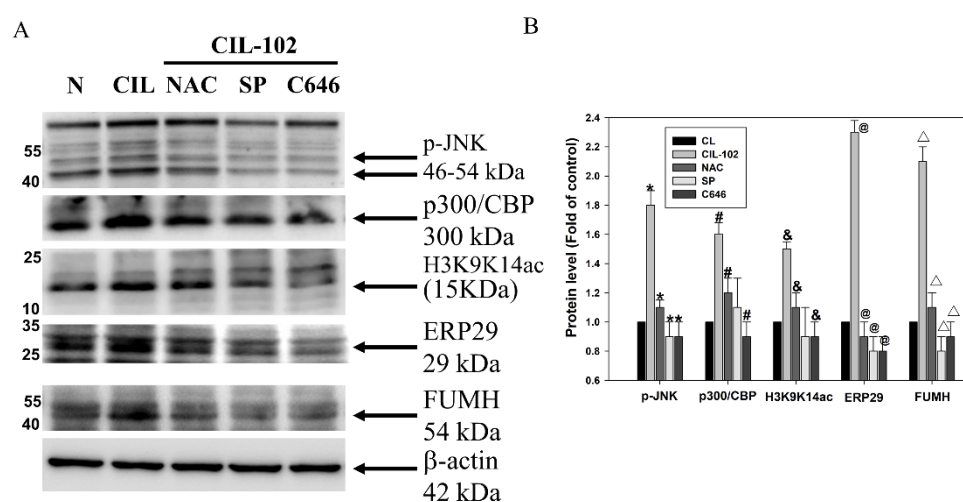


**Figure 6.** ROS production, histone acetylation, and JNK signal participate in the upregulation of ERP29 and FUMH by CIL-102. (A) DLD-1 cells were treated with kinase inhibitors (NAC for the inhibition of ROS production; SP is an inhibitor for the JNN signal; C646 is for the inhibition of acetyltransferase) in the presence or absence of CIL-102. One hour later, all cell lysates were prepared and subjected to a Western blot analysis. (B) The protein levels of phosphorylated JNK, p300/CBP and Histone H3 (H3K9K14ac), ERP29, FUMH, and β-actin were detected with the indicated antibodies and quantified by using a densitometric analysis. After normalization, β-actin served as loading control, and the data are presented as 100% of the untreated control group (means ± SD) from three independent experiments. \*  $p < 0.05$ , p-JNK when compared with the untreated control group. #  $p < 0.05$ , p300/CBP when compared with the untreated control group. &  $p < 0.05$ , H3K9K14ac when compared with the untreated control group. @  $p < 0.05$ , ERP29 when compared with the untreated control group. Δ  $p < 0.05$ , FUMH when compared with the untreated control group.

The results and the data showed that FUMH and ERP29 expression in DLD-1 cells is essential for the implication of oxidative stress ROS and JNK/P300 CBP signaling; this is along with the association that CIL-102 inhibited cell invasion and tumor growth. These results are consistent with the proteomic results, which indicates that a proteomic differential display model FUMH and ERP29 are applicable when assessing CIL-102-inhibited DLD-1 cells.

#### 4. Discussion

Colorectal cancer (CRC) is a sequential multistage process that includes tumor initiation, tumor promotion, and tumor metastasis [29]. Effective agents for CRC treatment have not yet been found. Therefore, bioactive safe compounds from foods have been considered a source for developing the chemo-preventive compounds for cancer chemoprevention

and metastasis suppression. Many reports demonstrate that these chemo-preventive compounds can also inhibit cancer cell metastasis [4,30,31] via a variety of mechanisms, such as ROS production. CIL-102, a derivative of the 9-anilino-furoquinoline from the bark and stems of *Camptotheca acuminata*, is used as an antiseptic drug [8,9]. Anti-cancer and chemo-preventive properties of CIL-102 have recently been reported, including the inhibition of tumor cell proliferation [10], the induction of cell apoptosis, and cell cycle arrest [11,12]. However, the biochemical effect of CIL-102 that triggers its anti-carcinogenic properties in CRC cells and its regulatory mechanism remains unclear. In this study, we found that CIL-102 reduces the aggressive status (migration and invasiveness) of DLD-1 cells (Figure 1). Furthermore, our data indicate the essential role of ROS generation and JNK/p300 CBP pathways during the execution of apoptosis and anti-invasion by using naturally extracted CIL-102 (Figures 2 and 3B, Table 2). This study elucidated the mechanism of the observed inhibition of the metastasis of CRC cells, suggesting that the inhibition of metastasis is related to the CIL-102.

Many studies demonstrate that cellular mechanisms contribute to the overall cancer-prevention effects of these dietary phytochemicals [31,32]. Our previous study demonstrated that CIL-102 causes mitotic arrest and the tumor-growth inhibition of human CRC cells via ROS generation [14–16]. In this study, our data showed how the method of CIL-102 treatment may be used to inhibit the tumor invasion of DLD-1 cells through ROS increment and the activation of the JNK/p300 CBP signaling pathway. With respect to the dosage and duration of inductive ROS production, phenolic phytochemicals activate signal transduction pathways, leading to either cell cycle arrest or apoptosis and invasiveness [4,13,16].

Our present study demonstrates that DLD-1 cells treated with CIL-102 show oxidative alterations in terms of signaling transduction events and ROS overloading that result in the therapeutic effects on cancer invasion (Figure 2, Table 2). To identify the novel CIL-102-regulating molecule and its anti-cancer mechanism, two-dimensional electrophoresis (2-DE)-based proteomic analysis was performed (Figure 4). The level of Endoplasmic Reticulum resident Protein 29 (ERP29) and Fumarate Hydratase (FUMH) were increased in CIL-102-treated DLD-1 cells (Figures 4 and 5). A recent study demonstrated that ERP29, a molecular chaperone, acts as a tumor-suppressor protein and a novel regulator, which leads to cell growth arrest and cell transition from a proliferative to a quiescent state. Furthermore, it leads to the reprogramming of molecular portraits to suppress tumor growth. Thus, ERP29 needs to be further assessed as a potential effect of medical intervention for CRC therapy by CIL-102 for inhibiting the malignant behavior of the CRC [33–35].

In addition, FUMH, an enzyme participating in the Tricarboxylic Acid (TCA) cycle, catalyzes the reversible hydration of fumarate to generate malate [36]. We also previously found the effect of CIL-102 on neuroblastoma cells and identified FUMH as having tumor suppressor- and tumor invasiveness-related proteins. CIL-102 elicits these proteins during the upregulation of FUMH. They play a central role in controlling the migratory potential of tumor cells by regulating the epithelial-to-mesenchymal transition (EMT)-associated gene expression, such as Vimentin and E-cadherin, in response to either oxidative stress or DNA damage [37]. Through JNK/p300 CBP signaling cascades, the trans-differentiation of the EMT pathway is a critical cellular event that controls the induction of cell apoptosis and migration in prostate, breast, and colon cancer cells; further studies are mediated actions in CIL-102-treated CRC cells.

Based on the proteomic differential displays of DLD-1 cells [21,22,27], our results showed the important finding that these activation effects result from a downstream gene of ERP29 and FUMH expression and the phosphorylation of the JNK/p300 CBP pathways, as well as the execution of apoptosis and anti-invasiveness by CIL-102 (Figures 5 and 6 and Table 2). Interestingly, these results, from lenti shRNA ERP29 and shRNA FUMH alone CRC, showed ERP29 and FUMH protected CRC cells from a reduction of malignancy to promote metastasis and may be a potential effect of medical intervention for CRC therapy (Table 2). We recently researched the novel CIL-102-induced protein for either the induction

of cell apoptosis or the inhibition of human DLD-1 cells and their molecular mechanism related to the targeted downstream protein; this was done by using two-dimensional electrophoresis (2-DE)-based proteomic analysis to identify the proteins involved in the activation of JNK/p300 CBP signaling pathway and oxidative stress. It suggested that the generation of ROS, as well as the JNK/p300 CBP pathway, to promote apoptosis and decrease invasiveness could be partly due to the Endoplasmic Reticulum resident Protein 29 (ERP29) and Fumarate hydratase (FUMH) expression by CIL-102. Thus, CIL-102, a derivative of *Camptotheca acuminata*, represents a novel chemotherapeutic agent worth investigating further. To validate these particular findings, further studies using other differential proteins are needed to determine whether there is mediated oxidative stress, DNA damage, and EMT pathway actions.

## 5. Conclusions

In conclusion, on the basis of proteomic differential proteins, we suggest the upregulation of ERP29 and FUMH expression by CIL-102 via the activation of the JNK/p300 CBP pathway and the induction of ROS production (Figure 7). This study is potentially interesting with respect to its novel chemotherapeutic approach of using CIL-102 to treat malignant CRC and cancer development.

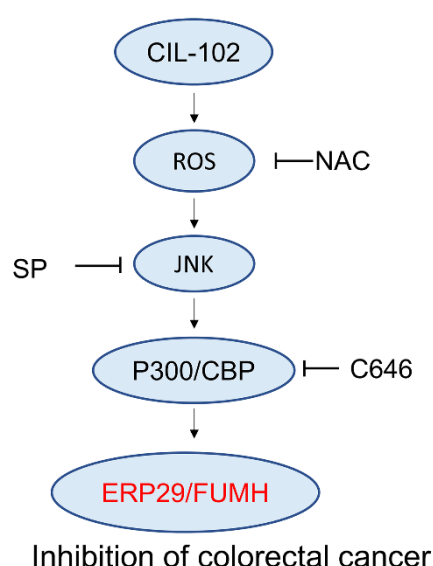


**Figure 7.** Working model of CIL-102 inhibits cell migration and the invasion of DLD-1 cells. ERP29 and FUMH are identified as novel CIL-102-upregulated proteins for the inhibition of cell migration and invasion in colorectal cancer. After the CIL-102 treatment, the activation of ROS and JNK/p300 CBP pathways are involved in cell migration and the invasion of colorectal cancer through the upregulation of ERP29 and FUMH.

**Author Contributions:** K.-C.C., Provision of study material, collection and assembly of data and histopathological evaluation, and manuscript writing, H.-C.K., Design, collection, assembly of data, C.-C.T., Collection, provision of study material, S.-Y.T., provision of study material, C.-H.S., M.-C.H. and C.-Y.H., Provision of study material, K.-F.L., Conception, histopathological evaluation. Y.-L.Y., Administrative support, collection, and assembly of data (flow cytometry). K.-C.L., Conception and design, financial support, administrative support, manuscript writing, final approval of manuscript. All authors have read and agreed to the published version of the manuscript.

**Funding:** The funding for this study was provided in part by research grants from the Chang Gung Memorial Hospital, Kaohsiung, Taiwan. This study was supported by grants CMRPG8J0491, CMRPG8J0492, CMRPG8J1051, and CMRPG8J1052 from Chang Gung Memorial Hospital, Kaohsiung, Taiwan, and Chang Gung University of Science and Technology, Chia-Yi Campus, Taiwan, and by the Ministry of Science and Technology, Taiwan (MOST 107-2320-B-255 -001 -MY3).



**Institutional Review Board Statement:** Not applicable.

**Informed Consent Statement:** Not applicable.

**Data Availability Statement:** All relevant data are within the paper.

**Acknowledgments:** The authors thank Chun-Hsien Chu (Institute of Molecular Medicine, College of Medicine, National Cheng Kung University) for the assistance with scientific consulting and manuscript editing. We thank the “Clinical Proteomics Core Laboratory, Chang Gung Memorial Hospital, Linkou and Genomic & Proteomic Core Laboratory, Kaohsiung Chang Gung Memorial Hospital, Taiwan” for their technical services.

**Conflicts of Interest:** The authors have declared that no competing interest exist. All authors declare no competing interest. This publication has had no significant financial support for this work that could have influenced its outcome.

## References

1. Brenner, H.; Kloor, M.; Pox, C.P. Colorectal cancer. *Lancet* **2014**, *383*, 1490–1502. [\[CrossRef\]](#)
2. Brenner, H.; Chen, C. The colorectal cancer epidemic: Challenges and opportunities for primary, secondary and tertiary prevention. *Br. J. Cancer* **2018**, *119*, 785–792. [\[CrossRef\]](#)
3. Li-Weber, M. New therapeutic aspects of flavones: The anticancer properties of Scutellaria and its main active constituents Wogonin, Baicalein and Baicalin. *Cancer Treat. Rev.* **2009**, *35*, 57–68. [\[CrossRef\]](#) [\[PubMed\]](#)
4. Lee, K.C.; Lee, K.F.; Tung, S.Y.; Huang, W.S.; Lee, L.Y.; Chen, W.P.; Chen, C.C.; Teng, C.C.; Shen, C.H.; Hsieh, M.C.; et al. Induction Apoptosis of Erinacine A in Human Colorectal Cancer Cells Involving the Expression of TNFR, Fas, and Fas Ligand via the JNK/p300/p50 Signaling Pathway with Histone Acetylation. *Front. Pharmacol.* **2019**, *10*, 1174. [\[CrossRef\]](#) [\[PubMed\]](#)
5. Sillars-Hardebol, A.H.; Carvalho, B.; de Wit, M.; Postma, C.; Delis-van Diemen, P.M.; Mongera, S.; Ylstra, B.; van de Wiel, M.A.; Meijer, G.A.; Fijneman, R.J. Identification of key genes for carcinogenic pathways associated with colorectal adenoma-to-carcinoma progression. *Tumor Biol.* **2010**, *31*, 89–96. [\[CrossRef\]](#)
6. Hanahan, D.; Weinberg, R.A. The hallmarks of cancer. *Cell* **2000**, *100*, 57–70. [\[CrossRef\]](#)
7. Li-Weber, M. Targeting apoptosis pathways in cancer by Chinese medicine. *Cancer Lett.* **2013**, *332*, 304–312. [\[CrossRef\]](#)
8. Chen, I.L.; Chen, Y.L.; Tzeng, C.C. An efficient synthesis of antitumor 4-anilino-furo[2,3-b]quinoline derivatives. *Chin. Pharm. J.* **2003**, *55*, 49–53.
9. Chen, Y.L.; Chen, I.L.; Wang, T.C.; Han, C.H.; Tzeng, C.C. Synthesis and anticancer evaluation of certain 4-anilino-furo[2,3-b]quinoline and 4-anilino-furo[3,2-c]quinoline derivatives. *Eur. J. Med. Chem.* **2005**, *40*, 928–934. [\[CrossRef\]](#)
10. Huang, Y.T.; Huang, D.M.; Guh, J.H.; Chen, I.L.; Tzeng, C.C.; Teng, C.M. CIL-102 interacts with microtubule polymerization and causes mitotic arrest following apoptosis in the human prostate cancer PC-3 cell line. *J. Biol. Chem.* **2005**, *280*, 2771–2779. [\[CrossRef\]](#)
11. Chen, Y.-L.; Lin, H.-C.; Yang, C.-N.; Lu, P.-J.; Tzeng, C.-C. Synthesis and Antiproliferative Evaluation of 4-Anilino-n-methoxyfuro[2,3-b]quinoline Derivatives (n = 6, 7). Part 5. *Chem. Biodivers.* **2008**, *5*, 267–278. [\[CrossRef\]](#)
12. Chen, Y.W.; Chen, Y.L.; Tseng, C.H.; Liang, C.C.; Yang, C.N.; Yao, Y.C.; Lu, P.J.; Tzeng, C.C. Discovery of 4-anilino-furo[2,3-b]quinoline derivatives as selective and orally active compounds against non-small-cell lung cancers. *J. Med. Chem.* **2011**, *54*, 4446–4461. [\[CrossRef\]](#) [\[PubMed\]](#)
13. Huang, W.S.; Kuo, Y.H.; Kuo, H.C.; Hsieh, M.C.; Huang, C.Y.; Lee, K.C.; Lee, K.F.; Shen, C.H.; Tung, S.Y.; Teng, C.C. CIL-102-Induced Cell Cycle Arrest and Apoptosis in Colorectal Cancer Cells via Upregulation of p21 and GADD45. *PLoS ONE* **2017**, *12*, e0168989. [\[CrossRef\]](#)
14. Teng, C.C.; Kuo, H.C.; Sze, C.I. Quantitative proteomic analysis of the inhibitory effects of CIL-102 on viability and invasiveness in human glioma cells. *Toxicol. Appl. Pharmacol.* **2013**, *272*, 579–590. [\[CrossRef\]](#)
15. Teng, C.C.; Kuo, H.C.; Cheng, H.C.; Wang, T.C.; Sze, C.I. The inhibitory effect of CIL-102 on the growth of human astrocytoma cells is mediated by the generation of reactive oxygen species and induction of ERK1/2 MAPK. *Toxicol. Appl. Pharmacol.* **2012**, *263*, 73–80. [\[CrossRef\]](#)
16. Teng, C.C.; Tung, S.Y.; Lee, K.C.; Lee, K.F.; Huang, W.S.; Shen, C.H.; Hsieh, M.C.; Huang, C.Y.; Sheen, J.M.; Kuo, H.C. Novel regulator role of CIL-102 in the epigenetic modification of TNFR1/TRAIL to induce cell apoptosis in human gastric cancer. *Food Chem. Toxicol.* **2021**, *147*, 111856. [\[CrossRef\]](#) [\[PubMed\]](#)
17. Huang, W.S.; Hsieh, M.C.; Huang, C.Y.; Kuo, Y.H.; Tung, S.Y.; Shen, C.H.; Hsieh, Y.Y.; Teng, C.C.; Lee, K.F.; Chen, T.C.; et al. The Association of CXCR4 Mediated Signaling Pathway with Oxaliplatin-Resistant Human Colorectal Cancer Cells. *PLoS ONE* **2016**, *11*, e0159927. [\[CrossRef\]](#) [\[PubMed\]](#)
18. Lu, C.C.; Huang, W.S.; Lee, K.F.; Lee, K.C.; Hsieh, M.C.; Huang, C.Y.; Lee, L.Y.; Lee, B.O.; Teng, C.C.; Shen, C.H.; et al. Inhibitory effect of Erinacines A on the growth of DLD-1 colorectal cancer cells is induced by generation of reactive oxygen species and activation of p70S6K and p21. *J. Funct. Foods* **2016**, *21*, 474–484. [\[CrossRef\]](#)

19. Lee, K.F.; Tung, S.Y.; Teng, C.C.; Shen, C.H.; Hsieh, M.C.; Huang, C.Y.; Lee, K.C.; Lee, L.Y.; Chen, W.P.; Chen, C.C.; et al. Post-Treatment with Erinacine A, a Derived Diterpenoid of *H. erinaceus*, Attenuates Neurotoxicity in MPTP Model of Parkinson's Disease. *Antioxidants* **2020**, *9*, 137. [\[CrossRef\]](#) [\[PubMed\]](#)
20. Kuo, H.C.; Kuo, Y.R.; Lee, K.F.; Hsieh, M.C.; Huang, C.Y.; Hsieh, Y.Y.; Lee, K.C.; Kuo, H.L.; Lee, L.Y.; Chen, W.P.; et al. A Comparative Proteomic Analysis of Erinacine A's Inhibition of Gastric Cancer Cell Viability and Invasiveness. *Cell. Physiol. Biochem.* **2017**, *43*, 195–208. [\[CrossRef\]](#) [\[PubMed\]](#)
21. Lee, K.C.; Kuo, H.C.; Shen, C.H.; Lu, C.C.; Huang, W.S.; Hsieh, M.C.; Huang, C.Y.; Kuo, Y.H.; Hsieh, Y.Y.; Teng, C.C.; et al. A proteomics approach to identifying novel protein targets involved in erinacine A-mediated inhibition of colorectal cancer cells' aggressiveness. *J. Cell. Mol. Med.* **2017**, *21*, 588–599. [\[CrossRef\]](#)
22. Tsai, J.J.; Kuo, H.C.; Lee, K.F.; Tsai, T.H. Proteomic analysis of plasma from rats following total parenteral nutrition-induced liver injury. *Proteomics* **2015**, *15*, 3865–3874. [\[CrossRef\]](#)
23. Huang, W.S.; Kuo, Y.H.; Chin, C.C.; Wang, J.Y.; Yu, H.R.; Sheen, J.M.; Tung, S.Y.; Shen, C.H.; Chen, T.C.; Sung, M.L.; et al. Proteomic analysis of the effects of baicalein on colorectal cancer cells. *Proteomics* **2012**, *12*, 810–819. [\[CrossRef\]](#)
24. Huang, W.S.; Chin, C.C.; Chen, C.N.; Kuo, Y.H.; Chen, T.C.; Yu, H.R.; Tung, S.Y.; Shen, C.H.; Hsieh, Y.Y.; Guo, S.E.; et al. Stromal cell-derived factor-1/CXC receptor 4 and beta1 integrin interaction regulates urokinase-type plasminogen activator expression in human colorectal cancer cells. *J. Cell. Physiol.* **2012**, *227*, 1114–1122. [\[CrossRef\]](#) [\[PubMed\]](#)
25. Huang, W.S.; Huang, C.Y.; Hsieh, M.C.; Kuo, Y.H.; Tung, S.Y.; Shen, C.H.; Hsieh, Y.Y.; Teng, C.C.; Lee, K.C.; Lee, K.F.; et al. Expression of PRDX6 Correlates with Migration and Invasiveness of Colorectal Cancer Cells. *Cell. Physiol. Biochem.* **2018**, *51*, 2616–2630. [\[CrossRef\]](#) [\[PubMed\]](#)
26. Ivanova, S.; Polajnar, M.; Narbona-Perez, A.J.; Hernandez-Alvarez, M.I.; Frager, P.; Slobodnyuk, K.; Plana, N.; Nebreda, A.R.; Palacin, M.; Gomis, R.R.; et al. Regulation of death receptor signaling by the autophagy protein TP53INP2. *EMBO J.* **2019**, *38*. [\[CrossRef\]](#)
27. Kuo, H.C.; Chiu, C.C.; Chang, W.C.; Sheen, J.M.; Ou, C.Y.; Kuo, H.C.; Chen, R.F.; Hsu, T.Y.; Chang, J.C.; Hsiao, C.C.; et al. Use of proteomic differential displays to assess functional discrepancies and adjustments of human bone marrow- and Wharton jelly-derived mesenchymal stem cells. *J. Proteome Res.* **2011**, *10*, 1305–1315. [\[CrossRef\]](#)
28. Guo, L.; Ma, L.; Liu, C.; Lei, Y.; Tang, N.; Huang, Y.; Huang, G.; Li, D.; Wang, Q.; Liu, G.; et al. ERp29 counteracts the suppression of malignancy mediated by endoplasmic reticulum stress and promotes the metastasis of colorectal cancer. *Oncol. Rep.* **2019**, *41*, 1603–1615. [\[CrossRef\]](#)
29. Tanaka, T. Colorectal carcinogenesis: Review of human and experimental animal studies. *J. Carcinog.* **2009**, *8*, 5. [\[CrossRef\]](#)
30. Loo, G. Redox-sensitive mechanisms of phytochemical-mediated inhibition of cancer cell proliferation (review). *J. Nutr. Biochem.* **2003**, *14*, 64–73. [\[CrossRef\]](#)
31. NavaneethaKrishnan, S.; Rosales, J.L.; Lee, K.Y. ROS-Mediated Cancer Cell Killing through Dietary Phytochemicals. *Oxid. Med. Cell. Longev.* **2019**, *2019*, 9051542. [\[CrossRef\]](#)
32. Ahmed, K.; Zaidi, S.F.; Cui, Z.G.; Zhou, D.; Saeed, S.A.; Inadera, H. Potential proapoptotic phytochemical agents for the treatment and prevention of colorectal cancer. *Oncol. Lett.* **2019**, *18*, 487–498. [\[CrossRef\]](#)
33. Bambang, I.F.; Xu, S.; Zhou, J.; Salto-Tellez, M.; Sethi, S.K.; Zhang, D. Overexpression of endoplasmic reticulum protein 29 regulates mesenchymal-epithelial transition and suppresses xenograft tumor growth of invasive breast cancer cells. *Lab. Invest.* **2009**, *89*, 1229–1242. [\[CrossRef\]](#) [\[PubMed\]](#)
34. Lafleur, M.A.; Stevens, J.L.; Lawrence, J.W. Xenobiotic perturbation of ER stress and the unfolded protein response. *Toxicol. Pathol.* **2013**, *41*, 235–262. [\[CrossRef\]](#) [\[PubMed\]](#)
35. Chen, S.; Zhang, D. Friend or foe: Endoplasmic reticulum protein 29 (ERp29) in epithelial cancer. *FEBS Open. Bio.* **2015**, *5*, 91–98. [\[CrossRef\]](#)
36. Fuhler, G.M.; Eppinga, H.; Peppelenbosch, M.P. Fumarates and Cancer. *Trends. Mol. Med.* **2017**, *23*, 3–5. [\[CrossRef\]](#) [\[PubMed\]](#)
37. Sciacovelli, M.; Goncalves, E.; Johnson, T.I.; Zecchini, V.R.; da Costa, A.S.; Gaude, E.; Drubbel, A.V.; Theobald, S.J.; Abbo, S.R.; Tran, M.G.; et al. Fumarate is an epigenetic modifier that elicits epithelial-to-mesenchymal transition. *Nature* **2016**, *537*, 544–547. [\[CrossRef\]](#) [\[PubMed\]](#)

Article

# Ailanthoidol, a Neolignan, Suppresses TGF- $\beta$ 1-Induced HepG2 Hepatoblastoma Cell Progression

Tsui-Hwa Tseng <sup>1,2</sup>, Huei-Jane Lee <sup>3</sup>, Yean-Jang Lee <sup>4</sup>, Ko-Chao Lee <sup>5</sup>, Chien-Heng Shen <sup>6,\*</sup>  
and Hsing-Chun Kuo <sup>7,8,9,10,\*</sup>

- <sup>1</sup> Department of Medical Applied Chemistry, Chung Shan Medical University, Taichung 40201, Taiwan; tht@csmu.edu.tw
  - <sup>2</sup> Department of Medical Education, Chung Shan Medical University Hospital, Taichung 40201, Taiwan
  - <sup>3</sup> Department of Biochemistry, School of Medicine, College of Medicine, Chung Shan Medical University, Taichung 40201, Taiwan; lhj@csmu.edu.tw
  - <sup>4</sup> Department of Chemistry, National Changhua University of Education, Changhua 50007, Taiwan; leeyj@cc.ncue.edu.tw
  - <sup>5</sup> Division of Colorectal Surgery, Department of Surgery, Chang Gung Memorial Hospital, Kaohsiung Medical Center, Chang Gung University College of Medicine, Kaohsiung 83301, Taiwan; kmch4329@gmail.com
  - <sup>6</sup> Department of Hepato-Gastroenterology, Chang Gung Memorial Hospital, Chiayi 61363, Taiwan
  - <sup>7</sup> Department of Nursing, Division of Basic Medical Sciences, Chang Gung University of Science and Technology, Chiayi 61363, Taiwan
  - <sup>8</sup> Research Fellow, Chang Gung Memorial Hospital, Chiayi 61363, Taiwan
  - <sup>9</sup> Research Center for Food and Cosmetic Safety, College of Human Ecology, Chang Gung University of Science and Technology, Taoyuan 33303, Taiwan
  - <sup>10</sup> Chronic Diseases and Health Promotion Research Center, Chang Gung University of Science and Technology, Chiayi 61363, Taiwan
- \* Correspondence: gi2216@adm.cgmh.org.tw (C.-H.S.); guscsi@gmail.com (H.-C.K.)



**Citation:** Tseng, T.-H.; Lee, H.-J.; Lee, Y.-J.; Lee, K.-C.; Shen, C.-H.; Kuo, H.-C. Ailanthoidol, a Neolignan, Suppresses TGF- $\beta$ 1-Induced HepG2 Hepatoblastoma Cell Progression. *Biomedicines* **2021**, *9*, 1110. <https://doi.org/10.3390/biomedicines9091110>

Academic Editor: Chung-Jung Liu

Received: 29 July 2021

Accepted: 25 August 2021

Published: 30 August 2021

**Publisher's Note:** MDPI stays neutral with regard to jurisdictional claims in published maps and institutional affiliations.



**Copyright:** © 2021 by the authors. Licensee MDPI, Basel, Switzerland. This article is an open access article distributed under the terms and conditions of the Creative Commons Attribution (CC BY) license (<https://creativecommons.org/licenses/by/4.0/>).

**Abstract:** Ailanthoidol (ATD), a neolignan, possessed an antitumor promotion effect in the mouse skin model in our previous investigation. However, other antitumor properties remain to be elucidated. Liver cancer is a major cause of death in the world, and its prognosis and survival rate are poor. Therefore, the prevention and therapy of liver cancer have received much attention. TGF (transforming growth factor)- $\beta$ 1, a cytokine, plays a critical role in the progression of liver cancer. This study determined the inhibitory effects of ATD on the migration and invasion induced by TGF- $\beta$ 1 in HepG2 hepatoblastoma cells. Furthermore, ATD reduced the TGF- $\beta$ 1-promoted colony number of HepG2 hepatoblastoma cells. In addition to reversing TGF- $\beta$ 1-induced cell scattering, ATD suppressed TGF- $\beta$ 1-induced expression of integrin  $\alpha$ 3, vimentin, N-cadherin, and matrix metalloproteinase 2 (MMP2). Finally, this study found that ATD significantly inhibited TGF- $\beta$ 1-promoted phosphorylation of p-38 mitogen-activated protein kinase (MAPK) and Smad 2. Furthermore, the administration of SB203580 (p38MAPK inhibitor) suppressed TGF- $\beta$ 1-induced expression of integrin  $\alpha$ 3, N-cadherin, and MMP2. These results demonstrate a novel mechanism of ATD against progression of liver cancer.

**Keywords:** Ailanthoidol; TGF- $\beta$ 1; p-38MAPK; anti-hepatic cancer progression

## 1. Introduction

Liver cancer is a common global malignancy with a high recurrence rate and poor prognosis [1]. Metastasis has been notably reported as the major cause of treatment failure in patients with liver cancer [2]. Metastasis, which is a multistep process, includes migration, invasion, implantation, colonization, and proliferation [3]. Migration and invasion of the primary tumor cells occur through the basement membrane and extracellular matrix, and form secondary tumors at distant sites, which are mediated by integrins and proteases. Recently, it has been suggested that epithelial to mesenchymal transition (EMT) contributes to the early spreading of cancer cells [4]. During EMT epithelial, polarized cells become motile mesenchymal appearing cells, where cell–cell attachment is lost, epithelial markers

are downregulated, and mesenchymal markers are upregulated [5]; thus, the search for an agent to block metastasis in liver cancer is a hope to sustain life.

Chronic inflammation is associated with the high incidence rate of several cancers, including liver cancer [6]. The inflammatory cells produce a vast number of cytokines, growth factors, prostaglandin, and chemokines, which may contribute to hepatic tumorigenesis and the progression of liver cancer. Transforming growth factor- $\beta$  (TGF- $\beta$ ) is a multifunctional cytokine that regulates cell growth, apoptosis, differentiation, cell motility, extracellular matrix production, and angiogenesis. TGF- $\beta$  is upregulated in liver cancer tissue and elevated in the plasma of liver cancer patients [7,8], and is reported to activate multiple signaling pathways, including Smad-dependent and Smad-independent pathways involving liver cancer progression. While many reports have demonstrated that TGF- $\beta$  activates Smad pathway mediating EMT, which contributes to hepatoma progression [9], it has been also demonstrated that the inhibition of p38MAPK, which is a downstream substrate of TGF- $\beta$ -activating kinase 1 (TAK-1), reversed TGF- $\beta$ -induced EMT [10]. Overall, developing agents to block TGF- $\beta$ -mediated signal activation may provide a novel preventive and therapeutic strategy to suppress hepatoma progression.

Within phytochemicals, phenolic compounds called lignans have attracted the interest of medicinal and food chemists over years due to their broad range of biological activities including antioxidant, anti-inflammatory, antitumor, and antiviral [11–13]. Growth evidence demonstrate that lignan derivatives possess potential in disease prevention and therapy. Traditionally, lignans are classified into two types: classical lignans and neolignans. Classical lignans are phenylpropane (C6-C3) dimers linked in a  $\beta$ - $\beta'$  linkage and neolignans are composed of two C6-C3 units but not  $\beta$ - $\beta'$  linked [13]. Many classical lignans have been isolated from food such as sesame, whole-grain cereals, and legumes. Lignan-rich diets have been shown to protect against cardiovascular diseases and diabetes [14,15]. In addition, neolignans isolated from Magnolia bark, such as magnolol and honokiol, exhibit efficient effects on inhibiting or preventing the growth of various cancers [16]. Ailanthoidol (ATD) (Figure 1), a neolignan, has been isolated from the barks of *Zanthoxylum ailanthoidol* and demonstrated to possess antioxidant, anti-inflammatory, and anti-adipogenic activities [17–19]. Our previous study showed that ATD displayed antitumor promotion effect using the multistep skin cancer model induced by 12-o-tetradecanoylphorbol-13-acetate [17]. While ATD is a neolignan, its anticancer properties have not been well clarified, thus, this study investigated the effect of ATD on TGF- $\beta$ 1-promoted HepG2 hepatoblastoma cell progression.

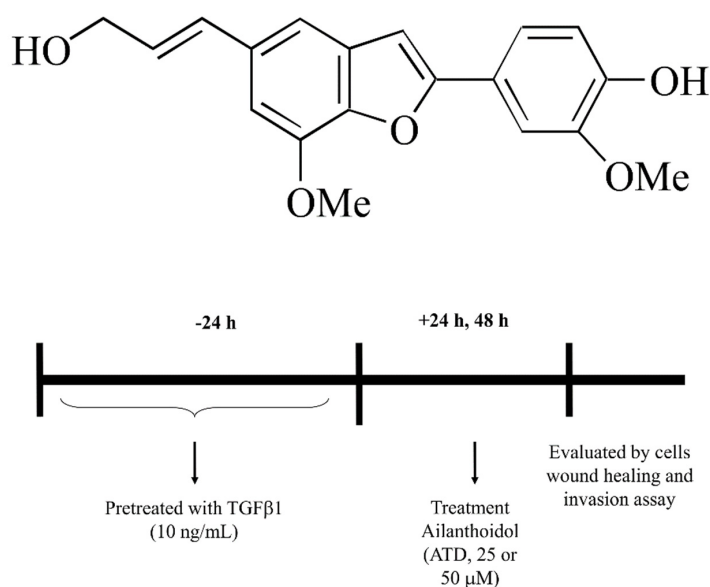


**Figure 1.** Chemical structure of ailanthoidol (ATD). Flow chart of ATD administered after initial of TGF- $\beta$ 1 pretreated HepG2.



## 2. Materials and Methods

### 2.1. Materials

Dulbecco's modified Eagle's medium (DMEM), phosphate-buffered saline (PBS), fetal bovine serum (FBS, catalogue 10437028, Gibco BRL, Grand Island, NY, USA), penicillin/streptomycin/neomycin (PSN, catalogue 15240062, Gibco BRL, Grand Island, NY, USA), and trypsin-EDTA were purchased from Gibco Ltd. (Grand Island, NY, USA). TGF- $\beta$ 1 was from PeproTech, Rocky Hill, NJ, USA (Catalog Number: 100-21). Primary antibodies against integrin  $\alpha$ 3 (sc-374242), vimentin (sc-6260), N-cadherin (sc-8424), MMP2 (sc-13595), Smad 2/3 (sc-398844), and tubulin (sc-5286) were obtained from Santa Cruz Biotechnology, Inc. (Santa Cruz, CA, USA). Anti-p-p38MAPK (#9211), anti-p38MAPK (#9212), and anti-p-Smad 2/3 (#8828) were from Cell Signaling Technology (Beverly, MA, USA). ATD was provided by Dr. Lee and synthesized from 5-bromo-2-hydroxy-3-methoxybenzaldehyde, as previously reported [20]. Matrigel is a solubilized basement membrane preparation extracted from murine sarcomas, and contains proteoglycans, type IV collagen, laminin, and growth factors (Catalog Number: 356234 BD Biosciences, Bedford, MA, USA). Triton X-100, tris base, crystal violet, and all other materials were purchased from Sigma Chemical Co. (St. Louis, MO, USA).

### 2.2. Cell Culture

Human hepatoma HepG2 hepatoblastoma cells, obtained from the American Type Culture Collection (ATCC, Manassas, VA, USA), were cultured in Dulbecco's modified Eagle's medium (DMEM; Gibco BRL, Grand Island, NY, USA) supplemented with 10% fetal bovine serum (FBS) and 1% penicillin–streptomycin–neomycin. The cell line was maintained at 37 °C in a humidified incubator with 5% CO<sub>2</sub>. HepG2 is also referred to as a hepatoblastoma cell line (PubMed: 6248960 and 19751877). ATD was dissolved in DMSO (stock solution: 100 mM).

### 2.3. Cytotoxicity Assay

The HepG2 hepatoblastoma cells were seeded into 24-well culture plates ( $2 \times 10^4$  cells/well), and then treated with various concentrations of ATD (0–100  $\mu$ M) for 24 h and 48 h, respectively, at 37 °C in a humidified incubator with 5% CO<sub>2</sub>. After treatment, the medium was changed and incubated in the presence of 3-[4,5-dimethylthiazol-2-yl]-2,5-diphenyltetrazolium bromide (MTT) dye solution for 4 h. The number of viable cells was directly proportional to the production of formazan, which was then dissolved with dimethyl sulfoxide (DMSO) and the optical density was measured at 540 nm using an ELISA multiwall plate reader.

### 2.4. Wound Healing Assay

Cells ( $5 \times 10^5$  cells per well) were cultured in 6-well plates and pretreated with or without (control group) TGF- $\beta$ 1 (10 ng/mL) for 24 h [21]. A wound was scratched by a 200  $\mu$ L pipette tip. After washing with PBS, the cultured medium was replaced with fresh medium and cotreated with ATD (0, 10, 25, or 50  $\mu$ M) and TGF- $\beta$ 1 (10 ng/mL) for an additional 24 h and 48 h, respectively, at 37 °C in a humidified incubator with 5% CO<sub>2</sub>. Cell migration into the wound area was photographed at 0, 24, and 48 h. The area of cell migration was evaluated in 6 random fields, compared with the wound area at 0 h using ImageJ software, and expressed as a percentage of the initial area. Data are represented as the mean  $\pm$  SD of the three independent experiments.

### 2.5. In Vitro Cell Invasion Assay

The invasion experiment was assessed using transwell plates. Matrigel (BD Transduction Laboratories) was diluted at 1:25 with serum-free DMEM, and fifty microliters of diluted Matrigel was used to coat the upper insert membrane. Cells were pretreated with or without (control group) TGF- $\beta$ 1 (10 ng/mL) for 24 h, then co-treated ATD (0, 25, 50  $\mu$ M) and TGF- $\beta$ 1 (10 ng/mL) for an additional 24 h at 37 °C in a humidified incubator with 5% CO<sub>2</sub>. Then the cells were harvested and the cells ( $2 \times 10^4$  cells/well) in 200  $\mu$ L of

serum-free DMEM were added to the top chamber, while the complete growth medium (15% FBS) was placed in the lower chamber. After incubation for 24 h, the cells on the upper surface of the filter were wiped with a cotton swab, while the cells on the lower surface of the filters were fixed for 15 min with 4% paraformaldehyde and stained with 0.1% crystal violet for 20 min. Then, the cells that had invaded the lower surface of the filter were photographed by light microscopy. The invading cells in 6 randomly selected fields were determined and the counts were averaged.

## 2.6. Colony Assay

HepG2 hepatoblastoma cells ( $2 \times 10^4$  cells/well) were seeded and incubated overnight. The cells were pretreated with or without (control group) TGF- $\beta$ 1 (10 ng/mL) for 24 h, then cotreated with ATD (0, 25, 50  $\mu$ M) and TGF- $\beta$ 1 (10 ng/mL) for an additional 24 h at 37 °C in a humidified incubator with 5% CO<sub>2</sub>. Afterwards, the cells were fixed with 4% paraformaldehyde for 20 min, then stained with 0.1% crystal violet solution in ethanol for 5 min and photographed. The colony number was quantified by ImageJ software that counts the spot of screen photos and expressed as a percentage of the control.

## 2.7. Preparation of Total Cell Extracts and Immunoblot Analysis

Cells were pretreated with or without (control group) TGF- $\beta$ 1 for 24 h, then co-treated with ATD (0, 25, 50  $\mu$ M) and TGF- $\beta$ 1 (10 ng/mL) for an additional 24 h at 37 °C in a humidified incubator with 5% CO<sub>2</sub>. The cells were collected by trypsin-EDTA and lysed in a RIPA buffer (50 mM Tris-HCl, 150 mM NaCl, 1 mM EDTA, 1% NP40, and 0.5% deoxycholic acid containing PMSF, NaVO<sub>4</sub>, DTT, and protease inhibitor). After mixing for 30 min at 4 °C, the mixtures were centrifuged ( $10,000 \times g$ ) for 10 min at 4 °C, and the supernatants were collected as whole-cell extracts. The protein content was determined with the Bio-Rad protein assay reagent using bovine serum albumin as the standard. After equal protein contents of the total cell extracts were boiled for 8 min, the extracts were separated by SDS-polyacrylamide gels and electrophoretically transferred to the PVDF membrane. Following SDS-polyacrylamide gel electrophoresis (PAGE) (10–12% running, 4% stacking), it was transferred to the PVDF member, and protein expression was detected. The blots were blocked with 5% skim milk in PBS for 1 h at room temperature, then incubated overnight with the indicated primary antibodies, followed by incubation with horseradish peroxidase-conjugated goat anti-mouse (or rabbit) IgG for 1 h. Proteins were then blotted onto NC membranes, and reacted with the primary antibodies (integrin  $\alpha$ 3 (1:10,000), vimentin (1:10,000), N-cadherin (1:2000), MMP2 (1:2000), Smad 2/3 (1:2000), and tubulin (1:10,000) were obtained from Santa Cruz Biotechnology, Inc. (Santa Cruz, CA, USA). Anti-p-p38MAPK (1:1000), anti-p38MAPK (1:1000), and anti-p-Smad 2/3 (1:2000) were from Cell Signaling Technology (Beverly, MA, USA)). The secondary antibody was a peroxidase-conjugated goat anti-mouse antibody (1:10,000), obtained from Santa Cruz Biotechnology, Inc., CA, USA. After binding for 1 h, the immune-reactive bands were revealed by enhanced chemiluminescence using an ECL commercial kit. The relative image density was quantitated by densitometry.

## 2.8. Statistical Analysis

Data were expressed as mean  $\pm$  S.D. ( $n = 6$ /group) of three independent experiments and analyzed by one-way ANOVA with Tukey's Multiple Comparison Test. Significant differences were established at  $p < 0.05$ . The data were analysed using the SAS software statistical package SigmaPlot, version 9.0 (SAS Institute Inc., Cary, NC, USA).

# 3. Results

## 3.1. The Cytotoxicity of ATD on HepG2 Hepatoblastoma Cells

The cytotoxic effect of ATD was evaluated in HepG2 hepatoblastoma cells by MTT assay. Various concentrations of ATD (0–100  $\mu$ M) were applied to the HepG2 hepatoblastoma cells for 24 and 48 h. As shown in Figure 2, doses of ATD up to 25  $\mu$ M exhibited

no significant growth inhibition on HepG2 cells regardless of treatment for 24 h or 48 h. In addition, 50  $\mu$ M ATD treated for 24 h inhibited cell viability as compared to control group ( $p < 0.05$ ), but that was not significant as compared to the 25  $\mu$ M ATD treated group. IC<sub>50</sub> of ATD on HepG2 cells for 48 h was near 100  $\mu$ M. To clarify the role of ATD on TGF- $\beta$ 1-induced progression of liver cancer, 0–50  $\mu$ M concentrations of ATD were used in this study.

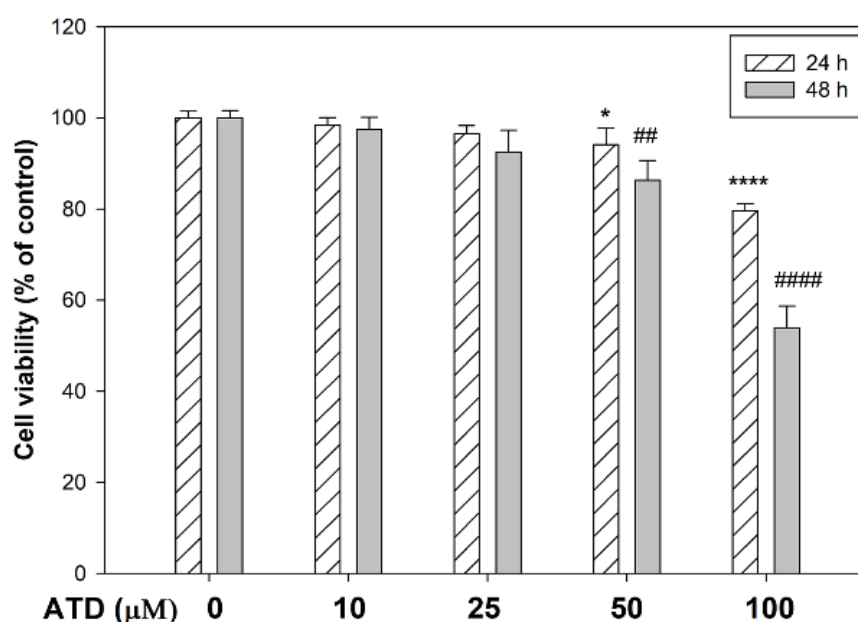


**Figure 2.** The cytotoxic effect of ATD on the HepG2 hepatoblastoma cells was measured by MTT assay. Cells were seeded in 24-well plates at  $2 \times 10^4$  cells/well. After attachment, cells were treated with various concentrations of ATD (0–100  $\mu$ M) for 24 h and 48 h. The cell viability was determined by MTT assay as described in the text. Data are represented as the mean  $\pm$  SD from three independent experiments. \*  $p < 0.05$ , \*\*\*\*  $p < 0.0001$ , compared with the control group (0.2% DMSO) of treatment for 24 h. ##  $p < 0.01$ , ####  $p < 0.0001$ , compared with the control group (0.2% DMSO) of treatment for 48 h.

### 3.2. Inhibitory Effect of ATD on TGF- $\beta$ 1-Promoted Migration and Invasion of HepG2 Hepatoblastoma Cells

Since metastasis depends on increased motility or invasion of tumor cells to successfully colonize a secondary site, the effect of ATD on TGF- $\beta$ 1-promoted cell motility growth in HepG2 hepatoblastoma cells was evaluated by wound healing assay. According to photographs (Figure 3), TGF- $\beta$ 1 treated for 48 h after the created wound displayed obvious migration growth. The continuous rapid movement was observed for HepG2 cells, but a resultant movement of a cell migration front was clearly evident at 48 h, where a highly confluent monolayer region gradually migrated into the cell-free ‘scratch’ region. In the presence of TGF- $\beta$ 1, migration was significantly increased after 24 and 48 h, whereas treatment with ATD lead to an inhibition of cell migration in a dose-dependent manner, shown as 91%, 83%, and 72% (Figure 3). As shown in Figure 3, TGF- $\beta$ 1 significantly ( $p < 0.01$ ) promoted cell migration, which was inhibited when cotreated with ATD (25  $\mu$ M and 50  $\mu$ M) for 48 h in HepG2 hepatoblastoma cells significantly. We further examined whether ATD affected TGF- $\beta$ 1-promoted invasion in HepG2 hepatoblastoma cells using the transwell assay, and the results show that treatment with ATD (25  $\mu$ M and 50  $\mu$ M) significantly inhibited TGF- $\beta$ 1-promoted cell invasion (Figure 4).

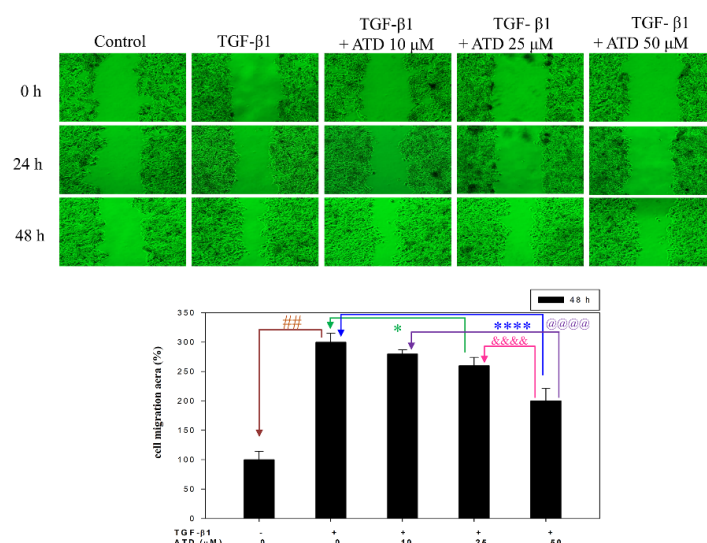


**Figure 3.** Effect of ATD on TGF-β1-induced migration of HepG2 hepatoblastoma cells by wound-healing assay. Cells were cultured in 6-well plates and pretreated with or without (control group) 10 ng/mL of TGF-β1 for 24 h. A wound was scratched by a 200 μL pipette tip. After washing with PBS, cultured medium was replaced with fresh medium and with or without coadministration of TGF-β1 and ATD (0, 10, 25, or 50 μM) for 24 h and 48 h, then photographed at 0 h, 24 h, and 48 h. Migration activity of cotreated with TGF-β1 and ATD for 48 h was quantified with ImageJ software. Data are represented as the mean  $\pm$  SD from three independent experiments. ##: TGF-β1 vs. control,  $p < 0.01$ ; \*: TGF-β1 vs. TGF-β1 + 25 μM ATD,  $p < 0.05$ ; \*\*\*\*: TGF-β1 vs. TGF-β1 + 50 μM ATD,  $p < 0.0001$ ; &&&&: TGF-β1 + 25 μM ATD vs. TGF-β1 + 50 μM ATD,  $p < 0.0001$ ; @@@@: TGF-β1 + 10 μM ATD vs. TGF-β1 + 50 μM ATD,  $p < 0.0001$ .

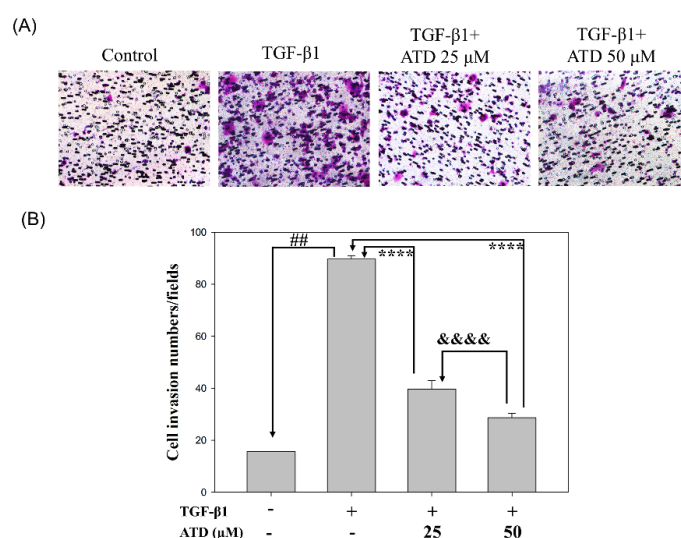


**Figure 4.** Effect of ATD on invasion induced by TGF-β1 in HepG2 hepatoblastoma cells. Cells were pretreated with or without (control group) TGF-β1 for 24 h, then co-treated indicated concentration of ATD and TGF-β1 for an additional 24 h. Cells were harvested and seeded onto upper chamber which was coated with Matrigel. The transwell chamber assay was performed as described in the text. (A) After incubation for 24 h, invasion cells in the lower surface of membrane were fixed, then stained with crystal violet solution and photographed at 200 $\times$  magnification. (B) The invasion cells were quantified in 6 randomly selected fields per well ( $n = 6$ ) using a light microscope. Data are represented as the mean  $\pm$  SD. ##: TGF-β1 vs. control,  $p < 0.01$ ; \*\*\*\*: TGF-β1 vs. TGF-β1 + 25 μM ATD or + 50 μM ATD,  $p < 0.0001$ ; &&&&: TGF-β1 + 25 μM ATD vs. TGF-β1 + 50 μM ATD,  $p < 0.0001$ .



### 3.3. Effect of ATD on Colonization of HepG2 Hepatoblastoma Cells

To further evaluate the effect of ATD on the TGF- $\beta$ 1-promoted colonization growth in vitro, a colony assay was performed. After various administrations of TGF- $\beta$ 1 and ATD for 24 h, one thousand cells were counted and seeded onto a dish, and the culture was maintained for 2 weeks. The result showed that administration of TGF- $\beta$ 1 increased the colony formation of HepG2 cells as compared to the control group (Figure 5). The cotreatment group showed that ATD significantly reduced TGF- $\beta$ 1-promoted colony formation of HepG2 cells (Figure 5).

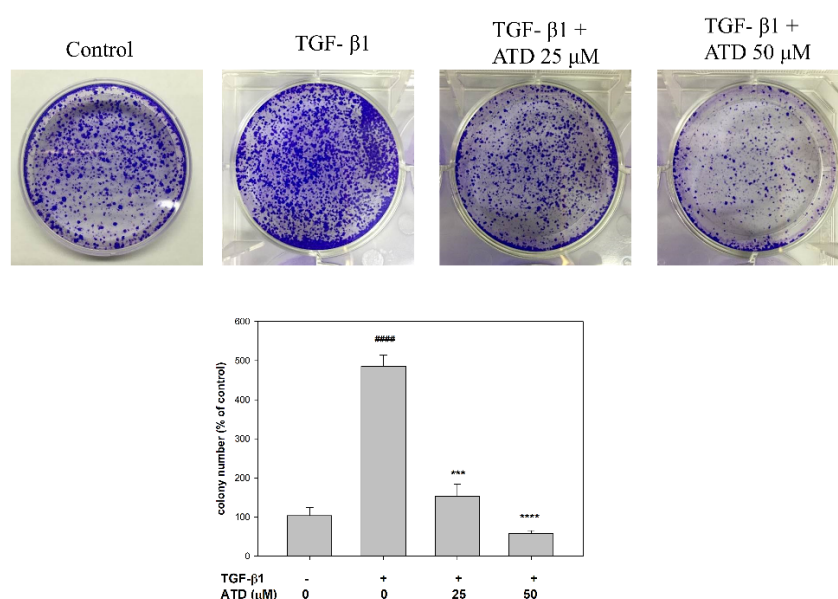


**Figure 5.** Effect of ATD on TGF- $\beta$ 1-promoted growth in HepG2 hepatoblastoma cells by colony formation assay. After treatment with ATD or cotreatment ATD and TGF- $\beta$ 1 for 24 h, 1000 cells were seeded on 6-well plate and cultured for 2 weeks, then cells were fixed with methanol and stained with crystal violet. Colony numbers were quantified by ImageJ software. Data are represented as the mean  $\pm$  SD from the three independent experiments. #  $p < 0.05$ , ##  $p < 0.01$ , #####  $p < 0.0001$ , compared with the control group treated (0.2% DMSO). \*\*\*: TGF- $\beta$ 1 vs. TGF- $\beta$ 1 + 25  $\mu$ M ATD,  $p < 0.001$ ; \*\*\*\*: TGF- $\beta$ 1 vs. TGF- $\beta$ 1 + 50  $\mu$ M ATD,  $p < 0.0001$ .

### 3.4. Effect of ATD on TGF- $\beta$ 1-Induced Cell Scattering

Cell scattering is a critical manifest of several physiological and pathological processes such as tissue regeneration and cancer cell invasion. In the morphology observation, we found that the cells exhibited remarkable cell scattering after treatment with TGF- $\beta$ 1, while the cultured HepG2 hepatoblastoma cells displayed a tight junction. Figure 6 shows that treatment with TGF- $\beta$ 1-induced cell scattering was reversed by co-treatment with ATD.

### 3.5. Alterations of ATD on TGF- $\beta$ 1-Induced Progression Associated Protein Marker Expression in HepG2 Hepatoblastoma Cells

Due to their diverse roles, integrins are key players in cancer metastasis, such as in cell motility [22]. It has been reported that TGF- $\beta$ 1 plays a critical role in liver cancer progression by stimulating integrin  $\alpha$ 3 expression [23]. In addition, the expression of N-cadherin and vimentin facilitates the process of EMT and promotes migration and invasion. ECM degradation by MMPs also promotes cell migration and invasion. This study examined the effect of ATD on TGF- $\beta$ 1-induced expression of cancer cell progression associated proteins, and the results showed TGF- $\beta$ 1 promoted the expression of integrin  $\alpha$ 3, N-cadherin, vimentin, and MMP2, while TGF- $\beta$ 1 cotreated with ATD inhibited such expression (Figure 7). It implicated that ATD suppressed TGF- $\beta$ 1-induced expression of progression-associated proteins.

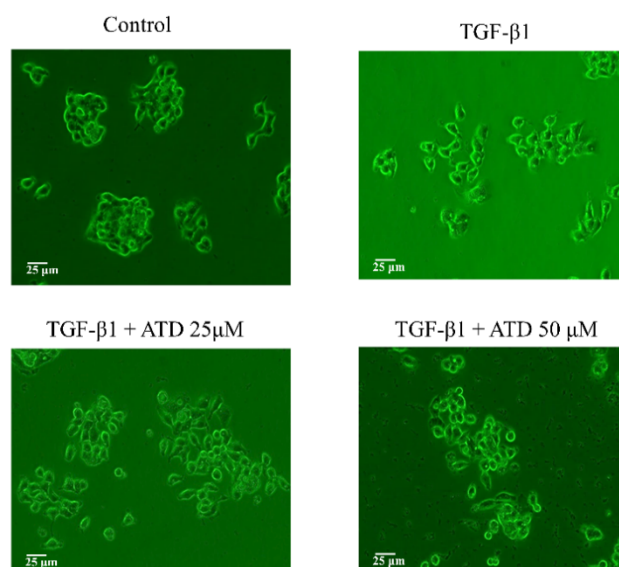


**Figure 6.** Reverse effect of ATD on TGF- $\beta$ 1-induced cell scattering in HepG2 hepatoblastoma cells. The cell was applied with or without (control group) TGF- $\beta$ 1 for 24 h, and then TGF- $\beta$ 1 co-treated with or without ATD for an additional 24 h. The cell was observed under phase contrast microscopy (200 $\times$ ) and photographed.

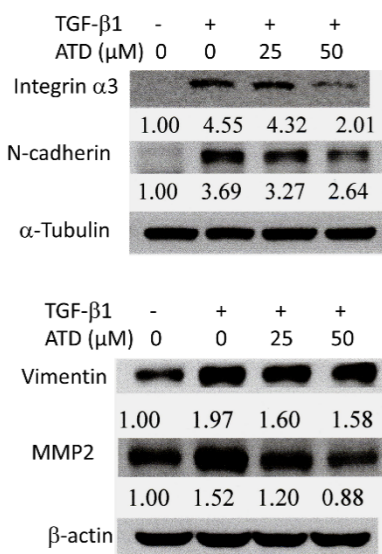


**Figure 7.** Effect of ATD on the cancer progression markers induced by TGF- $\beta$ 1 in HepG2 hepatoblastoma cells. Following the TGF- $\beta$ 1 and ATD treatment as described in the text, the cell lysates were prepared and subjected to the immunoblotting analysis using antibodies against integrin- $\alpha$ 3, vimentin, N-cadherin, MMP2, and  $\alpha$ -tubulin or  $\beta$ -actin as loading control. The relative image density was quantitated by densitometer.

### 3.6. ATD Inactivating TGF- $\beta$ 1-Induced p38MAPK and SMAD Signaling

In addition to activating the Smad signaling pathway, TGF- $\beta$ 1 activates kinase-1 (TAK1), which in turn triggers the activation of downstream p38MAPK [24]. p38MAPK has been implicated in a wide range of complex biologic processes, such as migration and invasion in solid tumors [25]. In order to resolve the mechanisms by which ATD inhibited migration and invasion, as induced by TGF- $\beta$ 1 in HepG2 hepatoblastoma cells, we examined the phosphorylation of p38MAPK and Smads. While TGF- $\beta$ 1 upregulated phosphorylation of Smad2 and p38MAPK, ATD (25 or 50  $\mu$ M) co-treated significantly

inhibited the phosphorylation of p38MAPK, and ATD (50  $\mu$ M) co-treated significantly inhibited the phosphorylation of Smad2 (Figure 8A). In addition, SB203580, which is a p38MAPK inhibitor, was used to confirm the effect of blocking p38MAPK and alleviating the TGF- $\beta$ -induced progression associated protein expression. The results showed that SB203580 (5  $\mu$ M) inhibited TGF- $\beta$ -enhanced expression of integrin  $\alpha$ 3, N-cadherin, and MMP2 (Figure 8B).

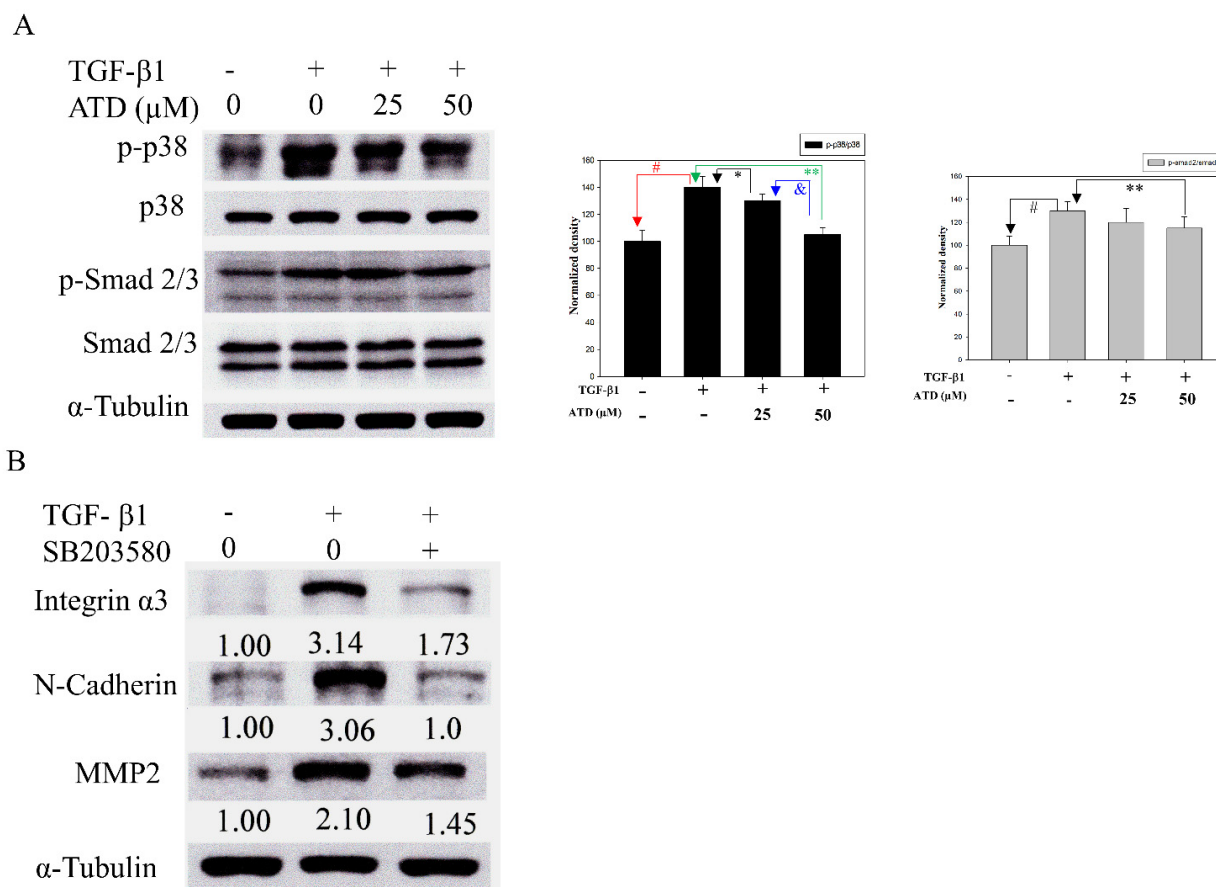


**Figure 8.** Effect of ATD on TGF- $\beta$ 1-induced p38MAPK and Smad 2/3 pathway. **(A)** After treatment of TGF- $\beta$ 1 and ATD as described in the text, the cell lysates were prepared and subjected to immunoblotting analysis using antibodies against p-p38MAPK, p-Smad 2/3, p38MAPK, Smad 2/3, and  $\alpha$ -tubulin (loading control). The average densitometric value was shown as mean  $\pm$  SD ( $n = 3$ ). #: TGF- $\beta$ 1 vs. control,  $p < 0.05$ ; \*: TGF- $\beta$ 1 vs. TGF- $\beta$ 1 + 25  $\mu$ M ATD,  $p < 0.05$ ; \*\*: TGF- $\beta$ 1 vs. TGF- $\beta$ 1 + 50  $\mu$ M ATD,  $p < 0.01$ ; &: TGF- $\beta$ 1 + 25  $\mu$ M ATD vs. TGF- $\beta$ 1 + 50  $\mu$ M ATD,  $p < 0.05$ . **(B)** Cells were pretreated with or without TGF- $\beta$ 1 for 24 h, then co-treated with 5  $\mu$ M p38 MAPK inhibitor (SB203580) and TGF- $\beta$ 1 for an additional 24 h. The cell lysates were subjected to immunoblotting analysis using antibodies against integrin- $\alpha$ 3, N-cadherin, MMP2, and  $\alpha$ -tubulin (loading control). The relative image density was quantitated by a densitometer.

#### 4. Discussion

Most liver cancer occurs in patients with chronic liver disease, which appears as hepatitis, fibrosis, and cirrhosis, and suggests that liver cancer is an inflammation-associated cancer [26]. Cytokines are key mediators of inflammation. TGF- $\beta$  is a multifunctional cytokine, which plays a critical role in arranging a favorable microenvironment for tumor growth and progression. TGF- $\beta$  promotes hepatocellular carcinoma progression via an autocrine or paracrine growth factor, which induces microenvironment changes that trigger cell migration and invasion [27]. TGF- $\beta$ 1 has been reported to promote HepG2 hepatoblastoma cell migration and invasion [28]. The occurrence of EMT is affected by various factors such as TGF- $\beta$ 1 [29]. Furthermore, TGF- $\beta$ 1 stimulates integrin  $\alpha$ 3 expression, which has been suggested to play an important role in liver cancer invasiveness [23]. In the

present study, in addition to reversing TGF- $\beta$ 1-promoted cell scattering, ATD attenuated TGF- $\beta$ 1-induced the expression of cancer progression-associated proteins (Figure 7), which is a novel action of ATD on antitumor progression.

Cancer is a multiple-cause disease in which many signaling pathways are affected [30]. MAPK mediates a wide variety of cellular behaviors in response to extracellular stimuli. As one of the main subgroups, p38MAPK has been implied in a broad range of complicated biological processes, including cell proliferation, cell death, cell differentiation, cell migration, and cell invasion. The specific function of p38MAPK appears to depend not only on the cell type, but also on the stimulants. Liver cancer development is controlled by both extracellular factors and intracellular signaling pathways. TGF- $\beta$ 1, which is a cytokine, plays a critical role in liver cancer progression involving Smad-dependent and independent pathways [31]. TGF- $\beta$ 1 activates the TGF- $\beta$ 1/II receptor, which phosphorylates Smad2 and Smad3, leading to the formation of a heteromeric Smad complex with cytosolic Smad4. The Smad complex translocates to the nucleus, where it regulates gene transcription of several transcription factors involved in the EMT induction. In addition to the Smad pathway, the activation of the p38MAPK pathway has been reported to contribute to the EMT in the primary tumor, as well as to the acquisition of tumor cell migration and invasion. It has been reported that TGF- $\beta$ 1 activates Smad and TAK1/p38MAPK pathways targeting ATF-2 synergistically induce trans-activation capacity [32]. Silencing ATF2 demonstrates anticancer effects in liver cancer [33]. This study found that ATD could attenuate TGF- $\beta$ 1-induced phosphorylation of nuclear ATF2 (data not shown), thus, whether ATD inactivated other transcription factors in the downstream of p38MAPK requires further clarification. The results show that ATD attenuated TGF- $\beta$ 1-promoted HepG2 hepatoblastoma cell progression by inhibiting Smad-dependent and independent pathways (Figure 9). According to Figure 8, it also reveals that ATD reduced TGF- $\beta$ 1-induced expression of invasion-associated proteins in large part through blocking p38MAPK signaling.

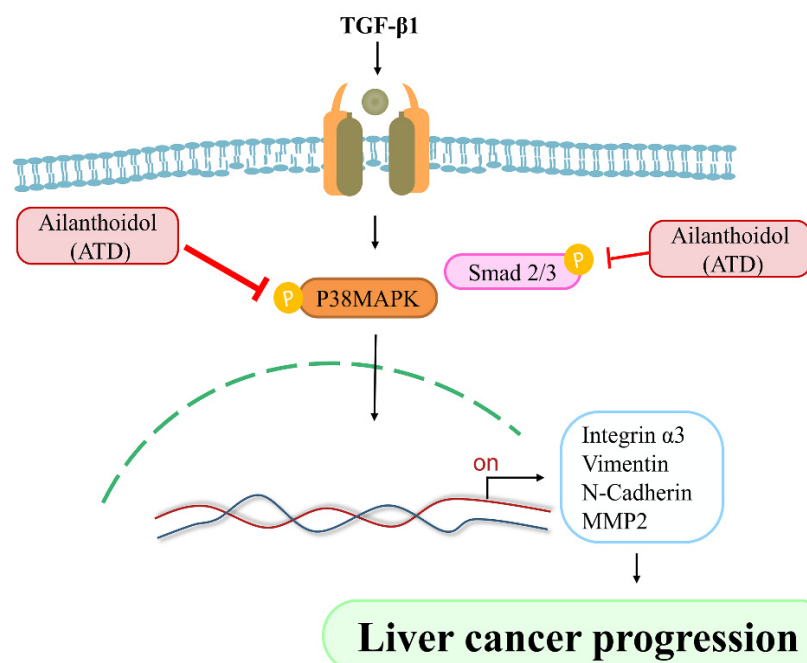


**Figure 9.** Effect of anti-tumor potential of Ailanthoidol (ATD), ATD blocks TGF- $\beta$ 1 activated two signaling axes: P38MARK pathway and Smad 2/3 pathway, resulting in down-regulation of liver cancer progression associated proteins.

Plants are the major food and pharmaceutical origins of humans. Some phytochemicals, such as alkaloids, diterpenoids, and sesquiterpenes, display therapeutic potential in cancer [34]. However, these therapeutic phytochemicals are also associated with adverse



side effects, such as cardiovascular diseases, vomiting, renal dysfunction, and myelotoxicity. In addition, certain polyphenol-rich foods have been reported to reduce the incidence and mortality rates of cancer, as well as delay cancer progression [35]. However, past studies have found that in order to exert the health benefits, the required dose of polyphenols is higher than humans can consume [36]. Therefore, it is imperative to develop chemotherapy or chemoprevention substances with minimal side effects and good bioavailability. Thus, it has been suggested that plants are still a reservoir possessing enormous potential to provide chemotherapy or chemoprevention. Recently, neolignan derivatives are suggested to possess great potential for chemoprevention and treatment [37]. In addition, it has been reported that compounds containing heterocyclic moieties can boost salt formation properties, which are important for bioavailability [38]. Recently, neolignan derivatives were suggested to possess great potential for chemoprevention and treatment [16]. Several neolignans from the Magnolia family are biphenyl neolignans found to possess a good safety profile while ATD is a neolignan with a 2-arylbenzofuran skeleton. [16] In addition, it has been reported that compounds containing heterocyclic moieties can boost salt formation properties, which are important for bioavailability [38]. For real application, animal studies of ATD are required to clarify the *in vivo* properties such as adsorption, distribution, metabolism, and elimination in the future. In addition, growing evidence has been shown that chronic inflammation is associated with high incidence of several cancers [6]. Targeting inflammatory pathways has proven effective in preventing the formation of colonic tumors and their malignant progression in both preclinical and clinical studies. Synthetic non-steroidal anti-inflammatory drugs have been recognized as potential colorectal cancer chemopreventive agents; however, most of these synthetic agents are associated with sometimes fatal or unwanted side effects [39]. A large amount of evidence supports the effectiveness of natural phytochemicals with anti-inflammatory activity in the prevention and treatment of cancer [40]. Our previous study found that ATD inhibited 12-o-tetradecanoylphorbol-13-acetate induced COX-2 expression and myeloperoxidase activation. It implicated that ATD possessed anti-inflammatory bioactivity [17]. Kim and Jun reported that ATD suppresses lipopolysaccharide-stimulated inflammatory in RAW 264.3 cells and endotoxin shock in mice [18]. The present investigation demonstrates that ATD exerts antitumor progression properties by modulating the effect of cytokine. While ATD is a neolignan with heterocyclic moiety and possesses antiinflammatory activity, whether it can play a role in chemoprevention requires further investigation.

## 5. Conclusions

This study first demonstrated a novel mechanism—that ATD exerted antitumor potential through suppressing TGF- $\beta$ 1-promoted HepG2 hepatoblastoma cell progression, which involves blocking p38MAPK and Smad 2 signaling (Figure 9). Further investigation is required to elucidate the universal anticancer properties of ATD against human hepatoblastoma cell lines.

**Author Contributions:** T.-H.T.: Provision of study material, collection and assembly of data, histopathological evaluation, and manuscript writing. H.-J.L., Y.-J.L. and K.-C.L.: Provision of study material, collection, and assembly of data. C.-H.S. and H.-C.K.: Conception and design, financial support, administrative support, manuscript writing, final approval of manuscript. All authors have read and agreed to the published version of the manuscript.

**Funding:** This work was supported by the Ministry of Science and Technology Grant (MOST 108-2320-B-040-016-MY3 and MOST 110-2320-B255-005-MY3), Taiwan. The instruments were performed in the Instrument Center of Chung Shan Medical University, which was supported by the Ministry of Science and Technology, Ministry of Education and Chung Shan Medical University, Taiwan. This study was supported by grants CMRPG6J0151, CMRPG6J0152, CMRPG6J0153, and ZRRPF6K0011 from Chang Gung Memorial Hospital, and Chang Gung University of Science and Technology, Chia-Yi, Taiwan.

**Institutional Review Board Statement:** Not applicable.

**Informed Consent Statement:** Not applicable.

**Data Availability Statement:** All relevant data are within the paper.

**Conflicts of Interest:** The authors declare no conflict of interest.

## References

- Bruix, J.; Gores, G.J.; Mazzaferro, V.M. Hepatocellular carcinoma: Clinical frontiers and perspectives. *Gut* **2014**, *63*, 844–855. [\[CrossRef\]](#)
- Song, P.-M.; Zhang, Y.; He, Y.-F.; Bao, H.-M.; Luo, J.-H.; Liu, Y.-K.; Yang, P.-Y.; Chen, X. Bioinformatics analysis of metastasis-related proteins in hepatocellular carcinoma. *World J. Gastroenterol.* **2008**, *14*, 5816–5822. [\[CrossRef\]](#) [\[PubMed\]](#)
- Jiang, W.; Sanders, A.; Katoh, M.; Ungefroren, H.; Gieseler, F.; Prince, M.; Thompson, S.K.; Zollo, M.; Spano, D.; Dhawan, P.; et al. Tissue invasion and metastasis: Molecular, biological and clinical perspectives. *Semin. Cancer Biol.* **2015**, *35*, S244–S275. [\[CrossRef\]](#) [\[PubMed\]](#)
- Giannelli, G.; Koudelkova, P.; Dituri, F.; Mikulits, W. Role of epithelial to mesenchymal transition in hepatocellular carcinoma. *J. Hepatol.* **2016**, *65*, 798–808. [\[CrossRef\]](#)
- Shankar, J.; Nabi, I.R. Actin Cytoskeleton Regulation of Epithelial Mesenchymal Transition in Metastatic Cancer Cells. *PLoS ONE* **2015**, *10*, e0119954. [\[CrossRef\]](#)
- Multhoff, G.; Molls, M.; Radons, J. Chronic Inflammation in Cancer Development. *Front. Immunol.* **2012**, *2*, 98. [\[CrossRef\]](#)
- Gupta, D.K.; Singh, N.; Sahu, D.K. Article Commentary: TGF- $\beta$  Mediated Crosstalk between Malignant Hepatocyte and Tumor Microenvironment in Hepatocellular Carcinoma. *Cancer Growth Metastasis* **2014**, *7*, CGM.S14205–8. [\[CrossRef\]](#) [\[PubMed\]](#)
- Refolo, M.G.; Messa, C.; Guerra, V.; Carr, B.I.; D'Alessandro, R. Inflammatory Mechanisms of HCC Development. *Cancers* **2020**, *12*, 641. [\[CrossRef\]](#) [\[PubMed\]](#)
- Peng, L.; Yuan, X.-Q.; Zhang, C.-Y.; Ye, F.; Zhou, H.-F.; Li, W.-L.; Liu, Z.-Y.; Zhang, Y.-Q.; Pan, X.; Li, G.-C. High TGF- $\beta$ 1 expression predicts poor disease prognosis in hepatocellular carcinoma patients. *Oncotarget* **2017**, *8*, 34387–34397. [\[CrossRef\]](#)
- Yu, L.; Hébert, M.C.; Zhang, Y. TGF-beta receptor-activated p38 MAP kinase mediates Smad-independent TGF-beta responses. *EMBO J.* **2002**, *21*, 3749–3759. [\[CrossRef\]](#)
- Durazzo, A.; Lucarini, M.; Camilli, E.; Marconi, S.; Gabrielli, P.; Lisciani, S.; Gambelli, L.; Aguzzi, A.; Novellino, E.; Santini, A.; et al. Dietary Lignans: Definition, Description and Research Trends in Databases Development. *Molecules* **2018**, *23*, 3251. [\[CrossRef\]](#)
- Teponno, R.B.; Kusari, S.; Spiteller, M. Recent advances in research on lignans and neolignans. *Nat. Prod. Rep.* **2016**, *33*, 1044–1092. [\[CrossRef\]](#) [\[PubMed\]](#)
- Pan, J.-Y.; Chen, S.-L.; Yang, M.-H.; Wu, J.; Sinkkonen, J.; Zou, K. An update on lignans: Natural products and synthesis. *Nat. Prod. Rep.* **2009**, *26*, 1251–1292. [\[CrossRef\]](#) [\[PubMed\]](#)
- Peterson, J.; Dwyer, J.; Adlercreutz, H.; Scalbert, A.; Jacques, P.; McCullough, M.L. Dietary lignans: Physiology and potential for cardiovascular disease risk reduction. *Nutr. Rev.* **2010**, *68*, 571–603. [\[CrossRef\]](#)
- Barre, D.E.; Mizier-Barre, K.A. Lignans' Potential in Pre and Post-onset Type 2 Diabetes Management. *Curr. Diabetes Rev.* **2019**, *16*, 2–11. [\[CrossRef\]](#)
- Ong, C.P.; Lee, W.L.; Tang, Y.-Q.; Yap, W.H. Honokiol: A Review of Its Anticancer Potential and Mechanisms. *Cancers* **2019**, *12*, 48. [\[CrossRef\]](#)
- Lee, Y.-J.; Kao, E.-S.; Chu, C.-Y.; Lin, W.-L.; Chiou, Y.-H.; Tseng, T.-H. Inhibitory effect of aianthoidol on 12-O-tetradecanoyl-phorbol-13-acetate-induced tumor promotion in mouse skin. *Oncol. Rep.* **2006**, *16*, 921–927. [\[CrossRef\]](#)
- Kim, J.-K.; Jun, J.-G. Ailanthoidol suppresses lipopolysaccharide-stimulated inflammatory reactions in RAW264.7 cells and endotoxin shock in mice. *J. Cell. Biochem.* **2011**, *112*, 3816–3823. [\[CrossRef\]](#)
- Park, J.-H.; Jun, J.-G.; Kim, J.-K. Anti-Adipogenic Activity of Ailanthoidol on 3T3-L1 Adipocytes. *Biomed. Sci. Lett.* **2014**, *20*, 62–69.
- Lin, S.-Y.; Chen, C.-L.; Lee, Y.-J. Total Synthesis of Ailanthoidol and Precursor XH14 by Stille Coupling. *J. Org. Chem.* **2003**, *68*, 2968–2971. [\[CrossRef\]](#)
- Lee, H.; Pyo, M.J.; Bae, S.K.; Heo, Y.; Choudhary, I.; Hwang, D.; Yang, H.; Kim, J.-H.; Chae, J.; Han, C.H.; et al. Nemopilema nomurai jellyfish venom exerts an anti-metastatic effect by inhibiting Smad- and NF- $\kappa$ B-mediated epithelial-mesenchymal transition in HepG2 cells. *Sci. Rep.* **2018**, *8*, 2808. [\[CrossRef\]](#) [\[PubMed\]](#)
- Ganguly, K.K.; Pal, S.; Moulik, S.; Chatterjee, A. Integrins and metastasis. *Cell Adhes. Migr.* **2013**, *7*, 251–261. [\[CrossRef\]](#)
- Giannelli, G.; Fransvea, E.; Marinosci, F.; Bergamini, C.; Colucci, S.; Schiraldi, O.; Antonaci, S. Transforming Growth Factor- $\beta$ 1 Triggers Hepatocellular Carcinoma Invasiveness via  $\alpha$ 3 $\beta$ 1 Integrin. *Am. J. Pathol.* **2002**, *161*, 183–193. [\[CrossRef\]](#)
- Hao, J.; Chen, D. TGF- $\beta$  signaling in hepatocellular carcinoma suppression and progression. *Tradit. Med. Res.* **2018**, *3*, 10–21. [\[CrossRef\]](#)
- Koul, H.K.; Pal, M.; Koul, S. Role of p38 MAP Kinase Signal Transduction in Solid Tumors. *Genes Cancer* **2013**, *4*, 342–359. [\[CrossRef\]](#)
- Yu, L.-X.; Ling, Y.; Wang, H.-Y. Role of nonresolving inflammation in hepatocellular carcinoma development and progression. *NPJ Precis. Oncol.* **2018**, *2*, 6. [\[CrossRef\]](#) [\[PubMed\]](#)
- Giannelli, G.; Villa, E.; Lahn, M. Transforming Growth Factor- $\beta$  as a Therapeutic Target in Hepatocellular Carcinoma. *Cancer Res.* **2014**, *74*, 1890–1894. [\[CrossRef\]](#) [\[PubMed\]](#)

28. Chen, B.; Zhou, S.; Zhan, Y.; Ke, J.; Wang, K.; Liang, Q.; Hou, Y.; Zhu, P.; Ao, W.; Wei, X.; et al. Dioscin Inhibits the Invasion and Migration of Hepatocellular Carcinoma HepG2 Cells by Reversing TGF- $\beta$ 1-Induced Epithelial-Mesenchymal Transition. *Molecules* **2019**, *24*, 2222. [[CrossRef](#)]
29. Yilmaz, M.; Christofori, G. EMT, the cytoskeleton, and cancer cell invasion. *Cancer Metastasis Rev.* **2009**, *28*, 15–33. [[CrossRef](#)]
30. Samadani, A.A.; Norollahi, S.E.; Rashidy-Pour, A.; Mansour-Ghanaei, F.; Nemati, S.; Joukar, F.; Afshar, A.M.; Ghazanfari, S.; Safizadeh, M.; Rostami, P.; et al. Cancer signaling pathways with a therapeutic approach: An overview in epigenetic regulations of cancer stem cells. *Biomed. Pharmacother.* **2018**, *108*, 590–599. [[CrossRef](#)]
31. Tu, S.; Huang, W.; Huang, C.; Luo, Z.; Yan, X. Contextual Regulation of TGF- $\beta$  Signaling in Liver Cancer. *Cells* **2019**, *8*, 1235. [[CrossRef](#)] [[PubMed](#)]
32. Luo, L.; Cai, L.; Luo, L.; Tang, Z.; Meng, X. Silencing activating transcription factor 2 promotes the anticancer activity of sorafenib in hepatocellular carcinoma cells. *Mol. Med. Rep.* **2018**, *17*, 8053–8060. [[CrossRef](#)]
33. Sano, Y.; Harada, J.; Tashiro, S.; Gotoh-Mandeville, R.; Maekawa, T.; Ishii, S. ATF-2 Is a Common Nuclear Target of Smad and TAK1 Pathways in Transforming Growth Factor- $\beta$  Signaling. *J. Biol. Chem.* **1999**, *274*, 8949–8957. [[CrossRef](#)] [[PubMed](#)]
34. Desai, A.; Qazi, G.; Ganju, R.; El-Tamer, M.; Singh, J.; Saxena, A.; Bedi, Y.; Taneja, S.; Bhat, H. Medicinal Plants and Cancer Chemoprevention. *Curr. Drug Metab.* **2008**, *9*, 581–591. [[CrossRef](#)] [[PubMed](#)]
35. Amawi, H.; Ashby, J.C.R.; Samuel, T.; Peraman, R.; Tiwari, A.K. Polyphenolic Nutrients in Cancer Chemoprevention and Metastasis: Role of the Epithelial-to-Mesenchymal (EMT) Pathway. *Nutrients* **2017**, *9*, 911. [[CrossRef](#)]
36. Manach, C.; Williamson, G.; Morand, C.; Scalbert, A.; Rémésy, C. Bioavailability and bioefficacy of polyphenols in humans. I. Review of 97 bioavailability studies. *Am. J. Clin. Nutr.* **2005**, *81*, 230S–242S. [[CrossRef](#)]
37. Ranaware, A.M.; Banik, K.; Deshpande, V.; Padmavathi, G.; Roy, N.K.; Sethi, G.; Fan, L.; Kumar, A.P.; Kunnumakkara, A.B. Magnolol: A Neolignan from the Magnolia Family for the Prevention and Treatment of Cancer. *Int. J. Mol. Sci.* **2018**, *19*, 2362. [[CrossRef](#)]
38. Leeson, P.D.; Springthorpe, B. The influence of drug-like concepts on decision-making in medicinal chemistry. *Nat. Rev. Drug Discov.* **2007**, *6*, 881–890. [[CrossRef](#)]
39. Ghanghas, P.; Jain, S.; Rana, C.; Sanyal, S. Chemopreventive action of non-steroidal anti-inflammatory drugs on the inflammatory pathways in colon cancer. *Biomed. Pharmacother.* **2016**, *78*, 239–247. [[CrossRef](#)] [[PubMed](#)]
40. Khor, T.; Yu, S.; Kong, A.-N. Dietary Cancer Chemopreventive Agents—Targeting Inflammation and Nrf2 Signaling Pathway. *Planta Medica* **2008**, *74*, 1540–1547. [[CrossRef](#)] [[PubMed](#)]